Lecture Notes in Electrical Engineering 386

Qilian Liang
Jiasong Mu
Wei Wang
Baoju Zhang
Editors

Proceedings of the 2015 International Conference on Communications, Signal Processing, and Systems

Springer

Lecture Notes in Electrical Engineering

Volume 386

About this Series

"Lecture Notes in Electrical Engineering (LNEE)" is a book series which reports the latest research and developments in Electrical Engineering, namely:

- Communication, Networks, and Information Theory
- Computer Engineering
- Signal, Image, Speech and Information Processing
- Circuits and Systems
- Bioengineering

LNEE publishes authored monographs and contributed volumes which present cutting edge research information as well as new perspectives on classical fields, while maintaining Springer's high standards of academic excellence. Also considered for publication are lecture materials, proceedings, and other related materials of exceptionally high quality and interest. The subject matter should be original and timely, reporting the latest research and developments in all areas of electrical engineering.

The audience for the books in LNEE consists of advanced level students, researchers, and industry professionals working at the forefront of their fields. Much like Springer's other Lecture Notes series, LNEE will be distributed through Springer's print and electronic publishing channels.

More information about this series at http://www.springer.com/series/7818

Qilian Liang · Jiasong Mu · Wei Wang
Baoju Zhang
Editors

Proceedings of the 2015 International Conference on Communications, Signal Processing, and Systems

Springer

Editors
Qilian Liang
University of Texas at Arlington
Arlington, TX
USA

Jiasong Mu
Tianjin Normal University
Tianjin
China

Wei Wang
Tianjin Normal University
Tianjin
China

Baoju Zhang
College of Physical and Electronic Information
Tianjin Normal University
Tianjin
China

ISSN 1876-1100 ISSN 1876-1119 (electronic)
Lecture Notes in Electrical Engineering
ISBN 978-3-662-49829-3 ISBN 978-3-662-49831-6 (eBook)
DOI 10.1007/978-3-662-49831-6

Library of Congress Control Number: 2016938650

This Springer imprint is published by Springer Nature
The registered company is Springer-Verlag GmbH Berlin Heidelberg

Preface

The 4th International Conference on Communications, Signal Processing, and Systems (CSPS) held in Chengdu, Sichuan, on October 23–24, 2015. Chengdu, the capital of Sichuan Province, lies in the hinterland of the Chengdu Plain, in central Sichuan. The city is known as the southwest technology center, business center, financial center, and hub of transportation and communication. CSPS 2015 brings together Chinese and international researchers and practitioners in communications, signal processing, and systems together.

The accepted papers of CSPS 2015 are from various regions around the world, which includes 13 different technical sessions include 'Heterogeneous Networks', 'Ad hoc and Short Range Networks,' 'Radar and Sonar Networks, Radar Signal Processing,' 'Spectrum access and optimization,' 'Interference Alignment,' 'Wireless Communication,' 'Millimeter Wave, UWB and Terahertz Technology,' 'Localization and Tracking,' 'Pattern Recognition,' 'Image and Video Processing,' 'Biological and Medical Signal Processing,' 'Circuit Processing System and System Design,','Signal Processing and Machine Learning Algorithm.'

The technical program team did an excellent job in soliciting submissions, coordinating the review process, and promoting the technical program. We would like to thank every one of them for taking leadership roles in organizing the various aspects of the technical program.

Also we would like to express our thanks to all members of the organizing committee and all the volunteer reviewers who have been working hard days and nights for this conference. We are grateful to the host institution, Tianjin Normal University, Chengdu University of Information Technology, and sponsorships from IEEE Fort Worth Section, University of Texas at Arlington, Beijing University of Posts and Telecommunications, University of Electronic Science & Technology of China. Finally, the publication support from Springer is deeply appreciated.

October 2015

Qilian Liang
Jiasong Mu
Wei Wang
Baoju Zhang

Welcome Message from the General Chairs

It is our great honor and pleasure to welcome you to Chengdu for the 4th International Conference on Communications, Signal Processing, and Systems (CSPS) held during October 23–24 2015. During this conference, scholars and practitioners from all over the world in communications, signal processing, and electronic systems will get together in Chengdu.

Chengdu is a famous scenic region for tourists in Southwest China, characterized by the all-season scenery and the ancient culture of the Shu Kingdom during the Three Kingdom Period at the end of the Han Dynasty about 2500 years ago. It has gained the eulogium by Li Bai, the poet immortal and Du Fu, the poet sage. As one of the birthplace of the tea culture and a major tea base of China, Chengdu has largest number of tea houses in the world. Besides, being one of the four major Chinese cuisines and with over 3000 varieties and hundreds of representative dishes, Chengdu snacks are well known for their low price, excellent appearance and taste, and exquisite shape.

CSPS 2015 is organized by an international team. The conference features nine technical sessions and two keynote sessions. We invite you to join us by attending the technical and social events held in CSPS 2015.

On behalf of the Organizing Committee, the Technical Program Committee, and all the volunteers that have been working hard for this conference, we warmly welcome you to CSPS 2015 and hope that you will enjoy the conference, and the beautiful city in which it takes place.

Tariq S. Durrani, Rabinder N. Madan, Qilian Liang, Yiming Pi, and Ling Yang
General Co-Chairs, CSPS 2015

Organization

The International Conference on Communications, Signal Processing, and Systems (CSPS) is organized by Tianjin Normal University, Chengdu University of Information Technology, University of Texas at Arlington, Beijing University of Posts and Telecommunications, University of Electronic Science and Technology, China.

General Co-chairs
Tariq S. Durrani, University of Strathclyde, UK
Rabinder N. Madan, George Washington University, USA
Qilian Liang, University of Texas at Arlington, USA
Yiming Pi, University of Electronic Science and Technology, China
Ling Yang, Chengdu University of Information Technology, China

TPC Co-chairs
P.P. Vaidyanathan, California Institute of Technology, USA
Zongjie Cao, University of Electronic Science and Technology, China
Haijiang Wang, Chengdu University of Information Technology, China
Baoju Zhang, Tianjin Normal University, China
Wei Wang, Tianjin Normal University, China

International Advisory Committee
Leon Chua, University of California at Berkeley, USA
Gene Frantz, Texas Instruments, USA
Er Meng Hwa, Nanyang Technological University, Singapore
Sanjit Mitra, University of Southern California, USA
Zhisheng Niu, Tsinghua University, China
Wan-Chi Siu, Hong Kong Polytechnic University, Hong Kong
Tieniu Tan, Chinese Academy of Science, China
Xiaorong Wu, Tianjin Normal University, China
Zheng Zhou, Beijing University of Posts and Telecommunications, China

Keynote Co-chairs
Jing Liang, University of Electronic Science and Technology, China
Qiangyu Zeng, Chengdu University of Information Technology, China

Local Arrangement Chair
Jun Xu, Chengdu University of Information Technology, China

Publication Co-chairs
Jiasong Mu, Tianjin Normal University, China
Tingting Han, Tianjin Normal University, China

Registration Chair
Jiasong Mu, Tianjin Normal University, China

Publicity Co-chair
Rui Min, University of Electronic Science and Technology, China
Zhong Zhang, Tianjin Normal University

Sponsoring Institutions
Tianjin Normal University
Chengdu University of Information Technology
IEEE Fort Worth Section, USA
University of Texas at Arlington
Beijing University of Posts and Telecommunications
University of Electronic Science and Technology, China

Contents

Part I
Heterogeneous Networks

An Enhanced Cost Efficient Resource Scheduling Algorithm for Dense Heterogenous Networks

Fudong Yang, Xiaodong Ji and Lei Li

Abstract In this paper, a frequency division and resource block allocation strategy are proposed based on the cost of the system and the different rates of user equipments. Small cell enhancement has been adopted by 3GPP LTE-advanced to improve system performance. However, since the number of small cells in one cluster increased, the interference between thee small cells and the cost of system will increase significantly. A new resource allocation scheme combing both the full frequency reuse and orthogonal strategy is proposed to address this problem. The proposed resource block allocation consider both the cost of the system and the different rates of user equipments. Simulation result are presented to verify the effectiveness of the proposed algorithm.

Keywords Small cell · Heterogenous network · Cost efficiency

1 Introduction

Work on standardizing long-term evolution (LTE) was completed at the end of 2010. As a major enhancement of LTE, the third generation partnership project (3GPP) LTE advanced (LTE-A) was standardized with the aim to fulfill the anticipated higher requirements of the fourth generation (4G) communication systems. The major goals in LTE-A is to support higher downlink throughput and high energy efficiency. Many of the corresponding techniques have been developed to support these requirements and the small cell enhancement (SCE) is one of the promising techniques to significantly improve downlink throughput [1].

Due to the low capital expenditure (CAPEX) and operating expense (OPEX) of the traditional cellular networks, dense small cells will be deployed to improve the network capacity in hotspots such as stadiums and shopping malls [2]. The small cell

F. Yang (✉) · X. Ji · L. Li
Key Laboratory of Universal Wireless Communications, Ministry of Education, Beijing University of Posts & Telecommunications, Beijing, China
e-mail: yangfudong@bupt.edu.cn

Q. Liang et al. (eds.), *Proceedings of the 2015 International Conference on Communications, Signal Processing, and Systems*, Lecture Notes in Electrical Engineering 386, DOI 10.1007/978-3-662-49831-6_1

layer accommodates most of the data traffic load in a network [3]. To support the high traffic load in these areas, a number of small cells can be deployed in a cluster. 3GPP has defined several scenarios as indicated in the Release-12 SCE study item [1]. In these scenarios, the macrocells and the small cells use the same frequencies. In scenario 1, small cells are deployed as the outdoor cells in the coverage area of a macrocell. In scenario 2b, small cells are deployed as the indoor cells in the coverage area of a macrocell, while small cells are deployed as the indoor cells outside of the coverage area of a macrocell in scenario 3.

As the number of small cells in one cluster increases, the interference, power consumption, and the system cost increases significantly [4]. There are many interference cancelation methods. In the time domain, enhanced intercell interference cancelation can reduce the interference by configuring almost blank subframes [5, 6]. However, more channel state information is needed for feedback in this case. In the frequency domain, fractional frequency reuse can reduce interference using different bandwidths for the cell edge user equipments (UEs) [7, 8]. However, problems arise in that the spectrum efficiency is low and centralized control is necessary, resulting in the system cost increased significantly. And the cost contains the deployment cost and transmission cost. The transmission cost is used to service the UEs and backhaul cost, while the resource block (RB) allocation problem should be considered as well [9]. In order to address these problems, a new RB allocation scheme has been proposed that provides a new frequency by combing the advantage full reuse and orthogonal strategies. In the RB allocation scheme, not only the different rates of UEs have been considered, but also the system cost has been considered. Moreover, the simulation results have demonstrated the effectiveness of the proposed algorithm. The rest of this paper is organized as follows. Section 2 introduces the system model and cost efficiency. In Sect. 3, the frequency divided is analytically derived, and RB allocation algorithm is then presented. System simulation results are shown in Sect. 4 to help us look into the effectiveness of the algorithm. Finally, conclusions are drawn in Sect. 5.

2 System Model

2.1 Topology

In this paper, the small cell in scenario 1 is considered in which the macrocell and the small cells use the same frequencies. For the macrolayer, the macrocell sites are deployed within a hexagonal grid and each cell site is divided into three sectors. For the small cell layer, a small cell cluster is dropped uniformly and randomly within the macro geographical area. There are ten small cells in cluster. Small cells are uniformly and randomly dropped within the cluster area. Among all small cells, 40 % small cells have ideal backhaul and the others have nonideal backhaul (wireless backhaul). There are 40 UEs in each sector. 2/3 UEs are uniformly distributed within the

small cell cluster, and the others are uniformly distributed within the sectors. Each UE is dropped without mobility during the entire simulation. Each UE will access the BS with the Min pathloss.

2.2 Cost Efficiency

According to the min requirement R_{min}, the UE was is divided into the high-speed UE and the low-speed UE. In this paper, the R_{min} of high-speed UE is 1.5 M, and the R_{min} of the low-speed UE is 150 K. While if the rate is large or equal the R_{min}, the UE cannot get any RB, as it is the same with the case that the UE data rate small or equal R_{min}. According to EARTH power model [1], the overall energy consumption of the base station (BS) can be simplified into a linear model, which can be written as

$$P_{in} = P_0 + \lambda P_{out}, 0 < P_{out} < P_{max}, \tag{1}$$

where P_{in} and P_{out} denote the overall energy consumption and radio frequency (RF) output power of the BS, P_0 is fixed power related to circuit processing, air-conditioning, etc. P_{max} is the maximum RF output power. λ is the utilization rate of RB. Pico BS and macro-BS have different parameters according to EARTH in Table 1.

Energy efficiency of the network can be calculated as

$$EE_{network} = \frac{\sum_i R_i}{\sum_j P_j}, \tag{2}$$

where $\sum_i R_i$ denotes the total data rate of all the UEs connecting to the network, and $\sum_j P_j$ is the summation of energy consumed by the BSs including the sets of macro-BSs and picos.

As the power model, the cost of BS is defined into a linear model, which is given by

$$\cos t = \cos t_0 + \sum_{i \in \{RB\}} \cos t_i, \tag{3}$$

Table 1 Power parameters

	P_{max} (dBm)	Fixed power (W)
Macro	46	130
Pico	23	6.8

where $\cos t_0$ is static cost related to construction of the base station, air-conditioning, etc. $\sum_{i\in\{RB\}} \cos t_i$ is the dynamic cost related to BS type, utilization rate of RB, backhaul type, etc. Pico BS and macro-BS have different parameters.

By considering the energy efficiency and the cost, the cost efficiency of the network can be defined as

$$CE_{network} = \frac{EE_{network}}{\sum_{i\in\{RB\}} \cos t_i}. \tag{4}$$

3 The Proposed Resource Allocation Scheme

In this section, the sequential MMSE channel estimation algorithm is developed along with the optimal training design for $\mathbf{H}_{r1}$ and $\mathbf{H}_{r2}$. The individual channel estimation of ACLs and WFLs is derived relying on the Kalman filter and EVD. According to the estimation MSE minimization criteria, the optimal training of the proposed estimators is obtained as well.

3.1 Training Design for $\mathbf{H}_{r2}$

3.2 Frequency Divide

As shown in Fig. 1, the frequency was divided into five parts: HPN Dedicated, HPN& LPN Shared, LPN Dedicated, inband backhaul, and outband backhaul. The size of these resource block is changed with the system load. The regularity of the change is shown as follows:

(1) *Light Load*
When the system is in the light load, the size of resource blocks shared by HPN and LPN is minimum, and the size of other resource blocks is the maximum. In this case,

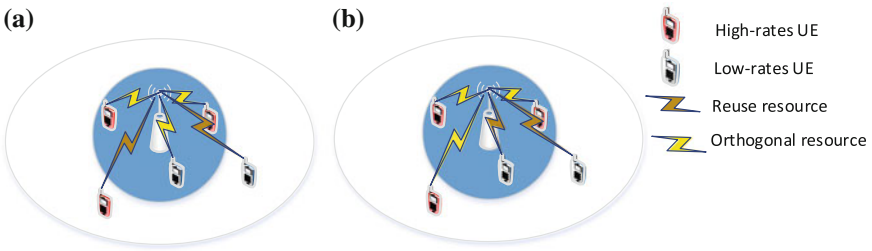

Fig. 1 System model

the wireless backhaul used the inband backhaul first. The outband backhaul is then used when inband backhaul resource has already been used.

(2) *Moderate Load*
When the system load increased, the size of each resource block is changed. The size of resource blocks shared by HPN and LPN is bigger than the light load. The size of other resource blocks is the smaller than the light load. Then, the wireless backhaul used the inband backhaul first, and the outband backhaul is used when inband backhaul resource has already been used.

(3) *High Load*
When the system load is in the high load, the size of each resource block is changed. The size of the resource blocks shared by HPN and LPN is maximum. The size of other resource blocks is the minimum. At this load, the wireless backhaul used the inband backhaul first or there is no inband backhaul. The outband backhaul is used when inband backhaul resource has already been used or there is no inband backhaul.

Advantage:

- Compared to the frequency reused strategy, where all the frequencies are shared by the HPN and the LPN, the proposed frequency divide strategy can avoid interference on some frequency.
- Compared to the frequency orthogonal strategy, where the frequency resource is divided into two parts and the BSs on different layers use completely orthogonal parts, the proposed frequency divide strategy can avoid interference on some frequency and provide more resource to the BSs at the same time.
- Compared to the traditional backhaul strategy (inband or outband), the proposed strategy uses the inband backhaul resource or outband backhaul resource according to the cost efficiency of the BS.

3.3 RB Allocation

The traditional SFR (Soft Frequency Reuse) is an efficient intercell and inter-tier interference coordination technique. The SFR partitions the service area into spatial regions, and each subregion is assigned with different frequency subbands as shown in Fig. 2a. Therefore, the cell-edge-zone UEs do not interfere with the cell-center-zone UEs. With an efficient channel allocation method, the cell-edge-zone UEs may not interfere with neighboring cell-edge-zone UEs. At the future network, the HPN is mainly used to deliver the control information and guarantee the seamless service. The LPN is mainly used to deliver the big traffic and bursty traffic. The HPN will service these UEs far away from the pico base station or having high move speed. The LPN will service these UEs moving very slowly and have big data traffic or is very closed to the LPN. The cell-edge-zone/cell-center-zone UEs can be the high-rate UEs and may also be the low-rate UEs. The location of UES cannot represent the needs of users. While the deployment of the small cell will be densified,

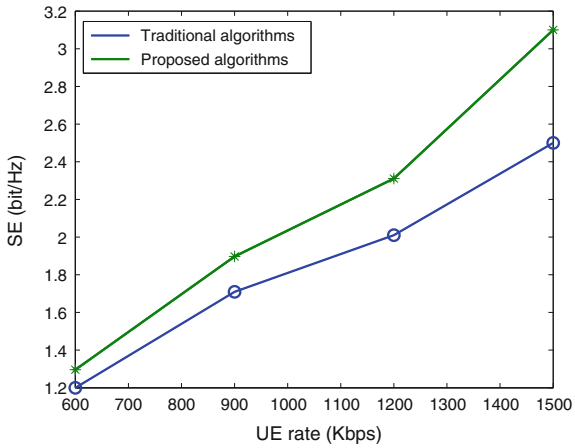

Fig. 2 SE versus UE rate with different algorithms

and the distance between the UE to the BS will be shorter. Then the needs of the cell-center-zone UEs may be bigger than the cell-edge-zone UES. Consequently, an enhanced RB allocation scheme is proposed to suppress the inter-tier interference between HPN and RRHs in Fig. 2b. In the proposed RB allocation scheme, the HPN/LPN dedicated resource block is used to service the high-rate UEs first. Then the resource shared by HPN/LPN is used after the dedicated resource block, and it is solely used by the low-rate users.

The traditional backhaul resource allocation is inband or outband, and the system cost is not considered. Therefore, a backhaul resource allocation scheme is proposed by taking the system cost and CQI (Channel Quality Indicator) into consideration. Backhaul resources will be allocated according to the following rule

$$LPN_{scheduled} = \arg \max_i \{ \frac{C_i}{\bar{R} \cos t} \}, \tag{5}$$

where C_i is the CQI, and $\bar{R}$ is the average transmission rate, $\cos t$ is the cost of the LPN to service wireless LPN.

Advantage:

- If the traditional S-FFR is utilized in the future network, the cell-center-zone UEs access to the LPN may be the high-rates UE, and will share the same radio resources with UEs access to the HPN, which decreases the spectral efficiency (SE) performance significantly.
- How to determine UEs located in the cell-edge or cell-center zone is a challenging work for the traditional SFR. However, it can be avoided in the proposed RB allocation scheme, where only the needs of rates for UEs access to the LPN should be distinguished.
- The dedicated resource is used to service the high-rates UEs, and the shared resource is used to service the low-rates UEs. This method can make a full use

of the resource. The usage of resource block and the service time is reduced in this scheme as well as the power consumption and the system cost.
- The channel quality and system cost are considered in the backhaul resource allocation.

4 Performance Analysis

The performance evaluation parameters are given in Table 2, and the cost parameters are shown in Table 3. The throughput performance, energy efficiency and cost efficiency of the network is considered in the simulation. In order to drop the small cell cluster, macrocell sites are deployed first. Nineteen macrocell sites are deployed within a hexagonal grid and each cell site is divided into three sectors. In each sector there is only one small cell cluster of 10 small cells. A cluster is dropped uniformly and randomly within the macro-geographical area. Small cells are uniformly and randomly dropped within the cluster area with a radius of 70 m. There are 40 UEs in each sector. Among all the UEs, 2/3 UEs are uniformly distributed within the small cell cluster, and the others are uniformly distributed within the sectors. The traffic mode is FullBuffer traffic model, but each UE has a rate limit. In this paper, the high rate is 600 K, 900 K, 1.2 M, and 1.5 M, while the low rate is 150 K. In the simulation, the system load is high load. The contrast scheme is the traditional SFR technology as described above.

Figures 2, 3, and 4 show the spectral efficiency (SE), energy efficiency (EE), and cost efficiency (CE) at different algorithms for different UE rates, respectively. The SE, EE, and CE of the proposed algorithm are significantly improved compared with the traditional algorithm in Figs. 2, 3, and 4, respectively.

These figures shows the proposed algorithm achieve a significant gain to the SE, EE and CE. From Figs. 2, 3, and 4, the higher the load is, the more obvious the gain can be. When the UE rate is as high as 1.5 M, the gain of SE is 20 %, the gain of the EE is 25 %, and the gain of the CE is 27 %, respectively.

Table 2 Simulation parameters

	Macrocell	Small cell
System bandwidth (MHz)	5	5
Carrier frequency (GHz)	2.0	2.0
Pathloss	ITU Uma with 3D distance	ITU Umi with 3D distance
Clusters and cells	1 cluster with 10 small cells	
Traffic model	Fullbuffer with rate-limited	
UE receiver	MMSE-IRC as baseline	
UE speed	3 km/h	
Backhual model	2/5 is ideal and 3/5 is wireless	

Table 3 Cost parameters

	Static cost ($1e^4$¥)	Unit cost ($1e^4$¥)
Macro	21	0.05
Ideal backhaul pico	1	0.05
Wireless backhaul pico	1	0.02

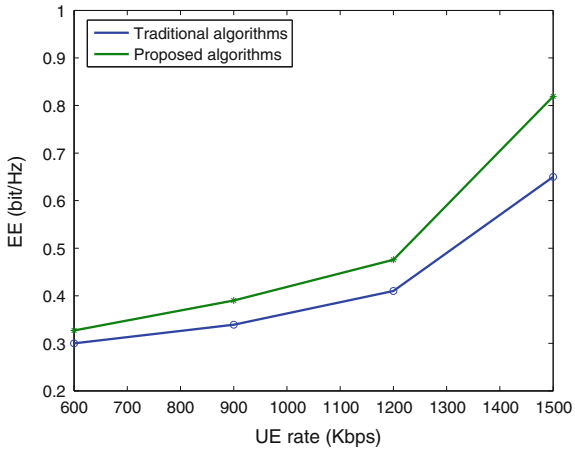

Fig. 3 EE versus UE rate with different algorithms

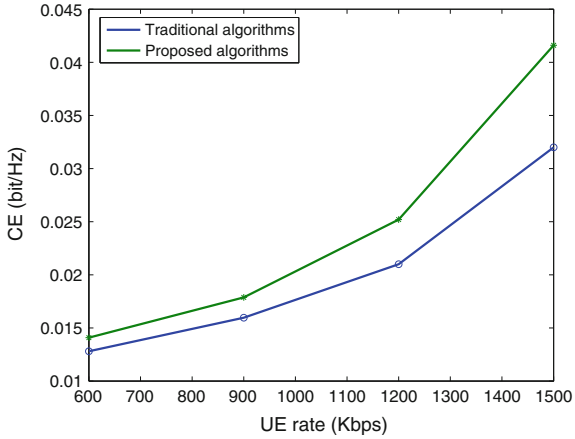

Fig. 4 CE versus UE rate with different algorithms

5 Conclusion

In this paper, a new frequency divide and RB allocation scheme has been proposed to reduce the interference and the system cost in the small cell networks. In order to mitigate the interference, the proposed scheme was divided the frequency into five parts by combining the advantages of the full reuse and orthogonal strategies. The

different rates of UEs and the system cost have been taken into consideration in the RB allocation scheme. Finally, the simulation results have shown the effectiveness of the proposed scheme.

References

1. 3GPP, Small cell enhancements for E-UTRA and E-UTRAN—Physical layer aspects, ser. TR, Mar. 2013, no. TR 36.872, Rel-12 v12.0.0
2. Pan Z et al (2013) Cell sizing based energy optimization in joint macro-femto deployments via sleep activation. In: IEEE wireless communications and networking conference (WCNC), pp 4765–4770
3. Miao G et al (2011) Distributed interferenceaware energy-efficient power optimization. IEEE Trans Wireless Commun 10(4):1323–1333
4. Chen X et al (2012) Energy efficient power allocation in generalized distributed antenna system. IEEE Commun Lett 16(7):1022–1025
5. Pedersen SB et al (2012) ICIC functionality and performance for LTE HetNet co-channel deployments. In: Proceedings of IEEE vehicular technology conference (VTC Fall)
6. Kamel EK et al (2012) Performance evaluation of a coordinated timedomain eICIC framework based on ABSF in heterogeneous LTE Advanced networks. In: Proceedings of IEEE global communications conference (GLOBECOM)
7. Fangmin X (2010) Fractional frequency reuse (FFR) and FFR-based scheduling in OFDMA systems. In: Proceedings of IEEE international conference in multimedia technology (ICMT)
8. Giovany PB et al (2013) Simulation and analysis of interference avoidance using fractional frequency reuse (FFR) method in LTE femtocell. In: Proceedings of IEEE international conference on information and communication technology (ICoICT)
9. Miao G et al (2010) Energy-efficient link adaptation in frequency-selective channels. IEEE Trans Commun 58(2):545–554

A Heterogeneous Ship Formation Network Selection Algorithm Based on Service Level and Load Balance

Xubin Yang, Wenqiang Zhang, Xinrong Wu, Lei Zhu and Xiang Zheng

Abstract Future ship formation tactical wireless communication networks will be heterogeneous and integrate several communication methods. To guarantee the end-to-end Quality of Service (QoS) for users in the heterogeneous ship formation network, one of the key problems is to design a proper network selection algorithm depending upon the QoS requirements of the service together with the network QoS parameters. In this paper, we propose a network selection algorithm based on service level and load balance. Analytic Hierarchy Process (AHP) method and entropy method are applied to compute the subjective weights and objective weights, respectively, and the final weights are determined by the combination weight process. The algorithm then adapts Technique for Order Preference by Similarity to an Ideal Solution (TOPSIS) method to rank the optional subnets. Taking the service level and load balance into consideration, the suboptimal subnet is also probably to be selected and service with high service level has better chance to access to the optimal subnet. Simulation results verify the validity as well as the load balance performance of the algorithm.

Keywords Heterogeneous ship formation network · Network selection · Service level · Load balance

1 Introduction

With the wireless communication technology and the network technology developing rapidly, future ship formation tactical wireless communication network (hereinafter referred to as ship formation network) will be a high-speed self-organized

X. Yang (✉) · W. Zhang (✉) · X. Wu · L. Zhu · X. Zheng
Institute of Communications Engineering, PLA University of Science and Technology, Nanjing, China
e-mail: yangxubin2015@163.com

W. Zhang
e-mail: zwq_yxb@163.com

Q. Liang et al. (eds.), *Proceedings of the 2015 International Conference on Communications, Signal Processing, and Systems*, Lecture Notes in Electrical Engineering 386, DOI 10.1007/978-3-662-49831-6_2

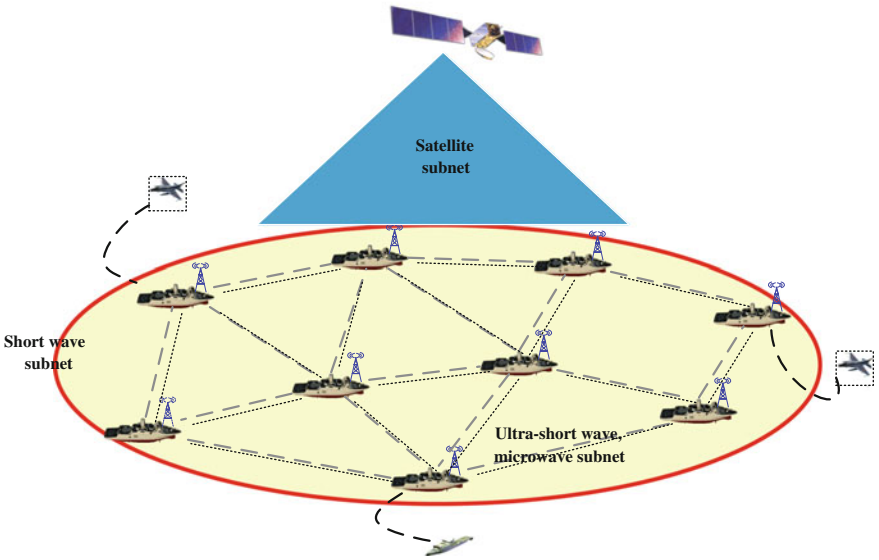

Fig. 1 The heterogeneous ship formation network

network center which is expected to integrate multiple communication methods. As shown in Fig. 1, nodes in the ship formation network all support server communication methods and each communication method forms a communication subnet. The network center should achieve the effective access of users which are flexible platforms composed of aircraft, submarines, and so on. Therefore in the environment of the heterogeneous ship formation network, how users select the Always Best Connected [1] network according to their own needs together with the network QoS parameters has become a new research points.

In recent years, numerous network selection algorithms have been proposed, among which multi-attribute decision-making (MADM) [2] algorithm has been used widely because of its comprehensive consideration of network attributes. In [3–5], TOPSIS method has been used to rank the alternative networks by computing the relative closeness coefficient of each alternative network to the ideal network. In [6], an improved AHP method is applied to solve the weights consistent problem in network selection. In [7], depending on the QoS requirements, a network selection algorithm based on the signal strength is proposed. To make the network selection more accurately, fuzzy AHP is used in [8] to assign the attribute weight. However, the above network selection algorithms are in the background of civil heterogeneous convergence networks. For a specific tactical communication network, to fully exert combat effectiveness only important users' communication

(e.g., the commander's communication) is guaranteed. Besides, to make the full use of the ship formation network, load balance among the multiple hosted networks also need to be taken into consideration.

In this paper, combined with the actual characteristics of the heterogeneous ship formation network, we proposed a network selection algorithm based on service level and load balance. The algorithm adapts a combination weight process to make each attribute assigned more accurately and TOPSIS is used to rank the alternative subnets. By classifying the service level and setting the relative closeness coefficient difference threshold, the suboptimal subnet is also probably to be chosen to balance the global traffic, and high level service is more likely to be guaranteed better QoS.

2 Service Classification

Based on users' perceived QoS of the service, 3GPP classifies next generation network service into four primary types, respectively are conversational service, streaming service, interactive service, and background service. However, the services in ship formation network are of specific military application background and are not suitable to be classified exactly according to the standard of the civil network service. Considering the actual QoS requirements of the services in the ship formation network, we sort them into voice service, messages service, data service, and streaming service, as described in Table 1, where B denotes bandwidth, D denotes delay, DJ denotes delay jitter, PLR denotes packet loss rate, BER denotes bit error rate.

Ship formation network contains different kinds of users, and the users' levels are diverse. In battlefield environment, users' service importance may also change according to mission's importance and urgency. Hence, we sort the service level (SL) into three classes based on the importance of the user and the service, as is shown in Table 2.

Table 1 Service classification in ship formation network

Service type	QoS requirements					Including service
	B	D	DJ	PLR	BER	
Voice	Low	Strict	Strict	Moderate	Moderate	Voice of different security classifications
Messages	Low	High	Low	Strict	Strict	Massages commands
Data	High	Low	Low	High	High	Mainly refer to large-capacity data
Streaming	Strict	Low	Moderate	High	High	Videos images

Table 2 Service level classification

SL	Service description	Importance degree
1	Important service of key users	Extremely
2	General service of key users or important service of normal users	Quite
3	General service of normal users	Moderate

3 Network Selection Algorithm

In heterogeneous ship formation network, due to the characteristics of the high delay in the satellite subnet and the low bandwidth in the short wave subnet, large-capacity service is mainly transmitted over ultra-short wave subnet and microwave subnet by multiple relay transmission. Satellite subnet and short wave subnet are normally for signaling channels or backup networks solely. Hence, we take user preference (UP) as one of the target attributes in the proposed algorithm, and the proposed algorithm process is shown as Fig. 2.

3.1 Combination Weight Process to Compute the Weights

In ship formation network, the QoS requirements between different types of service are greatly different, so we adapt AHP method to compute the subjective weights of

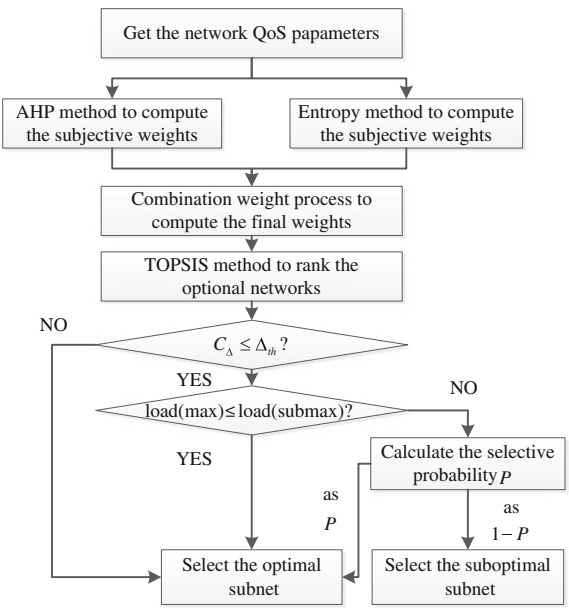

Fig. 2 The proposed algorithm process

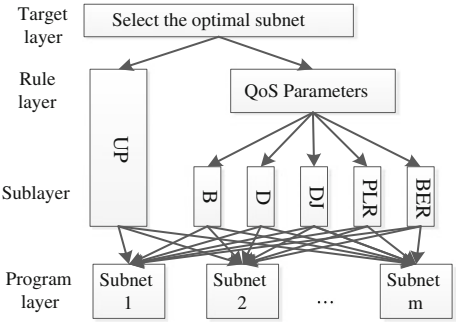

Fig. 3 The hierarchical structure of network selection

the target attributes. Besides, some QoS parameters are also distinct between each subnet, e.g., bandwidth in short wave subnet is quite low. Considering that sole AHP method is too subjective and does not take the network objective conditions into account. Hence, we adapt entropy method to compute the objective weights of the target attributes and the final weights is calculated by combination weight process. The hierarchical structure of network selection in AHP method is shown as Fig. 3.

In entropy method, we construct the original target decision-making matrix $\mathbf{A}$ by combining the user preference parameters with the QoS parameters:

$$\mathbf{A} = \begin{array}{c} \\ N_1 \\ N_2 \\ \vdots \\ N_m \end{array} \begin{array}{c} \begin{array}{cccccc} UP & B & D & DJ & PLR & BER \end{array} \\ \begin{bmatrix} a_{11} & a_{12} & a_{13} & a_{14} & a_{15} & a_{16} \\ a_{21} & a_{22} & a_{23} & a_{24} & a_{25} & a_{26} \\ \vdots & \vdots & \vdots & \vdots & \vdots & \vdots \\ a_{m1} & a_{m2} & a_{m3} & a_{m4} & a_{m5} & a_{m6} \end{bmatrix} \end{array} \tag{1}$$

Assume $\mathbf{W}^{'} = \left[w_1^{'}, w_2^{'}, w_3^{'}, w_4^{'}, w_5^{'}, w_6^{'}\right]$ is the subjective weight vector obtained by AHP method, and $\mathbf{W}^{''} = \left[w_1^{''}, w_2^{''}, w_3^{''}, w_4^{''}, w_5^{''}, w_6^{''}\right]$ is the objective weight vector obtained by entropy method. The final weight of ith target attribute w_i can be denoted as the linear combination of $w_i^{'}$ and $w_i^{''}$. That is:

$$w_i = \lambda w_i^{'} + (1-\lambda) w_i^{''} \quad (i = 1, 2, 3, 4, 5, 6) \tag{2}$$

where $0 < \lambda < 1$, denotes the proportional coefficient of the subjective weight. To get the optimal combination weights, make a game equilibrium between the subjective weights and the objective weights by minimizing the deviation to optimal weights, namely:

$$\min z = \sum \left[(w_i - w_i^{'})^2 + (w_i - w_i^{''})^2 \right] \tag{3}$$

Combine (3) with (2), the optimal proportional coefficient λ and the final combination weight vector can be obtained: $\mathbf{W} = [w_1, w_2, w_3, w_4, w_5, w_6]$. $\mathbf{W}$ will be used to construct the weighted target decision-making matrix in later TOPSIS method.

3.2 TOPSIS Method to Rank the Optional Subnets

TOPSIS method is a widely used ranking algorithm to conduct network selection scheme. Its basic idea is to rank the optional networks by computing the relative closeness coefficient of each alternative network to the ideal network. Suppose D_i^+ and D_i^- respectively denotes the Euclidean distance of each optional subnet to the positive ideal solution and negative ideal solution calculated by TOPSIS method. Then the relative closeness coefficient to the negative ideal solution can be given by

$$C_i = \frac{D_i^-}{D_i^- + D_i^+} \quad (i = 1, 2, \ldots, \mathrm{m}) \tag{4}$$

where C_i reflects the deviate degree between optional subnet N_i and the negative ideal solution. TOPSIS method generally selects the subnet whose C_i is the highest.

3.3 Network Selection Scheme Based on Service Level and Load Balance

As in Fig. 2, the proposed algorithm does not directly choose the subnet whose C_i is the highest to access. Instead, the algorithm calculates the relative closeness coefficient difference between the optimal subnet and the suboptimal subnet, defined as C_Δ:

$$C_\Delta = \max_i(C_i) - sub\max_i(C_i) \tag{5}$$

Then set a threshold of C_Δ in advance, denoted as Δ_{th}. The network selection scheme will be determined depending on the value of C_Δ and Δ_{th}. In the proposed scheme, the optimal subnet selective probability P is given by:

$$P = \alpha \frac{L(sub\max_i(C_i))}{L(\max_i(C_i))} \tag{6}$$

where α is a factor related to service level. $0 \le \alpha \le 1$, and the higher the service level, the smaller the α. That is to say service with high service level has better chance to receive the best QoS guarantee. $L(sub\max_i(C_i))$ denotes the load of the

suboptimal subnet and $L(\max_i(C_i))$ denotes the load of the optimal subnet. Denoted the ratio as $\beta, 0 < \beta < 1$, it indicates the load balance degree between the optimal subnet and the suboptimal subnet. From (6), we can see P is proportional with β. That is to say, the less balance of the load between the optimal subnet and the suboptimal subnet, the higher probability to access to the suboptimal subnet. On this account, the global traffic of the ship formation network can be balanced.

4 Simulation and Analysis

We consider a heterogeneous ship formation network integrating four different subnets, respectively are broadband short ground wave subnet with a total bandwidth of 76.8 Kbps, denoted as N_1, high-speed ultra-short wave subnet with a total bandwidth of 40 Mbps, denoted as N_2, high-speed microwave subnet with a total bandwidth of 20 Mbps, denoted as N_3, and the second generation communication satellite subnet with a total bandwidth of 34 Mbps, denoted as N_4.

The value of user preference is depending on the type of the service, Δ_{th} is set to 0.2, and $\alpha = 1/\sqrt{SL}$. To verify the validity as well as the load balance performance of the algorithm, we set the following three simulation scenarios:

4.1 Simulation Scenario 1

Scenario1 denotes the normal environment (without any electromagnetic interference). When the service comes, the network QoS parameters are set as Table 3, where B denotes the available bandwidth. 1000 times simulation is performed for each type of service and the service level is random. The network selection results are shown as in Figs. 4 and 5.

Figure 4 depicts the network selection proportion for each type of service in scenario 1. It is shown that the voice service and the messages service all select the microwave subnet whose bandwidth is relatively high and the delay, day jitter, packet loss rate, and bitter error rate are quite low as the optimal access network. Streaming service has strict requirements on bandwidth and messages service has strict requirements on delay, as a result, these two types of service select the

Table 3 The network QoS parameters in scenario 1

	B (Mbps)	D (ms)	DJ (ms)	PLR (%)	BER (10^{-4})	Load
N_1	0.06	40	10	0.4	0.5	0.2
N_2	24	20	6	0.5	0.2	0.4
N_3	14	24	6	0.3	0.05/10	0.3
N_4	27.2	270	40	0.5	1	0.2

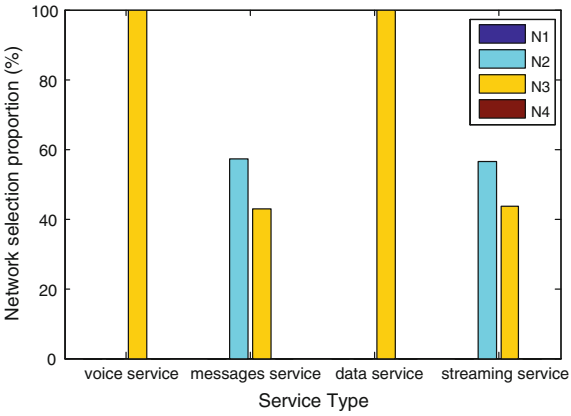

Fig. 4 The network selection proportion in scenario 1

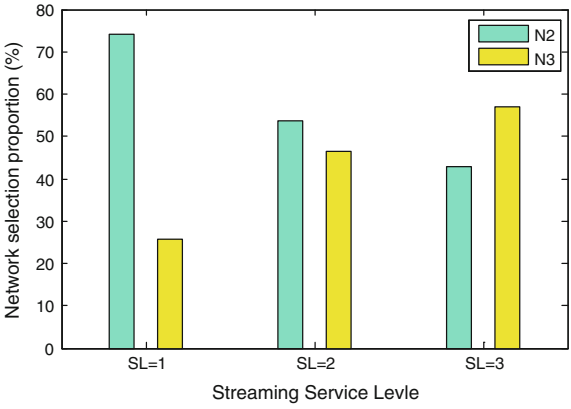

Fig. 5 The network selection proportion for streaming service

ultra-short wave subnet whose bandwidth is the highest, meanwhile the delay is the lowest as the optimal subnet. Besides, because of the high traffic load of the ultra-short wave subnet, streaming service and messages service partly select the suboptimal subnet (microwave subnet) to balance the global traffic. From the simulation result, we can dawn that in the normal environment, service transmission mainly depend on ultra-short wave subnet and microwave subnet, satellite subnet and short wave subnet are normally used solely as backup networks. The results are coincided with the fact.

Figure 5 depicts the network selection proportion for steaming service of different service level in scenario 1. The simulation results show that the higher the service level, the higher proportion for the service to select the optimal subnet. It indicates the proposed network selection algorithm can provide service of high service level with better chance to achieve the better QoS guarantee based on load balance.

4.2 Simulation Scenario 2

In the real combat environment, every band of the ship formation network is likely to be affected by enemy electromagnetic interference. Assuming the microwave band is affected by electromagnetic interference, the BER of the microwave subnet changes from 0.05×10^{-4} to 10×10^{-4} and the left network QoS parameters remain the same as Table 4. Then the network selection results are shown as in Fig. 6.

Figure 6 depicts the network selection proportion for each type of service in scenario 2. The simulation results show when the microwave subnet is affected by electromagnetic interference, large-capacity service can partly transfer to satellite subnet for service transmission and the voice service partly select the short wave subnet because of its low requirements on bandwidth. The results verify the backup role of the short wave subnet and the satellite subnet.

4.3 Simulation Scenario 3

In a period of time, assume the four types of service arrive at an independent Poisson process and the duration of the service obeys exponential distribution. The service level is assumed to be random. The network QoS parameters will change

Table 4 The initial network QoS parameters in scenario 2

	B (Mbps)	D (ms)	DJ (ms)	PLR (%)	BER (10^{-4})	Load
N_1	0.06	40	10	0.4	0.5	0.2
N_2	32	18	5	0.4	0.2	0.2
N_3	16	23	6	0.28	0.05	0.2
N_4	27.2	270	40	0.5	1	0.2

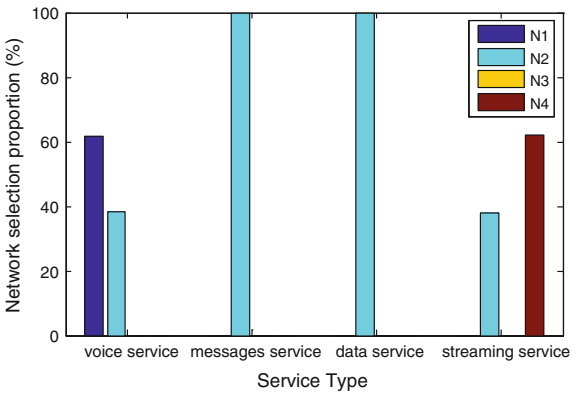

Fig. 6 The network selection proportion in scenario 2

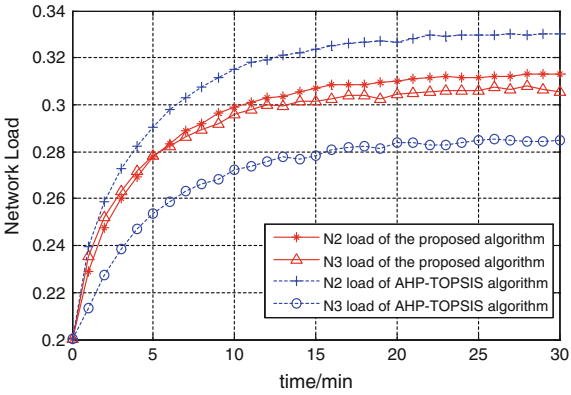

Fig. 7 The network load of N_1 and N_2 in scenario 3

correspondingly after the service successfully access to the ship formation network. The initial network QoS parameters are set as Table 4. The average of 1000 times simulation results is shown as in Fig. 6.

Figure 7 depicts the load of ultra-short wave subnet and the microwave subnet versus the time in scenario 3. The proposed algorithm is compared with the algorithm simply based on AHP-TOPSIS method, where AHP method is used to determine the target attribute weight while TOPSIS method is used to select the optimal subnet. It is clear that the load of the ultra-short wave subnet is always higher than the microwave subnet's in both of the two algorithms. It is because that the total bandwidth of the ultra-short wave is higher, hence the ultra-short wave can provide more available bandwidth under the same load. Simulation results show that the proposed algorithm achieves better load balance than the AHP-TOPSIS one in the steady state, thus the load balance performance of the proposed algorithm is verified.

5 Conclusion

To guarantee the end-to-end QoS and maximize the utilization of the resources in heterogeneous ship formation network, the proper network selection scheme is the one of the key technologies. Considering the actual characteristics, the proposed algorithm sorts the service level into three classes and the load balance is the key point to be concerned. The simulation results show that the proposed algorithm can select the suitable subnet based on the QoS requirements of the service, where the service with high service level has better chance to access to the optimal subnet, and the performance of load balance is verified in the end.

Acknowledgements This work is supported by National Natural Science Foundation of Jiangsu Province BK20140065.

References

1. Gustafsson E, Jomson A (2003) Always best connected. IEEE Wirel Commun 10(1):49–55
2. Zhang W (2004) Handover decision using fuzzy MADM in heterogeneous networks. In: Wireless communications and networking conference, 2004, WCNC, vol 2, pp 653–658. IEEE
3. Chamodrakas I, Drakoulis M (2011) A utility-based fuzzy TOPSIS method for energy efficient network selection in heterogeneous wireless networks. Appl Soft Comput 11(4):3734–3743
4. Chuang H-C, Huang CY, Chiang T (2007) Content-aware adaptive media palyout controls for wireless video streaming. IEEE Trans Multim 9(6):1273–1283
5. Farooq B, Victor CML (2007) Automated network selection in a heterogeneous wireless network environment. IEEE Netw 21:34–40
6. Lahby M, Cherkaoui L, Adib A (2012) Network selection algorithm based on Diff-AHP and TOPSIS in heterogenous wireless networks. In: 2012 International conference on IEEE 2012 multimedia computing and systems (ICMCS),, pp 485–490
7. Park H, Yoon S, Kim T, et al (2003) Vertical handoff procedure and algorithm between IEEE802.11 WLAN and CDMA cellular network. In: Mobile communications. Springer, pp 103–112
8. Mehbodniya A, Kaleem F, Yen KK (2012) A fuzzy MADM ranking approach for vertical mobility in next generation hybrid networks. In: 4th International congress on IEEE 2012 Ultra modern telecommunications and control systems and workshops (ICUMT), pp 262–267

Stackelberg Game-Based Dynamic Spectrum Access Scheme in Heterogeneous Network

Yunfeng Liao, Yong Chen, Aiwei Sun and Jianzhao Zhang

Abstract In this paper, we consider a problem of dynamic spectrum access in a heterogeneous network with spectrum database-assisted where spectrum operators (SOs) provide licensed spectrum and shared spectrum to secondary users (SUs) for maximizing their revenue. SUs can select a shared spectrum to transmit data with low price, but the quality of service (QoS) could be influenced by activities of primary users (PUs). SUs can also select licensed spectrum with high price for satisfactory QoS. We use the Stackelberg game to analyze the economic behavior of SUs and the optimal revenue of operators, respectively. Furthermore, we propose a price compensation scheme (PCS) to enhance the utility of SUs when PUs appear. Numerical results verify that the high activities of PUs can motivate SUs to purchase licensed spectrum and maximize revenue of spectrum operators. The proposed scheme could also enhance the utility of SUs several times than no compensation when channel condition is getting worse.

Keywords Dynamic spectrum access · Price compensation · Spectrum leasing · Cognitive radio

1 Introduction

With the concept of cognitive radio emerging, it is likely that the scarce spectrum resource could be utilized efficiently. With the development of research work, scientists find the existence of spectrum holes and propose a novel approach to access idle spectrum, Dynamic Spectrum Access [1]. In a typical dynamic spectrum

Y. Liao · A. Sun
Institute of Communications Engineering, PLA University of Science and Technology, Nanjing, China
e-mail: lyf631s@126.com

Y. Chen (✉) · J. Zhang
Nanjing Telecommunication Technology Institute, Nanjing, China
e-mail: chy63s@126.com

Q. Liang et al. (eds.), *Proceedings of the 2015 International Conference on Communications, Signal Processing, and Systems*, Lecture Notes in Electrical Engineering 386, DOI 10.1007/978-3-662-49831-6_3

access network, SUs are allowed to opportunistically exploit the unoccupied spectrum resource and utilize the idle channel to transmit data but not to cause harmful interference to PUs. However, the main challenge is how to exploit the idle spectrum efficiently with little consumption for SUs.

The most former researches are focused on spectrum sensing and channel estimation. However, a recent study shows that sensing is not an efficient approach since it has to pay high cost for the unsatisfied sensing performance. As an alternative, the Federal Communications Commission suggests to use geo-location database to obtain spectrum information [2]. With the assist of database, unlicensed device could get spectrum information instead of sensing wireless radio environment. In [3], Luo et al. investigate the white space ecosystem, and study the equilibrium behavior of secondary network operators. Since spectrum availability is determined by PUs' activities and changeful radio environment, Liu et al. [4] propose a joint local sensing and database scheme to confirm specific condition of channel and guarantee reliability for exploiting spectrum holes. Considering the stochastic and heterogeneous nature of SUs' demands, Jiang et al. [5] solve the revenue maximization of SOs with joint pricing of spectrum resources and admission control. The secondary market is a promising approach to provide different spectrum for variety of QoS demands [6]. In [7], the authors study the interaction between single primary spectrum owner and multiple unlicensed SUs, and design an optimal contract to maximize their profit, respectively. With the assist of spectrum database, SOs could design mechanism to provide shared spectrum for unlicensed users (such as SUs) with suitable price to satisfy their demands. However, consider the changeful wireless environment; it is not realistic that there is enough available spectrum resource to lease. Thus, operators would like to lease licensed spectrum from licensed users (such as PUs) with high price.

However, few papers have considered the activities of PUs in a dynamic access network with database-assisted. In that case, we use the Stackelberg game to investigate the interaction between SOs and SUs in a heterogeneous network where PUs would appear with stochastic probability. Furthermore, we study SUs' economic behavior with primary activities, and propose a price compensation scheme which could alleviate the loss of SUs when channel condition is getting worse.

The rest of this paper is organized as follows. In Sect. 2, we discuss the system model. And the problem analysis is given in Sect. 3. Section 4 provides the simulation results. Finally, Sect. 5 concludes the paper.

2 System Model

We consider a heterogeneous dynamic spectrum access network with database-assisted where SOs could provide two types of spectrum, the licensed spectrum and shared spectrum, for SUs. The licensed spectrum is owned by PU^Ls who would like to lease portion of spectrum to SOs in exchange for additional reward, and the channel quality could be guaranteed. The shared spectrum owned by PU^Ss who do

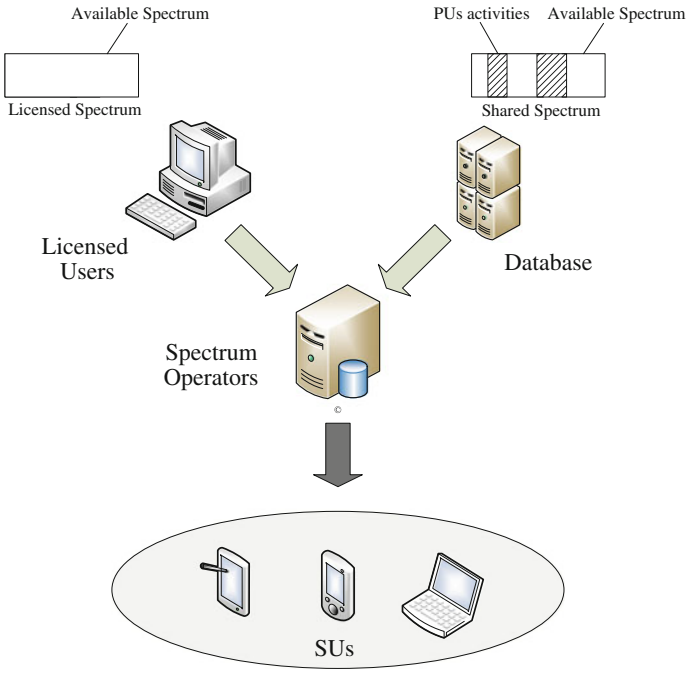

Fig. 1 System Model

not lease spectrum could be used by everyone if PU^Ss do not occupy the channel, but the channel quality could not be guaranteed for PU^Ss' activities. The spectrum database real-timely updates shared spectrum information from wireless environment and provides it to SOs. The SOs make corresponding licensed price according to the shared channel-occupied probability obtained from the database to attract more SUs for maximizing their revenue.

The system model is described in Fig. 1. We formulate their interaction with a three-stage Stackelberg game to investigate their optimal profit, respectively. In a duration T, PU^Ls charge operators with price ρ_0 first, then operators determine their leasing bandwidth B in stage one, but the maximum leasing bandwidth of PU^Ls provided is $B^{\max}$. Operators announce the licensed spectrum price ρ_l and shared spectrum price ρ_s to SUs in stage two. Simultaneously, operators send the channel-occupied probability obtained from database to SUs. According to the shared spectrum information and the two types of price, SU_i determines the licensed spectrum fraction $\theta_i \in [0, \theta]$ of the total bandwidth in stage three. It is obvious that the licensed bandwidth is finite, and SUs are willing to select shared spectrum if the price of licensed spectrum is too high. In that case, SOs have to make an optimal price strategy to motivate more SUs to purchase licensed spectrum for maximizing revenue.

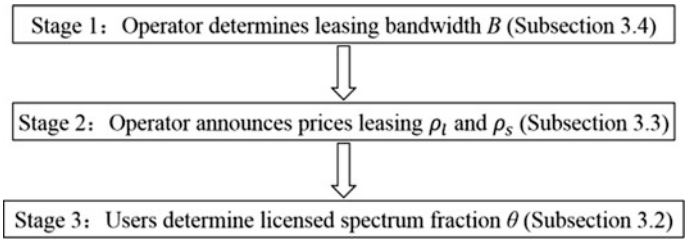

Fig. 2 Three-stage Stackelberg game

In this paper, we assume that there is one spectrum operator, and N number of SUs, $\mathcal{N} = \{1, 2, \ldots N\}$. The spectrum efficiency is denoted by η (Mbps/MHz), the traffic demand of SU_i is D_i and $\theta = \min\left\{\frac{\eta B}{D}, 1\right\}$ [8]. $D = \sum_{i=1}^{N} D_i$ is sum of all SUs' demands. Considering the activities of PUs in shared spectrum, we use φ to denote channel-occupied probability.

3 Problem Formulation and Analysis

To investigate the optimal profit of SO and SUs, we formulate their interaction as a three-stage Stackelberg game as shown in Fig. 2. In this section, we will describe the price compensation scheme first and then analyze their optimal profit and PUs' impact on SUs' economic behavior with backward induction method.

3.1 The Price Compensation Scheme

It is worth noting that the utility function of SU_i is increasing with D_i and more SUs would like to select licensed spectrum with the θ_i increasing because the worse QoS on shared spectrum could not satisfy users' traffic demands.

The utility function of SU_i could be defined as follows [8]:

$$u_i = D_i\left[\alpha - \varphi\, e^{\beta(1-\theta_i)}\right] - \left[(1-\varphi)\rho_s(1-\theta_i)D_i + \rho_l\theta_i D_i\right] \tag{1}$$

The first term is the profit of SU_i and the second term is the corresponding cost. Considering the QoS influenced by primary activities at shared spectrum, it is not reasonable that the shared spectrum price is ρ_s. So, the operator should adjust the price to $(1-\varphi)\rho_s$ as a compensation for alleviating the loss of SUs. It is obvious that the shared spectrum price is decreasing with channel-occupied probability and the detail analysis is presented in Sect. 4.

3.2 The Optimal Fraction in Stage Three

In stage three, SUs need to make the decision of how much to purchase. If a user SU_i purchase spectrum from operator, then its utility function u_i is given in (1). The optimal fraction of licensed spectrum that maximizes the profit of SU_i is

$$\theta_i^* = \arg\max_{\theta_i \in [0,\theta]} u_i(\theta_i, \rho_l) \tag{2}$$

Then we will characterize the optimization problem as follows:

$$\begin{aligned} (\mathrm{P1}) \quad & \max \quad u_i = D_i\left[\alpha - \varphi\, e^{\beta(1-\theta_i)}\right] - [(1-\varphi)\rho_s(1-\theta_i)D_i + \rho_l\theta_i D_i] \\ & s.t. \quad 0 \le \theta_i \le \theta \end{aligned} \tag{3}$$

Lemma 1 *The (P1) is a convex optimization problem with* $\{\theta_i\}$.

Proof It is clear that the Hessian matrix of function of u_i is negative, and constraints of (P1) are affine functions, so the (P1) is a convex problem [9].

Using the Lagrangian method, the Lagrangian function of u_i is

$$L(\theta_i, \lambda) = D_i\left[\alpha - \varphi\, e^{\beta(1-\theta_i)}\right] - [(1-\varphi)\rho_s(1-\theta_i)D_i + \rho_l\theta_i D_i] + \lambda(\theta_i - \theta) \tag{4}$$

with the KKT conditions [9], we could get the optimal fraction

$$\theta_i^* = \begin{cases} 1 - \frac{1}{\beta}\ln\dfrac{\rho_l - \rho_s(1-\varphi)}{\beta\varphi}, & \lambda = 0 \\ \theta, & \lambda \neq 0 \end{cases} \tag{5}$$

because of the $\theta_i \in [0, \theta]$, after algebra steps, we have

$$\rho_s(1-\varphi) + \beta\varphi\, e^{(1-\theta)\beta} \le \rho_l < \rho_s(1-\varphi) + \beta\varphi\, e^{\beta} \tag{6}$$

3.3 The Optimal Price in Stage Two

In stage two, the operator will make the optimal price strategies to maximize its revenue according to the demands in stage three. From the analysis in stage three, the utility function of SO could be presented as

$$U_{SO}=\begin{cases}\sum\limits_{i=1}^{N}(1-\phi)D_i\rho_s-\rho_0 B & \rho_l\geq\rho^H\\ \sum\limits_{i=1}^{N}\left[\frac{(1-\phi)\rho_s-\rho_l}{\beta}D_i\ln\frac{\rho_l-(1-\phi)\rho_s}{\beta\phi}+\rho_l D_i\right]-\rho_0 B & \rho^L\leq\rho_l<\rho^H\\ \sum\limits_{i=1}^{N}\left[(1-\phi)D_i\rho_s(1-\theta)+\rho_l\theta D_i\right]-\rho_0 B & \rho_l<\rho^L\end{cases} \tag{7}$$

when $\rho_l\geq\rho^H$, the revenue of PU^Ls is zero, this situation should be ignored.

When $\rho^L\leq\rho_l<\rho^H$, we have the optimization problem as:

$$\begin{aligned}(\text{P2.1})\quad &\max\quad U_{SO}^1=\frac{(1-\varphi)\rho_s-\rho_l}{\beta}D\ln\frac{\rho_l-(1-\varphi)\rho_s}{\beta\varphi}+\rho_l D-\rho_0 B\\ &s.t.\quad \rho^L\leq\rho_l<\rho^H\end{aligned} \tag{8}$$

(P2.1) is a convex problem as (P1). Using the same method, let the Lagrange multiplier equal to 0, the optimal licensed price is

$$\rho_l^*=\rho_s(1-\varphi)+\beta\varphi\, e^{\beta-1} \tag{9}$$

when $\rho_l<\rho^L$, the optimization problem is

$$\begin{aligned}(\text{P2.2})\quad &\max\quad U_{SO}^2=(1-\varphi)\rho_s D(1-\theta)+\rho_l\theta D-\rho_0 B\\ &s.t.\quad \rho_l<\rho^L\end{aligned} \tag{10}$$

Similarly, the optimal solution of problem (P2.2) is

$$\rho_l^*=\rho_s(1-\varphi)+\beta\varphi\, e^{(1-\theta)\beta} \tag{11}$$

It is obvious that $\rho_s(1-\varphi)+\beta\varphi\, e^{\beta-1}>\rho_s(1-\varphi)+\beta\varphi\, e^{(1-\theta)\beta}$, so the fraction $\theta>\frac{1}{\beta}$. From the analysis above, we substitute (9) and (11) into (5). When $\theta\leq\frac{1}{\beta}$,

$$\begin{aligned}\rho_l^*&=\rho_s(1-\varphi)+\beta\varphi\, e^{(1-\theta)\beta}\\ U_{SO}&=(1-\varphi)\rho_s D+\theta D\beta\varphi\, e^{\beta(1-\theta)}-\rho_0 B\\ \theta^*&=\theta\end{aligned} \tag{12}$$

when $\theta>\frac{1}{\beta}$,

$$\begin{aligned}\rho_l^*&=\rho_s(1-\varphi)+\beta\varphi\, e^{\beta-1}\\ U_{SO}&=(1-\varphi)\rho_s D+D\varphi\, e^{\beta-1}-\rho_0 B\\ \theta^*&=\frac{1}{\beta}\end{aligned} \tag{13}$$

3.4 The Optimal Leasing Bandwidth in Stage One

In stage one, operator will determine its leasing bandwidth B, but the maximum leasing bandwidth that PU^Ls could provide is $B^{\max}$. It means that operator could not increase the leasing bandwidth infinitely. According the analysis in stage two, the utility function of SO could be presented as

$$U_{SO} = \begin{cases} (1-\varphi)\rho_s D + \theta D\beta e^{\beta(1-\theta)} - \rho_0 B & \theta \le \frac{1}{\beta} \\ \varphi D e^{\beta-1} + D\rho_s(1-\varphi) - \rho_0 B & \theta > \frac{1}{\beta} \end{cases} \tag{14}$$

Since $\theta = \min\left\{\frac{\eta B}{D}, 1\right\}$, the utility function can be derived as follows:

$$U_{SO} = \begin{cases} (1-\varphi)\rho_s D + \eta B\varphi\beta e^{\beta\left(1-\frac{\eta B}{D}\right)} - \rho_0 B & B \le \frac{D}{\eta\beta} \\ \varphi D e^{\beta-1} + D\rho_s(1-\varphi) - \rho_0 B & B > \frac{D}{\eta\beta} \end{cases} \tag{15}$$

When $B \le \frac{D}{\eta\beta}$, we have optimization problem as:

$$\begin{aligned} (\text{P3}) \quad & \max \quad U_{SO} = \rho_s D(1-\varphi) + \eta B\beta\varphi\, e^{\beta\left(1-\frac{\eta B}{D}\right)} - \rho_0 B \\ & s.t. \quad 0 \le B \le B^{\max} \end{aligned} \tag{16}$$

The (P3) is a convex optimization problem for the same character as (P1), we could get the Lagrangian function as

$$L(B,\lambda) = \rho_s D(1-\varphi) + \eta B\beta\varphi\, e^{\beta\left(1-\frac{\eta B}{D}\right)} - \rho_0 B + \lambda(B - B^{\max}) \tag{17}$$

Giving the KKT conditions as follows:

$$\begin{aligned} \frac{\partial L}{\partial B} &= -\rho_0 + \eta\beta\varphi\, e^{\beta\left(1-\frac{\eta B}{D}\right)} + \eta\beta B\varphi\, e^{\beta\left(-\frac{\eta B}{D}\right)}\left(-\frac{\beta\eta}{D}\right) + \lambda = 0 \\ \lambda(B - B^{\max}) &= 0 \\ \lambda &\ge 0 \end{aligned} \tag{18}$$

if $\lambda = 0$, substituting it to (18), we have

$$\eta\beta\varphi\, e^{\beta\left(1-\frac{\eta B}{D}\right)} + \eta\beta B\varphi\, e^{\beta\left(-\frac{\eta B}{D}\right)}\left(-\frac{\beta\eta}{D}\right) = \rho_0 \tag{19}$$

$$\left(1 - \frac{B\beta\eta}{D}\right) e^{1-\frac{\beta\eta B}{D}} = \frac{\rho_0}{\eta B\varphi\, e^{\beta-1}} \tag{20}$$

with the *Lambert W* Function [10],

$$1 - \frac{B\beta\eta}{D} = W\left(\frac{\rho_0}{\eta\beta\varphi\, e^{\beta-1}}\right) \tag{21}$$

$$B^* = \frac{D}{\eta\beta}\left(1 - W\left(\frac{\rho_0}{\eta\beta\varphi\, e^{\beta-1}}\right)\right), W\left(\frac{\rho_0}{\eta\beta\varphi\, e^{\beta-1}}\right) \in [0,1] \tag{22}$$

if $\lambda \neq 0$,

$$B^* = B^{\max} \tag{23}$$

Thus, the optimal leasing bandwidth is

$$B^* = \min\left\{B^{\max}, \frac{D}{\eta\beta}\left(1 - W\left(\frac{\rho_0}{\eta\beta\varphi\, e^{\beta-1}}\right)\right)\right\} \tag{24}$$

when $B > \frac{D}{\eta\beta}$, from (15), utility function $\varphi De^{\beta-1} + D\rho_s(1-\varphi) - \rho_0 B$ increases with B, the $B^* = \frac{D}{\eta\beta}$.

Considering $W(\frac{\rho_0}{\eta\beta\varphi\, e^{\beta-1}}) \in [0,1]$, we obtain the optimal leasing bandwidth as

$$B^* = \min\left\{B^{\max}, \frac{D}{\beta\eta}\left(1 - W\left(\frac{\rho_0}{\eta\beta\varphi\, e^{\beta-1}}\right)\right)\right\} \tag{25}$$

4 Simulations

In this section, we analyze the numerical results to illustrate the performance of the system. In the simulation, we will find that profit of SUs and SO could achieve equilibrium solution. And the activities of primary users will impact secondary users' interest on licensed spectrum.

In this network, there are four SUs groups, the total traffic demands are $D_1 = 80, D_2 = 80, D_3 = 100, D_4 = 150$. When they access shared spectrum, the channel-occupied probability are $\varphi_1 = 0.3, \varphi_2 = 0.4, \varphi_3 = 0.5, \varphi_4 = 0.5$, respectively. The other parameters set as follows: $\alpha = 22, \beta = 3$, the licensed spectrum unit price determined by PU^Ls $\rho_0 = 1$.

Figure 3 shows the variation of licensed spectrum fraction θ under the heterogeneous network model. When channel condition of shared spectrum is getting worse, more users prefer licensed spectrum for high QoS. It denotes that the θ will increase with φ. Meanwhile, with θ increasing, the demands for licensed spectrum

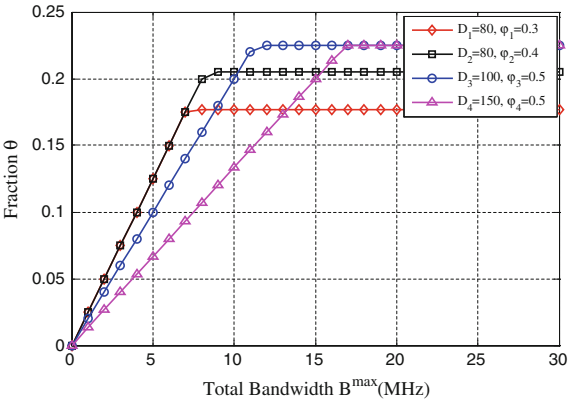

Fig. 3 Variation in licensed spectrum fraction

from PU^Ls increases, it is obvious in curve D_1 and D_2. That is to say, operator will lease more spectrum from PU^Ls to satisfy SUs' increasing licensed spectrum requirements. Furthermore, comparing with the two curve $D_3 = 100$ and $D_4 = 150$, we can find that the more SUs' traffic demands is required, the more licensed spectrum could be provided.

In Fig. 4 with the B^{max} increasing, operator will reduce the licensed price ρ_l to attract more users to select licensed spectrum for maximizing operator's revenue. If the channel condition is better, the ρ_l is lower. Because the shared spectrum could satisfy SUs' demands, the operator has to adjust ρ_l much lower to draw attention to SUs for achieving more revenue. It is worth noting that the price decreases faster in D_3 compared with D_4; the reason is that, operator adjusts the licensed price according to SUs demands of licensed spectrum. For example, the traffic demands on licensed spectrum are 50 in D_3 and 75 in D_4, respectively. Group D_4 must purchase more licensed spectrum to satisfy communication demands so that operator decreases the price slower.

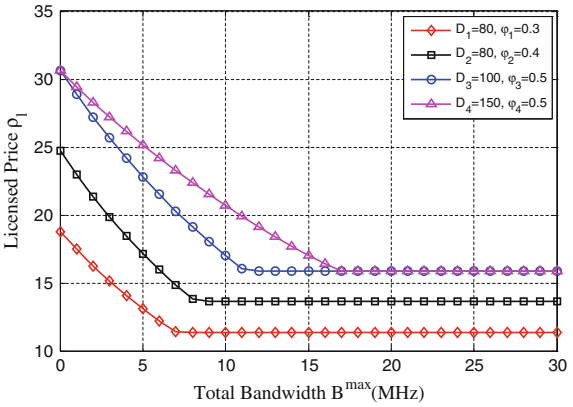

Fig. 4 Variation in licensed spectrum price

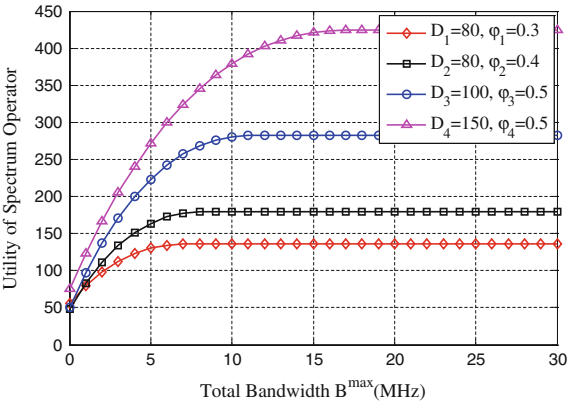

Fig. 5 Variation of utility of operator

From Fig. 5 the four curve denote when operator reduces the price ρ_l, he will achieve more revenue. The reason is due to when shared spectrum is getting worse and the licensed price is decreasing, the licensed spectrum becomes the most favorable choice. Simultaneously, operator will lease more licensed spectrum from PU^Ls.

From Fig. 6 the leasing licensed bandwidth B increases for the increasing traffic demands and worse shared spectrum (because of PU^Ss' activities). When SUs achieve their QoS demands, operator will not lease more licensed spectrum, for no user would like to purchase it. Thus, the leasing licensed bandwidth B will reach the equilibrium solution, meanwhile the revenue of operator could not increase in Fig. 5.

We can further see from Fig. 7 that under the proposed scheme, the SUs using worse channel will get more compensation to reduce their loss of profit. When $\varphi = 0.9$, the channel condition of shared spectrum is getting worse than that at $\varphi = 0.3$. But the utility of SUs could increase up 14.17 %, when $\varphi = 0.9$. However, the utility just increase up 1.92 % when $\varphi = 0.3$. Moreover, when shared spectrum

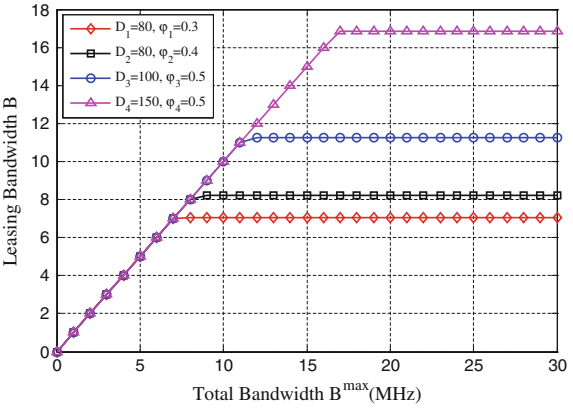

Fig. 6 Variation of leasing bandwidth

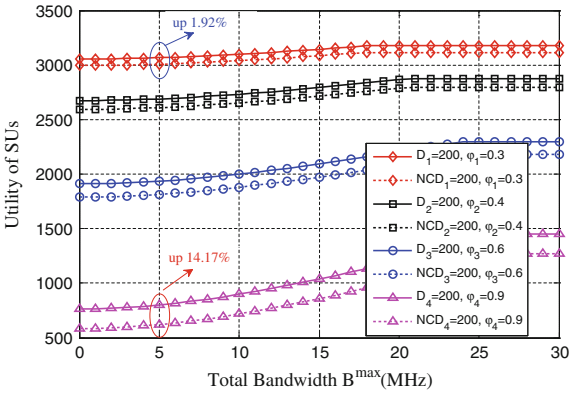

Fig. 7 Utility of SUs with price compensation and no compensation respectively

is worse, such as $\varphi = 0.9$, utility of SUs increases faster than that with $\varphi = 0.3$ under the PCS. Meanwhile, more licensed spectrum is required. From Fig. 7, the maximum leasing bandwidth for licensed spectrum is 24 MHz when $\varphi = 0.9$, and it is 18 MHz when $\varphi = 0.3$. Obviously, PU^Ls will achieve more profit when shared spectrum is getting worse.

5 Conclusions

In this paper, we have studied the economic behavior of SUs under the impact of PU^Ss' activities on shared spectrum. We use three-stage Stackelberg game to analyze the optimal revenue of operator and users, respectively. Furthermore, we propose a price compensation scheme (PCS) to enhance the utility of SUs when channel condition of shared spectrum is getting worse. Numerical results verify that the high activities of primary users could motivate SUs to purchase more licensed spectrum, which maximizes revenue of operator and PU^Ls, respectively. The proposed scheme could enhance the utility of users up to 14.17 % when $\varphi = 0.9$, that is better than the case of $\varphi = 0.3$.

Acknowledgments This research was supported in part by the National Nature Science Foundation of China (Grant No. 61301161, 61471395). And the Natural Science Foundation of Jiangsu Province (Grant No. BK20141070).

References

1. Zhao Q, Sadler B (2005) A survey of dynamic spectrum access: signal processing, network, and regulatory policy. IEEE Signal Process 24(3):201–220
2. Ofcom, Implementing Geolocation (2010)

3. Luo Y, Gao L, Huang J (2013) White space ecosystem: a secondary network operator's perspective. IEEE GLOBECOM. doi:10.1109/GLOCOM.2013.6831192
4. Liu Y, Yu R, Pan M, Zhan Y (2014) Adaptive channel access in spectrum database-driven cognitive radio networks. IEEE ICC. doi:10.1109/ICC.2014.6884102
5. Jiang C, Duan L, Huang J (2014) Joint spectrum pricing and admission control for heterogeneous secondary users. In: Modeling and optimization in mobile, Ad Hoc, and wireless networks (WiOpt), pp 497–504
6. Kun Z, Niyato D, Wang P, Han Z (2012) Dynamic spectrum leasing and service selection in spectrum secondary market of cognitive radio network. IEEE Trans Wirel Commun 11 (3):1136–1145. doi:10.1109/TWC.2012.010312.110732
7. Yin J, Sun G, Wang X (2013) Spectrum trading in cognitive radio network: a two-stage market based on contract and stackelberg game. In: IEEE WCNC, pp 1679–1684. doi:10.1109/WCNC.2013.6554816
8. Feng X, Zhang Q, Zhang J (2013) Dynamic spectrum leasing with users-determined traffic segmentation. In: IEEE ICC, pp 6069–6100. doi:10.1109/ICC.2013.6655578
9. Boydnad S, Vandenberghe L (2004) Convex optimization. Cambridge University Press
10. Corless RM, Gonnet GH, Hare DE, Jeffrey D, Knuth DE (1996) On the Lambert W function. Adv Comput Math 5

Distributed Estimation in Heterogeneous Sensor Networks Using Principal Component Analysis

Liang Han, Saichao Li and Jiasong Mu

Abstract This paper focuses on estimating a common unknown random vector in heterogeneous sensor networks (HSNs). We assume that both observation models and sensor operations are linear. The fusion center (FC) uses the received observations to find the minimum mean square error (MMSE) estimate of the signal. Two cases are considered: Raw data-based fusion and principal component analysis (PCA)-based fusion. We derive the mean square error (MSE) for both cases. It is shown by numerical and simulation results that PCA-based fusion can reduce the transmission requirement while satisfying the system performance requirement.

Keywords Heterogeneous sensor networks · Distributed estimation · Principal component analysis · MMSE

1 Introduction

Wireless sensor networks (WSNs) have attracted considerable interests due to a wide range of applications, such as environmental monitoring, remote surveillance, intelligent transportation, health care, to name a few [1, 2].

Traditional WSNs use only sensors of the same category, such as radars or sonars for detection of targets. In these WSNs, complete sensor observations are available and classical hypothesis testing procedures are employed for signal processing. In recent years, there is an increasing interest in simultaneously employing several different kinds of sensors, such as optical, EO/IR, acoustic/seismic, RF, electromagnetic, thermal and electrical sensors. This class of WSNs is called heterogeneous sensor networks (HSNs) [3]. The main goal of HSNs is to increase the accuracy of detection and estimation, which can be achieved by properly combining the information obtained from the sensors of different types.

L. Han (✉) · S. Li · J. Mu
College of Electronics and Communication Engineering, Tianjin Normal University, Tianjin 300387, China
e-mail: hanliang_tjnu@163.com

Q. Liang et al. (eds.), *Proceedings of the 2015 International Conference on Communications, Signal Processing, and Systems*, Lecture Notes in Electrical Engineering 386, DOI 10.1007/978-3-662-49831-6_4

Since HSNs have created a large amount of multi-sensor signals across multi-modality, sensors need to operate in a collaborative manner to solve a common signal processing problem [4]. In general, there are three major options for signal processing with HSNs. With the first option, complete sensor observations (raw data) can be transmitted to the central processor or fusion center (FC) [5, 6]. This requires transmission of sensor information with a large communication bandwidth. The full signals are processed at the FC based on the classical theory [7]. The second option is to make detection at each sensor and integrate the decision information at the FC [8–12]. Since much of the important sensor signal information has lost, this option will result in ineffective detection and estimation. With the third option, raw data can be quantized or compressed at the sensors. Upon receiving the quantized or compressed data, the FC combines them according to some fusion rules for ultimate detection or estimation. Since this option offers huge advantages in terms of cost, reliability, and communication bandwidth, it is more attractive for many applications. In [13], the authors studied the optimal compression matrix of sensor data in multiuser estimation fusion by using the matrix decomposition, pseudoinverse, and eigenvalue techniques. In [14], the authors investigated optimum compression of a noisy measurement for transmission over a noisy channel, and gave the closed-form expression for the optimal compression matrix that minimizes the trace or determinant of the error covariance matrix.

In this paper, we investigated the compression-estimation approach in HSNs by using principal component analysis (PCA), which focuses on recovering the principal covariance eigenvectors and projecting the data on the principal covariance eigenspace. Since each sensor can compress its data and reduce the data dimensionality before sending its data to a FC, PCA-based compression estimation can reduce the transmission requirement.

2 System Model

We consider an HSN as depicted in Fig. 1. Suppose that there are N sensors, each observing a common unknown random vector of interest $\boldsymbol{\theta} \in \mathbb{R}^{p\times 1}$, which has zero mean and covariance matrix $\mathbf{C}_\theta = E\left(\boldsymbol{\theta}\boldsymbol{\theta}^T\right)$. In this paper, we consider linear measurement of $\boldsymbol{\theta}$, then the observation at sensor m can be given as

$$\mathbf{x}_m = \mathbf{H}_m\boldsymbol{\theta} + \mathbf{w}_m, \quad m = 1, 2, \ldots N, \tag{1}$$

where $\mathbf{x}_m \in \mathbb{R}^{l_m\times 1}$ denotes the sensor's vector observation, $\mathbf{H}_m \in \mathbb{R}^{l_m\times p}$ denotes the known observation matrix, and $\mathbf{w}_m \in \mathbb{R}^{l_m\times 1}$ denotes the additive multivariate Gaussian noise with zero mean and covariance matrix $\mathbf{C}_{w_m} = E\left(\mathbf{w}_m\mathbf{w}_m^T\right)$. Note that since multiple sensors are heterogeneous, the observation matrix and the dimension of the observation are different across the sensors.

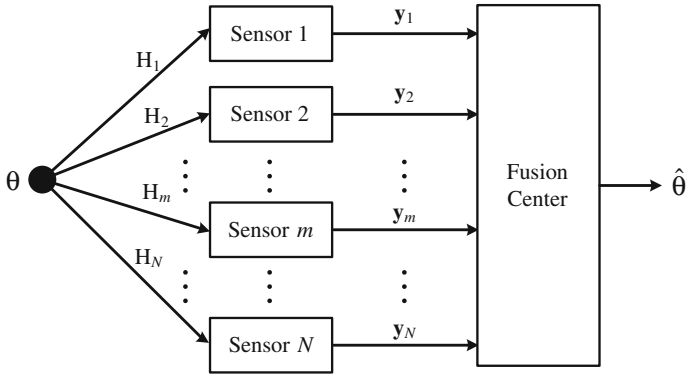

Fig. 1 System model

To reduce the transmission requirement, some operations should be performed at the sensor and a quantized or compressed version of the data is transmitted. For simplicity, we consider all the sensor operations are linear, i.e., sensor m encodes its observation by multiplying it with a matrix $\mathbf{T}_m \in \mathbb{R}^{k_m \times l_m}$. Thus, the transmitted signal $\mathbf{y}_m$ can be written as

$$\mathbf{y}_m = \mathbf{T}_m \mathbf{x}_m = \mathbf{T}_m \mathbf{H}_m \boldsymbol{\theta} + \mathbf{T}_m \mathbf{w}_m, \quad m = 1, 2, \ldots N. \tag{2}$$

We assume that the communication between the sensors and the FC is over orthogonal AWGN channels so that there is no multi-sensor interference, then the received signal of sensor m at FC is given as

$$\mathbf{r}_m = \mathbf{T}_m \mathbf{H}_m \boldsymbol{\theta} + \mathbf{T}_m \mathbf{w}_m + \mathbf{n}_m, \quad m = 1, 2, \ldots N, \tag{3}$$

where $\mathbf{n}_m \in \mathbb{R}^{k_m \times 1}$ is the additive multivariate Gaussian noise at FC with zero mean and covariance matrix $\mathbf{C}_{n_m} = E\left(\mathbf{n}_m \mathbf{n}_m^T\right)$. The FC can separate and concatenate vectors of individual sensors to form

$$\mathbf{r} = \mathbf{F}\theta + \mathbf{v}, \tag{4}$$

where $\mathbf{r} = \left[\mathbf{r}_1^T, \mathbf{r}_2^T, \ldots \mathbf{r}_N^T\right]^T$ is the $k \times 1$ received observations at all sensors with $k = \sum_{m=1}^{N} k_m$, $\mathbf{F} = \left[\mathbf{H}_1^T \mathbf{T}_1^T, \mathbf{H}_1^T \mathbf{T}_1^T, \ldots \mathbf{H}_N^T \mathbf{T}_N^T\right]^T$ denotes the $k \times p$ joint observation and operation matrix for all sensors, and $\mathbf{v} = \left[\mathbf{w}_1^T \mathbf{T}_1^T + \mathbf{n}_1^T, \mathbf{w}_2^T \mathbf{T}_2^T + \mathbf{n}_2^T, \ldots \mathbf{w}_N^T \mathbf{T}_N^T + \mathbf{n}_N^T\right]^T$ denotes the $k \times 1$ equivalent additive noise vector.

3 Distributed Estimation Using PCA

For different types and sizes of $\mathbf{T}_m$, the system performance will be dramatically different. We consider two cases in this paper.

3.1 Baseline Scenario

Here, we consider the case that complete sensor observations, i.e., raw data, can be transmitted to the FC, which means that $\mathbf{T}_m = \mathbf{I}_{l_m}$. In this case, the minimum mean square error (MMSE) estimation for $\boldsymbol{\theta}$ is given as

$$\boldsymbol{\theta} = \mathbf{C}_\theta \mathbf{H}^T \left(\mathbf{H}\mathbf{C}_\theta \mathbf{H}^T + \mathbf{C}_v\right)^{-1} \mathbf{y} \tag{5}$$

where $\mathbf{H} = \left[\mathbf{H}_1^T, \mathbf{H}_2^T, \ldots \mathbf{H}_N^T\right]^T$, $\mathbf{C}_v$ denotes the covariance matrix of $\mathbf{v}$. Assume that the noise is independent across the sensors, then $\mathbf{C}_v$ can be given as $\mathbf{C}_v = \mathrm{diag}[\mathbf{C}_{w_1} + \mathbf{C}_{n_1}, \mathbf{C}_{w_2} + \mathbf{C}_{n_2}, \ldots \mathbf{C}_{w_N} + \mathbf{C}_{n_N}]$, which is a $k \times k$ block diagonal matrix such that the mth diagonal element is the equivalent noise covariance matrix of the mth sensor. The mean square error (MSE) achievable by such estimator is

$$\mathrm{MSE} = \mathrm{tr}\left(\mathbf{C}_\theta - \mathbf{C}_\theta \mathbf{H}^T \left(\mathbf{H}\mathbf{C}_\theta \mathbf{H}^T + \mathbf{C}_v\right)^{-1} \mathbf{H}\mathbf{C}_\theta\right) \tag{6}$$

3.2 PCA Scenario

In this case, we resort to the well-known PCA. Assume that there is no inter-sensor communication since all sensors are distributed. Each sensor compresses its data and transmits the compressed data to the FC.

The covariance matrix of $\mathbf{x}_m$ is $\mathbf{C}_{x_m} = \mathbf{H}_m \mathbf{C}_\theta \mathbf{H}_m^T + \mathbf{C}_{w_m}$, and the eigendecomposition of this covariance matrix is given by

$$\mathbf{C}_{x_m} = \mathbf{Q}_m \boldsymbol{\Lambda}_m \mathbf{Q}_m^T = \sum_{i=1}^{l_m} \lambda_{m,i} \mathbf{q}_{m,i} \mathbf{q}_{m,i}^T \tag{7}$$

where $\mathbf{Q}_m = \left[\mathbf{q}_{m,1}, \mathbf{q}_{m,2} \cdots, \mathbf{q}_{m,l_m}\right] \in \mathbb{R}^{l_m \times l_m}$ is a unitary matrix whose columns are the eigenvectors of the matrix $\mathbf{C}_{x_m}$, and $\boldsymbol{\Lambda}_m = \mathrm{diag}[\lambda_{m,1}, \lambda_{m,2} \ldots, \lambda_{m,l_m}]$ is a diagonal matrix whose entries are eigenvalues and $\lambda_{m,1} \geq \lambda_{m,2} \geq \cdots \geq \lambda_{m,l_m} \geq 0$. We denote the orthonormal matrix formed by the eigenvectors corresponding to the largest k_m eigenvalues $\{\lambda_{m,i}\}_{i=1}^{k_m}$ with $\mathbf{Q}_{m,k_m}$. Then the PCA of $\mathbf{x}_m$ can be given as

$$\mathbf{y}_{m,k_m} = \mathbf{Q}_{m,k_m}^T \mathbf{x}_m = \begin{bmatrix} \mathbf{q}_{m,1}^T \mathbf{x}_m \\ \mathbf{q}_{m,2}^T \mathbf{x}_m \\ \vdots \\ \mathbf{q}_{m,k_m}^T \mathbf{x}_m \end{bmatrix} \tag{8}$$

where $\mathbf{F} = \left[\mathbf{H}_1^T \mathbf{T}_1^T, \mathbf{H}_1^T \mathbf{T}_1^T, \ldots \mathbf{H}_N^T \mathbf{T}_N^T\right]^T$ denotes the $k \times p$ joint observation and operation matrix for all sensors, and $\mathbf{v} = \left[\mathbf{w}_1^T \mathbf{T}_1^T + \mathbf{n}_1^T, \mathbf{w}_2^T \mathbf{T}_2^T + \mathbf{n}_2^T, \ldots \mathbf{w}_N^T \mathbf{T}_N^T + \mathbf{n}_N^T\right]^T$ denotes the $k \times 1$ equivalent additive noise vector.

In this setup, the joint observation and operation matrix for all sensors is $\mathbf{F} = \left[\mathbf{H}_1^T \mathbf{Q}_{1,k_1}, \mathbf{H}_1^T \mathbf{Q}_{2,k_2}, \ldots \mathbf{H}_N^T \mathbf{Q}_{N,k_N}\right]^T$ and the equivalent additive noise vector is $\mathbf{v} = \left[\mathbf{w}_1^T \mathbf{Q}_{1,k_1} + \mathbf{n}_1^T, \mathbf{w}_2^T \mathbf{Q}_{2,k_2} + \mathbf{n}_2^T, \ldots \mathbf{w}_N^T \mathbf{Q}_{N,k_N} + \mathbf{n}_N^T\right]^T$. The MMSE estimation for $\boldsymbol{\theta}$ is given as

$$\boldsymbol{\theta} = \mathbf{C}_\theta \mathbf{F}^T \left(\mathbf{F}\mathbf{C}_\theta \mathbf{F}^T + \mathbf{C}_v\right)^{-1} \mathbf{y} \tag{9}$$

where $\mathbf{C}_v = \text{diag}\left[\mathbf{Q}_{1,k_1}^T \mathbf{C}_{w_1} \mathbf{Q}_{1,k_1} + \mathbf{C}_{n_1}, \mathbf{Q}_{2,k_2}^T \mathbf{C}_{w_2} \mathbf{Q}_{2,k_2} + \mathbf{C}_{n_2}, \ldots \mathbf{Q}_{N,k_N}^T \mathbf{C}_{w_N} \mathbf{Q}_{N,k_N} + \mathbf{C}_{n_N}\right]$. The MSE achievable by such estimator is

$$\text{MSE} = \text{tr}\left(\mathbf{C}_\theta - \mathbf{C}_\theta \mathbf{F}^T \left(\mathbf{F}\mathbf{C}_\theta \mathbf{F}^T + \mathbf{C}_v\right)^{-1} \mathbf{F}\mathbf{C}_\theta\right) \tag{10}$$

4 Numerical and Simulation Results

In this section, we present some numerical and simulation results to validate our analysis. Suppose that there are three sensors, each observing a common unknown random vector $\boldsymbol{\theta} \in \mathbb{R}^{3\times 1}$, which has zero mean and covariance matrix $\mathbf{C}_\theta = \text{diag}[1, 2, 3]$. The known observation matrices are randomly chosen as

$$\mathbf{H}_1 = \begin{bmatrix} 2.93 & 1.40 & 2.16 \\ 0.69 & 0.23 & 0.33 \\ 0.13 & 1.52 & 2.04 \\ 0.65 & 1.48 & 0.96 \end{bmatrix}, \mathbf{H}_2 = \begin{bmatrix} 0.89 & 1.03 & 1.14 \\ 1.80 & 0.68 & 0.49 \\ 1.79 & 1.29 & 1.25 \\ 1.53 & 0.36 & 1.85 \\ 0.73 & 1.38 & 1.27 \\ 0.96 & 0.69 & 1.84 \end{bmatrix}, \mathbf{H}_3 = \begin{bmatrix} 1.02 & 1.79 & 0.08 \\ 1.74 & 0.49 & 1.53 \\ 0.14 & 0.52 & 1.80 \\ 1.70 & 2.97 & 0.38 \\ 0.36 & 0.50 & 0.37 \\ 1.25 & 2.49 & 0.57 \\ 0.36 & 0.93 & 3.14 \\ 1.10 & 0.56 & 0.51 \end{bmatrix} \tag{11}$$

The covariance matrices of the additive multivariate Gaussian noise are $\mathbf{C}_{w_1} = \sigma_{w_1}^2 \mathbf{I}_4, \mathbf{C}_{w_2} = \sigma_{w_2}^2 \mathbf{I}_6$ and $\mathbf{C}_{w_3} = \sigma_{w_3}^2 \mathbf{I}_8$. Moreover, we assume $\sigma_{w_1}^2 = \sigma_{w_2}^2 = \sigma_{w_3}^2 = \sigma_n^2 = \sigma^2$.

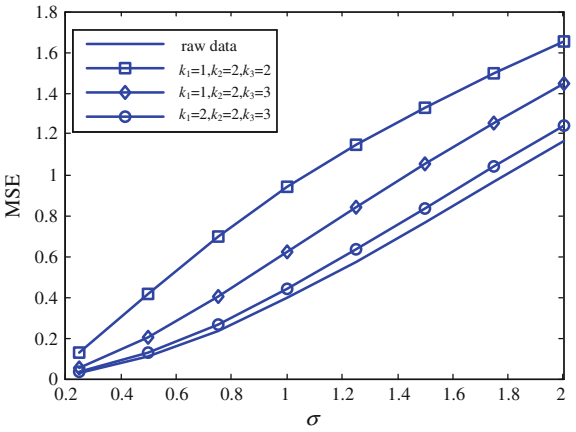

Fig. 2 MSE performance versus noise power with different dimensions of PCA

In Fig. 2, we illustrate the MSE performance with respect to σ for different dimensions of PCA. From Fig. 2, we can see that different compression matrices result in different MSE performances. As the dimensions increase, the MSE decreases. When $k_1 = 2,\ k_2 = 2,\ k_3 = 3$, the gap between the PCA-based estimation and raw data-based estimation is relatively small, while the transmission bandwidth can be reduced significantly.

5 Conclusion

In this paper, we investigated the estimation of a common unknown random vector in HSNs using the well-known PCA. We assume that there is no inter-sensor communication since all sensors are heterogeneous and distributed. Each sensor compressed its data using the eigendecomposition of the covariance matrix and transmitted the compressed data to FC. The FC uses the received observations to find the MMSE estimate of the signal. It was shown by numerical and simulation results that PCA-based fusion can reduce the transmission requirement while satisfying the system performance requirement.

Acknowledgments This work was supported by the National Natural Science Foundation of China (61401310) and the Doctoral Foundation of Tianjin Normal University (5RL135).

References

1. Yick J, Mukherjee B, Ghosal D (2008) Wireless sensor network survey. Comput Netw 52:2292–2330
2. Borges LM, Velez FJ, Lebres AS (2014) Survey on the characterization and classification of wireless sensor network applications. IEEE Commun Surv Tutor 16:1860–1890

3. Liang Q, Cheng X, Huang SC, Chen D (2014) Opportunistic sensing in wireless sensor networks: theory and application. IEEE Trans Comput 63:2002–2010
4. Chen B, Tong L, Varshney PK (2006) Channel-aware distributed detection in wireless sensor networks. IEEE Signal Process Mag 23:16–26
5. Bahceci I, Khandani AK (2008) Linear estimation of correlated data in wireless sensor neworks with optimum power allocation and analog modulation. IEEE Trans Commun 56:1146–1156
6. Ahmed MFA, Al-naffouri TY, Alouini MS, Turkiyyah G (2013) The effect of correlated observations on the performance of distributed estimation. IEEE Trans Signal Process 61:6264–6275
7. Kay SM (1993) Fundamentals of statistical signal processing: estimation theory. Prentice-Hall, Englewood Cliffs
8. Chair Z, Varshney PK (1986) Optimal data fusion in multiple sensor detection systems. IEEE Trans Aerosp Electron Syst AES 22:98–101
9. Thomopoulos SCA, Viswanathan R, Bougoulias DC (1987) Optimal decision fusion in multiple sensor systems. IEEE Trans Aerosp Electron Syst AES 23:644–653
10. Kam M, Zhu Q, Gray WS (1992) Optimal data fusion of correlated local decisions in multiple sensor detection systems. IEEE Trans Aerosp Electron Syst 28:916–920
11. Xiao J, Luo Z (2005) Universal decentralized detection in a bandwidth-constrained sensor network. IEEE Trans Signal Process 53:2617–2624
12. Niu R, Chen B, Varshney PK (2006) Fusion of decisions transmitted over rayleigh fading channels in wireless sensor networks. IEEE Trans Signal Process 54:1018–1027
13. Zhu Y, Song E, Zhou J, You Z (2005) Optimal dimensionality reduction of sensor data in multisensor estimation fusion. IEEE Trans Signal Process 53:1631–1639
14. Wang Y, Wang H, Scharf LL (2014) Optimum compression of a noisy measurement for transmission over a noisy channel. IEEE Trans Signal Process 62:1279–1289

An Adaptive Energy-Efficient Optimization Scheme in Future Massive MIMO HetNets

Na Chen, Songlin Sun and Junshi Xiao

Abstract In future wireless systems, implementation of massive multiple-input multiple-output (MIMO) and heterogeneous networks (HetNets) technologies will lead to higher capacity of networks, but also result in energy problems and resistance for operators to provide desirable services. In this paper, we focus on energy-saving problem, and try to improve the energy efficient (EE) with required quality of service (QoS) maintained. We will first indicate the problem of energy use in modern wireless communication systems, then address a massive MIMO-based HetNets framework with software defined network (SDN) as the central controller of radio resource management (RRM). After that, we will develop a scheme that reduces the energy use of the system, which is monitored and managed by SDN controller at the controlling pannel. Finally, we will deploy the scheme to achieve a higher EE with sufficient QoS.

1 Introduction

In 5G mobile communication systems, massive multiple-input multiple-output (MIMO) systems and heterogeneous networks (HetNets) are currently considered as two promising and effective solutions for achieving high data rates and coverage gains, as well as satisfying the galloping demand for ubiquitous broadband mobile services [1]. Exploiting pilot reuse and channel reciprocity in time division duplex (TDD) networks, a large number of users is served using the additional spatial degrees of freedom [2], which can significantly improve the quality of service (QoS) of the system.

N. Chen · S. Sun (✉) · J. Xiao
Beijing University of Posts and Telecommunications, Beijing, China
e-mail: slsun@bupt.edu.cn

N. Chen
e-mail: chn@bupt.edu.cn

J. Xiao
e-mail: 2012212930@bupt.edu.cn

Q. Liang et al. (eds.), *Proceedings of the 2015 International Conference on Communications, Signal Processing, and Systems*, Lecture Notes in Electrical Engineering 386, DOI 10.1007/978-3-662-49831-6_5

Despite lots of promising features can be provided by massive MIMO-based HetNets, deployment of these two technologies will also bring some side effects to the system. With the drastic increase of ultra-dense deployment of small cells in 5G networks, the total energy consumption may easily exceed the acceptable scope. Moreover, fluctuated volumes of traffic also bring considerable increase in energy consumption, which will also cause extra operating expense (OPEX) to service providers. Therefore, energy efficient (EE) has become one of urgent issues which prevents 5G provider to afford desirable performance.

To solve EE problem in 5G systems, plenty of work has been done in the previous literatures. Hu and Yi [3] provided a framework which supports centralized baseband processing, cooperative radio, and energy saving in HetNets. The spectral efficiency and EE trade-off of massive MIMO systems has recently been studied in [4]. However, it only considered the power consumed by the power amplifiers (PA) at the user terminals (UT).

In this paper, we propose a software defined network (SDN)-based EE optimization scheme in massive MIMO-based HetNets. We first analyze the energy use condition of a typical massive MIMO HetNet with single-antenna low power nodes (LPNs) and single-antenna UEs. Furthermore, we developed a scheme that reduces the energy use of the system by two means: (1) adaptively justify the access point of specific UE according to the channel status, (2) explore the solution hyperspace to achieve the optimal energy use. The whole scheme is controlled by SDN controller at the controlling panel. The numerical results have shown that the proposed scheme can help the systems achieve a higher energy efficient with sufficient QoS.

2 System Framework

As mentioned above, volume of the next generation network will increase as well as the number and density of subscribers, which makes 5G network more complex than previous generations. This ever-increasing network complexity is driving operators toward a virtualization of network functionality that calls for a paradigm shift from a hardware-based approach to a software-based approach. In this work, we address an intelligent management framework based on the concept of SDN, as illustrated in Fig. 1.

The bottom layer is composed of different categories of cells with multiple communication standards. In the middle layer, virtual gateways (VGs) can help different data access to corresponding virtual controllers (VCs). VCs provide HetNet support for loading cells and directly controlled by SDN controller located in the top layer. Implementation of SDN techniques enables this controller to analyze the current network status and topology through the data provided by all of the VCs. With the knowledge of the network and radio environment, the SDN controller selects appropriate operating parameters. This virtual entity resides at each network device and

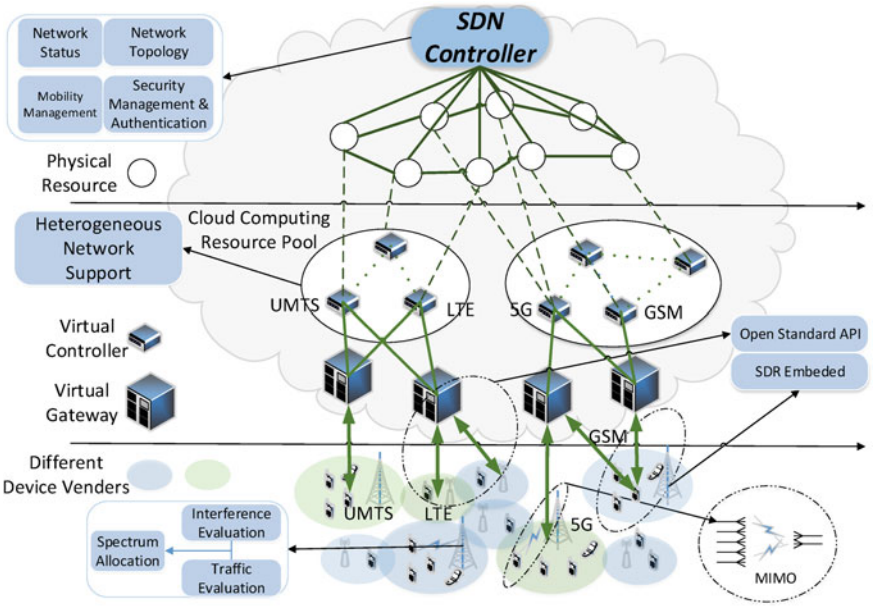

Fig. 1 A generalized architecture of SDN controlled adaptive HetNet

takes decisions with information collected from the lower layers. Furthermore, SDN controller exploits seamless cooperation amongst neighboring BSs and UEs. Such type of architecture design allows adaptive mechanisms that aim at achieving the right balance of energy savings amongst network devices. Finally, SDN controller achieves real-time interaction with its environment to adapt appropriate communication parameters. Taking advantage of the network virtualization, the whole network is under control of the central SDN controller. And we recognize the system is of sufficient computing capacity.

3 Proposed Scheme

Consider the uplink of a multiuser massive MIMO single-cell HetNet where a BS is equipped with M antennas. In the macrocell coverage area of the BS, there are Q single-antenna LPNs and K single-antenna UEs. The K UEs are served by the BS or an LPN or both BS and LPN simultaneously. Channel fading between any pair of antenna is assumed to be Rayleigh with unit mean and independent across nodes. With TDD-based communication applied, we assume perfect channel reciprocity.

3.1 Adaptive Coorperation

With the higher throughput supported, there are multiple services provided in upcoming future systems. Assume the data rate requirement of the k-th UE is Q_k. It is required that

$$Blog_2(1 + SINR_k) \geq Q_k, \tag{1}$$

For UEs located in coverage of an LPN, we reconsider some specific UEs' access method for better performance and efficiency. For the k-th UE with large data requirement (for example, multimedia services applied), we will perform a trade-off between accessing to the BS or an LPN or both of them. Here we assume the different LPNs located far enough from each other, i.e., their coverage do not overlap, and the BS is not within the coverage of any LPNs. If UE k can be served very well by either the BS or an LPN, we compare and choose the better one. Else, if the requirement cannot be satisfied, the k-th UE can access to both of them. The coverage probability of the k-th UE, i.e., $Pc_{q,k} = P(SINR_k > T_k), (T_k = 2^{\frac{Q_k}{B}} - 1)$, is computed by SDN controller to make the following justice.

$$J(k) = \begin{cases} 0, & Pc_{0,k} > T_p > Pc_{q,k} \\ q, & Pc_{q,k} > T_p > Pc_{0,k} \ \ or \ \ min\{Pc_{0,k}, Pc_{q,k}\} > Tp \\ Q + q + 1, & T_p > max\{Pc_{0,k}, Pc_{q,k}\} \end{cases} \tag{2}$$

Here $J(k)$ is the justice function, where k represents the index of the user. First we define T_p as the threshold of whether we apply cooperative situation, and we have the user set $K = \{K_0, K_1, \ldots, K_q, \ldots, K_Q, K_{Q+1}, \ldots, K_{Q+q+1}, \ldots, K_{2Q+1}\}$. The specific user k belongs to a subset of $K_{J(k)}$.

The SINR of macro cell UE k ($k \in K_0$) is given by

$$SINR_{0,k} = \frac{P_{0,k}||\mathbf{h}_{0,k}^H||^2 r_{0,k}^{-\alpha}}{\sum_{q=1}^{Q} P_q||\mathbf{h}_{q,k}^H||^2 r_{q,k}^{-\alpha} + \sum_{i=1, i\neq k}^{i\in K_0} P_{0,i}||\mathbf{h}_{0,k}^H||^2 r_{0,k}^{-\alpha} + N_0 B}, \tag{3}$$

where $P_{0,k}$ stands for the transmission power of the BS, $\mathbf{h}_{0,k}$ is the channel from the k-th UE to the BS. Here B is the channel bandwidth (Hz), and N_0 (W/Hz) is the power spectral density of the AWGN channel. Moreover, we assume the data transmission between the BS and LPNs does not affect the wireless transmission environment.

Similarly, the SINR of a small cell user j ($j \in K_q$) served by LPN q is

$$SINR_{q,j} = \frac{P_{q,j}||\mathbf{h}_{q,j}||^2 r_{q,j}^{-\alpha}}{\sum_{i=1, i\neq q}^{Q} P_q||\mathbf{h}_{i,j}^H||^2 r_{i,j}^{-\alpha} + \sum_{i=1}^{i\in K_0} P_0||\mathbf{h}_{0,j}^H||^2 r_{0,j}^{-\alpha} + N_0 B} \tag{4}$$

And the SINR of a UE l ($l \in K_{Q+q+1}$) served by both the BS and LPN q can be expressed as

$$SINR_{0,q,l} = \frac{P_{0,l}||\mathbf{h}_{0,l}^H||^2 r_{0,l}^{-\alpha} + P_{q,l}||\mathbf{h}_{q,l}||^2 r_{q,l}^{-\alpha}}{\sum_{i=1,i\neq q}^{Q} P_q||\mathbf{h}_{i,j}^H||^2 r_{i,j}^{-\alpha} + \sum_{i=1,i\neq l}^{i\in K_0} P_0||\mathbf{h}_{0,l}^H||^2 r_{0,l}^{-\alpha} + N_0 B} \tag{5}$$

3.2 Energy Efficiency Analysis and Optimization Scheme

Next, we analyze how EE can be described and optimized in massive MIMO HetNet systems. As we know, EE is measured in bit/Joule and a common EE definition is the ratio of the spectral efficiency (in bit/channel use) to the emitted power (in Joule/channel use). EE can be expressed as

$$EE = \frac{Throughput}{P}, \tag{6}$$

where P denotes the total power consumption as

$$P = P_0 + \sum_{q=1}^{Q} P_q + \sum_{k=1}^{K} P_k . \tag{7}$$

where

$$\begin{cases} P_0 = Mp_{t,0} + K_0 p_{dec,0} + p_{mud,0} + p_{s,0} \\ P_q = p_{t,q} + K_q p_{dec,q} + p_{mud,q} + p_{s,q} \\ P_k = \beta p_u + p_t \end{cases} \tag{8}$$

Let $p_{t,0}$ and $p_{t,q}$ be the average power consumed in each tranceiver antenna unit of the BS and the q-th LPN, respectively, and the average power consumed at the BS and the q-th LPN for decoding each user's coded information stream is averaged and modeled as $p_{dec,0}$ and $p_{dec,q}$. And $p_{mud,0}$ and $p_{mud,q}$ stands for the average power consumed for channel estimation and multiuser detection, $p_{s,0}$ and $p_{s,q}$ models the fixed power consumption which is independent of M and number of accessed UEs. At the UE side, $\beta > 1$ models the efficiency of the power amplifier and p_t is the power consumed by the other signal processing circuits inside the transmitter. The actual power consumption can be realized with different precoding and decoding methods applied, and some previous works have made optimal achievements on them [5, 6].

Massive MIMO is proven to be more effective with relatively more antennas. However, it depends on the situation whether massive is necessary for the system. According to previous work [7], when the average user channel gain is high or else

the BS/UE design is power inefficient, it is optimal to have a few BS antennas and a single user, i.e., nonmassive MIMO regime. Similarly, when the channel gain is small or else the BS/UT design is power efficient, it is optimal to have a larger (M, K), i.e., massive MIMO regime.

The scheme we proposed to optimize the system EE is described as below. The optimal power consumption and EE can be achieved after the process and all is under management of the SDN controller.

Algorithm 1 Adaptive EE optimization.

Input: Number of antenna equipped at the BS, M; number of the total users, K; number of the LPNs, Q; rate requirements of the users, Q_k; cooperation threshold, T_p; max times of iteration, J;

Initialization: Set the initial M, K, Q; $J(k) = -1(0 \leq k < K)$; UE index k; iteration index, j; optimal EE, EE_{opt}; power allocation matrix, $\mathbf{P}$; optimal power consumption, $\mathbf{P}_{opt}$; optimal increment vector, $\boldsymbol{\Delta}$.

Calculation:

```
do Channel estimation.
Update IsMassive = Ture or False.
if IsMassive
  M = M_mas.
else
  M = M_nonmas.
while j < J do
  while k < K do
    Calculate SINR_k, Pc_k.
    Calculate J(k) by Eq. (4).
    Update K_0, K_q, K_{0,q}.
    Update k = k + 1.
  end while
  Calculate EE.
  if EE < EE_opt
    Update EE_opt and P_opt.
  end if
  Update P = P + Δ.
  Update j = j + 1.
end while
```

Output:

```
return P_opt and EE_opt.
```

---

4 Numerical Results

In this section, we present numerical results and discuss the performance of the scheme developed in the paper. The default simulation parameters for the results are listed in Table 1.

In Fig. 2, we compare the energy-saving performance achieved by different iteration of the scheme. And it is shown that with the proposed scheme, the system can achieve a better EE after iterations.

Figure 3 shows the total power consumption impacted by the number of massive antennas at the BS. It can be observed that the total power consumption can be substantially reduced by increasing the number of antennas at the BS. Massive MIMO brings large improvements in energy efficiency and the increased antennas can be used to eliminate the interference to the victim users. Furthermore, the improvements in energy efficiency can be achieved by applying appropriate precoding algorithms, i.e., changing the transmitting power of the receivers.

Table 1 Main parameters in the numerical evaluation

Parameters	Values
Macro cell radius	500 m
Small cell radius	50 m
System bandwidth	100 MHz
Simulation scenario	ITU-UMa/UMi
Distribution of users	Uniform
Requirements of the rate (per user)	$Q \in \{2, 6, 10, 20\}$ Mbps

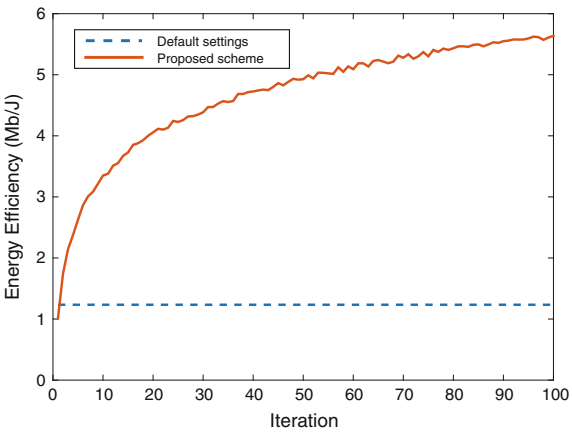

Fig. 2 EE performance achieved by proposed scheme

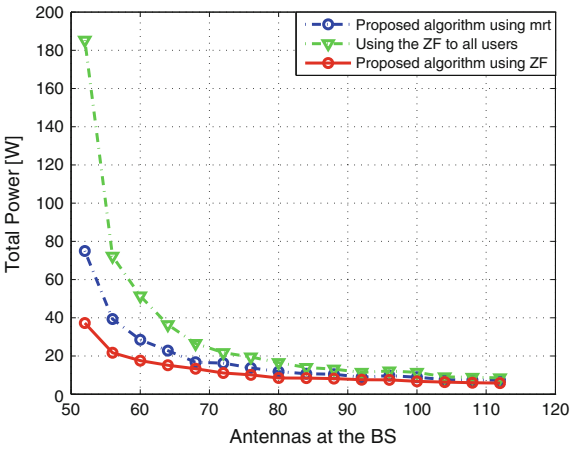

Fig. 3 Impact of different numbers of antennas

5 Conclusions

In this paper, focusing on energy-saving problem, we proposed an adaptive scheme and improved the energy efficient with sufficient QoS and spectrum efficiency maintained. We first indicated the problem of energy use in modern wireless communication systems. Then we introduced the framework of SDN to ensure the realizability of the system. Then we developed an adaptive optimization scheme to reduce the energy use of the system. At last we realized the scheme and it fulfilled our expectation. Some future work will be done to enhance the performance and effectiveness of the algorithms.

Acknowledgments This work is supported in part by National Natural Science Foundation of China (NSFC) under the Grant No. 61471066, and the scholarship from China Scholarship Council (CSC) under the Grant CSC No. 201506470023.

References

1. Bjornson E, Kountouris M, Debbah M (2013) Massive MIMO and small cells: improving energy efficiency by optimal soft-cell coordination. J Mol Med. doi:10.1109/ICTEL.2013.6632074
2. Marzetta TL (2010) Non-cooperative cellular wireless with unlimited numbers of base station antennas. IEEE Trans Wirel Commun 9(11):3590–3600
3. Hu RQ, Yi Q (2014) An energy efficient and spectrum efficient wireless heterogeneous network framework for 5G systems. J Mol Med. doi:10.1109/MCOM.2014.6815898
4. Ngo HQ, Larsson EG, Marzetta TL (2013) Energy and spectral efficiency of very large multiuser MIMO systems. IEEE Trans Commun 61(4):14361449
5. Bjornson E, Hoydis J, Kountouris M, Debbah M (2014) Massive MIMO systems with Non-ideal hardware: Energy efficiency, estimation, and capacity limits. J Mol Med. doi:10.1109/TIT.2014.2354403

6. Choi JW, Lee B, Shim B, Kang I (2013) Low complexity detection and precoding for massive MIMO systems. J Mol Med. doi:10.1109/WCNC.2013.6555014
7. Mohammed SK (2014) Impact of transceiver power consumption on the energy efficiency of zero-forcing detector in massive MIMO system. J Mol Med. doi:10.1109/TCOMM.2014.2364188

Signals Reconstruction in Heterogeneous Sensor Network with Distributed Compressive Sensing

Chengchen Mao, Fangqi Zhu, Huaiyuan Liu and Jing Liang

Abstract In this paper, we reconstruct signals in heterogeneous sensor network (HSN) with distributed compressive sensing (DCS). Combining different types of measurement matrices and different numbers of measurements, we investigate three different scenarios in which HSN is used to acquiring signals for the first time. In the first scenario, there are two different types of measurement matrices. One is Gaussian measurement and the other is Fourier measurement, and each sensor applies the same numbers of measurements. In the second scenario, all sensors use the same type of measurement matrices but the number of measurements are different from each other. The third scenario combines different types of measurement matrix and distinct numbers of measurements. Our simulation results show that in Scenario I, when the common sparsity is considerable, the DCS scheme can reduce the number of measurements. In Scenario II, the reconstruction situation becomes better with the increase of the number of measurements. In both Scenario I and III, joint decoding that use different types of measurement matrices performs better than that of all-Gaussian measurement matrices, but it performs worse than that of all-Fourier measurement matrices. Therefore, DSC is a good compromise between reconstruction percentage and the number of measurements in HSN.

C. Mao (✉) · F. Zhu · H. Liu · J. Liang
Department of Electrical Engineering, University of Electronic Science and Technology of China, Chengdu, China
e-mail: excellentmao@outlook.com

F. Zhu
e-mail: ZFQ_theodore@std.uestc.edu.cn

H. Liu
e-mail: louis.uestc@outlook.com

J. Liang
e-mail: liangjing@uestc.edu.cn

Q. Liang et al. (eds.), *Proceedings of the 2015 International Conference on Communications, Signal Processing, and Systems*, Lecture Notes in Electrical Engineering 386, DOI 10.1007/978-3-662-49831-6_6

1 Introduction

Compressive sensing (CS) is a rapidly growing field of signal processing. It predicts that sparse high-dimensional signals can be recovered from highly incomplete measurements by using efficient algorithms [1]. These algorithms can be classified as $L1$-minimization types [2] and greedy types, as orthogonal matching pursuit (OMP) [3] mentioned.

So far, many works have been reported on CS for sensor networks (SN). In [4], Liang applied CS to radar sensor network (RSN) to tremendously reduce the sampling rate. In [5], CS has been shown as an efficient and effective signal acquisition and sampling framework for wireless sensor networks (WSN). DCS extends the theory and practice of CS to multisignal, distributed settings [6]. In our work, considering the scenarios investigated in this work, we use joint sparsity model-1 (JSM-1).

HSN consists of sensor nodes with different abilities, such as different computing power and sensing range. Compared with conventional sensor networks, deployment and fusion rules are more complex in HSN [7]. In [8], Liang proposed optimized energy allocation schemes that not only optimize the energy allocation in heterogeneous radar sensor networks (HRSNs), but also offer an appropriate tradeoff between resource consumption and target detection performance.

In this work, we assume three scenarios in which HSN is used for signal acquisition. In the first scenario, there are at least two types of measurement matrices in whole HSN system. However, each sensor has the same numbers of measurements. In the second scenario, all sensors use the same type of measurement matrices but the number of measurements is different from each other. The third scenario combines different types of measurement matrix and distinct numbers of measurements.

In [9, 10], DCS has been applied in conventional SN and shows the superior potentials over non-CS methods, but they did not use DCS into an HSN. To the best of our knowledge, this is the first investigation about DCS usage in HSN and the first utilization of different types of measurement matrices, i.e., Gaussian and Fourier measurement matrices, at the same time.

The remainder of this paper is organized as follows. Section 2 describes the necessary background on CS. Section 3 describes DCS and JSM-1 in HSN, and proposes three scenarios in HSN. Section 4 presents simulation result and analysis. Finally, Sect. 5 summarizes our investigation.

2 Compressed Sensing

Consider a real-valued signal $x \in \mathbb{R}^N$, where is K-sparse, ($K \ll N$). Using the $N \times N$ basis matrix Ψ with the vectors $\{\psi_i\}$ as columns, x can be expressed as

$$x = \sum_{i=1}^{N} s_i \psi_i \qquad \text{or} \qquad x = \psi s \tag{1}$$

where s is the $N \times 1$ column vector of weighting coefficients $s_i = \langle x, \psi_i \rangle = \psi_i^T x$.

Consider a general linear measurement process that computes $M < N$ inner products between x and a collection of vectors $\{\phi_j\}_{j=1}^{M}$ as in $y_j = \langle x, \phi_i \rangle$. Arrange the measurements y_j in an $M \times 1$ vector y and the measurement vectors ϕ_j^T as rows in an $M \times N$ matrix $\boldsymbol{\Phi}$. Then, by substituting $\boldsymbol{\Psi}$ from (1), y can be written as

$$y = \boldsymbol{\Phi} x = \boldsymbol{\Phi}\boldsymbol{\Psi} s = \boldsymbol{\Theta} s \tag{2}$$

where $\boldsymbol{\Theta} = \boldsymbol{\Phi}\boldsymbol{\Psi}$ is an $M \times N$ matrix. Generally, $\boldsymbol{\Phi}$ is fixed and is independent of x.

Because $M < N$, the recovery of the signal x from y is ill-conditioned. A necessary and sufficient condition for this simplified problem to be well conditioned is restricted isometry property (RIP) and a related condition is incoherence. These two conditions can be achieved with high probability simply by selecting $\boldsymbol{\Phi}$ as a random matrix. Gaussian and Fourier measurements are commonly utilized random measurement matrices in CS framework. For Fourier measurements, after measuring, the costs of computing and communication are increasing.

Since $M < N$, to recover x from y is an under determined problem. Fortunately, optimization based on the L_1 norm

$$\hat{s} = \arg\min \|s\|_1 \quad \text{s.t.} \quad \boldsymbol{\Theta} s = y \tag{3}$$

can exactly recover K-sparse signals with high probability.

3 Joint Sparsity Model-1 and Heterogeneous Sensor Network

In an HSN, let $\Lambda := \{1, 2, \ldots, J\}$ represent the set of indices for the J sensors. Denote the corresponding signals in each sensor by $x_j \in \mathbb{R}^N$, $(j \in \Lambda)$. Without loss of generality, assume these signals are sparse in the canonical basis, i.e., $\boldsymbol{\Psi} = I_N$, where I_N is the $N \times N$ identity matrix. We denote the measurement matrix for signal j by $\boldsymbol{\Phi}_j$; $\boldsymbol{\Phi}_j$ is $M_j \times N$ and, the entries of $\boldsymbol{\Phi}_j$ are different for each j, in general. Thus, $y_j = \boldsymbol{\Phi}_j x_j$ consists of $M_j < N$ random measurements.

To compactly represent the signal and measurement ensembles, we denote $\overline{M} = \sum_{j \in \Lambda} M_j$ and define $X \in \mathbb{R}^{JN}$, $Y \in \mathbb{R}^{\overline{M}}$, and $\boldsymbol{\Phi} \in \mathbb{R}^{\overline{M} \times JN}$ as

$$X = \begin{bmatrix} x_1 \\ x_2 \\ \vdots \\ x_J \end{bmatrix}, \; Y = \begin{bmatrix} y_1 \\ y_2 \\ \vdots \\ y_J \end{bmatrix}, \; \boldsymbol{\Phi} = \begin{bmatrix} \boldsymbol{\Phi}_1 & \mathbf{0} & \cdots & \mathbf{0} \\ \mathbf{0} & \boldsymbol{\Phi}_2 & \cdots & \mathbf{0} \\ \vdots & \vdots & \ddots & \vdots \\ \mathbf{0} & \mathbf{0} & \cdots & \boldsymbol{\Phi}_J \end{bmatrix} \tag{4}$$

with $\mathbf{0}$ denoting a matrix of appropriate size with all entries equal to 0. We have $Y = \boldsymbol{\Phi} X$. Equation (4) shows that separate measurement matrices have a characteristic block diagonal structure when the entries of the sparse vector are grouped by signal.

DCS extends CS to the application of recovering a sparse signal ensemble. A JSM specifies the correlations that are present between the values and locations of the nonzero coefficients for each of the signals being acquired. In [6], three JSMs were described and three corresponding recovery algorithms were proposed. Considering different sensors measuring properties of physical processes that change slightly in time and space in an HSN, we focus on JSM-1 in this work.

In JSM-1, we assume that all signals are sharing a common sparse component z_C while each individual signal contains a sparse innovations component z_j:

$$x_j = z_c + z_j, \qquad j \in \Lambda \tag{5}$$

with $z_c = \boldsymbol{\Psi}\alpha_c$, $\|\alpha_c\|_0 = K_c$, and $z_j = \boldsymbol{\Psi}\alpha_j$, $\|\alpha_j\|_0 = K_j$. Thus, the signal z_c is common to all of the x_j and has sparsity K_c in the basis $\boldsymbol{\Psi}$. The signals z_j are the unique portions of the x_j and have sparsity K_j in the basis $\boldsymbol{\Psi}$. Similarly, we assume $\boldsymbol{\Psi} = I_N$. Using the vector and frame

$$Z = \left[z_c, z_1, z_2, \cdots, z_J\right]^T \quad \text{and} \quad \widetilde{\boldsymbol{\Phi}} = \begin{bmatrix} \boldsymbol{\Phi}_1 & \boldsymbol{\Phi}_1 & \mathbf{0} & \cdots & \mathbf{0} \\ \boldsymbol{\Phi}_2 & \mathbf{0} & \boldsymbol{\Phi}_2 & \cdots & \mathbf{0} \\ \vdots & \vdots & \vdots & \ddots & \vdots \\ \boldsymbol{\Phi}_J & \mathbf{0} & \mathbf{0} & \ldots & \boldsymbol{\Phi}_J \end{bmatrix} \tag{6}$$

we can represent the concatenated measurement vector Y sparsely using the concatenated coefficient vector Z to obtain $Y = \widetilde{\boldsymbol{\Phi}} Z$. From (6), we can see that because the common sparsity z_c appears only once in the equation, the total sparsity is reduced from $J \times (K_c + K_j)$ to $K_c + (J \times K_j)$. By using the weighted L_1-norm minimization, the FC can take advantage of exploiting inter-sensor correlation to recover a vector $\widehat{Z}$, which yields $x_j = \widehat{z_C} + \widehat{z_j}, j \in \Lambda$.

The γ weighted L_1-norm minimization is formulated as following:

$$\widehat{Z} = \arg\min \gamma_C \left\|z_C\right\|_1 + \gamma_1 \left\|z_1\right\|_1 + \gamma_2 \left\|z_2\right\|_1 \cdots + \gamma_J \left\|z_J\right\|_1 \qquad \text{s.t.} \quad y = \widetilde{\boldsymbol{\Phi}} Z \tag{7}$$

where the weights $\gamma_C, \gamma_1, \gamma_2, \ldots, \gamma_J \geq 0$ in (7) depend on the relative sparsities K_c, $K_j, j \in \Lambda$. We find the optimal γ_C using a line search optimization [11].

Since HSN consists of sensor nodes with different abilities, such as different types of measurement matrices and different numbers of measurements, we consider three possible designs for signal acquisition situation.

For convenience, we list these three scenarios in Table 1.

Table 1 Three simulated scenarios in HSN

Measurement matrix type	Numbers of measurements	
Same/different	Same/different	Scenario number
S	S	(Empty)
D	S	I
S	D	II
D	D	III

4 Simulation

In this section, we simulate signal acquisition situation of JSM-1 under three scenarios mentioned in Table 1. The γ weighted L_1-norm formulation (7) was used. We find the optimal γ_C as mentioned in Sect. 3. Since all K_j are the same in JSM-1, generally, we set all $\gamma_j = 1$. All signals are of length $N = 100$.

4.1 Different Types of Measurement Matrices and Same Numbers of Measurements (Scenario I)

In this scenario, suppose there are only two sensors with the same numbers of measurements and different types of measurement matrices. Specifically one is Gaussian measurements and another one is Fourier measurements. We restrict our attention to the symmetric setting in which $K_1 = K_2$ and $M_1 = M_2$. In our joint decoding simulations, we consider values of M_1 and M_2 in the range from 20 to 80.

The results of the simulation are summarized in Fig. 1a, b. From these two figures, we can see that percentage of exact reconstruction increases along with the increase of number of measurements per signal M in all cases. When using different types of measurement matrices, joint decoding shows better performance than when measurement matrices are all Gaussian, but it does not represent as good as all measurement matrices are Fourier.

For $K_C = 22$, $K_1 = K_2 = 4$, compared with separate decoding, joint decoding enjoys about 30 % reduction of M. For smaller K_C and larger K_j showed in Fig. 1b, since most of the measurements are expended on innovation components, joint decoding barely outperforms separate decoding.

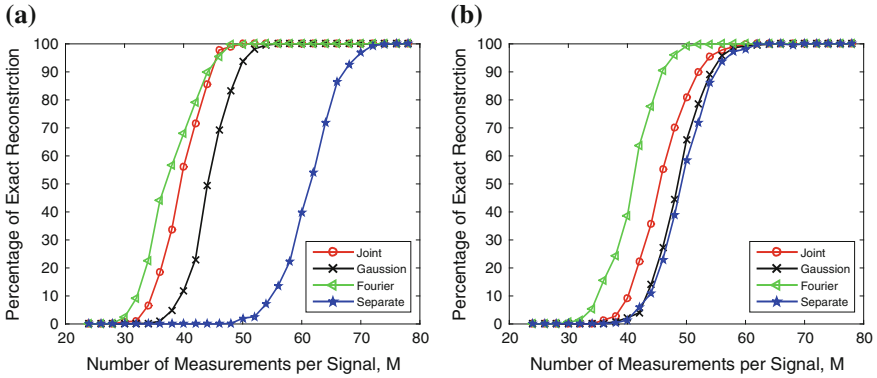

Fig. 1 Comparison of joint decoding, separate decoding with one sensor is Gaussian measurement and one sensor is Fourier measurement, all sensors are Gaussian or Fourier measurement. **a** $K_c = 22, K_1 = K_2 = 4, N = 100$. **b** $K_c = 6, K_1 = K_2 = 12, N = 100$

4.2 *The Same Types of Measurement Matrices and Different Numbers of Measurements (Scenario II)*

Without loss of generality, in this scenario, we suppose all sensors use Gaussian measurement matrices but the numbers of measurements of one kind of sensors are different with the other one. To be specific, we assume M_1 in one kind of sensors is fixed as 50 and M_2 in another kind of sensors is in the range from 10 to 90.

A common sparsity $K_C = 20$ and innovation sparsity $K_j = 5$ are investigated and suppose each kind of sensors has $J = 1, 2, 3$ sensors. The result is showed in Fig. 2a. From the simulation, we can find that the reconstruction situation is getting better

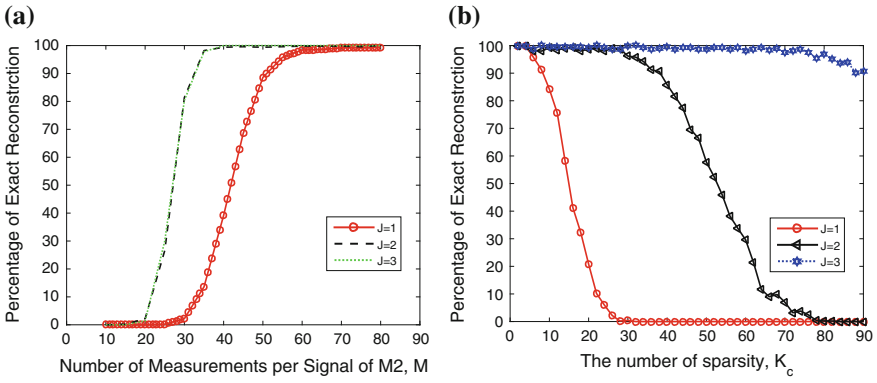

Fig. 2 Each kind of sensors has $J = 1, 2, 3$ sensors, Gaussian measurement matrices. **a** $K_c = 20$, $K_j = 5, M_1 = 50, N = 100$. **b** $K_j = 6, M_1 = 50, M_2 = 40, N = 100$

with the increase of M_2. The HSN reaches 100 % exact reconstruction at $M_2 = 50$ when $J = 1$, while it can achieve this at $M_2 = 40$ when J is 2 and 3. Actually, there are totally 4 and 6 sensors in this scheme.

Figure 2b shows another simulation result of scenario II. We increase the common sparsity K_c of each sensor and the number of each kind of sensors J while fixing the signal length and the innovation sparsity of each sensor at $N = 100$ and $K_j = 6$, respectively. In addition, the numbers of measurements of two kinds of sensors M_1 and M_2 are 50 and 40, respectively. The result shows that the percentage of exact reconstruction decreases along with the increase of number of common sparsity K_c. The HSN can reach 100 % exact reconstruction at $K_c < 70$ when $j = 3$, while the scheme cannot perform so well at $K_c > 30$ when $j = 2$. When $j = 1$, the performance of 100 % exact reconstruction drops quickly, and at $K_c = 30$ the scheme cannot recover the signals without errors.

4.3 *Different Types of Measurement Matrices and Different Numbers of Measurements (Scenario III)*

In this scenario, each one uses different types of measurement matrix and different numbers of measurements. In order to maintain consistency with the previous scenarios, we assume that one measurement matrix is Gaussian and the other is Fourier, and the rest simulation assumptions are just the same with scenario II, i.e., $K_j = 6$, $M_1 = 50$, $M_2 = 40$, $N = 100$.

Figure 3 shows the results of above assumptions. Figure 3a demonstrates when the number of each kind of sensors $J = 1$ and all sensors use Gaussian measurement matrices, the HSN scheme cannot recover the signals without errors at $K_c = 30$, but

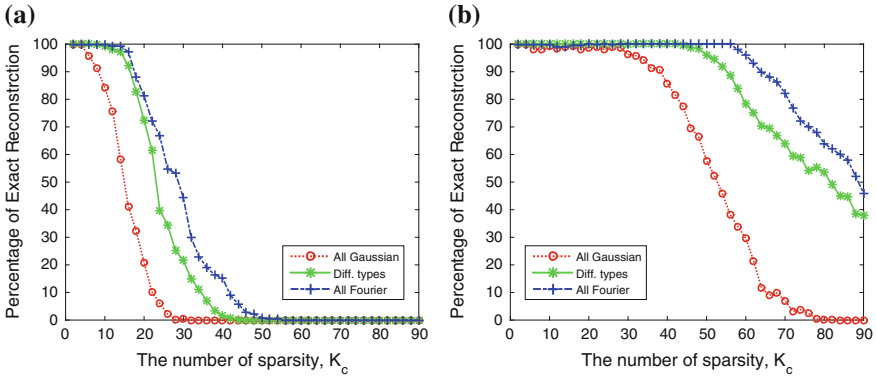

Fig. 3 Comparison of all measurement matrices are Gaussian, Fourier, and mix of these two measurement matrices when $K_j = 6$, $M_1 = 50$, $M_2 = 40$, $N = 100$, for the number of each kind of sensors $J = 1, 2$. **a** Each kind of sensors has $J = 1$. **b** Each kind of sensors has $J = 2$

when sensors in the HSN scheme use different types of measurement matrix, the number is 40. Figure 3b shows similar results but performs better for the number of each kind of sensors $J = 2$.

Although when the HSN uses both Gaussian and Fourier measurement matrices at the same time, the maximum K_c that achieves 100 % exact reconstructions less than that of all-Fourier measurement, it can reduce the computing and communication cost. So, as a compromise, the usage of DCS is still a good choice in HSN.

5 Conclusion

In this paper, combining different types of measurement matrix and different numbers of measurements, we assume three different scenarios in which HSN is used for signal acquisition and to investigate the usage of DCS in HSN. The simulation results illustrate:

1. The percentage of exact reconstruction increases along with the increase of number of measurements per signal M in all cases.
2. The percentage of exact reconstruction decreases along with the increase of number of common sparsity K_c in all cases.
3. Joint decoding that uses different types of measurement matrices performs better than that of all-Gaussian measurement matrices. However, it performs worse than that of all-Fourier measurement matrices.

In view of the computing and communication cost, DSC is a good compromise between reconstruction percentage and the number of measurements.

Acknowledgments This work was supported by the National Natural Science Foundation of China Project No. 61102140, Doctoral Fund of Ministry of Education of China Project No. 20110185120003, and the Fundamental Research Funds for the Central Universities Project No. ZYGX2012J015.

References

1. Eldar YC, Kutyniok G (2012) Compressed sensing: theory and applications. Cambridge University Press
2. Baraniuk RG (2007) Compressive sensing. IEEE Sig Process Mag 24(4)
3. Tropp J, Gilbert AC et al (2007) Signal recovery from random measurements via orthogonal matching pursuit. IEEE Trans Inf Theor 53(12):4655–4666
4. Liang Q (2010) Compressive sensing for radar sensor networks. In: Global telecommunications conference (GLOBECOM, 2010) IEEE, pp 1–5
5. Hu F, Hao Q (2012) Intelligent sensor networks: the integration of sensor networks. CRC Press, Signal Processing and Machine Learning
6. Baron D, Duarte MF, Wakin MB, Sarvotham S, Baraniuk RG (2009) Distributed compressive sensing. arXiv:0901.3403

7. Liang J, Wang Z, Liang Q (2011) Adaptive sensor selection for multitarget detection in heterogeneous sensor networks. Ad Hoc Sens Wireless Netw 12(3–4):325–342
8. Liang J, Huo Y, Mao C (2015) Multitarget detection in heterogeneous radar sensor network with energy constraint. Sig Process. doi:10.1016/j.sigpro.2015.07.020
9. Xu W, Lin J, Niu K, He Z (2012) A joint recovery algorithm for distributed compressed sensing. Trans Emerg Telecommun Technol 23(6):550–559
10. Schnelle SR, Laska JN, Hegde C, Duarte MF, Davenport M et al (2010) Texas hold'em algorithms for distributed compressive sensing. In: IEEE international conference on acoustics speech and signal processing (ICASSP), 2010, pp 2886–2889
11. Baron D, Duarte MF, Wakin MB, Sarvotham S, Baraniuk RG (2006) Distributed compressive sensing. Tech Rep TREE0612

Analysis for the Enhanced Cell Reselection Mechanism in Heterogeneous Wireless System

Xinran Zhang and Songlin Sun

Abstract This work proposes an enhanced algorithm for cell reselection mechanism in heterogeneous wireless system. A Markov model-based analytical method is proposed to describe system behavior and derive performance metric. The optimal QoS control parameter for the algorithm is derived based on system model and analyzed in numerical results. It is shown that the network performance can be improved by utilizing the proposed algorithm, and the optimal value of QoS control parameter varies according to system traffic condition, which provides insight for network deployment and radio resource management.

1 Introduction

The cell reselection process of user equipment (UE) is an important physical-layer process of cellular wireless communication system. It is defined and described in third generation partner project (3GPP) physical layer specifications [1, 2], and essentially specifies UE's behavior to choose other access cells when the power or quality of the received signal varies. In tradition, simple scenarios of cellular system like global system for mobile communication (GSM) system or third generation (3G) wideband code division multiple access (WCDMA) system, the radio access network (RAN) is constituted by the so-called macrocells, where the base station (BS) or node B (NB) serves as the access point for UEs in a wide coverage area. In that case, the cell reselection behavior happens when UE moves through the edge of different cells and requires handoff to the cell with best access quality. This scenario can be construed as homogeneous wireless system. With the emergence of fourth generation (4G) long-term evolution (LTE) standard and its rapid deployment

X. Zhang (✉) · S. Sun
Beijing University of Posts and Telecomm, No.10 Xitucheng Road, Beijing, China
e-mail: zhangxr.wspn@gmail.com

S. Sun
e-mail: slsun@bupt.edu.cn

Q. Liang et al. (eds.), *Proceedings of the 2015 International Conference on Communications, Signal Processing, and Systems*, Lecture Notes in Electrical Engineering 386, DOI 10.1007/978-3-662-49831-6_7

around the world, more complex network scenarios unlike traditional homogeneous wireless system are introduced and referred as the heterogeneous wireless systems.

The concept of heterogeneity and its related theories have become heated research topics in the past decade. In the family of 3GPP cellular systems, the typical scenario of heterogeneous wireless system consists of GSM system: enhanced data rate for GSM evolution (EDGE) system, WCDMA system, LTE system, and even in the future, fifth generation (5G) system. Within theses systems, different nodes are involved such as pico nodes and femto nodes, along with macro nodes deployed in a overlapping manner. To make the scenario more complicated, the wireless local area network (WLAN) system are also considered in heterogeneous wireless system, since the convergence of different radio access technologies (RATs) is a fundamental aspect for 3GPP cellular system and an inevitable trend of future wireless communication system. These conditions provide a much more complicated scenario for UE mobility management problem, in which the cell reselection problem has already become an important technique applied in current cellular wireless systems as well as an interesting theoretical research point.

In the field of mobility management and radio resource management (RRM) research, the Markov-related model is extensively studied and discussed in existing literatures [3–7] due to its accuracy, simplicity and validity, and is considered to be an ideal research methodology to model the cell reselection mechanism in heterogeneous wireless system. In this work, we first present the proposed mechanism for cell reselection in heterogeneous wireless system defined in 3GPP specifications, then derived a Markov mode-based analytical method for the system to obtain system performance metric, then provide detailed analysis for optimal parameter in the algorithm.

The paper is organized as follows: in Sect. 2 the cell reselection mechanism in [1] and the proposed algorithm is described. Then in Sect. 3 we present the mathematical model for the system, and derived the optimal parameter solutions to the model. Section 4 presents the main results for the optimal quality of service (QoS) parameter analysis. Section 5 concludes the paper.

2 Enhanced Cell Reselection Mechanism for Heterogeneous Wireless System

2.1 Cell Reselection Mechanism in 3GPP TS 36.304

We first present cell reselection process defined in the latest technical specification (TS) [1] in 3GPP protocol in a mathematical manner. This protocol is essentially designed for 3GPP cellular wireless system. To provide more theoretical insight, we model the system in a general manner. Consider 4G LTE system and its evolution

scenario, where adjacent macro evolved node Bs(MeNBs) form wide-area coverage for UEs in each corresponding cell (macro cell), and low power nodes (LPNs) within each cell form hot-spot coverage. The criterion for UE to perform cell reselection is the value of reference signal power denoted by P_k, where k denotes the index of different types of nodes and cells. In real application scenarios, all overlapping RAT cells in the heterogeneous wireless system have the rank of priority, according to which UE will perform cell reselection to the specific cell when P_k meets certain thresholds requirements. Priority rank parameters are broadcasted to all UE by system information or dedicated signallings [1].

For UE that has camped on others' cells adjacent to cell k, if P_k is large enough, the UE will try to reselect to cells k for better access service. Define T_k^{in} as the threshold for P_k when UE tries to camp on cell k, above which UE will try to perform cell reselection to cell k. For UE already camped on cell k, if P_k is too small, it will try to reselect to other cells. Define T_k^{out} as the threshold for P_k when UE tries to camp on other cells, below which UE will try to perform cell reselection to other cells. Assume UE currently camps on cell k, and try to perform cell reselection to other cells with different priority ranks. Let the cell with index h represent the cell with higher priority, and let the cell with index l represent the cell with lower priority. The algorithm for cell reselection is summarized as follows:

- If $P_h > T_h^{in}$ holds for a consecutive time $t_{reselection}$, UE shall perform cell reselection from cell k to cell h.
- If $P_l > T_l^{in}$ and $P_k < T_k^{out}$ hold for a consecutive time $t_{reselection}$, UE shall perform cell reselection from cell k to cell l.

If more than one cell meets the above requirements, UE shall perform cell reselection to the cell with highest priority.

2.2 Enhanced Algorithm for Admission Control

Consider the scenario where 4G LTE MeNB or LPN nodes bear large amount of traffic and has potential risk of data congestion. The admission control mechanism is needed to prevent overload and protect QoS for UEs. We derive our new algorithm on the basis of previous algorithm in [7] for general heterogeneous wireless environment. Consider the scenario when cell k is overload and admission control is needed. We aim to prevent UEs in other cell to perform cell reselection to cell k and encourage UEs on the edge of cell k to perform cell reselection to other cells. When overload happens in cell k, an indicator bearing the index of k is broadcasted to all UEs within the system in the same manner as the rank of priority parameters for the purpose of informing UEs to initiate the admission control mechanism for cell k.

Define multiplication factor $\phi \in [0, 1]$. UE will adjust thresholds for cell reselection to achieve admission control as follows:

- For all UEs:
  - replace T_k^{in} with $T_k^{in} \times (1 + \phi)$, and replace T_k^{out} with $T_k^{out} \times (1 - \phi)$.
  - replace T_l^{in} with $T_l^{in} \times (1 - \phi)$.
  - replace T_h^{in} with $T_h^{in} \times (1 - \phi)$.
- For UEs in cell l that meet $P_k > T_k^{in} \times (1 + \phi)$, UE performs cell reselection to cell k with probability $Pr^{in}(P_k, T_k^{in}, \phi)$
- For UEs in cell k that meet $P_h > T_h^{in} \times (1 - \phi)$, UE performs cell reselection to cell h with probability $Pr^{in}(P_h, T_h^{in}, \phi)$
- For UEs in cell k that meet $P_l > T_l^{in} \times (1 - \phi)$ and $P_k < T_k^{out} \times (1 - \phi)$, UE performs cell reselection to cell l with probability $Pr^{out}(P_k, T_k^{out}, \phi)$
- For UEs in cell h that meet $P_k > T_k^{in} \times (1 + \phi)$ and $P_h < T_h^{out} \times (1 - \phi)$, UE performs cell reselection to cell k with probability $Pr^{out}(P_h, T_h^{out}, \phi)$

The function $Pr^{in}(P, T, \phi)$ and $Pr^{out}(P, T, \phi)$ represent the probability of UEs to perform extra reselection behavior according to the proposed algorithm. To maintain consistency with 3GPP protocols, the function should be an interpolation between the probability of $[0, 1]$ in the domain of $[T, T \times (1 + \phi)]$ and $[T \times (1 - \phi), T]$. ϕ represents the admission control intensity. Let ρ denote the order of polynomial interpolation which is not deeply discussed in this paper, and $U(x)$ denotes the unit step function. Denote $T \times (1 + \phi)$ as $\hat{T}$, and $T \times (1 + 0.5\phi)$ as T_m. We propose the following theorem for the functions:

Theorem 1 *Define polynomial interpolation of $Pr^{in}(P, T, \phi)$ and $Pr^{out}(P, T, \phi)$ as follows:*

$$Pr^{in}(P, T, \phi) = \mathbb{P} \times U(P - T) + (1 - \mathbb{P}) \times U(P - \hat{T}). \tag{1}$$

$$Pr^{out}(P, T, \phi) = (\mathbb{P} - 1) \times U(P - T) - \mathbb{P} \times U(P - \hat{T}) + 1. \tag{2}$$

$$\mathbb{P} = 0.5 \left[\left(\frac{P - T}{0.5\phi T} \right)^{\rho} - 1 \right] U(T_m - P) + 0.5 \left[1 - \left(\frac{\hat{T} - P}{0.5\phi T} \right)^{\rho} \right] U(P - T_m) \tag{3}$$

When $\phi \to 0$ and $\rho \to \infty$, the proposed algorithm will degrade to the original cell reselection algorithm.

Proof By performing some algebra manipulations, the polynomial interpolation function will degrade to step function $U(P - T)$ with $\phi = 0$ and $\rho \to \infty$, which is equivalent to the function for the original cell reselection algorithm. □

3 Optimal Parameter Analysis Model

3.1 Markov Chain-Based System Model

In order to evaluate the performance of our proposed model, we utilize Markov model to describe system behavior. Due to limitation of space, we adopt a simple co-sited integrated LPN–MeNBs heterogeneous wireless system where two MeNBs serve as macrocells for 4G LTE and 3G CDMA RANs, and one LPN in the center of the cell serves for hot-spot coverage. The radius of 4G LTE MeNB cell is assumed to be larger than LPN cell and smaller than 3G CDMA cell. We leave more complicated scenarios where MeNB is coupled with various LPN nodes and adjacent MeNBs for future work. To model the system behavior, we adopt the Markov model and define the three-dimension state vector as follows:

$$\mathbf{s} = (n_{3G}, n_{4G}, n_{LPN}), \tag{4}$$

where n_{3G}, n_{4G}, and n_{LPN} denote the numbers of UEs camped on 3G CDMA MeNB cell, 4G LTE MeNB cell and LPN cell, respectively, with their maximum load number denoted by n_{3G}^{MAX}, n_{4G}^{MAX}, and n_{LPN}^{MAX}, respectively.

The mobility of UEs is described by the arrival rates of events that occur when UEs perform powering on or off and choose the best cell to camp on, as known as cell selection, or when UEs move through the edges of the cells and perform cell reselection. Those events are modeled as the Poisson process for analysis convenience. For simplicity we assumed that $T_k^{out} = T_k^{in} = T_k$, and adopt the simplified path loss model and ignore fading impacts. Let d_k denotes the radius of cell k, we have the following equation:

$$T_k = P_t K \left[\frac{d_0}{d_k}\right]^{\gamma}, \tag{5}$$

where P_t denotes the transmission power of the node, K denotes the constant determined by antenna parameters and average channel loss, and d_0 denotes the reference distance of antenna in far field. In such scenario, T_k multiplied by $(1 \pm \phi)$ in the algorithm in Sect. 2.2 is equivalent to d_k multiplied by $(1 \pm \phi)^{-\frac{1}{\gamma}}$.

To model events in the system based on geology assumptions above, denote λ^N as the arrival rate of event per unit area in which case new UEs power on and perform cell selection. Also, denote μ as the departure rate for UEs that power off and leave the system. For 3G CDMA MeNB cell, 4G LTE MeNB cell and LPN cell, the corresponding arrival rates of new UEs are given as follows:

$$\lambda_{3G}^N = \lambda^N \times \pi(d_{3G}^2 - d_{4G}^2), \tag{6}$$

$$\lambda_{4G}^N = \lambda^N \times \pi(d_{4G}^2 - d_{LPN}^2), \tag{7}$$

$$\lambda_{LPN}^{N} = \lambda^{N} \times \pi d_{LPN}^{2}. \tag{8}$$

For each cell, the corresponding departure rate of events in which case UEs power off is denoted by $\mu_{3G} = \mu \times n_{3G}$, $\mu_{4G} = \mu \times n_{4G}$ and $\mu_{LPN} = \mu \times n_{LPN}$ respectively.

Denote λ_k^R as the arrival rate of event per unit in which case UEs perform cell reselection when roaming through the edge of cell k. Consider the ring area on the edge of the cell, the number of UEs within this ring is proportional to its size. Thus the rates of cell reselection events are given as follows:

$$\lambda_{3G-4G}^{R} = \lambda^{R} \times \frac{2\pi d_{4G} \times \Delta d_{4G}}{\pi \left(d_{3G}^{2} - d_{4G}^{2}\right)} \times n_{3G}, \tag{9}$$

$$\lambda_{4G-3G}^{R} = \lambda^{R} \times \frac{2\pi d_{4G} \times \Delta d_{4G}}{\pi \left(d_{4G}^{2} - d_{LPN}^{2}\right)} \times n_{4G}, \tag{10}$$

$$\lambda_{4G-LPN}^{R} = \lambda^{R} \times \frac{2\pi d_{LPN} \times \Delta d_{LPN}}{\pi \left(d_{4G}^{2} - d_{LPN}^{2}\right)} \times n_{4G}, \tag{11}$$

$$\lambda_{LPN-4G}^{R} = \lambda^{R} \times \frac{2\pi d_{LPN} \times \Delta d_{LPN}}{\pi d_{LPN}^{2}} \times n_{LPN}, \tag{12}$$

where Δd_k denotes the width of the ring on the edge of cell k, and $2\pi d_k \times \Delta d_k$ denotes the estimated size of the ring.

$$P_{\mathbf{mn}} = \begin{cases} \lambda_{3G}^{N}/\lambda_{sum}, & \text{if } n_{3G} = m_{3G} + 1, n_{4G} = m_{4G}, n_{LPN} = m_{LPN} \\ \lambda_{4G}^{N}/\lambda_{sum}, & \text{if } n_{3G} = m_{3G}, n_{4G} = m_{4G} + 1, n_{LPN} = m_{LPN} \\ \lambda_{LPN}^{N}/\lambda_{sum}, & \text{if } n_{3G} = m_{3G}, n_{4G} = m_{4G}, n_{LPN} = m_{LPN} + 1 \\ \lambda_{3G-4G}^{N}/\lambda_{sum}, & \text{if } n_{3G} = m_{3G} - 1, n_{4G} = m_{4G} + 1, n_{LPN} = m_{LPN} \\ \lambda_{4G-3G}^{N}/\lambda_{sum}, & \text{if } n_{3G} = m_{3G} + 1, n_{4G} = m_{4G} - 1, n_{LPN} = m_{LPN} \\ \lambda_{4G-LPN}^{N}/\lambda_{sum}, & \text{if } n_{3G} = m_{3G}, n_{4G} = m_{4G} - 1, n_{LPN} = m_{LPN} + 1 \\ \lambda_{LPN-4G}^{N}/\lambda_{sum}, & \text{if } n_{3G} = m_{3G}, n_{4G} = m_{4G} + 1, n_{LPN} = m_{LPN} - 1 \\ \mu_{3G}/\lambda_{sum}, & \text{if } n_{3G} = m_{3G} - 1, n_{4G} = m_{4G}, n_{LPN} = m_{LPN} \\ \mu_{4G}/\lambda_{sum}, & \text{if } n_{3G} = m_{3G}, n_{4G} = m_{4G} - 1, n_{LPN} = m_{LPN} \\ \mu_{LPN}/\lambda_{sum}, & \text{if } n_{3G} = m_{3G}, n_{4G} = m_{4G}, n_{LPN} = m_{LPN} - 1 \\ 0, & \text{otherwise} \end{cases}. \tag{13}$$

3.2 Dynamic Equations and Performance Metric

For a given state, its transition behavior depends on the cumulation of all possible Poisson events. To describe the transition probability of the state vector, define

Table 1 Parameters configuration

Parameter	Value	Parameter	Value	Parameter	Value
d_{3G}	1.2 km	n_{3G}^{MAX}	10	ρ	1
d_{LTE}	1.0 km	n_{4G}^{MAX}	10	ϕ	0–0.5
d_{LPN}	0.6 km	n_{LPN}^{MAX}	10	η	0.8
λ^N	0.12–0.22/s/km^2	λ^R	0.1/s/km^2	μ	0.01/s/km^2
γ	2.2	Q^S	1	θ	0.5
Δd_k	$0.01 \times d_k$				

cumulative event rate as follows:

$$\begin{aligned}\lambda_{sum} = \lambda_{3G}^N + \lambda_{4G}^N + \lambda_{LPN}^N + \lambda_{3G-4G}^N \\ + \lambda_{4G-3G}^R + \lambda_{4G-LPN}^R + \lambda_{LPN-4G}^R + \mu_{3G} + \mu_{4G} + \mu_{LPN}.\end{aligned} \tag{14}$$

For the state transition from state $\mathbf{m} = (m_{3G}, m_{4G}, m_{LPN})$ to state $\mathbf{n} = (n_{3G}, n_{4G}, n_{LPN})$, its transition probability denoted by $P_{\mathbf{mn}}$ conforms to the cumulation characteristics of Possion process and is given as Eq. (13).

Let $p_{\mathbf{n}}$ denote the static probability of state $\mathbf{n}$. The static probability conforms the constraints in Eq. (15) and can be solved by numerical methods.

$$p_{\mathbf{n}} \geq 0, p_{\mathbf{n}} = \sum_{\mathbf{m}} P_{\mathbf{m},\mathbf{n}} \times p_{\mathbf{m}}, \sum_{\mathbf{n}} p_{\mathbf{n}} = 1, \forall \mathbf{n}. \tag{15}$$

Due to the limitation of space, we only present the QoS analysis method for the system. Consider the evaluation for the average QoS for cell k. For non-congestion traffic status, define Q^S as the standard QoS value for each UE. If the number of UEs camping on the cell is too large, the average QoS of UEs in the cell is likely to be degraded and the system needs to perform admission control. Define overload fraction factor $\eta \in (0, 1)$, and QoS penalty factor $\theta \in (0, 1)$. If $n_k > \eta n_k^{MAX}$ holds, the QoS value for each UE is degraded to be θQ^S. Hence the average QoS metric for the system is denoted by the Eq. (16). Apparently, the reselection control intensity ϕ and the order of interpolation ρ will affect the system performance and reflects on the value of Q_k. Thus, the optimal parameter in the enhanced cell reselection mechanism for admission control of cell k is given in Eq. (17).

$$Q_k = \sum_{n_k > \eta n_k^{MAX}} p_{\mathbf{n}} n_k \theta Q^S + \sum_{n_k \leq \eta n_k^{MAX}} p_{\mathbf{n}} n_k Q^S \tag{16}$$

$$\phi^* = \arg\max_{\phi} [Q_k(\phi, \rho)], \phi \in [0, 1] \tag{17}$$

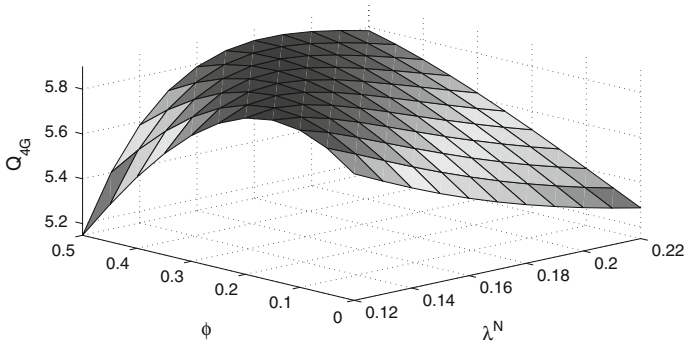

Fig. 1 Impact of ϕ on average QoS for 4G cell

4 Numerical Results

The parameters of the network model is configured as shown in Table 1. We set the maximum UE number to be very small to avoid the well-known computation complexity of Markov model. Due to limited space of this work, we leave the complex model and its solution for future work. The result for average QoS metric for 4G cell is shown in the following figure (Fig. 1). As we can see, the optimal admission control intensity parameter ϕ varies in different traffic condition. Also, if ϕ is too large the performance will degrade since the admission control algorithm affects UEs within the local cell. If ϕ is too small, the algorithm will not effectively prevent overload and achieve best performance. The optimal ϕ can be obtained by numerical methods when utilizing our algorithm.

5 Conclusion

In this work, we propose the enhanced algorithm for cell reselection in heterogeneous wireless system and the analytical model to evaluate system performance. Numerical result shows that the proposed algorithm achieves best performance when assigned a suitable parameter of admission control intensity. Further work includes more complex mathematical model and parameter scenarios for the system, and effective methods to evaluate the performance in such complex system scenarios.

References

1. 3GPP TS 36.304 V12.3.0 (2014–2012) Technical Specification Group Radio Access Network; Evolved Uniervesal Terrestial Radio Access (E-UTRA); User Equipment (UE) procedures in

idle mode (Release 12)
2. 3GPP TS 36.133 V12.6.0(2014–2012) Technical Specification Group Radio Access Network; Evolved Uniervesal Terrestial Radio Access (E-UTRA); Requirements for support of radio resource management (Release 12)
3. Lee Y, Chuah T, Lo J, Vinel A (2014) Recent advances in radio resource management for heterogeneous LTE/LTE-A networks. IEEE Commun Surv Tutorials 16(4):2142–2180
4. Olmos J, Ferrus R, Galeana-Zapien H (2013) Analytical modeling and performance evaluation of cell selection algorithms for mobile networks with backhaul capacity constraints. IEEE Trans Wirel Commun 12(12):6011–6023
5. Kim T, Yang Y, Hou J, Krishnamurthy V (2013) Resource allocation for qos support in wireless mesh networks. IEEE Trans Wirel Commun 12(5):2046–2054
6. Zhang X, Jin H, Ji X, Li Y, Peng M (2012) A separate-SMDP approximation technique for RRM in heterogeneous wireless networks. In: Proceedings of IEEE wireless communication networking conference WCNC (WCNC'12), pp 2087–2091
7. Zhang X, Jin H, Ji X, Jia Y, Wang W, Peng M (2012) An enhanced cell reselection mechanism and network analysis model in 3G/LTE heterogeneous system. In: Proceedings of international conference on wireless communication signal process (WCSP'12)

Part II
Ad Hoc and Short Range Networks

Energy Dissipation Balance Scheme in Dynamic Ad Hoc Networks

Yuheng Fang, Jianyi Shi, Zhuo Sun, Song Kong and Sese Wang

Abstract In order to balance energy allocation to extend the lifetime of dynamic ad hoc networks, the Relay Node Backup Power Control (RNBPC) scheme is proposed using Markov decision process. Through theoretical proof and simulations, an expected energy-balanced network can be achieved by collecting information of transmission probability of every node in the network and predict the future transmission situation in preprocess period. During preprocess period, we initialize the network by the combination of two proved schemes. Once we find the nodes which have heavy communication task, evaluated by the transmission probability, then the scheme searches the feasible backup relay node to share the communication task to avoid energy running out too quickly. Simulation results show that the RNBPC scheme can relieve traffic nodes and then balance the energy dissipation of every node as well to extend the lifetime of the whole network.

1 Introduction

Recent years, mobile ad hoc networks (MANETs) have become the major short-distance wireless networks, especially when the Internet of Things has been emerging. Most of the sensors and communication ends in MANETs have power dissipation

Y. Fang (✉) · J. Shi · Z. Sun · S. Kong · S. Wang
Key Laboratory of Universal Wireless Communications,
Beijing University of Posts and Telecommunications, Beijing, China
e-mail: yhfang@bupt.edu.cn

J. Shi
e-mail: Shijianyi@bupt.edu.cn

Z. Sun
e-mail: zhuosun@bupt.edu.cn

S. Kong
e-mail: kongsong@bupt.edu.cn

S. Wang
e-mail: buptyt@bupt.edu.cn

Q. Liang et al. (eds.), *Proceedings of the 2015 International Conference on Communications, Signal Processing, and Systems*, Lecture Notes in Electrical Engineering 386, DOI 10.1007/978-3-662-49831-6_8

sensing due to the lack of sustainable and stable energy supply, for the reason of that battery cannot be recharged once the network starts working. Therefore, power consumption control and energy saving schemes are very important for MANETs to improve network stability and prolong the lifetime of whole communication system.

Traditional power control schemes have been proposed to reduce the interference and energy consumption in MANETs. Many adaptive power control schemes have been proposed, mainly including the centralized and distributed methods. Centralized optimizations require a centralized controller, which assists to collect the information of all the rest of the nodes and adjusts the transmission power for each of them. But the obvious defect is the extra power which would be wasted when the centralized controller is collecting the information and this will also result in network latency.

Many research works put the efforts on distributed power control schemes. In Ref. [1], a distributed power control algorithm, DTRNG, was put forward based on the Relative Neighborhood Graph (RNG) [2]. The DTRNG aims to minimize the total transmission power while maintaining the connectivity of the network. The DTRNG first searches the neighbor nodes and determines the minimal transmission power by reducing the power gradually for every node. Then the DTRNG algorithm removes the largest edge of each triangle of RNG to reduce the transmission power and keep the network connected. Furthermore, the DTRNG is developed to be the DTCYC algorithm, which removes the largest edge of each circle when the DTRNG work has done. Therefore, the DTCYC is more efficient in saving energy and can thus prolong the lifetime of the network.

However, the DTCYC algorithm only focuses on the total transmission power and has not taken the influence of dynamic communication environment into consideration. Therefore, the DTCYC algorithm is not suitable when delay-sensitive applications need to be transmitted across the multi-hop wireless networks. An autonomic and distributed joint routing and power control scheme was proposed in Ref. [3], which enables the nodes to autonomously determine their routing and transmission power to maximize the network utility in a dynamic environment. In this method, the problem was formulated as a Markov decision process. According to the state transition probability, a distributed scheme, which can find the optimal policy through reinforcement learning when the dynamics are unknown, is presented for only a restricted braid topology.

Energy consumption is an important performance metric for wireless sensor networks, and in many cases wireless transmission is the major factor, which largely depends on the distance between transceivers. In Ref. [4], a precise model based on probabilistic distance distributions using the geometric properties of grid-based clustering is presented. An optimal power control scheme for mobile ad hoc networks, which optimizes the hop count according to the distance between the source and the destination nodes for improving the network's capacity, is proposed in Ref. [5]. Considering that the total length of the path segments is usually much larger than the Euclidean distance between the source–destination pair in the multi-hop routing methods, which results in more total power consumption of the involved mobile nodes. In Ref. [6], an adaptive and distance-driven power control (ADPC) scheme,

which determines the optimal number of relay nodes and the best position of these relay nodes, is proposed. The ADPC algorithm first computes the optimal number and the sites of relay nodes between the source and the destination nodes. Then the ADPC scheme searches feasible relay nodes around the optimal virtual relay-sites and selects one link with the minimal total transmission energy consumption for data transmission. The ADPC scheme can both save energy and reduce the end-to-end latency of the transmission.

2 Problem Formulation

In DTCYC algorithm, we can achieve the minimal total power consumption in mobile ad hoc networks. However, this algorithm does not take the realistic communication situation into consideration. Given that if Node A communicates to Node F most frequently in Fig. 1, according to DTCYC algorithm, we only have the communication route: ACDEGF. Obviously, this link is not the best route to transmit data packets from Node A to Node F, when comparing to the link: ACF, on the efficient of saving energy. Another problem is that if the total probability of Node A transmits data to Node F and Node B communicates to Node G is over 50 % or more higher, Node C would be the most frequent relay node in communication and thus the power consumption of Node C would be the highest, so its lifetime would be the shortest. And once one relay node dies, the whole system would have a disaster in further communication.

In Ref. [6], an adaptive and distance-driven power control scheme was proposed by means of distance research in random geometrics. According to the ADPC scheme, the optimal number of relay nodes and the optimal location of each node for data transmission can be obtained when a distance is given. Furthermore, we can choose an optimal communication route between source–destination pair by searching around the optimal location. The search range is a circle with the virtual relay-site

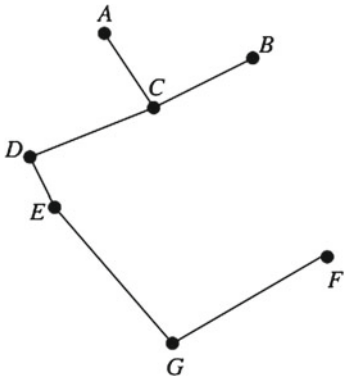

Fig. 1 Application of DTCYC algorithm

(OVS) as the center and r as the radius. This scheme can help find the optimal communication route. However, the ADPC scheme also encounters the problem that the DTCYC has been facing with, the Node C would also become the most frequent relay node. Therefore, the ADPC also has not taken the case that one or more specific nodes would bear heavy task on forwarding data, which would shorten the node's lifetime, into careful consideration.

Considering that transmission probability in a network usually keeps a distribution over the restricted range, which can be figured out by statistics. In this paper, we introduce a scheme to improve the performance of ADPC scheme using Markov decision process, called Relay Node Backup Power Control (RNBPC) scheme. The simulation results demonstrate that the RNBPC algorithm achieves a more optimal performance in saving total energy in a dynamic environment.

3 Relay Node Backup Power Control Scheme

Now the problem to be solved in this paper can be stated as: Given a mobile ad hoc network, assume that the nodes transmission probability can be described as a matrix **P**, then the total power consumption could be optimized using Markov decision process (MDP) based on the DTCYC algorithm and the ADPC scheme.

In this section, we put forward a distributed scheme to balance energy allocation and optimize the total power consumption. We first use DTCYC algorithm to start the communication inside the network and record every node's neighbor nodes. Then we use ADPC scheme to determine the optimal route of source–destination pairs and update the record table of each node. Second, we collect the information of every node's transmission probability during a certain period T and then use the collection to initialize the transmission probability matrix **P**. Finally, we analyze **P** to determine whether some nodes have excessive communication task. If these nodes do exist, we use matrix **P** to pick up a backup node for these nodes to get a relief in communication. Through the Relay Node Backup Power Control (RNBPC) scheme, we achieve an optimal energy consumption balance for nodes in the network, which would greatly extend the lifetime of the network.

3.1 Initialize Transmission Probability Matrix P Using the DTCYC Algorithm and the ADPC Scheme

In our scheme, initializing the transmission probability matrix **P** correctly is very important. At first, the situation of the network is not known, especially when the network is dynamic. We first choose the DTCYC algorithm to determine and record each node's theoretical minimal transmission power while maintaining the connectivity of the network. However, the DTCYC algorithm does not help us to select an

optimal route between source and destination nodes, except the minimal total power consumption. Subsequently, we choose the ADPC scheme to get an optimal route for each node's transmission. After the calculation, the record table for every node should get updated with the optimal route information. Then we run the network according to the records for a certain period T. During this period, we collect the transmission statistics. When T runs out, we use the statistics to initialize the matrix **P**. The above process can be described as Transmission Probability Matrix Initialization (TPMI) algorithm.

According to the DTCYC algorithm, we can adjust transmission power $p_1, p_2, \ldots, p_n$ to minimize total power consumption $\sum_{i=1}^{n} p_i$ while maintaining the connectivity of the network. Then, the ADPC scheme helps us to choose the optimal route in the topology that the DTCYC algorithm has built. According to mathematical proof in Refs. [1] and [6], we achieve a balance between total power consumption and optimal route. Finally, we choose a time threshold T, which should be determined by practical situation, to run the network to collect transmission information. Therefore, the initialization algorithm is convincing in maintaining low power consumption.

3.2 Determine Backup Nodes for Traffic Relay Nodes

Once we get the transmission probability matrix **P**, which can be stated as formulation (1), then we can predict the transmission probability of next period.

$$\mathbf{P} = \begin{bmatrix} p_{11} & \cdots & p_{1n} \\ \vdots & \ddots & \vdots \\ p_{n1} & \cdots & p_{nn} \end{bmatrix} \tag{1}$$

The variable p_{ij} presents the data forwarding probability between Node i and Node j, where Node i is the transmitter and Node j is the receiver.

Considering the theory of Markov decision process, once we do a matrix multiply, we get $\mathbf{P} \times \mathbf{P}$ or $\mathbf{P}^2$, thus we can achieve the transmission probability of next period. According to the meaning of $\mathbf{P}^2$, we can figure out the transmission probability of Node i in next stage by just adding the probability of ith column together. Thus, we can predict the transmission situation of every node in the next period T. We introduce a variable marked as p_0, which presents the threshold to determine whether the state of one node is overloaded. If $p_i > p_0$, then we claim that Node i has too much communication task, which would break the balance of the overall energy consumption. Then we search the route table of Node i to find a suitable backup node, which should be much less busy and its communication probability is far under the threshold. If we find one, we use it as a backup for Node i to reallocate the communication task between Node i and this node to achieve a communication power consumption balance. In Fig. 2, for example, we set p_0 to 35 % and assume that Node C has heavy communication task, and then we choose Node D as the backup node for Node C

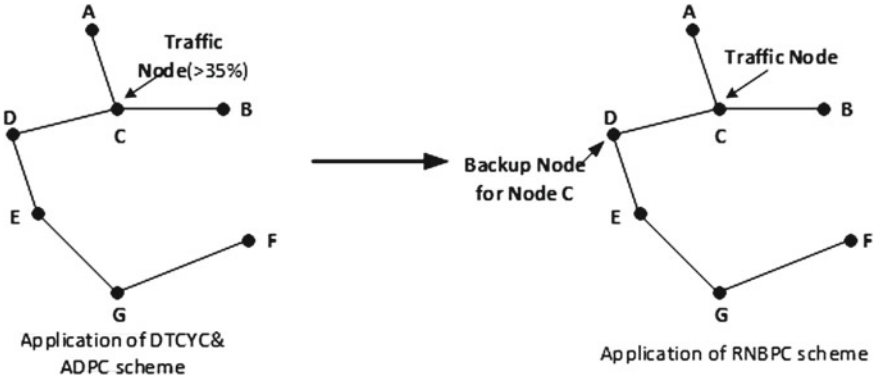

Fig. 2 Finding backup node for traffic node using RNBPC

which is determined by the transmission probability of next period. At the end of each period, the matrix **P** should be updated to keep the information of every node being real time.

According to Markov decision process, we can achieve the next state transition probability. When the variable T is big enough, the prediction is more precise. Thus we could predict the situation of each node in order to determine whether choose a backup node for the traffic node from its optimal neighbor nodes and then adjust the transmission route.

4 Performance Evaluation

In order to evaluate the performance of the proposed RNBPC scheme, we compare it with the ADPC scheme, mentioned before.

We consider a square field with a size of $500 \times 500\,\mathrm{m}^2$, where 150 nodes are randomly deployed. Assume that the amount of data generated by each node per round is 1 KB. In preprocess period, we here set the time threshold T as 1 h and set the baseline of p_0 to judge whether a node is traffic as 35 %.

According to Ref. [6], we get the basic simulation parameters and calculation formulations. Thus, we let $E = E_{tx} + E_{rx}$ be the total energy consumption for each node, which is composed of two parts: the receiving cost $E_r x = Q(i)E_{elec}$ and the transmission power $E_{tx} = Q(i)(E_{elec} + \varepsilon d^{\lambda})$. Here, d is the distance between the source and the destination; λ represents the path loss exponent ($\lambda \geq 2$); and $Q(i)$ represents the amount of data transmitted/received by a node. According to Ref. [7], E_{tx} can be computed as formulation (2):

$$\mathrm{E_{tx}} = \begin{cases} Q\,(\mathrm{i}) \times \left(\mathrm{E_{elec}} + \varepsilon_{\mathrm{Friis}} \mathrm{d}^2\right) & d \leq \mathrm{d}_0 \\ Q\,(\mathrm{i}) \times \left(\mathrm{E_{elec}} + \varepsilon_{\mathrm{two-ray}} \mathrm{d}^4\right) & d \geq \mathrm{d}_0 \end{cases} \tag{2}$$

Here, we let the energy consumed per bit in the transceiver electronics be $E_{elec} =$ 50nJ/bit, the coefficients $\varepsilon_{Friis} = 10pJ/(bit{\cdot}m^2)$, $\varepsilon_{two-ray} = 0.0013pJ/(bit{\cdot}m^4)$, and the threshold distance $d_0 = 75$m.

Considering that RNBPC is designing for balancing the overall energy allocation and the power consumption of the entire network, we conduct two simulation experiments to examine the average power consumption and max energy dissipation of certain single node, respectively. Figure 3 shows the average dissipated energy of all the nodes with a varying number of relay nodes. Obviously, the RNBPC curve wastes 4 % more power consumption than the ADPC does.

Figure 4 shows the max energy dissipation of single node. In RNBPC, we achieve 15 % less energy dissipation than the ADPC scheme does, which means we can get a more balanced network through RNBPC scheme. Therefore, the main concept of RNBPC scheme is to sacrifice little power consumption to achieve overall energy allocation balance and thus, to extend the lifetime of whole network.

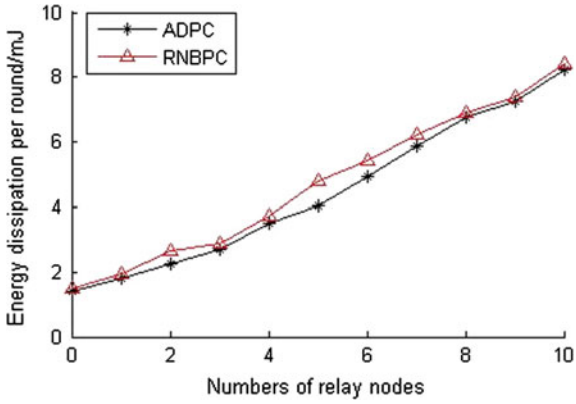

Fig. 3 Total energy consumption RNBPC versus ADPC

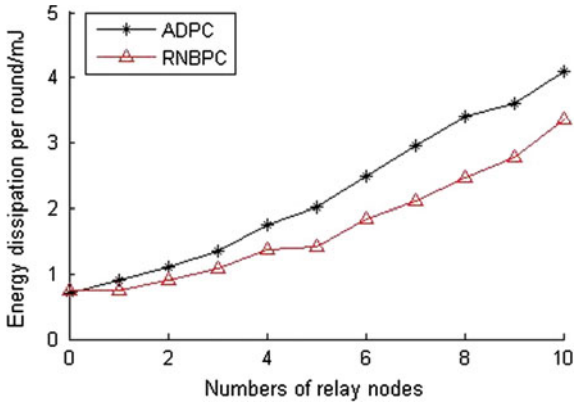

Fig. 4 Single node's max energy consumption RNBPC versus ADPC

5 Conclusion

Aiming at finding optimal energy allocation scheme to extend the lifetime of the whole network and achieving optimal average energy dissipation, we study the problem of transmitting probability of every node while packets are transmitted from the source to the destination. The proposed RNBPC scheme, which is based on the DTCYC algorithm and the ADPC scheme, uses MDP to predict transmission situation in next period and get the optimal energy allocation using backup relay nodes to relieve traffic ones. The simulation results show that we achieve a balance of energy allocation by sacrificing little energy consumption than the minimal dissipation. In future, we plan to study an optimal scheme to decrease the average energy consumption while ensuring the best energy allocation balance.

Acknowledgments This work was supported by The China National Natural Science Fund under grant 61271181 and 61171109, and the joint project with China Southwest Institute of Electronic and Telecommunication Technology.

References

1. Chen X, Rowe N (2011) Saving energy by adjusting transmission power in wireless sensor networks. In: IEEE Global Telecommunications Conference. Houston, TX, USA, pp 6134029-1–6134029-5
2. Santi P (2005) Topology control in wireless ad hoc and sensor networks. Wiley, New York
3. Lin Z, Schaar M (2011) Autonomic and distributed joint routing and power control for delay- sensitive applications in multi-hop wireless networks [J]. IEEE Trans Wirel Commun 10(1):102–113
4. Zhuang Y, Pan J, Cai L (2010) Minimizing energy consumption with probabilistic distance models in wireless sensor networks. In: 30th IEEE International conference on computer communications (INFOCOM). San Diego, CA, USA, pp 1–9
5. Ramaiyan V, Kumar A, Altman E (2012) Optimal hop distance and power control for a single cell, dense, ad hoc wireless network. IEEE Transactions on Mobile Comput 11(11):1601–1612
6. Tao J, Liu Y, Xiao P, Zhu L, Chen W (2012) Adaptive and distance-driven power control scheme in mobile ad hoc networks. J Southeast Univ 29(3):252–258
7. Rapport T (1996) Wireless communications: principles and practice. Prentice Hall, NewJersey

Research and Design of Monitoring Smog System Based on Wireless Intelligent Network

Yanping Wu, Jincheng Wu, Jian Chen, Yingjie Wang, Yongyue Yang, Xin Lu and Qiufang Yu

Abstract This paper is based on the wireless intelligent network which implement for real-time monitoring of smog, using STM32F407 as master chip, combining with the smog sensor module, 2.4 G wireless communication module, GSM communication module, and the corresponding peripheral hardware and software to realize monitoring smog. In the end, with LCD screen displaying, web pages to monitor and message reception mode to realize the real-time monitoring of smog concentration. Wireless network can be moved, do not need large wiring and convenient erection because of its flexibility, replacing the traditional wired network, becoming the new trend in the development of communication technology gradually. Using wireless network technology can also reduce the intelligent network system limitation which causes of terrain, geography and price factors, making the intelligent network system widely used in various fields, meeting needs of the wireless monitoring on the most occasions. After the test, the design has been basically achieved the functions and the expected effect and it has a good application prospect.

Keywords STM32F407 · NRF24L01 · Smog monitoring · GSM

1 Introduction

The wide application of computer network and embedded technology [1], the continuous development of electronic information and communication technologies are further to improve people's lives and ensure people's health. Wireless intelligent network based on embedded technology as a kind of advanced and cheap monitoring technology, providing a new solution for the development of video surveillance equipment.

Y. Wu · J. Wu (✉) · J. Chen · Y. Wang · Y. Yang · X. Lu · Q. Yu
College of Electronic and Communication Engineering,
Tianjin Normal University, Tianjin, China
e-mail: wdxywjc@mail.tjnu.edu.cn

Q. Liang et al. (eds.), *Proceedings of the 2015 International Conference on Communications, Signal Processing, and Systems*, Lecture Notes in Electrical Engineering 386, DOI 10.1007/978-3-662-49831-6_9

Wireless monitoring has played a great role in smog monitoring, warning when the concentration of smog is overproof, reminding people of going out less often to protect themselves. At present, the smog monitoring technology is not very perfect around the world, people also have more and more high requirement of smog monitoring, traditional way of monitoring and transmission has lost its advantages, wireless intelligent network monitoring which based on ARM of plays an important role. The system is low cost, practical performance, high reliability, flexible, easy installation, etc., can be widely used in various places of monitoring.

In recent years, wireless intelligent network monitoring technology has developed rapidly all over the world [2], and becomes more and more practical in people's daily life. As the wireless communication has been gradually perfect, and has a considerable advantage, this system adopts the wireless communication way of connection control receiver. This topic chooses wireless intelligent monitoring system design in the wireless intelligent system, studying aims at market demands, and develops based on STM32F407, the corresponding hardware and application software.

2 Background of the Research and Significance

The rapid expansion of economic scale and accelerating urbanization process, causes more serious smog problems, seriously affected the physical and mental health of the people, the governance of smog has become a top priority. But in terms of the situation, our country and the world for the management measures of smog has not reached an ideal state, and cannot govern fundamentally smog. The smog in the outside air goes into our body through the mouth, nose breathing. Although not directly blocking the smog into the body's way, we can use the indirect method, some appropriate measures to prevent the inhalation of smog. This topic is from this perspective, Based on ARM wireless intelligent network monitoring smog, to send air quality information to the people to do the appropriate measures and adjust the time to go out.

Usually, people will wear a mask to the outside, but it is also unable to avoid smog enter human body. By observation, not many people wearing masks to go out to work or play, even if most people have awareness, but they still feel that wearing a mask is a trouble thing. At this point, we can predict the air quality situation of the destination in advance, according to their own time and other conditions to do the appropriate adjustments to avoid going out when the impact of the smog. They make their time and peak stagger out smog, to ensure that the amount of human inhalation of smog can be greatly reduced. Therefore, wireless intelligent network monitoring system for the elderly, the younger generation, and children is very practical and effective, and is very simple, easy to understand, the most important is that it provides an important measure to avoid the inhalation of smog.

3 The Overview of System Architecture Diagram

System structure as shown in Fig. 1, the system adopts STM32F407 as the master chip, using wireless module for data collection and transmission. The data of detecting from smog sensor through the wireless module is transferred to the CPU, and judged by the CPU whether smog concentration is excessive (with set value compared) or to reach a predetermined value, real-time displaying at the same time by the LCD screen and the web,driving corresponding linkage, sending real-time information to mobile phone SIM card, and reminding of the user in the period of time to avoid traveling or to do the corresponding protective measures.

3.1 Smog Sensor Module

The principle and structure of smog sensor are shown in Fig. 2, sensors collecting moisture and impurities, getting current signal converts the voltage signal through the amplifier, inputting amplified signal to the successive compared A/D converter, disposed by the CPU, displayed on the LCD screen. As STM32F407 based on development system, with high-performance 32-bit processor, with ARM Cortex-M4F architecture kernel, processing capacity of 210DMIPS at 168 MHz, containing 1 M bytes FLASH and 196 K bytes of SRAM, with 1 10 M/100 M Ethernet interface, STM32F407 processor internal IEEE 1588 V2 hardware with National Semiconductor Corporation of industrial Ethernet PHY chip standard RJ45 interface, with 1 USB OTG 2.0 interface, can be used as SLAVE USB, with 1 SD card interface, 2 2.4G wireless communication module interface realizes the transmission of data and information, the detected information through the wireless

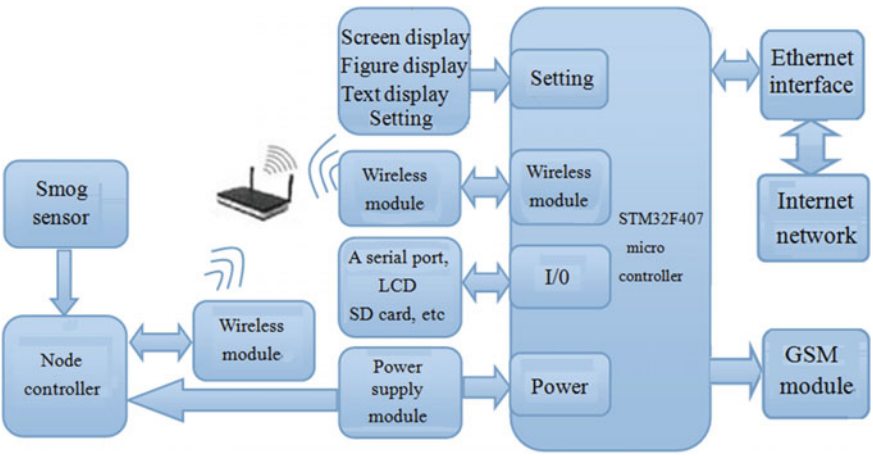

Fig. 1 System structure

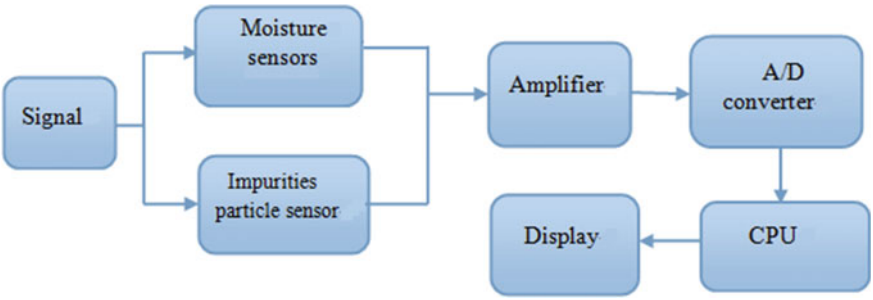

Fig. 2 The principle and structure of smog sensor

module to transmit to the master chip, through the analysis of processing the surroundings of the PM2.5 sensor read back information to determine whether the excessive PM2.5 particles in the air, the real-time information will be displayed by the TFT LCD screen. The realization of wireless transceiver can be achieved, which is easy to operate.

3.2 GSM Module

GSM module can send messages to users who set a good number in ahead of time as notification reminders when caught in serious smog.

As shown in Fig. 3 for the GSM module [3]. The system using GSM module to send text messages and call the alarm, GSM network after years of development has become increasingly mature, less blind area, signal stability, automatic roaming, and communication distance is not affected by the surrounding environment, especially the short information, flexible and convenient, and across the province intercity even multinational transfer, reliable and cheap, so the use of GSM module for alarm is a very good choice.

As shown in Table 1 for GSM communication commonly used AT instruction set.

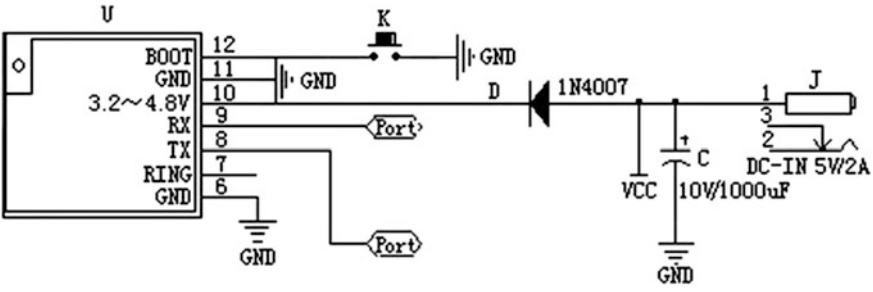

Fig. 3 The principle of GSM module

Table 1 AT Instruction Set

Instruction	Function
AT&F	Module initialization
AT+CMGF=1	Set the text to text format
AT+CMGF=0	Set the text to the PDU format
AT +CSCS="GSM"	Choose TE character set
AT +CMGS="number"	The number of settings to send text messages
ATD number	Dial instructions
ATH	Hang up the instructions

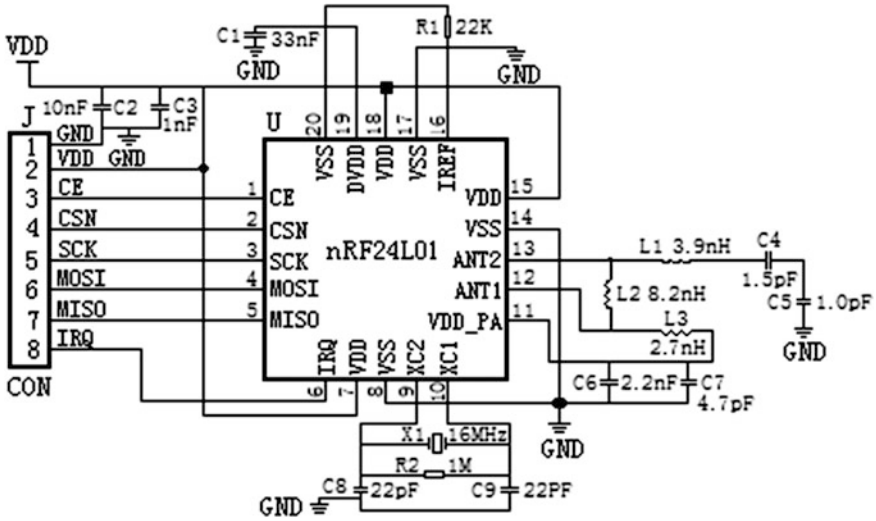

Fig. 4 The principle diagram of the wireless communication module

3.3 Wireless Communication Module

As shown in Fig. 4 for the principle diagram of the wireless communication module, choose the Nordic companies nRF24L01 chip [4], work in ISM frequency band, which can be connected with various microcontroller chip to complete the wireless transmitting data, its highest rate up to 2 MBPS, wide working voltage range, have more than one communication channel and data channel. It USES efficient GFSK (gaussian frequency shift keying), strong antijamming capability, its work mode is shown in Table 2.

Table 2 NRF24L01 working mode

Mode	PWR_UPregister	PRIM_RX register	CE	FIFO state
RX mode	1	1	1	–
TX mode	1	0	1	Data in TX FIFO
TX mode	1	0	1 → 0	Stays in TX mode until packet transmission is finished
Standby-II	1	0	1	TX FIFO empty
Standby-I	1	–	0	No ongoing packet transmission
Power Down	0	–	–	–

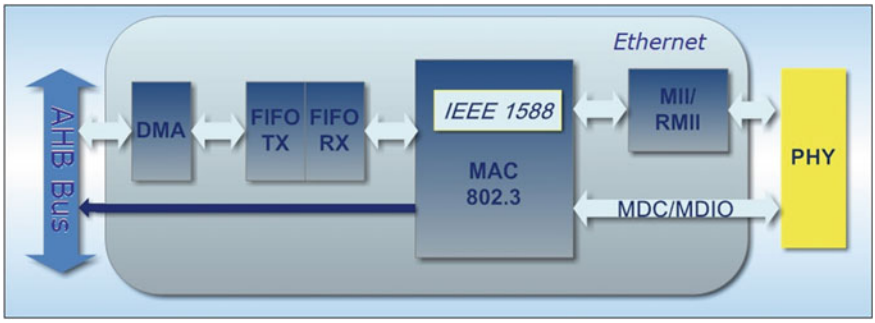

Fig. 5 STM32F407 internal MAC structure

3.4 Ethernet Module

STM32F407 internally integrated Ethernet card (MAC) [5, 6], its structure as shown in Fig. 5, this function allows the user only internal registers configuration can be easily connected to the network physical layer (PHY), and do not have to buy in addition to the transceiver card chip.

3.5 SD Card

SD card highly integrated flash memory, serial and random access ability. It can pass through the serial interface to access special optimization speed, reliable data transmission. Interface allows a few card cribs, by their external connections. SD card system is a new mass storage system. It is a kind of based on flash memory device of a new generation of semiconductor memory device, the size is like a postage stamp, only 2 g in weight, has high memory capacity, fast data transfer rate, great flexibility, and good security.

4 Software Implementation

As shown in Fig. 6 software flow chart, there is an initialization interface in liquid crystal display part after electric automatic reset or button manual reset of single-chip microcomputer, monitoring the surrounding environment by the smog sensor, the real-time data which is read back is displayed on the LCD screen. The current smog concentration of system shows on the LCD display screen and Internet browsing page, and sends short message to user numbers in advance through GSM, in order to prompt the user current outdoor smog concentration is too high, taking corresponding measures to ensure the user's health.

Smog concentration index as shown in Table 3, according to the world health organization(WHO) 2005 edition of the "air quality guidelines", PM2.5 standard values measures the quality of the air we breathe, according to research of WHO, which is the most harm to human body is largest ultrafine particles PM2.5 (diameter is less than or equal to 2.5 micron particles). PM2.5 refers to the diameter less than or equal to 2.5 micron particles in atmosphere, also known as can go directly to the alveoli. Scientists said PM2.5 is particles per cubic meter in the air, the higher the value is the more serious the air pollution.

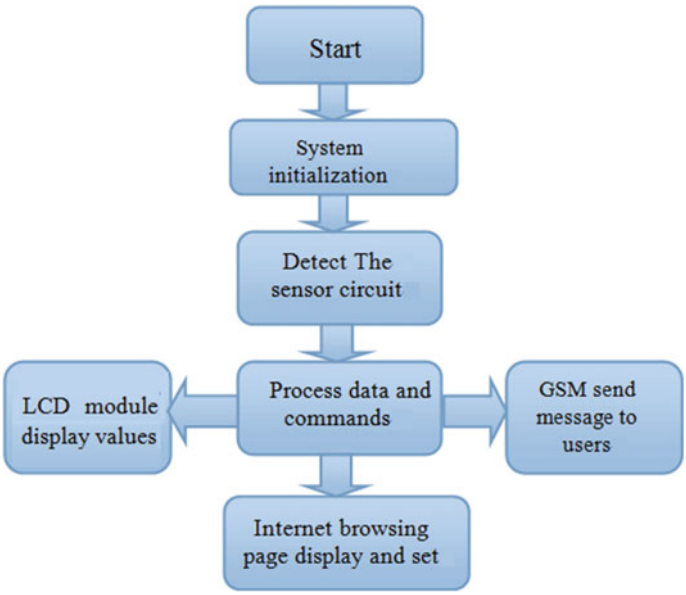

Fig. 6 Software flow chart

Table 3 Smog concentration index

PM2.5 index	Level	Matters needing attention
0–50	Level 1 optimal	participate in outdoor activities, breath fresh air
50–100	Level 2 good	outdoor activities can be normal
101–150	Level 3 mild	Sensitive crowd reduce large physical exertion outdoor activities
151–200	Level 4 moderate	A larger effect on sensitive crowd
201–300	Level 5 severe	All people should be appropriate to reduce outdoor activities
>300	Level 6 serious	Try not to stay outside

5 Conclusion

This paper based on the smog weather system research of ARM wireless intelligent network monitoring and design to combine the traditional Internet and new type of wireless sensor network, surveying outdoor smog through the probe, transmitting smog situation to a wireless receiving device such as mobile phone with a screen through sensor, so as to prompt whether it is suitable to go out. In this design, the detection head can be free replacement due to the difference of time and place, its application range is wide, can also be applied to other areas.

Acknowledgments This research was supported by the Tianjin College Students' Innovation and Entrepreneurship Training Program project Fund (project number: 201510065062)

References

1. Guo L (2007) Based on ARM embedded system design. University of electronic science and technology
2. Guo H (2006) Zigbee wireless network communication system based on ARM. The research and design of Shandong University of Science and Technology
3. Wu J, Du A (2014) The Research and application of wireless intelligent network system based on STM32F407. In: The Proceedings of the third international conference on communications, signal processing, and system. Springer, Huhehaote, 14 July 2014
4. Liu P (2012) The short distance wireless communication based on nRF24L01 application. Inf Comput 2:155–156
5. Wu J, Yu J (2013) Research and application of building monitoring platform based on the internet of things. In: The Proceedings of the second international conference on communications, signal processing, and system. Springer, Tianjin. Accessed 1, 2 Sept 2013
6. xu day (2011) Arm9-based embedded and industrial Ethernet in the mine gas monitoring system research. Xi 'an University of Science and Technology

Optimal Cooperation Strategy in Cognitive Relay Networks with Energy Harvesting

Kaiqiang Yan, Guochun Ren, Jin Chen, Guoru Ding and Huidong Liu

Abstract In this paper, we consider cognitive relay networks with energy harvesting and cooperative communications, the secondary user (SU) can get energy and idle spectrum by helping primary user (PU) to transmit its information for each slot. In such a scenario, we propose an optimal cooperation strategy in order to maximize the overall networks' throughput. We compare the results of the optimal cooperation strategy with the other collaboration strategy. The results show that the optimal cooperation strategy is always superior to the other collaboration strategy.

Keywords Energy harvesting · Relay channel · Cooperative communication

1 Introduction

With the growing environmental concerns and the increasing demand of wireless services, energy efficiency and spectral efficiency are two essential design metrics in wireless communications [1]. Recently, it has been shown that the wireless information and power transfer technology could make one device harvest energy from the environment RF signal, and process the information at the same time [2]. On the other hand, cognitive radio is a promising way to improve spectrum utilization by allowing spectrum sharing. Therefore, combining cognitive radio networks with energy harvesting offers an efficient way in terms of both energy and spectrum [3, 4].

Cognitive radio was proposed to improve the spectrum utilization by allowing SUs to opportunistically exploit the spectrum unused by PUs [5, 6]. In [7], the authors investigate optimization for the cooperative spectrum sensing with an improved energy detector to minimize the total error rate (sum of the probability of false alarm and miss detection). Follow-up works extend the scenario in [7] to imperfect reporting channels [8] and SUs with multiple antennas [9], respectively.

K. Yan (✉) · G. Ren · J. Chen · G. Ding · H. Liu
College of Communications Engineering, PLA University of Science and Technology, Beijing, China
e-mail: kaiqiang_yan@163.com

Q. Liang et al. (eds.), *Proceedings of the 2015 International Conference on Communications, Signal Processing, and Systems*, Lecture Notes in Electrical Engineering 386, DOI 10.1007/978-3-662-49831-6_10

Cooperative spectrum sensing based on finite number of primary signal samples is investigated in [10, 11], where the local and global thresholds are optimized in order to minimize the total error rate. In [12–15], the authors investigate transmission policies to guarantee that the energy constrained relay could carry out simultaneously the energy harvesting and information processing in wireless cooperative systems. Our research is inspired by [16]. In [16], the authors have proposed the optimal cooperation protocol in cognitive radio system where the direct link between the PUs is available and the SU's energy is harvested from ambient radio signal.

In this paper, we consider cognitive relay networks with one pair of primary transceivers and one pair of secondary transceivers, which operate in time-slotted mode. The secondary transmitter is powered exclusively by energy extracted from the primary transmitter's signal. The main contributions of this paper are summarized as follows:

(1) We characterize a new transactional relationship between the PU and SU. The PU provides sufficient energy and idle spectrum for the SU. In return, the SU can act as a relay node to complete PU's transmission.
(2) We formulate the problem of the SU's achievable throughput maximization. In such a scenario, there exist energy transfer (e.g., fraction of dedicated time), cooperative transmission (e.g., allocated power for cooperative relay), and data transmission. To tackle such trade-off, we investigate the optimal cooperation strategy in cognitive relay networks, namely, the optimal action (to spend how much time on energy harvesting and to allocate how much power for cooperative relay).
(3) We derive the expression of the optimal cooperation strategy and illustrate the strategy by numerical computation and simulation analysis. Our numerical results show that the optimal cooperation strategy can maximize the throughput.

The paper is organized as follows. Section 2 sets up the energy harvesting, information transfer, and cooperative communication model. The problems are formulated and analyzed in Sect. 3. Simulations are presented in Sect. 4, followed by conclusions in Sect. 5.

2 System Model

We consider cognitive relay networks with energy harvesting as shown in Fig. 1. The PU has the ownership of a licensed channel. In each timeslot, the PU has a certain amount of data stored in its buffer. Because the direct link between the PUs is not available, the PU must rely on a relay node to use the licensed channel to transmit its data. After PU's transmission is finished, the PU turns into silence and the licensed channel is vacated. On the contrary, the SU does not have any licensed

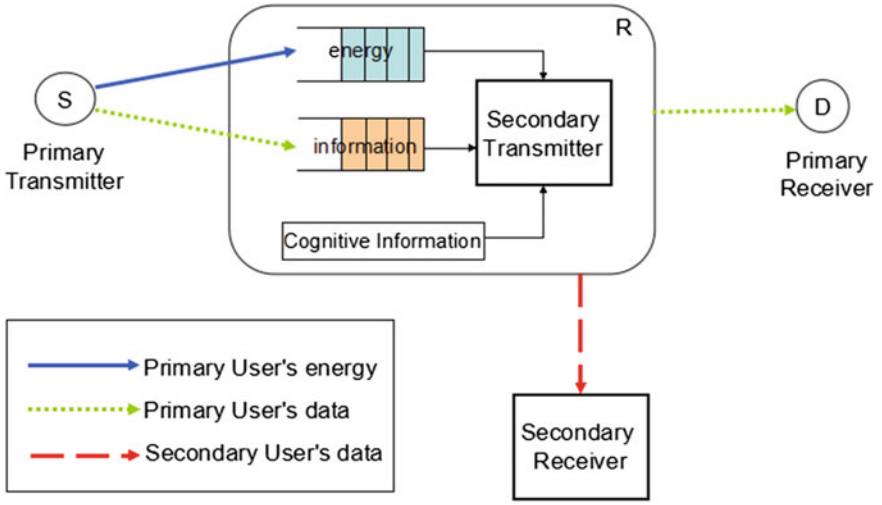

Fig. 1 Cognitive relay networks with cooperation between PU and SU

spectrum and is allowed to transmit its own data only when the licensed channel is unused by the PU in order to avoid collision with the PU. Moreover, the self-powered SU has no fixed power supplies and extracts energy exclusively via energy harvested from the PU's radio signal. We also assume that the SU's transmitter follows a save-then-transmit protocol. This is because practically rechargeable energy storage devices cannot charge and discharge simultaneously (which is termed energy half-duplex constraint). In each timeslot, the SU first devotes a fraction (referred to as save-ratio) of time exclusively to energy harvesting, then it uses the harvested energy for data transmission.

In such cognitive relay networks, the PU needs a relay to transmit the data and the SU lacks energy and spectrum. Therefore, we assume that there is a transaction between the PU and SU. The SU can act as a cooperative relay to help the PU finish its certain transmission. In exchange, the PU provides ambient radio signal, which the SU can harvest energy from, and idle spectrum. After all of PU's data is transmitted, the SU can transmit its own data on the idle channel by consuming the remaining energy. As a result, the PU and the SU can achieve a win-win. Moreover, the PU sever as a power source can make the harvested energy assured.

In order to do so, the SU must consume its harvested energy to help relay the PU's data. This cooperation can take place in several ways depending on the cooperative protocol being used. In this paper, we assume the cooperative communication between PU and SU follows the decode-and-forward (DF) protocol, which is one of the commonly used protocols. In the DF protocol, the relays first decode the received signal, re-encode it, and then transmit it to the destination. Finally, the destination decodes the data.

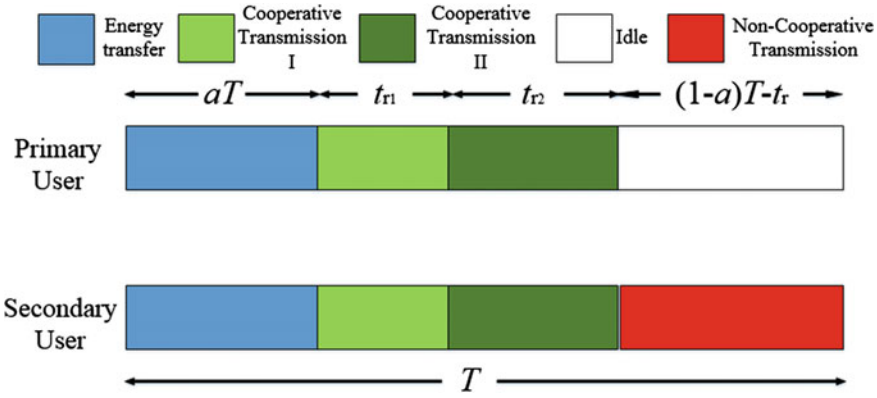

Fig. 2 Timeslot structure of cooperation mode

In the proposed mode shown in Fig. 2, a timeslot is partitioned into three fractions synchronous for both PU and SU, which can be detailed as follows:

(1) During time interval $(0, aT]$, the SU harvests energy from ambient signal. The SU's harvested energy amounts to XaT, where X denotes the SU's energy harvesting rate (average energy harvested in unit time).

(2) During time interval $(aT, aT + t_r]$, where the cooperative communication duration is given by

$$t_r = t_{r1} + t_{r2} = Qlog2(1 + r_{PS}) + Qlog2(1 + w\gamma_{SR}) \quad (1)$$

the PU and the SU cooperate with each other to complete the PU's transmission, Q denotes the data amount of PU in each timeslot, r_{PS} denotes signal-to-noise ratio of link between PU transmitter (source) and SU transmitter (relay), and γ_{SR} denotes channel-power-gain-to-noise-power ratio of link between SU transmitter (relay) and PU receiver (destination). Here, we specify that $t_r \leq (1 - a)T$. Because the PU must be able to complete its transmission within one timeslot. After consuming wt_{r2} of energy for cooperative relay, $X\alpha T - wt_{r2}$ of energy remains. Following the DF protocol, the PU transmitter (as source) transmits its data to the SU transmitter (as relay) and PU receiver (as destination) in the first part of cooperation interval $(aT, aT + t_{r1}]$. Then in the second part of cooperation interval $(aT + t_{r1}, aT + t_r]$, the SU transmitter relays the PU's data to the PU receiver. Here, we focus on fully decoding at the SU's transmitter (i.e., repetition-coded scheme without error).

(3) During time interval $(aT + t_r, T]$, when PU's transmission is completed and the licensed channel is vacated, the SU starts to transmit its own data. The PU keeps silent and of energy remains for secondary transmission. We assume that the SU must exhaust all the harvested energy in each timeslot for data transmission. While operating in cooperation mode, in addition to the save-ratio, the SU can decide how much of its harvested energy is allocated to help relay the

PU's data as well. Evidently, with more energy consumed for cooperative relay, the PU's transmission could be completed earlier such that more opportunities could be available for secondary transmission, whereas less energy is reserved, which inevitably limits the SU's achievable throughput.

3 Problem Formulation

In this section, problem of the SU's achievable throughput maximization is formulated. In the proposed mode as shown in Fig. 2, the SU's achievable throughput in each timeslot is given by

$$R(a,w) = [(1-a)T - t_r]\log_2\left[1 + \frac{(\mathrm{X}aT - wt_{r2})\gamma_S}{(1-a)T - t_r}\right] \tag{2}$$

Note that the SU's achievable throughput in (2) is normalized with $1/T$, and γ_S denotes channel-power-gain-to-noise-power ratio of link between SU transceiver pair. We aim at jointly optimizing the SU's save-ratio (a) and allocated power (w) for cooperative relay to maximize SU's achievable throughput and the problem can be formulated as the following:

$$\begin{aligned} &\max_{a,w}\ R(a,w) \\ &\text{s.t.}\quad (1-a)T - t_r \geq 0 \\ &\qquad \mathrm{X}aT - wt_{r2} \geq 0 \\ &\qquad a, w \geq 0 \\ &\qquad Q = t_{r1}\log_2(1 + r_{PS}) = t_{r2}\log_2(1 + w\gamma_{SR}) \\ &\qquad t_r = t_{r1} + t_{r2} \end{aligned} \tag{3}$$

The first constraint in (3) refers to the time causality constraint which guarantees that the cooperative communication duration should not exceed the remaining time after energy harvesting. The second one refers to the energy causality constraint which guarantees that the energy consumed for cooperative relay should not exceed the SU's harvested energy. We ensure the PU's transmission by the two constraints. The one can guarantee the transmission time and the other one can satisfy the transmission power. We aim at jointly optimizing the SU's save-ratio (a) and allocated power (w) for cooperative relay to maximize SU's achievable throughput in (2). The analysis of (3) did turn up that it is a typical convex optimization problem [17], and its *Lagrange Equation* is given by

$$L(a,w,\lambda_1,\lambda_2)=R(a,w)+\lambda_1[(1-a)T-t_r]+\lambda_2(XaT-wt_{r2}) \tag{4}$$

We first investigate the convexity of the optimization problem in (2) and then derive the optimal by solving the equation system of Karush–Kuhn–Tucker (KKT) optimality conditions. Thus, the global optimum of (3) exists and the optimal can be derived by comparing all the candidate KKT points.

The KKT optimality condition of (4) is given by

$$\begin{cases} \frac{\partial R}{\partial a}-\lambda_1 T+\lambda_2 XT=0 \\ \frac{\partial R}{\partial w}-\lambda_1 W+\lambda_2(-t_{r2}+wW)=0 \\ W=\frac{Q\gamma_{SR}}{(1+w\gamma_{SR})\log_2^2(1+w\gamma_{SR})} \\ (1-a)T-t_r>0, XaT-wt_{r2}>0 \\ \lambda_1[(1-a)T-t_r]=0, \lambda_2(XaT-wt_{r2})=0 \\ \lambda_1,\lambda_2\geq 0 \end{cases} \tag{5}$$

Therefore, we eliminate the complementary slackness conditions and dual variables concerning these cases.

(1) Candidate KKT point 1: $\lambda_1=\lambda_2=0$: Deriving the optimal and while is equivalent to solving the following equation system:

$$\begin{cases} \frac{\partial R}{\partial a}=0 \\ \frac{\partial R}{\partial w}=0 \end{cases} \tag{6}$$

The candidate KKT point (a_1, w_1) can be expressed as

$$\begin{cases} a_1=\frac{(A_1+B_1)\ln\left(1+\frac{A_1}{B_1}\right)}{XT}-\frac{\gamma_S A_1}{T}+\frac{w_1 Q}{XT\log_2(1+w_1\gamma_{SR})} \\ w_1=\frac{(A_1+B_1)\gamma_{SR}\ln\left(1+\frac{A_1}{B_1}\right)+\gamma_S(1+w_1\gamma_{SR})\ln(1+w_1\gamma_{SR})+B_1\gamma_{SR}}{A_1\gamma_{SR}} \end{cases} \tag{7}$$

where

$$\begin{cases} A_1=(1-a_1)T-t_{r1}-\frac{Q}{\log_2(1+w_1\gamma_{SR})} \\ B_1=\left(Xa_1T-\frac{w_1 Q}{\log_2(1+w_1\gamma_{SR})}\right)\gamma_S \end{cases} \tag{8}$$

Then the feasibility of (a_1, w_1) can be tested with the constraints in (3).

(2) Candidate KKT point 2: $\lambda_2=0$ and $\lambda_1\geq 0$: In this case, we have

$$a_2 = 1 - \frac{Q}{T\log_2(1+r_{PS})} - \frac{Q}{T\log_2(1+w_2\gamma_{SR})} \tag{9}$$

(3) Candidate KKT point 3: $\lambda_1 = 0$ and $\lambda_2 \geq 0$: In this case, we have

$$a_3 = \frac{w_3 Q}{XT\ \log_2(1+w_3\gamma_{SR})} \tag{10}$$

However, we tested (9) and (10) with the constraints in (2), it can be concluded that (a_2, w_2) and (a_3, w_3) are both practically infeasible. The values of R(a_2, w_2) and R(a_3, w_3) are zero, obviously they do not meet with the maximum throughput.

4 Numerical Results

In this section, we illustrate how the optimal strategy depends on the system parameters in cooperation. We respectively evaluate numerically the optimal save-ratio and allocated power for cooperative relay in the proposed mode by setting $X = 150$, $T = 1$, $r_{PS} = 15$ dB, $\gamma_{SR} = \gamma_S = 5$ dB/W.

We set $Q = 2$, $a \in [0, 0.4]$ and $w \in [0, 80]$. Simulation results are shown in Fig. 3. In Fig. 3, it can be observed that: the figure of results is convex, and it exists in the peak. We first set an initial value. Then, according to the formula (3), the optimal save-ratio and the optimal allocation power are obtained by the iteration. We mark the optimal point and corresponding throughput by plus sign (+), which coincides with the peak. Therefore, the optimal cooperation strategy can be verified.

Optimal save-ratio in the proposed mode with different system parameters is shown in Fig. 4. In Fig. 4, we can see that the SU's achievable throughput R decreases as PU's data amount Q increases, and the optimal save-ratio varies with different Q. When the allocated power for cooperative relay is optimum, the

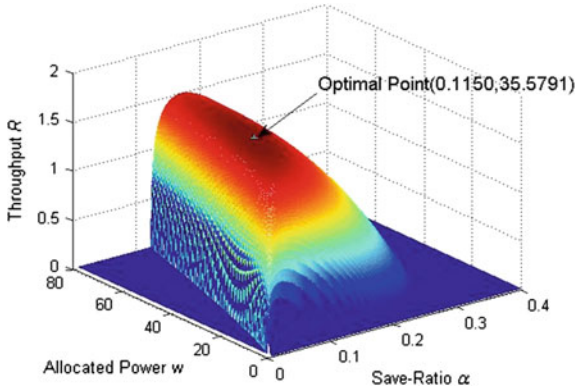

Fig. 3 The global throughput

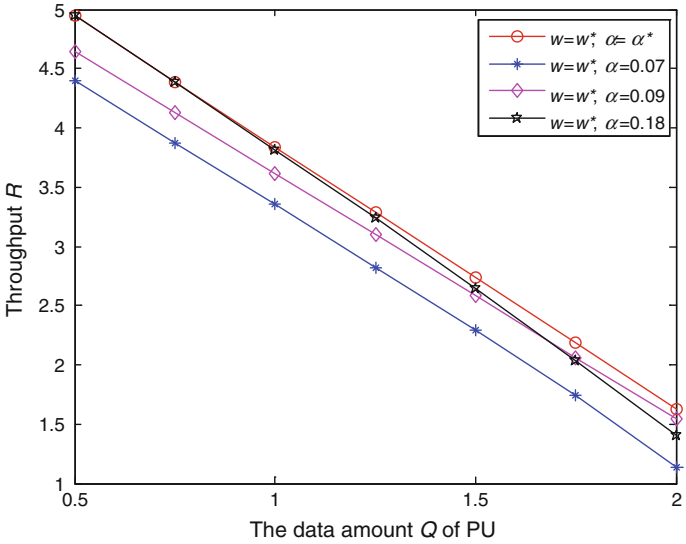

Fig. 4 The throughput with the optimal allocated power and different save-ratio

throughput which the optimal save-ratio achieves is always equal or greater than the other save-ratio's achievable throughput.

Optimal allocated power for cooperative relay in cooperation mode with different system parameters is shown in Fig. 5. In Fig. 5, we can see that the save-ratio

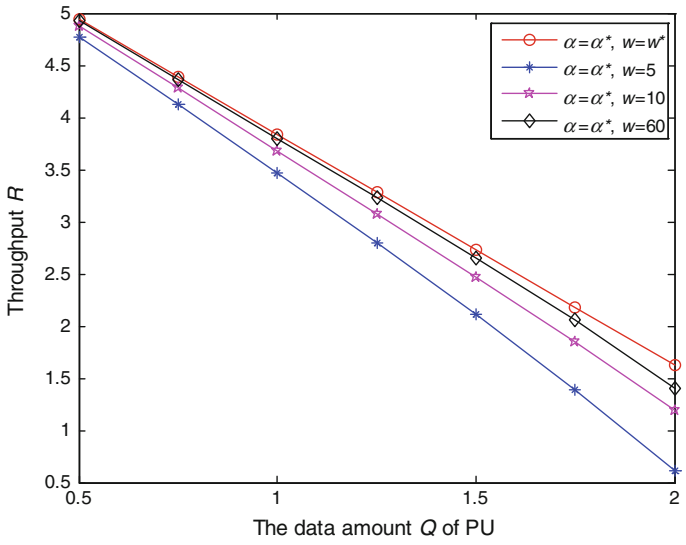

Fig. 5 The normalization throughput with the optimal save-ratio and different allocated power

is optimum, the optimal allocated power's achievable throughput is always equal or greater than the others. The difference between them increases as the PU's data amount Q increases. The reason of the phenomenon is that the influence of the allocated power is not obvious when the value of Q is small.

5 Conclusions

In this paper, we consider cognitive relay networks with one PU and one SU and both of their transmitters operate in time-slotted mode. The SU, which has no fixed power supplies and extracts energy exclusively via energy harvested from ambient radio signal, can optionally cooperate with the PU to help PU's complete transmission such that enough energy and idle channel can be available for its own transmission. To tackle the trade-off in energy harvesting, cooperative relay, and secondary transmission, we investigate the optimal action to maximize the SU's achievable throughout and derive the optimal closed-form solutions with numerical analysis. Based on the analytical results, we further propose the optimal cooperation protocol (OCP) to make the optimal cooperation decision. Simulation results demonstrate the effectiveness of the proposed strategy.

References

1. Hu Z, Chen Z, Liu H, Shao X, Xing G (2013) System design for broadband digital radio broadcasting. IEEE Commun Mag 51(4):58–65
2. Varshney LR (2008) Transporting information and energy simultaneously. In: Proceedings of the IEEE ISIT
3. Haykin S (2005) Cognitive radio: brain-empowered wireless communications. IEEE J Sel Areas Commun 23(2):201–220
4. Zhou X, Zhang R, Ho CK (2012) Wireless information and power transfer: architecture design and rate-energy tradeoff. http://arxiv.org/abs/1205.0618
5. Ding G, Wu Q, Yao Y, Wang J, Chen Y (2013) Kernel-based learning for statistical signal processing in cognitive radio networks: theoretical foundations, example applications, and future directions. IEEE Signal Process Mag 30(4):126–136
6. Ding G, Wang J, Wu Q, Zhang L, Zou Y, Yao Y, Chen Y (2014) Robust spectrum sensing with crowd sensors. IEEE Trans Commun 62(9):3129–3143
7. Singh A, Bhatnagar MR, Mallik RK (2011) Cooperative spectrum sensing with an improved energy detector in cognitive radio network. In: Proceedings of the NCC, pp 1–5
8. Singh A, Bhatnagar MR, Mallik RK (2011) Optimization of cooperative spectrum sensing with an improved energy detector over imperfect reporting channels. In: Proceedings of the IEEE VTCł Fall, pp 1–5
9. Singh A, Bhatnagar MR, Mallik RK (2012) Cooperative spectrum sensing in multiple antenna based cognitive radio network using an improved energy detector. IEEE Commun Lett 16 (1):64–67
10. Singh A, Bhatnagar MR, Mallik RK (2012) Threshold optimization of finite sample based cognitive radio network. In: Proceedings of the NCC, pp 1–5

11. Singh A, Bhatnagar M, Mallik R (2013) Threshold optimization of a finite sample-based cognitive radio network using energy detector. EURASIPJ Wirel Commun Netw 2013(1):165
12. Chen Z, Wang B, Xia B, Liu H (2013) Wireless information and power transfer in two-way amplify-and-forward relaying channels. http://arxiv.org/abs/1307.7447
13. Chen Z, Liu H, Wang W (2011) On the optimization of decode-and-forward schemes for two-way asymmetric relaying. In: Proceedings of the IEEE ICC
14. Liu Y, Mo J, Tao M (2013) QoS-aware transmission policies for OFDM bidirectional decode-and-forward relaying. IEEE Trans Wirel Commun 12(5):2206–2216
15. Lee S, Huang K, Zhang R (2012) Cognitive energy harvesting and transmission from a network perspective. In: Proceedings of the IEEE ICCS
16. Yin S, Zhang E, Qu Z, Yin L, Li S (2014) Optimal cooperation strategy in cognitive radio systems with energy harvesting. IEEE Trans Wirel Commun 13(9):4693–4707
17. Boyd S, Vandenberghe L (2004) Convex optimization. Cambridge University Press, Cambridge, pp 243–249

Improving the End-to-End Delay in Cognitive Radio Ad Hoc Networks

Jing Gao

Abstract The end-to-end delay is an important performance indicator for ad hoc networks since it usually needs multi-hops to propagate a packet from source to destination. In order to improve the performance of *Farthest-node routing* (*FNR*) protocol, we evaluated the local delay of Cognitive Radio (CR) networks with Poisson Point Process model. Then, we deduced the upper bound of end-to-end delay based on the local delay. We also assess the sensitivity of CR local delay and end to end delay with respect to the primary users' activity, secondary users' transmission radius and nodes density via numerical and simulation methods.

1 Introduction

Delay, reliability, and throughput provide a comprehensive metric for the ability of delivering information. And the local delay has been well investigated in [1–3], which is defined as the mean time (in numbers of time slots) until a packet is successfully received over a link between nearest neighbors.

Since the seminal work of Gupta and Kumar [4], the scaling law of the multi-hop delay in homogeneous ad hoc networks has been an active topic. The end-to-end delay of a multi-hop transmission scheme is evaluated by taking into account both the access and waiting time in [5]. Additionally, the delay of CR networks becomes an interesting topic with the rapid development of CR technology [6–8]. But the heterogeneous nature causes more difficulty to quantify the delay of CR networks than that of homogeneous networks. In this paper, we evaluate both local delay and end-to-end delay of CR network and further provide an optimal method to minimize the delay.

The rest of the paper is organized as follows. Section 2 presents the system model of the CR network, FNR protocol, and the definition of CR local delay.

J. Gao (✉)
School of Electronics and Communication Engineering,
Tianjin Normal University, Tianjin 300387, China
e-mail: jing401@126.com

Q. Liang et al. (eds.), *Proceedings of the 2015 International Conference on Communications, Signal Processing, and Systems*, Lecture Notes in Electrical Engineering 386, DOI 10.1007/978-3-662-49831-6_11

Section 3 provides the analysis of CR local delay. In Sect. 4, we study the multi-hop delay and delay-minimized transmission radius. In Sect. 5, we discuss the numerical and simulation results of local delay and multi-hop delay. Section 6 concludes the paper.

2 System Model and CR Local Delay

2.1 Primary Network Model

We assume that there is one channel available for primary transmissions. The occupancy of the licensed channel by the primary user (PU) is modeled as independent continuous-time Markov processes with idle $(S=0)$ and busy state $(S=1)$. The mean time is exponentially distributed with parameter λ^{-1} and μ^{-1} for the busy state and idle state, respectively. The transition probability of channel from idle state to idle and busy state within time t are given by

$$P_{II}(t)=\frac{\mu}{\lambda+\mu}+\frac{\lambda}{\lambda+\mu}e^{-(\lambda+\mu)t} \tag{1}$$

2.2 Secondary Network Model

We consider secondary network as a mobile Ad Hoc network where secondary users (SUs) hierarchically access the spectrum when the licensed channel is idle. The positions of terminals follow a two-dimensional Poisson Point Process (PPP) Φ_S [9] with spatial density λ_S. A slotted transmission structure is adopted with slot length L. In each slot, SUs could sense the licensed channel perfectly and decide whether to transmit over the channel based on the sensing outcome. Once the channel is idle at the beginning of a certain time slot, SUs randomly access the channel with probability p, hence the potential secondary transmitters form a PPP Φ_S^t with density $\lambda_S p$ and accordingly the potential receivers follow another homogeneous PPP Φ_S^r with density $\lambda_S(1-p)$.

2.2.1 SIR-Based Packet Success Probability

The wireless channel combines Rayleigh fading with path-loss. All nodes have the same transmission power (normalized to 1) and transmission radius R. A packet is successfully received by a typical receiver j at origin if $SIR(d)=\frac{hd^{-\alpha}}{I_{\Phi_S^t}}>\beta$, where h is the fading coefficient, exponentially distributed with unit mean, $\alpha>2$ is the path-loss exponent, d is the random transmission distance from j to its associated

transmitter, $I_{\Phi_S^t} = \sum_{k \in \Phi_S^t} h d_{k,j}^{-\alpha}$ is the shot-noise process of Φ_S^t, β is a threshold predetermined.

According to Corollary 3.2 in [10], The SIR-based packet success probability is

$$p_S = P(SIR(d) > \beta) = e^{-\lambda_S p C_\alpha d^2}, \qquad C_\alpha = \frac{2\pi^2 \beta^{2/\alpha}}{\alpha \sin(2\pi/\alpha)}. \tag{2}$$

2.2.2 Routing Protocol

Farthest-node routing (*FNR*) *protocol*: Considering a multi-hop transmission scenario, each node selects the farthest node in the selection region similar to that in [11] to propagate packets. For each node along the route to the destination, a selection region is determined by two parameters: a direction angle φ and a transmission radius R. That is to say, selection region is the area within angle φ and inside the arc AB with $\rightharpoonup |OA| = R$.

Based on *FNR* protocol above and the properties of PPP, the PDF of random transmission distance in one hop d is

$$f_d(x) = \varphi \lambda_S x e^{-\frac{\varphi}{2}\lambda_S (R^2 - x^2)} \quad 0 < x \le R \tag{3}$$

Thus we have the average one-hop distance as

$$\bar{d} = E(d) = \int_0^R x f_d(x) dx = R - \frac{\text{DawsonF}[\sqrt{\varphi \lambda_S/2} R]}{\sqrt{\varphi \lambda_S/2}}. \tag{4}$$

And the mean packet success probability of FNR protocol transmission is

$$\bar{p}_S = \frac{\varphi\left(e^{-\frac{\varphi}{2}\lambda_S R^2} - e^{-\lambda_S p C_\alpha R^2}\right)}{2(pC_\alpha - \varphi/2)}. \tag{5}$$

2.3 The Definition of CR Local Delay

Supposing source initiate the packets when $t = 0$, $P_{s,l}$ denotes the packets are successfully received by the receiver in one hop when $t = lT$, $l \in N_+$. And

$$P_{s,l} = p(1-p) p_s P_I(0) P_I(lT). \tag{6}$$

Theorem 1 *Let L denote the random variable of number of slots which success events happens in CR Ad Hoc networks,* ***CR local delay*** *defined as the expectation of L is*

$$D = E(L) = \sum_{k=1}^{\infty} kP_{s,k} \prod_{l=1}^{k} (1 - P_{s,l}), \tag{7}$$

where $P_{s,l} = p(1-p)p_s P_I(0) P_I(lT)$.

Proof The probability mass function of L is

$$P(L = k) = \prod_{l=1}^{k-1} P_{s,k}(1 - P_{s,l}). \tag{8}$$

And the expectation of L yields CR local delay is obtained.

3 The Upper Bound of CR Local Delay

3.1 The Upper Bound of CR Local Delay

Theorem 2 *Supposing a node successfully transmits packets at the beginning of time slots k, let*

$$P_{SUC} = P_{s,1} = P_{s,2} \cdots = P_{s,k} = p(1-p)p_s P_I(0) P_I(kT),$$

we get the upper bound of CR local delay $D^{'}$ *is the solution of next equation*

$$D^{'} P_I(D^{'}T) p(1-p) \mathbf{E}(p_S) P_I(0) = 1. \tag{9}$$

Proof is omitted.

3.2 The Closed Form Expression of the Upper Bound

In this section, we try to solve the Eq. (9) and give the closed form expression of the upper bound of CR local delay D'. After some calculations we have

$$\frac{\mu x}{\lambda + \mu} \left(\frac{\mu}{\lambda + \mu} + \frac{\lambda}{\lambda + \mu} e^{-(\lambda + \mu)xT} \right) = \frac{1}{p(1-p)\bar{p}_S}. \tag{10}$$

It is difficult to solve the Eq. (10) directly, we give the solution by employing Proposition 1 in the following.

Proposition 1 *As* $(\lambda+\mu)T<<1$, *the necessary condition of*

$$\frac{\mu}{\lambda+\mu}+\frac{\lambda}{\lambda+\mu}e^{-(\lambda+\mu)DT}\approx e^{k\mu}e^{-(\lambda+\mu)DT} \tag{11}$$

is $DT<k<<1$.

Proof is omitted.

By Proposition 1, the upper bound of CR local delay is approximately

$$\tilde{D}'=\frac{-1}{(\lambda+\mu)T}W(Z), \tag{12}$$

where $Z=\frac{-(\lambda+\mu)^2T\left(pC_\alpha-\frac{\varphi}{2}\right)e^{-k\mu}}{\mu\left(p(1-p)\frac{\varphi}{2}\left(e^{-\lambda_S\frac{\varphi}{2}R^2}-e^{-\lambda_S pC_\alpha R^2}\right)\right)}$, and omega function $y=W(x)$ is the unique solution of equation $ye^y=x$.

4 The Analysis of the End-to-End Delay

4.1 The Upper Bound of the End-to-End Delay

Let D_i^u denote the upper bound of CR local delay of ith hop, the upper bound of end-to-end delay is derived as

$$D_i^u=\frac{1}{p(1-p)\bar{p}_sP_{II}\left(\sum_{k=1}^{i}D_k^uT\right)}.$$

If average h_n hops are needed for a typical end-to-end link, the upper bound of the end-to-end delay is

$$D_S^u=\sum_{i=1}^{h_n}D_i^u \tag{13}$$

4.2 End-to-End Delay-Minimized Transmission Radius

Considering time slot T is a small value in units of tens of microseconds, it is reasonable to optimize $\bar{D}_S^u$ in the following instead of D_S^u .

$$\bar{D}_S^u\approx h_nD_1^u, \tag{14}$$

where $h_n = \frac{L_{S-D}}{d} = L_{S-D} / \left(R - \frac{\text{DawsonF}\left[\sqrt{\varphi\lambda_S/2}R\right]}{\sqrt{\varphi\lambda_S/2}} \right)$, L_{S-D} denotes the distance from a typical source to the destination. And

$$\bar{D}_S^u = -L_{S-D} W\left(K_0 / \left(e^{-\lambda_S \frac{\varphi}{2} R^2} - e^{-\lambda_S p C_\alpha R^2} \right) \right) / T(\lambda+\mu) \left(R - \frac{\text{DawsonF}[\sqrt{\varphi\lambda_S/2}R]}{\sqrt{\varphi\lambda_S/2}} \right) \tag{15}$$

where $K_0 = \frac{-(\lambda+\mu)^2 T\left(pC_\alpha - \frac{\varphi}{2}\right) e^{-k\mu}}{\mu p (1-p)\frac{\varphi}{2}}$. In order to get the optimal transmission radius R_{opt} that minimizes $\bar{D}_S^u$, let $f(R) \equiv R - \frac{\text{DawsonF}\left[\sqrt{\varphi\lambda_S/2}R\right]}{\sqrt{\varphi\lambda_S/2}}$ and $g(R) \equiv W(z(R))$, where $z(R) \equiv K_0 / \left(e^{-\lambda_S \frac{\varphi}{2} R^2} - e^{-\lambda_S p C_\alpha R^2} \right)$. For the derivative of omega function W: $\frac{dW}{dz} = \frac{W(z)}{z(1+W(z))}$, after some algebra, we have

$$\frac{K_0^2 [1 + W(z)]}{\lambda_S R f(R)} = \frac{\varphi e^{-\lambda_S \frac{\varphi}{2} R^2} - 2pC_\alpha e^{-\lambda_S p C_\alpha R^2}}{\left(e^{-\lambda_S \frac{\varphi}{2} R^2} - e^{-\lambda_S p C_\alpha R^2} \right)}. \tag{16}$$

And R satisfies

$$\varphi e^{-\lambda_S \frac{\varphi}{2} R^2} - 2pC_\alpha e^{-\lambda_S p C_\alpha R^2} > 0. \tag{17}$$

Hence the end-to-end delay-minimized transmission radius

$$R_{opt} > \sqrt{\ln \frac{\varphi}{2pC_\alpha} / \lambda_S \left(\frac{\varphi}{2} - pC_\alpha \right)}. \tag{18}$$

5 Simulation Results

In our simulations, $\alpha = 4, T = 20\,\mu\text{s}$, $\beta = 1\,\text{dB}, \lambda = 0.03, \mu = 0.05, p = 0.2$, $\varphi = 7\pi/9$, $\lambda_S = 0.02$ nodes/m^2.

In Fig. 1, we compare the simulation results of end-to-end delay with its upper bound D_S^u . As shown in the figures, it is practicable to improve the performance of the multi-hop delay by optimizing D_S^u. Specifically, the optimal transmission radius $R_{opt} = 10$ satisfies the analytic inequality in Sect. 4.2.

Figure 2 illustrates the simulated end-to-end delays using *FNR* and Dijkstra algorithms. In the figure, the transmission radius R is set to be a feasible value which satisfies Sect. 4.2 ($R_{opt} = 10$). The figure also shows that the multi-hop

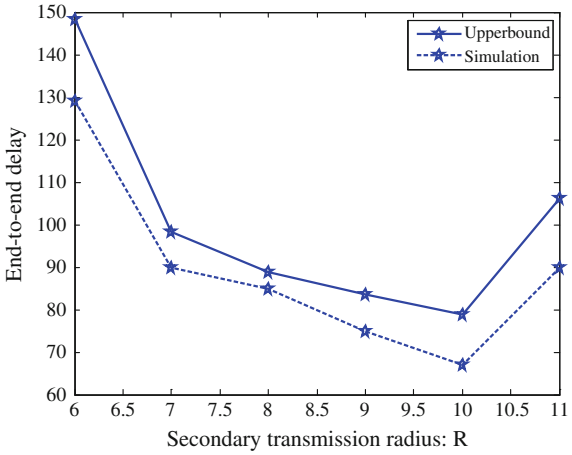

Fig. 1 The end-to-end delay versus secondary transmission radius R

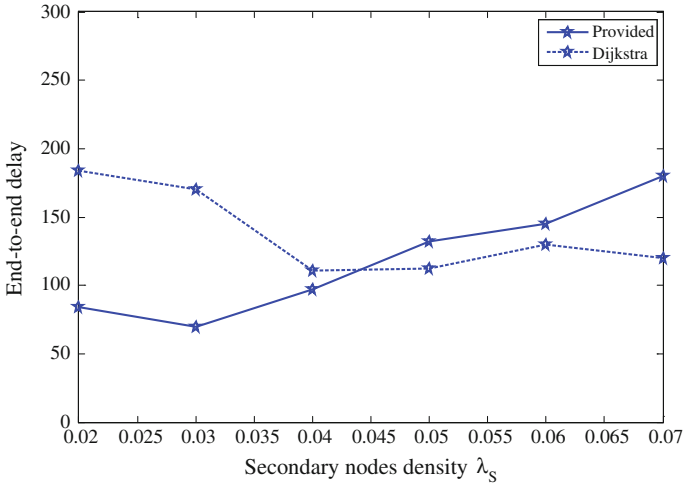

Fig. 2 The end-to-end delay versus λ_S with a different routing algorithm

delay-minimizing FNR algorithm outperforms Dijkstra algorithm in terms of multi-hop delay when secondary nodes density λ_S is a small value. There is an opposite result when λ_S increases to a certain value. This is due to the interference which in creases with the secondary node density and then reduces the accuracy of the approximation.

6 Conclusions

We have provided a comprehensive analysis of the local delay in Poisson CR Ad Hoc networks. The upper bounds of CR local delay and the end-to-end delay are derived by an approximation of exponential function and the iterative method. Furthermore, by numerical and simulation results, we illustrate the relationship between these delays and some important secondary network parameters: nodes density and transmission radius. It is achievable to promote the performance of CR network by optimizing transmission radius in FNR protocol when secondary nodes density is small. In addition, the presence of more than two licensed channels is not treated in this paper, and this will be studied in our future investigation.

Acknowledgments This work is supported by the National Natural Science Foundation of China (NSFC) under Grant 61501325, and the Doctor Foundation of Tianjin Normal University under Grant 52XB1507, and National Natural Science Foundation of China under Grant No. 11404240

References

1. Baccelli F, Blaszczyszyn B (2010) A new phase transition for local delays in manets. In: Proceedings of IEEE INFOCOM, 15–19 March 2010, San Diego, USA, pp 1–9
2. Haenggi M (2010) Local delay in static and highly mobile poisson networks with ALOHA. In Proceedings of IEEE international conference on communications (ICC'10), 23–27 May 2010, Cape Town, South Africa, pp 1–5
3. Haenggi M (2013) The local delay in Poisson networks. IEEE Trans Inf Theory 59(3): 1788–1802
4. Gupta P, Kumar PR (2000) The capacity of wireless networks. IEEE Trans Inf Theory 46(2): 388–404
5. Stoyan D, Kendall WS, Mecke J (1995) Stochastic geometry and its applications. Wiley, Chichester
6. Baccelli F, Blaszczyszyn B, Muhlethaler P (2006) An ALOHA protocol for multi-hop mobile wireless networks. IEEE Trans Inf Theory 52(2):421–436
7. Li D, Yin C, Chen C et al (2010) A selection region based routing protocol for random mobile ad hoc networks. In: Proceedings of IEEEGLOBECOM, 6–10 Dec 2010, Miami, USA, pp 104–108
8. Stamatiou K, Haenggi M (2013) Delay characterization of multi-hop transmission in a poisson field of interference. IEEE/ACM Trans Netw 1:99
9. Yin C, Gao L, Cui S (2010) Scaling laws for overlaid wireless networks: A cognitive radio network vs. a primary network. IEEE/ACM Trans Netw 18(4):1317–1329
10. Wei R, Zhao Q, Anantheram S (2011) On the connectivity and multi-hop delay of Ad Hoc cognitive radio networks. 29(4):805–818
11. Han C, Yang Y (2011) Information propagation speed study in multi-hop cognitive radio networks. In: Proceedings of IEEE INFOCOM, 10–15 April 2011, Shanghai, China, pp 226–230

A Design on Monitoring Data Acquisition System Based on ZigBee Sensor Network for Unconventional Gas Wells

Zhiguo Li, Shubin Wang, Dongyu Liu, Junfei Chang and Yanhong Ge

Abstract In order to improve the collection efficiency for some production data on unconventional gas wells, and ensure the real time and accuracy of getting data, this paper uses the ZigBee wireless sensors to set up a monitoring network for some production data. ZigBee wireless sensor nodes are distributed in gas wells to collect oil pressure, set pressure, gas temperature, voltage of sensor nodes, etc. These parameters are transferred from the terminal node to the coordinator nodes, and then transmitted to remote monitoring center through GSM wireless transceiver module. The system can periodically transmit data, and also can transmit paroxysmal production parameters.

Keywords Unconventional gas wells · ZigBee wireless sensor networks · Data acquisition

1 Introduction

Traditional mining and monitoring technology cannot support the exploiting of unconventional gas efficiently. With the development of wireless sensor network, more and more wireless sensors are applied into the oil or natural gas industry [1–3]. ZigBee technology is a wireless communication technology which is unified by the technical standards IEEE802.15.4, and can set up a wireless transmission network whose number of nodes is not fixed for different tasks and different venues. ZigBee technology has the characteristics of low power consumption, low cost, and low

Z. Li · S. Wang (✉) · D. Liu · J. Chang · Y. Ge
College of Electronic Information Engineering, Inner Mongolia University, Hohhot, China
e-mail: wangshubin@imu.edu.cn

Q. Liang et al. (eds.), *Proceedings of the 2015 International Conference on Communications, Signal Processing, and Systems*, Lecture Notes in Electrical Engineering 386, DOI 10.1007/978-3-662-49831-6_12

rate. It meets the requirement of unconventional gas monitoring [4–6]. For meeting the production monitoring for unconventional gas, this paper applies ZigBee wireless sensor networks to monitor the production data of unconventional gas.

2 System Design

Unconventional gas well monitoring and data acquisition system collects environmental data from an area of gas well group. The gas tree of each gas well is responsible for acquiring oil pressure, set pressure, temperature, and the voltage of ZigBee node. Each gas tree is a ZigBee network, and each gas tree transfers the data acquired from respective network to the upper sensor nodes, then, to the coordinator node, and finally coordinator uses GSM wireless module to transfer the gathered data to the remote monitoring center through the gateway. Overall system design is shown in Fig. 1.

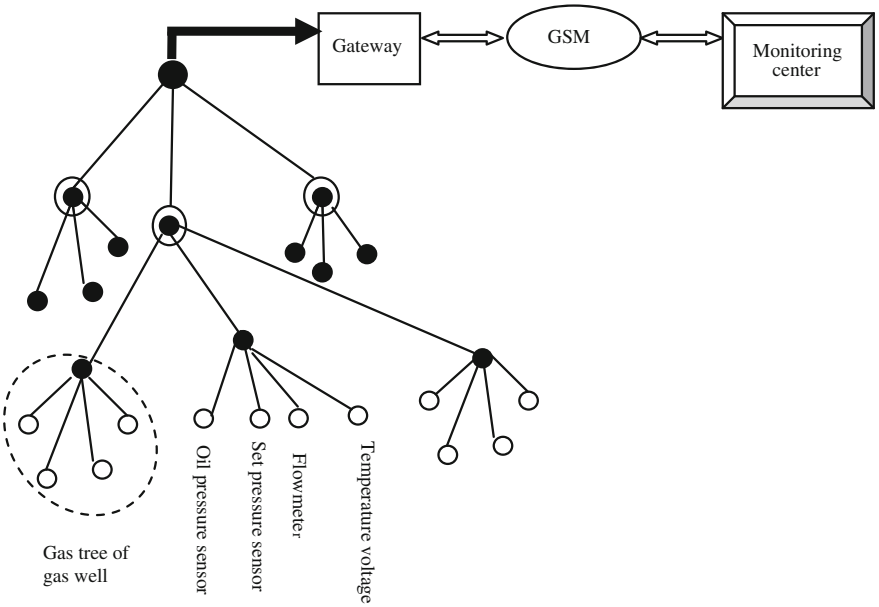

Fig. 1 System design

The function of the system includes the following three points:

1. Uploading the parameters acquired from various gas trees to the coordinator, including oil pressure, set pressure, temperature, and node voltage. Replacing the battery timely when the node voltage is below a certain voltage value and cannot complete the acquisition and transmission ensures the acquisition system work uninterruptedly.
2. Proactive and reactive data transmission.
   There is no need to send data ceaselessly because gas wells environmental monitoring data changes continuously, it will not change by leaps and bounds. The system adopts two means of transmission. The first one is a cyclical data transmission. System sets count time (CT). Nodes are awakened when the count time arrives and transmit data to the coordinator. The second is reactive data transmission. The oil pressure and set pressure threshold values are preset by system. Nodes are awakened to transmit data immediately when the oil pressure or set pressure exceeds the threshold regardless of whether it reaches the count time (CT).
3. The acquired data is transmitted to the remote monitoring center using GSM wireless module through the gateway.
   The sensor that acquires oil pressure is installed on the position where gas tree trachea connects to the gas nozzle, and the oil pressure mainly reacts to the ability of gas tree of supplying liquid gas. The sensor that acquires set pressure is mounted on the position on which sleeve valve of gas tree is, and the set pressure mainly reacts to gas well's differential pressure of production. The distribution of various sensors in gas well's gas tree is shown in Fig. 2.

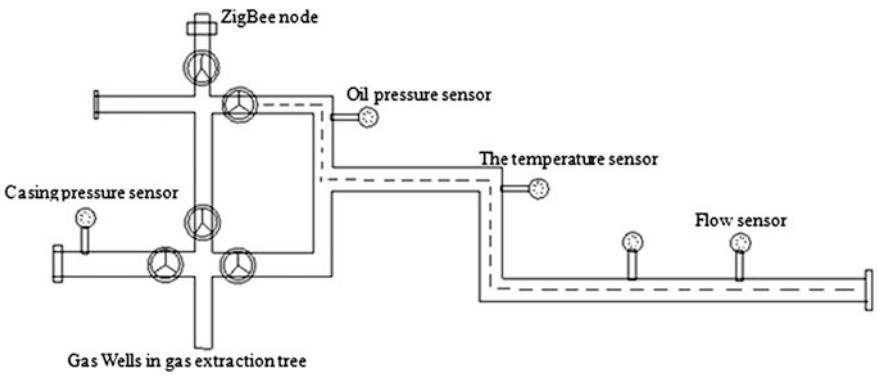

Fig. 2 Sensors distributed on the tree of gas wells

3 Software Design

The operations and sensor tasks need to be added to the APP folder sequentially in IAR project, and it needs to compile two functions to add a new task: initialization function and event handler function. Initialization function should be added to the end of osalInitTasks() and the address of the event handler function should be added to the array(tasksArr[]) and we must ensure the sequence of events and event handler functions is one-to-one correspondence.

3.1 The Data Acquisition Software Design of Oil Pressure and Set Pressure Sensor

It needs to compile terminal node program and coordinator node program separately in the software implementation process in which oil pressure and set pressure sensors acquire the data. The software flow chart of terminal node is shown in Fig. 3. Terminal nodes mainly transmit the data acquired by the pressure transmitter to the coordinator through ZigBee wireless module and we need to compile two

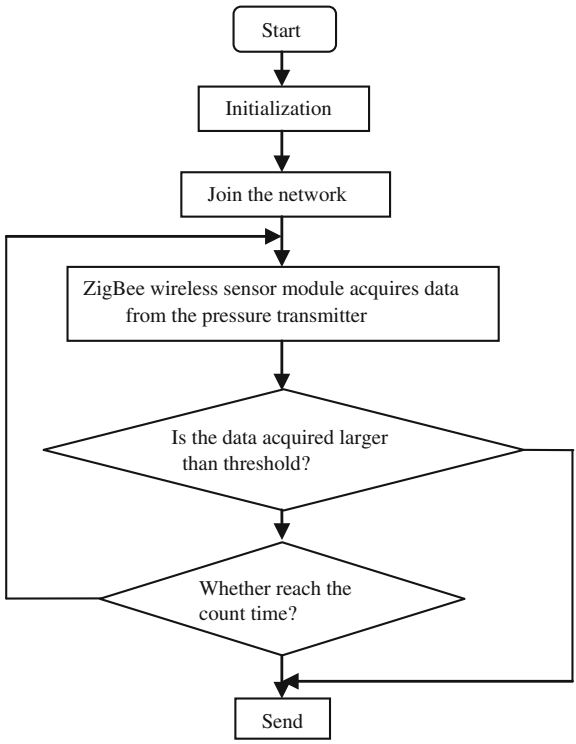

Fig. 3 The terminal node software flow chart

functions in the terminal node program: initialization function of the pressure transmitter (void_GenericApp_Init()), event handler function(GenericApp_ProcessEvent()), and send function(sendPress()). The cycle and response to events of the terminal node data transmission should be set in the function-osal_start_timerEx (uint8 taskID, uint16 event_id, uint16 timeout_value).

The general steps on adding new task of pressure data acquisition in Z-Stack protocol stack are as follows:

1. Adding the function declaration folder (press.h) of the pressure sensors and the folder of implement function (press.c) to the source folder and adding it to the APP directory in the IAR software.
2. Adding the function pointer of oil pressure (set pressure) acquisition tasks to the array (tasksArr[]).
3. Adding the initialization function (GenericApp_Init()) of oil pressure(set pressure) acquisition tasks to the function (osalInitTasks(void)).
4. Compiling oil pressure (set pressure) acquisition event handler function (Generic App_Process Event()), initialization function(Generic App_Init()), and send function(send Press ()).

Coordinator is mainly responsible for creating a network, controlling the join of terminal node, sending commands and uploading data. In the program, coordinator is mainly used to receive the data which is transmitted from the terminal nodes and show it on the upper computer through the serial ports. Coordinator software flow chart is shown in Fig. 4.

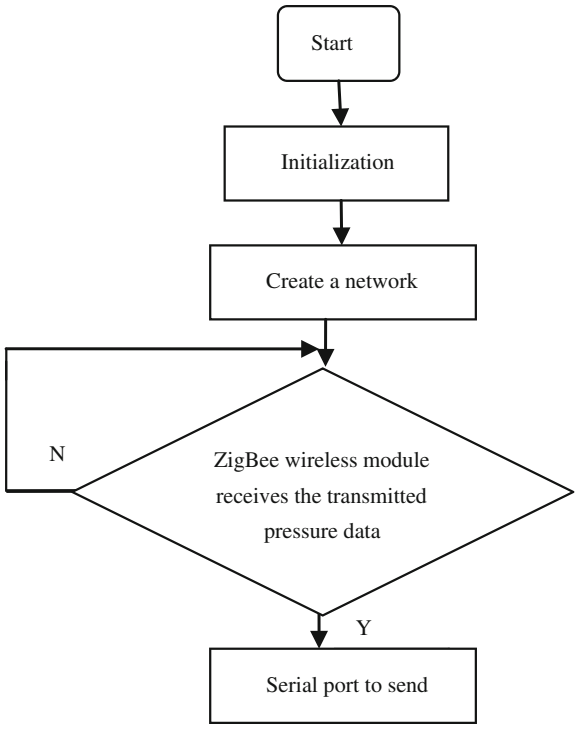

Fig. 4 The coordinator software flow chart

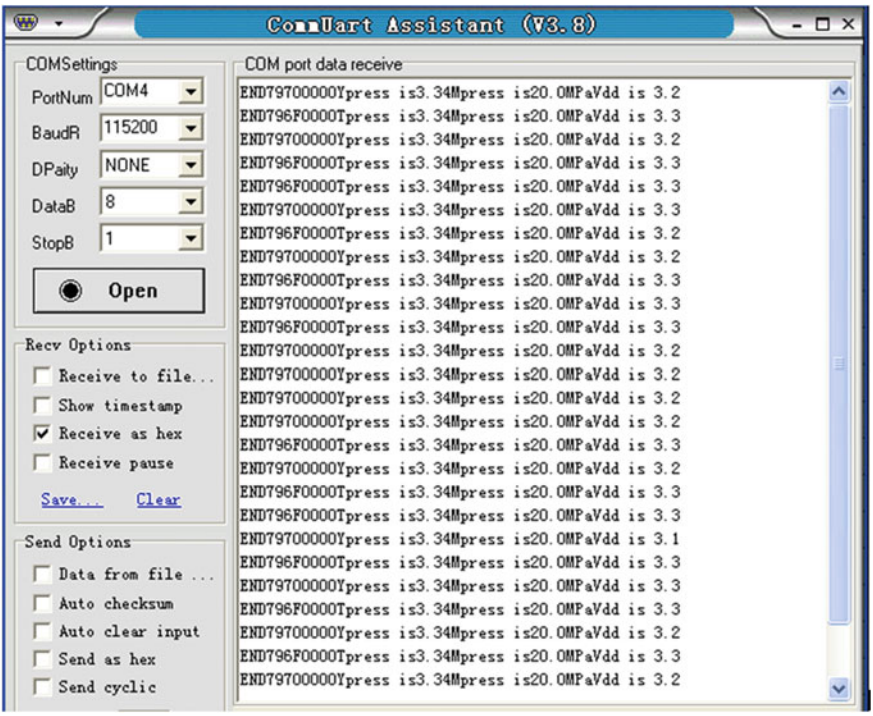

Fig. 5 Debugging results of oil pressure and set pressure

The debugging result of oil pressure and set pressure data is shown in Fig. 5 after the program is downloaded to the appropriate development board. Because the pressure acquired by the pressure transmitter is equal to the value of the pressure on the sensor itself, the pressure value is 0 when the sensor is not installed on the gas tree, the oil pressure threshold is 15 Mpa, set pressure threshold is 20 MPa, and the voltage value is equal to the voltage value of ZigBee node battery in the program.

3.2 The Software Design of Temperature and Node Voltage Data Acquisition

It also needs to compile, respectively, node and coordinator node program in the software implementation process of the temperature and node voltage data acquisition, and it is necessary to download them to appropriate ZigBee wireless module board in different types when you compile.

Compiling the coordinator program should mainly complete the following three points:

1. GenericApp_Init()-task initialization function, it mainly achieves the initialization of the port and the serial port and finishes the initialization of hardware circuit implementation;
2. GenericApp_ProcessEvent0-taskevent handler function, it mainly processes the data transmitted by the nodes;
3. GenericApp_MessageMSGCB() shows the data through the serial port on the PC after it processes the data packet. The debugging result of temperature and node voltage data is shown in Fig. 6. The temperature in the figure is the gas tree temperature and the voltage value is the voltage value of ZigBee node battery.

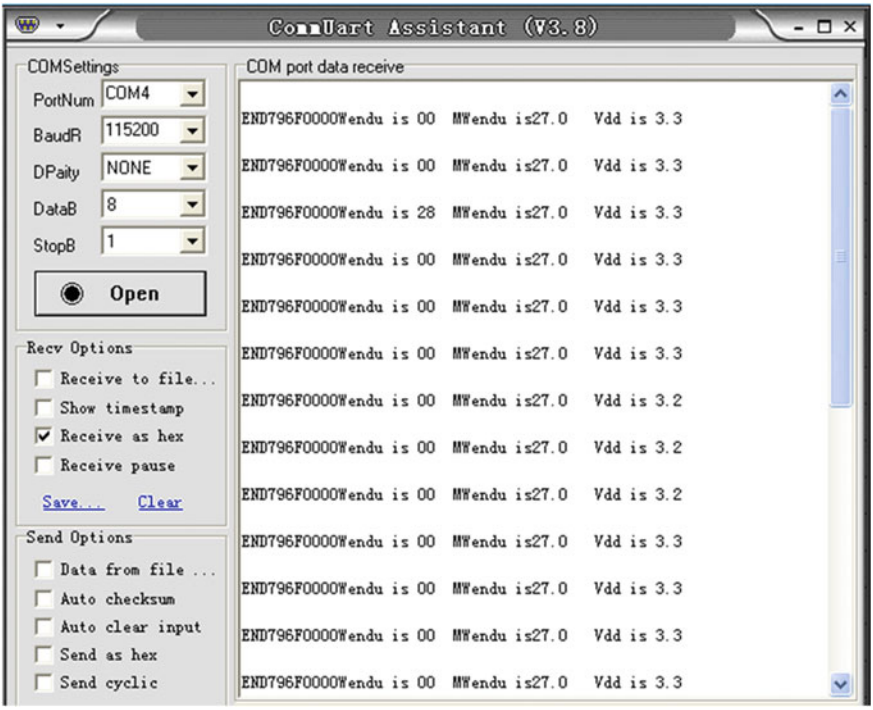

Fig. 6 Debugging results of temperature and voltage

4 System Debugging Results

We can get the data information that is acquired by the sensor through respectively debugging the data acquired by the system above. Now, we combine all the sensors with ZigBee wireless module and establish the monitoring and data acquisition system of unconventional gas environment. The system hardware connection is shown in Fig. 7. In the system, ZigBee module is Net Bee Company's production, Pressure transmitter is Beijing Kunlun Cuhk Company's production, gateway is ARM's learning development board which is made in Feiling Company and GSM wireless module is GTM900Bmodule made in Huawei Company.

The data uploaded is received through GSM wireless module and connected to the computer through the serial port. The results are shown in Fig. 8 through the serial port assistant.

All sensor nodes data acquired by the coordinator is transmitted to remote monitoring center through GSM module and stored in SQL Server database. The data extracted from the SQL Server database is shown in Fig. 9. The address shown in the figure refers to the ZigBee node address assigned by the coordinator, we can judge which specific ZigBee node on which well according to the address value.

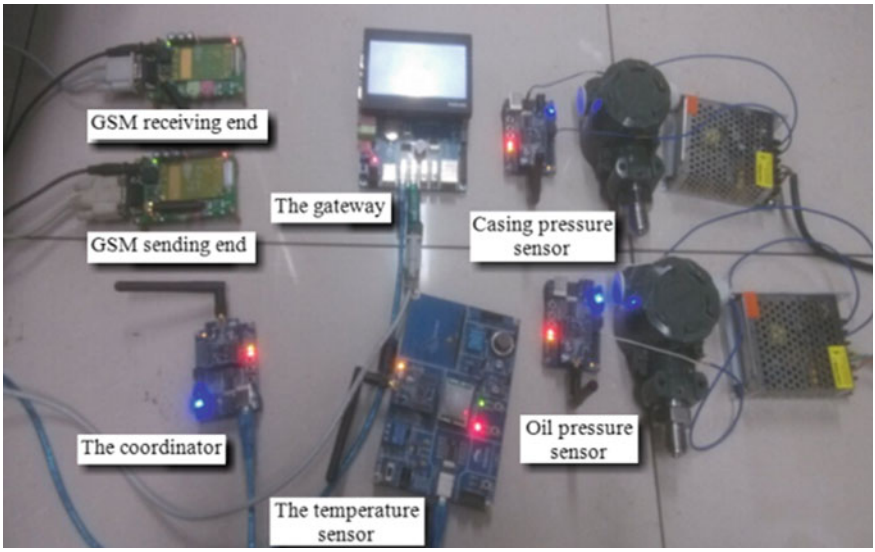

Fig. 7 The system hardware connection diagram

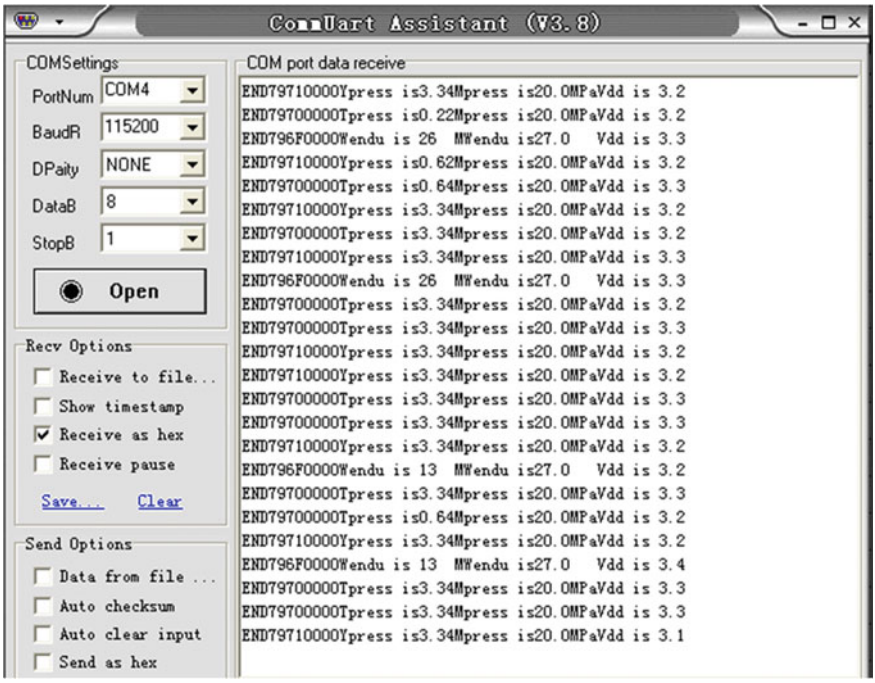

Fig. 8 System debugging result

Address	Oil pressure	Casing pressure	Temperature	Threshold value	Voltage
796F0000	NULL	NULL	28	27.0	3.z2
79710000	NULL	00	NULL	20	3.3
79700000	00	NULL	NULL	15	3.3
796F0000	NULL	NULL	28	27.0	3.z2
79710000	NULL	00	NULL	20	3.3
79700000	00	NULL	NULL	15	3.3
796F0000	NULL	NULL	28	27.0	3.z2
79710000	NULL	00	NULL	20	3.3
79700000	00	NULL	NULL	15	3.3
796F0000	NULL	NULL	28	27.0	3.z2
79710000	NULL	00	NULL	20	3.3
79700000	00	NULL	NULL	15	3.3
796F0000	NULL	NULL	28	27.0	3.z2
79710000	NULL	00	NULL	20	3.3
79700000	00	NULL	NULL	15	3.3
796F0000	NULL	NULL	28	27.0	3.z2
79710000	NULL	00	NULL	20	3.3
79700000	00	NULL	NULL	15	3.3

Fig. 9 Data in the SQL Server database

5 Conclusion

Proactive and reactive wireless sensors are used in the network establishment of ZigBee wireless sensor to ensure the real time and accuracy of the data acquisition according to the characteristics and the actual needs of unconventional gas wells. The system uses wireless transmission in acquiring and transmitting data. It solves the monitoring difficulty that unconventional gas distributes dispersedly in the wild, enhances the safety index of gas production, and improves the productive life of wireless sensor network. The system mainly solves the following problems: (1) The wireless sensor networks based on ZigBee protocol specifications acquire gas environment parameters hierarchically, then, the data is hierarchically transmitted up in turn, and finally converged to the coordinator. In fact, the acquired gas monitoring data includes oil pressure, set pressure, flow, the temperature, and sensor node voltage. (2) Setting the count time CT and the threshold value of oil pressure and set pressure during the sensor acquires the data to ensure that the system can acquire the environmental parameters periodically, in addition, it can respond to emergencies and rapidly reacts to the emergencies. (3) The acquired data is transferred to the remote monitoring center through the gateway using GSM wireless module. It realizes the wireless acquisition and the wireless transmission of the data.

Acknowledgments Shubin Wang (wangshubin@imu.edu.cn) is the correspondent author and this work was supported by the PetroChina Innovation Foundation (2014D-5006-0603).

References

1. Gislason D (2009) ZigBee wireless networking, vol 1. Newnes
2. Elahi A, Gschwender A (2009) ZigBee wireless sensor and control network, vol 1. Prentice Hall
3. Farahani S (2008) ZigBee wireless networks and transceivers. Ph.D. Newnes
4. Gao M, Xu J, Tian J, Zhang F (2008) ZigBee wireless mesh networks for remote monitoring system of pumping unit. Intell Control Autom 7
5. Magbool S, Chandra N (2013) Real time wireless monitoring and control of water systems using ZigBee 802.15.4. In: 2013 5th International conference on computational intelligence and communication networks (CICN), pp 150–155
6. Seesaard T, Seaon S, Khunarrak C, Lorwongtragool P, et al (2014) A novel creation of thread-based ammonia gas sensors for wearable wireless security system. In: 2014 11th International conference on electrical engineering/electronics, computer, telecommunications and information technology (ECTI-CON), pp 1–4

Nearest Access Routing Algorithm for the ZigBee Network in 5G Environment

Jiasong Mu and Shu Jiang

Abstract ZigBee network uses a mixed routing mechanism combined with hierarchical tree routing (HRP) and ad hoc on demand distance vector (AODV) to meet the different demands. However, the existing scheme cannot fully satisfy the applications. The 5G communication network is featured by the smarter devices and the native support for the M2 M communication. The 5G terminals have the potential to optimize the data transmission in the ZigBee network. In this paper, we proposed a nearest access routing algorithm for the ZigBee network in 5G environment. Based on the accessibility to various kinds of wireless network of the 5G terminal, the data flow in its neighbourhood is converged and transmitted in the IP network. By that mechanism, the bandwidth and energy resources in the ZigBee network can be saved. The simulation results show that the proposed algorithm effectively share the traffic for the ZigBee network by reducing and balancing the throughput.

Keywords ZigBee · Routing algorithm · 5G · Throughput

1 Introduction

ZigBee technology is characterized by low cost, low power, low data rate, and simplicity [1]. It uses a mixed routing mechanism combined with hierarchical tree routing (HRP) and ad hoc on demand distance vector (AODV) [2]. HRP, which is based on the address distribution, provides a simple and reliable measure for data transmission, though it is not always efficient and robust. For AODV, each node may initiate a routing discovery when necessary, a global shortest path between the

J. Mu (✉)
College of Electronic and Communication Engineering, Tianjin Normal University, Tianjin, China
e-mail: mujiasong@aliyun.com

S. Jiang
704 Institute, China Shipbuilding Industry Corporation, Shanghai 200031, China

Q. Liang et al. (eds.), *Proceedings of the 2015 International Conference on Communications, Signal Processing, and Systems*, Lecture Notes in Electrical Engineering 386, DOI 10.1007/978-3-662-49831-6_13

source and destination is obtained during the process and the data frame was sent along the route. Due to the limited processing capabilities, storage, power supplies, and communication bandwidth for the ZigBee devices, current network formation and routing protocols described in the ZigBee specification cannot fully address power consumption issues [3]. To optimize the routing performance, we could not only try to improve the algorithms based on the existing network, but also look for the measurements from the deployed environment, which includes the coming 5G communication network.

5G Technology is a name to indicate the next most important stage of mobile communication standards beyond the 4G standards. Due to the extremely higher aggregate data rates and the much lower latencies required, along with other disruptive technologies, the smarter devices and the native support for the M2 M communication are two of the most important features in the 5G communication network [4]. The smarter devices will have access to different wireless technologies at the same time [5]. Meanwhile, a native inclusion of M2 M communication in 5G involves satisfying three fundamentally different requirements associated with different classes of low data rate services: support of a massive number of low-rate devices, sustaining a minimal data rate in virtually all circumstances, and very low latency data transfer [6]. Based on the above functionalities, it is reasonable to take the ubiquitous smarter terminals into account to improve the ZigBee routing performance in the 5G environment.

A sample of the ZigBee network with 5G terminals is shown in Fig. 1. As the accessibility to various kinds of wireless network, the 5G devices in the coverage may be utilized to optimize the data transmission for the ZigBee network. Different from the existing relay or external node, note that the 5G terminal could also access the IP network. That means, beside the existing sink, the network have more devices that could communicate with the management devices. Our work is to utilize these links to share the traffic in the ZigBee network to lighten the overload for the ZigBee devices with limited resources.

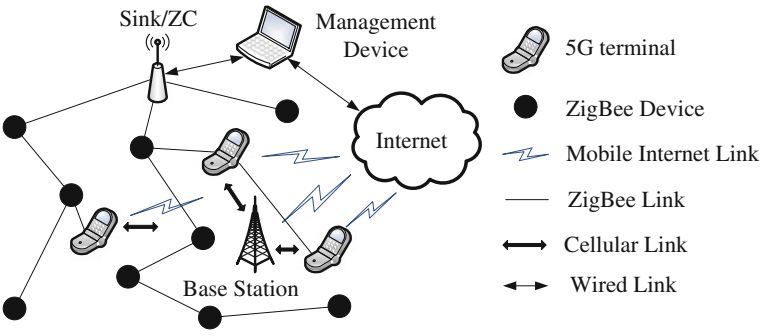

Fig. 1 The ZigBee network in 5G environment

To the best of our knowledge, this is the first work on the ZigBee routing improvement in the 5G environment. The key problem of our task is to design a proper routing algorithm that allows the 5G terminal to converge the data flows in its neighbourhood and has no conflicts against the existing ZigBee specification. Considering the dual ZigBee routing algorithms, the AODV-based method requires the 5G terminal broadcast its accessibility of the Internet when it joins the network. The ZigBee nodes also have to cache the information and then find the path to the 5G device by sending routing discovery. Finally, the 5G node needs to announce its leaving. The procedure described may generate a lot of data and consume the bandwidth and energy resources for the ZigBee devices. So we have to exploit the HRP-based routing algorithm to control the routing cost.

In our previous work [7], the physical depth is introduced to the routing discovery optimization. In this paper, we are going to develop the concept. On that basis, a nearest access routing (NAR) algorithm is proposed to improve the ZigBee network in the 5G environment.

The rest of this paper is organized as follows: Sect. 2 will briefly introduce the related contents in the ZigBee specification, the nearest access routing algorithm will be proposed in Sect. 3. In Sect. 4, simulation results are presented. Finally, the conclusion is shown in Sect. 5.

2 ZigBee Specification and Routing Methods

2.1 Address Allocation and HRP

In ZigBee specification, it is recommended to use Distributed Address Allocation Mechanism (DAAM) for address assignment to form tree structure. The parameter *Cm* represents the largest number of children nodes, *Rm* means the number of children nodes which can be a router, and *Lm* decides the maximum depth in the network. And for the same network, different nodes usually have constant *Cm* and *Rm*. Every potential parent is provided with a finite sub-block of the address space, which is used to assign network addresses to its children. Given *Cm*, *Lm*, and *Rm*, we can compute the function *Cskip*(*d*) as the size of the address sub-block distributed by each parent at depth *d* as (1) [1].

$$Cskip(d) = \begin{cases} 0, & Rm = 0, \\ 1 + Cm \times (Lm - d - 1), & Rm = 1, \\ (1 + Cm - Rm - Cm \times R^{Lm-d-1})/(1 - Rm), & Rm > 1. \end{cases} \quad (1)$$

The network addresses $A_{d+1,rn}$ and $A_{d+1,el}$ shall be assigned to the *n*-th router child and *l*-th end device child at depth $d + 1$ in a sequential manner, respectively, as shown in (2):

$$\begin{aligned} A_{d+1,rn} &= A_{parent} + Cskip(d) \cdot (n-1) + 1 \\ A_{d+1,el} &= A_{parent} + Cskip(d) \cdot R_m + l \end{aligned} \tag{2}$$

where A_{parent} represents the address of the parent and $1 \leq n \leq Rm$.

The hierarchical topology in ZigBee network is based on DAAM. In this tree shape structure, if the destination address is in the address space that a node is managing, the node forwards the packet to one of its child nodes. Otherwise, it forwards the packet to its parent.

The depth is defined as the transmission hops in the HRP. It indicates the topology distance between the local device and the ZC.

2.2 Neighbour Table

Each ZigBee device maintains a neighbour table which has all its neighbour's information in the 1-hop transmission range. The contents for a neighbour entry are the network's PAN (Personal Area Network) identifier; node's extended address, network address, device type, relationship, LQI and etc. Optionally, additional information such as the depth can be included. Entries in the table are created when the node joins to an existing network. Conversely, the neighbour entry is removed when the neighbour node leaves the network. Since the information on the neighbour table is updated every time a device receives any frame from the some neighbour node, the information of the neighbour table can be said to be up-to-date all the time.

3 Nearest Access Routing Algorithm

The original depth limits the transmission to parent–child links. Here, we introduce the concept of the physical depth (PD), which is defined as the minimum hop counts from a certain node to its nearest device which is able to access the internet/management device. So the *PD* indicates the minimum hops to the network where the resource is not such limited. Thus, the *PD* of the ZC and the 5G terminals is 0.

For a device in the neighbourhood of a zero-*PD* device, if the *PD* information is required in the neighbour table, its *PD* may be set 1 as it may find a neighbour table entry that indicates a device with 0 *PD*. Similarly, all the nodes within the transmission range of the *PD* 1 devices may have *PD* 2, the *PD* of any device can be recursively decided. The principle can be simply stated as: the *PD* value of a certain node is one plus the minimum *PD* value in its neighbour table.

However, there is no such content in the neighbour table for the ZigBee specification. Fortunately, the node depth is an optional term. Moreover, if the network

address is assigned as the DAAM and the network address is given, the node depth can be calculated as the following pseudo codes [8]:

Pseudo codes: Algorithm of deciding the topology depth for node X

Q_0 = ADDR(X)
for d = 0 to Lm **do**
if Q_d == 0 **then**
D(X) = d **break**;
else if d > 0 and $Q_{d-1} \geq Rm \cdot Cskip(d-1)$ **then**
D(X) = d **break**;
else
$Q_{d+1} = (Q_d - 1) \bmod (Cskip(d))$
end if

where Q_d is introduced to determine whether the node X is a router node or an end device at depth *d*. One can see that the depth information is redundant in this case. Therefore, it can be replaced by the *PD*. On that basis, the nearest access routing algorithm will be discussed.

Based on the physical depth maintenance mechanism above, the NAR routing is simple. The diagram is shown in Fig. 2. When a node is receiving a packet, it may look through its neighbour table. If a device has the unique minimum *PD*, it may be chosen as the next hop destination. Otherwise, a parameter *Txed* is introduced to represent the times a neighbour is selected as the next hop in the case that not a best route can be found. For the neighbours with the same minimum *PD* value, the receiving node may compare the *Txed* value, which is initialized 0 when a new neighbour entry is created. If a unique minimum *Txed* value is found, the packet may be forwarded by unicast to the node, and its *Txed* is added 1. Otherwise, the receiving node may randomly choose the next hop destination among the neighbours with the same minimum *PD* and *Txed* values.

Note that the NAR does not change any mandatory contents in the existing ZigBee routing methods. It is fully compatible with the ZigBee specification.

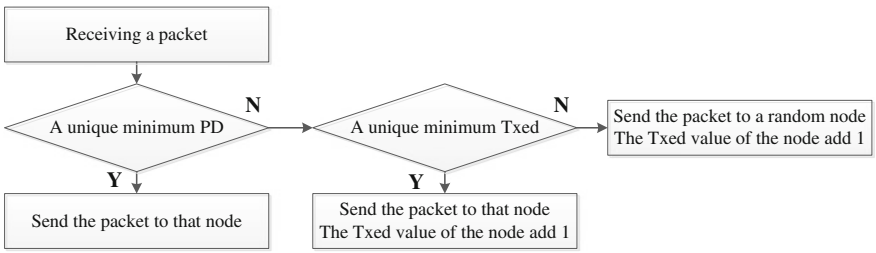

Fig. 2 The diagram of the nearest access routing algorithm

4 Simulations

The performance of the proposed NAR algorithm is discussed in this section. The simulation was implemented in the MATLAB. The NAR was compared with the HRP and AODV routing methods. Some parameters in the simulation were set as follows: the time duration was 300 s; the simulation area was 100 m × 100 m; 100 ZigBee nodes were randomly deployed following the uniform distribution; *Cm, Rm,* and *Lm* were set 4, 4, and 5 separately; the packet size is 1024 bits; the packet interval time was 0.1 s (only the ZigBee nodes generated the packets); the first packet arrival time followed a uniform distribution from 0 to 1 s for each node; the number of 5G terminal varied from 1 to 10; the joining time for each 5G terminal varied from 1 to 50 s; for each scenario, the simulation was carried out 500 times to calculate the average.

The average hop counts in the ZigBee network (excluded the transmission in the 5G terminals) is shown in the Fig. 3. In the HRP, because the hierarchical topology had been constructed when the 5G terminal joined the network, they could not improve the ZigBee routing due to their descendant roles. For the AODV, more nodes meant better opportunities to find a better route; thus the 5G nodes slightly reduced the average hop counts. Compared with the existing algorithm, NAR was able to significantly reduce the transmission in the ZigBee networks. Since each 5G terminals could be regarded as an access to the internet, part of the packet flows were forwarded along with the external links. Moreover, as the slope shown in the figure, we could also conclude that the more 5G terminals were involved, the better improvement the NAR could make.

Figure 4 illustrates the network throughput in the ZigBee network for different routing algorithms. The HRP had little change due to the static network topology, and the AODV had a minor decreasing because of the better route. Note that the

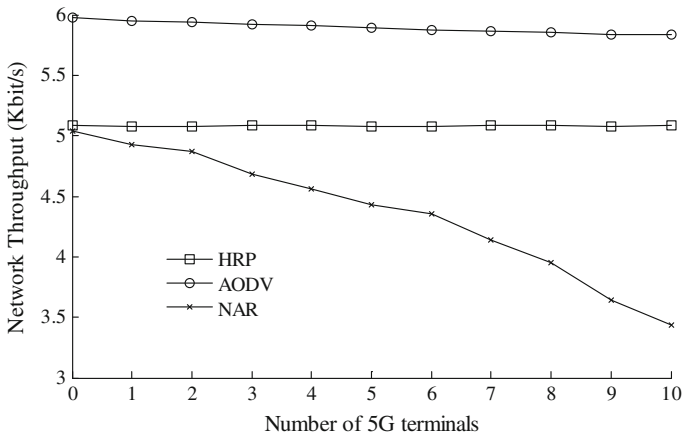

Fig. 3 The average hop counts in the ZigBee network for different routing algorithm

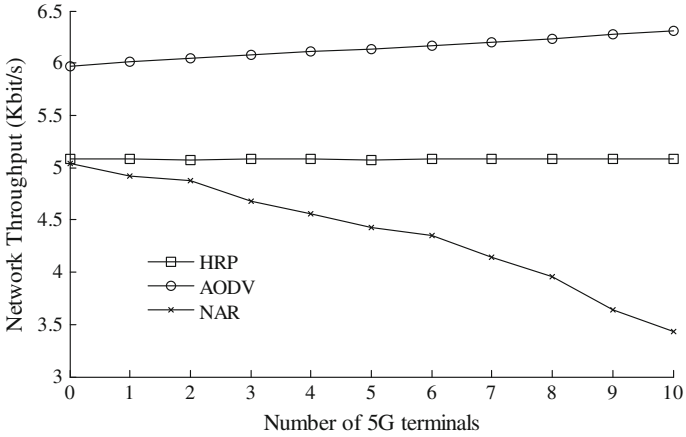

Fig. 4 The throughput in the ZigBee network for different routing algorithm

routing overhead led to a higher average throughput in the AODV, although it had a shorter path. On the contrary, the NAR achieved a lower overall throughput based on its simple forwarding mechanism. Moreover, as the numbers of 5G terminal increased, the packets were further reduced in the ZigBee networks.

To observe the balancing effect of the NAR, the maximum node load in the ZigBee network for different routing algorithm is drawn as the Fig. 5. One could see that the maximum node loads for the HRP and AODV were randomly changed in a higher level; the extra 5G nodes did not change the situation that some low depth nodes were overused. However, the maximum node load was effectively reduced by the sharing of the packets. In the 10 5G nodes case, the maximum node

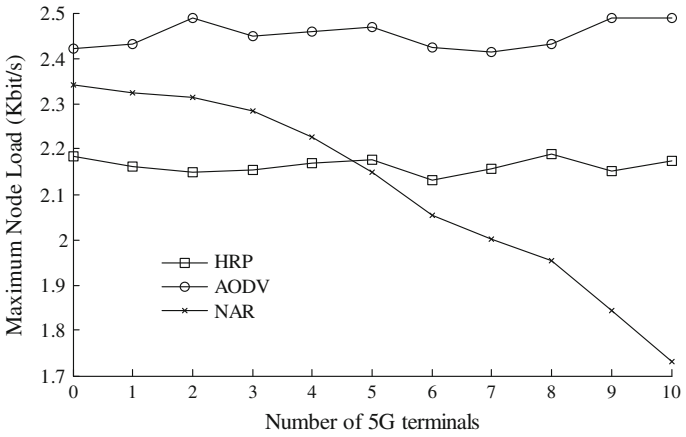

Fig. 5 The maximum node load in the ZigBee network for different routing algorithm

load was 30.3 and 20.3 % lower than the AODV and HRP respectively. Since the data flows in the neighbourhood of the 5G terminals were converged and transmitted by other networks, the traffic and the energy cost were balanced.

5 Conclusions

In this paper, we propose a nearest access routing algorithm for the ZigBee network in the 5G environment. By the introduction of the physical depth, which is defined as the minimum hop counts from a certain node to its nearest device with the accessibility to the internet/management device, a simple forward mechanism is designed to converge the traffic in the 5G terminals' neighbourhood. The simulation results show that the NAR could effectively reduce the throughput and average hop counts in the ZigBee network. Moreover, the traffic is also balanced by decreasing maximum node load.

For our future work, the replacement of the 5G terminals and the different device types will be taken into consideration.

Acknowledgments This work is funded by the National Science Foundation of China, (NSFC: 61401310), the Project of Tianjin University Technology Development Fund (20130714).

References

1. ZigBee Standard Organization (2007) ZigBee specification document 053474r17. ZigBee Alliance, San Ramon
2. Cuomo F, Luna SD, Monaco U, Melodia T (2007) Routing in ZigBee benefits from exploiting the IEEE 802.15.4 association tree. Paper presented at the IEEE international conference on communications. Glasgow, pp 3271–3276. doi:10.1109/ICC.2007.542
3. Metin T, Ibrahim K, PSAR: Power-source-aware routing in ZigBee networks. Wirel Netw 18 (6):635–651. doi:10.1007/s11276-012-0424-5
4. Boccardi F, Heath RW, Lozano A, Marzetta TL, Popovski P (2013) Five disruptive technology directions for 5G. IEEE Commun Mag 52(2):74–80
5. Andrews JG, Buzzi S, Choi W, Hanly SV, Soong ACK, Zhang JC (2014) What will 5G be? IEEE J Sel Areas Commun 32(6):1065–1082
6. Gohil A, Modi H, Patel SK (2013) 5G Technology of mobile communication: a survey. In: 2013 International conference on intelligent systems and signal processing (ISSP). pp 288–292
7. Jiasong Mu, (2014) A minimum physical distance delivery protocol based on ZigBee in smart grid. EURASIP J Wirel Commun Netw 108
8. Li J, Zhu X, Tang N, Sui J (2010) Study on ZigBee network architecture and routing algorithm. Paper presented at the 2010 2nd International conference on signal processing systems (ICSPS), vol 2. Dalian, pp 389–393. doi:10.1109/ICSPS.2010.5555486

Optimal Relay Placement for WSN-Based Home Health Monitoring System

Yanjun Li, Chung Shue Chen, Jianhui Zhang and Kaikai Chi

Abstract Due to the increasing need of health monitoring at home or in senior center, we study the optimal relay node placement problem for wireless sensor networks with data collection and localization requirements. The problem can be modeled as finding a minimum connected k-dominating set. We consider realistic indoor wireless environment and explicitly take into account the effect of obstacles to the radio coverage, instead of using idealistic disc model. We prove the problem is NP-hard and propose an efficient greedy method called optimal relay placement algorithm (ORPA) to derive the best network setup. Results show that by using the proposed method, the number of relays required can be significantly reduced in comparison to two baseline algorithms. The method presented would be also relevant to other systems of similar network connectivity and relay deployment criteria.

1 Introduction

Wireless sensor networks (WSN) have been a promising solution for home health monitoring systems [5, 8] due to its low power, low cost, and easy deployment. It can provide intelligent senior home monitoring service. Since the world population is aging, there is a rapidly increasing demand for being capable of monitoring patients

Y. Li · K. Chi
School of Computer Science and Technology,
Zhejiang University of Technology, Hangzhou, China
e-mail: yjli@zjut.edu.cn

K. Chi
e-mail: kkchi@zjut.edu.cn

C.S. Chen (✉)
Alcatel-Lucent Bell Labs, 91620 Nozay, France
e-mail: cs.chen@alcatel-lucent.com

J. Zhang
School of Computer Science and Technology,
Hangzhou Dianzi University, Hangzhou, China
e-mail: jhzhang.zju@gmail.com

Q. Liang et al. (eds.), *Proceedings of the 2015 International Conference on Communications, Signal Processing, and Systems*, Lecture Notes in Electrical Engineering 386, DOI 10.1007/978-3-662-49831-6_14

in hospital or senior citizens living alone or in nursing home environment so as to offer feedback and assistance for accidence or emergency. Equipped with wearable sensors, vital signs can be automatically collected, processed, and relayed to a remote base station (BS) or gateway. Once the vital signs exceed certain thresholds, alert messages can be sent to a contact or adviser such as doctor or nurse. The doctor or nurse can also query the user's health status anytime and anywhere via Internet.

In such a health monitoring system, there are some immobile relay nodes to communicate with the wearable sensor node carried by the patient or person and to connect to the BS to make the system scalable and more energy-efficient [7, 10]. To maintain pervasive monitoring of the patient, there are two basic requirements. First, there exists at least one bidirectional path from the sensor node to the BS or gateway. Secondly, to locate the patient, the standard is the sensor node should be covered by at least three relays for using triangulation or centroid based positioning methods. In general, localization accuracy can be further improved if more relays are in contact. These issues are in the scope of relay node placement for WSN. There are various works and system designs. For example, in [7], the problem has been generally classified as single-tiered or two-tiered relay placement problems w.r.t. different routing assumptions. Notice that we will focus on the two-tiered case in which the sensor node will transmit data to relays and will not do packet forwarding for other sensor nodes. In single-tiered case, a sensor node also forwards packets.

We model the above problem as *finding a minimum connected k-dominating* ($k \geq 3$) *set*, where the relay set is interconnected and each sensor is adjacent to at least k relays. Related work can be found in for example [1, 6]. Note that in indoor environment, the radio propagation would be significantly affected by obstacles [9]. Existing results often adopt oversimplified radio models for simplicity but cannot be directly applied to address practical systems.

Besides, in our system, we consider the relays are low-power wireless devices. Therefore, the relays do not require wireline connection and can be more flexibly placed. They just need to form a connected wireless network. Moreover, the wearable sensor node needs to be covered by at least three wireless relays for localization, which is for intelligent and automatic home health monitoring service.

The major contributions of our paper are summarized below.

1. To the best of our knowledge, this is the first paper to study optimal relay placement for connected k-radio coverage for above location aware home health monitoring system and model it as minimum connected k-dominating set problem.
2. We explicitly consider the effect of indoor obstacles to radio in the optimization.
3. We prove it is NP-hard and propose an efficient greedy algorithm (ORPA) to optimize the relay placement and minimize the number of required relays.
4. Experiment and simulation work are conducted to evaluate the performance. Results have shown that ORPA can significantly reduce the number of relay nodes.

The rest of the paper is organized as follows. Section 2 describes the system model and problem setup. Section 3 shows the problem is NP-hard and presents ORPA to solve the problem in polynomial time. Section 4 evaluates the performance in comparison to two baseline algorithms. Finally, Sect. 5 concludes the paper.

2 System Model and Problem Setup

In the following, we present the WSN, system model, and technical notations. The architecture of home health monitoring system is shown in Fig. 1a. A wearable sensor node is attached to the patient for sampling vital signs (e.g., body temperature, blood pressure, motion) to be transmitted to the gateway directly or through the relays (e.g., attached to the ceiling) in multiple hops to a remote contact or server [2]. The goal is to allow the remote contact be able to know the patient's state and location any time. For this, there are two basic requirements: (1) there always exists at least one bidirectional path between the sensor and the gateway, and (2) the sensor node can communicate with at least 3 relays wherever the patient moves in the house.

2.1 Radio Propagation Model

In practice, we need to determine the radio coverage of relay nodes for optimal deployment. A generic method for assessing the radio range of a transmitter is as follows: first assume a radio model with some unknown parameters, then collect radio measurements from the environment as training data, and finally feed these

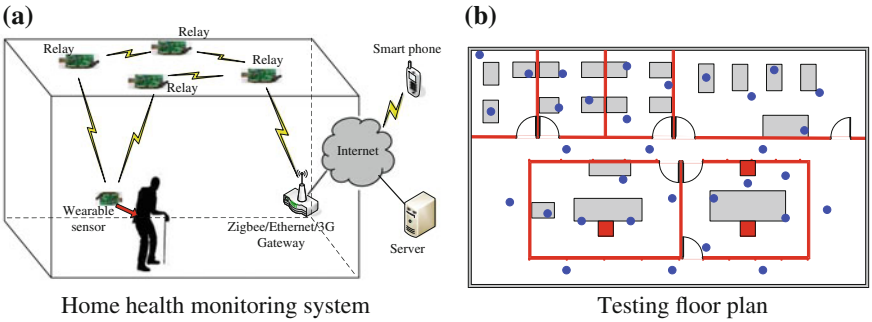

Fig. 1 **a** System architecture. **b** Floor plan: *red lines* are walls (drywall, wooden wall, glass wall, cement pillar), *red squares* are pillars, *gray rectangles* are tables, *blue dots* are possible relays

measurements to the radio model for determining the unknowns. After determining the radio model, each relay's radio range can be estimated with respect to the realistic environment and certain thresholds. For indoor environment, it has been shown in [3] that a radio model that can incorporate the attenuation and blocking effect of obstacles is necessary: Consider each obstacle $o_i \in I_{s,r}$ can attenuate the transmitted signal by a factor γ_{o_i}, where $I_{s,r}$ is the set of obstacles intersecting the line from the transmitter s to receiver r, and denote the distance between s and r by $d(s,r)$, the received signal strength (RSS) at receiver r is expressible as:

$$P(s,r) = P_t - \alpha - 10\beta \log_{10} d(s,r) - \sum_{o_i \in I_{s,r}} \gamma_{o_i}, \tag{1}$$

where P_t is the transmission power, α is the path loss at reference distance equal to 1 meter, β is the path loss exponent. Here, P_t, α and γ_{o_i} are in their decibel values.

There could be a large number and also various types of obstacles see for example our experiment testbed in Fig. 1b, which would require a large amount of training data and also bring high complexity in determining the unknowns of Eq. (1). One can classify obstacles into groups of similar attenuation to reduce the number of unknown parameters and offer similar accuracy as follows [3]: Given a set of groups G, a mapping function $\Pi : I_{s,r} \rightarrow G$, and an attenuation coefficient Γ_g for each group $g \in G$, the RSS at the receiver r can be rewritten as

$$P(s,r) = P_t - \alpha - 10\beta \log_{10} d(s,r) - \sum_{o_i \in I_{s,r}} \Gamma_{\Pi(o_i)}, \tag{2}$$

where the unknowns are α, β and $\Gamma_{\Pi(o_i)}$ with $\Pi(o_i) = 1, 2, \ldots, |G|$, and $|G|$ is the number of classified groups. Clearly, now the number of unknowns equal to $|G| + 2$.

Here, we provide an automatic and efficient algorithm to classify the obstacles into groups with minimum estimation error. The pseudocode of the algorithm is presented in Algorithm 1. The *inputs* to Algorithm 1 are the set of RSS measurements denoted by vector P_r, the distances between senders and receivers denoted by vector d, and the sets of obstacles and classified groups denoted by O and G. The *outputs* are the obstacle classification function Π, the values of α and β, and the attenuation coefficient Γ_g for each obstacle group g, where $g = 1, 2, \ldots, |G|$. Algorithm 1 is guaranteed of convergence and also much faster than exhaustive search.

2.2 Problem Formulation and Definitions

In our system, the sensor nodes are mobile whereas the relays are immobile. In this two-tiered architecture, say relay tier Π_r and sensor tier Π_s as shown in Fig. 2a,

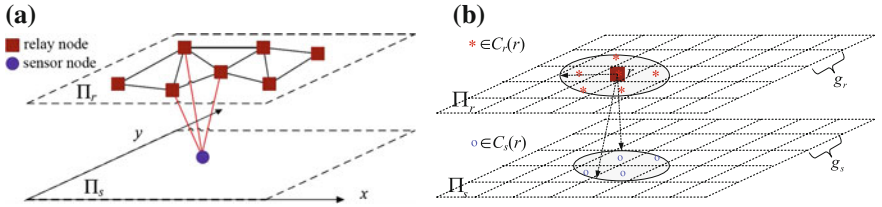

Fig. 2 **a** Illustration of Definitions 1 and 2. **b** Illustration of $C_r(r)$ and $C_s(r)$

a sensor node has to communicate with at least three relays for localizing itself. For practical simplicity, we consider the relay and sensor nodes are in discretized coordinates such that the relay and sensor tiers consist of n_x, n_y and n'_x, n'_y grid points in the x, y dimensions, respectively. Let R denote the set of relays, R_r denote the set of grid points in Π_r, and R_s denote the set of grid points in Π_s.

Definition 1 (*Relay Communication Graph*) The relay communication graph RCG is an undirected graph $RCG(V, E)$ with vertex set $V = R$ and edge set E, defined as: for any two relays $r_i, r_j \in R$, there is an undirected edge (r_i, r_j) if the RSS at the receiver exceeds a threshold, i.e., the receiver sensitivity (e.g., −85 dBm).

Definition 2 (*Connected k-dominating set*) Given R_r and R_s, a connected k-dominating set is a subset $R \subseteq R_r$ that satisfies: (i) each point in R_s is dominated by k relays in R, and (ii) the RCG induced by R is connected (there is at least one path between each pair of relays in R).

Since more relay nodes incur higher system cost, we aim to determine optimal relay placement strategy for minimizing the total number of relay nodes (say N) under the connectivity requirement (say C) in maintaining a connected RCG and all reachable grid points in sensor tier Π_s to be k-dominated ($k \geq 3$) by the relays.

Definition 3 (*Optimal Relay Placement Problem*) Given the set of grid points R_s in sensor tier Π_s and the set of grid points R_r in relay tier Π_r, the optimal relay placement for a home health monitoring system is to determine the relay location points $R \subseteq R_r$ such that R forms a connected k-dominating set with minimum size.

Theorem 1 *The optimal relay placement problem in Definition 3 is NP-hard.*

Proof The problem of constructing a minimum connected dominating set is NP-hard [4]. Our problem is equivalent to the problem if $k = 1$. It is therefore a superset of the minimum connected dominating set problem and thus also NP-hard.

We will therefore provide an efficient heuristic solution in the next section.

Algorithm 1: Obstacle Classification and Parameter Estimation Algorithm

Input: P_r, d, O, G
Output: α, β, Γ, Π
for $k = 1 : K$ **do**
  $SSE_{min} = \infty$; //Remark: SEE refers to sum of squared errors//
  foreach obstacle $o \in O$ **do**
    $\Pi(o)$ =rand($|G|$); //Remark: each obstacle is classified into a random group//
  end
  while (improvement) **do**
    improvement = false;
    foreach obstacle $o \in O$ in random order **do**
      $\Pi_{new} = \Pi$;
      foreach group $g \in G$ **do**
        $\Pi_{new}(o) = g$;
        $[\alpha, \beta, \Gamma] = \text{regress}(P_r, [d\ \Pi_{new}])$; //Remark: linear regression to estimate//
        for $i = 1 : |P_r|$ **do**
          $\hat{P}_r(i) = P_t - \alpha - 10\beta \log_{10} d(s, r) - \Sigma_{o \in I_{s,r}} \Gamma_{\Pi_{new}(o)}$;
        end
        $SSE(g) = \Sigma_{i=1}^{|P_r|} (P_r(i) - \hat{P}_r(i))^2$;
      end
      if $\min SSE \leq SSE_{min}$ **then**
        $SSE_{min} = \min SSE$; //Remark: do group update, replace optimal SSE_{min}//
        $\Pi(o) = \arg_g \min SSE$;
        improvement = true;
        break;
      end
    end
  end
  $\widetilde{SSE}(k) = SSE_{min}$;
  $\widetilde{\Pi}(k) = \Pi$;
end
$\Pi = \arg_{\widetilde{\Pi}} \min \widetilde{SSE}$;
$[\alpha, \beta, \Gamma] = \text{regress}(P_r, [d\ \ \Pi])$.

3 Proposed Optimal Relay Placement

We propose an efficient algorithm, called optimal relay placement algorithm (ORPA), see Algorithm 2. The basic ideas are as follows. (1) The candidate point in Π_r is chosen only within the radio ranges of already chosen points to ensure that relays are all connected. (2) The candidate point in Π_r that can maximize the number of undominated points in Π_s is chosen to place the relays. (3) The unchosen points in Π_r are iteratively checked until all the points in Π_s are k-dominated. The radio range of each placed relay can be estimated using aforementioned Algorithm 1.

The inputs to Algorithm 2 are the transmission power P_t, the dominating requirement k, the set of sensor points R_s, the set of relay points R_r, and the channel parameters (by Algorithm 1). For a relay at point $r \in R_r$, the set of points in R_r that lie in the radio range of r is denoted by $C_r(r)$, as shown in Fig. 2b. Similarly, the set of points $s \in R_s$ that lie in the radio range of r is denoted by $C_s(r)$. Let $|C_s(r)|$ be the

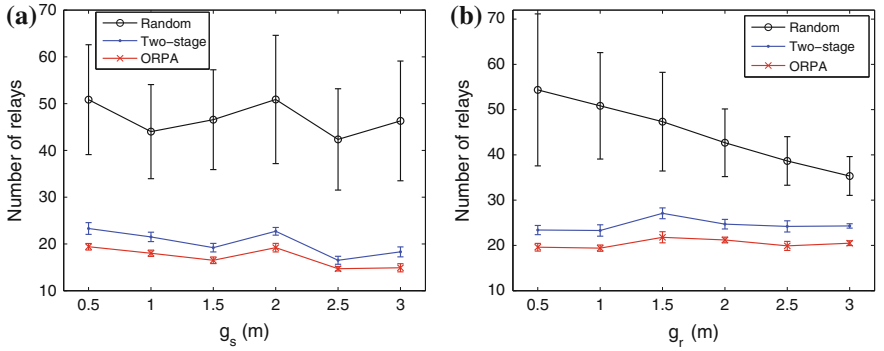

Fig. 3 The number of relays required by the three algorithms. **a** $g_r = 1$ m, $p_t = -19$ dBm, $k = 3$. **b** $g_s = 1$ m, $p_t = -19$ dBm, $k = 3$

cardinality of $C_s(r)$. For a sensor node at point $s \in R_s$, the dominated degree $D(s)$ is defined as the number of already-placed relays which it can communicate with. In other words, if s is k-dominated, $D(s) = k$.

Initially, the point $r^* \in R_r$ that can maximize $|C_s(r^*)|$ is chosen and a relay node is placed (line 6–9). So, points in $C_s(r^*)$ are all 1-dominated (line 10–12). Then, the algorithm checks the points in R_r within the radio range of the placed relay at point r^*, and selects the point (a new r^*) that can maximize the number of undominated points in R_s to place the relay (line 16–20). The dominated degree of each point in $C_s(r^*)$ is thus updated (line 21–23). Since we always check the points within the radio range of already-placed relays, the resultant RCG is guaranteed to be connected.

4 Performance Evaluation

We conduct extensive simulation and experiments to evaluate the proposed solution in comparison to the following two baseline algorithms:

- **Random placement**: first randomly selects a point from the candidate locations, then iteratively selects the points within the communication range of the already-placed relays randomly until the relays satisfy the k-dominating requirement.
- **Two-stage optimization**: first ignores the requirement of connected RCG and selects the grid points that can maximize the number of uncovered points to place the relays [9] so that the k-dominating requirement can be satisfied, then constructs a minimum spanning tree (MST) for the partitioned components.

We consider a 24.2 × 13.3 m office floor area (see Fig. 1b). The testbed includes 17 obstacles with different constructing materials. Since the granularity of the grid points in Π_s and Π_r can impact the performance and also computation complexity, we will simulate various grid sizes of Π_s and Π_r, denoted by g_s and g_r, respectively. First, we fix g_r to be 1 m and vary g_s from 0.5 to 3 m with step size of 0.5 m. Figure 3a

shows the required number of relays by the three algorithms with increasing g_s. We can see that the number of relays required by random placement is more than twice of that required by the other two algorithms.

Algorithm 2: Optimal Relay Placement Algorithm

Input: P_t, k, R_r, R_s, channel parameters
Output: the set of grid points R where the relays are placed

```
//Initialization//
R = ∅;
foreach s ∈ R_s do
    D(s) = 0;
end
foreach r ∈ R_r do
    Compute the sets C_r(r) and C_s(r);
end
r* = arg_r max |C_s(r)|;
foreach s ∈ C_s(r*) do
    D(s) = 1;
end
R = R ⋃ {r*};
// Select a grid point in R_r that can maximize the number of undominated points in R_s //
while k do
    while ∃s ∈ R_s: D(s) < 1 do
        foreach r ∈ R_r && r ∈ C_r(R) do
            Compute the sets C_r(r) and C_s(r);
        end
        r* = arg_r max(|C_s(r)| − Σ_{s∈C_s(r)} D(s));
        foreach s ∈ C_s(r*) do
            D(s) = D(s) + 1;
        end
        R = R ⋃ {r*}, R_r = R_r − {r*};
    end
    foreach s ∈ R_s do
        D(s) = D(s) − 1;
    end
    k = k − 1;
end
```

Secondly, we set g_s to be 0.5 m and vary g_r from 0.5 to 3 m with step size of 0.5 m. Figure 3b shows the required number of relays by the three algorithms with increasing g_r. We can see that the proposed ORPA always requires a smaller number of relays than the other two algorithms. Besides, its performance is quite stable.

5 Conclusion

In the paper, we study the two-tiered relay placement problem for a WSN-based home health monitoring system, which requires that the relays form a connected network and the patient carrying the sensor node is at least k-radio covered ($k \geq 3$).

Instead of using idealistic disc radio model, we explicitly take into account the effect of obstacles to the radio propagation. We show that the problem is NP-hard and propose an efficient greedy algorithm (ORPA) to solve the optimal relay placement problem. Results have verified the superiority of the proposed ORPA in comparison to the random and two-stage algorithms. Note that the method used could be also beneficial for solving other similar problems.

Acknowledgments This work is supported in part by ANR project IDEFIX under grant number ANR-13-INFR-0006, China NSF under grant No. 61003264, and Zhejiang Provincial NSF under grant No. LY13F020028. A part of the work was carried out at LINCS (www.lincs.fr).

References

1. Bai X, Yun Z, Xuan D, Jia W, Zhao W (2010) Pattern mutation in wireless sensor deployment. In: IEEE INFOCOM, pp 1–9 (2010)
2. Chen CS, Li Y, Song YQ (2008) An exploration of geographic routing with *k*-hop based searching in wireless sensor networks. In: International conference on communications and networking in China, pp 376–381
3. Chipara O, Hackmann G, Lu C, Smart W, Roman G (2010) Practical modeling and prediction of radio coverage of indoor sensor networks. In: ACM/IEEE IPSN, pp 339–349
4. Gary MR, Johnson DS (1979) Computers and intractability: a guide to the theory of NP-completeness. WH Freeman and Company, New York
5. Hung K, Lee C, Choy SO (2015) Ubiquitous health monitoring: Integration of wearable sensors, novel sensing techniques, and body sensor networks. In: Mobile health pp 319–342
6. Lloyd E, Xue G (2007) Relay node placement in wireless sensor networks. IEEE Trans Comput 56(1):134–138
7. Misra S, Hong S, Xue G, Tang J (2010) Constrained relay node placement in wireless sensor networks: formulation and approximations. IEEE/ACM Trans Netw 18(2):434–447
8. Suryadevara NK, Mukhopadhyay SC (2012) Wireless sensor network based home monitoring system for wellness determination of elderly. IEEE Sens J 12(6):1965–1972
9. Xue C, Zhu Y, Ni L, Li M, Li B (2012) Optimal relay placement for indoor sensor networks. In: IEEE DCOSS, pp 209–215
10. Yang D, Misra S, Fang X, Xue G, Zhang J (2012) Two-tiered constrained relay node placement in wireless sensor networks: computational complexity and efficient approximations. IEEE Trans Mobile Comput 11(8)

Part III
Radar and Sonar Networks, Radar Signal Processing

A Multi-hop Acknowledgment Technique Based on Network Coding for Underwater Acoustic Communication

Danfeng Zhao, Xiangyu Song and Guiyang Lun

Abstract Underwater acoustic sensor networks (UASNs) are prone to packet loss due to their poor link condition with high noise and high bit error rate. Therefore, a multi-hop acknowledgment technique based on network coding and multi-path (MHA-NCMR) is proposed for UASNs to guarantee the reliable message delivery. The improved scheme introduces acknowledgment node to the network to judge information of partial network, and adds a feedback mechanism to the acknowledgment and destination node. The proposed scheme is simulated on the platform of OPNET network simulators. Simulation results demonstrate that MHA-NCMR plays better than NCMR from the perspective of transmission reliability and normalized redundancy.

Keywords Underwater acoustic sensor networks · NCMR · Normalized redundancy · Multi-hop acknowledgement

1 Introduction

As terrestrial wireless sensor network (WSN) technologies mature, underwater acoustic sensor networks (UASNs) are gaining popularity recently. Underwater acoustic channel is by far one of the most complicated wireless communication channels, which has a narrow band, high error rates, and long propagation delays, bringing great challenges to the reliability of the underwater acoustic sensor networks researches [1, 2].

D. Zhao · X. Song (✉) · G. Lun
College of Information and Communication Engineering,
Harbin Engineering University, Harbin 150001, China
e-mail: song_xiang_yu@126.com

D. Zhao
e-mail: zhaodanfeng@hrbeu.edu.cn

G. Lun
e-mail: lunguiyang@hrbeu.edu.cn

Q. Liang et al. (eds.), *Proceedings of the 2015 International Conference on Communications, Signal Processing, and Systems*, Lecture Notes in Electrical Engineering 386, DOI 10.1007/978-3-662-49831-6_15

In consideration of the particularity of underwater acoustic channel, traditional methods used in WSN cannot be applied to the UASNs directly. Using common error-recovery techniques such as Automatic Repeat reQuest (ARQ), Forward Error Correction (FEC), and Multipath forwarding in underwater sensor networks has the following drawbacks. Because of the fixed rate, FEC-based schemes cannot adapt to the complex and changeable underwater acoustic channel. ARQ-based schemes require the receiver to detect loss and then request the sender to retransmit packets. This may lead to long propagation delays to deliver a packet successfully to the receiver in underwater sensor networks. And in harsh channel conditions it will inevitably produce a lot of feedback information, which will consume a lot of resources [3, 4]. Multipath forwarding improves the redundancy by sending packets through multiple paths, which may lead to unnecessary redundancy. So these three techniques do not apply to the underwater network. Network coding is a novel mechanism proposed to improve network throughput, transmission reliability, energy consumption especially in the broadcast environment. Studies show that network coding is a promising technique for efficient error recovery in underwater sensor networks When it is applied to multipath forwarding, it cannot only improve the reliability of underwater sensor networks, but also can reduce redundancy. Therefore, network coding based on multipath forwarding scheme is of great significance to the study of the transmission protocol applied to the underwater environment [6].

In the study of ReInForM [5], the author applied network coding to the multipath routing, and analyzed the network coding model. Simulation results show that the improved scheme achieves higher packet delivery ratio as well as less redundancy. But the algorithm required more paths under harsh channel conditions. Guo Zheng et al. first proposed an efficient error-recovery scheme that carefully couples network coding and multipath routing (NCMR) for underwater sensor networks, and evaluated the performance of the scheme using simulation. However, network coding efficiency is dependent upon the quality of the established paths in the algorithm. Too much or too little relay nodes can influence the performance of the network [6]. Simulation results confirmed the analytical study that the scheme is efficient in both error recovery and energy consumption. Junhong Cui et al. proposed a novel Multi-path Power-control Transmission scheme, MPT, for time-critical applications in underwater sensor networks [7]. The results demonstrate that MPT can achieve low end-to-end packet delay and relatively high energy efficiency. Cai Shaobin et al. proposed Multiple Paths and Network Coding, MPNC [8]. In MPNC, three disjoint paths are established, and then, two groups of packets A and B, which are individually coded by network coding, are transmitted over two side paths, and another group of packets, $A \oplus B$, are transmitted over the middle path. The simulation results show that, MPNC acquires low energy consumption. Yuhuai Peng et al. put forward a fault-tolerant routing mechanism based on network coding to quickly recover local information [9]. The scheme obtained very good results in improving latency and throughput. However, when these existing schemes are applied to the underwater environment with poor channel conditions,

or there is a long distance between the source node and the destination node, the reliability and the redundancy can not be balanced.

To take the reliability and the redundancy into account, based on the analysis of the existing reliability mechanism, this paper proposes a multihop acknowledgment transmission scheme based on network coding and multipath routing (MHA-NCMR), and incorporating feedback retransmission mechanism in the acknowledgment and sink node. By analyzing its transmission reliability and redundancy in the network, we realize that MHA-NCMR can further improve the packet delivery reliability, and reduce the redundancy of the network.

The rest of the paper is organized as follows. In Sects. 2 and 3, we describe network coding scheme and multipath transmission based on network coding. In Sect. 4, we describe the proposed scheme and analyze it via mathematics. Section 5 presents our simulation results. A conclusion is brought in Sect. 6.

2 Network Coding Scheme

Linear random network coding is a distributed network coding method. It can adapt to the dynamic changes of the network topology. Network coding is no longer limited to a particular network topology and centralized algorithm by applying it to wireless networks [10].

Packets from the source are divided into generations, each generation contains k packets. More specifically, let $X_1, \ldots, X_k$ denote the K packets in a generation. The source node randomly selects k × K elements from a Galois field to be a coefficient matrix, and code these k original packets in a generation into K new packets, denoted as $Y_1, Y_2, \ldots, Y_K$, where

$$Y_i = \sum_{j=1}^{k} a_{ij} X_j, \quad i = 1, 2, \ldots, K. \tag{1}$$

We choose $K \geq k$ since adding a small amount of redundancy to the source reduces the impact of packet loss on the first hop and improves error recovery at the sink.

A relay in forwarding paths stores incoming packets from different paths for a certain period of time, then linearly combines the received packets belonging to the same generation. Suppose a relay receives m incoming packets, $Y_1, Y_2, \ldots, Y_m$. Let $Z_1, Z_2, \ldots, Z_M$ denote the coded packets,

$$Z_i = \sum_{j=1}^{m} b_{ij} Y_j, \quad i = 1, 2, \ldots K, \tag{2}$$

where b_{ij} is picked randomly from the finite field F_{2q}. Then

$$h_{ij} = \sum_{l=1}^{m} b_{il} a_{lj}, \tag{3}$$

$$Z_i = \sum_{j=1}^{k} h_{ij} X_j, \quad i = 1, 2, \ldots M, \quad j = 1, 2, \ldots k. \tag{4}$$

Then sending these recoded packets to the next hop. Finally, the sink can recover the original packets when it receives at least k independent packets.

Whether the destination node can decode the original packets successfully, is dependent on the rank of the encoding coefficient matrix. For random network coding, coding coefficients are randomly picked out from a finite field. The probability of associated coding coefficient received by the destination node can be reduced if we increase the finite field. When the capacity is limited to 2^8 fields, the successful decoding probability is 0.996 [11]. However, when the limited field capacity is too large, it will decrease the storage efficiency and increase the computational complexity. Thus, in practical applications, the capacity of a finite field is not necessary to use 2^8. Furthermore, the generation size should be selected properly. It will consume more computing resources and storage overhead, if the size is too large. However, if the size is too small, it will be unable to give full play to the potential advantages of network coding.

3 The Multipath Transmission Scheme Based on Network Coding

From the network topology point, multipath routing can be divided into disjoint multipath and braided multipath, as shown in Figs. 1 and 2. Disjoint multipath routing establishing conditions are harsh and the robustness is poor. Disjoint

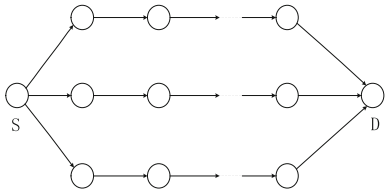

Fig. 1 Disjoint multipath model

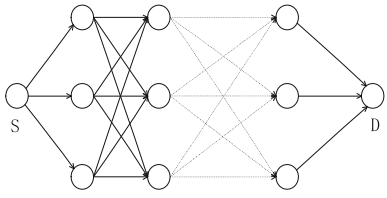

Fig. 2 Braided multipath model

multipath routing can be expanded from single-path routing. When packets are forwarded hop by hop, they could be received by multiple relays in the next hop simultaneously, conforming to the broadcast characteristics of radio channel [12]. This study focused on the braided multipath network model. Multipath transmission mechanism increases transmission redundancy by forwarding packets through multiple paths, to improve packet transfer efficiency and reliability [13]. However, the repeated packets will be deleted directly, which consume energy but not increase the useful information. If multipath transmission mechanism is applied directly to the underwater sensor networks, it will inevitably lead to the rapid demise of the nodes, thus only multipath transmission is not enough. Linear random network coding can solve the problem of multipath transmission redundancy, that is, on the basis of multipath, joining the encoding mechanism to the nodes. Namely, the source (S) encodes and forwards the data packets. Then packets received by relay nodes will be re-encoded. Finally, the original packets will be recovered until the destination node (D) receives enough packets.

4 Implementation and Analysis of MHA-NCMR

4.1 MHA-NCMR Scheme

In this paper, we adopt linear random network coding and multipath transmission mode by selecting one hop between the source node and destination node as an acknowledgment node to determine whether it has received sufficient information. The selected hop is determined by the total hops of the network and the condition of the channel. We will study the relationship in our future work. Specific steps are as follows:

First, we need to determine whether the node is the acknowledgment node. If not, then we continue coding and forwarding. The acknowledgment node starts its timer as soon as it receives the first packet. When time is out, the acknowledgment node will weigh the rank of the received coefficient. If the received coefficient is of full rank, the node will recode and forward the packets, if not, it will add the value of the current rank to the feedback packet and send the NACK packet to the nodes in the previous hop. The relay nodes in the previous hop will get the rank value after receiving NACK. According to this value, the number of packets to be retransmitted is determined, then recoded and retransmitted with proper redundancy. Because the transmission reliability of NCMR has been high, usually, the nodes in the local area closer to the acknowledgment node can complete the retransmission, without introducing too long delay.

For the sink node, it will start its timer when it receives the first packet. It uses on the fly Gaussian elimination (OFG) [14] decoding algorithm. If the decoding fails in certain time, the value of the current rank is added to the feedback packet, and then the NACK packet will be sent to the previous hop. The relay nodes received NACK

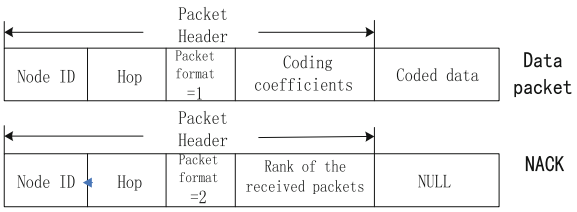

Fig. 3 Transmission packet format

packet will get the value of the rank, and determine the number of retransmission packets according to this. The relay nodes will recode the packets with proper redundancy and forward them to the next hop. The sink continues decoding when it receives retransmission packets until the sink recovers the original packets successfully. Since the number of retransmission packets is dependent on the rank in the feedback, so often, the original packets can be decoded successfully with only one retransmission. Transmission packet format is shown in Fig. 3.

4.2 *Analysis of Transmission Reliability and Normalized Redundancy*

Transmission reliability is characterized through packet delivery ratio (PDR) in this paper. PDR is defined as the probability of the sink successfully obtaining the original packets by receiving or decoding in a transmission.

$$PDR = \frac{the\ number\ of\ successful\ transmation}{the\ number\ of\ transmation} \tag{5}$$

Normalized redundancy (NR) is defined as the total number of packets sent by the nodes of the network in a successful transmission. Normalized redundancy reflects the redundancy packets generated in the network and energy consumption of the network.

$$NR = \frac{\sum_{all\_node} the\ sent\ packet\ number\ of\ a\ node}{the\ successful\ decoding\ packet\ number} \tag{6}$$

Node redundancy ratio (NRR) is defined as the ratio of the number of packets sent by a node with the generation size.

$$NRR = \frac{the\ sent\ packet\ number\ of\ a\ node}{the\ generation\ size} \tag{7}$$

Taking the amount of calculation problem into account, here q is set to 2. We use MATLAB to generate a random matrix of different orders in the finite field, and compare the proportion of full rank. When the order of the matrix is 10, the

Table 1 The ratio of the full rank

Order	Full rank ratio
5	0.9174
6	0.9527
7	0.9746
8	0.9887
9	0.9955
10	0.9982

probability of full rank matrix is close to 1. Thus, we set the initial setting of generation size to 10 and the generation number to 1000 (Table 1).

Considering an arbitrary generation of K packets, the number of hop between the source node and the acknowledgment node is H_1. There are H_2 hops between the acknowledgment node and the sink node. The source and the acknowledgment node redundancy ratio are r_1, and the relay node redundancy ratio is r_2. We have N paths in the network. The total number of packets has been sent by the nodes in the network is (Fig. 4)

$$total\_packet = [2r_1 + N * r_2(H_1 + H_2) - 2N * r_2] * K, \tag{8}$$

NR is

$$NR = 2r_1 + N * r_2(H_1 + H_2) - 2N * r_2. \tag{9}$$

To analyze the reliability of the network, we do not differentiate between the nodes in the same hop. The packet loss ratio is p. Let $\alpha_{i,k}$ be the probability that a node in the ith relay set receives k packets (when $1 \le i \le H_1$, $0 \le k < K$) or at least k packets (when k = K) from all nodes in the previous relay set. Since the acknowledgment is in the H_1th relay set, we have

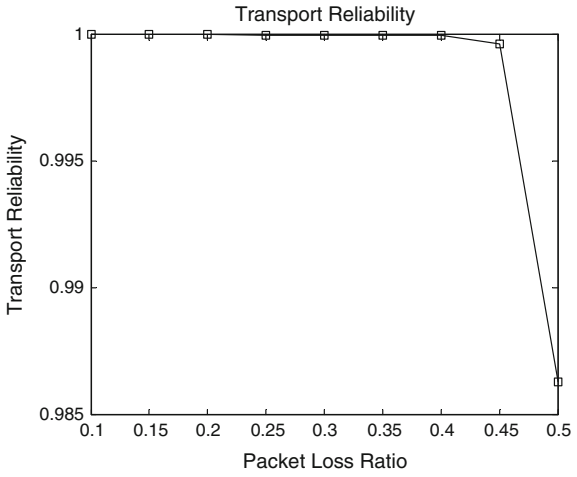

Fig. 4 Transport reliability of the analysis

$$PDR_1 = \alpha_{H_1,K}. \tag{10}$$

We next derive $\alpha_{i,k}$, $1 \le i \le H_1, 0 \le k < K$. The nodes in the first relay set receive packets from the source.

Therefore

$$\alpha_{1,k} = \begin{cases} C_{r_1 K}^{k}(1-p)^{k} p^{r_1 K - k}, & 0 \le k < K \\ 1 - \sum_{j=0}^{K-1} \alpha_{1,j}, & k = K \end{cases} \tag{11}$$

For $1 \le i \le H_1$, $0 \le k < K$, we obtain $\alpha_{i+1,k}$ as follows. We index the nodes in the ith relay from 1 to N. Let $\beta_{i,k}$ denote the probability that a node in the ith relay set receives k packets from the jth node in the previous relay set, $1 \le i \le H_1$, $0 \le k < K$. Since each relay transmits no more than K packets, we have

$$\beta_{i,k} = \sum_{n=k}^{K} \alpha_{i-1,k} C_n^k (1-p)^k p^{n-k}, \; 0 \le k < K \tag{12}$$

To obtain $\beta_{i,k}$, we need to consider all combinations of k_j, such that $k_j = 0, \ldots k. \quad s.t \sum_{j=1}^{N} k_j = k$. That is

$$\alpha_{i+1,k} = \begin{cases} \sum_{k_j = 0, \ldots k.s.t \sum_{j=1}^{N} k_j = k} \prod_{j=1}^{N} \beta_{i+1,k_j}, & 0 \le k < K \\ 1 - \sum_{k=0}^{K-1} \alpha_{i+1,k}, & k = K \end{cases} \tag{13}$$

Then we can get the reliability of the whole network

$$PDR = \alpha_{H_1,K} * \alpha_{H_2,K} \tag{14}$$

We analyzed transmission reliability on MALAT platform.

In the simulation, H_1 and H_2 are set as 3; N is set as 3; K is set as 10 and r_1 is set as 1.

5 Simulation Study

In order to verify the performance of MHC-NCMR, this paper built a network model on the platform of OPNET network simulators, studied the number of source packets in each generation, packet loss ratio and the node redundancy ratio impact on transmission protocol, and compared them with NCMR.

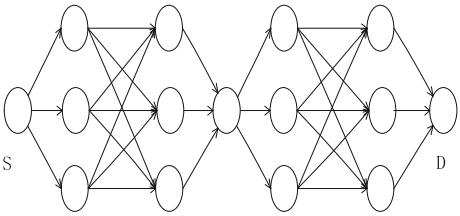

Fig. 5 MHA-NCMR model

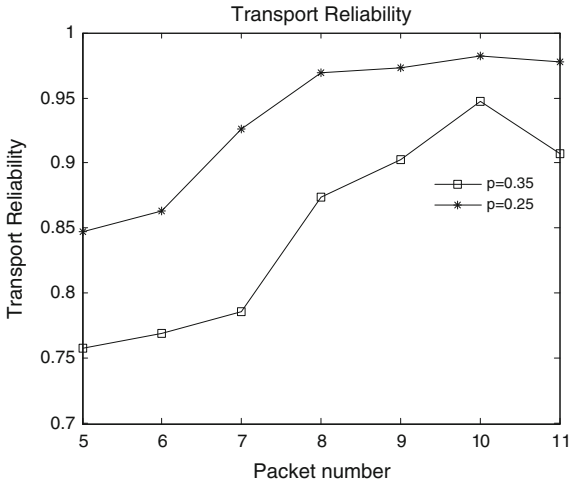

Fig. 6 Transport reliability comparison of different packet numbers in each generation

To examine the parameters impact on transmission reliability and redundancy in NCMR and MHA-NCMR, this study fixed source node to acknowledgment node and acknowledgment node to the sink node at three hops, the path number is three, as shown in Fig. 5. In discussing normalized redundancy, the node redundancy must ensure that the sink can successfully decode the original packets with minimum redundancy and the number of retransmissions is less than or equal to 1. In exploring the reliability, we set the source node and the acknowledgment node redundancy to 1.5, the relay node redundancy to 0.8.

In Figs. 6 and 7, we examined the impact of generation size under different packet loss ratio ($p = 0.25, 0.35$). It shows that when the number is greater than eight, it can achieve a higher reliability, and the reliability is highest when the number is up to ten. Normalized redundancy decreases with the increasing of the number until it reaches ten to the minimum. It demonstrates that the energy efficiency improves with increasing generation size. Therefore, in exploring redundancy and normalized reliability, the number in each generation is set to ten.

According to the set parameters in the earlier paper, Figs. 8 and 9 plot normalized redundancy and transmission reliability for NCMR and MHA-NCMR. From the results, we can observe that higher packet loss ratio results in better packet delivery reliability, but higher normalized redundancy. Compared to NCMR, normalized

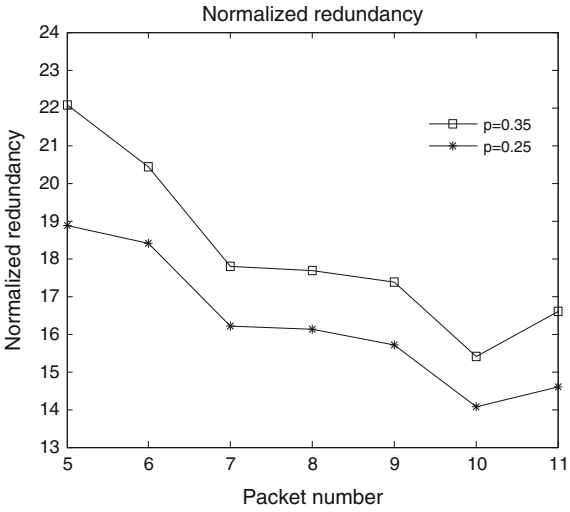

Fig. 7 Normalized redundancy comparison of different packet numbers in each generation

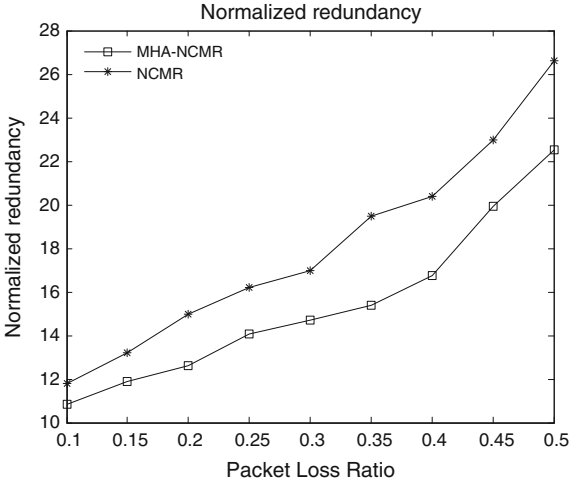

Fig. 8 Normalized redundancy comparison of MHA-NCMR and NCMR in different packet loss ratios

redundancy of MHA-NCMR decreased obviously, especially in the packet loss ratio from 0.3 to 0.4, the standard redundancy decreases by about 20 %. From the result of the normalized redundancy, we can draw that the energy consumption of MHC-NCMR is lower. When p is less than 0.25, transmission reliability of the two schemes is high, and MHA-NCMR has better performance in packet delivery reliability, especially when the packet loss ratio is up to 0.35 or larger.

Figure 10 demonstrates that, when the source node redundancy is less than 1.3, the transmission reliability increases with the increasing of the source node redundancy. When the source node redundancy is up to 1.3, the reliability is greater than

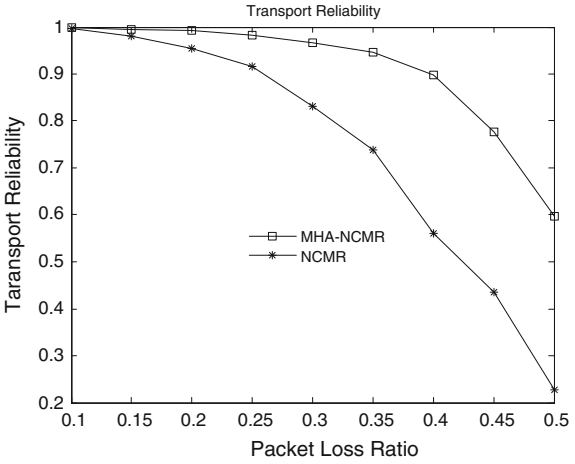

Fig. 9 Transport reliability comparison of MHA-NCMR and NCMR in different packet loss ratios

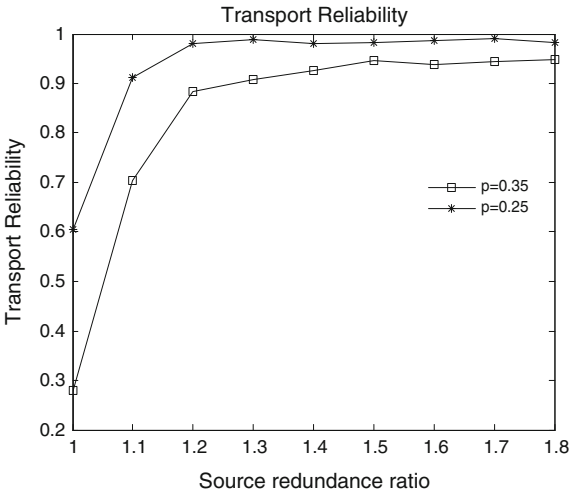

Fig. 10 Transport reliability under different source node redundancy ratios

0.9, and transmission reliability of little change with the source node redundancy increasing, which indicates that too much redundancy will not increase the reliability.

6 Conclusion

This paper presents a reliable multi-hop acknowledgment transmission scheme based on network coding and multi-path to achieve a lower coding redundancy and higher transmission reliability, which can be applied in underwater acoustic

communication networks. The multi-hop acknowledgment mechanism was added to NCMR. On this basis, we joined feedback retransmission mechanism in the acknowledgment node and the destination node to realize efficient coding transmission. The simulation results show that, compared to NCMR scheme, this design enables a lower transmission coding redundancy, higher energy efficiency and obtains higher transmission reliability. Considering the characteristics of the underwater acoustic network, this design is more suitable for underwater acoustic network.

Acknowledgments The work is supported by the International Exchange Program of Harbin Engineering University for Innovation-oriented Talents Cultivation and National Science foundation of China (61371099).

References

1. Otnes R, Asterjadhi A, Casari P et al (2012) Underwater acoustic networking techniques. Springer, Berlin
2. Hamidzadeh M, Forghani N, Movaghar A (2011) A new hierarchal and scalable architecture for performance enhancement of large scale underwater sensor networks. Kuala Lumpur
3. Liu B, Garcin F, Ren F et al (2008) A study of forward error correction schemes for reliable transport in underwater sensor networks. Sensor, mesh and Ad Hoc communications and networks. pp 197–205
4. Stojanovic M (2005) Optimization of a data link protocol for an underwater acoustic channel
5. Shan-Shan L, Pei-Dong Z, Xiang-Ke L, et al (2006) Energy efficient multipath routing using network coding in wireless sensor networks. In: Ad-Hoc, mobile, and wireless networks. pp 114–127
6. Guo Z, Wang B, Cui JH (2007) Efficient error recovery using network coding in underwater sensor networks. Ad Hoc and sensor networks, wireless networks. pp 227–238
7. Zhou Z, Cui JH (2008) Energy efficient multi-path communication for time-critical applications in underwater sensor networks. Mobile Ad Hoc Netw Comput 5346(2):221–230
8. Cai S, Gao Z, Yang D et al (2013) A network coding based protocol for reliable data transfer in underwater acoustic sensor. Ad Hoc Netw 11(5):1603–1609
9. Peng Y, Song Q, Yu Y et al (2014) Fault-tolerant routing mechanism based on network coding in wireless mesh networks. J Netw Comput Appl 37:259–272
10. Ho T, Medard M, Koetter R et al (2006) A random linear network coding approach to multicast. IEEE Trans Inf Theory 52(10):4413–4430
11. Jaggi S, Sanders P, Chou PA et al (2005) Polynomial time algorithms for multicast network code construction. IEEE Trans Inf Theory 51(6):1973–1982
12. Yang Y, Gu L, Ju Y et al (2010) Reliable braided multipath routing with network coding for underwater sensor networks. China Ocean Eng 24(3):565–574
13. Guo Z, Wang B, Xie P et al (2009) Efficient error recovery with network coding in underwater sensor networks. Ad Hoc Netw 7(4):791–802
14. Bioglio V, Grangetto M, Gaeta R et al (2009) On the fly Gaussian elimination for LT codes. Commun Lett IEEE 13(12):953–955

An Envelope Alignment Method for Terahertz Radar ISAR Imaging of Maneuvering Targets

Tong Liu, Zongjie Cao and Rui Min

Abstract A novel envelope alignment technique for terahertz radar ISAR imaging of maneuvering targets is presented in this paper. This method selects a single pulse echo as the envelope alignment benchmark through the correlation coefficient of adjacent range profiles, which solves the problems of jump error and drift error in the conventional adjacent amplitude correlation method. The imaging results of measured terahertz data demonstrate the effectiveness of this improved envelope alignment technique based on the adjacent amplitude correlation method.

Keywords Terahertz radar · Maneuvering targets · Envelope alignment · ISAR imaging

1 Introduction

As terahertz wave can penetrate nonpolar materials and has a strong reflect character towards metal materials, and is easy to achieve large bandwidth modulated signal, terahertz radar can obtain high resolution images of concealed threats, such as knives and guns hidden in clothing or luggage. Meanwhile, due to the low photon energy, terahertz wave is harmless to human body. It is an attractive technology to do the security checks and the monitoring of concealed threats at a standoff range utilizing terahertz radar nowadays [1, 2]. Considering the practical application demands and the convenience requirements, the research on terahertz radar ISAR imaging of maneuvering targets is necessary.

The relative motion between maneuvering targets and radar can be divided into the translation component and the rotation component. The translation component

T. Liu (✉) · Z. Cao · R. Min
School of Electronic Engineering, University of Electronic Science and Technology of China, Chengdu, China
e-mail: liutong013@163.com

Q. Liang et al. (eds.), *Proceedings of the 2015 International Conference on Communications, Signal Processing, and Systems*, Lecture Notes in Electrical Engineering 386, DOI 10.1007/978-3-662-49831-6_16

makes no contribution to ISAR imaging, but it will cause range cell migration and Doppler variation to degrade the imaging quality. The impact of the translation component should be eliminated by envelope alignment and phase correction before imaging. Envelope alignment is the base of phase correction and imaging. Because terahertz wave has a shorter wavelength than microwave or millimeter wave, the rotation angle that terahertz radar ISAR imaging required is smaller, for which the envelope of terahertz radar echo is very similar. Traditionally, the adjacent amplitude correlation method can gain a good envelope alignment effect, but it has the jump error and drift error problems [3] which would cause the terahertz radar image defocusing.

An improved envelope alignment technique based on the adjacent amplitude correlation method is presented in this paper. The single pulse echo is sifted as the envelope alignment benchmark through the correlation coefficient of adjacent range profiles, and the problems of jump error and drift error in the conventional adjacent amplitude correlation method are solved. The imaging results of measured terahertz data demonstrate the effectiveness of this improved envelope alignment method.

2 Theory and Methodology

2.1 Received Signal Model

The relative motion between maneuvering targets and radar can be divided into the translation component (Maneuvering targets move from point 3 to point 2) and the rotation component (Maneuvering targets rotate from dotted line position to solid line position at point 2), as shown in Fig. 1. Since the rotation angle that terahertz radar ISAR imaging required is small, the rotation velocity is approximately uniform. After eliminating range cell migration and Doppler variation that the translation component caused by envelope alignment and phase correction, the ISAR imaging of maneuvering targets will be converted into the basic concepts of Range-Doppler imaging for ISAR [4].

Terahertz radar transmits line frequency modulation signal with the pulse repetition interval T. The transmitted signal can be expressed as

$$s(\hat{t}, t_m) = \mathrm{rect}\left(\frac{\hat{t}}{T_p}\right) e^{j2\pi\left(f_c t + \frac{1}{2}\gamma \hat{t}^2\right)} \tag{1}$$

where $\mathrm{rect}(u) = \begin{cases} 1 & |u| \le \frac{1}{2} \\ 0 & |u| > \frac{1}{2} \end{cases}$, T_p is the pulse width, f_c is the center frequency, γ is the chirp rate of the transmitted signal. The moments at which the signal is transmitted $t_m = mT(m = 0, 1, 2, \ldots)$ are called slow time. $\hat{t}$ denotes the time variable varying

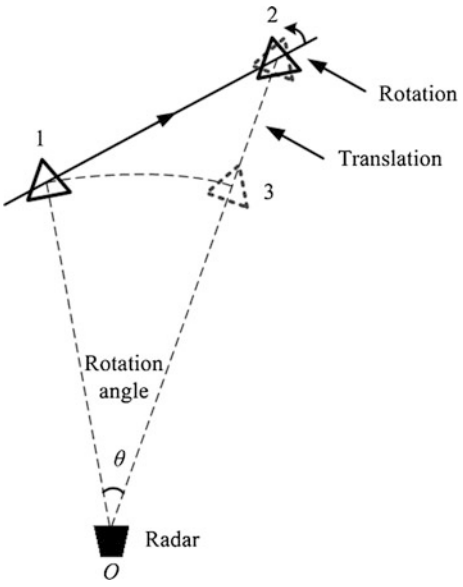

Fig. 1 ISAR imaging geometry of maneuvering targets

within the pulse repetition interval, which is called fast time. The relationship between t_m and $\hat{t}$ is $\hat{t} = t - mT$.

Assume that the maneuvering target is an ideal geometric point, the instantaneous distance between the maneuvering target and the radar is $R(t_m)$ at t_m. The received signal reflected from the maneuvering target can be denoted as

$$s_r(\hat{t}, t_m) = A\mathrm{rect}\left(\frac{\hat{t} - 2R(t_m)/c}{T_p}\right) e^{j2\pi\left(f_c\left(t - \frac{2R(t_m)}{c}\right) + \frac{1}{2}\gamma\left(\hat{t} - \frac{2R(t_m)}{c}\right)^2\right)} \tag{2}$$

where A denotes the echo signal amplitude and c is the speed of light. The intermediate frequency signal can be expressed as

$$\begin{aligned} s_{if}(\hat{t}, t_m) &= s_r(\hat{t}, t_m) \cdot s^*(\hat{t}, t_m) \\ &= A\mathrm{rect}\left(\frac{\hat{t} - 2R(t_m)/c}{T_p}\right) e^{-j\frac{4\pi}{c}f_c R(t_m)} e^{-j\frac{4\pi}{c}\gamma R(t_m)} e^{j\frac{4\pi\gamma}{c^2}R^2(t_m)} \end{aligned} \tag{3}$$

Applying the Fourier transform to $s_{if}(\hat{t}, t_m)$ with variable $\hat{t}$ and removing the residual video phase and envelope migration phase, the expression of the radar echo in frequency domain becomes

$$S_{IF}(f_i, t_m) = AT_p \sin c\left[T_p\left(f_i + 2\frac{\gamma}{c}R(t_m)\right)\right] e^{-j\frac{4\pi}{c}f_c R(t_m)} \tag{4}$$

2.2 ISAR Imaging of Maneuvering Targets

$u(i), i = 1, 2, \ldots, \mathrm{M}-1$ is the correlation coefficient of adjacent range profiles of radar data $A(m, n)$, where $m(m = 1, 2, \ldots, M)$ denotes sequence of azimuth, n $(n = 1, 2, \ldots, N)$ denotes range cell. L samples are taken from $u(i)$ as a group in turn and their mean is computed. The one whose mean is maximal in those groups is picked out

$$K = \max_{1 \le i \le M-L} \left\{ \frac{1}{L} \cdot [u(i) + u(i+1) + \cdots + u(i+L-1)] \right\} \tag{5}$$

where K is the index of groups.

The single pulse echo corresponding to the maximal correlation coefficient of adjacent range profiles in the Kth group is selected as the envelope alignment benchmark.

$$J = \max_{K \le j \le K+L-1} \{u(j)\} \tag{6}$$

$A(J, n)$ is the unity benchmark of envelope alignment. The cross-correlation function of $A(m, n)$ and $A(J, n)$ is

$$R_{mJ}(\tau) = \sum_{\tau=0}^{N} A(m, n)\mathrm{A}(J, n-\tau) \tag{7}$$

After searching for the peak and computing the range cells corresponding to τ, the envelope alignment is completed. In order to achieve high accuracy requirement for envelope alignment, the range cell is processed with a 16-time interpolation before the cross-correlation function is computed.

The focused image makes the entropy of image minimal, which is the principle of phase correction based on the minimum entropy method [5].

$f(m, n)$ denotes the signal after envelope alignment. Applying the Fourier transform to the result of $f(m, n)$ multiplying the phase correction term, the image is obtained.

$$\begin{aligned} g(k, n) &= \mathrm{fft}[f(m, n) \cdot \exp[\phi(m)]] \\ &= \sum_{m=0}^{M-1} f(m, n) \cdot \exp[\phi(m)] \cdot \exp\left(-j\frac{2\pi}{M} km \right) \end{aligned} \tag{8}$$

where k denotes the Doppler frequency index, $\phi(m)$ is the correction phase.

Ignoring the constant term, the entropy of image is defined as

$$\varepsilon\left[|g(k,n)|^2\right] = \sum_{k=0}^{M-1}\sum_{n=0}^{N-1}|g(k,n)|^2 \ln|g(k,n)|^2 \tag{9}$$

When the entropy of image is minimal, the correction phase $\phi(m)$ satisfies the following condition:

$$\frac{\partial\varepsilon\left[|g(k,n)|^2\right]}{\partial\phi(m)} = 2M\,\mathrm{Im}\left\{\exp[j\phi(m)]a^*(\mathrm{m})\right\} = 0 \tag{10}$$

where $a(\mathrm{m}) = \sum_{n=0}^{N-1} f^*(m,n)\cdot\frac{1}{M}\sum_{k=0}^{M-1}\left[1+\ln|g(k,n)|^2\right]g(k,n)\exp\left(j\frac{2\pi}{M}km\right)$.

Therefore,

$$\phi(m) = \arg[a(m)] \tag{11}$$

The correction phase $\phi(m)$ can be estimated by iterative process. The termination condition for the iteration is

$$\max_{m=0}^{M-1}\{|\exp[j\phi_i(m)] - \exp[j\phi_{i-1}(m)]|\} \le \mu \tag{12}$$

where $\phi_i(m)$ and $\phi_{i-1}(m)$ are the values of $\phi(m)$ in current iteration and last iteration, respectively. μ is a constant decided by the accuracy of $\phi(m)$.

Because the phase error still exists after the translation compensation, and the velocity of the small angle rotation is approximately uniform but not strictly uniform, the image obtained by applying Fourier transform to the azimuth of the signal after the translation compensation is defocusing. The time-frequency transform instead of the Fourier transform is used for the ISAR imaging of maneuvering targets to make image focus [6]. Due to the multiple scattering points, the smoothed pseudo Wigner Ville distribution (SPWVD) is selected for imaging.

$$SPWVD_s(t,\omega) = \int h(t')\int g(u)\cdot s(t-u+\frac{t'}{2})s^*(t-u-\frac{t'}{2})du\,e^{-j\omega t'}dt' \tag{13}$$

where $s(t)$ denotes any signal, $g(t)$ and $h(t)$ are the time-domain window function and the frequency-domain window function, respectively. The SPWVD suppresses cross-term interference at the expense of the time resolution and the frequency resolution.

The flow chart of terahertz radar ISAR imaging of maneuvering targets is shown in Fig. 2.

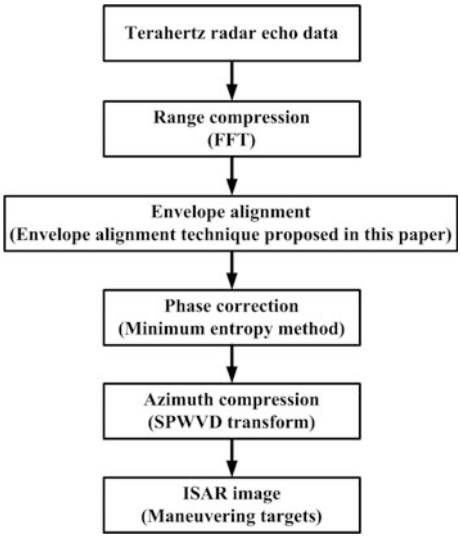

Fig. 2 Flowchart of ISAR imaging of maneuvering targets

3 Experiment and Results

The terahertz radar system works at 0.34 THz with a bandwidth of 10.08 GHz, which leads to a range resolution of 1.5 cm [7]. The image of the terahertz radar is shown in Fig. 3a. The maneuvering target consists of two corner reflectors inlaid on the foam board, as shown in Fig. 3b. The foam board slides within the scope of the radar beam at a distance of 10 m off the radar by the fine line traction.

2800 radar pulse echoes are collected and the accumulation angle of azimuth is about 1.7°, which leads to an azimuth resolution of 1.5 cm matched to the range

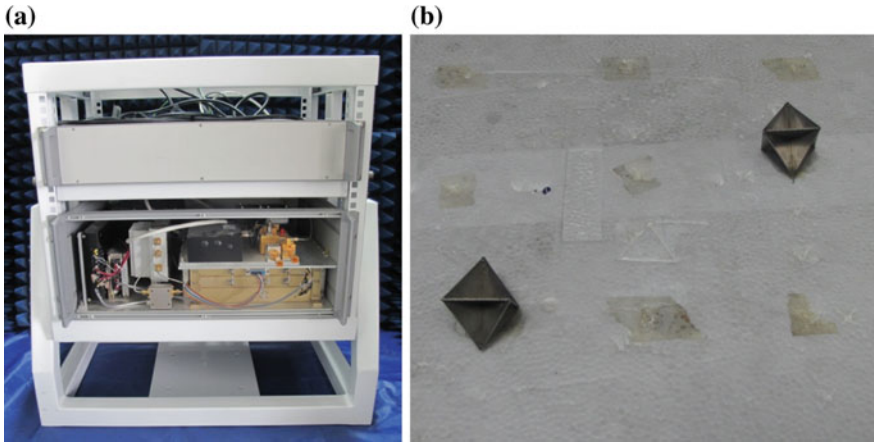

Fig. 3 Image of the terahertz radar and the maneuvering target. **a** Image of the terahertz radar. **b** Maneuvering target

resolution. The envelope of the radar echoes after range compression is shown in Fig. 4a. The translation component leads to range cell migration. The envelope after envelope alignment via the adjacent amplitude correlation method is shown in Fig. 4b. The ISAR image is shown in Fig. 4c with the SPWVD in azimuth imaging. The correlation coefficient of adjacent range profiles of the terahertz radar data is

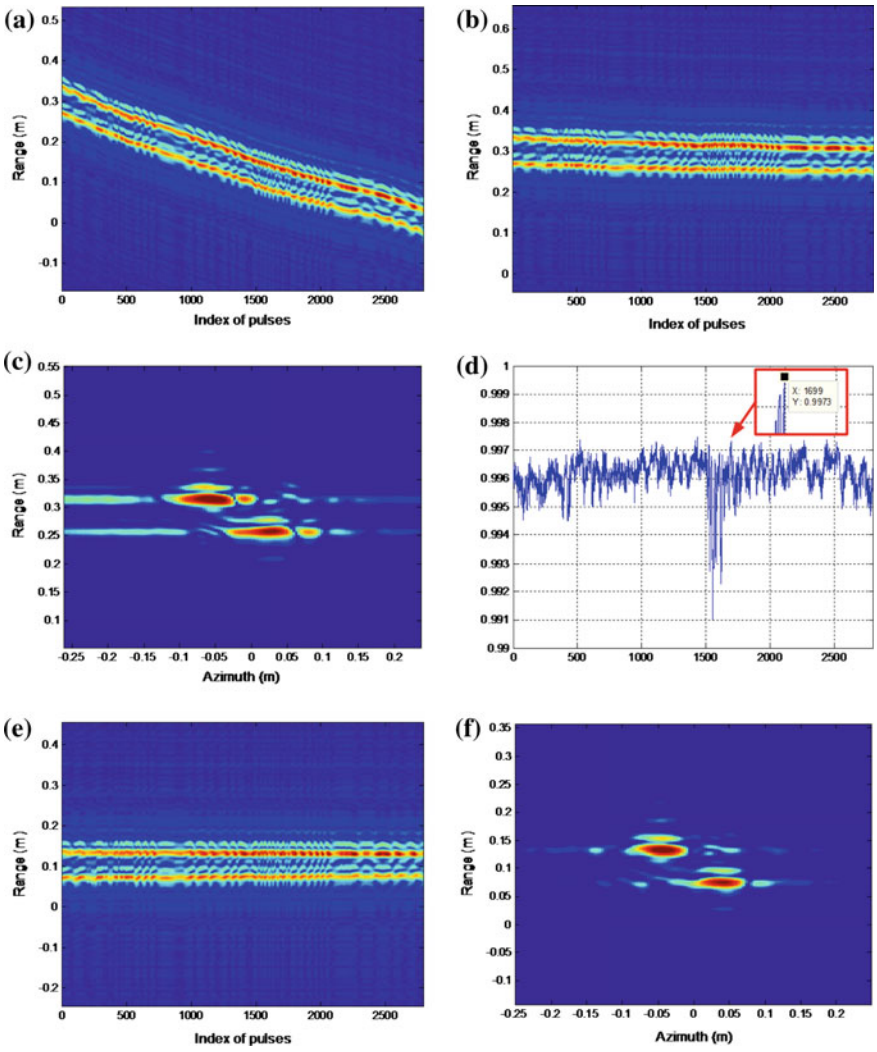

Fig. 4 ISAR imaging of maneuvering target. **a** Envelope after range compression. **b** Envelope after envelope alignment via the adjacent amplitude correlation method. **c** ISAR image gained via azimuth SPWVD transform. **d** The correlation coefficient of adjacent range profiles. **e** Envelope after envelope alignment via the envelope alignment technique proposed in this paper. **f** ISAR image gained via azimuth SPWVD transform

shown in Fig. 4d. The correlation coefficient of adjacent range profiles of the terahertz radar data keep above 0.99 and the envelope of terahertz radar echo is very similar. The 1699th pulse echo is selected as the unity benchmark of envelope alignment. The envelope after envelope alignment via the envelope alignment technique proposed in this paper is shown in Fig. 4e. The ISAR image is shown in Fig. 4f with the SPWVD in azimuth imaging.

We can observe that the envelope alignment technique proposed in this paper has a higher envelope alignment accuracy than that the adjacent amplitude correlation method has from Fig. 4b, e. Comparing Fig. 4c, f, a higher quality ISAR image is acquired via the envelope alignment technique proposed in this paper. Because the ISAR image of the maneuvering target in Fig. 4f is generated with the SPWVD transform in azimuth imaging, the azimuth resolution is expanded.

4 Conclusion

In this paper, a novel envelope alignment technique is presented, which solves the problems of jump error and drift error in the conventional adjacent amplitude correlation method. This method is suitable for terahertz radar ISAR imaging of maneuvering targets with a small rotation angle. Experiments have demonstrated the effectiveness of the envelope alignment technique proposed in this paper.

Acknowledgments This work was supported by the National Nature Science Foundation of China under Grants 61271287, 61301265, U1433113.

References

1. Cooper K, Dengler R, Llombart N et al (2011) THz imaging radar for standoff personnel screening. IEEE Trans Terahertz Sci Technol 1(1):169–182
2. Gu S, Li C, Gao X et al (2012) Terahertz aperture synthesized imaging with fan-beam scanning for personnel screening. IEEE Trans Microw Theory Technol 60(12):3877–3885
3. Chen CC, Andrews HC (1980) Target motion induced radar imaging. IEEE Trans Aerosp Electron Syst 16(1):2–14
4. Cheng B, Jiang G, Wang C et al (2013) Real-time imaging with a 140 GHz inverse synthetic aperture radar. IEEE Trans Terahertz Sci Technol 3(5):594–605
5. Li X, Liu GJ, Ni L (1999) Autofocusing of ISAR images based on entropy minimization. IEEE Trans Aerosp Electron Syst 35(4):1240–1252
6. Chen V, Hao L (1999) Joint time-frequency analysis for radar signal and image processing. IEEE Signal Process Mag 16(2):81–93
7. Zhang B, Pi Y, Li J (2015) Terahertz imaging radar with inverse aperture synthesis techniques: system structure, signal processing, and experiment results. Sens J IEEE 15(1):290–299

Terahertz Radar for Imaging Spinning Space Debris

Xu Yang, Zongjie Cao and Rui Min

Abstract With the increasing of human space activities, the resulting space debris could post a potential threat to on-orbit objects around the Earth, therefore, their size estimation is a vital task in the observation of space debris. Imaging with high-resolution terahertz radar is a promising technique to extract the dimensional and structural feature of the space debris. This paper employs a radar system operating at 340 GHz with the bandwidth of 28.8 GHz to do an emulating experiment. In terms of the spinning nature of space debris, 2-D inverse synthetic aperture radar (ISAR) imaging geometry and echo model is established. Then, a time-varying spectral analysis instead of conventional range Doppler algorithm is proposed to solve the blurring problem of radar imaging incurred by the nonuniform spinning motion. The experiment result verifies the validity of this algorithm.

Keywords ISAR · Terahertz radar · Space debris · Time-varying spectral analysis · Radar imaging

1 Introduction

With the rapid development of space technologies, many manmade targets have been launched into space or outer space, meanwhile, the human space activities lead to hundreds of millions of space debris [1]. Space debris have become a great threat to the safety of spacecraft and on-orbit satellite, which can be classified into two categories in terms of their origin, the one is space artificial target destroyed and the other one is micrometeoroids from the universe [2]. Usually, the space debris travel at a high speed with respect to the orbiting aircraft on the order of even 10 km/s as estimated by the available literature [3]. Such speed can seriously destroy operational on-orbit targets and penetrate the space suit; therefore, the measurements and

X. Yang (✉) · Z. Cao · R. Min
School of Electronic Engineering, University of Electronic Science and Technology of China, Chengdu, China
e-mail: joyodsp@163.com

Q. Liang et al. (eds.), *Proceedings of the 2015 International Conference on Communications, Signal Processing, and Systems*, Lecture Notes in Electrical Engineering 386, DOI 10.1007/978-3-662-49831-6_17

observations of space debris are of great importance. In this paper, we mainly focus on the imaging of space debris whose diameter ranges from 1 to 10 cm. Because the populations of space debris mainly concentrate the low earth orbit and geosynchronous orbit with altitude of ranging from 300 to 40000 km [4], the space-based radar is the closest and the most efficient observing mean of detecting space debris. To recognize space debris whose sizes are mentioned above, we employ space-based radar that operates at 340 GHz with the bandwidth of 28.8 GHz to image space debris.

ISAR is one of radar imaging modes that seeks to employ relatively fine range resolution and Doppler processing to discern target features not otherwise resolvable. Due to the attribute of the rotation angle of the spinning space debris with respect to radar, we can employ ISAR technique to image spinning space debris. Typical ISAR RD imaging algorithm is on the basis of three assumptions [5–8], i.e., (1) targets to be imaged is fully within the beam of radar; (2) the angular speed of spinning targets is constant; and (3) the integration angle of targets with respect to radar is a small angle, whereas, the motion of practical space debris is very complex [9]. To solve the blurring problem of radar image, Yuan et al. proposed general Radon transform in reassigned spectrogram to obtain a more focused image of space debris in [10], but this imaging algorithm will lose information. On the premise that the rotational angular speed of space debris is unchanged, Xueru Bai et al. proposed a 3-D imaging method based on the complex-valued back-projection transform according to the spinning nature of space debris [11]. Song et al. proposed a single range matching filtering algorithm based on the hypothesis that the angular velocity is constant [12]. In terms of the time-varying nature of Doppler domain, therefore, we employ time-varying spectral analysis methods instead of the traditional RD imaging algorithm to image space debris. The real data demonstrate that the proposed imaging algorithm can well solve the image blurring problem for spinning space debris.

The remainder of this paper is organized as follows. The overview of high-resolution THz radar imaging system is founded in Sect. 2. Then, the echo model of space debris is analyzed in Sect. 3. In Sect. 4, the real turntable data is used to verify the validity of the proposed time-varying spectral analysis method for solving the problem of image blurring. Conclusions are drawn in Sect. 5.

2 Radar System

The block diagram of the 340 GHz FMCW imaging radar system is illustrated in Fig. 1a. This system employs double point frequency sources to drive transmitter chain and receiver chain respectively to realize coherent reception of radar signal [6]. Due to the conversion loss of mixer and low power of single frequency source, single frequency source can hardly simultaneously drive the frontend of the transmitter chain and the receiver chain; therefore, this system structure can well solve the problem of low power assumption in terahertz band. The chirp source of

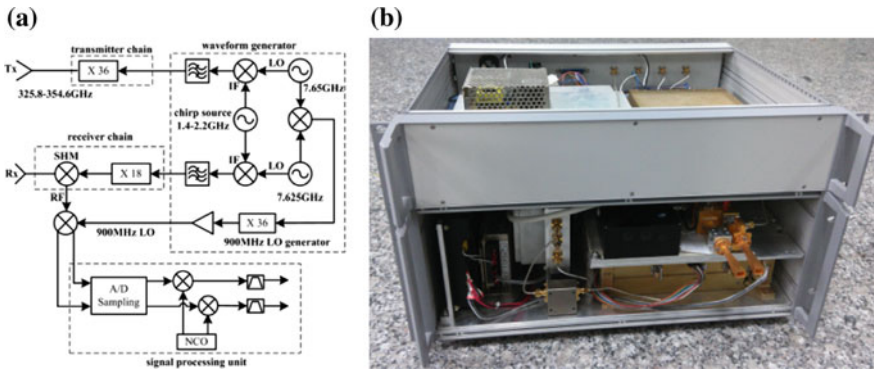

Fig. 1 **a** Block diagram and **b** photograph of 340 GHz FMCW imaging radar system

the imaging radar system employs the pre-distortion technique to improve its amplitude flatness; whose frequency linearly sweeps range from 1.4 GHz up to 2.2 GHz during the dwell time of 300 μs. The bandwidth of this radar system is 28.8 GHz, whose theoretical 3-dB range resolution is 4.61 mm.

As shown in Fig. 1a, the radar system consists of the receiver chain, the transmitter chain, the waveform generator, and the signal processing unit, in which the NCO module is used to choose the scene of interest. The photograph of the imaging radar system is shown in Fig. 1b.

As illustrated in Fig. 2, the real 3-dB resolution of 4.71 mm in range profile is well approximated as the theoretical 3-dB resolution of 4.61 mm. To examine the imaging performance of this THz radar system, three corner reflectors with the diameter of 1 cm are aligned within the illumination beam and the distance from each other is 0.5 cm along the radar line-of-sight. The three corner reflectors are mounted on the foam turntable with the angular speed of 1°/s and the integration

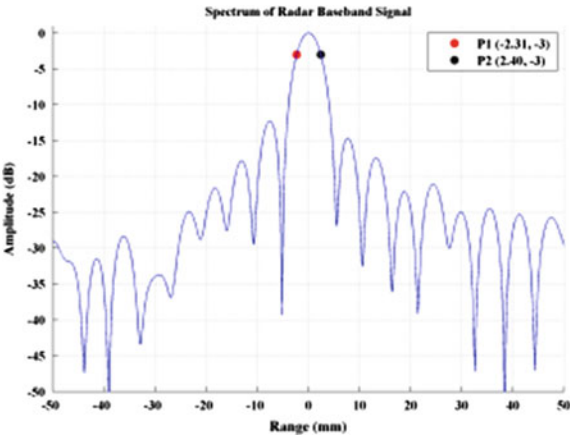

Fig. 2 Resolution measurement of 1D range profile

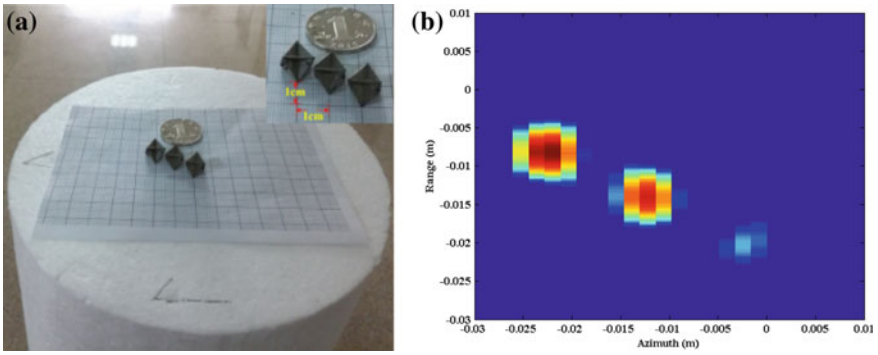

Fig. 3 **a** Imaging scene and **b** imaging result of 2D resolution experiment

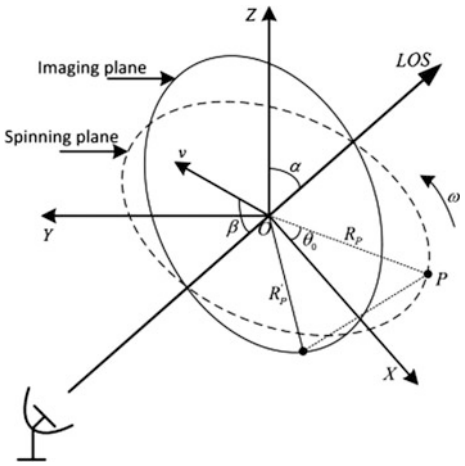

Fig. 4 Imaging geometry of spinning space debris

angle of 5.14°. The photograph of the test scene is illustrated in Fig. 3a and the imaging result of the three corner reflectors is presented in Fig. 4b. Figure 3b demonstrates that this THz radar system is capable of achieving high resolution in range profile.

3 Echo Model of Spinning Space Debris

The imaging geometry of spinning space debris [10] is illustrated in Fig. 4. The spinning plane is projected into the imaging plane, which can be simplified as the model of 2-D turntable plane imaging.

As shown in Fig. 4, the echo signal model of the point target P can be expressed as

$$s_p(t) = \sigma_p \exp\left\{ j2\pi f_c \left[t - \frac{2R_p(\tau)}{c} \right] \right\}, \tag{1}$$

where σ_p is the backscattering coefficient, f_c is the center frequency of the transmitter, t is the fast time in range profile, τ is the slow time in azimuth profile, c is the speed of light, and $R_k(\tau)$ is the instantaneous distance of point P from the radar. After the echo signal mixes with local oscillator signal, the baseband signal is given by

$$s_p(t) = \sigma_p \exp\left\{ -j\frac{4\pi}{\lambda} R_p(\tau) \right\}, \tag{2}$$

where λ is the wavelength of the transmitter, the instantaneous distance of point P from the radar can be expressed as

$$R_p(\tau) = R_0 + v\tau \cos\beta + \frac{\alpha\tau^2 \cos\beta}{2} + R_p' \sin\alpha \sin(\omega\tau + \theta_0), \tag{3}$$

where R_0 is the initial distance between the radar and the center of spinning space debris, v and α is the residual velocity and acceleration of the space debris, respectively, after the motion compensation, α denotes the angle between the XOZ plane and the radar line-of-light (RLOS), β denotes the angle between the velocity vector of the space debris and the RLOS, R_p' denotes the distance from the scattering point p to the spinning center of the space debris, ω is the angular velocity of the space debris, θ_0 denotes the initial angle of the scattering point p with respect to the X axis.

Due to the Doppler frequency shift corresponding to the time derivative of this radial distance, the instantaneous Doppler frequency shift can be expressed as

$$f_d = \frac{2}{\lambda}\frac{d}{d\tau} R_p(\tau) = 2\left\{ v\cos\beta + \alpha\tau \cos\beta + \omega R_p' \sin\alpha \cos(\omega\tau + \theta_0) \right\} / \lambda, \tag{4}$$

where the terms $v\cos\beta$ and $\alpha\tau\cos\beta$ are the translational motion components, which have no contribution to imaging. After the translational motion components are well compensated, the Doppler frequency shift can be expressed as

$$f_d = 2\omega R_p \cos(\omega\tau + \theta_0)/\lambda, \tag{5}$$

where $R_p = R_p' \sin\alpha$ denotes the projected radius of the scattering point p to the rotational center in imaging plane. Because the spinning space debris is composed

of the discrete scattering points, therefore, the echo model of the spinning space debris can be expressed as

$$s_p(\tau) = \sum_{p=1}^{P} \sigma_p \exp\left\{ -j\frac{4\pi}{\lambda} R_p \sin(\omega\tau + \theta_0) \right\}. \quad (6)$$

Equation (6) is on the basis of the assumption that the angular velocity ω is constant, whereas the angular velocity of practical spinning space debris varies with time of t. Due to the time-varying behavior of the Doppler frequency shift, a high resolution time-varying spectral analysis instead of direct Fourier transform is applied to the time-varying Doppler spectrum to solve the blurring problem of radar image.

4 Imaging Experiment and Analysis

The complex motion of spinning space debris can be decomposed into the translational motion component with respect to the RLOS and the rotational motion component with respect to the spinning axis, the translational motion component has no contribution to imaging, therefore, the rotational motion component is our focus. To emulate the real spinning space debris with the translational motion component well compensated, we use the turntable model instead of the real rotational motion component of space debris.

In our experiment, the real turntable data of three corner reflectors with the diameter of 1 cm is used to verify that the time-varying spectral analysis methods to solve the blurring problem of radar image induced by using the Fourier transform to the time-varying Doppler spectrum. The main experiment parameters are listed in Table 1. We define the R_0 as the distance from the radar to the center of the turntable, the ω as the initial angular velocity of the turntable, the N_a as the number of sampling points in cross-range profile, the N_r as the number of sampling points in range profile, the $\Delta\theta$ as the integration angle, and the a as the angular acceleration. The associated imaging scene is shown in Fig. 5; three corner reflectors are mounted on the foam turntable.

Figure 6a is the imaging result applying the Fourier transform to time-varying spectrum, the radar image becomes blurred, in which we can see that two corner reflectors are blurred. By using the time-varying spectral analysis instead of the

Table 1 Experiment parameters

Parameter	Value
R_0 (m)	3.66
ω $(°/s)$	1
$\Delta\theta$ $(°)$	5.41
a $(°/s^2)$	1

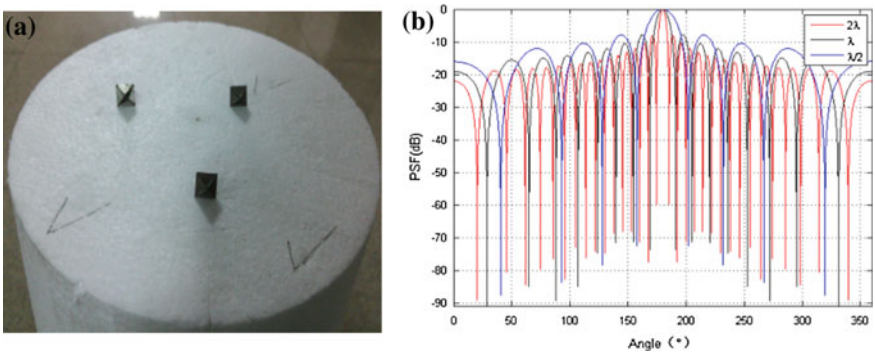

Fig. 5 **a** Photograph of imaging scene and **b** PSF of different radii

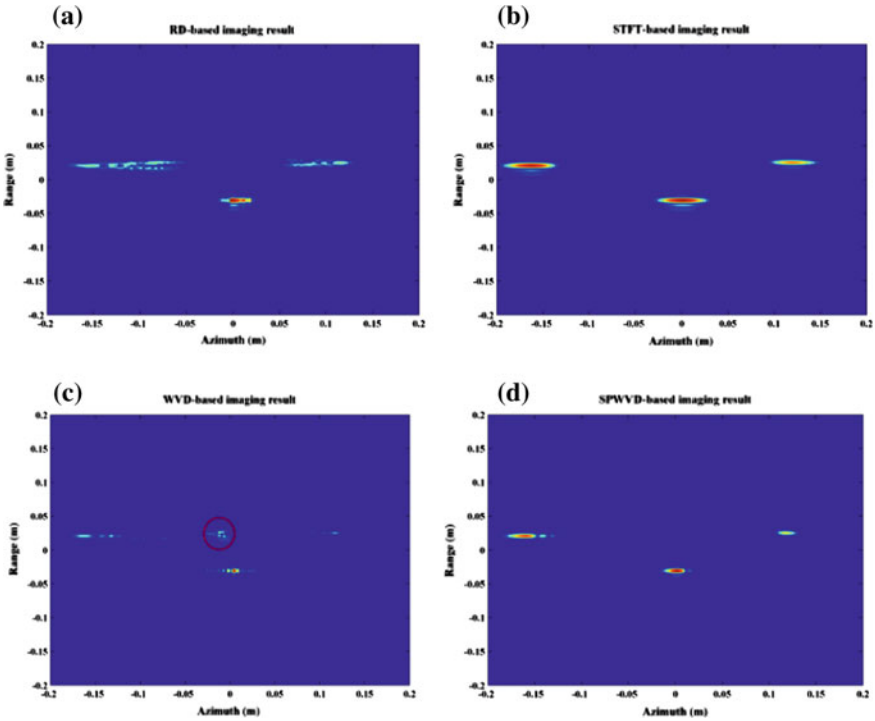

Fig. 6 **a** RD-based imaging result, **b** STFT-based imaging result, **c** WVD-based imaging result, and **d** SPWVD-based imaging result

Fourier transform, a single Fourier image frame becomes a sequence of time-varying image frames. Each represents a full radar RD image at a specific time instant. Figure 6b is one of the image frames using the STFT imaging algorithm, which can well solve the blurring problem of radar image as opposed to the

traditional RD imaging algorithm, but the resolution is worse than the traditional RD algorithm. Figure 6c is one of the image frames using the WVD imaging algorithm, in which ghost targets enclosed by a red circle emerges due to the existing inherent cross-terms. Figure 6d is one of image frames using the SPWVD imaging algorithm. As shown in Fig. 6, compared with the traditional RD imaging algorithm, the STFT, WVD, and SPWVD time-varying spectral analysis not only can well solve the blurring problem of radar image, but also exhibit the Doppler change and range walk with time. Among the three time-varying spectral analysis methods, the resolution of the WVD imaging algorithm is the best one but exists cross-terms resulting in ghost targets in radar image, in contrast to the WVD imaging algorithm, although the STFT is the worst one but has no ghost target, the SPWVD imaging algorithm is a trade-off between the resolution and the problem of cross-terms. As shown in Fig. 5b, SRMF exhibits different angular resolutions for different radii; whereas, the angular resolution of the proposed algorithm is only dependent on the integration angle and wavelength of a carrier frequency.

5 Convolutions

To meet high-resolution requirement for space debris, the 340 GHz radar system with the bandwidth of 28.8 GHz is proposed. The real data show that the presented radar system can achieve the practical 3-dB resolution of 4.7 mm. To solve the blurring problem of radar image induced by the non-uniform spinning motion of space debris, the time-varying analysis is proposed.

The real turntable data of three corner reflectors were used to demonstrate the capability of the time-varying analysis for radar imaging of spinning space debris. The results clearly illustrate that time-varying spectral analysis can well eliminate the blurring problem of radar image.

Acknowledgments This work was supported by the National Nature Science Foundation of China under Grants 61271287, 61371048, U1433113.

References

1. Gong S (2006) The simulated research of effectiveness for space debris mitigation measures. Aerospace, vol 2, Shanghai
2. Wang Q, Xing MD et al (2008) High-resolution three-dimensional radar imaging for rapidly spinning targets. IEEE Trans Geosci Remote Sens 46(1):22–31
3. Paté-Cornell E, Sachon M (2000) Risks of particle hits during space walks in low Earth orbit. IEEE Trans Aerosp Electron Syst 36(1):134–146
4. Cong L (2007) Overview of the world's space based radar technique development. National Defense Industry Press, Beijing, p 2
5. Cheng B, Jiang G et al (2013) Real-Time imaging with a 140 GHz inverse synthetic Aperture radar. IEEE Trans Terahertz Sci Technol 3(5):594–605

6. Zhang B, Pi Y et al (2013) Terahertz imaging radar with aperture synthetic techniques for object detection. In: IEEE International communications workshops (ICC), pp 921–925
7. Caner O (2012) Inverse synthetic aperture radar imaging with MATLAB algorithms, vol 210. Wiley
8. Zhang B, Pi Y, Li J (2015) Terahertz imaging radar with inverse aperture synthesis techniques: system structure, signal processing, and experiment results. IEEE Sens J 15(1):290–299
9. Chen VC, Miceli WJ (1998) Time-varying spectral analysis for radar imaging of manoeuvring targets. In: IEEE proceedings radar, sonar and navigation, vol 145, issue no 5, pp 262–268
10. Yuan B, Chen ZP et al (2013) Space debris narrowband imaging via general radon transform in reassigned spectrogram. In: IET International radar conference, pp 1–5, 14–16 April 2013
11. Bai X, Xing M et al (2009) High-resolution three-dimensional imaging of spinning space debris. IEEE Trans Geosci Remote Sens 47(7):2352–2362
12. Song D, Shang S (2011) Microwave radar imaging and detection algorithm for space debris. In: International conference electronics, communications and control (ICECC), pp 4378–4381, 9–11 Sept 2011

Cluster-Head Election Using Fuzzy Logic Systems in Radar Sensor Networks

Yaoyue Hu, Huaiyuan Liu and Jing Liang

Abstract In this paper, we propose three cluster-head election schemes using fuzzy logic systems (FLSs) for clustered radar sensor networks. Three factors of a radar sensor (RS) are considered in our FLS design: its remaining energy (RE); the fading envelope of the signal transmitted by the RS to base station (FESTRBS); its distance to base station (DBS). The three cluster-head election schemes are named FF (FLS with two-antecedents & fuzzy-c means (FCM)), FFSVD (FLS with two-antecedents, FCM, and singular value decomposition-QR (SVD-QR)), and FF3SVD (FLS with three-antecedent FLS, FCM, and SVD-QR). Their clustering performances in terms of detection performances and networks' lifetime are compared and analyzed. Monte Carlo simulations show that among these three cluster-head election schemes, FF3SVD provides the lowest energy consumption and moderate probability of target detection (PD), and FFSVD offers moderate power loss and the highest PD, whereas FF has the worst clustering performances.

1 Introduction and Motivation

Among the existing research on radar sensor networks (RSN), three criteria for RSN design have been used.

(1) Detection performance optimization: the PD and constant false alarm rate (CFAR) are used as the optimality standards. RSNs using ultra-wideband impulse have been investigated in [1–3] to reduce clutter and interference.

Y. Hu · H. Liu · J. Liang (✉)
Department of Electrical Engineering, University of Electronic Science and Technology of China, Chengdu, China
e-mail: liangjing@uestc.edu.cn

Y. Hu
e-mail: kalina_hu@163.com

H. Liu
e-mail: louis.uestc@outlook.com

Q. Liang et al. (eds.), *Proceedings of the 2015 International Conference on Communications, Signal Processing, and Systems*, Lecture Notes in Electrical Engineering 386, DOI 10.1007/978-3-662-49831-6_18

(2) Energy-efficient optimization [4, 5]: these networks should function as long as possible, because RSs may need to be deployed in remote or dangerous environments, and thus it may be inconvenient or impossible to timely recharge RS batteries.
(3) SNR maximization: In [6], SVD-QR with threshold approach has been applied to select the channel with high SNR in virtual multiple-input-multiple-output wireless sensor networks. It is shown that SVD-QR with threshold approach can reduce the redundance and the bit error rate.

Although the aforementioned papers provide dazzling advantage in their own study field, current investigations have not considered combining above three criteria together in the RSN design.

In this paper, we consider a set of RSs deployed in large numbers over a rectangular field. Some assumptions about the properties of the network are as follows: (1) all RSs have similar capabilities (processing/communication), but different initial energy; (2) RSs in the network are quasistationary and location aware; (3) all RSs are left unattended after the deployment; (4) when clustering approaches are applied, the non cluster-head (NCHs) are responsible for detecting the targets and transmitting the decision results to the corresponding cluster heads (CHs). CHs receive and fuse messages and transmit their own decisions to the base station (BS), which makes the second fusion and the final decision.

The novelty and contributions of this paper are threefold:

(1) The idea behind the three cluster-head schemes is that not only the energy consumption and FESRBS are taken into account in the FLS design, but also FLSs and SVD-QR approach are used to maximize the SNR in the BS and CHs. The method—combining FLSs and SVD-QR, to the best of our knowledge—is used for the first time for cluster-head election in RSN.
(2) We investigate a CFAR decision fusion approach for clustered RSN.
(3) We present extensive simulation results, which help to illustrate the clustering performances in cases of different cluster numbers.

The rest of the paper is organized as follows: Sect. 2 elaborates these three cluster-head election algorithms. Section 3 addresses a CFAR decision fusion approach for clustered RSN. In Sect. 4, the clustering performances of these three cluster-head election algorithms are evaluated. Finally, Sect. 5 draws the conclusion.

2 Cluster-Head Election Algorithms

The following assumptions are used in our analysis.

(1) The RSN is clustered by FCM clustering approach based on RSs' locations.
(2) Three factors of a RS are considered in our FLS design: RE, FESTRBS and DBS. All these antecedents use the same type of membership functions (MFs)

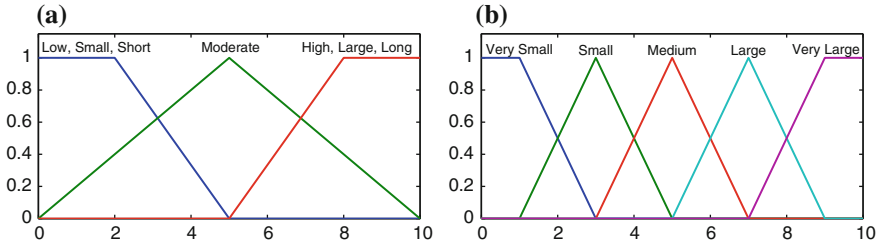

Fig. 1 MFs. **a** Antecedents, consequent of FF and FFSVD, **b** consequent of FF3SVD

and the MF parameters are initialized consistently. The linguistic variables that represent each antecedent are divided into three levels: low, moderate and high for RE; small, moderate and large for FESTRBE; short, moderate and long for DBS. We apply trapezoidal MFs and triangular MFs to map linguistic variables to a membership value between 0 and 1, which are shown in Fig. 1a. Note that the input of these three antecedents MFs have been normalized to $\in [0, 10]$.

(3) The FLS consequent for FF and FFSVD is divided into 3 levels: small, medium, large, using the same type and parameters of MFs as in Fig. 1a.

(4) The FFSVD and FF3SVD can be presented in three steps:

Step 1: Use FLSs to set the probability of becoming a temporary CH (TCH);
Step 2: Use FCM to choose TCHs;
Step 3: Use SVD-QR to decide the final CH of the cluster and set TCHs as NCHs.

2.1 FF

In FF, FLS is designed to minimize the energy consumption. The energy consumed for a CH include two parts: the energy for receiving signals from NCHs and for transmitting signals to BS. So to achieve the load balance of the whole network, the CH should have high remaining power to communicate with NCHs and BS. A CH can consume less energy if it is located closer to BS. Therefore, we choose RE and DBS as antecedents for FF. The consequent denotes the probability that a RS is elected to be a CH. Since there are two-antecedents and each antecedent has three fuzzy subsets, we need to set up $3^2 = 9$ rules for this FLS, which are summarized in Table 1. For every current input (x_1, x_2) of each RS, the output—the probability of a RS being elected to be a CH—is computed using

$$y(x_1, x_2) = \frac{\sum_{l=1}^{9} \mu_{F_1^l(x_1)} \mu_{F_2^l(x_2)} c^l}{\sum_{l=1}^{9} \mu_{F_1^l(x_1)} \mu_{F_2^l(x_2)}} \tag{1}$$

Table 1 Rules in FF for CH election

Rule	RE	DB	Consequent
1	Low	Short	Medium
2	Low	Moderate	Small
3	Low	Long	Small
4	Moderate	Short	Large
5	Moderate	Moderate	Medium
6	Moderate	Long	Medium
7	High	Short	Large
8	High	Moderate	Medium
9	High	Long	Small

Thus, the final CH is the RS with the highest probability of a RS being elected to be a CH.

2.2 FFSVD

(1) FLS Design: in FFSVD, FLS is designed to optimize the detection performance. We choose RE and FESTRBE as antecedents. In view of the detection performances, the fading channel gain of the signal sent by CHs should be as large as possible. The consequent denotes the probability of a RS being elected to be a TCH and can be computed use formula (1). Fuzzy rules for FFSVD are summarized in Table 2.

(2) FCM: FCM clustering [7] approach is a data clustering technique where each data point belongs to a cluster to a degree specified by a membership grade. Here we apply FCM clustering to choose TCHs. Assume the probability of a RS being elected to be a TCH of N_i RSs in the ith cluster is $p = p_1, p_2, \ldots, p_{N_i}$, we use FCM to part the vector p to mc_i minimal clusters, and choose the cluster with larger center as the TCH cluster, $tp = (tp_1, tp_2, \ldots, tp_{tN_i})$. mc_i is an integer and can be computed by $mc_i = floor(C_{prob} * N_i)$, where C_{prob} (say 30 %) is a constant ratio tN_i is the number of TCHs in the ith cluster.

(3) We propose SVD-QR as follows:

Step 1: Suppose h_{jk} is the channel gain from the jth RS to the kth RS in the ith cluster, where $1 \leq j, k \leq N_i$ and $j \neq k$, and H is the $(N_i - 1) \times N_i$ matrix made of h_{jk}. The index set of TCHs chosen by FCM is $tp = (tp_1, tp_2, \ldots, tp_{tN_i})$ and $tN_i > 1$. Therefore, the channel gain matrix of TCHs is $H_t = H(:, tp)$ and $r = rank(H_t) \leq tN_i$.

Step 2: Calculate the singular value decomposition of H_t, $H_t = U\Sigma V^T$, where U is an $(N_i - 1) \times (N_i - 1)$ matrix of orthonormalized eigenvectors of $H_t {H_t}^T$, V is an $tN_i \times tN_i$ matrix of orthonormalized eigenvectors of ${H_t}^T H_t$, and Σ is

Table 2 Rules in FFSVD for TCH election

Rule	RE	FESRBS	Consequent
1	Low	Small	Small
2	Low	Moderate	Medium
3	Low	High	Medium
4	Moderate	Small	Small
5	Moderate	Moderate	Medium
6	Moderate	High	Large
7	High	Small	Small
8	High	Moderate	Medium
9	High	High	Large

the diagonal matrix $\Sigma = diag(\sigma_1, \sigma_2, \ldots, \sigma_j, \ldots, \sigma_r)$, $\sigma_j = \sqrt{\lambda_j}$ and λ_j is the jth eigenvalue of $H_t {H_t}^T$ and $\sigma_1 \geq \sigma_2 \geq \cdots \geq 0$. σ_j is the singular value of H_t. We choose σ_1. $V = (v_1, v_2, \ldots, v_k, \ldots, v_{tN_i})$, where v_k is the kth $tN_i \times 1$ vector of V.

Step 3: Using QR decomposition with column pivoting, determine E such that ${v_1}^T E = QR$, where Q is a unitary matrix; and E is the permutation matrix. The position of 1 in the first column of E correspond to the final CH.

2.3 FF3SVD

In FF3SVD, we set up fuzzy rules in view of the following three antecedents of a RS: RE, FESTRBS, and DBS. The consequent—PRET—is divided into five levels: very small, small, medium, large, and very large, which are illustrated in Fig. 1b. 27 rules are applied here, which are summarized in Table 3. Based on the FLS output, the final CHs is selected using FCM and SVD-QR approaches mentioned in the FFSVD algorithm.

3 An CFAR Decision Fusion Approach for Clustered RSN

Assumption is that a RSN with N RSs is parted to c clusters, and each cluster has N_i RSs except the CH, $1 \leq i \leq c$.

Assume the additive Gaussian noise is with zero mean and variance σ^2. When one target appears in the surveillance area, the kth NCHs ($1 \leq k \leq N - c$) makes a binary decision $u_k \in \{-1, +1\}$ to either "target absent"—H_0, or "target present"—H_1, with a probability of detection P_{dk}.

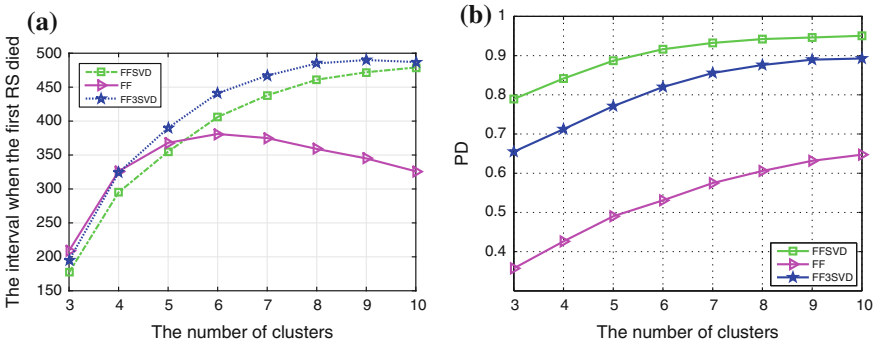

Fig. 2 The lifetime (first RS death) and the PD of the RSN in FF, FFSVD and FF3SVD versus different cluster numbers. **a** the lifetime (first RS death), **b** the PD

Table 3 Rules in FF3SVD for TCH election

RE	FESTRBS	DBS	Consequent	RE	FESTRBS	DBS	Consequent
Low	Small	Short	Small	Moderate	Moderate	Long	Small
Low	Small	Moderate	Very small	Moderate	High	Short	Very large
Low	Small	Long	Very small	Moderate	High	Moderate	Large
Low	Moderate	Short	Medium	Moderate	High	Long	Medium
Low	Moderate	Moderate	Small				
Low	Moderate	Long	Very small	High	Small	Short	Large
Low	High	Short	Large	High	Small	Moderate	Medium
Low	High	Moderate	Medium	High	Small	Long	Small
Low	High	Long	Small	High	Moderate	Short	Very large
Moderate	Small	Short	Medium	High	Moderate	Moderate	Large
Moderate	Small	Moderate	Small	high	Moderate	Long	Medium
Moderate	Small	Long	Very small	High	High	Short	Very large
Moderate	Moderate	Short	Large	High	High	Moderate	Very large
Moderate	Moderate	Moderate	Medium	High	High	Long	Large

The received signal at the ith CH from the kth RS within the ith cluster is $y_k^i = h_k^i u_k + n_k^i$, where h_k^i is a real valued fading envelope with $h_k^i \geq 0$, $n_k^i \sim N(0, \sigma^2)$, $1 \leq k \leq N_i$. The fusion statistic of the ith CH Λ_a [8] is

$$\Lambda_a = \frac{1}{N_i} \sum_{k=1}^{N_i} (P_{dk} - P_f^{(l)}) y_k^i h_k^i \tag{2}$$

where $P_f^{(l)}$ is the CFAR for all RSs. Obviously, Λ_a is the sums of independent and identically distributed (i.i.d.) random variables whose probability distribution functions can be approximately obtained through the central limit theorem. For both

Table 4 Mean and variance of Λ_a^L under H_0 and H_1 with N_i RSs in the ith cluster

H_0	$\mu_{i_0} = \frac{2P_f^{(l)}-1}{N_i} \sum_{k=1}^{N_i} A_{ki}$
	$\sigma_{i_0}^2 = \frac{1}{N_i^2}(\sigma^2 \sum_{k=1}^{N_i} B_{ki} + 4P_f^{(l)}(1-P_f^{(l)}) \sum_{k=1}^{N_i} {A_{ki}}^2)$
H_1	$\mu_{i_1} = \frac{1}{N_i} \sum_{k=1}^{N_i} (A_{ki}(2P_{dk}-1))$
	$\sigma_{i_1}^2 = \frac{1}{N_i^2}(\sigma^2 \sum_{k=1}^{N_i} B_{ki} + 4 \sum_{k=1}^{N_i} ({A_{ki}}^2 P_{dk}(1-P_{dk})))$

analysis and numerical simulation, here we assume Rayleigh fading channel. Provided $E[{h_k^i}^2] = 1$, the first and second statistics of Λ_{di}, are derived and summarized in Table 4.

Given the CFAR of the CHs $P_f^{(c)}$, the decision threshold is derived as

$$T_i^{(c)} = \sigma_{i_0} Q^{-1}(P_f^{(c)}) + \mu_{i_0} \tag{3}$$

The ith CH also makes a binary decision $u_i \in \{+1, -1\}$. The received signal from the ith CH is $y_i^c = h_i^c u_i + n_i^c$. Similar as formula (2), the fusion statistic of BS is $\Lambda_b = \frac{1}{c} \sum_{i=1}^{c} (P_{di}^{(c)} - P_f^{(c)}) y_i^c h_i^c$, where $P_{di}^{(c)}$ is the estimated PD of the ith CH and $P_{di}^{(c)} = Q(\frac{T_i^{(c)} - \mu_{i_1}}{\sigma_{i_1}})$. The first and second statistics of Λ_b can also be derived the same way as the formulas in Table 4, if N_i, $P_f^{(l)}$, P_{dk} are displaced by c, $P_f^{(c)}$, P_{di}, respectively. Similarly, given the CFAR of the RSN $P_f^{(b)}$, the decision threshold of the BS can be obtained in the same way as the formula (3).

4 Performances Evaluation

In our experiment, 100 RSs with the random initial energy, from 0.3 to 0.5 J/batery, are uniformly dispersed into a square field from (0, 0) to (100, 100 m). The BS is at (50 m, 175 m). The CFAR of NCHs and CHs, $P_f^{(l)}$ and $P_f^{(c)}$, are fixed as 0.05 and 0.01, respectively.

Figure 2a illustrates the lifetime of the RSN in FF, FFSVD and FF3SVD, where network lifetime is the time until the first RS dies. The energy of the network is primarily consumed for detection and data transmission. Energy consumption model for data transmission is the same in [4]. This graph shows that: (1) in FF, the optimum cluster number is 6 for the 100-RS network to reduce the energy consumption; (2) in both FFSVD and FF3SVD, the lifetime of a RSN is increasing with the rise of cluster number; (3) FF3SVD offers the longest lifetime and FFSVD outperforms FF in prolonging the RSN's lifetime.

Figure 2b shows the PD of the RSN in FF, FFSVD and FF3SVD at different cluster numbers when CFAR and SNR are fixed as 10^{-3} and 7 dB, respectively. This graph

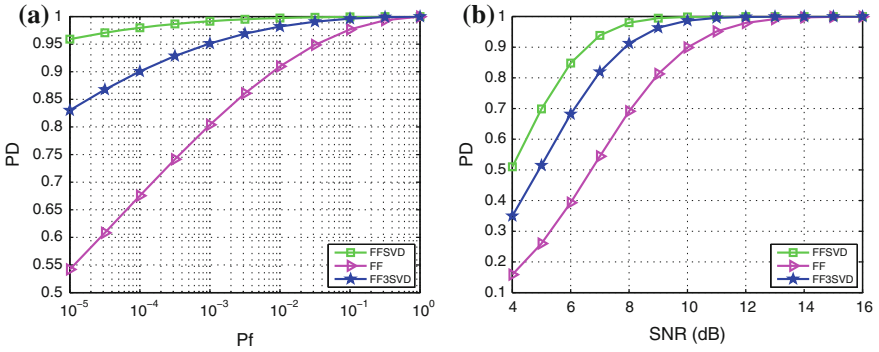

Fig. 3 The PD of the RSN in FF, FFSVD and FF3SVD when cluster number is 6. **a** Various CFARs of the system (SNR = 7 dB), **b** different SNRs (CFAR = 10^{-3})

demonstrates that at the fixed SNR and CFAR, all the PD of FF, FFSVD and FF3SVD is increasing with the rise of cluster number.

Figure 3 presents the PD of the RSN in FF, FFSVD and FF3SVD at various CFARs of the system (SNR = 7 dB) and different SNRs (CFAR = 10^{-3}) when the number of cluster is 6. From this figure, we obtain that FFSVD offers highest PD whenever the CFAR and SNR is different, and the PD of FF3SVD is higher than that of FF.

5 Conclusion

In this paper, three cluster-head election schemes—FF, FFSVD, and FF3SVD—using FLSs are proposed and compared for clustered RSN. FCM clustering approach is used to cluster the RSN based on the RSs' locations. Monte Carlo simulations show that among these three cluster-head election schemes:

(1) In the case of qusistatic channel environment, FF3SVD provides lowest energy consumption and moderate PD, and FFSVD offers moderate power loss and the highest PD, whereas FF have worst clustering performances.
(2) The clustering performances of a RSN in FFSVD or FF3SVD can be improved by increasing the cluster number.

References

1. Liang J, Liang Q (2009) UWB radar sensor networks detection of targets in foliage using short-time fourier transform. In: 2009 IEEE international conference on commucations, pp 1–5

2. Win MZ, Scholtz RA (2000) Ultra-wide bandwidth time-hopping spread-spectrum impulse radio for wireless multiple-access communications. IEEE Trans Commun 48(11):679–691
3. Liang J, Liang Q (2011) Design and analysis of distributed radar sensor networks. IEEE Trans Parallel Distrib Syst 22(11):1926–1933
4. Alirezaei G, Reyer M, Mathar R (2014) Optimum power allocation in sensor networks for passive radar applications. IEEE Trans Wirel Commun 13(6):3222–3231
5. Heinzelman WB, Chandrakasan AP, Balakrishnan H (2002) An application-specific protocol architecture for wireless mmicrosensor networks. IEEE Trans Wirel Commun 1(4):660–670
6. Liang J, Liang Q (2009) Channel selection in virtual MIMO wireless sensor networks. IEEE Trans Veh Technol 58(5):2249–2257
7. Bezdek JC (1981) Pattern recognition with fuzzy objective function algorithms. Plenum, New York
8. Chen B, Jiang R, Kasetkasem T, Varshney PK (2004) Channel aware decision fusion in wireless sensor networks. IEEE Trans Sig Process 52(12):3454–3458

Raw Data Reduction for Synthetic Aperture Based on SVD-QR

Na Wu and Qilian Liang

Abstract Singular-Value-QR Decomposition (SVD-QR) is a new data reduction algorithm, which can be applied to compress high data redundancy in wireless communication system and radar system. It selects the most important part of the original data which can represent other information as well. Based on the analysis of synthetic aperture radar (SAR) history data in slow-time domain, we prove that it satisfies the condition of SVD-QR approach. In addition, backprojection image reconstruction algorithm is also presented in this work, which is more efficient than matched filter method. Simulations are performed according to the Gotcha Volumetric SAR Data Set, which is collected in a real 2D/3D scenario. From the simulation results, the effectiveness of this new algorithm is verified and the compression ratio can be achieved by 2:5. Comparing with the uniform down sampling method, SVD-QR algorithm can save about 60 % data and have a better performance.

1 Introduction

Synthetic aperture radar (SAR) is an on-board radar system that can provide high-resolution images for remote objectives even in a bad weather situation. The research of SAR is mainly focused on image and target recognition algorithm. In the past few years, it has been successfully applied in remote sensing, satellite ocean observation, and ground mapping, for example, in [1, 2], the authors studied SAR related with soil properties. SAR processing includes two distinct steps, which are range imaging and cross-range imaging. The former is performed in fast time and the latter is in slow time. During the flight interval, the antenna collects echoes at appropriate positions along the flight path. As a consequence, the slow-time resolution is made much finer.

N. Wu (✉) · Q. Liang
Department of Electrical Engineering, University of Texas at Arlington, Arlington, TX 76019, USA
e-mail: na.wu@mavs.uta.edu

Q. Liang
e-mail: liang@uta.edu

Q. Liang et al. (eds.), *Proceedings of the 2015 International Conference on Communications, Signal Processing, and Systems*, Lecture Notes in Electrical Engineering 386, DOI 10.1007/978-3-662-49831-6_19

However, with a high sampling rate, the SAR data is collected in a large amount which requires to be compressed. There are several different strategies to reduce the capacity of the data. The author in [3] compared different approaches for on-board SAR raw data reduction. In [4], Gabor transform is proposed for SAR image compression and in [5, 6], compressive sensing algorithms are applied. Nonetheless, data compression will cause a loss of information and affect the resolution of the image. Moreover, some methods are too complex to be applied on real data. Within these approaches, in [7], the author proposed a Singular-Value-QR Decomposition (SVD-QR) algorithm which is less complicated and in [8], it was used for radar sensor network reduction successfully.

SVD-QR algorithm has also been used in reducing the redundancy of wireless sensor network [9, 10] for its advantage of low complexity. SVD-QR selects several independent datasets which minimize the residual error in a least-square sense. In wireless sensor networks, since the sensors are densely deployed and the information collected among adjacent sensor nodes is possible alike with each other, this approach can be very efficient. The SAR images formed from the phase histories are also spatially overlapped, taking advantage of this property, we apply SVD-QR method in synthetic aperture radar in a similar way.

For the SAR image reconstruction, different algorithms are developed, such as range Doppler algorithm [11], time-domain reconstruction [12] and wavelets basis [13]. There is a tradeoff between computation complexity and image accuracy when we design these methods. Two basic SAR imaging algorithms are matched filter method and backprojection method [14]. Due to the high computational complexity of the former algorithm, it is hard to be used in practical situations. Backprojection algorithm is more efficient than matched filter method, which also results in precise images based on the range information in the collected data. There are several papers studying the complexity of backprojection algorithm, such as the fast backprojection method in [15].

In this paper, Gotcha Volumetric SAR Data Set is provided for the simulation. Gotcha is a prototype airborne radar platform which is developed by the Air Force Research Laboratory [16, 17]. The trace of the aircraft is a circle over an area of parking lot and the on-board, side-looking radar transmits and receives electromagnetic waves at a constant pulse repetition interval (PRI), which constructs phase history raw data.

The rest of this paper is organized as follows. In Sect. 2, we give a brief overview of Gotacha data set and the backprojection algorithm. SVD-QR method is detailed described in Sect. 3. In Sect. 4, we apply the simulations and analyze the results. Conclusions are presented in Sect. 5.

2 Preliminaries

2.1 Background of Gotcha Data Set

Gotcha SAR Dataset is an open source for radar algorithm research, which collects signal at a 640 MHz bandwidth and the on-board radar covers eight different elevation angles of phase history data with full polarization. The paths of the radar system are circular along with different altitudes while the imaging scene is made up of several civilian cars and calibration targets. In the document, the data over one degree of azimuth is for a single pass and a single polarization in each file. There are still several challenging problems existing in this dataset.

2.2 Signal Model

The following SAR model is introduced in [18] which is on the basis of polar format algorithm (PFA). In Fig. 1, we illustrate the circular SAR geometry as an example. The civilian vehicles and calibration target locate in the monitored area.

The real path in the figure can be written as

$$\mathbf{r}_a(\tau) = (x_a(\tau), y_a(\tau), z_a(\tau)) \tag{1}$$

where τ denotes the slow-time domain.

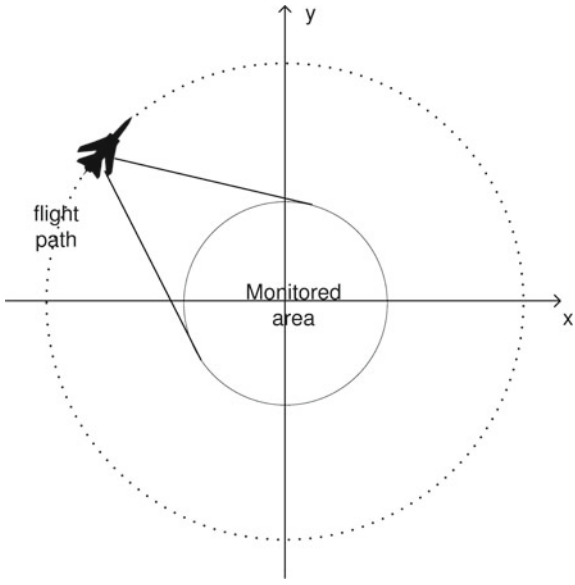

Fig. 1 Imaging system geometry in circular SAR

If we define the distance with respect to the origin (0, 0, 0), it is

$$d_a(\tau) = \sqrt{(x_a(\tau))^2 + (y_a(\tau))^2 + (z_a(\tau))^2} \tag{2}$$

A target in the range is located at

$$\mathbf{r}(\tau) = (x(\tau), y(\tau), z(\tau)) \tag{3}$$

We assume that this target is stationary, as a result, the distance between the antenna phase center and the target can be calculated by

$$d_{a0}(\tau) = \sqrt{(x_a(\tau) - x)^2 + (y_a(\tau) - y)^2 + (z_a(\tau) - z)^2} \tag{4}$$

Along the flight path, the radar transmits and receives pulses. In a given synthetic aperture, N_p pulse used to construct the image and the transmission time, of each pulse is $\{\tau_n, n = 1, 2, \ldots, N_p\}$. There are K frequency samples per pulse, which are $\{f_k, k = 1, 2, \ldots, K\}$.

Furthermore, we assume the output of the receiver at a given time τ, which is the time delayed by the round-trip to the target, sampled on band-limited frequency domain of a pulse and the scene center has zero phase. Therefore, the receiving signal is written as

$$S(f_k, \tau_n) = e^{-2\pi f(2(d_{a0}(\tau_n) - d(\tau_n))/c)} \tag{5}$$

We will substitute (5) into the backprojection algorithm for SAR image formation.

3 Data Reduction in Slow-Time

In this paper, we use the backprojection algorithm [19, 20] that sums total data across the aperture with high resolution. Assuming at a discrete range bin m, the range profile is calculated through the given SAR phase history (5):

$$s(m, \tau_n) = \sum_{k=1}^{K} S(f_k, \tau_n) e^{(2\pi f(2(d_{a0}(m,\tau_n) - d(m,\tau_n))/c)} \tag{6}$$

The detailed process of backprojection algorithm is plotted in Fig. 2, $f(x_a, y_a, z_a)$ means the reflector at (x_a, y_a, z_a). For each position, this process is repeated once.

The image formation result is decided by the reflectivity of the target scene, for instance, some areas with small reflectivity values can be considered as no target, which are shown in dark color in the figure. This motivates us to separate a space into principle and sub-principle subspaces.

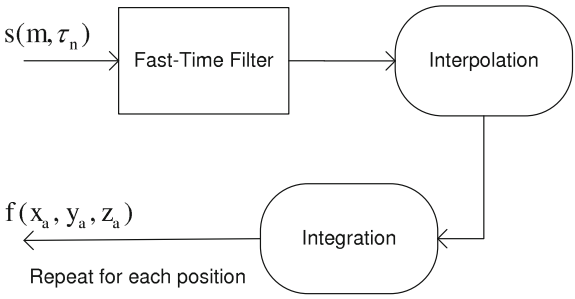

Fig. 2 Block diagram of SAR reconstruction via backprojection algorithm

3.1 SVD-QR Algorithm

SVD-QR algorithm is proposed in [21, 22], which is a preferable method in rank deficient problems. In a least-square sense, it chooses a subset from the independent data which have the minimum residual error. Here, the main mathematical notations are

(1) Given the phase history data set matrix $\mathbf{P} \in R^{N\times M}$, $r = \text{rank}\ (\mathbf{P}) \leq M$ and r' is the numerical estimation of rank r through Eq. (7)

$$P = \mathbf{U} \begin{bmatrix} \Sigma & 0 \\ 0 & 0 \end{bmatrix} \mathbf{V}^T \tag{7}$$

where $\mathbf{U}$ is a size $N \times N$ matrix of orthonormalized eigenvectors of $\mathbf{PP}^T$, $\mathbf{V}$ is an $M \times M$ matrix of orthonormalized eigenvectors of $\mathbf{P}^T\mathbf{P}$, and Σ is the diagonal matrix which is

$$\Sigma = diag(\sigma_1, \sigma_2, \ldots, \sigma_r), \sigma_i = \sqrt{\lambda_i}. \tag{8}$$

here λ_i is the ith eigenvalue of $\mathbf{HH}^T$ and select $\hat{r} \leq r'$.

(2) Compute a permutation matrix $\mathbf{E}$ such that the columns of the matrix $\Gamma_1 \in R^{N\times\hat{r}}$ in

$$\mathbf{PE} = [\Gamma_1, \Gamma_2] \tag{9}$$

are independent. The permutation matrix $\mathbf{E}$ is obtained from the QR decomposition of the sub-matrix comprised of the right singular vectors, which correspond to the $\hat{r}$ ordered most significant singular values.

The specific procedures of this algorithm could be presented as following:

Step 1: Create a matrix $\mathbf{P}$ which is selected from the phase history data.

Step 2: Execute SVD-QR as describing above to the slow-time history phase data and decide the most important collections to be used in the image formation.

Step 3: Partition

$$V = \begin{bmatrix} V_{11} & V_{12} \\ V_{21} & V_{22} \end{bmatrix} \tag{10}$$

where $V_{11} \in R^{\hat{r}\times\hat{r}}$, $V_{12} \in R^{\hat{r}\times(M-\hat{r})}$, $V_{21} \in R^{(M-\hat{r})\times\hat{r}}$ and $V_{22} \in R^{(M-\hat{r})\times(M-\hat{r})}$. For $\hat{r}$, it could be selected smaller than r' in many practical cases.

Step 4: Pivoting the column by using QR decomposition, determine $\mathbf{E}$ such that

$$\mathbf{Q} \times \mathbf{R} = [V_{11}^T, V_{21}^T]\mathbf{E} \tag{11}$$

here $\mathbf{Q}$ represents a unitary matrix, $\mathbf{R}$ forms an upper triangular matrix with decreasing elements, and $\mathbf{E}$ is the permutation matrix.

After decomposition and pivoting, the most significant $\hat{r}$ can be decided, which in short is the set used to construct the image.

3.2 An Example of Data Reduction in Phase History

First, SVD a matrix P and get $diag(\Sigma) = (0.059510004, 0.042771991, \ldots, 0.0043679429, 0.0041228784)$. It's necessary to decide the value of $\hat{r}$, here in Fig. 3, we plot the singular values Σ.

It is clearly to see that the slope of the curve changes from steeply to slightly, and around after 40, the singular values are much smaller than before. As a result, in the simulation we define $\hat{r} = 40$.

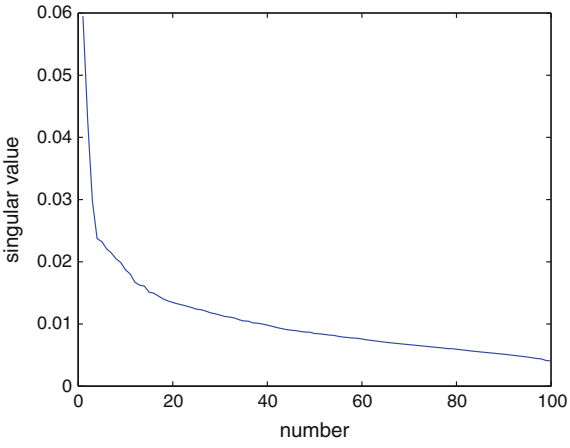

Fig. 3 Applying SVD-QR algorithm, the results of singular values

Second, in order to get V_{11} and V_{21}, V needs to be partitioned before QR decomposition. V_{11} is a size of $R^{40\times40}$ matrix and V_{21} is $R^{(M-40)\times40}$.

Third, with column pivoting and QR decomposition, the economy matrix $\mathbf{E}$ is determined. In this instance, $\hat{r} = 40$, we only care about sixty columns of $\mathbf{E}$. For example, if

$$\mathbf{E} = \begin{bmatrix} 0 & 0 \\ 0 & 0 \\ 0 & 1 \\ 1 & 0 \\ 0 & 0 \\ 0 & 0 \\ 0 & 0 \\ 0 & 0 \end{bmatrix}$$

the values of 1 appears in the forth and third columns of the input matrix $\mathbf{P}$, which means that the data collected only from these two angular are the most significant, and they can effectively represent all the others.

4 Simulation Results

In [23], a challenging problem of two dimensional image formation of stationary targets is released, which aims to construct an area of numerous civilian vehicles and calibration targets.

In our simulation, we randomly choose 21 files of the history data with total number of 2462 datasets and no windowing is applied to the data before imaging. After the SVD-QR algorithm, we only depend on about half of the original data to recover the scenario. In Fig. 4, we show the original image formation result by using backprojection algorithm.

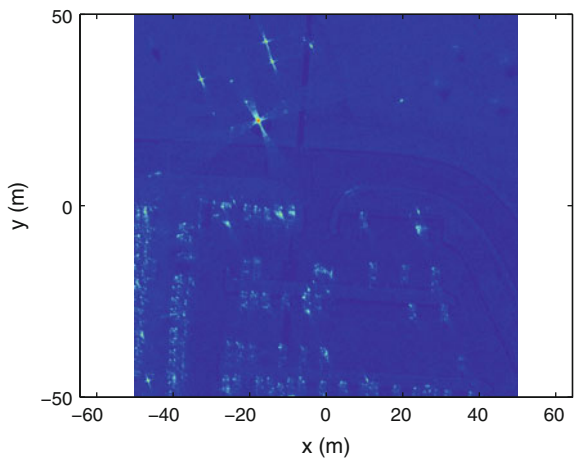

Fig. 4 Original image formation via backprojection algorithm using Volumetric Challenge Problem data set

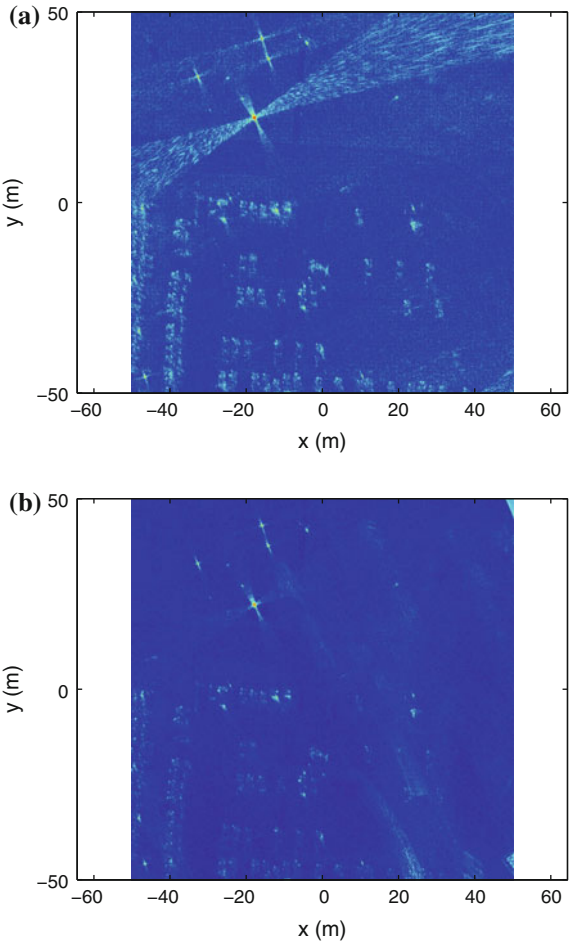

Fig. 5 Compression image formation via Volumetric Challenge Problem dataset. **a** SVD-QR algorithm, **b** uniform down sampling

If we employ the SVD-QR method explained in Sect. 3 before backprojection algorithm, the phase history data could be compressed by a ratio about 2:5. The output of the image is plotted in Fig. 5a.

We can see that even if some information is lost, the main properties of the scenario are preserved well. It proves the validity of SVD-QR algorithm in 2D SAR environment. In order to show the importance of correctly selecting echoes, in Fig. 5b, we compare it with the uniform down sampling of the data, which achieves the compression ratio as 1:2. It seems that if we uniformly sample the data, we will miss more significant information than SVD-QR algorithm.

To further illustrate the performance of SVD-QR algorithm, we process the figures through MATLAB imaging processing toolbox. In Fig. 6, several highlight parts

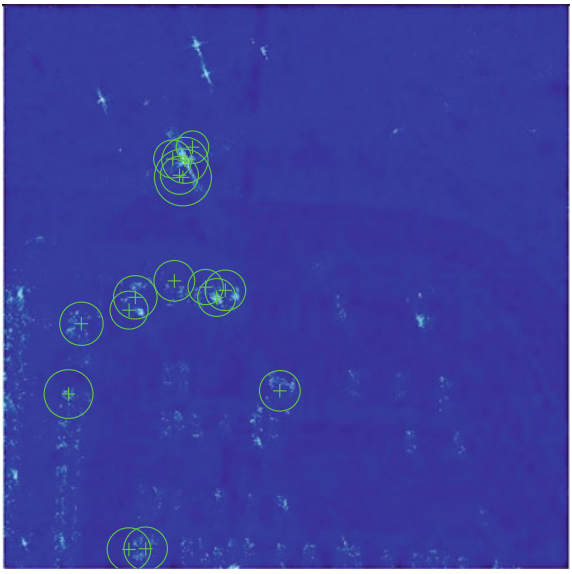

Fig. 6 Object detection via point feature matching of the original image

are circled, which stands for the strongest points in the original image. Figure 5a and b are processed by the toolbox as well and the outputs are shown in Fig. 7. It indicates that in Fig. 7a, it can detect more targets than in Fig. 7b because more highlight parts are circled.

5 Conclusions and Future Works

In this work, we compressed the high redundant SAR raw data of the signal echoes by exploiting SVD-QR algorithm in slow-time domain of the data set before using backprojection image reconstruction method. This is less complicated than many compressive sensing algorithms and can achieve better performance than uniform down sampling method. We test our algorithm and compare it with uniform down sampling on Volumetric Challenge Problem data set, which is collected in a real scenario. The results show that this algorithm can successfully recover the image without losing important information such as the vehicles and calibration targets and the compression ratio could achieved by 2:5 overall. This is the first time that SVD-QR algorithm is applied to the real 2D SAR data.

Our future work will be focused on extending the compression method in slow-time domain to fast-time domain and study on other SAR data set. Moreover, we plan to apply opportunistic sensing [24] on SAR data reduction from slow-time domain and further optimizing our algorithm.

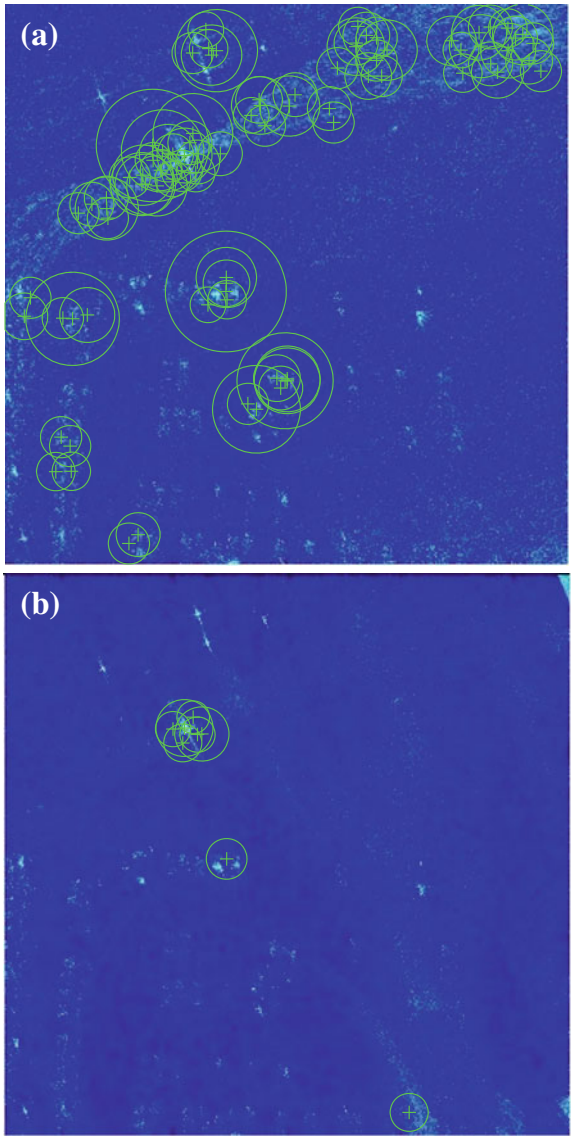

Fig. 7 Object detection via point feature matching after image compression. **a** After SVD-QR algorithm, **b** after uniform down sampling

References

1. Aly Z, Bonn FJ, Magagi R (2007) Analysis of the backscattering coefficient of salt-affected soils using modeling and RADARSAT-1 SAR data. IEEE Trans Geosci Remote Sens 45(2):332–341
2. Srivastava HS, Patel P, Sharma Y, Navalgund RR (2009) Large-area soil moisture estimation using multi-incidence-angle RADARSAT-1 SAR data. IEEE Tran Geosci Remote Sens 47(8):2528–2535
3. Strodl K, Benz UC, Moreira A (1994) Comparison of several algorithms for on-board SAR raw data reduction. In: International society for optics and photonics, satellite remote sensing
4. Baxter RA (1999) SAR image compression with the Gabor transform. IEEE Trans on Geosci Remote Sens 37(1):574–588
5. Baraniuk R, Steeghsm P (2007) Compressive radar imaging. In: IEEE radar conference. Waltham, Massachusetts
6. Chen J, Liang Q, Paden J, Gogineni P (2012) Compressive sensing analysis of synthetic aperture radar raw data. In: IEEE international conference on communications (ICC)
7. Liang Q (2011) Compressive sensing for synthetic aperture radar in fast-time and slow-time domains. In: Asilomar conference on signals, systems and computers (ASILOMAR), pp 1479–1483
8. Liang Q (2010) Compressive sensing for radar sensor networks. In: IEEE global telecommunications conference. Miami, FL
9. Liang Q, Wang L (2005) Redundancy reduction in wireless sensor networks using SVD-QR. IEEE Conf Mil Commun 3:1857–1861
10. Liang J, Liang Q (2009) Channel selection in virtual MIMO wireless sensor networks. IEEE Trans Veh Technol 58(5):2249–2257
11. Neo YL, Wong FH, Cumming IG (2008) Processing of azimuth-invariant bistatic SAR data using the range doppler algorithm. IEEE Trans Geosci Remote Sen 46(1):14–21
12. Ribalta A (2011) Time-domain reconstruction algorithms for FMCW-SAR. IEEE Geosci Remote Sens Lett 8(3):396–400
13. Bhattacharya S, Blumensath T, Mulgrew B, Davies M (2007) Fast encoding of synthetic aperture radar raw data using compressed sensing. In: IEEE/SP 14th workshop on statistical signal processing, pp 448–452
14. Gorham LeRoy A, Moore Linda J (2010) SAR image formation toolbox for MATLAB. In: International society for optics and photonics SPIE defense, security, and sensing
15. Yegulalp AF (1999) Fast backprojection algorithm for synthetic aperture radar. In: Proceedings 1999 IEEE radar conference, April 2022. Waltham, MA, p 6065
16. Perlovsky L, Ilin R, Deming R, Linnehan R, Lin F (2010) Moving target detection and characterization with circular SAR. In: IEEE radar conference, pp 661–666
17. Austin CD, Ertin E, Moses RL (2009) Sparse multipass 3D SAR imaging: applications to the GOTCHA data set. In: International society for optics and photonics SPIE defense, security, and sensing
18. Rigling BD, Moses RL (2005) Taylor expansion of the differential range for monostatic SAR. IEEE Trans Aerosp Electron Syst 41(1):60–64
19. McCorkle J, Nguyen L (1994) Focusing of dispersive targets using synthetic aperture radar, No. ARL-TR-305. Army Research Laboratory, Adelphi, MD
20. Soumekh M (1999) Synthetic aperture radar signal processing. A Wiley-Interscience publication, USA
21. Golub GH, Van Loan CF (2012) Matrix computations, vol 3. JHU Press
22. Golub G (1965) Numerical methods for solving linear least squares problems. Numerische Mathematik 7(3):206–216
23. Casteel Jr CH, Gorham LA, Minardi MJ, Scarborough SM, Naidu KD, Majumder UK (2007) A challenge problem for 2D/3D imaging of targets from a volumetric data set in an urban environment. In: International Society for optics and photonics, defense and security symposium
24. Liang Q, Cheng X, Chen D (2014) Opportunistic sensing in wireless sensor networks: theory and application. IEEE Trans Comput 63(8):2002–2010

A Novel Artificial Bee Colony Algorithm for Radar Polyphase Code Design

Xiu Zhang and Xin Zhang

Abstract When designing a radar system based on pulse compression technique, optimization problem needs to be handled to achieve a good system efficiency. Polyphase code is a popular method to implement pulse compression. To deal with the design problem, a novel artificial bee colony (ABC) algorithm is proposed which includes a population reduction method and a boundary repair method. Large population is initially taken for exploration search, while population is reduced by half for exploitation search. Moreover, a new boundary repair method is proposed to amend infeasible candidate solutions. It hybridizes four commonly used repair methods in literature. The resulting algorithm is called population reduction and hybrid repair ABC (PRHRABC). Experiments result shows that PRHRABC presents promising performance in dealing with the problem compared with a state of the art ABC algorithm.

1 Introduction

In the design of radar and commercial satellite communication systems, optimization problems are usually involved to achieve a good system efficiency [3, 5, 6]. One example is when designing a radar system that uses pulse compression, a key issue is to choose appropriate waveform. Polyphase code is an attractive method that could do pulse compression. The advantages of this method is their lower side lobes in the compressed signal and easier implementation of digital processing methods. Dukic and Dobrosavljevic [5] modeled the compression problem as a min-max nonlinear non-convex optimization problem. This problem was verified to be a multimodal one with numerous local optima.

X. Zhang · X. Zhang (✉)
College of Electronic and Communication Engineering,
Tianjin Normal University, Tianjin, China
e-mail: ecemark@mail.tjnu.edu.cn; xinzhang9-c@my.cityu.edu.hk

X. Zhang
e-mail: zhang210@126.com

Q. Liang et al. (eds.), *Proceedings of the 2015 International Conference on Communications, Signal Processing, and Systems*, Lecture Notes in Electrical Engineering 386, DOI 10.1007/978-3-662-49831-6_20

The aforementioned problem is very difficult to handle and effective algorithms are of high demand. This paper proposes a novel algorithm based on artificial bee colony (ABC) paradigm. A population reduction method is used in the proposed algorithm. The purpose of this method is to assist exploration search by keeping a large population in the former evolutionary stage, and turn to a small population for promoting exploitation search in the latter evolutionary stage. Moreover, a new boundary repair method is proposed which hybridizes four commonly used repair methods in literature.

The paper is organized as follows. Section 2 describes standard ABC algorithm. Section 3 explains the proposed algorithm. Experimental result is shown in Sects. 4 and 5 gives the conclusion.

2 Standard Artificial Bee Colony Algorithm

This section describes standard ABC algorithm. It contains three main phases: employed bee phase, onlooker bee phase, and scout bee phase.

Initially, a population is randomly created within search space Ω. The size of population is denoted as N_p. Each solution in population is considered as a food source for honey bees. After evaluating all initialized solutions, their fitness values are calculated as follows:

$$fit(\mathbf{x}_i) = \begin{cases} \frac{1}{1+f(\mathbf{x}_i)}, & \text{if } f(\mathbf{x}_i) \geq 0 \\ 1 + |f(\mathbf{x}_i)|, & \text{otherwise} \end{cases}, \tag{1}$$

where $f(\mathbf{x}_i)$ is the function value of solution $\mathbf{x}_i$, $i = 1, 2, \ldots, N_p$.

Employed bee phase. A swarm of employed bees is sent out to search around food sources for making honey. Usually, the number of employed bees is equal to N_p so that one employed bee searches one food source. Candidate solution $\mathbf{v}_i$ produced by employed bee i is implemented by

$$v_{i,j} = \begin{cases} x_{i,j} + \varphi_{i,j}(x_{i,j} - x_{r1,j}), & \text{if } j = j1 \\ x_{i,j}, & \text{otherwise} \end{cases}, \tag{2}$$

where $v_{i,j}$, $x_{i,j}$ and $x_{r1,j}$ denote the jth variable of $\mathbf{v}_i$, $\mathbf{x}_i$ and $\mathbf{x}_{r1}$, respectively; $\varphi_{i,j} \in [-1, 1]$ is a random number. $j1 \in [1, D]$ is a random integer and D is the number of variables. $\mathbf{x}_i$ and $\mathbf{x}_{r1}$ are different solutions of population. After evaluating $\mathbf{v}_i$, a greedy selection is implemented between $\mathbf{v}_i$ and $\mathbf{x}_i$. The winner survives and is saved as the new $\mathbf{x}_i$ as follows.

$$\mathbf{x}_i = \begin{cases} \mathbf{v}_i, & \text{if } f(\mathbf{v}_i) < f(\mathbf{x}_i) \text{ or } fit(\mathbf{v}_i) > fit(\mathbf{x}_i) \\ \mathbf{x}_i, & \text{otherwise} \end{cases}, \tag{3}$$

Onlooker bee phase. A swarm of onlooker bees is sent out. The number of onlooker bees is also equal to N_p. The behavior of onlooker bees is different from employed bees. An onlooker bee chooses a food source depending on the quality/goodness of that food source. High quality food sources would attract more onlooker bees, while low quality sources have small chances to be searched. This behavior is realized first calculating a probability value for each solution; then using roulette wheel selection method to choose a food source. The prob ability value of $\mathbf{x}_i$ is calculated by the following equation:

$$p_i = \frac{fit_i}{\sum_{j=1}^{N_p} fit_j}. \tag{4}$$

After choosing a food source, an onlooker bee produces a modification following (2). Then a greedy selection is performed between the newly produced solution and the old one.

Scout bee phase. Scout bees are sent out occasionally looking for new food sources. If a food source has been searched for a long time, its nectar amount would decrease and it might be abandoned by honey bees. In this case, scout bees are send out exploring for new food sources. In standard ABC, a predefined parameter called *limit* is set to determine if a food source should be abandoned. In case a solution cannot be improved after *limit* times, then it is abandoned and the associated employed bee becomes a scout bee. The abandoned solution is replaced by a randomly created solution. This is the scout bee phase. Note that the number that a solution (food source) is searched but not improved is counted as follows:

$$l_i = \begin{cases} 0, & \text{if} f(\mathbf{v}_i) < f(\mathbf{x}_i) \text{ or } fit(\mathbf{v}_i) > fit(\mathbf{x}_i) \\ l_i + 1, & \text{otherwise} \end{cases}. \tag{5}$$

Clearly, standard ABC includes two parameters: *Np* and *limit*. The impact of both parameters on the algorithm has been studied on a set of benchmark functions. Studies show that the proper setting of both parameters depends on the characteristics of application problem [4, 7]. Parameter *limit* is not sensitive to the difficulty of problems; $limit = 0.5NpD$ could solve many benchmark functions and thus becomes default setting [7, 11].

In standard ABC, both employed bees and onlooker bees use formula (2). This formula could not fully reflect the behavior of onlooker bees. A new formula is introduced in quick ABC (qABC) algorithm for mimicking the behavior of onlooker bees [8].

$$v_{i,j} = \begin{cases} x_{i,j}^{nbest} + \phi_{i,j}(x_{i,j}^{nbest} - x_{r1,j}), & \text{if} j = j1 \\ x_{i,j}, & \text{otherwise} \end{cases}, \tag{6}$$

where $\mathbf{x}_i^{nbest}$ represents the best solution amongst the neighbors of $\mathbf{x}_i$ and itself. Euclidean distance is used to define neighborhood of a solution. Denote $d(i,m)$ as the Euclidean distance between $\mathbf{x}_i$ and $\mathbf{x}_m$. The mean Euclidean distance of $\mathbf{x}_i$ is computed by

$$md_i = \frac{\sum_{m=1}^{N_p} d(i,m)}{N_p - 1} . \tag{7}$$

Then the neighbor of $\mathbf{x}_i$ is defined as the set of solutions with distance $d(i,m) \neq r \times md_i$. parameter r is "neighborhood radius." When $r = 0$, qABC becomes standard ABC. Experimental results show that qABC improves the convergence performance of stand ABC when r is properly set. Note that r is suggested to be 1 in qABC [8].

3 Population Reduction and Boundary Repair Methods

3.1 Population Reduction Method

The mapping of algorithmic parameter and application problem can be expressed as:

$$N_p^{new} = g(A, S, N_p^{cur}) , \tag{8}$$

where A represents the problem attributes; S is the evolutionary state of algorithm; N_p^{cur} is the size of current population. Mapping g is very hard to quantify and is simplified as follows. Consider two problem attributes D and a fixed-budget termination condition. Termination budget is the maximum number of function evaluations (MFE). Based on the search scope, evolutionary status of an algorithm could be divided into exploration, intermediate, and exploitation. Initial population size N_p^{init} has to be set so that formula (8) could start working. N_p^{init} is related with D by $N_p^{init} = 4D$. A decreasing step function is taken to approximate g as shown in Fig. 1. The step function is expressed as

$$N_p = \begin{cases} N_p^{init}, & \text{if } 1 \leq f_{eval} \leq MFE/3 \\ 0.5N_p^{init}, & \text{if } MFE/3 < f_{eval} \leq 2MFE/3 \\ 0.25N_p^{init}, & \text{otherwise} \end{cases} . \tag{9}$$

As in (9), MFE is equally split into three evolutionary stages. In exploration stage, a large population size is used so that the algorithm could perform global search. Then population size is reduced to half; solutions with high fitness are kept and those with low fitness are discarded. By doing this, elitist solutions survive. In exploitation stage, N_p is equal to one forth of N_p^{init}. Algorithm could search around good solutions and perform local search to attain a promising solution.

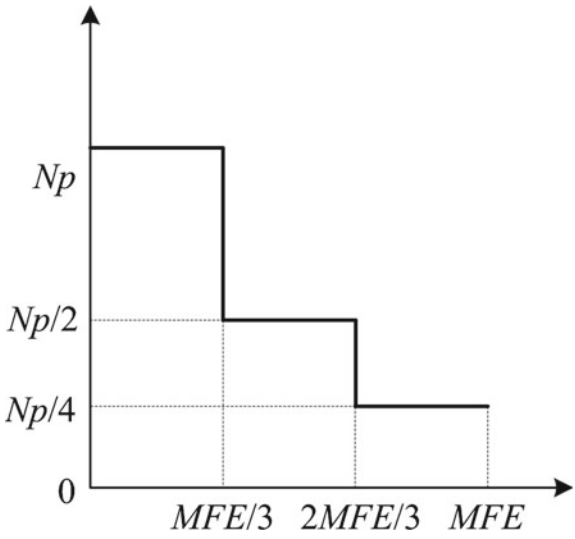

Fig. 1 A population size reducing method

Differing from existing researches on algorithmic parameter control methods [2, 11], the proposed population size reducing method could adapt parameters to handle problems with different budget without the interface of users.

3.2 Boundary Repair Method

A recent study proves that boundary repair methods have great impact on the performance of evolutionary algorithms [1]. Popularly used repair methods in literature include reinitialization, projection, resampling, conservatism, wrapping, reflection, and parent medium [1, 9].

Inspired by previous researches of various repair methods, a new scheme is proposed which is a hybrid of four repair methods: reinitialization, resampling, projection, and parent medium. Resampling is first used, whereas the computational cost of resampling method could not be guaranteed. In the worst case, an infinite loop happens if none of the combinations produces a feasible solution. In our implementation, resampling is performed three times at most. For example, if $\mathbf{v}_{i,g}$ is infeasible using (2) or (6), two parents $\mathbf{x}_{r1,g}$ and $\mathbf{x}_{r2,g}$ are resampled not more than three times; if a feasible vector is generated, then repair step is finished and turn to proceed the next individual; otherwise, turn to the following steps.

If $\mathbf{v}_{i,g}$ is infeasible and its associated parent lies in the boundary of search space, reinitialization method is applied. If vector $\mathbf{v}_{i,g}$ is infeasible and its associated parent is feasible but not in boundary, then projection and parent medium methods have equal chance to be selected. Because both methods are good choices, i.e.,, projection

is the second choice and parent medium is suggested in [10], hence each method is assigned a probability 0.5 to be chosen for execution.

3.3 The Proposed Algorithm

Population size reducing and boundary repair methods are attached with qABC [8]. The resulting algorithm is called population reduction and hybrid repair ABC (PRHRABC). The pseudocode of the algorithm is shown in Algorithm 1.

Algorithm 1 Pseudo code of the PRHRABC algorithm

Require: $f(\cdot)$, MFE, D, $\mathbf{x}^{min}$, $\mathbf{x}^{max}$, $N_p = N_p^{init}$, $limit$, r
Ensure: the best solution obtained by the algorithm
randomly create N_p solutions $\mathbf{x}_1, \mathbf{x}_2, \cdots, \mathbf{x}_{N_p}$;
evaluate function values of solutions and their fitness by (1);
set counter l_i, $i = 1, 2, \cdots, N_p$ to 0;
repeat
    send out employed bees by (2);
    repair infeasible candidate solutions;
    evaluate candidate solutions and their fitness by (1);
    do greedy selection by (3) and update l_i by (5);
    send out onlooker bees depending on their nectar amounts by (4);
    repair infeasible candidate solutions;
    evaluate candidate solutions and their fitness by (1);
    do greedy selection by (3) and update l_i by (5);
    send out scout bees if l_i reaches $limit$;
    evaluate candidate solutions and their fitness by (1);
    reset l_i to 0;
    update N_p by (9);
until termination criteria are met

4 Experimental Evaluation and Analysis

In this section, the proposed algorithm is applied to deal with a polyphase code design problems. Polyphase code design contains 20 variables.

4.1 Experimental Configuration

PRHRABC and qABC are chosen for experiment. The parameter setting for qABC is $N_p = 25$, $limit = 0.5N_pD$, and $r = 1$ as suggested in [4, 7, 8]. For PRHRABC, N_p^{init} is set to $4D$, $limit = 0.5N_pD$, and $r = 1$. Both algorithms are implemented in

Table 1 Statistics of the best function values found by PRHRABC and qABC

Polyphase code	Min	Med	Max	Std	p
PRHRABC	1.1035	1.3000	1.4441	0.0885	0.0199
qABC	1.1175	1.3454	1.5769	0.0933	+

Matlab and simulated on a PC with 3.4 GHz 4-core CPU and 4GB of memory. Each problem is conducted 25 independent runs with $MFE = 50000$. The source code of PRHRABC can be obtained from the first author upon request.

4.2 Experimental Results

The experimental result is shown in Table 1. This table presents the best function values in four kinds of statistics, which are minimum (min), median (med), maximum (max), and standard deviation (std). For polyphase code design, PRHRABC obtains better results than qABC. To gain a statistical view of the results, Mann–Whitney U test (U test) is utilized with significant level $\alpha = 0.05$. The p-values comparing PRHRABC and qABC is given in the last column Table 1. Symbol "+" indicates cases in which the null hypothesis is rejected and PRHRABC displays a statistically superior performance by U test.

The convergence curves of PRHRABC and qABC for dealing with polyphase code design are shown in Fig. 2. It is plotted as the median best objective function value found over 25 trials. From the beginning, the proposed PRHRABC attains

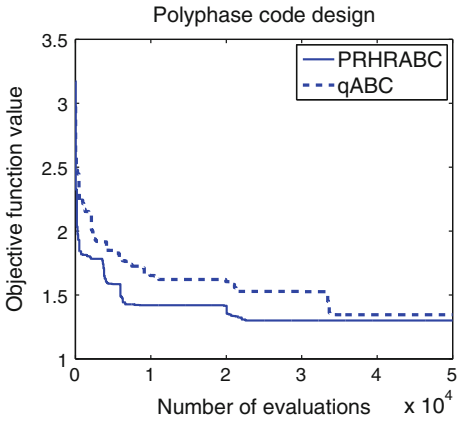

Fig. 2 Convergence graph of the proposed algorithm and qABC for antenna array design

better solution than qABC and leads the evolutionary process until the end. Thus, the proposed algorithm shows good performance to deal with such design optimization problem.

5 Conclusion

Optimization problems widely exist in radar and commercial communication system designs. These problems are featured with multidimension and numerous local optima. Based on the artificial bee colony (ABC) paradigm, this paper proposes a population reduction method and a boundary repair method. Different from existing researches on algorithmic parameter control, the proposed method could adapt parameters to handle problems with different budget setting without the interface of users.

The proposed algorithm is tested on a polyphase code design problem. Quick ABC (qABC), which is a state-of-the-art ABC variant, is chosen as benchmark. Experimental result shows that the proposed algorithm significantly outperforms qABC accessed on four statistical measures. This suggests that the novel algorithm is good at solving optimization problems in radar, and communication system designs.

Acknowledgments This research was supported by the Tianjin Thousand Youth Talents Plan Project of Tianjin Normal University (ZX110023).

References

1. Arabas J, Szczepankiewicz A, Wroniak T (2010) Experimental comparison of methods to handle boundary constraints in differential evolution. In: PPSN XI, pp 411–420
2. Brest J, Maucec MS (2008) Population size reduction for the differential evolution algorithm. Appl Intell 29(3):228–247
3. Dessouky M, Sharshar H, Albagory Y (2006) A novel tapered beamforming window for uniform concentric circular arrays. J Electromagn Waves Appl 20
4. Diwold K, Aderhold A, Scheidler A, Middendorf M (2011) Performance evaluation of artificial bee colony optimization and new selection schemes. Memet Comput 3(3):149–162
5. Dukic M, Dobrosavljevic Z (1990) A method of a spread spectrum radar polyphase code design. IEEE J Sel Areas Comm 8
6. Guo L, Deng H, Himed B, Ma T, Geng Z (2015) Waveform optimization for transmit beamforming with mimo radar antenna arrays. IEEE Trans Antennas Propag 63(2):543–552. doi:10.1109/TAP.2014.2382637
7. Karaboga D, Basturk B (2008) On the performance of artificial bee colony (ABC) algorithm. Appl Soft Comput 8(1):687–697
8. Karaboga D, Gorkemli B (2014) A quick artificial bee colony (qABC) algorithm and its performance on optimization problems. Appl Soft Comput 23:227–238
9. Wessing S (2013) Repair methods for box constraints revisited. In: Proceedings of the 16th European conference on applications of evolutionary computation, Springer, Berlin, Heidelberg, EvoApplications'13, pp 469–478

10. Zhang J, Sanderson AC (2009) JADE: adaptive differential evolution with optional external archive. IEEE Trans Evol Comput 13(5):945–958
11. Zhang X, Zhang X, Ho SL, Fu WN (2014) A modification of artificial bee colony algorithm applied to loudspeaker design problem. IEEE Trans Magn 50(2):737–740

A New Rain/Snow Clutters Suppression Algorithm for Ship Navigational Radar

Zengshan Tian, Shuang Li and Zhengwu Yuan

Abstract Rain/snow clutters have a significant impact on the performance of navigation radar, and the suppression for rain/snow clutters has been significantly studied. Different from the traditional Constant False Alarm Rate (CFAR)-based suppression, in this paper, a novel suppression algorithm combining median filtering and wavelet denoising is proposed based on the characteristics of rain/snow clutters. First, the median filtering is applied to the data. Then, we adopt wavelet denoising for the sake of reconstructing the data based on decomposed coefficients. Experiments show that our proposed algorithm outperforms the traditional CFAR-based scheme.

Keywords Rain/snow clutters · Ship navigation radar · Median filtering · Wavelet denoising · Constant false alarm rate

1 Introduction

The ship navigation radar has been an indispensable equipment for ships. Meanwhile, the suppression techniques for rain/snow clutters in radar siganl are widely studied in order to enhance navigation performance. As for analog radar, the Fast Time Constant (FTC) circuit is normally used to weaken the rain/snow clutters which makes use of the rising edge of echo signal. The FTC circuit is a signal differential processing module, which can automatically detect and retain the front edge of echo signal. After the processing of the FTC, only the leading edges of clutters are retained and at the same time the intensity of clutters becomes weak. While other useful radar echoes are generally narrower and stronger than rain/snow returns, thus, the energy

Z. Tian · S. Li (✉) · Z. Yuan
Chongqing Key Lab of Mobile Communications Technology,
Chongqing University of Posts and Telecommunications,
Chongqing 400065, People's Republic of China
e-mail: 1522102479@qq.com

Z. Tian
e-mail: tianzs@cqupt.edu.cn

Q. Liang et al. (eds.), *Proceedings of the 2015 International Conference on Communications, Signal Processing, and Systems*, Lecture Notes in Electrical Engineering 386, DOI 10.1007/978-3-662-49831-6_21

losses of removing trailing edges of useful echoes are much smaller than that of clutters. Therefore, the Signal-to-Noise Ratio (SNR) is improved after FTC. But the performance of FTC depends on the parameter setting according to the actual environment, and the detection performance will drop dramatically with inappropriate parameter setting [1]. In digital radar, the Constant False Alarm Rate (CFAR) algorithm is adopted to improve the detection ability. Finn and Johnson [2] first presented the CA-CFAR method. There are many researches focusing on the detection performance of CA-CFAR in the environment with multiple targets [3, 4] which show that the performance of CA-CFAR declines seriously in multiple targets environment. The estimation of average value is unstable due to the limited reference units which causes noise fluctuation accordingly. In this paper, we propose a novel suppression algorithm for rain/snow clutters combining the median filtering and wavelet denoising. The pulse noise in the signal is eliminated after the median filtering, then signal is restructured with the deposed coefficients after wavelet denoising. Finally rain/snow clutters are suppressed.

The rest of this paper is summarized as follows. In Sect. 2, we introduce traditional method of clutter suppression. The proposed approach is discussed in detail in Sect. 3. Experimental results are shown in Sect. 4. Finally, Sect. 5 concludes the paper and presents some future work.

2 Traditional Method of Clutter Suppression–Constant False Alarm Rate Processing

2.1 Analysis of Rain/snow Clutters

Radar beams will be scattered by the rain/snow particles and some of the scattered waves are merged with echoed signal and are received by radar which causes rain/snow clutters in the image generated by the echo signal.

The rain/snow clutters are composed of a large number of scattered waves. And they follow that the amplitudes of two orthogonal scattered waves form the normal distribution. Therefore, the amplitude of clutter forms the Rayleigh distribution. So the mathematical model of rain/snow clutters can be described as follows:

$$f_0(x) = \frac{1}{2\delta^2} \exp\left(-\frac{x}{2\delta^2}\right), \quad (x \geq 0) \tag{1}$$

where δ^2 is the variance of clutter.

2.2 The CFAR Algorithm

In the environment with time-varied interference, the False Alarm Rate (FAR) of signal keeps constant with self-adapted threshold so as to minimize the impact of clutter, which forms CFAR. CFAR is widely used for radar clutter suppression but it will cause the loss of SNR which is called CFAR loss. Especially, the flowchart of Cell-Averaging CFAR (CA-CFAR) algorithm is shown in Fig. 1.

In Fig. 1, echo data, $v(t)$, first passes through a matched filter. Then, the output will be processed by envelope detector which is followed by sliding window detector. After that, the miscellaneous wave power level, Z, is obtained by averaging $2n$ reference units. Next, the detection threshold, S, is obtained by multiplying the normalized threshold, T, and Z. Finally, the detection unit, D, is compared with, S, then output the result. Moreover, protective units are also applied in case of energy leaking to the reference units.

On the other hand, the FAR will increase with raised noise under fixed threshold. And the detection threshold should be set according to the number of reference cells for keeping a constant FAR. Meanwhile, the SNR of input should also be increased accordingly which forms the disadvantage of CA-CFAR. In multiple targets environment, the performance of CA-CFAR declines seriously since the detection threshold will increase with the existence of other jamming targets as for one target to be detected, which will eventually shorten radar horizon and lose targets.

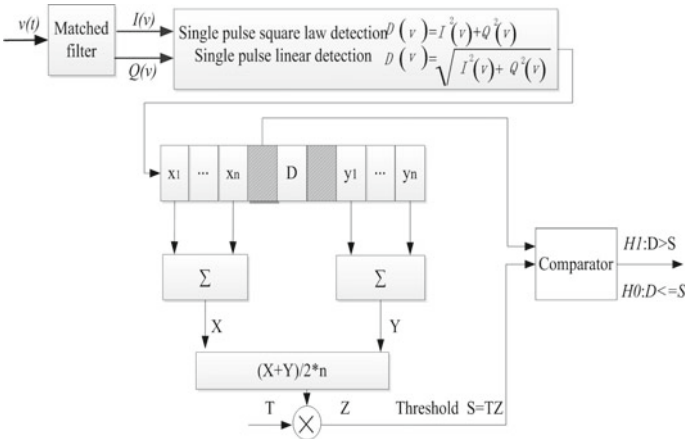

Fig. 1 Flowchart of CA-CFAR detector

3 The Design of New Rain/Snow Clutters Suppression Algorithm

In order to deal with the detection of multiple targets, in this section, we will describe the proposed suppression for rain/snow clutters combining median filtering and wavelet denoising.

3.1 Wavelet Denoising

In wavelet theory, the discrete wavelet transform has a convolution expression as follows.

$$\begin{cases} c^{j-1} = D\left(c^j * \bar{h}^*\right) \\ d^{j-1} = D\left(c^j * \bar{g}^*\right) \end{cases} \tag{2}$$

$$c^j = \left(Uc^{j-1}\right) * h + \left(Ud^{j-1}\right) * g \tag{3}$$

where c^{j-1} and d^{j-1} are the approximate and detail coefficients of next layer; $*$ is the convolution operation; h and g represent coefficients of low pass filter and high pass filter respectively. $D(\bullet)$ represents the down sampling operation while U represents the up sampling operation [5].

The iterative process of wavelet decomposition as well as wavelet reconstruction for one dimension is shown in Fig. 2 [6]. M represents the number of layers for decomposition and reconstruction. Wavelet analysis has the localized characteristic that the different frequency components match with different time resolution, making it particularly suitable for the processing of non stationary signal.

Especially, the expression for haar wavelet is shown as follows [7].

$$\phi(x) = \begin{cases} 1, & x \in [0, 1/2) \\ -1, & x \in [1/2, 1) \\ 0, & others \end{cases} \tag{4}$$

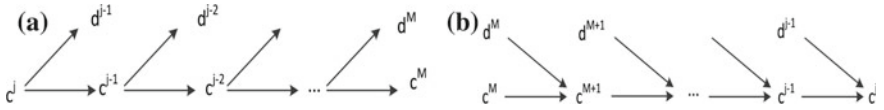

Fig. 2 The iterative process of wavelet decomposition as well as wavelet reconstruction. **a** Wavelet decomposition. **b** Wavelet reconstruction

And the coefficients of low pass filter and high pass filter used in the wavelet decomposition and reconstruction are $\left[\sqrt{2}/2\ \sqrt{2}/2\right]$ $\left[-\sqrt{2}/2\ \sqrt{2}/2\right]$ and $\left[\sqrt{2}/2\ \sqrt{2}/2\right]$ $\left[\sqrt{2}/2\ -\sqrt{2}/2\right]$ respectively.

3.2 New Suppression for Rain/Snow Clutters

Given a discrete sampling sequence, $h_1, h_2, h_3 \cdots h_n$, the median filtering process is illustrated in Fig. 3, where L is the length of filtering window, m is the center of the window which satisfies $L = 2m + 1$, and n is the length of sequence. Meanwhile, the median filtering is formulized in Eq. (5) [8].

$$h_i = median\left(h_{i-m}, \cdots, h_i, \cdots h_{i+m}\right) \tag{5}$$

The pulse with the width of signal sequence not greater than m is removed by the median filtering. The process of median filtering algorithm is as follows:

Step 1: Move the center of filtering window from $2m + 1$ to $n - m$ with interval of $+1$;
Step 2: As for each move, sort the data within each window with ascending or descending order;
Step 3: Select the median in the sorted data.

After the median filtering processing, wavelet denoising is carried out. The process of wavelet denoising algorithm is as follows.

Step 1: Select a wavelet basis to decompose the signal to N layers, and obtain the approximate coefficients and detail coefficients;
Step 2: Select an appropriate threshold, then deal with the detail coefficient of each layer (If the absolute value of the coefficient is greater than or equal to the threshold, value keeps constant. Otherwise it will be turned 0);
Step 3: Use the detail coefficients after processing and approximate coefficients to restore the original signal.

The proposed suppression for rain/snow clutters is shown in Fig. 4. First, set a neighborhood window size, sort the data inside the window size and then take the value corresponding to the middle term instead of its own. Next, decompose the new signal sequence and do threshold processing of coefficients. Finally restructure the signal based on coefficients after processing.

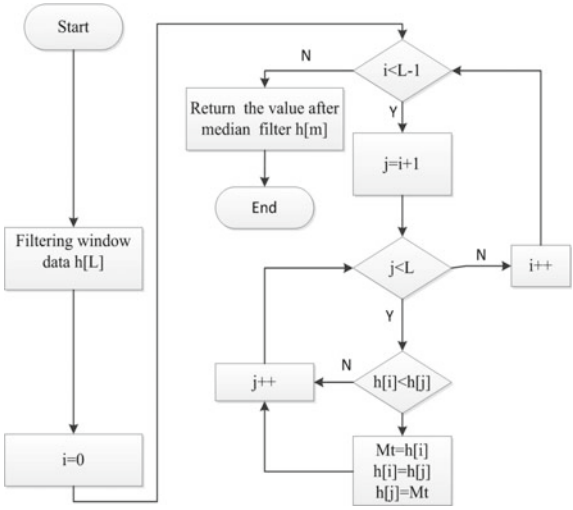

Fig. 3 Flow chart of median filtering

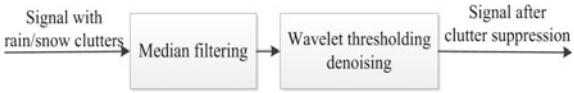

Fig. 4 The process of suppression for rain/snow clutters

4 Experimental Results

4.1 Simulation Results

The simulation signal is composed of 2000 sampled points forming 3 rectangular waves and 3 sine waves. And the radar echo signal superposed with rain/snow clutters is shown in Fig. 5 accordingly. From Fig. 5 we can see that the rain/snow clutters can affect the whole signal, which makes it more difficult to deal with than other clutters.

In the simulation, we chose the scale of wavelet noise reduction to be 4, 5, and 6 respectively [9]. Next, three kinds of Haar wavelet transforms with different scales for the median-filtered signal are shown in Fig. 6.

From Fig. 6, we can see that the wavelet transform can effectively suppress the high-frequency components of rain/snow clutters, and the transform result keeps stable as the scale increases while the computational cost raises. Considering the computational complexity on FPGA, we choose 4 to be the scale.

We assumed that the number of reference units is 32 and protection units is 2, then CA-CFAR is applied to radar echo signal with rain/snow clutters. Figure 7 shows the comparison between CA-CFAR and the proposed suppression. From Fig. 7, we can see that both of the radar echo signal and clutters are suppressed after CA-CFAR and some clutters can be treated as useful signals. While the target and clutters can be distinguished clearly using the proposed suppression. So our proposed approach can detect the target more effectively.

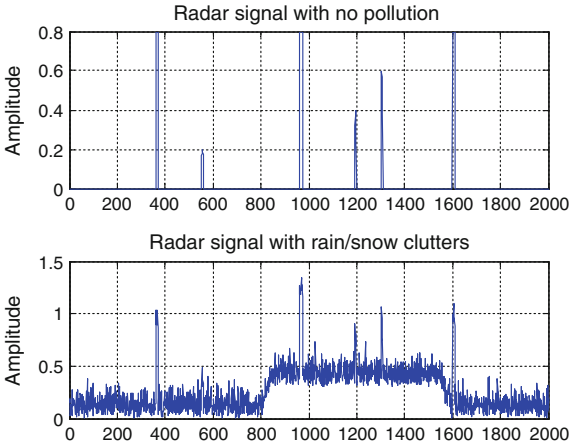

Fig. 5 Radar echo signal with clutter

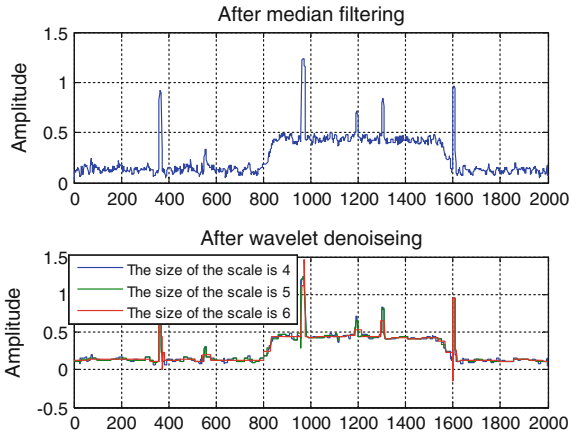

Fig. 6 Output after wavelet denoising

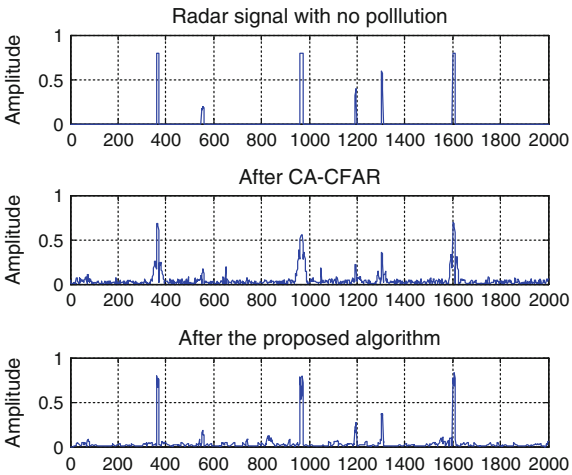

Fig. 7 Comparison between CA-CFAR and proposed suppression

4.2 Actual Experiments

We use FPGA board to make signal processing, then display in the windows 7 system. And the radar antenna is set in model 1832. We test and verify the proposed algorithm in the actual environment and the results are shown in Fig. 8. Figure (a) and (b) represent radar target with or without clutter respectively. Figure (c) is (b) after CA-CFAR processing and figure(d) is radar target with rain/snow clutters after processing by the proposed approach.

From simulation results and actual experiments, we observe that our proposed suppression for rain/snow clutters combining median filtering and wavelet denois-

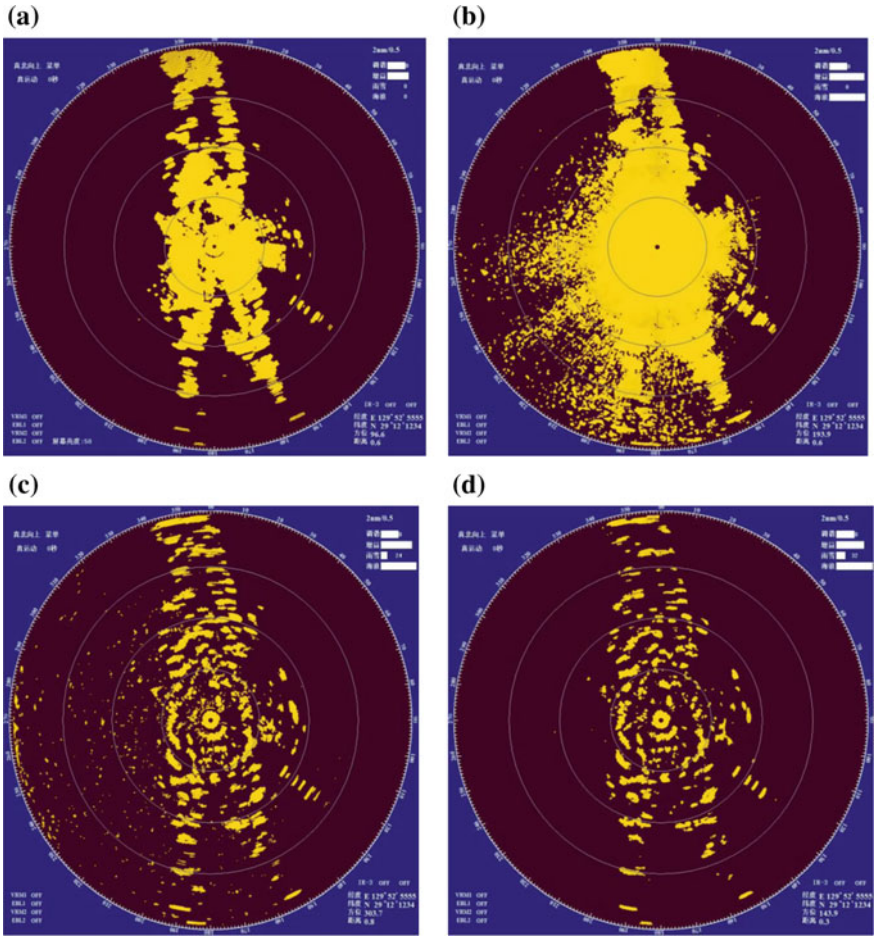

Fig. 8 Results in actual environment. **a** Radar target with no clutter. **b** Target with rain/snow clutters. **c** Target after CA-CFAR. **d** Target after the proposed approach

ing can detect the target in more accurate manner. Compared with traditional CA-CFAR processing, rain/snow clutters can be suppressed effectively by the proposed approach in the same conditions. After CA-CFAR processing, clutters are filtered partly, but the rest clutters still affect target detection. While clutters are filtered quite clearly by the the proposed approach. By the comparison of FPGA and MATLAB simulation results, we can find the theoretical simulation results are basically consistent with the test results. The above experimental results verify the effectiveness of the designed rain/snow clutters suppression algorithm in this paper. And it has obvious advantages over the traditional constant false alarm processing.

5 Conclusions

Rain/snow clutters have a serious impact on target detection in ship navigation. In this paper, a suppression approach for rain/snow clutters with the combination of median filtering and wavelet denoising is proposed. We verify the proposed method in simulation and in actual environment and they show that the proposed suppression algorithm is superior to the CA-CFAR processing. Moreover, considering the realization of FPGA, we choose Haar wavelet whose coefficients are special to do the wavelet denoising. However, using other wavelet basis to conduct the wavelet denoising forms an interesting work in future.

References

1. Liu T, Zhang B (2013) Nautical Navigation Instruments. Dalian Maritime University Press, Dalian, pp 109–112
2. Rohling H (1983) Radar CFAR thresholding in clutter and multiple target situations. IEEE Trans Aerosp Electron Syst 19(4):608–621
3. Barboy B, Lomes A, Perkalski E (1986) Cell-averaging CFAR for multiple target situations. IEE Proc-F 133(2):176–186
4. MashadeM MB (1994) M-sweeps detection analysis of cell-averaging CFAR processors in multiple-target situations. IEE Proc-F 141(2):103–108
5. Quellec G, Lamard M, Cazuguel G, Cochener B, Roux C (2010) Adaptive nonseparable wavelet transform via lifting and its application to content-based image retrieval. IEEE Trans Image Process 19(1):25–35
6. Kumar K, Mustafa N, Jian-Ping L, Shaikh RA, Khan SA, Khan A (2014) Image edge detection scheme using wavelet transform. In: International computer conference on wavelet active media technology and information processing, pp 261,265,19–21
7. Cordova JJ, Wen Y, Xiaoou L (2012) Haar wavelet neural networks for nonlinear system identification. IEEE Int Symp Intell Control 276,281,3-5
8. Eng HL, Ma KK (2001) Noise adaptive soft-switching median filter. IEEE Trans Image Process 10(2):242–251
9. Popeseu B, Costa P et al (1996) Extraction of parameters from a wavelet packet analysis for terrain matching. In: Proceedings of the IEEE-SP International Symposium, pp 493,496, 18–21

Interferometric Phase Error Correction for Ka-Band InSAR via BP

Danni Xuan, Jun Shi, Daiqi Shi, Shunjun Wei and Xiaoling Zhang

Abstract This paper discusses the dynamic baseline phase error correction capacity of the back projection (BP) algorithm. Because of the short wavelength, the imaging method with a better phase-preserved capacity is necessary to obtain the high-quality interferograms for Ka-band InSAR systems. We find that the BP algorithm can remove the flat-earth phase automatically. With this ability, it can be used to correct the majority of the phase distortion caused by the attitude errors via calculating the antenna phase centers of the master and slave antennas separately in the consideration of the dynamic baseline. Actual Ka-band InSAR experiments show that BP algorithm is a sound choice in the face of high-resolution airborne InSAR system with the accurate inertial measurement unit data.

Keywords Back projection algorithm · Dynamic baseline · IMU data · Interferometric phase distortion correction · Ka-band insar

1 Introduction

Compared with other bands, Ka-band InSAR has smaller size, lighter weight, and lower penetrating capacity (means higher DEM accuracy), which has become one of the hot points of InSAR researching [1, 2]. On the other hand, however, since the wavelength of Ka-band is shorter than the others, the imaging methods with a better phase-preserved capacity are necessary to obtain high-quality interferograms.

For airborne SAR systems, because of the existence of wind fields and turbulence, the antenna phase center (APC) deviates from the desired trajectory severely, which degrades the imaging and interferometric performances greatly.

D. Xuan · J. Shi (✉) · S. Wei · X. Zhang
University of Electronic Science and Technology of China (UESTC), Chengdu, People's Republic of China
e-mail: cn.papyrus@gmail.com

D. Shi
Institute of Electronics, Chinese Academy of Sciences, Beijing, China

Q. Liang et al. (eds.), *Proceedings of the 2015 International Conference on Communications, Signal Processing, and Systems*, Lecture Notes in Electrical Engineering 386, DOI 10.1007/978-3-662-49831-6_22

Back projection (BP) algorithm [3–5] that calculates the accurate range delays one pixel by one pixel is more suitable to process the complex trajectory SAR data by combining with the high-accuracy IMU data.

Besides degrading the imaging performance, the motion errors will cause the baseline vector to vary with time, i.e., a dynamic baseline. Since the interferometric phase is sensitive to the baseline, the dynamic baseline will lead to some significant phase distortion.

As it has been shown in the literature [6], because of its imaging strategy, the interferometric phase of BP is different from the traditional one and the flat-earth phase is removed, which is beneficial to correct the phase error too. In this paper, the dynamic baseline phase error correction capacity of BP is discussed in detail based on actual high-resolution Ka-band InSAR experiments.

The organization of this paper is as follows. In Sect. 2, the flat-earth-removing capacity of BP is reviewed briefly. In Sect. 3, the effect of the dynamic baseline on the interferometric phase of BP is discussed in detail. In Sect. 4, a discussion on the interferometric capacity is presented based on the actual high-resolution Ka-band InSAR images. A summary is presented in Sect. 5.

2 Interferometic Phase of BP

In InSAR systems, the interferometric phase is defined as the phase difference associated with the distances from a scatterer to the master and slave antennas. For the standard BP algorithm, however, since the accurate ranges are calculated and compensated, the points of closest approaches (POC) ranges used to calculate the interferometric phase are changed significantly.

To be compatible with the InSAR processing, the POC ranges should be preserved during imaging and the phase compensation of BP should be expressed as:

$$\mathbf{I}(u,v) = \sum_{n} \mathbf{s}(R(u,v;n),n) e^{-j2K_0(R(u,v;n)-R(u,v;0))} \tag{1}$$

where $\mathbf{I}(u,v)$ denotes the SAR image, n denotes the slow time, $\mathbf{s}(r,n)$ denotes the range-compressed SAR echoes, $R(u, v; n)$ denotes the range from radar to the pixel (u, v) at the nth pulse, and $R(u, v; 0)$ means the POC range of the pixel (u, v).

Since $R(u, v; 0)$ is independent of the slow time n, it can simply be moved out of the sum operation and we have:

$$\mathbf{I}(u,v) = e^{j2K_0R(u,v;0)} \sum_{n} \mathbf{s}(ID_{\mathbf{p},n},n) e^{-j2K_0R(u,v;n)} \tag{2}$$

Equation (2) indicates that to ensure the BP algorithm to be compatible with the InSAR processing, one can simply focus the images via the standard BP and restore the over-compensated phases using Eq. (2) after imaging.

Combining the interferometric phase and Eq. (2), we have:

$$\varphi_{BP} = \varphi_{In} - 2K_0(R_M(u, v; 0) - R_S(u, v; 0)) \tag{3}$$

The second term of Eq. (3) has a clear physical meaning: the flat-earth phase of the pixel (u, v). That is to say, BP algorithm can remove the flat-earth phases from the interferograms.

3 Interferometric Phase of Dynamic Baseline

Because of the instability of the flight environment, such as turbulence, the master and slave APCs vary with time irregularly. The motion errors affect the InSAR performance in two aspects: First, the high-frequency turbulence in the same aperture will impose an additional phase noise in the echo that deteriorates the coherence of different images. Second, the low-frequency turbulence (between different apertures) will change the baseline vector, which leads to the SAR image mismatch and the interferometric phase distortion [7].

The mismatch can be corrected during the BP imaging or via the coregistration technique [8]. This section will discuss the influence of the motion errors on the interferometric phase.

3.1 Effect of Motion Errors on Baseline

To facilitate the analysis, the APC trajectory is considered as a virtual array antenna, whose equivalent phase center (EPC) is denoted as $\mathbf{e}_Q$, $Q = \{M, S\}$.

Assuming that there is a turbulence imposed on the master's APCs (or equivalently on the IMU center), the actual EPC $\tilde{\mathbf{e}}_M$ is:

$$\tilde{\mathbf{e}}_M \approx \sum_n w_n \tilde{\mathbf{p}}_Q(n) = \mathbf{e}_M + \delta\mathbf{e}, \quad \sum_n w_n = 1 \tag{4}$$

where w_n is a group of weighted coefficients, $\tilde{\mathbf{p}}_M(n)$ denotes the APCs with a turbulence error, $\delta\mathbf{e}$ denotes the EPC offset.

When there is no attitude error, the baseline vector does not change with time. The actual EPC of the slave antenna $\tilde{\mathbf{e}}_S$ can be written as:

$$\tilde{\mathbf{e}}_S = \tilde{\mathbf{e}}_M + \mathbf{b} = \mathbf{e}_S + \delta\mathbf{e} \tag{5}$$

Equation (5) indicates that the actual baseline vector is fixed as $\mathbf{b}$ without the attitude errors, i.e., the motion errors of the IMU center have no effect on the baseline vector.

When the attitude of the platform varies with time during flight, the attitude errors (roll, pitch, and yaw) can be expressed as a time-variant rotation matrix $\mathbf{H}(n)$ [9].

Subtracting the APCs of the slave antennas by master's, the APCs of the slave antenna can be expressed as:

$$\tilde{\mathbf{p}}_S(n) = \tilde{\mathbf{p}}_M(n) + \mathbf{H}(n)\mathbf{b} \tag{6}$$

where $\mathbf{d}_S = \mathbf{d}_M + \mathbf{b}$, $\mathbf{d}_M$ and $\mathbf{d}_S$ denote the displacements of the master and slave antennas relative to the IMU center.

Thus, the EPC of the slave antenna can be expressed as:

$$\tilde{\mathbf{e}}_S = \tilde{\mathbf{e}}_M + \mathbf{b} + \left(\sum_n w_n \mathbf{H}(n) - \mathbf{I}\right)\mathbf{b} = \mathbf{e}_S + \delta\mathbf{e} + \left(\sum_n w_n \mathbf{H}(n) - \mathbf{I}\right)\mathbf{b} \tag{7}$$

Equation (7) indicates that with the existence of the attitude errors, the baseline vector varies with time, i.e., a dynamic baseline.

3.2 *Effect of Dynamic Baseline on Phase*

Approximating the interferometric phase error caused by the motion errors via the firstst-order multiple Taylor's theorem, $\Delta\varphi$ can be written as:

$$\Delta\varphi \approx 2K_0\left(\frac{(\mathbf{e}_M - \mathbf{p})^T\delta\mathbf{e}}{\|\mathbf{e}_M - \mathbf{p}\|_2} - \frac{(\mathbf{e}_S - \mathbf{p})^T\delta\mathbf{e}}{\|\mathbf{e}_S - \mathbf{p}\|_2}\right) \tag{8}$$

When there is no attitude error, by substituting Eqs. (4) and (5) into (8), we have:

$$\Delta\varphi \approx 2K_0\left(\frac{(\mathbf{e}_M - \mathbf{p})^T\delta\mathbf{e}}{\|\mathbf{e}_M - \mathbf{p}\|_2} - \frac{(\mathbf{e}_S - \mathbf{p})^T\delta\mathbf{e}}{\|\mathbf{e}_S - \mathbf{p}\|_2}\right) = \frac{-2K_0\mathbf{b}^T\delta\mathbf{e}}{\|\mathbf{e}_M - \mathbf{p}\|_2} \tag{9}$$

That is to say, the interferometric phase error caused by the IMU center errors is smaller.

When there are some attitude errors, the interferometric phase error is:

$$\begin{aligned}\Delta\varphi_{In} &\approx 2K_0\left(\frac{(\mathbf{e}_M - \mathbf{p})^T\delta\mathbf{e}}{\|\mathbf{e}_M - \mathbf{p}\|_2} - \frac{(\mathbf{e}_S - \mathbf{p})^T\left(\delta\mathbf{e} + (\overline{\mathbf{H}} - \mathbf{I})\mathbf{b}\right)}{\|\mathbf{e}_S - \mathbf{p}\|_2}\right) \\ &\approx \frac{-2K_0\mathbf{b}^T\delta\mathbf{e}}{\|\mathbf{e}_M - \mathbf{p}\|_2} - \frac{2K_0(\mathbf{e}_S - \mathbf{p})^T(\overline{\mathbf{H}} - \mathbf{I})\mathbf{b}}{\|\mathbf{e}_S - \mathbf{p}\|_2}\end{aligned} \tag{10}$$

The first term of Eq. (10) is the phase error caused by the IMU center errors, the second term is the phase error caused by the attitude errors. Assuming that the baseline length is 0.5 m and the attitude errors are all 0.1°, the interferometric phase error caused by the second term is about 78°, which is far larger than the former term.

For further analyses, we can divide the second term of Eq. (10) into two terms:

$$\frac{2K_0(\mathbf{e}_S-\mathbf{p})^T(\overline{\mathbf{H}}-\mathbf{I})\mathbf{b}}{\|\mathbf{e}_S-\mathbf{p}\|_2}=\frac{2K_0(\mathbf{e}_S-\mathbf{p}_{u,v})^T(\overline{\mathbf{H}}-\mathbf{I})\mathbf{b}}{\|\mathbf{e}_S-\mathbf{p}\|_2}+\frac{2K_0(\mathbf{p}_{u,v}-\mathbf{p})^T(\overline{\mathbf{H}}-\mathbf{I})\mathbf{b}}{\|\mathbf{e}_S-\mathbf{p}\|_2} \tag{11}$$

where $\mathbf{p}_{u,v}$ denotes the three-dimensional (3D) position of the pixel (u,v). Note that since the SAR images are a projection from 3D space to two-dimensional (2D) image space, $\mathbf{p}_{u,v}\neq\mathbf{p}$, if the scatterer is not literately located in the image plane.

The first term of Eq. (11) is the phase error associated with the flat-earth phase; the second term is the phase error associated with the displacement of the scatterer relative to the image plane. Since $\|\mathbf{e}_S-\mathbf{p}_{u,v}\|_2\gg\|\mathbf{p}_{u,v}-\mathbf{p}\|_2$, the phase distortion caused by the first term is far larger than that caused by the second term.

Thus, with the flat-earth-removing ability, BP algorithm can correct the majority of the phase distortion in the consideration of the dynamic baseline.

4 Experimental Results

This section continues the error based on the actual InSAR data. The system is worked at Ka-band with a range resolution of about 0.2 m and the azimuth resolution of about 0.1 m. The height of the radar to the ground is about 1,000 m with the incident angle about 45°. The length of the baseline is about 0.2 m, which is vertical to the line of sight and the velocity direction. The pixel interval of the image space is selected as 0.1 m (range) × 0.05 m (azimuth) and the size of the image is about 8,000 (pixel) × 8,000 (pixel).

According to the elevation formula of InSAR [10], we have the relationship between the interferometric phase.

Figure 1 plots the interferograms after removing the flat-earth phases by BP. Figure 1a is the photograph of the scene in the bird's-eye view. Figure 1b is the interferogram after removing the flat-earth without the consideration of the dynamic baseline. We find that there are some fluctuations at the left-top, which do not exist in the photograph.

Figure 1c is the interferogram after removing the flat-earth with the consideration of the dynamic baseline. Comparing it with Fig. 1b, we find that the undesired fluctuations are eliminated. Furthermore, some indistinct features (such as the stripe centered at x = 350 m, y = 50 m) appear.

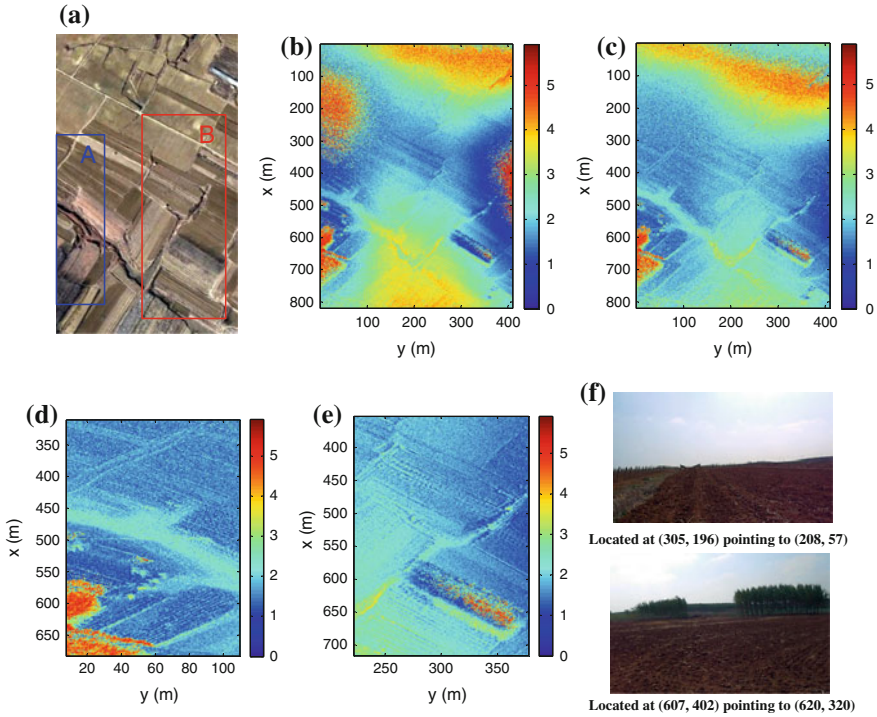

Fig. 1 Interferograms after removing the flat-earth phase via BP. **a** Photograph of the scene in the bird's-eye view. **b** Interferogram without the dynamic baseline correction. **c** Interferogram with the dynamic baseline correction via BP. **d** Interferogram corresponding to the area A. **e** Interferogram corresponding to the area B. **f** Photographs of the scene

Figure 1d, e plot the local regions of Fig. 1c corresponding to the areas A and B in Fig. 1a. Some typical landforms, such as the L-shaped woods, the farm lanes, the rectangle woods, the ridges, and the ditch, can easily be recognized.

For further analysis, the imaging scene has been inspected after the experiment, and some photographs are taken at positions (305, 196) and (607, 402) (the same coordinate system with those interferograms) that point to (208, 57) and (620, 320), respectively, which are shown in Fig. 1f.

From Fig. 1f (top), we learn that the left-top region of the imaging scene is fairly flat, and the fluctuation in Fig. 1b is caused by the attitude errors. By compensating the dynamic baseline, the undesired fluctuation is eliminated accurately. Combining with the discussion in the last section, we can conclude that the BP algorithm can correct the irregular flat-earth phase error caused by the attitude errors by calculating the APCs in the consideration of the dynamic baseline.

Figure 1f (bottom) plots the rectangle woods in the area B (the middle part has been chopped down when taking the photos). From it, we find that those trees far away from the camera are lower than those near, which matches the interferogram in Fig. 1e (note that since $h = -3.8\varphi$, a small phase indicates a high elevation.

5 Summary

Through the studies, we find that the phase error caused by the attitude errors dominates the interferogram distortion. With the flat-earth-removing ability, BP can correct the majority of the phase distortion in the consideration of the dynamic baseline. Actual Ka-band InSAR experiments show that BP algorithm is a sound choice in the face of high-resolution airborne InSAR system.

Acknowledgments The authors thank the 23rd Institute of CASIC for providing the actual SAR data. This work is supported by the China Postdoctoral Science Foundation under Grant 2013M530395 and 2014T70857 and High-Resolution Earth Observation Major Special Projects—"Youth Innovation Funding" under Grant GFZX04060103-5-25.

References

1. Moller D, Hensley S, Sadowy GA, Fisher CD, Michel T, Zawadzki M, Rignot E (2011) The glacier and land ice surface topography interferometer: an airborne proof-of-concept demonstration of high-precision ka-band single-pass elevation mapping. IEEE Trans Geosci Remote Sens 49(2):827–842. doi:10.1109/TGRS.2010.2057254
2. Fjortoft R, Gaudin JM, Pourthie N, Lalaurie JC, Mallet A, Nouvel JF, Martinot-Lagarde J, Oriot H, Borderies P, Ruiz C, Daniel S (2014) KaRIn on SWOT: characteristics of near-nadir Ka-band interferometric SAR imagery. IEEE Trans Geosci Remote Sens 52(4):2172–2185. doi:10.1109/TGRS.2013.2258402
3. Ash JN (2012) An autofocus method for backprojection imagery in synthetic aperture radar. IEEE Geosci Remote Sens Lett 9(1):104–108. doi:10.1109/LGRS.2011.2161456
4. Tan WX, Li DJ, Hong W (2008) Airborne spotlight SAR imaging with super high resolution based on back-projection and autofocus algorithm. IEEE Int Geoscience Remote Sens Symp (IGARSS) 2008:1300–1303. doi:10.1109/IGARSS.2008.4779969
5. Shi J, Ma L, Zhang X (2013) Streaming BP for non-linear motion compensation SAR imaging based on GPU. IEEE J Sel Top Appl Earth Obs Remote Sens 6(4):2035–2050. doi:10.1109/JSTARS.2013.2238891
6. Ma L, Shi J, Wei S, Shi D, Xu S (2014) Ka-band InSAR data processing of BP method. In: IEEE international conference on signal processing, communications and computing (ICSPCC), pp 316–320. doi: 10.1109/ICSPCC.2014.6986206
7. Fattahi H, Amelung F (2013) DEM error correction in InSAR time series. IEEE Trans Geosci Remote Sens 5(7):4249–4259. doi:10.1109/TGRS.2012.2227761
8. Li Z, Bao Z, Suo Z (2007) A joint image coregistration, phase noise suppression, and phase unwrapping method based on subspace projection for multibaseline InSAR systems. IEEE Trans Geosci Remote Sens 45(3):584–591. doi:10.1109/TGRS.2006.888143
9. Goel S, Lohani B (2014) A motion correction technique for laser scanning of moving objects. IEEE Geosci Remote Sens Lett 11(1):225–228. doi:10.1109/LGRS.2013.2253444
10. Richards MA (2007) A beginner's guide to interferometric SAR concepts and signal processing. IEEE A&E Syst Mag 22(9):5–29. doi:10.1109/MAES.2007.4350281

SAR Image De-noising Based on Generalized Non-local Means in Non-subsample Shearlet Domain

Liu Shuaiqi, Geng Peng, Shi Mingzhu, Fang Jing and Hu Shaohai

Abstract How to suppress and remove the speckle of SAR image has been a hot research issue. Combining the advantages of non-subsample Shearlet transform (NSST) with the generalized non-local means de-noising algorithm, we proposed a new SAR image de-noising algorithm in this paper. This algorithm is appropriate for the characteristics of the speckle noise, so it can improve the quality of de-noised image. Meanwhile, the algorithm holds the characteristics of translational invariance, which can suppress Gibbs phenomenon effectively.

1 Introduction

Due to the specificity of the speckle, the de-noised images by using the traditional image processing methods are not very good. SAR image de-noising is mainly divided into two categories. One is spatial filtering including Frost filter [1], total variation [2] and non-local means de-noising [3, 4], and the other is de-noising based on some transform domain like the Bayesian de-noising in Wavelet domain [5], the Bayesian de-noising in Shearlet domain [6], and multi-scale products thresholding based on directionlet domain [7]. The de-noised SAR image is darkened due

L. Shuaiqi (✉)
College of Electronic and Information Engineering, Hebei University, Hebei, China
e-mail: shdkj-1918@163.com

L. Shuaiqi
Key Laboratory of Digital Medical Engineering of Hebei Province, Hebei, China

G. Peng
School of Information Science and Technology,
Shijiazhuang Tiedao University, Hebei, China

S. Mingzhu
College of Electronic and Communication Engineering,
Tianjin Normal University, Tianjin, China

F. Jing · H. Shaohai
Institute of Information Science, Beijing Jiaotong University, Beijing, China

Q. Liang et al. (eds.), *Proceedings of the 2015 International Conference on Communications, Signal Processing, and Systems*, Lecture Notes in Electrical Engineering 386, DOI 10.1007/978-3-662-49831-6_23

to spatial filtering, so SAR images de-noising mainly uses de-noising methods in transform domain. For image processing systems, Curvelet and Contourlet are the most effective and useful multi-resolution analysis tools. Curvelet is generated from the action of operators on a non-single function, so the discrete implementation of Curvelet is very challenging [8, 9]. Contourlet overcomes this limitation and its base function with anisotropy and direction selectivity can effectively capture the geometric regularity in the image. It adaptively gives the optimal representation of the image. But the theory of Contourlet transform does not comply with the multi-resolution analysis (MRA) and it is sensitive for shifts. To overcome these disadvantages, based on a simple and rigorous mathematical framework, a new representation called Shearlet is proposed. Shearlet is both a more flexible theoretical tool for the geometric representation of images and more natural for implementation. What is more, the Shearlet approach can be associated to a multi-resolution analysis and the Shearlet transform also has highly directional sensitivity, spatially localized and well localized [10, 11]. So, we use non-subsample Shearlet in [10] to suppress the speckle in this paper.

So far, many methods have been proposed to suppress and remove the speckle noise. For thanking about natural images contained many repeat patterns, a non-local image denoising algorithm is proposed by making use of the information encoded in the whole image [12]. In [3, 4], non-local means is applied to SAR image de-noising by improving anisotropic diffusion filtering and using stochastic distances. In [13], non-local means is applied to transform domain called BM3D, which can get a perfect de-noising effect. And BM3D is applied to SAR image de-noising in [14], one of which is the best speckle suppression methods. There are also some improvements in non-local de-noising based on transform domain such as improved in computing speed like [15]. Though the de-noising methods in [14, 15] have achieved good speckle suppression effect. The correlated noises in the image cannot be filtered directly by NL-means. And in [14, 15], the author applied homomorphic transform to SAR image to change speckle to Gaussian noise, and it will make serious artificial texture in de-noised image. To overcome this disadvantage of non-local means, in [16], they proposed a generalized non-local means (GNL-means) de-noising method for non-identically distributed image noise. GNL-means performs better than NL-means in speckle suppression, and archive almost the same de-noising effect of BM3D. So, in this paper, we proposed a new speckle suppression method based on GNL-means in non-subsample Shearlet domain. The new method can get the better de-noising performance.

2 Non-subsample Shearlet

The implementation of Shearlet is easier than Curvelet and more flexible than Contourlet [17]. In dimension $n = 2$, Shearlet can be represented by the collections as follows:

$$\Omega_{AB}(\psi) = \left\{\psi_{j,l,k}(x) = |\det \mathbf{A}|^{j/2}\psi\left(\mathbf{B}^l\mathbf{A}^j x - k\right) : j, l \in \mathrm{Z}, k \in \mathrm{Z}^2\right\} \quad (1)$$

where $\psi \in L^2(\mathrm{R}^2)$, $\mathbf{A}, \mathbf{B}$ are 2×2 invertible matrices and $|\det \mathbf{B}| = 1$. Let $\mathbf{A} = \mathbf{A}_0 = \begin{pmatrix} 4 & 0 \\ 0 & 2 \end{pmatrix}$ is the anisotropic dilation matrix, and $\mathbf{B} = \mathbf{B}_0 = \begin{pmatrix} 1 & 1 \\ 0 & 1 \end{pmatrix}$ is shear matrix in form (1), then, a tiling of the frequency supported on many pairs of trapezoids is constructed.

Let $\psi^{(d)}_{j,l,k}(x) = 2^{\frac{3j}{2}}\psi^{(d)}\left(\mathbf{B}_1^l\mathbf{A}_1^j x - k\right)$, if $f \in L^2\left(\mathrm{R}^2\right)$ then its continuous Shearlet transform is defined as:

$$SH_\psi = \left\langle f, \psi^{(d)}_{j,l,k}\right\rangle \quad (2)$$

where $j \geq 0, l = -2^j, \ldots, 2^j - 1, k \in Z^2, d = 0, 1$.

The discretization process of NSST [17] can be constructed by multi-scale transform and multi-orientation transform. Typically, multi-scale transform is achieved by non-subsampled pyramid (NSP). NSP can produce $k + 1$ sub-images which consist of k high frequency images and one low frequency image, where k denotes the number of decomposition levels. And the sizes of these images are all the same as the source image. The multi-orientation transform in NSST is realized via improved shearing filters, i.e., NSST makes the standard shearing filter map from pseudo-polar coordinate systems into Cartesian system to satisfy the property of shift-invariance [17]. Applying NSST in image de-noising cannot only reduce the noise sharply, but also preserve more useful information of source image [17].

3 GNL-means

NL-means can be applied to image de-noising easily. First, NL-means looks for the similar pixels. And then, the similar pixels is used to estimate the real value as a weighted average (the weights should decay exponentially as the similarities decrease). U_i and V_i denotes the values of the noise-free pixel and noise, respectively. The observed noisy pixel can be represented by $Z_i = U_i + V_i$ for $i = 1, 2 \ldots, M$ (M represents the number of pixels in the image). U_i can be estimated by NL-means as follows.

$$\hat{Z}_i = \frac{1}{C}\sum_{j \in N_i} W_{ij} Z_j \quad (3)$$

where N_i is the search window centered at i, W_{ij} is the weight, and $C = \sum_{j \in N_i} W_{ij}$ is a normalization term. The weight W_{ij} is defined as Euclidean distance between Z_i and Z_j. NL-means faced with a bias-variance dilemma, many methods have proposed to improve NL-means. Luo et al. [16] proposed a two-stage de-noising process that iterates NL-means. For any image with i.i.d. Gaussian noises, NL-means is used to

get a filtered image firstly. Next, as the filtered image doesn't have the same variance and they are correlated, NL-means can not be applied directly, so they make some changes to handle the non-i.i.d. noises and put it to the filtered image at the first step. The weight in NL-means can be determined by using patch-based Euclidean distance. Let $Z_i(k)$ and $Z_j(k)$ represent the pixels in the patches centered at the i-th and j-th pixels, respectively, and d represent the sizes of the patch. Notice that each pair of pixels $Z_i(k)$ and $Z_j(k)$ are correspondent to Gaussian distribution. Let

$$\Delta_{ij}(k) \overset{def}{=} Z_i(k) - Z_j(k) \tag{4}$$

Then $\Delta_{ij}(k)$ is correspondent to Gaussian distribution and $Var(\Delta_{ij}(k)) = 2\sigma^2$. Then, NL-means uses the following patch

$$D_{patch}(Z_i, Z_j) \overset{def}{=} 2\sigma^2 \sum_{k=1}^{d} [\frac{\Delta_{ij}(k)^2}{Var(\Delta_{ij}(k))} - 1] \tag{5}$$

And W_{ij} can be formulated as a generalized weight like

$$W_{ij}^G \overset{def}{=} \exp\left(-\frac{\max\left\{ \sum_{k=1}^{d} \left[\frac{\Delta_{ij}(k)^2}{Var(\Delta_{ij}(k))} - 1 \right], 0 \right\}}{dT^2/2} \right) \tag{6}$$

If we replaceW_{ij} with W_{ij}^G, NL-means will be generalized. The author called this Generalized NL-means (GNL-means). As the case is that patchwise NL-means is used, the weights will be calculated for patches rather than pixels. At the same time, all the pixels of same patch also will be de-noised simultaneously. The numbers of estimates for each pixel and patches that cover it are same, and we can get the last of the de-noised value by calculating the average of all these estimates.

4 Speckle Suppressed by GNL-means via NSST Domain

In fact, speckle is the main noise in SAR images. And the speckle noise model can be represented by the following equation

$$Y(x, y) = F(x, y) * N(x, y) \tag{7}$$

where $Y(x, y)$ denotes observed image with speckle. $F(x, y)$ denotes the noise-free SAR image. $N(x, y)$ indicates speckle, which is suited to a Γ distribution. To make de-noised processing be convenient, Logarithmic transform is applied to two sides

of (7), that is, multiplicative noise is translated to additive noise, as (8) shows

$$\log(Y(x,y)) = \log(F(x,y)) + \log(N(x,y)) \tag{8}$$

In [19], they consider that the present noise $\log(N(x,y))$ fits Gaussian distribution, but may not non-identical. When image with Gaussian noise decomposed by NSST, the noise is also fit Gaussian distribution in the high-bands frequency. So, whether NL-means de-noising methods or transform domain de-noising methods, all will make severe artificial texture in de-noised image. But this station can be dealt by GNL-means well. So, in this paper, we will combine NSST and GNL-means to suppress speckle. The following is the de-noising steps.

Step 1: First, apply logarithmic transform to the original image, we can get $F_{noise} = \log(Y)$, see (7). And we can change the multiplicative noise to Gaussian noise.
Step 2: Apply NSST to F_{noise}, we can get the low-band coefficients F^{l}_{noise} and high-band coefficients F^{h}_{noise}.
Step 3: Apply GNL-means to high-band coefficients F^{h}_{noise}, we can get F^{h}_{clear}.
Step 4: After de-noising, we can use invert NSST to get the de-noised SAR image F_{clear}.
Step 5: Apply exponential operator to F_{clear}, we get the final de-noised image.

5 Experimental Results and Discussion

In order to verify the reliability and validity of the proposed algorithm, we compared the proposed algorithm with existing algorithms to de-noise: Frost filter [1], Bayesian wavelet shrinkage de-noising (BWS) [5], Image de-noising based on NSST [4], non-local SAR image de-noising based on LLMMSE (NL-LMSE) [14], GNL-means

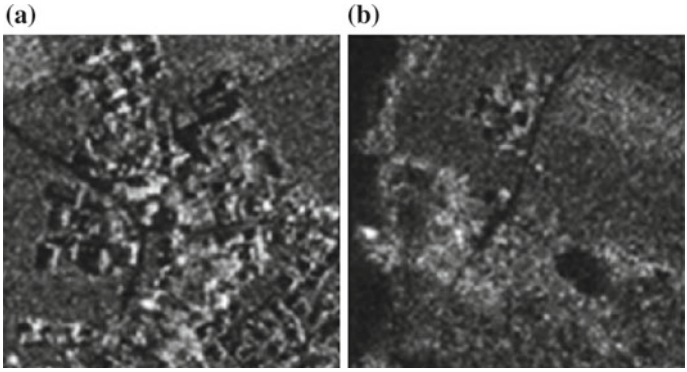

Fig. 1 The natural SAR image: **a** Fields SAR image. **b** Woods SAR image

de-noising [16], wavelet de-noising via spare representation (WSP) [18], Bayesian shearlet shrinkage de-noising via spare representation (BSSR) [19]. Figure 1 shows the test SAR images which are shot by TerraSar-X of the European Space Agency. Then, Fig. 1a shows fields SAR image, and Fig. 1b shows woods SAR image. Apply

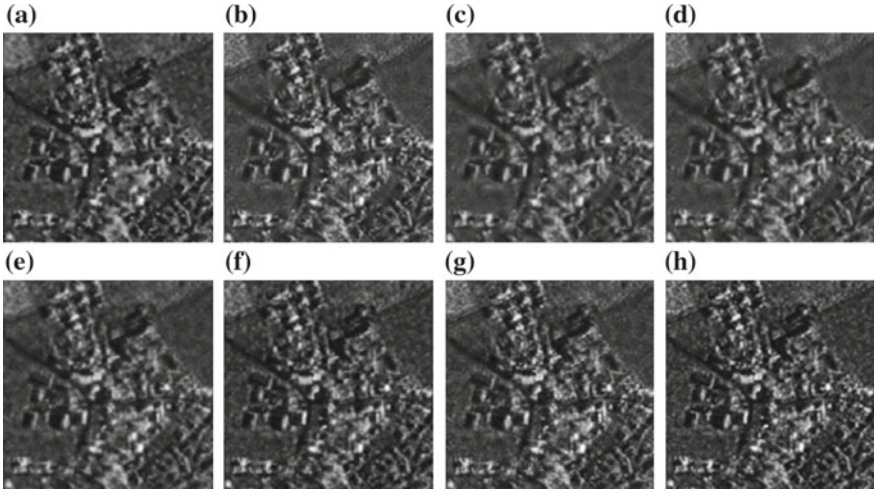

Fig. 2 Comparison of results on fields SAR image. **a** De-noised result of Frost. **b** De-noised result of BWS. **c** De-noised result of NSST. **d** De-noised result of NL-LMSE. **e** De-noised result of GNL. **f** De-noised result of WSP. **g** De-noised result of BSSR. **h** De-noised result of ours

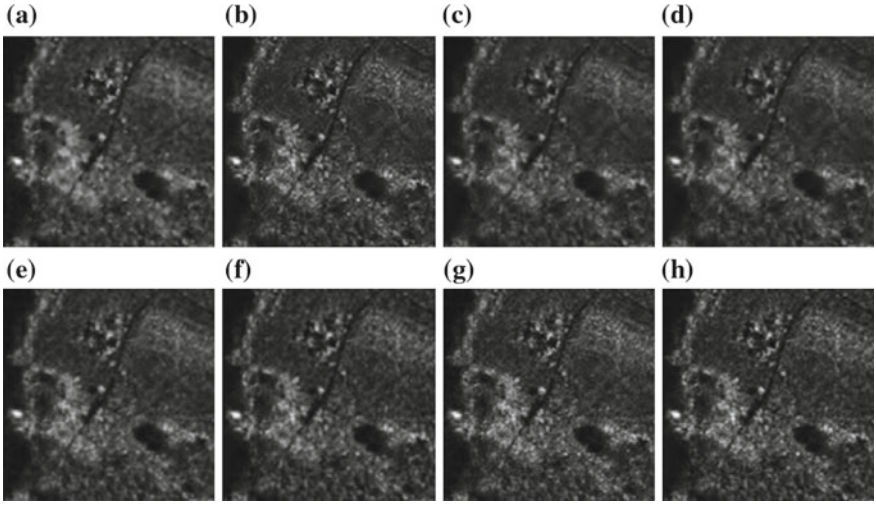

Fig. 3 Comparison of results on woods SAR image. **a** De-noised result of Frost. **b** De-noised result of BWS. **c** De-noised result of NSST. **d** De-noised result of NL-LMSE. **e** De-noised result of GNL. **f** De-noised result of WSP. **g** De-noised result of BSSR. **h** De-noised result of ours

the above de-noising methods to the test images. Figures 2 and 3 show the de-noising effect of all the methods on fields and woods SAR image.

Figures 2 and 3 show that the Frost filter perform the worst effect in the all de-noising methods. After de-noising, some textures of the edge are removed by the BWS and GNL. NSST makes the edge blurry, and NL-LMSE, WSP make some artificial texture, and the proposed method can retain the edge and texture of the image as well as suppress the artificial texture. As we known, these two figures are very special that Fig. 1a has rich texture; while, Fig. 1b has poor texture relatively. It means that the two SAR images are very representative. In order to evaluate the performance of the algorithms above more objectively, some common parameters is calculated. And these de-noising performance parameters are peak signal-to-noise ratio (PSNK), equivalent number of looks (ENL), standard deviation (Sd), and edge preservation index (EPI), and they are shown in Tables 1 and 2. What is more, larger the PSNK is, stronger the capability of de-noising algorithm is; greater the ENL is, better the visual effects of the de-noising images are; and greater the EPI is, more details of the images can be preserved. From Tables 1 and 2, our algorithm has highest PSNR, ENL, Sd, and EPI. The image which is obtained by our algorithm not only has smooth image, but also suppresses artificial texture, and obviously improves the image visual effect.

Table 1 The performance of de-nosing methods in Fig. 2

The de-nosing methods	PSNR (db)	ENL	Sd	EPI
Frost	27.28	7.44	33.03	0.68
BWS	30.75	12.65	29.62	0.84
NSST	31.65	15.57	28.74	0.88
NL-LMSE	32.43	20.11	29.07	0.92
GNL	31.78	19.89	27.35	0.90
WSP	33.65	19.75	28.55	0.93
BSSR	34.33	19.90	29.57	0.94
Ours	35.01	20.65	29.78	0.95

Table 2 The performance of de-nosing methods in Fig. 3

The de-nosing methods	PSNR (db)	ENL	Sd	EPI
Frost	28.05	27.15	30.75	0.72
BWS	32.78	32.78	32.79	0.88
NSST	33.01	32.55	33.45	0.90
NL-LMSE	35.77	33.78	34.01	0.97
GNL	34.56	32.94	33.59	0.93
WSP	35.23	33.66	34.49	0.96
BSSR	35.85	34.29	35.15	0.97
Ours	36.67	35.65	35.67	0.98

6 Conclusion

In this paper, we propose a new algorithm that combines the NSST with GNL-means for de-noising of SAR images. The experiment has proven that the edge detail and texture features can be well preserved by the method of this paper. Besides, its visual effect is good. Nevertheless, there are some imperfections of the proposed method. For example, PSNK could be improved and the computation time is still a little long. So, the next study will be solving these problems.

Acknowledgments This work was supported by National Natural Science Foundation of China (61572063, 61401308), Natural Science Foundation of Hebei University (2014-303), Natural Science Foundation of Hebei Province (F2016201122), Science research project of Hebei Province (QN2016085, ZC2016040).

References

1. Frost V, Stiles J, Shanmugan K et al (2011) A model for radar images and its application to adaptive digital filtering of multiplicative noise. IEEE Trans Pattern Anal Mach Intell PAMI-4(2):157–166
2. Yu P, Zhang C, Xie L (2012) A multiplicative Nakagami speckle reduction algorithm for ultrasound images. Multidimension Syst Signal Process 23(4):499–513
3. Fabbrini L, Greco M, Messina M et al (2013) Improved anisotropic diffusion filtering for SAR image despeckling. Electron Lett 49(10):672–674
4. Torres L, Frery A (2013) Improved anisotropic diffusion filtering for SAR image despeckling. arXiv preprint arXiv:1308.4338, pp 1–6
5. Dai M, Peng C, Chan A (2004) Bayesian wavelet shrinkage with edge detection for SAR image despeckling. IEEE Trans Geosci Remote Sens 42(8):1642–1648
6. Hou B, Zhang X, Bu X (2012) SAR image despeckling based on nonsubsampled shearlet transform. IEEE J Sel Topics Appl Earth Obs Remote Sens 5(3):809–823
7. Sethunadh R, Thomas T (2013) SAR iamge despeckling using adaptive multiscale products thresholding in directionlet domain. Electron Lett 49(18):1183–1184
8. Liu S, Hu S, Xiao Y (2014) Image separation using wavelets-complex shearlets dictionary. J Syst Eng Electron 25(2):314–321
9. Cands E, Donoho D (2004) New tight frames of curvelets and optimal representations of objects with piecewise C^2 singularities. Comm Pure Appl Math 57(2):219–266
10. Lim W (2010) The discrete shearlets transform: a new directional transform and compactly supported Shearlets frames.IEEE Trans Image Proc 19(5):1166–1180
11. Liu S, Hu S, Shi M et al (2004) Apply hyperanalytic shearlet transform to geometric separation. EURASIP J Adv Signal Process 1:63–70
12. Buades A, Coil B, Morel J (2005) A non-local algofithm for image denoising. In: CVPR 05, San Diego, USA, pp 60–65
13. Dabov K, Foi A, Katkovnik V et al (2007) Image denoising by sparse 3-D transform-domain collaborative filtering. IEEE Trans Image Process 16(8):2080–2095
14. Parrilli S, Poderico M, Angelino C et al (2012) Nonlocal SAR image denoising algorithm based on LLMMSE wavelet shrinkage. IEEE Trans Geosci Remote Sens 50(2):606–616
15. Cozzolino D, Parrilli S, Scarpa G et al (2012) Fast adaptive nonlocal SAR despeckling. IEEE Geosci Remote Sens Lett 11(2):524–528
16. Luo E, Pan S, Nguyen T (2012) Generalized non-local means for iterative denoising. In: 2012 Proceedings of the 20th European signal processing conference (EUSIPCO), Bucharest, Romania, pp 260–264

17. Easley G, Labate D, Lim W (2008) Sparse directional image representation using the discrete Shearlets transform. Appl Comput Harmonic Anal 25(1):25–46
18. Zhao R, Liu X, Liu C et al (2009) Wavelet denoising via sparse representation. Sci China Ser F 52(8):1371–1377
19. Liu S, Hu S, Xiao Y et al (2014) Bayesian shearlet shrinkage for SAR image de-noising via sparse representation. Multidimension Syst Signal Process 25(4):683–701

A Global Routing Algorithm Based on Physical Depth for Abnormal Data in Radar Sensor Networks

Jiasong Mu and Liang Han

Abstract Considering the issue of low latency and link robustness in the radar sensor networks, a global routing algorithm based on physical depth is proposed in this paper. We introduce the concept of physical depth, which is defined as the minimum possible hop counts from the current node to the sink or the cluster head, to indicate the distance between them. And a maintenance mechanism of the parameter is designed. On that basis, the routing optimization is proposed. To reduce the routing overhead, we integrate the routing discovery with the first time data transmission. Since, it is a global algorithm and featured by the shortest path and low latency, it could be used to transmit the abnormal data which are highly important in the radar sensor networks. The simulation results showed that the proposed algorithm could effectively reduce the hop counts in the transmission, and it achieved a lower latency. The robustness was also improved; our algorithm had higher packet delivery ratios when different numbers of nodes were disabled in the networks.

Keywords Routing · Radar sensor networks · Latency · Robustness · Abnormal data

1 Introduction

Radar sensor networks (RSN) are the networks of distributed radar sensors which are deployed ubiquitously on airborne, surface, and unmanned vehicles in a large geographical area. Since, a single node has limited transmission range and resources, they have to collaboratively operate to acquire different kinds of data and

J. Mu (✉) · L. Han
College of Electronic and Communication Engineering, Tianjin Normal University, Tianjin, China
e-mail: mujiasong@aliyun.com

Q. Liang et al. (eds.), *Proceedings of the 2015 International Conference on Communications, Signal Processing, and Systems*, Lecture Notes in Electrical Engineering 386, DOI 10.1007/978-3-662-49831-6_24

send them back to the sink in multi-hop method. Radar sensors have capabilities for radar sensing, signal processing, and wireless communications. In RSN, radar sensors are networked together in an ad hoc fashion, that is, they do not depend on any preexisting infrastructure. In fact, they are self-organizing entities that are deployed on demand to perform various tasks such as surveillance, search and rescue, disaster relief, and so forth [1].

A RSN is always organized into clusters, which are independently controlled and dynamically reconfigured to observe targets such as tactical weapons, missiles, aircraft, ships, and so on, in the surveillance area [2]. In a cluster, sensors receive the signals backscattered by targets in the presence of interference and noise. Then, the observed signals from all radar sensors are forwarded to a cluster head where received data set will be combined to perform fundamental tasks such as detection, localization, identification, classification, and tracking. After finished processing the data from the radar sensors, the cluster head transmits the data to the sink node. In a RSN, the cluster head must have a function such as data collection, fusion, transition, and so on [3].

From that mechanism, one can see that there are two steps in the RSNs working flow.

- (Intra-cluster phase) In some cluster, each distributed radar sensor has to send the observed signals to the cluster head;
- (Inter-cluster phase) The cluster head is in charge of processing the data from the nodes within the cluster, and then transmit the packets to the sink.

A simple example of the RSN is given in the Fig. 1. For convenience, only 2 radar sensors for a cluster are illustrated.

The routing algorithm has become one of the hot topics in the RSN Research. The performances of intracluster and intercluster transmission, the cluster hierarchy

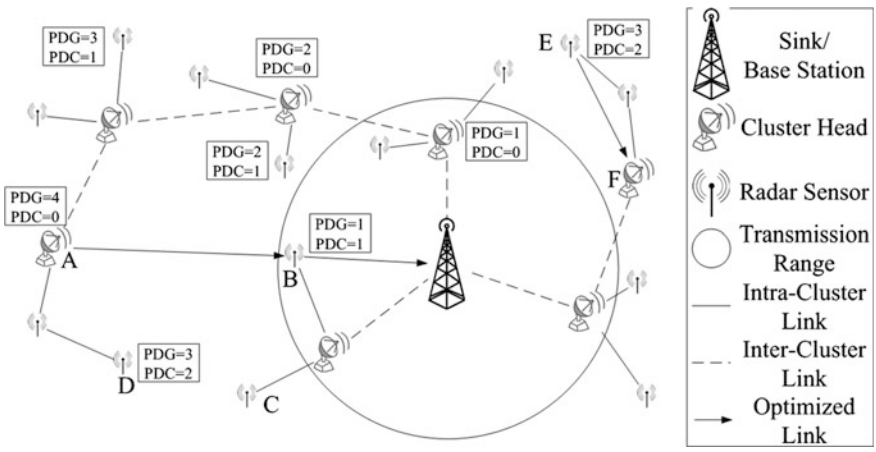

Fig. 1 A simple example of the RSN

and the cluster deciding have been studied and improved in different works. To find the best route, several routing algorithms have been proposed, such as the ACO in [4], EEABR in [5], MACS in [6], and EPACOR in [7]. One of the most famous methods is LEACH [8]; the protocol assumes that the deployed sensors are far from the sink. The network is clustered according to a certain rule and the cluster head collects data from all the sensor nodes within its cluster. Once the data from each sensor node are received, the cluster head aggregates and transfers them directly to the base station. In order to make all the sensor nodes use up their energy approximately and simultaneously, the role as the cluster head is randomly rotated among all sensor nodes in the same cluster. In [9], an efficient routing algorithm for large-scale WSN is proposed. In the intracluster phase, cluster members send data directly to their cluster head and the cluster head is selected by LEACH; in the intercluster phase, the cluster head uses ant colony optimization to find a route to the base station.

The existing routing algorithms are quite effective from the viewpoint of being able to find the best route. However, they also may have a higher latency caused by the routing discovery. For the regular scanning, it is tolerable. Since the RSNs are used for surveillance, we hope the delay become as less as possible when some abnormal data are detected and the corresponding packets can be forwarded to the sink with a high probability. On that purpose, we want to develop a routing algorithm only for these abnormal signals. Being different from the goal of low energy consumption for the regular data, the routing for the abnormal data should be more focused on the low latency and high robustness. The routing discovery by sending routing request in the ad hoc networks is an effective method to get the global shortest path with quite high robustness. But it also has a high latency. To overcome this defect, we want to integrate the routing discovery with the first time transmission. This task is achievable if the nodes are aware of the rough distances from the base station.

For the wireless nodes, there is an attribute called depth which can be defined as the packet hop counts to the sink (which means the depth of the sink is 0). However, this depth is related to the routing method, the depth is decided by the accessible links that the data transmission can only use. To indicate the real distance, we introduce the physical depth (PD) into the routing optimization. The PD is defined as the possible minimum hop counts to the sink. If a proper mechanism is designed to generate and maintain this parameter, the value could be used to improve the routing performance. For a certain node that receiving a packet with abnormal data, if it can decide whether retransmit or abandon the frame based on the PD information calculation. And the PD is taken as a network attribute, the routing is real time and does not require any extra peripherals.

The rest of this paper is organized as follows. Section 2 introduces the preliminary knowledge such as the concept of PD and the maintaining mechanism, the routing algorithm RBPD is proposed in Sect. 3. In Sect. 4, simulation results are presented. Finally, the conclusion is shown in Sect. 5.

2 Preliminary Knowledge

2.1 Neighbor Table

In most wireless networks, each device maintains a neighbor table which has all its neighbors' information in the 1-hop transmission range. The contents for a neighbor entry may include (but not limited to) some of the following parameters: the network's identifier, address, device type, cluster identifier, relationship, link quality indicator, and the depth. Entries in the table are created when the node joins to an existing network. Conversely, the neighbor entry is removed when the neighbor node leaves the network. Since the information on the neighbor table is updated every time a device receives or monitors any frame from the some neighbor node, the information of the neighbor table can be said to be up-to-date all the time. For the RSNs, one more advantage is that the radar sensors keep sending beams for scanning. Some mechanism may be design to fuse the depth information in the radar beams. It is one of our goals in the further work.

2.2 Energy Consumption

In RSN, the radar node transmits the radio in free space. The path loss model [10] is as follows:

$$P_r = \frac{P_t \cdot G_r \cdot G_t \cdot \lambda^2}{(4n)^2} \cdot \left(\frac{d_0}{d_{ij}}\right)^2 \tag{1}$$

where P_t is radar node's transmission power, P_r is the radar node's received power, d_{ij} is distance between radar node S_i and S_j, and G_r and G_t are antenna gain of receiving antenna and transmitting antenna, respectively. λ is the wavelength of carrier. α is the path loss exponent which indicates the rate at which the path loss increases with distance; d_0 is the close-in reference distance which is determined from measurement close to the radar node transmitter.

Based on the Eq. (1), one can see the transmission range of radar which is proportional to the square of transmitter power, and the path loss should be taken into consideration for long distance communication in the practical condition. Thus, in popular viewpoints, the transmitter power should be controlled, and the data are forwarded to the sink by multi-hop methods. However, it may not be a universal rule for all types of data in all applications. In our routing optimization, the nodes are allowed to send the abnormal data packets with a higher power if it could achieve a shorter path, while the energy consumption of the transmitter is also controlled for regular data.

Equation (2) represents the amount of energy consumption in the transmitting packet with bits over distance according to the first-order model. E_{elec} is the amount of energy consumption per bit to run the transmitter or receive circuitry. ε_{fs} and ε_{mp} are the amount of energy per bit dissipated in the RF amplifier according to the distance d_0 which can be obtained from (3). E_{radar} represents the energy consumption for scanning of radar sensor node in every round.

$$E_{tx} = \begin{cases} I \cdot \left(E_{elec} + \varepsilon_{fs} \cdot d^2\right) + E_{radar} & \text{if } d < d_0 \\ I \cdot \left(E_{elec} + \varepsilon_{mp} \cdot d^2\right) + E_{radar} & \text{if } d \geq d_0 \end{cases} \tag{2}$$

$$d_0 = \sqrt{\varepsilon_{fs} / \varepsilon_{mp}} \tag{3}$$

2.3 Physical Depth

As mentioned before, the node depth, which is a topology distance in essential, may not always be able to reflect the real distance from the sink since it is related to the routing algorithms. Thus, to distinguish from the previous one, we introduce the concept of PD, which is able to indicate the spatial distance to some extents.

In the clustering sensor networks like RSNs, there are 2 types of "PD" we should pay attention to. One is the physical depth from the sink, which is a global and intercluster parameter. We call it physical depth in global (PDG). The other, on the contrast, is called physical depth in Clusters (PDC) to imply the rough distance to the cluster head. In our algorithms, the former parameter is used to optimize the intercluster transmission initialized by a cluster head, and the latter one can improve the routing performance with some cluster.

Thus, the sink is the only device with the PDG 0 in the network. Also, as the unique terminal that belongs to no clusters; its PDC is set 0. For a device in the neighborhood of the sink, it is able to receive frames from the base station because of the broadcasting nature in wireless channels and the omnidirectional radar scanning. It may store an entry of the sink in its neighbor table and set the value of PDG by one. Similarly, all the nodes within the transmission range of the PDG 1 devices may have PDG 2, the PDG of any device can be recursively decided. The principle can be simply stated as: the PDG value of a certain node is one plus the minimum PDG value in its neighbor table. Similarly, a cluster member could decide and maintain its PDC based on the minimum PDC value (then plus one) in its neighborhood. The example of PDG and PDC are also shown in the Fig. 1.

3 A Global Routing Algorithm Based on Physical Depth for Abnormal Data

In this section, we will describe the global routing algorithm based on the physical depth (RBPD) for abnormal data that is RSNs. For convenience, the processed data sent from the cluster heads will be discussed first.

In the RBPD, we focus on the following parameters in the transmission. The address of the source cluster head which initializes the sending SCH; the frame type that indicate the direction of packets forwarding, F/T (From or To the sink, for the cluster head sending data to the base station, it should be set T.); the sequence number, SN, which is used as the unique identifier for the packets sent from the cluster head (SCH), this value should be added one every time a new packet is generated; the retired times, RT, this value is set 0 for the first attempt and added by one for each retries; the address of the device that sending the frame, SA (This value is same to the SCH in the first hop); the PDG of the sending device, SPDG; the transmitted hops, TH, which is 0 at the beginning and added by one after a retransmission; and the routing discovery enable flag, EN, which will decide whether a node can retransmit the frame unless it finds a corresponding routing table entry. All the variables above are included in the frame header. With the vector of [SCH, F/T, SN, RT, SA], which we called packet identifier (PI), the frame can be uniquely recognized in the network. And the parameters SPDG, TH, and EN are used to control the transmission.

Our algorithm is based on an assumption that all the transmission links are duplex/half-duplex and symmetric, which can be satisfied in RSNs. The diagram of the retransmission deciding in the RBPD is shown in Fig. 2. To make it more clear, the RTE is short for routing table entry and RDSE is short for routing discovery entry. When a certain cluster head finds something abnormal based on the data processing, it may send the packets instantly. In the frame header, the SCH and SA are both the address of the sending node, whose PDG is put into the SPDG, the F/T is T, TH is 0, the EN must be one for the first time transmission, and the SN and RT are based on the rules mentioned above. As discussed, in RBPD, a larger transmitter power is allowed that may lead to a wider coverage. A receiving device may decide whether it will retransmit this packet by the following rules.

(1) Find if the current node could contribute for the RBPD routing. According to the Fig. 2, only if it has a 2 or 3 more less PDG value than the sending device, or it is the next hop in the regular routing, it will participate in the RBPD routing.
(2) Find the corresponding RTE based on the parameters of the SCH and SA. If yes, it may send this frame; otherwise, to step 3;
(3) Based on the SCH and SN value, try to find a corresponding RDE, if found, go step 4; or, the packet will be sent and the RDE is established.

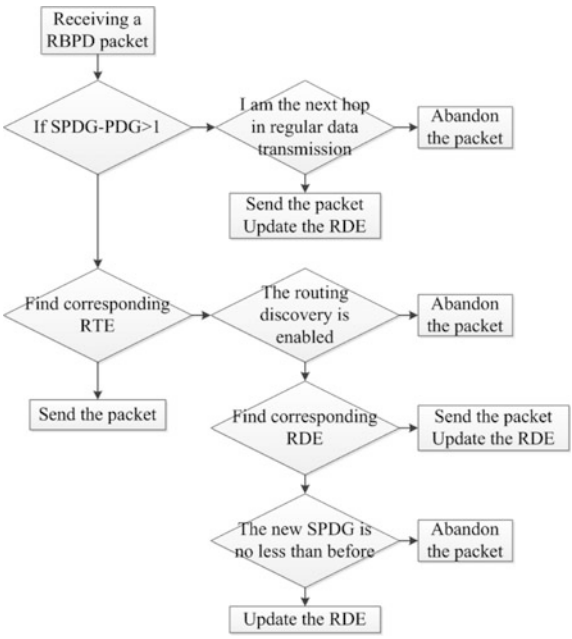

Fig. 2 The packet delivery ratio for different routing methods

(4) Compare the SA between the newly incoming frame and the previous one, if the new value is less or equal, the packet will be directly abandoned; otherwise, the RDE information will be updated with the recently SA.

One can see that the base station may receive several duplicates of the packets sent in different paths. Once it receive a RBPD packet, it may compare the HT with the previous entry which has the same SCH, and the sink will only keep the lowest HT entry. If they have equal HT, in our work, we simply ignore the newly received one. However, more parameters or algorithms may be introduced to evaluate the routing, that is also another topic for our further work. After a fixed duration, the sink has to send a confirmation to the link it has chosen. Similar as the routing discovery confirmation, this packet will be backward transmitted to the SCH based on the SA information stored in the routing discovery entries of intermediate nodes. And the routing discovery entry in each node will be erasable after a prefixed time. Thus, when the cluster head is trying to send an abnormal packet to the sink again, the new RBPD packet could set EN to 1, and the frame can be sent to the base station in the only path based on the routing table, although the receiving device address in each hop is not specified. Since the F/T parameter implies the packet is gathering data or distributing orders, both frame types can be optimized in our algorithm. One example of optimized path can be found in the Fig. 1.

In our algorithm, the steps 3–4 take the similar function with the routing discovery. To reduce the extra energy consumption, the participating nodes are limited,

thus RBPD may not guarantee the global shortest path which is able to be found. However, based on the simulation results given in the next section, we may find it could improve the transmission path effectively. In the worst case, the routing will degenerate to the regular routing path.

The mentioned mechanism is based on the PDG to improve the intercluster data transmission. Similarly, the intracluster transmission can be optimized by substituting the PDG by the PDC and the participating devices are limited to the members of the given cluster.

4 Simulation and Analysis

The performance of the proposed global routing algorithm based on physical depth for abnormal data in RSN is discussed in this section. Since different radar sensors have quite different features, such as the transmission range, data rate, packet size. This made a difficulty to our work. Trying to let the simulation make more sense, for some parameters, we used the ratios to the simulation boundary to run our program. The simulation area is a square with *l***l*. The number of cluster heads, N, varied from 20–100, stepped by 20. Considering, the fact that the rate of cluster heads is always from 5–15% in the RSNs, we made each cluster head manage 9 members in the simulation. It meant there were 10 nodes in a cluster, including the head, and the total nodes in a network is 10*N. The transmission radius for a node is set to $l/\sqrt{2 \cdot N}$ and the transmitter power was *P0*. We compared our algorithm with the famous ant colony optimization (ACO) in the RSNs. We also testified with different transmitter power to see how the parameter would affect the performances. The energy *Pt* was set 2**P0*, 3**P0,* and 4**P0,* respectively. The transmission ranges were calculated based on the Eqs. (2) and (3). Each scenario was run 1000 times for the average.

As shown in the Fig. 3, the average hop counts were firstly analyzed. The retransmission times was effectively reduced in the RBPD. As the node number

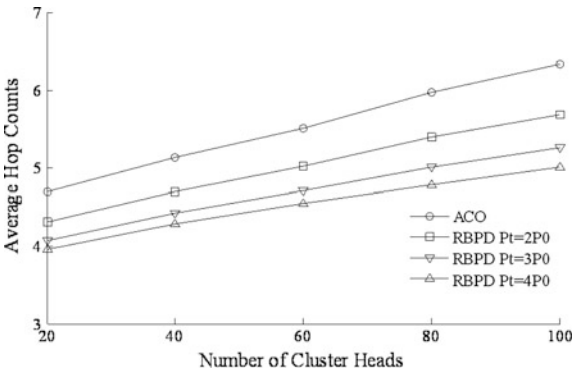

Fig. 3 The average of hop counts with different transmitter power in the RBPD

increased, the improvement was larger. It was because the more nodes were in the networks, the more options a node might have to optimize the routing. Besides, as the *Pt* added, the hop counts were less. The longer transmission radius led to the less hops. However, since the range is proportional to the power according to Eq. (1), we could also see that the improvement was not a linear function to the *Pt*. It implied that the transmitter power in the RBPD was a compromise between the effectiveness and the efficiency.

The simulation on the packet delay was a tough task, because the latency is not only related to the routing algorithms but also the MAC layer features. Since the radar sensors in the network were not specified, it was impossible to determine which model should be used to run the program. In this paper, we made an approximation. The delay is mainly composed of three parts; the first one is the transmission time in the channel which is related to the distance, the second one is the node processing time, and the third one is caused by the channel access. We made the length of the simulation boundary 10 km to calculate the first part. As to the processing time, noted that the RBPD just decided whether to retransmit the packet after several searching and comparing courses and the ACO required an ant colony algorithm based on the probability to find the next hop. One could find the RBPD had a processing time no longer than the ACO. Thus, we made a finite processing time of 20 ms for both the ACO and RBPD. The most common CSMA/CA was used as the channel access control method to deal with the third part.

The simulation result was shown in the Fig. 4. We could see that the RBPD had lower delays than the ACO. Since the routing discovery in the RBPD was integrated with the first time transmission, it cost no more time even if some cluster head had never transmitted abnormal data to the base station before. The tendency of the chart was accordance with the hop counts. Due to the independence to the routing table, it might imply that the hop count was the main factor that affected the latency.

At last, we evaluated the robustness with the packet delivery ratio (PDF) of different routing methods. In the Fig. 5, the curve of the RBPD $Pt = 3*P0$ was now drawn because it was so close to the others. Its position was just between the curves

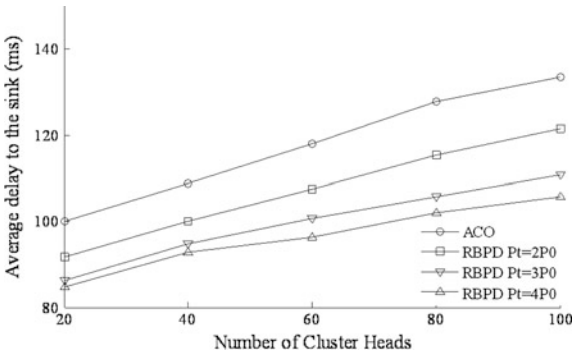

Fig. 4 The average delay to the sink with different transmitter power in the RBPD

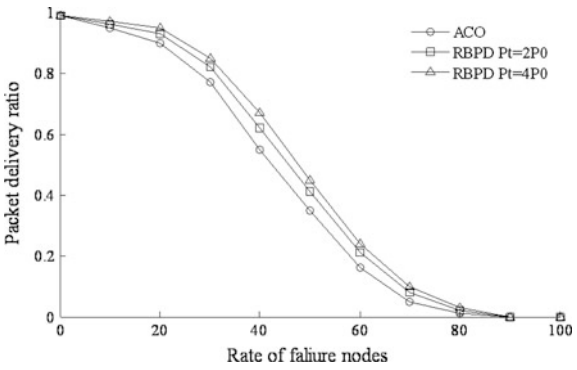

Fig. 5 The packet delivery ratio for different routing methods

of $Pt = 2*P0$ and $Pt = 4*P0$. From this illustration, it could be proved that the RBPD had a higher probability for successful packet forwarding. Since the RBPD had a longer transmission range, it had a better chance to find some substitution. That was why it had a larger tolerance to the failure nodes.

5 Conclusion

In this paper, we proposed a global routing algorithm based on the physical depth for abnormal data in the RSNs. By the introduction of the physical depth and its maintaining mechanism, the node is aware of its rough distance to the sink. On that basis, we describe the RBPD algorithm. The device is allowed to use a higher transmitter power for the abnormal data transmission. To eliminate the extra delay caused by the routing discovery, we combined the routing finding procedure with the first time transmission. Since both the PDG and PDC are considered, the RBPD could improve the performances for the intracluster and intercluster transmission. The simulation results showed the effectiveness of the RBPD, compared with the famous ACO algorithm. It had less average hop counts, lower latency, and higher packet delivery ratio.

For our further work, as mentioned, one is to find some mechanism of fusing the depth information in the radar beams to optimize the physical depth maintaining. Another one is to improve the judging method in routing selection. Besides, the flooding control and the energy efficiency are needed to be more considered.

Acknowledgments This work is funded by the National Science Foundation of China, (NSFC: 61401310), the Project of Tianjin University Technology Development Fund (20130714), and the Doctoral Scientific Foundation of Tianjin Normal University (52XB1106).

References

1. Ly HD, Liang Q (2007) Collaborative multi-target detection in radar sensor networks. In: Proceedings of the military communications conference (MILCOM '07), Orlando, Fla, USA, pp 1–7
2. Liang Q (2011) Radar sensor wireless channel modeling in foliage environment: UWB versus narrowband. IEEE Sens J 6(11):1448–1457
3. Akyildiz IF, Su W, Sankarasubramaniam Y, Cayirci E (2002) A survey on sensor networks. IEEE Commun Mag 40(8):102–105
4. Dorigo M, Maniezzo V, Colorni A (1996) Ant system: optimization by a colony of cooperating agents. IEEE Trans Syst Man Cybern Part B 26(1):29–41
5. Camilo T, Carreto C, Silva JS, Boavida F (2006) An energy-efficient ant-based routing algorithm for wireless sensor networks. In: Proceedings of the 5th international workshop on ant colony optimization and swarm intelligence. Lecture Notes in Computer Science, vol 4150, Brussels, Belgium, pp 49–59
6. Ren X, Liang H, Wang Y (2008) Multipath routing based on ant colony system in wireless sensor networks. In: Proceedings of the international conference on computer science and software engineering (CSSE '08), Wuhan, China, pp 202–205
7. Shen Z, Zhu Y, Tian X (2008) An ant colony system based energy prediction routing algorithms for wireless sensor networks. In: Proceedings of the 4th International conference on wireless communications, networking and mobile computing (WiCOM '08), pp 1–4
8. Heinzelman W, Chandrakasan A, Balakrishnan H (2000) Energy-efficient communication protocol for wireless microsensor networks. In: Proceedings of the 33rd annual Hawaii international conference on system sciences, Maui, Hawaii, USA, pp 1–10
9. Salehpour A, Mirmobin B, Afzali-Kusha A, Mohammadi S (2008) An energy efficient routing protocol for cluster-based wireless sensor networks using ant colony optimization. In: Proceedings of the international conference on innovations in information technology, pp 455–459
10. Rappaport TS (1996) Wireless communications: principles and practice. Prentice Hall, Upper Saddle River

Part IV
Spectrum Access and Optimization

Carrier Frequency Offset Estimation Based on Compressed Sensing: A Preliminary Study

Chaojin Qing, Xin Tong, Yi Guo, Xi Cai, Mintao Zhang and Ling Xia

Abstract Based on the compressed sensing technique, the carrier frequency offset (CFO) is estimated in this paper. For the traditional maximum likelihood (ML)-based CFO estimation, we first confirm the CFO estimation metrics are compressible. Then the coarse CFO estimation is implemented by referencing compressive sampling matching pursuit (CoSaMP) algorithm, and a metric characteristic-based CoSaMP (MCB-CoSaMP) algorithm is proposed. According to the estimated value of coarse CFO estimation, the equivalent likelihood function is interpolated to search the frequency value of fine CFO estimation. The analysis and simulation results show that the sampling rate can be reduced. Compared to the classical CoSaMP algorithm, the better mean squared error (MSE) performance can be obtained when the proposed MCB–CoSaMP is employed for coarse CFO estimation.

C. Qing (✉) · X. Tong · Y. Guo · X. Cai · M. Zhang · L. Xia
School of Electrical Engineering and Electronic Information,
Xihua University, Chengdu 610039, China
e-mail: chjqing@mail.xhu.edu.cn

X. Tong
e-mail: 1050205361@qq.com

Y. Guo
e-mail: lpngy@126.com

X. Cai
e-mail: caixi-1983@163.com

M. Zhang
e-mail: zhangmt@vip.163.com

L. Xia
e-mail: xialing.cd@gmail.com

Q. Liang et al. (eds.), *Proceedings of the 2015 International Conference on Communications, Signal Processing, and Systems*, Lecture Notes in Electrical Engineering 386, DOI 10.1007/978-3-662-49831-6_25

1 Introduction

The carrier frequency offset (CFO), which is well-understood radio frequency (RF) impairment, may result in severe performance degradation at the receiver [1]. To improve receiver performance, the CFO estimation has been investigated in many literatures. Although various methods of CFO estimation are proposed, the sampling rate of existing methods for CFO estimation needs to be at least the Nyquist rate, resulting in excessive power consumption and design difficulty for analog-to-digital converter (ADC) when high sampling rate is experienced [2].

To reduce the sampling rate, the recently proposed compressive sensing (CS) approach [3], which enables sub-Nyquist sampling of sparse or compressible signals in some domain, can be employed for to reduce system complexity and to save power significantly. In [4], a fast and rough estimate of pseudonoise (PN) code phase and Doppler frequency with a reduced number of parallel correlators (i.e., compressed correlators) is proposed by Kong, where the sparse expression is based on autocorrelation. Although the number of correlators is reduced, the compressed correlator technique can only rough estimate Doppler frequency using correlation method. Without using correlation method, the compressed correlator technique will encounter application difficulties. Furthermore, the CFO estimation (includes coarse estimation and fine estimation) is not very intensively investigated in [4].

Whether the CS technique can be introduced into CFO estimation to reduce sampling rate while keeping estimation performance be not deteriorated significantly? A preliminary study is investigated in this paper. First, we confirm the compressibility of CFO estimation metrics in traditional maximum likelihood (ML)-based CFO estimation. By referencing compressive sampling matching pursuit (CoSaMP) algorithm [5], an metric characteristic-based CoSaMP (MCB–CoSaMP) algorithm is then proposed to implement the CFO estimation. By the analysis and simulation, it is shown that CS-based CFO estimation can be implemented, and the better CFO estimation performance of mean squared error (MSE) can be obtained when the proposed MCB–CoSaMP is utilized.

Notation: We use boldface letters to denote matrices and column vectors; $\mathbf{0}$ denotes the zero vector of arbitrary size; $(\cdot)^T$, $(\cdot)^H$, $(\cdot)^{-1}$, $(\cdot)^\dagger$, and $\lfloor\cdot\rfloor$, denote the transpose, conjugate transpose, matrix inversion, Moore–Penrose matrix inversion, and floor operation, respectively; $\mathbf{I}_P$ is $P \times P$ identity matrix; $G(i,j)$ is the (i,j)th element of the matrix of $\mathbf{G}$; we write $\|\cdot\|_p$ for the usual ℓ_p vector norm: $\|\mathbf{x}\|_p = \left(\sum x_i^p\right)^{1/p}$; $\mathrm{supp}\,(\mathbf{x}) = \{i : x_i \neq 0\}$ is the support set that denotes the index set of nonzero elements in $\mathbf{x}$; $\mathbf{A}_\mathrm{T}$ denotes the column submatrix comprising the T columns of $\mathbf{A}$; $\mathbf{x}\big|_\mathrm{T}$ denotes the entries of the vector $\mathbf{x}$ in the set T; and the complementary set of set T is denoted by T^c.

2 Compressive Sampling for CFO Estimation

2.1 Traditional Maximum Likelihood-Based CFO Estimation

From [6], without compressive sampling, the observation of the sampled signal can be expressed as

$$r_k = e^{j(2\pi \Delta f k T_s + \theta)} + v_k, \quad 1 \le k \le N, \tag{1}$$

where Δf is the frequency to be estimate, $T_s \le 1/(2 \cdot \Delta f)$ is the sampling interval, θ is an unknown random phase with uniform probability density in $[0, 2\pi)$, and v_k is a sample of complex additive white Gaussian noise (AWGN) with zero mean and variance σ^2. The carrier-to-noise ratio (CNR) ρ, which is the ratio between the signal and noise powers in (1), is defined as $\rho \overset{\Delta}{=} \frac{1}{2\sigma^2}$ [6].

In the traditional estimation method [6], denoting tentative value for Δf as $\Delta \tilde{f}$, the problem of maximum likelihood (ML) estimation of the frequency Δf is let to seek the maximum of the equivalent likelihood function

$$\Lambda\left(\Delta \tilde{f}\right) \overset{\Delta}{=} \left| \sum_{i=1}^{N} r_i e^{-j2\pi \Delta \tilde{f} \cdot i T_s} \right|^2 = \sum_{k=1}^{N} \sum_{m=1}^{N} r_k r_m^* e^{-j2\pi \Delta \tilde{f} T_s (k-m)}. \tag{2}$$

2.2 Compressibility of CFO Estimation Metrics

Assume $B\left(\Delta \tilde{f}\right) = \sum_{i=1}^{N} r_i e^{-j2\pi \Delta \tilde{f} \cdot i T_s}$, then the matrix form of $B\left(\Delta \tilde{f}\right)$ is

$$B\left(\Delta \tilde{f}\right) = \mathbf{r}^T \cdot \mathbf{C}\left(\Delta \tilde{f}\right), \tag{3}$$

where $\mathbf{r} = \left[r_1, r_2, \ldots, r_N\right]^T$ and $\mathbf{C}\left(\Delta \tilde{f}\right) = \left[e^{-j2\pi \Delta \tilde{f} \cdot T_s}, e^{-j2\pi \Delta \tilde{f} \cdot 2T_s}, \ldots, e^{-j2\pi \Delta \tilde{f} \cdot N T_s}\right]^T$.

In this paper, we call $B\left(\Delta \tilde{f}\right)$ as *CFO estimation metric*. From (2), the equivalent likelihood function $\Lambda\left(\Delta \tilde{f}\right)$ can be rewritten as

$$\Lambda\left(\Delta \tilde{f}\right) \overset{\Delta}{=} \left| B\left(\Delta \tilde{f}\right) \right|^2 = \left| \mathbf{r}^T \cdot \mathbf{C}\left(\Delta \tilde{f}\right) \right|^2. \tag{4}$$

For grid search, P ($P \ge N$) tentative values of Δf, denoted as $\Delta \tilde{f}_1, \Delta \tilde{f}_2, \ldots, \Delta \tilde{f}_P$, are considered. According to the P tentative values, we form a estimation metric vector $\widetilde{\mathbf{B}}$ as

$$\widetilde{\mathbf{B}} = \left[B\left(\Delta \tilde{f}_1\right), B\left(\Delta \tilde{f}_2\right), \ldots, B\left(\Delta \tilde{f}_P\right)\right]^T. \tag{5}$$

Substituting $B\left(\Delta\tilde{f}_p\right) = \mathbf{r}^T\mathbf{C}\left(\Delta\tilde{f}_p\right), p = 1, 2, \ldots, P$ into (5), then we have

$$\widetilde{\mathbf{B}} = \left[\mathbf{C}\left(\Delta\tilde{f}_1\right), \mathbf{C}\left(\Delta\tilde{f}_2\right), \ldots, \mathbf{C}\left(\Delta\tilde{f}_P\right)\right]^T\mathbf{r} = \widetilde{\mathbf{C}}\mathbf{r}. \tag{6}$$

In (5), the CFO estimation metric is approximately sparse. That is, for the amplitudes of CFO estimation metrics (i.e., $\left|B\left(\Delta\tilde{f}_1\right)\right|, \left|B\left(\Delta\tilde{f}_2\right)\right|, \ldots, \left|B\left(\Delta\tilde{f}_P\right)\right|$), only a few amplitudes are significant and the rest are zero or negligible when relatively high CNR can be obtained. An example is given in Fig. 1 to illustrate the compressibility of CFO estimation metrics. Where $N = 256$, $P = 512$, $T_s = 10^{-8}$ s, $\Delta f.T_s = 0.1$ (normalized CFO), and $\rho = 10$ dB. From Fig. 1, only a few amplitudes are significant, and the significant amplitudes gather a cluster. Thus, the estimation metric vector $\widetilde{\mathbf{B}}$, which describes the CFO estimation metrics in Eq. (5), can be compressed according to the compressed sensing theory [3].

Based on the compressed sensing theory [3], an $M \times P$ ($M \ll N \leq P$) measurement matrix $\mathbf{A}$ is employed to compress the estimation metric vector $\widetilde{\mathbf{B}}$. Then, an $M \times 1$ measurements, denoted as $\mathbf{y}$, can be obtained, i.e.,

$$\mathbf{y} = \mathbf{A}\widetilde{\mathbf{B}}. \tag{7}$$

Substituting $\widetilde{\mathbf{B}} = \widetilde{\mathbf{C}}\mathbf{r}$ (see 6 into 7), we can obtain

$$\mathbf{y} = \mathbf{A}\widetilde{\mathbf{C}}\mathbf{r} = \mathbf{D}\mathbf{r}. \tag{8}$$

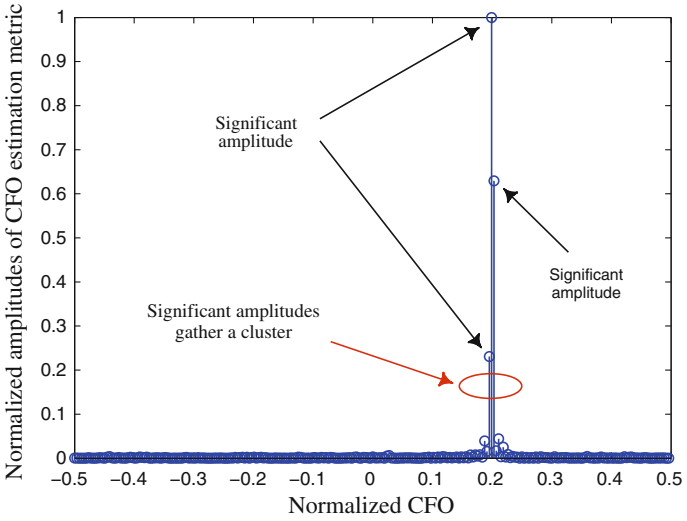

Fig. 1 An example of the compressibility of CFO estimation metrics

In (8), $\mathbf{D} = \mathbf{A}\widetilde{\mathbf{C}} = \left[\mathbf{D}_1, \mathbf{D}_2, \ldots, \mathbf{D}_M\right]^T$, where $\mathbf{D}_m = \left[D_{m1}, D_{m2}, \ldots, D_{mN}\right]^T, m = 1, 2, \ldots, M.$, and the pseudorandom signal wave $\mathbf{D}_m(t)$ can be generated by $\mathbf{D}_m$. By viewing $\mathbf{D}$ as a sensing matrix, the compressive sampling of received signal can be performed by employing the generic analog-to-information converter (AIC) circuit architecture.

3 CFO Estimation Method

The proposed CFO estimation method requires a two-step procedure. The first step, called coarse CFO estimation, reconstructs the estimation metric vector $\widetilde{\mathbf{B}}$ (denoted as $\breve{\mathbf{B}}$) and determines the coarse CFO estimation $\Delta\hat{f}_{\text{coarse}}$. In the second step (i.e., fine CFO estimation), the $\Lambda\left(\Delta\tilde{f}\right)$-values are interpolated according to $\Delta\hat{f}_{\text{coarse}}$, and the local maximum $\Delta\hat{f}_{\text{fine}}$ nearest to Δf is found.

3.1 Coarse CFO Estimation Based on Sparse Reconstruct

Since the estimation metric vector $\widetilde{\mathbf{B}}$ is sparse and the received signal $\mathbf{y}$ is obtained by compressive sampling, we need to exploit reconstruct algorithms to reconstruct the estimation metric vector, i.e., to reconstruct $\widetilde{\mathbf{B}}$. Then the coarse CFO estimation is implemented on the basis of reconstructed $\breve{\mathbf{B}}$.

In this paper, the reconstruct algorithm is exploited according to the currently available CS signal recovery algorithms and the characteristics of estimation metric vector $\widetilde{\mathbf{B}}$. Among these currently available CS signal recovery algorithms, we reference the compressive sampling matching pursuit (CoSaMP) due to its high reconstruction accuracy and excellent robustness to noise [5]. The characteristic that the significant amplitudes of the CFO estimation metrics in estimation metric vector gather a cluster (see Fig. 1) is also utilized. Then an metric characteristic-based CoSaMP (MCB–CoSaMP) algorithm is proposed.

The proposed MCB–CoSaMP algorithm is exhibited in Table 1, where the $P \times 1$ vector $\mathbf{u}$ is expressed as $\mathbf{u} = [u_1, u_2, \ldots, u_P]^T$. Comparing the proposed MCB–CoSaMP algorithm with the classical CoSaMP algorithm in [5], they have quite similar procedure except employing the different support set $\mathbf{W}_1$. In CoSaMP algorithm $\mathbf{W}_1$ locates the $2K$ largest components of $\mathbf{u}$, while the $2K$ indexes nearest the index of the maximum amplitude in $\mathbf{u}$ are chosen for MCB–CoSaMP algorithm.

On the basis of $\breve{\mathbf{B}}$, the coarse CFO estimation $\Delta\hat{f}_{\text{coarse}}$ can be estimated. We denote the reconstructed $\breve{\mathbf{B}}$ as $\breve{\mathbf{B}} = \left[\breve{B}\left(\Delta\tilde{f}_1\right), \breve{B}\left(\Delta\tilde{f}_2\right), \ldots, \breve{B}\left(\Delta\tilde{f}_P\right)\right]^T$, then we have

Table 1 MCB-CoSaMP Algorithm

Input: Measurement matrix $\mathbf{A}$, noisy measurements $\mathbf{y}$, and sparsity level K.

Output: CFO estimation metric vector $\breve{\mathbf{B}}$.

Initial: $\breve{\mathbf{B}}^{(0)} \leftarrow \mathbf{0}$, $\mathbf{v} \leftarrow \mathbf{y}$, $k \leftarrow 0$.
Repeat:
a). $k = k + 1$.
b). Form metric-vector proxy: $\mathbf{u} = \mathbf{A}^H \mathbf{v}$.
c). Identify circle-cluster location according to $\mathbf{u}$:
$W_1 = \{i : |u_i| = \max\{|u_1|, |u_2|, \cdots, |u_P|\}\}$;
$\mathbf{W}_1 \leftarrow$ the $2K$ indexes nearest to W_1 in index set $\{1, 2, \cdots, P\}$ including W_1.
d). Merge support set:
$\mathrm{T} \leftarrow \mathrm{supp}\left(\breve{\mathbf{B}}^{(k-1)}\right) \bigcup \mathbf{W}_1$.
e). Least square estimation: $\mathbf{b}|_{\mathrm{T}} \leftarrow (\mathbf{A}_{\mathrm{T}})^{\dagger}\mathbf{y}$.
f). $\mathbf{b}|_{\mathrm{T}^c} \leftarrow \mathbf{0}$.
g). Prune to obtain next approximation: $\breve{\mathbf{B}}^{(k)} \leftarrow \mathbf{b}$.
h). Update current samples $\mathbf{v} \leftarrow \mathbf{y} - \mathbf{A}\breve{\mathbf{B}}^{(k)}$.
Until: $k = K$
$\breve{\mathbf{B}} \leftarrow \breve{\mathbf{B}}^{(K)}$.

$$\Delta\hat{f}_{\mathrm{coarse}} = \arg\max_{\Delta\tilde{f}_p} \left\{ \left| \breve{B}\left(\Delta\tilde{f}_p\right) \right|^2 \right\}. \tag{9}$$

3.2 Fine CFO Estimation

By using the estimated $\breve{\mathbf{B}}$ and $\Delta\hat{f}_{\mathrm{coarse}}$, we employ interpolation method to implement the fine CFO estimation, where we search $\Delta\hat{f}_{\mathrm{fine}}$ near to $\Delta\hat{f}_{\mathrm{coarse}}$. In this subsection, we assume the frequency range for searching $\Delta\hat{f}_{\mathrm{fine}}$ is $\left[\Delta\hat{f}_{\mathrm{coarse}} - \zeta, \Delta\hat{f}_{\mathrm{coarse}} + \zeta\right]$ with $\zeta > 0$.

From (6), we have $\mathbf{r} = \widetilde{\mathbf{C}}^{\dagger}\widetilde{\mathbf{B}}$. Assuming $N \times 1$ noise vector caused by inaccurate reconstruction of $\widetilde{\mathbf{B}}$ be $\mathbf{n}$, the received signal $\mathbf{r}$ sampled as Nyquist rate can be expressed as

$$\mathbf{r} = \widetilde{\mathbf{C}}^{\dagger}\breve{\mathbf{B}} + \mathbf{n}, \tag{10}$$

where we replace $\widetilde{\mathbf{B}}$ with the estimated $\breve{\mathbf{B}}$. Since the recovery algorithm can accurately reconstruct $\widetilde{\mathbf{B}}$ (i.e., $\widetilde{\mathbf{C}}\mathbf{r}$) when the CNR is relatively high (e.g., 10 dB), we can ignore the noise vector $\mathbf{n}$ for relatively high CNR. Then we have

$$\mathbf{r} \approx \breve{\widetilde{\mathbf{C}}}^{\dagger}\breve{\mathbf{B}}. \tag{11}$$

In this paper, we use the tentative frequency $\breve{\Delta f}$ in $\left[\Delta\hat{f}_{\text{coarse}} - \zeta, \Delta\hat{f}_{\text{coarse}} + \zeta\right]$ to construct $N \times 1$ vector $\breve{\mathbf{C}}\left(\breve{\Delta f}\right)$ as

$$\breve{\mathbf{C}}\left(\breve{\Delta f}\right) = \left[e^{-j2\pi\breve{\Delta f}\cdot T_s}, e^{-j2\pi\breve{\Delta f}\cdot 2T_s}, \ldots, e^{-j2\pi\breve{\Delta f}\cdot NT_s}\right]^T. \tag{12}$$

Substituting (12) and (11) into (3), the equivalent likelihood function $\Lambda\left(\breve{\Delta f}\right)$ can be expressed as

$$\Lambda\left(\breve{\Delta f}\right) = \left|\left(\breve{\widetilde{\mathbf{C}}}^{\dagger}\breve{\mathbf{B}}\right)^T \breve{\mathbf{C}}\left(\breve{\Delta f}\right)\right|^2. \tag{13}$$

Then the fine CFO estimation $\Delta\hat{f}_{\text{fine}}$ can be obtained by seeking the maximum of the equivalent likelihood function $\Lambda\left(\breve{\Delta f}\right)$, i.e.,

$$\Delta\hat{f}_{\text{fine}} = \arg\max_{\breve{\Delta f}} \left\{\left|\left(\breve{\widetilde{\mathbf{C}}}^{\dagger}\breve{\mathbf{B}}\right)^T \breve{\mathbf{C}}\left(\breve{\Delta f}\right)\right|^2\right\}. \tag{14}$$

In fact is that the Eq. (14) can be viewed as employing the same estimation method of the traditional ML-based CFO estimator for good enough CNR.

4 Numerical and Simulation Results

Computer simulation results are presented in this section. Some basic simulation parameters are as follows: $N = 1024$, $P = 1024$, $T_s = 10^{-9}$ s, $K = 40$, measurement matrix $\mathbf{A}$ is Gaussian random matrix, and the CRLB is given in [6].

The comparison of MSE of CFO estimation is plotted in Fig. 2, where $M = 512$. The processing of fine CFO estimation is same, while the coarse CFO estimation employs CoSaMP and MCB–CoSaMP algorithm respectively. In coarse CFO estimation, Fig. 2 indicates that adopting the proposed MCB–CoSaMP recovery algorithm can obtain better MSE performance than the classical CoSaMP recovery algorithm. On the other hand, only 512 samples are considered here while 1024 samples are required in [6], i.e., the ratio between M and N is M/N = 0.5.

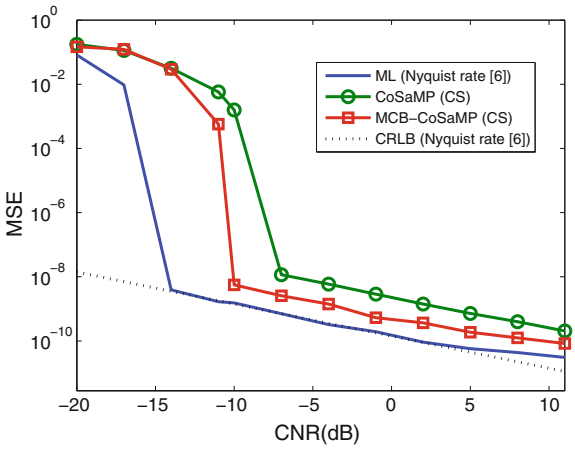

Fig. 2 The MSE of CFO estimation with different recovery algorithms (i.e., CoSaMP and MCB–CoSaMP) for coarse CFO estimation, where $M = 512$

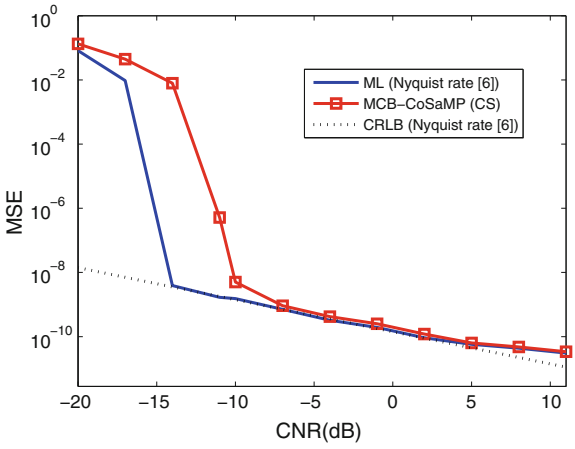

Fig. 3 The MSE of CFO estimation with $M = 819$, where ML algorithms in [6] and the proposed MCB–CoSaMP are compared

Increasing M/N further, an example is given in Fig. 3 to illuminate comparative MSE performance of Nyquist rate in [6] can be obtained for relative high CNR, where $M = 819$, i.e., $M/N \approx 0.8$. That is, compared to Nyquist rate in [6], we can obtain comparative MSE with 20 % samples are discarded when $\rho > -6$ dB.

5 Conclusion

In this paper, a preliminary study for CFO estimation based on compressed sensing has been exhibited. For conventional ML-based CFO estimation, we have confirmed that the CFO estimation metrics are compressible. An MCB–CoSaMP algorithm is proposed to reconstruct the metrics of coarse CFO estimation from the compressed

samples. According to the coarse estimation, the equivalent likelihood function is interpolated to implement the fine CFO estimation. Compared to the classical CoSaMP algorithm, the analysis and simulation results have shown that the better MSE performance can be obtained when the proposed MCB–CoSaMP is employed for coarse CFO estimation.

Acknowledgments This work is supported in part by the Science Foundation for Post Doctorate Research (Grant No. 2012M511920), the project of Meteorological information and Signal Processing Key Laboratory of Sichuan Higher Education Institutes (Grant No. QXXCSYS201402), the Xihua University Young Scholars Training Program (Grant No. 01201408), the key scientific research fund of Xihua University (Grant No: Z1120941, Z1120945, Z1320927), the project of science and technology plan of Sichuan Province (Grant No. 2015JY0138), the key projects of Education Department of Sichuan Province (Grant No. 15ZA0134), the Open Research Subject of Key Laboratory (Research Base) of signal and information processing (Grant No. szjj2015-071), and the major cultivation project of Education Bureau of Sichuan Province (Grant No. 13ZC0003) of China.

References

1. Wang X, Hu B (2014) A low-complexity ml estimator for carrier and sampling frequency offsets in OFDM systems. IEEE Commun Lett 18(3):503–506
2. Zhou J, Ramirez M, Palermo S, Hoyos S (2012) Digital-assisted asynchronous compressive sensing front-end. IEEE J Emer Sel TopicsCircuits Syst 2(3):482–492
3. Donoho D (2006) Compressed sensing. IEEE Trans Inf Theor 52(4):1289–1306
4. Kong SH (2013) A deterministic compressed GNSS acquisition technique. IEEE Trans Veh Technol 62(2):511–521
5. Needell D, Tropp J (2010) Cosamp: Iterative signal recovery from incomplete and inaccurate samples. Commun ACM 53(12):93–100
6. Luise M, Reggiannini R (1995) Carrier frequency recovery in all-digital modems for burst-mode transmissions. IEEE Trans Commun 43(234):1169–1178

A Stackelberg Game Spectrum Sharing Scheme in Cognitive Radio-Based Heterogeneous Wireless Sensor Networks

Songlin Sun, Na Chen, Junshi Xiao and Tao Tian

Abstract In this paper, we focus on spectrum sharing in heterogeneous wireless sensor networks (HWSNs) and consider Stackelberg game exploiting the cognitive radio (CR) technology to utilize those resources. In the game, the licensed network controls and prices the improvable spectrum that the wireless sensor networks (WSNs) relay: can purchase and use to serve the attached sensor nodes as well as offload some nodes in licensed network. When on spectrum trading, actor nodes and sensor nodes would try to maximize their data rates, gaining, and expenditures. During the process of the game, the interference coordination functions of the heterogeneous sensor network and CR technology are employed so that the difference of spectrum allocation can be completely used. According to simulation result, we evaluate the impact on throughput performance after implementing proposed game strategy in HWSNs. And we prove that the proposed method can observably improve the capacity of victim licensed nodes with slightly decreasing network's throughput.

1 Introduction

Wireless sensor network (WSN) is one of the most striking technologies in monitoring and supervising. It is a self-organizing ad hoc network consisted of a great quantity of sensor nodes [1]. Generally, large scale of WSN applications would like to exploit the unlicensed spectrum bands. The rare and scant unlicensed radio spectrum are contended by a mass of wireless applications and there are less and less

S. Sun (✉) · N. Chen · J. Xiao · T. Tian
Beijing University of Posts and Telecommunications, Beijing, China
e-mail: slsun@bupt.edu.cn

N. Chen
e-mail: chn@bupt.edu.cn

J. Xiao
e-mail: 2012212930@bupt.edu.cn

T. Tian
e-mail: tiantao@bupt.edu.cn

Q. Liang et al. (eds.), *Proceedings of the 2015 International Conference on Communications, Signal Processing, and Systems*, Lecture Notes in Electrical Engineering 386, DOI 10.1007/978-3-662-49831-6_26

unlicensed bands as the quantity of wireless communication devices sharply increases because more and more people choose mobile devices, etc. Therefore, the interference and coexistence issues of wireless systems restrict the development of WSN [2].

As a way to solve the problem of spectrum resources' shortage, we adopt the dynamic spectrum access (DSA) technology, i.e., CR system to obtain a better result of WSN communications efficiency. In this paper, we will propose a game theory-based spectrum sharing algorithm exploiting CR technology for WSN [3].

We formulate a Stackelberg game [4] spectrum sharing scheme where licensed user can price the shared frequency band and if the cognitive radio sensor network (CRSN) nodes would like to use the band they will have to purchase it. However, the base station sets up the original spectrum hole ratio and according to it, the actor node can decide whether to purchase the bandwidth and the number of licensed nodes to offload. As the result of the dynamic game, we can achieve the balance with the most suitable parameters.

The rest of this paper is organized as follows. System model is described in Sect. 2. In Sect. 3, the spectrum sharing problem is solved by the use of Stackelberg game strategy. In Sect. 4, numerical results are shown with evaluation the performance of the proposed scheme. The final conclusions are drawn in Sect. 5.

2 System Model

In this work, we adopt a heterogeneous and hierarchical CRSN architecture [5]. In this architecture, we introduced special nodes which are provided with more or renewable power sources such as actor nodes. They may perform additional tasks like local spectrum bargaining. What is more, because of longer transmission ranges, these nodes can also act as relay nodes [6].

Suppose the heterogeneous CRSN totally has J co-channel actor nodes. The set of base stations and actor nodes can be presented by $j \in \mathscr{B} = \{0, 1, \ldots, J\}$, where $j = 0$ indexing the BS and $j \geq 1$ representing the ANs. Considering external interference, the set of I external interference power nodes can be indicated by $i \in \mathscr{B}_I = \{1, 2, \ldots, I\}$. N_0 and N_j, respectively, represents the number of users in licensed network and the number of nodes in the j-th actor node. Moreover, each actor node j is surrounded by $N_j^{offload}$ licensed nodes in their coverage area.

The channel condition in our model is assumed to be block-fading and the additive noises at licensed network and CRSN are independent circularly symmetric complex Gaussian (CSCG) whose variance is σ^2 and mean is zero.

According to above assumptions, the signal to interference plus noise ratio (SINR) of the kth sensors of the network served by the j-th power node during the non-spectrum hole period can be denoted by

$$SINR_{j,k}^{(0)} = \frac{P_j h_{j,k}}{\sum_{s\in\mathscr{B}/j} P_s h_{s,k} + \sum_{i\in\mathscr{B}_I} P_i^{'} h_{i,k}^{'} + \sigma^2}. \tag{1}$$

Similarly, the SINR during the spectrum hole period is

$$SINR_{j,k}^{(1)} = \frac{P_j h_{j,k}}{\sum_{s\in\mathscr{B}/\{0,j\}} P_s h_{s,k} + \sum_{i\in\mathscr{B}_I} P_i^{'} h_{i,k}^{'} + \sigma^2}. \tag{2}$$

In these two expressions, P_j and $P_i^{'}$, respectively, represent the transmitted power of actor node j and external power node i. The path gain between sensor k and actor node j is denoted by $h_{j,k}$ and $h_{i,k}^{'}$ indicate the path gain between sensor k and external power node i. We also make the assumption that the actor nodes are sparsely located in the licensed network and the interference between them is able to be ignored.

For an actor node, the minimum user data rate without offloading licensed users can be calculated by

$$r_j = \frac{F_j(1-\gamma)}{N_j} \log(1 + SINR_{j,min}^{(0)}), \tag{3}$$

where γ and F_j, respectively, denote spectrum hole ratio and the relay j's bandwidth, and $SINR_{j,min}^{(0)}$ is the minimum SINR among N_j sensor served by actor node j in non-spectrum hole period. Similarly, the j-th actor node's minimum user data rate after offloading the licensed users is denoted by

$$r_j^{offload} = \frac{F_j\gamma}{N_j^{offload}} \log(1 + \frac{SINR_{j,min}^{(1)}}{\beta_j}), \tag{4}$$

where β_j is the offloading factor, $SINR_{j,min}^{(1)}$ is the minimum SINR can be obtained among N_j in spectrum hole period. Note that $N_j^{offload} = f_j(\beta_j)$ is an increasing function whose variable is β_j, and In practice, we can obtain the $f_j(\cdot)$ through analyzing long-term statistic with particular distributions of users and actor nodes. Hence, a licensed network's minimum user data rate can be written by

$$r_M = \frac{F(1-\gamma)}{N_M} \log(1 + SINR_{0,min}^{(0)}), \tag{5}$$

where F is the base station's total available bandwidth and $SINR_{0,min}^{(0)}$ represents the minimum SINR among the N_M nodes served by base station. $N_M = f_0(\beta_1, \beta_2, \ldots, \beta_J)$ is a non-increasing function whose variable is offloading factors. The relationship between N_M and $N_j^{offload}$ satisfies $N_M + \sum_{j=0}^{J} N_j^{offload} = N_0$.

3 The Proposed Algorithm

3.1 Utility Function and Stackelberg Game Formulation

For an random node, let r^0 be the minimum data rate which is demanded by a node and the licensed network r is the true minimum user data rate. Then as for a node, which is belong to N attached nodes, $U = N \ln\left(\frac{r}{r^0}\right)$ is its general utility function.

The actor node will try to use smallest cost to obtain maximum data rates in CRSN, their utility function is $U_j = CN_j \ln\left(\frac{r_j}{r^0}\right) - (1-\gamma)AF_j$, where C is a positive constant, and the frequency band's unit price is A. In order to optimize relay j, there is

$$\max_{F_j} \; U_j \quad st. 0 \le F_j \le F. \tag{6}$$

For licensed network, the correspondent utility function is shown as follows:

$$U_M = \sum_{j\ge 1}(1-\gamma)AF_j + C\left(N_M \ln\left(\frac{r_M}{r^0}\right) + \sum_{j\ge 1} N_j^{offload} \ln\left(\frac{r_j^{offload}}{r^0}\right)\right). \tag{7}$$

Hence,for licensed network, the optimization problem can be formulated as

$$\begin{aligned} &\max_{\gamma,\boldsymbol{\beta}} \; U_M \\ &st. \; 0 \le \gamma \le 1 \\ &\quad \beta_j \ge 1, \; j = 1, 2, \ldots, J, \end{aligned} \tag{8}$$

where $\boldsymbol{\beta} = \left(\beta_1, \beta_2, \beta_3 ... \beta_F\right)$.

3.2 Stackelberg Game Solution

The licensed network's base station initializes parameters γ and $\boldsymbol{\beta}$ randomly, after solving the optimization problem given by (6), actor nodes will make a decision about how much bandwidth should be purchased, in order to solve (8) for new γ and $\boldsymbol{\beta}$, actor nodes will purchase some bandwidth, in this process, the base station will perform a backward induction all the way and in the end the balance can be obtained [7].

Consider U_j as function in F_j, the second derivative is formulated as $\frac{\partial^2 U_j}{\partial {F_j}^2} = \frac{-N_j C}{{F_j}^2} < 0$.

Given γ, after solving the following formulation $\frac{\partial U_j(F_j)}{\partial F_j} = \frac{N_j C}{F_j} - (1-\gamma)A$, the maximal F_j, shown as F_j^*, can be obtained.

And the solution is as follows:

$$F_j^* = \begin{cases} F & 1 - \frac{N_j C}{AJ} \le \gamma \le 1 \\ \frac{N_j C}{A(1-\gamma)} & 0 \le \gamma < 1 - \frac{N_j C}{AJ}. \end{cases} \tag{9}$$

Generally, the actor node cannot occupied all the spectrum of the licensed network, so the condition $\gamma < 1 - \frac{N_j C}{AJ}$ will be feasible in most occasions. Therefore, to simplify the problem, we assume that $F_j^*(\gamma)$ be equal to $\frac{N_j C}{A(1-\gamma)}$.

As for the backward induction, we can transform U_M into the following form given $F_j^*(\gamma)$

$$\begin{aligned} U_M(\gamma, \boldsymbol{\beta}) = C \sum_{j \ge 1} N_j + C f_0(\boldsymbol{\beta}) \ln\left((1-\gamma) Q_0(\boldsymbol{\beta})\right) \\ + C \sum_{j \ge 1} f_j(\beta_j) \ln\left(\frac{\gamma Q_j(\beta_j)}{1-\gamma}\right), \end{aligned} \tag{10}$$

where

$$\begin{aligned} Q_0(\boldsymbol{\beta}) &= \frac{F}{f_0(\boldsymbol{\beta}) r^0} \log\left(1 + SINR_{0,min}^{(0)}\right) \\ Q_j(\beta_j) &= \frac{N_j C}{A f_j(\beta_j) r^0} \log\left(1 + \frac{SINR_{j,min}^{(1)}}{\beta_j}\right) \\ \boldsymbol{\beta} &= \left(\beta_1, \beta_2, \beta_3 ... \beta_F\right). \end{aligned} \tag{11}$$

To solve the problem, $\boldsymbol{\beta}$ need to be dependent. There are two cases, first $\boldsymbol{\beta}$ is predetermined, second for each actor node $\boldsymbol{\beta}$ is changed until finally achieving maximum access data rate.

3.2.1 Predetermined Offloading Factor $\boldsymbol{\beta}$

Observe that $\sum_{j \ge 1} N_j^{offloading} < N_M$, the second derivative of Eq. (10) on γ is given by $\frac{\partial^2 U_M(\gamma)}{\partial^2 \gamma} = \frac{-N_M}{(1-\gamma)^2} - \sum_{j \ge 1} \left(\frac{N_j^{offload}}{\gamma^2} - \frac{N_j^{offload}}{(1-\gamma)^2}\right) < 0.$

According to above equation, $U_M(\gamma)$ is concave in $\boldsymbol{\beta}$. Thus, by solving $\frac{dU_M(\gamma)}{d\gamma} = \frac{-N_M}{1-\gamma} + \frac{\sum_{j\geq 1} N_j^{offload}}{\gamma} + \frac{\sum_{j\geq 1} N_j^{offload}}{1-\gamma} = 0$, we can obtain the optimal γ^* which maximizes $U_M(\gamma, \boldsymbol{\beta})$. Hence, $\gamma^* = \frac{\sum_{j\geq 1} N_j^{offload}}{N_M}$.

And then we consider the condition [8] that the nodes in the licensed network will attach to the base station which can provide the maximal date rate without considering the node's utility, and this standard is viewed as the Max-rate access principle. According to this principle, offloading factor β_j is used to satisfy $r_j^{offload} = r_{M,j}$, $j = 1, 2, \ldots, J$, where $r_{M,j}$ denotes the average data rate provided by the j-th actor node in its coverage area.

4 Performance Evaluation

4.1 System Throughput

As shown in Fig. 1, we compare the throughput performance of the proposed Stackelberg scheme with the existed method without implementing CR technology and the traditional static scheme. As the CR technology takes advantage of the spectrum hole to improve victim licensed nodes' throughput and our model does not consider other nodes' interest, the throughput achieved by the scheme we proposed is smaller than that of the scheme without implementing CR technology. However, as we can see, the degradation is not obvious, the improvement in victim licensed nodes' access rates is still meaningful.

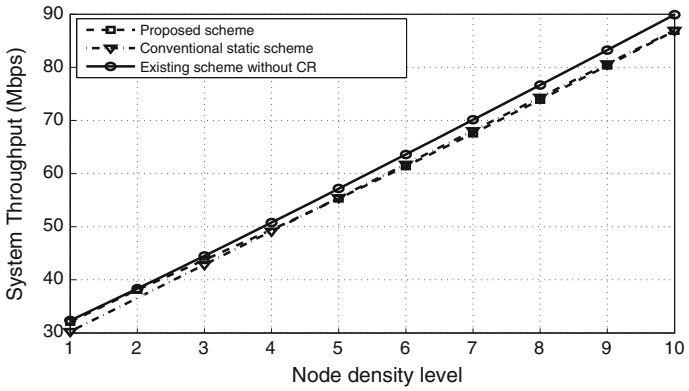

Fig. 1 Throughput performance of the whole system

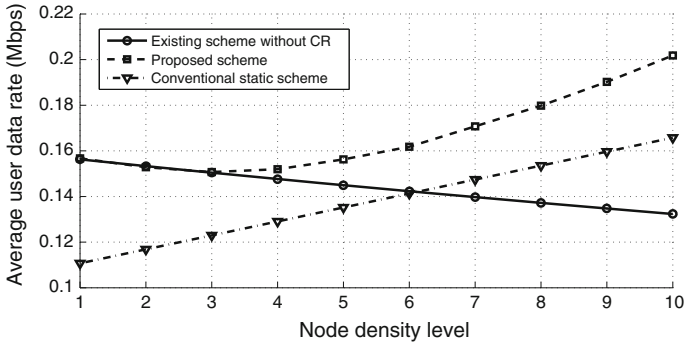

Fig. 2 Average data rate performance of actor nodes

4.2 Data Rate of Relay-Nodes

As compared in Fig. 2, thanks to the CR technique that relays can serve wholly for the victim licensed nodes in spectrum hole period. By the game we proposed, actor nodes are stimulated to purchase more bandwidth, as a result, more sensor nodes are linked and the stronger interference is induced which can be handled in a great extent by our algorithm. As a result, the proposed scheme is the best one over three schemes with slight degradation of overall throughput.

4.3 Data Rate of Edge Nodes

The data rate performance of nodes near the boundary of CRSN cells versus the spectrum price is shown in Fig. 3, where the offloading factor is determined by the two cases discussed in Sect. 3.2.

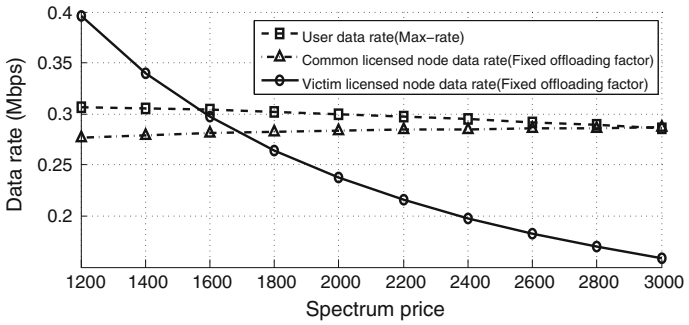

Fig. 3 Data rate performance of the edge nodes in actor node coverage area

For the case where offloading factor is determined before, when the spectrum price goes to high, the victim nodes' data rates cannot be ensured, since the actor node needs to make the spending on spectrum purchasing and the income of user offloading in balance for licensed network and if price rises, they would like to reduce offloading. However, using max-rate access principle, all nodes can work in the same rate, because when spectrum price rises, the actor node can shrink the offloading factor and let some victim nodes resort to the licensed network for more same service.

5 Conclusions

In this paper, we proposed a spectrum sharing scheme between licensed network and actor nodes in HWSNs which is based on the Stackelberg game and employment of CR techniques.

Due to the Stackelberg game, the licensed network and actor nodes can dispose the frequency deployment issue dynamically and smartly, and the underlying HWSN can work in a self-organized fashion. The features brought by CR technique are the crucial factors that enable the game. From simulation results, we learn that the frequency resource can be deployed efficiently between licensed network and actor nodes as the change of nodes density. Thanks to the adjustment in actor nodes' offloading action in the light of the change in spectrum hole proportion and offloading factor, the victim nodes and edge nodes' date rate can be ensured, though with a slight reduction in overall network throughput.

Acknowledgments Project 61471066 supported by NSFC.

References

1. Yau K-LA, Komisarczuk P, Teal PD (2009) Cognitive radio-based wireless sensor networks: conceptual design and open issues. J Mol Med. doi:10.1109/LCN.2009.5355016
2. Xiao-Hui L, Hui W (2012) On using game theory to balance energy consumption in heterogeneous wireless sensor networks. J Mol Med. doi:10.1109/LCN.2012.6423676
3. Vijay G, Ben Ali Bdira E, Ibnkahla M (2011) Cognition in wireless sensor networks: a perspective. J Mol Med. doi:10.1109/JSEN.2010.2052033
4. Zhu J, Liu KJR (2007) Cognitive radios for dynamic spectrum access—dynamic spectrum sharing: a game theoretical overview. J Mol Med. doi:10.1109/MCOM.2007.358854
5. Asokan A, AyyappaDas R (2014) Survey on cognitive radio and cognitive radio sensor networks. J Mol Med. doi:10.1109/ECS.2014.6892784
6. Jiang CX, Chen Y, Gao Y, Liu KJR (2013) Joint spectrum sensing and access evolutionary game in cognitive radio networks. IEEE Trans Wirel Commun 12(5):2470–2483
7. Scutari G, Jong-Shi P (2013) Joint sensing and power allocation in nonconvex cognitive radio games: quasi-nash equilibria. J Mol Med. doi:10.1109/ICDSP.2011.6004984
8. Tabassam AA, Suleman MU (2012) Game theory in wireless and cognitive radio networks—coexistence perspective. J Mol Med. doi:10.1109/ISWTA.2012.6373837

Research on Maximal Weighted Independent Set-Based Graph Coloring Spectrum Allocation Algorithm in Cognitive Radio Networks

Yuanyuan Bao, Shubin Wang, Bingxin Yan, Kun Liu and Fangfang Meng

Abstract The traditional graph coloring spectrum allocation algorithm takes into account the efficiency in the different spectrum, but in one allocation period, it can only be assigned one spectrum to the corresponding user. Spectrum allocation algorithm based on maximal independent set can assign a spectrum to multiple users simultaneously and does not constitute interference. However, it does not consider the efficiency in the different spectrum as well as the aggregated interference as it allocates one spectrum to multiple users simultaneously. Based on this, we propose an improved maximal weighted independent set-based graph coloring spectrum allocation algorithm in cognitive radio networks. The algorithm allocates spectrum to the nodes with maximal weighted independent set and fully considers the differences in spectral efficiency and interference spectral differences. The simulation results validates the feasibility of the algorithm, and with the usage of power control technology, it improves the spectrum utilization at the premise of ensuring the received signal to interference plus noise ratio at each intended cognitive radio receivers.

Keywords Cognitive radio · Maximal independent set · Power control · Spectrum allocation

Y. Bao · S. Wang (✉) · B. Yan · K. Liu · F. Meng
College of Electronic Information Engineering,
Inner Mongolia University, Hohhot, China
e-mail: wangshubin@imu.edu.cn

Y. Bao
e-mail: candy_6666@163.com

B. Yan
e-mail: yanbingxin@163.com

K. Liu
e-mail: lkspecial@163.com

F. Meng
e-mail: 15754815731@163.com

Q. Liang et al. (eds.), *Proceedings of the 2015 International Conference on Communications, Signal Processing, and Systems*, Lecture Notes in Electrical Engineering 386, DOI 10.1007/978-3-662-49831-6_27

1 Introduction

In recent years, with the rapid development of wireless communication technology, there occurs a sharp increase in the number of wireless users, and the available spectrum resources become increasingly scarce. A study from US concluded that the existing spectrum management and allocation strategy is one of the important reasons for the shortage of spectrum resources [1]. A research from the National Radio Network Test Bed project [2] is a measurement report shows that at the bands below 3GHz, the average spectral efficiency is only 5.2 %. So the spectrum sharing technology, which can realize the recycling in the nonrenewable resources, received widespread attention in recent years.

The cognitive radio effectively solves the existing problem of the low utilization of spectrum resources. Dr. Joseph Mitola proposed cognitive radio based on the concept of software defined radio in 1999, who pointed out that cognitive radio "is an intelligent wireless communication technology, and analyzes, understands and makes judgment to the environmental information through continuously sensing the surrounding wireless communication environment, then adjusts its operating frequency, coding method, transmission power and other parameters to adapt to the changes in wireless communication environment. " The main function of the cognitive radio is sensing the surrounding environment, and then dynamically allocate spectrum resources to the secondary users (brief in SU) while not interfere with the primary users (brief in PU). Spectrum allocation in cognitive radio networks considers the number of cognitive users and different communication needs and allocates resources to one or more cognitive users in the network according to a certain spectrum allocation algorithm so as to attain the optimal system performance.

Current works on cognitive radio spectrum allocation model can be loosely categorized into four classes: interference temperature model, game theory model, auction bidding model, and graph coloring models. In this paper we use graph coloring models. In cognitive radio networks, the available spectrum varies as cognitive user differs in locations, which is equivalent to "the number of colors" in graph theory. Similarly, the interference between cognitive users can be equivalent to the "edge." So by this way, we can use the graph coloring theory to analyze and study the spectrum allocation issue in cognitive radio. Works on spectrum allocation in cognitive radio networks with opportunistic spectrum access include [3–6]. In the literature [3], the list-coloring algorithms are proposed based on the graph coloring model. Among this, the list-coloring greedy algorithm's goal is to get the maximum number of allocated spectrum under the existing interference constraints. The degree of the connection of node is an important consideration when it allocates spectrums, which can lead to poor fairness among users, because in general, nodes that with less connection degree tend to get more resources. In contrast, nodes with more degree may be assigned to less channels or even no channels to be assigned. In addition, it does not take into account the differences in spectrum efficiency and the spectral interference differences. Based on this, Peng and Zheng proposed a color sensitive graph coloring algorithm, referred CSGC algorithm [4]. CSGC algorithm is a

heuristic algorithm tends to select a most valuable vertex that corresponds to a color. However, the main drawback lies in that the operation will form a nonlinear increase with the increase in the number of users and the number of spectrum. The optimal coloring problem is a NP-Hard problem. Therefore, it can hardly adapt to the fast time-varying environment in cognitive radio.

The paper [5] proposed a spectrum allocation algorithm based on maximal independent set. In order to reduce the distribution of cycles and the convergence time, they use maximal independent set method in graph theory to solve the problem, in this way, more users will be allocated spectrum in a distribution period as they divide a graph into several independent set groups. Neither does it consider the differences in spectrum efficiency nor the spectral interference differences as well as the aggregated interference constrains as it allocate channels to more users simultaneously. Combination of the above, this paper proposes a maximal weighted independent set-based graph coloring spectrum allocation algorithm in cognitive radio, which reduces the distribution cycles and ensures the feasibility of transmission and improves the utilization rate of the spectrum.

The rest of the paper is organized as follows: in Sect. 2, we introduce the system model and related restraint. The proposed algorithm and the simulation are introduced in Sects. 3 and 4. Finally, the conclusions are presented in Sect. 5.

2 System Model and Related Restraint

The interference graph is established according to the physical model [6], which is based on the encoding and decoding mechanisms at the physical layer in the actual communication system. In the physical model, if and only if the signal to interference plus noise ratio at each receiver reaches a certain threshold, the transmission is successful. It can accurately express the behavior of the physical layer, and this interference model is also believed to be accurate in that it has corresponding coding schemes in the actual communication system.

2.1 Establish the Interference Graph

In this paper, G(V, E) represent the interference graph, V is the set of vertex in graph and each vertex represents a transmission link in the network. E is the set of edge in graph G. Here if two adjacent vertex have an edge between them, it means that there exists interference between the two transmission links when they use the same spectrum.

Independent sets are sets of mutually non-adjacent nodes of a graph, if added to any vertex, it is no longer an independent set, we call it maximal independent set [7]. Maximal weighted independent set may be any one in all the independent sets, this is related to the weight of each vertex. Hence, first we must obtain all the

independent set, and then find out the maximal weighted independent set by calculating the weighted value at each vertex. We obtain the independent set of a graph by first obtaining the minimum vertex cover, and then with the relationship between the minimum vertex cover and the maximal independent set, we find out the maximal independent set of a graph. Cover set h represents a subset of vertex in G and each side has at least one endpoint belongs to K, then K is called a cover set. If any vertex removed from K and it is no longer a cover set, we call it minimum vertex cover.

The calculation of the minimum vertex cover: the Boolean expression, $B = \prod_{i=1}^{n}(v_i + \prod_{u \in N(v_i)} u)$, n is the total vertex in graph G, $N(v_i)$ represents the neighbor vertex. According to the complementary relationship between the maximal independent set and the minimal cover set, we can get the maximal independent set.

We construct the interference graph with the principle in literature [6], and let us assume that the transmissions $i_1 \to j_1$ and $i_2 \to j_2$ are the only transmissions in the network. Then simultaneous transmission is a transmission scenario if and only if

$$\gamma^{2/\alpha} \qquad < \frac{d(i_1,j_2)d(i_2,j_1)}{d(i_1,j_1)d(i_2,j_2)} \tag{1}$$

This is a necessary condition but not a sufficient and necessary condition.

2.2 Related Restraint

We assume that the cognitive radio network is based on interference prohibited spectrum sharing model, and each spectrum is strictly orthogonal, so we do not need to consider the interference to the primary user, only need to consider the aggregated interference when simultaneous transmission happens in a same spectrum. Assume there are k simultaneous transmission links that requesting a spectrum, we note that $X = \{i_1 \to j_1, i_2 \to j_2, \ldots i_k \to j_k\}$, by judging a successful transmission at the receiver, we assign a spectrum to the link $i_n \to j_n$, $n \in \{1, 2, \ldots n\}$. That is, at each receiver, according to literature [6], the signal to interference plus noise ratio at each receiver must satisfy following inequality

$$\frac{\frac{p_n}{d^{\alpha}(i_n j_n)}}{N_0 + \sum_{r=1, r\neq n}^{k} \frac{p_r}{d^{\alpha}(i_r j_n)}} \geq \gamma \tag{2}$$

Before moving on to present our spectrum allocation algorithm in Sect. 3, we must consider the problem of assigning a particular spectrum simultaneously to a set of transmissions toward k links, i.e., we must check the feasibility, and feasibility means there exists a set of positive transmit power levels $p = \{p_1, p_2, \ldots p_k\}$ such that all signal to interference plus noise ratio constraints of the k links are met. Based on the Perron–Frobenius theorem [8], transmission scenario $X = \{i_1 \to j_1, i_2 \to j_2, \cdots i_k \to j_k\}$ is feasible if and only if

$$p(I - F) \geq u \tag{3}$$

The above inequality has a positive component-wise solution p if and only if the maximum eigenvalue of F is less than one. In that case, the Pareto-optimal transmit power vector $p* = (I - F)^{-1}u$ is a nonnegative component wise, whereby

$$F_{rs} = \begin{cases} 0, r = s \\ \gamma \frac{d^{\alpha}(i_r, j_r)}{d^{\alpha}(i_s, j_r)}, otherwise \end{cases} \tag{4}$$

and

$$u = (\gamma N_0 d^{\alpha}(i_1, j_1), \gamma N_0 d^{\alpha}(i_2, j_2), \ldots, \gamma N_0 d^{\alpha}(i_k, j_k)^{\mathrm{T}} \tag{5}$$

Here Pareto-optimal means that if p is a positive power vector that satisfies (3), then $p \geq p*$ component-wise. Due to this fact, Pareto-optimal is a resource allocation state, which expressed that in the case of does not make the distribution result bad, never again have some kind of better way of distribution. Therefore, any other power vector under which simultaneous transmissions of the same set of transmission requests are received successfully at their intended receivers satisfies $p' \geq p*$, component-wise. As a result, assuming $p_{max} < \infty$, transmission scenario $X = \{i_1 \to j_1, i_2 \to j_2, \ldots i_k \to j_k\}$ is feasible if and only if $0 < p_i* < p_{max}$, $i = \{1, 2, \ldots, k\}$, where $p_1, p_2, \ldots, p_k$ represents the transmission power of the each requesting links, d represents the distance, N_0 represents the noise power, γ represents the signal to interference plus noise ratio threshold at each receiver, α represents attenuation factor, I represents identity matrix.

3 The Proposed Algorithm

The available matrix: $L = \{l_{n,m} \mid n, m \in (0, 1)\}_{N \times M}$, indicates the availability of spectrum, where N represents the transmission link, M represents the number of spectrum in the network. $l_{n,m} = 1$ represents link $i_n \to j_n$ can use spectrum m , otherwise not.

The interference matrix: $C = \{c_{n,k} \mid n, k \in (0, 1)\}_{N \times N}$, indicates the interference relationship between two vertexes in the network. $c_{n,k} = 1$ means there exists interference between two links when they use the same channel. $c_{n,k} = 1$ means they have no impact on each other when selecting the spectrum. The interference matrix is a symmetric matrix.

The beneficial matrix: $B = \{b_{n,m}\}_{N \times M}$, $b_{n,m}$ represents the benefits when spectrum M occupied by the cognitive user n.

The allocation matrix: $A = \{a_{n,m} \mid n, m \in (0, 1)\}_{N \times M}$, represents the spectrum M allocated to the link $i_n \to j_n$, Otherwise, the value refers to 0. When $C_{n,k} = 1$, $a_{n,m} \cdot a_{k,m} = 0, \forall 1 \leq n, k \leq N, 1 \leq m \leq M$.

In our proposed algorithm, first we must find out a list of the available links under each spectrum in accordance with the available matrix and then we construct the interference graph and find out the maximal independent set. Unlike in the past, it added to consider the efficiency in the different spectrum as well as the integrated interference when it allocate one spectrum to multiple users simultaneously and power control techniques was used to determine the allocation feasibility. The weights for the each node can be expressed as

$$W_i = \frac{b_{i,m}}{\sum_{j=0}^{M-1} a_{i,j} b_{i,j}}, i \in V_m \tag{6}$$

Here V_M represents a subgraph. In each subgraph, we find out all the independent sets, calculate the weights for each node and select the maximum one to be input parameters to determine the feasibility, in this way, we fully consider the accumulated weight, and take this as a priority when selecting the links; if feasible, the spectrum will be assigned to the maximal weighted independent set that includes one or more nodes. When assigned with spectrum, the assigned users would exit from the allocation process, that is, we must update the available matrix, the allocation matrix and then proceed to the next allocation process. In this way, the assigned links will not participate in the distribution of the next allocation period. Further, by adding the power control technology in the allocation process, the comprehensive interference was reduced. Until all users get allocated, we accomplish our allocation process.

Figure 1 shows the allocation process. The performance of total system reward and fairness among users were defined as follows: Total system reward can be expressed as

$$U = \sum_{n=0}^{N-1} \sum_{m=0}^{M-1} a_{n,m} \cdot b_{n,m} \tag{7}$$

Fairness of distribution can be expressed as

$$F_{fair} = \{\prod_{n=1}^{N} (\sum_{m=1}^{M} a_{n,m} \cdot b_{n,m} + 10^{-4})\}^{\frac{1}{N}} \tag{8}$$

We modify the definition of the total system reward to facilitate the simulations. We use mean reward, i.e., we use formula (9), instead of sum reward in formula (7), the expression is as follows:

$$U_{mean} = \frac{1}{N} \sum_{n=0}^{N-1} \sum_{m=0}^{M-1} a_{n,m} \cdot b_{n,m} \tag{9}$$

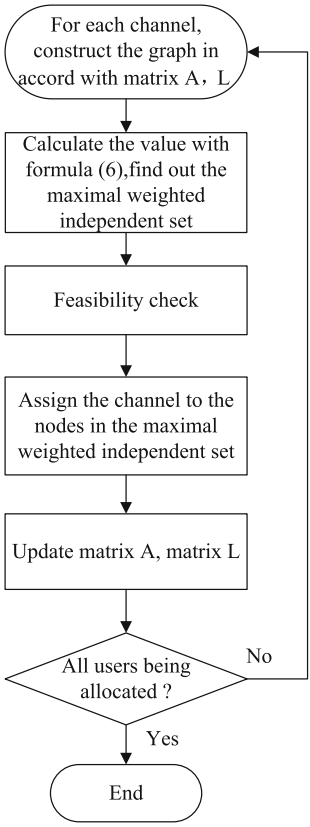

Fig. 1 The flowchart of the allocation process

Table 1 Simulation parameters

Parameters	Value	Parameters	Value
Attenuation factor α	4	The SINR threshold	15 dB
Available spectrum M	10	Beneficial reward	7–14
Requesting links	10–30	Available matrix	Random 0/1
Noise power	−10 dBm	Maximum transmit power	20 mw

4 Simulation

Here we analyze and verify the performance of the proposed algorithm. The simulation parameters are shown in Table 1. The performance of fairness and the total system reward are compared between the proposed algorithms and the CSGC algorithms.

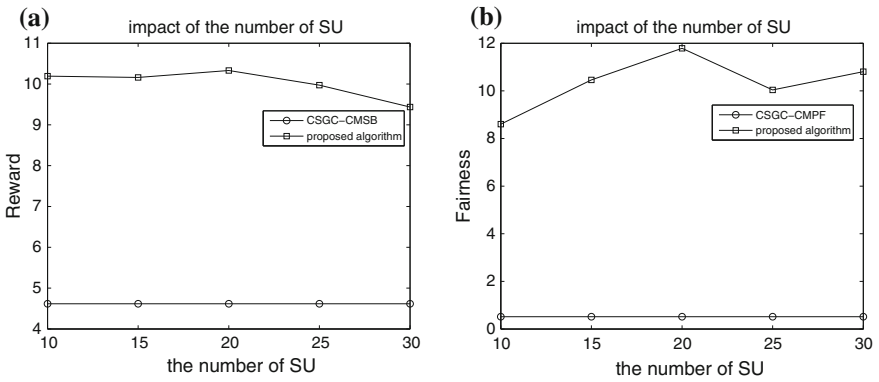

Fig. 2 Comparison of the two algorithm. **a** Comparison of the system reward. **b** Comparison of the fairness

It can be seen from Fig. 2a, as the number of users increases, the system reward of the proposed algorithm performs much better than the CSGC–CMSB algorithm. So the proposed algorithm is considered to be inferior to CSGC algorithm in the system reward.

Figure 2b shows that along with increased number of users, the fairness of the proposed algorithm also performs better than the CSGC–CMPF algorithm. This is because, in the allocation process, the proposed algorithm fully considers the fairness among users in its distribution period.

5 Conclusion

In this paper, a spectrum allocation algorithm in cognitive wireless networks was proposed based on the maximal weighted independent set. Simulation results show that compared with traditional CSGC algorithm, the proposed algorithm improved greatly in the total reward and fairness among users. Besides added with the power control technology, the feasibility of communication is also ensured.

Acknowledgments Shubin Wang (wangshubin@imu.edu.cn) is the correspondent author and this work was supported by the National Natural Science Foundation of China (61261020), and the Natural Science Foundation of Inner Mongolia, China (2012MS0903), and PetroChina Innovation Foundation (2014D-5006-0603), and the Scientific Research Initial Fund for Higher Talents Program of Inner Mongolia University, China.

References

1. Jiang C, Chen Y, Liu KJ, Ren Y (2013) Renewal-theoretical dynamic spectrum access in cognitive radio network with unknown primary behavior. IEEE J Sel Areas Commun 31(3):406–416
2. Berthold U, Fu F, van der Schaar M, Jondral FK (2008) Detection of spectral resources in cognitive radios using reinforcement learning. In: 3rd IEEE symposium on new frontiers in dynamic spectrum access networks, DySPAN 2008. IEEE, pp 1–5
3. Wang W, Liu X (2005) List-coloring based channel allocation for openspectrum wireless networks. In: IEEE vehicular technology conference, vol 62(1). Citeseer, p 690
4. Zheng H, Peng C (2005) Collaboration and fairness in opportunistic spectrum access. In: 2005 IEEE international conference on communications. ICC 2005, vol 5. IEEE, pp 3132–3136
5. Fan L, Liu Y, Tan X, Jiang M (2009) Spectrum allocation algorithm based on graph theory in cognitive radio network. Sci Technol Eng 16:4645–4648
6. Behzad A, Rubin I (2004) Multiple access protocol for power-controlled wireless access nets. IEEE Trans Mobile Comput 3(4):307–316
7. Duffus D, Frankl P, Rodl V (2011) Maximal independent sets in bipartite graphs obtained from boolean lattices. Eur J Comb 32(1):1–9
8. Chang K-C, Pearson K, Zhang T et al (2008) Perron-frobenius theorem for nonnegative tensors. Common Math Sci 6(2):507–520

Hybrid Full-/Half-Duplex Relaying in Cognitive Networks

Zhi Lin, Yueming Cai, Weiwei Yang and Wendong Yang

Abstract In cognitive radio full-duplex (FD) relay networks, self-interference (SI) generated from the relay and harmful interference from secondary user (SU) on primary user (PU) would jointly deteriorate the system performance. In this paper, we analyze the physical layer security issue of a cognitive relay network. Specially, a SU source transmits message to a SU receiver through multi-antenna relay under the interference constraints on PU. In practical, FD and half-duplex (HD) model have its own advantages. Thus, we employ the hybrid protocols that switch adaptively between FD and HD relaying models. The motivation for hybrid adaptive protocols selection comes from trade-off of spectral efficiency and SI suppression: The HD model avoids inherently the SI at the cost of halving the data rate while FD model is spectral efficiency that achieve full data rate, but it suffers from severe SI. We propose a combination of hybrid protocols selection and secure on–off transmission to enhance the system performance. Simulation results demonstrate that our hybrid strategy with secure on–off transmission outperforms the system design that utilizes either relay mode.

Keywords Physical layer security · Full-duplex · Cognitive networks · Self-interference

1 Introduction

Recently, cognitive radio technology has become a hot research issue, as it can figure out spectrum scarcity problem by allowing unlicensed user to share the same spectrum with licensed user [1–4]. To achieve it, cognitive radio technology usually adopts underlay, overlay or interweave approaches [5]. For the underlay approach, the

Z. Lin (✉) · Y. Cai · W. Yang · W. Yang
College of Communication Engineering, PLA University of Science and Technology, Nanjing, China
e-mail: lz945@sina.cn

Q. Liang et al. (eds.), *Proceedings of the 2015 International Conference on Communications, Signal Processing, and Systems*, Lecture Notes in Electrical Engineering 386, DOI 10.1007/978-3-662-49831-6_28

secondary user (SU) is permitted to utilize the same spectrum with the primary user (PU) as long as the interference is below a certain threshold that the PU can tolerate.

Owing to the broadcast nature of wireless channels which makes communication inherently accessible, security becomes one of the most important issues in wireless communications. Unlike conventional cryptographic system, physical layer security (PLS) technology exploits the randomness of wireless channels to achieve secure transmission. Since cooperative relay communication system usually employs half-duplex (HD) protocol, it will cause 50% lose in spectral efficiency (SE) while two time slots are intended to transmit same data packet. Therefore, full-duplex (FD) model has attracted extensive attention, which transmits and receives signals in the entire bandwidth [6]. A range of theoretical researches have showed advantages of FD model over HD model in terms of either having increased throughput and decreased outage probability [7]. However, even after cancelation technology, FD relay networks would still be suppressed by the large power difference between the FD received antennas and low-power received signals from a remote destination. Some works also indicate that FD model may not always outperform HD model, while hybrid scheme that switches adaptively between FD and HD models can be employed to effectively suppress the self-interference (SI) and achieve better secrecy performance [8].

To sum up, the researches above only investigate the secrecy performance in either FD or cognitive system, and little works have been done for cognitive FD relay networks. Moreover, hybrid FD/HD strategy is not widely considered in relay networks. In this paper, we investigate the secrecy performance of hybrid FD/HD relay network, in which hybrid strategy is employed to suppress SI and secure on–off transmission is adopted to control the interference from SU on PU under a certain threshold.

Notation Bold uppercase and lowercase letters denote matrices and vectors, respectively. $\mathrm{E}\{\bullet\}$ denotes the expectation operator.

2 System Model

In this paper, we consider a communication scenario in cognitive relay network. The system shown in Fig. 1 consists of a SU source node S, a relay node R, a SU legitimate receiver D and N primary users (PU) $P_n\{n \in 1, \ldots, N\}$, in which all nodes are equipped with single antenna. In particular, we assume the direct path between S and D is very weak, but the direct channel still exists. To extend coverage, system employ relay to enhance performance. $h_{SD}, h_{SR}, h_{RD}, h_{SP_n}, h_{RP_n}$ and h_{RR} denote the channel coefficients of S-D, S-R, R-D, S-P_n, R-P_n and self-interference links respectively, and these channels are Rayleigh random variables with parameter λ. We assume all the channels involved are considered to remain constant during one operation period. The normalized transmit power at the source and relay are subjected to individual power constraints $P_S \leq 1$ and $P_R \leq 1$.

Fig. 1 Hybrid relay model

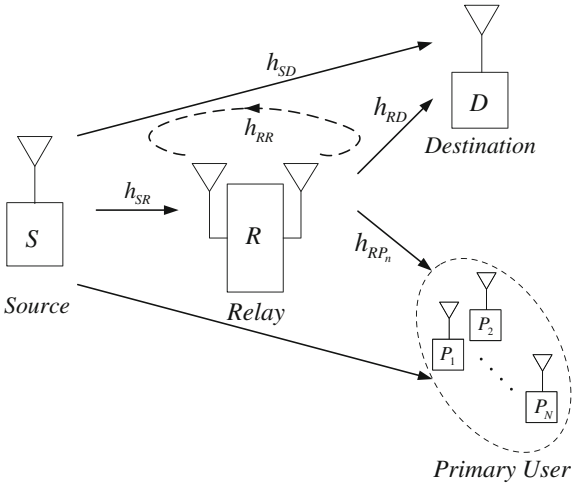

2.1 Full-Duplex Model

The relay would receive and forward signals simultaneously in FD model, which enhance the spectral efficiency. However, the communication is degraded by SI from relay transmission to relay reception.

At time slot t, source S sends private message $x(t)(\mathrm{E}\left\{|x(t)|^2\right\}=1)$, R receives $r(t)$ and transmit signal $u(t)$. Thus the received signals at relay, SU destination and primary users P_n can be expressed as

$$\begin{aligned} r(t) &= \sqrt{P_S}h_{SR}(t)x(t)+\sqrt{P_R}h_{RR}(t)u(t)+n_R(t) \\ y_D(t) &= \sqrt{P_S}h_{SD}(t)x(t)+\sqrt{P_R}h_{RD}(t)u(t)+n_D(t) \\ y_{P_n}(t) &= \sqrt{P_S}h_{SP_n}(t)x(t)+\sqrt{P_R}h_{RP_n}(t)u(t)+n_{P_n}(t) \end{aligned} \tag{1}$$

The power of white Gaussian noise at relay, D and P_n are subject to $\mathrm{E}\left\{|n_R(t)|^2\right\}=\mathrm{E}\left\{|n_D(t)|^2\right\}=\mathrm{E}\left\{|n_{P_n}(t)|^2\right\}=\sigma^2$.

According to (1), the relay would utilize cancelation technology to eliminate the part of $\sqrt{P_R}h_{RR}(t)u(t)$. Practically, complete suppression is impossible to achieve because of imperfect channel estimation and signal processing. Then we analyze $u(t)$ in two different relay protocols.

With the AF protocol, the relay amplify received signals by factor $\beta>0$. We normalize the factor $\beta$to guarantee the transmit power P_R at the relay. The received signal power at the relay is $\mathrm{E}\left\{|r(t)|^2\right\}=P_S|h_{SR}|^2+P_R|h_{RR}|^2+\sigma^2$. The amplification factor in AF protocol is obtained as

$$\beta = \sqrt{\frac{1}{P_S|h_{SR}|^2 + P_R|h_{RR}|^2 + \sigma^2}} \tag{2}$$

We find that the upper bound of the factor $\beta < 1/\left(\sqrt{P_R}|h_{RR}|\right)$ makes sure the stability of relay and avoids the oscillation. With DF protocol, the transmit signals of relay can be written as

$$u(t) = \begin{cases} \beta r(t-1) & \text{with AF,} \\ x(t-1) & \text{with DF.} \end{cases} \tag{3}$$

In FD model, the SU destination decodes the signals $u(t)$ from $y_D(t)$ and treats the weak direct signals $x(t)$ as interference.

2.2 Half-Duplex Model

Traditionally, the HD relay communication is usually divided into two time slots. Source transmits signals $x(2t)$ at even time slot, relay receives signals $r(2t)$ at even time slot and transmits signals $u(2t+1)$ at odd time slot. Thereby, the received signals at relay, SU receiver and PU P_n can be expressed as

$$r(2t) = \sqrt{P_S}h_{SR}(2t)x(2t) + n_R(2t) \tag{4}$$

$$\begin{aligned} y_D(2t) &= \sqrt{P_S}h_{SD}(2t)x(2t) + n_D(2t) \\ y_D(2t+1) &= \sqrt{P_R}h_{RD}(2t+1)x(2t+1) + n_D(2t+1) \end{aligned} \tag{5}$$

$$\begin{aligned} y_{P_n}(2t) &= \sqrt{P_S}h_{SP_n}(2t)x(2t) + n_{P_n}(2t) \\ y_{P_n}(2t+1) &= \sqrt{P_R}h_{SR}(2t+1)u(2t+1) + n_{P_n}(2t+1) \end{aligned} \tag{6}$$

The signal processing in HD model is similar with (2) and (3), except that the loop interference is neglected.

3 Performance Analysis

In our hybrid relaying cognitive networks, to eliminate the interference from SU on PU, we should define an interference constraint to protect the PU communication. In particular, we consider the on–off transmission: SU decides whether or not to transmit signals according to the instantaneous interference on N PU. Transmission would take place while the interference IN_{P_n} is smaller than a certain threshold Γ. Using this on–off transmission scheme is necessary for improving energy efficiency and protecting PU communication.

3.1 Secure on–off Transmission

Since h_{ij} are Rayleigh random variables and $|h_{ij}|^2$ are exponential variables with parameter λ. The PDF and CDF of $|h_{ij}|^2$ can be written as $f_X(x) = \lambda e^{-\lambda x}$ and $F_X(x) = 1 - e^{-\lambda x}$. The instantaneous interference is expressed as

$$IN_{P_n} = P_S |h_{SP_n}|^2 + P_R |h_{RP_n}|^2 + \sigma^2 \tag{7}$$

Under the assumption of high SNR region and $P_S = P_R = P$, we define $Y = |h_{SP_n}|^2 + |h_{RP_n}|^2$, the PDF of the variable $Y$is written as

$$f_Y(y) = \lambda^2 y e^{-\lambda y} \tag{8}$$

Then we define a new variable that the variable Y multiple by constant P, $G = PY$, the PDF and CDF of G are obtained as

$$\begin{aligned} f_G(g) &= \frac{\lambda^2}{P^2} g e^{-(\lambda g/P)} \\ F_G(g) &= 1 - e^{-(\lambda g/P)} \left(\frac{\lambda g}{P} + 1 \right) \end{aligned} \tag{9}$$

From (7) and (8), the probability that interference on a certain PU is below the threshold can be expressed as

$$\Pr(IN_{P_n} \le \Gamma) = 1 - e^{(-\lambda/P)\Gamma} \left(\frac{\lambda}{P} \Gamma + 1 \right) \tag{10}$$

Note that there are N different primary users, using order statistics, we can obtain the following probability

$$\Pr\left(\max_{n=1,\ldots,N} \{IN_{P_n}\} \le \Gamma \right) = \left[1 - e^{(-\lambda/P)\Gamma} \left(\frac{\lambda}{P} \Gamma + 1 \right) \right]^N \tag{11}$$

Then we will consider the secrecy rate of different protocols. First, we define the channel SNR as $\gamma_{ij} = |h_{ij}|^2 / \sigma^2$. In FD model, the received signal power at destination D is expressed as $\mathrm{E}\left\{ |y_D(t)|^2 \right\} = P_S |h_{SD}|^2 + P_R |h_{RD}|^2 + \sigma^2$. The signal-to-interference and noise ratio (SINR) at relay and SU destination are given as

$$\gamma_R = \frac{P_S \gamma_{SR}}{P_R \gamma_{RR} + 1} = \frac{\gamma_{SR}}{\gamma_{RR} + 1} \quad \textit{and} \quad \gamma_D = \frac{P_R \gamma_{RD}}{P_S \gamma_{SD} + 1} = \frac{\gamma_{RD}}{\gamma_{SD} + 1} \tag{12}$$

We can obtain the received SNR of AF and DF protocols in FD model as

$$\gamma_{FD} = \begin{cases} \frac{\gamma_R \gamma_D}{\gamma_R + \gamma_D + 1} & \text{with AF,} \\ \min\{\gamma_R, \gamma_D\} & \text{with DF.} \end{cases} \tag{13}$$

And we assume the FD model uses the maximum power at source and relay ($P_S = P_R = 1$). In HD model, since the source and relay transmit double time compared with FD model, HD model should double power budget ($P_S = P_R = 2$) to equalize the average power in the two models.

In HD model, the destination receive two independent signals at two time slots, we assume the destination apply maximum ratio combination (MRC). The received SNR in HD model with MRC can be written as

$$\gamma_{HD} = = \begin{cases} 2\gamma_{SD} + \frac{4\gamma_{SR}\gamma_{RD}}{2\gamma_{SR} + 2\gamma_{RD} + 1} & \text{with AF,} \\ \min\{2\gamma_{SR}, 2\gamma_{SD} + 2\gamma_{RD}\} & \text{with DF.} \end{cases} \tag{14}$$

We define $\hat{\gamma}_{HD} = \sqrt{1 + \gamma_{HD}} - 1$ to represent the equivalent SNR of transformed expression of HD model, because it can make expressions similar in two modes. The secrecy rates of FD and HD models are given by

$$\begin{aligned} C_{FD} &= \log_2(1 + \gamma_{FD}) \Pr\left(\max_{n=1,\ldots,N} \{IN_{P_n}\} \le \Gamma | P = 1 \right) \\ C_{HD} &= \frac{1}{2} \log_2(1 + \gamma_{HD}) \Pr\left(\max_{n=1,\ldots,N} \{IN_{P_n}\} \le \Gamma | P = 2 \right) \\ &= \log_2(1 + \hat{\gamma}_{HD}) \Pr\left(\max_{n=1,\ldots,N} \{IN_{P_n}\} \le \Gamma | P = 2 \right) \end{aligned} \tag{15}$$

3.2 Hybrid Relaying Strategy

In this section, we propose a hybrid strategy to utilize the advantages of two models. Necessary condition for the FD model to outperform HD model is that the loop interference received SNR γ_{RR} is below threshold Γ_{RR}.

$$C_{FD} \ge C_{HD} \quad \text{if and only if } \gamma_{RR} \le \Gamma_{RR} \tag{16}$$

To optimize the performance, we apply hybrid relaying mode that switches to a proper model according to the instantaneous CSI. The secrecy rate is given by

$$C_{Hybrid} = \log_2(1 + \max\{\gamma_{FD}, \hat{\gamma}_{HD}\}) \tag{17}$$

To further analyze the hybrid strategy, we would obtain the optimal switching boundary Γ_{RR} between models.

As demonstrated below, the SI channel SNR γ_{RR} is the key parameter for switching between FD and HD models. According to (14), the HD model is preferred over the FD model if $\min\{\gamma_R, \gamma_D\} \leq \hat{\gamma}_{HD} = \sqrt{1+\gamma_{HD}} - 1$, otherwise, the FD model outperforms HD model and the switching boundary Γ_{RR} is obtained as

$$\Gamma_{RR} = \begin{cases} \frac{\gamma_{SR}(\gamma_D - \hat{\gamma}_{HD})}{\hat{\gamma}_{HD}(\gamma_D + 1)} - 1 & \text{with AF,} \\ \frac{\gamma_{SR}}{\hat{\gamma}_{HD}} - 1 & \text{with DF.} \end{cases} \tag{18}$$

Proof First, we can find that if $\gamma_D \leq \hat{\gamma}_{HD} = \sqrt{1+\gamma_{HD}} - 1$, the secrecy rate of HD model always outperforms FD model whatever switching boundary Γ_{RR} is defined. While $\gamma_D > \hat{\gamma}_{HD} = \sqrt{1+\gamma_{HD}} - 1$, according to (17), we deduce the upper bound of γ_{RR} to achieve $C_{FD} > C_{HD}$ in AF and DF protocols. To demand (18), the upper bound of γ_{RR} is the optimal switching boundary Γ_{RR}.

4 Simulations

In this section, we present simulation and numerical results to illustrate the performance analysis. For convenience, we assume threshold SNR of PU is $\Gamma = 3$ dB, and the noise power is $\sigma^2 = 1$.

In Fig. 2, we present the secrecy rate comparison against SI channel SNR γ_{RR} between our hybrid scheme with FD and HD models of different protocols. We let $\gamma_{SD} = \gamma_{RR} - 10$ dB, $\gamma_{SR} = 3$ dB and $\gamma_{RD} = 6$ dB. We can find that hybrid scheme outperforms FD and HD schemes because of hybrid strategy, which can enhance security and suppress SI in relay networks. Furthermore, while the SI channel SNR

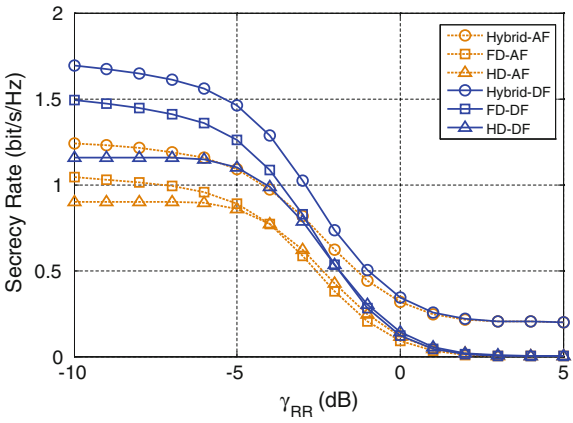

Fig. 2 Secrecy rate versus SI channel SNR γ_{RR} with different schemes

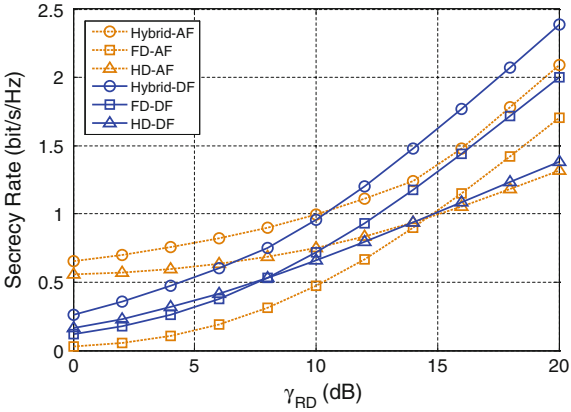

Fig. 3 Secrecy rate versus channel SNR γ_{RD} with different schemes

increases, the hybrid scheme guarantees higher secrecy rate, while the FD and HD schemes decline quite seriously especially for large γ_{RR}.

Figure 3 presents the secrecy rate of different schemes versus R-D channel SNR γ_{RD}, where we assume $\gamma_{SR} = \gamma_{RD} - 5\,\text{dB}$, $\gamma_{SD} = 3\,\text{dB}$ and $\gamma_{RR} = -2\,\text{dB}$. It is intuitively shown in Fig. 3 that hybrid scheme yields higher secrecy rate than FD and HD schemes. While the secrecy rate threshold increases, the optimal protocols also change. It also can be observed from Fig. 3 that the scheme with DF protocol would perform better than the scheme with AF protocol in low SNR regions, while in high SNR regions, the performance reverse.

5 Conclusions

In this paper, we analyze the performance of hybrid full-/half-duplex relaying strategy in cognitive networks. To eliminate the self-interference of FD model and enhance the spectral efficiency, we propose on–off transmission strategy and hybrid strategy to utilize the advantages of FD and HD models. Specially, if interference of source and relay on PU is beyond some threshold, the outage of transmission would occur to protect the PU communication. Furthermore, we deduce the optimal self-interference threshold to adaptively switch between FD and HD models on different protocols. Simulation results demonstrate that the hybrid FD/HD relaying is an attractive technique because of significant improvement of our scheme.

Acknowledgments This work is supported by the National Natural Science Foundation of China (No.61371122 and No.61471393), and the China Postdoctoral Science Foundation under a Special Financial Grant No. 2013T60912.

References

1. Kolodzy PJ (2006) Interference temperature: a metric for dynamic spectrum utilization. Int J Netw Manage 16(2):103–113
2. Sakran H, Shokair M, Nasr O et al (2012) Proposed relay selection scheme for physical layer security in cognitive radio networks. IET Commun 6(16):2676–2687
3. Lee J, Wang H, Andrews JG, Hong D (2011) Outage probability of cognitive relay networks with interference constraints. IEEE Trans Wirel Commun 10(2):390–395
4. Zou Y, Yao YD, Zheng B (2011) Cognitive transmissions with multiple relays in cognitive radio networks. IEEE Trans Wirel Commun 10(2):648–659
5. Goldsmith A, Jafer SA, Maric I, Srinivasa S (2009) Breaking spectrum gridlock with cognitive radio: an information theoretic perspective. Proc IEEE 59(5):894–914
6. Ju H, Oh E, Hong D (2009) Improving efficiency of resource usage in two-hop full duplex relay systems based on resource sharing and interference cancellation. IEEE Trans Wirel Commun 8 (8):3933–3938
7. Chen G, Gong Y, Xiao P (2015) Physical layer network security in the full-duplex relay system. IEEE Trans Forensics Secur 10(3)
8. Zhang Z, Chai X, Long K, Vasilakos AV, Hanzo L (2015) Full duplex techniques for 5G networks: self-interference cancellation, protocol design, and relay selection. IEEE Commun Mag 53(5):128–137

Low-SNR Energy Detection Based on Relevance in Power Density Spectrum

Xuemeng Wang, Tao Peng and Wenbo Wang

Abstract Energy detection is the most commonly used spectrum sensing method in cognitive radio because of its simplicity and there is no need for priori information. However, the performance of energy detection will seriously deteriorate under low-SNR condition. Various improved methods have been proposed to solve this problem, but at the expense of high complexity. This paper introduces an energy detection method based on the relevance in power density spectrum. It uses an iterative method to precisely estimate the noise power without any priori information and makes use of the relevance between occupied frequency points to detect low-SNR signals effectively. Simulation results show that the proposed method has better performance and lower complexity than traditional methods.

1 Introduction

Rapid development of wireless communications results in a large demand for radio spectrum resources. But fixed spectrum allocation policy causes a horrible waste of it [1]. Cognitive radio technology uses a more flexible way called dynamic spectrum access to improve the spectrum utilization. Spectrum sensing, as a key technology of cognitive radio, aims to find out the spectrum holes [2]. Without interference to the primary user(PU), these spectrum holes can be used by the second users to improve the utilizable ratio. There are three main spectrum sensing methods: energy detection, cyclostationary feature detection, and matched filtering detection [3–5].

X. Wang (✉) · T. Peng · W. Wang
Key Laboratory of Universal Wireless Communications,
Beijing University of Posts and Telecommunications, Beijing, China
e-mail: xuemeng@bupt.edu.cn

T. Peng
e-mail: pengtao@bupt.edu.cn

W. Wang
e-mail: wbwang@bupt.edu.cn

Q. Liang et al. (eds.), *Proceedings of the 2015 International Conference on Communications, Signal Processing, and Systems*, Lecture Notes in Electrical Engineering 386, DOI 10.1007/978-3-662-49831-6_29

Energy detection is widely used because it is simple and does not need any priori information.

The performance of energy detection deteriorates seriously under low-SNR condition, various improved algorithms have been proposed to solve this problem, but at the expense of increased complexity or longer observation time. Paper [6] introduces an improved energy detection method which outperforms the classic energy detection scheme. However, it needs a long observation time when detecting a low-SNR signal. Algorithm proposed in paper [7] has good performance in low-SNR conditions but has high complexity. In addition, they are both conducted on the premise of a known noise power. Zixuan Lao has put forward a totally blind spectrum sensing method which combines noise estimation with energy detection and the simulation results show that it can obtain a good performance if the observation time is longer than a certain value [8]. However, its performance will deteriorate as the SNR declines like other energy detection methods. Traditional algorithms neglect the relevance between adjacent frequency points in power density spectrum. The bandwidth of a signal is always wider than the frequency resolution so the powers of occupied frequency points are continuously greater than the noise power, but noise has no relevance between adjacent frequency points so the powers of unoccupied frequency points will float around the noise power. We can use this difference to detect low-SNR signals if we know the noise power.

In this paper, we propose a new iterative algorithm combining noise estimation and relevance-based energy detection. It does not need any priori information including the noise power and has low complexity. What is more, it has good performance under low-SNR condition. The simulation results show that it works well even when the SNR of signal is smaller than −5 dB.

The rest part of the paper is organized as follow. Section 2 introduces the system model, including signal generating and the calculation of test statistic. The relevance-based energy detection algorithm will be proposed in Sect. 3. In Sect. 4, we present the simulation parameters and detection results to demonstrate the superiority of the proposed algorithm. The conclusion and future work are shown in Sect. 5.

2 System Model

We study the energy detection methods on signals within a wide band, the signals have multiple bandwidths and powers. Sample the time signal with frequency f_s greater than the Nyquist frequency. Denote N as the number of sampling points each time and N_t as the time span of observation which means sampling is repeated N_t times to get the average power of each frequency point.

Assume that the cognitive system has no priori information about signals. We can only judge the presence of PU by detecting the average power of each frequency point and there are only two different results: occupied and unoccupied in that the energy detection can be reduced to a binary hypothesis-testing model. H_0 denotes the frequency point which is unoccupied and H_1 denotes those being occupied.

Denote ${\sigma_\omega}^2$ as the power of the additive white Gaussian noise, ${\sigma_s}^2$ as signal power, $\gamma = {\sigma_s}^2/{\sigma_\omega}^2$ as the signal-to-noise ratio (SNR), and $Y_k(k = 1, 2, \ldots, N)$ as the result of FFT to sampling points each time. The test statistic is given by

$$T_k = (1/N_t)\sum_{N_t} \left|Y_k\right|^2 \tag{1}$$

T stands for the average power of frequency points and roughly follows the normal distribution based on the central-limit theorem [9].

$$\begin{aligned} H_0 &: T \sim Normal({\sigma_\omega}^2, {\sigma_\omega}^4/N_t) \\ H_1 &: T \sim Normal({\sigma_\omega}^2 + {\sigma_s}^2, ({\sigma_\omega}^2 + {\sigma_s}^2)^2/N_t) \end{aligned} \tag{2}$$

If we choose V_{th} as the energy detection threshold, the probability of false alarm is $P_f = P\left\{T > V_{th}\left|H_0\right.\right\}$, the detection rate is $P_d = P\left\{T > V_{th}\left|H_1\right.\right\}$, and $P_e = P_f P(H_0) + (1 - P_d)P(H_1)$ is the error rate. They are commonly used parameters to measure the performance of an energy detection method.

3 The Proposed Relevance-Based Energy Detection Algorithm

We can use the relevance between adjacent frequency points in power density spectrum to detect signals with relatively high SNR and low SNR. But relevance-based method has higher complexity than traditional methods, a two-stage method can be used to solve this. We can use a traditional algorithm to detect signals with relatively high SNR first and estimate the noise power at the same time. After that relevance-based method will be applied to detect signals which cannot be detected by traditional methods.

3.1 The First Stage Energy Detection

There are two most commonly used energy detection criteria, constant false alarm rate (CFAR) and constant detection rate (CDR). Denote $V_{th,CFAR}$ as threshold calculated by CFAR criteria, $V_{th,CDR}$ as threshold calculated by CDR criteria and they are given below. P_f in (3) is the target false alarm rate and P_d in (4) is the target detection rate, γ in (4) is the minimum detectable SNR, $Q(\cdot)$ is the complementary distribution function of the standard Gaussian.

$$V_{th,CFAR} = \frac{Q^{-1}(P_f){\sigma_\omega}^2}{\sqrt{N_t}} + {\sigma_\omega}^2 \tag{3}$$

$$V_{th,CDR} = \frac{Q^{-1}(P_d)\sigma_\omega{}^2(1+\gamma)}{\sqrt{N_t}} + \sigma_\omega{}^2(1+\gamma) \tag{4}$$

The performances of CDR and CFAR do not differ much, but CDR has one more target value γ and different values will bring about different performances. In order to decrease the uncertainty brought by target value, we choose CFAR as the first energy detection method. Because there is no priori information about signals, we use the totally blind spectrum sensing method mentioned above to calculate the first threshold and estimate the noise power. First, we set an initial threshold $V_{th,1}$ to detect the frequency points and estimate the noise power according to the detection result; and then we use the estimated noise power to get a new threshold $V_{th,2}$ and detect the frequency points again. Repeat the process until the difference between two contiguous thresholds is no longer greater than a presupposed value, $\left|V_{th,1} - V_{th,2}\right| < \lambda V_{th,2}$ (a smaller λ indicates a higher accuracy and more iterations). Then use the latest threshold to detect the frequency points.

3.2 The Location of Undetected Signal

The powers of occupied frequency points are commonly greater than the unoccupied ones. But the opposite situation could happen because of the existence of variance especially under low-SNR condition. In addition, in the first energy detection, frequency points whose powers are not greater than the threshold are detected to be unoccupied. So after the first detection, there must be many points whose powers close to V_{th} detected to be unoccupied. How to find the location of an undetected signal becomes a problem.

The principle of a moving average window is to take the average of variables within the window as the midpoint's value in the new sequence, so it can work as a low-pass filter. Denote seq_1 as the sequence of points first detected to be noise. We can use a moving average window on seq_1 and then get a new sequence, name it as seq_2. The variance of seq_2 is much smaller than seq_1. So if there exists an undetected signal, the variables around the location of the signal are supposed to be greater than others, which makes signal easier to be distinguished from noise. Denote S_w as the size of moving average window, variables in seq_2 as T_{seq_2}. We can get the probability distribution function of T_{seq_2} according to the central limit theorem.

$$\begin{aligned} H_0 &: T_{seq_2} \sim Normal(\sigma_\omega{}^2, \sigma_\omega{}^4/(S_w N_t)) \\ H_1 &: T_{seq_2} \sim Normal((1+\gamma)\sigma_\omega{}^2, (1+\gamma)^2\sigma_\omega{}^4/(S_w N_t)) \end{aligned} \tag{5}$$

Denote *loc* as the location of the max value in seq_2, normally *loc* is the most probable location of an undetected signal if it does exist. The moving average window makes the borders between signal and noise more smoothed and harder to detect. So

seq_2 is only used to find the probable location of undetected signals. The following relevance-based detection is conducted on the original sequence seq_1.

3.3 Noise Estimation and Relevance-Based Detection

In seq_1, as a single frequency point, the probability of an unoccupied one's power greater than ${\sigma_\omega}^2$ is 0.5. The probability of an occupied frequency point's power greater than ${\sigma_\omega}^2$ is proportional to N_t and γ. In formula (6), if we set $N_t = 200$, $\gamma = -8$ dB, then $H_1 : P(T > {\sigma_\omega}^2) = 0.973$. If the detection threshold is set to be ${\sigma_\omega}^2$, almost a half of the unoccupied points will be false alarmed. But considering the case of several consecutive unoccupied frequency points, the probability of most of their powers greater than ${\sigma_\omega}^2$ is very small. Compared with unoccupied ones, the probability will be much greater for several consecutive occupied frequency points, just as formula (8) indicates. $\Phi(\cdot)$ is the distribution function of standard Gaussian. Figure 1 illustrates the situation described above.

$$H_1 : P(T > {\sigma_\omega}^2) = \Phi\left(\frac{((1+\gamma){\sigma_\omega}^2 - {\sigma_\omega}^2)\sqrt{N_t}}{(1+\gamma){\sigma_\omega}^2}\right) = \Phi\left(\frac{\gamma\sqrt{N_t}}{1+\gamma}\right) = 0.973(N_t = 200, \gamma = -8\,dB) \tag{6}$$

$$H_0 : P(T > {\sigma_\omega}^2) = \Phi(0) = 0.5 \tag{7}$$

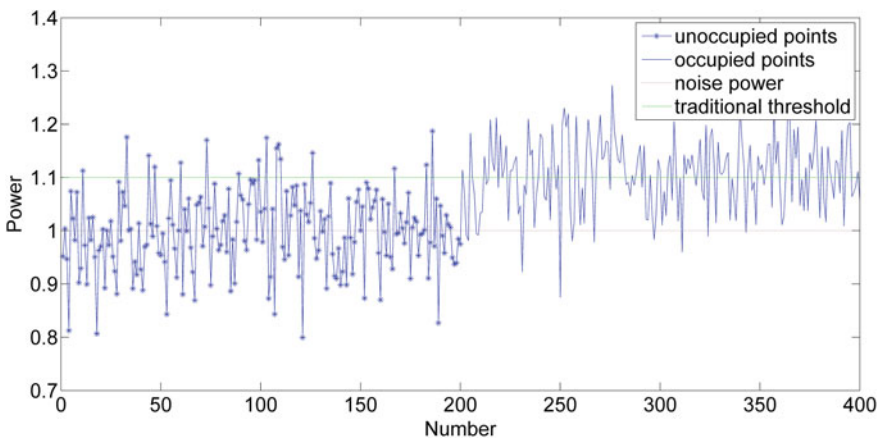

Fig. 1 Occupied and unoccupied cases

The probability of more than 90 % consecutive points' power greater than ${\sigma_\omega}^2$ in two different cases:

$$\begin{aligned} H_0 &: C_{10}^9 0.5^9(1-0.5) + C_{10}^{10} 0.5^{10} = 0.0107 \\ H_1 &: C_{10}^9 0.973^9(1-0.973) + C_{10}^{10} 0.973^{10} = 0.9716 \end{aligned} \tag{8}$$

The occupied frequency points are very likely to be greater than ${\sigma_\omega}^2$ consecutively because of the relevance between them, we can use this to distinguish signal from noise. In seq_1, search from the location *loc* to both sides. If there exists an undetected signal, the powers of nearby undetected frequency points are almost all greater than ${\sigma_\omega}^2$, but there is still exceptions. So if a point's power is lower than ${\sigma_\omega}^2$ in the search, we should analyze the adjacent frequency points to judge if it is an exception. For example, if there are more than nine whose powers greater than ${\sigma_\omega}^2$ in the subsequent ten points, we can confirm them occupied and continue searching. Else stop searching and update the detection results.

There is no priori information about the noise power ${\sigma_\omega}^2$, so we use an iterative algorithm to estimate it. First, we calculate the mean power of seq_1 and denote it as $\hat{\sigma}_\omega^2$. Use $\hat{\sigma}_\omega^2$ to detect seq_1 with method above. After that, we can get a new unoccupied sequence ${seq_1}'$ and estimated noise power ${\hat{\sigma}_\omega}^{2'}$. If the difference between $\hat{\sigma}_\omega^2$ and ${\hat{\sigma}_\omega}^{2'}$ is greater than a presupposed value, detect ${seq_1}'$ again as before. The cyclic process will not finish until the difference between two contiguous estimated noise powers is smaller than the presupposed value. Figure 2 shows the flow diagram of iterative algorithm. ρ is the iteration precision.

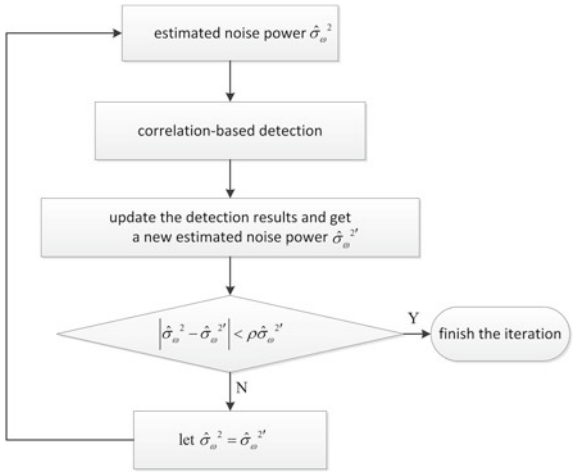

Fig. 2 The flow diagram of iterative algorithm

4 Simulation Results

In this section, the simulation results are listed to prove the performance improvement of relevance-based energy detection method compared with traditional methods in paper [8]. Denote ICDR as the joint iterative algorithm of CDR energy detection and noise estimation in [8], ICFAR as the joint iterative algorithm of CFAR energy detection and noise estimation, RBED as relevance-based algorithm proposed in this paper.

Signals with different SNRs and bandwidths are simulated in a 50 M bandwidth including a low-SNR CDMA signal. The bandwidth and SNR of CDMA are changeable so we can observe their influence on detection performance, while other signals have fixed bandwidth and SNR higher than 0 dB. The other parameters are as follows. Frequency resolution $f_r = 10$ KHz, the number of frequency points $N = 5000$, observation time $N_t = 200$, and the size of moving average window $S_w = 10$. We set the target false alarm rate $P_f = 0.005$ in CFAR and target detection rate $P_d = 0.95$, minimum detectable SNR $\gamma = -5$ dB in CDR because repeated simulations show that they have best performances with these parameters.

First, we study the effect of noise on the detection performance. Keep the other parameters fixed and change the SNR of CDMA from -10 to 0 dB. Figure 3 shows the detection rate on CDMA. When SNR is smaller than -5 dB, the traditional methods have bad detection performances, but RBED still can detect the signal completely even under -8 dB. When the SNR is smaller than -8 dB, the performance of RBED will decline either, but is still much better than traditional methods.

RBED can increase the detection rate effectively as Fig. 3 shows. Normally, the increase of detection rate will cause higher false alarm rate at the same time. But we can see from Fig. 4 that RBED does not increase the false alarm rate. That is because if there is no signal undetected, only a few frequency points will be judged

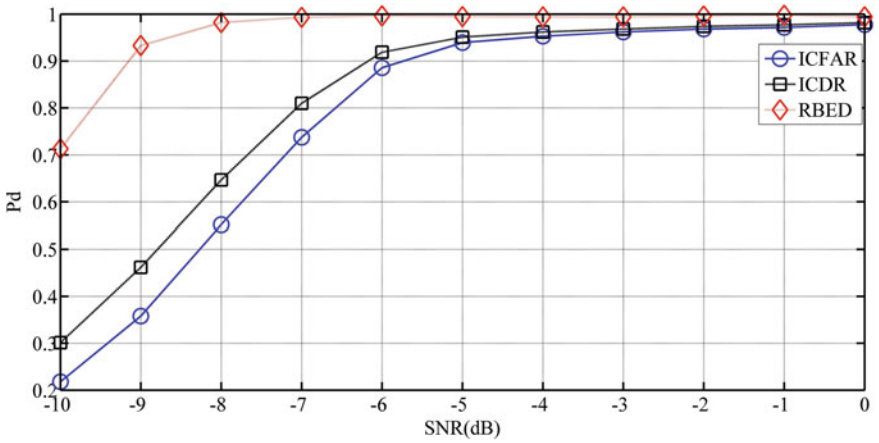

Fig. 3 The detection rate on the low-SNR signal

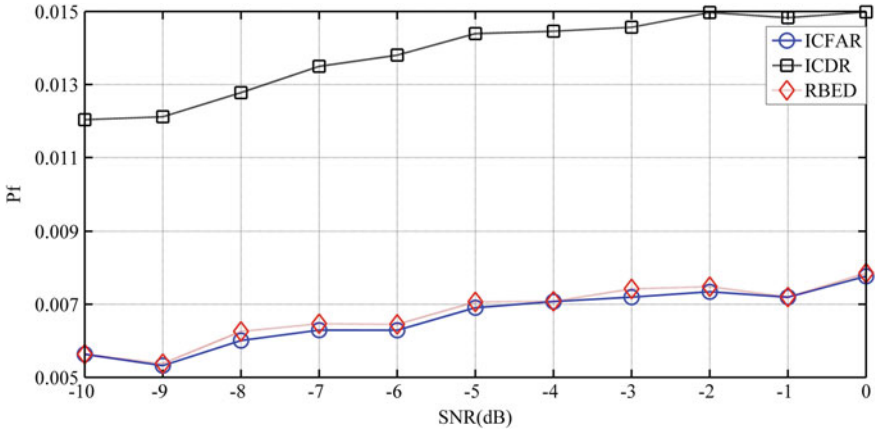

Fig. 4 The false alarm rate

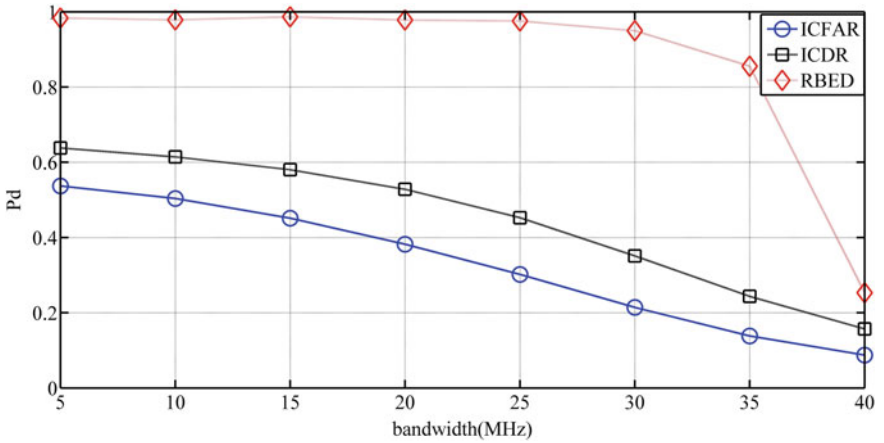

Fig. 5 The detection rate on the low-SNR signal

to be occupied and the estimated noise power almost has no change. The iteration will be terminated soon so the false alarm rate will not increase.

The detection results listed above have already proved that RBED have better performance under low-SNR condition. Next we will research whether the bandwidth of CDMA affect the detection results by fixing the SNR of CDMA as -8 dB and the iteration precision ρ as 0.0001.

Figure 5 shows that the detection rates of traditional methods on the low-SNR signal declined with increasing bandwidth. RBED has good performance when the bandwidth is smaller than 30 MHz. The occupancy rate of low-SNR signal is proportional to its bandwidth. If the occupancy rate is too high, there will be many frequency points remain undetected in the first energy detection and the estimated

noise power will be much higher than the real value. Setting the starting value of noise power in the iteration process too high will result in inaccurate noise power estimation which leads to poor detection performance. A feasible solution for that is decreasing the iteration precision with the cost of more iteration times.

5 Conclusions

In this paper, a relevance-based energy detection method is proposed. It is easy to implement and has low complexity. The simulation results prove that this method has better performance compared with traditional energy detection methods because it can effectively detect low-SNR signals. In addition, this method will not increase the false alarm rate. But the performance of RBED will also be declined when the SNR is lower than −8 dB or the occupancy rate of the low-SNR signal is too high. Further study can be conducted in the future.

References

1. FCC (2002) Spectrum policy task force report, FCC 02-155
2. Cao Lili, Zheng Haitao (2012) Balancing reliability and utilization in dynamic spectrum access. IEEE/ACM Trans Networking 20(3):651–661
3. Sobron I, Diniz PSR, Martins WA (2015) Energy detection technique for adaptive spectrum sensing. IEEE Trans Commun 63(3):617–627
4. Shen JC, Alsusa E (2013) Post-combining based cyclostationary feature detection for cognitive radio over fading channels. In: Global communications conference (GLOBECOM)
5. Wang Pu, Sahinoglu Z, Pun Man-On (2012) Persymmetric parametric adaptive matched filter for multichannel adaptive signal detection. IEEE Trans Sig Process 60(6):3322–3328
6. Lopez-Benitez M, Casadevall F (2010) Improved energy detection spectrum sensing for cognitive radio. IET Commun 6(8):785–796
7. Aly, OAM (2013) Two-stage spectrum sensing algorithm for low power signals in cognitive radio. In: Electronics, communications and photonics conference(SIECPC)
8. Lao Zixuan, Liu Ziyang, Peng Tao (2013) Totally-blind spectrum sensing: a joint iterative algorithm of noise estimation and energy detection. J Electron Inf Technol 35(8):1958–1963
9. Yuan Long, Xing Lu, Peng Tao (2014) An iterative spectrum sensing algorithm based on accurate noise estimation. J Electron Inf Technol 36(3):655–661

A Comprehensive Framework to Evaluate the Utilization of Spectrum Resource

Sun Jian and Jinnan Zhang

Abstract As the industries based on spectrum were developing rapidly in recent decades, spectrum management is getting more complex and difficult. Aside for technical factors, other aspects need to be considered. The report ITU-R SM.2012-2 took economic aspects into account. It is urgent to set up a new framework for spectrum management. Evaluation on technology, economic and other field is valuable for spectrum management in China. This paper builds a novel spectrum management framework on the basis of big data. The objective of the model is to evaluate the efficiency of the utilization of spectrum resource. The framework classifies spectrum resource into two kinds commercial spectrum and non-commercial spectrum. Each kind of spectrum can be evaluated by several indices. The indices contain four dimensions: technology, micro economy, macro economy and sustainability. The application result of this framework in Ningbo is presented in this paper to illustrate its validity.

Keywords Spectrum resource · Spectrum management · Economics · Utilization efficiency

1 Introduction

Wireless services are developing at a speed beyond people's expectation, especially IMT technology, which has been updating from 2G–4G. While data traffic demand is growing faster than network capacity grows. GSMA estimated that in 2020

S. Jian (✉) · J. Zhang
Institute of Information Photonics and Optical Communications,
Beijing University of Posts and Telecommunications, Beijing, China
e-mail: sjyanger@163.com

J. Zhang
e-mail: zhangjinnan@bupt.edu.cn

Q. Liang et al. (eds.), *Proceedings of the 2015 International Conference on Communications, Signal Processing, and Systems*, Lecture Notes in Electrical Engineering 386, DOI 10.1007/978-3-662-49831-6_30

demand for IMT service spectrum would be 1600–1800 MHz [1]. As service based on spectrum is becoming prosperous and its economic value begins to emerge, the disadvantage of allocating spectrum by administrative measures is obvious: administrative allocation measure considers more of regulations than utilization, the value of spectrum is not carefully calculated nor fully realized [2].

Spectrum in China has been managed administratively for decades, along with explosive developing of wireless services, which causes two serious problems in spectrum industry, one is that spectrum utilization is not balanced, the other is that spectrum business distribution is not reasonable. For example, 700 MHz frequency band is far from busy while public mobile communication frequency band is almost 100 % occupied. To increase spectrum's utilization efficiency, one way is to invent technique like MIMO or DSA [3, 4], which can make fixed bandwidth carry more data. The other way is to change spectrum management policy according to marketing environment, eliminating low value industry to make room for high value industry, like 700 M frequency band used to adopt analog technique, in recent decades it has transformed to digital technique [5]. This paper focuses on market solutions.

Market regimes play more important role in recent decades [6]. The existing market approaches are varied, one approach is licensed approach and the other is the open access model. There has been some debates about the merit of these two extremes [7, 8], but the basis of the approaches and almost all effective spectrum management regimes is about the evaluation of the spectrum utilization. No matter deciding the auction bid or changing the use of some frequency bands, bidders, or spectrum regulators need to know how the frequency is used and the value of it. Evaluation of spectrum utilization is the foundation of spectrum market and spectrum allocation.

Current spectrum utilization evaluation mostly focuses on technical parameters. ITU-R SM.2256 proposed economic aspect consideration on spectrum management, but the knowledge is not systematic. Besides, Ningbo Radio Authority proposed several indices on spectrum evaluation [9], which is practical but the coverage is not wide enough. The evaluation system in [10] focuses mostly on qualitative aspects rather than quantifiable aspects. This paper considers their results and also puts more indices into consideration, such as technology, economy, and sustainability, proposing a new framework to evaluate spectrum utilization and the value of specific frequency band.

The rest of the article is organized as follows: Sect. 2 presents theoretical foundation of the spectrum utilization evaluation framework. Section 3 presents the framework, including the four kinds of indices and definition of commercial and non-commercial spectrum, cost, income, and value of each kind of spectrum. Three applications of the framework in Ningbo are presented in Sects. 4, and 5 draws the conclusions.

2 The Foundation of the Evaluation Framework

There are four principles of building our framework [10]: First, the indices should be comprehensive, covering up as many aspects as possible, to avoid the disadvantages of existing spectrum resource evaluation frameworks. Second, the framework should be built on the properties of spectrum. Spectrum is electromagnetic wave and it is invisible, which makes it hard to evaluate its utilization. Third, the indices should be computable and quantifiable, so that the results from different conditions can be compared. Last, the framework should be directive, reflecting the trend of spectrum utilization and management.

According to the four principles above, the framework takes four aspects into consideration. The most important aspect is technology. Technical indices such as frequency range or spectrum occupancy rate can influence the band's economic value mostly. Besides, all spectrum regulation institutions make management measures according to technical indices.

Except for technical condition, spectrum users and administrators need to know how much the spectrum values and how spectrum utilization affects economy, in order to put spectrum to better use. So this framework brings in micro and macro economy indices. There are several methods to estimate the value of spectrum, this paper refers to [11]. This method takes spectrum resource as a general production element in the market. Like land resource and other natural resources in the market, spectrum resource has a price that depends on demand-and-supply-curve. The macro economy indices reflect influence between spectrum-based industry and national economy.

As radio technology is updating rapidly, reallocation of spectrum resource is more often than before. The reallocation process of spectrum can be several years long and complicate. To evaluate the value of spectrum resource in future, the framework introduces sustainability indices. Sustainability indices also evaluate how much resource we can use in the future and what is the cost of using it.

3 The Spectrum Resource Utilization Evaluation Framework

The framework contains four kinds of indices, technology, micro economy, macro economy, and sustainability. Technology and sustainability indices emphasize on spectrum's properties and use. Economy indices emphasize on spectrum's value in the market. The importance of each kind of indices may be different in different conditions. Users can select influential indices from the framework according to practical application.

There are three judging standards in this framework [12]: whether the industry's main products or services use spectrum as carrier; whether the industry is making profits; whether spectrum brings direct or indirect profit for the industry. Normally,

Table 1 Technology indices

Num	Index	Formula	Classification
A1	Radio station growth rate	$\left(\frac{BSNum_{Current\ Year}}{BSNum_{Last\ Year}} - 1\right)$	Spatial domain
A2	Radio station spatial density	$\frac{BSNum_{district}}{Area_{district}}$	Spatial domain
A3	Radio station frequency density	$\frac{BSNum_{Frequency\ Band}}{Width_{Frequency\ Band}}$	Frequency domain
A4	Frequency band occupancy	$\frac{\sum_{Band} width_{Occupied}}{Width_{Band}}$	Frequency domain
A5	Maximum continuous idle spectrum	$\max\left(Width_{Idle\ Spectrum}\right)$	Frequency domain
A6	Radio station time density	$\frac{Num_{Active\ Radio\ Station}}{Hour_{Duration}}$	Time domain
A7	Channel occupancy	$\frac{Num_{Effective\ Signal}}{Num_{Scan}}$	Time domain
A8	Complaint ratio	$\frac{Num_{Complaints}}{Num_{User}}$	Order domain
A9	Investigation ratio	$\frac{Num_{Solved\ Complaints}}{Num_{Total\ Complaints}}$	Order domain
A10	Registered signal ratio	$\frac{Num_{registered\ Signal}}{Num_{Total\ Signal}}$	Order domain
A11	Technique efficiency	$\frac{Amount_{Valid\ Data}}{Width_{Frequency\ Band}}$	Technology domain

spectrum used in public mobile communication, satellite communication, radio broadcast is commercial. Spectrum used in public services like railway transportation, weather forecast, national security is non-commercial.

Commercial spectrum utilization can be evaluated by four kinds of indices, but non-commercial spectrum do not provide direct economic value and its impact on macroeconomic situation is hard to evaluate, only technology and part of sustainability indices can be applied to non-commercial spectrum. Definitions and explanations of indices are listed in Table 1.

There are some commonly used indices in telecommunication and radio monitoring industry, which can be introduced directly into the framework. Normally, these indices are classified into spatial domain, frequency domain, time domain, and code domain. In practice, radio order is a potential condition to guarantee the effectiveness of the communication system, and order is an important aspect to consider in radio management. For these two reasons, this paper adds order domain into the framework. As indices in code domain vary greatly in different fields, this paper uses a universal index to evaluate transmission efficiency in different systems. Numerator of A11, amount of valid data represents data received (Table 2).

Table 2 Micro economy indices

Num	Index	Formula	Unit
B1	Cost	$\frac{Cost}{Width_{Frequency\ Band}}$	$\frac{Yuan}{MHz}$
B2	Income	$\frac{Income}{Width_{Frequency\ Band}}$	$\frac{Yuan}{MHz}$
B3	Spectrum license fee	$\frac{Fee_{Spectrum\ License}}{Width_{Frequency\ Band}}$	$\frac{Yuan}{MHz}$
B4	Input–output ratio	$\frac{Income}{Cost}$	Null

Cost of natural resources like land, water, or spectrum is hard to decide. In some way they are priceless. In another way, people use spectrum as raw material to produce services, and charge for these services. The more work of processing spectrum involves, the higher cost is. Spectrum's commercial value equals income minus cost. Usually spectrum users hope for higher value, which means higher profit.

For commercial spectrum, this paper defines cost as all the money takes to provide spectrum-based services, including three parts described in the formula below

$$Cost_{Commercial\ Spectrum} = Cost_{production} + Cost_{processing} + Cost_{marketing} \tag{1}$$

Production cost represents the cost to get spectrum resource, like price paid in an auction or spectrum license fee. Sometimes, spectrum management organization may attach some additional conditions to spectrum license. Cost caused by these additional conditions is also included in production cost. Processing cost represents the cost to turn spectrum into service, like research and development cost, infrastructure cost, cost to keep services running. Marketing cost represent the cost to sell spectrum productions, like marketing cost, staff cost.

In public mobile communication, spectrum is the carrier of service, but in factories or ports, spectrum is used as a supporting way to improve production efficiency or avoid safety accidents. Therefore, there are two methods to calculate income of commercial spectrum. For industries the spectrum produces direct commercial value, formula of income is as below:

$$\begin{aligned} Income_{ComSpec-direct} = {} & Income_{ser} + Income_{cooper} \\ & + Income_{adv} + Income_{lease} \end{aligned} \tag{2}$$

Service income represents revenue received in service, like 3G or 4G service fee. Cooperation income represents revenue received in cooperation, like telecom operators and internet companies cooperation fee. Advertisement income represents revenue received in offering advertisement for other products, like advertisements

in FM broadcast. Lease income represents revenue received in renting spectrum to others.

For industries that spectrum is used as a supporting resource, income can be calculated as below:

$$Income_{Commercial\ Spectrum-indirect} = Income_{Efficiency\ Improvement} + Income_{Avoided\ Loss} \quad (3)$$

$$Income_{Efficiency\ Improvement} = \left(\sum_{i=1}^{n} (N_i + OLD_i) \cdot \overline{p} - \sum_{i=1}^{n} (S_i + O_i) - F - \frac{D-L}{Y} \cdot n \right) \quad (4)$$

$$Income_{Avoided\ Loss} = \left(\sum_{n=1}^{\infty} P_n \cdot n \cdot \bar{L} - \sum_{i=1}^{n} (S_i + O_i) - F - \frac{D-L}{Y} \cdot n \right) \quad (5)$$

i: the *i*th year
r: discount rate, fixed value
n: time limit of license, fixed value
S: staff cost
D: device cost
L: residual value
Y: tenure of use, fixed value
F: frequency occupancy fee
N: annual production after spectrum applying
OLD: annual production before spectrum applying
$\bar{p}$: average price of product
O: operation cost
$\bar{L}$: average loss of an accident
P_n: probability of happening n accidents per year

Efficiency improvement income represents revenue received by using spectrum. For example, at Ningbo port, efficiency of loading and uploading has been improved greatly since digital modulation technology was applied. Avoid loss income represents revenue received in avoiding safety accidents, like in chemical plants radio is used to detect hazard.

For non-commercial spectrum, like spectrum used in weather forecast, military defense, there is no income, because income of non-commercial spectrum cannot be accurately calculated. Cost formula of non-commercial spectrum is as below:

$$Income_{Non-\text{commercial Spectrum}} = \frac{\frac{D-L}{Y} \cdot n + \sum_{i=1}^{n} (S_i + O_i) + F}{\sum_{i=1}^{n} (i+r)^i \cdot n} \quad (6)$$

Table 3 Macro Economy Indices

Num	Index	Formula	Unit
C1	Income growth rate	$\frac{Income_{This\ Year} - Income_{Last\ Year}}{Income_{Last\ Year}}$	Null
C2	Subdivision industry ratio	$\frac{Output_{Subdivision\ Industry}}{Output_{whole\ Industry}}$	Null
C3	GDP joint coefficient beta	$\ln Y = C + \beta \ln X + \varepsilon$	Null

Table 4 Sustainability Indices

Num	Index	Formula	Unit
D1	Available spectrum ratio	$\frac{Width_{unoccupied\ Frequency\ Band}}{Width_{Allocated\ Frequency\ Band}}$	Null
D2	Industry transfer time	The time needed to change the use of frequency band	Year
D3	Industry transfer cost	The money needed to change the use of frequency band	Yuan
D4	Expected cost	$\frac{Cost_{Developing\ New\ Frequency\ Band}}{Width_{New\ Frequency\ Band}}$	$\frac{yuan}{MHz}$
D5	Expected income	$\frac{Income_{Developing\ New\ Frequency\ Band}}{Width_{New\ Frequency\ Band}}$	$\frac{yuan}{MHz}$
D6	Expected input-output ratio	$\frac{Income_{Expected}}{Cost_{Expected}}$	Null

i: the *i*th year
r: discount rate, fixed value
n: time limit of license, fixed value
S: staff cost
L: residual value
D: device cost
Y: tenure of use, fixed value
F: frequency occupancy fee (Table 3)

C3 reflects how much spectrum's contribution in telecommunication and broadcast industry influences national GDP [12] (Table 4).

D3 cost of industry transfer can be estimated by:

$$Cost_{Industry\ Transfer} = Cost_{compensation} + Cost_{Devices\ Adjustment} + Cost_{business\ Loss} + Cost_{Potential\ Loss} \tag{7}$$

Cost of devices adjustment including discarding or adjusting old devices and buying new devices. Cost of potential loss including redlined patents and so on.

4 Assessment of Spectrum Resource Utilization in Ningbo

This section compares spectrum utilization between different business and users in Ningbo area. The indices may illustrate how spectrum is used and what to do with spectrum management. Some of the indices are not shown because they are not suit for the selected frequency bands.

There are three public mobile communication companies in China, China mobile, China unicom, and China telecom. Ningbo Radio Authority offered radio monitoring data of the three companies Figs. 1, 2, 3, 4, 5, 6, 7, 8, and 9.

Analyzing the charts above, conclusions are as follows: in year 2014 radio station growth rate of China Mobile is significantly higher than that of the other two

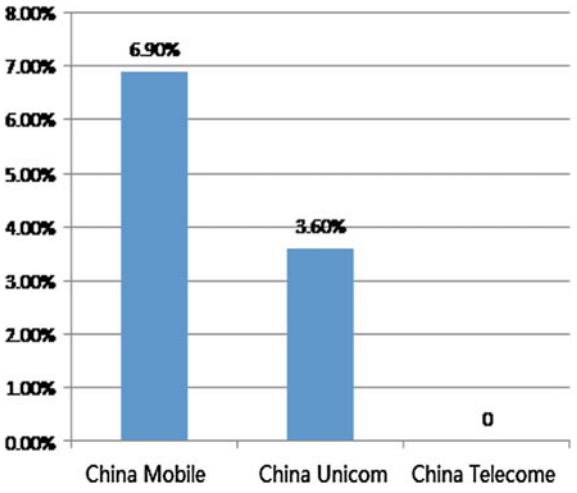

Fig. 1 Radio station growth rate

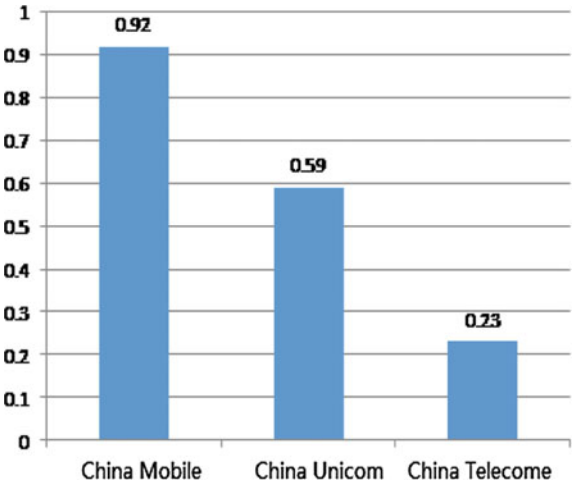

Fig. 2 Radio station spatial density

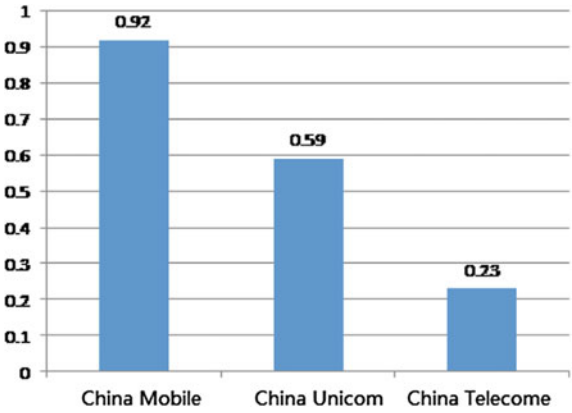

Fig. 3 Radio station frequency density

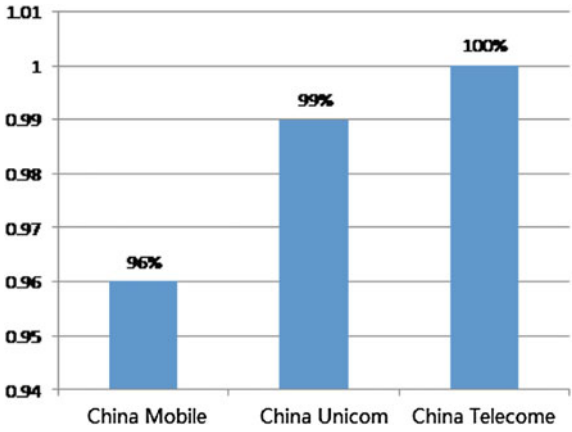

Fig. 4 Frequency band occupancy

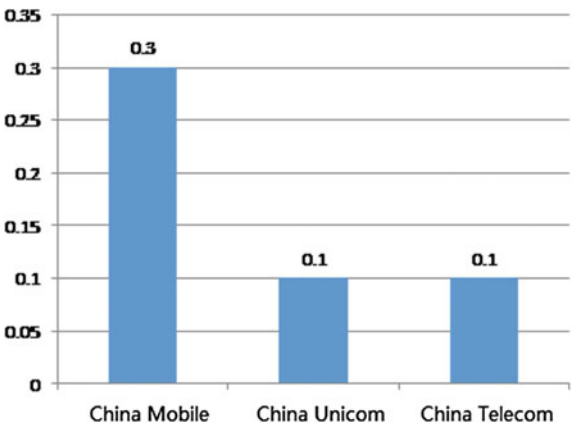

Fig. 5 Max continuous idle spectrum

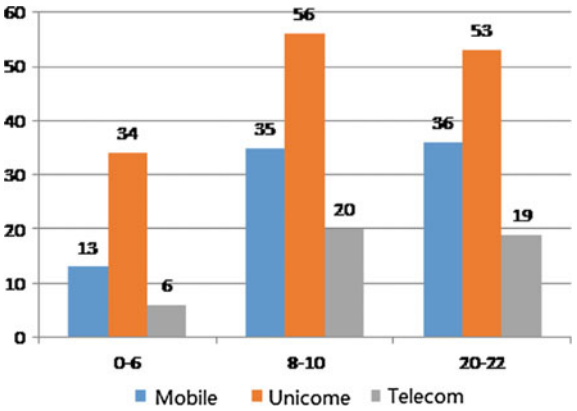

Fig. 6 Radio station time density

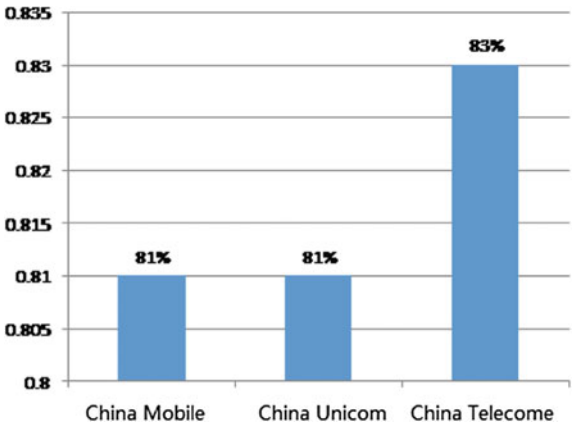

Fig. 7 Registered signal ratio

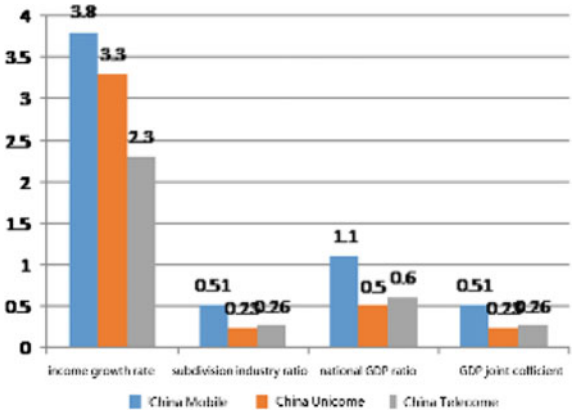

Fig. 8 Macro economy indices

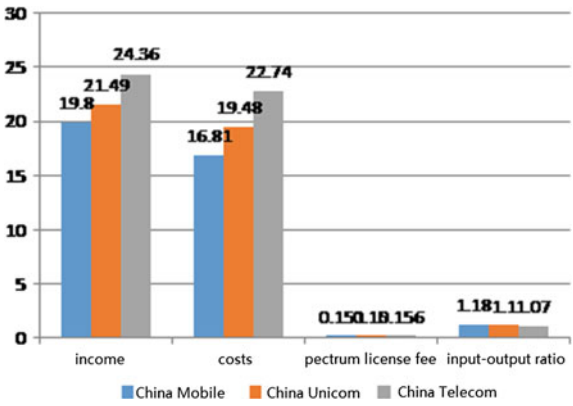

Fig. 9 Micro economy indices

companies, which is related to its deployment in 4G. Their frequency band occupancy, channel occupancy is close to 100 %, Maximum continuous idle spectrum is little, indicating public mobile communication frequency band is quite busy. Indices difference of the three companies is small, which means communication industry pattern in Ningbo is stable. China Mobile's economy performance is better because its input–output ratio, income growth rate, subdivision industry ratio are higher.

We select public mobile communication business and broadcast and wireless television business for comparison, using China Mobile's mobile communication frequency band in Ningbo and 700 MHz broadcast and wireless television frequency band(700 MHz band for short). The range is Figs. 10, 11, 12, 13, 14, 15, and 16.

Conclusions are: utilization efficiency of 700 M band is far lower than mobile communication band. 700 M band's Radio station growth rate has been 0 for many years, while mobile communication band's radio station growth rate has been high. Mobile communication band's radio station frequency density is several times as

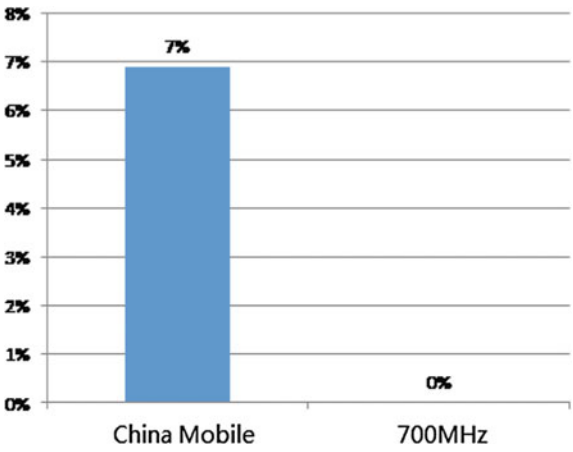

Fig. 10 Radio station growth rate

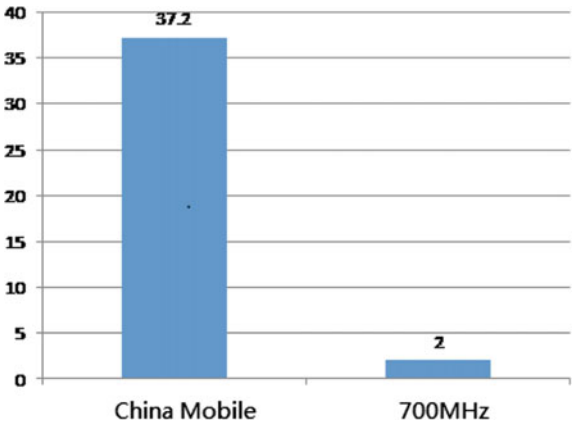

Fig. 11 Radio station frequency density

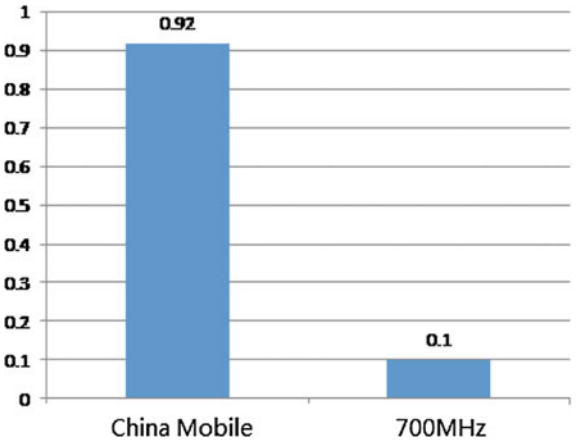

Fig. 12 Radio station spatial density

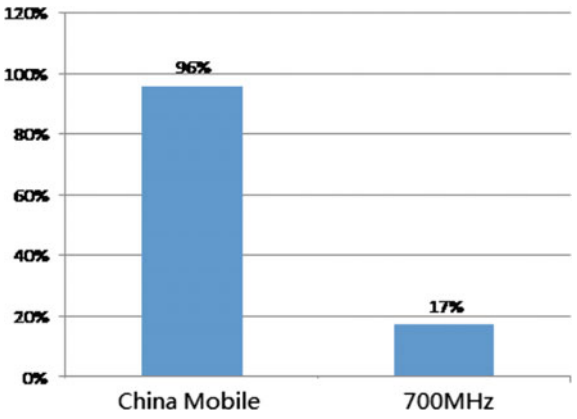

Fig. 13 Frequency band occupancy

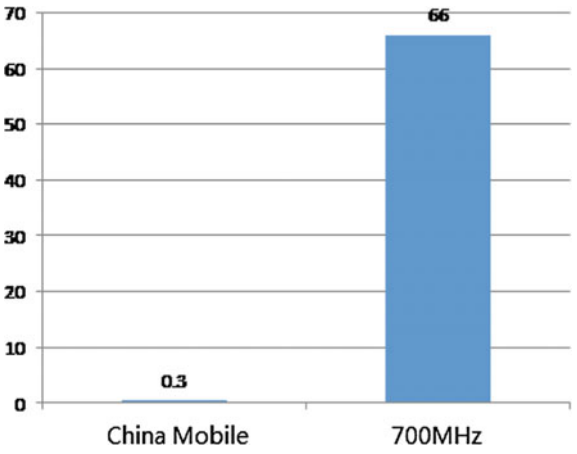

Fig. 14 Max continuous idle spectrum

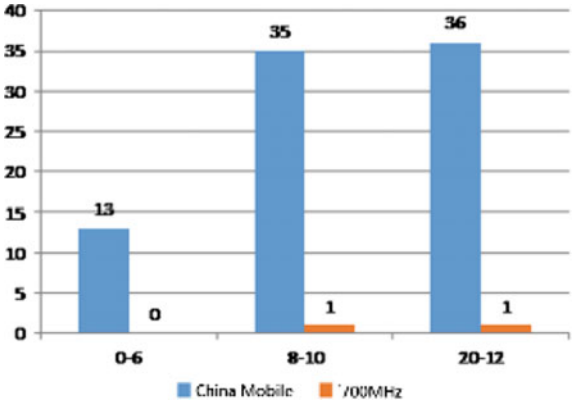

Fig. 15 Radio station time density

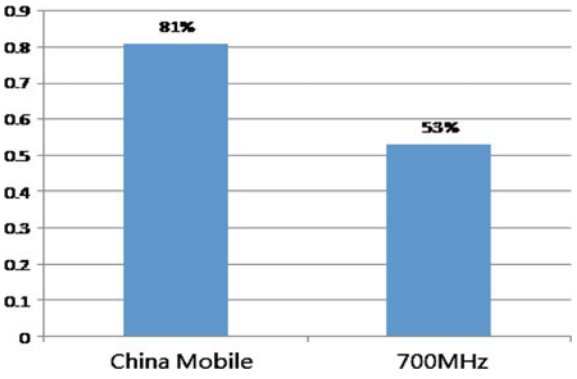

Fig. 16 Registered signal ratio

much as 700 M band, its radio station spatial density is higher, too. Mobile communication band's frequency band occupancy remains at close to 100 % for a long time, averagely 700 M band's frequency band occupancy is below 20%. Maximum continuous idle spectrum in 700 M band is 66 M, which means more than half of the band is idle, along with little changing radio station time density, we can conclude that for most time during the day, most 700 M frequency band is idle. Registered signal ratio of 700 M band is much lower than that of public communication band, suggesting that 700 MHz band is offering continuous room for illegal occupation. Analog TV to digital TV conversion process in China started at 2003, and will complete at 2020, this schedule is much slower than most developed countries in the world.

As for industrial users evaluation, we picked Ningbo port group and Sinopec Zhenhai Refining & Chemical Company Ningbo branch(ZRCC for short).

Ningbo Port Group and ZRCC are two representative companies who are using spectrum for dispatch communication and industrial use Figs. 17, 18, 19, 20, 21, 22, and 23.

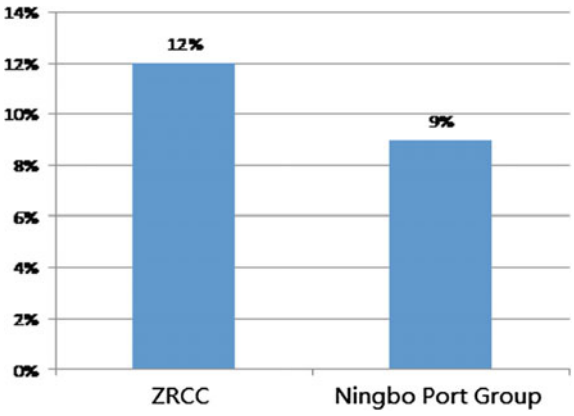

Fig. 17 Radio station growth rate

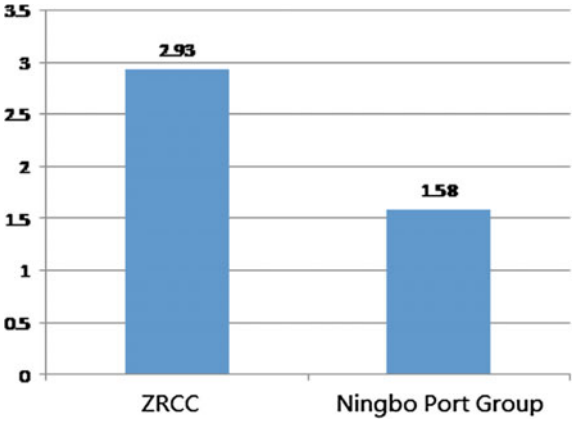

Fig. 18 Radio station spatial rate

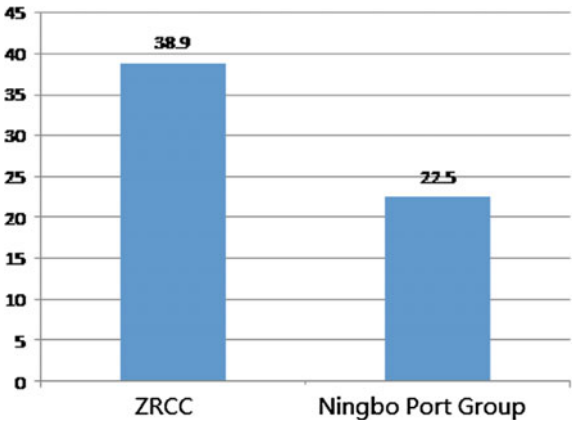

Fig. 19 Radio station frequency density

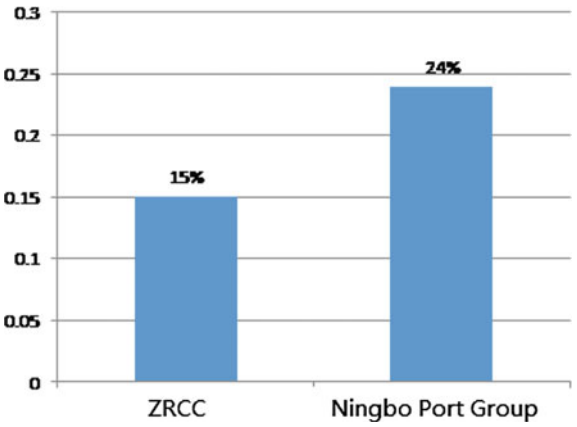

Fig. 20 Frequency band occupancy

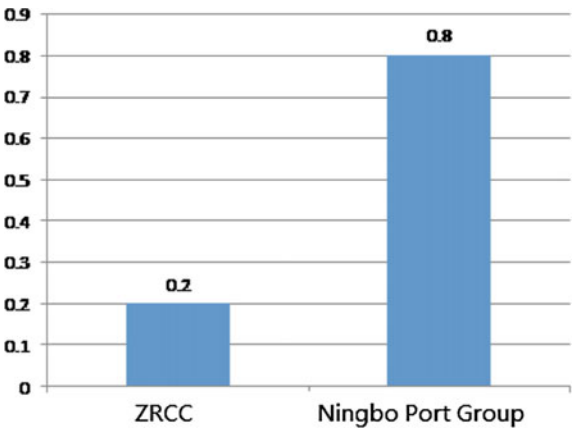

Fig. 21 Max continuous idle spectrum

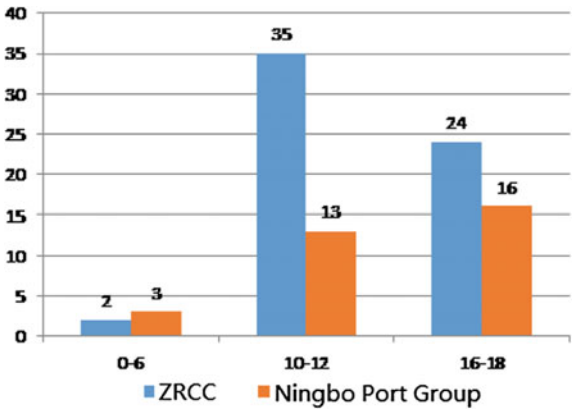

Fig. 22 Radio station time density

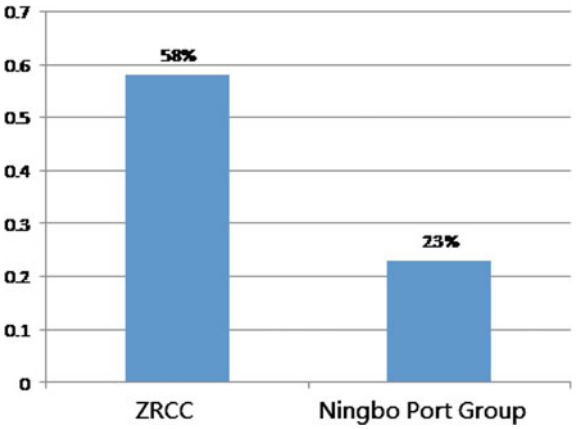

Fig. 23 Registered signal ratio

Table 5 The spectrum value of several frequency bands

Year	Frequency band	Value (million/MHz)
2014	China mobile	313
2014	China Unicom	201
2014	China Telecom	162
2014	Ningbo Port Group	55

Conclusions are: Radio station growth rate, radio station spatial density, and radio station frequency density of ZRCC are higher than those of Ningbo Port Group, this is because ZRCC's production base is centralized in space. Both of their frequency band is idler during the night, but diurnal difference of ZRCC's frequency band occupancy is bigger, because ports are open and ships coming from other countries may anchor at any time. ZRCC's registered signal ratio is higher because Ningbo Port Group uses both public frequency band and exclusive frequency band, many ships using 150 MHz band are not registered in local database.

By calculating collected data from annual report of telecom companies and government, we list spectrum value of several frequency bands in Table 5.

5 Conclusion

This paper proposed a novel framework to evaluate the utilization of spectrum, by analyzing indices in technology, micro economy, macro economy, and sustainability, and we give three examples of applying the framework on practical spectrum utilization evaluation in Ningbo. Results showed that in Ningbo area, spectrum utilization is not balanced, some frequency bands need authority intervention and rearrangement.

By applying this framework, users and regulators can get a comprehensive picture of how spectrum is used and how much spectrum values, this framework can be reference for spectrum auction or spectrum management.

References

1. Pang J, Wang T, Li J et al (2013) Spectrum requirements estimation for the future imt systems: current work and way forward. Commun Netw 5
2. Review of Radio Spectrum Management, Martin Cave, 2002. ofcom.org.uk
3. Adachi K, Adachi F, Nakagawa M (2007) On cellular MIMO spectrum efficiency. IEEE Veh Technol Conf, 417–421
4. Chakravarthy V, Li X, Wu Z et al (2009) Novel overlay/underlay cognitive radio waveforms using Sd-Smse framework to enhance spectrum efficiency-part I: theoretical framework and analysis in awgn channel. IEEE Trans Commun 57(12):3794–3804
5. Kishi M, Tajima J, Kanmuri N et al (1983) Digital signal processing spectrum inversion for analog speech channels. IEEE Trans Veh Technol 32(4):254–259
6. Doyle L, Forde T (2007) Towards a fluid spectrum market for exclusive usage rights. In: 2nd IEEE International symposium new frontiers in dynamic spectrum access networks, DySPAN, pp 620–632
7. Lehr W, Crowcroft J (2005) Managing shared access to a spectrum commons. In: First IEEE International symposium new frontiers in dynamic spectrum access networks, Dyspan, pp 420–444
8. Hazlett TW (2006) The spectrum-allocation debate: an analysis. IEEE Internet Comput 10 (5):68–74
9. Liu L, Chen R (2013) Construction of big data model for radio management. In: Proceedings of the national radio application and management
10. Li Y, Shen J (2006) The tentative ideas of establishing the radio management capability comprehensive evaluation index system. China Radio 1:23–28
11. Lunndborg M (2013) Spectrum pricing—theoretical approaches and practica, In: Summit LS (ed) Implementation, Lichtenau, 3 July 2013
12. Yan J, Lv T (2011) Study on the economic value assessment system of radio spectrum. J Beijing Univ Post Telecommun: Soc Sci Ed 4:51–56. doi:10.3969/j.issn.1008-7729.2011.04.010

Part V
Interference Alignment

Internetwork Interference Avoidance Mechanism for WBAN Based on Nested-Complex-Superframe Structure

Boya Zhang, Weixia Zou, Feng Wei and Ting Jiang

Abstract As the existing internetwork interference avoidance mechanism for wireless body area network remains having problems, an internetwork interference avoidance mechanism based on nested-complex-superframe structure for wireless body area network is designed. First, the nested-complex-superframe is designed, and the related frame structure is improved. Second, the communication mechanism for this structure is proposed in the form of communication process. Simulation results show that this method can effectively avoid internetwork interference, reduce packet loss rate, and improve the throughput.

Keywords Body area network · Internetwork interference · Medium access control · Two-tier network

1 Introduction

In China, the population is large and the aging problem is increasing, human and material resources for health care is scarce, it is urgent to study new ways to solve the health care problems for the elderly [1]. The human-based wireless body area network monitors physiological indicators of human body through the sensor deployed in or on the surface of the body, and wirelessly transmits to the remote terminal by the coordinator, which avoids the influence of device circuit to patient activity, provides new solutions for hypertension, diabetes and other chronic diseases' care. Therefore, wireless body area network has more extensive application prospects in the fields of medical support and health monitoring [2].

B. Zhang (✉) · W. Zou · F. Wei · T. Jiang
Key Laboratory of Universal Wireless Communications, MOE, Beijing University of Posts and Telecommunications, Beijing 100876, People's Republic of China
e-mail: zhangb_y@yeah.net

B. Zhang · W. Zou · F. Wei · T. Jiang
State Key Laboratory of Millimeter Waves, Southeast University, Nanjing 210096, People's Republic of China

Q. Liang et al. (eds.), *Proceedings of the 2015 International Conference on Communications, Signal Processing, and Systems*, Lecture Notes in Electrical Engineering 386, DOI 10.1007/978-3-662-49831-6_31

As Wireless body area networks (WBAN) [3, 4] relate to life safety, it has strict demands on reliability. However, in the country like China with large population, the internetwork interference [5–7] problem is serious, thus is necessary to study the internetwork interference avoidance for WBAN, especially the interference problem in the sense that WBAN equipment is used densely, such as nursing home and hospital ward.

Currently, inter-interwork interference avoidance mechanism based on physical layer is mainly power control mechanism, frequency hopping mechanism, etc., and that based on medium access control (MAC) layer is mainly distributed or centralized networking mechanism, this article studies from MAC layer. Beacon shifting and active superframe interleaving mechanism [8] in IEEE802.15.6 [9] are two internetwork interference avoidance mechanisms based on MAC. Beacon shifting reduces the internetwork interference by increasing the randomness of access time of medium, however, it just avoids the collision of beacon, but neglects the collision between other phases, and too many repetition of time series in beacon shifting makes collision still difficult to avoid. Another mechanism avoids the interference by interleaving WBANs' active superframes, but the mechanism for more than two WBANs is not explicit and the channel resource utilization will decrease after multiple interactive because there is active time reducing process but no increasing process. In addition, the literature [10] proposed a distributed dynamic coexistence management mechanism to enable WBAN to relieve dynamic coexistence problem caused by movement of users, it can improve data transmission success rate, however, since it is a distributed solution, the synchronization problem between WBANs is prominent, and the payload is high with frequent control messages interact. The literature [11] proposed an internetwork avoidance mechanism based on the theory of random incomplete coloring, but is limited by the number of WBAN users.

Based on the above-described issues, an internetwork interference avoidance mechanism based on nested-complex-superframe is proposed. The scene is abstract as two-tier model with star topology, the nested-complex-superframe is designed according to the model, and the communication mechanism is given under the structure. This mechanism can effectively avoid internetwork interference between WBANs, reduce frame loss rate, improve throughput, and improve the WBAN products' user experience in medical scenes in China.

2 Interference Avoidance Mechanism Based on Nested-Complex-Superframe Structure

This paper is to propose solutions for the sense like nursing home and hospital ward, which will normally deploy total-hub indoors whose function is similar with the hub. This paper uses the total-hub to schedule each WBAN's hub uniformly,

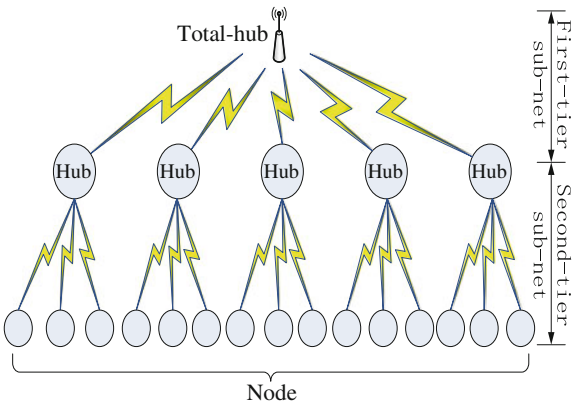

Fig. 1 Two-tier network topology structure

and the use of channel resources is coordinated through the hub compete with each other, thus coordinate the time of WBAN occupying the channel and avoid internetwork interference.

2.1 Model of Two-Tier Network

The two-tier network topology structure [12] built by scene like nursing home and hospital ward is showed in Fig. 1. For convenience of description, hub of WBAN is called sub-hub, the beacon it sends is called sub-beacon, and superframe mains nested-complex-superframe. The second-tier subnet is composed of nodes and sub-hub in each WBAN, the first-tier subnet is composed of the sub-hubs and the total-hub. Transmission in different subnet is transparent.

The super-hub decides the start and end time of the superframe and its each phase, and also coordinates the time and sequence of each WBAN occupying the channel. Weather each WBAN can occupy the channel in managed access phase (MAP) and the sequence they occupy are all completed by sub-hubs with each other, and finally decided by the total-hub.

2.2 Nested-Complex-Superframe Structure Base on Two-Tier Network

The superframe constructed by two-tier network is shown in Fig. 2. In which, total-beacon (TB) and hub contend phase (HCP) is used for first-tier subnet, sub-beacon (SB), exclusive access phase (EAP), random access phase (RAP) and managed access phase (MAP) is used for second-tier subnet. MAP is divided equally into multiple sub-MAPs, and then the sub-hub assigned one of the

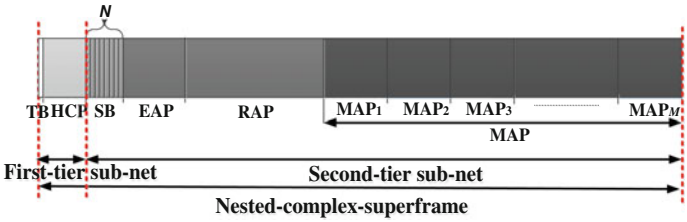

Fig. 2 Nested-complex-superframe structure based on two-tier network

sub-MAPs to its nodes according to the sequence the sub-hub obtains by competing in the first-tier subnet for related communication.

In this paper, the communication mechanism of the two-tier network is introduced based on protocol of IEEE802.15.6, some related frames are slightly changed in units of field, and the changed part is shown in italics and shaded in the figure of frame structure,while the rest uses 15.6. Changes made under this mechanism are equally applicable to other WBAN standard like 4n and 4j.

TB is used for total-hub to send total-beacon to each sub-hub, the frame structure is shown in Fig. 3. In which, SB Start field represents the start time of SB, the SB contains N slot, N indicates the maximum number of WBAN that a limited area can hold, namely to insure that all the WBANs in the area can have the chance to send sub-beacon, but in the actual scene the WBAN number L is generally not larger than N; Number of MAP fields is the number of sub-MAP(MAP_i,$i = 1, 2, \ldots, M$), the value is M, indicating that the MAP in a superframe is divided equally into M sub-MAPs, namely there are no more than M WBANs in each superframe obtain the right to use sub-MAP by compete under this mechanism, M is generally not larger than N.

HCP is used for sub-hub to compete sequence, the sequence not only determines the sequence of sub-hub sending sub-beacon in SB, but also determines the situation of WBAN obtaining time slot in MAP. During HCP, sub-hub and total-hub send Hub Contend frame and Contend Ack frame, respectively, that are designed based on the existing Disconnect frame. The frame structures are shown in Figs. 4 and 5. Contend Ack frame contends a Contend Sequence Number field, indicating the sequence the sub-hub obtains by competes.

MAC Frame Header	Sender Address	Beacon Period Length	Allocation Slot Length	*SB Start*	RAP Start	RAP End	*Number of MAP*	MAC Capalibity	PHY Capalibity	FCS
	MAC Frame Body									

Fig. 3 Frame structure of total-beacon

Fig. 4 Frame structure of Hub Contend frame

MAC Frame Head	Recipient Address	Sender Address	MAC Capalibity	PHY Capalibity	FCS
	MAC Frame Body				

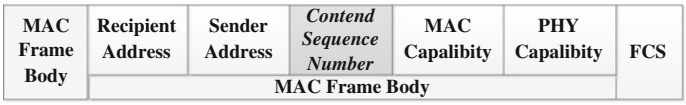

Fig. 5 Frame structure of Contend Ack frame

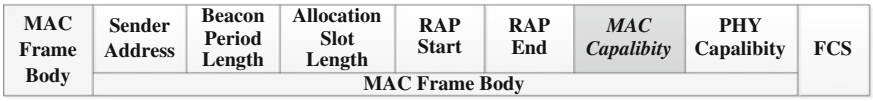

Fig. 6 Frame structure of sub-beacon

SB is used for sub-hubs in second-tier subnet to broadcast sub-beacons to their own nodes, the frame structure is shown in Fig. 6. In which, 1 bit of the reserved field in MAC Capability is used to indicate whether the WBAN can occupy MAP in next superframe. The transmission in different subnet is transparent, the nodes in second-tier subnet do not know the time assignment about the superframe which communicated in first-tier subnet, and just obtain the information of the start and end time of each phase from the sub-beacon sending by their sub-hub, therefore, the RAP Start field and RAP End field is still contained in the sub-beacon, and the value of these two fields are the same as corresponding fields in total-beacon. But sub-beacon needs not telling their nodes the start and end time of sub-MAP, because nodes just request the length of time interval when they compete for the time slot in MAP, however, the detailed time assignment is assigned by their sub-hub.

2.3 Communication Mechanism of Two-Tier Network

The sequence number WBAN obtained determines its channel occupation in superframe. The following describes the channel occupation of different WBAN in the same superframe, and set L is 8, N is 10, M is 5 as an example.

During network initialization, the sub-hub listens to the channel first. When it receives the total-beacon that the total-hub sends at the beginning of each superframe, it synchronizes with the total-hub, and obtains the start and end time of the superframe and each phase. The sub-hub accesses the channel in the next superframe according to the time set of total-beacon. The sub-hub accesses to HCP immediately when it receives the next total-beacon. During this HCP, the sub-hub sends Hub Contend frame to the total-hub by CSMA/CA to compete sequence for accessing channel. The total-hub responses Contend Ack frame to the sub-hub when it receives the Hub Contend frame, and sets the Contend Sequence Number field to the number of the sequence that the sub-hub obtains. For convenience of description, it is assumed that the number responses to $WBAN_i$ is i, namely $WBAN_1$ to $WBAN_8$ obtains the number of 1 to 8, respectively.

The following describes the communication mechanism of $WBAN_1$ that obtains sub-MAP and $WBAN_6$ that does not obtain sub-MAP as examples.

(1) **Communication process of $WBAN_1$**

$WBAN_1$ accesses to SB at the time that the total-hub sets after it obtains the sequence during HCP. The sub-hub of $WBAN_1$ sends its sub-beacon at the first time slot of SB, as it obtains number 1. Nodes of all WBANs start to listen to their sub-beacon at the first time slot of next SB in order to synchronize with their sub-hub accurately, since the sequence that sub-hub obtains will change with time goes on.

The nodes synchronize with their sub-hub and get the schedule of second-tier when they receive the sub-beacon, and access to EAP immediately after receiving the sub-beacon of the next superframe. EAP is used to transmit emergent data of high user priority, the sub-hub or the nodes will send this kind of data frame to each other by CSMA/CA if they have.

The nodes start to communicate by CSMA/CA and decide whether to upload management frame or data frame according to whether the MAP of next superframe can be occupied, when it comes to the start time of RAP. Nodes of $WBAN_1$ compete to upload management frame to request and get assigned of the time interval in MAP_1, since they can occupy channel in MAP_1.

The length of time interval in MAP that each node in $WBAN_1$ obtains by competes is various depending on the communication requirement of each node, and it may have the case that some nodes does not obtain time slot or the sub-MAP is not fully allocated. The nodes in $WBAN_1$ will be in hibernation from MAP_2 to MAP_5 and TB, HCP in the following superframe, and will be in active during SB to receive next sub-beacon.

The communication process of $WBAN_2$ to $WBAN_5$ is similar with $WBAN_1$.

(2) **Communication process of $WBAN_6$**

The sub-hub can only broadcast sub-beacon in the corresponding time slot of SB, but cannot occupy cannel in MAP, if the sequence number that the sub-hub obtains by compete is larger than M. For instance, the sequence number that sub-hub of $WBAN_6$ obtains is 6, so it broadcast sub-beacon at the sixth time slot to its nodes, and the value of MAC Capability field in sub-beacon is set to indicates that nodes cannot occupy channel in MAP of next superframe. The communication process of $WBAN_6$ in TB, HCP, and EAP is the same as $WBAN_1$, this section focuses on other phase. The nodes of $WBAN_6$ listen to the channel from the start of SB, ready to receive sub-beacon, they do not upload management frame to their sub-hub in RAP but upload the data they collect to sub-hub by CSMA/CA directly in the form of data frame, as they receive the sub-hub and acknowledged that MAP in next superframe is not accessibly for them. The nodes are in hibernation from the start of MAP, and not be awake until the start of next SB.

The communication process of $WBAN_7$ and $WBAN_8$ is similar with $WBAN_6$.

3 Simulation and Performance Analysis

This simulation uses visual studio 2013 as simulation tool, through implementing a discrete event simulator, to simulate and compare different internetwork interference avoidance mechanisms. The main parameters of the simulation are set as in Tables 1 and 2 [13].

In the simulation analysis, the beacon shifting mechanism in IEEE802.15.6 and the superframe mechanism of this paper is mainly compared. To satisfy the communication amount and control the variable, the length of allocated portion of MAP in 15.6 is the same as the length of each sub-MAP in the mechanism of this paper, namely to ensure that the traffic amount of nodes in MAP under the two mechanism is the same.

First, the change of frame loss rate with the increase in the number of WBAN in the scene is shown in Fig. 7, the loss of frame is just caused by collision in the ideal channel. As can be seen, under the mechanism of IEEE802.15.6, the chance of

Table 1 Common parameter setting

Parameter name	Value
Transmission rate	75.9 kbps
Length of date frame	2024 bit
Maximum interference distance	2 m
Slot length of CSMA/CA	870 μs
Business generation period	32 s
Time of simulation	1000 s

Table 2 Parameter setting unique in nested-complex-superframe mechanism

Parameter name	Value
M	5
N	10
L	8
S	10

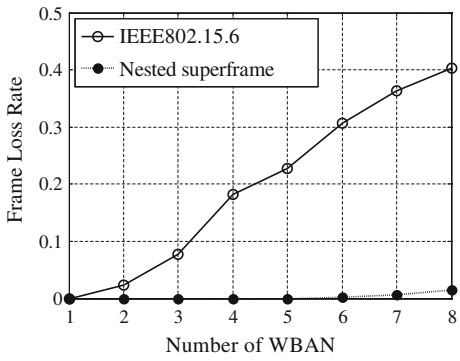

Fig. 7 Simulation result of averaged frame loss

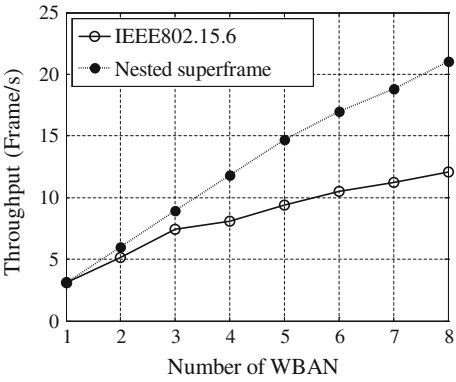

Fig. 8 Simulation result of rate throughout

collision that caused by different WBANs send frames at the same time is increased, which means that the frame loss rate is increased. However, under the mechanism of this paper, the possibility of internetwork interference is avoided since each WBAN communicate at different time interval under the coordination of total-hub, even though there may be interference since all the WBAN communicate together in RAP, and result in the frame loss, but the interference is still a small amount as the collision avoided CSMA/CA is used, it is also proved by the simulation results that the frame loss rate is indeed nearly zero. The frame loss rate gets a bit higher when the number of WBAN is larger than five, because the communication amount in RAP is larger than before since there are nodes send data frame in RAP.

The change of throughput with the increase in the number of WBAN in the scene is shown in Fig. 8. As can be seen, the throughput is nearly the same under the two mechanisms when there is only one WBAN, since the traffic amount in MAP is the same; when the number of WBAN is larger than two, the internetwork interference is increasingly frequent under the mechanism of IEEE802.15.6, so that the throughput is affected and gradually decreased. However, under the mechanism of this paper, it still maintains high throughput performance, and not affected by the increased of WBAN number, and the larger the number of WBAN is, the obvious the advantages is.

4 Conclusion

In this paper, the problem of internetwork interference of Wireless Body Area Networks is studied from the perspective of MAC layer. The nested-complex-superframe is designed, and the communication mechanism under the superframe structure is given. Through the theoretical analysis and simulation comparison, it is found that under the scheduling of total-sub, different WBAN that uses the same channel can occupy the channel exclusively at different or compete to use the channel by collision avoided CSMA/CA in the same time interval, the interference

frequency and frame loss rate is reduced, and the throughput is improved, therefore the proposed mechanism has a certain value and practical significance.

Acknowledgments This work was supported by the 863 Program of China under Grant No. 2015AA01A703, the Fundamental Research Funds for the Central Universities under grant No.2014ZD03-02,NSFC(No. 61571055, No.61171104), fund of SKL of MMW (No. K201501).

References

1. Movassaghi S, Abolhasan M, Lipman J, Smith D, Jamalipour A (2014) Wireless body area networks: a survey. IEEE Commun Surv Tutor 16:1658–1686
2. Xiao L, Li RF, Luo J (2013) Recognition of human activity based on compressed sensing in body sensor networks. J Electron Inf Technol 35:119–125
3. Alam MM, Hamida BE (2014) Towards accurate mobility and radio link modeling for IEEE 802.15.6 wearable body sensor networks. In: IEEE international conference on wireless and mobile computing, networking and communications. pp 298–305
4. Shuai J, Zou WX, Zhou Z (2013) Priority-based adaptive timeslot allocation scheme for wireless body area network. In: 13th International symposium communications and information technologies (ISCIT). pp 4–6
5. Zhao Z, Shang PF et al (2013) Interference identification and classification mechanism for wireless sensor network. J Commun 34:28–36
6. Fatehy M, Kohno R (2013) Variable spread slotted aloha simulation analysis over IEEE 802.15.6 using IR-UWB for wireless body area networks. In: Modelling symposium (EMS), pp 20–22
7. Zou WX, Guo C, Kang FY (2015) An interference avoidance method of wireless body area network based on Chinese medical band. In: An interference avoidance method of wireless body area network based on chinese medical band
8. Zou WX, Kang FY, Du GL, Zhang CQ (2015) Physical layer proposal design and interference analysis based on Chinese medical band in wireless body area network. J Electron Inf Technol 37:429–434
9. Wireless Body Area Networks, IEEE Std. 802.15.6, 2012
10. Deylami MN, Jovanov E (2014) A distributed scheme for managing the dynamic coexistence of IEEE 802.15.4-based health monitoring WBANs. IEEE J Biomed Health Inf 18:327–334
11. Cheng SH, Huang CY (2013) Coloring-based inter-WBAN scheduling for mobile wireless body area networks. IEEE Trans Parallel Distrib Syst 24:250–259
12. Rashwand S, Misic J (2012) Two-tier WBAN/WLAN healthcare networks; Priority considerations. In: Global communications conference (GLOBECOM), pp 5398–5403
13. Huque MTI, Munasinghe KS, Jamalipour A (2014) Body node coordinator placement algorithms for wireless body area networks. Internet Things J 2:94–102d

On Gradient Ascend for Single Data Stream Multifrequency Channel Interference Alignment

Guanglong Du, Weixia Zou and Zheng Zhou

Abstract This paper explores multifrequency channel interference alignment (IA) system with single data stream transmit for each user. This paper first proves that a M frequency independent fading channels and $2M - 2$ users IA system will have only single optimal IA solution when the transmit signal power reduce to 0. Then based on this idea, and by derivation of the sum rate gradient function, this paper proposes gradient ascend with power increase method to search interference alignment solution. At last, the numerical simulation results show that the proposed method will obtain a better network sum rate performance than the classical maximum signal to interference plus noise (Max-SINR) algorithm and minimum interference leakage (Min-IL) algorithm.

Keywords Interference alignment · Multifrequency channels · Degrees of freedom · Gradient ascend · Network sum rate

G. Du (✉)
Key Lab of Universal Wireless Communications, MOE, Beijing, China
e-mail: dglbupt@gmail.com; guanglong108@sina.com

W. Zou
Beijing University of Posts and Telecommunications, Beijing 100876, China
e-mail: zwx0218@bupt.edu.cn

Z. Zhou
State Key Laboratory of Millimeter Waves, Southeast University,
Nanjing 210096, People's Republic of China
e-mail: zzhou@bupt.edu.cn

Q. Liang et al. (eds.), *Proceedings of the 2015 International Conference on Communications, Signal Processing, and Systems*, Lecture Notes in Electrical Engineering 386, DOI 10.1007/978-3-662-49831-6_32

1 Introduction

The degrees of freedom (DoF) of wireless interference networks have been widely researched in the recent years. In a symmetric wireless network with M antennas for transmitters and receivers, and nondegenerate channel conditions, the DoF for K user multiinput multioutput (MIMO) network is no more than twice of the DoF achieved by each user in the absence of interference [1–6]. Hence, if there have only single data stream transmit for each user at such a MIMO interference alignment (IA) network, then the IA network can accommodates $2M - 1$ users communicating. But in diagonal channel conditions, i.e., multifrequency independent fading channel system, a M-independent-fading-channel IA network can only accommodates $2M - 2$ users communicating [7], which can be denoted as $(M \times M, 1)^{2M-2}$ system. This means that compared with interference alignment, the traditional frequency division multiplexing method to cancel interference and support multi user is inefficient for spectrum resource utilization.

Although the DoF result, or user capacity conclusion for multifrequency channel IA system is clear, there are still lack of methods which can obtain a optimal network sum rate IA solution. In spite of the wildly used iterative maximize signal to interference plus noise ratio (Max-SINR) and iterative minimum interference leakage (Min-IL) algorithms can realize interference alignment perfectly [8], however, the network sum rate performance of Max-SINR and Min-IL are not good enough. Actually, the iterative Max-SINR and Min-IL algorithms are not considered as the network sum rate. In this paper, we start form the gradient function derivation of the network sum rate function, then propose the gradient ascend method to search the interference alignment solution for $(M \times M, 1)^{2M-2}$ multifrequency channel IA system.

This paper is organized as follows: Sect. 2 introduces the system model of $(M \times M, 1)^{2M-2}$ multifrequency channel IA system; Sect. 3 derives the network sum rate gradient function; then the gradient ascend method under power increase is given in Sect. 4; Sect. 5 presents some numerical results; at last, Sect. 6 is the conclusion of this paper.

2 System Model

Consider a SISO multifrequency channel system with M independent fading channels, hence it can accommodate $K = 2M - 2$ users communication. The channel output at the kth receiver can be written as follows:

$$\boldsymbol{Y}^{(k)} = \sum_{l=1}^{K} \boldsymbol{H}^{(kl)} \boldsymbol{X}^{(l)} + \boldsymbol{Z}^{(k)} \tag{1}$$

where $\boldsymbol{H}^{(kl)} = diag\{h^{(kl)}[f_1], h^{(lk)}[f_2], ..., h^{(kl)}[f_M]\}$ is $M \times M$ diagonal channel matrix whose j-th diagonal component $h^{(kl)}[f_j]$ denotes the jth channel fading coefficient from the kth transmitter to the lth receiver, $\boldsymbol{Z}^{(k)}$ is zero mean additive Gaussian noise with unit covariance matrix, i.e., $E[\boldsymbol{Z}^{(k)}\boldsymbol{Z}^{(k)^H}] = \boldsymbol{I}$. $E[||\boldsymbol{X}^{(l)}||^2] = P^{(l)}$ is the lth transmitter's signal power. Here the transmit signal $\boldsymbol{X}^{(l)} = \sqrt{P^{(l)}}\boldsymbol{V}^{(l)}x^{(l)}$, where $\boldsymbol{V}^{(l)}$ denotes the unit precoding vector of lth transmitter and $x^{(l)}$ denotes the corresponding data stream.

The goal of interference alignment is to design all the K precoding vectors $\boldsymbol{V}^{(l)}, 1 \le l \le K$, to limit the interference signals into an interference subspace at each receiver, so that the desired signal is linearly independent from the interference subspace. At the kth receiver, a $M \times 1$ filter denoted by $\boldsymbol{U}^{(k)}$ is used to extract the desired signal. So the interference alignment solutions of interference network are required to satisfy the following conditions:

$$\boldsymbol{U}^{(k)^H}\boldsymbol{H}^{(kl)}\boldsymbol{V}^{(l)} = 0, \forall k \neq l \tag{2}$$

$$\boldsymbol{U}^{(k)^H}\boldsymbol{H}^{(kk)}\boldsymbol{V}^{(k)} \neq 0, 1 \le k \le K \tag{3}$$

where $()^H$ denotes the conjugate transpose operator.

3 Grad of Sum Rate

Similar with a MIMO interference alignment system [9, 10], the sum rate of multi-frequency channel IA system is the sum of each user's channel rate, and is given by

$$R = \sum_{k=1}^{K} \log_2 \left| \boldsymbol{I} + \left(\boldsymbol{B}^{(k)} + \boldsymbol{I}_N\right)^{-1}\boldsymbol{A}^{(k)} \right| \tag{4}$$

where $\boldsymbol{A}^{(k)}$ and $\boldsymbol{B}^{(k)}$ denotes the correlated matrix of desired signal and interference signal of the kth receiver correspondingly:

$$\begin{aligned} \boldsymbol{A}^{(k)} &= \boldsymbol{H}^{(kk)}\boldsymbol{V}^{(k)}\boldsymbol{V}^{(k)^H}\boldsymbol{H}^{(kk)^H}P^{(k)} \\ \boldsymbol{B}^{(k)} &= \sum_{l \neq k} \boldsymbol{H}^{(kl)}\boldsymbol{V}^{(l)}\boldsymbol{V}^{(l)^H}\boldsymbol{H}^{(kl)^H}P^{(l)} \end{aligned} \tag{5}$$

By strictly mathematical deduction, the network sum rate function can be written as

$$\begin{aligned} R &= \sum_{k=1}^{K} \left(\log_2 \left| \boldsymbol{A}^{(k)} + \boldsymbol{B}^{(k)} + \boldsymbol{I}_N \right| - \log_2 \left| \boldsymbol{B}^{(k)} + \boldsymbol{I}_N \right| \right) \\ &= \sum_{k=1}^{K} \left(\boldsymbol{\Phi}_k - \Psi_k \right) \end{aligned} \tag{6}$$

where $\boldsymbol{\Phi}_k$ and Ψ_k denotes the first part and second part of sum rate function R. Based on (6), the network sum rate gradient function respect to encoding vectors $\boldsymbol{V}^{(k)}$ can be easily obtained by some mathematical deductions.

From the differential formula $d(\ln|\boldsymbol{X}|) = tr\{\boldsymbol{X}^{-1}d\boldsymbol{X}\}$, the gradients of $\boldsymbol{\Phi}_l$ and Ψ_l with respect to the kth encoder vector $\boldsymbol{V}^{(k)}$ are given by

$$\begin{aligned}\frac{\partial \boldsymbol{\Phi}_l}{\partial \boldsymbol{V}^{(k)}} &= \frac{2P^{(k)}}{\ln 2}\boldsymbol{H}^{(lk)H}\left(\boldsymbol{A}^{(l)} + \boldsymbol{B}^{(l)} + \boldsymbol{I}_N\right)^{-1}\boldsymbol{H}^{(lk)}\boldsymbol{V}^{(k)} \\ \frac{\partial \Psi_l}{\partial \boldsymbol{V}^{(k)}} &= \frac{2P^{(k)}}{\ln 2}\boldsymbol{H}^{(lk)H}\left(\boldsymbol{B}^{(l)} + \boldsymbol{I}_N\right)^{-1}\boldsymbol{H}^{(lk)}\boldsymbol{V}^{(k)}\end{aligned} \tag{7}$$

Then the gradient function of network sum rate respect to the kth encoder vector $\boldsymbol{V}^{(k)}$ can be get from (7):

$$\nabla_k R = \sum_{l=1}^{K}\frac{\partial \boldsymbol{\Phi}_l}{\partial \boldsymbol{V}^{(k)}} - \sum_{l\neq k}\frac{\partial \Psi_l}{\partial \boldsymbol{V}^{(k)}} \tag{8}$$

From gradient function (8), a fact about $\nabla_k R$ can be presented as

$$\lim_{P_m\to 0}\frac{\nabla_k R}{P^{(k)}} = \frac{2}{\ln 2}\boldsymbol{H}^{(kk)H}\boldsymbol{H}^{(kk)}\boldsymbol{V}^{(k)} \tag{9}$$

where $P_m = \max\{P^{(1)}, \ldots, P^{(k)}\}$. This is because that when the signal power $P_m \to 0$, then $\boldsymbol{A}^{(k)} \to \boldsymbol{0}$, $\boldsymbol{B}^{(k)} \to \boldsymbol{0}$. As the channel matrixes are diagonal matrixes, so when signal power reduce to 0, the optimal IA solution is:

$$\boldsymbol{V}^{(k)} = v_m\left(\boldsymbol{H}^{(kk)H}\boldsymbol{H}^{(kk)}\right) \tag{10}$$

where $v_m(\boldsymbol{X})$ denotes the eigenvector corresponding to the biggest eigenvalue of matrix $\boldsymbol{X}$. This means the following theorem:

Theorem 1 *The network sum rate function* (6) *have single global optimal value when the signal power close to 0, and the optimal solution will approach to* (10).

This conclusion is correct because that, when the signal power close to 0, the other eigenvectors of $\boldsymbol{H}^{(kk)H}\boldsymbol{H}^{(kk)}$ except (10) are only stagnation points but cannot obtain local optimal. Therefore, the solution (10) will be the global optimal point when the signal power reduced to infinitesimal.

4 Grad Ascend Algorithm

From Theorem 1, we know that when the signal power is small enough, there will be global optimal solution. Hence we can design a method to search the global optimal solution at small signal power, and then track the optimal solution with the increasing of the signal power. Based on this idea, this section propose a gradient ascend algorithm with power increase, i.e., GAPI algorithm.

Based on the gradient function (8), and start from a small enough signal power parameters P, the GAPI algorithm will execute a number of searching epochs. In each epoch, the signal powers of each transmitter are set to $min(P, P^{(k)})$, and the GAPI algorithm will use gradient ascend method to searching optimal network sum rate, i.e., solving the following problem by gradient ascend method:

$$\begin{aligned} &\max \ R\left(\boldsymbol{V}^{(1)}, \ldots, \boldsymbol{V}^{(K)}\right) \\ &s.t. \ \boldsymbol{V}^{(k)^H}\boldsymbol{V}^{(k)} = 1 \end{aligned} \tag{11}$$

where R is the sum rate function defined by (6), and the subject condition $\boldsymbol{V}^{(k)^H}\boldsymbol{V}^{(k)} = 1$ insures that $\boldsymbol{V}^{(k)}$ in the Grassmann manifold and have unit length. After each epoch of gradient ascend searching, the GAPI algorithm will update signal power parameter using the following step:

$$\rho P \to P \tag{12}$$

where ρ is the amplification parameter which bigger than 1.

The steps of GAPI algorithm are illustrated in Table 1. In the algorithm, Steps 3–6 composes gradient ascend searching algorithm, and $\mathcal{O}\{\boldsymbol{x}\}$ denotes the unit vector along with the same direction of $\boldsymbol{x}$, i.e., $\mathcal{O}\{\boldsymbol{x}\} = \boldsymbol{x}/\|\boldsymbol{x}\|$.

Table 1 Gradient ascend with power increaser algorithm

Step 1	Initialize $\boldsymbol{V}^{(l)}$, $k = 1, 2, \ldots, K$, the original power $P = P_0$, and the magnitude parameter ρ
Step 2	Update signal power parameter by (12), start a new epoch of gradient ascend searching, i.e., solving problem (11)
Step 3	Calculate gradient functions $\nabla_k R$ by (8), $1 \le k \le K$ Searching along with the direction of $\nabla_k R$, i.e., maximize 1-D
Step 4	function $R(\mathcal{O}\{\boldsymbol{V}^{(k)} + \eta^* \nabla_k R\})$, and obtain the optimal step parameter η^*
Step 5	Update the encoding vectors by $\mathcal{O}\{\boldsymbol{V}^{(k)} + \eta^* \nabla_k R\} \to \boldsymbol{V}^{(k)}$
Step 6	Return to Step 3, until this epoch converged
Step 7	Return to Step 2 and begin another epoch, until $P \ge P^{(k)}$ for all $1 \le k \le K$

5 Numerical Simulations

This section illustrates some numerical simulations about the proposed GAPI algorithm.

From the conclusion of [7], a multiuser interference network with M independent fading channels can accommodate $2M - 2$ users transmit, i.e., three channels can accommodate four users transmit and four channels can accommodate six users transmit. Figure 1 illustrates the network sum rate performance of three channels and four users. Figure 2 illustrates the network sum rate performance of fpur channels and six users. Figures 1 and 2 compare the performance of the following schemes:

(1) Iterative Max-SINR algorithm: each realization is initialized from random unit precoding vectors, i.e., $\boldsymbol{V}^{(k)}$, and iterates sufficient number of iterations until convergence.
(2) Iterative Min-IL algorithm: each realization is initialized from random unit precoding vectors, i.e., $\boldsymbol{V}^{(k)}$, and iterates sufficient number of iterations until convergence as well.
(3) Gradient ascend with power increase algorithm: each realization is initialized from random unit precoding vectors, and the initial parameters P_0 and ρ are set to $P_0 = -10\,\text{dB}$ and $\rho = 1.2$;

The performance is measured by average network sum rate, i.e., the sum channel capacity of all users in the network. From Figs. 1 and 2, it can be seen that, GAPI, Max-SINR, and Min-IL can work well and realize the goal of interference alignment, and the performance of Min-IL is much worse than Max-SINR and GAPI. Compared with Max-SINR algorithm, the GAPI algorithm obtains a similar sum rate performance at small SNR region, and obtains much better sum rate performance at high SNR region. In our opinion, this is because that, as the $(M \times M, 1)^K$ system is a under

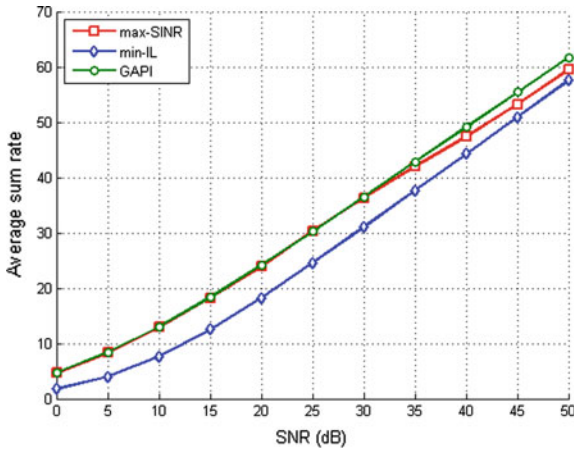

Fig. 1 Performance of 3 channel 4 user system

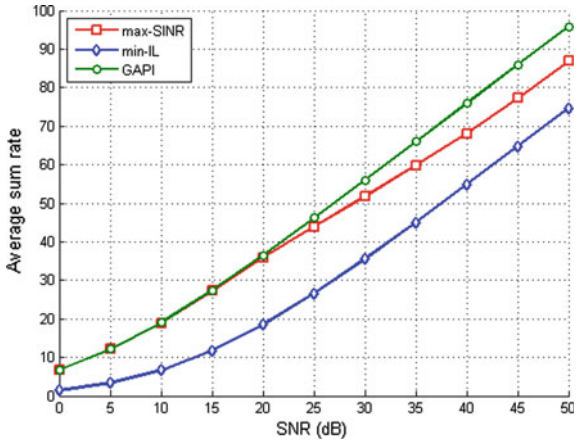

Fig. 2 Performance of 4 channel 6 user system

determinate system, the IA solutions of $(M \times M, 1)^K$ system will span a continuous manifold. Besides, there may have the following reasons:

- The goal of Min-IL algorithm is to find a interference alignment, i.e., satisfy (2), and converged once a IA solution find but regardless the sum rate performance, while the goal of GAPI and Max-SINR algorithms are concern about the sum rate, hence the performance of Min-IL algorithm is worse than Max-SINR and GAPI;
- From Theorem 1, there will be single optimal sum rate point when the signal power parameter P is small enough, and also is the Max-SINR algorithm. Hence the Max-SINR algorithm can obtain a similar network sum rate performance with GAPI algorithm at small SNR region, and both can converge to global optimal sum rate value.
- With SNR increasing, there will be more and more local optimal values of Max-SINR algorithm, which lead to more and more possibility that iterative Max-SINR algorithm converge to a local optimal value. Hence the average sum rate obtained by Max-SINR algorithm worse than GAPI algorithm at high SNR region.

Compare with Figs. 1 and 2, a pronounced tendency is that, the sum rate performance of GAPI will more and more larger than Max-SINR algorithm at moderate and high SNR regions. This is because that, with the increase of channels and users in a multifrequency channel interference alignment system, the dimension of the solution manifold will increase and becomes complex, which leads to that the Max-SINR algorithm converge to local optimal value with higher possibility.

6 Conclusions

This paper proves that, at a multifrequency channel interference alignment system with M channels and $K \leq 2M - 2$ users, and single data stream transmit for each user, there will be only one global optimal interference alignment solution when

the signal power reduce to infinitesimal. Then we derive the gradient function for network sum rate respect to all the encoding vectors of each transmitter. Based on these results, we propose gradient ascend with power increase algorithm to trace the optimal interference alignment solution and realize interference alignment. The proposed algorithm composed a series of gradient ascend searching epochs, and after each epoch, the algorithm will magnitude the signal power to trace the optimal interference alignment solution. At last, the numerical simulations shows that the proposed algorithm can realize interference alignment and obtains a better network sum rate performance than the classical Max-SINR algorithm.

References

1. Cadambe V, Jafar S (2008) Interference alignment and degrees of freedom of the k-user interference channel. IEEE Trans Inf Theor 54(8):3425–3441
2. Cadambe V, Jafar S (2008) Interference alignment and spatial degrees of freedom for the k user interference channel. In: IEEE International conference on communications, 2008. ICC '08, pp 971–975
3. Etkin R, Ordentlich E (2009) On the degrees-of-freedom of the k-user gaussian interference channel. In: IEEE international symposium on information theory, 2009. ISIT 2009, pp 1919–1923
4. Ruan L, Lau V, Win M (2013) The feasibility conditions for interference alignment in mimo networks. IEEE Trans Sig Process 61(8):2066–2077
5. Liu T, Yang C (2013) On the feasibility of linear interference alignment for mimo interference broadcast channels with constant coefficients. IEEE Trans Sig Process 61(9):2178–2191
6. Jafar SA (2014) Topological interference management through index coding. IEEE Trans Inf Theor 60:529–568
7. Long Du G, Xia Zou W, Zhou Z, Han Liu J (2014) On feasibility of linear interference alignment for single-input-single-output multi-frequency interference channel. Commun IET 8:2207–2212
8. Gomadam K, Cadambe V, Jafar S (2011) A distributed numerical approach to interference alignment and applications to wireless interference networks. IEEE Trans Inf Theor 57(6):3309–3322
9. Santamaria I, Gonzalez O, Heath R, Peters S (2010) Maximum sum-rate interference alignment algorithms for mimo channels. In: Global telecommunications conference (GLOBECOM 2010), 2010 IEEE, pp 1–6
10. Shang X, Chen B, Kramer G, Poor H (2010) Capacity regions and sum-rate capacities of vector gaussian interference channels. IEEE Trans Inf Theor 56:5030–5044

A New Distributed Interference Alignment Technology Scheme Under the Condition of Partial Interference Alignment

Weixia Zou, Tiefei Wang and Chao Xu

Abstract This paper is based on the idea of partial interference alignment, studies the OBSS (Overlap Basic Service Set) scene that the strong and weak interference coexist, while mainly to strong interference. When only adopting distributed interference alignment for the strong interference region, since distributed interference alignment can only align the interference of strong interference region, if the SNR is relatively large, weak interference can severely limit the system's channel capacity. For solving this problem, in this paper, weak interference is added to the covariance matrix of distributed interference alignment as a constant in order to eliminate the weak interference while eliminating the strong interference in the iteration, which effectively improves the system's channel capacity under the condition of partial interference alignment. Then the simulation results show that the algorithm can effectively improve the channel capacity of the system, and greater power attenuation factor, the improved effect is more obvious.

Keywords OBSS · Partial interference alignment · Channel capacity · Strong and weak interference

W. Zou · T. Wang (✉)
Key Laboratory of Universal Wireless Communications, MOE, Beijing, China
e-mail: 752069746@qq.com

W. Zou · T. Wang
Beijing University of Posts and Telecommunications,
Beijing 100876, People's Republic of China

W. Zou
State Key Laboratory of Millimeter Waves, Southeast University,
Nanjing 210096, People's Republic of China

C. Xu
State Grid Electric Power Co. Ltd., Northern Hebei Zhangjiakou Power Company,
Nanjing, China

Q. Liang et al. (eds.), *Proceedings of the 2015 International Conference on Communications, Signal Processing, and Systems*, Lecture Notes in Electrical Engineering 386, DOI 10.1007/978-3-662-49831-6_33

1 Introduction

n order to provide higher data transmission rate within limited spectral resources, the multi-antenna technology with higher spectral efficiency has been introduced to the next generation wireless LAN. However, with the increase of the number of BSS (basic service set), multiple BSS using MIMO (multiple-input multiple-output) technology will inevitably produce CCI (Co-Channel Interference), and the CCI will seriously weaken spectral efficiency brought by MIMO technology [1]. Therefore, it is necessary to study and control the interference of multiple BSS system.

In the study of the interference,as a new thought of interference management, interference alignment can effectively improve the degree of freedom in the communication system, so it has received extensive research and attention. At present, the realization mechanism of the interference alignment has been studied in depth. For K-user interference channel, it achieves interference alignment mainly through the method of continuous iterative optimization [2–6]. However, for the wireless network having determined antenna configuration, the interference alignment can be achieved only when the number of users meets the feasibility constraint, at this time, In order to improve the channel capacity, we can only achieve interference alignment for partial interference links.

Partial interference alignment technology achieves interference alignment by choosing partial interference links in order to improve system's channel capacity under the condition of limited antenna resource. The research of partial interference alignment at present mainly focuses on different scenarios. For instance, the paper [7, 8] studies the partial interference alignment in the scene of the downlink of MIMO system with multi-cell and multi-user. The paper [9, 10] studies the partial interference alignment in the heterogeneous network. There is no research on the OBSS scene in the above literature. In the OBSS scene, because the user cannot cooperate, the distributed interference alignment technology can only be used. The main idea of distributed interference alignment is using the dual nature of the communication system, that if a receiving node in a certain signal dimension has the least interference suffered by other transmitting nodes, then viewing this receiving node as sending node, the interference for other sending nodes is also the smallest while sending signal along the same signal dimension [11]. Using distributed interference alignment technology in partial interference alignment, for the scene that strong and weak interference coexist in OBSS, mainly to strong interference in a certain geographical distribution at the same time, the weak interference is seen as noise, namely in the iterative process, the interference covariance matrix weakens the effect of weak interference. This paper uses the idea of partial interference alignment, sees weak interference as constant in the covariance matrix of distributed interference alignment. The simulation results show that the channel capacity of the system can be significantly improved if the effect of weak interference is properly considered, rather than as noise.

2 System Model

For the scene that strong and weak interference coexist in OBSS,establish system model as shown in Fig. 1. Assuming that the BSS_i ($i = 1, 2, \ldots, K$) is close to each other, and form together the area of strong interference (Strong Zone, $Zone_s$). There is a BSS_w from a certain distance away from $Zone_s$, which constitutes weak interference to $Zone_s$. Here mainly to explain the improvement of the algorithm, and in order to facilitate the description, it is assumed that the weak interference BSS only has one, that is BSS_w. For any BSS, multiple terminal STA can communicate in the way of frequency division multiplexing, so this paper only studies the case that one BSS contains an AP (Point Access) and a terminal STA. Assuming the channel in the network is block fading MIMO channel, block fading channel coefficient is $\boldsymbol{H}_{ji}(1 \leq i, j \leq K)$, $\boldsymbol{H}_{ji}$ represents the channel matrix from AP_i to STA_j, its elements are sampled from independent identically distributed complex Gaussian random variables with mean 0 and variance 1. Supposing that there exists feedback channel with no delay and error for each STA and AP in the network, STA can feed the channel state information and the receiving interference suppression matrix back to AP, each AP can send its precoding matrix to all STA by the way of broadcasting.

Since BSS_w has a certain distance from $Zone_s$, it has a certain path loss from BSS_w to $Zone_s$. Assuming that the attenuation from BSS_w to each BSS of $Zone_s$ is approximately same. Supposing the power attenuation value is ρ, for BSS_j in $Zone_s$, the receiving signal of STA_j is:

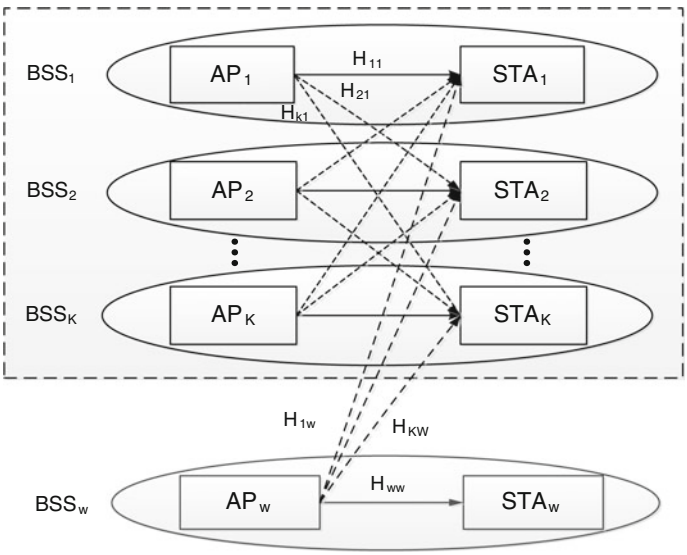

Fig. 1 OBSS scene in the scheme

$$Y_j = H_{jj}V_jX_j + \sum_{i=1,\,i\neq j}^{K} H_{ji}V_iX_i + \sqrt{\rho}H_{jw}I_wX_w + Z_j \tag{1}$$

where $\boldsymbol{X}_j$ is the useful signal from AP_j to STA_j in BSS_j, $\boldsymbol{V}_j$ is used to donate the precoding matrix in AP_j. The second term in the formula indicates the interference signal from other AP to STA_j in Zones. The third term in the formula indicates the interference signal from BSS_w to STA_j. Iw donates unit matrix, $\boldsymbol{Z}j$ donates additive complex Gauss white noise contained in terminal STA_j.

3 The Improved Algorithm

For the system model of Fig. 1, Using distributed interference alignment technology under partial interference alignment, at the begin of the procedure, randomly generate precoding matrix and the receiving interference suppression matrix, and then achieve interference alignment by gradually iterative update. At the STA_j of $Zone_s$, the total interference caused by the non expected AP is:

$$Q_j = \sum_{i=1,\,i\neq j}^{K} \frac{P_i}{d_i} H_{ji}V_i(H_{ji}V_i)^{\mathrm{H}} + \rho\frac{P_w}{d_w}H_{jw}I_w(H_{jw}I_w)^{\mathrm{H}} \tag{2}$$

where we use P_i to donate the signal transmission power of AP_i, d_i donates the freedom of AP_i, $\boldsymbol{Q}_j$ donates interference covariance matrix of STA_j. The receiving interference suppression matrix at the STA_j of $Zone_s$ is shown in the formula (3).

$$U_j^d = \nu_d(Q_j), \quad d = 1, \ldots, d_j \tag{3}$$

In the formula (3), U_j^d donates the corresponding receiving interference suppression matrix at the dth data stream of STA_j in $Zone_s$, $\nu_d(Q_j)$ donates the feature vector for the dth minimum eigenvalue of $\boldsymbol{Q}_j$. At the STA_j, the total interference energy caused by the non expected AP side is:

$$I_j = \mathrm{tr}(U_j^{\mathrm{H}}Q_jU_j) \tag{4}$$

In the same way, in the dual network, the total interference covariance matrix at the AP_j of $Zone_s$ is:

$$Q_j = \sum_{i=1,\,i\neq j}^{K} \frac{P_i}{d_i} H_{ji}U_i(H_{ji}U_i)^{\mathrm{H}} + \rho\frac{P_w}{d_w}H_{jw}I_w(H_{jw}I_w)^{\mathrm{H}} \tag{5}$$

In the dual network, the precoding matrix at the AP_j:

$$V_j^d = \nu_d(Q_j), \quad d = 1, \ldots, d_j \tag{6}$$

where we use V_j^d to donate the precoding matrix at the dth data stream of AP_j in Zones. At the AP_j, the total interference energy caused by the non expected STA side is:

$$I_j = \text{tr}\ (V_j^{\text{H}} Q_j V_j) \tag{7}$$

Referring to the iterative method of paper [12], the iterative procedure of the distributed interference alignment algorithm based on partial interference alignment is following:

(1) Initialize the precoding matrix $\boldsymbol{V}_i$ at the AP_i (i = 1, 2, …, K) of $Zone_s$, and meet $V_i^{\text{H}} V_i = I_{d_i}$.
(2) calculate the interference covariance matrix of each STA in the corresponding BSS, and then get the corresponding receiving interference suppression matrix $\boldsymbol{U}_j$ at each STA side.
(3) Reverse the direction of the communication, take the receiving interference suppression matrix $\boldsymbol{U}_j$ at each STA in the original network as the precoding matrix at the sending side in the inverted network, calculate the receiving interference covariance matrix at each receiving terminal in the dual network, and get the receiving interference suppression matrix $\boldsymbol{V}_j$ in the dual network.
(4) Reverse the direction of the communication again, take the $\boldsymbol{V}_j$ as transmitter's precoding matrix. Continue the iterative procedure until eventually converge. The condition of ultimate convergence is that the receiving interference leakage power at each STA in Zones is close to 0.

4 Channel Capacity and Algorithm Analysis

4.1 Channel Capacity

In the OBSS scene shown in Fig. 1, for BSS_j in $Zone_s$, the channel capacity is:

$$C_{BSS_j} = \log_2 \left[\det \left(I_{d_j} + \frac{P_j}{d_j} \frac{U_j^{\text{H}} H_{jj} V_j V_j^{\text{H}} H_{jj}^{\text{H}} U_j}{Inter_s + Inter_w + U_j^{\text{H}} I_{N_r} U_j} \right) \right] \tag{8}$$

where det (.) means to get determinant, $\boldsymbol{Inter}_s$ donates the interference suffered from other BSS in Zones at the BSS_j, $\boldsymbol{Inter}_w$ donates the interference suffered from BSS_w at the BSS_j. $\boldsymbol{Inter}_s$ and $\boldsymbol{Inter}_w$ is shown in formula (9):

$$Inter_s = \sum_{i=1, i\neq j}^{K} \frac{P_i}{d_i} U_j^{\mathrm{H}} H_{ji} V_i V_i^{\mathrm{H}} H_{ji}^{\mathrm{H}} U_j \quad Inter_w = \rho \frac{P_w}{d_w} U_j^{\mathrm{H}} H_{jw} H_{jw}^{\mathrm{H}} U_j \tag{9}$$

Thus, the total channel capacity of Zones is:

$$C_{Zone_s} = \sum_{j=1}^{K} C_{BSS_j} \tag{10}$$

4.2 Algorithm Analysis

4.2.1 The Partial Interference Alignment Technology

The thought of partial interference alignment is to achieve interference alignment for only partial BSS, while the rest of the interference is processing as noise. That is in the scene as is shown in Fig. 1, only adopt distributed interference alignment technology within BSS of $Zone_s$, the interference from BSS_w to $Zone_s$ is treated as noise. That is to say, while using distributed iterative interference alignment, as is shown in formula (11), the interference covariance matrix $\boldsymbol{Q}_j$ should have only the interference from BSS_i (i = 1, 2, …, K, i ≠ j) of $Zone_s$ to BSS_j, not include the interference from BSS_w to BSS_j, In this way, the interference covariance matrix produced in iterative process is only affected by the strong interference signal. Thus, after iteration, the distributed interference alignment can only eliminate the influence by $\boldsymbol{Inter}_s$, but the value of $\boldsymbol{Inter}_w$ is not affected. At this time, the channel capacity of BSS_j is still limited by $\boldsymbol{Inter}_w$. By formula (8) and (10), when SNR (signal to noise ratio) is larger, the value of $\boldsymbol{Inter}_w$ is larger, the impact on channel capacity of BSS_j is more obvious.

$$Q_j = \sum_{i=1, i\neq j}^{K} \frac{P_i}{d_i} H_{ji} V_i \; V_i^{\mathrm{H}} H_{ji}^{\mathrm{H}} \tag{11}$$

4.2.2 The Improved Part

For the influence of the interference from $\boldsymbol{Inter}_w$ on the channel capacity of BSS_j, the idea of this paper is that the effect of $\boldsymbol{Inter}_w$ can also be eliminated in the iterative process of partial interference alignment when eliminate the influence of $\boldsymbol{Inter}_s$. Therefore, the weak interference factor is considered in the interference covariance matrix $\boldsymbol{Q}_j$ in formula (5). While achieving iterative interference alignment for the strong interference, the interference covariance matrix $\boldsymbol{Q}_j$ is added to the interference from BSS_w at the same time. So, it can decrease the value of $\boldsymbol{Inter}_w$ when the value of $\boldsymbol{Inter}_s$ that is reduced in the iterative process. By the formula (8)

and (10), the channel capacity of BSS_j can be effectively improved in this way, further more, the channel capacity of the whole system can also be improved. In addition, different from the full interference alignment, the scheme still uses the idea of partial interference alignment, which achieves interference alignment only for $Zone_s$. The full interference alignment is used to achieve interference alignment for all BSS, including not only $Zone_s$, but also BSS_w. In many cases, especially when the number of user is very large, it is not able to meet the feasible conditions of achieving full interference alignment. Therefore, in these cases, we can use the scheme of this paper to improve the channel capacity of the system.

5 Performance Simulation

In order to verify the performance of the algorithm, we simulate the OBSS scene in Fig. 1. In the simulation, assuming the number of BSS in $Zone_s$ $K = 3$, the number of antennas at each AP $M_t = 4$, the number of antennas at each STA $N_r = 4$, the sending data stream d of each BSS is 2, the number of iteration is 15 times, all BSS in the network transmit signal in qual power. What shown in Fig. 2 is the improved $Zone_s$'s channel capacity, the power attenuation factor ρ takes 0.05 as interval, from the beginning of 0, and continues to increase, to the end of 0.3. By Fig. 2, as the value of increasing, the interference of BSS_w to $Zone_s$ becomes larger, which makes the channel capacity of $Zone_s$ decrease.

Figure 3 shows that before and after the algorithm is improved, the channel capacity's change of Zones when $M_t = 4$, $N_r = 4$, $K = 3$, $d = 2$, the number of iteration is 15 times. Seen from the Fig. 3, compared with the previous algorithm, the improved distributed interference algorithm's performance has improved. When SNR is the same, As the value of increases, the interference from BSS_w to

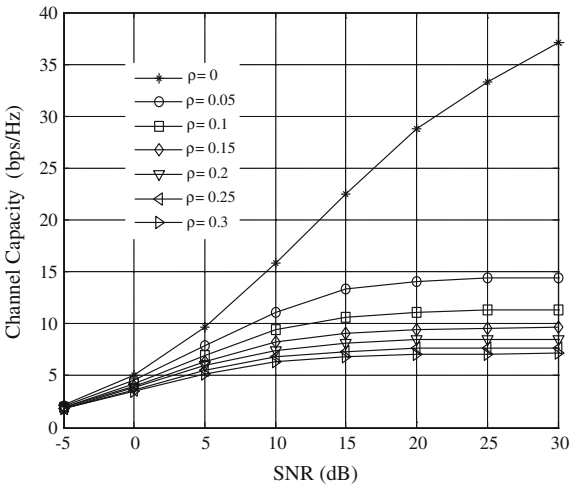

Fig. 2 The improved Zones's channel capacity

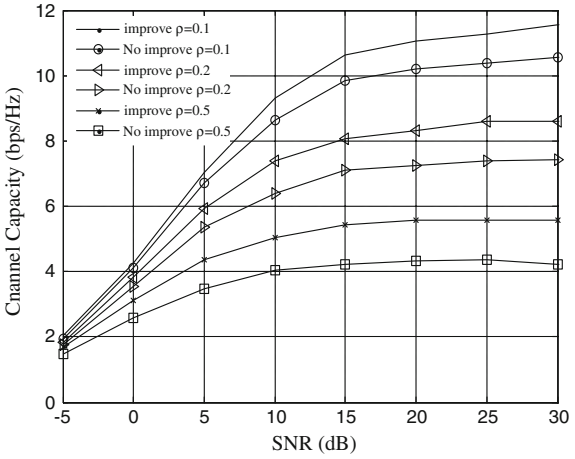

Fig. 3 Performance comparison before and after the improvement of the algorithm

Zone$_s$ is greater, the improved effect is more obvious. For example, in Fig. 3, when SNR is equal to 15 dB, ρ is equal to 0.1, the performance is about to improve 0.79 bps/Hz, $\rho$is equal to 0.2, the performance is about to improve 0.97 bps/Hz, ρ is equal to 0.5, the performance is about to improve 1.19 bps/Hz. That is, as the value increases, the improved effect of the channel capacity is becoming more and more significant. Finally, the reason that the channel capacity is tend to stable before and after the algorithm is improved is that the interference cannot be completely eliminated in the part iterative interference alignment.

6 Conclusion

For the coexisting scene of strong and weak interference in OBSS, this paper takes strong interference region as the research object, improves the algorithm of distributed interference alignment under the condition of partial interference alignment. The simulation results show that the algorithm can effectively improve system's channel capacity. The improved algorithm can provide reference for the application of partial interference alignment technology. In some scenes, for example, for urban and rural living area (there are more than one BSS in a region), which is influenced by some weak interference outside a certain distance, or for the region with very many BSS, which can not achieve full interference alignment due to the limitation of the terminals' antenna number, the algorithm can be used to further improve the system's channel capacity.

Acknowledgments This work was supported by the 863 Program of China under Grant No. 2015AA01A703, the Fundamental Research Funds for the Central Universities under grant No.2014ZD03-02, NSFC (No. 61571055,61171104), fund of SKL of MMW (No. K201501).

References

1. Catreux S, Driessen PF, Greenstein LJ (2000) Simulation results for an interference-limited multiple-input multiple-output cellular system. In: Global telecommunications conference, 2000. GLOBECOM '00. IEEE, pp 334–336
2. Gomadam K, Cadambe VR, Jafar SA (2011) A distributed numerical approach to interference alignment and applications to wireless interference networks. IEEE Trans Inf Theory 57 (6):3309–3322
3. Schreck J, Wunder G, Jung P (2015) Robust iterative interference alignment for cellular networks with limited feedback. IEEE Trans Wirl Commun 14(2):882–894
4. Santamaria I, Gonzalez O, Heath RW, Peters SW (2010) Maximum sum-rate interference alignment algorithms for MIMO channels. In: Global telecommunications conference (GLOBECOM 2010), Miami FL, pp 1–6
5. Ben Halima S, Saadani A (2012) A reduced complexity clustering algorithm for the K-user MIMO interference channel. In: 2012 IEEE 13th international workshop on signal processing advances in wireless communications (SPAWC). IEEE, pp 284–288
6. Rihan M, Elsabrouty M, Muta O, et al (2014). Iterative interference alignment in macrocell-femtocell networks: a cognitive radio approach. In: 2014 11th international symposium on wireless communications systems (ISWCS). IEEE, pp 654–658
7. Zhang W, Yu Y, Wang C, et al. ()2013 Partial interference alignment for multi-cell and multi-user MIMO downlink transmission. In: 2013 IEEE 78th vehicular technology conference (VTC Fall). IEEE, pp 1–5
8. Zhang Y, Zhou Z, Li B et al (2015) Partial interference alignment for downlink multi-cell multi-input–multi-output networks. IET Commun 9(6):836–843
9. Seo J, Yang C, Park G, et al. (2013) Partial interference alignment in heterogeneous networks. In: Military communications conference, MILCOM 2013–2013 IEEE, San Diego, pp 1553–1557
10. Liu G, Sheng M, Wang X et al (2015) Interference alignment for partially connected downlink MIMO heterogeneous networks. IEEE Trans Commun 63(2):551–564
11. Zhou R, Lv T, Long W (2012) A distributed iterative interference alignment scheme for K-User MIMO interference channel. In: 2012 8th international conference on wireless communications, networking and mobile computing (WiCOM), Shanghai, pp 1–4
12. Yang Zhang, Zheng Zhou, Lei Shi, Bin Li (2013) Distributed interference alignment with grassmannian codebook. J Beijing Univ Posts Telecommun 36(4):71–75

CFO Estimation with Model-Based CoSaMP Over Flat Fading Channel

Chaojin Qing, Xin Tong, Yi Guo, Xi Cai, Mintao Zhang and Ling Xia

Abstract In flat Rayleigh fading channel, the estimation of carrier frequency offset (CFO) is investigated based on compressed sensing (CS) technique in this paper. The CFO estimation metrics for traditional maximum likelihood (ML)-based CFO estimation are confirmed to be compressible when there is relatively high signal-to-noise ratio (SNR). By analyzing the metric characteristic and referencing the classical compressive sampling matching pursuit (CoSaMP) algorithm, we introduce model-based CoSaMP algorithm into the recovery of coarse CFO estimation metrics. In the phase of fine CFO estimation, the equivalent likelihood function is interpolated in the vicinity of the frequency of coarse CFO to search local maximum nearest to the true CFO. The analysis and simulation results show that the mean squared error (MSE) performance employed model-based CoSaMP for coarse CFO estimation better than the classical CoSaMP is employed for coarse CFO estimation.

C. Qing (✉) · X. Tong · Y. Guo · X. Cai · M. Zhang · L. Xia
School of Electrical Engineering and Electronic Information,
Xihua University, Chengdu 610039, China
e-mail: chjqing@mail.xhu.edu.cn

X. Tong
e-mail: 1050205361@qq.com

Y. Guo
e-mail: lpngy@126.com

X. Cai
e-mail: caixi-1983@163.com

M. Zhang
e-mail: zhangmt@vip.163.com

L. Xia
e-mail: xialing.cd@gmail.com

Q. Liang et al. (eds.), *Proceedings of the 2015 International Conference on Communications, Signal Processing, and Systems*, Lecture Notes in Electrical Engineering 386, DOI 10.1007/978-3-662-49831-6_34

1 Introduction

In wireless communication systems, an accurate estimation of carrier frequency offset (CFO) is a crucial task for the reason that the CFO may result in severe performance degradation at the receiver [1]. In [2], the traditional maximum likelihood (ML)-based CFO estimation for flat fading is investigated. However, the CFO estimation is based on Nyquist sampling. For high sampling rate of wireless communication systems, the analog-to-digital converter (ADC) for existing CFO estimation methods will experience excessive power consumption and design difficulty [3, 4].

Based on the compressed sensing (CS) methods, a fast and rough estimate of pseudonoise (PN) code phase and Doppler frequency with the reduced number of parallel correlators is proposed by Kong [3, 4]. Although the number of correlators can be reduced, the compressed correlator technique can only rough estimate Doppler frequency, i.e., the fine CFO estimation cannot be obtained. Furthermore, the compressed correlator technique will encounter application difficulties without using correlation method. Thus, the CFO estimation (includes coarse estimation and fine estimation) is not very intensively investigated in [3, 4].

In this paper, we investigate the CS-based CFO estimation in the scenario of flat Rayleigh channel. First, we confirm the compressibility of CFO estimation metrics in traditional ML-based CFO estimation, and the compressive sampling is directly employed for the radio signals. Then, we analyze the metric characteristic and introduce model-based CoSaMP [5] algorithm into the reconstructing of coarse CFO estimation metrics from compressed samples. Finally, we construct equivalent likelihood function according to the coarse CFO estimation, and the equivalent likelihood function is interpolated in the vicinity of the frequency of coarse CFO to search local maximum nearest to the true CFO for fine CFO estimation. By the analysis and simulation, it is shown that CS-based CFO estimation can be implemented with reduced sampling rate, and the proposed method can improve the mean squared error (MSE) of CFO estimation.

The notation used in this paper follows usual convention–vectors denoted by symbols in boldface, $(\cdot)^*$, $(\cdot)^T$, $(\cdot)^H$, $(\cdot)^\dagger$ are complex conjugate, transpose conjugate transpose, and Moore–Penrose matrix inversion of $(\cdot)$, respectively. $\mathbf{b}|_{\mathrm{T}}$ denotes the entries of the vector $\mathbf{b}$ in the set T, T^c represents the complementary of given set T; $\mathbf{D}_{\mathrm{T}}$ denotes the column submatrix comprising the T columns of $\mathbf{D}$.

2 Compressibility of CFO Estimation Metric

2.1 ML-Based CFO Estimation over Flat Fading Channel

Concentrating on CFO estimation over flat Rayleigh channel, the sampled signals can be expressed in matrix form as [2]

$$\mathbf{x} = \mathbf{H}(\nu)\,\mathbf{A}h + \mathbf{w}, \tag{1}$$

where $\mathbf{x} = [x(0), x(1), \ldots, x(N-1)]^T$ is the received signal vector, diagonal matrix $\mathbf{H}(\nu) = diag\left\{1, e^{j2\pi\cdot\nu}, \ldots, e^{j2\pi\cdot(N-1)\nu}\right\}$, ν denotes the the carrier frequency offset normalized to $1/T_s$ (T_s is the sampling interval), the training symbols are represented as $\mathbf{A} = \left[a_0, a_1, \ldots, a_{N-1}\right]^T$, h is a zero-mean complex Gaussian random variable with unit variance that models the flat Rayleigh fading, and $\mathbf{w} = [w(0), w(1), \ldots, w(N-1)]^T$ is a zero-mean Gaussian vector with covariance matrix $\sigma_n^2\mathbf{I}_N$, where $\mathbf{I}_N$ is the identity matrix.

The signal-to-noise ratio (SNR) is defined as $SNR = \frac{\sigma_s^2}{\sigma_n^2}$, where $\sigma_s^2 = \frac{1}{N}\sum_{n=0}^{N-1}\left|ha_n\right|^2$. In traditional estimation method [2], the problem of ML estimation of the frequency ν is to seek the maximum of the equivalent likelihood function

$$g\left(\widetilde{\nu}\right) = \frac{1}{\sum_{n=0}^{N-1}\left|a_n\right|^2}\left|\mathbf{A}^H\mathbf{H}^H\left(\widetilde{\nu}\right)\mathbf{x}\right|^2, \tag{2}$$

where $\widetilde{\nu}$ is a tentative value of ν.

2.2 Compressibility of ML-Based CFO Estimation

By ignoring the constant $\sum_{n=0}^{N-1}\left|a_n\right|^2$ in (2), the *CFO estimation metrics* is

$$\mathbf{B}\left(\widetilde{\nu}\right) = \mathbf{A}^H\mathbf{H}^H\left(\widetilde{\nu}\right)\mathbf{x}. \tag{3}$$

Then, the equivalent likelihood function can be expressed as

$$g\left(\widetilde{\nu}\right) = C\left|\mathbf{B}\left(\widetilde{\nu}\right)\right|^2, \tag{4}$$

where the constant C represents the part that does not depend on $\widetilde{\nu}$.

Without loss of generality, the maximum of the equivalent likelihood function is found according to (4) using the grid search. For grid search, P ($P \geq N$) tentative values of ν, denoted as $\widetilde{\nu}_1, \widetilde{\nu}_2, \ldots, \widetilde{\nu}_P$, are considered. According to the P tentative values, we form a estimation metric vector $\widetilde{\mathbf{B}}$ as

$$\widetilde{\mathbf{B}} = \left[\mathbf{B}\left(\widetilde{\nu}_1\right), \mathbf{B}\left(\widetilde{\nu}_2\right), \ldots, \mathbf{B}\left(\widetilde{\nu}_\mathbf{P}\right)\right]^T. \tag{5}$$

Substituting $\mathbf{B}\left(\widetilde{\nu}_p\right) = \mathbf{A}^H\mathbf{H}^H\left(\widetilde{\nu}_p\right)\mathbf{x}$, $p = 1, 2, \ldots, P$, into Eq. (4), we have

$$\widetilde{\mathbf{B}} = \begin{pmatrix} \mathbf{A}^H\mathbf{H}^H\left(\widetilde{\nu}_1\right) \\ \mathbf{A}^H\mathbf{H}^H\left(\widetilde{\nu}_2\right) \\ \vdots \\ \mathbf{A}^H\mathbf{H}^H\left(\widetilde{\nu}_P\right) \end{pmatrix}\mathbf{x} = \widetilde{\mathbf{H}}\mathbf{x}, \tag{6}$$

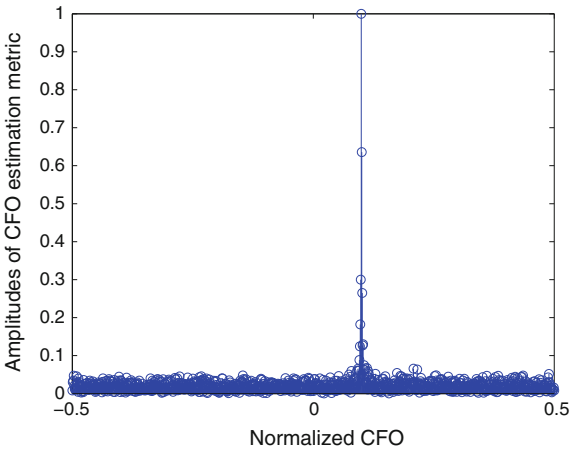

Fig. 1 An example of the compressibility of CFO estimation metrics. Where $N = 1024$, $P = 1024$, $T_s = 10^{-9}$ s, the normalized CFO $\nu = 0.1$, $SNR = 20$ dB, and the amplitudes are normalized to the maximum amplitude

where $\widetilde{\mathbf{H}} = \left[\widetilde{\mathbf{H}}\left(\widetilde{\nu}_{\mathbf{0}}\right), \widetilde{\mathbf{H}}\left(\widetilde{\nu}_1\right), \ldots, \widetilde{\mathbf{H}}\left(\widetilde{\nu}_{N-1}\right)\right]^T$. For relatively high SNR, the estimation metric vector $\widetilde{\mathbf{B}}$ is approximately sparse. That is, the amplitudes of CFO estimation metrics, i.e., $\left|B\left(\widetilde{\nu}_1\right)\right|, \left|B\left(\widetilde{\nu}_2\right)\right|, \ldots, \left|B\left(\widetilde{\nu}_P\right)\right|$, only a few amplitudes are significant and the rest are zero or negligible with relatively high SNR. A typical example is given in Fig. 1. From Fig. 1, only a few amplitudes are significant, and the significant amplitudes gather a cluster. Thus, the estimation metric vector $\widetilde{\mathbf{B}}$ can be compressed according to the compressed sensing theory [6].

Since the CFO estimation metrics are sparse, we may employ an $M \times P$ ($M \ll N \leq P$) measurement matrix $\mathbf{D}$ to compress $\widetilde{\mathbf{B}}$ according to the compressed sensing theory [6]. An $M \times 1$ measurements, denoted as $\mathbf{y}$, is given by

$$\mathbf{y} = \mathbf{D}\widetilde{\mathbf{B}}. \tag{7}$$

By substituting Eq. (6), i.e., $\widetilde{\mathbf{B}} = \widetilde{\mathbf{H}}\mathbf{x}$, into Eq. (7), we have

$$\mathbf{y} = \mathbf{D}\widetilde{\mathbf{H}}\mathbf{x} = \mathbf{J}\mathbf{x}, \tag{8}$$

where $\mathbf{J} = \mathbf{D}\widetilde{\mathbf{H}}$ can be viewed as a sensing matrix. Then, the generic analog-to-information converter (AIC) circuit architecture can be formed to perform compressive sampling of received signal $\mathbf{x}$. Note that, the case that the estimation metric vector $\widetilde{\mathbf{B}}$ can be compressed, cannot illuminate we can perform compressive sampling of received signal $\mathbf{x}$. In this paper, we are fortunate to obtain (8) that enables us to directly compress the received signal $\mathbf{x}$.

3 CFO Estimation Method with Model-Based CS

3.1 Coarse CFO Estimation with Model-Based CoSaMP

Using compressive sampling, the $M \times 1$ measurements $\mathbf{y}$ are obtained by exploiting the sparsity of the estimation metric vector $\widetilde{\mathbf{B}}$. We first reconstruct the estimation metric vector $\widetilde{\mathbf{B}}$, and denote the reconstructed $\widetilde{\mathbf{B}}$ as $\breve{\mathbf{B}}$.

Among these available CS reconstruct algorithms, we reference the CoSaMP method [7] due to its high reconstruction accuracy and excellent robustness to noise. Meanwhile, the characteristic that the significant amplitudes of the CFO estimation metrics gather together (see Fig. 1) indicates that the model-based CoSaMP [5] algorithm can be introduced into the reconstructing of coarse CFO estimation metrics. The detail of the model-based CoSaMP algorithm for reconstructing of coarse CFO estimation metrics is exhibited in Table 1, where $\mathbf{u} = [u_1, u_2, \ldots, u_P]^T$, $\mathbf{b} = [b_1, b_2, \ldots, b_P]^T$, the superscript "$c$" represents the complementary of given set,

Table 1 Model-based CoSaMP for reconstruction of coarse CFO estimation metrics

Input: Measurement matrix $\mathbf{D}$, noisy measurements $\mathbf{y}$, and sparsity level K.

Output: CFO estimation metric vector $\breve{\mathbf{B}}$.

Initial: $\breve{\mathbf{B}}^{(0)} \leftarrow \mathbf{0}$, $\mathbf{v} \leftarrow \mathbf{y}$, $k \leftarrow 0$;
Repeat:
- $k = k + 1$;
- $\mathbf{u} \leftarrow \mathbf{D}^H \mathbf{v}$;
- $W_1 = \{i : |u_i| = \max\{|u_1|, |u_2|, \cdots, |u_P|\}\}$;
- $\mathbf{W}_1 \leftarrow$ The $2K$ indexes nearest to W_1 in index set $\{1, 2, \cdots, P\}$ including W_1;
- $\mathrm{T} \leftarrow \mathrm{supp}\left(\breve{\mathbf{B}}^{(k-1)}\right) \cup \mathbf{W}_1$;
- $\mathbf{b}|_{\mathrm{T}} \leftarrow (\mathbf{D}_{\mathrm{T}})^{\dagger}\mathbf{y}$;
- $\mathbf{b}|_{\mathrm{T}^c} \leftarrow \mathbf{0}$;
- $W_2 = \{i : |b_i| = \max\{|b_1|, |b_2|, \cdots, |b_P|\}\}$;
- $\mathbf{W}_2 \leftarrow$ The K indexes nearest to W_2 in index set $\{1, 2, \cdots, P\}$ including W_2;
- $\mathbf{b}|_{\mathbf{W}_2^c} \leftarrow \mathbf{0}$;
- $\breve{\mathbf{B}}^{(k)} \leftarrow \mathbf{b}$;
- $\mathbf{v} \leftarrow \mathbf{y} - \mathbf{D}\breve{\mathbf{B}}^{(k)}$;

Until: $k = K$
$\breve{\mathbf{B}} \leftarrow \breve{\mathbf{B}}^{(k)}$.

and the support set $\mathrm{supp}(\mathbf{x})$ denotes the index set of nonzero elements in $\mathbf{x}$, i.e., $\mathrm{supp}(\mathbf{x}) = \{i : x_i \neq 0\}$.

For reconstructing coarse CFO estimation metrics, the model-based CoSaMP algorithm is instantiated in two parts. One is that $\mathbf{W}_1$ locates $2K$ nearest indexes (including the index of maximum amplitude) of the index of the maximum amplitude (i.e., W_1) in $\mathbf{u}$. The other is the K nearest indexes of the index of the maximum amplitude in $\mathbf{b}$ for updating $\breve{\mathbf{B}}^{(k)}$ is employed.

Note that, model-based CoSaMP in [5] does not provide the method details of choosing $2K$ indexes for $\mathbf{W}_1$ and choosing K indexes for $\mathbf{W}_2$. We employ the the most credible values W_1 and W_2 (i.e., the respective maximum amplitudes of $\mathbf{u}$ and $\mathbf{b}$) to find the nearest $2K$ indexes of W_1 for $\mathbf{W}_1$ and the nearest K indexes of W_2 for $\mathbf{W}_2$, respectively.

On the basis of $\breve{\mathbf{B}}$, the coarse CFO estimation $\hat{\nu}_{\text{coarse}}$ can be estimated. We denote the reconstructed $\breve{\mathbf{B}}$ as $\breve{\mathbf{B}} = \left[\breve{B}\left(\tilde{\nu}_1\right), \breve{B}\left(\tilde{\nu}_2\right), \ldots, \breve{B}\left(\tilde{\nu}_P\right)\right]^T$, then we have

$$\hat{\nu}_{\text{coarse}} = \arg\max_{\tilde{\nu}_p} \left\{ \left| \breve{B}\left(\tilde{\nu}_p\right) \right|^2 \right\}, \tag{9}$$

where $p = 1, 2, \ldots, P$.

3.2 Fine CFO Estimation Using Interpolating

Using the estimated $\breve{\mathbf{B}}$ and $\hat{\nu}_{\text{coarse}}$, we employ interpolation method to implement the fine CFO estimation by searching $\hat{\nu}_{\text{fine}}$ near to $\hat{\nu}_{\text{coarse}}$. In this subsection, we assume that the frequency range for searching $\hat{\nu}_{\text{fine}}$ is $\left[\hat{\nu}_{\text{coarse}} - \zeta, \hat{\nu}_{\text{coarse}} + \zeta\right]$ with $\zeta > 0$.

From (6), we have $\mathbf{x} = \widetilde{\mathbf{H}}^{\dagger}\widetilde{\mathbf{B}}$. Assuming $N \times 1$ noise vector caused by inaccurate reconstruction of $\widetilde{\mathbf{B}}$ be $\mathbf{n}$, the received signal $\mathbf{x}$ sampled as Nyquist rate can be expressed as $\mathbf{x} = \widetilde{\mathbf{H}}^{\dagger}\breve{\mathbf{B}} + \mathbf{n}$, where we replace $\widetilde{\mathbf{B}}$ with the estimated $\breve{\mathbf{B}}$. For relatively high SNR (e.g., 20 dB), the recovery algorithm can accurately reconstruct $\widetilde{\mathbf{B}}$ (i.e., $\widetilde{\mathbf{H}}\mathbf{x}$), and the noise vector $\mathbf{n}$ can be ignored. Then we have

$$\mathbf{x} \approx \widetilde{\mathbf{H}}^{\dagger}\breve{\mathbf{B}}. \tag{10}$$

According to Eq. (3), we use the tentative frequency $\breve{\nu}$ in $\left[\hat{\nu}_{\text{coarse}} - \zeta, \hat{\nu}_{\text{coarse}} + \zeta\right]$ to construct $N \times 1$ vector $\breve{\mathbf{H}}\left(\breve{\nu}\right)$ as

$$\breve{\mathbf{H}}\left(\breve{\nu}\right) = \left[a_0^*, a_1^* e^{-j2\pi\cdot\breve{\nu}}, \ldots, a_{N-1}^* e^{-j2\pi\cdot(N-1)\breve{\nu}}\right]^T. \tag{11}$$

Substituting (11) and (10) into (2), the equivalent likelihood function $g\left(\breve{\nu}\right)$ can be expressed as

$$g\left(\breve{\nu}\right) = \left|\left(\widetilde{\mathbf{H}}^{\dagger}\breve{\mathbf{B}}\right)^{T}\breve{\mathbf{H}}\left(\breve{\nu}\right)\right|^{2}. \tag{12}$$

Then, the fine CFO estimation $\hat{\nu}_{\text{fine}}$ can be obtained by seeking the maximum of the equivalent likelihood function $g\left(\breve{\nu}\right)$.

4 Numerical and Simulation Results

Computer simulation results are presented in this section. The training sequence employs Zadoff–Chu sequence, and the Cramér-Rao Bound (CRB) is referenced from [2]. We first verify the effectiveness of coarse CFO estimation of proposed method. Considering Gaussian random matrix as the measurement matrix **D**, an example of coarse CFO estimation is given in Fig. 2, where three cases for coarse CFO estimation, i.e., $\nu = 0.1$, $\nu = 0.2$, and $\nu = 0.3$ are considered. In Fig. 2, the CoSaMP and model-based CoSaMP algorithms obtain nearly the same CFO estimation values of ML method described in Eq. (2) with relatively high SNR, e.g., $SNR \geq 10$ dB. Thus, the proposed method can ensure good performance of coarse estimation. Furthermore, the estimated values of model-based CoSaMP is much closer to the classical ML-based method than CoSaMP algorithm when $SNR \leq 5$

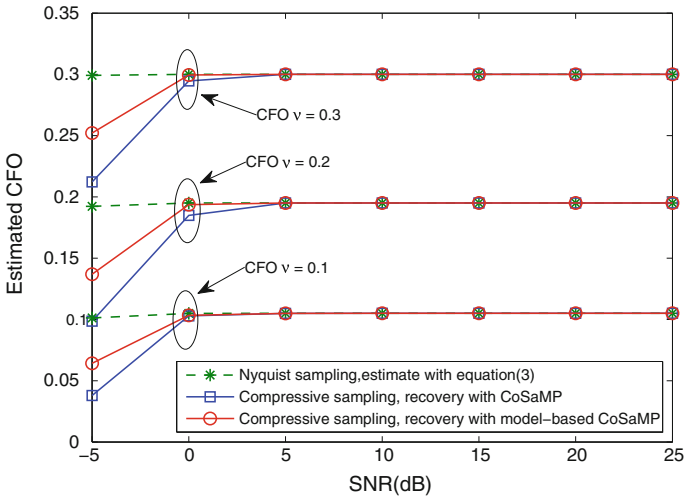

Fig. 2 CoSaMP and model-based CoSaMP for coarse CFO estimation, where $N = P = 64$, $T_s = 10^{-9}$ s, $M = 32$, $K = 6$, the CFOs, i.e., $\nu = 0.1$, $\nu = 0.2$, and $\nu = 0.3$ are considered, **D** employs a Gaussian random matrix

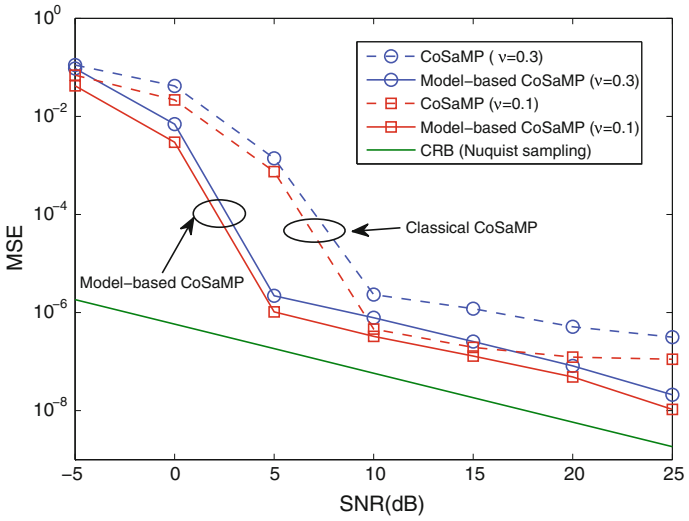

Fig. 3 The MSE of CFO estimation, where $N = 64, P = 128, M = 32, K = 6, \nu = 0.1$, and $\nu = 0.3$ are considered. **D**, respectively, employs a Gaussian random matrix and an optimized measurement matrix for $\nu = 0.1$ and $\nu = 0.3$

dB, which illuminates that the model-based CoSaMP can improve the performance of classical CoSaMP algorithm for coarse CFO estimation.

For fine CFO estimation, the comparison of MSE performance is given in Fig. 3. For $\nu = 0.3$ and $\nu = 0.1$, we, respectively, consider the measurement matrix **D** as a Gaussian random matrix and a optimized measurement matrix in [8]. With same method of fine CFO estimation and different coarse CFO estimation methods, Fig. 3 shows that the model-based CoSaMP can produce better MSE performance than the classical CoSaMP recovery algorithm. The main reason is that the model-based CoSaMP adopts the prior information of metric characteristic. Although the same values of coarse CFO estimation can be obtained with relatively high SNRs, the reconstructed estimation metrics $\breve{\mathbf{B}}$ using model-based CoSaMP is much closer to $\widetilde{\mathbf{B}}$ than using CoSaMP algorithm. Thus, the model-based CoSaMP can effectively improve the MSE performance compared to the classical CoSaMP algorithm for CFO estimation.

5 Conclusion

In this paper, the CS-based CFO estimation method in flat fading channel has been investigated. We have confirmed that the compressive sampling can be employed for CFO estimation in flat fading channels. On the basis of the prior information of metric characteristic, the model-based CoSaMP algorithm is introduced into the

reconstructing the metrics of CFO estimation to interpolate the equivalent likelihood function for fine CFO estimation. Compared to the classical CoSaMP algorithm, the analysis and simulation results have shown that the better estimation performance (including coarse estimation and fine estimation) can be obtained when the model-based CoSaMP is employed.

Acknowledgments This work is supported in part by the Science Foundation for Postdoctorate Research (Grant No. 2012M511920), the project of Meteorological information and Signal Processing Key Laboratory of Sichuan Higher Education Institutes (Grant No. QXXCSYS201402), the Xihua University Young Scholars Training Program (Grant No. 01201408), the key scientific research fund of Xihua University (Grant No: Z1120941), the project of science and technology plan of Sichuan Province (Grant No. 2015JY0138), the key projects of Education Department of Sichuan Province (Grant No. 15ZA0134), and the Open Research Subject of Key Laboratory (Research Base) of signal and information processing (Grant No. szjj2015-071).

References

1. Haring L, Czylwik A, Speth M (2004) Analysis of synchronization impairments in multiuser OFDM systems. In: Proceedings of 2004 international OFDM-workshop, pp 91–95
2. Kuo WY, Fitz MP (1997) Frequency offset compensation of pilot symbol assisted modulation in frequency flat fading. IEEE Trans Commun 45(11):1412–1416
3. Kong SH (2013) A deterministic compressed GNSS acquisition technique. IEEE Trans Veh Technol 62(2):511–521
4. Kim B, Kong SH (2014) Two-dimensional compressed correlator for fast acquisition of BOC (m, n) signals. IEEE Trans Veh Technol 63(6):2662–2672
5. Baraniuk RG, Cevher V, Duarte MF, Hegde C (2010) Model-based compressive sensing. IEEE Trans Inf Theor 56(4):1982–2001
6. Cands E, Romberg J, Tao T (2006) Robust uncertainty principles: Exact signal reconstruction from highly incomplete frequency information. IEEE Trans Inf Theor 52:489–509
7. Needell D, Tropp J (2010) Cosamp: iterative signal recovery from incomplete and inaccurate samples. Commun ACM 53(12):93–100
8. Zelnik-Manor L, Rosenblum K, Eldar Y (2012) Dictionary optimization for block-sparse representations. IEEE Trans Sig Process 60(5):2386–2395

Modeling and Analyzing Electromagnetic Interference Signal in Complex Battlefield Environments

Chuntong Liu, Rongjing Wu, Zhenxin He, Xiaofeng Zhao, Hongcai Li and Pengzhi Wang

Abstract Electronic jamming is the key technology of electronic warfare, for which models and simulation are studied on noise jamming deception jamming and chaff jamming. In the noise jamming, the simulation analysis of radio frequency noise jamming is conducted and the theoretical models of other forms of noise jamming are built. The simulation analysis of RGPO is carried out in the deception jamming. In addition, theoretical modeling and simulation analysis of chaff jamming are carried out with the Monte Carlo method. Simulation results show that the models are correct and can be used to simulate the statistical characteristics of chaff jamming.

Keywords Battlefield environment · Electronic jamming · Mathematical model · Simulation analysis

1 Introduction

The Gulf War and the Kosovo war show that the electronic warfare kicks off and exists in the whole process of war, affecting the war process and pattern, which is the mainstream and a significant feature of information warfare [1]. Radar jamming and antijamming ability have become the key factors in the electronic warfare. The detection and intentional electronic interference of launch task of the foreign spy satellites are inevitable to affect the electromagnetic safety of the launch site, which seriously threatens the space launch task of each country [2]. Missiles under electromagnetic interference cannot be properly guided and lose targets. Therefore, it is significant to study electromagnetic interference in complex battlefield environment, which will play an indispensable role in the construction of information army and in the war of information technology. It also has practical significance in anti-interference research for missile weapons.

C. Liu · R. Wu · Z. He (✉) · X. Zhao · H. Li · P. Wang
Xi'an Research Institute of High Technology, Xi'an 710025, Shaanxi, China
e-mail: hezhenxin1986@126.com

Q. Liang et al. (eds.), *Proceedings of the 2015 International Conference on Communications, Signal Processing, and Systems*, Lecture Notes in Electrical Engineering 386, DOI 10.1007/978-3-662-49831-6_35

Electronic attack is the fighting force which can destroy the target directly by the active use of the electromagnetic spectrum or directional energy. Electronic attacks against radar include nondestructive actions and destructive actions. Nondestructive action is to reduce or offset the operational effectiveness of enemy radar by using suppressing jamming and deception jamming [3].

The development of electronic jamming and antijamming technology has brought unprecedented challenges to the guided weapons. Radar jamming reduces the lethality of the guided weapon, yet improves the survival ability of the target [4]. The new strategy should be proposed in air defense missile weapon system to meet the current electronic warfare needs after carefully studying the development of airborne electronic countermeasure technology [5]. At present, there has been a large number of researches concerning the electronic interference, but most of them are based on a certain kind of interference. The research scope is relatively scattered and lack comprehensive interference analysis and model study [6]. This paper analyzes the theory of mathematical modeling and simulation of common types of electronic jamming, which will play an important role in the identification of enemy electronic jamming and electronic jamming to enemies. It has important practical significance in the current form of electronic warfare technology, and pushes forward the researches of radar antijamming technology.

2 Classification and Mathematical Model of Radar Jamming

Electronic warfare is a military action where both sides interfere with weapons' usage of the electromagnetic spectrum and electromagnetic information and attack enemies and their weapons by using electromagnetic energy or directional energy; in the meantime it guarantees weapon equipment normal function and personnel's safety [7]. The interference of radar is mainly classified into background and artificial interference and the latter is the focus of our study. Artificial interference can be classified into active jamming and passive jamming. Active jamming can be further classified into the suppression of jamming and deception jamming according to the principle of interference signal. The mathematical modeling and analysis of common jamming signals are discussed in the following parts.

2.1 Radio Frequency Noise Jamming

Masking jamming basic principle is as follows, internal noise and external noise exist in any radar; detection of radar targets is conducted in these noises; the detection is based on a certain probability criterion.

Radio frequency noise jamming is one of the effective ways of masking jamming. The RF noise jamming can be obtained by direct amplification of microwave noise and its mathematical model can be expressed as follows,

$$u_j(t) = u_n(t) \cdot \cos(\omega_j t + \phi(t)) \tag{1}$$

where $u_n(t)$ satisfies the Rayleigh distribution and $\phi(t)$ satisfies uniform distribution in [0, 2pi]; $u_n(t)$ and $\phi(t)$ are independent of each other; ω_j is the carrier frequency and it is a constant.

The noise is a power signal and its power is limited, but the energy is unlimited. So, the power spectrum is used to express its frequency characteristics. Its power spectral density expression is,

$$G_j(f) = \begin{cases} \frac{\sigma^2}{\Delta f_j} & |f - f_j| \le \frac{\Delta f_j}{2} \\ 0 & others \end{cases} \tag{2}$$

where σ^2 is the average power of noise; Δf_j is interference bandwidth; f_j is the center frequency of RF noise jamming. If medium frequency of the receiver has a rectangular feature, after the radio frequency noise is received by the receiver, the output interference signal of the medium-frequency amplifier is still narrow band Gauss noise, and its power spectrum $G_i(f)$ is as follows,

$$G_j(f) = |H_i(f)|^2 \cdot G_j(f - f_i) = \begin{cases} \frac{\sigma_i^2}{\Delta f_i} & |f - f_i| \le \frac{\Delta f_r}{2} \\ 0 & others \end{cases} \tag{3}$$

where f_i is the center frequency of the receiver; Δf is medium bandwidth of receiver. The correlation function of the RF noise can be obtained according to Fourier transform relation between the correlation function and the power spectrum density function of the signal. The correlation function of the RF noise satisfies:

$$R_i(\tau) = \int_0^\infty G_i(f) \cos 2\pi f \tau df = \sigma_i^2 \frac{\sin \pi \Delta f_r \tau}{\pi \Delta f_r \tau} \cos 2\pi \Delta f_i \tau \tag{4}$$

After the linear detector, the Gauss white noise distribution becomes Rayleigh distribution,

$$P_i(U_v) = \frac{U_v}{\sigma_v^2} \cdot e^{\frac{U_v^2}{2\sigma_v^2}}, \; U_v > 0 \tag{5}$$

where $\sigma_v^2 = k \cdot \sigma^2$ (k is the amplification factor of the linear detector).

In practice, the RF noise signals and radar signals are often simultaneously entered into the radar receiver, and built the model for the mixed signal of both.

Set target echo signal as single frequency signal, and then

$$s(t) = u_s \cdot \cos(w_0 t) \tag{6}$$

The expression of the mixed signal of output signal of the receiver and the noise is,

$$\begin{aligned} u_j(t) + s(t) &= u_{\mathrm{n}}(t) \cdot \cos(\omega_j t + \phi(t)) + u_s \cdot \cos(w_0 t) \\ &= u_i(t) \cdot \cos(\omega_i t + \phi(t)) \end{aligned} \tag{7}$$

where $u_i(t)$ is the amplitude of the synthesized signal, and the probability distribution is the rice distribution.

2.2 Range-Gate Pull Off

RGPO can be applied to radar systems of different ranging systems. RGPO can be roughly divided into three stages: stop delay period, towing period and termination period. In the first period, jammers amplify and forward signals quickly to make time delay difference between the target echo and itself short enough to enter the radar range gate, due to its higher power of interference signal, the range gate cannot lock the exact interference signal. When the stop delay period ends or when the range gate locks interference signal, it comes to the second period, towing period. In this period, time delay of jammer's forwarding signal is gradually extended to increase distance between the interference signal and target signal in range dimension. Because the range gate is locked in the interference signal, the target has been dragged out of range gate gradually. Then the change rule of time delay of interference signal can be expressed as $d\tau(t)/dt = v(t)$, wherein, $\tau(t)$ and $v(t)$ are towing distance and towing speed. Finally, when the target is dragged out of range gate, it comes to the termination period, in which the jammer is turned off or stops forwarding the interference signal, and the radar returns back to the search state because there is no signal within range gate.

Based on analysis of the target echo model, the target echo signal received by receiver can be obtained,

$$s(t) = A_s \exp[j(\omega_c + \omega_d)(t - \frac{2R(t)}{c})] \tag{8}$$

signal of RGPO satisfies,

$$J(t) = A_j \exp[j(\omega_c + \omega_d)(t - \frac{2R(t)}{c} - \Delta t_j(t))] \tag{9}$$

where A_s is the signal amplitude of the real target; A_j is amplitude of interference signal and $A_j > A_s$; ω_c is the carrier frequency of radar; ω_d is the Doppler frequency; $R(t)$ is the real distance of the target; $\Delta t_j(t)$ is delay time of signal of RGPO compared with normal echo signal of the target, it changes with time; C is the speed of light.

Assuming that the target is moving at a constant speed, when adopting the linear or parabolic dragging ways, the distance function of the false target can be expressed as follows,

$$\Delta t_j(t) = \begin{cases} R + v_1 t & 0 \le t < t_1 \text{ (stop } delay \text{ period)} \\ R + v_1 t_1 + v_2(t - t_1) \text{ or } R + v_1 t_1 + a(t - t_1)^2 & t_1 \le t < t_2 \text{ (towing period)} \\ jamming\ off & t_1 \le t < t_2 \text{ (terminaton period)} \end{cases} \tag{10}$$

where R is the distance of the target; v_1 is velocity of the target; v_2 is the towing speed of linear towing and a is the towing acceleration of parabolic towing. According to the principle of radar delay ranging, the distance change of the interference signal is converted into time delay and we can obtain,

$$\Delta t_j(t) = \begin{cases} R + v_1 t & 0 \le t < t_1 \text{ (stop } delay \text{ period)} \\ \frac{2v_2}{c}(t - t_1) \text{ or } \frac{2a}{c}(t - t_1)^2 & t_1 \le t < t_2 \text{ (towing period)} \\ jamming\ off & t_1 \le t < t_2 \text{ (termination period)} \end{cases} \tag{11}$$

3 Computer Simulation Analysis

3.1 RF Noise Jamming Simulation

We design MATLAB program for RF noise and carry out computer simulations. The simulation parameters are set as follows, the sampling frequency is 100 MHz; the bandwidth of bandpass filter is 30 MHz; the Noise Figure is 1.2. Simulation flow chart is shown in Fig. 1.

Simulation results are shown in Figs. 2 and 3.

It can be seen from the graph that the envelope of the RF noise obeys the Rayleigh distribution and the phase obeys the uniform distribution, which is consistent with the theoretical analysis.

Through the filter, autocorrelation function and power spectrum density function of RF noise are shown in Figs. 4 and 5. It can be seen that power spectral density shows the filter shape through bandpass filter and autocorrelation function shows characteristics of single frequency signal, which is consistent with the theoretical analysis.

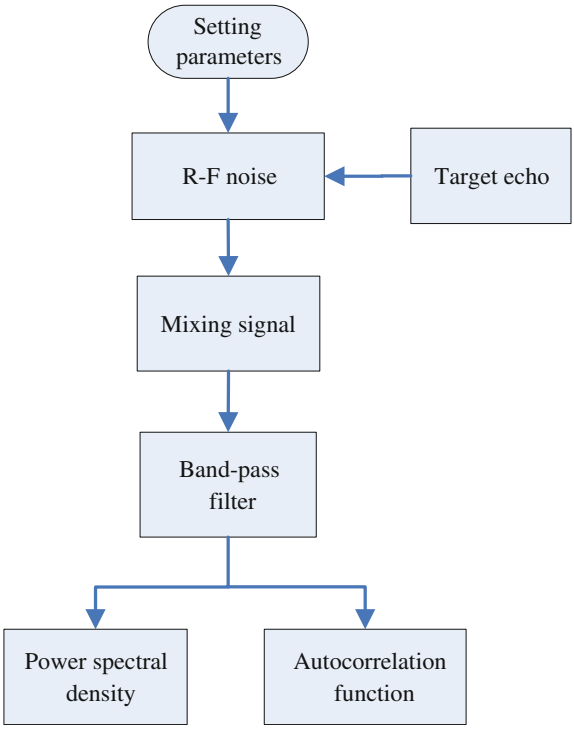

Fig. 1 Simulation flow chart of RF noise

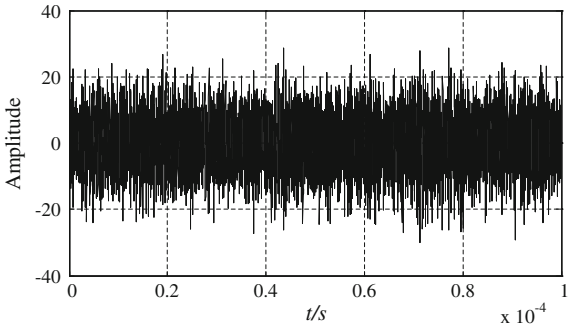

Fig. 2 Time-domain wave of band-limited RF noise

Respectively, $u_s/\sigma_i = 0.1$; 1; 10, the computer simulation results of the signal superimposed with noise are shown in Figs. 6, 7 and 8. It can be seen that the output amplitude of the receiver under RF noise jamming shows following distribution. Echo signals' magnitude is no longer original form of rectangular pulse under the influence of RF noise jamming and varies around the average potential of noise. As the interference power increases, the signal is submerged in the noise interference and it cannot be detected and identified.

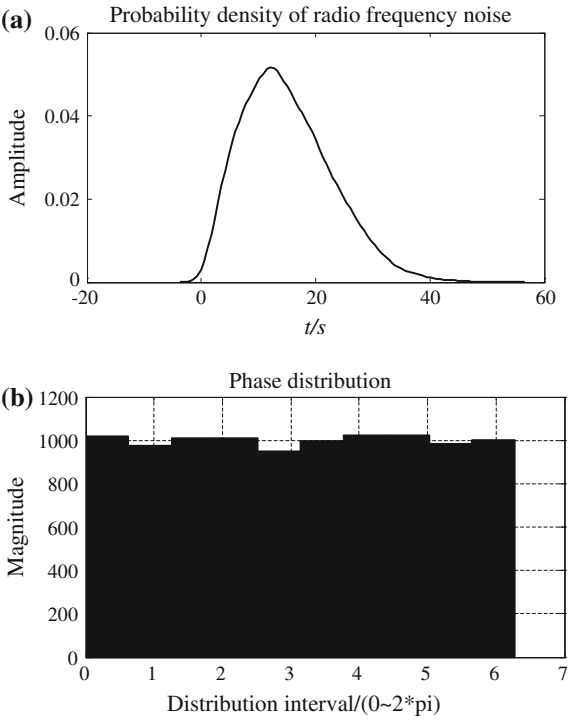

Fig. 3 Envelope distribution and phase distribution of RF noise jamming. **a** The envelope obeys the Rayleigh distribution, **b** the phase obeys the uniform distribution

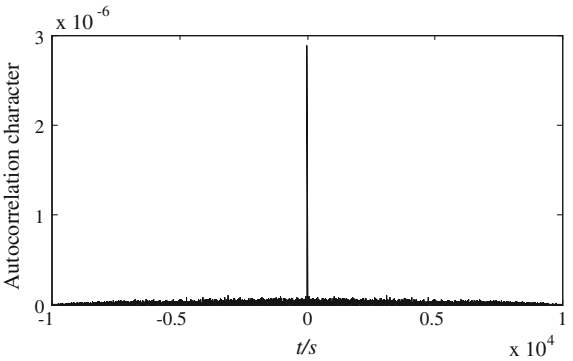

Fig. 4 Autocorrelation function of RF noise

3.2 RGPO Simulation

Assume that carrier frequency of the radar emission signal is 10 MHz; pulse repetition frequency is 2.5 kHz; duty ratio is 1/4; sampling frequency is 100 MHz; range gate is towed at a constant speed. Simulation parameters are as follows,

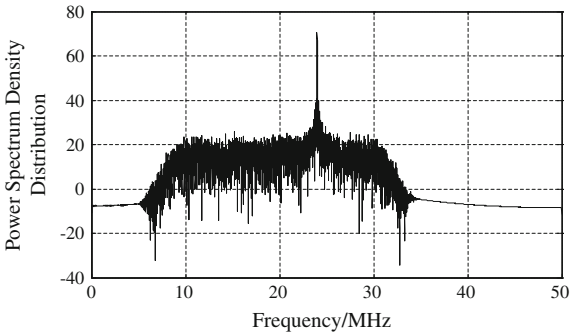

Fig. 5 Power spectral density of RF noise

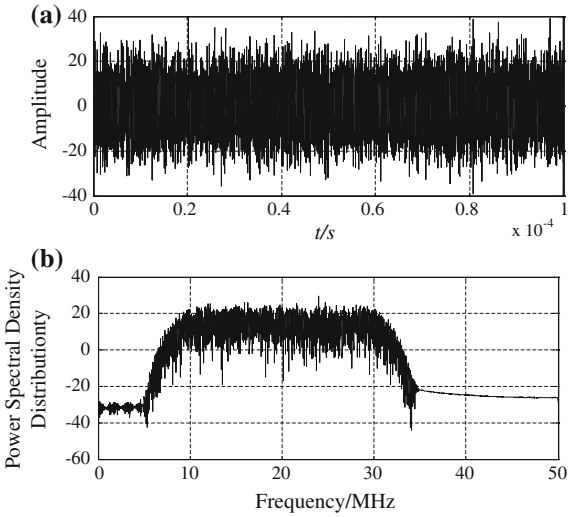

Fig. 6 Performance simulation of echo with RF noise when $u_s/\sigma_i = 0.1$. **a** Time-domain waveform. **b** Power spectral density

R = 2 km; v1 = 0 m/s; t1 = 0.2 ms; t2 = 2 ms; V2 = 105 m/s; jamming to signal ratio is 10 dB. Flow chart of deception jamming simulation algorithm is shown in Fig. 9.

Figure 10 shows that interference signal is formally exactly the same as the target signal except amplification of amplitude before 0.2 ms. They both have same time delay compared to emission signal, about 13 us which is consistent with the target distance. Distance towing begins at 0.2 ms, interference signal and target signal differs. Compared with emission signal, time delay of interference signal is gradually increased within each pulse period and the delay of target signal remains unchanged, so the distance between interference signal and the target signal becomes larger, which is consistent with the theoretical analysis. It verifies the validity of the simulation model.

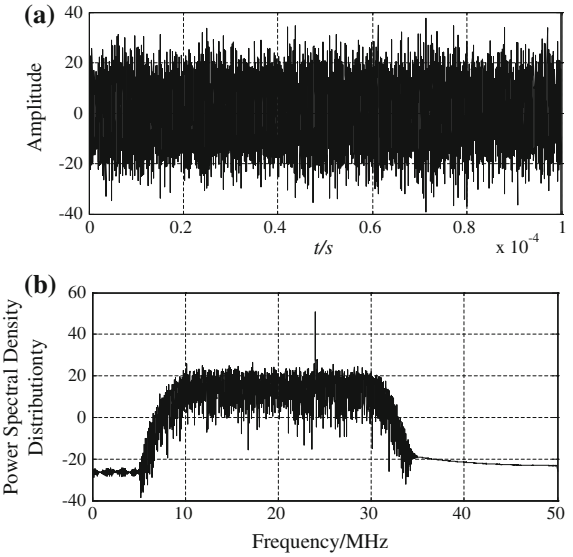

Fig. 7 Performance simulation of echo with RF noise when $u_s/\sigma_i = 1$. **a** Time-domain waveform. **b** Power spectral density

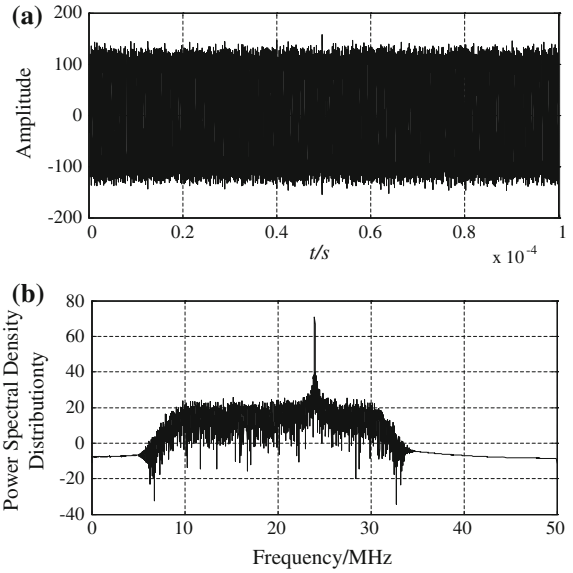

Fig. 8 Performance simulation of echo with RF noise when $u_s/\sigma_i = 10$. **a** Time-domain waveform. **b** Power spectral density

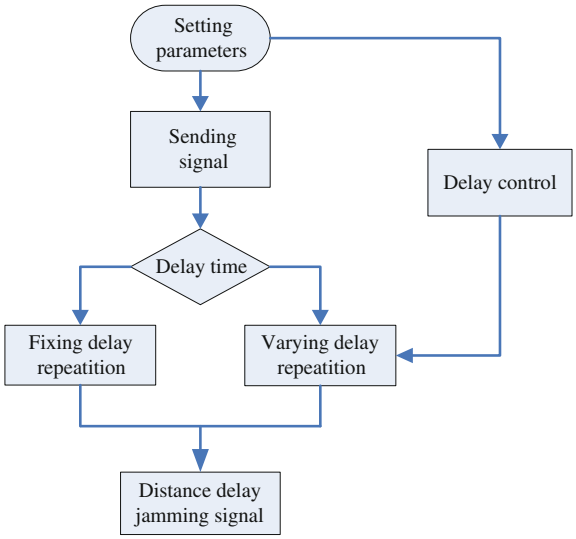

Fig. 9 Algorithm flow chart of distance deception jamming

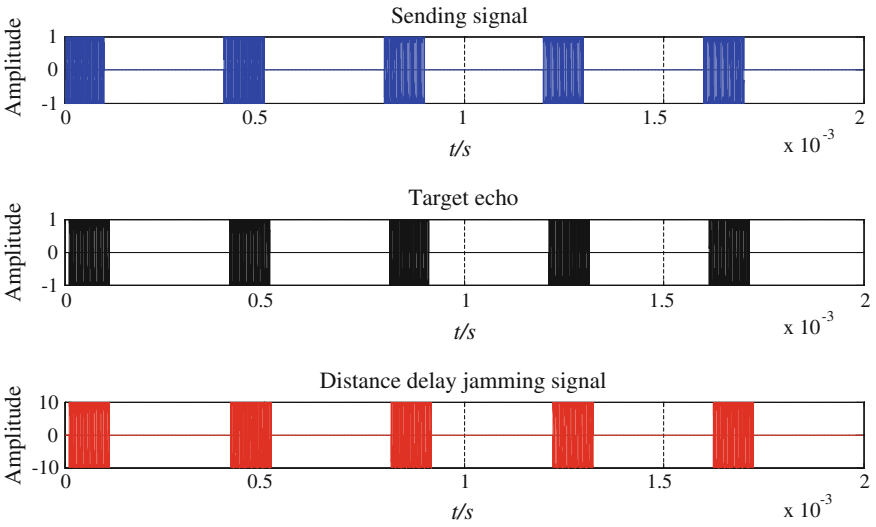

Fig. 10 Simulation of distance deception jamming

4 Conclusions

As new systems of radar and electronic systems and new communication equipment continue to emerge, the corresponding electronic countermeasure tactics technology has also been rapidly developed. In order to meet the objective requirements of the electronic warfare theory research and practical testing, benefiting from the favorable conditions that modeling theory and computer and the network technology obtained the rapid development, many electronic warfare simulation systems are produced at home and abroad. We analyzed the mathematical model of the common electronic interferences in complex battlefield environment and conducted computer simulation of RF noise jamming, RGPO, and chaff jamming. Simulation analyzes verify the validity of the mathematical model of the electronic interference. This study will be helpful in further study on the electronic interference and suppression.

Acknowledgments This work is partially supported by the National Nature Science Foundation of China under Grant 41404022 and the Nature Science Foundation of Shaanxi Province under Grant 2015JM4128.

References

1. Gao B, Lv S-W, Zhao J-H (2005) Implementation of effectiveness evaluation simulation system for ECM. Syst Eng Electron 27(10):1738–1739
2. Li Z-L (2009) Research on complicated electromagnetic environment and its applications for launch mission. Chinese Academy of Sciences, China
3. Zhang Y-S, Tong N-N, Zhao G-Q (2006) Principle of radar electronic warfare. National Defense Industry Press, Beijing
4. Su J, Song Z-Y, Fu Q, et al (2014) Joint tracking method for the unresolved decoy and target with monopulse radar. J Radars 4(2):160–163
5. Tao B-R (1993) An ECCM model and the technical development trends to the demands of the future EW combat. Syst Eng Electron 10:49–50
6. Ji F (2013) Modeling and simulation of radar electronic jamming. Dalian University of Technology, China
7. Zhao G-Q (2005) Principle of radar countermeasure. Xidian University Press, Xi'an

Part VI
Wireless Communication

An 8-Cycle Construction Scheme for Latin Square LDLC

Zhao Dan-feng and Xie Feng

Abstract A novel method for constructing the Latin square Low Density Lattice Codes (LDLC) parity check matrix is proposed in this paper. Based on the permutation matrix, a 6-cycle matrix is build firstly. Then the elements involved in the 6-cycle are detected and swapped, which is on the basis of the theory of adjacency matrix. Therefore, we obtain a check matrix, which is 6-cycle free and the nonzero elements obeying random distribution. Simulation results demonstrate that the proposed method has a lower symbol error rate (SER) compared with the previous works.

Keywords Lattice codes · LDLC · Parity check matrix · Symbol error rate

1 Introduction

Low Density Lattice Codes which were proposed in [1], are efficient and practical lattice codes for the reason that in LDLC both the encoder and the channel use the same real algebra, which is very convenient for the continuous-valued AWGN channel. LDLC codes are characterized by a sparse matrix, refers to the parity check matrix. Similar to LDPC codes, the parity check matrix is restricted to be sparse so that we can use the belief propagation (BP) algorithm to develop a linear complexity iterative decoding scheme [2, 3]. Simulation results show that LDLC can obtain the capacity of the AWGN channel [1, 4].

LDLC codes are designed by constructing the sparse parity check matrix in the Euclidean space. In [1], a constructing method was presented. In this method a

Z. Dan-feng · X. Feng (✉)
College of Information & Communication Engineering,
Harbin Engineering University, Harbin 150001, China
e-mail: 15663638668@163.com

Q. Liang et al. (eds.), *Proceedings of the 2015 International Conference on Communications, Signal Processing, and Systems*, Lecture Notes in Electrical Engineering 386, DOI 10.1007/978-3-662-49831-6_36

random permutation matrix is generated first, and then the 2-cycle and 4-cycle are detected and removed sequentially by swapping the elements involved in these cycles. Finally the check matrix is built from this permutation matrix. This scheme can obtain a check matrix without 4-cycle, and the nonzero elements are randomly distributed. But there still exist 6-cycle in the check matrix and it is difficult to remove using the same method as removing the 4-cycle. In [5], a construction scheme which eliminates the size 6-cycles based on the cyclic shift has been suggested. However, the un-randomly distributed nonzero elements in the parity check matrix lead to poor performance. In order to obtain better check matrices, we proposed in this work an efficient scheme to construct the parity check matrix of Latin square LDLC. This check matrix is 6-cycle free and the nonzero elements are randomly distributed.

Specifically, in the new scheme a 6-cycle matrix is generated first based on the permutation matrix, then the elements involved in a 6-cycle are detected through the theory of the adjacency matrix [6, 7]. When such an element is found, swap it without creating any new 6-cycles. Finally we obtain an 8-cycle parity check matrix until all the 6-cycles have been eliminated. Simulation results indicate that this 8-cycle check matrix has better performance than previous works.

The outline of this paper is as follows. In Sect. 2 we introduce the lattice and lattice codes. Section 3 gives the definition of LDLC codes and Sect. 4 describes the iterative decoding algorithm of the LDLC codes. The proposed construction method of the LDLC codes is presented in Sects. 5, 6 gives simulation results, followed by some conclusions in Sect. 7.

2 Lattice and Lattice Codes

A n dimensional lattice $\boldsymbol{\Lambda}$ in $\boldsymbol{R}^n$ is defined as the set of all linear combinations of n linearly independent vectors in $\boldsymbol{R}^n$ with integer coefficients [8] i.e.

$$\boldsymbol{\Lambda} = \{b_1\boldsymbol{g_1} + \cdots + b_n\boldsymbol{g_n}\} = [\boldsymbol{g_1}\cdots\boldsymbol{g_n}] \cdot [b_1\cdots b_n]^T \tag{1}$$

where the column vectors $\boldsymbol{g_1}\boldsymbol{g_2}\ldots\boldsymbol{g_n}$ are referred to as the basis vectors. The generator matrix of $\boldsymbol{\Lambda}$ is defined as

$$\boldsymbol{G} = [\boldsymbol{g_1}\boldsymbol{g_2}\cdots\boldsymbol{g_n}] = \begin{pmatrix} g_{11} & \cdots & g_{1n} \\ \vdots & \ddots & \vdots \\ g_{n1} & \cdots & g_{nn} \end{pmatrix} \tag{2}$$

With the above definition, the n dimensional lattice can be denoted as follows:

$$\boldsymbol{\Lambda} = \{\boldsymbol{G} \cdot \boldsymbol{b} : \boldsymbol{b} \in \boldsymbol{Z}^n\} \tag{3}$$

A n dimensional lattice code is defined by a lattice $\boldsymbol{G}$ and a shaping region $\boldsymbol{B} \subset \boldsymbol{R}^n$, where the codewords are all the lattice points that lie within the shaping region $\boldsymbol{B}$ [8]. All codewords are generated by $\boldsymbol{x} = \boldsymbol{G} \cdot \boldsymbol{b}, \boldsymbol{b} \in \boldsymbol{Z}^n$, where $\mathbf{b} = [b_1\ b_2 \cdots b_n]^T$ is a n dimensional integer vector.

3 Low Density Lattice Codes

Low Density Lattice Codes (LDLC) are n dimensional lattice codes represented by a sparse parity check matrix $\boldsymbol{H} = \boldsymbol{G}^{-1}$, where $\boldsymbol{G}$ is the LDLC generator matrix. A n dimensional Latin square LDLC is a special kind of LDLC that every row and column of the parity check matrix $\boldsymbol{H}$ has the same d nonzero values, except for a possible change of order and random signs. These d sorted values $h_1 \geq h_2 \geq \cdots \geq h_d > 0$ constitute a sequence which is referred to as the generator sequence.

For example, the matrix $\boldsymbol{H}$ is a parity check matrix of a Latin square LDLC with lattice dimension $n = 6$, degree $d = 3$ and generating sequence $h = \{1, 0.6, 0.3\}$.

Just like low density parity codes (LDPC), LDLC codes can also be represented by the bipartite graph as illustrated in Fig. 1b. In the graph, we put the variable nodes on the top and the check nodes down below. An edge connects variable node i and check node j when $H_{j,i} \neq 0$. A cycle is a closed path with no repeated nodes, and must therefore be of even length [7]. For example, the path $x_1 \to c_1 \to x_3 \to c_3 \to x_1$ forms a 4-cycle in the bipartite graph.

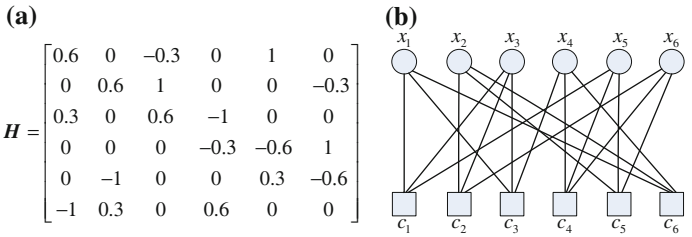

Fig. 1 **a** Parity check matrix of Latin square LDLC and **b** its bipartite graph

4 LDLC Iterative Decoder

A LDLC codeword $\boldsymbol{x}=(x_1, \ldots, x_n)$ is generated by $\boldsymbol{x}=\boldsymbol{G}\cdot\boldsymbol{b}, \boldsymbol{b}\in\boldsymbol{Z}^n$ and then transmitted over the AWGN channel, where noise w_i with variance σ^2 is added to each code symbol. Denoting the received sequence as $\boldsymbol{y}=(y_1, \ldots, y_n)$.

$$y_i = x_i + w_i, i = 1, 2, \ldots, n \tag{4}$$

The LDLC iterative decoder can be illustrated over the corresponding bipartite graph. A n dimensional Latin square LDLC with degree d contains nd variable-to-check messages $f_k(z)$ and nd check-to-variable messages $q_k(z)$ in each iteration, $k = 1, 2, \ldots, nd$.

Initialization: Each variable node x_i sends the initialization message $f(z)$ to the d check nodes connected to it.

$$f(z) = \frac{1}{\sqrt{2\pi\sigma^2}} e^{-\frac{(y_i - z)^2}{2\sigma^2}} \tag{5}$$

Check node: For a specific check node (without lose of generality) denote the appropriate check equation by $\sum_{i=1}^{d} h_i x_i = b$. For convenience, consider computing the check-to-variable message $q_d(z)$ using the $d-1$ input variable-check messages $f_k(z), k = 1, 2, \ldots, d-1$, as shown in Fig. 2a. The output message $q_d(z)$ is mainly calculated in three steps.

First compute the convolution of the $d-1$ expanded input messages

$$\widetilde{q}_d(z) = f_1(\frac{z}{h_1}) * f_2(\frac{z}{h_2}) * \cdots * f_{d-1}(\frac{z}{h_{d-1}}) \tag{6}$$

Then stretch the convolution results by $-h_d$

$$\overline{q}_d(z) = \widetilde{q}_d(-h_d z) \tag{7}$$

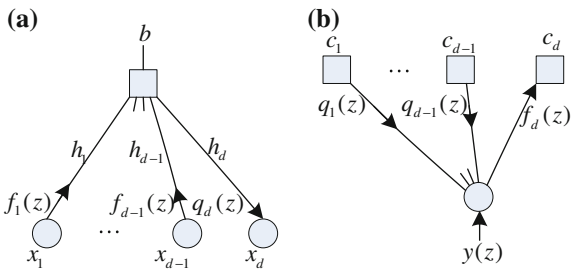

Fig. 2 Message operations at **a** check node and **b** variable node

Finally, extend the result to a periodic function for every possible value of b

$$q_d(z) = \sum_{b=-\infty}^{\infty} \overline{q}_d(z - \frac{b}{h_d}) \tag{8}$$

Variable node: Without lose of generality, suppose the input messages of a variable node are $q_i(z), i = 1, 2, \ldots, d-1$, and the output message is $f_d(z)$, as shown in Fig. 2b. the output message is calculated in two basic steps.

First product the incoming check-to-variable messages and the channel message:

$$\overline{f}_d(z) = \frac{1}{\sqrt{2\pi\sigma^2}} e^{-\frac{(y_i - z)^2}{2\sigma^2}} \prod_{i=1}^{d-1} q_i(z) \tag{9}$$

Then normalize the result:

$$f_d(z) = \frac{\overline{f}_d(z)}{\int_{-\infty}^{\infty} \overline{f}_d(z) dx} \tag{10}$$

Final decision: After an appropriate number of iterations between check nodes and variable nodes, we obtain the final variable node message:

$$\overline{f}_{i,final}(z) = \frac{1}{\sqrt{2\pi\sigma^2}} e^{-\frac{(y_i - z)^2}{2\sigma^2}} \prod_{i=1}^{d} q_i(z) \tag{11}$$

Then, we find the peak of the final message to estimate each x_i:

$$\overline{x}_i = \arg\max_x \overline{f}_{i,final}(z), i = 1, 2, \ldots, n \tag{12}$$

At last, the transmit integer vector $\boldsymbol{b}$ is estimated as $\overline{\boldsymbol{b}}$:

$$\overline{\boldsymbol{b}} = \lfloor \boldsymbol{H}\overline{x} \rceil \tag{13}$$

Where $\lfloor \cdot \rceil$ denote round operation.

5 Construction of 8-Cycle Check Matrix for Latin Square LDLC

Due to the message passing used in LDLC iterative decoder, cycles, especially short cycles degrade the performance of LDLC decoder, since they affect the independence of the extrinsic information exchanged in the iterative decoding [9, 10]. Thus, it is crucial to construct a check matrix with long cycle, for example, 8-cycle is desired. The following 8-cycle construction scheme has two basic steps: constructing a 6-cycle sparse matrix and eliminating the size 6-cycles.

5.1 Construct a 6-Cycle Matrix H

Given the block length n, degree d and generating sequence $\{h_1, h_2, \ldots, h_d\}$, to construct a 6-cycles matrix $\boldsymbol{H}_1$, first we generate d random permutations and then searches for 2-cycles and 4-cycles. when such a cycle is found, remove one of the permutations to eliminate the cycle.

Step 1: Generate a $d \times n$ permutation matrix $\boldsymbol{F}$, each row of $\boldsymbol{F}$ is a random permutation on $\{1, 2, \ldots, n\}$.

Step 2: Sequentially search for 2-cycle in $\boldsymbol{F}$: A 2-cycle is found in column c if the condition $i \neq j, \boldsymbol{F}_{i,c} = \boldsymbol{F}_{j.c}$ is satisfied, then mark the row index i.

Step 3: If there is no 2-cycle in column c, sequentially search for 4-cycle: A 4-cycle is found if there exists $c_0 \neq c$ such that $\boldsymbol{F}_{:,c}$ and $\boldsymbol{F}_{:,c_0}$ have two identical elements at least. Then we mark the row index for which the first identical element appears in column c.

Step 4: Modify the permutations in the row which was marked in step 2 and step 3: Randomly select an integer $1 \leq k \leq n$, and then exchange the position c with k in this row.

Step 5: Repeat step 2 $\sim$ step 4 until no 2-cycle or 4-cycle exist in every column of $\boldsymbol{F}$.

Step 6: Construct $\boldsymbol{H}_1$ from the $d \times n$ permutation matrix $\boldsymbol{F}$: $\boldsymbol{H}_1(\boldsymbol{F}(j,i), i) = \pm h_j$ for $1 \leq i \leq n, 1 \leq j \leq d$.

Through the above steps, we obtain a 6-cycle matrix $\boldsymbol{H}_1$. Simulation results show that the performance of this check matrix is poor due to the 6-cycle structure. In order to improve the performance, these cycles must be eliminated.

5.2 Eliminate the 6-Cycle in $\boldsymbol{H}_1$

When locating a 6-cycle, the position of nonzero elements in a cycle is our concern, the value of these elements can be ignored. With this in mind, we defined the related binary matrix of $\boldsymbol{H}_1$ as $\boldsymbol{H}_1^r$:

$$\boldsymbol{H}_1^r = \begin{cases} 1 & \boldsymbol{H}_1(i,j) \neq 0 \\ 0 & \boldsymbol{H}_1(i,j) = 0 \end{cases}, 0 < i,j \leq n \tag{14}$$

Denote the nodes of a bipartite graph of LDLC as $v_1, v_2, \ldots, v_{2n}$, where n is the number of variable nodes. The cycles are found by calculating different powers of the adjacency matrix. Adjacency matrix is a $2n \times 2n$ symmetric binary matrix which satisfies that if node v_i is connected to node $v_j, \boldsymbol{A}(i,j) = 1$ and zero otherwise. For LDLC, the adjacency matrix is defined as

$$\boldsymbol{A} = \begin{pmatrix} 0 & \boldsymbol{H}_1^r \\ (\boldsymbol{H}_1^r)^T & 0 \end{pmatrix} \tag{15}$$

In [6], a theorem to detect cycles in the bipartite graph was suggested. We declare it in Theorem 1.

Theorem 1 *In a graph with girth l two nodes v_i and v_j are directly opposite each other in a l-cycles if and only if*

$$\boldsymbol{A}_{i,j}^{l/2} \geq 2 \tag{16}$$

$$\text{And} \boldsymbol{A}_{i,j}^{(l/2)-2} = 0 \tag{17}$$

Theorem 1 is convenient to detect a 6-cycle. When such a cycle is found we try to eliminate it. We present our locating and removing step in detail as follows.

Step 1: Locate one element in a 6-cycle.

According to the above theorem, when $\boldsymbol{A}_{i,j}^3 \geq 2$ and $\boldsymbol{A}_{i,j}^1 = 0$, we can determine that variable i is involved in a 6-cycle. Assuming the position of this element is (i,k), where the column ordinate k satisfies the conditions: $\boldsymbol{A}_{i,k}^1 = 1$ and $\boldsymbol{A}_{k,j}^2 > 0$.

Step 2: Move this element to eliminate the 6-cycle.

Let $\boldsymbol{H}_1(i,k) = h_s$, then we find another element whose value is also h_s in $\boldsymbol{H}_1$. Denote the coordinate of this element as (p,q) i.e., $\boldsymbol{H}_1(p,q) = h_s$. When the following conditions are met, move these two elements: $\boldsymbol{H}_1(i,q) = \boldsymbol{H}_1(p,q)$, $\boldsymbol{H}_1(p,k) = \boldsymbol{H}_1(i,k)$, $\boldsymbol{H}_1(p,q) = 0$, $\boldsymbol{H}_1(i,k) = 0$. If we can not find such a (p,q), locate another element in the cycle and try the moving step.

Condition 1: The values at (i,q) and (p,k) must be equal to zero, i.e., $\boldsymbol{H_1}(i,q) = \boldsymbol{H_1}(p,k) = 0$.

Condition 2: This moving step does not produce any 4-cycles.

In order to determine whether condition 2 is satisfied, we perform the inner product between two rows of $\boldsymbol{H}_1^r$ after this moving step: $dot\left(\boldsymbol{H}_1^r(i,:), \boldsymbol{H}_1^r(l,:)\right)$, $l = 1, i-1, i+1, \ldots, n$ and $dot\left(\boldsymbol{H}_1^r(p,:), \boldsymbol{H}_1^r(m,:)\right), m = 1, p-1, p+1, \ldots, n$, where $\boldsymbol{H}_1^r(i,:)$ represents the ith row of $\boldsymbol{H}_1^r$. If all of these results are less than 2, then it means that this moving step does not produce any 4-cycles.

Condition 3: This moving step can eliminate the detected 6-cycles, and does not produce any new 6-cycles.

Because the moving operation will put a zero-value to the corner of the detected 6-cycle, to destroy the 6-cycle structure, then the detected cycle is eliminated. According to the properties of the adjacency matrix, if $\boldsymbol{A}^5(i,(q+n))=0$ and $\boldsymbol{A}^5(p,(k+n))=0$ which means that there is no length 5 path from node $i(p)$ to node $q(k)$, so this moving step does not create any new 6-cycles.

Step 3: Repeat Step 1 and Step 2 until we cannot find any 6-cycle element in Step 1, which means there is no 6-cycle exists.

After completing the above steps, all the size 6-cycles are eliminated, finally we get the 8-cycle parity check matrix, denote as $\boldsymbol{H}$.

6 Simulation Result

A Latin square LDLC based on the proposed construction method was simulated for the AWGN channel. The parity check matrix $\boldsymbol{H}$ was constructed using the parameters shown in Table 1, and then normalized by $\sqrt[n]{|\det(\boldsymbol{H})|}$. In the simulation, we use the iterative decoding algorithm suggested in [1] to decode the received messages. The simulation parameters are given in Table 2.

Finally we compare our scheme with the algorithm proposed in [1]. The performance is measured in symbol error rate (SER), versus the distance to the noise variance σ^2 from the capacity in dB. Simulation results are presented in Fig. 3. We observe that the performance of SER is improved efficiently, for example, there is a gain of 0.2 dB for lattice dimension $n=500$.

Table 1 Parameter for constructing check matrix

Dimension (n)	Degree (d)	Generate sequence (h)
200	4	$h=\{\frac{1}{2.31},\frac{1}{3.17},\frac{1}{5.11},\frac{1}{7.33}\}$
500	5	$h=\{\frac{1}{2.31},\frac{1}{3.17},\frac{1}{5.11},\frac{1}{7.33},\frac{1}{11.71}\}$
1200	6	$h=\{\frac{1}{2.31},\frac{1}{3.17},\frac{1}{5.11},\frac{1}{7.33},\frac{1}{11.71},\frac{1}{13.11}\}$

Table 2 Parameters for BP decoder

Resolution (Δ)	Message length (L)	Message range (D)	Number of iterations (t)
1/128	512	4	50

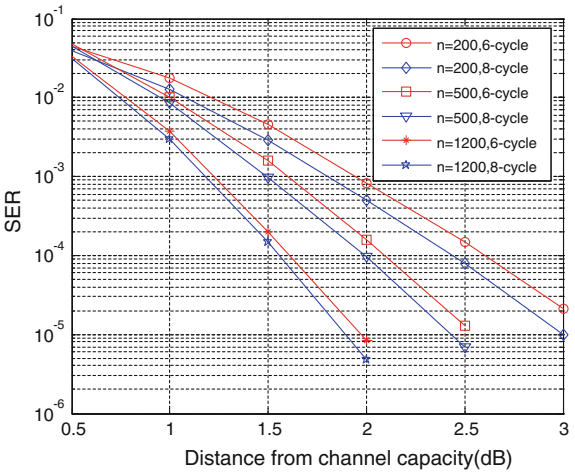

Fig. 3 Symbol Error Rate for different construction schemes and block lengths

7 Conclusion

LDLC are close to optimal lattice codes and can be decoded efficiently employing the BP iterative decoder. In this work we presented a novel algorithm for constructing the parity check matrix of Latin square LDLC, which is 6-cycle free and the nonzero elements are randomly distributed. Simulation results indicate that the performance of these matrices is improved efficiently.

Ackonowledgment The work is supported by the international exchange program of harbin engineering university for innovation-oriented talents cultivation.

References

1. Sommer N, Feder M, Shalvi O (2008) Low-density lattice codes [J]. IEEE Trans Inf Theor 54 (4):1561–1585
2. Thorpe J (2003) Low-density parity-check (LDPC) codes constructed from protographs [J]. IPN progress report 42(154):42–154
3. Fossorier MPC, Mihaljevic M, Imai H (1999) Reduced complexity iterative decoding of low-density parity check codes based on belief propagation [J]. IEEE Trans Commun 47 (5):673–680
4. Erez U, Zamir R (2004) Achieving 1/2 log (1 + SNR) on the AWGN channel with lattice encoding and decoding [J]. IEEE Trans Inf Theor 50(10):2293–2314
5. Wang X, Chang G (2008) A method to construct girth-8 low density lattice codes[C]. In: 2008 11th IEEE singapore international conference on communication systems, pp 258–262
6. McGowan JA, Williamson RC (2003) Loop removal from LDPC codes[C]. In: Proceedings. 2003 IEEE information theory workshop, pp 230–233
7. Fan J, Xiao Y (2006) A method of counting the number of cycles in LDPC codes[C]. In: 2006 8th international conference on signal processing, p 3

8. Zamir R (2014) Lattice coding for signals and networks: a structured coding approach to quantization, modulation, and multiuser information theory[M]. Cambridge university press
9. Wiberg N (1996) Codes and decoding on general graphs[M]. Department of electrical engineering, linköping university, Sweden
10. Kschischang FR, Frey BJ, Loeliger HA (2001) Factor graphs and the sum-product algorithm [J]. IEEE Trans Inf Theor 47(2):498–519

DME Pulse Interference Suppression Based on WRELAX for GPS L5 Signal

Wei Fang and Jie Li

Abstract A new algorithm is proposed in this paper to solve the problem of multisource distance measurement equipment (DME) pulse interference suppression for global positioning system (GPS) L5 signal. The problem can be treated as DME signal estimation, and then can be taken as a problem of optimization. Based on nonlinear least squares (NLS) criterion, using WRELAX iteration method, the optimization problem can be solved to estimate the multisource DME signal. Once DME pulse interference signal is estimated, then it can be reconstructed, and finally can be eliminated and suppressed. Compared with traditional method, the proposed method can reserve more useful GPS satellite data. The performance of proposed method is verified by numerical simulations.

Keywords GPS L5 · DME · Interference suppression

1 Introduction

GPS L5 signal is used for civil aviation exclusively, and takes up exclusive frequency band. Moreover, the compass (Beidou) system will be compatible with GPS system via sharing the same frequency band. The compass B2 signal and GPS L5 signal share the same band with central frequency 1176.45 MHz.

However, there exists a lot of interference equipment working at the L5 frequency band, among which distance measurement equipment (DME) pulse interference makes greatest influence on L5 signal. DME interference can cause degradation of signal to interference and noise ratio (SINR) at GPS receiver, reduce the sensitivity of acquisition, thus lead to the failure of convergence of tracking

W. Fang (✉)
Beijing Aeronautical Science & Technology Research Institute of COMAC, Beijing, China
e-mail: davidf8@163.com

J. Li
Zhonghuan Information College, Tianjin University of Technology, Tianjin, China

Q. Liang et al. (eds.), *Proceedings of the 2015 International Conference on Communications, Signal Processing, and Systems*, Lecture Notes in Electrical Engineering 386, DOI 10.1007/978-3-662-49831-6_37

loop, and finally make it difficult to decode the navigation information [1–4]. DME signal also interferes with compass B2 signal. Therefore, it is very necessary to solve the problem of DME interference.

Many researches have been carried out to study on the problem of DME interference, and many anti-interference techniques have been developed, most frequently used of which are pulse blanking, notch filter and hybrid method [5–9].

The traditional methods mentioned above eliminate the interference in time or frequency domain, and at the same time, the useful signal will suffer from loss more or less to a certain extent. In this paper, we propose a new DME interference suppression method. This method firstly estimates the parameters of DME signal under nonlinear least squares (NLS) criterion, then reconstructs the DME signal as the signal of interest, and finally suppresses the DME interference. This method can maintain useful GPS signal to a large extent while suppressing the interference. So this method can enhance the availability of the GPS signal. The efficiency of the proposed approach is verified in the numerical experiments.

2 Data Model and Problem Formulation

The DME equipment works at the frequency ranged from 962 to 1213 MHz. Unfortunately, this frequency band covers the GPS L5 signal with central frequency 1176.45 MHz and bandwidth 24 MHz. So the DME interference to GPS L5 mainly comes from the ground DME devices.

The baseband signal of DME equipment has the structure of pulse pair. The signal can be modeled as

$$s(t) = e^{-\frac{\alpha}{2}\left(t-\frac{\Delta t}{2}\right)^2} + e^{-\frac{\alpha}{2}\left(t+\frac{\Delta t}{2}\right)^2} \tag{1}$$

among which the constant α determines the width of pulse pair, and Δt determines the interval, where $\alpha = 4.5 \times 10^{11}\,\mathrm{s}^{-2}$, and $\Delta t = 12 \times 10^{-6}\,\mathrm{s}$. The half-amplitude width of each single pulse is 3.5 μs, and the interval between two single pulses is 12 μs. The waveform of DME pulse pair has been shown in Fig. 1.

When the airplanes are near the ground base of DME, the airborne GPS receiver will be interfered by the pulses with high power sent by DME ground base stations nearby. Because of the relative movement between the airplane and DME station, the frequency of interference signal received by the GPS receiver will have Doppler frequency shift in frequency domain.

When the GPS receiver is interfered by only one DME ground station, the interference can be eliminated by the method based on NLS criterion, which can be seen in reference [10].

Consider the scenario that the DME pulse interference comes simultaneously from two or more different ground base stations. Due to the difference of distances

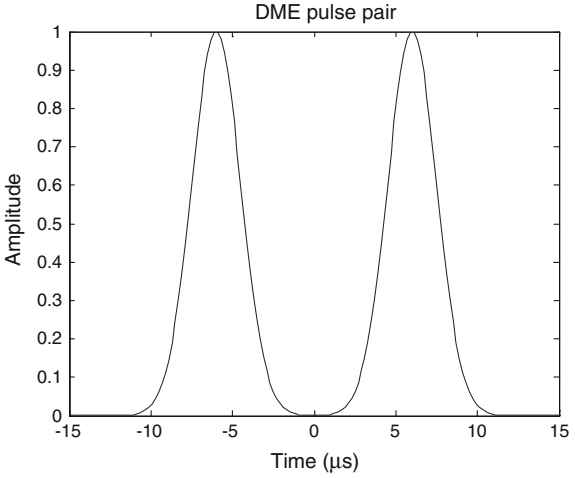

Fig. 1 DME pulse pair

between GPS receiver and the two DME ground base, the GPS receiver will be interfered by two DME pulses with different Doppler shifts.

When there exit multiple interferences from DME ground base station, the signal received by GPS receiver can be modeled as:

$$y(t) = \sum_{l=1}^{L} \beta_1 s(t-\tau_l) e^{j\omega_l(t-\tau_l)} + e(t) \tag{2}$$

where $s(t)$ stands for DME signal, β_l and ω_l is complex amplitude and frequency to be estimated separately.

The sampled signal is

$$y(nT_s) = \sum_{l=1}^{L} \beta_l s(nT_s-\tau_l) e^{j\omega_l(nT_s-\tau_l)} + e(nT_s), \quad n=1,2,\ldots,N \tag{3}$$

The signal received by GPS receiver can be modeled as below

$$y(t) = \sum_{k=1}^{K} \beta_k s(t) e^{j\omega_k t} + e(t), \quad t=1,2,\ldots,N, \tag{4}$$

where $s(t)$ is the DME signal, β_k is the complex amplitude to be estimated, ω_k is the frequency equal to carrier frequency plus the Doppler frequency shift due to relative movements of airplane and DME ground base station, and $e(t)$ includes noise and satellites signals buried under the noise level. In the scenario of two DME base stations, K is equal to 2.

3 Algorithm Implementation

Due to the much stronger power of DME pulse than satellite signal, we can take the DME signal as the signal of interest. Once the DME signal is detected in the range of interest (ROI), we can estimate the frequency and complex amplitude of DME signal under the criterion of NLS [10, 11]. Then the DME signal can be reconstructed using the already known waveform information of DME signal. Finally the goal of suppressing interference can be achieved by subtracting the estimated DME signal from the received signal by the GPS receiver.

As for the problem of estimating multiple group of parameters, we can utilize the theory of WRELAX to estimate each group of parameters via iteration [12]. Take the problem of estimating two groups of parameters for example. That is to say, we need to estimate the parameters of $\{\beta_l, \tau_l, \omega_l\}_{l=1}^{2}$. The problem of parameter estimation can be transferred to solve the problem of optimization as below

$$\min_{\beta,\tau,\omega}\left|y(nT_s)-\sum_{l=1}^{L}\beta_l s(nT_s-\tau_l)e^{j\omega_l(nT_s-\tau_l)}\right|^2,\quad n=1,2,\ldots,N \tag{5}$$

This is a problem of nonlinear least squares. To solve the problem, firstly let

$$y_l(nT_s)=y(nT_s)-\sum_{i=1,i\neq l}^{L}\beta_i s(nT_s-\hat{\tau}_i)e^{j\hat{\omega}_i(nT_s)-\hat{\tau}_i)},\quad n=1,2,\ldots,N \tag{6}$$

where the parameters $\{\beta_i, \hat{\tau}_i, \hat{\omega}_i\}_{i=1,i\neq l}^{L}$ are supposed to be known.

Solve the problem of optimization in Eq. (5) and we can get

$$\hat{\omega}_l=\arg\max_{\omega_l}\left|\sum_{n=1}^{N}y_l^2(nT_s)e^{-j2\omega_l nT_s}\right|^2,\quad n=1,2,\ldots,N \tag{7}$$

$$\hat{\tau}_l=-\frac{N}{2\pi f_s}\arg\max_{\omega_{dl}}\left|\mathbf{a}^H(\omega_{dl})(\mathbf{X}^*\mathbf{Y}_l)\right|^2 \tag{8}$$

$$\beta_l=\left.\frac{\mathrm{a}^H(\omega_{dl})(\mathbf{X}^*\mathbf{Y}_l)}{\|\mathbf{X}\|^2}\right|_{\omega_{dl}=\hat{\omega}_{dl}} \tag{9}$$

where

$$\begin{aligned}
&\mathbf{Y}=[Y(N/2)\quad Y(-N/2+1)\quad\ldots\quad Y(N/2-1)]^T,\ Y(k)=\mathrm{DFT}\{y(nT_s)\},\\
&\mathbf{X}=\mathrm{diag}\{X(-N/2)\quad X(-N/2+1)\quad\ldots\quad X(N/2-1)\},\\
&X(k)=\mathrm{DFT}\{x(nT_s)\},\\
&\mathbf{a}(\omega_d)=[e^{j\omega_d(-N/2)}\quad e^{j\omega_d(-N/2+1)}\quad\ldots\quad e^{j\omega_d(N/2-1)}]^T.
\end{aligned}$$

The steps of solving the problem of optimization using the theory of WRELAX are as below

Step 1 Suppose $L = 1$, take $\beta_1 s(nT_s - \tau_1)$ as unknown waveform, then estimate the parameters $\hat{\omega}_1, \hat{\tau}_1$ and β_1.

- Step 1(a) Calculate the frequency estimation $\hat{\omega}_1 = \arg\max \left| \sum_{n=1}^{N} y^2(nT_s) e^{-j2\omega_1 nT_s} \right|^2$, using the NLS algorithm [10].
- Step 1(b) After we get the estimation $\hat{\omega}_1$, then we can estimate the complex amplitude $\beta_l = \left. \frac{\mathrm{a}^H(\omega_d)(\mathrm{X}^* \mathrm{Y})}{\|\mathrm{X}\|^2} \right|_{\omega_d = \hat{\omega}_1}$, and time delay $\hat{\tau}_1 = -\hat{\omega}_1 N / (2\pi f_s)$.
- Step 1(c) Reconstruct the signal using the estimated complex amplitude β_l and time delay $\hat{\tau}_1$, and then reestimate the frequency $\hat{\omega}_1$.
- Step 1(d) Return to Step 1(b) and reestimate β_l and $\hat{\tau}_1$, using the estimated value $\hat{\omega}_1$. Repeat the iteration from Step 1(b) to Step 1(c) until it is converged. (The convergence condition is that the value of the cost function in the Eq. (5) during two iterations is smaller than the predefined value.)

Step 2 Suppose $L = 2$, calculate $\hat{y}_2(nT_s), n = 1, 2, \ldots, N$, using $\hat{\omega}_1, \beta_l$ and $\hat{\tau}_1$ obtained from Step 1 and Eq. (6). Then estimate $\hat{\omega}_2, \beta_2$ and $\hat{\tau}_2$, using $\hat{y}_2(nT_s)$ and the method similar to the iteration steps in Step 1(a)–(d).

- Step 2(a) Using $\hat{y}_2(nT_s)$ and Eq. (7) to calculate estimated frequency β_2.
- Step 2(b) After $\hat{\omega}_2$ is estimated, using (8) and (9) to estimate complex amplitude β_2 and time delay $\hat{\tau}_2$.
- Step 2(c) Then use β_2 and $\hat{\tau}_2$ to reconstruct the signal, and estimate the frequency $\hat{\omega}_2$.
- Step 2(d) Go back to Step 2(b) and reestimated β_2 and $\hat{\tau}_2$, using got $\hat{\omega}_2$ in Step 2(c). Repeat the iteration from Step 2(b) to 2(c), until it is converged under the condition that the changed value of the cost function in the Eq. (5) during two iterations is smaller than the predefined value.

Then compute $\hat{y}_1(nT_s)$, $n = 1, 2, \ldots, N$, using the estimated value $\{\beta_l, \hat{\tau}_l, \hat{\omega}_l\}_{l=2}$ and Eq. (6). When $\hat{y}_1(nT_s)$ is got, reestimate $\{\beta_l, \hat{\tau}_l, \hat{\omega}_l\}_{l=1}$. Repeat iteration progress between Step 1 and Step 2 until it is converged, under the condition that the changed value of the cost function in the Eq. (5) during two iterations is smaller than the predefined value.

Step 3 Suppose $L = 3$, compute $\hat{y}_3(nT_s)$ using the estimated parameters $\{\beta_l, \hat{\tau}_l, \hat{\omega}_l\}_{l=1}^{2}$ got in upper steps. Then estimate $\{\beta_l, \hat{\tau}_l, \hat{\omega}_l\}_{l=3}$ using $\hat{y}_3(nT_s)$. Then recompute $\hat{y}_1(nT_s)$ using $\{\beta_l, \hat{\tau}_l, \hat{\omega}_l\}_{l=2}^{3}$, and reestimate $\{\beta_l, \hat{\tau}_l, \hat{\omega}_l\}_{l=1}$. Then estimate $\hat{y}_2(nT_s)$ using $\{\beta_l, \hat{\tau}_l, \hat{\omega}_l\}_{l=1,3}$, and calculate

parameters $\{\beta_l, \hat{\tau}_l, \hat{\omega}_l\}_{l=2}$. Repeat the above steps until it is converged. Then we can get the estimation $\{\beta_l, \hat{\tau}_l, \hat{\omega}_l\}_{l=1}^{3}$.

Remaining Steps. Repeat the above process until reach the desired L.

Then the estimated value $\{\beta_l, \hat{\tau}_l, \hat{\omega}_l\}_{l=1}^{L}$ is obtained.

Finally we can reconstruct the DME interference signal using the estimated frequency, complex amplitude and time delay $\{\beta_l, \hat{\tau}_l, \hat{\omega}_l\}_{l=1}^{L}$.

$$\hat{y}_1(nT_s) = \sum_{l=1}^{L} \beta_l s(nT_s - \hat{\tau}_l) e^{j\hat{\omega}_l(nT_s - \hat{\tau}_l)},\ n = 1, 2, \ldots, N \tag{10}$$

Eliminate the DME interference signal from received GPS signal, and the DME interference can be suppressed

$$\hat{y}_{GPS}(nT_s) = y(nT_s) - \hat{y}_1(nT_s),\ n = 1, 2, \ldots, N \tag{11}$$

As for the problem of two interference sources, that is to say when L = 2 in above analysis, we can estimate the amplitude and frequency using the iteration process of WRELAX algorithm, then reconstruct the interference signal and suppress it.

4 Numerical and Experimental Results

In order to illustrate the performance of the proposed method, the numerical experiments have been carried out. In the experiments, the satellite data are interfered by DME pulse, and are down-converted at the intermediate frequency of 1.25 MHz. The sample rate is 5 MHz, the signal-to-noise ratio (SNR) is—18 dB, and the jammer-to-noise ratio (JNR) of DME is 40 dB.

Figure 2 demonstrates the results of interference suppression using the proposed method. Figure 2a is the satellite data interfered by two DME signal, with time delay 2 and 2.5 ms. Due to the stronger JNR, the DME interference can make the GPS receiver fail in tracking and acquisition. Use the proposed method to suppress the interference, and the results is shown in Fig. 2b in time domain. We can see that the DME interference is suppressed, and the useful satellite signal remains.

As is shown in Fig. 3, the proposed method has prevailed performance, compared with traditional notch filtering method. The result is achieved after Monte-Carlo trails under different JNR. As we can see from the figure, the root mean square error (RMSE) of proposed method is much lower than the traditional method, which means that after processing using the proposed method, the data are closer to the original satellite data than the traditional method. So the proposed approach has better performance than the latter one. Thus the proposed method can

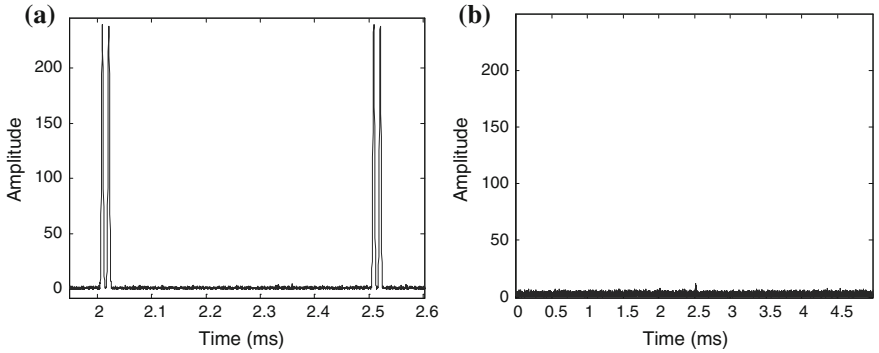

Fig. 2 DME pulse interference suppression. **a** Satellite data interfered by DME signal. **b** Satellite data after DME suppression

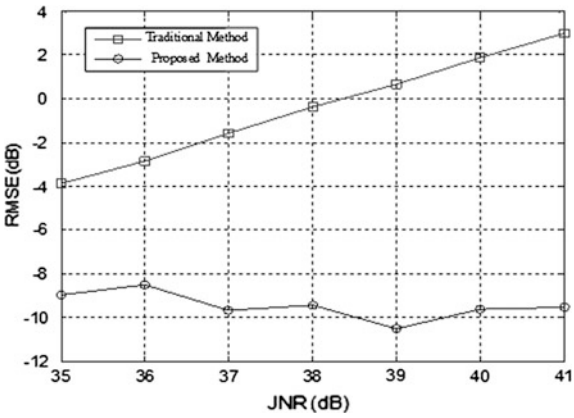

Fig. 3 Performance comparison

maintain more useful satellite after interference suppression. In other words, the proposed algorithm has lower loss of useful data, and so this method is with better performance than other approaches.

5 Conclusions

In this paper, we propose a new DME interference suppression method based on WRELAX algorithm, when the DME interference comes from more than one base stations. Using WRELAX iteration process, the frequency, amplitude and time delay of DME interference signal can be estimated and then reconstructed. Then the interference signal can be eliminated and suppressed, and the useful satellite signal can be remained. The results of numerical experiments show that the proposed

method can maintain more useful satellite data compared with traditional method. So the proposed method is with good performance in solving the problem of multisource DME interference suppression.

References

1. Steingass A, Hornbostel A, Denks H (2010) Airborne measurements of DME interferers at the European hotspot. In: Proceedings of the fourth European conference on antennas and propagation (EuCAP), pp.1–9, 12–16
2. Hegarty C, Kim T, et al (1999) Methodology for determining compatibility of GPS L5 with existing systems and preliminary results. In: Proceedings of the institute of navigation annual meeting, Cambridge, MA
3. Fang W, Wu R, Lu D, Wang W (2011) A new interference suppression method in GPS based on modified GAPES. Sig Process 27(12):1860–1864
4. Angelis M, Fantacci R, Menci S, Rinaldi C (2005) Analysis of air traffic control systems interference impact on Galileo aeronautics receivers. In: IEEE international radar conference, pp 585–595
5. Gao G (2007) DME/TACAN interference and its mitigation in L5/E5 bands. In: The ION conference on global navigation satellite systems
6. Brandes S, Epple U, et al (2009) Physical layer specification of the L-band digital aeronautical communications system (L-DACS1). In: Integrated Communications, Navigation and Surveillance Conference, pp 1–12
7. Grabowski J (2002) Characterization of L5 receiver performance using digital pulse blanking. In: The ION conference
8. Zhang Q, Zheng Y, Wilson SG, Fisher JR, Bradley R (2005) Excision of distance measuring equipment interference from radio astronomy signals. Astron J 129:2933–2939
9. Anyaegbu E, Brodin G, Cooper J, Aguado E, Boussakta S (2008) An integrated pulsed interference mitigation for GNSS receivers. J Navig 61:239–255
10. Fang Wei, Renbiao Wu, Wang Wenyi, Dan Lu (2012) DME pulse interference suppression based on NLS for GPS. Int Conf Signal Process 1:174–178
11. Christensen MG, Jensen SH (2011) New results on perceptual distortion minimization and nonlinear least-squares frequency estimation. IEEE Trans Audio Speech Lang Process 19 (7):2239–2244
12. Li J, Wu RB (1998) An efficient algorithm for time delay estimation. IEEE Trans Signal Process 46(8):2231–2235

Multi-stack Decoding of Polar Codes

Dongsheng Wu, Qingshuang Zhang and Yingxian Zhang

Abstract A successive cancellation multi-stack (SCMS) decoding is proposed to improve the performance of polar codes. Unlike the successive cancellation stack (SCS) decoding algorithm which just uses one ordered stack to store the candidate partial paths and attempts to find out the optimal estimation in the stack, the SCMS algorithm uses several stacks to obtain better performance at the same space complexity. Simulation results in binary-input additive white Gaussian noise channel (BI-AWGN) show that the SCMS algorithm can achieve an improvement of about 0.2 dB.

Keywords Polar codes · SCS · SCMS · Space complexity

1 Introduction

For any given binary-input discrete memoryless channel (B-DMC), it has been proved that the polar codes which were introduced in [1] by Arikan can achieve the symmetric capacity. There is a prove in [2] that, for polar codes with large enough code length, if the code rate $R < I(W)$, its block error probability can be wrote as $P(N, R) \leq 2^{-N^{\beta}}$ for any $\beta < \frac{1}{2}$.

However, the performance under SC in the case of finite-length is unsatisfactory. As the SC decoding process goes, if a bit is decided incorrect, it cannot be rectified, and it will have influence on the decision of the following bits. To reduce the similar mistakes, the successive cancellation list (SCL) decoder keep L candidates paths simultaneously, then we pick up one path as the final decision from the L paths with the maximal sequence probability. It has been proved in [3] that the SCL decoder can effectively improve the performance and when the size of L is appropriate it

D. Wu (✉) · Q. Zhang · Y. Zhang
College of Communications Engineering, PLA University of Science and Technology, Nanjing 210007, China
e-mail: dongshengwu@yeah.net

Q. Liang et al. (eds.), *Proceedings of the 2015 International Conference on Communications, Signal Processing, and Systems*, Lecture Notes in Electrical Engineering 386, DOI 10.1007/978-3-662-49831-6_38

can approach the performance of the ML decoder. However, compared with the SC decoder there is a remarkable increase of the time complexity.

To reduce the time complexity of the SCL algorithm, the successive cancellation stack (SCS) decoder was introduced by K. Chen. The SCS decoder has very low time complexity and its performance is very close to that of the SCL decoder [4]. However, as the time complexity reduced, the space complexity of SCS becomes slightly larger.

The performance of the SCS decoder is unsatisfying when the depth of the stack is insufficient. To overcome this shortcoming, inspired by the stack decoding of multi-stack structure [5], we propose a new decoding strategy called the successive cancellation multi-stack (SCMS) decoder algorithm in this paper. The SCMS can achieve better performance than SCS at the same space complexity.

The structure of this paper is organized as follows: Part II present the background of the polar codes. Part III describes the SCMS algorithm, the processes are present by details. Part IV gives the simulation result and the corresponding analyses. Finally, Part V concludes the paper.

2 Background

2.1 Polar Coding

The cutoff rate $R_0(W)$ of a discrete memoryless channel (DMC) W is often used as a figure of merit, alongside the channel capacity $C(W)$, and it can be improved by methods of channel combining and splitting [6].

Channel polarization is realized via the operation of channel combining and splitting. Polar coding is a method which takes the advantage of polarization effect to construct codes that can achieve the symmetric channel capacity $I(W)$.

We use notation x_1^N and u_1^N to denote a row vector $(x_1, \ldots, x_N)$ and $(u_1, \ldots, u_N)$, respectively. Then we can define the polarization as

$$x_1^N = u_1^N G_N \tag{1}$$

where $G_N = B_N F^{\otimes n}$, $\otimes n$ is a shorthand for the *nth* Kronecker power, B_N is a bit-reversal permutation and $F = \begin{bmatrix} 0 & 1 \\ 1 & 1 \end{bmatrix}$ [1].

We obtain a set of N binary-input coordinate channels $\left\{ W_N^{(i)} \right\}, i = 1, 2, \ldots, N$ via channel polarization and the symmetric capacity terms $\left\{ I(W_N^{(i)}) \right\}$ will be changed when the code length N tends to be large, in which some of that will tend towards 0 and the others will tend towards 1. Figure 1 shows the distribution of $I(W_N^{(i)})$.

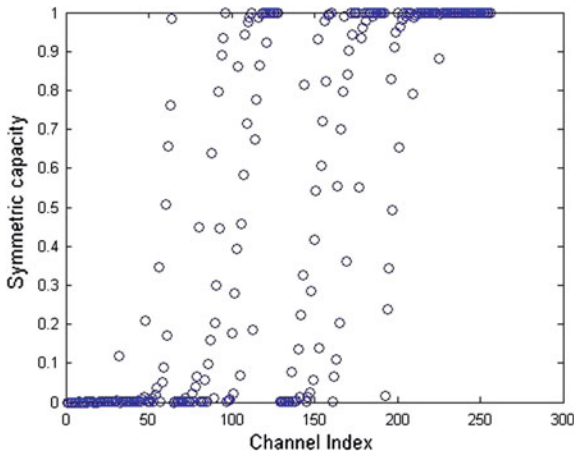

Fig. 1 Plot of $I(W_N^{(i)})$ versus index i

When we need to communicate at a rate R, we pick out the most reliable NR channels, and then we send information bits through these channels only, while the rest send fixed values. Conventionally, the bits transmitted over the unreliable channels are called frozen bits and the values are always set to be zero.

Supposing that, let the binary vector x_1^N be the input of the N copies of B-DMC W, and $y_1^N(y_1, y_2, \ldots, y_N)$ denotes the output of $W_N^{(i)}$. Then we have the transition probability of the *ith* channel:

$$W_N^{(i)}(y_1^N, u_1^{i-1}|u_i) = \sum_{u_{i+1}^N} \frac{1}{2^{N-1}} W_N(y_1^N|u_1^N) \tag{2}$$

2.2 Stack Successive Cancellation Decoding

In [1], the successive cancellation decoding (SC) algorithm was introduced with low complexity $O(N \log N)$. We write $\hat{u}_1^N = (\hat{u}_1, \hat{u}_2, \ldots, \hat{u}_N)$ to denote the estimation vector which we have received. In SC decoder, we decide the bits step by step. For a frozen bit, it is obvious that $\hat{u}_i = 0$. For the information bits, the decoding rule can be wrote as follows:

$$\hat{\mathrm{u}}_i = \begin{cases} 0, & \frac{W_N^{(i)}(y_1^N, u_1^{i-1}|u_i=0)}{W_N^{(i)}(y_1^N, u_1^{i-1}|u_i=1)} > 1 \\ 1, & otherwise \end{cases} \tag{3}$$

Although the performance of polar codes with large code length N is astonishing, the performance will be unsatisfied as the code length becomes small. Then the successive cancellation list (SCL) decoder was proposed to improve the performance

with high time complexity. In [4], the successive cancellation stack (SCS) decoding was proposed and it figures out the shortcoming of the SCL decoder.

In the SCS decoder, an ordered stack was used to store the candidate paths and attempts to find out the optimal estimation in the stack by using metrics as labels of probabilities. The decoding process would not stop until the top path in the stack reaches length N, then the top path is the decode result [7]. If the stack is full before the result comes out, we abandon the paths from the bottom of the stack.

3 The Multi-stack Successive Cancellation Decoding

The SCMS decoder used two stacks $\mathbb{S}1$ and $\mathbb{S}2$ to store the candidate paths. Metrics were used to judge the reliability of a path. For a path $u_1^i(u_1, u_2, \ldots, u_i)$, the metric can be calculate as follows:

$$M(u_1^i) = \log W_N^{(i)}(y_1^N, u_1^{i-1}|u_i) \tag{4}$$

The SCMS decoding algorithm has two working status called *on-going* and *transfer*. Let $D1$ and $D2$ denote the maximal depths of $\mathbb{S}1$ and $\mathbb{S}2$, respectively. Similarly, $T1$ and $T2$ denote the instantaneous depths of $\mathbb{S}1$ and $\mathbb{S}2$ respectively.

Initially, the SCMS decoder works in the *on-going* mode of $\mathbb{S}1$, which is similar to SCS. However, when the number of candidate paths in the stack is about to achieve $D1$, SCMS stops searching forward in the $\mathbb{S}1$ and switches to the *transfer* mode. In the *transfer* mode, SCMS moves several paths from the bottom of the $\mathbb{S}1$ to the $\mathbb{S}2$. The number of the paths which will be transferred to the $\mathbb{S}2$ is set to be M. Then the SCMS works in the *on-going* mode of $\mathbb{S}2$ until we got a result. We reserve the result and the corresponding metric as a candidate decision. Then, SCMS switches back to the *on-going* mode of $\mathbb{S}1$. The process goes on until the $\mathbb{S}1$ got a result. Figure 2 shows a graphic illustration of the process. Figure 3 gives an example of the paths in the stacks of SCMS.

The SCMS decoding algorithm is summarized as follows:

1. Initialization: Push a null path into $\mathbb{S}1$, then set the value of the corresponding metric to be 0. The instantaneous stack depth are $T1 = 1$ and $T2 = 0$. The working mode flag f_{mode} is initialized to 0, where $f_{mode} = 0$ denote the *on-going* mode, and $f_{mode} = 1$ denote the transfer mode. A stack flag f_{stack} is also needed and the initial value is set to be 1, where $f_{stack} = 1$ indicates the algorithm is now working in the $\mathbb{S}1$, and $f_{stack} = 2$ indicates the algorithm is now working in the $\mathbb{S}2$.
2. Popping: When $f_{stack} = 1$, a path is popped from the top of $\mathbb{S}1$ then $T1 = T1 - 1$; otherwise, pop the path from the top of $\mathbb{S}2$ then $T2 = T2 - 1$.
3. Expansion: A label u_1^i is used to denote the path in the stack. If the u_i is a frozen bit, the path is simply extended to $u_1^i = (u_1^{i-1}, 0)$; otherwise, if u_i is an information bit, the path is extended to $(u_1^{i-1}, 0)$ and $(u_1^{i-1}, 1)$. The path metric(s) will be calculated by using (3).

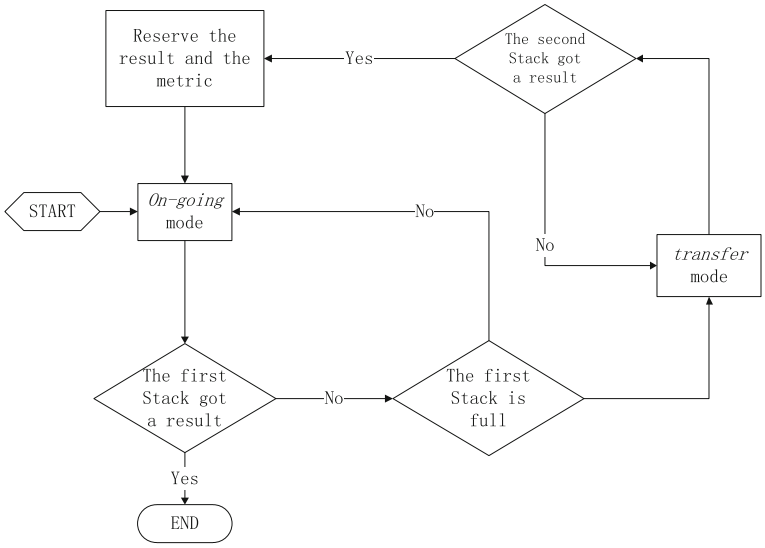

Fig. 2 Mode transition diagram of SCMS decoding

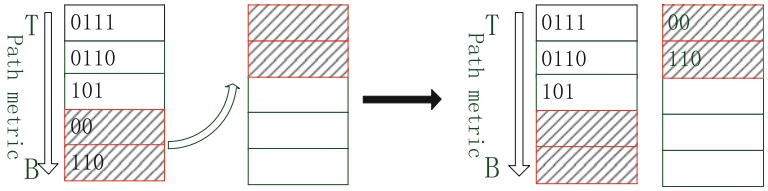

Fig. 3 Example of decoding paths in the stack of SCMS

4. Pushing: For $f_{stack} = 1$, push the extended path(s) into $\mathbb{S}1$; otherwise, push the extended path(s) into $\mathbb{S}2$. If the u_i is a frozen bit, $T_{(1,2)} = T_{(1,2)} + 1$; otherwise, if u_i is an information bit, $T_{(1,2)} = T_{(1,2)} + 2$.
5. Sorting: Depending on the metric reorder the paths in the stack in descending.
6. Mode Switching:

   a. When $f_{stack} = 1$ and the $\mathbb{S}1$ is full without a result, the working mode is switched to *transfer* mode, then move the M paths from the bottom of $\mathbb{S}1$ to $\mathbb{S}2$, $f_{stack} = 2$, the process goes back to step 2;
   b. When $f_{stack} = 2$ the $\mathbb{S}2$ is full without a result, then the process goes back to step 2;
   c. When $f_{stack} = 2$ and the top path in $\mathbb{S}2$ reaches a leaf node of the code tree, then reserve the result and the corresponding metric as a candidate decision, $f_{stack} = 1$, the process goes back to step 2;
   d. When $f_{stack} = 1$ and the $f_{stack} = 2$ comes out a result, the process goes on to step 7.

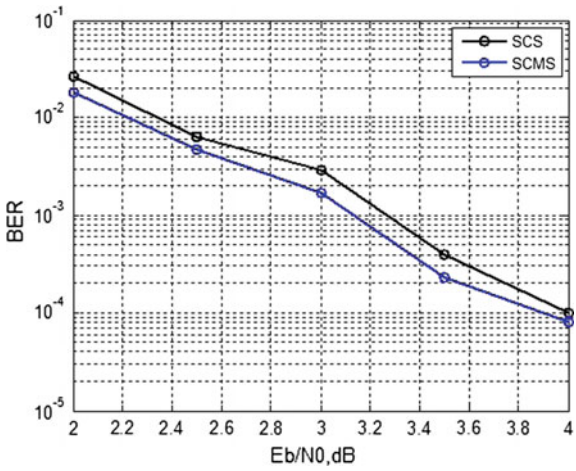

Fig. 4 Performance comparison of SCS, SCMS algorithm of (256, 128) polar code under the BI-AWGN

7. Determination: Pick up the path form the candidates and the result of $\mathbb{S}1$ with the maximum metric as the final decision.

4 Result

Figure 4 gives the BER performance of different decoding algorithms of (256, 128) polar code under the BI-AWGN channel. The maximal depth of the stack in the SCS decoder is $D = 30$. For the SCMS, the depth of the two stacks is 15 either. Compare with the SCS decoding, the SCMS algorithm can achieve a performance improvement of 0.2 dB.

To analyze the complexity of the decoder, the space complexity of SCMS is just the same as SCS. However, because of the interactive structure between the two stacks, the time complexity is much higher than SCS. Further work is needed to reduce the time complexity.

5 Conclusion

The successive cancellation multi-stack (SCMS) decoding algorithm is proposed to improve the performance of polar codes. The SCMS can achieve better performance than SCS at the same space complexity when the depth of the stack is limited. However, the cost is that the time complexity is high.

References

1. Arikan E (2009) Channel polarization: a method for constructing capacity achieving codes for symmetric binary-input memoryless channels. IEEE Trans Inf Theory 55(7):3051–3057
2. Arikan E, Telatar E (2009) On the rate of channel polarization. In: Proceeding of 2009 IEEE International Symposiumon Information Theory, pp 1493–1495
3. Chen K, Niu K, Lin JR (2012) List successive cancellation decoding of polar codes. Electron Lett 48(9):500–501
4. Niu K, Chen K (2012) Stack decoding of polar codes. Electron Lett 48(12):695–696
5. Huang J, Li W, Zhang T, Jiang H (2013) An improved stack decoding algorithm. Wirel Commun Technol 4:7–10
6. Arikan E (2006) Channel combing and splitting for cutoff rate improvement. IEEE Trans Inf Theory 52(2):628–639
7. Chen K, Niu K, Lin JR (2013) Improved successive cancellation decoding of polar codes. IEEE Trans Commun 61(8):3100–3107

STDMA for Inter-satellite Communication in Low Earth Orbit

Hailong Kang, Xiujie Jiang and Weiming Xiong

Abstract Distributed small satellites flying in close formations are deployed in the low Earth orbit for Earth observation (EO) missions owing to their unique ability to increase observation sampling in spatial, spectral, angular, and temporal dimensions simultaneously. All these missions require inter-satellite links (ISLs) with guaranteed performance to track and maintain the satellites in a desired geometric configuration. The data exchanged should then be arrived timely in order to control the inter-satellite distance collaboratively. Although many protocols are developed to apply in different communication layer, there has been little work done in self-organizing time division multiple access (STDMA) in data link layer for the inter-satellite communication.This paper addresses an adaption of STDMA in order to reduce the overall development costs of novel space missions. Besides, STDMA has been simulated in a mesh formation scenario with periodic broadcast packets compared to Carrier Sense Multiple Access/Collision Avoidance (CSMA/CA). Finally, simulation results show that STDMA has a higher packet reception probability in the scenario and thereby a better reliability.

Keywords Satellite communication · STDMA · LEO · Wireless network

1 Introduction

Distributed Space Missions (DSMs) are gaining momentum in their application to Earth Observation (EO) missions owing to their unique ability to increase observation sampling in spatial, spectral, angular, and temporal dimensions simultaneously [1]. Characteristics of these DSMs are achieved using multiple satellites in

H. Kang (✉) · X. Jiang · W. Xiong
National Space Science Center, Chinese Academy of Sciences, Beijing 100190, China
e-mail: kanghailong@gmail.com; khldragon@163.com

H. Kang
University of Chinese Academy of Sciences, Beijing 100190, China

Q. Liang et al. (eds.), *Proceedings of the 2015 International Conference on Communications, Signal Processing, and Systems*, Lecture Notes in Electrical Engineering 386, DOI 10.1007/978-3-662-49831-6_39

flight formation which can be changed into different formations depending on the mission requirements. Most of the DSMs can be considered combinations of monolithic satellite, including heterogeneous ad-hoc flyers like the A-Train, autonomous formation flying clusters such as Edison (EDSN) [2], fractionated spacecraft such as the system F6 program.

All these missions require inter-satellite links (ISLs) with guaranteed performance to build a network in space. In literature, there are some discussions on the potential network architecture for formation flying. Marszalek [3] discussed the potentials and limitations of IEEE 802.11 for satellite swarms and adapted all critical parameters of WIFI for the long-range satellite communication. Similar proposals also include [4–6]. The main requirement for the inter-satellite link is to acquire and maintain the satellite in a desired relative geometric configuration. The data exchanged should then be arrived timely in order to control the inter-satellite distance collaboratively. However, WIFI will not be applicable due to the time-criticality. The CSMA/CA method used in the 802.11 MAC protocol causes transmission uncertainty because of the detection of the medium. Sun [7] proposed half-duplex Code Division Multiple Access (CDMA) with roles rotating which enables both code and carrier phase measurements at variable mission phases and detect some satellites while tracking others. But total number of simultaneous cross-link transmissions is limited by the CDMA code noise floor. Complexity in design adds to communications system cost.

Considering the lack of CSMA/CA and CDMA MAC protocol, A completely different MAC method, where the available time is divided into slots and the nodes choose their slots according to an algorithm called self-organizing time division multiple access (STDMA) is capable to our requirement. It is not only crucial for an application to provide the real-time communication with high reliability properties, but divides the shared communication channel in a fair and predictable way. This paper addresses an adaption of STDMA in order to reduce the overall development costs of novel space missions.

2 The STDMA Algorithm

In this section, STDMA is briefly introduced. For a more detailed description, we invite the readers to refer to [8]. STDMA is a deterministic channel access mechanism, in which the time dimension of channel is divided into frames. These frames are further divided into fixed length slots, whose duration typically corresponds to one data packet duration plus a necessary guard interval. The medium access strategy is based on a slot reservation process, including four different phases: initialization, network entry, first frame and continuous operation. Figure 1 shows the STDMA algorithm flowchart.

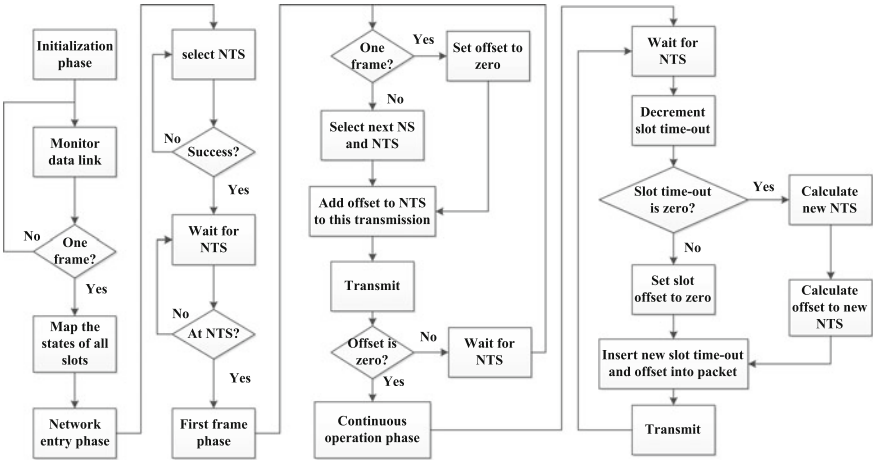

Fig. 1 The STDMA algorithm flowchart

2.1 Initialization Phase

When a satellite node powers up at the first time, it will begin with an initialization phase which takes one frame. During this frame, the node will monitor the data link to determine channel activity and current slot assignments. The state of a slot can either be free, busy or allocated. After one frame has elapsed, the node enters the Network Entry Phase.

2.2 Network Entry Phase

During the network entry phase, the node selects its first transmission slot which is randomly chosen according to a p-persistent algorithm, and then advertises itself on the data link. The probability $p(i)$ for a transmission in a potential transmission slot i is defined as

$$\begin{aligned} p(0) &= \frac{1}{n(0)} \\ p(i) &= p(i-1) + \frac{1-p(i-1)}{n(i)}, i > 0 \end{aligned} \tag{1}$$

where $n(i)$ denotes the number of free slots.

In this phase, some parameters must be determined:

Nominal Increment (NI)—The satellite node first determines its NI by dividing the number of slots per second (N) with the desired report rate(r) representing the ideal interval between two consecutive transmitted packets:

$$NI = \left\lfloor \frac{N}{\mathrm{r}} \right\rfloor \tag{2}$$

Nominal Start Slot (*NSS*)—To select the first transmission slot, the satellite node selects a *NSS* which is randomly selected from the current slot and *NI* slots ahead of time.

Selection Interval (*SI*)—After this, the search range for free time slot (*SI*) is determined which is given by

$$SI = \mathrm{k} \times NI \tag{3}$$

where $\mathrm{k}(0 < k < 1)$ is an adjustment factor and placed so that the NSS is in the middle, i.e.,

$$SI = \{NSS - 0.5 \times SI, NSS + 0.5 \times SI\} \tag{4}$$

Nominal Transmission Slot (*NTS*)—A slot is randomly selected within *SI*. This slot is checked to see if it is available for use. If not, the adjacent slot to the left and right is checked. This process is continued until an available slot is found within *SI*. There shall always be a set of available slots. If the link is approaching maximum capacity, slots are reused from nodes at the greatest distance from the own position. The selected slot becomes the Nominal Transmission Slot (*NTS*). Each *NTS* is assigned a random time-out. Upon reaching the *NTS*, the first frame phase is entered.

2.3 First Frame Phase

During the first frame phase, the node continuously allocates its *NTS*. When one frame has elapsed, the initial transmissions have been allocated and then the offset is set to zero in the last transmission to indicate that no more allocations will be made. Upon reaching the first *NTS*, a new Nominal Slot (*NS*) and *NTS* is selected for the following transmission. Meanwhile, the offset to next *NTS* is calculated and saved. The *NS* is selected by adding *NI* to the *NTS*.

2.4 Continuous Operation Phase

In the continuous operation phase, the node transmits in the allocated NTSs and decrements the slot time-out. When the time-out reaches zero, a new NTS is selected within the SI as described above. The relative offset (slot offset) is inserted into the data packet and transmitted so that receiving nodes are made aware of the intentions. This phase is maintained until the system is shut down, enters other mode.

3 Simulation Model

3.1 Assumptions and Satellite Formation

The following assumptions are made without loss of generalization:

(1) all satellite nodes generate packets at a fixed (report) rate *r*,
(2) all packets have a fixed maximum size (which translates to a fixed transmission duration),
(3) internal clocks of satellite nodes are synchronized. In the aspect of network protocol stack, we adopt the same the physical (PHY) layer derived from [9]. The MAC method is STDMA, compared the results against CSMA/CA.

The number *N* of available slots per second depends on the channel and packet characteristics: considering a 20 MHz wide control channel with 1Mbps transfer rate, this translates to N = 384 slots/s for 300 bytes according to the paper ([10]–5.2.3.1). Table 1 summarizes the modified parameters used in the simulationPlease provide appropriate citation for 5.2.3.1 to crossrefer in this chapter.

Satellite mesh flying formation is used and each node can communicate with each other. Figure 2 shows the mesh flying formation.

3.2 Performance Metrics

Performance metrics which have been used to evaluate the MAC method are channel access delay and packet reception probability.

Table 1 Parameters used in the simulation

Parameter	Value
Simulator	NS-3 (version 3.21)
Operating system	GNU/Linux (Ubuntu 14.04 -32 bit)
Simulation time	60 s
Min. number of candidate slots	4 slots
Frame duration	1 s
Min. reservation time-out	3 frames
Max. reservation time-out	7 frames
Selection interval ratio	0.2
Max. duration of network entry	50 slots
Guard interval (per slot)	6 us
Max. packet size	300 bytes
Report rate	10 Hz

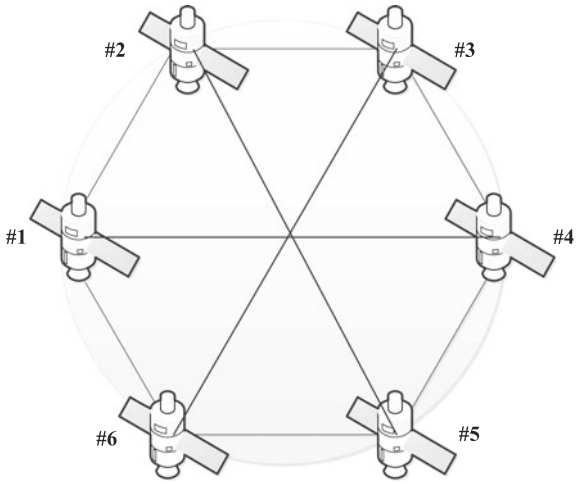

Fig. 2 Mesh formation

The channel access delay which can be used to evaluate the fairness between nodes is defined as the time elapsing from the channel access request until the actual channel access takes place.

The packet reception probability is measured similar to the throughput, but it relates the successful received packets to the overall sent packets, which given by:

$$Packet\ reception\ probability = \frac{\sum received\ packets}{\sum transmitted\ packets} \tag{5}$$

4 Simulation Results

The cumulative distribution function (CDF) for the channel access delay in STDMA and CSMA is shown in Fig. 3. As the channel access delay in CSMA is random, there is generally longer delays than STDMA. The channel access delay is upper bounded in STDMA since a satellite node is always allowed to transmit regardless of the number of nodes. When all slots are occupied, a satellite node will transmit at the same time as another node but it selects the one situated furthest away from itself.

Figure 4 shows the packet reception probability for ISL distances. With the increase of the ISL distance and Bit Error Rate degradation, packet reception probability decreases. STDMA performs better than CSMA because of the synchronized transmissions, scheduling of transmissions in space and nodes avoid using allocated slots when there still is available resources in the system. Due to the scheduling of transmissions the packet reception probability for STDMA is always better then CSMA regardless of setting. STDMA has a higher packet reception probability

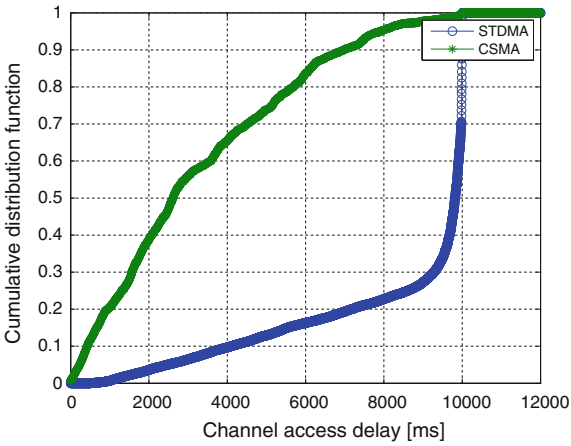

Fig. 3 Channel access delay

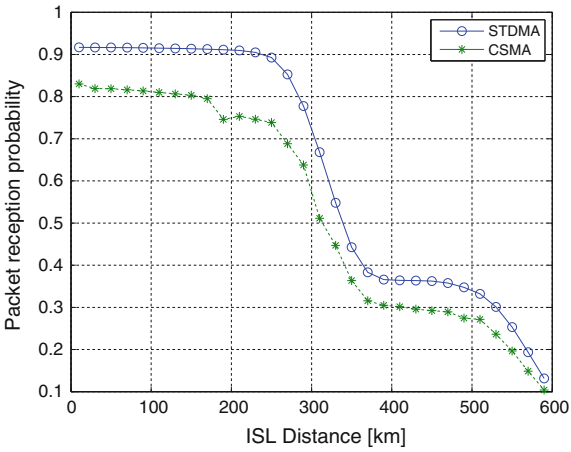

Fig. 4 Packet reception probability

compared to CSMA in the satellite scenario and thereby a better reliability. The STDMA algorithm always grants packets channel access since slots can be reused if all slots are currently occupied within the selection interval of a node.

5 Conclusion

In this paper, a self-organizing time division multiple access (STDMA) is proposed for distributed satellite formation and the parameters of STDMA are modified to adapt the satellite scenario. Channel access delay and packet reception probability are selected as performance measures. In the aspect of channel access delay, STDMA has lower delays than CSMA due to the deterministic depends on SI. On the other

hand, as the ISL distance increases, packet reception probability of two MAC methods degrades because of Bit Error Rate degradation. However, STDMA performs better than CSMA in the periodic broadcast.

Acknowledgments The authors would like to thank Jionghui Li of NSSC, CAS and the anonymous reviewers for their constructive comments that improved the presentation of this paper.

References

1. Nag S, LeMoigne J, Miller et al (2015) A framework for orbital performance evaluation in distributed space missions for earth observation. In: IEEE Xplore, aerospace conference 2015
2. Yost B (2013) EDSN-edison demonstration for smallsat networks overview.presented at the small satellite conference, Logan, Utah
3. Marszalek M, Rummelhagen M, Schramm F (2014) Potentials and limitations of IEEE 802.11 for satellite swarms. In: Aerospace conference, 2014 IEEE, pp 1–9
4. Vladimirova T, Sidibeh K (2008) WLAN for earth observation satellite formations in LEO. In: BLISS'08. ECSIS Symposium on Bio-inspired learning and intelligent systems for security, pp 119–124
5. Sidibeh K, Vladimirova T (2006) IEEE 802.11 Optimisation techniques for inter-satellite links in LEO networks. In: 2006 8th international conference advanced communication technology
6. Clare LP, Gao JL, Jennings EH, Okino C (2005) A network architecture for precision formation flying using the IEEE 802.11 MAC protocol. In: Aerospace conference, 2005 IEEE, pp 1335–1347
7. Sun R, Guo J, Gill EKA, Maessen DC (2012) Potentials and limitations of CDMA networks for combined inter-satellite communication and relative navigation. Int J Adv Telecommun 5(1–2)
8. Gaugel T, Mittag J, Hartenstein H, Papanastasiou S, Strom EG (2013) In-depth analysis and evaluation of Self-organizing TDMA. In: Vehicular networking conference (VNC), 2013 IEEE, pp 79–86
9. Kang H, Jiang X, Xiong W (2015) Research on wireless networking mode for the distributed satellite communication system. J Comput Inform Syst 11(12):1–10
10. ETSI, TR. 102 861 (2012) Intelligent Transport Systems (ITS). STDMA recommended parameters and settings for cooperative ITS. ETSI, Technical Report

DME Interference Mitigation Algorithm Based on Signal Separation Estimation Theory for GPS L5

Jie Li and Wei Fang

Abstract L5 signal is set up for civil aviation exclusively in GPS (Global Positioning System), and takes up exclusive frequency band. However, the DME (Distance Measurement Equipment) signal which has already applied for distance measurement works as the same frequency band as GPS L5. DME signal with high power will decrease SINR (Signal to Interference and Noise Ratio) of GPS L5 and even give rise to acquisition failure. On DME interference suppression, the traditional methods will bring loss to useful satellite data. Thus the performance of GPS L5 receiver will suffer from serious degradation. In the light of the received signal model, a new DME interference mitigation algorithm is presented in this paper. Firstly, frequency is estimated with time-modulated windowed all-phase DFT (tmwapDFT). Then, we use the estimated frequency to get amplitude and signal delay information with signal separation estimation theory. Compared with traditional method, the proposed method can reserve more useful satellite data. The performance of proposed method is verified by simulations.

Keywords GPS L5 signal · DME interference mitigation · Time-modulated windowed all-phase DFT · Signal separation estimation theory · Precise estimation of parameters

1 Introduction

GPS L5 signal is used for civil aviation exclusively, and takes up exclusive frequency band. Compared with L1 and L2 signal, L5 signal has more power at receiver, more positioning accuracy, stronger anti-interference capability, and can be implemented more conveniently. However, there are a lot of interference

J. Li (✉)
Zhonghuan Information College, Tianjin University of Technology, Tianjin, China

W. Fang
Beijing Aeronautical Science and Technology, Research Institute of COMAC, Beijing, China
e-mail: davidf8@163.com

Q. Liang et al. (eds.), *Proceedings of the 2015 International Conference on Communications, Signal Processing, and Systems*, Lecture Notes in Electrical Engineering 386, DOI 10.1007/978-3-662-49831-6_40

equipment working at the L5 frequency band, among which DME (Distance Measurement Equipment) signals make greatest influence on L5 signal. DME interference can cause degradation of SINR (Signal to Interference and Noise Ratio) at GPS receiver, reduce the sensitivity of acquisition, thus lead to the failure of convergence of tracking loop, and finally make it difficult to decode the navigation information [1–4].

Lots of research organizations and universities have been seeking for the methods to mitigate the error brought from DME interference. Many anti-interference techniques have been developed, most frequently used of which are pulse blanking, notch filter and hybrid method.

Pulse blanking method sets the part of signal to zero which is beyond the threshold in time domain, and thus achieves the goal of suppressing the interference [5, 6]. It is easy to implement and has already verified on hardware receiver [7]. However, the main deficiency of this method is that a large part of useful GPS signal will be gotten rid of as well when the interferences are suppressed. And what's more, this method will also cause a great amount of data gaps, which will make the failure of acquisition, tracking and then positioning of the receiver. Notch filter method mitigates the interference by letting the signal pass a narrow band notch filter involving DME frequencies [5, 8]. Hybrid method uses a moving window in time domain to detect the DME pulse interference and filter data in the frequency domain [5, 9]. Although the next two methods can preserves more useful signals, the data missing problem still exists.

In this paper, we propose a new DME interference suppression method which can keep useful GPS signal to a large extent meanwhile suppress the interference. The efficiency of the proposed approach is verified in the experiments.

2 Data Model and Problem Description

DME baseband signal is a pulse pair which can be modeled as:

$$s(t) = e^{-\alpha/2(t-\Delta t/2)^2} + e^{-\alpha/2(t-\Delta t/2)^2} \tag{1}$$

When the airborne DME equipment take advantage of the channel 64–126 X for communication, the ground equipment may respond frequencies ranged from 1151 to 1213 MHz [3, 5]. Unfortunately, this frequency band covers the GPS L5 signal with central frequency 1176.45 MHz and bandwidth 24 MHz. Generally, the peak power of DME signal varies from 50 W to 2 kW. The maximum of the pulses from transponder may be up to 2700 per second. The interference of DME will seriously degrade the SINR of GPS receiver and then cause the failure of acquisition.

When the GPS receiver is interfered by only one DME base station, the interference can be eliminated by the method based on NLS criterion [10]. Consider the scenario that the DME pulse interference comes simultaneously from two or more

different ground base stations. Due to the difference of distances between GPS receiver and the two more DME ground bases, the GPS receiver will be interfered by two more DME pulses with different Doppler shifts.

It is supposed that there are P DME interferences received, the signal can be modeled as:

$$y(t) = \sum_{p=1}^{P} \alpha_p x(t-\tau_p) e^{j\omega_{dp}(t-\tau_p)} + u(t) + e(t) \tag{2}$$

where $x(t)$ is DME signal, $u(t)$ is GPS signal, $e(t)$ is the thermal noise. $\alpha_p, \tau_p, \omega_{dp}$ represent the complex amplitude, time delay and frequency of DME signal respectively.

After A/D conversion, the transformed signal model is given as:

$$y(nT_s) = \sum_{p=1}^{P} \alpha_p x(n-\tau_p) e^{j\omega_{dp}(n-\tau_p)} + u(n) + e(n) \tag{3}$$

Because GPS satellites signals are buried under the noise level, GPS signals can be taken as noise compared with DME signals. Accordingly, the Eq. (3) can be rewritten as:

$$y(n) = \sum_{p=1}^{P} \alpha_p x(n-\tau_p) e^{j\omega_{dp}(n-\tau_p)} + e_1(n) \tag{4}$$

3 Algorithm Implementation

3.1 Signal Separation Estimation Theory

Due to the DME pulse is much stronger than GPS signal, it is no need to analyze GPS signal separately. Once DME signal is detected and estimated, we can estimate the frequency and complex amplitude of DME signal under the criterion of NLS [10, 11]. DME pulse pairs can be simply detected by means of calculating the correlation of received signal and a moving window with the width of 12 μs.

In order to get a more precise estimate accuracy, each group of unknown parameters is to be estimated with signal separation estimation theory via iteration. We consider below estimating the unknown parameters $\left\{\hat{\alpha}_p, \hat{\tau}_p, \hat{\omega}_{dp}\right\}_{p=1}^{P}$ by minimizing the Nonlinear Least Squares (NLS) criterion [12]

$$Q\left(\left\{\hat{\alpha}_p, \hat{\tau}_p, \hat{\omega}_{dp}\right\}_{p=1}^{P}\right) = \min_{\alpha,\tau,\omega_d} \left| y(n) - \sum_{p=1}^{P} \alpha_p x(n-\tau_p) e^{j\omega_{dp}(n-\tau_p)} \right|^2 \tag{5}$$

Let $s(n-\tau_p) = x(n-\tau_p)e^{j\omega_{dp}(n-\tau_p)}$, then Eq. (5) can be expressed as

$$Q\left(\left\{\hat{\alpha}_p, \hat{\tau}_p, \hat{\omega}_{dp}\right\}_{p=1}^{P}\right) = \min_{\alpha,\tau,\omega_d}\left|y(n) - \sum_{p=1}^{P}\alpha_p s(n-\tau_p)\right|^2 \tag{6}$$

Solving the problem of optimization in Eq. (6) yields the estimate $\hat{\alpha}_p, \hat{\tau}_p, \hat{\omega}_{dp}$ of $\alpha_p, \tau_p, \omega_{dp}$ as:

$$\hat{\omega}_{dp} = \arg\max_{\omega_{dp}}\left|\mathbf{b}^H(\omega_{dp})\mathbf{y}_p^2\right|^2 \tag{7}$$

$$\hat{\tau}_p = -\frac{N}{2\pi f_s}\arg\max_{\tau_p}\left|\mathbf{a}^H(\omega_p)\hat{\mathbf{S}}^*\mathbf{Y}_p\right|^2 \tag{8}$$

$$\hat{\alpha}_p = \left.\frac{\mathbf{a}^H(\omega_p)(\hat{\mathbf{S}}^*\mathbf{Y}_p)}{\left\|\hat{\mathbf{S}}\right\|^2}\right|_{\omega_p=\hat{\omega}_p} \tag{9}$$

where $\mathbf{y} = [y(-N/2), y(-N/2+1), \ldots, y(N/2-1)]^T$, $\mathbf{Y} = \mathrm{DFT}(\mathbf{y})$, $\mathbf{b}(\omega_{dp}) = \left[e^{j2\omega_{dp}(-N/2)}, e^{j2\omega_p(-N/2+1)}, \ldots, e^{j2\omega_p(N/2-1)}\right]^T$, $S(k) = \mathrm{DFT}(s(n))$, $\mathbf{S} = diag\{\hat{S}(-N/2), \hat{S}(-N/2+1), \ldots, \hat{S}(N/2-1)\}$, $\mathbf{a}(\omega_p) = \left[e^{j\omega_p(-N/2)}, e^{j\omega_p(-N/2+1)}, \ldots, e^{j\omega_p(N/2-1)}\right]^T$, f_s is the sampling rate.

Note that the values of $2\hat{\omega}_{dp}$ and $\hat{\omega}_p$ can be obtained by the FFT of vectors $\mathbf{y}_p^2$ and $\hat{\mathbf{S}}^*\mathbf{Y}_p$ respectively.

The steps of optimized method of signal separation estimation theory are given as follow:

Step 1 Assume $p=1$, take $\alpha_1 s(n-\tau_1)$ as unknown waveform. Then calculate $\hat{\omega}_{d1}$, $\hat{\alpha}_1$, $\hat{\tau}_1$ according to Eqs. (7), (8) and (9) respectively

Step 2 Assume $p=2$, calculate $\hat{y}_2(n)$ by using $\hat{\alpha}_1, \hat{\tau}_1, \hat{\omega}_{d1}$ obtained in Step1. After that, $\hat{\alpha}_2, \hat{\tau}_2, \hat{\omega}_{d2}$ can be gotten with the method similar to Step 1

Step 3 Compute $\hat{y}_1(n)$ by using $\hat{\alpha}_2, \hat{\tau}_2, \hat{\omega}_{d2}$ and then redetermine $\hat{\alpha}_1, \hat{\tau}_1, \hat{\omega}_{d1}$ from $\hat{y}_1(n)$

Step 4 Iterate the previous two steps until convergence is achieved to get the final estimates

Step 5 Assume $p = 3, 4 \ldots P$, repeat the above steps until all parameters of P DME signals are estimated and the convergence conditions are satisfied in the meantime

Finally, the reconstructed DME signals can be expressed as:

$$\hat{y}_{DME}(n) = \sum_{p=1}^{P}\hat{\alpha}_p x(n-\hat{\tau}_p)e^{j\hat{\omega}_{dp}(n-\hat{\tau}_p)} \tag{10}$$

Eliminate the DME interference signal from received signal and get the suppressed GPS signal as:

$$\hat{u}(n) = y(n) - \hat{y}_{DME}(n) \tag{11}$$

3.2 *Frequency Estimation with Time-Modulated Windowed All-Phase DFT*

Although a rather effective method has been afforded above, it is difficult to analyze frequency component accurately with DFT from Eq. (7) because of spectral leakage and picket-fence effect [13]. In this paper, time-modulated windowed all-phase DFT(tmwapDFT) is taken advantage of to deal with the problem [14, 15].

The original windowed all-phase DFT can be implemented as below

$$Y_{ap}(k) = DFT([y(n)R_w(n) + y(n-N)R_w(n-N)]) \tag{12}$$

where, $R_w(n)$ is the correlation window function. FFT can be used here to reduce computation complexity.

In order to improving the deficiency of missing a half of information, a complex factor W_{2N}^{n} is modulated to the received signal in time domain.

$$y_{tm}(n) = y(n)\, W_{2N}^{n} \tag{13}$$

Hence, the time-modulated windowed all-phase DFT is defined as

$$Y_{ap}(k) = DFT([y_{tm}(n)R_w(n) + y_{tm}(n-N)R_w(n-N)]) \tag{14}$$

It is a better choice to get estimate $\hat{\omega}_{dp}$ of ω_{dp} by tmwapDFT instead of original DFT.

4 Experimental Results

To test and verify the performance of the proposed method, the experiments have been carried out. Where, the satellite data are interfered by DME pulse and down-converted at the intermediate frequency of 1.25 MHz same as the GPS signal. The sample rate is 5 MHz, the SNR (Signal-to-Noise Ratio) is 18 dB.

Mean square error (MSE) of time delay and frequency change with JNR (Jammer-to-Noise Ratio) are shown in Figs. 1 and 2. Frequency estimation error of

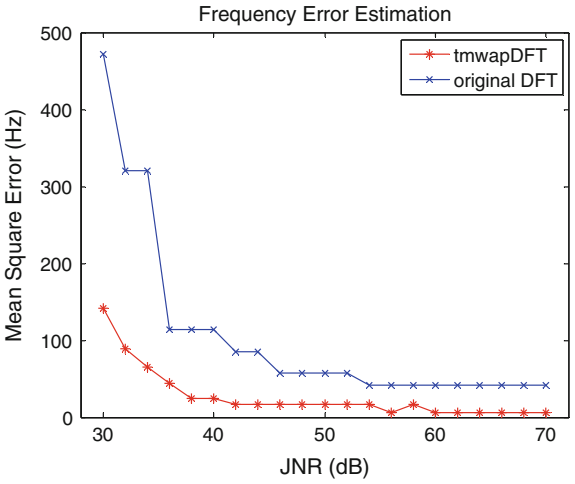

Fig. 1 Frequency error changes with JNR

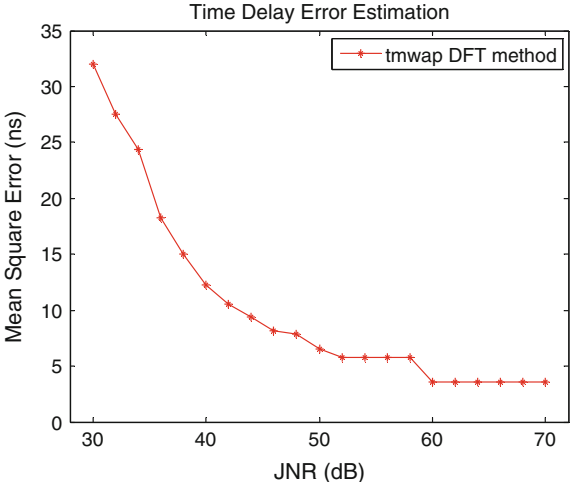

Fig. 2 Time delay error changes with JNR

original DFT is too large to reconstruct the DME signal exactly while the proposed method in this paper has a better performance. Frequency error after fine estimation has been further declined in lower JNR condition, while there is no distinct improvement after fine estimation with the JNR increasing because the error of tmwap DFT method is already very small. Time delay error before precise estimation is accurate enough to reconstruct the DME signal exactly. Nevertheless, more little error estimate can be attained after precise estimation which further improve the anti-jamming performance.

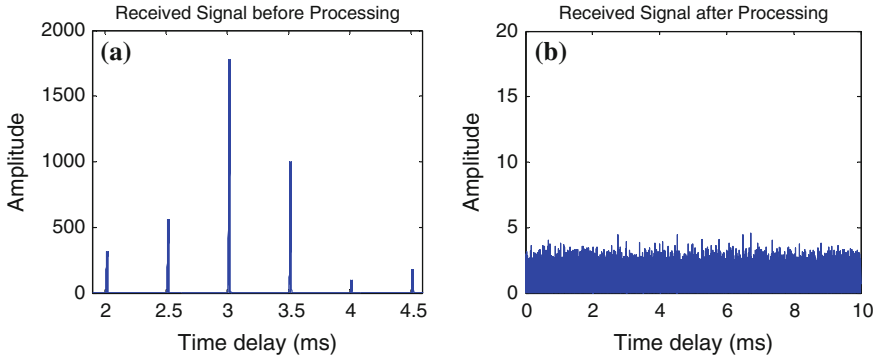

Fig. 3 DME interference mitigated by proposed method

Six DME signals from different base stations are received in company with the four GPS signals during the experiment. The JNR of them are 50, 55, 65, 60, 40, 45 dB and the time delays are 2, 2.5, 3, 3.5, 4, 4.5 ms correspondingly. The comparison results between the original signal and the suppressed signal with the proposed method is demonstrated in Fig. 2. The DME signal is mitigated after processing while the useful satellite signal still remains.

The acquisition results of the original and proposed method is given in Fig. 3. Pulse blanking method which lose a lot of useful GPS signal will result in the correlation peaks of acquisition lower than the threshold. The useful data missing problem still exists in hybrid method. Although the correlation peaks are higher than pulse blanking method, the results still do not reach the threshold. Further descending the threshold may let the GPS signal be detected, but the signal power could be too low to finally get an accurate position. The proposed method has prevailed performance and easily acquire the signal. It is slightly bad than GPS only circumstance because the proposed method almost maintain entirely useful signal.

5 Conclusions

The traditional DME interference suppression methods which bring about the loss of GPS signal will suffer from serious performance degradation of GPS receiver. In this paper, a new DME interference suppression method for GPS L5 signal are proposed, when the DME interferences come from more than one base station. Firstly, frequency is estimated with time-modulated windowed all-phase DFT

(tmwapDFT). Then, we use the estimated frequency to get amplitude and signal delay information with signal separation estimation theory. In order to further improve the estimation accuracy, a two-dimension fine estimation method is proposed, which takes the previous estimated results as the initial values. Experiment results show that the proposed method could estimate the parameters precisely, by which DME signal can be reconstructed and eliminated. It can be shown from the experiment results that the proposed method which keeps more useful satellite data has a better performance compared with conventional ones.

Acknowledgment The work of this paper is supported by the Project of the National Natural Science Foundation of China (Grant No. 61172112, 61179064 and 61271404), Science and Technology Fund of Civil Aviation Administration of China (Grant No. MHRD0606), and the Fundamental Research Funds for the Central Universities (Grant No. ZXH2009A003).

References

1. Steingass A, Hornbostel A, Denks H, (2010) Airborne measurements of DME interferers at the European hotspot. In: Proceedings of the fourth European conference on antennas and propagation (EuCAP), pp 1–9
2. Hegarty C, Kim T, et al (1999) Methodology for determining compatibility of GPS L5 with existing systems and preliminary results. In: Proceedings of the institute of navigation annual meeting, Cambridge, MA
3. Fang W, Wu R, Lu D, Wang W (2011) A new interference suppression method in GPS based on modified GAPES. Sig Process 27(12):1860–1864
4. Angelis M, Fantacci R, Menci S, Rinaldi C (2005) Analysis of air traffic control systems interference impact on Galileo aeronautics receivers. In: IEEE international radar conference, pp 585–595
5. Gao G (2007) DME/TACAN interference and its mitigation in L5/E5 bands. In: The ION conference on global navigation satellite systems
6. Brandes S, Epple U et al (2009) Physical layer specification of the L-band digital aeronautical communications system (L-DACS1). In: Integrated communications, navigation and surveillance conference, pp 1–12
7. Grabowski J (2002) Characterization of L5 receiver performance using digital pulse blanking. In: The ION conference
8. Zhang Q, Zheng Y, Wilson SG, Fisher JR, Bradley R (2005) Excision of distance measuring equipment interference from radio astronomy signals. Astron J 129:2933–2939
9. Anyaegbu E, Brodin G, Cooper J, Aguado E, Boussakta S (2008) An integrated pulsed interference mitigation for gnss receivers. J Navig 61:239–255
10. Fang Wei, Renbiao Wu, Wang Wenyi, Dan Lu (2012) DME Pulse interference suppression based on NLS for GPS. Int Conf Signal Process 1:174–178
11. Christensen MG, Jensen SH (2011) New results on perceptual distortion minimization and nonlinear least-squares frequency estimation. IEEE Trans Audio Speech Lang Process 19 (7):2239–2244
12. Li J, Wu RB (1998) An efficient algorithm for time delay estimation. IEEE Trans Signal Process **46**(8):2231–2235
13. Oppenheim AV, Schafer RW (2010) Discrete-time signal processing, 3rd edn, pp 793–840. Prentice Hall, Upper Saddle River

14. Huang XD, Wang ZH (2007) Principle of all-phase DFT restraining spectral leakage and the application in correcting spectrum. J Tianjin Univ 40(7):882–886
15. Liu JZ (2001) Multidimensional all phase digital filtering theory and image multiscale geometric representation. Ph.D. dissertation, pp 23–28

Wireless Video Transmission Optimization Based on Error Resilience and Unequal Packet Loss

Haiyun Sun, Yumei Wang and Yu Liu

Abstract On account of the wireless channel interference, transmission data tends to be erroneously decoded at the receiver. Even received with errors in some extent, the video can still be successfully recovered because of its error resilience, e.g. videos encoded with H.264/AVC. According to recent research, when a bit sequence is modulated to constellation symbols, different bit positions of symbols may have different probabilities of error occurrence. To exploit whether differential protection could be provided to different data bits of a video streaming based on this feature, our experiment implements this UEP (unequal error protection) scheme together with the data partitioning mechanism in H.264/AVC video encoding standards. The experiment results show the UEP scheme gains 5 dB of PSNR improvement in average than the EEP (equal error protection) scheme. While once massive errors occur, packets must be discarded and retransmissions are required, so additional resource consumption is unavoidable. To solve this problem, unequal loss protection (ULP) for H.264 bit stream is proposed in this paper. And we find a fact through experiments that when bandwidth resource is limited, insignificant partial data of H.264 bit stream could be discarded selectively without arousing obvious video quality degradation. Our simulation shows that when the unimportant network abstraction layer units (NALU) of H.264 bit stream are discarded, approximately 20 % of bandwidth resource is saved.

This work is partially supported by the Fundamental Research Funds for the Central Universities under grant No. 2014ZD03-02, Huawei Research fund, National Science Foundation of China (No. 61201149 and No. 61171098), the Beijing Higher Education Young Elite Teacher Project, and the 111 Project (No. B08004).

H. Sun (✉) · Y. Wang · Y. Liu
Key Lab of Universal Wireless Communication, Ministry of Education of PRC, Beijing University of Posts and Telecommunications, Beijing, China
e-mail: hyunsun@bupt.edu.cn

Y. Wang
e-mail: ymwang@bupt.edu.cn

Y. Liu
e-mail: liuy@bupt.edu.cn

Q. Liang et al. (eds.), *Proceedings of the 2015 International Conference on Communications, Signal Processing, and Systems*, Lecture Notes in Electrical Engineering 386, DOI 10.1007/978-3-662-49831-6_41

Keywords Constellation mapping · Error resilience · Unequal error protection · H.264/AVC · Unequal loss protection

1 Introduction

In recent years, with the rapid development of the mobile Internet, the demand for mobile video is expanding. As a result, more and more video services are extended to the wireless networks, such as video chatting, video conferencing, and video streaming, which requires the wireless networks to provide higher service quality and wireless access speed. Although the wireless networks evolve very rapidly for higher capacity in recent years, wireless video transmission still presents great challenges for nowadays wireless networks.

On account of the time-variation and heterogeneity of the wireless network, as well as the high error rate and the unpredictable nature of wireless channels, which has a great influence on the quality of the wireless video transmission.

In order to resist the impact of the transmission errors to the video quality, some error resilience tools are added in newer class of video coding standards. For example, when an original YUV file is encoded with H.264/AVC, error resilience tools are added, e.g. flexible macroblock order (FMO) [1], and data partitioning. When video data is encoded with H.264/AVC, the H.264/AVC bit stream will be divided into three partitions with different priorities. We find that partition with higher priority could tolerate the least bit errors, while the partition with lower priority could tolerate the most bit errors. As a result, the differential protection according to different priorities of data could be conducted to improve the overall video transmission quality.

Traditionally, redundant bits are added to each data unit during video source encoding or channel encoding at the physical layer [2–4], which will then help to detect and correct transmission errors at the receiver. Since the different significance of H.264/AVC partitions could be discriminated, more redundant check bits are added to more significant partitions and less check bits added to less significant partitions [1]. In this way, the recovered video quality are enhanced indeed, but it introduces additional bandwidth consumption by adding more redundancy, which equivalently reduces the capacity of wireless network.

Recently, a systematic structure is proposed in [5]. It demonstrates that when a bit stream is modulated into a set of symbols, some bit positions of a symbol are less error-prone compared to others during wireless transmission. That is to say, differential protection could be provided for different bits at different positions. If the transmitter is aware of the relative importance of different data bits, we can place those data bits with higher significance into positions with stronger protection and those with lower significance into less protected positions. In other words, the transmitter can provide an unequal error protection (UEP) of its data by simply arranging different data bits onto specific bit positions without consuming additional resources.

Nowadays, there are also some valid MAC-PHY schemes that can recover errors from partially erroneous packets, including partial packet recovery(PPR) [6], SOFT [7], ZipTx [8], and Maranello [9]. Errors could be corrected by these schemes in some extent. But when it comes to long error bursts, these error correction schemes may fail. In this case, the erroneous transport data units must be discarded, and retransmission will be invoked by the receiver. However, retransmission is not feasible for all of video applications [10], e.g. wireless video broadcast and multicast. Additionally, retransmission demands more wireless resources. While our experiments in part V show that almost half of insignificant NALUs could be dropped without deteriorating the recovered video quality. For this reason, an unequal loss protection scheme is proposed in part IV of this paper by discriminating the priorities of NALUs and discarding the NALUs with relative low priorities. Our experiments in Sect. 5 shows that almost half of insignificant NALUs could be dropped and approximately 20 % of bandwidth resource is saved without degrading the recovered video quality much.

The rest of the paper is organized as follows. Section 2 gives a detailed explanation of the error resilience and different priorities of H.264 bit stream. Section 3 respectively presents the UEP scheme and ULP scheme. The simulation results and analyses of the UEP and ULP schemes are presented in Sect. 4. Finally, the paper is concluded in Sect. 5.

2 Intensive Research on H.264 Bit Stream

2.1 Introduction of Error Resilience in H.264/AVC

Since video data transmission through wireless channel is error-prone, some error resilience tools are adopted in new video encoding standard, e.g. H.264/AVC [1], which is composed of video coding layer (VCL) and network abstraction layer (NAL). Originally, one frame of a YUV file could be divided into one or several slices. Under normal circumstances, one frame corresponds to one slice. And one slice is encoded to bits included in one NALU. When a NALU is decoded, its corresponding frame is decoded.

As we all know, several profiles [1] of H.264/AVC can be selected for video encoding, such as base profile, extended profile, and high profile, etc. In order to realize the error resilience, some error resilience tools are added into the extended profile, including flexible macroblock order(FMO), data partitioning and etc. Data partitioning is allowed in extended profile to exploit the unequal significance of video data. The extended profile can be selected during H.264/AVC encoding process.

The H.264/AVC bit stream with no data partitioning contains parameter set (SPS), picture parameter set (PPS), instantaneous decoding refresh (IDR) slice, and ordinary slices (as indicated by “No Data Partitioning” in Fig. 1). When data partitioning is used, the encoded data for an ordinary slice is divided into three

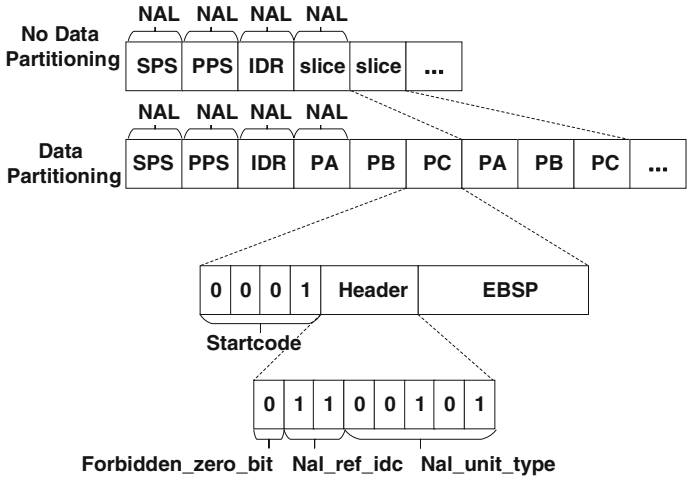

Fig. 1 Data partitioning in H.264/AVC and the structure of NALU

separate partitions, i.e. Partition A (PA), Partition B (PB), and Partition C (PC), as shown in Fig. 1 by "Data Partitioning".

During the decoding process, the decoding of PB depends on the corresponding PA. Likewise, decoding PC depends on the corresponding PB [11]. Hence, Partition A (PA) has the highest priority, and Partition C (PC) is least significant. Actually, PAs, PBs and PCs are uniformly distributed in H.264/AVC bit stream. Hence, we need to exploit further into NALU.

2.2 Discriminating the Different Priorities of H.264/AVC Bit Stream [1]

As shown in Fig. 1, H.264 bit stream is composed of a series of NALUs. To discriminate the NALU boundaries, the start code 0001 is added at the beginning of each NALU. If a NALU corresponds to the slice at the beginning of a frame, a 4-byte 0001 is added additionally as start code prefix; otherwise, a 3-byte 001 is added, which are specified in Annex B of H.264/AVC specification for the byte stream format.

To construct a NALU, one slice of original video data is first compressed into a string of data bit stream (SODB) in VCL(video coding layer). And then some ending bits with one "1" and some "0"s are added to the SODB, which is called *raw byte sequence payload* (RBSP). Then byte alignment is implemented. To avoid repetition with the starting bytes, a byte of 0X03 is inserted into the RBSP, which is called *extended byte sequence load* (EBSP). Most importantly, a NALU header is added in front of the EBSP.

The NAL header is crucial to distinguish the different priorities of NALUs. As displayed in Fig. 1, the NAL header is composed of 8 bits. The first bit is *forbidden_zero_bit*. And the following two bits represent the priority of this NAL unit, whose values vary between 0 ~ 3. The larger the value is, the more important the NALU is. The remaining 5 bits indicate the type of current NALU. Some common values are like 2, 3, 4, 5, 6 and 7. Among these, 2, 3 and 4 represent PA, PB and PC, respectively; the value of 5 indicates that current NALU is an IDR slice, which is one of the most important NAL units; and the values of 7 and 8 represent SPS and PPS respectively.

In our simulations, the project JM8.6 is used to encode a YUV file into a H.264 bit stream. Encoding parameters are set in the configuration file before encoding. Firstly, the extended profile is selected. The GOP structure is set as IPBPBPB. The constrained intra prediction option is selected. FMO is also adopted to implement error concealment. And data partitioning is used to discriminate the differential significance of the H.264 bit stream.

Given that 447 NALUs are contained in a H.264 bit stream of our experiment, which is shown in Fig. 2. Particularly, NALUs are distinguished by the NAL header in hexadecimal format, which are 67, 68, 65, 42, etc. Furthermore, with data partitioning, the original NALUs containing PAs, PBs and PCs are uniformly distributed, as shown by "The Original 264 Bit-stream" in Fig. 2. PAs need to be placed together for cancellation mapping convenience. Likewise for PBs and PCs.

According to our large amount of experiments, if the values of NAL header are 67, 68, 65, 42, and 43, the corresponding NALUs belong to the foremost significant NALUs. Meantime, 2 and 44 belong to the secondary significant NALUs. And, 3 and 4 belong to the least significant NALUs. In Sect. 3, for the convenience of mapping different partitions into different bit positions of symbols in the constellation map, we need to reorder the bit stream. As shown by "The rearranged 264 Bit-stream" in Fig. 2, NALUs are reordered in turn of descending importance to form Segment A (SA), Segment B (SB) and Segment C (SC).

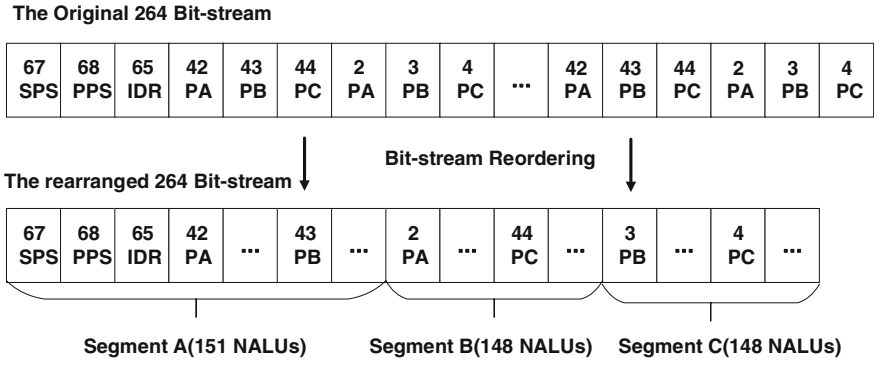

Fig. 2 NALU reordering of H.264 bit-stream

3 UEP Scheme Implementation and Proposed ULP Scheme

3.1 The UEP Implementation Based on Bit Stream Reordering

After the video sequence is encoded into a bit stream with H.264/AVC encoding, the wireless transmitter modulates this bit sequence into symbols for transmitting across the wireless channel. When the receiver tries to detect the received symbols, sometimes errors occur. As a result, when wrong symbols are mapped back into a bit sequence, bit errors might occur. An UEP structure [5] is proposed that different bit positions of a transmitted symbol have different bit error rates. This phenomenon could be explained through an example based on Quadrature Amplitude Modulation (e.g. 16QAM and 64QAM).

When an erroneous symbol is received by the receiver, it would be easier to be decoded to a symbol closer to the correct symbol. For example, in Fig. 3, we adopt the gray code in 16QAM constellation mapping as an example, which maps bit sequence to symbols in a way that increases the error resilience of certain bits. We can calculate the BER of different bits in a symbol to define the most significant bit (MSB) and the least significant bit (LSB).

For example, when an error occurs in any symbol within the shaded region in Fig. 3, there will be no errors in the first and the third bit of a symbol, while the BER of the second and the fourth bits of a symbol are 1/2 or 1/3 respectively. For the remaining symbols, the error probability of the four bit is 1/3 or 1/4. In this way, we can separately calculate the BER of each bit in a symbol.

In Table 1, the bit error rates of 4 different bit positions in a 16QAM symbol are listed. We can conclude that the first and the third bites of a symbol are MSBs, the rest ones are LSBs.

Same as 16QAM with gray code, we can calculate the error probabilities of six bits in the constellation map of 64QAM with gray code, as shown in Table 2. We

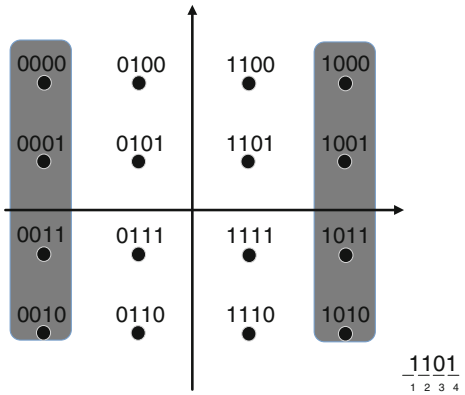

Fig. 3 The constellation map for 16-QAM with *gray code*

Table 1 Ber of different bit positions in a 16qam symbol

Bit position	MSB		LSB	
	1	3	2	4
16QAM	7/48		17/48	

Table 2 Ber of different bit positions in a 64qam symbol

Bit position	MSB		MID		LSB	
	1	4	2	5	3	**6**
16QAM	13/192		26/192		57/192	

can also summarize that the first bit and the fourth bit are MSBs, the second bit and fifth bits are middle bits, while the third and the sixth bits are LSBs.

After NALU reordering of H.264 bit stream in Part B of Sect. 2, the reordered H.264 bit stream is {SA, SB and SC}, as shown in Fig. 2.

In our UEP scheme, MSBs will carry SA, middle bits carry SB, whereas LSBs carry data of least significance, i.e. SC. In this way, the UEP scheme could be implemented without consuming additional network resources, unlike most of existing UEP schemes.

3.2 The ULP Scheme Based on Packet Discarding

In some extent, minor errors could be corrected with above UEP scheme. But when it comes to long error bursts, most of error correction schemes may fail. Additionally, some limitations still exist, e.g. only a limited number of errors allowed in current UEP scheme. Conclusions could be drawn from Part C of Sect. 4 that the maximum approximate BER the video transmission could bear is $2.2*10^{-5}$, which means that only one bit is permitted to be in error for every 45000 bits. When the channel condition is so poor that the BER is higher than $2.2*10^{-5}$, the UEP scheme implemented in Sect. 3 is not enough for error correction.

In this case, the erroneous transport data units at the receiver must be discarded, or retransmission will be requested. In fact, not all packets of transmitted data are of the same importance. Especially, as NALUs are the basic unit of H.264 bit stream, dropping some unimportant NALUs won't degrade the recovered video quality. For this reason, unequal loss protection (ULP) is proposed in this paper to decrease the cost of bandwidth resources without arousing obvious video quality degradation. More details will be provided in Part D of Sect. 4.

4 Simulations

In this section, the unequal BER of different bits in the constellation symbols and the error resilience of H.264/AVC bit stream are validated with simulations in part A and B. And then, part C and D give the experimental results of the UEP and the ULP scheme in terms of PSNR of video transmission performance.

4.1 The BER of Different Bit Positions in a 16/64QAM Symbol

First of all, we need to verify that the UEP constellation mapping in Sect. 3 can reduce the BER of the MSB by increasing the BER of LSB indeed. In this experiment, we assume that a bit sequence is divided into three sub-sequences, i.e. A, B and C. Here, sequence A is of the most importance, B is of the medium, and C is the least. Each sub-sequence is composed of 5000 bits.

Assume that 16QAM is adopted here. We map the 15000 bits onto the constellation diagram sequentially in the EEP (equal error protection) scheme. While in the UEP scheme, we place sub-sequence A and half of sub-sequence B sequence onto MSBs, and the rest are on LSBs. After the bit sequence is recovered by the receiver, the BERs of A and B are calculated separately.

When the bit sequence is modulated with 64QAM, we put sub-sequence A onto the positions of MSBs, B onto the positions of medium bits, and C onto LSBs. Then the BERs of sub-sequence A, B and C are calculated respectively. For simplicity, only the results of 64QAM are displayed in Fig. 3.

We can conclude from Fig. 4 that with the EEP scheme, sub-sequence A, B and C have almost the same BERs; while with the UEP scheme, the BER of A decreases, that of C increases, and that of B remains unchanged essentially. In addition, the BER decrease of sub-sequence A corresponds to the BER increase of sub-sequence C, which indicates that the UEP scheme does provide differential protection for different bit positions of transmitted symbols. In part C of this section, a new UEP implementation will be given based on this feature and H.264 bit stream reordering.

4.2 The PSNR of H.264 Video with Different Error Rates in SA, SB and SC

In order to validate whether the bit stream encoded with H.264/AVC is able to tolerate errors, different number of error bits are added. And then the PSNRs of recovered videos are calculated. 64QAM is used in this part.

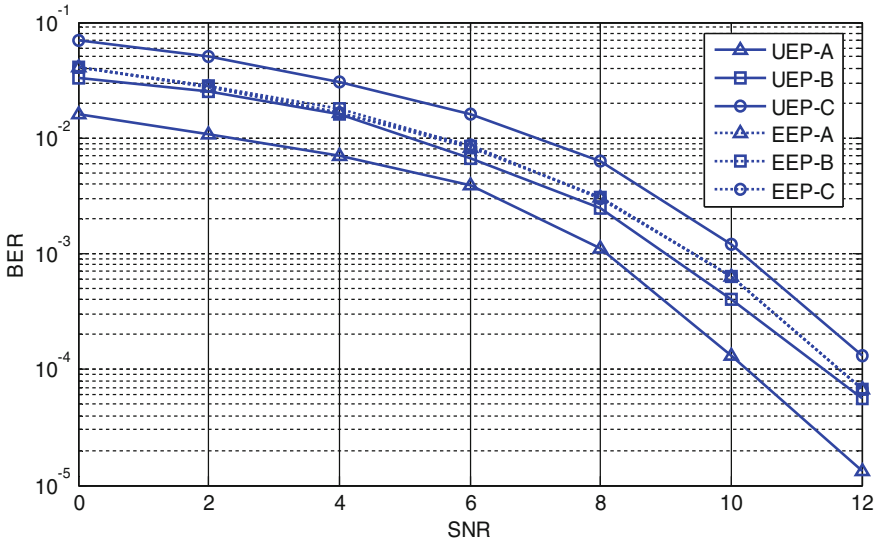

Fig. 4 BER comparisons of 64QAM with the UEP and the EEP scheme

To verify the different error resilience extents of SA, SB and SC of H.264 bit stream, we add error bits randomly into SA, SB and SC of the reordered H.264 bit stream, as illustrated in part B of Sect. 2. Then, the erroneous H.264 bit stream is decoded into YUV file and the average PSNRs of the YUV file are calculated.

In our experiments, we adopt two YUV files. One is 'soccer_176*144_15_qcif.yuv' ('soccer' for short hereinafter) with 149 frames, which features rapid movement. The resolution is 176*144, and the frame rate of is 15. Another YUV file is 'suzie_176*144_15.yuv' ('suzie' for short hereinafter) with 149 frames. Opposite to 'soccer', it has slow moving frames, and the other parameters are the same as 'soccer'.

According to our extensive experiments we find that if the PSNR of the decoded YUV file is higher than 30 dB, the clarity and the fluency of the video is satisfactory enough to watch. On the basis of this finding, the simulation results in Fig. 5 reveal that when the source file is 'soccer', the maximum BER that SA could tolerate is $1.2*10^{-6}$. The maximum BER for SB is $4.5*10^{-6}$, and that of SC is $1.7*10^{-5}$. As for 'suzie', the frames change less dramatic compared to 'soccer'. The conclusions could be drawn from Fig. 5 that the BER tolerance of SA is $1.2*10^{-5}$, that of SB is $2.18*10^{-5}$, and that of SC is $4.5*10^{-5}$.

Obviously, 'suzie' could tolerant more errors than 'soccer'. The reason is that the frames of 'suzie' change more slowly, thus the effect of error estimation and error concealment is much better.

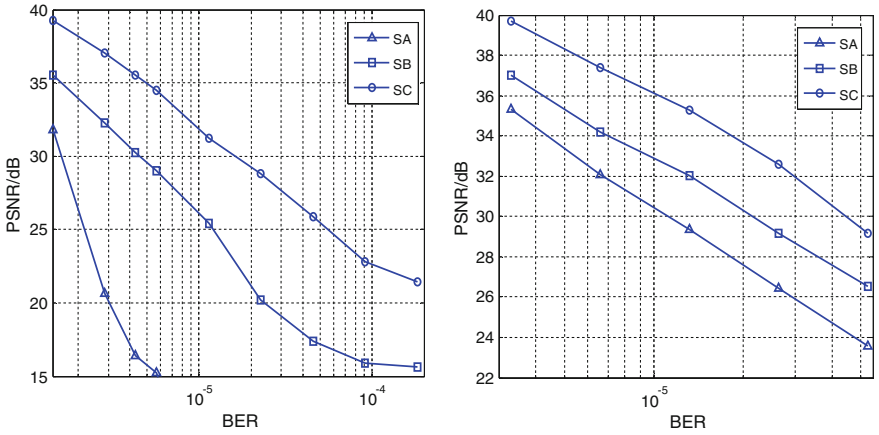

Fig. 5 PSNR of H.264 videos (e.g. 'soccer' and 'suzie') with different error rates of SA, SB and SC

4.3 The PSNR of the UEP Scheme with H.264 Bit Stream Reordering

We have verified that proper constellation mapping could reduce the BER of data with higher priorities by sacrificing the BER of lower priorities data in part A of Sect. 4. What's more, we have learned from part B of Sect. 4 that once data partitioning is implemented in H.264/AVC, SA containing the foremost significance has the weakest error resilience, SB has better error resilience than SA, and SC has the best error resilience. As a result, in the following simulations, the two properties verified in part A and B of this section are employed to provide differential protection to SA, SB and SC.

First of all, 'soccer' is encoded into a H.264 bit stream with the bit rate of 156kbps, and then the reordered bit stream is mapped to the 64QAM symbols on the gray constellation diagram. When 64QAM symbols are transmitted through AWGN channel, different channel conditions may result in different bit error rates. At the receiver, the reordered bit stream is recovered at the receiver to the original order of NALUs. And after decoding, the PSNR of the reconstructed video is computed.

As for the EEP scheme, there are neither NALU reordering at the transmitter nor NALU de-reordering at the receiver. The simulation results in Fig. 6 show that the UEP scheme with H.264 bit stream reordering (i.e. UEP in Fig. 6) has 5 dB improvement of PSNR in average compared with the EEP scheme. What's more, as the bit error rate increases, it provides smoother degradation of video performance, which indicates more graceful degradation of the received video quality than EEP.

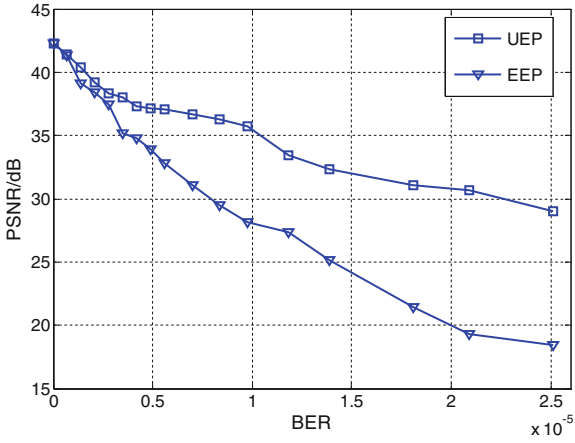

Fig. 6 The PSNR comparison of UEP and EEP schemes

Table 3 Segment statistics of 'Soccer' and 'Suzie'

	Soccer	Suzie
SA (%)	43.49	70.86
SB (%)	37.66	25.61
SC (%)	18.85	3.53
Aver. size of NALU (Byte)	980	144

4.4 The PSNR of Unequal Loss Protection (ULP) Scheme

In this part, some insignificant NALUs identified by the NAL header are dropped from some segments. And then the PSNR of the decoded YUV file is calculated to verify whether the ULP scheme could reduce the cost of bandwidth resources without arousing obvious video quality degradation.

After the analysis of the H.264 bit stream of 'soccer' and 'suzie', corresponding parameters could be calculated. Firstly, the statistics of SA, SB and SC of 'soccer' and 'suzie' are shown in Table 3. The reason why the ratio of SA of 'suzie' is much higher than that of 'soccer' is that the content of frames changes more slowly, which results in a small amount of inter-frame information. Secondly, the NALU size of SA varies more dramatically than that of SB or SC, whose NALU size is quite small. In addition, the average NALU size of 'suzie' is much smaller than that of 'soccer', which is due to the better error resilience and error concealment of 'suzie'.

In our simulations, for 'soccer', all NALUs of SC are dropped, i.e. almost 20 % of the whole bit stream data, or equally 1/3 of all NALUs are discarded. As for 'suzie', if all SC is dropped, only 5 % of the whole bit stream is discarded. In order to discard 20 % of all bit data, the relatively unimportant half NALUs of SB are also dropped. The PSNR of the decoded YUV file is shown in Fig. 7 with the variation of NALU loss rate. It's worth noting that for fast-moving YUV like 'soccer', when 1/3 of all the NALUs are discarded, it won't degrade the video quality obviously; but when the drop rate becomes even higher, the video quality will deteriorate

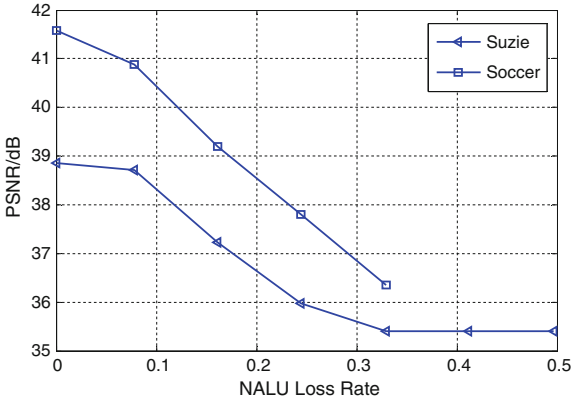

Fig. 7 PSNR versus NALU loss rate for 'soccer' and 'suzie'

quickly. While for slow-moving YUV, even half of NALUs are dropped, it doesn't lead to significant quality degradation. We can conclude that the bandwidth could be saved by approximately 20 % with our proposed ULP scheme.

5 Conclusions

The UEP constellation mapping can provide differential protection for different bit positions of transmitted symbols. And different segments of H.264 bit stream can tolerate different numbers of error bits for successful video reconstruction. Based on this error resilience feature of wireless video application and the UEP systematic structure provided by the constellation mapping at physical layer, we implement an UEP scheme with H.264 bit stream reordering, and propose an ULP packet discarding mechanism in this paper. Extensive experiments show that the UEP scheme gains 5 dB of PSNR improvement in average than the EEP scheme. When the unimportant network abstraction layer units (NALU) of H.264 bit stream are discarded, approximately 20 % of bandwidth resource is saved.

Acknowledgment We'd like to express my gratitude to Dr. Chunchang Tian in Huawei Technologies Co. LTD, Beijing, for his constructive suggestions and joint work during our research on wireless video transmission optimization.

References

1. ITU-T Rec.H.264/ISO/IEC 14496-10:2005, H.264 Advanced video coding for generic audiovisual services[S] (2005)
2. Wang Y, Zhu Q-F (1998) Error control and concealment for video communication: a review. Proc IEEE 86(5):974–997

3. Nguyen T, Zakhor A (2002) Distributed video streaming with forward error correction. In: Proceedings of the packet video workshop
4. Horn U, Stuhmuller K, Link M, Girod B (1999) Robust internet video transmission based on scalable coding and unequal error protection. In: Signal processing: image communication
5. Sen S, Gilani S, Srinath S, Schmitt S, Banerjee S (2010) Design and implementation of an "Approximate" communication system for wireless media applications. In: SIGCOMM
6. Jamieson K, Balakrishnan H (2007) PPR: partial packet recovery for wireless networks. In: SIGCOMM
7. Woo GR, Kheradpour P, Shen D, Katabi D (2007) Beyond the bits: cooperative packet recovery using physical layer information. In: MOBICOM
8. Lin KC-J, Kushman N, Katabi D (2008) ZipTx: exploiting the gap between bit errors and packet loss. In: ACM Mobicom. ACM, New York, pp 351–362
9. Han B, Schulman A, Gringoli F, Spring N, Bhattacharjee B, Nava L, Ji L, Lee S, Miller R (2010) Maranello: practical partial packet recovery for 802.11. In: NSDI
10. Jumisko-Pyykkö S, Vinod Kumar MV (2006) Unacceptability of instantaneous errors in mobile television: from annoying audio to video. In: MobileHCI'06, Sept 12–15
11. Zhang X, Peng X (2010) Robust H.264/AVC video transmission using data partitioning and unequal loss protection. CIT

A Scheme Against Spectrum Sensing Data Falsification Attacks Based on Improved Energy Detection Algorithm

Kaixuan Du, Xiaodi Han and Lexin Yu

Abstract An advanced scheme against the Spectrum Sensing Data Falsification (SSDF) is proposed in this paper. An improved energy detector in the cognitive radio network is achieved by replacing the squaring operation of the signal amplitude in the conventional energy detector with an arbitrary positive power. In addition, the sensing threshold, decision threshold and arbitrary positive power can be found accurately to ensure that the probability of SSDF detected by users is large enough and the honest user is not recognized as an attacker. The simulation results show that the proposed scheme can detect the SSDF attack efficiently.

Keywords Cognitive radio · Improved energy detection · Spectrum sensing data falsification attack

1 Introduction

In the past decade, Cognitive Radio (CR) technology has been used to improve spectrum utilization which allows unlicensed users to access the licensed frequency bands without interfering the licensed users [1]. Most research institutes have paid a great amount of attention to develop a safe, efficient, and reliable spectrum sensing system. Primary Users (PU) and Secondary Users (SU) are the foremost two candidates for the CR network. Generally, energy detector is applied to discriminate the difference between the energy of signals and the sensing threshold so as to confirm the existence of the primary user (PU) [2]. Meanwhile, secondary users (SU) send the local sense results to the system fusion center independently in the centralized cooperative sensing process. However, fusion center cannot judge the accuracy of the sense information reported by secondary users due to the intangible state of the licensed frequency band. In addition, the selfish node and a part of the

K. Du (✉) · X. Han · L. Yu
School of Electronics and Information Engineering,
Tianjin Polytechnic University, Tianjin, China
e-mail: 1310940202@stu.tjpu.edu.cn

Q. Liang et al. (eds.), *Proceedings of the 2015 International Conference on Communications, Signal Processing, and Systems*, Lecture Notes in Electrical Engineering 386, DOI 10.1007/978-3-662-49831-6_42

SU nodes who have lost the ability to sense the spectrum will transmit the false information to the fusion center, which makes the data fusion center produce a wrong decision in reducing the utilization of the secondary users to the idle spectrum.

The two above phenomenon are regarded as Spectrum Sensing Data Falsification (SSDF), which may trigger wrong decision of the fusion center and leads a reduction in the utilization of frequency spectrum for the SU. At present, the research on SSDF attack are almost about how to find out the SSDF attacker [3–5], but how to find out the SSDF attacker quickly is an open topic.

The rest of paper is organized as follows: Sect. 2 discusses the improved energy detector model in literature [6, 7] and analyzes the various SSDF attack modes. In Sect. 3, the proposed scheme is analyzed in detail. In this scheme, the sensing threshold, decision threshold and P are found to ensure that the probability of SSDF detected by the users is large enough and the honest user is not recognized as an attacker. In Sect. 4, we show the results of simulation. Finally, our work is concluded in Sect. 5.

2 System Model

In the cooperative spectrum sensing, we assume there are N secondary users and one Primary User (PU). System model was shown in Fig. 1. The two hypothesis H_0 and H_1 can be written as

$$H_0: Y_i(n) = v_i(n), \text{if PU is absent} \tag{1}$$

$$H_1: Y_i(n) = s(t) + v_i(n), \text{if PU is present} \tag{2}$$

where $i = 1, 2, \ldots, N$, $s(n) \sim N\left(0, \sigma_s^2\right)$ denotes the signal of the PU, $v_i(n) \sim N\left(0, \sigma_n^2\right)$ means additive white Gaussian noise. It is assumed that each secondary user contains an improved energy detector. The fusion center makes decisions based on the information from each SU and the fusion criterion. The ith SU utilizes the following statistic to decide of the presence of the PU

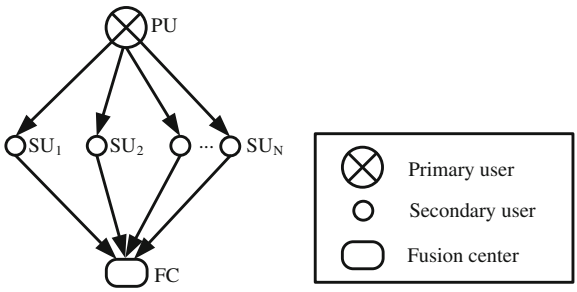

Fig. 1 System model

$$Y = |Y_i|^P, P > 0 \tag{3}$$

In this paper, we use hard fusion expressed in *K out of N* as the fusion methods, where K stands for the threshold of fusion criterion. Each secondary user sends the binary decision (0 or 1) to the fusion center using an improved energy detector depicted as follows

$$X = \sum_{i=1}^{N} x_i \tag{4}$$

where X is the sum of the all 1-bit decisions from the secondary users.

Since the fusion center could makes a decision according to the following hypothesis,

$$H_0: X < K \text{ if PU is absent} \tag{5}$$

$$H_1: X \geq K, \text{if PU is present} \tag{6}$$

the false alarm probability and detection probability of the local decision can be achieved by

$$P_{fi} = \int_{\lambda}^{+\infty} f_{Y|H_0}(y)dy = \Gamma\left(0.5, 0.5\lambda^{2/P}/\sigma_n^2\right)/\Gamma(0.5) \tag{7}$$

$$P_{fi} = \int_{\lambda}^{+\infty} f_{Y|H_0}(y)dy = \Gamma\left(0.5, 0.5\lambda^{2/P}/\left(\sigma_n^2 + \sigma_s^2\right)\right)/\Gamma(0.5) \tag{8}$$

where λ is the decision threshold. $\Gamma(a)$ is the gamma function, and $\Gamma(a, x)$ indicates the upper incomplete gamma function [8].

In the CR system, the anti attack not only increases the probability of false alarm system, but also reduces the probability of detection system [4]. The larger the error probability of the system became, the worse the system performs. It has been proved that destructive of the of anti attack is larger than the others. Our work concentrates on the impact of anti attack and the specific solutions.

Assume that the parameters P and the threshold are same in the local detector, P_{db} and P_{fb} are defined as the local detection probability and the false alarm probability respectively. Considering the detection probability P_{db} and false alarm probability P_{fb} not correct due to the SSDF attack, the real detection probability and false alarm probability can be deducted as

$$P_{dr} = P_r \cdot P_{db} + P_w \cdot (1 - P_{db}) = P_w + (P_r - P_w) \cdot P_{db} \tag{9}$$

$$P_{fr} = P_r \cdot P_{fb} + P_w \cdot \left(1 - P_{fb}\right) = P_w + (P_r - P_w) \cdot P_{fb} \tag{10}$$

where P_w is the attack probability of a SSDF attacker, P_r is the probability without attack.

When an intelligent counter attacker exists in the system, the detection probability and false alarm probability can be obtained with the help of K out of N criterion

$$P_f = P_{fr} \sum_{i=k-1}^{N-1} C_{N-1}^{i} P_{fb}^{i} \left(1 - P_{fb}\right)^{N-i-1} + \left(1 - P_{fr}\right) \sum_{i=k}^{N-1} C_{N-1}^{i} P_{fb}^{i} \left(1 - P_{fb}\right)^{N-i-1} \tag{11}$$

$$P_d = P_{dr} \sum_{i=k-1}^{N-1} C_{N-1}^{i} P_{db}^{i} \left(1 - P_{db}\right)^{N-i-1} + \left(1 - P_{dr}\right) \sum_{i=k}^{N-1} C_{N-1}^{i} P_{db}^{i} \left(1 - P_{db}\right)^{N-i-1} \tag{12}$$

Obviously, the detection probability will decline as the probability of false alarm system rises. Thus, the system performance would be deteriorated greatly when the total error probability increases.

3 Scheme of SSDF Attack Detection Based on Trust Mechanism

The main idea of the proposed scheme is based on the trust mechanism described above. Let the fusion center ensures that the probability of SSDF detected by users is large enough and the honest user is not recognized as an attacker. In this section, we first analyze the probability under different state of PU, and then propose the scheme against SSDF attacks.

3.1 Probability Analysis

In case H_0, the fusion center judges that the wrong probability of the information sent by the attacker is P_{wf}, and the correct probability is P_{rf}.

The SSDF attacker's sensing information is judged mistakenly in two cases. First case: The final decision of the fusion center is 0, while local sensing result sent by the SSDF attacker is 1, that is the SSDF attacker makes false alarm when the fusion center makes the correct judgment. In this case, the fusion center judges that the wrong probability of the information sent by the attacker is $P_{wf1} = P_{fr}\left(1 - P_f\right)$. Second case: The final result of judgment by the fusion center is 1, while local sensing result sent by the SSDF attacker is 0, that is the SSDF attacker makes wrong decision when the fusion center make the correct judgment. In this case, the fusion center judges that the wrong probability of the information sent by the attacker is $P_{wf2} = P_f\left(1 - P_{fr}\right)$. In summary, the fusion center judges that the wrong

probability of the information sent by the attacker is $P_{wf} = P_{wf1} + P_{wf2} = P_{fr}(1 - P_f) + P_f(1 - P_{fr})$.

The SSDF attacker's sensing information is judged correctly in two cases. First case: The final decision of the fusion center is 0, while local sensing result sent by the SSDF attacker is 0. In this case, the fusion center judges that the right probability of the information sent by the attacker is $P_{rf1} = (1 - P_f)(1 - P_{fb})$. Second case: The final decision of the fusion center is 1, while local sensing result sent by the SSDF attacker is 1. In this case, the fusion center judges that the right probability of the information sent by the attacker is $P_{rf1} = P_f P_{fb}$. In summary, the fusion center judges that the right probability of the information sent by the attacker is $P_{rf} = P_{rf1} + P_{rf2} = (1 - P_f)(1 - P_{fb}) + P_f P_{fb}$.

In case H_1, the fusion center judges that the wrong probability of the information sent by the attacker is $P_{wd} = P_{wd1} + P_{wd2} = P_{dr}(1 - P_d) + P_d(1 - P_{dr})$, and the right probability of the information sent by the attacker is $P_{rd} = P_{rd1} + P_{rd2} = (1 - P_d)(1 - P_{db}) + P_d P_{db}$.

Assuming that the occurrence probability of the primary user within a detection period is 0.5, the fusion center judges that the wrong probability of the information sent by the attacker is $P_{zg} = P_{wf}/2 + P_{wd}/2$, and the right probability of the information sent by the attacker is $P_{zc} = P_{rf}/2 + P_{rd}/2$. In order to detect SSDF attacker as soon as possible, the fusion center should ensure that the probability of SSDF detected by the users is large enough and the honest user is not recognized as an attacker. Once an honest SU is judged as a SSDF attack and kicked out of the cognitive system which makes the number of cooperative users less, the performance of the system is decreased.

3.2 Proposed Scheme

According to the analysis illuminated above, an optimization scheme for the SSDF attacker detection is proposed as follows:

Step1: Select appropriate system parameters (the local detector parameters P, the local detection threshold λ, and the fusion center decision threshold K). Assume that the number of nodes involved in the detection is N. Initialize the trust value r_i of each SU. Set the upper trust value $r_{\max}$, the lower trust value $r_{\min}$, reward factor k_1, and penalty factor $k_2 (k_1 < k_2)$. Set the symbolic parameter n_i(the times that the SU sent the wrong sensing information continuously) and the decision threshold r_P and M.

Step2: The fusion center renew r_i according to the final decision result (0 or 1). When the sensing information judged by the fusion center is correct, let $r_i = r_i + k_1$. When the sensing information judged by the fusion center is wrong, let $r_i = r_i - k_2$ and renew n_i.

Step3: Compare r_i and n_i with r_P and M respectively, and judge whether the user is a SSDF attacker or not. When $r_i \le r_p$ or $n_i \ge M$, SU is identified as SSDF attacker. When $r_i > r_p$ or $n_i < M$, return to the previous step.

The condition of selecting system parameters: when $P_{zc} \ge \varepsilon$ (determine the value of the ε according to the parameters of the trust mechanism), find the K, P, λ according to the condition, and the value of $K^{'}, P^{'}, \lambda^{'}$ when P_{zg} is maximum. Let the fusion center ensure that the probability of SSDF detected by the users is large enough and the honest user is not recognized as an attacker.

4 Simulations

Simulation parameters are set as follows: $s_i(t)$ obeys a Gaussian distribution with mean 0 and variance 1. The SNR from PU to SU are same. λ is the SU local decision threshold. K is the threshold of the fusion center. The correctness of the detection probability and false alarm probability of the intelligent SSDF attacker should be verified first. The probability of SSDF attack launched by the attacker in each detection cycle is $P_w = 0.75$ and the appearance probability of user is $P(H_1) = 0.5$.

Figures 2 and 3 show that the error between the theoretical value and the simulation value is very small. It is proved that the SSDF false alarm probability and the detection probability are correct. The fast detection method of SSDF based on trust mechanism and improved energy detection algorithm were analyzed. Decision threshold in setting scheme $r_p = \sum_{i=1}^{N} (r_i - \Delta)/N$, $\Delta = 100$ indicates the offset of the mean. Let $M = 20$. The maximum value of the trust value is $r_{\max} = 100$, the minimum value of the trust value is $r_{\min} = -1000$. The reward factor is $k_1 = 1$, and the penalty factors are $k_2 = 2$, $r_i = 0, n_i = 0$, $\varepsilon = 0.95$. Assume that the cycle of each detection is $T_s = 0.1$ μs, the probability of SSDF attack launched by the intelligent

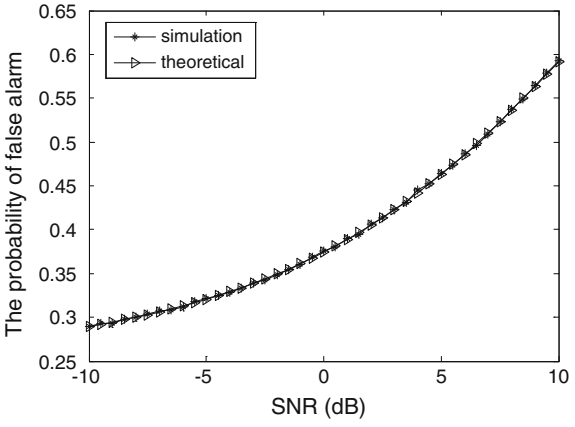

Fig. 2 Comparison between theoretical value and the probability of detection

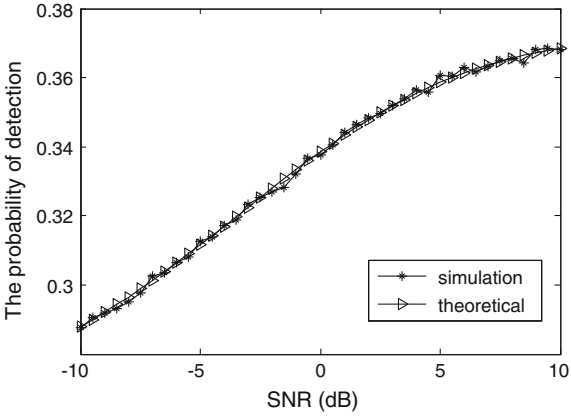

Fig. 3 Comparison between theoretical value and the probability of false alarm

SSDF attacker in each detection cycle is $P_w = 0.5$, and the probability of the main user is $P(H_1) = 0.5$. Find a set of system parameters according with the optimization scheme $K = 2, P = 0.1, \lambda = 0.1$, and then take the other system parameters $K = 2, P = 0.1, \lambda = 0.9$ which do not meet the optimization scheme. In order to compare the two cases which can identify the SSDF attacker more quickly with the same signal under the same conditions, the number of experiments is set 500.

Figure 4 is the required time which the SSDF attacker is detected under the system parameters 1 and the system parameters 2. Table 1 shows the test results of the time which the SSDF attacker is detected in the 10 set of the same test conditions. Tables 1 and 2 show that the detection time which the SSDF attacker is detected with the proposed scheme is littler in the same experimental conditions.

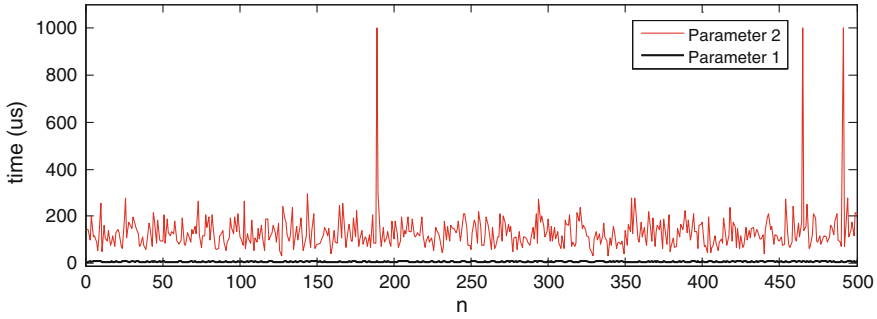

Fig. 4 Detection time of experimental results

Table 1 Experimental results were extracted (unit US)

Parameter 1	7.2	9.6	7	7	7.8	7.4	7	8.6	8.4	6.8
Parameter 2	99.8	131.2	72	116	99.4	38.4	90.6	83	174.2	168

Table 2 Experimental results were extracted (The attacker sort)

Parameter 1	10	10	10	10	10	10	10	10	10	10
Parameter 2	10	10	7	10	10	10	10	2	10	10

There is no miscarriage of justice with the proposed scheme, while there are two cases of false positives without using the proposed scheme. The simulation results demonstrate that the proposed scheme can detect the SSDF attacker more quickly and more accurately.

5 Conclusions

In this paper, a fast detection scheme for SSDF based on trust mechanism and improved energy detection algorithm is proposed. Three SSDF attacks and their effects on the system are analyzed. The proposed scheme using the improved energy detection algorithm and trust mechanism ensure that the probability of SSDF detected by users is large enough and the honest user is not recognized as an attacker. Good simulation results are obtained with the proposed scheme.

References

1. Mitola III J, Maguire Jr GQ Cognitive radio: making software radios more personal. Personal Commun 6(4):13–18. doi:10.1109/98.788210
2. Urkowitz H Energy detection of unknown deterministic signals. Proc IEEE 55(4):523–531. doi:10.1109/PROC.1967.5573
3. Pang DM, Hu G, Xu M (2011) Trust model-based secure sensing techniques for cognitive radio networks. In: The tenth international conference on networks. pp 1–6
4. Vu-Van H, Koo I Cooperative spectrum sensing with collaborative users using individual sensing credibility for cognitive radio network. Consum Electron 57(2):320–326. doi:10.1109/TCE.2011.5955162
5. Zeng K, Paweczak P, Cabric D Reputation-based 'Reputation-based cooperative spectrum sensing with trusted nodes assistance. Commun Lett 14(3):226–228. doi:10.1109/LCOMM.2010.03.092240
6. Chen Y Improved energy detector for random signals in Gaussian noise. Wireless Commun 9(2):558–563. doi:10.1109/TWC.2010.5403535
7. Singh A, Bhatnagar MR, Mallik RK Cooperative spectrum sensing in multiple antenna based cognitive radio network using an improved energy detector. Commun Lett 16(1):64–67. doi:10.1109/LCOMM.2011.103111.111884
8. Luo L, Ghosh C, Roy S (2010) Joint optimization of spectrum sensing for cognitive radio networks. In: global telecommunications conference. Miami, pp 1–5. doi:10.1109/GLOCOM.2010.5683435

NOMA Based on User Grouping and Multiple Layer Modulation

Sicong Qu, Zhongwei Si, Zhiqiang He and Kai Niu

Abstract In Non-orthogonal multiple access (NOMA) system, different users utilize the same time and frequency resource to achieve a higher spectral efficiency. However, for conventional NOMA multiplexing in the power domain, the number of users carried in the system is very limited due to the requirement of perfect interference cancelation in the successive decoding. In this paper, we propose a novel NOMA scheme based on user grouping and multiple layer modulation with constellation scaling and rotation. Users are first grouped according to their channel conditions, and transmit power is allocated among the groups. Then multiple layer modulation is employed within each group where each user is identified by a unique rotation parameter. Simulation results in terms of bit error rate (BER) are provided. Compared to the conventional NOMA scheme, the proposed scheme can afford a larger number of users under the same power constraints, and it has clear advantages in both system throughput and BER performance.

This work was supported in part by the National Natural Science Foundation of China (No. 61401037), the 863 project (No. SS2015AA011303), and the Fundamental Research Funds for the Central Universities (No. BUPT2015AA01A709).

S. Qu (✉) · Z. Si · Z. He · K. Niu
Beijing University of Posts and Telecommunications, Beijing, China
e-mail: qscbupt@163.com

Z. Si
e-mail: sizhongwei@bupt.edu.cn

Z. He
e-mail: hezq@bupt.edu.cn

K. Niu
e-mail: niukai@bupt.edu.cn

Q. Liang et al. (eds.), *Proceedings of the 2015 International Conference on Communications, Signal Processing, and Systems*, Lecture Notes in Electrical Engineering 386, DOI 10.1007/978-3-662-49831-6_43

1 Introduction

Nowadays, the explosive traffic growth in mobile communications has motivated research activities on the next generation (5G) of wireless networks that can offer significant improvements in coverage and user experience [1]. With the demand of highly spectral-efficient multiple access techniques, non-orthogonal multiple access (NOMA) has been considered as a promising candidate for future radio access. Since NOMA does not require orthogonal division of time or frequency, it has higher spectrum efficiency and system throughput than orthogonal multiple access (OMA) techniques.

Various NOMA schemes have been proposed in the literature. One of the NOMA schemes has been proposed in [2] where users are multiplexed in the power domain. On the transmitter side, users are allocated with different transmit power. On the receiver side, multiuser detection is conducted based on successive interference cancelation (SIC). From an information-theoretic perspective, the combination of superposition coding at the transmitter and SIC decoding at the receiver not only outperforms orthogonal multiplexing, but also is optimal in the sense of achieving the capacity region of the channel [3].

In this paper, we propose a novel method which can support a larger number of users for the uplink non-orthogonal transmission compared to the conventional NOMA. At the transmitter, instead of multiplexing in the power domain directly, users are first grouped by their channel magnitudes. Then multiple layer modulation (MLM) is used to multiplex all the signals within the same group. At the receiver, different groups' MLM symbols are detected by an SIC–MMSE decoder, and users' messages in the same group can be recovered according to the detected MLM symbols. Power allocation is employed to maximize the throughput or to guarantee the fairness of all groups. The tradeoff between spectrum efficiency and fairness among users is also considered. Simulation results show that the proposed scheme clearly outperforms the conventional NOMA scheme in terms of the number of users and bit error rate.

The remainder of the paper is organized as follows. In Sect. 2, we briefly review the concept of NOMA. Section 3 introduces the proposed uplink NOMA scheme based on user grouping and multiple layer modulation. Section 4 illustrates the numerical results. Finally, Sect. 5 concludes the paper.

2 NOMA in the Power Domain

The advantages of NOMA is discussed in the following from an information-theoretic perspective. We suppose User-1 and User-2 can reliably communicate at rate R_1 and R_2 respectively. The set of rates (R_1, R_2) satisfies the following three constraints:

$$R_1 \leq \max I(X_1; Y|X_2), \tag{1}$$

$$R_2 \leq \max I(X_2; Y|X_1), \tag{2}$$

$$R_1 + R_2 \leq \max I(X_1X_2; Y). \tag{3}$$

The sum-rate (3) can be rewritten by the chain rule of mutual information as follows:

$$R_1 + R_2 \leq \max\{I(X_1; Y) + I(X_2; Y|X_1)\} \tag{4}$$

or:

$$R_1 + R_2 \leq \max\{I(X_2; Y) + I(X_1; Y|X_2)\}. \tag{5}$$

This indicates that the capacity region can be achieved by utilizing the successive decoding provided perfect interference cancelation.

However, in order to ensure the correctness of the interference cancelation, the received power of each user is supposed to decrease exponentially. Thus, pure power domain multiplexing access cannot afford many users within the same time and frequency resource block. In the following we propose to increase the number of users by considering user grouping and utilizing multiple layer modulation.

3 NOMA Based on User Grouping and Multiple Layer Modulation

3.1 Multiple Layer Modulation

In orthogonal multiple access schemes, all users employ the same modulation constellation since they can be distinguished by the index of the time/frequency resource blocks. In NOMA schemes, all the users' modulated symbols are added together both in time domain and in frequency domain. Therefore, if the same constellation is applied by all the users, we obtain the superimposed symbol as follows [4],

$$x = \sum_{l=1}^{L} x_l, \tag{6}$$

where L is the number of the users (layers), and $x_l \in \mathscr{A}$ is the modulated symbol at layer l. Without the loss of generality, we assume that $\mathscr{A} = \{-1, +1\}$. Then the set of the superimposed symbols obeys $|\mathscr{A}| \leq 2^L$. The reduced cardinality makes the mapping from the user symbols to the superimposed symbol ambiguous, i.e., several combinations of x_l result in the same constellation x. When $|\mathscr{A}| \neq 2^L$, the resultant sum-rate will be strictly lower than the sum of the individual layers' rates.

In the multiple layer modulation, each user is allocated with a user-specific modulation featured by an amplitude scaling factor ρ_l and/or a phase rotation parameter

θ_l. Then the superimposed symbol is written as

$$x = \sum_{l=1}^{L} \rho_l x_l e^{j\theta_l}. \tag{7}$$

By proper scaling and rotating, the superimposed symbol x has 2^L distinct constellation points, which allows the maximum sum-rate as L bits per superimposed symbol.

3.2 NOMA Based on User Grouping and Multiple Layer Modulation

The above multiple layer modulation can be used as a NOMA transmission scheme. Since each user is identified by two parameters—the scaling factor and the rotation factor, the entire system is complicated especially when the number of users is large. Therefore, in the following we combine the multiple layer modulation and the user grouping to realize the non-orthogonal multiple access. An uplink scenario is considered. There are in total N users in the system, and h_n ($n \in [1, N]$) is the channel coefficient of the n-th user. We write h_n as

$$h_n = \left|h_n\right| e^{j\beta_n}, \tag{8}$$

where $\left|h_n\right|$ is the magnitude and β_n is the phase. In our proposed scheme, users with the same channel magnitude form a group. Within a group, equal power is allocated for the users. We assume that the number of groups is K, and N users are distributed into K groups equally. Denote $x_{k,l}$ as the modulated symbol of l-th user in the k-th group, $l \in [1, L]$, $k \in [1, K]$ and $L = N/K$. The received signal at the base station can be represented as

$$y = \sum_{k=1}^{K} \sqrt{P_k}\left|h_k\right| \sum_{l=1}^{L} x_{k,l} e^{j(\alpha_{k,l}+\beta_{k,l})} + n, \tag{9}$$

where $\alpha_{k,l}$ and $\beta_{k,l}$ are the phase rotation parameter of the multiple layer modulation and the channel phase of the l-th user of the k-th group, respectively. The notation P_k is the transmit power of the k-th group and $|h_k|$ is the corresponding channel magnitude. The additive white Gaussian noise is denoted by n with the power spectral density N_0. The block diagram of the proposed NOMA scheme at the transmitter is depicted in Fig. 1.

To simplify (9), we define y_k as

$$y_k = \sum_{l=1}^{L} x_{k,l} e^{j(\alpha_{k,l}+\beta_{k,l})} = \sum_{l=1}^{L} x_{k,l} e^{j\theta_{k,l}}, \tag{10}$$

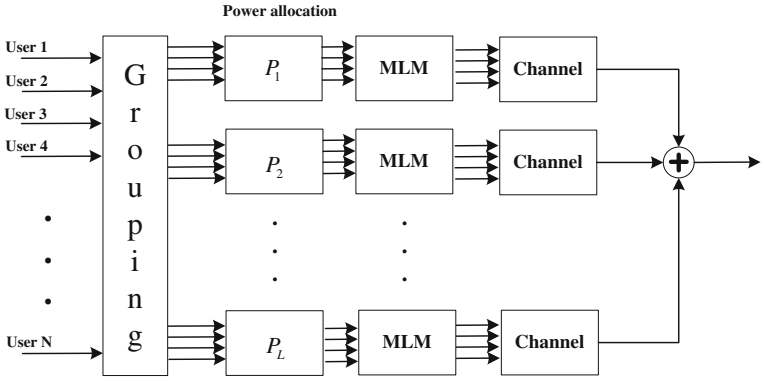

Fig. 1 User grouping and MLM at the transmitter

where $\theta_{k,l}$ is the sum of the MLM phase rotation $\alpha_{k,l}$ and the channel phase $\beta_{k,l}$. By substituting (10) into (9), we obtain

$$y = \sum_{k=1}^{K} \sqrt{P_k}|h_k|y_k + n. \tag{11}$$

3.3 SIC-MMSE Decoding

At the receiver, based on the user grouping and the power allocation at the transmitter, an SIC-MMSE decoder is utilized to decode $x_{k,l}$. The block diagram of the decoder at the receiver is depicted in Fig. 2. We assume that $\sqrt{P_k}|h_k|$ is decreasing as k grows. The steps for decoding are given as follows:

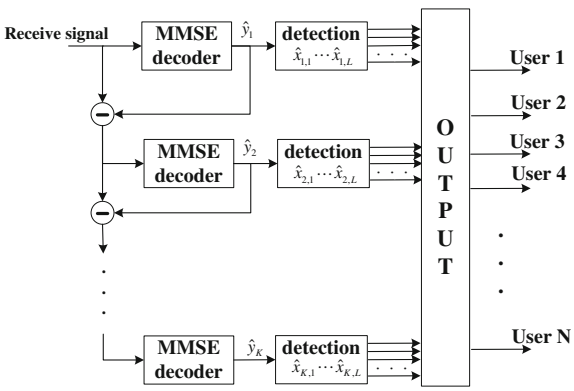

Fig. 2 The SIC-MMSE decoder at the receiver

- Initial setting
  - Define $k = 1$.
  - Remaining signal is initialized with the received signal.
- The SIC-MMSE decoder
  - Decode $\hat{y}_k$ from the remaining signal according to the MMSE criterion.
  - Recover the transmitted symbol of l-th user in the k-th group, $\hat{x}_{k,l}$, through $\hat{y}_k$.
  - Remove $\hat{y}_k$ from the remaining signal and update it.
- If $k \neq K$ repeat step (2), and $k = k + 1$.

3.4 Power Allocation and Selection of Rotation Parameter

In this section, we discuss the power allocation among the groups and the selection of the rotation parameters within the group. We assume that the base station has perfect channel state information of all the links. To maximize the throughput of the system, LP algorithm will be used. To avoid complicated optimization, a simple but suboptimal power allocation method is proposed. We assume that the K groups are sorted in the order of decreasing channel magnitude $|h_k|$. The transmit power of the i-th group, represented as P_i, can be calculated by satisfying

$$|h_{i+1}|^2 P_{i+1} = \lambda |h_i|^2 P_i, \quad \sum P_i = P. \tag{12}$$

The parameter λ ($\lambda > 0$) controls the system's throughput and the users' fairness. As λ increases, the system tends to allocate more power to the users experiencing poor channel conditions.

The selection of rotation parameter θ is independent of the power allocation. The selecting criterion of θ is to maximize the mutual information within each group. It has been proved in [5] that, in the high SNR region, the maximization of mutual information is equivalent to maximizing the minimum Euclidean distance among the constellation points. Once the optimal θ is obtained, the phase rotation $\alpha_{k,l}$ of the MLM can be determined according to $\theta_{k,l} = \alpha_{k,l} + \beta_{k,l}$.

4 Simulation Results and Discussions

In this section, we evaluate the performance of the proposed scheme through the numerical results. For all the simulations, the error-correcting code is the Turbo code of length 1024 and of rate 1/3.

In Fig. 3, we investigate a basic model to compare the proposed scheme with the conventional NOMA scheme in the power domain. The parameters for the simulations are listed in Table 1.

Figure 3 shows that, for the same number of users and under the same power constraint, the conventional NOMA cannot be recovered when users' number is increasing. The newly proposed scheme provides considerable gain compared to the conventional NOMA scheme. Similar conclusion can be drawn for both the BPSK modulation and the QPSK modulation. We also noticed that when the selection of θ in the BPSK modulation is changed from $(0, \pi/4)$ to the optimal $(0, \pi/2)$, a gain of 2 dB is obtained. In Fig. 4, we evaluate the number of users carried by the newly proposed scheme and the conventional NOMA scheme. For all the schemes, BPSK modulation is employed. The selection of θ is listed in Table 2. The red curve represents the average BER of 6 users for the conventional NOMA scheme without user grouping and multiple layer modulation. The blue curves represent the proposed schemes which have 2 users in each group, and have 2, 3, 4, 5 groups, respectively. The parameter

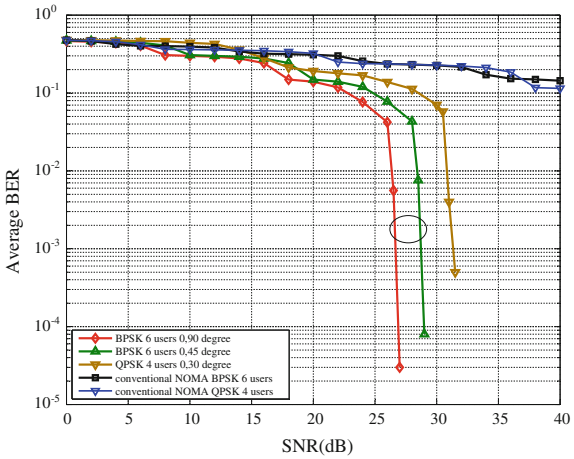

Fig. 3 Comparison between conventional NOMA and our proposed scheme under the same power constraint

Table 1 The parameters for the simulations

Scheme	Proposed Uplink NOMA			Conventional NOMA	
User number	6	6	4	6	4
Modulation	BPSK	BPSK	QPSK	BPSK	QPSK
Groups	3	3	2	–	–
User per group	2	2	2	–	–
selection of θ	$0, \pi/2$	$0, \pi/4$	$0, \pi/6$	–	–
λ	0.1	0.1	0.03	0.1	0.03

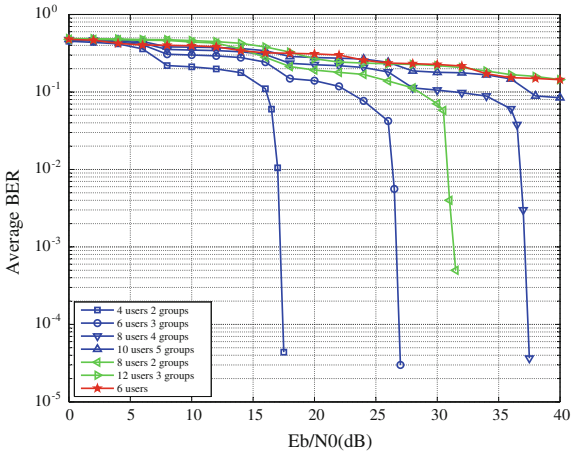

Fig. 4 Comparison between the conventional NOMA and our proposed scheme

Table 2 The selection of theta

Rotation	1st user	2nd user	3rd user	4th user
2 users	0	$\pi/3 - 2\pi/3$	–	–
4 users	0	$\pi/6$	$\pi/2$	$2\pi/3$

λ is set to be 0.1 for these cases. It can be seen that the proposed scheme clearly performs the conventional NOMA even when it carries a larger number of users. Similar simulations have been done for the cases that the number of users in each group is up to 4. For these cases, we set $\lambda = 0.01$. we can see that the performance has been further improved. The advantages of the proposed scheme is observed in terms of both the BER performance and the number of users.

5 Conclusions

In this paper, we have proposed a novel non-orthogonal multiple access scheme based on user grouping and multiple layer modulation. Users are first grouped according to their channel conditions, and then multiple layer modulation modified by constellation scaling and rotation is employed within each group. The users are multiplexed by the user-specific scaling factor and the rotation parameter. Simulation results show that the proposed scheme can afford a larger number of users compared with the conventional NOMA scheme under the same power constraints. A significant improvement in system throughput and BER performance is obtained by using the newly proposed scheme.

References

1. Thompson J, Ge X, Wu H-C, Irmer R, Jiang H, Fettweis G, Alamouti S (2014) 5G wireless communication systems: prospects and challenges [Guserst Editorial]. IEEE Commun Mag 52(2):62–64
2. Schaepperle J, Ruegg A (2009) Enhancement of throughput and fairness in 4G wireless access systems by non-orthogonal signaling. Bell Labs Tech J 13(4):59–77
3. Tse D, Viswanath, P (2005) Fundamentals of wireless communication. Cambridge University Press
4. Rong Z, Hanzo L (2011) A unified treatment of superposition coding aided communications: theory and practice. IEEE Commun Surv. tutorials 13(3):503–520
5. Wulich D, Dabora R, Tsouri GR (2009) On increasing spectral efficiency of frequserncy division multiple access using synchronized superposition-modulation. IEEE international conference on microwaves, communications, antennas and electronics systems, pp 1–4

Part VII
Millimeter Wave, UWB and Terahertz Technology

Performance Analysis and Comparison of CFAR Methods for FOD Detection in Airport Runway Environment

Zhongjin Zhang, Yuguo Wang, Qi Zhong, Huaqiong Li and Xuelian Yu

Abstract In recent years, airport runway FOD (Foreign Object Debris) detection system that usess millimeter-wave radar as the main means of detection becomes a hot research topic in the field of Civil Aviation. The radar clutter background that airport runway FODs situate is complex and relatively strong, therefore, need to use constant false alarm rate (CFAR) technology to obtain a satisfactory detection performance. Focus on this problem, application of FOD detection in airport runway environment is simulated by matlab. Simulation results show the detection performance of some CFAR methods, and provide theoretical basis for practical engineering application.

Keywords FOD detection · Adjacent unit CFAR technique · Clutter map CFAR technique · Millimeter-wave radar

1 Introduction

Airport runway FOD refers to the foreign objects in the airport runway that may damage track aircraft, such as metal parts, broken stones, constitute a major hidden danger to the safety of civil aviation aircraft taking off and landing [1, 2]. At present, the monitoring of FOD in domestic airport is relied on manual inspection. This backward method is poor reliability and low efficiency that take up valuable track time and the number of flights is forced to reduce. Consequently, some FOD detection systems have been developed and tested on airports recently, such as Tarsier, FODetect and, etc. [3, 4]. Most of them are based on millimeter-wave radar.

Z. Zhang (✉) · Y. Wang · Q. Zhong · H. Li
The Second Research Institute of CAAC, Chengdu, China
e-mail: jinsbm@163.com

X. Yu
University of Electronic Science and Technology of China, Chengdu, China
e-mail: iceyu@126.com

Q. Liang et al. (eds.), *Proceedings of the 2015 International Conference on Communications, Signal Processing, and Systems*, Lecture Notes in Electrical Engineering 386, DOI 10.1007/978-3-662-49831-6_44

The radar clutter background that airport runway FODs situate is complex and relatively strong, in order to obtain a predictable and stable detection performance, background clutter power level must be real-time estimated from radar echo data, and use constant false alarm rate (CFAR) processing to adjust the detection threshold. The main process of CFAR method is to estimate the clutter mean power, there are two categories of this method: One is the spatial CFAR, that uses the measured value from reference units which adjacent to detecting unit in space to estimate the clutter mean power, called adjacent unit CFAR technique [5]; another kind is the time-domain CFAR, which uses the measured value of detecting unit in past times scanned to estimate the clutter mean power, and mean power level is iteratively updated by new measurement, called clutter map CFAR technique [6].

However, the detection performance and applicability of CFAR methods is different. In this paper, adjacent unit CFAR technique and Clutter map CFAR technique are introduced and their simulations are given in Sects. 2 and 3. The simulation results are analyzed in Sect. 4. Finally, conclusions are drawn in Sect. 5.

2 Adjacent Unit CFAR Technique

2.1 *Principle of Adjacent Unit CFAR*

Figure 1 is the typical structure block diagram of adjacent unit CFAR detector. Among them, V(T) is measurement of radar echo signal, I(V) and Q(V) are in-phase and quadrature components of the echo signal that constitute detection statistics D(V) through square law detector. In the figure, D is detecting unit, the units before and after D called reference unit. CFAR detector sets the detection threshold through estimating the background clutter power of detecting unit by the total $2N$ reference units in front and back windows, and then gets CFAR decision of existence of target in detecting unit. The shadow marked units close to detecting unit on both sides are protection unit that prevent energy leakage into the reference unit, does not participate in the estimation of background clutter power.

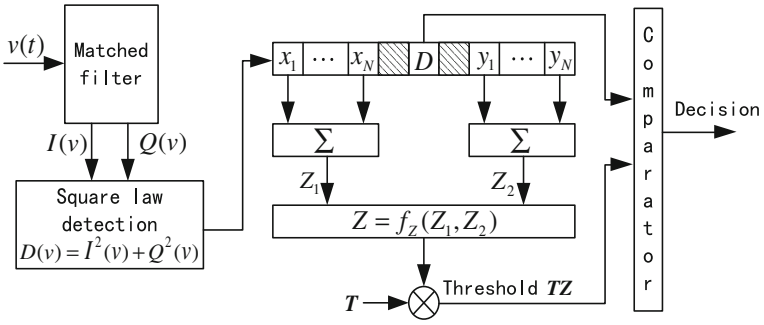

Fig. 1 Structure block diagram of adjacent unit CFAR detector

Let $Y = TZ$ be the detection threshold, the CFAR criterion can be expressed as:

$$D \begin{array}{l} > H_1 \\ < H_0 \end{array} TZ \tag{1}$$

where T is threshold factor, Z is the estimation of background clutter power.

Cell average CFAR is the most commonly used detection method among adjacent unit CFAR technique, its estimation of background clutter power is obtained by the calculated mean power value of $2N$ reference units that can be expressed as:

$$Z = (Z_1 + Z_2)/2N = (\sum_{i=1}^{N} x_i + \sum_{i=1}^{N} y_i)/2N \tag{2}$$

2.2 Simulation of CA-CFAR Detection

2.2.1 Single Target Detection in Homogeneous Clutter Environment

In simulation, Rayleigh distribution clutter sequences is generated with 20 dB-power and let target with 35 dB-power located in 100th distance unit. Assuming the probability of false alarm is $P_{fa} = 10^{-3}$ and the sliding window before and after detecting unit contains three protection units and ten reference units. As is shown in Fig. 2, the CA-CFAR detector can correctly detect the target and no false alarm in other distance unit happen.

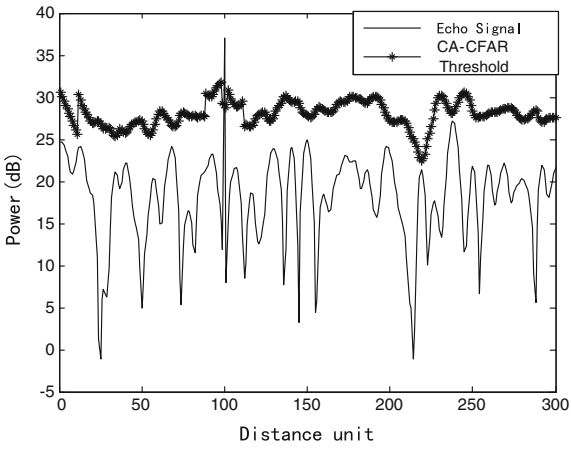

Fig. 2 Example of single target detection

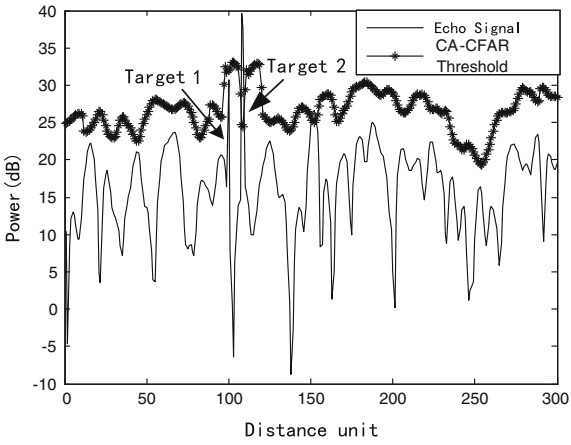

Fig. 3 Example of multi-targets detection

2.2.2 Multi-targets Detection in Homogeneous Clutter Environment

When one or more interference targets exist in the reference window of the detecting target, the total level of clutter power is elevated so that the main target may be shadowed and cannot be detected effectively. This is the truth when two or more FOD targets locate closely on the runway.

In simulation, let target 1 with 35 dB-power located in 100th distance unit and target 2 with 40 dB-power located in 108th distance unit. Other conditions are the same as the 2.2.1. It can be seen from Fig. 3 that when target 1 is located in the detecting unit, target 2 is located in the reference sliding window, and its higher power increases the estimated value of the background power, so the threshold of CA-CFAR detector is raised, as a result, target 1 is not detected.

2.2.3 Target Detection in Clutter Edge Environment

In practical FOD detection, the radar beam radiation area could include part of airport runway ground and part of the grass ground. When the detecting unit is located near the boundary of two different reflectance regions, the reference sliding window in CFAR processing will contain clutter edge, which may result in the target with low power being missed.

In simulation, the average power of Rayleigh clutter of the first 150 distance units is 20 dB and is up to 30 dB in the following 150 distance units. Assuming one FOD target is located in the 145th distance unit with 35 dB-power. Other conditions are the same as 2.2.1. The detection result is shown in Fig. 4, the FOD target is missed, because the detection threshold is elevated by those clutter units in the high reflectance region of its reference sliding window.

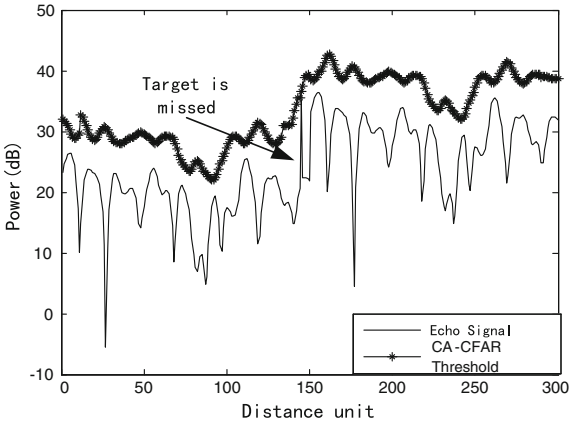

Fig. 4 Example of target detection in clutter edge environment

3 Clutter Map CFAR Technique

3.1 Principle of Clutter Map CFAR Point Technique

When clutter intensity changes violently in airspace, it is hard to maintain a constant false alarm rate because the reference units which traditional CA-CFAR method can use are insufficient. In normal circumstance, even the clutter changing violently in range and azimuth, but the change of clutter intensity of the same unit is relatively slow with time, so clutter map CFAR point technique [7] that iteratively processing the measurements of radar echo in previous repeat periods can be adopted.

The clutter map CFAR processing mainly includes two steps: clutter map update and clutter map detection. The iterative formula of clutter map update is

$$p_n = (1 - w)p_{n-1} + wq_n \tag{3}$$

where p_{n-1} is the clutter power update measurement of one clutter map unit after $n - 1$ times scan, q_n is echo measurement of this unit in nth time scan, w is attenuation factor. The actual storage of clutter map p_{n-1} is detection threshold of each clutter map unit, and this value will be updated when the next scanning echo measurement arriving. The criterion of clutter map detection can be expressed as:

$$\frac{q_n}{p_{n-1}} \begin{matrix} > H_1 \\ < H_0 \end{matrix} T \tag{4}$$

where T is the threshold factor. According to (4), when q_n/p_{n-1} more than T, then judged as target exist; otherwise, update clutter power according to (3). The principle diagram of clutter map CFAR point technique is shown in Fig. 5.

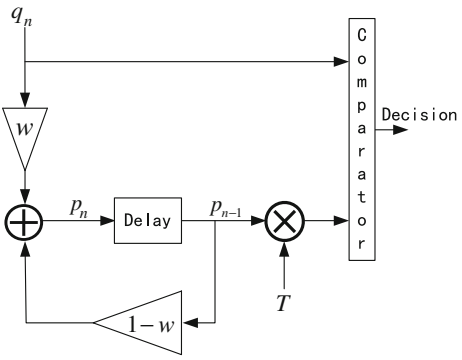

Fig. 5 Principle diagram of clutter map CFAR point technique

3.2 Principle of Clutter Map CFAR Plane Technique

Shen et al. proposed a clutter map CFAR plane technique based on point technique [8]. The basic principle of clutter map CFAR plane technique is do average processing to clutter map units firstly in each scan cycle, then obtain background clutter power estimation of detecting unit by the iteration of clutter power mean value of clutter map units. The iterative formula of clutter map CFAR plane technique is the same as point technique according to (3), but q_n is clutter power mean value of clutter map units, it can be expressed as (5):

$$q_n = \sum_{i=1}^{K} q_n^i / K \tag{5}$$

where $K = M \times N - p \times q$, q_n^i is the echo measurement of ith clutter map unit in nth scan (Fig. 6).

3.3 Simulation of Clutter Map CFAR Detection

In simulation, radar scanning space is divided into 30 azimuth units and 300 distance units, so clutter map size is 30 * 300. The average power of Rayleigh clutter of the first 150 distance units is 20 dB and is up to 30 dB in the follow 150 distance

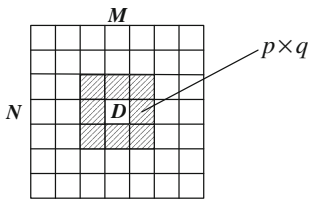

Fig. 6 Schematic diagram of clutter map CFAR plane technique

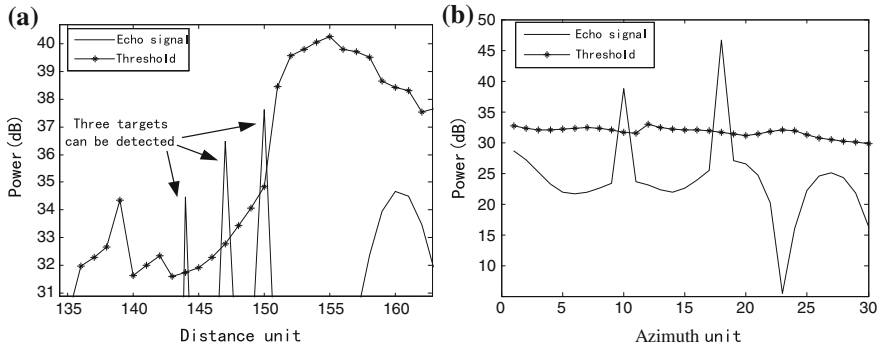

Fig. 7 Example of target detection with clutter map CFAR point technique. **a** Detection result in distance. **b** Detection result in azimuth

units and formed stable clutter map after 49 times scan, let four targets located into clutter edge in 50th scan. Assuming the probability of false alarm is $P_{fa} = 10^{-3}$, M and N is 7, p and q is 3. For point technique, w is 0.0625, T is 18.1255 and for plane technique, w is 0.125, T is 0.3498. The information of four targets is as follows: target 1 with 35 dB-power located in 150th distance unit and 10th azimuth unit; target 2 with 40 dB-power located in 150th distance unit and 18th azimuth unit; target 3 with 35 dB-power located in 147th distance unit and 10th azimuth unit; target 4 with 35 dB-power located in 144th distance unit and 10th azimuth unit.

The simulation results of point technique are shown in Fig. 7. The four targets with average SNR above 15 dB are located in low clutter power region of clutter edge. Because the estimation of background clutter power is only related to the unit itself and will not be affected by high power of clutter edge, so the four targets can be detected successfully.

The simulation results of plane technique are shown in Fig. 8. Because half reference units of target 1 are from high power clutter region, the detection threshold

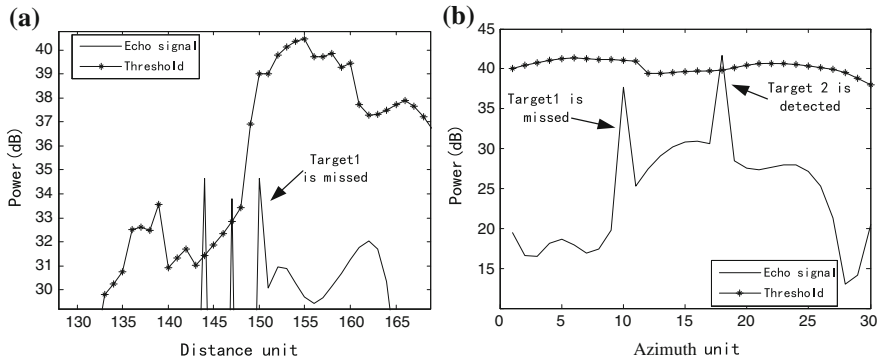

Fig. 8 Example of target detection with clutter map CFAR plane technique. **a** Detection result in distance. **b** Detection result in azimuth

is elevated obviously, so it cannot be detected.The threshold of target 2 is also elevated, but because of its relatively high SNR, target 2 can still be detected. Target 3 is located near the edge of the clutter, the detection threshold is elevated relatively little, so target 3 just can be detected. Target 4 is far from the edge of clutter, the reference units are main from low clutter power region, it can be detected successfully.

4 Analysis of Simulation Results

Based on the analysis and simulation of adjacent unit CFAR technique and clutter map CFAR technique, conclusions are drawn as follow:

1. In homogeneous clutter background environment and meet the requirement of SNR, the two CFAR techniques have satisfactory performance in single target detection.
2. In clutter edge environment and multi-targets interference detection, the detection performance of CA-CFAR is decline seriously. In contrast, it has not any influence to clutter map CFAR point technique. The detection performance of clutter map CFAR plane technique declines slightly in clutter edge environment, and still maintains a good detection performance in multi-targets interference detection.
3. Clutter map CFAR technique needs to form stable clutter map after several times scan before target detecting. The selection of attenuation factor w is very important. If the value of w is smaller, the probability of detection will be higher, but if it is slower then the detection performance becomes stable [9]. Point technique is much stronger and relies on the selected value of w than plane technique to get a better detection performance.

Based on the above three conclusions, although the speed of clutter map CFAR point technique achieve stable performance is relatively slow, but its detection performance is better than the other two kinds of methods, choose point technique can obtain a better detection performance for FOD target.

5 Conclusions

Adopt airport runway FOD detection system with millimeter-wave radar is more efficient and reliable than traditional manual inspection. Choose suitable CFAR methods which can get a better detection performance, ensure the safety of civil aircraft taking off and landing and also improve economic efficiency. Computer simulation can provide a theoretical basis for practical engineering application, saves time and manpower resources. This work will be continued in the future to improve the performance of detection system.

Acknowledgments This work is partially supported by the National Natural Science foundation of China(No.61139003). The authors would like to thank the anonymous reviewers and editors for their helpful comments and suggestions.

References

1. Security and technology center of department of airport CAAC (2009) FOD precaution manual, pp 1–5
2. FAA.AC 150/5220-24 (2009) Airport Foreign Object Debris Detection Equipment, pp 1–13
3. MH 5001-2000 (2007) Technical standards for airfield area of civil airports, pp 8–25
4. Mazouni K, Kohmura A (2010) 77 GHz FMCW Radar for FODs detection. In: Proceeding of 7th European Radar Conference Paris, France:EuMA, 2010, pp. 451–454
5. You H, Jian G, Xiangwei M (2001) Survey of automatic radar detection and CFAR processing. Syst Eng Electron 12(11):9–85
6. Xiulin Y (2004) Application of the clutter-map technology to signal processing in radar terminals. Mod Radar 24(5):34–36
7. Yong L, You H, Xiangwei M (1998) CFAR point technique on amplitude clutter map. Syst Eng Electron 9:7–18
8. Fuming S, Zheng L (1996) An approach of CFAR plane detection of radar targets based on integration of clutter image. Syst Eng Electron 18(7):9–14
9. You H, Yong L, Xiangwei M (1999) Performance of clutter map CFAR plane technique in homogeneous background. Acta Electron Sinica 27(3):119–121

Clutter Simulation for FOD Detection in Airport Runway Environment

Zhongjin Zhang, Yuguo Wang, Huaqiong Li and Qi Zhong

Abstract Focusing on the effective detection of FOD (foreign object debris) targets in airport runway complex clutter environment, this paper describes modeling and simulation of radar clutter by ZMNL (Zero Memory Nonlinearity) method. An experiment comparing the simulation data generated in MATLAB with the data collected by radar in airport runway is conducted; results show the validity of the method.

Keywords Clutter simulation · Airport runway environment · ZMNL method · FOD detection

1 Introduction

Airport runway foreign object debris (FOD) [1, 2] may cause damages or disasters to aircrafts. The crash of a Concorde jet in France in 2000 is an example of disasters due to FOD. Moreover, a lot of money is spent each year by airlines for repairing the damages caused by FOD to aircrafts. Consequently, some FOD detection systems have been developed and tested on airports recently, such as Tarsier system, FODetect, iFerret, and etc. Most of them are based on millimeter-wave radar and an optical sensor [3].

One of the key problems of FOD detection is how to find small target under relatively strong clutter background. The millimeter-wave linear frequency modulated continuous wave (LFMCW) radar is very suitable to FOD detection since it has excellent properties such as high range resolution, high sensitivity, no range blind area, and etc., which is helpful to detect small targets.

The clutter situation on airport runway faced by the FOD detection radar is rather complex. With the rapid development of digital electronic technology, computer

Z. Zhang (✉) · Y. Wang · H. Li · Q. Zhong
The Second Research Institute of CAAC, Chengdu, China
e-mail: jinsbm@163.com

Q. Liang et al. (eds.), *Proceedings of the 2015 International Conference on Communications, Signal Processing, and Systems*, Lecture Notes in Electrical Engineering 386, DOI 10.1007/978-3-662-49831-6_45

simulation has been widely used in various fields such as radar system that can be reduce the cost and cycles of radar design.

The essence of radar clutter simulation is generating a related sequence with certain probability distribution. FOD detection radar is operating in the vicinity of the airport runway, and its ground clutter is mainly from the runway ground and nearby grass echo. Combined with various runway types, vegetation, wind, rain, fog, and other weather conditions, study the statistical properties of the clutter in the airport runway environment, establishing appropriate clutter statistical model can provide the basis for clutter suppression algorithm and runway FOD clutter map CFAR technique to obtain a satisfactory detection performance.

In this paper, aiming at accurate clutter simulation of airport runway environment, clutter power spectrum is introduced first. Then, the principle of clutter simulation is given in Sect. 3 and the simulation result is compared with FOD detection radar data that verified its correctness in Sect. 4. Finally, conclusions are drawn in Sect. 5.

2 Signal Model

The transmit signal of LFMCW radar in a sweep frequency cycle is

$$S_t(t) = A_0 \cos[2\pi(f_0 t + \frac{1}{2}\alpha t^2) + \varphi_0], 0 \le t \le T \tag{1}$$

where f_0 is the radar's initial frequency, $\alpha = B/T$ is frequency modulation rate, B is frequency sweep bandwidth, T is frequency sweep cycle, and φ_0 is initial phase.

Note that the airport runway FOD is static target and thus the main detection task for LFMCW radar is to estimate the distance of FOD targets. Assuming there is only one FOD target existed, the time delay of each target is

$$\tau = \frac{2r}{c} \tag{2}$$

where r is the radial distance of target, and $c = 3 \times 10^8$ m/s is the speed of light. So the echo signal received can be expressed as

$$S_r(t) = B \cos\{2\pi[f_0(t-\tau) + \frac{1}{2}\alpha(t-\tau)^2] + \varphi\}, 0 \le t \le T \tag{3}$$

Then, the difference frequency signal after frequency mixing can be obtained as

$$S_{IF}(t) = A \cos\{2\pi[\frac{2r}{c}(f_0 - \frac{\alpha r}{c}) + \frac{2\alpha r}{c}t] + \varphi_0 - \varphi\}, 0 \le t \le T \tag{4}$$

3 Clutter Power Spectrum

3.1 Power Spectrum of Clutter

Clutter power spectrum plays a crucial influence on radar detection performance, so power spectrum characteristic is an important aspect of clutter simulation. Before generating the scattering signal sequence of a single clutter unit, we need to determine the feature of probability distribution and power spectrum characteristics, and then based on these parameters to meet the requirements of desired sequence of ground clutter. Clutter power spectrum is assumed to be Gaussian-shape that can be expressed as

$$S(f) = \frac{P}{\sqrt{2\pi}\delta} e^{-\frac{(f-f_0)^2}{2\delta^2}} \tag{5}$$

where f_0 is clutter mean Doppler frequency, δ is standard deviation, P is the scattering power calculation of single clutter unit that can be defined as (6).

$$P = \frac{p_0 G^2 \gamma^2 \sigma S}{(4\pi)^3 R^4 L} \tag{6}$$

In (6) where p_0 is radar average power, G is radar antenna gain, L is radar integrated loss, γ is radar working wavelength, σ is backscattering coefficient (depending on topography, geomorphology, radar parameters, and spatial geometry parameters factors to set according to the specific circumstance), S is the scattering area of single scattering unit, R is slant range of single scattering unit.

3.2 Backscattering Coefficient

Kulemin proposed a scattering coefficient empirical model [4] that is applicable to the frequency in a 3–100 GHz range within the grazing angle Less than 30°. It is suitable for describing the backscattering coefficient in complex airport runway environment that FOD millimeter-wave radar faced. In the case of a variety of ground roughness (including whether the vegetation cover, snow and urban areas), the empirical model can be expressed as

$$\sigma = A_1 + A_2 \log \varphi / 20 + A_3 \log f / 10 \tag{7}$$

where f is frequency in GHz, φ is grazing angle in degree, the coefficients A_1, A_2, A_3 varies with different ground targets. These coefficients in case of concrete floor and grass ground less than 0.5 m height are shown in Table 1.

Table 1 The coefficients of the different surface

Target species	A_1	A_2	A_3
Concrete floor	–49	32	20
Grass ground less than 0.5 m height	–21	10	6

4 Principle of Clutter Simulation

4.1 Weibull Clutter Model

In case of high-resolution radar at low grazing angles, the general ground clutter can accurately described by the Weibull distribution [5]. Weibull distribution probability density function can be expressed as

$$f(x) = \frac{p}{q}\left(\frac{x}{q}\right)^{p-1} \exp\left[-\left(\frac{x}{q}\right)^{p}\right], x \geq 0 \tag{8}$$

where q is the scale parameter, it is relevant to mean square value of the distribution. p is the shape parameter, controlling the shape of the distribution tail.

4.2 ZMNL Method

The block diagram of ZMNL method is shown in Fig. 1, first put an independent white Gaussian process V through filter $H(\omega)$ to obtain the relevant Gaussian sequence W, then introduce correlation characteristic to obtain non-Gaussian sequence Z by some kind of nonlinear transformation [6].

4.3 Weibull Clutter Generation

The process of generating related Weibull distribution clutter sequences is shown in Fig. 2. If we take two independent and identically distributed random variables $W_1, W_2 \sim N(0, \sigma^2)$, then the random variable $Z = \left(W_1^2 + W_2^2\right)^{1/p}$ obey two-parameter Weibull distribution and $q = (2\sigma^2)^{1/p}$.

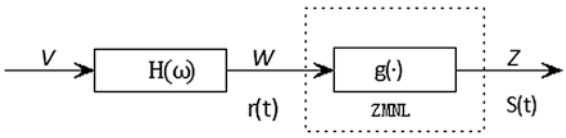

Fig. 1 Block diagram of ZMNL method

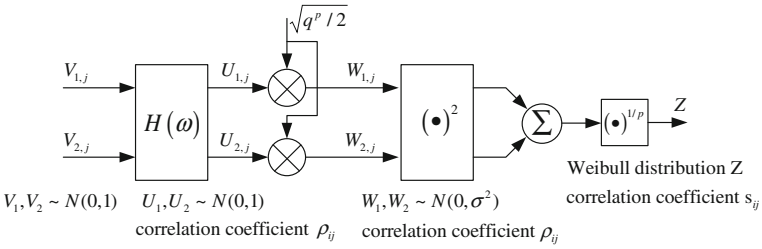

Fig. 2 Generation diagram of related Weibull clutter sequence

Correlation coefficient is defined as

$$\rho_{ij} = \frac{E\left[W_{k,i}, W_{k,j}\right] - E[W_{k,i}]E\left[W_{k,j}\right]}{\sqrt{D[W_{k,i}]D\left[W_{k,j}\right]}} \quad k = 1, 2 \tag{9}$$

In (9) $W_{1,i}, W_{1,j}$ are correlated, the correlation coefficient is ρ_{ij}. As the same, correlation coefficient of $W_{2,i}$ and $W_{2,j}$ is ρ_{ij}. $W_{1,i}, W_{2,j}$ are independent. The relationship between ρ_{ij} and s_{ij} is

$$s_{ij} = \frac{\Gamma^2\left(1+\frac{1}{p}\right)}{\Gamma^2\left(1+\frac{2}{p}\right) - \Gamma^2\left(1+\frac{1}{p}\right)} \cdot \left[{}_2F_1\left(-\frac{1}{p}, -\frac{1}{p}; 1; \rho_{ij}^2\right) - 1 \right] \tag{10}$$

where $\Gamma(\cdot)$ is the gamma function, ${}_2F_1(\cdot)$ is hypergeometric distribution.

How to get system response $H(\omega)$ is the key to clutter generating, the basic implementation process is as follows:

1. Obtained s_{ij} according to the Fourier transform relationship between correlation coefficient and power spectrum density, then calculate ρ_{ij} according to (10).
2. Select appropriate phase angle function φ to construct the system response $H(\omega) = \sqrt{\frac{S_U(\omega)}{S_V(\omega)}} e^{j\varphi(\omega)}$

Then, required Weibull clutter can be generated by following the process as in Fig. 2. In the next section we will do specifically the experiment in MATLAB simulation.

5 Simulation Experiment

The clutter data in the area outside of airport runway will be removed by the distance filter in signal processing unit of FOD radar, so we just simulate the clutter in concrete floor. In the simulation, assumed clutter power spectrum is Gaussian-shape

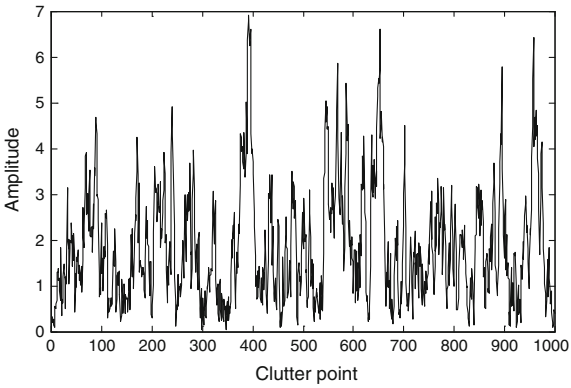

Fig. 3 Generation of related Weibull clutter sequence

defined in (1), f_0 is 0, δ is 1.0. The parameters in (6) is according to FOD detection radar that p_0 is 20 mW, G is 45 dB, γ is 4 mm, R is 150 m, L is –10 dB, S is 0.25 m^2. σ is selected with Kulemin model defined in (7) and its value is –38.74 dB. The Weibull clutter parameters p is 1.5 and q is 2.2. The related Weibull clutter sequence generated by MATLAB simulation is shown in Fig. 3.

It can be seen from Fig. 4 that the amplitude characteristic and spectral characteristic of clutter simulation data coincide well with the data collected by radar in airport runway that fully in line with expectation. From experimental results, it can be concluded that the simulation has some practical value and the clutter data generated by this effective method can be used for FOD radar optimized design to reduce the cost and cycles of radar design.

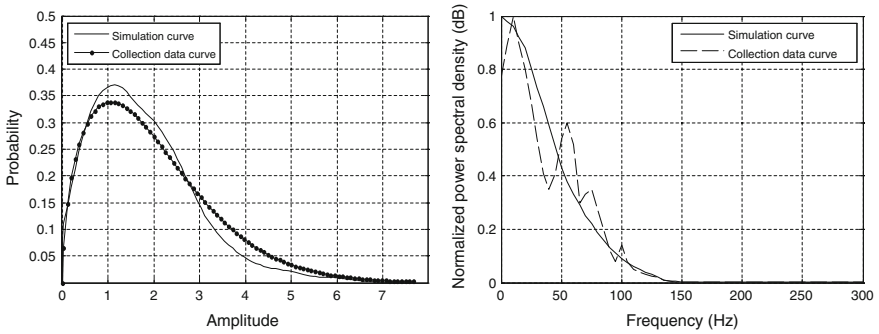

Fig. 4 Experiment results

6 Conclusions

The basic task of FOD detection is to find small target in complex airport runway environment, establishing appropriate clutter statistical model by computer simulation can provide the basis for clutter suppression algorithm and runway FOD clutter map CFAR technique to obtain a satisfactory detection performance. It also reduced the cost and cycles of radar design. In the next step, we studied the influence that variety environmental factors on the p, q parameters of Weibull clutter and types of clutter power spectrum will be conducted, so to make the generated clutter practicality broader and more accurate.

Acknowledgments This work is partially supported by the National Natural Science foundation of China (No.61139003). The authors would like to thank the anonymous reviewers and editors for their helpful comments and suggestions.

References

1. Security and technology center of department of airport CAAC (2009). FOD precaution manual, pp 1–5
2. FAA.AC 150/5220-24 (2009) Airport Foreign Object Debris Detection Equipment, pp 1–13
3. Mazouni K, Kohmura A (2010) 77 GHz FMCW Radar for FODs detection. In: Proceedings of the 7th European Radar Conference, Paris, France:EuMA, pp. 451–454
4. Tarnavsky EV, Kulemin GP (2004) Modeling of radar land clutter map for small grazing angles. SPIE (5484):702
5. Li G, Yu K (1989) Modeling and simulation of coherent Weibull clutter. IEEE Proc F Radar Signal Process 136(1):2–12
6. Liu B, Munson Jr DC (1982) Generation of a Random Sequences Giving a Jointly Specified Marginal Distribution and Auto covariance. IEEE Trans ASSP, ASSP-30:973–983

Integrated Narrow Band and UWB Reconfigurable Antenna

Jian Wu, Jian-Feng Pang, Wen-Xiang Cai, Ya-Hua Ran and Jiang-Jiang Li

Abstract A microstrip-fed planar ultra-wideband (UWB) monopole antenna with two added tunable bands is presented. The proposed antenna consists of a heptagon radiating patch that covers the 3.1–10.6 GHz (UWB) and two added arms which form the frequency bands 1.8 GHz (GSM) and 2.4 GHz (WLAN). Two PIN diode switches are placed on the slots between the patch and arms. By switching the PIN diodes ON or OFF, the antenna can work on GSM and UWB mode, WLAN and UWB mode, or single UWB mode. Surface current distributions are used to analysis the effects of the added structures. Simulated and measured results show that the antenna has good impedance match and stable radiation patterns across the whole band. The proposed antenna, which integrates narrowband and UWB, will be a suitable candidate for multiband applications and cognitive radio (CR).

Keywords Reconfigurable antenna · Ultra-wideband antenna · Multiband · Equivalent circuit model

1 Introduction

As the rapid development of modern wireless communication system, reconfigurable antennas [1–9] which can dynamically change their characteristics such as resonant frequency [1–4], radiation pattern [5, 6], or polarized type [7, 8] according to different needs and varieties of applications to realize the efficient use of the frequency spectrum have attracted much attention. Reconfigurable antenna has such salient features as simple structure, low profile, flexibility, and easy to integrate, so it is a good candidate to be used in Cognitive radio (CR) systems with the

J. Wu (✉) · J.-F. Pang
Sichuan Broadcasting Research, Chengdu 610017, China
e-mail: 1216139138@qq.com

W.-X. Cai · Y.-H. Ran · J.-J. Li
School of Electronic Engineering, University of Electronic Science and Technology of China, Chengdu 611731, China

Q. Liang et al. (eds.), *Proceedings of the 2015 International Conference on Communications, Signal Processing, and Systems*, Lecture Notes in Electrical Engineering 386, DOI 10.1007/978-3-662-49831-6_46

enough frequency bandwidth and excellent reconfigurability to achieve their smart applications. For CR scanning and communication, the UWB mode can be used to scan the available spectrum, while the narrow band mode can be used to communicate in free frequency band.

In the recent years, UWB antennas [10–15], as the key component of the UWB Communication systems, have attracted a lot of research. In [13], a planar monopole antenna with a added arm at the corners of the patch is designed. The antenna exhibits a dual-band operation covering 2400–2484 MHz (Bluetooth) and 3100–10600 MHz (UWB) frequency bands. In [14], by using a triangular-shaped patch and a pair of arms integrated on the patch, a dual-band is created. In [15], a multiband antenna which covers the frequency bands 1.3, 1.8, 2.4, and 3.1–10.6 GHz is presented. By removing the center part of a diamond-shaped patch, Ali Foudazi et al. added three narrow strips to the main radiating patch. The design realizes multiband and small size simultaneously. In [16], a reconfigurable UWB antenna with a diversity notched band is presented. Two PIN-diodes and a lumped varactor are located in the inverted U slot of the radiation patch. By controlling switches and varactor, a notched band tunability of 2.7–7.2 GHz is obtained. In [17], by using a switchable slotted structure on the ground plane, a reconfigurable antenna that has an ultrawideband (UWB) mode, three narrowband modes, and a dual-band mode has been designed. However, for the literature [13–15], the added bands cannot be controlled. The design of [17], UWB mode, and narrow band mode cannot work at the same time.

In this paper, we have designed a microstrip-fed UWB monopole antenna with two added arms in the radiating patch. We optimize two narrow strips at a suitable site to create two narrowband at 1.8 and 2.4 GHz. Two pin diode switches are placed in the slots between patch and strips. UWB mode and UWB integrated narrowband mode is obtained by switching "ON/OFF" the two diodes. The size of the proposed antenna, including the feeding mechanism, is 38 × 30 mm^2. Simulated and measured results match reasonably well. The designed antenna can be used for narrowband applications such as GSM and WLAN or UWB operations from 3.1–10.6 GHz and it can also be used for CR application.

2 Reconfigurable Antenna Design

The configuration of the heptagon monopole antenna, operating over the UWB frequency range, is shown in Fig. 1a. The dielectric substrate used in this work is a FR4 substrate with thickness of 1.6 mm, relative permittivity $\varepsilon_r = 4.6$, and a loss tangent of 0.025. In order to match with 50 Ω coaxial line, the width (W) 1.86 mm and the length 10 mm of the microstrip-fed line are chosen. The ground plane is designed to have two beveled edges and a notch in the middle of the upper edge to improve the antenna impedance matching. Figure 2 shows the simulated reflection coefficient of the UWB antenna.

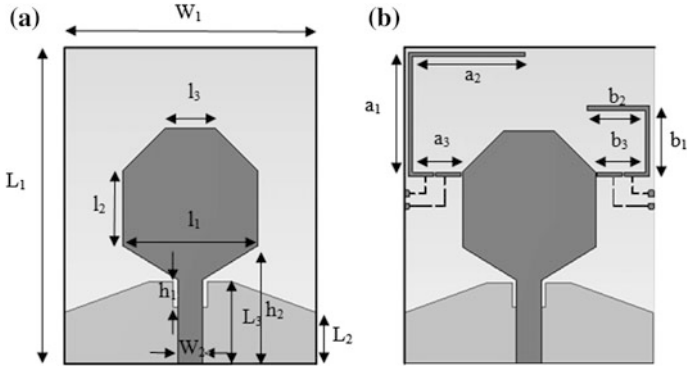

Fig. 1 Geometry of the proposed reconfigurable ultra-wideband antenna: **a** UWB antenna; **b** UWB antenna with tunable strips. And the main dimensions of the antenna are $L_1 = 38$ mm; $L_2 = 6$ mm; $L_3 = 9.7$ mm; $l_1 = 16$ mm; $l_2 = 9$ mm; $l_3 = 6$ mm; $l_2 = 9$ mm; $W_1 = 30$ mm; $W_2 = 3$ mm; $h_1 = 3$ mm; $h_2 = 14$ mm; $a_1 = 15$ mm; $a_2 = 13.5$ mm; $a_3 = 5.8$ mm; $b_1 = 8.5$ mm; $b_2 = 7$ mm; $b_3 = 5.8$ mm

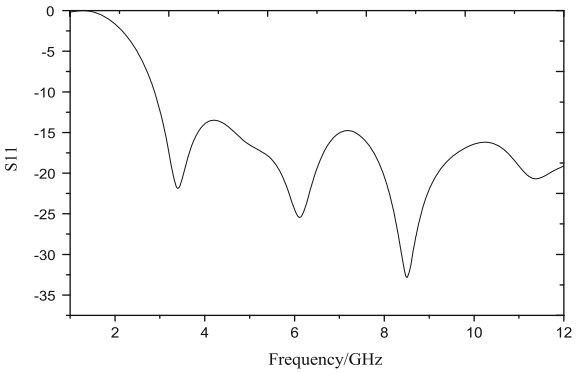

Fig. 2 The simulated reflection coefficient of the UWB antenna

Figure 1b shows the configuration of the frequency reconfigurable UWB antenna. Compared to the structure in Fig. 1a, two narrow strips which is designed to produce two tunable bands at frequency 1.8 and 2.4 GHz and dc biasing network are integrated to the heptagon patch. The length of the resonant strips L_a ($a_1 + a_2 + a_3$) and L_b ($b_1 + b_2 + b_3$) can be calculated approximately by the equations [14] as follows:

$$L_a = \frac{c}{4f_1\sqrt{\varepsilon_{\text{reff}}}} \tag{1}$$

$$L_b = \frac{c}{4f_2\sqrt{\varepsilon_{\text{reff}}}} \tag{2}$$

where c is the speed of light, f_1 and f_2 is the resonant frequency, $\varepsilon_{\text{reff}}$ is effective permittivity which can be calculated by the following formula:

$$\varepsilon_{\text{reff}} \approx \frac{\varepsilon_r + 1}{2} \tag{3}$$

The equations above do not put the mutual coupling into consideration, and the accurate size of the two added arms need to be optimized by simulation software.

To decrease the influence of dc network on antenna radiation, the dc lines are very thin (0.1 mm) and short. Two 100 pF capacitances are used to separate DC current and the AC source. Four 100 nH inductances are used to prevent the AC signal flowing along the biasing line, and 120 Ω resistances are used to protect the bias circuit (as shown in Fig. 3). All simulations above are carried using the commercial simulation software CST Microwave Studio.

Two PIN diodes (BAR64-02 V) are placed at the little gaps (0.2 mm) between the added arms and the heptagon radiating patch. As shown in the PIN diode datasheet, the diode can be regarded as a forward resistance of 2.1 Ω for the ON state. And when there is no voltage on it (off state), the diode presents a parallel circuit of a capacitance 0.17 pF and a resistance about **7** kΩ. However, in order to increase the RF signal impedance and prevent the RF current flowing pass through the diode, we choose reverse bias (–5 V) rather than zero bias (0 V) as the diode off state.

Figure 4 shows the top view and back view of the fabricated reconfigurable UWB antenna. The added arm can be approximately seen as a monopole. Thus, the arm will produce a narrow resonant band outside the UWB band when RF current flows on it. The relationships between switch state and antenna working mode is summarized in Table 1. In mode 1, the left arm is on and radiating as well as the main patch, thus dual bands of UWB and GSM are produced. Similarly, in mode 2, the antenna will radiate UWB and WLAN band with the right arm on. In mode 3, the two arms are switched off and only the heptagon patch radiate, the antenna only works at UWB band. However, when both the two diodes are switched on, the input reflection coefficient of 3.1−10.6 GHz is too high to be used, so this model will not be adopted.

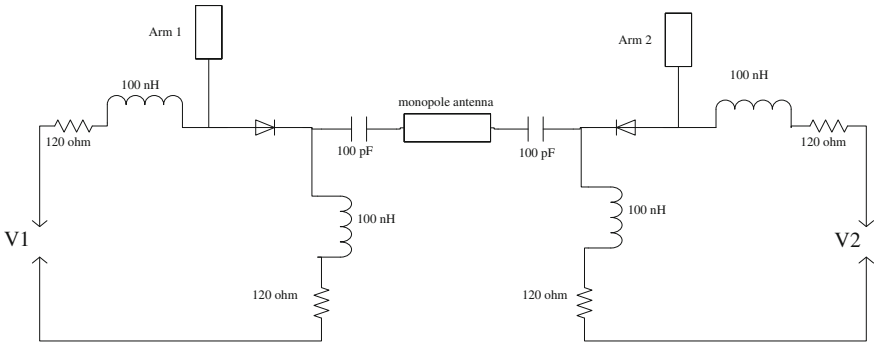

Fig. 3 The dc-bias circuit diagram of the proposed reconfigurable UWB antenna

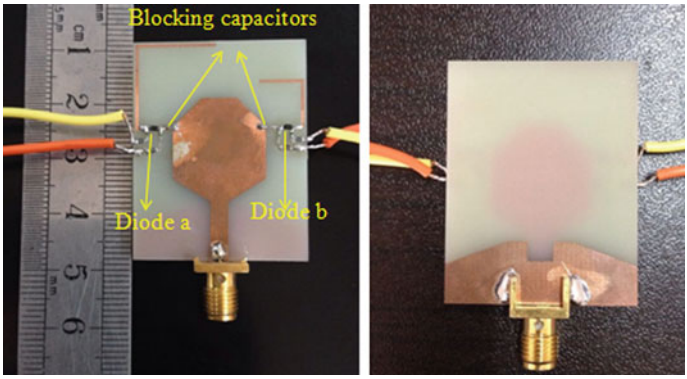

Fig. 4 Photo of the fabricated antenna with two arms

Table 1 Switch state and antenna working mode

Switch state	Antenna mode		
	Mode 1	Mode 2	Mode 3
Diode 1	ON	OFF	OFF
Diode 2	OFF	ON	OFF

3 Antenna Results and Discussion

The proposed reconfigurable ultra-wideband antenna has been measured using Rohde and Schwarz ZVB20 network analyzer. Figure 5 shows the simulated and measured reflection coefficient of the three modes. For Fig. 5a, b, as either of the diodes is on, the antenna produce a narrow band and UWB band simultaneously. The measured impedance bandwidth ($S_{11} \leq -10$ dB) of mode 1 and mode 2 is 1.4–1.83 GHz and 3.2–12 GHz, 2–2.75 GHz and 3.4–12 GHz, respectively. When both the diodes are off, the two arms are separated and the antenna is equal to a UWB monopole antenna which radiates a band of 2.7–12 GHz (as shown in Fig. 5c). Compared to the mode 3, the UWB band in mode 1 and mode 2 has a higher starting frequency of 3.2 and 3.4 GHz. It is because the added arms change the current distribution on the main patch which in turn reduces the equivalent electrical length of the patch. For the narrow band in mode 1 and mode 2, the measured reflection coefficient has a wider range below −10 dB than the simulated results. The differences between the simulated and measured reflection coefficient are owing to the manufacturing tolerance and the parasitic parameters (such as parasitic capacitance and inductance) introduced by the bias circuit and improper welding. Furthermore, the approximate simulation model of real PIN diode, electromagnetic interference in the surrounding environment, and the operation error in testing process are also the important factors to influence results.

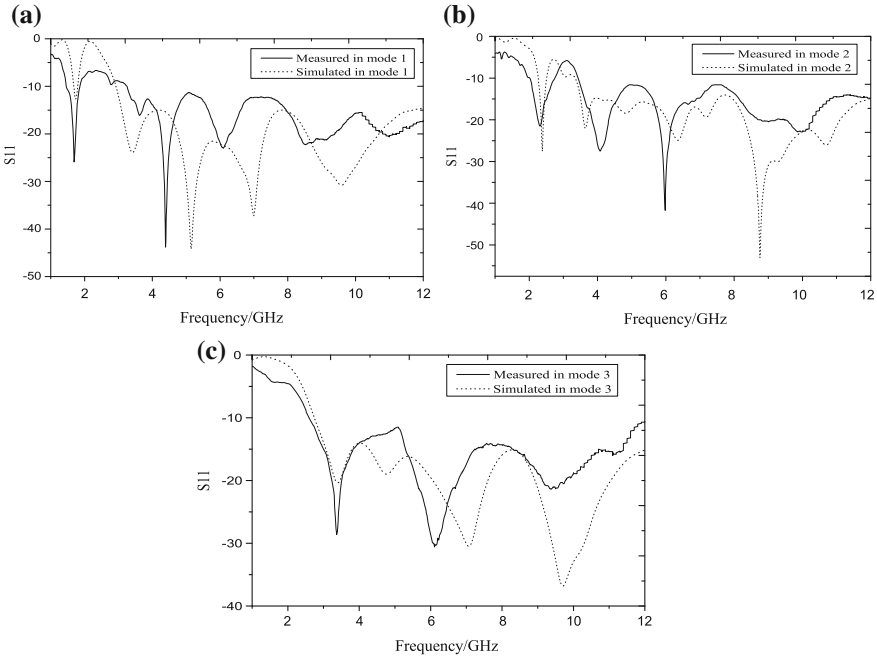

Fig. 5 The simulated and measured reflection coefficient of the antenna. **a** Mode 1: ON−OFF. **b** Mode 2: ON−OFF. **c** Mode 3: OFF−OFF

To further understand the operating principle of the added structures, the surface current of the antenna has been studied. Figure 6 shows the simulated surface current distribution at the fundamental resonance frequency of 1.8 and 2.4 GHz in mode 1 and mode 2, respectively. It can be found that the surface current mainly concentrates on the left arm near the resonant frequency 1.8 GHz in mode 1, while the surface current on the main patch and right arm is weak. Similarly, at the

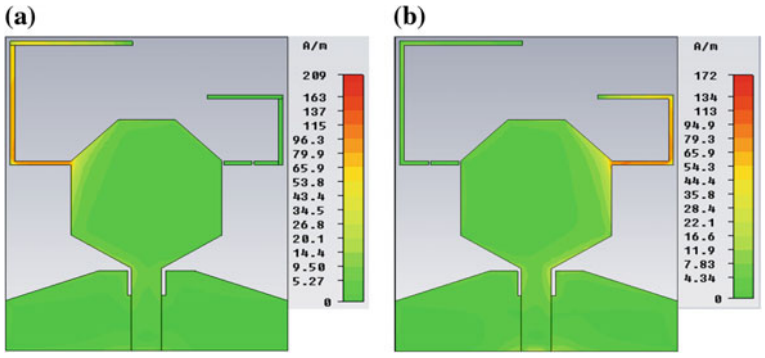

Fig. 6 Simulated current distributions of the antenna. **a** 1.8 GHz in mode 2. **b** 2.4 GHz in mode 3

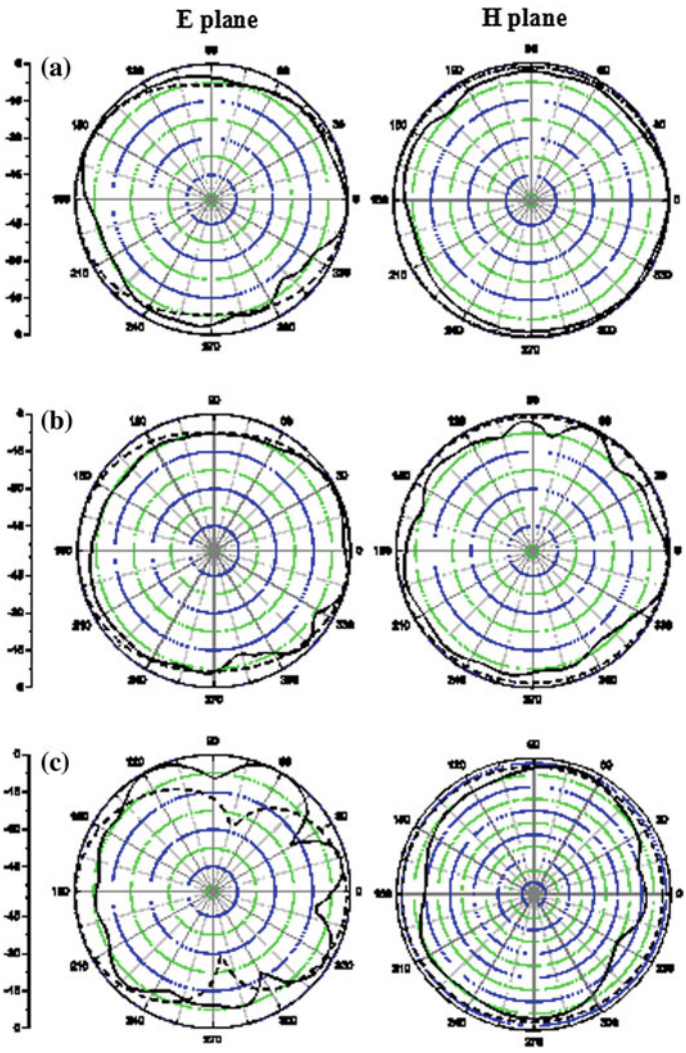

Fig. 7 Simulated and measured normalized radiation patterns of the antenna. **a** 1.75 GHz (mode 1). **b** 2.4 GHz (mode 2). **c** 4 GHz (mode 3)

resonant frequency 2.4 GHz in mode 2, surface current mainly flows through the right arm. It shows that the two arms have little coupling and keep well-separated to each other.

The radiation patterns of the reconfigurable UWB antenna are measured in SATIMO near-field multi-probe microwave anechoic chamber. Figure 7 shows the simulated and measured normalized patterns at 1.75 GHz in mode 1, 2.4 GHz in mode 2, 4 GHz in mode 3. The left column shows the E-plane and the right column shows the H-plane, respectively. Good agreements between simulation and

measurement are observed. It can be seen that antenna provides omnidirectional radiation patterns in the H-plane and reasonably stable patterns in the E-plane, which is similar to the ordinary monopole antenna.

4 Conclusion

A simple reconfigurable UWB monopole antenna is proposed in this letter. A heptagon patch and two narrow strips have been designed to radiate UWB, GSM, and WLAN frequency band, respectively. By selecting ON or OFF of the two PIN diodes, the antenna can be operated in two different dual-band modes or a UWB mode. The equivalent circuit model has been used to understand the principle of the antenna. The measured and simulated results show that the antenna can achieve a good performance over the whole band. The antenna has such advantages of compact size, simple structure, and low price. Thus, it may be a suitable candidate for wireless communication applications.

References

1. Chiu C-Y, Li J, Song S, Murch RD (2012) Frequency-reconfigurable pixel slot antenna. IEEE Trans Antennas Propag 60(10):4921–4924
2. Abutarboush HF, Nilavalan R, Cheung SW et al (2012) A reconfigurable wideband and multiband antenna using dual-patch elements for compact wireless devices. IEEE Trans Antennas Propag 60(1):36–42
3. Zhu HL, Liu XH, Cheung SW, Yuk TI (2014) Frequency-reconfigurable antenna using metasurface. IEEE Trans Antennas Propag 62(1):80–85
4. Ban Y-L, Sun S-C, Li P-P, Li JL-W, Kang K (2014) Compact eight-band frequency reconfigurable antenna for LTE/WWAN tablet computer applications. IEEE Trans Antennas Propag 62(1):471–475
5. Aboufoul T, Parini C, Chen X, Alomainy A (2013) Pattern-reconfigurable planar circular ultra-wideband monopole antenna. IEEE Trans Antennas Propag 61(10):4973–4980
6. Kittiyanpunya C, Krairiksh M (2013) A Four-beam pattern reconfigurable Yagi-Uda antenna. IEEE Trans Antennas Propag 61(12):6210−6214
7. Yoon W-S, Baik J-W, Lee H-S et al (2010) A reconfigurable circularly polarized microstrip antenna with a slotted ground plane. IEEE Antennas Wireless Propag 9:1161–1164
8. Yang X-X, Shao B-C, Yang F, Elsherbeni AZ, Gong Bo (2012) a polarization reconfigurable patch antenna with loop slots on the ground plane. IEEE Antennas Wireless Propag 11:69–72
9. Anagnostou DE, Chryssomallis MT, Braaten BD, Ebel JL, Sepúlveda N (2014) Reconfigurable UWB antenna with RF-MEMS for on-demand WLAN rejection. IEEE Trans. Antennas Propag 62(2):602−608
10. Wu S-J, Kang C-H, Chen K-H, Tarng J-H (2010) Study of an ultrawideband monopole antenna with a band-notched open-looped resonator. IEEE Trans Antennas Propag 58 (6):1890–1897
11. Dong YD, Hong W, Kuai ZQ, Chen JX (2009) Analysis of planar ultrawideband antennas with on-ground slot band-notched structures. IEEE Trans Antennas Propag 57(7):1886–1893

12. Chu Q-X, Yang Y-Y (2008) A compact ultrawideband antenna With 3.4/5.5 GHz dual band-notched characteristics. IEEE Trans Antennas Propag 56(12):3637–3644
13. Yildirim BS, Cetiner BA, Roqueta G, Jofre L (2009) Integrated bluetooth and UWB antenna. IEEE Trans Antennas Propag 8:149–152
14. Chu Q-X, Ye L-H (2010) Design of compact dual-wideband antenna with assembled monopoles. IEEE Trans Antennas Propag 58(12):4063–4066
15. Foudazi A, Hassani HR, Nezhad SMA (2012) Small UWB Planar Monopole Antenna With Added GPS/GSM/WLAN Bands. IEEE Trans Antennas Propag 60(6):2987−2992
16. Aghdam SA (2013) Reconfigurable antenna with a diversity filtering band feature utilizing active devices for communication systems. IEEE Trans Antennas Propag 61(10):5223−5228
17. Boudaghi H, Azarmanesh M, Mehranpour M (2012) A frequency-reconfigurable monopole antenna using switchable slotted ground structure. IEEE Antennas Wireless Propag 11:655–658

On the Spatial Modulation for 60 GHz Millimeter Wave Communications with Nonlinear Distortions

Xuebin Lin, Tiehong Tian, Chenglin Zhao and Bin Li

Abstract This paper suggests a promising spatial modulation scheme for the emerging 60 GHz millimeter wave communications, which is mainly designed to improve the system capacity and also combat the nonlinear distortions. The spectral efficiency can approach ($n_T - 2 + \log_2 M$) bpcu, where n_T is the number of transmit antennas and M is the modulation order. In order to combat nonlinear distortions, a novel spatial phase modulation code optimization scheme, relying on some specific rules amending the distribution of the spatial constellation points, is designed to enhance the transmission performance. Experimental simulations show that the new proposed method can acquire competitive performance at the same time of improving the transmission efficiency, which is hence of great significance to the 5G millimeter-wave communications.

Keywords Millimeter wave · Spatial modulation · Nonlinear distortion · Phase optimization · Offline optimization

1 Introduction

With the increasing demand of explosive transmission rate and higher capacity of wireless local area network (WLAN), multi-Gbps WLAN using 60 GHz millimeter-wave band has drawn a great deal of attentions [1–3]. Compared to existing short-range wireless communications technologies, the 60 GHz has richer spectrum resources [4] and allowed to have greater effective isotropic radiated power (EIRP) [3]. With the above features, the millimeter-wave communication has also become a potential candidate for future 5G wireless communications.

X. Lin (✉) · C. Zhao · B. Li
Key Lab of Universal Wireless Communications, Beijing University of Posts and Telecommunications, Beijing, China
e-mail: linxuebin@bupt.edu.cn

T. Tian
China Unicom System Integration Limited Corporation, Beijing, China

Q. Liang et al. (eds.), *Proceedings of the 2015 International Conference on Communications, Signal Processing, and Systems*, Lecture Notes in Electrical Engineering 386, DOI 10.1007/978-3-662-49831-6_47

As a double-edge sword, however, the hardware components in the context of ultrahigh frequency and enormous bandwidth will inevitably bring some challenges to the realistic implementations [5]. Among this, the nonideal or imperfect radio-frequency (RF) devices lead to serious nonlinear distortions, which may greatly deteriorate the transmission performance of millimeter-wave communication systems.

In order to overcome the nonlinear distortion of 60 GHz millimeter-wave transmission systems, a number of schemes have been proposed. Such existing methods are mainly divided into two kinds, i.e., the power back-off and peripheral circuits designing [6, 7]. The method of power back-off will push the nonlinear amplifier solely in a linear subregion, resulting in the undistorted or less distorted emission signals, but at the expense of a low SNR at the receiver. Another method is feedback compensation technologies or predistortion technologies [8], which can maintain the performance of nonlinear RF device. However, the integration of additional circuits of high operating frequency will greatly increase the additional power consumption and the implementation complexity.

Except for the nonlinear distortions, another problem in millimeter-wave communications is how to improve its spectrum efficiency. For future 5G communications, a target objective of 10–100 Gbps transmission rate [4, 9] can be hardly achieved by current modulation framework, given an allocated bandwidth less than 2 GHz. In this paper, a novel modulation scheme of higher spectrum efficiency is proposed for future 60 GHz millimeter-wave communications.

In order to enhance the transmission performance, in sharp contrast to existing power back-off or pre-distortion schemes, we further suggest a spatial modulation [10] and joint coding scheme. By simply adjusting the mapping phase of code-words of spatial modulation, the new scheme can avoid the huge implementation complexity of existing methods, while acquiring the performing detection performance and also the higher spectrum efficiency, even in the realistic nonlinear RF distortions. Experimental simulations have also validated the proposed scheme.

The rest of this paper is organized as follows. Section 2 presents the system model proposed in this work. Section3 describes the design of the SC code-words [11]. Numerical simulations and performance analysis are provided in Sect. 4. Finally, conclusion is generalized in Sect. 5.

2 System Model

Figure 1 shows the transmitter architecture of the proposed SM-OSTBC with nonlinear PA scheme. The encoding can be summarized as follows. Every two consecutive symbol periods, $(2m + l)$ bits, $(m = \log_2 M, l = 2 \times (n_T - 2))$, enter the SM-OSTBC transmitter. Then, after serial to parallel conversion, the input $(2m + l)$ bits signal is convert into an l bits signal and two m bits signals. The first

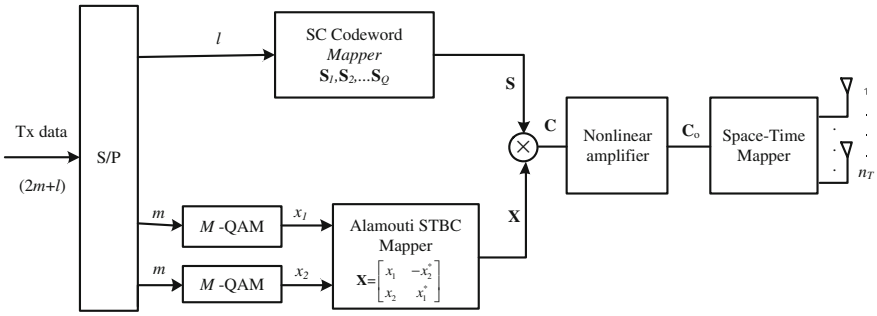

Fig. 1 Block diagram of the SM-OSTBC transmitter with nonlinear power amplifier

l bits are fed into the SC code-words Mapper in order to select 1 out of Q SC code-words, (S_1, …, S_Q, $Q = 2^n$), as the transmitted SC code-words $\mathbf{S}$. The remaining $2m$ bits ($m = \log_2 M$) are modulated by the M-QAM modulators, which provide the pair of symbols (x_1, x_2), are then fed into the Alamouti STBC Mapper, aiming to generate the Alamoui space-time block coding (STBC) code-word $\mathbf{X}$. The SM-OSTBC code-word $\mathbf{C}$ is obtained by multiplying $\mathbf{S}$ with $\mathbf{X}$, i.e., $\mathbf{C} = \mathbf{SX}$. The $\mathbf{C}_o$ is generated by feeding $\mathbf{C}$ into the nonlinear power amplifier, and subsequently transmitted via the n_T available at the transmitter.

By assuming the receiver as n_R available antennas and the channel as a Rayleigh fading channel, the receive $n_R \times 2$ signal matrix $\mathbf{Y}$ can be formulated as

$$\mathbf{Y} = \sqrt{\gamma}\mathbf{H} \times \mathbf{C}_o + \mathbf{N} \tag{1}$$

where γ is the average SNR at each receive available antenna. $\mathbf{H}$ is a $n_R \times n_T$ channel matrix and $\mathbf{N}$ is a $n_R \times 2$ noise matrix. The entries of $\mathbf{H}$ and $\mathbf{N}$ are assumed to be independent and identically distributed (i.i.d) complex Gaussian random variables with zero mean and unit variance. Besides, $\mathbf{H}$ is assumed to remain constant within a code-word of 2 symbol periods and to change independently from one code-word to another. $\mathbf{C}_o$ denotes an $n_T \times 2$ code-word, generated by feeding $\mathbf{C}$ into the nonlinear amplifier. $\mathbf{C} = \mathbf{SX}$, where $\mathbf{C}$, $\mathbf{X}$, and $\mathbf{S}$ denote a $n_T \times 2$ SM-OSTBC code-word, a 2×2 Alamouti STBC code-word, and a $n_T \times 2$ SC code-word, respectively. In addition, the transmit code-word $\mathbf{C}$ is normalized so that the ensemble average of the trace of $\mathbf{C}^H\mathbf{C}$ is equal to 2, i.e., $E\{\mathrm{tr}(\mathbf{C}^H\mathbf{C})\} = 2$.

Assume the perfect channel state information that is available at the receiver. Then the demodulator of the proposed scheme can be formulated as follows:

$$\begin{aligned}(\hat{\mathbf{S}}, \hat{\mathbf{X}}) &= \arg \min_{\mathbf{S} \in S, \mathbf{X} \in X} \left\| \mathbf{Y} - \sqrt{\gamma}\mathbf{H}\mathbf{C}_O \right\| \\ &= \arg \min_{\mathbf{S} \in S, \mathbf{X} \in X} \left\| \mathbf{Y} - \sqrt{\gamma}\mathbf{H} \times \mathbf{P}(\mathbf{SX}) \right\|\end{aligned} \tag{2}$$

Here, Ω_S, Ω_X are the search space associated with the SC code-words **S** and the Alamouti STBC code-words **X**, respectively. **P**(•) denotes to the function model of nonlinear power amplifier.

Finally, we can conclude with the result of Eq. (2) and estimate the $(2m + l)$ information bits.

3 SC Codeword Design

In this section, the spatial distribution characteristics of constellation encoded outputs **C** is modified, by optimizing the phase of SC code-words, which aims to enhance the capability of combating the nonlinear distortions. In the following, we will elaborate on the construction of SC code-words and the principle of phase optimization mechanism.

3.1 Construction of SC Codewords

Before redesigning the SC code-words, we may introduce the following $n_T \times 2$ generator matrix:

$$\mathbf{G}(\mathbf{s}) = \frac{1}{\|\mathbf{s}\|}\begin{bmatrix} s_1 & s_2 \\ -s_2^* & s_1^* \\ \vdots & \vdots \\ s_{n_T-1} & s_{n_T} \\ -s_{n_T}^* & s_{n_T-1}^* \end{bmatrix} \tag{3}$$

In Eq. (3), $\mathbf{s} = [s_1, s_2, \ldots, s_{n_T}]$ is a $1 \times n_T$ vector with complex valued entries s_n. $\|\mathbf{s}\|$ is the magnitude of vector **s**.

Assume the number of transmit antennas that are simultaneously activated as n_T. Then, the procedure for designing the SC code-words can be summarized as follows:

(1) Set the first two entries the $1 \times n_T$ vector $\mathbf{a}_q$ equal to 1,i.e., $\mathbf{a}_{q,1} = \mathbf{a}_{q,2} = 1$.
(2) Randomly select the remaining $(n_T - 2)$ entries from the set $\{\pm 1, \pm \mathrm{j}\}$ and ensure that all are different from each other. Then, the vector as following:

$$\mathbf{a}_q = [a_{q,1}, a_{q,2}, \ldots, a_{q,n_T}] \tag{4}$$

(3) Denote the $1 \times n_T$ phase optimized vector by $\mathbf{s}_q$. Then, adjust the phase of first entry to $\theta 1$, i.e., $\mathrm{s}_{q,1} = \mathrm{a}_{q,1} \times \mathrm{e}^{j\theta_1}$.

(4) If $a_{q,2k-1}$ and $a_{q,2k}$ ($2 \le k \le n_T/2$) both are real number or imaginary number, adjust the $a_{q,2k-1}$ as θ_{2k-1} and the $a_{q,2k}$ as θ_{2k}, i.e., $s_{q,2k-1} = a_{q,2k-1} \times e^{j\theta_{2k-1}}$, $s_{q,2k} = a_{q,2k} \times e^{j\theta_{2k}}$.

$$\mathbf{s}_q = [s_{q,1}, s_{q,2}, \ldots, s_{q,n_T}] \tag{5}$$

(5) Generate the SC code-words as $n_T \times 2$ matrix $\mathbf{S}_q = \mathbf{G}(\mathbf{s}_q)$, where $q = 1, 2, \ldots, Q$.

3.2 Principle of Phase Optimization

The Eq. (6) implies that adjusting the phase of $2r - 1$ and $2r$ ($1 \le r \le n_T/2$) rows of matrix $\mathbf{S}_q$ only influences the same rows of SM-OSTBC code-words $\mathbf{C}$, while it does not affect the remaining ones. Further, assume that the matrix $\mathbf{X}$ remains constant. Then, adjusting the $2r - 1$ and $2r$ entries of vector $\mathbf{s}_q$, it will only affect the same rows of matrix $\mathbf{S}_q$. That is, we may consider that the $2r - 1$ and $2r$ entries of the vector $\mathbf{s}_q$ as a whole, which will be completely independent of the others.

$$\mathbf{C} = \mathbf{S}_q\mathbf{X} = \frac{1}{\|\mathbf{s}\|} \times \begin{bmatrix} s_{q,1}x_1 + s_{q,2}x_2 & -s_{q,1}x_2^* + s_{q,2}x_1^* \\ -s_{q,2}^*x_1 + s_{q,1}^*x_2 & s_{q,2}^*x_2^* + s_{q,1}^*x_1^* \\ \vdots & \vdots \\ s_{q,n_T-1}x_1 + s_{q,n_T}x_2 & -s_{q,n_T-1}x_2^* + s_{q,n_T}x_1^* \\ -s_{q,n_T}^*x_1 + s_{q,n_T-1}^*x_2 & s_{q,n_T}^*x_2^* + s_{q,n_T-1}^*x_1^* \end{bmatrix} \tag{6}$$

Here, $\mathbf{C}$, $\mathbf{X}$, and $\mathbf{S}_q$ denote a $n_T \times 2$ SM-OSTBC code-word, a 2×2 Alamouti STBC code-word, and a $n_T \times 2$ SC code-word.

Besides, the entries of matrix $\mathbf{X}$ are mapped constellation generated by the M-QAM modulator. Since the whole shape of the $\mathbf{C}$ is symmetry with л/2, the rotation on the original constellation can be restricted to (0, л/2) [12]. In view of reducing the complexity of the phase adjusting, we may simply set θ_{2k-1} equal to $-\theta_{2k}$. As a result, θ_1 and θ_{2k-1} ($2 \le k \le n_T/2$) are ranged from 0–л/2, and meanwhile, θ_{2k} equal to $-\theta_{2k-1}$, i.e., θ_1- $\in$[0, л/2), $\theta_{2k-1} \in$ [0, л/2), $\theta_{2k} = -\theta_{2k-1}$.

In this paper, an offline optimization scheme is proposed. In the scheme, we will first send a sequence of specific data, which is assumed to uniformly traverse all code-words, and then adjust each phase subgroup, respectively. By doing so, we may easily acquire the received bit error rate (BER) with respect to various different rotation angles, given the specific signal to noise ratio (SNR). To sum up, the optimization process can be formulated as below:

$$\begin{cases} \theta_1 = \arg \min\limits_{\theta_1' \in [0,90)} r_{\mathrm{BER}} \\ \theta_{2k-1} = \arg \min\limits_{\theta_{2k-1}' \in [0,90), \theta_{2k}' = -\theta_{2k-1}'} r_{\mathrm{BER}}, \quad 2 \le k \le \frac{n_T}{2} \\ \theta_{2k} = \theta_{2k-1} \end{cases} \tag{7}$$

4 Simulation Experiments

In this section, we will evaluate the performance of proposed scheme, namely the optimized SM-OSTBC scheme. The comparative experiments are performed on both the new scheme and traditional ones, including classical SM-OSTBC scheme operating both in the presence of the linear amplifier [13] and the nonlinear amplifier. In the following simulations, two back-off conditions are concerned, i.e., 0, 3 dB.

In the simulation, the nonlinear amplifier model, introduced by the 802.11ad task group [14], is considered. The amplitude modulation-amplitude modulation (AM-AM) model and the amplitude modulation-phase modulation (AM-PM) can be respectively given by:

$$\mathrm{G}(A) = g \frac{A}{\left(1 + (gA/A_{\mathrm{sat}})^{2s}\right)^{1/(2s)}} \tag{8}$$

$$\Psi(A) = \frac{\alpha A^{q_1}}{(1 + (A/\beta)^{q_2})} \tag{9}$$

where A and $\mathrm{G}(A)$ denote input voltage amplitude and output voltage amplitude, respectively. $A_{\mathrm{sat}} = 0.58$ V denotes output voltage saturation point. $g = 4.65$ denotes the degree of distortion inflection smooth. $\Psi(A)$ denote the value of generating phase distortion, which is angle system. The values of α, β, q_1, q_2 are 2560, 0.114, 2.4, 2.3.

In the numerical experiment, the number of activated transmit antennas n_T is configured to 4 and the number of activated transmit antennas n_R is also equal to 4, i.e., $n_T = 4$, $n_R = 4$. The modulation order M of M-QAM modulators is set to 16.

In the first experiment, the value of power back-off is set to 0 dB, and the derived result is shown as Fig. 2a. It is seen from Fig. 2a that, compared with the traditional SM-OSTBC scheme operating in the nonlinear PA, the optimized SM-OSTBC with the additional phase rotation will improve the BER performance significantly, in the context of nonlinear distortions. As a benchmark, we also plotted the traditional SM-OSTBC scheme operating in the linear PA, i.e., there is no nonlinear distortion. It is found that, compared with the linear PA, our suggested optimized SM-OSTBC scheme's performance degradation is still noticeable. This is

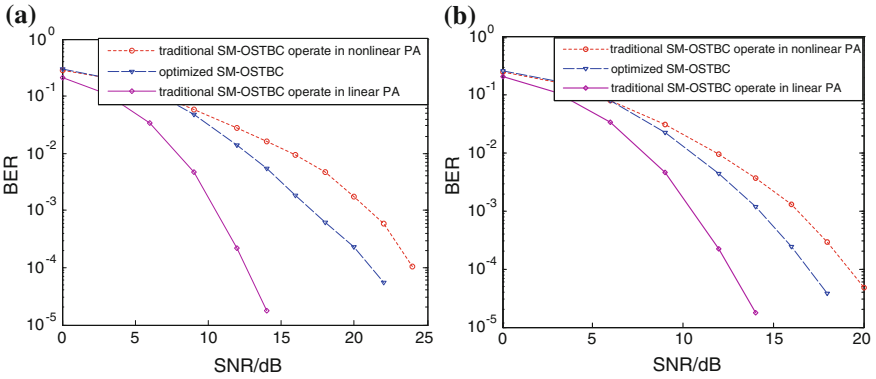

Fig. 2 **a** BER of system on condition of 0 dB back-off. **b** BER of system on condition of 3 dB back-off

mainly because that, with the nonlinear distortions, the emission signals will be mostly operated in the saturated zone, by distorting the constellation sharply.

In the second experiment, the value of power back-off is 3 dB, and the numerical result is shown in Fig. 2b. It is observed from Fig. 2b that, compared with traditional SM-OSTBC scheme operating in the nonlinear PA, the optimized SM-OSTBC with additional phase rotation can acquire the detection gain of 2 dB in the case of the value of BER is 10^{-4}. It is considered that this detection gain is mainly attributed to the additional freedom introduced by the addition phase, and the optimized constellation distribution which is more robust to the nonlinear distortions.

From the above experimental analysis, the optimized scheme can substantially improve the BER performance when the back-off power condition is set to 0 dB, compared to traditional SM-OSTBC without phase rotation optimization. In this case, as almost all the signals constellations will experience serious nonlinear distortions when operating in the saturation zone, the derived performance of the optimized scheme is still kept far away from the linear case. Even so, the new scheme can acquire 3 dB gain, compared with traditional one. However, this detection gain will be reduced as the value of power back-off increases. For example, a rough detection gain of 2 dB can be achieved when the power back-off is set to 3 dB.

5 Conclusion

In this work, we propose a new spatial modulation scheme for 60 GHz millimeter-wave communications in order to further improve the spectrum efficiency and also troubleshoot the problem induced by nonlinear power amplifier, and the simulation results have demonstrated the excellent performance. The advantages of this scheme could be summarized into two-fold. First, the

SM-OSTBC model is applied to 60 GHz millimeter-wave communications, which can maximize the spectral efficiency furthermore. Thus, the spectral efficiency can even approach ($n_T - 2 + \log_2 M$) bpcu. Second, we modify the spatial distribution characteristics of constellation encoded outputs, by optimizing the phase of SC code-words, leading to enhance system's capability of combating the nonlinear distortions, without the assistance of any additional processing. Given the advantages aforementioned, the proposed method provides a promising solution to enhance the performance in realistic 60 GHz millimeter-wave communications, and induce the 60 GHz to become a competitive candidate for future 5G wireless communications.

Acknowledgments This research is financially supported by the National Natural Science Foundation of China (61271180) and Research Fund for the Doctoral Program of Higher Education of China (20130005110016).

References

1. Yong SK, Chong C-C (2006) An overview of multigigabit wireless through millimeter wave technology: potentials and technical challenges. In: EURASIP journal on wireless communications and networking 2007
2. Law CY, Pham A-V (2010) A high-gain 60 GHz power amplifier with 20 dBm output power in 90 nm CMOS. In: 2010 IEEE international on solid-state circuits conference digest of technical papers (ISSCC), IEEE, 2010
3. Yong S-K, Pengfei X, Alberto V-G (2011) 60 GHz technology for Gbps WLAN and WPAN: from theory to practice. Wiley
4. Pietraski P et al (2012) Millimeter wave and terahertz communications: feasibility and challenges. ZTE Commun 10.4: 3–12
5. Lei M et al (2008) Hardware impairments on LDPC coded SC-FDE and OFDM in multi-Gbps WPAN (IEEE 802.15. 3c). In: Wireless communications and networking conference, WCNC 2008. IEEE, 2008
6. Black HS (1941) Wave translating system. U.S. Patent No. 2,258,128. 7 Oct. 1941
7. Kim B et al (2002) A new adaptive feed forward amplifier using imperfect signal cancellation. In: 2002 3rd international conference on microwave and millimeter wave technology, Proceedings. ICMMT 2002. IEEE, 2002
8. Kao K-Y et al (2013) Phase-delay cold-FET pre-distortion linearizer for millimeter-wave CMOS power amplifiers. IEEE Trans Microwave Theory Tech 61.12:4505–4519
9. Roh W et al (2014) Millimeter-wave beamforming as an enabling technology for 5G cellular communications: theoretical feasibility and prototype results. IEEE Commun Mag 52.2:106–113
10. Sugiura S, Chen S, Hanzo L (2010) Coherent and differential space-time shift keying: A dispersion matrix approach. IEEE Trans Commun 58(11):3219–3230
11. Le M-T et al (2012) High-rate space-time block coded spatial modulation. In: 2012 International Conference on Advanced Technologies for Communications (ATC), IEEE, 2012
12. Oppenheim AV, Alan SW (1997) Signals and systems. Prentice-Hall
13. Le M-T et al (2014) Spatially modulated orthogonal space-time block codes with non-vanishing determinants. IEEE Trans Commun 62.1:85–99
14. Perahia E, Park M, Stacey R (2010) IEEE P802. 11 wireless LANs TGad evaluation methodology. IEEE 802:9–15

3D-Beamforming Codebook Design Based on Reduced-Dimension and Decomposition for Millimeter-Wave Communications

Weixia Zou, Longfei Wang, Chao Guo, Guanglong Du and Zhaoxia Song

Abstract To improve the reliability of received signal of millimeter-wave communications, 3D-beamforming is discussed in this paper. This paper proposes a codebook design scheme, which can transforms 3D-beamforming problem into two 2D-beamforming problems by using a coordinate system to instead of spherical coordinate system. The scheme can generate the 3D codebook by the direct product of two codebooks of horizontal dimension and vertical dimension. It reduces the complexity of the two-dimension codebook generation.

Keywords 3D-beamforming · Codebook design · Decomposition · Coordinate system

1 Introduction

With increasing demand for high rate multimedia services in work, live, and entertainment, millimeter-wave communications which can achieve Gbps and even several Gbps transfer rate attract more and more attention and become the new hot spot in wireless communications prospective study [1, 2].

Although the millimeter-wave communication technology can theoretically provide several Gbps transmission rate, the attenuation of millimeter-wave is significant, and a huge path loss makes reliable signal transmission and reception of communications become difficult. However, because of the high millimeter-wave frequencies, it happens to employ large scale array antennas to improve the link quality by beamforming technology [3].

W. Zou · L. Wang (✉) · C. Guo · G. Du · Z. Song
Key Laboratory of Universal Wireless Communications, MOE, Beijing University of Posts and Telecommunications, Beijing 100876, People's Republic of China
e-mail: 513640883@qq.com

W. Zou · L. Wang · C. Guo · G. Du · Z. Song
State Key Laboratory of Millimeter Waves, Southeast University, Nanjing 210096, People's Republic of China

Q. Liang et al. (eds.), *Proceedings of the 2015 International Conference on Communications, Signal Processing, and Systems*, Lecture Notes in Electrical Engineering 386, DOI 10.1007/978-3-662-49831-6_48

For common scenarios in millimeter-wave communications in wireless personal area network (WPAN) and wireless local area network (WLAN), Ref. [4] utilized the nonlinear objective optimization approach to design an arbitrary shape of the beam to satisfy the requirements of communications. However, traditional 2D-beamforming technology can dynamically change the horizontal angle of the beam but cannot adjust the vertical angle of the beam. The vertical coverage is fixed, hence it cannot satisfy the growing demand for data services [5–7]. 3D-beamforming technology can dynamically change vertical angle of the beam to optimize vertical coverage of the antenna, so that the users at the edge can effectively receive signals [8–10], this paper will apply the method in the reference to 3D-beamforming technology. First, to make the planar array of two-dimensional codebook can easily generated by direct product of the codebooks of horizontal dimension and vertical dimension. This paper uses a coordinate system to instead of spherical coordinate system, whose definition method of the angle of incident signal is similar to that of a one-dimensional linear array. Second, the 3D target beam is decomposed into two 2D target beams in horizontal and vertical dimensions. The 2D target beam is generated by two ways, and then the codebook of one-dimension linear array is obtained by searching method in [4]. Finally, the 3D codebook is obtained by using the direct product of two codebooks.

2 Beam Response

2.1 *Planar Array Beam Response in Spherical Coordinate System*

Assuming that an antenna array is incident from a point source with a spherical angle $\vartheta = (\theta, \phi)$, the θ, ϕ represents the horizontal azimuthal angle and the vertical elevation angle. The components of X- and Y-axis of the unit vector in the direction of the signal propagation is

$$v(\vartheta) = -\left[\sin\phi\cos\theta,\ \sin\phi\sin\theta\right]^{\mathrm{T}} \tag{1}$$

In the spherical coordinate system, the beam response is expressed as

$$\begin{aligned} p(\theta) = w^{\mathrm{H}} a(\theta) &= \sum_{m=0}^{M-1} w_m^* \exp(-jw\tau_m) \\ &= \sum_{m_x=0}^{M_x-1}\sum_{m_y=0}^{M_y-1} w_{m_x,m_y}^* e^{j\frac{2\pi}{\lambda}(m_x d\sin\phi\cos\theta + m_y d\sin\phi\sin\theta)} \\ &= \sum_{m_x=0}^{M_x-1} w_{m_x}^* e^{j\frac{2\pi}{\lambda}m_x d\sin\phi\cos\theta} \sum_{m_y=0}^{M_y-1} w_{m_y}^* e^{j\frac{2\pi}{\lambda}m_y d\sin\phi\sin\theta} \end{aligned} \tag{2}$$

In the above equation, the planar array beam response is decomposed into product of two parts where each part is related to two angles in the coordinate system, and the definition of the two angles is different from the definition of incident angle in a linear array, the codebooks of horizontal and vertical dimensions cannot be produced by using the method of one-dimensional linear array codebook design. Thus, the two-dimension codebook of planar array in this coordinate system cannot be obtained easily by using the direct product of the codebooks of horizontal dimension and vertical dimension. Hence, this paper adopts another coordinate system so that the beam response of the planar array can be decomposed into the product of two linear array beam response.

2.2 Planar Array Beam Response in New Coordinate System

Similar to the linear array, this paper uses the angle deviating from the midperpendicular of linear array to express the direction of arrival. The horizontal and vertical direction angles $(\theta x, \theta y)$ represent the incident wave direction deviates from the Z-axis in plane XOZ and plane YOZ, respectively, as shown in Fig. 1. Assuming that an antenna array is incident from a point source with a spherical angle $\vartheta = (\theta x, \theta y)$, the component of X- and Y-axis of the unit vector in the direction of the signal propagation is

$$v(\vartheta) = -\left[\frac{\tan \theta x}{\sqrt{\tan^2 \theta x + \tan^2 \theta y + 1}}, \frac{\tan \theta y}{\sqrt{\tan^2 \theta x + \tan^2 \theta y + 1}}\right]^{\mathrm{T}} \tag{3}$$

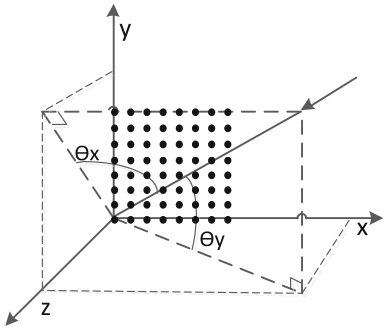

Fig. 1 Coordinate system used in this paper

In this coordinate system, the beam response is expressed as

$$\begin{aligned} p(\theta) = w^{\mathrm{H}} a(\theta) &= \sum_{m=0}^{M-1} w_m^* \exp(-jw\tau_m) \\ &= \sum_{m_x=0}^{M_x-1} \sum_{m_y=0}^{M_y-1} w_{m_x,m_y}^* \mathrm{e}^{j\frac{2\pi}{\lambda}\left(m_x d \frac{\tan\theta x}{\sqrt{\tan^2\theta x+\tan^2\theta y+1}} + m_y d \frac{\tan\theta y}{\sqrt{\tan^2\theta x+\tan^2\theta y+1}}\right)} \\ &= \sum_{m_x=0}^{M_x-1} w_{m_x}^* \mathrm{e}^{j\frac{2\pi}{\lambda} m_x d \frac{\tan\theta x}{\sqrt{\tan^2\theta x+\tan^2\theta y+1}}} \sum_{m_y=0}^{M_y-1} w_{m_y}^* \mathrm{e}^{j\frac{2\pi}{\lambda} m_y d \frac{\tan\theta y}{\sqrt{\tan^2\theta x+\tan^2\theta y+1}}} \end{aligned} \tag{4}$$

By the Eq. (4), with the coordinate system in this paper, the beam response is also decomposed into product of two parts, although each part is related to two angles in the coordinate system. Because the definitions of the two angles are similar with the definition of that in linear array, the two-dimension planar array beamforming codebook design problem can be transformed into two one-dimensional linear array beamforming codebook design problems.

$$\mathrm{e}^{j\frac{2\pi}{\lambda} m_x d \frac{\tan\theta x}{\sqrt{\tan^2\theta x+\tan^2\theta y+1}}} = \begin{cases} \mathrm{e}^{j\frac{2\pi}{\lambda} m_x d \sin\theta x} & \theta y = 0^\circ \quad \text{(a)} \\ \mathrm{e}^{j\frac{2\pi}{\lambda} m_x d \sin\theta x * \eta} & 0 < \eta < 1,\ \theta y \neq 0^\circ \quad \text{(b)} \end{cases} \tag{5}$$

In the Eq. (5), when $\Theta_y = 0°$, equation (a) is exactly same with linear array beam response equation, the codebook can be generated by one-dimensional linear array codebook design method. When $\Theta_y \neq 0°$, equation (b) is equal to multiply η by sin Θ_x comparing with linear array beam response equation, equation (a) is not much different from equation (b), when $\Theta_y \neq 0°$, the optimal codebook is approximate to the one-dimensional linear array codebook generated by equation (a). So the method of one-dimensional linear array codebook design can be used to generate the codebook of the horizontal and vertical dimension, respectively, and the two codebooks are able to approximately replace the optimal codebook of each part in Eq. (4). So that the two-dimensional codebook of planar array in this coordinate system can easily be obtained by using the direct product of the codebooks of horizontal and vertical dimension. The coordinate system has been used in [11] before this paper, the purpose is to describe the area covered by the satellite antenna better, the benefit is the same in millimeter-wave communications.

3 Arbitrary Shaped 3D-Beamforming Codebook Design

In this paper, an arbitrary shaped 3D-beamforming codebook design scheme for planar array antenna is provided. According to the above, the two-dimensional codebook can be obtained by using the direct product of the codebooks of horizontal and vertical dimension. Therefore, some symmetric 3D-beamforming problem can be transformed into two arbitrary shaped 2D-beamforming problems.

3.1 The Decomposition of Two-Dimensional Codebook

By the above, 2D-beamforming uses an angle to describe the direction of the main lobe and the only variable of beam response is the angle, and 3D-beamforming uses two angles to describe the direction of the main lobe and the two variables of the beam response are horizontal angle and vertical angle. In addition, according to the Eq. (4), the beam response of a planar array antenna is represented as a product of the beam response of the two linear array antennas. For a 3D-beamforming problem, if planar array antenna beam pattern has only one main lobe, and the gain of the angle range of the main lobe is normalized, and assuming normalized values in this range are 1, the angle range outside the main lobe is approximately 0, as the 3D target beam pattern is decomposed, the horizontal and vertical angle ranges of the main lobe in the beam pattern of the linear array antenna are also 1, as shown in Fig. 2. The square grid box represents the main lobe of the 3D target, and the rectangular shadow box represents the main lobe of the 2D beam. At this point, a 3D-beamforming problem is transformed into two 2D-beamforming problems. The two target beams of linear array antenna with horizontal and vertical dimensions are obtained, respectively. Therefore, this method can be used to transform some symmetrical 3D-beamforming problems into two arbitrary shaped 2D-beamforming problems.

Reference [4] proposed a method to design arbitrary shape 2D-beamforming codebook. It utilized optimization approach to search for the required codebook of the phased array. We can generate one-dimensional linear array codebook based on the method of Ref. [4].

If we obtain the horizontal dimension and vertical dimension codebooks $\mathbf{w}_x$ and $\mathbf{w}_y$, according to the Eq. (6), two-dimensional codebook can be obtained by using the direct product of the two codebooks.

$$\mathbf{w} = \mathbf{w}_y^{\mathrm{T}} . \mathbf{w}_x = \begin{bmatrix} w_{x_0} . w_{y_0} & \cdots & w_{x_m} . w_{y_0} & \cdots & w_{x_{M-1}} . w_{y_0} \\ \cdots & \cdots & \cdots & \cdots & \cdots \\ w_{x_0} . w_{y_m} & \cdots & w_{x_m} . w_{y_m} & \cdots & w_{x_{M-1}} . w_{y_m} \\ \cdots & \cdots & \cdots & \cdots & \cdots \\ w_{x_0} . w_{y_{M-1}} & \cdots & w_{x_m} . w_{y_{M-1}} & \cdots & w_{x_{M-1}} . w_{y_{M-1}} \end{bmatrix}, |w_m| = 1 \quad (6)$$

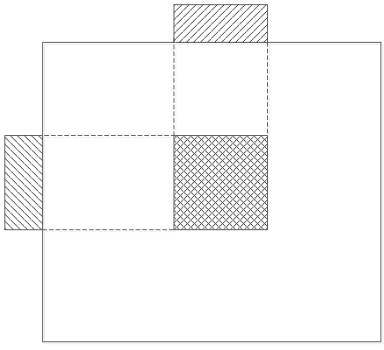

Fig. 2 Beam response decomposition

3.2 Simulation Example

Take 8 × 8 planar array antenna as an example, using the codebook design scheme proposed in this paper, simulation can produce a variety of different-shaped beams, including wide main lobe beam, multimain lobe equal width beam, multimain lobe unequal width beam, and symmetric multimain lobe beam, to meet the communication requirements of different scenarios. At the same time, for arbitrarily-shaped beam, two different object beam generation methods are, respectively, the rectangular box and superposition of codebook, where the method of codebook superposition uses N phase codebook [12]. In this paper, we take the decomposition and simulation of multimain lobe equal width beam as example.

In daily life, equipment often needs to communicate with other devices in different directions, or PNC needs to broadcast in different directions. Therefore, a beam with several main lobes needs to be produced. We called the beam as multimain lobe equal width beam in this paper.

A. **Rectangular box method to generate the target beam**

According to Sect. 3.1 decomposition method, it is the first step to decompose the 3D target beam into two wide target beams of the horizontal and vertical dimensions, as shown in Fig. 3. We can set three rectangular boxes in direction (–40°, –30°), (–5°, 5°), (30°, 40°) in the horizontal dimension and a rectangular box in direction (–10°, 10°) in the vertical dimension as the two 2D target beams. The beam generated by the two-dimensional codebook is shown in Fig. 4a.

B. **Superposition of codebook method to generate the target beam**

The two 2D target beams generated by decomposition can be obtained through superposition by the codebook number $Q = \{5, 8, 11\}$ in the horizontal dimension and the codebook number $Q = \{8, 9\}$ in the vertical dimension. The beam generated by the two-dimensional codebook is shown in Fig. 4b.

Fig. 3 Beam decomposition

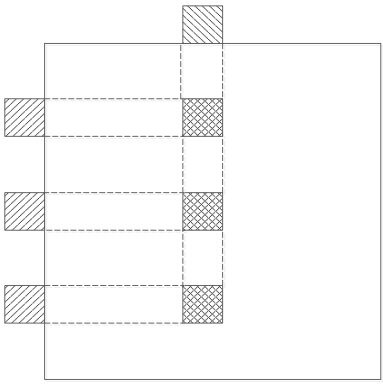

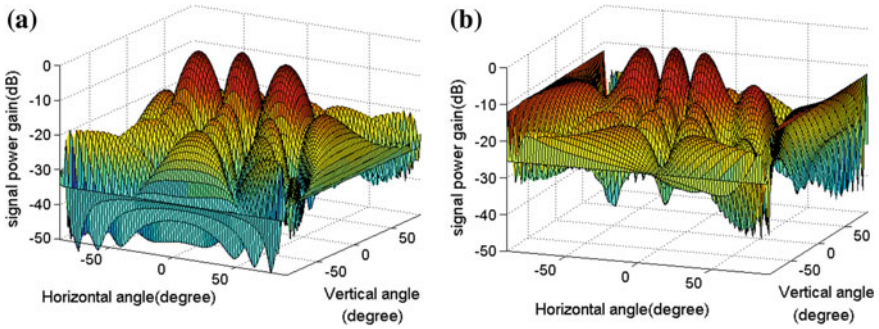

Fig. 4 Multimain lobe equal width beam, **a** rectangular box, **b** superposition of codebook

3.3 Performance Analysis

3.3.1 Flexibility

This method is flexible. First, we can generate a beam with arbitrary direction, width main lobe, and the number of the main lobes is arbitrary. Second, different methods to generate target beam can be used in a linear array. In short, this method can generate different kinds of beams for different application scenarios.

3.3.2 Gain Loss

Because the whole antenna radiation power is limited, the larger the main lobe width is, the smaller the main lobe gain is. In the same way, the number of the main lobes of the antenna increases and the gain of every main lobe obtained by the array will be reduced. The following simulations analyze the extent of the gain loss of array from the two aspects (Figs. 5 and 6).

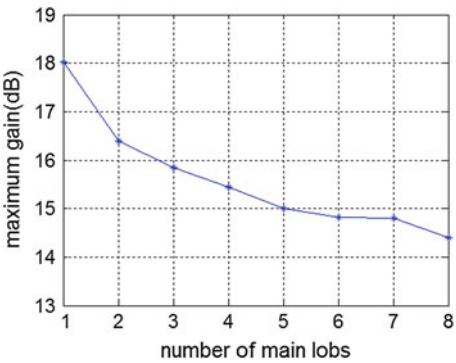

Fig. 5 Array gain and the number of main lobe

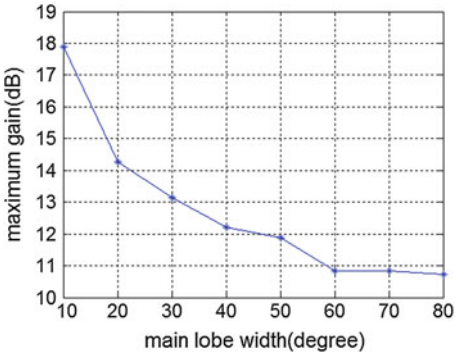

Fig. 6 Array gain and the width of main lobe

3.3.3 Search Complexity

The codebook design scheme proposed in this paper will transforms a two-dimensional matrix codebook search problem into horizontal and vertical two one-dimensional matrix codebook search problems, respectively. The number of variables of the two-dimensional codebook search problem is n^2, after the transformation, the number of variable of the one-dimensional codebook search problem dropped to n. Therefore, the scheme transforms the optimal search problem with n^2 variables into two optimal search problems with n variables. When n value is large, the search size is significantly reduced. The search speed is significantly improved.

4 Conclusion

In this paper, we propose a scheme for generating 3D codebook with arbitrary-shaped beams. This scheme not only has strong flexibility, but also can satisfy the communication requirements of different application scenarios. In addition, the method transforms a two-dimensional matrix codebook search problem into respectively horizontal and vertical two one-dimensional matrix codebook search problems. It reduces the size of search, and improves the codebook search efficiency. It produces the two-dimensional codebook by using the direct product of the codebooks of the horizontal dimension and vertical dimension. The beam generated by the codebook must be symmetric and cannot be used for asymmetric angles of main lobe beam and other asymmetric width multiple main lobes. It lacks a stronger flexibility, so we will seek better method and wider application range of arbitrarily shaped 3D codebook design scheme.

Acknowledgments This work was supported by the 863 Program of China under Grant No. 2015AA01A703, the Fundamental Research Funds for the Central Universities under grant No.2014ZD03-02, NSFC (No. 61571055,61171104), fund of SKL of MMW (No. K201501).

References

1. Laskar J, Pinel S, Dawn D et al (2007) The next wireless wave is a millimeter wave. Microwave J 50(8):22
2. Xia P, Qin X, Niu H et al (2007) Short range gigabit wireless communications systems: potentials, challenges and techniques. In: Proceedings of IEEE international conference on ultra-wideband, ICUWB, Singapore, pp. 123–128, 24–26 Sep
3. Yong SK, Chong CC (2007) An overview of multigigabit wireless through millimeter wave technology: potentials and technical challenges. EURASIP J Wireless Commun Networking 1:50–50
4. Zou W-X, Du G-L, Guo C Arbitrary shaped beamforming codebook design for millimeter-wave communications. Wireless personal communications, in press
5. Kumbar KA (2015) Adaptive beamforming smart antenna for wireless communication system. Int Res J Eng Technol 2(3):2038–2043
6. Godara LC (1997) Application of antenna arrays to mobile communications. II. Beam-forming and direction-of-arrival considerations. Proc IEEE 85(8):1195–1245
7. Van Veen BD, Buckley KM (1988) Beamforming: a versatile approach to spatial filtering. IEEE Assp Mag 5(2):4–24
8. Koppenborg J, Halbauer H, Saur S et al (2012) 3D beamforming trials with an active antenna array. In: 2012 international ITG workshop on smart antennas (WSA), pp 110–114. IEEE
9. Zhang W, Zhou X, Yang L et al (2011) 3D beamforming for wireless data centers. In: Proceedings of the 10th ACM workshop on hot topics in networks, p 4. ACM
10. Halbauer H, Saur S, Koppenborg J et al (2013) 3D beamforming: performance improvement for cellular networks. Bell Labs Tech J 18(2):37–56
11. Cheng A-Q, Wang H-L (2008) Adaptive modulation zero and interference location technology based on multi beam satellite planar array antenna beam space. Chin J Electron 36 (7):1279–1283
12. Zou W-X, Cui Z-F, Li B, Zhou Z, Hu Y-C (2012) N phases based beamforming codebook design scheme for 60 GHz wireless communication. J Beijing Univ Posts Telecommun 35(3):1–5

An Experimental Low-Complexity Noncoherent Ultra-Wideband Ranging System

Xinxin Zhu, Yue Wang, Yuling Guo, Jiayu Chen, Na Li and Bin Zhang

Abstract High-accuracy and low-complexity ranging is essential to a number of wireless applications, especially wireless localization networks. Since ultra-wideband (UWB) signals can realize accurate ranging even in harsh environments, we design and implement an experimental low-complexity noncoherent UWB ranging system. This system adopts two-way time-of-arrival (TW-ToA) ranging protocol and uses the time-to-digital-converter (TDC) to measure time difference between the transmission and the reception of ranging frames. Preliminary experimental results show that this system can achieve sub-meter ranging accuracy.

1 Introduction

Real-time and high-accuracy position information is essential to a variety of wireless applications, such as logistics, search and rescue operations, automotive safety, various military systems, internet of things (IoTs), as well as emerging wireless sensor networks (WSNs) [1]. Although global navigation satellite systems (GNSSs) are excellent solutions for many scenarios and typically have fine precision outdoors, they fail to provide the desired accuracies in harsh environments, such as in buildings, in urban canyons, under tree canopies, in caves, and under the ground, due to multipath and non-line-of-sight (NLoS) effects. In addition, GNSSs devices are usually too expensive for many applications, such as IoTs and WSNs.

Pulse-based ultra-wideband (UWB) technique has a number benefits, including accurate ranging/positioning, robustness to multipath fading, superior obstacle penetration, and low complexity/power-consumption/cost, which make pulse-based

This work was supported by the College Students' Innovation and Entrepreneurship Training Program (No. 201510065051) and the Doctor Foundation of Tianjin Normal University (No. 52XB1417).

X. Zhu · Y. Wang (✉) · Y. Guo · J. Chen · N. Li · B. Zhang
College of Electronic and Communication Engineering,
Tianjin Normal University, Tianjin 300387, China
e-mail: ywang_tjnu@163.com

Q. Liang et al. (eds.), *Proceedings of the 2015 International Conference on Communications, Signal Processing, and Systems*, Lecture Notes in Electrical Engineering 386, DOI 10.1007/978-3-662-49831-6_49

UWB an excellent signaling choice for high-accuracy localization in harsh environments [2]. In 2007, IEEE 802.15.4a standard was approved [3], which adopts pulse-based UWB signals to achieve mediate-range (<300 m) low-data-rate (110 kbps to 27.24 Mbps) communication combined high-accuracy (<1 m) localization applications, such as IoTs and WSNs.

Range-based localization is widely adopted in IoTs and WSNs, and time-based ranging can achieve high accuracy using UWB signals [4]. Although time-of-arrival (ToA) estimation using maximum likelihood (ML) estimator can asymptotically achieves the Cramr-Rao bound (CRB) in high signal-to-noise-ratio (SNR) region [5], it usually require implementation at the Nyquist sampling rate or higher, and these sampling rates can be impractical or high-cost due to the large bandwidth of UWB signals. As an alternative, non-coherent subsampling ToA estimation schemes based on energy detectors (EDs) or amplitude detectors have recently received significant attention due to their advantages, such as low complexity, low cost, and low power consumption.

In this paper, we present an experimental low-complexity UWB ranging system, which mainly uses two-way time-of-arrival (TW-ToA) ranging protocol as well as time-to-digital-converter (TDC) [6] to realize high-accuracy range measurements. This system is featured as single-pulse measurements, low-power consumption, and no need of an external counter.

This paper is organized as follows. Section 2 describes the system and node architecture as well as related implementation issues. Section 3 presents some preliminary experimental results, and Sect. 4 gives the conclusions and future research directions.

2 Architecture

This section introduces both the overall ranging system architecture with the ranging protocol and the node architecture with detailed hardware implementation.

2.1 System Architecture

As illustrated in Fig. 1, our ranging system comprises two nodes and adopts the TW-ToA ranging protocol, which does not require time synchronization between ranging nodes. Let RFRAME represent a ranging frame and assume node A needs to perform ranging with node B. Then, the procedure of the TW-ToA ranging protocol would be as follows.

(i) Node A sends a ranging request frame, $\text{RFRAME}_{\text{req}}$, to node B, and records the time instance t_1^A when the frame departs from its antenna according to its time recorder.

(ii) Node B records the time instance when it receives the $\text{RFRAME}_{\text{req}}$ at its antenna according to its time recorder. This time instance is denoted as t_1^B.

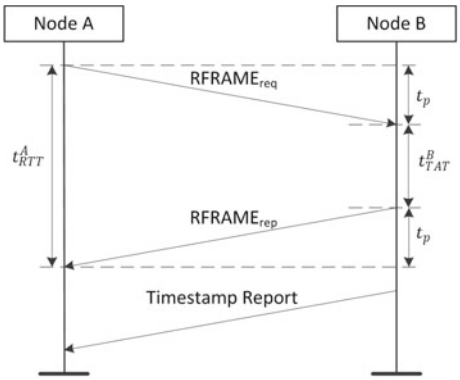

Fig. 1 Two-way time-of-arrival ranging protocol

(iii) Node B sends back to node A a ranging reply frame, RFRAME$_{rep}$, and records the time instance t_2^B when the frame departs from its antenna according to its time recorder.
(iv) Node A records the time instance when it receives the RFRAME$_{rep}$ at its antenna according to its time recorder. This time instance is denoted as t_2^A.
(v) Node A calculates the time difference between its two recorded time instances, which is called the round-trip-time (RTT), i.e., $t_{RTT}^A = t_2^A - t_1^A$.
(vi) Node B calculates the time difference between its two recorded time instances, which is called the turn-around-time (TAT), i.e., $t_{TAT}^B = t_2^B - t_1^B$. Then node B sends the value of t_{TAT}^B to node A via one timestamp report.
(vii) After receiving the timestamp report, node A computes the range using the formula $d = c \cdot (t_{RTT}^A - t_{TAT}^B)/2$, where c is the propagation speed of ranging signals.

Besides TW-ToA ranging protocol, symmetric-double-sided (SDS) TW-ToA ranging protocol [7, 8] can also be adopted using the hardware described as follows.

2.2 Node Architecture

As illustrated in Fig. 2, one ranging node mainly comprises five parts: one pulse generator, one pulse detector, one time-to-digital-convertor (TDC), one transmit/receive (T/R) switch combined one wideband antenna, and one controller. The timing of the pulse generator is determined by controller, and pulse departure time is recorded by the TDC from the pulse generator. In addition, the pulse arrive time is also recorded by the TDC from the pulse detector. Therefore, both round-trip-time and turn-around-time can be obtained, and inter-node range can be calculated using TW-ToA ranging protocol.

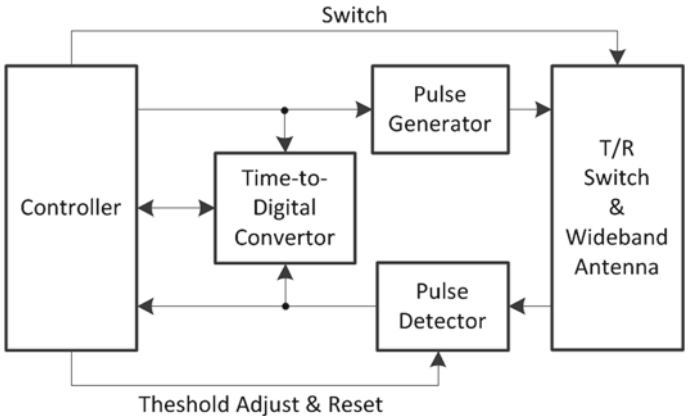

Fig. 2 Block diagram of the ranging node architecture

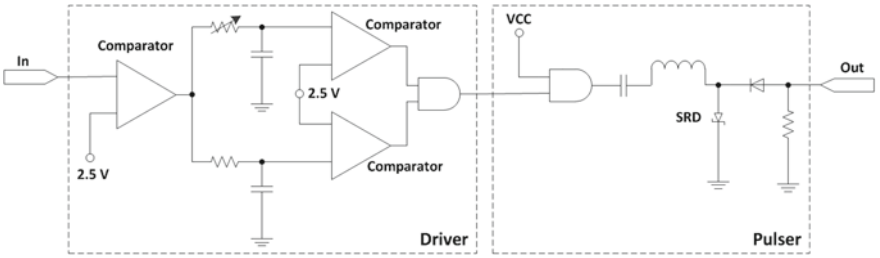

Fig. 3 Block diagram of a SRD-based pulse generator

2.3 Implemenation Issues

The pulse generator has been designed and implemented based on a step-recovery-diode (SRD) and followed a modular approach [9, 10]. The block diagram of the pulse generator is depicted in Fig. 3, which is comprised by one driver module and one pulser modules. When triggered by the rising edge of the input, the driver module produces an adjustable-duration positive pulse, whose duration can be modified by changing the value of the variable resistor. In our system, this duration has been set at approximately 200 ns. This positive pulse serves as the input for the pulser module. A BiCMOS logic buffer gate with high-drive capability in the pulser module is used to realize a current driver and its output is connected to a pulse-shaping network and to the SRD. The SRD stores charge when it is forward-biased and the stored charge is removed by the reverse current. An abrupt increment in the junction impedance occurs when all charge has been removed, which generates very fast sub-nanosecond rise or fall times. Under our circuits and triggered by the falling edge of the driving signal, a negative pulse is generated by the shunt SRD while the positive portion of this signal is canceled by the clipping diode. The particular SRD used is HP5082-0180.

As illustrated in Fig. 4, the pulse detector is a tunnel diode based threshold detector [11, 12], where tunnel diode bias can be adjusted to obtain a desired receiver operating characteristic, i.e., probability of detection versus false-alarm rate. The tunnel diode has numbers of advantages, such as requiring no bias, having an extremely broad-band and flat frequency response (extending well into millimeter waves), exhibiting excellent temperature stability (typically ±0.5 dB typical over temperature extremes), and having very low noise. As shown in Figs. 4 and 5, the tunnel diode has been used with a constant current bias source and adjusted to its bias point (or operating point), which is near and just before the peak of its *I-V* curve. Under this configuration, the tunnel diode acts as a charge sensitive device where a small amount of receive charge forces the diode to transition its negative resistance region (the transition typically measured in tens of picoseconds) to produce a large voltage swing at output. This threshold detector has one important advantage that the receive pulse shape is irrelevant, which becomes particularly advantageous in severe multipath conditions where pulse-shape distortion occurs due to time-varying frequency-selective fading. The particular tunnel diode used is obtained from General Electric, Model No. TD262A. The particular two digital-to-analog-converters (DACs) are Linear Technology, Model No. LTC1453, which have 12-bit resolution and a serial input. The particular fast comparator is Analog Devices, Model No. AD9696.

The time-to-digital-convertor is implemented using commercial chip TDC-GP2, which is produced by Acam Messlectronic Gmbn, and has 50-ps rms resolution. One Vivaldi wideband antenna is installed on each ranging node to transmit and receive ranging frames, respectively. The timing and control functions of the ranging node are performed by the controller, which is implemented by a field-programmable-gate-array (FPGA). The timing of the ranging node should be designed to prevent

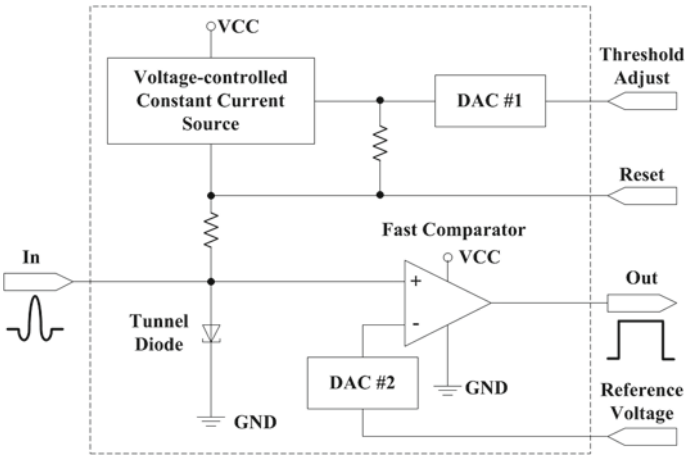

Fig. 4 Block diagram of the tunnel diode threshold detector

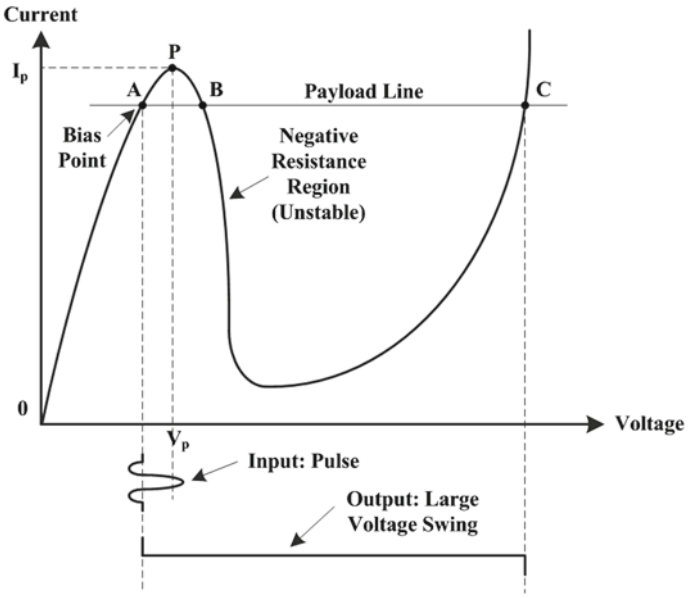

Fig. 5 Current-to-voltage (*I-V*) characteristics of a tunnel diode

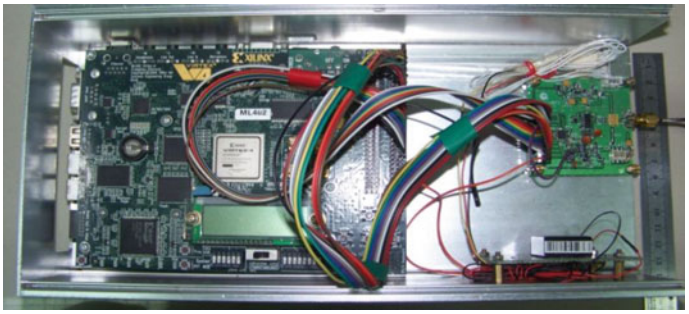

Fig. 6 Prototype of a ranging node

the self-interference, i.e., the transmitted frame is immediately received by the same node. In addition, the FPGA is also used to set the TDC and to read measurement data through the serial peripheral interface (SPI). The particular FPGA used is obtained from Xilinx, Model No. Virtex-4, and a lower power consumption and lower cost FPGA (e.g., Xilinx Artix-7 family) can replace it in our future works.

The prototype of the ranging node is shown in Fig. 6, where we use the Xilinx Virtex-4 ML402 evaluation platform as the controller, both pulse generator and detector are implemented on the same circuit board.

3 Experimental Results

Measured by Agilent Infiniium 19304 A wideband real-time sampling oscilloscope, the pulse generator provides a negative pulse with an amplitude of about −5 V and a measured fall time of about 100 ps, which is shown in Fig. 7.

We conduct some indoor ranging experiments to evaluate the performance of the implemented ranging system. The experimental setting is depicted in Fig. 8, where one signal generator implemented by the ML402 FPGA board is used to generate two trigger signals to two ranging node with controllable time difference. After receiving the stop trigger signal carried by the UWB pulse, the TDC on node A can measure the time difference between start trigger signal and stop trigger signal. Comparing this measured time difference with the presetting time difference gives the time errors.

Fig. 7 Time-domain waveform of the UWB pulse signal

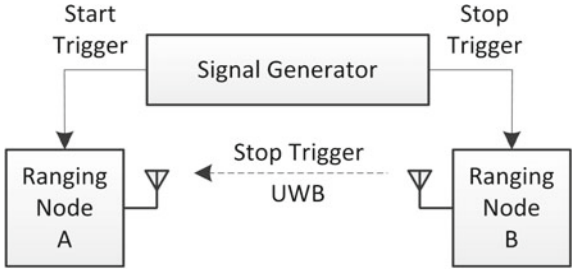

Fig. 8 Experimental settings of the UWB ranging

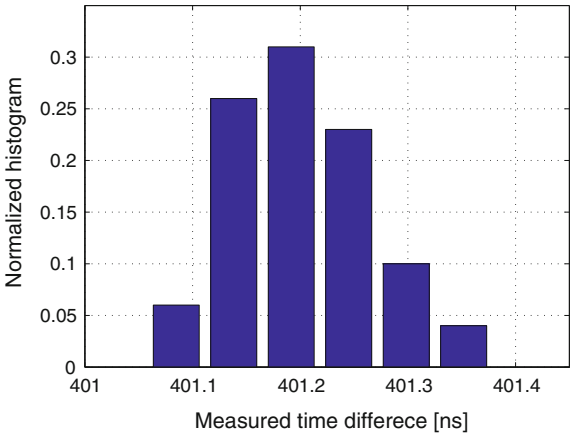

Fig. 9 Time difference measurement results for the 400 ns presetting

In addition, the inherent time delay caused by hardware of the whole system can be measured and calibrated. We set the time difference be 200, 400, 600 ns and repeatedly conduct each experiment 100 times, experimental results show that the time difference measurements are biased and all the time errors are less than 1.5 ns after the calibration. As an example, the time difference measurement results after calibration for the 400 ns presetting is depicted in Fig. 9. Therefore, the ranging error of our system using TW-ToA ranging protocol can be controlled within 1 m.

4 Conclusion

In this paper, we design and implement an experimental low-complexity noncoherent UWB ranging system, which adopts TW-ToA ranging protocol and uses the TDC to measure the time difference between the transmission and reception of ranging frames. Preliminary experimental results show that this system can achieve submeter ranging accuracy. Our future works are mainly focusing on the implementation of all the modules of the ranging node on one circuit board to reduce its size and power-consumption, self-adaptive threshold adjusting of the UWB detection module, and the accuracy measurement and analysis of ranging experiments with two nodes using TW-ToA ranging protocol and its various.

References

1. Dardari D, Luise M, Falletti E (2012) Satellite and terrestrial radio positioning techniques: a signal processing perspective. Elsevier, Oxford
2. Shen Y, Win MZ (2010) Fundamental limits of wideband localization-Part I: a general framework. IEEE Trans Info Theory 56(10):4956–4980 Oct

3. Amendment to IEEE Std. 802.15.4, IEEE Std. 802.15.4a-2007, IEEE Computer Society, Aug. 31, 2007
4. Gezici S, Poor HV (2009) Position estimation via ultra-wide-band signals. Proc IEEE 97(2):386–403
5. Dardari D, Conti A, Ferner U, Giorgetti A, Win MZ (2009) Ranging with ultrawide bandwidth signals in multipath environments. Proc IEEE 97(2):404–426
6. Song J, An Q, Liu S (2006) A high-resolution time-to-digital convertor implemented in field-programmable-gate-arrays. IEEE Trans Nucl Sci 53(1):236–241
7. Hach, R (2005) Symetric double sided- two way ranging, Technical Report, IEEE-802.15-05-0334-00-004a. http://www.mentor.ieee.org/802.15/documents
8. Xing LJ, Zhiwei L, Shin, FCP (2007) Symmetric double side two way ranging with unequal reply time. In: Proceedings of 66th IEEE Vehicular Technology Conference (VTC), Baltimore, MD, 30 Sept–3 Oct, pp 1980–1983
9. Angelis AD, Dionigi M, Giglietti R, Carbone P (2011) Experimental comparison of low-cost sub-nanosecond pulse generators. IEEE Trans Instrum Meas 60(1):310–318
10. Angelis AD, Dionigi M, Carbone P (2009) Characterization and modeling of an experimental UWB pulse-based distance measurement system. IEEE Trans Instrum Meas 58(5):1479–1486
11. Fontana RJ (2004) Recent system applications of short-pulse ultra-wideband (UWB) technology. IEEE Trans Microwave Theory Tech 52(9):2087–2104
12. Fontana RJ, Larrick JF (1999) Ultra wideband receiver with high speed noise and interference tracking threshold, U.S. Patent 5 901 172, 4 May

The Optimization of Terahertz Collimating Lens

Wang Guangzhen and Hou Yu

Abstract Terahertz is widely used in nondestructive testing, sensing, remote sensing of broadband communications, and other important key areas. However, terahertz applications must depend on the lenses or reflectors to match and couple radiation source. Based on one specified engineering requirements, the collimating optimization method is applied in this article for terahertz lens. The aspheric parameters of the surface are used as optimization parameters. A terahertz collimating plane-convex lens is designed. Results show that the designed lens conducts the terahertz radiation to the specified area with high efficiency. The lens helps the terahertz detector to receive and conduct the terahertz radiation and it fully meets the specified engineering requirements.

Keywords Terahertz · Collimating · Optimization · Lens

1 Introduction

The terahertz [1–3] has become a hot research subject for researchers. Because its wavelength is between wireless and microwave, it has the characteristics of both. To fully use the terahertz source, it requires a coupling lens for transmission and detection research. Terahertz collimating lens can meet the requirements. The design method includes complex computations, differential equations [4], and SMS [5]. But these methods are either complicate or time-consuming. In this paper, based on one specified project, optimization design [6] is used. The designed terahertz collimating lens can meet the requirements of the project more quickly and efficiently.

W. Guangzhen (✉)
Foundation Department, Tangshan University, Tangshan, Hebei 063000, China
e-mail: wanggz@opt.cn

H. Yu
Physics Department, Tangshan Normal University, Tangshan, Hebei 063000, China

Q. Liang et al. (eds.), *Proceedings of the 2015 International Conference on Communications, Signal Processing, and Systems*, Lecture Notes in Electrical Engineering 386, DOI 10.1007/978-3-662-49831-6_50

2 The Design Process

Collimating lens includes flat convex, double convex, and freeform, etc. But processing of double convex lens is relatively complex. The processing of freeform surface lens is time-consuming and expensive. Even if the engineers design a lot of excellent lenses, it is difficult to translate them into products. So conic flat convex lens is designed here, which is easy to fabricate. First, according to the requirements, set the initial structure for the flat convex lens. Then, establish the terahertz radiation source and receiving surface, which is about 250 mm, radius 1 m distance from the terahertz source. The convex conic surface is chosen as the initial structure with the diameter 300 mm. Parameters of the conic surface are conic coefficient constant k and curvature C as shown in the following:

$$k = -\frac{a^2 - b^2}{a^2} \cdot C = \frac{1}{R} = \frac{a}{b^2} \tag{1}$$

If the conic surface is hyperbolic, the parameters are shown in Fig. 1. Parameters a and b are half axis lengths of the conic surface.

Here k is 0 and C is 0.006. The terahertz radiation source emits from the origin position. Other parameters are shown in Table 1.

If the radiation source, lens, and receiver are established in the system, ray tracing can be processed. The result after ray tracing is shown in Fig. 2 using the initial structure. From Fig. 2, most of the radiation is strong converged and edge

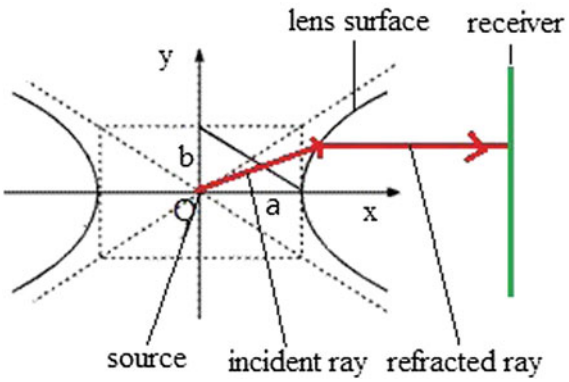

Fig. 1 Conic curve for lens surface

Table 1 Parameters of initial system

Parameter	Value
Radiation angle	40°
Wavelength	1 THz
Center thickness	50 mm
Refractive index	1.53

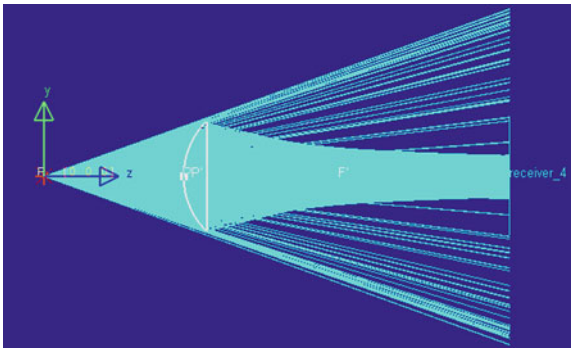

Fig. 2 The ray tracing of initial model

rays cannot reach the receiver. That is to say, the initial structure cannot realize collimating.

The next step is to optimize. Before the optimize processing, the optimize variables of the lens need to be set up. The two variables k and C are set as optimization variables. Then select the evaluation function, which is defined as follows:

$$\mathrm{MF} = \sum W_j \left(V_j - T_j\right)^2 \tag{2}$$

where W_j is a weighting factor, V_j is the current value, and T_j is the target value. The optimization process is to make the current value closer to the target value infinitely. The collimating optimization function of the software is used, which sets the direction cosine of the refracted ray 0. Finally, operate optimization program.

3 The Result

The simulation result is shown in Fig. 3. From the result, the optimization has been successfully completed. Table 2 shows the parameters of lens before and after optimization. It is found that k is –2.3409, that it a hyperboloid and C is 0.0062893. The lens diameter is 278 mm, but the effective part is 246 mm.

Fig. 3 Ray tracing after optimization

Table 2 Parameters of lens before and after optimization

Parameters of lens	Before optimization	After optimization
k	0	–2.3409
c	0.006	0.0062893
D	300 mm	278 mm

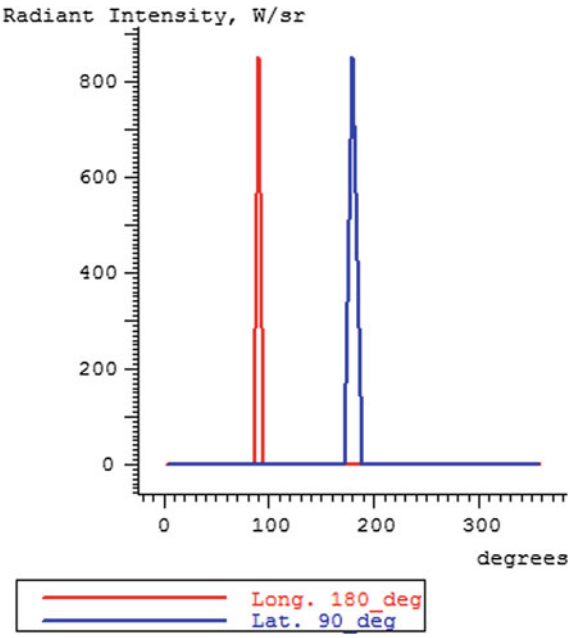

Fig. 4 Intensity map in 90° and 180° direction

In order to quantitatively describe the effect of collimation, Fig. 4 shows the intensity distribution in the position of 90° and 180°. As you can see, the radiant intensity is focused on the specified direction. The divergence angle is nearly equal to 0, which shows that the lens collimates radiation very well.

The next important item is the radiation distribution on the target surface, which shows the energy efficiency. Figure 5 shows the radiation distribution on the target surface after optimization. The efficiency is defined as the ratio of the radiation on the target to that form source. Simulation result shows that the radiation spot is concentrated in the circular area with a diameter of 250 mm. Almost all of the radiation comes to the target surface, which fully meet the engineering requirements.

For a complete optimization process, not only ray tracing but also the optimization function after several iterations is needed to be investigated. The optimization function which is also called the error function must reach a reasonable value. Its value becomes smaller during the optimization. Figure 6 is the change of

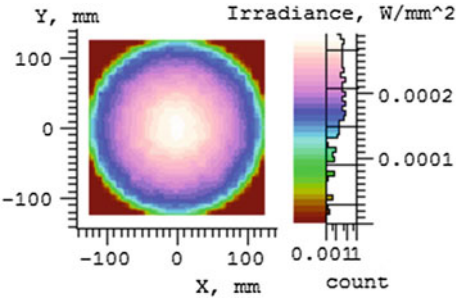

Fig. 5 Radiation distribution on the surface of the target

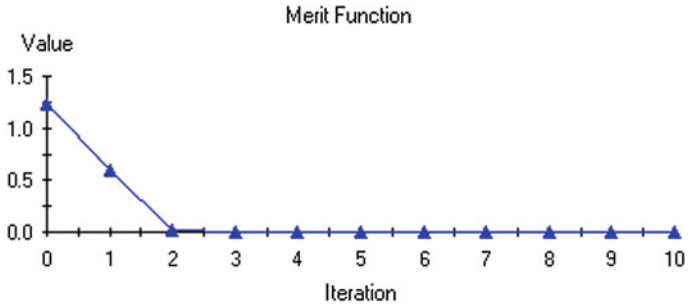

Fig. 6 Change of the evaluation function value

the optimization function in the optimization process. It can be seen, after five iterations, that the optimization function is basically kept zero.

When an evaluation function is based on the Monte Carlo ray tracing, the noise will appear. This is because statistical sampling is carried out during the ray tracing. In order to get an effective optimization, evaluation function value must be bigger than that of the noise. A smaller scope of variables can be estimated for parameter sensitivity analysis. Figure 7 shows the change of optimization function with

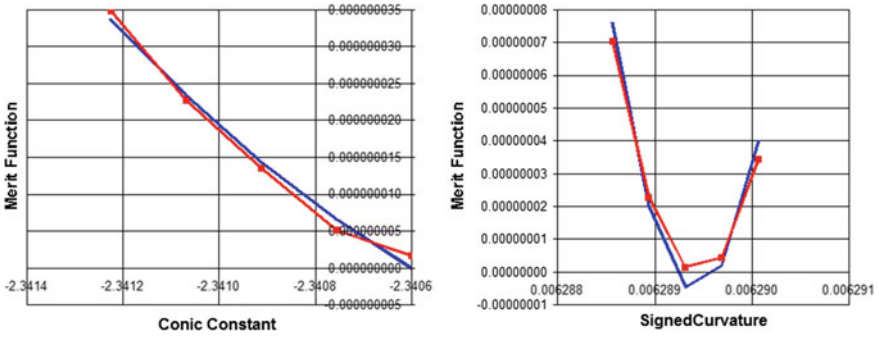

Fig. 7 Sensitivity analysis

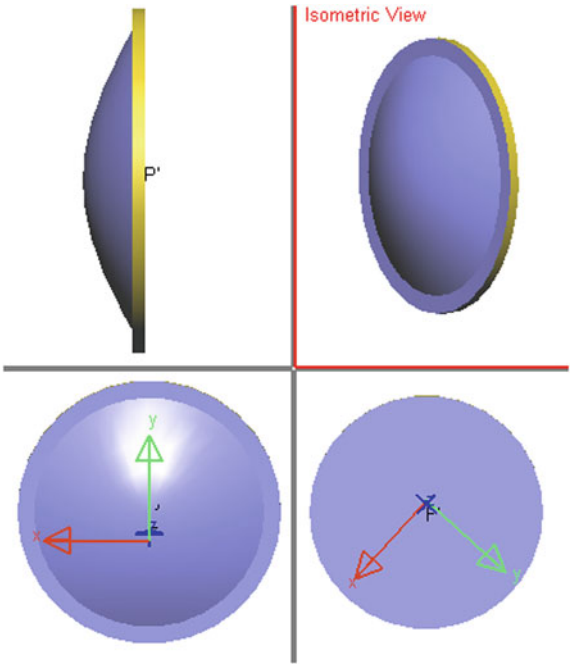

Fig. 8 The entity of the lens

changing k and C. It can be seen from the diagram, that C more likely lead the function to float, and which shows the curvature is more sensitive.

Finally, lens's flat edge is needed as in the following Fig. 8 for installation. The effective diameter of curved surface is 246 mm, edge thickness is 10 mm, and the diameter of the whole lens is 278 mm.

4 Conclusion

Collimating optimization function is used to design a lens for terahertz collimating coupling. Compared with other methods, this process is simple and timesaving without complex computation. Second, this lens satisfies the need of the specified project well. According to the requirements of this project, flat convex lens is established based on the conic surface. Then the optimization parameters are set up for several iterative optimizations. The lens surface is obtained by satisfying the requirements. The convex surface is hyperboloid, which collimates the radiation to the specified position with high efficiency after ray tracing. Finally, this lens can be fabricated much easily compared with the freeform lens.

Acknowledgment The work was jointly supported by the Doctoral Fund of Tangshan College (Grant No. tsxybc201310), Project of Science and Technology Plan of Tangshan (Grant No. 15110215a) and Doctoral Fund of Tangshan normal University (Grant No. 2014A07).

References

1. Wu Q, Zhang X-C (1995) Free-space electro-optic sampling of terahertz beams. Appl Phys Lett 67:3523–3526
2. Hou Y, Fan F, Wang X et al (2012) Terahertz switch and polarization controller based on photonic crystal fiber. Sci China-Inform Sci 55:106–113
3. Hou Y, Zhang H, Fan F et al (2012) Terahertz single-polarization single-mode hollow core fiber based on index-matching coupling. IEEE Photon Technic Let 8:637–639
4. Wang G, Wang L, Li F et al (2012) Design of optical element combining Fresnel lens with microlens array for uniform light-emitting diode lighting. J Opt Soc Am A 29:1877–1884
5. Grabovičkić1 D, Benítez P, Miñano JC (2010) Aspheric V-groove reflector design with the SMS method in two dimensions. Opt Express 18:2515–2521
6. Florian Fournier and Jannick (2008) Rolland. optimization of freeform lightpipes for light-emitting-diode projectors. Appl Opt 47:957–966

An Improved STFT Approach in Foliage Target Detection of UWB Radar Sensor Networks

Na Wu and Qilian Liang

Abstract Short-time Fourier transform (STFT) has been widely applied on non-stationary signals. In this paper, we propose two improved STFT methods namely nested sampling-based STFT (NS-STFT) algorithm and coprime sampling-based STFT (CS-STFT) algorithm. Nested sampling and coprime sampling are studied on the premise of stationary signals, but few researches has proposed for non-stationary signal, especially with the implementation of real data. Compared with existing STFT method, NS-STFT and CS-STFT can achieve the same performance with much less data, which saves the storage space. In this work, the estimation of autocorrelation is also applied. Results show that NS-STFT and CS-STFT approaches can work successfully on condition of both good quality data and poor quality data of radar echoes. In addition, the new methods can save about 50 % of the data without increasing the computation complexity.

1 Introduction

Since forests environment is a strong clutter background, ultra-wideband (UWB) radars have been employed in foliage environment because of the exception range resolution coupled with penetrating capability and low power [1, 2]. Target detection in forest environment attracted a lot of interest since it not only benefits military area, but also helps the detection in other scenarios, such as sense-through-wall. Some studies [3–5] have shown that the channel measured by UWB backscatter signals in foliage leads to inaccuracy of the K-distributions description [6], thus the signal in this condition is obvious time-varying and non-stationary. In existing works of UWB radar detection of targets in foliage, [7, 8] applied two methods, in the aspect

N. Wu (✉) · Q. Liang
Department of Electrical Engineering, University of Texas at Arlington, Arlington, TX 76019-0016, USA
e-mail: na.wu@mavs.uta.edu

Q. Liang
e-mail: liang@uta.edu

Q. Liang et al. (eds.), *Proceedings of the 2015 International Conference on Communications, Signal Processing, and Systems*, Lecture Notes in Electrical Engineering 386, DOI 10.1007/978-3-662-49831-6_51

of frequency domain and time domain, respectively. Liang and Liang [9] proves that STFT based approach is more straightforward because no threshold needs to be set.

Big data is a hot topic recently, and due to its large size, data compression becomes very important. In radar target detection, we often need to process a large amount of data. In principle, if the signal can be recovered after down sampling, the sampling rate should be larger than the Nyquist sampling rate. However, Nyquist sampling is less efficient in the background of big data, thus some sub-Nyquist sampling algorithms were studied, such as compressive sensing [10]. Among these research, a new sampling algorithm was mentioned in [11], which was systematically nesting two or more uniform linear arrays and [12] proposed coprime sampling afterward. One advantage of nested sampling and coprime sampling is that wide-sense stationary (WSS) signals sampled by these two sub-Nyquist sampling algorithm can keep the same second-order statistics and achieve enhanced degrees of freedom. Nonetheless, the signals in target detection of foliage environment are non-stationary. As a result, nested sampling and coprime sampling cannot be directly applied. Short-time Fourier transform provides a way to deal with the non-stationary signal. It segments the signal into small windows, treating each part approximate stationary. STFT determines the sinusoidal frequency and phase content of local sections of a signal as it changes over time. In this article, we combine nested sampling and coprime sampling with STFT in order to utilize them in the scenario of non-stationary signal.

Our work is based on the Foliage Penetration (FOPEN) database and the signals processed in this work are measured in late summer, fall and early winter foliage environment. If the signal data is collected using high amplitude pulses, it is called good quality signal, otherwise, it is poor quality signal. In the case of poor signal, radar sensor networks (RSN) and RAKE structure are exploited to detect the target.

The rest of this paper is outlined as follows. In Sect. 2, we give a brief overview of the experiment background. Theory of coprime sampling and nested sampling are introduced in Sect. 3. Then in Sect. 4, the details of our improved STFT methods NS-STFT and CS-SFTF are described respectively. Simulation results will be provided in Sect. 5. In Sect. 6, conclusions are presented.

2 Previous Work

In this experiment, the Barth pulse source was operated and there are two sets of data collected, good quality and poor quality. Each sample is spaced at 50 picoseconds interval, 16,000 samples were collected for each collection for a total time duration of 0.8 μs at the rate about 20 Hz. Some existing works about sense-through-foliage target detection based on these data were reported in [13, 14].

In Fig. 1, good quality signal with target and without target are plotted but it is difficult to tell the difference. If we expand views from sample 13001–15000, it is shown in Fig. 2. When there is target in the range, the difference of Fig. 2a, b will be the response of target, which is Fig. 2c. Based on the knowledge of appearance of target, we can tell that the target is around at sample 14,000. But in practice, we

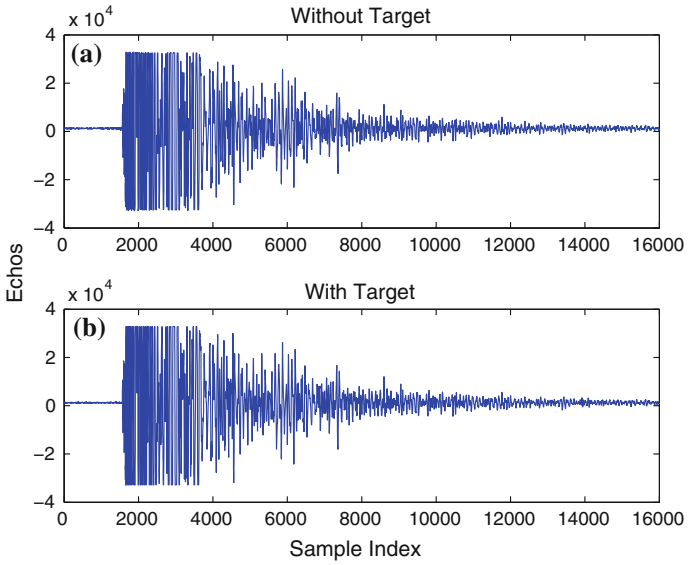

Fig. 1 Measurement with very good signal quality and 100 pulses average. **a** No target on range, **b** with target on range (target appears at around sample 14,000)

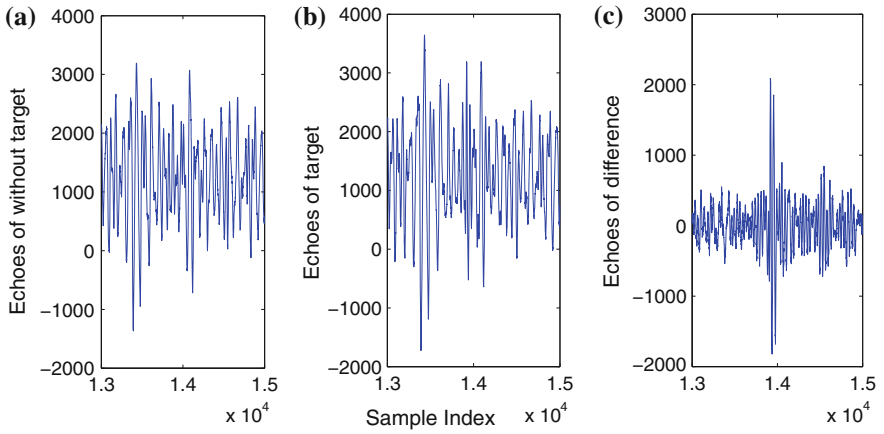

Fig. 2 Measurement with very good signal quality and 100 pulses average. **a** Expanded view of traces (with target) from samples 13,001–15,000. **b** Expanded view of traces (without target) from samples 13,001–15,000. **c** The differences between (**a**) and (**b**)

obtain clutter echoes without acquiring the knowledge about target, so the problem is how can we detect the target only rely on Fig. 2b? Moreover, if the signal quality is poor, it would be more difficult to find the position of the target.

3 Theory of Nested Sampling and Coprime Sampling

3.1 Nested Sampling

Nested sampling has been applied in beam-forming and Direction-of-Arrival [11], which is obtained by down sampling a set of data using two or more uniform linear arrays. For a two-level nested sampling of $x_c(t)$, the level 1 samples and level 2 samples are separately located at N_1 and N_2, and satisfy

$$1 \le l \le N_1 \tag{1}$$

$$(N_1 + 1)m, \quad 1 \le m \le N_2 \tag{2}$$

In Fig. 3, we give an example of two-level nested sampling.

For simplicity of describing nested sampling, several properties of nested sampling are concluded as follows:

Property 1 *Given the cross-difference* $k_n = (N_1 + 1)m - l$, $1 \le m \le N_2, 1 \le l \le N_1$, *the range of cross-differences lie in* $-[(N_1 + 1)N_2 - 1] \le k_n \le [(N_1 + 1)N_2 - 1]$.

Property 2 *There are some 'holes' in the range of cross-difference, such as* $(N_1 + 1), 2(N_1 + 1), \ldots, (N_2 - 1)(N_1 + 1)$, *which can be calculated by self differences* $(N_1 + 1)(m_1 - m_2)$, $1 \le m_1, m_2 \le N_2$.

Property 3 *For spatially wide-sense stationary signal, the correlation at all lags before nested sampling will be equal to that after nested sampling. If the signal is non-stationary, for a small period, this equality still holds.*

The proofs of Properties 1 and 2 can be referred in [12], and Property 3 is derived from the theory of STFT.

The period of nested sampling is represented as $(N_1 + 1)N_2$, for example, $N_1 = 3$ and $N_2 = 5$. It means that in each period, there are 20 values which are indicated by 8 numbers. The average sampling rate is

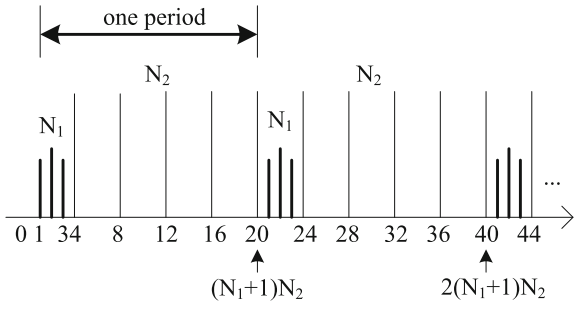

Fig. 3 Two-level of nested sampling with $N_1 = 3, N_2 = 5$

$$f_s = \frac{N_1 + N_2}{(N_1 + 1)N_2} \approx \frac{1}{N_1} + \frac{1}{N_2} \tag{3}$$

With the increasing of N_1 and N_2, the sampling rate will be smaller than the Nyquist sampling, thus causing nested sampling a Sub-Nyquist sampling.

3.2 Coprime Sampling

Different from nested sampling, coprime sampling deals with a set of data into two sets of uniformly spaced samplers MT and NT, where M and N must be mutual coprime numbers. The instance is shown in Fig. 4. After coprime sampling, the WSS signal $x_c(t)$ is divided into:

$$\begin{aligned} x_c(t) &= x(Mn) \\ x_c(t) &= x(Nn) \end{aligned} \tag{4}$$

and the difference between two sets is

$$k_c = Mn_1 - Nn_2 \tag{5}$$

which is defined as difference co-array.

From [12], we know that the range of k_c should be between

$$-MN + 1 \leq k_c \leq MN - 1 \tag{6}$$

There are also several properties of coprime sampling:

Property 4 *If* $0 \leq n_1 \leq N - 1$ *and* $0 \leq n_2 \leq M - 1$, *then* $x(n_1, n_2) = Mn_1 - Nn_2$ *can achieve* MN *distinct values in the previous range of* k_c.

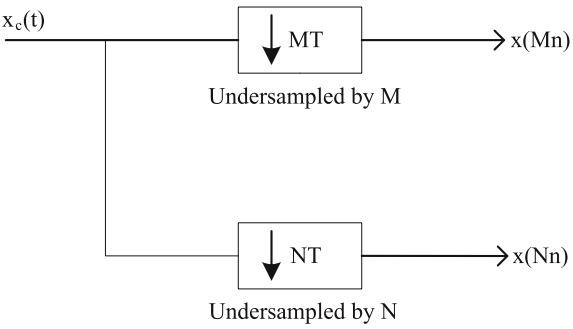

Fig. 4 Coprime sampling in the time domain using M, N

Property 5 *There are 'holes' in the difference co-array. In order to generate full range of* $[-MN+1, MN-1]$*, the ranges of* n_1 *and* n_2 *are defined as* $0 \le n_1 \le N-1$*,* $-M+1 \le n_2 \le M-1$*, and the self-difference* $Mi_1 - Mi_2$*,* $Ni_1' - Ni_2'$ *are considered.*

The average sampling rate of coprime sampling is

$$f_s = \frac{M+N}{MN} \approx \frac{1}{M} + \frac{1}{N} \tag{7}$$

when $T = 1$.

4 Coprime Sampling and Nested Sampling with STFT Based Approach in Target Detection

In this section, we present the NS-STFT algorithm and CS-STFT algorithm to realize target detection relying on much less data. From Wiener–Khinchin theorem, the relationship between autocorrelation function and power spectral density (PSD) for wide-sense stationary signal is defined below:

For discrete signal $x[n]$,

$$S(f) = \sum_{k=-\infty}^{+\infty} R_x(k) e^{-i2\pi fk} \tag{8}$$

where

$$\begin{aligned} R_x(k) &= E[x(n)x^*(n-k)] \\ &= \begin{cases} \frac{1}{N} \sum_{n=0}^{N-k-1} x(n)x^*(n-k), & 0 \le k \\ R_x(-k), & k < 0 \end{cases} \end{aligned} \tag{9}$$

and N is the length of echo x.

Another way to calculate PSD of $x(n)$ is through the N-point discrete Fourier transform (DFT),

$$X(f) = \sum_{n=0}^{N-1} x(n) e^{-i2\pi/Nkn} \tag{10}$$

$$S(f) = |X(f)|^2 \tag{11}$$

From Property 1, the cross-difference is given in the range $-[(N_1+1)N_2 - 1] \le k \le [(N_1+1)N_2 - 1]$ and thus the estimate of autocorrelation of nested sampling for all lags k can be obtained by

$$\hat{R}_n(k_n) = E[x(n)x^*(n-k)] = \frac{1}{P}\sum_{p=0}^{P-1} x(n)x^*(n-k) \tag{12}$$

and for coprime sampling, the estimate autocorrelation is [12]

$$\hat{R}_c(k_c) = \frac{1}{P}\sum_{p=0}^{P-1} x(M(n_1+Np))x^*(N(n_2+Mp)) \tag{13}$$

When target appears, the sample strength changes more abruptly, which implies that the echo contains more AC values than that without targets. In [9], the author introduced short-time Fourier transform to deal with the non-stationary signal. For a continuous-time signal, the definition of STFT is

$$Y(m,w) = \int_{-\infty}^{+\infty} x(t)w(t-m)e^{-jwt}dt \tag{14}$$

Here, $x(t)$ is the echo signal and $w(t)$ is the window function. $Y(m,w)$ represents sinusoidal values in every window at time position m. When moving the window, $x(t)$ is supposed to be stationary in corresponding window duration. The window's interval defines the frequency resolution of the STFT analysis, as a result, we should choose the window's length short so that it can approximate the signal's spectrum well.

If the signal is discrete, (14) is expressed as

$$Y(m,w) = \sum_{n=0}^{N-1} x(n)w(n-m)e^{-iwn} \tag{15}$$

There are different kinds of windows to choose, such as Gaussian window and rectangular window. No matter what kind of window is chosen, the result only represents that the PSD of the signal is changing with time. In this work, we apply a rectangular window, with the length L and step size M,

$$w(n) = \begin{cases} 1 & if \;\; 0 \le n \le L-1 \\ 0 & otherwise \end{cases} \tag{16}$$

After each step of STFT, we cumulate the power of AC values as following:

$$P(m) = \sum_{w=4}^{L-1} |Y(m,w)|^2 \tag{17}$$

Combining (11) and (15), $P(m)$ of NS-STFT and CS-STFT can be expressed as

$$P_n(m) = \sum_{w=4}^{L-1} S_n(m, w), w = 2\pi f \tag{18}$$

$$P_c(m) = \sum_{w=4}^{L-1} S_c(m, w), w = 2\pi f \tag{19}$$

where

$$\begin{aligned} S_n(m, w) &= \sum_{n=0}^{N-1} \hat{R}_n(k_n) w(n-m) e^{-iwk} \\ &= \sum_{n=0}^{N-1} \{ \frac{1}{P} \sum_{p=0}^{P-1} x(n) x^*(n-k) w(n-m) e^{-iwk} \} \end{aligned} \tag{20}$$

and

$$\begin{aligned} S_c(m, w) &= \sum_{n=0}^{N-1} \hat{R}_c(k_c) w(n-m) e^{-iwk} = \sum_{n=0}^{N-1} \\ &\{ \frac{1}{P} \sum_{p=0}^{P-1} x(M(n_1 + Np)) x^*(N(n_2 + Mp)) w(n-m) e^{-iwk} \} \end{aligned} \tag{21}$$

We detect the target through the power of AC values $P_n(m)$ and $P_c(m)$ respectively in NS-STFT method and CS-STFT method.

Several important variables in the new algorithms are listed in Table 1.

Table 1 Variables used in this section

Notations	Meaning
(M, N)	Coprime pair used in the sampling
P	Number of period of nested sampling or coprime sampling
$x(n)$	Discrete echo signal
$R(k)$	Autocorrelation of the discrete signal
$\hat{R}_n(k)$	Autocorrelation of the nested sampling signal
$\hat{R}_c(k)$	Autocorrelation of the coprime sampling signal
$S_n(m, w), S_c(m, w)$	Power spectral density
$P_n(m), P_c(m)$	power of AC values

5 Experimental Results of Good Quality Data and Poor Quality Data

5.1 NS-STFT Approach

Firstly, we show the results of existing STFT method in Fig. 5. Along with the moving of slicing window, we can acquire the power values of the echo $P(m)$ from sample 10,000–15,000. In [15], it has pointed out that generally the clutter has Gaussian distribution in the frequency domain. Therefore, when there is a target in the range, the power of AC values will behave like random noise. In Fig. 5a, b, we plot the good quality signal. It is clearly to see that in Fig. 5b, when there is target on range, the curve around 14,000 sample index is smooth. But in Fig. 5a, the curve is like chaotic impulses.

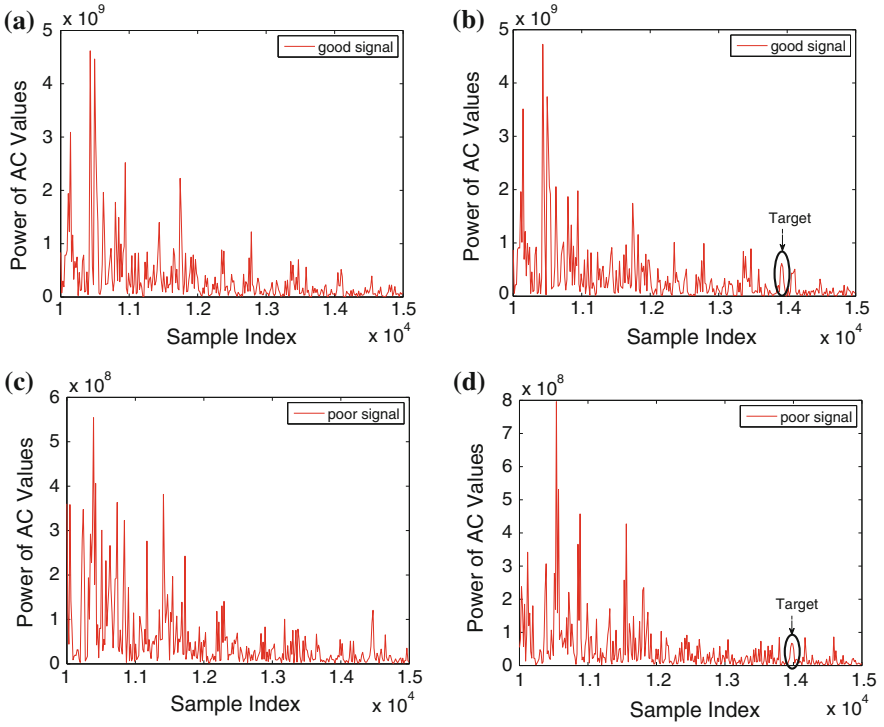

Fig. 5 The power of AC values versus sample index of good quality data with window length $L = 30$, step size $M = 16$ and poor quality data with window length $L = 25$, step size $M = 15$. **a**, **b** No target on range, **c**, **d** with target on range

For the poor quality of data, since pulse-to-pulse variability exists in the echoes at different time or different site, we rely on radar sensor networks (RSN) to solve this problem. In this paper, the RAKE structure proposed in [9] is chosen and the power of AC values are plotted in Fig. 5c, d, where the target is circled in the figure.

According to (20), we can plot the power spectral density of NS-STFT approach and the results are shown in Fig. 6. As Property 3 states, the autocorrelation $\hat{R}_n$ will approximately equal to R_x, so we can detect the target based on (20). From the simulations we find that the window length L will affect the performance of target detection. When NS-STFT approach is employed on good quality data, $L = 24$ is a little smaller than 30. This is because the existing variations of estimated autocorrelation.

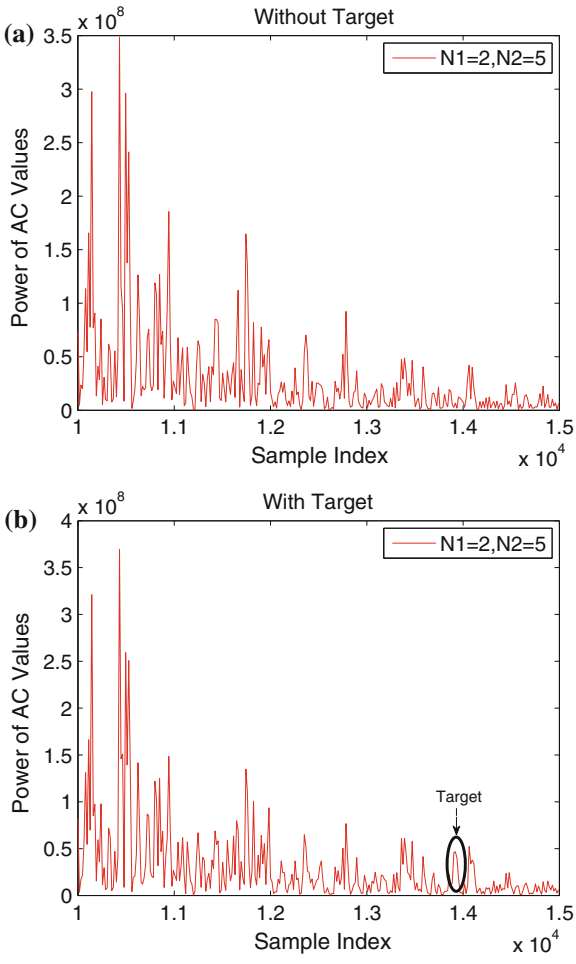

Fig. 6 The power of AC values versus sample index of good quality data after nested sampling, with sampling pairs $N_1 = 2, N_2 = 5$. **a** No target on range, **b** with target on range (target appears at around sample 14,000)

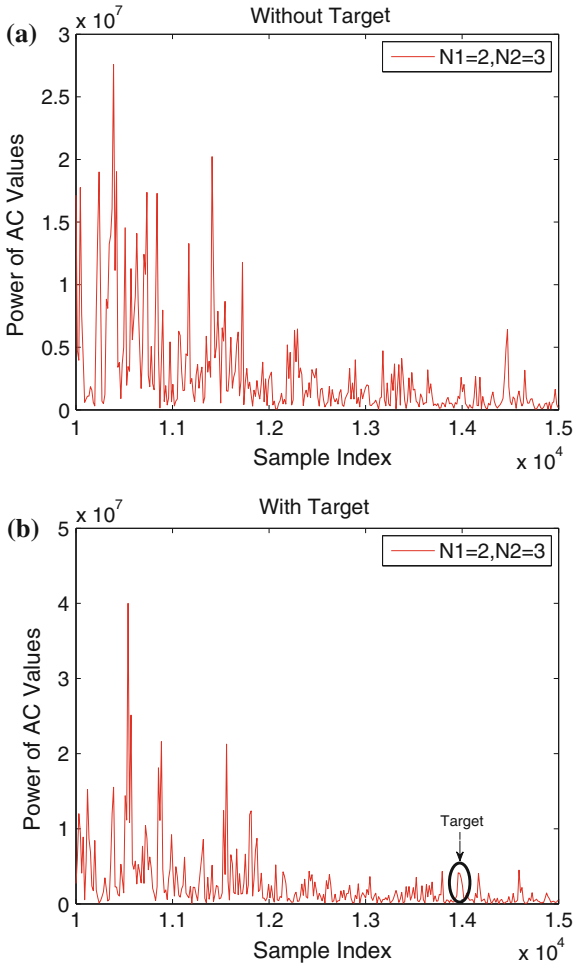

Fig. 7 The power of AC values versus sample index of poor quality data after nested sampling, with sampling pairs $N_1 = 2, N_2 = 3$. **a** No target on range, **b** with target on range (target appears at around sample 14,000)

Based on the sampling rate (3), we can calculate the compression ratio of nested sampling. For example, in Fig. 7a, the pair of nested sampling is $N_1 = 2, N_2 = 5$. Therefore, the compression ratio is decreased to about 46.67 %, this saves almost half of the space, which is quite desirable for large amount of data.

5.2 CS-STFT Approach

The results of CS-STFT on good quality data and poor quality data are presented in Figs. 8 and 9. For good data, coprime pairs $M = 3, N = 4$ are chosen and for poor quality signal, we use the sampling pair (2, 3). When target appears, the curve around

14,000 behaves like a Gaussian pdf as circled in Figs. 8b and 9b. The window length L in CS-STFT method is almost the same as in NS-STFT method, which is 23 for good quality data. The compression ratio of coprime sampling in Fig. 8 could be calculated by (7) and it is 58.3 %. If the sampling rate f_s keeps increasing, the window length L must decrease. However, in the case of poor quality signal, compression becomes more difficult since there will be more noise included in the data, so we only choose the sampling pair (2, 3).

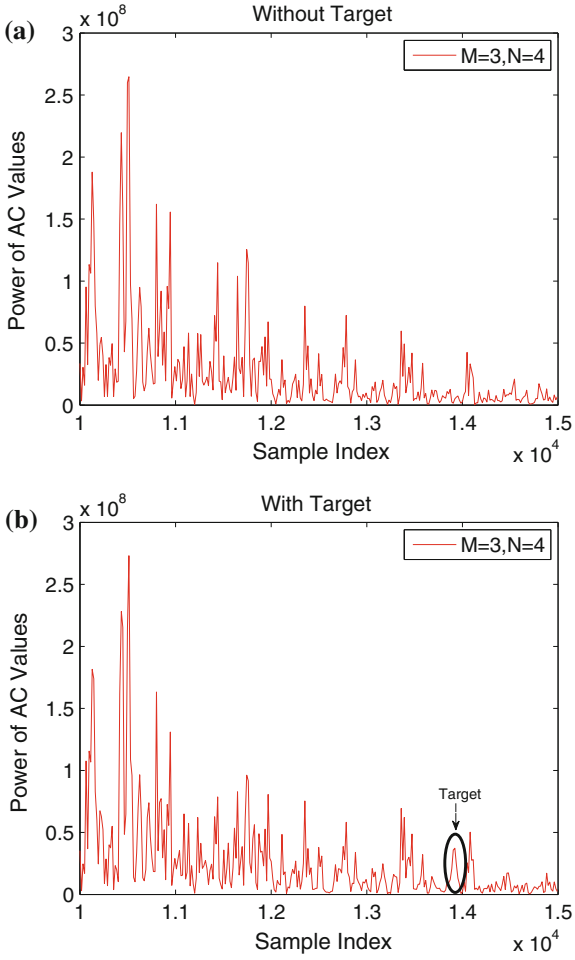

Fig. 8 The power of AC values versus sample index of good quality data after coprime sampling, with sampling pairs $M = 3, N = 4$. **a** No target on range, **b** with target on range (target appears at around sample 14,000)

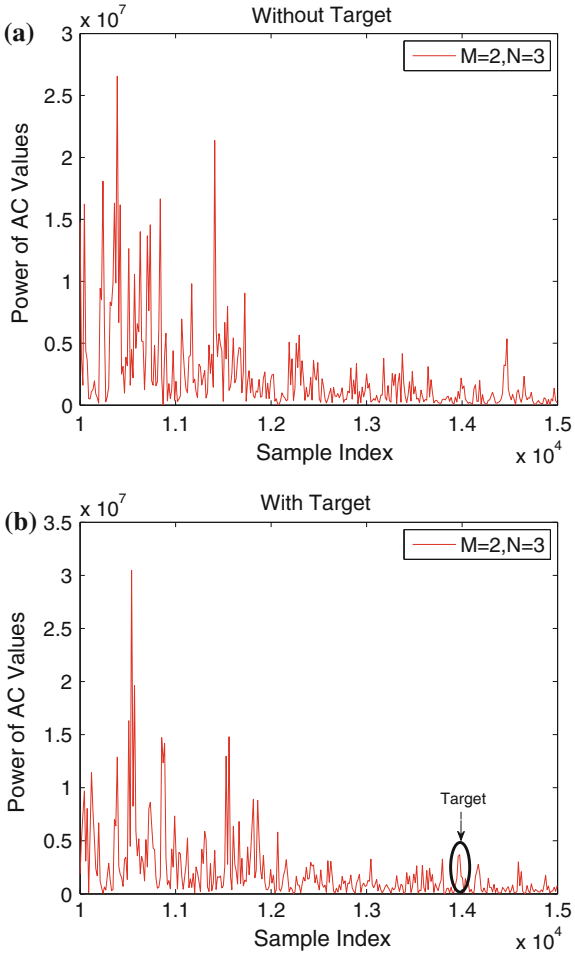

Fig. 9 The power of AC values versus sample index of poor quality data after coprime sampling, with sampling pairs $M = 2, N = 3$. **a** No target on range, **b** with target on range (target appears at around sample 14,000)

6 Conclusion

In this paper, we develop two target detection algorithms in foliage environment, which are NS-STFT approach and CS-STFT approach. Since nested sampling and coprime sampling are sub-Nyquist sampling, the NS-STFT methods and CS-STFT method can save about half the quantity of the data comparing with the original approach. The results show that as long as we choose suitable window length and step size, the new methods can achieve the same performance. The window length falls when the sampling frequency increases. The poorer the quality of the signal is, the more difficult to compress. Besides, if the signal quality is poor, with the help of RSN and RAKE structure, it is easy to detect target on range intuitively. In our

future research, the extended application of nested sampling and coprime sampling on non-stationary signal will be studied further.

Acknowledgments This work was supported in part by U.S. Office of Naval Research under Grants N00014-13-1-0043, N00014-11-1-0865, and U.S. National Science Foundation under Grants CNS-1247848, CNS-1116749, CNS-0964713. The authors would like to thank Dr. Sherwood W. Samn in Air Force Research Laboratory for providing the sense-through-foliage data used in this paper.

References

1. Ferrell B (1994) Ultrawideband foliage penetration measurements. In: Radar conference, 1994, Record of the 1994 IEEE National. IEEE
2. Xu X, Narayanan RM (2001) FOPEN SAR imaging using UWB step-frequency and random noise waveforms. IEEE Trans Aerosp Electron Syst 37(4):1287–1300
3. Fleischman JG, Ayasli S, Adams EM, Gosselin DR (1996) Foliage attenuation and backscatter analysis of SAR imagery. IEEE Trans Aerosp Electron Syst 32(1, part 3):135–144
4. Mccorkle JW (1993) Early results from the Army Research Laboratory ultrawide-bandwidth foliage penetration SAR. Underground and obscured object imaging and detection, April 1993, Orlando, Fla, USA, Proceedings of SPIE 1942
5. Sheen DR, Malinas NP, Kletzli DW, Lewis TB, Roman JF (1994) Foliage transmission measurements using a ground-based ultrawide band (300–1300 MHz) SAR system. IEEE Trans Geosci Remote Sens 32(1):118–130
6. Watts S (1987) Radar detection prediction in K-distributed sea clutter and thermal noise. IEEE Trans Aerosp Electron Syst 23:40–45
7. Liang Q, Samn SW, Cheng X (2008) UWB radar sensor networks for sensethrough-foliage target detection. In: IEEE 205 international conference on communications. ICC08. IEEE, pp 2228–2232
8. Liang J, Liang Q (2008) A differential based approach for sense-through-foliage 210 target detection using UWB radar sensor networks. In: IEEE international conference on communications. ICC08. IEEE, pp 1952–1956
9. Liang J, Liang Q (2009) UWB radar sensor networks detection of targets in foliage using short-time Fourier transform. In: Proceedings of the 2009 IEEE international conference on communications. IEEE Press
10. Cands EJ, Michael BW (2008) An introduction to compressive sampling. Signal Process Mag, IEEE 25.2 (2008): 21–30
11. Pal P, Vaidyanathan PP (2010) Nested arrays: a novel approach to array processing with enhanced degrees of freedom. IEEE Trans Signal Process 58(8):4167–4181
12. Vaidyanathan PP, Pal P (2011) Sparse sensing with co-prime samplers and arrays. IEEE Trans Signal Process 59(2):573–586
13. Liang J, Liang Q (2010) Sense-through-foliage target detection using UWB radar sensor networks. Pattern Recognit Lett 31(11):1412–1421
14. Liang Q, Zhang B, Wu X (2012) UWB radar for target detection: DCT versus matched filter approaches. In: Globecom workshops (GC Wkshps), 2012 IEEE. IEEE
15. Barton DK (2005) Radar system analysis and modeling. Artech House, Norwood

Part VIII
Localization and Tracking

Effect of Inaccurate Range Measurements on Hybrid TOA/RSS Linear Least Squares Localization

Xinxin Zhu, Yue Wang, Yuling Guo, Jiayu Chen, Na Li and Bin Zhang

Abstract Linear least squares (LLS) estimation is a sub-optimum but low-complexity localization method based on measurements of location-related parameters. It has been proved that hybridization of different types of measurements can enhance localization accuracy from Cramer-Rao lower bound (CRLB) analysis. In this paper, a hybrid time-of-arrival and received-signal-strength (TOA/RSS) LLS localization algorithm is derived, where TOA-based ranging has higher accuracy than RSS-based ranging. In many situations such as the case investigated in this paper, accuracies of different measurements are difficult to obtain, and hence no weighting factors are applied to different ranging measurements. In this case, incorporating extra inaccurate measurements into hybrid TOA/RSS LLS localization may degrade its original localization accuracy in some scenarios. Simulation results confirm the theoretical analysis and show that signal-to-noise ratio, path-loss exponent, anchors placement, as well as geometric relation between the agent and anchors all affect the hybrid TOA/RSS LLS localization accuracy in different ways.

1 Introduction

Real-time and high-accuracy position information is essential to a variety of wireless applications [1]. Range information is usually adopted and it can be measured from time-of-arrival (TOA) or received-signal-strength (RSS) estimates [2]. If the information about the measured range variances is unavailable, a nonlinear least squares (NLS) estimator can be obtained by assuming the variances are identical and using uniform weighting. Solving the NLS problem requires an explicit minimization of

This work was supported by the College Students' Innovation and Entrepreneurship Training Program (No. 201510065051) and the Doctor Foundation of Tianjin Normal University (No. 52XB1417).

X. Zhu · Y. Wang (✉) · Y. Guo · J. Chen · N. Li · B. Zhang
College of Electronic and Communication Engineering,
Tianjin Normal University, Tianjin 300387, China
e-mail: ywang_tjnu@163.com

Q. Liang et al. (eds.), *Proceedings of the 2015 International Conference on Communications, Signal Processing, and Systems*, Lecture Notes in Electrical Engineering 386, DOI 10.1007/978-3-662-49831-6_52

a nonlinear cost function, which cannot in general be solved analytically. In order to obtain a closed form solution and avoid explicit minimization of the NLS cost function, the nonlinear expressions of observations can be linearized using the least squares (LS) calibration method [3]. An alternative way for linear least squares (LLS) solution based on subtraction of the reference measured range is discussed in [4]. Moreover, the LLS localization performance for both line-of-sight (LOS) and non-line-of-sight (NLOS) cases is studied in [5]. Although LLS estimation is a sub-optimum localization technique [6], it usually has a reasonable localization accuracy and lower implementation complexity.

Hybrid localization techniques [1, 7], such as hybrid TOA/RSS, TDOA/RSS, TOA/TDOA, and TDOA/AOA techniques, are proposed to enhance localization accuracy and gives alternatives for the lack of location-related parameters. Although the analysis of CRLB shows that incorporating extra location-related measurements into the location estimator can improve its localization accuracy and extra accurate location-related measurements can drastically improve the original localization accuracy when the original location-related measurements are inaccurate, there is no study focusing on whether LLS localization technique can still benefit from fusion with extra inaccurate measurements, to the best of our knowledge.

In this paper, we take hybrid TOA/RSS LLS localization technique for example to analyze the effect of inaccurate measurements on hybrid LLS localization systems. A hybrid TOA/RSS LLS localization algorithm is introduced. In many situations such as the case investigated in this paper, accuracies of different measurements are difficult to obtain, and hence no weighting factors are applied to different ranging measurements. In this case, incorporating extra inaccurate measurements into hybrid TOA/RSS LLS localization may degrade its original localization accuracy in some scenarios. Simulation results confirm the theoretical analysis and show that signal-to-noise ratio, path-loss exponent, anchors placement, as well as geometric relation between the agent and anchors all affect the hybrid TOA/RSS LLS localization accuracy in different ways.

The rest of the paper is organized as follows. Section 2 introduces and analyzes the hybrid TOA/RSS LLS localization algorithm. Section 3 gives numerical simulation results and discussions. A conclusion in Sect. 4 wraps up this paper.

2 Hybrid TOA/RSS LLS Localization

We assume that the agent is connected to different anchors, which are able to measure the range between the agent and anchors via two types of parameters, i.e., TOA and RSS. Let N be the total number of all anchors in the hybrid localization system. Without loss of generality, we assume that the agent can measure TOA-based ranges from anchors with indexes $i \in \{1, 2, \ldots, S\}$ and measure RSS-based ranges from anchors with indexes $i \in \{S+1, S+2, \ldots, N\}$ $(S \leq N)$.

In the first step of two-step localization method, the range measurement between the agent and the ith $(i = 1, 2, \ldots, N)$ anchor is denoted as $\hat{d}_i$. Let $\mathbf{p} = [x\ y]^T$ be the

unknown two-dimensional (2-D) position of the agent, which is to be estimated, and let $\mathbf{p}_i = [x_i\ y_i]^T$ be the known 2-D coordinate of the ith anchor. The error-free range between the agent and the ith anchor is given by

$$d_i = \|\mathbf{p} - \mathbf{p}_i\| = \sqrt{(x - x_i)^2 + (y - y_i)^2}.$$

The range measurement is modeled as

$$\hat{d}_i = d_i + n_i, \tag{1}$$

where n_i is the ranging error in $\hat{d}_i$, which results from TOA or RSS estimation disturbance. It is assumed that $\{n_i\}$ are zero-mean independent Gaussian processes with variances $\{\sigma_i^2\}$.

For TOA-based ranging, we can adopt two-way TOA ranging protocol [2] and the range can be calculated as

$$\hat{d} = c \cdot \frac{\hat{\tau}_{\mathrm{RTT}} - \hat{\tau}_{\mathrm{TAT}}}{2},$$

where c is the propagation speed of ranging signals, $\hat{\tau}_{\mathrm{RTT}}$ is measured round-trip-time at the ranging start node, and $\hat{\tau}_{\mathrm{TAT}}$ is measured turn-around-time at the ranging respond node. Ideally, the CRLB of mean square ranging error from the ith ($i \in \{1, 2, \ldots, S\}$) anchor in additive white Gaussian noise (AWGN) channel is [1]

$$\sigma^2_{i,\mathrm{CRLB,TOA}} = \frac{c^2}{8\pi^2 \mathrm{SNR}_i \beta^2}, \tag{2}$$

where $\mathrm{SNR}_i = \mathscr{E}_i / \mathscr{N}_0$ is SNR from the ith anchor with $\mathscr{E}_i$ denoting the received-signal energy and $\mathscr{N}_0$ denoting the one-side power spectral density of AWGN, and β is the effective signal bandwidth defined by

$$\beta = \left(\frac{\int_{-\infty}^{+\infty} f^2 |K(f)|^2 df}{\int_{-\infty}^{+\infty} |K(f)|^2 df} \right)^{1/2}$$

with $K(f)$ denoting the Fourier transform of the ranging signal. When adopting ultra-wideband (UWB) signals for ranging, high-accuracy range measurements can be achieved even in harsh multipath environments, such as in buildings, in urban canyons, under tree canopies, and in caves [8].

For RSS-based ranging, a common model used to calculate range from path-loss is given by

$$\bar{P}_r(d) = P_0 - 10\gamma \log_{10}(d/d_0) + V,$$

where $\bar{P}_r(d)$ is the average received power in decibels at a distance d, P_0 is the received power in decibels at a short reference distance d_0, γ is the path-loss exponent

that typically assumes values between 2 and 6, and V represents the large-scale fading variations (i.e., shadowing) in decibels, which is commonly modeled as a Gaussian random variable with zero mean and standard deviation σ_{sh} [2]. The CRLB of mean square ranging error from the ith ($i \in \{S+1, S+2, \ldots, N\}$) anchor is [1]

$$\sigma^2_{i,\text{CRLB,RSS}} = \left(\frac{(\ln 10)\sigma_{\text{sh}} d_i}{10\gamma}\right)^2. \tag{3}$$

It is quite challenging to obtain the exact relation between them in a practical wireless environment due to complicated propagation mechanisms. Therefore, RSS-based ranging commonly has low accuracy.

In the second step of two-step localization method, we adopt the LS calibration method [3] to convert the range measurements into linear models in $\mathbf{p}$ and give a close form location estimate $\hat{\mathbf{p}}$. We introduce a dummy variable $R = x^2 + y^2$ and define $\theta \triangleq [x\ y\ R]^T$. Then, the LLS estimate of θ is give by

$$\hat{\theta} = \left(\mathbf{A}^T\mathbf{A}\right)^{-1}\mathbf{A}^T\mathbf{b}, \tag{4}$$

where

$$\mathbf{A} = \begin{bmatrix} -2x_1 & -2y_1 & 1 \\ -2x_2 & -2y_2 & 1 \\ \vdots & \vdots & \vdots \\ -2x_N & -2y_N & 1 \end{bmatrix},\ \mathbf{b} = \begin{bmatrix} \hat{d}_1^2 - x_1^2 - y_1^2 \\ \hat{d}_2^2 - x_2^2 - y_2^2 \\ \vdots \\ \hat{d}_N^2 - x_N^2 - y_N^2 \end{bmatrix}.$$

The hybrid TOA/RSS LLS location estimate is simply extracted from the first and second entries of $\hat{\theta}$, that is

$$\hat{\mathbf{p}}_{\text{TOA/RSS}} = \left[[\hat{\theta}]_1\ [\hat{\theta}]_2\right]^T. \tag{5}$$

On the other hand, non-hybrid TOA LLS localization techniques can also uniquely determine the 2-D position of the agent with S ($S \geq 3$) anchors. Similar to the hybrid TOA/RSS LLS localization result shown in (4) and (5), the location estimates of the agent based on non-hybrid TOA LLS localization technique is

$$\hat{\mathbf{p}}_{\text{TOA}} = \left[[\hat{\theta}']_1\ [\hat{\theta}']_2\right]^T,$$

where

$$\hat{\theta}' = \left(\mathbf{A}'^T\mathbf{A}'\right)^{-1}\mathbf{A}'^T\mathbf{b}',$$

$$\mathbf{A}' = \begin{bmatrix} -2x_1 & -2y_1 & 1 \\ -2x_2 & -2y_2 & 1 \\ \vdots & \vdots & \vdots \\ -2x_S & -2y_S & 1 \end{bmatrix},\ \mathbf{b}' = \begin{bmatrix} \hat{d}_1^2 - x_1^2 - y_1^2 \\ \hat{d}_2^2 - x_2^2 - y_2^2 \\ \vdots \\ \hat{d}_S^2 - x_S^2 - y_S^2 \end{bmatrix}.$$

Note that there is no method (e.g., weighting factor) in hybrid TOA/RSS LLS localization technique to control the effect of each measurement on the whole localization accuracy, and this may be due to that the priori information about variances of all measurements is unavailable. Therefore, incorporating inaccurate measurements to original accurate measurements can improve the original localization accuracy if extra position-related information is properly exploited. On the other hand, incorporating inaccurate measurements may degrade the original localization performance when no weighting parameters are applied in hybrid TOA/RSS LLS localization technique.

3 Numerical Simulation Results

A hybrid network with $N = 8$ anchors is used to localize one agent. The area is a square of $L \times L$ m^2 and L is fixed to 10 m. There are two sets of anchors (set I and set II). Set I contains $S = 4$ TOA-based ranging anchors located at $(0, 0)$, $(L, 0)$, (L, L), and $(0, L)$, respectively. Set II contains $N - S = 4$ RSS-based ranging anchors located at $(L/2, 0)$, $(L, L/2)$, $(L/2, L)$, and $(0, L/2)$, respectively. We randomly set the agent location at $(2, 3)$ for example unless otherwise specified.

According to (2) and [1], we simply assume that the agent and anchors have the same configuration and let TOA-based ranging error variance $\sigma^2_{\mathrm{TOA},i}$ be reversely proportional to SNR_i, which is

$$\sigma^2_{\mathrm{TOA},i} = \frac{1}{\mathrm{SNR}_i} = \frac{1}{\mathrm{SNR}_0}\left(\frac{d_i}{d_0}\right)^{\gamma},\ i \in \{1, 2, \ldots, S\},$$

where SNR_0 is the SNR at the reference distance d_0, and γ is the path-loss exponent. According to (3) and [9], we simply assume RSS-based ranging error variance $\sigma^2_{\mathrm{RSS},i}$ as

$$\sigma^2_{\mathrm{RSS},i} = \frac{\eta^2}{\mathrm{SNR}_i} = \frac{\eta^2}{\mathrm{SNR}_0}\left(\frac{d_i}{d_0}\right)^{\gamma},\ i \in \{S+1, S+2, \ldots, N\},$$

where η ($\eta \geq 1$) controls the relation between the two ranging error variances since TOA-based ranging usually has higher accuracy than RSS-based ranging, especially when adopting UWB signals. In the following simulations, we assume $d_0 = 1$, $\mathrm{SNR}_0 \in [20 : 60]$ dB with increasing step $\Delta = 5$ dB, and $\gamma = 2$ unless otherwise specified. We set η to be $\{1, 2, 3, 4\}$, respectively, and compare localization accuracy of hybrid TOA/RSS LLS localization technique with that of non-hybrid TOA LLS localization technique. For each simulation setting, 10^4 simulations are run to get the average performance.

The mean square position error (MSPE) versus SNR_0 for non-hybrid TOA and hybrid TOA/RSS LLS localization techniques is illustrated in Fig. 1. It is clear that larger η leads to worse hybrid localization performance since lesser accurate RSS-based range measurements are equally fused with accurate TOA-based range

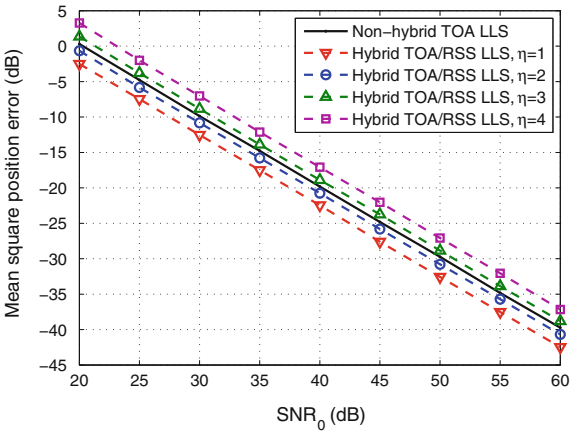

Fig. 1 Mean square position error (dB) comparison between non-hybrid TOA and hybrid TOA/RSS LLS localization, the agent locates at $(2, 3)$, $\gamma = 2$

measurements. When the RSS-based ranging is comparably accurate as the TOA-based ranging, i.e., $\eta = 1, 2$, the hybrid TOA/RSS LLS localization outperforms the non-hybrid TOA LLS localization since more location-related information from different anchors is obtained. On the other hand, if the RSS-based ranging is inaccurate compared with the TOA-based ranging, i.e., $\eta = 3, 4$, the localization accuracy degrades after incorporating inaccurate RSS-based range measurements to accurate TOA-based range measurements. This confirms our intuitive observation and is due to the fact that no weighting factors are applied to the hybrid TOA/RSS LLS localization algorithm.

Since the absolute difference between TOA-based and RSS-based ranging variances increases if the path-loss exponent increases. For example, we change the path-loss exponent γ from 2 to 4, which represents some indoor scenarios, and rerun the previous simulation. MSPE in decibels comparison and absolute MSPE comparison are depicted in Fig. 2. Since the path-loss exponent becomes larger, we narrow the SNR_0 range down to $[40 : 60]$ dB to get reasonable localization results. In Fig. 2, the MSPE becomes larger for each SNR_0 value compared with Fig. 1 since larger path-loss leads to larger variances of the ranging estimates for both TOA-based and RSS-based range estimations. Note that the inaccurate RSS-based range measurements ($\eta = 3$) becomes unharmful to the hybrid TOA/RSS LLS localization accuracy, which is a contrast to the case in Fig. 1. This seems counterintuitive as well as opposite to the above analysis that larger path-loss exponent leads to larger absolute difference between TOA-based and RSS-based ranging variances under the same distance condition, thus leads to larger absolute MSPE difference. However, another impact factor is anchors placement. Due to the fact that the anchors in set II (distance $L/2$ from the center) cover the area better than the anchors in set I (distance $\sqrt{2}L/2$ from the center) [10], the path-loss magnification effect from the anchors in set I is larger than that from the anchors in set II, thus the RSS-based ranging variances do not increase as much as the TOA-based ranging variances. Therefore, the positive effect due to anchors placement cancels the negative effect due to larger absolute

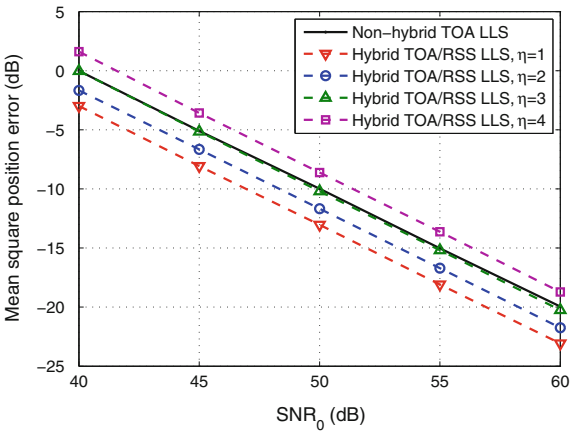

Fig. 2 Mean square position error (dB) comparison between non-hybrid TOA and hybrid TOA/RSS LLS localization, the agent locates at $(2, 3)$, $\gamma = 4$

ranging variance difference, and the overall effect of adding extra inaccurate RSS-based ranging with $\eta = 3$ on hybrid TOA/RSS LLS localization accuracy is marginal compared with non-hybrid TOA LLS localization.

Furthermore, the geometric relation between the agent and anchors can also influence the effect of inaccurate measurements on hybrid TOA/RSS LLS localization technique. For example, we change location of the agent from $(2, 3)$ to $(4, 5)$ and rerun the simulation as in Fig. 1. The localization performance comparison is depicted in Fig. 3, where the MSPE becomes smaller for each SNR_0 value compared with Fig. 1 and inaccurate RSS-based range measurements with $\eta = 3$ do not lead to lower accuracy of hybrid TOA/RSS LLS localization than non-hybrid TOA LLS localization, which is an opposite result to Fig. 1.

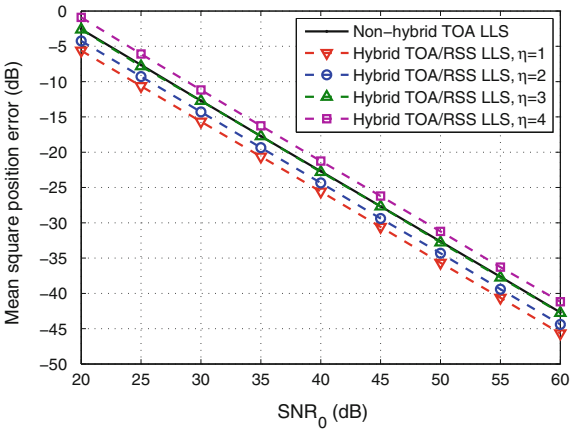

Fig. 3 Mean square position error (dB) comparison between non-hybrid TOA and hybrid TOA/RSS LLS localization, the agent locates at $(4, 5)$, $\gamma = 2$

4 Conclusions

Incorporating extra inaccurate measurements into hybrid TOA/RSS LLS localization may degrade its original localization accuracy in some scenarios, if no weighting factors are applied to different ranging measurements in the corresponding hybrid TOA/RSS LLS localization algorithm. Moreover, signal-to-noise ratio, path-loss exponent, anchors placement, as well as geometric relation between the agent and anchors all affect the hybrid TOA/RSS LLS localization accuracy in different ways.

References

1. Dardari D, Luise M, Falletti E (2012) Satellite and terrestrial radio positioning techniques: a signal processing perspective. Elsevier, Oxford
2. Dardari D, Conti A, Ferner U, Giorgetti A, Win MZ (2009) Ranging with ultrawide bandwidth signals in multipath environments. Proc IEEE 97(2):404–426
3. Chen JC, Hudson RE, Yao K (2002) Maximum-likelihood source localization and unknown sensor location estimation for wideband signals in the near field. IEEE Trans Signal Process 50(8):1843–1854
4. Guvenc I, Gezici S, Watanabe F, Inamura, H (2008) Enhancements to linear least squares localization through reference selection and ML estimation. In: Proceedings of IEEE Wireless Communications and Networking Conference (WCNC), Las Vegas, pp 284–289
5. Guvenc I, Chong CC, Watanabe F (2007) Analysis of a linear leastsquares localization technique in LOS and NLOS environments. In: Proceedings of IEEE Vehicular Technology Conference (VTC), Dublin, Ireland, pp 1886–1890
6. Li Z, Trappe W, Zhang Y, Nath B (2005) Robust statistical methods for securing wireless localization in sensor networks, in Proceedings of IEEE International Symposium on Information Processing in Sensor Networks (IPSN), Los Angeles, CA, pp 91–98
7. Reza RI (2000) Data fusion for improved TOA/TDOA position determination in wireless systems, Ph.D. dissertation, Virginia Tech
8. Shen Y, Win MZ (2010) Fundamental limits of wideband localization-Part I: a general framework. IEEE Trans Info Theory 56(10):4956–4980 Oct
9. Gadeke T, Schmid J, Kruger M, Jany J, Stork W, Glaser KDM (2013) A bi-modal ad-hoc localization scheme for wireless networks based on RSS and ToF fusion. In: Proceedings of Workshop Positioning Navigation and Communication (WPNC), Dresden, Germany, pp 1–6
10. Shen Y, Wymeersch H, Win MZ (2010) Fundamental limits of wideband localization-Part II: cooperative networks. IEEE Trans Info Theory 56(10):4981–5000 Oct

The Real-Time Target Tracking Algorithm Based on Improved Template Matching and its Hardware Implementation

Daqun Li, Jie Guo and Tingfa Xu

Abstract In order to solve the long-time tracking problem in the video stream, this paper proposes a real-time target tracking algorithm based on improved template matching. On the basis of the traditional template matching algorithm, we apply the random forests to generate and train those characteristics. During the process of template matching, we use the improved normalized correlation coefficient to evaluate the similarity. It can also update the real-time template library and ensure the tracking is not lost. Algorithm can achieve a long-term tracking, and able to deal with the complex background, part of the covering, and so on. The algorithm has been applied in the hardware processing platform which uses the FPGA and DSP as the core processing. The result is satisfactory.

Keywords Target tracking · Random forests · Improved normalized correlation coefficient

1 Introduction

We named the whole process as 'long-term tracking' which is dealing the video streaming with frame rate and keep the whole dealing process long enough. Long-term tracking has extending use in daily life, military, and industry. And it is also a vital component of computer vision field. Furthermore, this tracking is the key and difficult point in security monitor and control research field [1].

D. Li · J. Guo
Beijing Institute of Technology University, Beijing, China
e-mail: 452551566@qq.com

J. Guo
e-mail: 1101860289@qq.com

T. Xu (✉)
Section of Photoelectronic Imaging and Information Engineering,
Beijing Institute of Technology University, Beijing, China
e-mail: ciom_xtf1@bit.deu.cn

Q. Liang et al. (eds.), *Proceedings of the 2015 International Conference on Communications, Signal Processing, and Systems*, Lecture Notes in Electrical Engineering 386, DOI 10.1007/978-3-662-49831-6_53

The template matching technology is using the known target template matched in the waited research image field, then find the location in image field for this target template. The tradition template matching has slow speed, short of real time, and template drift situation. In this condition, researchers from domestic and overseas provide lots of improved solutions. In 2000, Peacock got a conclusion that after comparing the updated strategies for templates they do not depend on initial template. The conclusion is using the Kalman template they updated the filter to filtering which has the strongest robustness for drift and noisy of templates [2]. Based on this, Haworth and Renshaw had further research on how to choose templates to update filter and Kalman coefficient [3]. Yanmei Zhang and others applied the templates matching for high speed target tracking [4]. And then they designed a cross template to enhance the matching speed. Renting Song and others improved the similarity measure function for templates matching and then got a fast correlative matching regulation [5]. In 2008, Yan Ji and others used the wavelet transform match in the frequency domain. And then they applied this to recognize the satellite remote sensing images [6].

This paper depends on tradition templates matching algorithm, using random forest to generate and exercise the characters. In the process of templates matching, we used the improved normalized correlation coefficient to evaluate the similarity and updating the templates library. And we also got the better real-time tracking effects in the platform which uses DSP and FPGA as the core processing.

2 Improved Template Matching Algorithm

2.1 The Generation and Training of Characteristics

This part is improved and simplified on the basis of the literature [7]. In the first 100 frames of video, we use the rectangular box which is in the center of the image to determine the goal, and bring it into the template library. After that, we do block processing in each frame of the video. We divide the image into the image blocks which have a certain number, so that we can create the scanning grids. Then chose 10 grids which are closest to the initial rectangular box. Using each grid to do the geometric transformation (plane rotary in $\pm 10°$) and generating 20 different image blocks. In this way, we could get 200 positive samples in total. In order to increase the real-time performance of the algorithm, the selection of the negative samples was around the initial rectangular box by certain steps. This process was without the geometric transformation. In those positive and negative samples, we used random forests (ten trees in all) to generate the characteristics. Each tree randomly generated 10 pairs of determine nodes. Through comparing the two corresponding pixels in each pair, we got 0 or 1. Then we used the result to create a binary code, composed of 10 0 or 1, as the feature of the corresponding tree. Each feature has its posterior probability P(y|x),

$$P(y|x) = P_F / (P_F + N_F) \tag{1}$$

In the formula, P_F is the number of positive samples which have the same characteristic, N_F is the number of negative samples which have the same characteristic. In this condition, we can train the features by calculating the posterior probability, and increase its reliability.

After that, we deal with the whole scanning grids to let every block has its features. Then accumulate the posterior probabilities of every image block. We consider the image block which contains prospect target if the result is bigger than the threshold T and then we record it. At the same time, features in this block should be trained in order to increase their reliability.

2.2 The Processing of the Target Area

Each frame of the video image must have lots of image blocks which contain prospect target, we name them as good blocks. Label them as: g_1, g_2, …, g_n. Regarding the vertexes of each good block as the center of the circle, and the variable R as the radius to statistic the number of the good blocks within this scope. When carries on the statistics, we adopt the bilinear sampling to reduce the computational complexity. It can also improve the convergence speed and the real-time performance of the algorithm. Namely, one vertex of the good block correspondingly searches only the odd rows and odd columns (or even rows and even columns). To avoid the false missing and error, the search method of the vertexes which are adjacent to it should be opposite. Finally, we regard the area that contains the most number of good blocks as the target area. Use the formula:

$$M_h = \frac{1}{K} \sum_{x_i \in S_k} (x_i - x) \tag{2}$$

Quickly find the center of the target area, and compress it into the same size as the template block. In the formula, x_i is vertexes' abscissa of the good blocks in the target area; S_k is the target area; K is the number of the good blocks which should be calculated.

2.3 Improved Normalized Correlation Coefficient

In the traditional template matching algorithm, using the following normalized correlation coefficient as the similarity measure:

$$R(i,j)=\frac{\sum_{m=1}^{M}\sum_{n=1}^{M}S^{i,j}(m,n)\times T(m,n)}{\sqrt{\sum_{m=1}^{M}\sum_{n=1}^{M}\left[S^{i,j}(m,n)\right]^2}\sqrt{\sum_{m=1}^{M}\sum_{n=1}^{M}\left[T(m,n)\right]^2}} \tag{3}$$

$T(m,n)$ is the template; $S^{i,j}(m,n)$ is the target image; M is template's height and width.

This normalized correlation coefficient has low sensitivity, when the illumination of the image has changed, or the target has deformation. The similarity between the target and the template will decrease. For this problem, the literature [8] had proposed a kind of normalized correlation coefficient which has the weight:

$$\rho=\frac{\sum_{i=1}^{n}\omega_i(x_i-\overline{x})(y_i-\overline{y})}{\sqrt{\sum_{i=1}^{n}\omega_i(x_i-\overline{x})^2\sum_{i=1}^{n}\omega_i(y_i-\overline{y})^2}} \tag{4}$$

In the formula, $\overline{x}=\frac{1}{n}\sum_{i=1}^{n}\omega_i x_i$, $\overline{y}=\frac{1}{n}\sum_{i=1}^{n}\omega_i y_i$, $\omega_i=\frac{1}{2}\left[\frac{1}{x_i}+\frac{1}{y_i}\right]$.

This normalized correlation coefficient with height, improve the sensitivity of the calculation and the quality of the matching. However, the selection of weight value is too simple, and the improvement is not obvious. The coordinates in the formula are also too complicated to calculate and transplant to the hardware. To solve this problem, we combined the formulas (3) and (4), the improved normalized correlation coefficient formula is as follows:

$$\begin{gathered}\rho=\frac{\sum_{m=1}^{M}\sum_{n=1}^{M}\omega_i\left[S^{i,j}(m,n)-\overline{S^{i,j}}(m,n)\right]\times\left[T(m,n)-\overline{T}(m,n)\right]}{\sqrt{\sum_{m=1}^{M}\sum_{n=1}^{M}\omega_i\left[S^{i,j}(m,n)-\overline{S^{i,j}}(m,n)\right]^2}\sqrt{\sum_{m=1}^{M}\sum_{n=1}^{M}\omega_i\left[T(m,n)-\overline{T}(m,n)\right]^2}} \\ \overline{S^{i,j}}(m,n)=\frac{1}{MM}\sum_{m=1}^{M}\sum_{n=1}^{M}\omega_i S^{i,j}(m,n),\overline{T}(m,n)=\frac{1}{MM}\sum_{m=1}^{M}\sum_{n=1}^{M}\omega_i T(m,n) \\ \omega_i=\frac{1}{2}\left(1/\left[S^{i,j}(m,n)\right]^{3/2}+1/\left[T(m,n)\right]^{3/2}\right)\end{gathered} \tag{5}$$

Using the formula (5), we are able to evaluate the similarity between the target blocks and the template. It not only decreases the amount of calculation, but also enhances the real-time performance of the algorithm and the sensitivity of the formula.

3 Experiments

In order to verify the tracking effect of the improved template matching algorithm, we completed the software simulation. We simulated the algorithm and compared it with the traditional template matching algorithm. The resolution of the camera we used is 640 × 480 and the frame rate is 25 f/s. The results are shown in Figs. 1 and 2.

In the experiments, we also analyzed the real-time performance of two algorithms. When used the traditional template matching algorithm, the total time is 0.35946 s. When used the improved template matching algorithm, the total time is only 0.020423 s. Obviously, the running speed of the algorithm has been greatly improved. It also successfully satisfies the real-time requirement.

4 Hardware System Based on DSP and FPGA

4.1 Hardware System

The hardware system based on DSP and FPGA is shown in Fig. 3. It mainly includes image acquisition, image processing, and image output with three parts. The image acquisition and the image processing are mainly completed by the

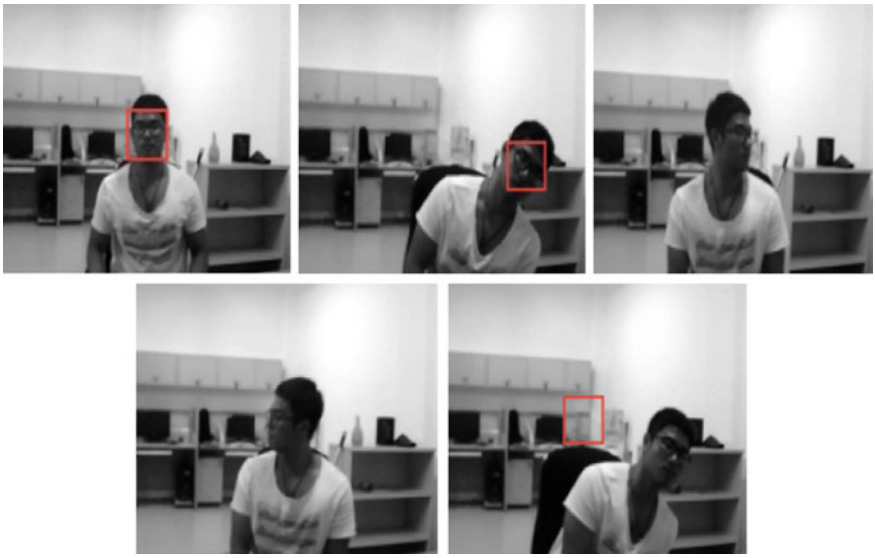

Fig. 1 Traditional template matching tracking algorithm

Fig. 2 The improved template matching tracking algorithm

DSP. Image output is mainly completed by FPGA. The camera we used in the system is Mintron Company's MTC-62V1. The total pixels of CCD are 795 × 596 (PAL). DSP is TMS320C6416, and it has 600 MHz clock rate, 4800MIPS processing ability. FPGA is Altera Cyclone III EP3C120F780. We connected it with DDR2 to complete data's quick storage.

4.2 System Design

Figure 4 is the flow chart of the hardware system. We use the CCD camera to acquire image. In the first 100 frames (PAL, frame rate is 25 f/s), we ensured that the target need to be tracked and initialized the system. After that, storage of data into FIFO and to send the stored data to the image data memory by the logical circuit. Then DSP can use the data in the memory. Finally, process the data by FPGA and use the LCD to display the image.

Fig. 3 Real-time tracking system based on DSP and FPGA processing platform

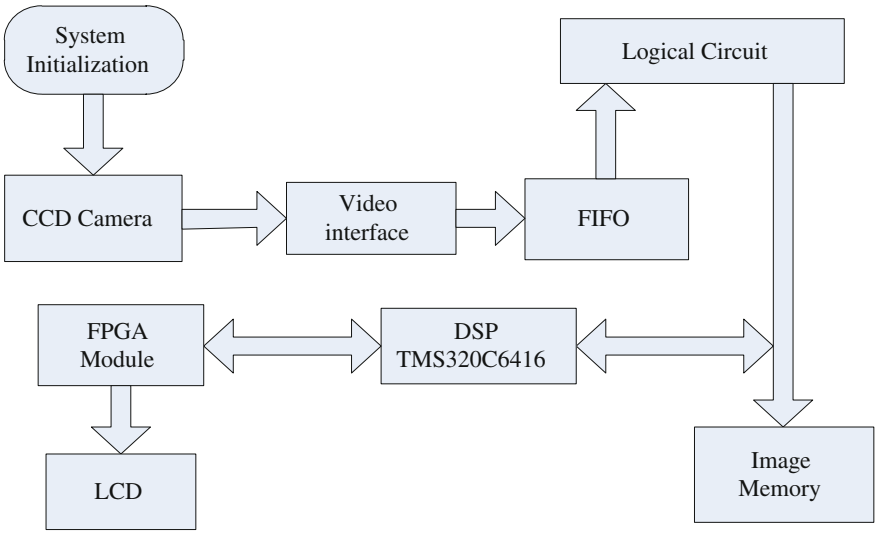

Fig. 4 Framework of hardware processing system

4.3 Results

The actual real-time effect of the hardware is shown in Fig. 5. According to the test, the running speed of the system is 0.015424 s. Obviously, the speed is much faster than the software simulation.

Fig. 5 The tracking effect of hardware system

5 Conclusion

This paper depends on the tradition templates matching algorithm, and using random forest and improved normalized correlation coefficient to improve the arithmetic speed and accuracy of algorithm. It can also complete the real-time tracking when targets have twist and swing. The method in paper effectively enhances the real-time feature of algorithm. Through transplanting the algorithm into the hardware, we used the DSP and FPGA as the core of it, giving the affirmative to transplant algorithm. Through a series of field experimentation, the algorithm shows the real time and feasibility features. Furthermore, this software platform is small, has better performance and real-time tracking with the targets. Meanwhile, the reasonable design for this software platform has simplified the design tasks for DSP and has the high value of engineering application.

Eventhough the algorithm has improved compared with before, this algorithm has also shortcomings when it meets small targets and weak targets situation.

Therefore, the algorithm needs continuing debugged and improved. In addition, there are more enhanced works on DSP and FPGA compatibility issues. The major direction of research in future is expressing the fusion system function extremely.

References

1. Gong Y, Xue T, Dongyang W, Sun Y (2010) Adaptive target tracking algorithm based on template matching. Comput Programing Skills Maintenance 22:14–15
2. Peacock AM et al (2000) Reference block updating when tracking with block matching algorithm. Electron Lett 36(4):309–310
3. Haworth C, Peacock AM, Renshaw D (2001) Performance of reference block updating techniques when tracking with the block algorithm. University of Edinburgh
4. Zhang Y, Song Y (2006) Application of the template matching method in high speed target tracking. Trans Beijing Inst Technol 26(11):1026–1029
5. Song R, Y Weiping, Yang M (2007) Improved template matching algorithm for moving target tracking. Infrared Laser Eng 36:197–200
6. Ji Y, Zhang Y (2008) Method research based on wavelet transformation template match. J Univ Sci Technol China 38(3):293–296
7. Kalal Z, Mikolajczyk K, Matas J (2010) Tracking-learning-detection. Pattern Anal Mach 34 (7):1409–1422
8. Liu Y, Meng Q, Chen R (2004) Improvement of similarity measure: pearson product-moment correlation coefficient. J Chin Pharm Sci 13(3):180–185

A Novel NLOS Mobile Node Localization Method in Wireless Sensor Network

Xiaosheng Yu, Nan Hu, Ming Xu and Meichen Wu

Abstract Mobile location estimation using wireless sensor network (WSN) is one of the important technologies in the past decades. A main challenge in mobile location is non line of sight (NLOS) propagation caused by the complicated practical environments. The NLOS effects will seriously reduce the accuracy of localization algorithms. In this paper, we present a novel NLOS mobile node localization algorithm based on probabilistic data association. First, we propose an improved residual weighting (Rwgh) algorithm which can efficiently mitigate the NLOS errors to provide different position estimates by using different subgroups of range measurements. And then a probabilistic data association filter is employed to determine the final position estimate. Experimental results demonstrate that the proposed algorithm is robust to the NLOS errors and provides higher location accuracy over the other traditional filter methods.

Keywords Location · Wireless sensor network · Non line of sight · Residual weighting algorithm · Probabilistic data association

X. Yu (✉) · N. Hu · M. Xu
College of Information Science and Engineering, Northeastern University, Shenyang, China
e-mail: yuxiaosheng7@163.com

N. Hu
e-mail: neuhunan0806@gmail.com

M. Xu
e-mail: 13998872060@163.com

M. Wu
School of Foreign Languages, Dalian Maritime University, Dalian, China
e-mail: 739774259@qq.com

Q. Liang et al. (eds.), *Proceedings of the 2015 International Conference on Communications, Signal Processing, and Systems*, Lecture Notes in Electrical Engineering 386, DOI 10.1007/978-3-662-49831-6_54

1 Introduction

In the recent years, mobile localization estimation using wireless sensor network (WSN) plays a significant issue and has been widely used in robotic industry, health surveillance, national security, and so on [1]. The WSN-based location algorithms have many advantages such as easy flexibility, low cost, and convenient maintenance.

WSN utilizes the beacon nodes with the priori location information to locate the unknown node. There are many fundamental WSN-based location methods to realize the localization, such as received signal strength indicator (RSSI), time of arrival (TOA), time difference of arrival (TDOA), and angle of arrival (AOA). Several study work has been done based on these measures. Generally, accurate location estimation can be obtained if the signal propagation state between the unknown node and all beacon nodes is line of sight (LOS) path. However, the complicated practical environment often causes the non line of sight (NLOS) environment, where the direct propagation path between the target and a beacon node may be blocked by obstacles. It results in the NLOS errors included in the erroneous measurements because of the reflection and diffraction of signal. The NLOS effects will decrease the accuracy of localization.

The existing methods to deal with the NLOS errors are generally categorized into two types: parametric methods and nonparametric methods. The parametric methods are proposed with the assumption that NLOS errors distribution is certain. For the parametric method, there are two strategies to obtain the location result. The first one is to identify the NLOS propagation, and then correct the NLOS errors. There are many methods based on this strategy, such as the hypothesis test-based method [2], likelihood ratio test-based methods, and statistical analysis-based methods [3]. However, in these methods, once the wrong identification occurs, the accuracy location cannot be realized. The second one is to locate the target by combining both the LOS and NLOS measurements. In [4–6], different filtering technologies based interacting multiple model (IMM) methods are presented.

Unlike the parametric methods, the nonparametric method does not need the prior statistical information of the NLOS errors. Chen [7] proposed a residual weighting (Rwgh) algorithm which can efficiently reduce the NLOS errors. Yu [8] reduce the computational complexity of the Rwgh algorithm. Wang [9] model the distribution of the LOS and NLOS errors by using Gaussian mixture model.

In this paper, we propose a novel NLOS mobile node localization algorithm based on probabilistic data association. The proposed is robust to NLOS errors and does not need any prior information.

2 The Proposed Algorithm

2.1 System Model

In this paper, we assume that N beacon nodes are randomly deployed in the field. The distance between each beacon node and unknown node can be estimated. The coordinate of the beacon nodes are represented as $\theta_i = [x_i, y_i]^{\mathbf{T}}, i = 1, 2, \ldots, N$, and the coordinate of the unknown node is represented as $X = [x, y]^{\mathbf{T}}$. At time k, the real distance between the ith ($i = 1,\ldots, N$) beacon node and target is:

$$d_i(k) = \sqrt{(x(k) - x_i(k))^2 + (y(k) - y_i(k))^2} \tag{1}$$

For LOS condition, the measured distance between the mobile node and the i-th beacon node at the time k is:

$$r_i(k) = d_i(k) + n_i \tag{2}$$

where n_i is the white Gaussian noise.

For NLOS condition, the measured distance between the mobile node and the i-th beacon node at the time k is

$$r_i(k) = d_i(k) + n_i + b_{\text{NLOS}} \tag{3}$$

where b_{NLOS} denotes the NLOS error which is independent of the n_i.

For different practical environment, the positive bias error b_{NLOS} could obey exponential distribution, Gaussian distribution, or uniform distribution.

At the time k, the state vector is modeled as

$$X(k) = [x(k), \dot{x}(k), y(k), \dot{y}(k)]^T \tag{4}$$

where $(x(k), y(k))$ denotes the position of the unknown node, and $(\dot{x}(k), \dot{y}(k))$ denotes the velocity of the unknown node.

The state model is expressed as

$$X(k+1) = AX(k) + Gw(k) \tag{5}$$

where A is the state transition matrix, and A and G are expressed as

$$A = \begin{bmatrix} 1 & 1 & 0 & 0 \\ 0 & 1 & 0 & 0 \\ 0 & 0 & 1 & 1 \\ 0 & 0 & 0 & 1 \end{bmatrix} \quad G = \begin{bmatrix} t^2/2 & 0 \\ t & 0 \\ 0 & t^2/2 \\ 0 & t \end{bmatrix} \tag{6}$$

where t is the period of localization.

2.2 Improved Rwgh Algorithm

In this section, we first build $R = C_N^{N-1}$ different subgroups of range measurements, and then we propose an improved Rwgh algorithm to estimate the position using each subgroup of range measurements. At time k, the improved Rwgh algorithm is described as follows.

Step 1. The area where the nodes deployed is split into a gird Φ with $W \times W$ cells. The centers of these cells are denoted by $C(i, j)$ $i, j = 1,\ldots,W$. $C(i, j)$ is described in a matrix form. We build a $W \times W$ matrix V which is named voting matrix. Each element of V can be computed by the following equation:

$$V(i,j) = \sum_{n=1}^{N} b_n(i,j), \quad i,j = 1, \ldots, W \tag{7}$$

where

$$b_n(\mathrm{i},\mathrm{j}) = \begin{cases} 1, & r_n - \varepsilon \le d_{ijn} \le r_n + \varepsilon \\ 0, & \text{otherwise} \end{cases} \tag{8}$$

where $r_n$is the measured distance between the mobile node and the n-th beacon node, and d_{ijn} is the Euclidean distance between $C(i, j)$ and the n-th beacon node.

Step 2. Let $C^* = \left[C_1^*, \ldots, C_m^*\right]$ denote the initial location results which contains all elements owning the same maximum value in the matrix V. For each element of C^*, the average residual is defined by

$$\overline{\mathrm{RES}_m} = \frac{\mathrm{RES}(C_m^*, \Theta)}{N}, m = 1, \ldots, M \tag{9}$$

where $\mathrm{RES}(C_m^*, \Theta) = \sum_{n=1}^{N} \left(r_n - \left\|C_m^* - \theta_n\right\|\right)^2$ is the residual.

Step 3. The location estimate of the unknown node is

$$Z = \frac{\sum_{m=1}^{M} C_m^* \left(\overline{\mathrm{RES}_m}\right)^{-1}}{\sum_{m=1}^{M} \left(\overline{\mathrm{RES}_m}\right)^{-1}} \tag{10}$$

2.3 Probabilistic Data Association Filter

The probabilistic data association is a statistical approach to solve the uncertainty of the measurement. In this section, we use the PDA filter to mitigate the measurement noise. There are four steps to form the PDA filter.

Step 1. The first step is Kalman prediction. The state and covariance for the i-th beacon node at time k, can be estimated by the following equations:

$$\hat{X}(k+1|k) = A\hat{X}(k|k) \tag{11}$$

$$P(k+1|k) = AP(k|k)A^T + \mathrm{GQG}^T \tag{12}$$

As mentioned above, we have estimated the position with each subgroup of range which is denoted by $Z_r(k+1), r = 1, \ldots, R$. The measure residual is defined by

$$\nu_r(k+1) = Z_r(k+1) - H\hat{X}(k+1|k), r = 1, 2, \ldots, R \tag{13}$$

Step 2. The second step is NLOS detection. If $\nu_r(k+1)$ is computed in the LOS condition

$$\nu_r(k+1) \sim N(0, S_r)(k+1)), r = 1, 2, \ldots, R \tag{14}$$

where $S_r(k+1) = HP(k+1|k)H^T + V_r(k+1)$ is the innovation covariance. The test statistic is defined by

$$\Gamma_r(k+1) = \nu_r(k+1)S_r^{-1}(k)\nu_r(k+1) \tag{15}$$

$\Gamma_r(k+1)$ is compared with a threshold γ. If $\Gamma_r(k+1)$ is larger than γ, $\nu_r(k+1)$ is computed in the NLOS condition, otherwise, $\nu_r(k+1)$ is computed in the LOS condition. We eliminate the positions in the NLOS condition, and obtain the $Z_u(k+1), u = 1, \ldots, U$.

Step 3. The third step is data association. At time k, the data association of measurement residual is expressed as

$$\varepsilon(k+1) = \sum_{u=1}^{U} \beta_u(k+1)\nu_u(k+1) \tag{16}$$

where $\beta_u(k+1) = \frac{e_u}{q + \sum_{u=1}^{U} e_u}, \beta_0(k+1) = \frac{q}{q + \sum_{u=1}^{U} e_u}, e_u = \exp\left(-\frac{[\varepsilon_u]^T S_u^{-1}(k+1)\varepsilon_u}{2}\right)$, $q = \lambda|2\pi S_u(k+1)|\frac{1-P_D}{P_D}$.

Step 4. The fourth step is filter update. This step includes the following equations:

$$K_u(k+1) = P(k+1|k)H^T S_u^{-1}(k+1) \tag{17}$$

$$\hat{X}(k+1|k+1) = \hat{X}(k+1|k) + K_u(k+1)\varepsilon(k+1) \tag{18}$$

$$\begin{aligned} P(k+1|k+1) = {} & \beta_0 P(k+1|k) + (1-\beta_0) \\ & \times \left[P(k+1|k) - K_u(k+1)HP(k+1|k)\right] \\ & + K_u(k+1) \times \left[\sum_{r=1}^{R} \beta_u(k+1)v_u(k+1)(\beta_u(k+1))^T \right. \\ & \left. - \varepsilon_u(k+1)\varepsilon_u^T(k+1)\right] K_u^T(k+1) \end{aligned} \tag{19}$$

The output of the proposed algorithm can be expressed as

$$[\hat{x}(k+1), \hat{y}(k+1)] = \Psi \cdot \hat{X}(k+1|k+1) \tag{20}$$

where $\Psi = \begin{bmatrix} 1 & 0 & 0 & 0 \\ 0 & 0 & 1 & 0 \end{bmatrix}$.

3 Performance Evaluation

In this section, we design various experiments to validate the effectiveness of the proposed algorithm. The proposed algorithm is compared with the Rwgh algorithm and Rwgh-based Kalman filter. We consider a 100 × 100 square area, where 6 beacon nodes are randomly deployed. We assume that the communication range of sensor node is 150 m. Figure 1 shows the deployment environment of this experiment. The measurement noise obeys Gaussian distribution whose mean value is zero and the standard deviation is 1. We use the root mean square error (RMSE) to evaluate the performance of these methods:

$$\text{RMSE} = \sqrt{\frac{1}{MC}\sum_{k=1}^{MC} (x(k) - \hat{x}(k))^2 + (y(k) - \hat{y})(k))^2} \tag{20}$$

where, $[x(k), y(k)]$ and $[\hat{x}(k), \hat{y}(k)]$ denote the true position of the unknown node and the estimated position of the unknown node at time k, respectively. We perform 500 Monte Carlo runs to obtain the following results.

We assume NLOS errors obey uniform distribution, and the minimum and maximum values of parameters of uniform distribution are 2 and $U_{\max}$, denoted by

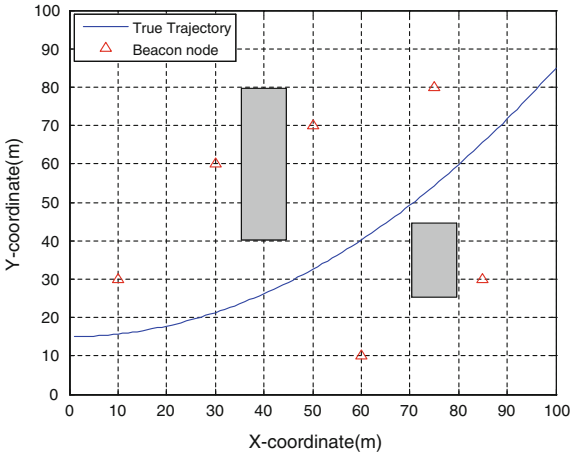

Fig. 1 The schematic diagram of the deployment environment

$U(2,\ U_{\max})$. Figure 2 shows the relationship between $U_{\max}$ and root mean square error. Obviously, the proposed algorithm has the highest localization accuracy.

We evaluate the performance of these three algorithms when NLOS errors obey Gaussian distribution, the mean of Gaussian distribution are 3. Figure 3 shows the impact of standard deviation of NLOS errors on root mean square error. Obviously, the proposed algorithm has the best performance.

We evaluate the performance of these three algorithms when NLOS errors obey Exponential distribution. Figure 4 shows the relationship between mean parameter and root mean square error. It can be observed that the proposed algorithm has the highest localization accuracy.

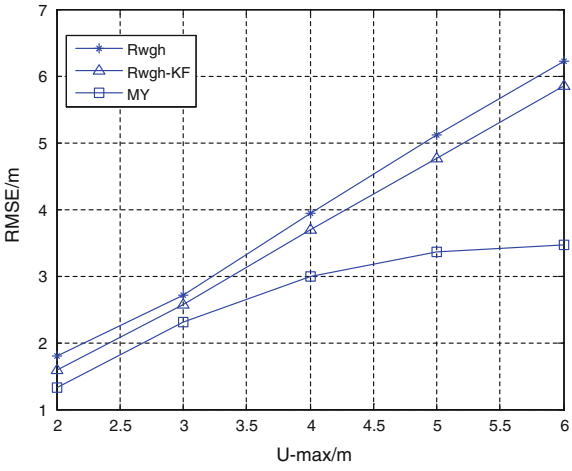

Fig. 2 The U-max versus root mean square error

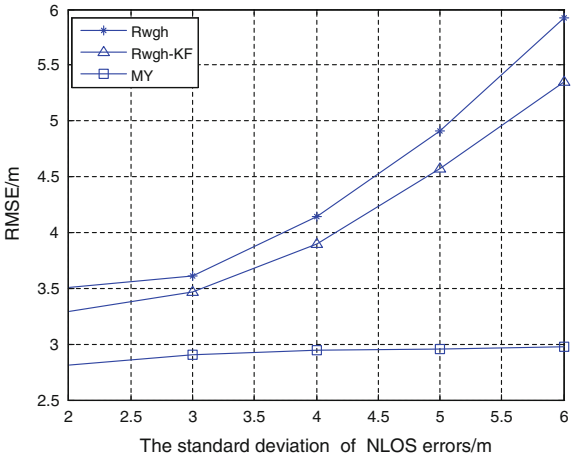

Fig. 3 The standard deviation of NLOS errors versus root mean square error

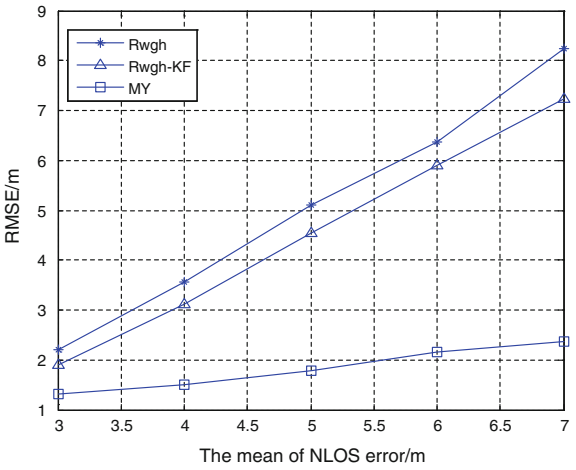

Fig. 4 The mean of NLOS errors versus root mean square error

4 Conclusion

In this paper, we propose a novel NLOS mobile node localization algorithm based on probabilistic data association which is robust to the NLOS errors. The proposed algorithm is a nonparametric method which does not need any prior information on error model. We compared the proposed algorithm with the Rwgh algorithm and Rwgh-based Kalman filter. The promising simulation results show that our algorithm has better performance in terms of robustness and accuracy.

Acknowledgments We are supported by National Science Foundation of China (61403068, 61273078, 61302012)), and Fundamental Research Funds for the Central Universities (N140403005, N140404014).

References

1. Ou CH (2011) A localization scheme for wireless sensor networks using mobile anchors with directional antennas. IEEE Sens J 11(7):1607–1616
2. Cong L, Zhuang W (2005) Nonline-of-sight error mitigation in mobile location. IEEE Trans Wireless Commun 4(2):560–573
3. Venjkatraman S, Caffery J, You HR (2004) A novel TOA location algorithm using LOS range estimation for NLOS environments. IEEE Trans Veh Technol 53(5):1515–1524
4. Liao JF, Chen BS (2006) Robust mobile location estimator with NLOS mitigation using interacting multiple model algorithm. IEEE Trans Wireless Commun 5(11):3002–3006
5. Chen BS, Yang CY, Liao JF (2009) Mobile location estimator in a rough wireless environment using extended Kalman-based IMM and data fusion. IEEE Trans Veh Technol 58 (3):1157–1169
6. Hammes U, Zoubir AM (2011) Robust MT tracking based on M-estimation and interacting multiple model algorithm. IEEE Trans Signal Process 59(7):3398–3409
7. Chen PC (1999) A non-line-of–sight error mitigation algorithm in location estimation. In: Proceedings of the wireless communication and networking conference, pp 316–320
8. Yu XS, Wu CD, Cheng L (2014) Indoor localization algorithm for TDOA measurement in NLOS environments. IEICE Trans Fundam Electron Commun Comput Sci E97-A (5):1149–1152
9. Wang QH, Balasingham M, Zhang M, Huang X (2011) Improving RSS-based ranging in LOS-NLOS scenario using GMMs. IEEE Commun Lett 15(10):1065–1067

Design and Development of Positioning System of Cable Trench Based on VLC + PLC

Hui Fan, Shuaihua Li, Liang Meng, Xiao Yang and Peng Luo

Abstract Aiming at the problems of city underground cable trench, a serious shortage of illumination light, GPS system receives signal which is very faint, proposed to visible light communication technology (VLC, visible light communication) and the power line carrier communication technology (PLC, power line communication) positioning system design and development scheme of combining. The technical principles and characteristics of VLC description, analysis function, and the key technology of the underground cable channel positioning system, and explain the application of the system and the effect of.

Keywords Visible light communication · Power line carrier communication · Cable channel · Positioning

1 Outline

With the rapid development of China's economy and the continuous expansion of city size, urban power transmission cable is gradually changed from the overhead wire power cables. Cable channel as a channel of cable lines, its construction speed and mileage annually [1]. The vast majority of underground cable channel illuminating light exists a serious shortage; GPS systems and other characteristics of the received signal are very weak, GPS technology in such a case cannot be effectively utilized. Therefore, the power company cable work area cable channel patrol officers and the lack of full-time full positioning emergency response capabilities, increasing the difficulty of maintenance inspection personnel, while job security is also compromised.

Compared with the traditional lighting, white light-emitting diode (LED) having a low driving voltage, low power consumption, long life, and other advantages, is a

H. Fan · S. Li (✉) · L. Meng · X. Yang · P. Luo
State Grid Electric Power Research Institute Hebe Electric Power Company, Shijiazhuang 050021, China
e-mail: dyy_lishuaihua@163.com

Q. Liang et al. (eds.), *Proceedings of the 2015 International Conference on Communications, Signal Processing, and Systems*, Lecture Notes in Electrical Engineering 386, DOI 10.1007/978-3-662-49831-6_55

green lighting device, and is regarded as the fourth generation of energy saving lighting equipment [2]. Since the white LED has high response sensitivity, it can be used for high-speed data communications, VLC technically developed a new wireless optical communication technology. Compared with conventional radio communication with high transmission power, electromagnetic interference does not need to apply for spectrum resources, etc. [3]. Combined with the unique power of communication systems, PLC uses the existing lighting power lines, by way of the carrier signal high-speed transmission. Used in urban underground cable trench, to avoid the inherent shortcomings of the PLC: signal loss distribution transformers barrier effect of power line carrier signals and three-phase power line between do not exist.

Therefore, the design and development based on VLC and PLC combination program are proposed for urban underground cable channel positioning system. Cable channel dedicated patrol officers in epaulets position by assembling LED communication module, and to the cable ditch unilateral "Lighting and communications integration" LED interact real-time location information via VLC + PLC converter module.

2 VLC + PLC Technology Introduction

2.1 VLC Technology Principle

VLC technology is the use of naked fluorescent or light-emitting diodes emitting a flashing light and dark which cannot see the high-speed signals to transmit information. Compared with the currently used for various wireless communication, VLC can take advantage of lighting equipment to replace the radio base station transmit signals, both lighting effects, but also has the communication function. The speed is up to tens of megabytes to hundreds of megabytes per second. Using a dedicated, capable of sending and receiving signals enabled mobile information terminals, as long as the light exposure to the place, it can be a long download and upload of all kinds of information and data.

At present, many research institutions and telecom companies, especially in Japan, Europe, the United States, and other countries in the field of visible light communication has launched an in-depth study. Calculated from a preliminary mathematical analysis and simulation-based white light visible light communication channel [4], the German Heinrich Hertz laboratory researchers created a visible light communication speed world record, reaching 513 Mbit/s [5], made rich results.

Our study of visible light communication started relatively late; there is no more mature commercialization of visible light communications systems. Peking University in 2006 first proposed the ultra-wide scheme based on visible light signal received wide-angle lens, and conducted a series of theoretical and experimental

work. In addition, the LED modulation drive, the layout of the LED array optimization, and high-sensitivity receiver and other aspects of certain research and visible light communication with the passive optical network (PON) in the converged access the physical layer, link layer, and other aspects of the transport layer to carry out exploration and research.

2.2 VLC + PLC Fusion Technology

Global Communications Conference visible Guangzhou International Conference Center and the China visible light communication technology innovation and application of Alliance Assembly, first proposed VLC (visible light communication) and PLC (power line communication) technology perfect fusion, low-cost system solutions.

PLC technology is a mode of communication; it has been widely used in power systems (including smart grids) networking and digital home. When information is sent, simply intended user information transmitted digitally modulated and coupled to low pressure (or MV) power lines, you can use the power line as a medium for transmission. At the receiving end, go through the filter which will filter out the modulated signal, and then through the corresponding demodulation with the originating process, you can recover the original information to achieve information transmission. Additional information transmission controls features of PLC system, low cost, wide coverage, plug and play, easy installation, so that "there is electricity where you can have a signal." VLC technique is used as the illumination source emitting diode (LED) light to transmit information. At the receiving end, a simple photo detector can restore the high-speed optical signals into electrical signals, and ultimately recover the original information to achieve information transmission and information services at the same time lighting functions. VLC technique has the advantage of the available spectrum and without wide spectrum authorization, anti-electromagnetic interference, no electromagnetic radiation, privacy, and human security, can be combined with extensive coverage of lighting networks. VLC + PLC, has all the advantages of fusion technology and VLC independent system to inherit, compared to other network combinations has a natural advantage. PLC technology can provide a ready-made visible light-based communications backbone network of LED lights. LED lights so that there is no longer one of the "islands of information", but the connection has become a cover having a certain scale of visible light communication network. Similar relationships are with such, the computer and the wireless Wi-Fi network cable. Power line networking VLC can meet the electricity demand-driven and information fed into two, fully capable of "electric light there, where there is light, there is a network signal." The architecture diagram of network showed in Fig. 1.

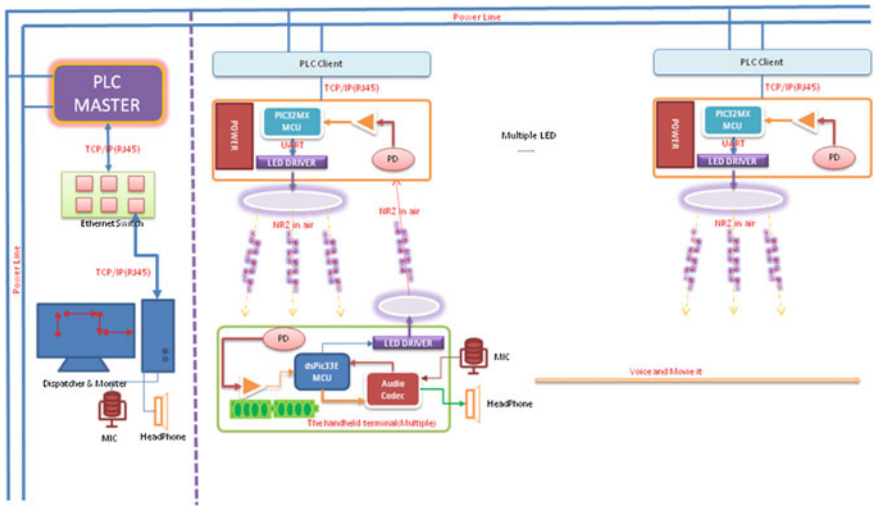

Fig. 1 Cable channel positioning system network architecture schematic

3 System Components and Key Technologies

Positioning principle of the system uses a single lamp positioning method, sets different LED lighting ID information associated with its own position. When the terminal receives ID information, the terminal is located at the corresponding LED light source. In the receiving terminal will receive the data analysis to the navigation map, to achieve positioning and navigation functions. The method is simple, positioning accuracy of LED lighting radius, and wide coverage.

3.1 System Components

System consists of "photo pass integration" LED light source, a mobile terminal, backstage PC scheduling, and monitoring of three parts. The "photo pass integration" LED light source by the explosion-proof LED lighting, the modem circuit composed of two parts, a mobile terminal consists of two parts, a photoelectric conversion module and display terminal composition, background PC scheduling and monitoring include a base station and PLC master station, and positioning display software.

3.2 PLC + VLC Depth Converged Communications Transmission Technology

This article will sparse time–frequency noise on the scale of the complexity of the system for the Joint Communications News Agency channel, system optimization, and design from the perspective of a number of key transmission technology, coding modulation technology, channel estimation, and relay scheme design propose new Robust and efficient broadband PLC system with VLC Joint Communications News Agency.

(1) For the power line and the visible channel transmission signal attenuation, more noise and more fading serious features, combined with the power line and visible transmission device principle and characteristics, to study the signal transmission mechanism of the power lines and visible Joint Communications News Agency in the system, then study Joint Communications News Agency system channel model in a variety of typical application scenarios and various probability models typical noise.
(2) Against noise and interference characteristics Joint Communications system channels, research performance-enhanced coded modulation mechanism, improve the system in harsh noise environments communications efficiency and robustness; challenges for VLC peak power and average power constraints PLC each other, approximation research peak, average power dual channel theoretical constraints limit the capacity of the constellation mapping; break through all the bits to be modulated equally misunderstanding, unequal protection features based on a reasonable allocation method to enhance the ratio of the bit map system error correction capability.
(3) Breaking the traditional frame structure of OFDM communication system to carry only the idea of a single time or frequency domain training sequence, frequency two-dimensional design, and the flexibility to meet the training sequence frame structure power line and visible light communication system requirements, allowing the system to achieve high spectral efficiency and high energy efficiency; Combining power line channel, visible light channels each having a frequency domain sparsely and temporal sparsely, based on compressive sensing theory framework and algorithms—frequency two-dimensional training sequence based precision, channel estimation method of low complexity.

3.3 Characteristics PLC + VLC Joint Channel Characteristics and Noise Analysis

(1) For the power line and the visible channel transmission signal attenuation, more noise and more fading serious features, combined with the power line

and visible transmission device principle and characteristics, to study the signal transmission mechanism of the power lines and visible Joint Communications News Agency in the system, then study Joint Communications News Agency system channel model in a variety of typical application scenarios and various probability models typical noise.

(2) In terms of VLC channel path loss, the communication received signal power at the receiving end of "Three-sensitive" characteristics. In visible light communication system noise aspect, the system noise with the "three none" features. For such a system model, based on coding theory and optimization theory, "Three-sensitive" Channel link attenuation coefficient distribution, research, "three none" closed-form expression noise model error performance and channel capacity. Based on this study the optimal signal modulation method and analysis, "Three-sensitive" channel model and noise model coded modulation system performance "three none" appropriate mathematical methods for further studies such as color keying modulation, dynamic code modulation, approximation theory, and other new coding and modulation method capacity limit.

(3) Against noise and interference characteristics Joint Communications system channels, research performance-enhanced coded modulation mechanism, improve the system in harsh noise environments communications efficiency and robustness; challenges for VLC peak power and average power constraints PLC each other, Approximation research peak, average power dual channel theoretical constraints limit the capacity of the constellation mapping; break through all the bits to be modulated equally misunderstanding, unequal protection features based on a reasonable allocation method to enhance the ratio of the bit map system error correction capability.

4 Application Examples and Effect Analysis

VLC and the depth of integration using PLC communication networks of the cable channel positioning presentation systems, demonstration sites located in Hebe Province, State Grid Electric Power Research Institute micro-grid demonstration zone, "distributed generation and micro-grid laboratory" and underground distribution long outdoor gallery conduct line and lighting equipment modification.

Underground power distribution outdoor promenade placed 16 white LED light source, lamp height is 3 m, two lamp spacing 2 m, respectively, and three positions in the same corridor. Background scheduling and monitoring software PC communication via PLC to "shine through integrated" LED light source transmits a location service data, LED light source is loaded with its own ID and position location services data from the PC side, and then broadcast it through the spatial light transmission. Received by the photoelectric conversion to electrical signals and transmitted to the mobile phone display terminals (loaded navigation software),

the received information is displayed on the map, to achieve positioning function. When the receiving terminal user moves to a different area of LED lighting, display terminal will automatically update the current location and location service information. For example, the handheld mobile terminal transmits the position data to the LED light source, when the receiving terminal is moved to the illumination area can be automatically updated to the real-time location and shows the location of service data. When receiving terminal moves to another LED lighting area, the same real-time automatic update to a different location and shows the location of the service information.

5 Conclusions

VLC is an emerging wireless optical communication technology, which can simultaneously achieve the dual function of illumination and communication. Since the urban underground cable tunnel illumination light in a serious shortage of memory, GPS system receives the signal which is very weak, etc., and therefore, in such environments, VLC + PLC technology based on positioning and communication broadcasting system with low power consumption, location high precision, fast transfer rate, and other advantages. Also, you can locate anywhere, anytime, without laying additional auxiliary equipment, it has a long life, green pollution-free, real-time to provide users with ubiquitous access. The system has been used in a demonstration in Hebe EPRI Micro-grid Demonstration Zone "distributed generation and micro-grid laboratory" and underground distribution outdoor promenade, to good effect.

References

1. Chen D (2009) Cable channel monitoring system based on ARM and CAN bus. Electronic Science and Technology master's degree thesis, Xi'an University
2. Nakamura S (1997) Present performance of InGaN based blue/green/yellow LEDs[C]. In: Proceedings of the SPIE conference on light-emitting diodes: research, manufacturing, and applications, San Jose, CA, USA. vol 3002 13−14 Apr 2007. SPIE, Bellingham, WA, USA, pp 26−35
3. Wei C (2008) White LED indoor visible light communication system based on research. Technology master's degree thesis, Changchun University
4. Tanaka Y, Haruyama S, Nakagawa M (2000) Wireless optical transmissions with white colored LED for wireless home links[C]. In: Proceedings of the 11th IEEE international symposium on personal, indoor and mobile radio communications (PIMRC'00), vol 2, London, UK, 18–21 Sept 2000. IEEE, Piscataway, NJ, USA, pp 1325−1329
5. Vucic J, Kottke C, Nerreter S (2010) 513 M bit/s visible light communications link based on DMT-modulation of a white LED. J Light Wave Technol 28(24):3512−3518
6. Liu R (2013) Research on indoor positioning technology in the visible light communication. Posts and master's degree thesis, Beijing University

A Novel Solution for the Optimal Deployment of Readers in Passive RFID Location System

Weiguang Shi, Xiaodi Han, Kaixuan Du and Jianxiong Li

Abstract The spatial relationship between the tag and the reader plays a great role in the performance of passive LANDMARC system. Since it is not easy to change the assignment of the whole reference tags frequently, most research aims at searching for the optimal deployment of readers. Instead of providing the exact RSSI values, the readers in passive system only can provide discrete power grades. In this paper, the detection radius under given power grade is discussed first. Then we explore the power grade management of the reader and propose the time consuming model for the passive LANDMARC, which leads to an objective function suffered from the position of readers. Finally, an enhanced particle swarming optimization algorithm is brought up to find the optimal deployment that bears the least time consuming. Simulation result showed that, the proposed solution provides a better design compared with the uniform deployment.

Keywords RFID · Deployment of readers · Time consuming in passive localization

1 Introduction

Passive UHF RFID is a promising approach towards indoor localization due to its advantages of noncontacting, non line of sight, short-delay, high accuracy, and low cost. Readers and passive tags are the foremost candidates for the passive RFID system. At the first of identification, each reader transmits interrogation signal via antenna to wake up passive tags within the detection area. After harvesting enough power from the interrogation signal, passive tags activate internal circuit and response back item data to reader. The process described above is generally called backscattering [1]. In backscattering, most passive RFID location algorithm

W. Shi (✉) · X. Han · K. Du · J. Li
School of Electronics and Information Engineering, Tianjin Polytechnic University, Tianjin, China
e-mail: shiweiguang12345@126.com

Q. Liang et al. (eds.), *Proceedings of the 2015 International Conference on Communications, Signal Processing, and Systems*, Lecture Notes in Electrical Engineering 386, DOI 10.1007/978-3-662-49831-6_56

captures the location information in the form of received signal strength indicator (RSSI) and calculates the tags' position on the basis of LANDMARC algorithm [2, 3]. Passive LANDMARC, another location algorithm based on passive tags, discards a large amount of computational complexity and achieves higher accuracy with lower cost compared with ranging algorithms like TOA and TDOA. However, passive LANDMARC still suffers from some drawbacks. First, readers have to decrease power grades step by step to identify the minimal grade for each tag. Obviously, unnecessary time consuming will be emerged in the case of readers and tags set closely. Second, a tag probably can not receive the interrogation signal even there is a reader around it when the turbulence from the electric accessory exist. Furthermore, severe multipath phenomenon, caused by the reflection, refraction, and scattering of radio waves, will affect the accuracy the RSSI.

Hence, the relative spatial location between the tag and the reader plays a great role in the performance of passive LANDMARC system. To obtain a satisfactory precision, a huge number of reference tags is usually fixed in the form of regular grid and serves as neighbours for the tracking tags. Since it is not easy to change the assignment of the whole reference tags, most research focuses on the optimal deployment strategy of the readers [4–6]. Nevertheless, few research pays attention to the effect of the deployment of the readers on the time consuming in the RFID location system, especially for the passive LANDMARC. In this paper, our objective is to propose a solution for the optimal deployment of readers with the least time consuming. The rest of this paper is organised as follows. We analyse the detection radius under given power grade in Sect. 2. In Sect. 3, an objective function associated with the position of readers is established. Enhanced particle swarming optimization algorithm combined with the simulated annealing algorithm (SAA) is brought up in Sect. 4 to find optimal deployment. In Sect. 5, we show the results of simulation. Finally, our work is concluded in Sect. 6.

2 Detection Radius Under Given Power Grade

Because of the level of radio frequency hardware, the readers in RFID system, whether active and passive, cannot provide exact RSSI values but only discrete power grades. At the beginning of the identification, the readers need to operate at the maximum power grade to transmit interrogation signal and wait for the response from tags. For the ith tag, if the response is only available for the power grade greater than or equals to j, j is regarded as its RSSI value. In theory, the maximum power grade has the greatest radius while the minimum power grade corresponding to the smallest radius. To identify each tag's RSSI value, readers have to diminish power grade step by step until none response can be heard.

For analysing the effect of the diminishing manner on the time consuming in localization, distance loss model is introduced to estimate the detection radius under each given power grade. Define the reader's transmitting power value as P_t whose maximum degree is $P_t^{\max}$, radius of the detection area can be obtained as:

$$R = \left(G_r G_t \lambda^2 R_0^{(\varepsilon - 2)} P_t / \left(16\pi^2 R^{\varepsilon} P_r^{\text{th}} \right) \right)^{1/\varepsilon} \tag{1}$$

where R_0 is the reference distance, λ is the wavelength of the RF signal, P_r is the activation threshold of passive tags, ε is path loss coefficient, G_r and G_t, respectively, represent the transmitting gain of the reader's antenna and the receiving gain of the tag's antenna.

Assume the maximum and minimum of the discrete power grade are, respectively, 1 and $G^{\max}$, the power value of jth discrete power grade can be evaluated by the linear interpolation

$$P_t^j = P_t^{\max} - (G^{\max} - j) * I_p \tag{2}$$

where I_p measured in dB denotes the step between the adjacent power grade. Substitute formula (2) into formula (1) and take log function on the both side, detection radius under the jth power grade can be given by:

$$R^j \le e^{P_t^{\max} - P_r^{\text{th}} - (G^{\max} - j) * I_p - 20lg(4\pi/\lambda) + 10(\varepsilon - 2)lg(R_0) + G_r + G_t + X_\sigma} - e^{10\varepsilon} \tag{3}$$

where X_σ is Gaussian noise in the transmission channel with mean zero and standard deviation σ, e is the Euler's constant.

3 Objective Function Based on the Time Consuming Model

According to the principle of the LANDMARC and the half duplex mode of the passive system, time consuming model can be established as follows:

Step1: Each reader operates at the maximum power grade and records the IDs of the reference tags and the tracking tags. During the process of the lth location service, take the uth reader for example, time consuming of the tag anti-collision is obtained as $T_{Ru}^0 = J(N_{Ru}^0, N_{Tu}^0, \delta)$, where N_{Ru}^0 and N_{Tu}^0 are the number of reference tags and the tracking tags, respectively, J is a time consuming function which related to the anti-collision algorithm, δ denotes the slot length.

Step2: Each reader decreases power grade to $(G^{\max} - 1)$ and detects the tags like Step 1. Similarly, the time consuming of tag anti-collision can be expressed as $T_{Ru}^1 = J(N_{Ru}^1, N_{Tu}^1, \delta)$. Suppose tuning word is utilized to control the power grade, time spent on the grade switching cannot be negligible and is given by t_z.

Step3: Each reader keeps working as the power grade decreased gradually until none response from the tracking tags is available. For the uth reader, suppose the power grade has declined to $G^{\max} - h_u$ when the number of

tracking tags fall to zero. Then the time consuming of the uth reader can be drew as $T_u = h_u \cdot t_z + \sum_{j=0}^{h_u} T_{Ru}^j$.

Step4: Consider all the readers work simultaneously and independently, the time consuming of the location system can be expressed as

$$T_l = \max_{u \in [1, U]} T_u + C \cdot t_c \tag{4}$$

where U denotes the total number of the readers, C denotes the total number of the tracking tags, t_c stands for computing time of algorithms for one tracking tag. Also, the average value of the computing time T can be obtained when the Monte Carlo method is executed

$$T = 1/\sum_{l=1}^{L} T_l \tag{5}$$

where L is the number of the location service.

Our objective described in formula (6) and formula (7) is to search the deployment with the least time consuming of the location system. The solution is represented as set of two-dimensional coordinates Ω indicating the positions of all readers included in the design.

$$\Omega = \left[(x_1^{\text{reader}}, y_1^{\text{reader}}), (x_2^{\text{reader}}, y_2^{\text{reader}}), \ldots, (x_U^{\text{reader}}, y_U^{\text{reader}}) \right] \tag{6}$$

$$O_S(\Omega) = \arg(\min(T)) \tag{7}$$

where $(x_u^{\text{reader}}, y_u^{\text{reader}})$ is the two-dimensional coordinate of the uth reader.

4 Enhanced PSO Algorithm

Combining SAA to regulate the inertia weight dynamically, we put forward an optimization mechanism based on PSO to find the optimal deployment of the readers.

4.1 Condition of Evolution

At the beginning of optimization, an initial population Z is generated based on the readers' initial position given by $Z = [Z_1 \quad Z_2 \quad \ldots \quad Z_W]^T$, where $Z_\varphi = [Z_{\varphi 1} \quad Z_{\varphi 2} \quad \ldots \quad Z_{\varphi U}]$, $[]^T$ denotes the transpose of matrix, W is the total number of particles, $\varphi \in (1, W)$. Assume $Z_{\varphi u} = (x_{\varphi u}, y_{\varphi u})$ and $V_{\varphi u} = (v_{\varphi u}^x, v_{\varphi u}^y)$ are the position

and the velocity of the uth reader in particle φ. $Pbest_{\varphi}^{\tau}$ and $Gbest^{\tau}$ represent the individual best position and the global best position of τth iteration, respectively. $\tau \in (1, \rho)$, where ρ is the maximum number of the iterations [7].

During the optimization process, the position and the velocity of all the particles are updated as follows:

$$V_{\varphi u}^{\tau+1} = \omega V_{\varphi u}^{\tau} + c_1 r_1^{\tau}\left(Pbest_{\varphi u}^{\tau} - Z_{\varphi u}^{\tau}\right) + c_2 r_2^{\tau}\left(Gbest^{\tau} - Z_{\varphi u}^{\tau}\right) \tag{8}$$

$$Z_{\varphi u}^{\tau+1} = Z_{\varphi u}^{\tau} + V_{\varphi u}^{\tau+1} \tag{9}$$

where ω denote the inertia weight, c_1 and c_2 are the acceleration coefficients, r_1^{τ} and r_2^{τ} are two uniformly distributed random numbers independently generated within $[0, 1]$.

To improve the effectiveness of the optimization, we define the same searching radius S for each reader and regard the circle region as the detection area, whose centre at the readers' initial position and radius is S. The maximum velocity of each particles is defined as $V_{\max} = \eta \cdot S$, where η is the limiting factor. In addition, we employ the penalty function Q to prevent readers outside the detection area and rewrite the objective function in formula (7)

$$M = T + Q,\ Q = (K_2/K_1) \cdot \sum_{u=1}^{U} s_u \tag{10}$$

$$O_S(\Omega) = \arg(\min(M)) \tag{11}$$

where K_1 and K_2 are penalty factor. If the uth reader has flown out the detection area, let $s_u = 1$. If not, let $s_u = 0$.

4.2 Adjustment Strategy of Inertia Weight Based on SAA

As mentioned in [8], inertia weight is a significant element for the balance between the local searching capability and the total searching capability. Usually, a small inertia weight means a strong local searching capability and a rapid convergence rate, while a big inertia weight may lead to a strong total searching capability and a large iterations. In this paper, an adjustment strategy of inertia weight based on the SAA is applied to regulate the inertia weight dynamically for a better and faster global searching process.

Define the annealing temperature ξ of the τth iteration as

$$\xi_{\tau} = \left[F(Pbest^{\tau})_{avg}/F(Gbest^{\tau})\right] - 1 \tag{12}$$

$$F(Pbest^{\tau})_{\text{avg}} = \sum_{i=1}^{W} F\left(Pbest_i^{\tau}\right)/W \tag{13}$$

where $F(Pbest^{\tau})_{avg}$ is the average fitness value of the τth iteration. The annealing probability p is also obtained as follows:

$$p = \begin{cases} 1, & if\ F(Gbest^{\tau-1}) \le F(Gbest^{\tau}) \\ \exp([F(Gbest^{\tau}) - F(Gbest^{\tau-1})]/\xi_{\tau}), & if\ F(Gbest^{\tau-1}) > F(Gbest^{\tau}) \end{cases} \quad (14)$$

Then, the inertia weight can be given by:

$$\omega = \begin{cases} \alpha_1 + 0.5\beta, & p \ge \beta \\ \alpha_2 + 0.5\beta, & p < \beta \end{cases} \quad (15)$$

where β is a random number within $(0, 1)$. α_1 and α_2 are fixed constant, $0 < \alpha_2 < \alpha_1 < 1$. If $F(Gbest^{\tau-1}) \le F(Gbest^{\tau})$, a larger inertia weight is selected to push particles to a broader region by the probability p. If $F(Gbest^{\tau-1}) > F(Gbest^{\tau})$, which denotes the result of τth iteration is desirable, a smaller inertia weight is selected by the probability p. As the number of iteration increases, the annealing temperature ξ_{τ} decreases gradually, which acquires a convergent of the optimization process.

5 Simulations

In the simulation experiment, we place 100 reference tags randomly and arrange four readers uniformly in 10 m × 10 m indoor environment. To measure the effectiveness and the flexibility of the proposed solution, we repeat the simulation and gather data from two typical environments. As illustrated in Fig. 1, 30 tracking

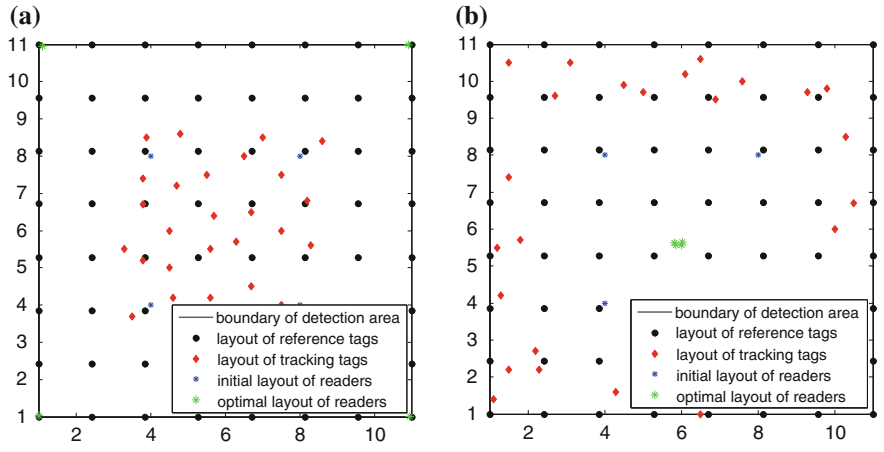

Fig. 1 The layout of the different environments **a** Environment 1 **b** Environment 2

tags in Environment 1 are distributed intensively near the centre of the indoor area, while 30 tracking tags in Environment 2 distributed dispersedly around the boundary. Dynamic frame length ALOHA algorithm is applied to check the tags. Some parameters in the simulation were set as follows: $c_1 = c_2 = 1.4962$, $\eta = 0.3$, $\alpha_1 = 0.7$, $\alpha_2 = 0.3$, $W = 40$, $U = 4$, $G_t = 1.2$ dBi, $G_r = 8$ dBi, $P_t = 36$ dBm, $\rho = 300$, $K2/K1 = 200$, $S = 3.5$, $I_p = 0.25$, $G^{\max} = 128$, $\delta = 64$, $t_z = t_c = 50$ ms, $L = 50$, $\sigma = 0$.

Figure 2 indicates that the proposed solution could converge rapidly to a deployment of readers with smaller T. From Fig. 2a, it can be seen that the final T of the proposed solution reaches 60.3476 s, while that of the uniform pattern is around 119.0156 s. Similarly conclusions can be drawn from the environment 2. Figure 1 also describes the best layout found by the proposed solution. In Environment 1, the proposed algorithm pushes all the readers to the corner of the area, which could avoid the superfluous switch during the power grade decreased from $G^{\max}$ to the desired value. In the Environment 2, as the tracking tags distributed dispersedly near the boundary, the readers are pulled to the centre of the area.

Because the optimal deployment of the readers is achieved on the condition $\sigma = 0$, we bring the noise interference into the simulation and receive cumulative distribution function (CDF) by 200 times Monte Carlo method to evaluate the stabilities of the best design under different σ. Figure 3 illuminates the comparison of CDF between the best design and the uniform pattern. In Environment 1, when $\sigma = 1.1$, 80 percentile of the best design has a $T = 57$ s with its maximum less than 59 s, while 80 percentile of uniform pattern is $T = 114$ s. As σ increases from 1.1 to 3.3, the maximum time consuming under uniform pattern and best design, respectively, are 119 s, 110 s, and 108 s and 59 s, 51 s, and 48 s.

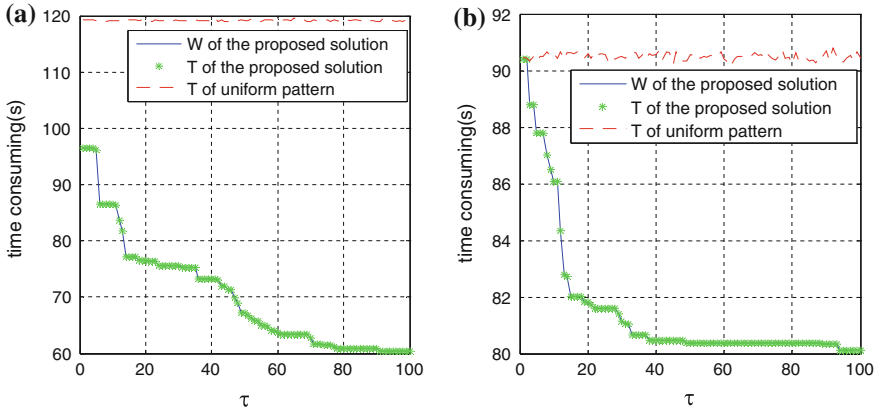

Fig. 2 The comparison of performance curves **a** Environment 1 **b** Environment 2

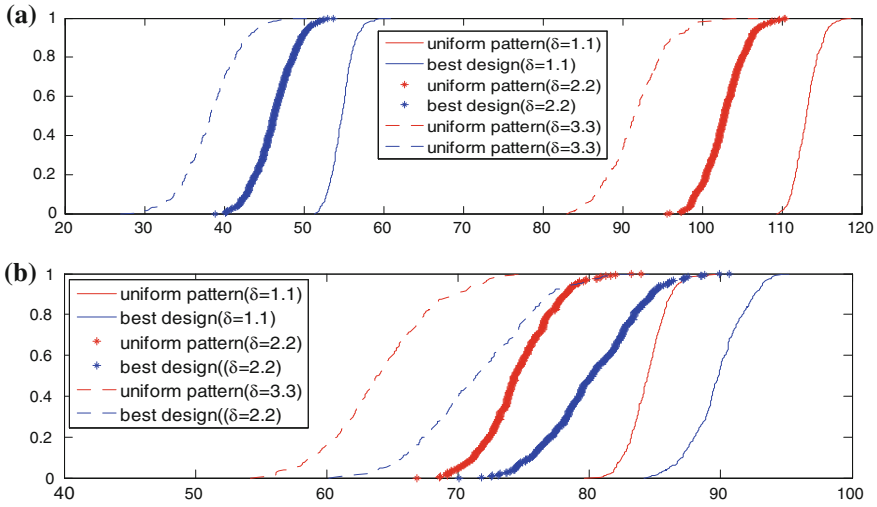

Fig. 3 The comparison of CDF under different noise interference **a** Environment 1 **b** Environment 2

6 Conclusions

The paper presents a novel optimization algorithm to obtain the optimal deployment of readers for passive LANDMARC. The detection radius under a given power grade is discussed first. Then, we explore the power grade control of the reader and propose the time consuming model for the passive LANDMARC, which leads to an objective function associated with the position of readers. Finally, an enhanced particle swarming optimization algorithm is proposed to provide the optimal deployment of readers. Simulation results indicate that, the proposed solution achieves a better design with less time consuming compared with the uniform deployment.

Acknowledgments The work in this paper is funded by National Nature Science Foundation of China under Grant (61372011).

References

1. Nakamori E, Tsukuda D, Fujimoto M, et al (2012) A new indoor position estimation method of RFID tags for continuous moving navigation systems. In: International conference on indoor positioning and indoor navigation (IPIN), Sydney NSW, pp 1–8. doi:10.1109/IPIN.2012.6418858
2. Ni LM, Liu Y, Lau YC, et al LANDMARC: indoor location sensing using active RFID. In: Wireless networks, vol 10(6), pp 701–710. doi:10.1109/PERCOM.2003.1192765

3. Zhao Y, Liu Y, Ni LM (2007) VIRE: Active RFID-based localization using virtual reference elimination. In: International conference on parallel processing, Xi'an, pp 56–56. doi:10.1109/ICPP.2007.84
4. Chang YC, Fong CJ, Lin YS, et al (2010) Optimal deployment strategy of RFID networks using Tabu search mechanism. In: The 12th International Conference on Advanced Communication Technology (ICACT), Phoenix Park, pp 1397–1400
5. Zhang D, Zhu Y, Chen H (2008). An algorithm for deployment of RFID readers in EPC network. In: 4th international conference on wireless communications, networking and mobile computing, Dalian, pp 1–4. doi:10.1109/WiCom.2008.2880
6. Zhao J, Zhang X, Guan S, et al (2009). Reader cellular deployment for RFID system. In: IEEE international conference on communications technology and applications, Beijing, pp 44–48. doi:10.1109/ICCOMTA.2009.5349240
7. Yue-lin G, Yu-hong D (2007) A new particle swarm optimization algorithm with random inertia weight and evolution strategy. In: International conference on computational intelligence and security workshops, Harbin, pp 199–203. doi:10.1109/CISW.2007.4425479
8. Smith K, Everson RM, Fieldsend JE, et al Dominance-based multi objective simulated annealing. Evolutionary Computation, vol 12(3), pp 323–342. doi:10.1109/TEVC.2007.904345

Algorithm for Optimal Placement of Cooperative Nodes in 2D TOA Cooperative Localization System

Weiguang Shi, Xin Feng and Xiaoli Qi

Abstract Cooperative localization provides an attractive solution for target positioning in recent years. It has been proved that the layout of the cooperative nodes plays a great role in the performance of the system such as the accuracy, stability, and capacity. Usually, geometric dilution of precision (GDOP) is used to measure the effect of the geometry on the accuracy. The smaller GDOP is, the lower positioning error is. In this paper, we choose 2D localization scene and derive the expression of the GDOP in TOA cooperative system. The term in GDOP that related to the position of cooperative node is chosen as the observation function. By analyzing the characteristic of its second order derivative, a fast algorithm on the basis of cosine direction coefficient, aimed to the lowest GDOP, is proposed to place cooperative nodes quickly and precisely. Simulation results demonstrate the effectiveness of the algorithm.

Keywords GDOP · Optimal placement · TOA · Cooperative node

1 Introduction

Recently, most mobile stations (MS) have been equipped with near field communication module like radio frequency identification (RFID), wireless sensor networks (WSN), bluetooth (BT), and could work in the cooperative mode to harvest auxiliary characteristic of the indoor channel for a higher precision, which called cooperative localization [1, 2]. As illustrated in Fig. 1, there are four different components in the cooperative localization system. The cooperative nodes (CN) represent fix-deployed infrastructures like RFID reader, wireless router and BT receiver, etc., which can provide ranging information. The general nodes (GN) are the base station that could offer typical cellular positioning service.

W. Shi (✉) · X. Feng · X. Qi
School of Electronics and Information Engineering, Tianjin Polytechnic University, Tianjin, China
e-mail: shiweiguang12345@126.com; shiweiguang12345@127.com

Q. Liang et al. (eds.), *Proceedings of the 2015 International Conference on Communications, Signal Processing, and Systems*, Lecture Notes in Electrical Engineering 386, DOI 10.1007/978-3-662-49831-6_57

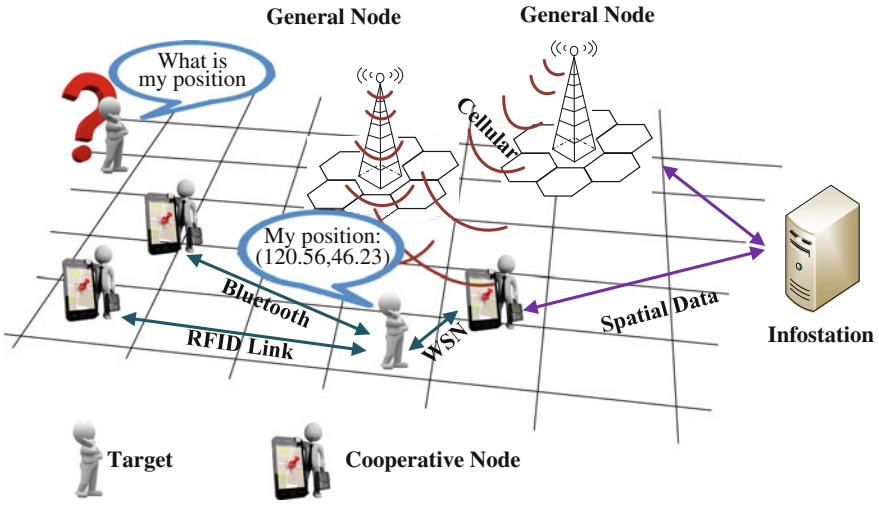

Fig. 1 The components of a cooperative localization system

The targets are the high-end mobile stations equipped with cellular positioning module and near field communication module. The work station is a server connecting to both the general nodes and the CN to collect spatial information about the target. When a target moves to indoor scenario, the communications with CN will be established quickly, which lead to a great mount of ranging information such as time stamp, power attenuation, and phase difference obtained by the work station. Obviously, the more the CN employed, the higher accuracy will be achieved as well as more computational costs involved.

Geometry deployment and measurement precision are the foremost candidates for the performance of the cooperative localization system. Previous research on the geometry deployment relies on employing the geometric dilution of precision (GDOP) to evaluate the effect of the geometry on the different ranging algorithms [3–7]. In literature [7], a solution of CN in time of arrival positioning systems, which aims to minimize the geometric dilution of precision, is presented based on generalized eigenvalue decomposition [7]. However, the solution only described the execution processes rather than deducing the expression of the eigenvalue. Since the distribution principle of the CN has not been summarized, a great amount of calculation is inevitable when the number of general nodes is huge.

Motivated by this fact, this paper addresses the optimal assignment of the CN in two-dimensional TOA systems and proposes another quick algorithm. The rest of paper is organized as follows: Sect. 2 introduces the Cramer–Rao bound (CRB) based on fisher information matrix (FIM). Section 3 gives the expression of the GDOP in two-dimensional TOA cooperative system. An algorithm for the assignment of the CN is derived in Sect. 4. In Sect. 5 we show the results of simulation. Finally, our work is concluded in Sect. 6.

2 Cramer–Rao Bound Based on FIM

Generally, the GDOP is computed on the basis of CRB which provides a theoretical lower bound for the variance of any unbiased estimator. Suppose there are totally P unknown parameters implicate in the received vector κ. Define the estimated vector as $\boldsymbol{\theta} = \left[\theta_1, \theta_2, \ldots \theta_p\right]^T$, consider the joint probability density function of κ follows q dimension Gaussian distribution with the expectation $\boldsymbol{\mu}(\boldsymbol{\theta})$ and the error covariance matrix Q, then the fisher information matrix $\mathbf{J}(\boldsymbol{\theta})$ can be given by

$$\mathbf{J}(\boldsymbol{\theta}) = \left(\partial\boldsymbol{\mu}(\boldsymbol{\theta})/\partial\boldsymbol{\theta}^{\mathrm{T}}\right)^{\mathrm{T}} Q^{-1}\left(\partial\boldsymbol{\mu}(\boldsymbol{\theta})/\partial\boldsymbol{\theta}^{\mathrm{T}}\right) \tag{1}$$

Define $H = \partial\boldsymbol{\mu}(\boldsymbol{\theta})/\partial\boldsymbol{\theta}^{\mathrm{T}}$ as the Jacobian matrix, the CRB can be expressed as follows

$$\mathbf{CRB} = \mathbf{J}^{-1}(\boldsymbol{\theta}) = \left(\mathbf{H}^{\mathrm{T}}\mathbf{Q}^{-1}\mathbf{H}\right)^{-1} \tag{2}$$

3 GDOP in Two-Dimensional TOA Cooperative System

For the two-dimensional TOA system, suppose $\kappa = \left[d_1, d_2, \ldots d_p\right]^T$ and let d_i stand for the range from the target to the ith GN given by $d_i = \sqrt{(x-x_i)^2 + (y-y_i)^2} = \overline{d_i} + e_i$, where $i \in [1, p]$, (x_i, y_i) is the coordinate of the ith GN, $\boldsymbol{\theta} = [x, y]^T$ is the position of the target, $\overline{d_i}$ is the theoretical value, e_i denotes the measurement errors with zero mean. Then the Jacobian matrix $\boldsymbol{H}$ in TOA system can be derived as

$$\mathbf{H}_{\mathrm{TOA}} = \frac{\partial\boldsymbol{\mu}(\boldsymbol{\theta})}{\partial\boldsymbol{\theta}^{\mathrm{T}}} = \begin{bmatrix} (x-x_1)/d_1 & (x-x_2)/d_2 & \ldots & (x-x_p)/d_p \\ (y-y_1)/d_1 & (y-y_2)/d_2 & \ldots & (y-y_p)/d_p \end{bmatrix}^T \tag{3}$$

Assume each e_i has an identical root mean square value σ_d, the error covariance matrix can be derived as $Q = \sigma_d^2 I$, where I is an $N \times N$ identity matrix, then the GDOP in two-dimensional TOA system can be obtained as

$$\mathrm{GDOP} = \sqrt{\sigma_x^2 + \sigma_y^2}/\sigma_d = \sqrt{G_{11} + G_{12}} \tag{4}$$

where $G = \left(\mathbf{H}^{\mathrm{T}}\mathbf{H}\right)^{-1}$, σ_x^2 and σ_y^2, respectively, stand for the variance of x and y.

It has been proved that the more CN employed, the lower GDOP received. Suppose there are totally M cooperative nodes, such as RF readers and wireless sensors, to be assigned to decrease GDOP. Geometry of the nodes in two-dimensional scenarios is illustrated in Fig. 2. For the ith GN, define the angle of arrival relative to the baseline as α_i, then we have $(x-x_i)/r_i = -\cos\alpha_i$,

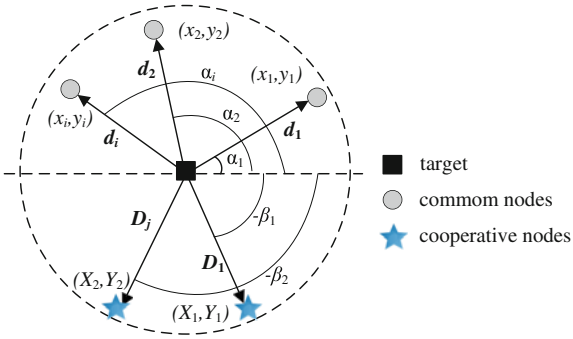

Fig. 2 Geometry of the nodes in two-dimensional scenarios

$(y-y_i)/r_i = -\sin\alpha_i$. Similarly, β_j can be defined as the angle of arrival relative to the baseline for the jth cooperative node, where $j \in [1, M]$.

Step by step strategy is utilized to arrange the whole cooperative nodes. The Jacobian matrixes of the received vector are refreshed to H'_{TOA} after first cooperative node being employed

$$H'_{\mathrm{TOA}} = \begin{bmatrix} -\cos\alpha_1 & -\cos\alpha_2 & \cdots & -\cos\alpha_p & -\cos\beta_1 \\ -\sin\alpha_1 & -\sin\alpha_2 & \cdots & -\sin\alpha_p & -\sin\beta_1 \end{bmatrix}^{\mathrm{T}} \tag{5}$$

Substituting (6) into (4), the value of GDOP in cooperative system can be deducted as

$$\mathrm{GDOP}^1_{\mathrm{TOA}} = \sqrt{(p+1)/\left(\sum_{i=1}^{p}\sin^2(\beta_1-\alpha_i) + \sum_{i=1}^{p-1}\sum_{j=i+1}^{p}\sin^2(\alpha_j-\alpha_i)\right)} \tag{6}$$

Meanwhile, we could come to a conclusion that GDOP in TOA system is only affected by the angles of the GN and the CN.

4 Optimal Assignment of the Cooperative Nodes

In the literature [7], a solution which aims to the minimum GDOP is presented on the basis of generalized eigenvalue decomposition of Jacobian matrix. However, the solution only described the execution processes rather than deducing the expression of the eigenvalue. A great amount of calculation of the eigenvalue decomposition is inevitable when the number of GN is huge. Motivated by this fact, our work will focus on providing another algorithm to the find the optimal assignment with less calculation.

Since value of GDOP is only related to β_1, we choose $Q(\beta_1) = \sum_{i=1}^{p}\sin^2(\beta_1-\alpha_i)$ as the observation function. Let $\partial Q(\beta_1)/\partial\beta_1 = 0$ and define β^1_{T1} and β^2_{T1} as the arrest points of $Q(\beta_1)$, then we have

$$\sin 2\beta_{\mathrm{T1}}^{1}/\cos 2\beta_{\mathrm{T1}}^{1} = \sin 2\beta_{\mathrm{T1}}^{2}/\cos 2\beta_{\mathrm{T1}}^{2} = \sum_{i=1}^{p} \sin 2\alpha_i / \sum_{i=1}^{p} \cos 2\alpha_i \tag{7}$$

Assume $\beta_{\mathrm{T1}}^{2} > \beta_{\mathrm{T1}}^{1}$, the value of β_{T}^{1} and β_{T}^{2} can be deduced as

$$\beta_{\mathrm{T1}}^{1} = 0.5 \times \arctan\left(\sum_{i=1}^{p} \sin 2\alpha_i / \sum_{i=1}^{p} \cos 2\alpha_i\right), \beta_{\mathrm{T1}}^{2} = \beta_{\mathrm{T1}}^{1} + 0.5\pi \tag{8}$$

Let $\beta_1 \in [\beta_{\mathrm{T1}}^{1}, \beta_{\mathrm{T1}}^{1} + \pi]$, then $\mathrm{GDOP}_{\mathrm{TOA}}^{1}$ can be considered as a periodic function of β_1 with period π. Substitute β_{T1}^{1} and β_{T1}^{2} into the second derivative $Q^{''}(\beta_1)$ respectively, then

$$Q^{''}(\beta_{\mathrm{T1}}^{1}) = 2\left|\vec{A}_{\mathrm{T1}}\right|\left|\vec{B}_{\mathrm{T1}}^{1}\right|\cos\gamma_1,\ Q^{''}(\beta_{\mathrm{T1}}^{2}) = 2\left|\vec{A}_{\mathrm{T1}}\right|\left|\vec{B}_{\mathrm{T1}}^{2}\right|\cos\gamma_2, \tag{9}$$

where $\vec{A}_{\mathrm{T1}}$, $\vec{B}_{\mathrm{T1}}^{1}$ and $\vec{B}_{\mathrm{T1}}^{2}$ are the direction vectors given by

$$\begin{aligned} &\vec{A}_{\mathrm{T1}} = \left\{\sum_{i=1}^{p} \cos 2\alpha_i,\ \sum_{i=1}^{p} \sin 2\alpha_i\right\}, \\ &\vec{B}_{\mathrm{T1}}^{1} = \left\{\cos 2\beta_{\mathrm{T1}}^{1},\ \sin 2\beta_{\mathrm{T1}}^{1}\right\}, \vec{B}_{\mathrm{T1}}^{2} = \left\{\cos 2\beta_{\mathrm{T1}}^{2},\ \sin 2\beta_{\mathrm{T1}}^{2}\right\} \end{aligned} \tag{10}$$

γ_1 is the angle between $\vec{A}_{\mathrm{T1}}$ and $\vec{B}_{\mathrm{T1}}^{1}$, γ_2 is the angle between $\vec{A}_{\mathrm{T1}}$ and $\vec{B}_{\mathrm{T1}}^{2}$. On the basis of formula (7), the value of $\cos(\gamma_1)$ is either 1 or -1, so does $\cos(\gamma_2)$. In addition, since $\beta_{\mathrm{T1}}^{2} = \beta_{\mathrm{T1}}^{1} + 0.5\pi$, the direction of $\vec{B}_{\mathrm{T1}}^{1}$ is opposite to that of $\vec{B}_{\mathrm{T1}}^{2}$.

For ease of analysis, define $\Re_1 = \sum_{i=1}^{p} \cos 2\alpha_i$ as the initial cosine direction coefficient. Obviously, if $\Re_1 < 0$, the vector angle of $\vec{A}_{\mathrm{T1}}$ is between $\pi/2$ and $3\pi/2$, then $\mathrm{GDOP}_{\mathrm{TOA}}(\beta_{\mathrm{T1}}^{1})$ achieves the minimum value since $\cos\gamma_1 = -1$ and $Q^{''}(\beta_{\mathrm{T1}}^{1}) < 0$. On the other hand, if $\Re_{\mathrm{T}} > 0$, the vector angle of $\vec{A}_{\mathrm{T1}}$ is between $-\pi/2$ and $\pi/2$, then $\mathrm{GDOP}_{\mathrm{TOA}}(\beta_{\mathrm{T1}}^{2})$ achieves the minimum value since $\cos\gamma_2 = -1$ and $Q^{''}(\beta_{\mathrm{T1}}^{2}) < 0$. Thus, a selection mechanism of the first cooperative node could be concluded as

$$\beta_{\mathrm{T1}} = \begin{cases} \beta_{\mathrm{T1}}^{1} & \text{if} \quad \Re_1 < 0 \\ \beta_{\mathrm{T1}}^{2} & \text{if} \quad \Re_1 > 0 \end{cases} \tag{11}$$

where β_{T1} is the best angle with the least GDOP. After the first cooperative node is assigned at the best position provided by formula (8) and (11), the second cooperative node should be taken into consideration. As observation function is updated to

$$Q(\beta_2) = \sum_{i=1}^{p} \sin^2(\beta_2 - \alpha_i) + \sin^2(\beta_2 - \beta_{\mathrm{T1}}) \tag{12}$$

The arrest points of $Q(\beta_2)$ can be found as β_{T2}^{1} and β_{T2}^{2}, which are given by

$$\frac{\sin 2\beta_{\mathrm{T2}}^{1}}{\cos 2\beta_{\mathrm{T2}}^{1}}=\frac{\sin 2\beta_{\mathrm{T2}}^{2}}{\cos 2\beta_{\mathrm{T2}}^{2}}=\frac{\sum_{i=1}^{p}\sin 2\alpha_i+\sin 2\beta_{\mathrm{T1}}}{\sum_{i=1}^{p}\cos 2\alpha_i+\cos 2\beta_{\mathrm{T1}}}=\frac{\sum_{i=1}^{p}\sin 2\alpha_i}{\sum_{i=1}^{p}\cos 2\alpha_i} \tag{13}$$

$$\beta_{\mathrm{T2}}^{1}=\beta_{\mathrm{T1}}^{1},\quad \beta_{\mathrm{T2}}^{2}=\beta_{\mathrm{T1}}^{2} \tag{14}$$

Also, it is clear that the cosine direction coefficient has been refreshed to $\mathfrak{R}_2=\sum_{i=1}^{p}\cos 2\alpha_i+\cos 2\beta_{\mathrm{T1}}$. Then the best position of the second cooperative node β_{T2} can be acquired by the similar mechanism depicted in formula (11). Finally, the global minimum GDOP can be achieved after the total M cooperative nodes arranged in the best location $\beta_{\mathrm{T}j}$ successively where $j\in[1,M]$.

Here, the algorithm for the optimal placement of the total cooperative nodes can be concluded as follows:

Step1: According to the position of the fixed GN, establish the initial observation function, and compute the values of $\mathfrak{R}_1$, β_{T1}^{1} and β_{T1}^{2};

Step2: Choose the best angle of the first cooperative node from β_{T1}^{1} and β_{T1}^{2} according to the polarity of $\mathfrak{R}_1$;

Step3: Arrange the first cooperative node in the best angle and update $\mathfrak{R}$;

Step4: Arrange the former uth CN in the same angle as that of first CN until $\mathfrak{R}_1\mathfrak{R}_u\le 0$;

Step5: Arrange the $(u+1)$th CN in the orthogonal angle to that of first CN, which is given by

$$\beta_{\mathrm{T}(u+1)}=\begin{cases}\beta_{\mathrm{T1}}^{2} & \text{if}\quad \beta_{\mathrm{T1}}=\beta_{\mathrm{T1}}^{1}\\ \beta_{\mathrm{T1}}^{1} & \text{if}\quad \beta_{\mathrm{T1}}=\beta_{\mathrm{T1}}^{1}\end{cases} \tag{15}$$

Step6: Deploy the rest of the CN in the angle of β_{T1}^{1} and β_{T1}^{2} alternately to obtain the global minimum $\mathrm{GDOP}_{\mathrm{TOA}}$.

5 Simulation

Simulation results and analysis are presented in this section, which intend to demonstrate the validity of the proposed algorithm. The location of target, general node, and cooperative node are denoted by polar coordinate (distance, angle). For simplicity, the coordinate of target is chosen to be (0,0). Assume that five general nodes are fixed at $(15,\pi/18),(12,\pi/6),(8,\pi),(10,11\pi/9),(10,3\pi/2)$, while six CNs are to be arranged successively to improve the precision of localization. Table 1 describes the best position obtained by the proposed algorithm. It can be seen that the minimum value of $GDOP_{\mathrm{TOA}}^{7}$ declines to 0.6043 when the angle of the mth node equals to 2.039 and the angle of the nth node equals to 0.4682 where $m=1, 2, 3, 5$ $n=4, 6$.

Table 1 Best position obtained by the proposed algorithm

Introduction of the mth CN	$\mathfrak{R}_i$	β_{Ti}	$\min(GDOP^i_{\mathrm{TOA}})$
$m = 1$	1.6133	2.0390	0.8524
$m = 2$	1.0207	2.0390	0.7600
$m = 3$	0.4281	2.0390	0.7075
$m = 4$	−0.1645	0.4682	0.6688
$m = 5$	0.4281	2.0390	0.6327
$m = 6$	−0.1645	0.4682	0.6043

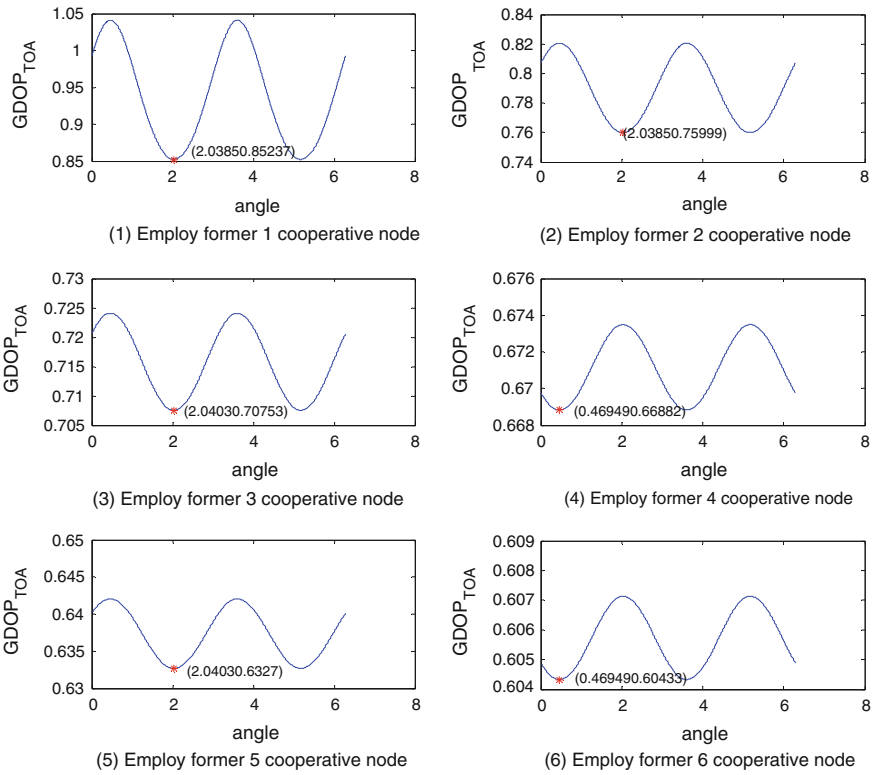

Fig. 3 Best position obtained by the exhaustive method

Figure 3 illustrates the best position of each CN obtained by the exhaustive method. The resolution of angle is $\pi/1800$. Clearly, the minimum GDOP and the best angle of the presented algorithm are always nearly the same as those of the exhaustive method. However, it should be mentioned that the computational complexity of the proposed algorithm is much smaller than the exhaustive method. In addition, the proposed algorithm only needs to compute $\mathfrak{R}_1$, β^1_{T1} and β^2_{T1} rather

than the eigenvalue and the eigenvector of Jacobian matrix in literature [7], which reduces a certain amount of computational complexity, especially in the case of huge p.

6 Conclusion

This paper aims to find the optimal placement of cooperative nodes which has the least effect of the geometry on the accuracy. First, the expression of GDOP in cooperative location system is provided. Second, the term in GDOP that related to the position of cooperative node is chosen as the observation function. After analyzing the characteristic of its second order derivative, a fast algorithm based on cosine direction coefficient, is proposed to achieve the assignment with the lowest GDOP. Simulation results indicate that, the proposed algorithm, which can receive the nearly the same performance for the cooperative nodes, can dramatically save the computational complexity compared with exhaustive method and the algorithm in the literature [7].

Acknowledgments This work was supported by the National Natural Science Foundation of China (no. 61372011).

References

1. Li W, Hu Y, Fu X, Lu S, Chen D (2014) Cooperative positioning and tracking in disruption tolerant networks. IEEE Trans Parall Distrib 99(PrePrints):382–392
2. He Z, Ma Y, Tafazolli R (2011) Accuracy limits and mobile terminal selection scheme for cooperative localization in cellular networks. In: Proceedings of IEEE VTC'11-Spring, Budapest, pp 1–5, May 2011
3. Lee H (1975) A novel procedure for assessing the accuracy of hyperbolic multilateration systems. IEEE Trans Aerosp Electron Syst AES-11:2–15
4. Tonieri DJ (1984) Statistical theory of passive location systems. IEEE Trans Aerosp Electron Syst AES-20:183–198
5. Levanon N (2000) Lowest GDOP in 2-D scenarios. In: IEE Proceedings of Radar, Sonar and Navigation, vol 147, no 3, pp 149–155, June 2000
6. Dempster AG (2006) Dilution of precision in angle-of-arrival positioning systems. Electron Lett 42(5):291–292
7. Lv X, Liu K, Hu P (2010) Efficient solution of additional base stations in time-of-arrival positioning systems. Electron Lett 46(12):861–863

Path Matching Indoor Positioning with WiFi Signal Strength

Sheng Su, Haijie Yu and Gaoli Zhang

Abstract A new indoor positioning technology based on path matching is proposed in this paper. It records the signal strength of WiFi hop points when a signal collector goes through a path in a building. The data is stored in a database as fingerprint data. Based on the fingerprint data and the building map, position of a walker can be estimated in the building. The fingerprint data of path, not point is used to the positioning. It is the innovation of the technology compared to the current indoor positioning methods. The experiments show that the path matching technology can gain the better position accuracy than KNN.

Keywords Indoor positioning · Path matching · WiFi signal strength

1 Introduction

With the rapid development of urbanization, building with large size is more popular. It is easy to lose his or her way in the building to the person who is not familiar with the building. Indoor positioning and navigation become important in order to address the issue. This paper presents an indoor positioning algorithm by path matching based on WiFi signal strength. Its realization is divided into two stages. At the offline stage, indoor WiFi signals are collected and stored in the database. At the online stage, the real-time WiFi signal is matched with the signals stored in the database. Person's locations are then estimated.

Different from the K-Nearest Neighbor algorithm (KNN), this method not only considers the values of WiFi signal, but also applies the historic data and direction sensors to arrange each WiFi device according to the signal strength. The signal

S. Su (✉) · G. Zhang
School of Information and Software Engineering,
University of Electronic Science and Technology of China, Chengdu, China
e-mail: susheng@uestc.edu.cn

H. Yu
School of Economic and Management, Southwest Petroleum University, Nanchong, China

Q. Liang et al. (eds.), *Proceedings of the 2015 International Conference on Communications, Signal Processing, and Systems*, Lecture Notes in Electrical Engineering 386, DOI 10.1007/978-3-662-49831-6_58

strength sequences at online and offline stages are matched. The current position of the device can be calculated. Compared to KNN, the problem that positioning results are back and forth jumping is avoided and related parameters are adjusted flexibly.

2 Related Works

As mentioned earlier, precise positioning is the key to the positioning and navigation in the indoor environment. A lot of research about indoor positioning has been made, such research can be divided into three categories, namely positioning based on trilateration, fingerprint matching, and dead matching. The most relevant is fingerprint matching.

Fingerprint matching algorithms have to obtain related signal information. "Closest Point" and "Nearest neighbors in signal space-average" are two algorithms that are used frequently. The results of these two methods are lack of stability, and influence the accuracy of positioning due to the unstable WiFi signal. RADAR [1] is a WLAN-based indoor positioning system that uses Nearest-Neighbor and Radio Map Modeling algorithms to estimate the target position, but the accuracy is not enough. HORUS [2] is an indoor WLAN positioning system completely based on fingerprint database, which is presented by Youssef. HORUS does not use the wireless signal propagation model, so the positioning accuracy is higher than RADAR system. However, modeling with signal distribution needs to gather a lot of signal data, and the signal intensity of each AP must be seen as irrelevant, which are not consistent with the actual situation. Kuo et al. [3] improved the performance of the positioning system by finding out the correlation between the signal intensity and positioning according to the relevance of signal intensity. For multipath propagation phenomenon in indoor environments, Fang et al. [4] proposed a method to reduce the interference of multipath propagation. Yin et al. [5] obtain the variation of system signal intensity by increasing the number of fixed observation point. Pan et al. [6] applied nuclear canonical correlation analysis technology to build the relationship between signal intensity and position coordinates. Kushid et al. [7] build fingerprint database by nuclear-based approach. In addition, Kuo et al. [8], Fang et al. [9], Tseng et al. [10], Chai et al. [11], Kushki et al. [12], also proposed a different approach for enhancing system performance.

3 Algorithm Description

This algorithm records WiFi signal intensity data for each WiFi devices recorded in working process in order of walking paths. We can get signal distribution from several WiFi signals in a path because there are multiple wifi devices, then use these signals to match the signal of WiFi in the corresponding sections stored in the database, and the

location is determined by matching sections and walking directions. Algorithm is divided into two stages, which will be introduced separately below.

3.1 Data Acquisition and Processing

Data acquisition is the first step to realize this algorithm. At this stage, we need to collect and store continuous signal intensity from all WiFi devices which can be received in every path in the indoor area. They will be used in the following signal matching. Since different WiFi devices have different transmit power, and there are large differences in highest signal intensity that can be achieved from different devices, the indoor environment which WiFi device in also affects size of the measured signal values. However, according to signal propagation law, received signal intensity will be larger when WiFi launch locations are closer. Based on this principle, WiFi location is able to achieve.

The left in Fig. 1 shows the signal intensity distribution of two WiFi devices at different locations collected when walking in a path in real environment. It can be seen from the left, attenuation of the WiFi signal will be greater because of the effects of walls, windows and doors, interior layouts in the environment. The collected WiFi signal intensity is significantly different in a different location because of the influence of signal wave reflection and diffraction, so there are large changes between signal intensity of two points at neighboring location. Irregular changes of signals make finding the regular transformation difficult when processing the number of WiFi signal data. In order to make the signal more stable to get better matching results, equation (1) is used to process data for smooth filtering. That is current value of the signal W_i under the influence of a signal value W_{i-1}, thereby reducing the collected signal amplitude.

$$W_i = (1-\alpha)W_{i-1} + \alpha W_i \tag{1}$$

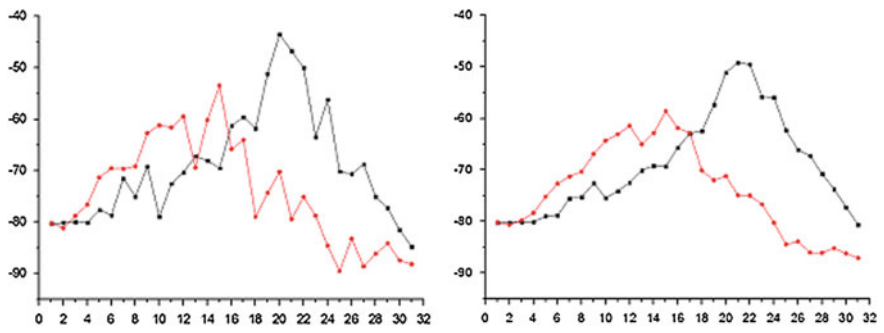

Fig. 1 *Left* is the collected raw data, *right* is the processed data

The right in Fig. 1 is a relation graph of WiFi signal changed by location after processed with equation (1). WiFi signal intensity is more stable after filtering, which is conducive to follow-up signal matching. The processed data stored in the database will finish WiFi signal data collection process at the offline stage.

3.2 Location Calculation Stage

On the basis of data collection and processing, this phase details the algorithm realization and problems in the process of algorithm realization. The detail of the algorithm is as following.

Algorithm 1 Algorithm of PathMatch

```
for x= 0 -> wifi_nums do
  for y = 0 -> position_nums -min_length do
    for z = y + min_length -> position_nums do
      if isSimilar(online_levels, offline_levels, y, z) then
        if similar_part[x][0] = similar_part[x][1] or z - y >
          similar_part[x][1] - similar_part[x][0] then
            similar_part[x][0] = y
            similar_part[x][1] = z
        end if
      end if
    end for
  end for
end for
for x = 0 -> wifi_nums do
  matched_nums = similar_part[x][1] - similar_part[x][0]
  step = len(online_levels[x]) / match_nums
  for y = 0 -> matched_nums do
    offline_levels_matched[y] = offline_levels[x][similar_part[x][0] + y]
    online_levels_matched[y] = online_levels[x][step * y]
  end for
  tmp <- calc_ppmcc(offline_levels_matched, online_levels_matched)
  if abs(tmp) > THRESHOLD_CC then
    matched_result[x][0] = y
    matched_result[x][1] = z
    if orient = 0 then
      if tmp > 0 then
        orient <- 1
      else
```

```
29:                orient <- -1
30:            end if
31:        end if
32:    end if
32:end for
33:for x = 0 -> len(matched_result) do
34:    if matched_result[x][0] != matched_result[x][1] then
35:        count++
36:        for y = matched_result[x][0] -> matched_result[x][1] do
37:            matched_road[y] += 1
38:        end for
39:     end if
40:end for
41:for x = 0 -> len(matched_road) do
42:    matched_road /= count
43:end for
44:for x = 0 -> len(matched_road) do
45:    if matched_road[x] > THRESHOLD_ROAD_COVER do
46:        begin_index = matched_road[x]
47:        break
48:    end if
49:end for
50:for x = len(matched_road) -> 0 do
51:    if matched_road[x] > THRESHOLD_ROAD_COVER do
52:        end_index = matched_road[x]
53:        break
54:    end if
55:end for
56:if orient is equal to 1 then
57:    return end_index
58:else
59:    return bigin_idnex
```

For the first WiFi device, the values read from the database and walking make up a group. Successive sections with similar characteristics $(W_{p-j}, W_{p-(j+1)}, \ldots, W_{p-(j+k)})$ between data in WiFi signal database and data recorded in the process of walking in this group are calculated.

Data features are several values to broadly represent the distribution of data values. These are initial value, end value, maximum, minimum, and average. Because the WiFi signal intensity and the distance of WiFi device in the test present negative relations and WiFi signal intensity is between -100 and -30, these values from a number of continuous WiFi signal values can reflect generally distances between the location recording the series of signals and the location of WiFi device.

When all eigenvalues in the two sets of data with a WiFi device are all within the limits of the 20 %, both sets of data are similar.

The correlation coefficient between two data sets is computed. If the correlation coefficient between the two sets of data is less than the threshold value THRESHOLD_CC, route section that records this piece of data is fetch out, and this route is recorded according to the matched data in Step 5.

Correlation coefficient is used to measure the linear relationship between two variables. Equation (2) is the calculation formula. The value of the correlation coefficient r is from -1 to 1. When r's absolute value $|r|$ is 1, two variables are perfectly correlated. In this case, relationship between x and y is a linear function. When $|r|$ is smaller than 1, the value of $|r|$ is larger. Two sets of data between x and y are not relevant if the value of $|r|$ is equal to 0. Thus, we can easily determine whether two groups of WiFi signals data are consistent.

$$r = \frac{\sum_{i=1}^{n}(X_i - \bar{X})(Y_i - \bar{Y})}{\sqrt{\sum_{i=1}^{n}(X_i - \bar{X})^2}\sqrt{\sum_{i=1}^{n}(Y_i - \bar{Y})^2}} \tag{2}$$

For each of the other WiFi devices, the Steps 5 to 7 are repeated to get the closest matching section between the data recorded from each WiFi devices for the current walking and that of the WiFi devices in the WiFi signals database. Then the section that has the same or larger coverage rate than the threshold THRESHOLD_-ROAD_COVER in all of these sections is obtained. One of the endpoints of the section is the location positioned.

4 Computational Experiments

One floor of a business office building is used to test the effect of the path matching indoor positioning algorithm. The floor is about 60 m long. The corridor is located at the middle of the floor. Two sides of the corridor have many offices. Many offices have WiFi route devices. Our algorithm is installed in a smart phone with android mobile system.

First, we moved the smart phone from one end to the other end of the corridor. In order to collect a steady WiFi signal strength value, we recorded ten times at each location. The interval time between two records is 500 ms. The average value of the ten records is used to be the final value at the location. The average values of all WiFi devices formed a vector according to the walk sequence. Equation (1) is used to process the average values in the vector. Then signal distributions of all WiFi devices are obtained in the path and stored.

The next stage is the real-time positioning. One walks in the corridor with the smart phone which constantly collects WiFi signal in order to positioning calculation.

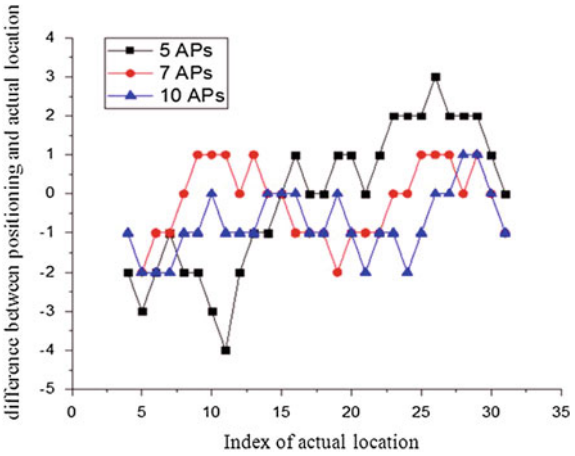

Fig. 2 Effects of different number of WiFi devices on positioning

The impact of the number of WiFi devices on positioning effect is shown in Fig. 2. According to the records of the offline data collection, all locations are numbered. The signal strength of all WiFi devices is stored by the sequence. As shown in Fig. 2, the x coordinate is the actual location of smart phone when positioning is executed. The y coordinate is the difference between the number of positioning location and that of actual location. The fluctuation of positioning result is smaller while the number of WiFi devices increase. It means that the positioning location is closer to the actual place and the effect of positioning is gradually accurate.

Figure 3 shows the impacts of the threshold of correlation coefficient on positioning. As shown in Fig. 3, the matching requirement of online and offline data is more restrict while the value of the threshold is larger. Offline data segment matched is shorter. The matching location tends to the end of the path. The comparisons of location obtained by three thresholds are illustrated in Fig. 3. Offline data

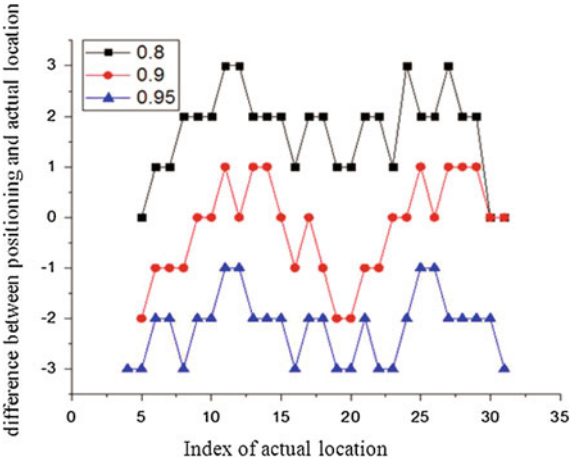

Fig. 3 Impacts of the threshold of correlation coefficient on positioning

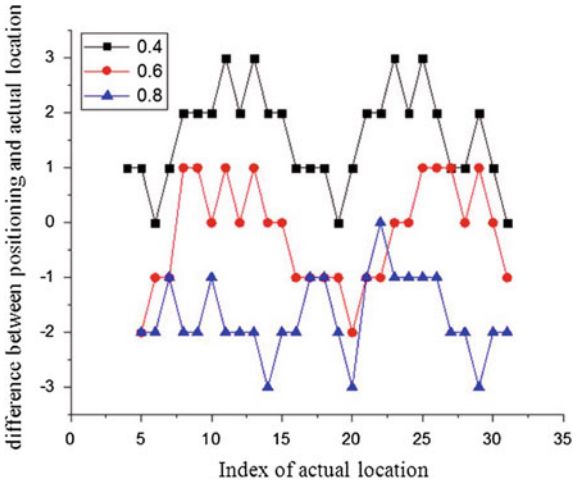

Fig. 4 Impacts of the threshold of coverage rate on positioning effect

segment is long while the threshold value is small. The positioning location is earlier than actual location. In the converse, offline data segment is short while the threshold value is large. The positioning location is later than actual location.

The impacts of the threshold of coverage rate on positioning are shown in Fig. 4. Similar to Fig. 3, the number of locations that is added to the matching path is fewer while the threshold of coverage rate is larger. The matched path is shorter. It means that the positioning location is later than the actual location.

In order to compare our algorithm with the KNN algorithm, seven WiFi devices are chosen in the next experiment. The threshold value of the correlation coefficient and coverage rate are set to 0.9 and 0.6, respectively. As shown in Fig. 5, the fluctuation of KNN is larger than our path matching algorithm. The positioning

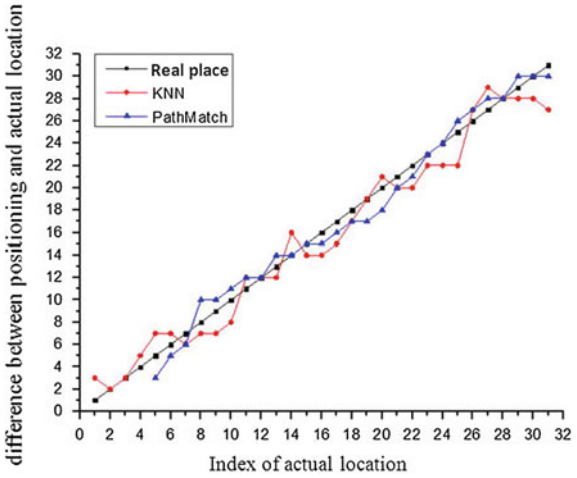

Fig. 5 Comparison of positioning of path matching and KNN

location jumps back and forth in some segments. The results of path matching algorithm are more stable and accurate.

5 Conclusions

The path matching indoor positioning algorithm utilizes the historic data of WiFi signal strength. The positioning is accurate. The accuracy of positioning is higher while the number of WiFi devices is larger. Compared to the KNN method, our path matching algorithm can obtain better positioning effect. Path matching algorithm is also more stable. In the future, we will focus on more complicate path and indoor building. It is challenger than positioning on simple indoor environment.

Acknowledgments This research was supported by the National Natural Science Foundation of China under Grant No. 60904072, 71301018.

References

1. Bahl P, Padmanabhan V (2000) RADAR: an in-building RF-based user location and tracking system. In: IEEE Infocom 2000. Tel Aviv:IEEE, pp 775–784
2. Youssef MA (2004) HORUS: a WALAN-based indoor location determination system. University of Maryland
3. Kuo S, Tseng Y (2008) A scrambling method for fingerprint positioning based on temporal diversity and spatial dependency. IEEE Trans Knowl Data Eng 20(5):678–684
4. Fang S, Lin T, Lee K (2008) A novel algorithm for multipath fingerprinting in indoor WLAN environments. IEEE Trans Wirel Commun 7(9):3579–3588
5. Yin J, Yang Q, Ni L (2008) Learning adaptive temporal radio maps for signal-strength-based location estimation. IEEE Trans Mob Comput 7(7):869–883
6. Pan J, Kwok J, Yang Q et al (2006) Multidimensional vector regression for accurate and low-cost location estimation in pervasive computing. IEEE Trans Knowl Data Eng 18 (9):1181–1193
7. Kushki A, Plataniotis K, Venetsanopoulos A (2007) Kernel-based positioning in wireless local area networks. IEEE Trans Mob Comput 6(6):689–705
8. Kuo S, Tseng Y (2011) Discriminant minimization search for large-scale RF-based localization systems. IEEE Trans Mob Comput 10(2):291–304
9. Fang S, Wang C (2011) A dynamic hybrid projection approach for improved Wi-Fi location fingerprinting. IEEE Trans Veh Technol 60(3):1037–1044
10. Tseng P, Feng K, Lin Y et al (2009) Wireless location tracking algorithms for environments with insufficient signal sources. IEEE Trans Mob Comput 8(12):1676–1689
11. Chai X, Yang Q (2007) Reducing the calibration effort for probabilistic indoor location estimation. IEEE Trans Mob Comput 6(6):649–662
12. Kushki A, Plataniotis K, Venetsanopoulos A (2010) Intelligent dynamic radio tracking in indoor Wireless Local Area Networks. IEEE Trans Mob Comput 9(3):405–419

Part IX
Pattern Recognition

Anomaly Detection in Big Data with Separable Compressive Sensing

Wei Wang, Dan Wang, Shu Jiang, Shan Qin and Lei Xue

Abstract Nowadays, the anomaly detection of big data is a key problem. In this setting, principal components analysis (PCA) as an anomaly detection method is proposed, but PCA also has scalability limitations. Thus, we proposed the feasibility measure to use the PCA and separable compression sensing to detect the abnormal data. Subsequently, we prove that volume anomaly detection using compressing data can achieve equivalent performance as it does using the original uncompressed and reduces the computational cost significantly.

Keywords Big data · Anomaly detection · Separable compression sensing · PCA

1 Introduction

The arrival of the era of big data promoted the development of information retrieval and data mining technology [1]. Detection of volume abnormal information is also becoming more and more important. There are a lot of detecting problem of large data in many practical applications. Furthemore, the exception will make network congestion and will cause serious influence to the user, thus analysis of abnormal problem is very important for us [2].

In recent work demonstrated a useful role for principal component analysis (PCA) to detect network anomalies. They showed that the minor components of PCA (the subspace obtained after removing the components with largest eigenvalues) revealed anomalies that were not detectable in any single node-level trace. This work assumed an environment in which all the data is continuously pushed to

W. Wang (✉) · D. Wang · S. Qin · L. Xue
College of Electronic and Communication Engineering, Tianjin, China
e-mail: weiwangvip@163.com

S. Jiang
Research Institute, China Shipbuilding Industry Corporation, No.704, Shanghai, China

Q. Liang et al. (eds.), *Proceedings of the 2015 International Conference on Communications, Signal Processing, and Systems*, Lecture Notes in Electrical Engineering 386, DOI 10.1007/978-3-662-49831-6_59

a centralsite for off-line analysis. Such a solution cannot scale either for networks with a large number of monitors nor for networks seeking to track and detect anomalies at very small time scales. Thus, anomaly detection in large data is still a problem to be studied.

In this paper we propose a general method to diagnose anomalies. This method is based on PCA (principal components analysis) algorithm and the CS (compression sensing) theory to realize the data anomaly detection. The goal of this article is in order to achieve the data of anomaly detection.

The paper is organized as follows. In Sect. 1, we introduced the data of the research status of anomaly detection and research content. In Sect. 2, we introduced anomaly detection theory and separable compression sensing theory. In Sect. 3, we first generate simulation data and then the data for training and testing results are obtained. In Sect. 4, we get the article conclusion.

2 Theory

2.1 Anomaly Detection

According to Lakhina et al. [2], we can learn a lot of anomalies which is very rare, and abnormal will be hidden in the normal data. PCA [3] is a small number of principal components derived from the original variables, so that they can retain the information of the original variables as much as possible [4]. Thus, we can use PCA algorithm which is easier to find abnormal.

First, let the network information by matrix $X = (X_1, X_2, \ldots, X_L)$ and each of these data $X_i \in R^N, i = 1, \ldots, L$ [5] after the normalization of matrix and we begin to decomposition for the normalized matrix by using PCA algorithm, then get the same covariance matrix:

$$\Sigma x = \left(\frac{1}{L}\right) XX^T = U\Lambda U^T \tag{1}$$

Given that $U = [U_1, \ldots, U_k]$ are the principal eigenvectors of $\sum_x$ corresponding to the largest K eigenvalues $\lambda_1, \ldots, \lambda_K$, the projection onto the residual subspace is $P = (I - UU^T)$ [6]. So, for the checked data X, its protection into the residual subspace is $Z = PX = (I - UU^T)X$. If Z follows a multivariate normal distribution, the squared prediction error (SPE) [7] statistic is given as:

$$tSPE = \|Z\|_2^2 = \left\|(I - UU^T)X\right\|_2^2 \tag{2}$$

and follows a noncentral chi-square distribution under the null hypothesis that the data is 'normal'. Hence, rejection of the null hypothesis can be based on whether

tSPE exceeds a certain threshold corresponding to a desired false alarm rate β. In [2], the Q-statistic was identified as threshold, it is usually expressed as:

$$Q_{\beta} = \theta_1 \left[\frac{c_{\beta}\sqrt{2\theta_2 h_0^2}}{\theta_1} + 1 + \frac{\theta_2 h_0(h_0-1)}{\theta_1^2}\right]^{\frac{1}{h_0}} \tag{3}$$

where $h_0 = 1 - \frac{2\theta_1\theta_3}{3\theta_2^2}$, $\theta_i = \sum_{j=K+1}^{N} \xi_j^i$ for $i = 1, 2, 3$, $c_{\beta} = (1-\beta)$ percentile in a standard normal distribution and Q_{β}, and ξ_j, $i = 1, \ldots, M$ are the eigenvalues of $\sum_y$.

Once the tspe $> Q_{\beta}$, then can estimate the data which is the abnormal state detection data.

2.2 *Theory of Separable Compression Sensing*

Separate compression sensing theory pointed out that the random measurement matrix through the tensor product can be expressed as $\Phi = \Phi_x \otimes \Phi_y$ [8], Depending on the theory of CS X Random projection value G can be represented as:

$$G = \Phi_x X \Phi_y \tag{4}$$

The (1) further the available data X of the sparse coefficient matrix is expressed as A:

$$G = \Phi_x \Psi_x A (\Psi_y)^T \Phi_y \tag{5}$$

The $\Psi = \Psi_x \otimes \Psi_y$ is sparse transformation matrix tensor product form. Depending on the random measured value, can reconstruct the original data:

$$\min \|A\|_1 \qquad \text{subject to } G = \Phi_x \Psi_x A (\Psi_y)^T \Phi_y \tag{6}$$

According to the Eq. (5), G represents the compressed of testing data, the G instead of type (2) in X, then carries on the data of the anomaly detection [9, 10].

3 Simulation and Experimental Results

3.1 *Synthetic Data*

There are two main purpose of the experiment. The first one is to prove that our method is feasible for Large N. The second is to show that it has a better time resolution property when processing the data stream in CS domain. First, we consider a model for the network data as follows:

$$x = s + n \tag{7}$$

where x is the snapshot of network traffic over N links: Which letter s represents original signal and the letter n is a gaussian noise that is added to the original data [6]. We selected matrix which is 500 lines of 2000 columns. In order to make the anomaly in the compression state as much as possible is detected, we selected the multiple compression matrix for the test, at the same time, we add the Gaussian noise average is zero-mean and mean square error is 0.01. To imitate the network abnormal, we added 40 sample sizes of exception information on the original signal following the procedure mentioned in [2].

3.2 Experiments Results

We investigated the uncompressed matrix and the compression degree of different matrix analysis as shown in the results. Horizontal axis represents the β from 0.1 to 0.9, ordinate represents anomaly detection accuracy. Specifically, Fig. 1 shows a plot of the eigenvalue distribution between original and compressed data. This is a

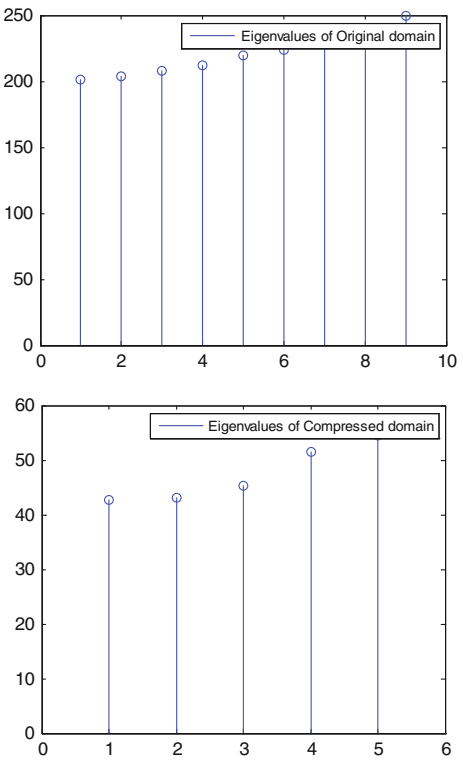

Fig. 1 Eigenvalues of original and compressed data

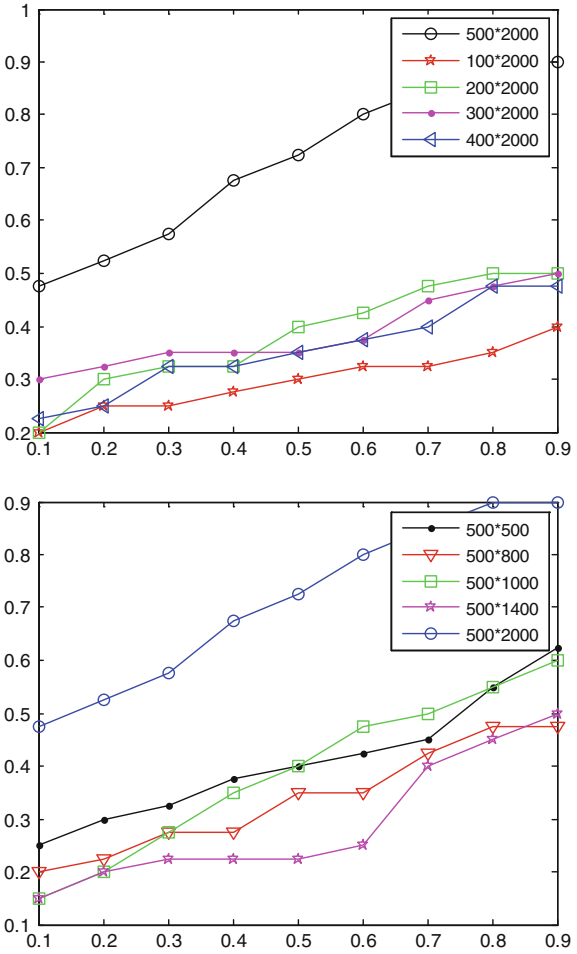

Fig. 2 The correct probability of anomaly detection with different matrix

very encouraging result from the point of view of detecting anomaly in CS domain. Under each beta we all joined the anomaly information with 40, the number of each matrix to detect abnormal is $Y/40$ and the anomaly detection accuracy can be calculated according to Fig. 2. Uncompressed curve as shown in Fig. 2, it can detect the abnormal information ratio which increases with the beta. As shown in Fig. 2 matrix compression degree can detect abnormal probability which is also different. The smaller the compression degree of anomaly detection the accuracy is higher.

4 Conclusions

Through simulation experiment, we use PCA and separable compression sensing to detect the different matrices, the matrix of uncompression is more easily to detect the abnormal than the matrix of compression. Thus, we have to choose the degree of compression in order to detect the abnormal information more accurately.

Acknowledgments This paper is supported by Natural Science Foundation of China (61271411), and cooperation project of 2014 annual national natural science fund committee with the Edinburgh royal society of British (613111215). It also supported by Tianjin Research Program of Application Foundation and Advanced Technology (15JCZDJC31500), National Youth Fund (61501326) and Research on real time topology optimization and efficient broadcasting transmission algorithm in ZigBee networks for smart grid (61401310).

References

1. Zhang J, Li H, Gao Q, Wang H, Luo Y (2014) Detecting anomalies from big network traffic data using an adaptive detection approach. J Inf Sci 318:91–110
2. Lakhina A, Crovella M, Diot C (2004) Diagonising network-wide traffic anomalies. In: Proceedings of the ACM SIGCOMM
3. Wang M (2007) A method for detecting wide-scale network traffic anomalies. J ZTE Commun 4:19–23, 1671-5799
4. Kanda Y, Fontugne R, Fukuda K, Sugawara T (2013) Anomaly detection method using entropy-based PCA with three-step sketches. J Comput Commun 36(5):575–588
5. Pham D-S, Venkatesh S, Lazarescu M, Budhaditya S (2014) Anomaly detection in large-scale data stream networks. J Data Min Knowl Disc 28:145–189. doi:10.1007/s10618-012-0297-3
6. Pham DS, Saha B, Lazarescu M, Venkates S (2009) Scalable network-wide anomaly detection using compressed data, Perth, W.A.
7. Ling H (2006) In-network PCA and anomaly detection. In: Proceedings of the twentieth annual conference on neural information processing systems 19, Vancouver, British Columbia, Canada, 4–7 Dec 2006
8. Rivenson Y (2009) Practical compressive sensing of large images. In: 2009 IEEE 16th international conference on digital signal processing. doi:10.1109/ICDSP.2009.5201205
9. Rivenson Y, Stern A (2009) Compressed imaging with a separable sensing operator. IEEE Signal Process Lett. doi:10.1109/LSP.2009.2017817
10. Wang W, Dunqiang L, Zhou X, Zhang B, Jiasong M (2013) Statistical wavelet-based anomaly detection in big data with compressive sensing. EURASIP J Wireless Commun. Networking. doi:10.1186/1687-1499-2013-269

Ground-Based Cloud Classification Using Pyramid Salient LBP

Zhong Zhang, Yue Zhang and Shuang Liu

Abstract Cloud classification of ground-based images is a challenging task due to extreme variations in the appearance of clouds under different atmospheric conditions. Recent research has focused on extracting discriminative image features, which play an important role in achieving competitive classification performance. In this paper, an novel feature extraction algorithm, pyramid salient LBP (PSLBP), is proposed for ground-based cloud classification. The proposed PSLBP descriptors take texture resolution variations into account by cascading the SLBP information of hierarchical spatial pyramids. PSLBP descriptors show their effectiveness for cloud representation. Experimental results using ground-based cloud images demonstrate that the proposed method can achieve better results than current state-of-the-art methods.

1 Introduction

Clouds play an important role in the energy balance of the earth because of their absorption and scattering of solar and infrared radiation, and their change is an important influence factor of the global climate [1]. Most of existing cloud related research requires the technology of ground-based cloud observation, such as ground-based cloud classification [2, 3], cloud cover evaluation [4], and cloud height measure. Among them, ground-based cloud classification, as an important cloud observation technique, has attracted much attention from the research community. It is because successful cloud classification can improve the precision of weather prediction and help us to understand climatic conditions. Nowadays, ground-based clouds

Z. Zhang · Y. Zhang · S. Liu (✉)
College of Electronic and Communication Engineering, Tianjin Normal University, Tianjin, China
e-mail: shuangliu.tjnu@gmail.com

Z. Zhang
e-mail: zhong.zhang8848@gmail.com

Y. Zhang
e-mail: qinlanruoshang@126.com

Q. Liang et al. (eds.), *Proceedings of the 2015 International Conference on Communications, Signal Processing, and Systems*, Lecture Notes in Electrical Engineering 386, DOI 10.1007/978-3-662-49831-6_60

are classified by the observers who have received professional training. However, different observers will obtain discrepant classification results due to different level of professional skill. Moreover, this work is complicated and time consuming. Therefore, automatic ground-based cloud classification technique is eagerly required in this area.

With the development of the remote sensing research and digital image processing technology, ground-based sky-imaging devices have been widely used for obtaining information on sky conditions. These devices, including WSI (whole sky imager) [5], TSI (total sky imager) [6], and ICI (infrared cloud imager) [7], can provide continuous sky images from which one can infer cloud macroscopic properties. Based on the above devices, a lot of methods have been proposed for ground-based cloud classification [2, 3, 8]. Singh and Glennen utilized cooccurrence matrix and autocorrelation to extract features from common digital images for cloud classification [9]. Calbó and Sabburg used fourier transformation and statistical features to classify eight predefined sky conditions [10]. Heinle et al. proposed an approach to extract spectral features and some simple textural features, such as energy and entropy for a fully automated classification algorithm, in which seven different sky conditions are distinguished [8]. Despite these recent works, many important problems for ground-based cloud classification have not yet been explored. For example, the extracted features are not discriminative enough to describe the ground-based cloud images, which might lead to poor classification performance.

Clouds can be thought of one kind of natural texture, and it is reasonable for ground-based cloud images to be handled with texture classification methods. As one kind of classical texture descriptors, local binary pattern (LBP) [11] is particularly popular due to its simplicity and efficiency, and various extensions are made for the conventional LBP descriptors [3, 12, 13]. Due to their excellent performances, LBP and its extensions have been successfully utilized in image classification and face recognition. The uniform patterns of LBP code (the uniform LBP for short) have been proposed as a means of improving the performance of LBP-based methods. However, the uniform LBP patterns do not account for a high proportion of the patterns in cloud images, therefore, they cannot capture the fundamental properties of these images. Liao et al. [13] proposed dominant LBP (DLBP) as an improved strategy to solve this problem, the method based on DLBP only considered the pattern occurrences of salient patterns, while the type of pattern information is lost. Liu et al. [3] proposed salient LBP (SLBP) descriptor which takes advantage of the most frequently occurring patterns to capture descriptive information. Although SLBP is effective for handling the disadvantage for conventional LBP, its basic assumption is that texture resolution of an image is fixed as shown in Fig. 1a. Actually, texture patches in a cloud image can be with various resolutions as shown in Fig. 1b. Each of the two examples shown in Fig. 1a is with same resolution. While the texture resolutions of each images shown in Fig. 1b are varying significantly. Usually, compared with various resolutions, texture information in a fixed resolution does not have significant discriminative power.

In order to obtain the resolution information of cloud image, an novel feature extraction algorithm named pyramid salient LBP (PSLBP) is proposed for ground-

Fig. 1 Ground-based cloud image patches with various resolutions. In **a** each image is with same resolution, images are with same content but with various resolutions. **b** The texture resolution are varying in each cloud image patch

based cloud classification. The proposed PSLBP descriptors take texture resolution variations into account by cascading the SLBP information of hierarchical spatial pyramids. The rest of this paper is organized as follows: In Sect. 2 the SLBP is briefly over viewed. and then the SLBP with pyramid representation is introduced in detail in Sect. 3. In Sect. 4 experimental results and discussions are given. Finally, conclusions are drawn in Sect. 5.

2 Brief Review of SLBP

Conventional local binary patterns (LBP) proposed by Ojala et al. [11] is considered as an effective descriptor for texture classification. The LBP operator labels each pixel in the image by computing the sign of the differences between the central pixel and its neighboring pixels. The result is a decimal number computed by the corresponding binary string. Then, the image is represented by the histogram of these decimal numbers. The LBP value for the central pixel is computed as

$$LBP^{ri}_{P,R} = \min_{0 \le l < P} \{ \sum_{p=0}^{P-1} s(g_p - g_c) \times 2^{[(p+l) mod\ P]} \} \quad (1)$$

where p_c represents the gray value of the central pixel, p_n $(n = 0, \ldots, N-1)$ denotes the gray value of the neighboring pixel on a circle of radius R, and N is the total number of neighbors. The step function $s(x)$ is described with $s(x) = 1$ if $x \geq 0$ and $s(x) = 0$ otherwise. The minimum value in Eq. (1) denotes the label of the rotation invariant LBP at the central pixel.

To ensure the robustness of feature representation, the most salient LBP descriptor [3] is proposed as the following steps. First, Liu et al. build rotation invariant LBP histogram by Eq. (1) for every cloud image, and then accumulate all of these histograms into a single histogram. Finally, we sort the histogram in descending order. The first several patterns in this sorted histogram are the most frequently occurring patterns in cloud images which are as the salient patterns. The minimum value k of determining the salient patterns are calculated by:

$$k = \arg\min_{S}\left(\frac{\sum_{j=0}^{k-1} H[j]}{\sum_{j} H[j]}\right) \geq T \tag{2}$$

Here, $H[1, 2, \ldots]$ denotes the sorted histogram of all rotation invariant patterns, and T is a threshold determining the proportion of salient patterns. The authors set $T = 80\,\%$. The salient patterns by solving Eq. (2) are denoted as $S[i]$.

3 The Proposed Pyramid Salient LBP

In order to capture the hierarchical spatial pyramids information of cloud images, the proposed PSLBP descriptors take texture resolution variations into account by cascading the SLBP information. Pyramid transform is an effective multi-resolution analysis approach. In this paper, we represent local binary pattern in spatial pyramid domain.

During pyramid transform, each pixel in the low spatial pyramid is obtained by down sampling from its adjacent high-resolution image as shown in Fig. 2. Thus in the low resolution images, a pixel corresponds to a region in its high resolutions.

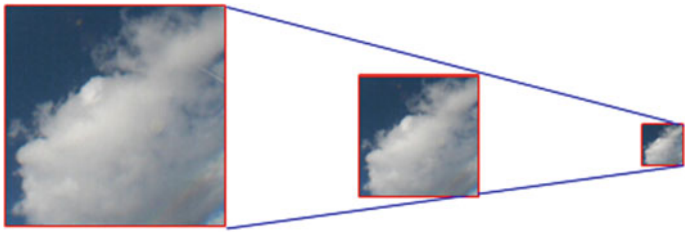

Fig. 2 The diagram of pyramid sampling in neighboring three resolutions

Each neighboring two images are with resolution variation rate 4. That is to say, the down sampling ratios in x and y directions are both 2.

Let $f(x, y)$ denote the original image. For the pyramids of adjacent two resolutions are determined as follows:

$$G_l(x, y) = \sum_i \sum_j G(R_x + i, R_y + j) \tag{3}$$

where $G_1 = f(x, y)$ and pyramid level $l > 1$. where R_x and R_y are the down sampling ratios in x and y directions, respectively. $R_x R_y > 1$ means down sampling is utilized during pyramid image generation, while $R_x = R_y = 1$ means no sampling is utilized.

Let T^k represent the texture information of the kth pyramid ($k = 1, ..., N$) and $SLBP_{P,R,k}$ denote the SLBP of a pixel at the kth spatial pyramid. Finally, the PSLBP is the combination of the SLBP histograms of the N spatial pyramid images as follows:

$$PSLBP_{P,R} = \bigcup_k SLBP_{P,R,k} = (SLBP_{P,R,1}; SLBP_{P,R,2}; \cdots; SLBP_{P,R,N}) \tag{4}$$

4 Experimental Results and Analysis

In this section, our proposed PSLBP is compared with the representative LBP [6], LTP [11] and CLBP algorithm For all descriptors, χ^2 metric is used to evaluate the performance of different descriptors. In the following experiments, each image is normalized to have an average intensity of 128 and a standard deviation of 20.

4.1 Database

Kiel database is provided by Kiel University in Germany. According to the International cloud classification system published in WMO, the dataset is divided into seven classes. The sample number of each class is different and the total number is 1500. This dataset has large illumination variations and intra-class variation. Samples for each class are shown in Fig. 3.

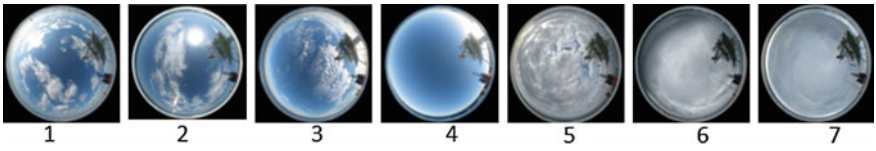

Fig. 3 Cloud samples from the Kiel database

Table 1 Average classification accuracy for the four algorithms on the Kiel database

LBP	DLBP	SLBP	PSLBP
70.53	75.16	77.42	83.21

4.2 Experimental Results and Analysis

In this experiment, 1/5 samples are randomly chosen from each class as training data while the remaining images are used for testing, and the process is repeated 100 times. The experiment results of different algorithms on the Kiel database are listed in Table 1. From the results, several conclusions can be drawn. First, the proposed PSLBP algorithm achieves the highest classification accuracies in the two databases. Second, the performance of our DSLBP method is over 12 % better than that of LBP method in the Kiel database. Third, the classification results of PSLBP are better than that of SLBP, indicating that adding texture resolution variation information is help to improve the classification performance.

5 Conclusions

In this paper, salient local binary pattern with pyramid representation approach is proposed. Texture information in spatial pyramid domain can improve the discriminative power of SLBP descriptors. Compared to the conventional LBP descriptors and SLBP descriptors, the pyramid representation for local binary patterns shows its effectiveness. The experimental results show that our method achieves better results than previous ones in ground-based cloud classification.

Acknowledgments This work is supported by National Natural Science Foundation of China under Grant No. 61401309, and No. 61501327, Natural Science Foundation of Tianjin under Grant No. 15JCQNJC01700, and Doctoral Fund of Tianjin Normal University under Grant No. 5RL134 and No. 52XB1405.

References

1. Taravat A, Del FF, Cornaro C, Vergari S (2014) Neural networks and support vector machine algorithms for automatic cloud classification of whole-sky ground-based images. IEEE Geosci Remote Sens Lett 12(3):666–670
2. Liu S, Wang C, Xiao B, Zhang Z, Cao X (2013) Tensor ensemble of ground-based cloud sequences: its modeling, classification and synthesis. IEEE Geosci Remote Sens Lett 10(5):1190–1194
3. Liu S, Wang C, Xiao B, Zhang Z, Shao Y (2013) Salient local binary pattern for ground-based cloud classification. Acta Meteorologica Sin 27(2):211–220

4. Yang J, Lv WT, Ma Y, Yao W, Li QY (2013) An automatic groundbased cloud detection method based on adaptive threshold. J Appl Meteorol Sci 20(6):713–721
5. Shields JE, Karr ME, Tooman TP (1998) The whole sky imagerłA year of progress. In: Proceedings of the eighth Atmospheric Radiation Measurement (ARM) science team meeting, pp 11–16
6. Long CN, Sabburg JM, Calbó J, Pagès D (2006) Retrieving cloud characteristics from ground-based daytime color all-sky images. J Atmos Oceanic Technol 23(5):633–652
7. Shaw JA, Thurairajah B (2003) Short-term Arctic cloud statistics at NSA from the infrared cloud imager. In: Proceedings of the thirteenth ARM science team meeting
8. Heinle A, Macke A, Srivastav A (2010) Automatic cloud classification of whole sky images. Atmos Meas Tech 3(1):557–567
9. Singh M, Glennen M (2005) Automated ground-based cloud recognition. Pattern Anal Appl 258–271
10. Calbó J, Sabburg J (2008) Feature extraction from whole-sky groundbased images for cloud-type recognition. J Atmos Oceanic Technol 3–14
11. Ojala T, Pietikäinen M, Mäenpää T (2002) Multiresolution gray-scale and rotation invariant texture classification with local binary patterns. IEEE Trans Pattern Anal Mach Intell 24(7):971–987
12. Tan X, Triggs B (2010) Enhanced local texture feature sets for face recognition under difficult lighting conditions. IEEE Trans Image Process 19(6):1635–1650
13. Guo Z, Zhang L, Zhang D (2010) A completed modeling of local binary pattern operator for texture classification. IEEE Trans Image Process 19(6):1657–1663

A Global Fast Fourier Transform Method for Target Recognition

Guang Zhu

Abstract A new algorithm about global fast Fourier transform (FFT) is introduced in this paper, which is more reasonable and scientific than old FFT. The algorithm of FFT is more reasonable and more scientific than in the past. Experiments indicate that this algorithm can detect oil storehouses fast and exactly. Furthermore, the relation between template scale feature and oil depot recognition is indicated, i.e., the algorithm speed is increased faster than direct convolution along with the template scale increasing, and small template can detect large oil storehouses, not vice versa. The precision of the detection will rise along with template scale reducing, but at the same time the false alert will appear. Meanwhile, the problem of this algorithm is pointed and will be solved in the further research.

Keywords Global FFT · Correlation match · Template scale · Oil storehouse

1 Introduction

Template matching [1–8] is an important part of digital image recognition. Spatial alignment of two or more images acquired from different sensors or the same sensor to a target at different times or under different conditions, or the processing method that according to the known pattern to find the pattern in the second picture is called the template match. In remote sensing image target recognition technology, the template-match technology is templates with image features in the tracking window, sliding, calculating the associated value of the template and the covered area according to certain criteria, the center of the best matched region can be thought as the center of the target. The algorithms for template match are various, such as minimum-absolute-add algorithm (MAD), amplitude-sort-related algorithm, FFT related algorithm, sequence-similar-detection algorithm (SSDA).

G. Zhu (✉)
State Key Lab Integrated Optoelect, College of Electronic Science and Engineering, Jilin University, Changchun 130012, China
e-mail: jlu_zg@163.com; txzzbit@163.com

Q. Liang et al. (eds.), *Proceedings of the 2015 International Conference on Communications, Signal Processing, and Systems*, Lecture Notes in Electrical Engineering 386, DOI 10.1007/978-3-662-49831-6_61

A pair of digital images is essentially expressed as a two-dimensional (2D) array. Assuming that taking the test image and the template image as two 2D arrays, convolving the test image (a larger matrix) with the template image (a smaller matrix) convolution, we can obtain a new matrix, i.e., the correlation matrix, where the elements indicate the correlation coefficient of the two matrices, then we normalize the correlation matrix, the greater the normalization factor, the better similarity of the test images on this point, then according to the needs of different targets, we can set a threshold value, the point that is greater than this threshold can be considered to be the target point. However, for the complex targets, such as various types of tanks, aircraft, aircraft carrier, the template should contain more detailed features in order to distinguish them better in the matching process. In terms of templates with lots of features, the convolution has large computational cost and matching time, and perhaps when matching results came out, the goal is no longer in that position. The convolution in time domain is equivalent to the multiplication in the frequency domain. For the same two $N \times N$ images, time consuming on convolution is probably $N/2$ times of the product time consuming. In order to be able to identify the target real-timely, relevant matching algorithm based on fast Fourier transform is proposed and applied to the target detection of a remote sensing image with a depot. Experiments show that the algorithm improves the speed of the related convolution algorithms, especially in the situation that the feature template is quite complex.

2 Global FFT

The main method of digital image processing is divided into two categories: image domain methods and frequency domain methods. By converting the image to the frequency domain can analyze the image features from another angle. This transformation is generally linear and reversible, especially the Fourier transform. In the

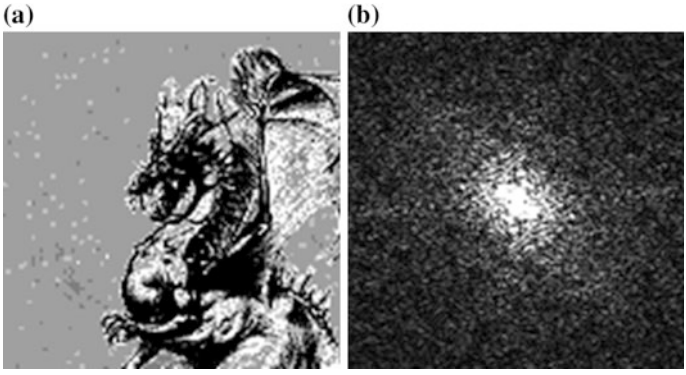

Fig. 1 FFT transform of an image with 128 × 128 pixels and 256 *gray scales*. **a** Incomplete image, **b**. FFT

frequency domain, the structure of the gray image becomes more significant, and the fast convolution and target recognition algorithm is easier to implement.

The fast Fourier transform (FFT) in some references and programs has some defects, that is not able to apply the FFT to the entire image, as shown in Fig. 1, for non-global FFT: 256 shades of gray images with 128 × 128 pixels:

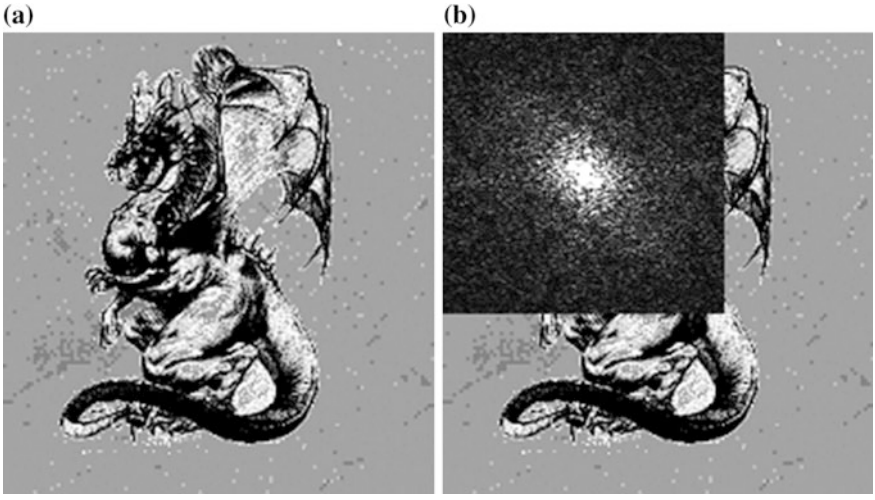

Fig. 2 Incomplete FFT of an image with 196 × 210 pixels and 256 *gray scales*. **a** Full image, **b**. Incomplete FFT

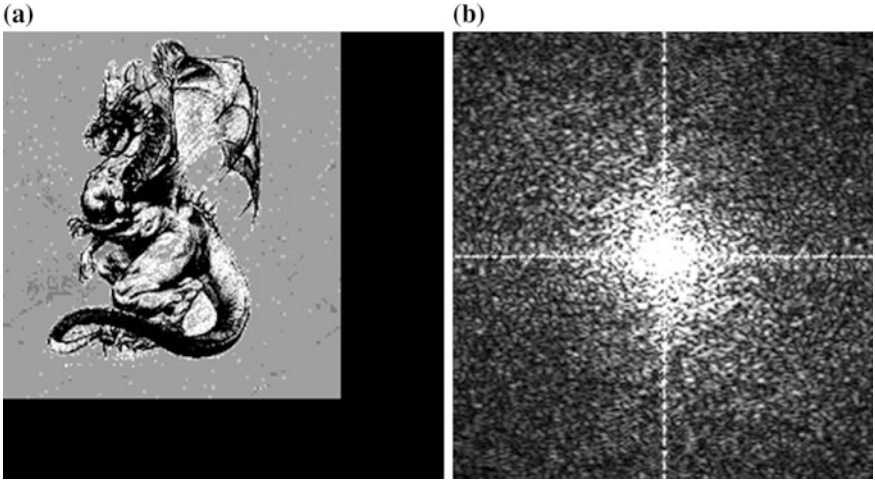

Fig. 3 Global FFT of an image with 196 × 210 pixels and 256 *gray scales*. **a** Expanded image, **b**. Global FFT

Comparing the FFT transform images of Figs. 1 and 2, the two are the same, expect for not getting rid of the excess part in Fig. 2, i.e., the FFT transformation of the second image is incomplete with the reason that the recognition of the discrete FFT butterfly processes is not impressive enough (Fig. 3).

3 Construction of the Feature Template Library of the Oil Depot

Template Library to establish a direct impact on subsequent matching algorithm accuracy and speed, the size of the image of the target to be measured on different scales are not the same, it must establish a multi-scale template library to meet different image target detection requirements, in order achieve the depot correlation matching algorithm, we must establish the characteristics of the depot template library, a multi-scale oil depot template in the following work is characterized mainly include: gray scale (brightness), contour (roughly circular, with a black shadow), and oil depots scale size; in algorithm program design process, the

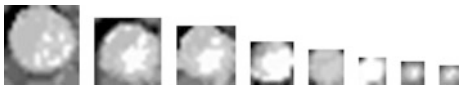

Fig. 4 The initial establishment of the feature template library of the oil depot

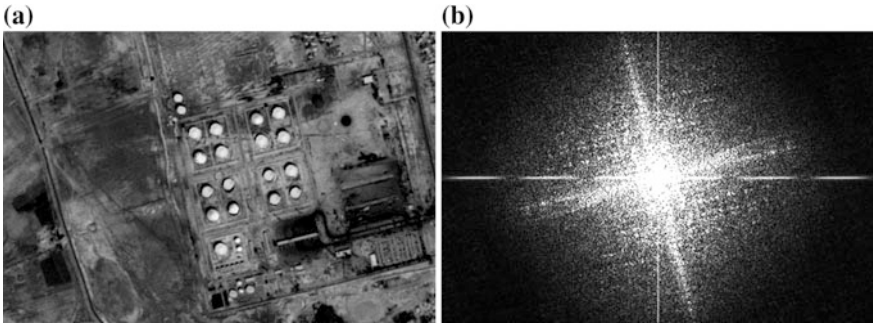

Fig. 5 The oil depot image and the global FFT image. **a** Test image with oil depot, **b**. Global FFT of oil depot image

template should take into account the rotation and scaling, since the objective is to test the depot, with full symmetry properties, and therefore, not considered in this rotation template, just consider scaling; as shown in the following figure, its size are 20×20, 17×17, 15×15, 11×11, 9×9, 7×7, 6×6, 5×5 pixels, whose gray are 256 (Figs. 4 and 5).

4 Matching Algorithms Related to FFT

From Fourier analysis theorems, two arrays defined in the domain convolution equals the product of the frequency domain and then take the inverse transform, convolution, and correlation is a particular form, as mentioned, FFT correlation algorithm is faster than direct convolution algorithm. For the depot target detection studied in this paper, the major steps are applying globally FFT transform, and then in the frequency domain, multiplying the two spectral images, followed by the inverse FFT transformation, normalizing, taking the fixed field value, and finding the target point that is larger than the field value.

The following images show the VC++ implementation results of the test image and eight matching templates (Fig. 6).

In the process of the acquisition target, starting with the large template matching, in general, the number of detected target will be increased, because of that the large template and small oil depot target have less relevant, but not with the same size of the depot target, with the decrease of the template scale, small template and large target depot also have a strong correlation, and can also detect the small oil depot goal, meanwhile, the accuracy of detection will be larger, and with further reduction of the template scales, false alarm occurs, then we should stop reducing the template scale, the minimal template without false alarms is the best matching template. With the increase of the detection images, we should update feature template library, making it more conducive to detect targets. Thus, a large oil depot template is not conducive to detecting small targets, while small oil depot templates but can also detect large oil depot goal, however, when the stencil small depot to a certain extent this is 6×6, it appeared false alarms, so, the depot template should be moderate, as shown in Table 1.

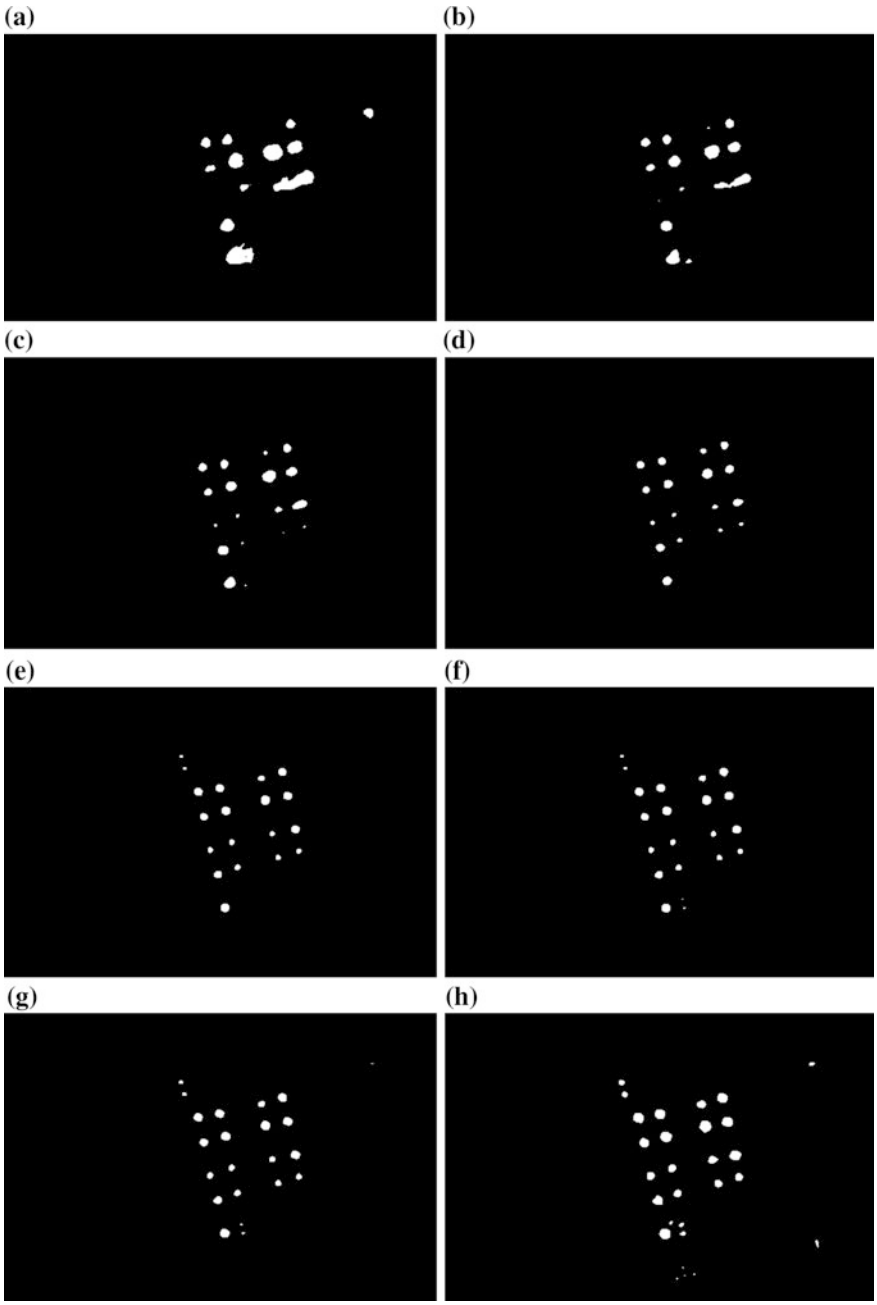

Fig. 6 The detecting results of templates with distinct scales

Table 1 The matching results of templates with distinct scales

Template size	20 × 20	17 × 17	15 × 15	11 × 11	9 × 9	7 × 7	6 × 6	5 × 5
Number of detecting targets	11	14	17	17	19	21	21	25
Number of false targets	1	0	0	0	0	0	1	3
Number of missing targets	14	11	8	8	6	4	4	0

5 Conclusions

In this paper, the overall FFT is applied to the design and implementation of the depot target matching algorithm, and achieved the method in the VC++ 7.0 environment. Experimental results show that the algorithm can accurately and rapidly detect oil depot target with a high recognition rate. This paper shows the relationship between the templates and the target detection results. At the same time there are still some problems, such as when a large piece gray area of the same depot template, even if a different contour, as long as the area is larger than the template, there will be false alarms, and to solve this problem also, more research and effective algorithm are needed. And the speed and accuracy of the algorithm needs to be further improved to meet the requirement of real-time detection.

References

1. Dufour RM, Miller EL, Galatsanos NP (2002) Template matching based object recognition with unknown geometric parameters. IEEE Trans Image Process 11(12):1385–1396
2. Myers V, Fawcett J (2010) A template matching procedure for automatic target recognition in synthetic aperture sonar imagery. IEEE Signal Process Lett 17(7):683–686
3. Bradley DA, Hashim S, Saripan MI et al (2011) Photon signature analysis using template matching. Nucl Instrum Methods Phys Res Sect A Accel Spectrom Dectect Assoc Equip 652 (1):466–469
4. Zhou JX, Shi ZG, Cheng X et al (2011) Automatic target recognition of SAR images based on global scattering center model. IEEE Trans Geosci Remote Sens 49(10):3713–3729
5. Zhu H, Deng L, Zhou G, et al (2012) Target recognition method based on template matching in downward-looking infrared image. In: Proceedings of the Audio, International Conference on Language and Image Processing (ICALIP), 2012, IEEE, pp. 898–902
6. Banharnsakun A, Tanathong S. (2014) Object detection based on template matching through use of best-so-far ABC. Comput. Intell. Neurosci. 2014, 7
7. Li B, Gong LG, Li Y.A (2014) Novel artificial bee colony algorithm based on internal-feedback strategy for image template matching. Sci World J, 2014, 14
8. Li Z Y, Li P F, Yu X P, et al (2014) Real-time tracking by double templates matching based on timed motion history image with HSV feature. Sci World J, 2014, 9

Ground-based Cloud Detection: A Comprehensive Study

Shuang Liu and Zhong Zhang

Abstract Ground-based cloud observation is an important factor in the hydrological cycle, the earth radiation balance, and climate change. Recently, the algorithms with cloud cover evaluation develop rapidly. Nevertheless, there is still no comprehensive study to compare the advantages and disadvantages of various algorithms. For this reason, we will give a comprehensive study on this subject in this paper. First of all, the development situation of cloud cover evaluation is presented. Then, we give a general idea of each method and compare the performance of several methods under two ground-based cloud databases. Finally, the theory of the results is analyzed.

1 Introduction

1.1 Motivation

Ground-based clouds have important influence in climate change and affect the earth radiation balance via interacting with terrestrial and solar energy conversion [1]. Many studies about ground-based clouds needs the knowledge of cloud observation, for example, cloud image classification [2, 3] and cloud cover evaluation [4]. Assessment cloud cover accurately is of great significance for climate research and early disaster warning. Until now, cloud cover assessment mainly relies on the manual visual inspection [4, 5]. However, this method relies the expertise of observers and different observations may obtain different results due variety of reasons, such as body, mind, and experience. As a result, the area of cloud observation needed automatically techniques to improve this situation.

S. Liu · Z. Zhang (✉)
College of Electronic and Communication Engineering, Tianjin Normal University, Tianjin, China
e-mail: zhong.zhang8848@gmail.com

S. Liu
e-mail: shuangliu.tjnu@gmail.com

Q. Liang et al. (eds.), *Proceedings of the 2015 International Conference on Communications, Signal Processing, and Systems*, Lecture Notes in Electrical Engineering 386, DOI 10.1007/978-3-662-49831-6_62

The cloud cover evaluation is a tough job due to the images being shot in outdoor. In order to accomplish this task, researchers have invented a number of devices to capture cloud images, such as TSI [6], WSI [7–9], and ICA [10]. Cloud detection is a key technique for cloud cover estimation, this is because each pixel in cloud image is divided into clouds or clear skies.

With these devices, the researchers proposed a number of methods to solve the problem of cloud detection. Due to the different scattering situation between air molecules and cloud particles, most existing cloud detection methods set color feature as the main factor to distinguish between cloud and sky. Based on this, the threshold technology are developed. Fixed thresholding methods include the saturation [11], ratio of R-channel to B-channel [6], and euclidean distance metric [12]. But, this kind of methods cannot adapt for different climatic conditions [6]. Alternatively, otsu algorithm which based on adaptive thresholding method was proposed [13]. Despite some improvements, the effect is not desirable due to inconsistent lighting. In order to overcome the influence by inconsistent lighting and fuzzy borders between cloud and clear sky regions, super-pixel segmentation [14] is utilized for ground-based cloud detection. While these methods can improve the detection results, there is always lack of a comprehensive study for this research domain. For this reason, we will give a comprehensive research on this theme in this manuscript. Several cloud detection techniques are presented and their differences are excavated. I believe that this paper is of great significance for future researchers.

1.2 Texonomy

Cloud detection is an application of image processing and pattern recognition, and many techniques show the superior performance in image processing [15, 16]. For a ground-based cloud image, the goal of cloud detection is to distinguish between clouds and sky pixels accurately. Currently, a mainstream approach is to use color feature as the primary differentiator. This is because that Pixels between the clouds and clear sky are different. Clearly, we set the existing cloud detection methods into three classes according to their motivations.

- Fixed thresholding methods use same value for all ground-based cloud images regardless of their imaging conditions. Typical methods include the ratio of R-channel to B-channel [6, 17] and euclidean distance metric [12]. But some researches indicate that this kind of methods cannot adapt for different climatic conditions.
- Adaptive thresholding methods set one or several thresholds for each ground-based cloud image. One of the typical methods is based on otsu algorithm, which is proposed in literature [13]. Despite some improvements, the effect is not desirable due to inconsistent lighting. Another method is introduced by Yang et al. [18]. They divide each cloud image into several regions with same size. For each region,

they calculate its threshold. But the kind of rigid division does not conform to the cloud images which belong to natural texture images.

- The above techniques use same value for all ground-based cloud images or set one or several thresholds for each ground-based cloud image. Despite some improvements, this kind of strategies is not suitable for ground-based cloud images due to inconsistent lighting and fuzzy borders regions. Based on the characteristics of cloud images, super-pixel segmentation [14] is utilized for ground-based cloud detection. In this strategy, we can obtain many super-pixels adaptively by the characteristics of cloud images (shape, size, and location). We will introduce this technique in detail as follows.

2 Ground-based Cloud Detection Techniques

2.1 Methods Based on Fixed Threshold

Fixed threshold method is the sample technique to detect ground-based cloud images. According to the radio of red to blue pixel value using a cloud image, literature [17] report an algorithm for ground-based cloud detection. In this strategy, we assign the pixels with radio R/B larger than 0.77 as clouds, and others are clear sky. Other features for fixed thresholding algorithms saturation [11] and Euclidean geometric distance (EGD) [12].

2.2 Methods Based on Adaptive Threshold

One of typical adaptive threshold methods is based on otsu algorithm, which is investigated in literature [13]. For each cloud image, literature [13] computes its feature image, and then use otsu algorithm to compute the threshold value T_g. The key factor of otsu algorithm is the different scattering between cloud and clear sky elements. Based on this, the distribution of histogram will appeared in a cloud image. Finally, a value is obtained by maximizing the variance according to cloud and clear sky. We can give the form solution of this problem as:

$$V(T) = P_C P_S(\mu_C - \mu_S) \tag{1}$$

where P_C is the probability of cloud elements, and P_S is the probability of sky elements. Finally, we can obtain T_g by this formula $\max\{V(T)\}(1 < T < 255)$;

Another method is introduced by Yang et al. [18]. They divide each cloud image into several regions with same size, as showed in Fig. 1b. For each region, they calculate its threshold.

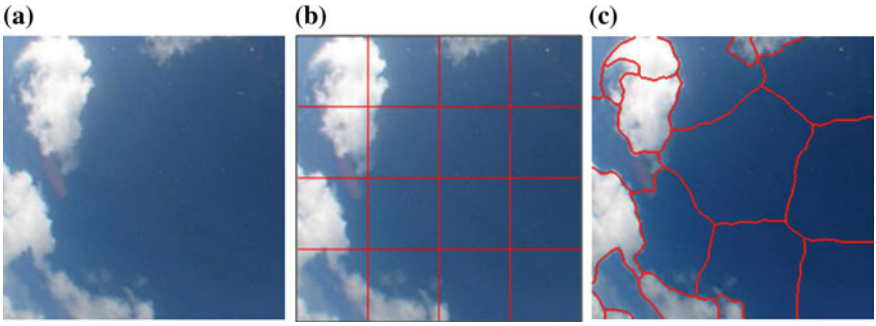

Fig. 1 **a** The initial cloud image; **b** The division by Yang et al. [18]; **c** Super-pixel segmentation of cloud image

2.3 Techniques Based on Super-Pixel Segmentation

Observing about researches, we can find that the majority only apply certain thresholds for cloud images. However, the characteristics of cloud images are ignored, which includes inconsistent lighting and fuzzy borders between cloud elements and sky ones. In order to overcome this insufficiency, literature [14] proposes to utilize super-pixel segmentation for ground-based cloud detection. The section below, we give a overview of super-pixel segmentation (SPS) [14]. In SPS strategy, we can obtain detect results by two steps. In this first step, according to the feature of cloud and sky elements, super-pixel segmentation is applied. Thereby, each cloud image is divided into several super-pixels, and each super-pixel is covered by cloud or sky elements as possible. In the second step, we calculate the threshold for each super-pixel, and then obtain the detection result.

2.3.1 Super-Pixel Segmentation

For a ground-based cloud image, the detect can be treated as a graph partitioning question. Based on this, a cloud image is considered to be a graph with weight where the nodes i and j are image pixels and the edge weights w_{ij} is a similarity measure between two image pixels. Thus, the segmentation can be performed by partitioning the pixels into groups using some criteria, We can use the following optimization function to solve this problem:

$$y = \arg\min Cut = \arg\min_{y} \frac{y^T(D - W)y}{y^T Dy} \tag{2}$$

Algorithm 1: Ground-based Cloud Cloud Detection

Input: an RGB cloud image, by super-pixel algorithm, we obtain the division of a cloud image.
Output: the result of cloud detection.

step1: After R color channel minus B color channel, we can obtain R-B as feature image;
step2: We convert the feature image R-B to the scope of 0∼255 as updated feature image;
step3: For each super-pixel, we calculate the threshold as its local threshold;
step4: After obtaining all thresholds for the detected cloud image, we obtain a threshold matrix using interpolation technique;
step5: For obtaining the final result, we contrast the threshold matrix to R-B feature image.

Fig. 2 Ground-based cloud detection algorithm

$W = \{w_{ij}\}$ is the incidence matrix W. D is the diagonal matrix. y equals to $\{a, b\}^N$, which is a vector. N is the number of pixels in a cloud image. Optimization y can be solved very efficiently by a generalized eigenvalue system. After applying super-pixel segmentation algorithm, we can obtain several super-pixels based on the features of clouds for each images, which is shown in Fig. 1c.

2.3.2 Detection Algorithm

In this part, we detect cloud based on the obtained super-pixels. The pseudocode of our cloud detection strategy is presented in Algorithm 1, which is shown in Fig. 2.

3 Experimental Results and Experimental Analysis

3.1 Database

In order to obtain the ground-based cloud images, a device with a fish-eye lens is utilized. Further information about the setting of this camera can refer to [19]. In this article, the above-mentioned detection methods will be used to test the data by this device. Database is shown as Fig. 1a. 500 samples make up this data.

3.2 Methods for Comparison

1. Fixed threshold (Fixed) [17]: we first calculate the radio of R/B. When the radio is large than 0.77, we assign it as cloud; on contrary, when the radio is small than 0.77, it will be assigned as sky.

2. Adaptive threshold 1 (Adaptive1) [13]: Using Otsu algorithm, we can obtain this threshold which is described in Eq. 2.
3. Adaptive threshold 2 (Adaptive2) [18]: We first obtain feature image by R-channel over B-channel, and then divide each image into 16 parts, Finally, we calculate its threshold for each part.
4. Super-pixel segmentation (SPS) [14]: super-pixel segmentation can adaptively divide the cloud image into several super-pixels by the feature of cloud image, which is described in Sect. 2.3.

3.3 Results and Analysis

In this section, we will evaluate the performance of different detect algorithms. Each algorithm is applied on the above database. We use the following formula as a judging standard:

$$\frac{NT_{cloud} + NT_{sky}}{N} \tag{3}$$

where NT_{cloud} actually represents the number of cloud elements, and NT_{sky} actually represents the number of sky elements, and N represents the number of elements in a detected cloud image. Table 1 gives the performance of the above four detection algorithms. We can obtain the following several conclusions. First, the performance by SPS algorithm is highest, which reach 93.65 %. Second, the fixed threshold algorithm obtains the least effective. Figure 3 gives several examples of results detected by the above four methods. From this results, several conclusions can be draw. The

Table 1 The correct rate of different algorithms

	Fixed	Adaptive1	Adaptive2	SPS
Precision (%)	71.53	72.46	82.36	**93.65**

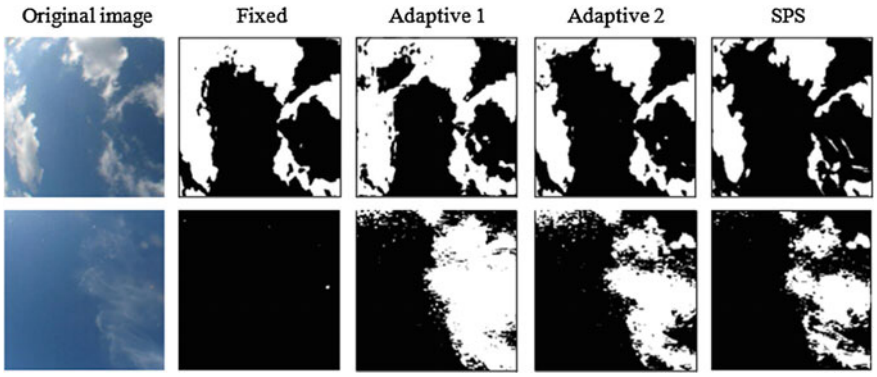

Fig. 3 The results for the above four different cloud detection algorithms

setting of 'Fixed' threshold method is difficult. Sometimes threshold slants big (the first row), sometimes small (the second row). 'Adaptive1' and 'Adaptive2' cannot adapt to the inconsistent lighting. Fortunately, the 'SPS' algorithm can adapt to different weather conditions.

4 Conclusions

In this manuscript, we make a comprehensive research on the different cloud cover evaluation algorithms. In addition, we contrast the advantages and disadvantages of various algorithms, and give their relationships. Finally, we find that SPS algorithm can obtain better detection results than other ones.

Acknowledgments This work is supported by National Natural Science Foundation of China under Grant No. 61401309, and No. 61501327, Natural Science Foundation of Tianjin under Grant No. 15JCQNJC01700, and Doctoral Fund of Tianjin Normal University under Grant No. 5RL134 and No. 52XB1405.

References

1. Taravat A, Del FF, Cornaro C, Vergari S (2014) Neural networks and support vector machine algorithms for automatic cloud classification of whole-sky ground-based images. IEEE Geosci Remote Sens Lett 12(3):666–670
2. Liu S, Wang C, Xiao B, Zhang Z, Cao X (2013) Tensor ensemble of ground-based cloud sequences: its modeling, classification and synthesis. IEEE Geosci Remote Sens Lett 10(5):1190–1194
3. Liu S, Wang C, Xiao B, Zhang Z, Shao Y (2013) Salient local binary pattern for ground-based cloud classification. Acta Meteorol Sin 27(2):211–220
4. Yang J, Lv WT, Ma Y, Yao W, Li QY (2013) An automatic groundbased cloud detection method based on adaptive threshold. J Appl Meteorol Sci 20(6):713–721
5. Liu S, Zhang Z, Xiao B, Cao X (2015) Ground-based cloud detection using automatic graph cut. IEEE Geosci Remote Sens Lett 12(6):1342–1346
6. Long CN, Sabburg JM, Calbó J, Pagès D (2006) Retrieving cloud characteristics from ground-based daytime color all-sky images. J Atmos Ocean Technol 23(5):633–652
7. Shields JE, Karr ME, Tooman TP (1998) The whole sky imagerŁA year of progress. In: Proceedings of Eighth Atmospheric Radiation Measurement (ARM) Science Team Meeting, pp 11–16
8. Feister U, Shield J (2005) Cloud and radiance measurements with the VIS/NIR Daylight Whole Sky Imager at Lindenberg (Germany). Meteorologische Zeitschrift 14(4):627–639
9. Heinle A, Macke A, Srivastav A (2010) Automatic cloud classification of whole sky images. Atmos Meas Tech 3(1):557–567
10. Genkova I, Long, CN, Besnard T, Gillotay D (2004) Assessing cloud spatial and vertical distribution with infrared cloud analyzer. In: Proceedings of the Fourteenth ARM Science Team Meeting, pp 22–26
11. Souza-Echer MP, Pereira EB, Bins LS, Andrade MAR (2006) A simple method for the assessment of the cloud cover state in high-latitude regions by a ground-based digital camera. J Atmos Ocean Technol, 23(3): 437–C447

12. Neto SLM, Wangenheim AV, Pereira EB, Comunello E (2010) The use of Euclidean geometric distance on RGB color space for the classification of sky and cloud patterns. J Atmos Ocean Technol, 27(9):1504–C1517
13. Yang J, Weitao L, Ying M, Wen Y, Qingyong L (2009) An automatic ground-based cloud detection method based on adaptive threshold. J Appl Meteorol Sci, 20(6):713–C721
14. Liu S, Zhang L, Zhang Z, Wang C, Xiao B (2015) Automatic cloud detection for all-sky images using superpixel segmentation. IEEE Geosci Remote Sens Lett 12(2):354–358
15. Zhang Z, Wang C, Xiao B, Liu S, Zhou W (2012) Multi-scale fusion of texture and color for background modeling. In: International Conference on Advanced Video and Signal-Based Surveillance, pp 154–159
16. Zhang Z, Wang C, Xiao B, Zhou W, Liu S, Shi C (2013) Cross-view action recognition via a continuous virtual path. In: IEEE Conference on Computer Vision and Pattern Recognition, pp 2690–2697
17. Kreuter A, Zangerl M, Schwarzmann M, Blumthaler, M (2009) All-sky imaging: a simple, versatile system for atmospheric research. Appl Opt 48(6):1091–1097
18. Yang J, Lv WT, Ma Y, Yao W, Li QY (2010) An automatic groundbased cloud detection method based on local threshold interpolation. Acta Meteorol Sin 68(6):1007–1017
19. Kalisch J, Macke A (2008) Estimation of the total cloud cover with high temporal resolution and parametrization of short-term fluctuations of sea surface insolation. Meteorologische Zeitschrift 17(5):603–611

Scene Text Detection with Adaptively Weighted Descriptors in Opponent Color Space

Yao Jiang, Aiwen Jiang and Mingwen Wang

Abstract This paper involves the challenging problem of text localization in complex scenes. Maximally Stable Extremal Regions (MSER) has recently been extensively employed in text detection methods. However, most efforts for MSERs are only put into a single intensity image. MSERs are therefore subjective to cases like low contrast and uneven lighting etc. In this paper, we investigate the opponent color theory and perform attempting to evaluate the benefit of MSER extraction on different opponent color channels. Furthermore, we propose to apply kernel descriptors for text classification and multi-kernel learning to learn relative weights for features. We have experimented our proposed strategy on 'Robust Reading Competition' dataset distributed by International Conference on Document Analysis and Recognition (ICDAR) 2003 and 2011. The experiment results demonstrate its effectiveness and efficiency. We can achieve general equivalently good performance with several compared state-of-the-art methods at lower computation cost.

1 Introduction

Detecting and reading text in scene images plays a great important role in many practical applications, such as helping visually impaired people for reading, automatical translation for tourists in an unfamiliar language environment, and semantic annotation for content based image retrieval, etc. However, scene text extraction is still an opening problem. To large extent, the difficulties are attributed to complex

Y. Jiang · A. Jiang (✉) · M. Wang
Jiangxi Normal University, Nanchang, China
e-mail: jiangaiwen@jxnu.edu.cn

Y. Jiang
e-mail: 867923593@qq.com

M. Wang
e-mail: mwwang@jxnu.edu.cn

Q. Liang et al. (eds.), *Proceedings of the 2015 International Conference on Communications, Signal Processing, and Systems*, Lecture Notes in Electrical Engineering 386, DOI 10.1007/978-3-662-49831-6_63

scene backgrounds, high text variations, uneven lighting etc. None of current state-of-the-art methods achieves sufficient accuracy for practical use. Therefore, in recent years, research on scene text extraction has received great attention in multimedia area [1, 2].

The entire process of scene text extraction includes localization and recognition. In this paper, we will be concentrated on the first step. Methods addressing scene text localization can be roughly divided into two categories: sliding window based methods and connected component (CCs) based methods.

The first group draws inspiration from object detection and exploit a sliding-window approach to localize individual characters or whole words. [3–5]. The drawbacks are the number of windows to be evaluated increases rapidly with image scales. The second group localizes characters as CCs based on some selected local properties like stroke width, edge, and color etc. [6–9]. The advantages of such methods are their low computing complexities and irrelevance to image scales. However, the disadvantage is their assumption is subjective to noises in many cases.

Recently, Maximally Stable Extremal Regions (MSER) has been extensively employed in text detection methods [10–14]. However, the limits existing in MSER based methods are they generally perform well but have problems on blurry images or characters with low contrast. Most efforts to detect MSER are performed only on a single intensity image. In this case, we observe that text regions are not always a sufficiently stable area for MSER detector in gray intensity channel. Text information will be lost when detecting MSERs.

The trichromatic theory known as the Young-Helmholtz theory, and opponent-process theory developed by Ewald Hering are two widely accepted theories for colour vision. The trichromatic theory explains colour vision phenomena at the photoreceptor level; while the opponent-process theory explains colour vision phenomena that result from the way in which photoreceptors are interconnected neurally. They interpreted different signal processing levels of vision system. In intuition, richer information like color perception may play a critical role in text detection stage, especially in cases of low contrast and uneven lighting. This motivates us to perform attempting for MSERs extraction in different color channels.

Furthermore, kernel descriptor proposed by Bo [15, 16], recently has been widely applied to generic object recognition problems. The advantages of kernel descriptors are their capacities to turn local pixel attributes into compact patch-level features with spatial structural information. Therefore, in this paper, instead of heuristically filtering out non-text components, we propose to extract kernel descriptor (KDES) as region representations, and employ multi-kernel learning strategy for text/nontext classifier training.

The contributions are twofold: (1) we have given a valuable attempting to detect MSERs on opponent color space and evaluated its effectiveness, especially in case of low contrast and uneven lighting; (2) the idea of applying multi-kernel learning on kernel descriptors for text classification is quite promising. We have experimented the proposed method on public datasets, and the results demonstrate that the proposed method can achieve good performance at relatively minimum computational cost.

2 The Proposed Method

2.1 Character Candidates Detection

Most prior work perform MSERs on grey image, which general perform well, but have problems in some special cases, such as low contrast, uneven lighting and different text colors. In this stage, we propose to obtain initial character regions by detecting MSERs on opponent color channels as well as intensity images.

The traditional trichromatic theory makes clear some of the processes involved in how we see color. However, it does not explain all aspects of color vision. Specifically, it cannot explain the pathology of red-green blindness and afterimage. The world in intensity image is colorless, in which much rich information will be lost. As shown in Fig. 1, the MSERs detection on gray image fails to extract complete text regions.

Furthermore, perception of color is usually not best represented in RGB, as shown in Fig. 2. According to the Opponent process theory, it suggests that color perception is controlled by the activity of two opponent systems: a yellow-blue mechanism and a red-green mechanism. The opponent color process works through a process of excitatory and inhibitory responses, with the two components of each mechanism opposing each other. For example, red creates a positive response while green creates a negative response. These responses are controlled by opponent neurons, which are neurons that have an excitatory response to some wavelengths and an inhibitory response to wavelengths in the opponent part of the spectrum. So It is more efficient

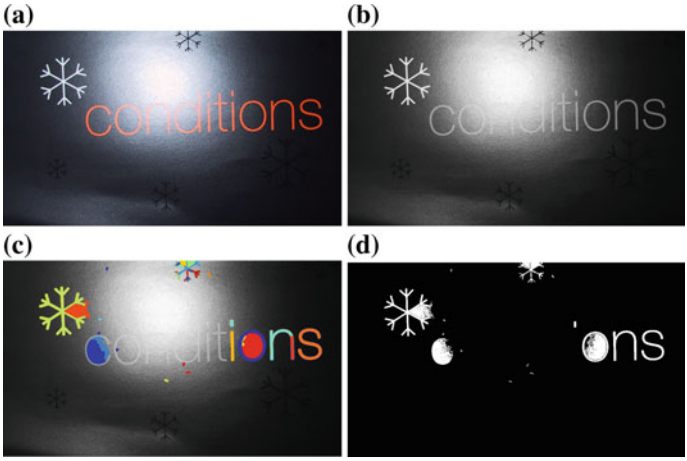

Fig. 1 Failing illusion for MSERs on single intensity channel. Input original RGB image shown in (**a**), its intensity channel image is shown in (**b**), the MSERs detection area and corresponding binary results are shown in (**c**) and (**d**) respectively

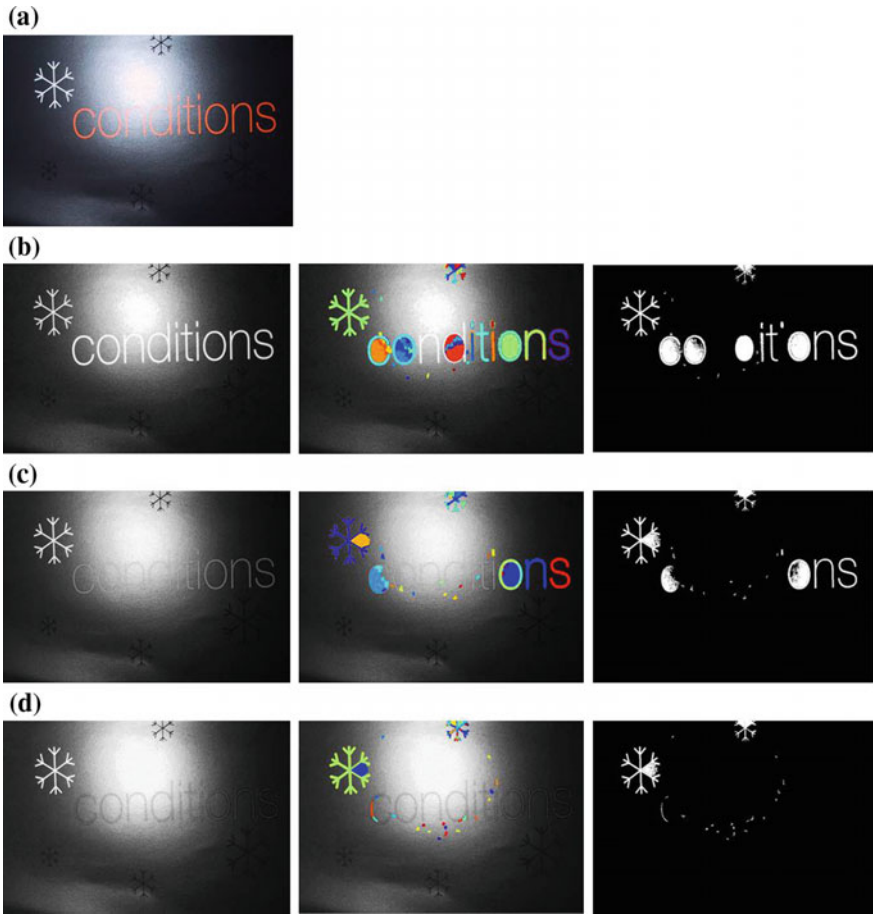

Fig. 2 Failing illusion for MSERs on RGB channel. Input original RGB image shown in (**a**), The channel image, the MSERs detection area and corresponding binary results of R, G, B are shown in (**b**), (**c**) and (**d**) respectively

for the visual system to record differences between the responses of neurons, rather than their individual responses.

According to the opponent color theory, we can compute the three opponent channels: red versus green O_1, yellow versus blue O_2 and white versus black O_3 as Eq. (1). It is not difficult to find that the O_3 channel (luminance) is achromatic and similar to our common grey intensity image. It detects the light-dark variation.

$$O_1 = (R - G)/\sqrt{2}, \quad O_2 = (R + G - 2B)/\sqrt{6}, \quad O_3 = (R + G + B)/\sqrt{3} \tag{1}$$

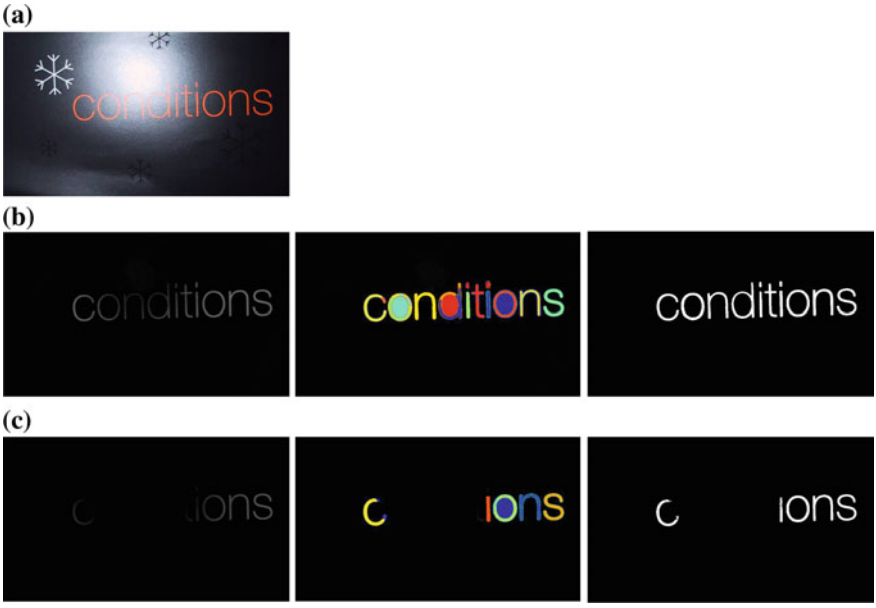

Fig. 3 Illusion for MSERs on opponent color channels. Input original RGB image shown in (**a**), The channel image, the MSERs detection area and corresponding binary results of *Red-Green*, *Yellow-Blue* channel are shown in (**b**), (**c**) respectively

There are at least two advantages, as suggested in [17]. It reinforces intensity edges, so that more importance is given to them. Another advantage of the opponent representation is that it depends less on the absolute intensity, because it computes differences between intensity values. In fact, it indeed retain these properties, as illusioned in Fig. 3.

Comparing Figs. 1, 2 and 3, we can find the advantage for MSERs brought by Opponent color transform. It can be treated as an important complements for intensity channel. Therefore, instead of traditional MSERs only on grey-intensity image, we suggest perform MSERs detection on opponent colour space as well. Applying MSERs on opponent color space can benefit MSER extraction robust to most cases, especially in case of low contrast and uneven lighting.

2.2 *Multiple Kernel Learning for Adaptive Feature Combination*

We will extract kernel descriptors based on three typical low level image attributes: gradient, local binary pattern and color attributes. As these kernel descriptors are extracted according to different information of text, they are in certain playing

complementary roles in text classification. Therefore, in order to select optimal combination for better performance, we consider using Multi-Kernel Learning strategy to learn their relative weights.

As described in [15], each proposed match kernel can be represented as the inner product of kernel descriptors of two patches, such as gradient descriptors shown in Eq. (2). Linear classifiers can be performed conveniently with similar performance as complex non-linear kernel classifiers.

$$K_{grad}(P, Q) = \left\langle F_{grad}(P), F_{grad}(Q) \right\rangle \tag{2}$$

The local binary pattern and color kernel descriptors are also extracted in a similar way.

In this paper, we employ simpleMKL [18] to settle the problem, for its efficiency and effectiveness. It addresses the MKL problem through a weighted L2-norm regularization formulation.

$$K\left(x_i, x_j\right) = \sum_m d_m k_m\left(x_i, x_j\right) \tag{3}$$

where $k_m\left(x_i, x_j\right)$ is a basis kernel, and d_m is a non-negative coefficient. It weights the combination importance of features. The simpleMKL algorithm is optimized based on performing gradient descent on the SVM objectives, as shown by (4):

$$\begin{aligned} &\min_d J(d) \\ &\text{s.t.} \sum_{m=1}^{M} d_m = 1, d_m \geq 0 \end{aligned} \tag{4}$$

where, $J(d) = \max_{\alpha} -\frac{1}{2} \sum_{i,j} \alpha_i \alpha_j \mathrm{y}_i \mathrm{y}_j \sum_m d_m K_m(\mathrm{x}_i, \mathrm{x}_j) + \sum_i \alpha_i$ with $\sum_i \alpha_i \mathrm{y}_i = 0, \mathrm{C} \geq \alpha_i \geq 0$

We run the above optimization problem to obtain its optimal solutions α_m^* and d_m^*.

As the basis kernels used can be formulated as linear product of selected kernel descriptors.

$$k_m(x, y) = \langle F_m(x), F_m(y) \rangle \tag{5}$$

Therefore, the optimal MKL solutions can be reformulated as (6):

$$\begin{aligned} &K_{MKL} = \textstyle\sum_{i=1}^{k} d_i^* K_i(x, y) = \sum_{i=1}^{k} \lambda_i^2 \langle F_i(x), F_i(y) \rangle \\ &= \langle F_{MKL}(x), F_{MKL}(y) \rangle \end{aligned} \tag{6}$$

where, $F_{MKL} = \left(\lambda_1 F_1, \lambda_2 F_2, ..., \lambda_k F_k\right)$ and $\lambda_i = \sqrt{d_i^*} \geq 0, i = 1, 2, ..., k$. λ_i represents the relative importance of ith kernel descriptor in the combinational feature. The resulted MKL-based features are fed into LinearSVM for solving text/nontext classification problems.

3 Experiment Results and Analysis

We evaluate our proposed method on two public datasets: ICDAR 2003 [1] and ICDAR 2011 [2]. Both datasets are widely used for text localization task. The ICDAR 2003 dataset includes 509 color images with image size ranging from 307×93 to 1280×960. They are divided into training set with 258 images and testing set with 251 images. In the ICDAR 2011 dataset, it contains 229 training images and 255 testing ones. About 1114 and 1186 words are annotated in train and test sets respectively.

To incorporate richer information for MSERs detection, we propose to combine the detection results on different opponent color channels. Furthermore, we employ kernel descriptors on three image attributes: gradient, LBP shape, color. Multiple kernel learning is performed to learn the adaptive relative importance of different features. More examples of the final scene text localization results under different conditions are shown in Fig. 4. We can observe that the performance is generally satisfied in different circumstance.

In order to evaluate performance more accurately, we accept the test procedure provided by ICDAR robust reading competition [2]. The performance comparisons of our proposed method with several state-of-the-art methods on ICDAR2003 and ICDAR2011 are shown in Tables 1 and 2, respectively. It should be note that in order

Fig. 4 More detection result for image with different text variations and complex background

Table 1 Experimental results on ICDAR 2003 dataset (%)

Method	Precision	Recall	F-measure
Pan [9]	67.0	71.0	69.0
Neumanne et al. [12]	65.0	64.0	63.0
Chen et al. [10]	73.0	60.0	66.0
Epshtein et al. [6]	73.0	60.0	66.0
Wang et al. [5]	42.0	36.0	39.0
Our Method	77.7	61.5	68.7

Table 2 Experimental results on ICDAR 2011 dataset (%)

Method	Precision	Recall	F-measure
Shi et al. [14]	83.3	63.1	71.8
Neumanne et al. [12]	73.1	64.7	68.7
Koo et al. [11]	83.0	62.5	71.3
Yi et al. [19]	67.2	58.1	62.3
Our Method	79.8	63.8	70.9

to evaluate the generalization ability of the proposed method, we train the classifier on ICDAR 2003 dataset and directly test its performance on ICDAR2011 without change.

From the experimental results, we can observe that our proposed method can achieve good performance. Because our method currently still treat some single letters as non-text regions. This may cause our results obtain a little less score than the best. However, it should be emphasized that our proposed method is efficient, because the extracted kernel descriptors are in kernel approximation strategy and the classifiers used is in linear style, which can scale very well.

4 Conclusions

In this paper, we have presented an effective text localization strategy by employing MSERs extraction on opponent color channels and doing multi-kernel descriptors learning for text classification. The experiment results on two public dataset have shown its advantages. Opponent color channels can be treated as an important complements for intensity channel. The idea of using kernel descriptors for text classification and applying multi-kernel learning to learn relative weights of features is quite promising. Experiments results on two public datasets have shown that our proposed method can achieve equivalently good performance with several state-of-the-art methods at less computation cost and complexities.

Acknowledgments This work is supported by Natural Science Foundation of China (under Grant No. 61365002, 61272212, 61462045), Natural Science Foundation of Jiangxi, China under Grant No. 20132BAB201030 and 20142BAB217010.

References

1. Lucas SM, Panaretos A, Sosa L, Tang A, Wong S, Young R (2003) Icdar 2003 robust reading competitions. In: International conference on document analysis and recognition (ICDAR), pp 682–687
2. Coates A, Carpenter B, Case C, Satheesh S, Suresh B, Wang T, Wu DJ, Ng AY (2011) Text detection and character recognition in scene images with unsupervised feature learning. In: International conference on document analysis and recognition (ICDAR)
3. Wang K, Babenko B, Belongie S (2011) End-to-end scene text recognition. In: IEEE international conference on computer vision (ICCV), pp 1457–1464
4. Lee J-J, Lee P-H, Lee S-W, Yuille A, Koch C (2011) Adaboost for text detection in natural scene. In: International conference on document analysis and recognition (ICDAR), pp 429–434
5. Wang T, Wu DJ, Coates A, Ng AY (2012) End-to-end text recognition with convolutional neural networks. In: 21st international conference on pattern recognition (ICPR), pp 3304–3308
6. Epshtein B, Ofek E, Wexler Y (2010) Detecting text in natural scenes with stroke width transform. In: IEEE conference on computer vision and pattern recognition (CVPR), pp 2963–2970
7. Huang W, Lin Z, Yang J, Wang J (2013) Text localization in natural images using stroke feature transform and text covariance descriptors. In: IEEE international conference on computer vision (ICCV), pp 1241–1248
8. Yao C, Bai X, Liu W, Ma Y, Tu Z (2012) Detecting texts of arbitrary orientations in natural images. In: IEEE conference on computer vision and pattern recognition (CVPR), pp 1083–1090
9. Pan Y-F, Hou X, Liu C-L (2011) A hybrid approach to detect and localize texts in natural scene images. IEEE Trans Image Process 20(3):800–813
10. Chen H, Tsai SS, Schroth G, Chen DM, Grzeszczuk R, Girod B (2011) Robust text detection in natural images with edge-enhanced maximally stable extremal regions. In: 18th IEEE international conference on image processing (ICIP), pp 2609–2612
11. IEEE Trans Image Process (2013) Scene text detection via connected component clustering and nontext filtering. 22(6):2296–2305
12. Neumann L, Matas J (2012) Real-time scene text localization and recognition. In: IEEE conference on computer vision and pattern recognition (CVPR), pp 3538–3545
13. Neumann L, Matas J (2013) Scene text localization and recognition with oriented stroke detection. In: IEEE international conference on computer vision (ICCV), pp 97–104
14. Shi C, Wang C, Xiao B, Zhang Y, Gao S (2013) Scene text detection using graph model built upon maximally stable extremal regions. Pattern Recogn Lett 34(2):107–116
15. Bo L, Ren X, Fox D (2010) Kernel descriptors for visual recognition. In: Advances in neural information processing systems (NIPS), pp 244–252
16. Bo L, Sminchisescu C (2009) Efficient match kernel between sets of features for visual recognition. In: Advances in neural information processing systems (NIPS), pp 135–143
17. Borer S, Süsstrunk S (2002) Opponent color space motivated by retinal processing. Conference on colour in graphics, imaging, and vision 2002:187–189
18. Rakotomamonjy A, Bach F, Canu S, Grandvalet Y (2008) Simplemkl. J Mach Learn Res 9:2491–2521
19. Yi C, Tian YL (2011) Text string detection from natural scenes by structure-based partition and grouping. IEEE Trans Image Process 20(9):2594–2605

Learning Representations for Steganalysis from Regularized CNN Model with Auxiliary Tasks

Yinlong Qian, Jing Dong, Wei Wang and Tieniu Tan

Abstract The key challenge of steganalysis is to construct effective feature representations. Traditional steganalysis systems rely on hand-designed feature extractors. Recently, some efforts have been put toward learning representations automatically using deep models. In this paper, we propose a new CNN based framework for steganalysis based on the concept of incorporating prior knowledge from auxiliary tasks via transfer learning to regularize the CNN model for learning better representations. The auxiliary tasks are generated by computing features that capture global image statistics which are hard to be seized by the CNN network structure. By detecting representative modern embedding methods, we demonstrate that the proposed method is effective in improving the feature learning in CNN models.

1 Introduction

The field of image steganalysis aims to reveal the presence of secret messages in digital images. It is often seemed as a pattern recognition problem. The key challenge of image steganalysis lies in building effective feature representations that are sensitive to stego signal while insensitive to image content. In order to obtain an accurate detection, it is important that the feature representations consider complex dependencies among individual image elements to capture the traces caused by embedding

Y. Qian
Department of Automation, University of Science and Technology of China, Hefei, China
e-mail: ylqian@mail.ustc.edu.cn

J. Dong (✉) · W. Wang · T. Tan
Center for Research on Intelligent Perception and Computing, Institute of Automation, Chinese Academy of Sciences, Beijing, China
e-mail: jdong@nlpr.ia.ac.cn

W. Wang
e-mail: wwang@nlpr.ia.ac.cn

T. Tan
e-mail: tnt@nlpr.ia.ac.cn

Q. Liang et al. (eds.), *Proceedings of the 2015 International Conference on Communications, Signal Processing, and Systems*, Lecture Notes in Electrical Engineering 386, DOI 10.1007/978-3-662-49831-6_64

operations. In the past years, researchers have focus on designing appropriate feature extractors, and various features have been constructed to capture different types of dependencies [4–6, 10, 18, 21–23]. A classifier is then trained based on these features to distinguish between cover and stego images. Though significant progress has been achieved, the detection accuracy is far from satisfactory, especially when against new and advanced steganographic methods. Moreover, these traditional steganalysis methods are heavily dependent on expert experiences, and it is difficult and time-consuming to design new features.

More recently, many efforts have been put toward learning feature representations automatically for steganalysis using deep learning models, which are powerful in learning complex representations by transforming the inputs through multiple layers of nonlinear processing. For example, Qian et al. [19] propose a novel framework for steganalysis based on Convolutional Neural Network (CNN). In the proposed framework, both the feature extraction and classification stages are unified under a single architecture, and are trained simultaneously. One obvious advantage of such method is that it would greatly reduce the amount of human labor by leaving the design of the feature extractor to the learning algorithm. Another is that the end-to-end training make the model possible to automatically discover useful information directly from data, while exploiting the guidance of classification.

Inspired by the recent progress on feature learning for steganalysis, this work takes a new CNN based approach, in which incorporation of prior knowledge to regularize the learning process is considered to boost the performance of steganalysis. In fact, though deep learning models have shown great promise in learning powerful features for pattern recognition, the difficulty of training thousands of or even millions of parameters still exists. They are easy to over-fitting and getting stuck in local minima, especially when trained on small datasets. To reduce these problems during training and to improve the performance of the model, many regularization methods have been developed, such as dropout [7], dropconnect [24], stochastic pooling [25], and data augmentation [3]. In this paper, we propose regularizing the CNN models for steganalysis by encoding prior knowledge via transfer learning from auxiliary tasks. The auxiliary tasks are generated by computing features that capture global statistics which are hard to be seized by the CNN network structure. We expect to encode such information in to the model, and encourage the learned feature representations to capture the global statistics for better detection performance.

2 Related Work

Our method is related to numerous works on deep learning, feature based steganalysis, and transfer learning. In this section, we briefly discuss them below.

Deep learning: Deep learning is a class of machine learning methods that addresses the problem of what makes better representations and how to learn them. The deep learning models have deep architectures that consist of multiple levels of non-linear

processing and can be trained to hierarchically learn complex representations by combining information from lower layers. There are many different types of deep models, such as Deep Boltzmann Machines [20], deep autoencoders [13], and Convolutional Neural Networks [14]. They have practically proved to be more powerful learning schemes for many artificial intelligence (AI) tasks such as object recognition, natural language processing, and image classification. In this paper, we focus on CNN as a base learner for steganalysis tasks. In a CNN model, trainable filters and pooling operations are applied alternatingly to the inputs, resulting in increasingly complex feature representations.

Feature based steganalysis: Most of the recent feature extraction methods for steganalysis follow a well-established paradigm of assembling a complex model as a combination of many diverse submodels to capture various dependencies among image elements [4–6, 10, 22, 23]. The submodels are constructed by firstly forming various noise residuals from pixels or DCT coefficients using a large number of designed linear or non-linear filters, and then computing global statistics such as high order co-occurrences from the residuals. Such methods rely heavily on expert human experiences to design different submodels to capture complementary information. Moreover, since the feature extraction and classification stages are independent, the guidance of classification can not be utilized for feature extraction. By contrast, our CNN based methods automatically learn features from data by training parameters in both feature extraction and classification stages. In [19], the authors also propose a CNN based model for feature learning in steganalysis. However,our method differs in that we exploit priori knowledge from auxiliary tasks to facilitate steganalysis feature learning for better performance.

Transfer learning: Transfer learning aims to leverage shared domain-specific knowledge contained in related tasks to help improving the learning of the target task. There has been a large amount of algorithms and techniques proposed on transfer learning to solve different problems. In this work, we mainly focus on transfer learning in the neural network. In [17], transfer learning with CNNs is explored for object recognition in a manner of reusing layers supervised trained on a large dataset to compute mid-level image representation for another dataset with limited training data. Differently to this work, we here transfer knowledge from some hand-engineered features. Similar ideas can also be found in other tasks [1, 11, 15], but its performance in steganalysis is not clear.

3 Proposed Framework

In this section, we will introduce the proposed framework in detail.

3.1 Exploiting Knowledge from Auxiliary Tasks with CNN

In our work, we use CNN, one of the most popular deep models, as the base learner to learn feature representations for steganalysis. A typical CNN model includes multiple convolutional layers, several fully-connected layers. The final layer is connected to a classifier for classification. In a convolutional layer, trainable filters, nonlinearity and local pooling of feature maps using a max or an averaging operation are applied in sequence. Detailed descriptions of CNNs can be found in [14].

Though CNN has been proved to be a powerful learning tool, the training of a large CNN architecture is still a challenging task, especially when facing limited training data. The key idea of this work is that the priori knowledge provided from auxiliary tasks through transfer learning can help CNN learn better feature representations for steganalysis as illustrated in Fig. 1.

In the proposed framework, the CNN model described in Sect. 3.2 extracts feature representations with multiple convolutional layers, and passes them to several fully-connected layers. The outputs of the last fully connected layer are fed to a two-way softmax for classification task, which is the target task in this work. The loss function here is the cross-entropy loss, which we call the target loss.

Meanwhile, the constructed auxiliary tasks from input described in Sect. 3.3 are used to regularize the CNN model. This is achieved by connecting the output units of the auxiliary tasks to the last fully-connected layer of the CNN structure and computing the least square loss, which we called the auxiliary loss. In this case, it encourages the fully-connected layer information to be close to the information provided by auxiliary tasks.

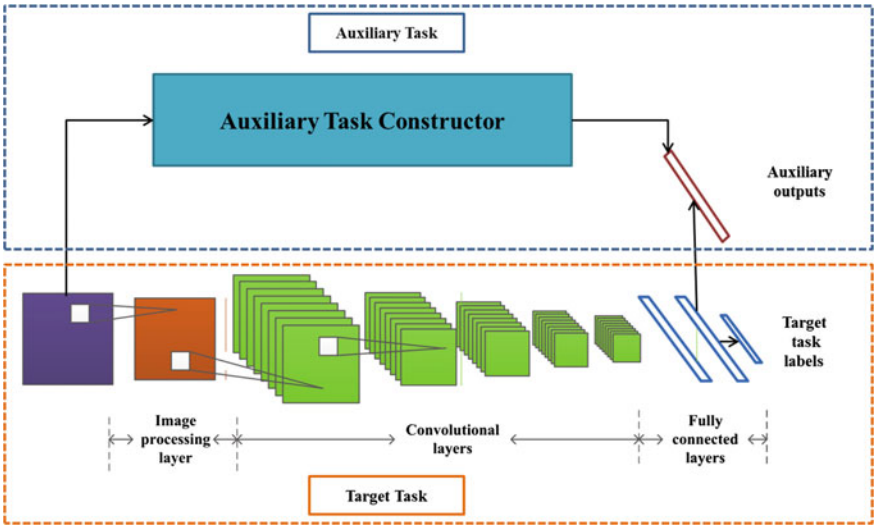

Fig. 1 Proposed framework for steganalysis

The overall loss function for the whole regularized model is a weighted summation of the target loss and the auxiliary loss. The network is then trained using backpropagation algorithm to minimize the overall loss, and thus the learning of features for steganalysis is guided by both the labeled information from the classification task and information from the auxiliary tasks simultaneously.

3.2 CNN Architecture

In this section, we describe the CNN architecture that is used for learning features for steganalysis as shown in Fig. 1. The architecture is composed of one image processing layer, five convolutional layers and three fully connected layers. It accepts an image patch of size 256×256 as input. Then the image processing layer computes the residuals with a predefined filter kernel of size 5×5. Here, we use the KV kernel, which is one of the commonly used kernels for preprocessing in traditional feature extractors, as shown below.

$$K_{kv} = \frac{1}{12} \begin{pmatrix} -1 & 2 & -2 & 2 & -1 \\ 2 & -6 & 8 & -6 & 2 \\ -2 & 8 & -12 & 8 & -2 \\ 2 & -6 & 8 & -6 & 2 \\ -1 & 2 & -2 & 2 & -1 \end{pmatrix} \tag{1}$$

The hard wired layer aims to strengthen the weak stego signal, hence to provide a much better initialization to drive the whole network as compared with random initialization. The first and fifth convolutional layer have 16 filter kernels of size 5×5, and the second to fourth convolutional layers have 16 filter kernels of size 3×3. The filtering stride of all the convolution operation is set to 1. Meanwhile, overlapping average pooling operation is applied to each convolutional layer with window size 3×3 and stride 2. Finally, the extracted features from the convolutional layers are passed to two fully connected layers. Each of the two layers has 128 neurons, and the output of each neuron is activated by the Rectified Linear Units (ReLUs) [16].

The settings of architecture we use here is the same as in [19], except that the activation function used in the five convolutional layers in this work is a variant of Gaussian function that has a better performance than Gaussian function. It is shown as below.

$$f(x) = 1 - e^{-\frac{x^2}{\sigma^2}}, \tag{2}$$

where σ is a parameter that determines the width of the curve.

3.3 Constructing Auxiliary Tasks

In this section, we introduce how to construct auxiliary tasks that are used for incorporate prior knowledge into the training of steganalysis models. Firstly, these tasks should be related to the specific steganalysis task. Secondly, we expect that they would provide complementary information that are useful for steganalysis while are hard to capture by the target task.

In steganalysis, effectively discovering and exploiting dependencies among individual image elements is crucial for the detectors to obtain a good performance. In different methods, different types of image statistics are exploited to model the dependencies. In traditional steganalysis systems, features are extracted by computing global statistics such as high order co-occurrences from noise residuals. These global statistics have been proved to be efficient for steganalysis. Differently, the CNN model describe the relationships among a large number of image elements through multi stage filtering and pooling operations, and the features extracted here are more related to local statistics from a neighborhood. It means that the useful global statistics in conventional steganalysis methods are hard to be captured by the CNN model. Hence, it is desirable that the auxiliary tasks can encode the global statistic information to the CNN model. To this end, we propose constructing the auxiliary tasks by computing features with a traditional method as mentioned before. In our experiments, we use a 169 dimensional feature vector formed from the noise residual computed using the KV kernel as auxiliary outputs. The detailed feature extraction step can be found in [5].

4 Experiments

To evaluate the effectiveness of the proposed framework, we conduct experiments on the BOSSbase 1.01 dataset [2], which contains 10,000 images acquired by seven digital cameras in RAW format and subsequently processed to the size of 512×512.

In our experiments, to further improve the network's generalization ability and to reduce the effects of overfitting during training, two commonly used regularization techniques are used in the CNN architecture. Firstly, the technique called "dropout" as detailed in [7] is applied for regularizing the two fully connected layers. Secondly, we take advantage of the data augmentation skill to artificially enlarge the dataset to reduce overfitting problem. It is applied by extracting random 256×256 patches as well as their flip version from the 512×512 images, and training the network on these extracted patches. At testing time, five 256×256 patches, including the four corner patches and the center patch, and their flip version are extracted. The network makes a prediction on each of these patches, and averages the ten predictions to produce a more robust estimate of the class probabilities.

Table 1 Detection error of different methods on BOSSbase 1.01

bpp	WOW			S-UNIWARD		
	0.3 (%)	0.4 (%)	0.5 (%)	0.3 (%)	0.4 (%)	0.5 (%)
SRM + Ensemble	25.57	20.90	16.60	26.12	20.92	16.70
CNN	28.93	21.98	17.35	32.03	24.20	20.65
Proposed	24.18	19.30	16.0	29.58	22.33	17.38

The proposed models are implemented using the code provided by Krizhevsky et al. [12], which allowed for rapid experimentation. We use a Tesla K40c GPU with 12GB of memory and two Tesla K20m GPU with 5GB of memory. In the overall loss function, the weight for the target loss is set to 1, and the weight for the auxiliary loss is set to 0.005 empirically. All the trainable parameters in the network are initialized randomly and trained by back-propagation algorithm as has been mentioned.

Table 1 shows the comparison of our results with two other methods. The detection error $P_E = min_{P_{FA}} \frac{1}{2}(P_{FA} + P_{MD}(P_{FA}))$ is used to evaluate the performance the these methods, where P_{MD} is the missed detection rate and P_{FA} is the false alarm rate. The "CNN" means the method proposed in [19]. In that work, the CNN model is trained without model regularization from auxiliary tasks. Here, for fair comparison, the CNN architectures in our proposed method and this method use the same settings. The "dropout" and the data augmentation are applied to both methods. The "SRM + Ensemble" means the method that based on training a ensemble classifier on SRM feature set, which is one of the representative traditional steganalysis schemes. The experiments are run on two content-adaptive steganographic algorithms, WOW [8] and S-UNIWARD [9], with three payloads respectively. From Table 1, we can observe that the proposed method achieves 1–4 % improvement in detection error over the "CNN" method in [19]. It means that model regularization via transfer learning from auxiliary tasks is helpful for learning features in steganalysis. And the detection performance for the WOW algorithm is better than the "SRM + Ensemble" method, which is one of the state-of-the-art methods in image steganalysis.

5 Conclusion

In this paper, we propose a new CNN based framework to effectively learn feature representations for steganalysis. In the framework, we use transfer learning from auxiliary tasks to encode priori knowledge into the learning process of CNN models. This would provide a good model regularization for improving the training of CNN. we construct auxiliary tasks by computing features to capture global image statistics which are useful for steganalysis but hard to be seized by the CNN network structure. Experimental results show the effectiveness of the proposed frame work on improving feature learning using CNN models for steganalysis. We also achieve a better performance on detecting the WOW algorithm against the traditional steganalysis scheme that using SRM feature set.

Acknowledgments This work is funded by the National Nature Science Foundation of China (Grant No.61303262).

References

1. Ahmed A, Yu K, Xu W, Gong Y, Xing E (2008) Training hierarchical feed-forward visual recognition models using transfer learning from pseudo-tasks. In: ECCV, pp 69–82
2. Bas P, Filler T, Pevnỳ T (2011) Break our steganographic system: the ins and outs of organizing boss. In: Information hiding, pp 59–70
3. Ciresan D, Meier U, Schmidhuber J (2012) Multi-column deep neural networks for image classification. In: IEEE conference on computer vision and pattern recognition, pp 3642–3649
4. Denemark T, Sedighi V, Holub V, Cogranne R, Fridrich J (2015) Selection-channel-aware rich model for steganalysis of digital images. In: National conference on parallel computing technologies (PARCOMPTECH), pp 48–53
5. Fridrich J, Kodovsky J (2012) Rich models for steganalysis of digital images. IEEE Trans Inf Forensics Secur 7(3):868–882
6. Gul G, Kurugollu F (2011) A new methodology in steganalysis: breaking highly undetectable steganograpy (hugo). In: Information hiding, pp 71–84
7. Hinton GE, Srivastava N, Krizhevsky A, Sutskever I, Salakhutdinov RR (2012) Improving neural networks by preventing co-adaptation of feature detectors. arXiv:1207.0580
8. Holub V, Fridrich J (2012) Designing steganographic distortion using directional filters. In: The IEEE international workshop on information forensics and security, pp 234–239
9. Holub V, Fridrich J (2013) Digital image steganography using universal distortion. In: Proceedings of the first ACM workshop on Information hiding and multimedia security, pp 59–68
10. Holub V, Fridrich J (2013) Random projections of residuals for digital image steganalysis. IEEE Trans Inf Forensics Secur 8(12):1996–2006
11. Ji S, Xu W, Yang M, Yu K (2013) 3D convolutional neural networks for human action recognition. IEEE Trans Pattern Anal Mach Intell 35(1):221–231
12. Krizhevsky A (2012) Cuda-convnet. http://code.google.com/p/cuda-convnet/
13. Larochelle H, Bengio Y, Louradour J, Lamblin P (2009) Exploring strategies for training deep neural networks. J Mach Learn Res 10:1–40
14. LeCun Y, Bottou L, Bengio Y, Haffner P (1998) Gradient-based learning applied to document recognition. Proc IEEE 86(11):2278–2324
15. Mobahi H, Collobert R, Weston J (2009) Deep learning from temporal coherence in video. In: Proceedings of the 26th annual international conference on machine learning, pp 737–744
16. Nair V, Hinton GE (2010) Rectified linear units improve restricted boltzmann machines. In: Proceedings of the 27th international conference on machine learning, pp 807–814
17. Oquab M, Bottou L, Laptev I, Sivic J (2014) Learning and transferring mid-level image representations using convolutional neural networks. In: IEEE conference on computer vision and pattern recognition, pp 1717–1724
18. Pevny T, Bas P, Fridrich J (2010) Steganalysis by subtractive pixel adjacency matrix. IEEE Trans Inf Forensics Secur 5(2):215–224
19. Qian Y, Dong J, Wang W, Tan T (2015) Deep learning for steganalysis via convolutional neural networks. In: IS&T/SPIE electronic imaging, pp 94,090J–94,090J
20. Salakhutdinov R, Hinton GE (2009) Deep boltzmann machines. In: International conference on artificial intelligence and statistics, pp 448–455
21. Shi YQ, Chen C, Chen W (2007) A markov process based approach to effective attacking jpeg steganography. In: Information hiding, pp 249–264
22. Shi YQ, Sutthiwan P, Chen L (2013) Textural features for steganalysis. In: Information hiding, pp 63–77

23. Tang W, Li H, Luo W, Huang J (2014) Adaptive steganalysis against wow embedding algorithm. In: Proceedings of the 2nd ACM workshop on information hiding and multimedia security, pp 91–96
24. Wan L, Zeiler M, Zhang S, Cun YL, Fergus R (2013) Regularization of neural networks using dropconnect. In: Proceedings of the 30th international conference on machine learning, pp 1058–1066
25. Zeiler MD, Fergus R (2013) Stochastic pooling for regularization of deep convolutional neural networks. arXiv:1301.3557

An Adaptive Ensemble Classifier for Steganalysis Based on Dynamic Weighted Fusion

Xikai Xu, Jing Dong, Wei Wang and Tieniu Tan

Abstract Recently, ensemble classifier is predominantly used for steganalysis of digital media, due to its efficiency when working with high-dimensional feature sets and large databases. While fusing the decisions of many weak base classifiers, the majority voting rule is often used, which has the disadvantage that all the classifiers have the same authority regardless of their individual classification abilities. In this paper, we propose a new dynamic weighted fusion method for steganalysis which can be adaptive to input testing samples. For each testing sample, the weight of each base classifier is dynamically assigned according to the distance between the testing sample and the classifier. Experimental results show that the proposed method is able to increase steganalysis performance.

Keywords Steganography · Steganalysis · Ensemble classifiers · Majority voting · Dynamic weighted fusion

1 Introduction

Steganography is a branch of information hiding which hides messages within an innocuous-looking cover object, for secret communication via public channel. Modern steganography works by replacing insignificant or redundant bits in regular

X. Xu · J. Dong (✉) · W. Wang · T. Tan
Center for Research on Intelligent Perception and Computing,
Institute of Automation, Chinese Academy of Sciences, Beijing, China
e-mail: jdong@nlpr.ia.ac.cn

X. Xu
e-mail: xikai.xu@nlpr.ia.ac.cn

W. Wang
e-mail: wwang@nlpr.ia.ac.cn

T. Tan
e-mail: tnt@nlpr.ia.ac.cn

Q. Liang et al. (eds.), *Proceedings of the 2015 International Conference on Communications, Signal Processing, and Systems*, Lecture Notes in Electrical Engineering 386, DOI 10.1007/978-3-662-49831-6_65

digital files (such as text, audio, image and video) with bits of given messages [10, 13, 16, 18]. As a countermeasure, steganalysis mainly aims to detect whether the media have hidden messages or not which can be viewed as a binary classification problem. For this task, like other classification systems, two basic operations are feature extraction and classification. Generally, discriminative features are extracted from cover and stego objects and then a classier as detector is trained using machine learning methods. In this paper, we use current existing steganalytic feature sets and focus on the classification stage of steganalysis.

Many popular classification algorithms, such as Linear Discriminant Analysis (LDA), Neural Network and Support Vector Machine (SVM), have been widely used in early steganalytic systems [5, 12, 17]. Among which, the SVM classifier with kernel methods once predominated in steganalysis [4, 12, 15, 19] for a long time because of its solid mathematical foundation and excellent performance on small sample learning problems [3]. Early steganalytic feature sets were low dimensional and the databases were also small, thus kernel SVMs could be trained quickly. But, currently, with growing feature dimensionality and increasing number of samples, nonlinear SVM is no longer suitable for its unbearable computational cost.

To detect new steganographic algorithms, especially content-adaptive image steganographic algorithms [6, 8, 9, 14], steganalysts have to use feature spaces of high dimensionality. For example, the state-of-the-art feature set for image steganalysis, "Rich Models" [7] even has a dimensionality of 34,671. To address problems caused by the curse of dimensionality in steganalysis, an ensemble classifier for steganalysis was proposed in [11] by Kodovský et al., which is a collection of FLD base learners (classifiers) trained on random subspaces of the feature space and on bootstrap samples of the training set. It is currently the most successful classifier for steganalysis which is very efficient and robust for dealing with high-dimensional feature spaces and large training data sets.

The fusion method of base classifiers in [11] is majority voting, which is very simple. The problem is that all the classifiers have the same 'authority' regardless of their individual classification abilities. To make an improvement, we can use weighted methods to combine base classifiers. In fact, the idea of weighted fusion has been used for many other classification tasks in literature [20–22]. But for steganalysis, the assignment of weights should be carefully designed with consideration of the characteristics of steganalysis. In this paper, we propose a dynamic weighted ensemble classifier for steganalysis which can be adaptive to testing samples. For each testing sample, the weight of each base classifier is dynamically assigned according to the distance between the testing sample and the classifier. Experimental results show that the proposed method outperforms majority voting on detecting different steganographic algorithms.

The remainder of the paper is organized as follows: In Sect. 2, we briefly review the ensemble classifier proposed in [11]. In Sect. 3, we demonstrate the proposed dynamic weighted fusion method for steganalysis. Experimental results are presented in Sect. 4. Finally, conclusions are drawn in Sect. 5.

2 The Kodovský's Ensemble Classifier

The ensemble classifier proposed by Kodovský et al. in [11] consists of L independently trained base learners. Each base learner, denoted as D_l with $l \in \{1, \ldots, L\}$ is trained on a random subspace of the feature space and on bootstrap samples of the training set. The dimensionality of the random subspace can be chosen to be much smaller than the full dimensionality, which significantly decreases the training complexity. Moreover, by using bootstrap samples drawn from the training set rather than all the training samples, the mutual diversity of the base learners can be further increased.

Let (X, y) be the training data, $X = \left[x_1, \ldots, x_i, \ldots, x_N\right]$, $y = \left[y_1, \ldots, y_i, \ldots, y_N\right]$, where $x_i \in R^d$ is the i^{th} sample and $y_i \in \{0, 1\}$ is its label with '0' standing for cover and '1' for stego, d is the number of features and N is the number of samples. (It is assumed that there are the same number of cover and stego images, since stego images are obtained by embedding messages in cover images).

A subspace is generated by randomly sampling without replacement, d_{sub} ($\ll d$) out of d features preserving their original order and the original data is projected onto the subspace. Meanwhile, the training samples for each subspace are obtained by bootstrap sampling (uniform sampling with replacement) from the original training set. Let $\left(\tilde{X}^{(l)}, y\right)$ be the projected data on the lth subspace, where $\tilde{X}^{(l)} = \left[\tilde{x}_1^{(l)}, \ldots, \tilde{x}_i^{(l)}, \ldots, \tilde{x}_{N_l}^{(l)}\right]$ and $\tilde{x}_i^{(l)} \in R^{d_{sub}}$. N_l, $\left|N_l\right| = N$ is the l^{th} bootstrap sampling of the set of indices $\{1, \ldots, N\}$. Then, the base learner D_l is trained on $\left(\tilde{X}^{(l)}, y\right)$.

After collecting L base learners, the final class predictor is formed by combining their individual decisions. For every testing sample $x \in X^{tst}$, the final prediction $C(x)$ is obtained by a majority vote:

$$C(x) = \begin{cases} 1 \ if \ \sum_{l=1}^{L} D_l(x) \geq L/2 \\ 0 \quad otherwise \end{cases}$$

Many kinds of classification tools can be used as base learners and in [11] the authors recommended to use Fisher Linear Discriminant (FLD) because of its low training complexity. Additionally, such weak and unstable classifiers desirably increase diversity.

The Kodovský's ensemble classifier achieves performance as good as or even better than the SVM and successfully solves the complexity issues of steganalysis in high-dimensional feature space. However, the simple voting strategy for combining base learners can be replaced by a weighted fusion method which has the potential to make the ensemble classifier more efficient and more robust.

3 Proposed Method

This paper proposes an adaptive ensemble classifier for steganalysis based on dynamic weighted fusion. First, we train base classifiers on random subspaces of the feature space and on bootstrap samples of the training set, as Kodovský did in [11]. Then, we dynamically assign a weight to each base classifier according to the distance between the input testing sample and the classifier. Finally, we combine the output of each classifier with the corresponding weight to give the final prediction for the input sample.

We dynamically determine the weights of classifiers for each input testing sample because the learned classifiers which can correctly classify the testing sample change as the testing sample varies. However, this is not an easy work since we know little prior knowledge about the dynamic performance of each classifier.

In order to validate the local performance of each base classifier, we have investigated the relationship between detecting errors and the distribution of testing samples. We found that when the testing samples are far away from the learned separating hyperplane (classifier), the classifier may fail in predicting their labels (acting out a high false positive rate or a high false negative rate). This is mainly because of one characteristic of the steganalysis problem: the difference between cover and its corresponding stego object is very small while the samples within the same category (cover or stego) scatter widely in the feature space. When the distance from the testing sample to a classifier is relatively large, the cover and stego versions of this sample may be on the same side of the separating hyperplane, hence the classifier cannot distinguish them. As the simplified examples illustrated in Fig. 1, C1, C2, and

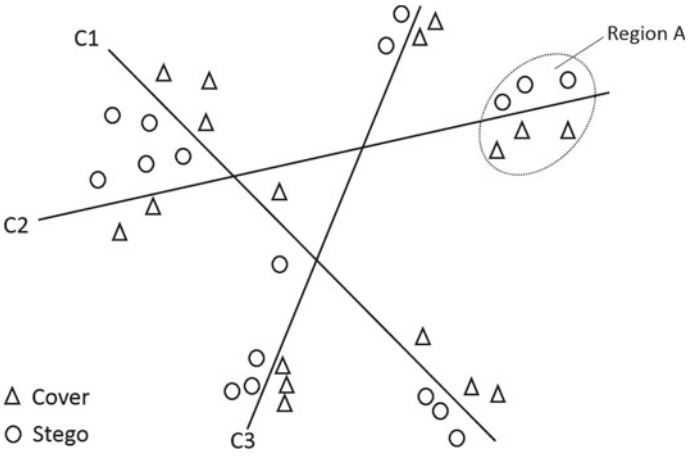

Fig. 1 The classifier has different performance in different area of the data space

C3 are three linear classifiers, they can separate cover and stego samples near them but cannot separate distant samples. For example, C1 and C3 may fail in separating samples in Region A.

The above observation motivated us to consider the sample–classifier distance when assigning weight to each base classifier for an input testing sample. Here, we also use FLD classifiers as base learners and to calculate the distance from a sample to a FLD classifier, the process of learning a FLD classifier should be made clear at first.

The FLD learning is to find the projection direction $\boldsymbol{w} \in \mathbf{R}_{\boldsymbol{sub}}^{\boldsymbol{d}}$ that maximizes the following Fisher's criterion:

$$J_F(\boldsymbol{w}) = \frac{\boldsymbol{w}^T \boldsymbol{S}_B \boldsymbol{w}}{\boldsymbol{w}^T \boldsymbol{S}_W \boldsymbol{w}},$$

$$\boldsymbol{S}_B = \left(\boldsymbol{u}_1 - \boldsymbol{u}_2\right)\left(\boldsymbol{u}_1 - \boldsymbol{u}_2\right)^T,$$

$$\boldsymbol{S}_W = \sum_j \left(\sum_{\boldsymbol{x} \in \boldsymbol{X}_j} \left(\boldsymbol{x} - \boldsymbol{u}_j\right)\left(\boldsymbol{x} - \boldsymbol{u}_j\right)^T \right), j = 1, 2.$$

where $\boldsymbol{X}_j$ is the set of the jth class samples and $\boldsymbol{u}_j$ is its centroid. $\boldsymbol{S}_B$ and $\boldsymbol{S}_W$ are known as the between-class scatter matrix and within-class scatter matrix, respectively. The decision rule of FLD is defined by

$$D(\boldsymbol{x}) = \begin{cases} 1 \ if \ \ \boldsymbol{w}^T \boldsymbol{x} - \boldsymbol{b} \geq 0 \\ 0 \ if \ \ \boldsymbol{w}^T \boldsymbol{x} - \boldsymbol{b} < 0 \end{cases}$$

The distance from a sample $\boldsymbol{x}$ to each FLD classifier D_l is:

$$r_l = \frac{\left|\boldsymbol{w}^T \boldsymbol{x} - \boldsymbol{b}\right|}{\|\boldsymbol{w}\|}$$

And the weight of D_l should be inversely proportional to the distance between $\boldsymbol{x}$ and D_l. Therefore, we define the weight of D_l as follows:

$$\mu_l = \frac{1}{r_l\left(\sum_{l=1}^{L} \frac{1}{r_l}\right)} = \frac{\prod_{l=1}^{L} r_l}{r_l\left(\sum_{l=1}^{L} r_l\right)}$$

Essentially, the weight μ_l is the normalized value of $\frac{1}{r_l}$. After calculating all the weights of base classifiers, the final decision rule of the ensemble classifier, for current testing sample $\boldsymbol{x}$, is:

$$C(\boldsymbol{x}) = \begin{cases} 1 \ if \ \sum_{l=1}^{L} \mu_l D_l(\boldsymbol{x}) \geq 0.5 \\ 0 \ if \ \sum_{l=1}^{L} \mu_l D_l(\boldsymbol{x}) < 0.5 \end{cases}$$

4 Experimental Results

To demonstrate the power and universality of the proposed dynamic weighted ensemble classifier, we carry out experiments on two image databases and involve the state-of-the-art image steganographic algorithms and high-dimensional features.

The first database is the BOSS V1.01 [1] composed of 10,000 images of size 512×512. All images in BOSS are captured by cameras of different types and stored in lossless RAW format. They are converted to gray images and processed by identical procedure. Contents of these images cover various themes. The second database is composed of 100,000 images, selected from the ImageNet [2]. ImageNet is a very famous image database with more than one hundred million images collected from the Internet. We randomly chose 100,000 images from those images that are larger than 400×400 and smaller than 1024×1024. We transformed the selected images into grayscale and denote the new database as ImageNet-S.

Stego images are generated by applying data hiding on above databases using three popular steganographic algorithms. The first one is LSB Matching Revisited (LSBMR) [13], a classical method which is an improvement of LSB Matching. The other two algorithms are HUGO [14] and S-UNIWARD [9]. They are all content-adaptive embedding algorithms which represent the state of the art in steganography. Four payloads are used for each algorithm, 0.10, 0.20, 0.30, 0.40 bpp (bits per pixel).

The steganalytic features are extracted using Spatial Rich Model (SRM) [7] which is the current state-of-the-art steganalytic method. SRM consists of many diverse submodels considering various types of correlations of neighboring elements of noise residuals obtained using various types of image filters. Multiple 4D co-occurrences matrices formed in the noise residuals are used to construct a feature set of 34,671 features.

The learning processes of base classifiers are run after the extraction of steganalytic features. The number of base classifiers, L, and the dimensional of subspace, d_{sub}, are determined in the training stage using the procedure proposed in [11]. After getting base classifiers, we compare our dynamic weighting with the original majority voting on detecting steganographic algorithms. We report the detection performance using the minimum detection error rate under equal priors:

$$P_E = \min_{P_{FA}} \frac{1}{2} \left(P_{FA} + P_{MD} \right),$$

Table 1 Error rates on detecting steganographic algorithms using ensemble classifier

		BOSSbase		ImageNet-S	
Algorithm	Payload (bpp)	Majority voting	Dynamic weighting	Majority voting	Dynamic weighting
LSBMR	0.10	0.1740	**0.1553**	0.0910	**0.0660**
	0.20	0.1163	**0.0990**	0.0458	**0.0235**
	0.30	0.0835	**0.0698**	0.0300	**0.0120**
	0.40	0.0650	**0.0505**	0.0130	**0.0028**
HUGO	0.10	0.3628	**0.3405**	0.2375	**0.2068**
	0.20	0.2533	**0.2330**	0.1283	**0.0980**
	0.30	0.1885	**0.1703**	0.0915	**0.0645**
	0.40	0.1280	**0.1145**	0.0610	**0.0375**
S-UNIWARD	0.10	0.4140	**0.3953**	0.2593	**0.2270**
	0.20	0.3163	**0.3005**	0.1610	**0.1303**
	0.30	0.2505	**0.2360**	0.1205	**0.0940**
	0.40	0.2020	**0.1885**	0.0980	**0.0713**

The proposed dynamic weighting is compared with the majority voting

where P_{FA} and P_{MD} are the probabilities of false alarm and missed detection. Each result is averaged over ten random splits of the database into 4/5 part for training and the rest 1/5 part for testing.

The error rates on detecting three steganographic algorithms at each payload are illustrated in Table 1. We can see that by using the proposed dynamic weighting the error rates decrease 1–4% on both databases compared with majority voting. The improvement seems a little bigger on database ImageNet-S, and this may be because there are more and diverse samples in ImageNet-S and the proposed dynamic weighting is more robust to high intraclass variations of samples.

Since we need to calculate the weights of classifiers for each testing sample, the testing time cost of the proposed method is higher but still acceptable. In our experiments, the average time on detecting 10,000 testing samples is about 4.9 s using majority voting and 12.4 s using dynamic weighting (The running environment: Intel Xeon E5620, 16GB memory, Windows Server 2008, Matlab R2011a).

5 Conclusions

The current trend in steganalysis is to train many classifiers on high-dimensional feature space and combine the decisions of multiple classifiers to obtain more accurate and robust detectors. While most steganalysts use the ensemble classifier based on majority voting, we proposed a new adaptive ensemble classifier for steganalysis based on dynamic weighted fusion. Experimental results show that the proposed scheme can effectively detect different steganographic algorithms and its

performance is better than that of the majority voting ensemble classifier. The future study will focus on designing better weighted method based on the sample-classifier distance.

Acknowledgments This work is funded by the National Nature Science Foundation of China (Grant No.61303262).

References

1. BOSS1.01. http://exile.felk.cvut.cz/boss/BOSSFinal/index.php
2. ImageNet. http://www.image-net.org/
3. Burges C (1998) A tutorial on support vector machines for pattern recognition. Data Min Knowl Disc 2:121–167
4. Chen X, Wang Y, Tan T, Guo L (2006) Blind image steganalysis based on statistical analysis of empirical matrix. Proc Int Conf Pattern Recogn 3:1107–1110
5. Farid H (2002) Detecting hidden messages using higher-order statistical models. Proc Int Conf Image Proc 2:08–905
6. Filler T, Fridrich J (2010) Gibbs construction in steganography. IEEE Trans Inf Forensics Secur 5(4):705–720
7. Fridrich J, Kodovsky J (2012) Rich models for steganalysis of digital images. IEEE Trans Inf Forensics Secur 7:868–882
8. Holub V, Fridrich J (2012) Designing steganographic distortion using directional filters. In: Proceedings of IEEE international workshop on information forensics and security. IEEE, pp 234–239
9. Holub V, Fridrich J, Denemark T (2014) Universal distortion function for steganography in an arbitrary domain. EURASIP J Inf Secur 2014(1)
10. Kawaguchi E, Eason RO (1998) Principle and applications of BPCS-steganography. In: SPIE: multimedia systems and applications, vol 3528. pp 464–472
11. Kodovsky J, Fridrich J, Holub V (2012) Ensemble classifiers for steganalysis of digital media. IEEE Trans Inf Forensics Secur 7:432–444
12. Lyu S, Farid H (2003) Detecting hidden messages using higher-order statistics and support vector machines. In: Proceedings of the 5th international workshop on information hiding. Springer, pp 340–354
13. Mielikainen J (2006) Lsb matching revisited. Sig Process Lett IEEE 13(5):285–287
14. Pevnỳ T, Filler T, Bas P (2010) Using high-dimensional image models to perform highly undetectable steganography. In: Information hiding, vol 6387. Springer, Berlin, pp 161–177
15. Pevnỳ T, Fridrich J (2007) Merging markov and dct features for multi-class JPEG steganalysis. In: Proceedings SPIE, electronic imaging, security, steganography, and watermarking of multimedia contents IX 6505
16. Provos N (2001) Defending against statistical steganalysis. In: Proceedings of the 10th conference on USENIX security symposium, vol 34. USENIX Association, pp 24–24. http://www.outguess.org/
17. Shaohui L, Hongxun Y, Wen G (2003) Neural network based steganalysis in still images. In: IEEE international conference on multimedia and expo, vol 1. Washington, DC, USA, pp 509–512
18. Sharp T (2001) An implementation of key-based digital signal steganography. In: Proceedings of the 4th international workshop on information hiding. Springer, pp 13–26
19. Shi Y, Xuan G, Yang C, Gao J, Zhang Z, Chai P, Zou D, Chen C, Chen W (2005) Effective steganalysis based on statistical moments of wavelet characteristic function. Proc Int Conf Inf Technol Coding Comput 1:768–773

20. Valdovinos R, Snchez J, Barandela R (2005) Dynamic and static weighting in classifier fusion. In: Pattern recognition and image analysis, vol 3523. Springer, Berlin, pp 59–66
21. Wozniak M (2008) Classifier fusion based on weighted voting—analytical and experimental results. Proc Eighth Int Conf Intell Syst Des Appl 2:687–692
22. Zhu Y, Ou J, Chen G, Yu H (2010) An approach for dynamic weighting ensemble classifiers based on cross-validation. J Comput Inf Syst 6(1):297–305

Technology of SCL Configuration File Content Difference Detection

Lei He, Ming Wei and Kun Wu

Abstract In engineering due to its frequent update, the SCL configuration file has too many versions and its management is chaotic. So the management of SCL files should be strengthened, and the content difference detection of SCL files should be carried out regularly. Due to the lack of full-featured configuration file comparison tools currently, this article describes how to develop new software based on MSXML4.0 parser tool. The XML file parsing and storage module, linked list creation and memory release module, and file content comparison module are introduced in detail. The application shows that the software can effectively reduce the workload of SCL file content difference detection and can improve the efficiency of the detection work.

Keywords IEC 61850 · Smart substation · Intelligent electronic device · Substation configuration language

1 Introduction

The IEC 61850 configuration file is using the substation configuration language (SCL) to describe the substation device object model for the exchange of configuration information between different manufacturers' configuration tools [1].

L. He (✉)
State Grid Hebei Electric Power Research Institute,
Shijiazhuang 050021, Hebei Province, China
e-mail: ksc200420042004@163.com

M. Wei
State Grid HanDan Electric Power Company,
Handan 056002, Hebei Province, China

K. Wu
State Grid Hebei Electric Power Company,
Shijiazhuang 050021, Hebei Province, China

Q. Liang et al. (eds.), *Proceedings of the 2015 International Conference on Communications, Signal Processing, and Systems*, Lecture Notes in Electrical Engineering 386, DOI 10.1007/978-3-662-49831-6_66

In the engineering of the substation, the SCL configuration files experience system integration, device manufacturers export, downloading the device and other processes, so they need a good fit of device manufacturers and system integrators to ensure the correctness of the configuration files [2].

At present, due to the continuous upgrading of the device, the change of the engineering design, the special needs put forward by the local users, the phenomenon of repeated modification of the device model and the replacement of the configuration file are still common. So the SCL files in engineering have too many versions, and management of the SCL files is chaotic.

In addition, some device manufacturers generate the CID by modifying the ICD file directly. So the CID file downloaded to the device and the SCD file is not consistent, which lead to the wrong signal, the error of communication services and other issues.

So in each stage of the substation commissioning, the SCL files of each device should be archived in time, and the configuration file and the recall of the archives are compared, as shown in Fig. 1.

In the substation expansion, the system integration engineer need to add new ICD file into the old version of the SCD file, the engineer should ensure that the newly imported ICD file will not cause damage to the old version of the SCD, and therefore also face the problem of checking the new version of the old version of the SCD file.

Although it can be used to compare the contents of the configuration file by using the software of the text, but the number of IEDs in the high-voltage substation is much more (containing hundreds of IEDs), and the configuration file capacity is quite large (containing hundreds of Logical Nodes). Using text comparison software to compare the various configuration files one by one has the problem with low efficiency and error prone, and the details of the different versions of SCL files cannot be output.

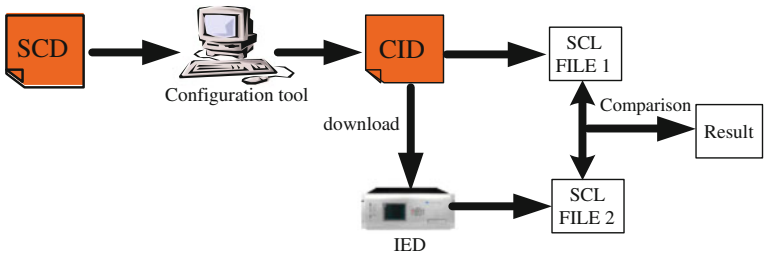

Fig. 1 The comparison process of SCL files

In this paper, a special software is developed, which can automatically accomplish the content comparison between different versions of the SCL files, and can output the differences in detail. It is helpful for the adjustment of the configuration file to be evaluated, which can improve the efficiency and quality of the project.

2 General Idea

The main process of software is shown in Fig. 2.

(a) The software uses the MSXML4.0 parser to load the SCL File 1 in the Fig. 1 into memory to form a DOM tree, and then each node of the DOM tree is stored in the linked list data structure.
(b) Load the SCL File 2 in the Fig. 1; Call the API interface function provided by MSXML4.0 to extract the DOM tree nodes, Compare each node of the DOM tree with the SCL element stored in the linked list data structure, if there are different the software will alarm;
(c) Save the test results to a text file;
(d) Finally release dynamically allocated memory when the list was created.

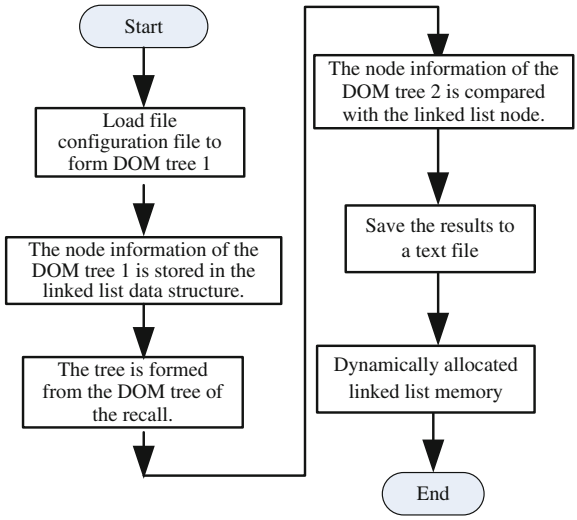

Fig. 2 The main process of software

3 Key Modules and Technologies

3.1 Parsing and Storage of SCL Files

Because the software needs to support the SCD file parsing, and the capacity of the SCD is generally large, so it requires higher speed and lower memory consumption in SCL File parsing. Since Microsoft's MSXML4.0 in these two aspects are excellent, so it is selected. After reading the XML document using the DOM interface, a data tree will be constructed in memory [3]. Using the API interface provided by MSXML4.0, the nodes in the DOM tree can be added, edited, moved, and so on [4].

Since the number of elements and attributes in the SCL configuration file is unknown, it is difficult to determine the length of the required memory cells in advance. If the memory is large enough to store any size of the file, it will be a waste of memory obviously. Data linked list does not has such a disadvantage. It opens up memory cells based on the need, so it is very suitable for storage of SCL configuration file.

According to the definition of schema SCL in IEC 61850-6, SCL configuration file uses a tree structure, as shown in Fig. 3. This software creates a tree of the chain structure, for storage of SCL configuration file. Take the IED part as an example, as shown in Fig. 4. The root node is IED, the child node of the root node is Server, and the server contains the logical device, and the logic device contains the logical node.

The software uses the structure body as the list node and the data list creation function of <Header>, <IED>, <Communication>, and <DataTypeTemplates> is written.

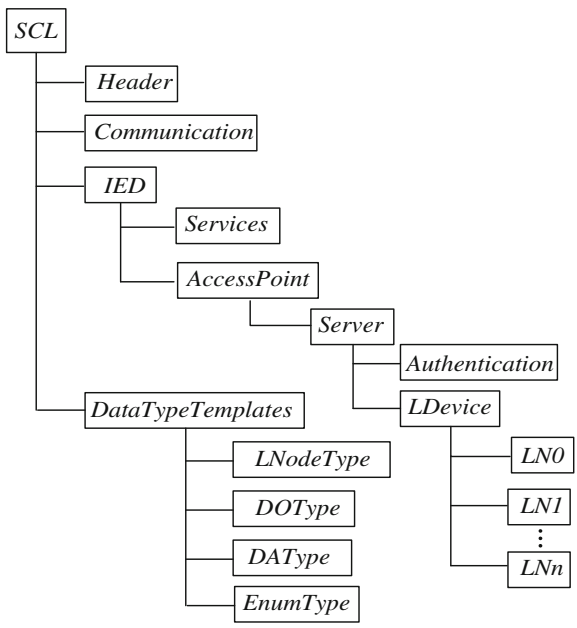

Fig. 3 Structure of SCL files

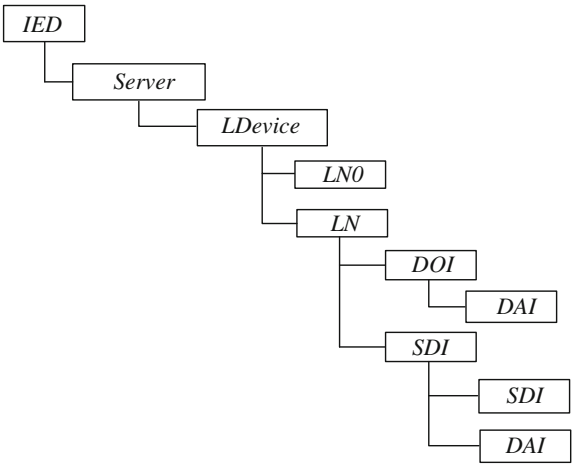

Fig. 4 Linked list of IED section

Figure 5 is the process of linked list creation and storage of the SCL file. LN in Fig. 5 does not represent LLN0, LLN0 also contains a data set, report control block, the setting value of the control block and other elements. The process of linked list creation and storage of LLN0 is more complicated.

C++ provides a simple and powerful <new> operator to dynamically allocate memory space, however, the memory unit of the <new> operator will not be automatically released at the end of the program. It needs to use the <delete> operator to undo. Therefore, for each type of linked list node, memory allocation and memory release functions are written to prevent memory leaks.

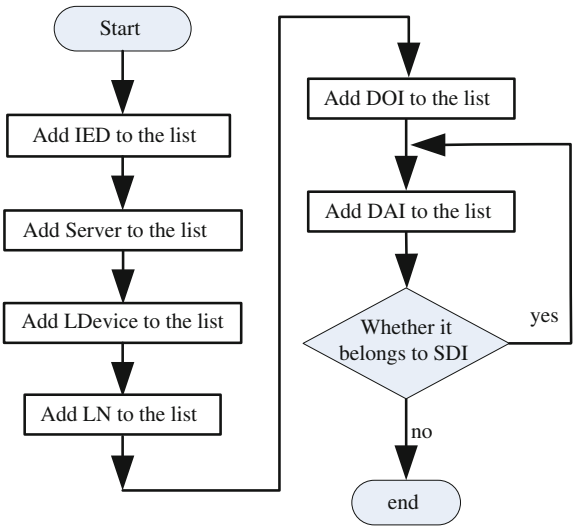

Fig. 5 Linked list of IED section

3.2 SCL Content Difference Detection

The main processes are as follows:

(1) First SCL File 1 in the Fig. 1 is read into memory and stored in the linked list data structure as the standard file;
(2) SCL File 2 in the Fig. 1 is read into memory to form a DOM tree, and then use the API function to extract the DOM tree node information;
(3) DOM tree node information and the list of the corresponding SCL file element information is compared

```
List1：
<LN desc="Bay 01 trip"  inst="1"  lnClass="PTRC" lnType="SZNR_PTRC_GOOUT_BP2C"
prefix="Bus">
<DOI desc=" Bay 01 trip_GOOSE" name="Tr">
    <DAI name="general" sAddr="GOOSEPin_EN_KO_
UNIT01_TRIP"/>
<DAI name="dU">
      <Val> Bay 01 trip _GOOSE</Val>
</DAI>
</DOI>
</LN>
```

The content difference detection of SCL configuration file adopts the method of hierarchical comparison.

Take the logical node "BusPTRC1" in Listing 1 as an example (assuming that the logical node is located in the DOM tree of the recall file, the software first searches all LNs in the same logical device of archived files, tries to find the LN of the same attribute values (desc, inst, lnClass, etc.). If corresponding LN cannot be searched an alarm is issued. If corresponding LN can be searched, then the child elements (such as DOI and SDI) of the LN will continue to be searched. And so on, SDI, DOI use the comparison process. Similar to LN.

In order to guarantee the integrity of the detection, comparison should be carried out in two directions. First, take the list of the archive file as the benchmark, files in the DOM tree are compared. Elements which are already present in the archive file but not in the recall file are checked. Then take the files in the DOM tree as the benchmark, the archive files are compared, elements which are already present in the recall file but not in the archive file are checked.

4 Engineering Application Examples

In the installation inspection of a substation, the software is used to compare the files which are archived at the end of the factory commissioning and the recalled files from the device. The problem of modifying the configuration file secretly by a device manufacturer is found. Practical engineering application can prove that the software can automatically detect the difference between the two versions of the configuration file, and can output the correct position in the configuration file. It reduces the workload of the configuration file content difference comparison effectively, and improve the test efficiency of the project site.

5 Conclusion

The problem faced in the application of SCL configuration file is that the SCL configuration file has too many versions and its management is chaotic. So the management of SCL files should be strengthened, and the content difference detection of SCL files should be carried out regularly. Aiming at the problem of the lack of a complete configuration file comparison tool, a dedicated SCL file content difference detection software is developed. The software can also be used as a function module embedded in the equipment manufacturer's model configuration tool.

References

1. He L, Tian X, Han Y-J (2011) Research on the testing of IEC 61850 configuration file in engineering [J]. Power Syst Prot Control 39(16):147–150
2. National energy administration of China. DL/T 1146-2009, Technical specification of DL/T 860 in engineering. Beijing, China Electric
3. Yong-chao W, Zeng-ping W, Yan-shi L (2009) Application and parsing of substation configrution language[J]. Power Syst Prot Control 37(15):38–41
4. He L, Tian X (2012) Design and achievement of test tool for IEC 61850 SCL configuration files [J]. Power Syst Prot Control 37 (12):82–85

Discrimination of Three-Dimensional Fluorescence Spectra of PAHs Mixture Using Parallel Factor Analysis

Guimei Dong, Renjie Yang, Yanrong Yang, Yaping Yu and Xiaotong Yang

Abstract Polycyclic aromatic hydrocarbons (PAHs), as one of petroleum pollutants, have increasingly threatened the ecological environment and human health due to its strong carcinogenicity, whose fast and efficient detection has consequently become a global subject. Nowadays, fluorescence spectrometry, especially three-dimensional fluorescence spectroscopy has been used to directly detect PAHs in the environment for the high sensitivity and selectivity. Parallel factor analysis is used for separation from the spectrum of different fluorescence matters. In the paper, taking anthracene, pyrene and phenanthrene as PAHs research object, parallel factor analysis was adopted to resolve respective characteristic spectrum from three-dimensional fluorescence spectrum of PAHs mixture. The experimental results showed that this kind of method achieved good separation for mixture of anthracene, pyrene and phenanthrene, which proved its feasibility and validity to discriminate overlapping spectra of multiconstituents of PAHs.

Keywords Three-dimensional fluorescence spectroscopy · Polycyclic aromatic hydrocarbons · Parallel factor · Multiconstituent

1 Introduction

Polycyclic aromatic hydrocarbons (PAHs) is a kind of hydrocarbons composed of two or more than two benzene rings that are connected together, such as naphthalene, anthracene, etc. [1–3]. PAHs are widely distributed in environment with high stability, refractory, heavy toxicity and accumulation effect [4–6], which received extensive attention of environmental researchers, and has been included in the blacklist or greylist of priority pollutants by many countries. Due to a great variety [7], the effective methods for determination and discrimination of PAHs

G. Dong (✉) · R. Yang · Y. Yang · Y. Yu · X. Yang
College of Engineering and Technology, Tianjin Agricultural University, Tianjin, China
e-mail: m13820408305@163.com

Q. Liang et al. (eds.), *Proceedings of the 2015 International Conference on Communications, Signal Processing, and Systems*, Lecture Notes in Electrical Engineering 386, DOI 10.1007/978-3-662-49831-6_67

mixture are essential. Fluorescence spectrometry is a sensitive and selective tool to probe various systems such as solutions, colloids, organic and inorganic solids, and polymers [8–11]. Despite the usefulness, the analysis of fluorescence spectra is sometimes difficult, especially when a heavy overlap of spectrum is generated from constituents in a mixture of PAHs [12–14]. To overcome this problem, three-dimensional fluorescence spectroscopy is employed, which can show excitation and emission spectra simultaneously in two dimensions to illustrate the dependence of fluorescence spectra on the excitation wavelength. Combined with parallel factor analysis (PARAFAC), it was applied to the analysis on fluorescence spectra of the mixture of anthracence, pyrene and phenanthrene in anhydrous alcohol solutions so as to separate out their respective characteristic spectra.

2 Methods and Principles

Total fluorescence of complex system is often represented by three parameters, including excitation wavelength, emission wavelength and fluorescence intensity. With excitation–emission matrix method (EEM), the rows order of the matrix indicates emission wavelength, while the columns order of the matrix indicates excitation wavelength, and the matrix elements indicate intensity of fluorescence [15]. This kind of expression method is also called three-dimensional fluorescence spectroscopy.

In a unique constituent system, the EEM is expressed as

$$M = \alpha xy \tag{1}$$

where EEM(M) is assumed as the product of three factors α, x and y. α represents coefficient that is not dependent of wavelength but dependent on concentration; x and y represent emission spectra and excitation spectra, respectively.

For a fluorescent system composed of n constituents, the EEM can be expressed as

$$\mathrm{M} = \sum_{k=1}^{n} \alpha^k x^k y^k \tag{2}$$

PARAFAC algorithm is a kind of multidimensional analysis method as well as a method of decomposition, which is an extension for principal component analysis (PCA) to a higher order array. During analyzing, a three-dimensional matrix (samples × excitation × emission) composed of multi-EEM is decomposed into three load matrices: A, B and C, which can be derived to make the fitting residual sum of squares the smallest.

PARAFAC employs the trilinear model

$$x_{ijk} = \sum_{f=1}^{F} \alpha_{if} b_{jf} c_{kf} + \varepsilon_{ijk} \tag{3}$$

where x_{ijk} represents fluorescence intensity of the ith sample, while excitation and emission wavelength correspond to excitation wavelength of kth row and emission wavelength of jth column in the matrix. α_{if} is the concentration ratio fraction of the fth fluorophore of the ith sample. b_{jf} and c_{kf} are emission spectra and excitation spectra, respectively, of the fth fluorophore. F is the number of factors, which is employed by the model. ε_{ijk} is the collection of model and random residual errors from fitting this trilinear model. Three load matrices A, B and C are derived from Eq. (3), which represent relative concentration, emission profiles and excitation profiles, respectively. The F columns of α_{if}, b_{jf} and c_{kf} can be estimated by alternating least squares (ALS) algorithm [16]. During the procedure, two of the load matrices are presumed reasonably first, and then other unknown parameters are calculated.

3 Experimentation

3.1 Main Reagents and Equipments

- PerkinElmer LS55 Fluorescence Spectrometer
- Anthracene (AN), pyrene (PY), phenanthrene (PH); anhydrous alcohol
- Unique constituent of AN, PY and PH solutions:
  Dissolve 25 mg solid AN in a beaker, adding proper amount of anhydrous alcohol solution and stirring it evenly until it dissolves completely. Transfer AN solution into 250 mL of volumetric flask along glass rod, and dilute with anhydrous alcohol solution to volume. Thus, 100 mg/L of AN solution was obtained. Dilute step by step to get 2×10^{-5} g/L of AN anhydrous alcohol solution. In the same way, 4×10^{-6} g/L of PY anhydrous alcohol solution and 6×10^{-5} g/L of PH anhydrous alcohol solution were prepared.
- Mixture of AN, PY and PH solutions:
  Take the same volume of 2×10^{-5}g/L of AN anhydrous alcohol solution, 4×10^{-6}g/L of PY anhydrous alcohol solution and 6×10^{-5}g/L of PH anhydrous alcohol solution to mix together to get the mixture solution.

3.2 Unique Constituent Spectra

The slit width of LS55 Fluorescence Spectrometer was set to 5 nm, with 1000 nm/min of scanning speed, and emission wavelength ranged from 300 to

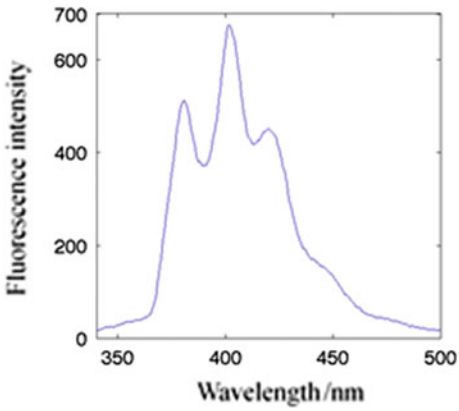

Fig. 1 Emission spectra of 2×10^{-5}g/L of AN in alcohol solution with excitation wavelength of 260 nm

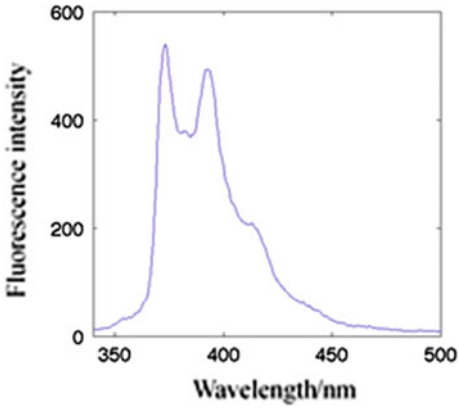

Fig. 2 Emission spectra of 4×10^{-6}g/L of PY in alcohol solution with excitation wavelength of 260 nm

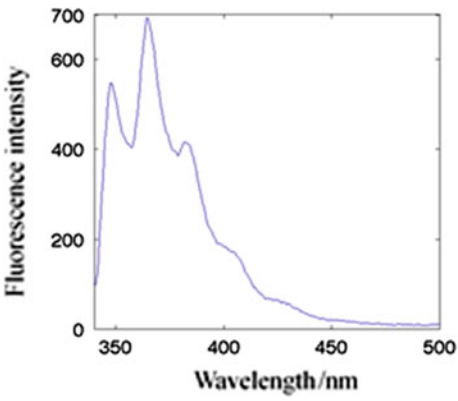

Fig. 3 Emission spectra of 6×10^{-5}g/L of PH in alcohol solution with excitation wavelength of 260 nm

500 nm. When excitation wavelength was 260 nm, the spectra of unique constituent of above AN, PY and PH solutions were as shown in Figs. 1, 2 and 3, respectively. From these spectra, we can know the position and shape of their characteristic peaks.

With experiments, the main fluorescence areas and corresponding excitation wavelength were determined. The main characteristic spectra of AN were located in $\lambda_{ex}/\lambda_{em}$ = 250/380 nm, 250/402 nm and 250/424 nm, and the strongest peak was around $\lambda_{ex}/\lambda_{em}$ = 250/402 nm. The main characteristic spectra of PY were located in $\lambda_{ex}/\lambda_{em}$ = 240/372 nm and 240/392 nm, and the strongest peak was around $\lambda_{ex}/\lambda_{em}$ = 240/372 nm. The main characteristic spectra of PH were located in $\lambda_{ex}/\lambda_{em}$ = 250/346 nm, 250/364 nm and 250/380 nm, and the strongest peak was around $\lambda_{ex}/\lambda_{em}$ = 250/346 nm.

3.3 *Mixed Three Constituents Spectra*

Mixture of AN, PY and PH solutions was taken as sample to be tested in three-dimensional fluorescence spectra mode. The slit width and scanning speed were kept the same, and start excitation wavelength was set to 260 nm, while emission wavelength ranged from 300 to 500 nm. The number of scans was 13 with excitation increment as 5 nm. The three-dimensional spectra of mixed solution of AN, PY and PH was shown as in Fig. 4.

As we can see from Fig. 4, the spectra of single constituent of AN, PY and PH in the mixture solution overlapped each other and hard to distinguish. Thus, PARAFAC algorithm was used to separate them out.

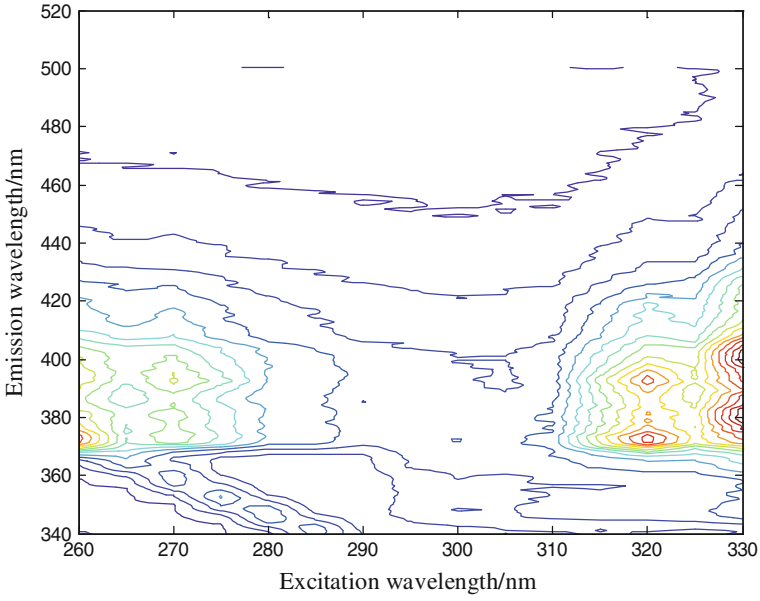

Fig. 4 Three-dimensional fluorescence spectra of AN, PY and PH mixture

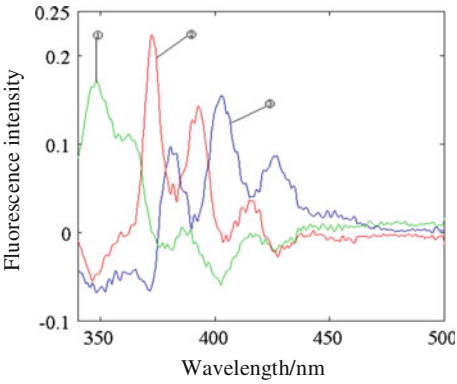

Fig. 5 Decomposition spectra of AN, PY and PH mixture with PARAFAC

4 Results and Discussion

PARAFAC was adopted to separate the three constituents from the three-dimensional spectra of the mixture solution. Three load matrices A, B and C were derived from solving Eq. (3), where matrix B was the emission spectra. Here, we plotted B on two dimension, then Fig. 5 was gained.

As Fig. 5 shows, we could easily find three kinds of spectral curves, which were named ①, ② and ③ in turn. Compared with the unique spectra curve of AN, PY and PH, which were shown in Figs. 1, 2 and 3, we observed that the characteristic spectra of the three curves corresponded to that of AN, PY and PH. It was obvious that curves ①, ② and ③ represented PH, PY and AN, respectively. It was proved that PARAFAC can separate different constituents from mixture spectra of PAHs effectively.

5 Conclusions

The PARAFAC model was adopted to analyze the three-dimensional fluorescence spectra of anthracene, pyrene and phenanthrene mixture in anhydrous alcohol solution in this pater. This method can realize mathematical separation instead of chemical separation, making the recognition and measurement in the mixed solution of different constituents accomplish at the same time. The experimental results showed that the three-dimensional spectra of mixed solution of anthracene, pyrene and phenanthrene was entirely separated using PARAFAC algorithm, which proved feasibility and validity for this method to achieve discrimination of overlapping spectra of PAHs mixture.

Acknowledgments This research was performed with financial support from Tianjin Science and Technology Development Fund of Higher School (20140621) and Tianjin Natural Science Foundation (14JCYBJC30400).

References

1. Haritash AK, KAUSHIK CP (2009) Biodegradation aspects of polycyclic aromatic hydrocarbons (PAHs): a review. J Hazard Mater 169:1–15
2. Lieberman SH, Apitz SE et al (1992) Subsurface screening of petroleum hydrocarbons in soil via laser induced fluorometry over optical fibers with a cone penetrometer system. Proc. SPIE 1716:392–402
3. Alarie JP, Watts W et al (1995) Field screening of polycyclic hydrocarbons contamination in soil using a portable synchronous scanning spectrofluorometer. Proc SPIE Int Soc Opt Eng 2504:512–519
4. Marowsky G, Lewitzka F, Karlitschek P, Buenting U, Niederkrueger M (1998) Miniaturized laser-induced fluorescence system with a fiber optic probe for the analysis of aromatic compounds. In: Proc. SPIE 3539, chemical microsensors and applications, p 2
5. Baumann T, Haaszio S, Niessner R (2000) Applications of a laser-induced fluorescence spectroscopy sensor in aquatic systems. Water Res 34(4):1318–1326
6. Boas G (2004) Laser-induced fluorescence checks soil clean up. Biophotonics Int. 11 (5):16–17
7. Lee CK, Ko EJ, Kim KW et al (2004) Partial least square regression method for the detection of polycyclic aromatic hydrocarbons in the soil environment using laser-induced fluorescence spectroscopy. Water Air Soil Pollut 158(1):261–275
8. Ko EJ, Kim YW, Wachsmuth U (2004) Remediation process monitoring of PAH-contaminated soils using laser-induced fluorescence. Environ Monit Assess 92 (2):179–191
9. Kuo DTF, Adams RG, Rudnick SM et al (2007) Investigating desorption of native pyrene from sediment on minute- to month-timescales by time-gated fluorescence spectroscopy. Environ Sci Technol 41(22):7752–7758
10. Valero NA, Fernandez SJF, Medina CAL et al (2007) A rapid, sensitive screening test for polycyclic aromatic hydrocarbons applied to Antarctic water. Chemosphere 67(5a):903–910
11. Kotzick R, Niessner R (1996) Application of time-resolved, laser-induced and fiber-optically guided fluorescence for monitoring of a PAH-contaminated remediation site. Fresenius J Anal Chem 354(1):72–76
12. Ko EJ, Kwak J, Kim JY et al (2011) Application of laser based spectroscopic monitoring into soil remediation process of PAH-contaminated soil. Geosyst Eng 14(1):15–22
13. Ko EJ, Kim YW, Park K et al (2010) Spectroscopic interpretation of PAH-spectra in minerals and its possible application to soil monitoring. Sensors 10:3868–3881
14. Goicoechea HC, Yu S, Moore AF et al (2012) Four-way modeling of 4.2 K time-resolved excitation emission fluorescence data for the quantitation of polycyclic aromatic hydrocarbons in soil samples. Talanta 101(15):330–336
15. Okparanma RN, Mouazen AM, Determination of total petroleum hydrocarbon (TPH) and polycyclic aromatic hydrocarbon (PAH) in soils: a review of spectroscopic and nonspectroscopic techniques. Appl Spectrosc. Rev 48(6):458−486
16. Yang X, Yang, S, B., Zhang Y., et al (2008) Identification of polycyclic aromatic hydrocarbons (PAHs) in soil by constant energy synchronous fluorescence detection. Spectrochim Acta Part A: Mol Biomol Spectrosc 69:400–406

Part X
Image and Video Processing

Signal Sensing with Sub-Nyquist Cyclic Feature

Sese Wang, Zhuo Sun, Weichen Zhao, Xuantong Chen and Haiwen Luo

Abstract Compressive sensing can be applied to reconstruct the signal with far fewer measurements than what is usually considered necessary. While in many scenarios, such as spectrum detection and modulation recognition, we only expect to acquire useful characteristics rather than the original signals. In this paper, we propose an effective method of digital communication signal detection based on the sub-Nyquist cyclic feature without the introduction of the reconstruction algorithm. By analyzing the difference between matrixes of cyclic autocorrelation for the two sceneries, it can be determined whether there exists signal or not. The simulation results show that the method performs well even at a low signal-to-noise ratio such as −10 dB, and complexity of both time and space is lowered considerably.

1 Introduction

Along with development of wireless communication, the lack of spectrum resources becomes increasingly prominent. Cognitive radio (CR) is raised for this issue, which allocates spectrum dynamically [1], and is widely applied in wireless communication systems on account of its spectrum sensing over wide band. As a premise for

S. Wang (✉) · Z. Sun · W. Zhao · X. Chen
Key Laboratory of Universal Wireless Communications,
Beijing University of Posts and Telecommunications, Beijing, China
e-mail: buptyt@bupt.edu.cn

Z. Sun
e-mail: zhuosun@bupt.edu.cn

W. Zhao
e-mail: goodwatermelon@126.com

X. Chen
e-mail: chxt@bupt.edu.cn

H. Luo
China United Telecommunications Co. Ltd, Beijing, China
e-mail: Luohw1@chinaunicom.cn

Q. Liang et al. (eds.), *Proceedings of the 2015 International Conference on Communications, Signal Processing, and Systems*, Lecture Notes in Electrical Engineering 386, DOI 10.1007/978-3-662-49831-6_68

spectrum allocation, signal detection is a vital task in this intelligent radio technology. However, considering Nyquist sampling theory, signal detection becomes difficult when it comes to wide spectrum.

Compressive Sensing (CS) theory can capture signal information at a rate significantly below the Nyquist sampling rate, which owes to the sparsity of the original signal in some transformation basis [2]. The introduction of this innovative theory has successfully settled the bottleneck problem of CR, which breaks down the power and scale of storage distinctly. Researchers usually reconstruct the original signal or features of the signal using compressive samples for further use [3], such as spectrum detection, modulation recognition, or others [4, 5]. While in some scenarios, compressive samples have already contain enough information, and it means that the reconstruction is not necessary.

Bing Liu has put forward a new method for signal detection, using numerical characteristics of compressive samples, without introduction of reconstruction algorithms [6]. Binwu Li also proposed a likelihood-based method based on compressive measurements [7]. Inspired by both of the researches, we focus on the physical layer process of CR, analyze the characteristics of the obtained samples and propose another effective method for the purpose of communication signal detection, without reconstruction, which has better performance than the previous ones. We apply the nature of partial Hadamard sampling matrix, and choose the cyclic autocorrelation matrix of compressive samples as sub-Nyquist detection features, for it performs quite differently when there exists signal or not. According to the simulations, the method can work efficiently with just few samples.

The following part of this paper is organized as follows: In Sect. 2, we introduce the system model applied in our method. In Sect. 3, we propose our new method for signal detection in detail. In Sect. 4, numerical results and correlated analysis are present. In Sect. 5, we draw conclusions for this method.

2 System Model

Consider a stream of communication signals, which are divided into K groups with N symbols in each group according to the received order. Then every group of data through channel can be described as (1)

$$\mathbf{y}_k = \mathbf{s}_k + \eta_k, k = 1, 2, \ldots, K. \tag{1}$$

where $\mathbf{s}_k$ and $\mathbf{y}_k$ respectively represent the kth group of transmitted signal and received signal, and η_k represents the noise introduced into the kth channel. In our analysis, we assume the noise to be additive white Gaussian noise (AWGN), and the modulation mode of signal is one of the multiple amplitude shift keying (MASK), multiple phase shift keying (MPSK), and multiple quadrature amplitude modulation (MQAM).

According to the theory of CS, we get compressive measurements $\mathbf{z}_k$ of every received group $\mathbf{y}_k$:

$$\mathbf{z}_k = \mathbf{A}\mathbf{y}_k \tag{2}$$

where $\mathbf{A}$ acts as the subsampling matrix, with scale of $M \times N$. In our method, we choose partial Hadamard matrix as compressive sampling matrix, which has been proved to comply with the restricted isometry property (RIP) [6].

3 Signal Detection with the Sub-Nyquist Cyclic Feature

In our method, we intend to apply the cyclic autocorrelation matrix of subsamples to fulfill signal detection. Therefore, for this part, we firstly introduce the calculation process of this sub-Nyquist cyclic feature, and then show the difference presentation between scenarios when there exists signal or not. BPSK is taken as example throughout the paper.

3.1 Nature of Partial Hardmard Matrix

For further analysis, we present nature of partial Hardmard matrix first, and give the reason why we choose it rather than Gaussian matrix.

Similar as Gaussian matrix, Hardmard matrix is an orthogonal matrix, meaning the inner product of any two rows of the matrix is zero. Hardmard matrix corresponds to a set of Walsh functions, and Walsh functions are periodical functions, with mean value zero, except the first one.

The composition of diagonal elements of the autocorrelation matrix of BPSK is also a periodical function with mean value zero, which we call diagonal function below. Then there exist three conditions:

1. For the Walsh function corresponded to the fist row of partial Hardmard matrix, inner product of this function and the diagonal function is zero, for it equals to integration of the diagonal function.
2. For the Walsh function not corresponded to the fist row of partial Hardmard matrix, if its cycle period is different than that of diagonal function, the inner product of these two functions is zero.
3. For the Walsh function not corresponded to the fist row of partial Hardmard matrix, if its cycle period is the same as that of diagonal function, the inner product of these two functions is also a periodical function, however the integration of it is not specific.

This nature of partial Hardmard matrix is vital in our method, which Gaussian matrix does not possess. Therefore, we apply the former one as our measurement matrix.

3.2 Sub-Nyquist Cyclic Feature

We first calculate the autocorrelation matrix of the compressive samples, and then get the cyclic autocorrelation matrix through transformation of it.

According to definition, we can represent the autocorrelation of subsamples as $r_z(n, v) = E\{z(n)z^*(n+v)\}$, where n, v respectively represent time and time delay. The autocorrelation matrix can be calculated by (5):

$$\mathbf{R}_z = E\{\mathbf{z}_k \mathbf{z}_k{}^H\} = \frac{1}{K}\sum_{k=1}^{K} \mathbf{z}_k \mathbf{z}_k{}^H \tag{3}$$

where $(\bullet)^H$ represents conjugate transpose.

For further calculation, we rearrange $\mathbf{R}_z$ as (6):

$$R = \begin{bmatrix} r_z(0,0) & r_z(0,1) & \cdots & r_z(0,M-1) \\ r_z(1,0) & r_z(1,1) & \cdots & 0 \\ \vdots & \vdots & & \vdots \\ r_z(M-1,0) & 0 & \cdots & 0 \end{bmatrix} \tag{4}$$

Referring to [4], the cyclic autocorrelation function of subsamples can be represented as (7):

$$r_z{}^{(c)}(a, v) = \{\frac{1}{N}\sum_{n=0}^{N-1-v} r_z(n, v) e^{-j\frac{2\pi}{N}an}\} e^{-j\frac{\pi}{N}av} \tag{5}$$

where $a \in [0, N-1]$ is the digital cyclic frequency. Then we can see, the cyclic autocorrelation matrix $\mathbf{R}_c$ is related to $\mathbf{R}$ through Fourier transformation:

$$\mathbf{R}_c = \mathbf{F}\mathbf{R} \tag{6}$$

$\mathbf{F} = [e^{-j2\pi ab/N}]_{(a,b)}$ represents the M-point FFT matrix.

3.3 Sub-Nyquist Cyclic Feature of AWGN and Signals

3.3.1 Cyclic Autocorrelation Matrix of AWGN

According to (6), the autocorrelation matrix $\mathbf{R_n}$ of AWGN is shown as Fig. 1a after calculation, which is a diagonal matrix.

When $\mathbf{s}_k = \mathbf{0}$, it can be obtained that $\mathbf{z}_k = \mathbf{A}\mathbf{y}_k = \mathbf{A}\eta_k, k = 1, 2, ..., K$, and then we obtain:

$$\mathbf{R}_z = E\{\mathbf{z}_k \mathbf{z}_k{}^H\} = E\{\mathbf{A}\eta_k \eta_k{}^H \mathbf{A}^H\} = \mathbf{A}E\{\eta_k \eta_k{}^H\}\mathbf{A}^H = \mathbf{A}\mathbf{R_n}\mathbf{A}^H \tag{7}$$

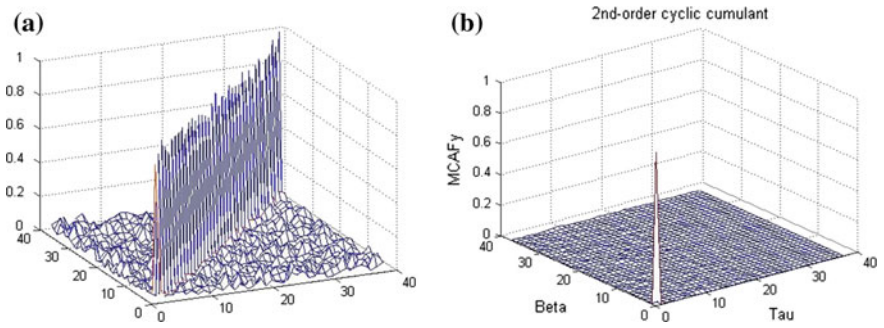

Fig. 1 The autocorrelation matrix and cyclic autocorrelation matrix of subsamples of AWGN. **a** Autocorrelation matrix. **b** Cyclic autocorrelation

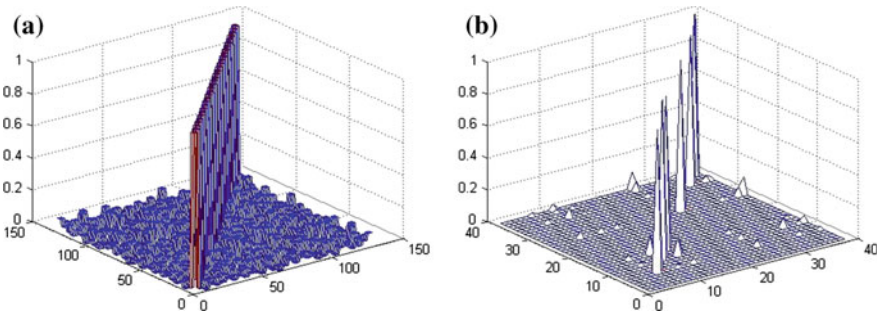

Fig. 2 The autocorrelation matrix of BPSK and subsamples of BPSK. **a** Autocorrelation matrix of BPSK. **b** Autocorrelation matrix of subsamples of BPSK

Since $\mathbf{R_n}$ is a diagonal matrix, it can be concluded that $\mathbf{R}_z = \mathbf{A}\mathbf{R_n}\mathbf{A}^H$ is also a diagonal matrix based on nature of it. After rearrangement and fourier transformation, the form of cyclic autocorrelation matrix of subsamples for AWGN is shown as Fig. 1b, with value only at $(Tau, Beta) = (0, 0)$.

3.3.2 Cyclic Autocorrelation Matrix of the Signal

We firstly analyze ideal situations, which means $\eta_k = 0$.

Based on Eq. (3), Fig. 2a shows the form of autocorrelation matrix of original signals, without noise. The parameters are set as follows: symbol rate $f_0 = 8000$ Baud, observation time $T = 0.002$ s, carrier frequency $f_c = 16000$ Hz, sampling rate $f_s = 32000$ Hz.

Since $\eta_k = 0$, it can be inferred that $\mathbf{z}_k = \mathbf{A}\mathbf{y}_k = \mathbf{A}\mathbf{s}_k, k = 1, 2, ...K$, and $\mathbf{R}_z$ can be calculated by (10):

$$\mathbf{R}_z = E\{\mathbf{z}_k {\mathbf{z}_k}^H\} = E\{\mathbf{A}\mathbf{s}_k {\mathbf{s}_k}^H \mathbf{A}^H\} = \mathbf{A}E\{\mathbf{s}_k {\mathbf{s}_k}^H\}\mathbf{A}^H = \mathbf{A}\mathbf{R_s}\mathbf{A}^H \tag{8}$$

where $\mathbf{R_s}$ is the autocorrelation matrix of BPSK. We take a_i and b_j as the ith row of subsampling matrix $\mathbf{A}$ and the jth column of autocorrelation matrix $\mathbf{R_s}$, where $i = 1, 2, ..., M$ and $j = 1, 2, ..., M$. Therefore, we have derivations as follows:

- when $a_i(\sum_{j=1}^{N} b_j) \neq 0$

$$\begin{aligned} &Rz(i,k) = \sum_{j=1}^{N} a_i b_j a_k{}^T(j) = a_i(\sum_{j=1}^{N} b_j) a_k{}^T = (a_i. * a_k)(\sum_{j=1}^{N} b_j) \\ &i = 1, 2, \ldots, M \\ &j = 1, 2, \ldots, N \end{aligned} \tag{9}$$

  $a_i. * a_k$ means dot product of the two vectors. According to the orthogonality nature of measurement matrix, $a_i. * a_k = 0$ when $i \neq k$, meaning $Rz(i,k) = 0$. Therefore, elements out of the diagonal are all zero. When $i = k$, $a_i. * a_k$ is a vector full of 1, meaning diagonal elements are 1, in this condition.

- when $a_i(\sum_{j=1}^{N} b_j) = 0$

$$Rz(i,k) = 0 \tag{10}$$

  In this condition, all elements are 0, including diagonal elements.

From analysis above, we can draw conclusion that diagonal elements are 1 or 0, and non-diagonal elements are all zero in theory. When the subsampling matrix is Hadamard matrix, most of diagonal elements are zero based on the nature of it. Therefore, the autocorrelation matrix of compressive samples is presented as Fig. 2b.

However, considering actual situations, signal is always accompanied with noises, meaning $\eta_k \neq 0$. Therefore, on the basis of summative nature of cumulants, autocorrelation of subsamples in actual situations is the addition of the two mentioned above, as shown in Fig. 3a.

The cyclic autocorrelation matrix of compressive measurements is presented as Fig. 3b after calculation.

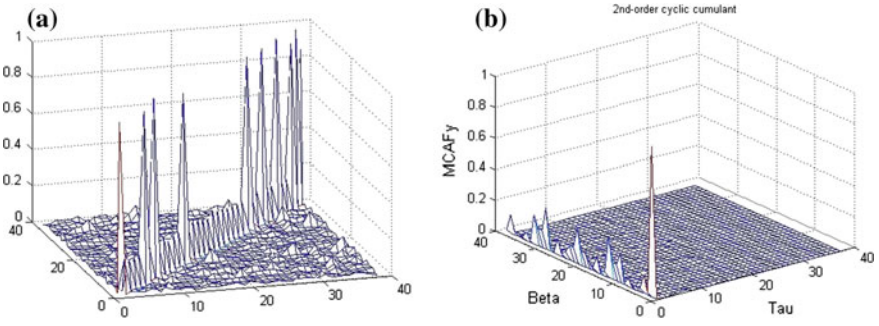

Fig. 3 Autocorrelation and cyclic autocorrelation of subsamples in actual situations. **a** Autocorrelation. **b** Cyclic autocorrelation

3.4 Signal Detection by Sub-Nyquist Cyclic Feature

Through comparison of Figs. 1b and 3b, the following conclusion can be drawn:

When there is no signal, cyclic autocorrelation of subsamples has the only value at $(0, 0)$. As a contract, when there exist signals, nearly all values exist when $Tau = 0$. We can distinguish the two situations by this evident difference.

In our method, we first calculate the average value when $Tau = 0$, except value at coordinate $(0, 0)$, and then compare it with the average value when $Tau \neq 0$, if the former one is significantly larger than the latter one, we can conclude there exist signals. For comparison, a threshold value is needed, and in our paper, we set it as twice the average value when $Tau \neq 0$.

4 Numerical Results and Analysis

In this section, we show simulation results of our method and analyze factors that influence the performance. Parameters are chosen as follows:

Symbol rate $f_0 = 8000$ bits/s, Carrier frequency $f_c = 16000$ Hz, Statistical time $K = 50$, Sampling rate $f_s = 32000$ bits/s, which is the Nyquist sampling rate.

The performance is closely related with signal-to-noise ratio (SNR). Compressive ratio actually represents number of subsamples, which has similar function with statistical time. Considering these, we carry out simulations with SNR and compressive ratio ranging among certain scopes.

Figure 4 shows performance with SNR ranging from -15dB to $\sim$ 0dB, and performance of the method by Bing Liu is taken as a comparison. It can be seen that the performance of our method is superior to the original one significantly. The probability of correct detection can reach nearly 100 % as long as SNR is higher than -10 dB.

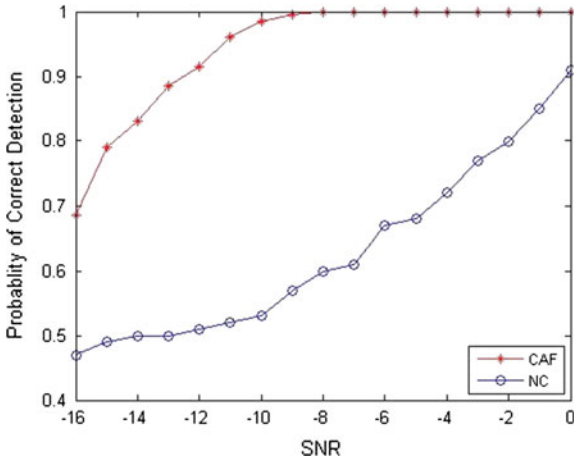

Fig. 4 Performance of the two methods at different SNRs

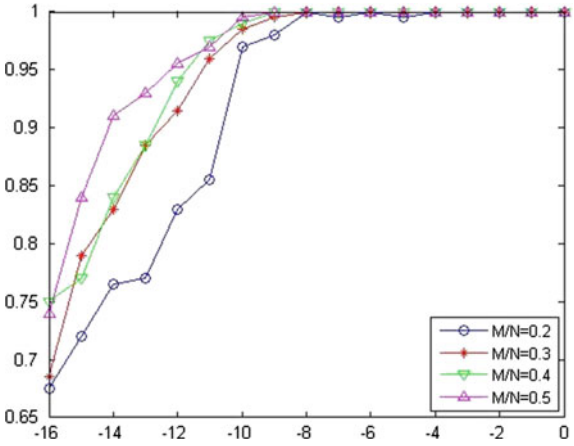

Fig. 5 Correct detection probability at different compressive ratios

Figure 5 shows the probability of correct detection at different compressive ratios. The larger the compressive ratio is, the higher probability of correct detection tends to be. However, the difference is not obvious. Therefore, we can carry out our method at a relatively low compressive ratio. In fact, the influence of statistic time is also not obvious when ranging in a small scale. Therefore, the scale of subsamples we need for our method can be relatively low.

5 Conclusions

In this paper, we proposed a method for signal detection using cyclic autocorrelation of subsamples, which successfully avoided reconstructing original signals or features. The method actually presents nature of subsampling matrix, and when we choose partial Hadamard matrix, the feature can be quite different. The most significant advantage of our method is that we can reach perfect detection effect with only few symbols, even at a low SNR such as -10 dB. Considering the simplicity and effectiveness of the method, it has much practical value, and for further work, we tend to carry out more research on compressive samples without reconstruction.

Acknowledgments This work was supported by The China National Natural Science Fund under grant 61271181 and 61171109, and the joint project with China Southwest Institute of Electronic and Telecommunication Technology.

References

1. Ganesan G, Ye L (2007) Cooperative spectrum sensing in cognitive radio, Part II: multiuser networks. IEEE Trans Wireless Commun 6(6):2214–2222
2. Cands EJ (2006) Compressive sampling. Marta Sanz Sol 25(2):1433–1452
3. Cohen D, Rebeiz E, Eldar YC, et al (2013) Cyclic spectrum reconstruction and cyclostationary detection from sub-Nyquist samples. In: IEEE 14th Workshop on Signal Processing Advances in Wireless Communications (SPAWC). IEEE, pp 425–429
4. Tian Z, Tafesse Y (2012) Cyclic feature detection with sub-nyquist sampling for wideband spectrum sensing. IEEE J Sel Top Sign Proces 6(1):58–69
5. Tian Z (2011) Cyclic feature based wideband spectrum sensing using compressive sampling. In: Communications (ICC)
6. Liu B, Fu P (2011) Compressive signal detection based on digital characteristics. Chin J Sci Instrum 32(3):577–582
7. Li BW, Li YG (2013) Radom signal detection and analysis based on the maximum likelihood criterion. J Sig Process 29(8):996–1002

A Novel Image Encryption Algorithm Based on Multiple Chaotic Systems and Self-adaptive Model

Chengqi Wang, Xiao Zhang and Zhiming Zheng

Abstract In recent years, image encryption has attracted much attention. Particularly, due to large data capacity and high correlation among pixels, chaos-based image encryption algorithms are more suitable to be applied in the digital image encryption. In this paper, we propose a novel chaotic image encryption algorithm, in which novel multiple chaotic systems and efficient self-adaptive model are initially mingled to enhance the security. Different from conventional algorithms, plaintext participates in the generation of cryptograph in a new way, which follows the idea from the perceptron model. The proposed algorithm enlarges the key space, enhances the randomness of the algorithm, and resists the differential attack effectively. Simulation results are demonstrated that proposed algorithm possesses the high security for the main current attacks, which is an excellent candidate for practical applications of image encryption.

Keywords Image encryption · Multiple chaotic systems · Self-adaptive model · Perceptron model

1 Introduction

Recently, chaos plays an important role in the field of image encryption, which is considered analogous to the confusion and diffusion process in the cryptosystem specified by Shannon [1, 2]. It possesses many pretty properties, such as the sensitivity to initial conditions and system parameters, non-periodicity, pseudo-randomness, and topological transitivity [3, 4]. In 1998, Fridrich applied the chaos to the image encryption algorithms for the first time [5]. Since then, there are three

C. Wang · X. Zhang (✉) · Z. Zheng
Key Laboratory of Mathematics, Informatics and Behavioral Semantics, Ministry of Education, and School of Mathematics and Systems Science, Beihang University, Beijing 100191, China
e-mail: xiao.zh@buaa.edu.cn

Q. Liang et al. (eds.), *Proceedings of the 2015 International Conference on Communications, Signal Processing, and Systems*, Lecture Notes in Electrical Engineering 386, DOI 10.1007/978-3-662-49831-6_69

different kinds of typical usages in the chaotic encryption algorithms design: (1) creating position permutation relations; (2) generating pseudorandom bit sequence (PRBS); (3) producing cryptograph directly with initial parameters of cryptosystem [6, 7]. Over the last few years, many image encryption algorithms based on chaotic maps have been presented [8–10].

Meanwhile, the cryptanalysis of chaotic image encryption algorithm is developing rapidly. According to the proposed paper, study about chosen and known plaintext attacks becomes the mainstream in the field of chaotic image encryption algorithm's cryptanalysis. Due to lack of the resistibility for these attacks, most algorithms which can resist the statistical analysis are vulnerable with some pairs of known plaintext and cryptograph obtained [11, 12].

To meet these challenges, we propose a novel chaotic image encryption algorithm to resist the differential attack effectively. Also, it is necessary to propose novel multiple chaotic systems and an efficient self-adaptive model, and design a new threshold function based on the perceptron model. The remaining of the paper is organized as follows. Section 2 describes the algorithm in detail. And Sect. 3 provides the security and efficiency analysis of our algorithm. The last section gives the conclusion.

2 The Proposed Algorithm

In this paper, for original image of size M × N, algorithm is divided into initialization, permutation, and diffusion. The proposed algorithm is described as follows:

2.1 Initialization

Before the permutation, obtain the initial value of the perceptron model. The details are described as follows:

Step 1: Let Chen's high-dimension hyper-chaotic system (1) iterate 3001 times.

$$\begin{cases} \dot{X} = a(Y - X) \\ \dot{Y} = -XZ + dX + cY - V \\ \dot{Z} = XY - bZ \\ \dot{V} = X + k \end{cases} \tag{1}$$

Step 2: Due to the transient effect, round the results of previous 3000 times and take the 3001th value as the initial value (X, Y, Z, V) of the perceptron model.

2.2 Permutation

In this section, permutation is applied to shuffle the image pixels with the self-adaptive model, which depends on the pseudorandom sequence generated by the tent map to reduce the pixel correlation. The details are described as follows:

Step 1: Acquire the sum of M × N pixels' value by calculating the Eq. (2),

$$D = \sum_{i=1}^{L} p_i \tag{2}$$

Step 2: Obtain the average of the pixels' values by calculating the Eq. (3),

$$average = \frac{D}{L}, \tag{3}$$

and obtain the fractional part of the average by calculating the Eq. (4),

$$E = average - \lfloor average \rfloor \tag{4}$$

Step 3: Let the tent map (5) iterates L times with the initial value E to acquire a real number sequence $\{e_i\}_{i=1}^{L}$.

$$x_{i+1} = \begin{cases} x_i/\alpha, & 0 \le x_i \le \alpha, \\ (1-x_i)/(1-\alpha), & \alpha \le x_i \le 1, \end{cases} \tag{5}$$

Step 4: Permute the real number sequence $\{e_i\}_{i=1}^{L}$ to obtain the permutation subscript sequence $\{y_i\}_{i=1}^{L}$, which is derived by $\{e_i\}_{i=1}^{L}$ with its sorted version, where e_{y_i} is the ith smallest number in the sequence $\{e_i\}_{i=1}^{L}$.

Step 5: Set $p_i^* = p_{y_i}$ to acquire the permutated sequence $\{p_i^*\}_{i=1}^{L}$.

2.3 Diffusion

In the stage of diffusion, perceptron model is employed to make the cipher-image dependent on the pixel values of permuted plain-image and the intermediate values in order to resist the differential attacks. The details are described as follows:

Step 1: Set the initial value B and let the piecewise linear map (6) iterates L times with the initial value B to acquire a real number sequence $\{B_i\}_{i=1}^{L}$.

$$x_{i+1} = \begin{cases} x_i/\beta, & 0 \le x_i \le \beta, \\ (x_i - \beta)/(0.5 - \beta), & \beta \le x_i \le 0.5, \\ (1 - x_i - \beta)/(0.5 - \beta), & 0.5 \le x_i \le 1 - \beta, \\ (1 - x_i)/\beta, & 1 - \beta \le x_i \le 1, \end{cases} \tag{6}$$

Step 2: Obtain the intermediate value sequence $\{b_i^*\}_{i=1}^{L}$ by calculating the Eq. (7),

$$b_i^* = \mod(\lfloor (B_i - \lfloor B_i \rfloor) \rfloor \times 10^8, 256) \tag{7}$$

Step 3: Obtain the diffusion sequence $\{b_i\}_{i=1}^{L}$ by calculating the Eq. (8),

$$b_i = \mod(p_i^* + b_i^*, 256) \tag{8}$$

Step 4: Do 8 iterations to get (X_k, Y_k, Z_k, V_k), $k \in [1, 8]$.
Calculate the Eq. (9) to get the (x_k, y_k, z_k, v_k), $k \in [1, 8]$:

$$t = \mod((Abs(T) - \lfloor Abs(T) \rfloor) \times 10^{14}, 256) \tag{9}$$

Calculate the Eq. (10):

$$x_k = \mod(x_k, 4) \tag{10}$$

Get the (B_{1k}, B_{2k}, B_{3k}), $k \in [1, 8]$ by the nonlinear transformation (11):

$$\begin{cases} (B_{1k}, B_{2k}, B_{3k}) = (x_k, y_k, z_k), & x_k = 0 \\ (B_{1k}, B_{2k}, B_{3k}) = (x_k, y_k, v_k), & x_k = 1 \\ (B_{1k}, B_{2k}, B_{3k}) = (x_k, z_k, v_k), & x_k = 2 \\ (B_{1k}, B_{2k}, B_{3k}) = (y_k, z_k, v_k), & x_k = 3 \end{cases} \tag{11}$$

Step 5: Get the *KeyX(k)*, *KeyY(k)*, *KeyZ(k)*, $k \in [1, 8]$ by the nonlinear transformation (12) which are the parameters of each perceptron model's weight

$$\text{Key} = \begin{cases} 1, & B \ge 128 \\ 0, & B < 128 \end{cases} \tag{12}$$

Step 6: According to the nonlinear transformation (13), (14), and (15)

$$w_{1,k} = \begin{cases} 1, & \text{KeyX(k)} = 1 \\ -1, & \text{KeyX(k)} = 0 \end{cases} \tag{13}$$

$$w_{2,k} = \begin{cases} 1, & \text{KeyY(k)} = 1 \\ -1, & \text{KeyY(k)} = 0 \end{cases} \tag{14}$$

$$w_{3,k} = \begin{cases} -0.5, & \text{KeyZ(k)} = 1 \\ 0.5, & \text{KeyZ(k)} = 0 \end{cases} \tag{15}$$

The results $w_{1,k}$, $w_{2,k}$, $w_{3,k}$, are perceptron model's weights.
According to the nonlinear transformation (16), (17), (18), and (19):

$$w'_{1,k} = \begin{cases} 1, & \text{KeyX(k)} = 1 \\ 0, & \text{KeyX(k)} = -1 \end{cases} \tag{16}$$

$$w'_{2,k} = \begin{cases} 1, & \text{KeyY(k)} = 1 \\ 0, & \text{KeyY(k)} = -1 \end{cases} \tag{17}$$

$$w'_{3,k} = \begin{cases} 1, & \text{KeyZ(k)} = 0.5 \\ 0, & \text{KeyZ(k)} = -0.5 \end{cases} \tag{18}$$

$$\theta_k = w'_{1,k} \oplus w'_{2,k} \oplus w'_{3,k} \tag{19}$$

The results θ_k is utilized for threshold function of each perceptron model, $k \in [1, 8]$, which is used to enhance the randomness of the algorithm.

Step 7: Use the strategy of stream cipher to encrypt image. For every pixel b from the scrambled image, b_k ($k \in [1, 8]$) denotes the kth bit of pixel b. And the c_k ($k \in [1, 8]$) denotes the kth bit of pixel c in the cryptograph. Do the nonlinear transformation (20):

$$c_k = \begin{cases} f(w_{1,k} \times b_k + w_{2,k} \times w_{3,k} - \theta_k), & w_{1,k} = 1 \\ f(w_{1,k} \times b_k + w_{2,k} \times w_{3,k} + \theta_k), & w_{1,k} = -1 \end{cases} \tag{20}$$

where $f(x) = \begin{cases} 1, & x \geq 0 \\ 0, & x < 0 \end{cases}$..

The result c_k is the kth bit of pixel c in the cryptograph, $k \in [1, 8]$.

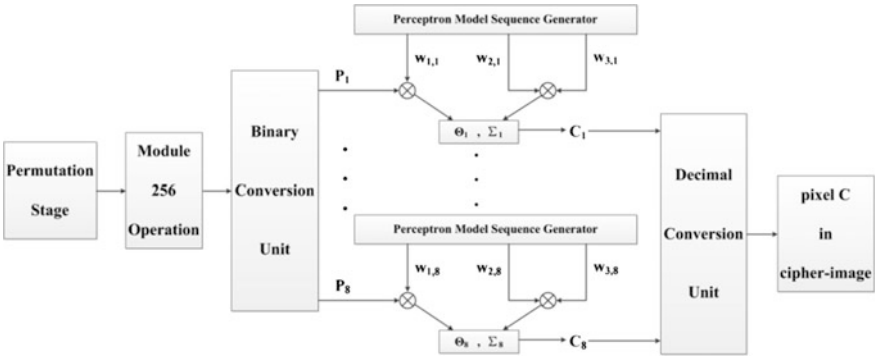

Fig. 1 The flowchart of the diffusion

Step 8: By parity of reasoning, repeat step 4–step 7, until the encryption is finished. Figure 1 shows the flowchart of the diffusion.

3 Security and Efficiency Analysis

Security and efficiency analysis usually includes key sensitivity analysis, histogram analysis, key space analysis, adjacent pixels correlation analysis, information entropy analysis, differential analysis, and speed performance analysis. From the details described in the Sect. 2, our algorithm obviously passes the key sensitivity analysis and histogram analysis. Thus, we focus more attention on the last five subsections.

3.1 Key Space Analysis

It is pointed out that the key space of image encryption algorithm should be larger than $2^{100} \approx 10^{30}$ to be capable of resisting the brute-force attack. The secret key $K = (\alpha, \beta, x_0, y_0, z_0, v_0)$ and the significant digits in each parameter are 15. Therefore, key space of the proposed algorithm is $\left(10^{15}\right)^6 = 10^{90} \approx 2^{300}$, which is much larger than the required size for an image encryption algorithm to forbid exhaustive search of the key space.

3.2 Adjacent Pixels Correlation Analysis

Figure 2 and Table 1 show the results of the adjacent pixels correlation analysis. In the Fig. 2(a), adjacent pixels are so correlated that original image can be deciphered using the statistical attack. Select 5000 pairs of pixel from plain-image and cipher-image randomly, and obtain the correlation of horizontal, vertical, and opposite angles direction. Table 1 shows the correlation of horizontal, vertical, and opposite angles direction before encryption and after encryption, respectively. The results indicate that the proposed chaotic image encryption algorithm makes almost no adjacent pixel correlation of cipher-plain, which increases the difficulty of deciphering by statistical analysis. Furthermore, proposed encryption algorithm has a nice ability of diffusion and confusion to resist the correlation attack.

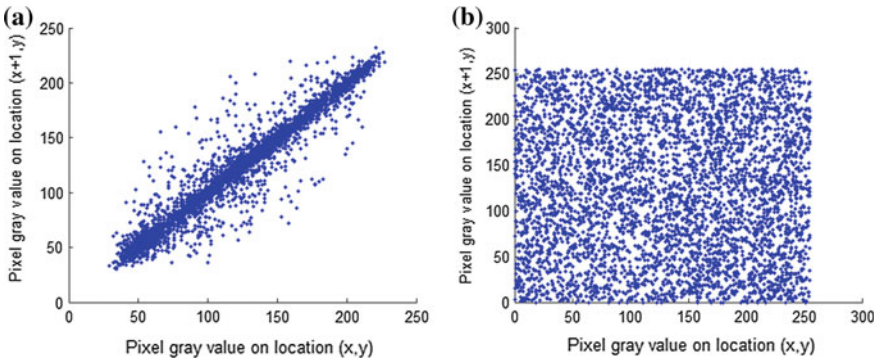

Fig. 2 The adjacent pixels correlation analysis: **a** before encryption, **b** after encryption

Table 1 The correlation of the adjacent pixel before and after encryption

Direction	Plain-image	Cipher-image
Horizontal	0.937084	−0.001959
Vertical	0.969142	−0.006196
Opposite angles	0.912509	−0.001665

Table 2 The results of the information entropy analysis

Category	Value
Expected value	8.00000
Plain-image	7.42662
The proposed algorithm	7.99765
Ref. [13]	7.99691
Ref. [14]	7.99685

3.3 Information Entropy Analysis

Information entropy is regarded as the most important feature of randomness, and the most commonly used information entropy, which is considered to be the crucial feature of randomness. As shown in the Table 2, the information entropy of the proposed algorithm is higher than two other algorithms. The information entropy of the proposed algorithm is 7.99748, which is very close to the ideal theoretical value 8 and makes the statistical attack infeasible.

3.4 Differential Analysis

Attackers usually make a slight change of the plain-image, and observe how differences of the inputs affect the corresponding outputs, which is named differential analysis. To test the influence of one pixel value change in the plain-image

Table 3 The results of the differential analysis

Category	NPCR (%)	UACI (%)
Expected value	99.6094	33.4635
The proposed algorithm	99.6069	33.4497
Ref. [13]	99.6170	33.4933
Ref. [15]	99.6063	33.4843

Table 4 The results of the speed performance analysis

Method	System feature	Time cost (ns)
The proposed algorithm	Multiple chaotic systems	387
Ref. [13]	Game of Life permutation and PWLCM	2837
Ref. [15]	Cellular Automata	1184

encrypted by the proposed algorithm, two common measures are used: NPCR and UACI to give a quantitative description [15]. With the gray-scale pixel values, the ideal NPCR and UACI are 99.6094 % and 33.4635 %, respectively. As shown in the Table 3, the NPCR and UACI of the proposed algorithm are better than two other algorithms. The NPCR and UACI of the proposed algorithm are 99.6069 % and 33.4497 %, which are very close to the expected NPCR and UACI, respectively. The results are demonstrated that the proposed algorithm resists the differential analysis effectively.

3.5 Speed Performance Analysis

As shown in the Table 4, the speed performance of the proposed algorithm without the optimization is faster than two other algorithms for comparison. The result means the proposed algorithm is performed in a fast manner, which satisfies the requiring speed.

4 Conclusion

In the present paper, we propose a novel chaotic image encryption algorithm, in which novel multiple chaotic systems and an efficient self-adaptive model are initially mingled to enhance the security. Different from conventional algorithm, plaintext participates in the generation of cryptograph in a new way, which follows the idea from the perceptron model. Furthermore, a minor change in the plain-image affects all the cryptographic operations and generates a completely different cipher-image, even though the same secret key is adopted in the algorithm.

From the results based on the experiments, proposed algorithm resists the statistical analysis. Benefited from the multiple chaotic systems, proposed algorithm also has a good dynamic characteristic and a larger key space, namely 2^{232}. In addition, proposed algorithm resists the differential attack effectively. Consequently, it is concluded that proposed algorithm is an excellent candidate for practical applications of image encryption, which is practical possesses the high security for the main current attacks.

References

1. Shannon CE (1949) Communication theory of secrecy systems. Bell Syst Tech J 28 (4):656–715
2. Wang XY, Xu DH (2014) Image encryption using genetic operators and intertwining logistic map. Nonlinear Dyn 78(4):2975–2984
3. Zhang X, Li W, Zheng ZM, Guo BH (2012) Optimized statistical analysis of software trustworthiness attributes. Sci China Inf Sci 11:2508–2520
4. Pareek NK, Patidar V, Sud KK (2005) Cryptography using multiple one-dimensional chaotic maps. Commun. Nonlinear Sci. Numer. Simul 10(7):715–723
5. Fridrich J (1998) Symmetric ciphers based on two-dimensional chaotic maps. Int. J. Bifurcat. Chaos 8(6):1259–1284
6. Khanzadi H, Eshghi M, Borujeni SE (2014) Image encryption using random bit sequence based on chaotic maps. Arab. J. Sci. Eng. 39(2):1039–1047
7. Hussain I, Gondal M (2014) An extended image encryption using chaotic coupled map and S-box transformation. Nonlinear Dyn 76(2):1355–1363
8. Chen GR, Mao YB, Chui CK (2004) A symmetric image encryption scheme based on 3D chaotic cat maps. Chaos, Solitons Fractals 21(3):749–761
9. Wang XY, Guo K (2014) A new image alternate encryption algorithm based on chaotic map. Nonlinear Dyn 76(4):1943–1950
10. Yao W, Zhang X, Zheng ZM, Qiu WJ (2014) A colour image encryption algorithm using 4-pixel Feistel structure and multiple chaotic systems. Nonlinear Dyn 81:151–168
11. Liu YS, Tang J, Xie T (2014) Cryptanalyzing a RGB image encryption algorithm based on DNA encoding and chaos map. Opt Laser Technol 60:111–115
12. Zhang YQ, Wang XY (2014) Analysis and improvement of a chaos-based symmetric image encryption scheme using a bit-level permutation. Nonlinear Dyn 77(3):687–698
13. Wang XY, Jin CQ (2012) Image encryption using game of life permutation and PWLCM chaotic sys-tem. Opt Commun 285:412–417
14. Zhang LY, Hu XB, Liu YS, Wong KW, Gan J (2014) A chaotic image encryption scheme owning temp-value feedback. Commun. Nonlinear Sci. Numer. Simul 19(10):3653–3659
15. Ping P, Xu F, Wang ZJ (2014) Image encryption based on non-affine and balanced cellular automata. Signal Process. 105:419–429

Smoggy Environment Recognition by Combining Infrared and Visible Images

Lujia Wang, Ying Tong, Zeng Liu, Jin Chen, Meili Zhou, Hengxin Liu and Ji Zhang

Abstract Smoke recognition is one of the research directions in the field of digital image processing, but common algorithms are mostly based on the video sequence of images. A combination of infrared and visible images is presented in this paper, by extracting the analyte infrared image outer contour, and complete comparison of the extent of the visible outline of the image in the same area. Then according to the measured object within the outer contour of the two bands contain the number of pixels ratio, determine the impact of smoggy on the visible image. Experiments show that the algorithm needs to be analyzed only for the infrared and visible band single still image. You can draw judgment of smoggy environment, and it can provide the basis for a fire alarm.

Keywords Smoggy recognition · Infrared image · Visible image · Edge extraction

1 Introduction

The application and theoretical research of Heterogeneous Sensor Networks (HSN) has been one of the most important fields in signal processing [1–3]. Image recognition and visual detection technology is based on visible light in the past decade gained a rapid development, and a lot of results have been achieved [4–6]. Compared with other bands such as infrared imaging technology, visible light has a clear imaging, low cost and other advantages. However, in a smoky environment such as fire, infrared imaging is far superior to the visible one. Therefore, we need to study the image recognition method combining infrared and visible light. In

L. Wang · Y. Tong (✉) · Z. Liu · J. Chen · M. Zhou · H. Liu
College of Electronic & Communication Engineering,
Tianjin Normal University, Tianjin 300387, China
e-mail: tongying2334@163.com

J. Zhang
Tianjin No.4 High School, Tianjin 300000, China

Q. Liang et al. (eds.), *Proceedings of the 2015 International Conference on Communications, Signal Processing, and Systems*, Lecture Notes in Electrical Engineering 386, DOI 10.1007/978-3-662-49831-6_70

addition to the results of this study apply to fire outside environment, it can also be used in special circumstances imaging and recognition of the occasion to dust, fog and haze, the battlefield and other smoke-filled, with good usability.

2 Smoggy Recognition Algorithm Design

Visible image of smoggy environment, because smoke obscured the image by impeding reflecting light of the measured object, can cause image blur. Sometimes, it can not even get a complete outline of the phenomenon. Infrared radiation of the measured object, however, can penetrate smoke. So the contour information of the measured objects can be reflected more correctly in the infrared image almost without smoggy affected. Thus, according to the integrity of the differences between the two bands of the image outline with reference to infrared images after registration, the measured object can be judged by the general situation of the smoggy obscured.

The basic idea of the algorithm is first to use edge detection algorithm to extract the edge visible image; then extract the foreground image in the infrared image segmentation algorithms; furthermore, extract the edge for foreground images. The purpose of the infrared image segmentation is foreground object to be measured in order to extract from the background and is to eliminate background environmental interference. After the edge portion of the two images is extracted, infrared edge as a reference to measure the degree of completeness edge of the visible image. If they are close to full extent, it is considered less affected by smoggy visible images, visible light can be used as a reference system working band; on the contrary, it is considered smoggy visible images with cover, and then according to the extent of the visible edge of the defect, determine whether infrared band as a system reference.

Step algorithm on **Matlab** platform is as follows:

(1) The system for the collection of images using **sobel** operator edge extraction of infrared image information, and calculates the gradient magnitude and gradient direction of each pixel of an edge.
(2) The gradient amplitude is less than a certain threshold of pixels from the edge of the set of pixels removed, retaining only the gradient magnitude larger edge pixels to eliminate the interference noise pixels.
(3) For the edge pixel set, based on the similarity of the pixel gradient magnitude and gradient direction, the slight edge discontinuities linking, try to keep the edge intact.
(4) For the visible image made (1)–(3), the same process step.
(5) On the infrared image binarization, and it does fill handle, using **bwperim** operator outside contour extraction.
(6) In step (5) extracted contour region infrared image as a reference, at the edge of a collection of two images, the comparison of infrared and visible image edge edge completeness in the same area.

(7) Set a threshold **T** (currently set up an experiment in T = 50 %), total number of pixels the edge of the visible image and infrared image edge than if the total number of pixels is less than the threshold value, it is determined that the impact of smoggy visible image on the larger environment; on the contrary, It can be considered a visible image can be more complete presentation of the measured object shape information.

3 Smoggy Recognition Experiments and Results Analysis

To test the effectiveness of the algorithm, we simulated the environment of different concentrations of smoggy experiment in laboratory conditions. For the same analytes images collected by the effect of the infrared image as a reference after registration are shown in Fig. 1.

After extracting the edge pixels and edge connection process, the edge of the infrared image is shown in Fig. 2a, the visible edges of the image results are shown in Fig. 2b.

Extracted in the infrared image of the measured object outer profile is shown in Fig. 3a. While the visible edges of the same area shown in Fig. 3b.

Finally, within the statistical range of the measured object contour region (IR edge expanded operations, maintain two-pixel-wide outline), the number of pixels of the visible image edge is 121, while that of the infrared image edge is 317, both of ratio about 38.17 %. It can be determined that the environment of visible smoggy obscured the more serious, the reference band infrared system should be selected, in the development of image fusion rules, it should be considered by an

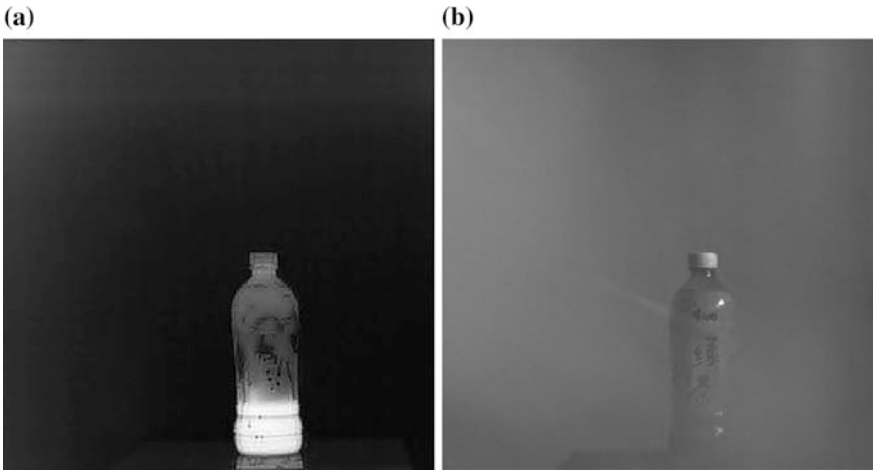

Fig. 1 Infrared and visible images in smoggy environment. **a** Infrared image. **b** Visible image

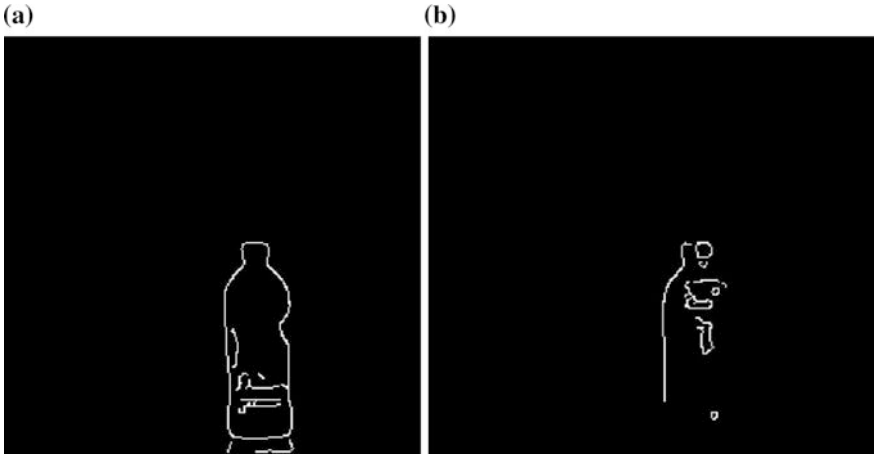

Fig. 2 Infrared and visible edge contrast in smoggy environment. **a** Infrared image edge. **b** The visible edges of the image

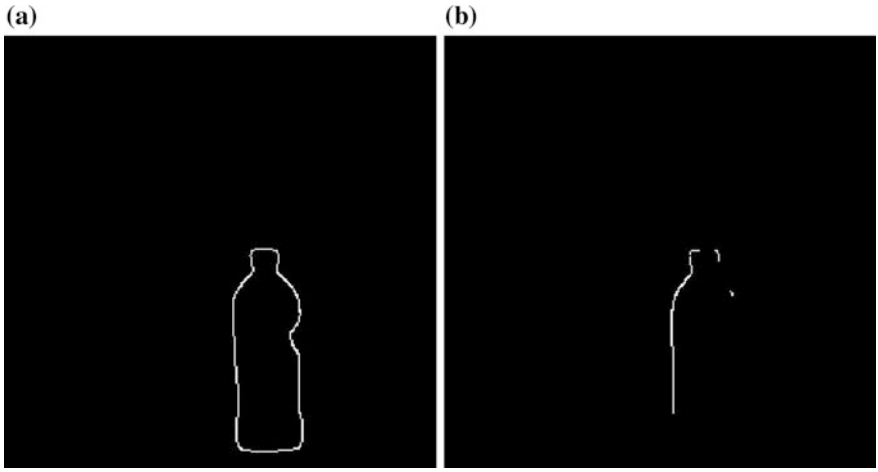

Fig. 3 Outer profile of the measured object. **a** An infrared image of the measured object outer profile. **b** Smoke-filled environment measured object visible band contour area

appropriate increase in the proportion of the infrared image of smoke on the way to weaken the influence of fused image (Fig. 4).

The measured object contour regions were shown in Fig. 5.

Within the statistical range of the measured object contour area, the number of pixels of the visible image edge is 291, while that of the infrared image edge is 317, both of the ratio close to 1. It can determine the visible image forming intact, unaffected smoke affected.

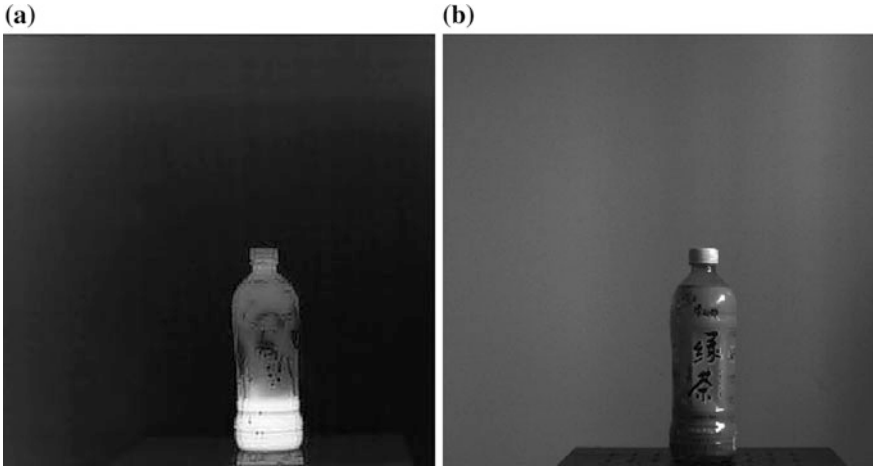

Fig. 4 Infrared and visible images under normal circumstances. **a** Infrared image. **b** Visible image

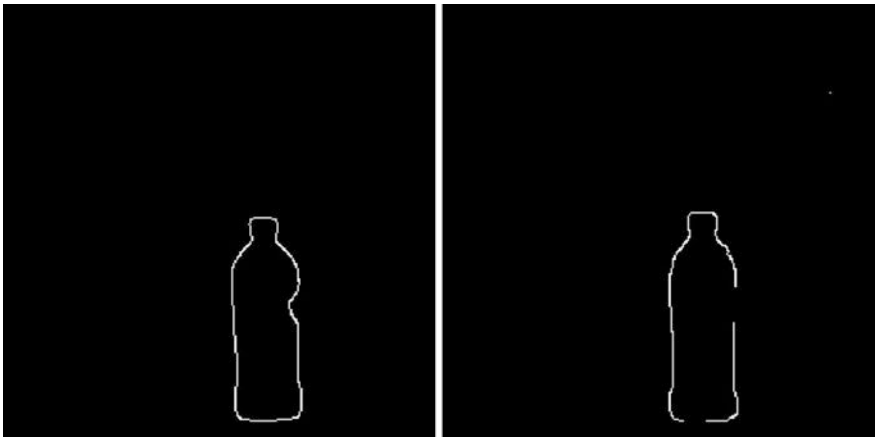

Fig. 5 Under normal circumstances the edge region of the integrity of the object to be measured contour contrast

4 Conclusion

As can be seen by the above experiment, the algorithm combined with dual-band image information to determine the impact of smoggy visible imaging environment by reference band chosen to achieve all-weather image recognition, and achieved certain results, the algorithm was concluded with the actual environment feature match, can provide the basis for a fire alarm.

Acknowledgments Thanks for the support by Tianjin Outstanding Young Teachers Program, Tianjin Edge Technology and Applied Basic Research Project (14JCYBJC15800), TJNUDP (52XK1206), and Google support for the Ministry of Education NCSIETPJF in China.

References

1. Liang Q, Cheng X, Huang S, Chen D (2014) Opportunistic Sensing in Wireless Sensor Networks: Theory and Applications. IEEE Trans Comput 63(8):2002–2010
2. Liang Q (2011) Situation understanding based on heterogeneous sensor networks and human-inspired favor weak fuzzy logic system. IEEE Syst J 5(2):156–163
3. Wang X, Liang Q (2013) On the throughput capacity and performance analysis of hybrid wireless networks over fading channels. IEEE Trans Wirel Commun 12(6):2930–2940
4. Zhao Peng, Wang Ni-Hong (2010) Precise perimeter measurement for 3D object with a binocular stereo vision measurement system. Optik—Int J Light Electron Optics 121(10):953–957
5. Shih Shen En, Tsai Wen Hsiang (2013) Optimal design and placement of omni-cameras in binocular vision systems for accurate 3-D data measurement. IEEE Trans Circ Syst Video Technol 23(11):1911–1926
6. Watkins WR, Tofsted DH, CuQlock-Knopp VG (2000) Navigation through fog using stereoscopic active imaging. In: Enhanced and synthetic vision, vol 4023, pp 20–28

Human Eye Detection via Sparse Representation

Chunning Meng and Taining Zhang

Abstract Eye detection is an active research area in machine vision and a major step in many applications such as intelligent human–machine interaction, driver behavior analysis, human identity verification, security control, and handicap-aiding interfaces. In this paper, we apply sparse representation algorithm to the problem of human eye detection in still color images. Considering the eye detection task as a pixel-wise classification problem, we use our framework to discriminate "patches centered on a pixel located on eye" against "patches centered on a pixel located elsewhere". Our experimental results show that our method achieves high detection accuracy on face (without spectacles) viewed under varying lighting conditions, general poses and viewpoints, and is highly robust to background variation.

Keywords Eye detection · Sparse representation · Classification · Color images

1 Introduction

Eye detection has been an active research topic for many decades due to its potential applications in various fields. A large number of works have been focused on this problem, which can be roughly classified into two categories: traditional image based passive approaches and the IR based approaches. The first category assumes that the eyes appear different from the rest of the face both in shape and intensity. Eyes can be detected and tracked based on their unique intensity distribution and shape. The IR based approach, on the other hand, exploits the spectral properties of pupils in the near infrared range to produce the bright/dark pupil effect.

C. Meng (✉)
Department of Electronic Technology, China Maritime Police Academy, Ningbo, China
e-mail: mengchunning123@163.com

T. Zhang
ShenYang Aerospace University, Shenyang, China

Q. Liang et al. (eds.), *Proceedings of the 2015 International Conference on Communications, Signal Processing, and Systems*, Lecture Notes in Electrical Engineering 386, DOI 10.1007/978-3-662-49831-6_71

Traditional passive approach usually consists of two stages. In the first stage, a face detection algorithm is adopted to locate faces in a given cluttered image [1]. Then, eyes can be located from their unique intensity distribution and shape by numerous methods based on the detected face, such as singular value decompositions (SVD) [2], principal component analysis (PCA) [3], support vector machines (SVM) [4], or neural network [5]. These methods use whole eye patches as training samples to train a classifier to determine whether the small patches of an image contain eye or not. As the face detection algorithms are mature, it is reasonable to adopt an existing algorithm for face detection. However, the way of using the whole eye as training patches is so sensitive to position perturbation that the training samples have to be carefully aligned before training.

The IR based eye detection approach is simple and effective. It exploits the spectral properties of the pupil in the near infrared range. Numerous techniques have been developed based on this principle [6–8]. In practice, however, these methods would not be widely used because in many real applications the face images are not IR illuminated.

In this paper, we focus on the research of direct search for eyes in still color images. We propose the use of sparse representation method to locate the positions of eyes directly from color images captured in natural light, while skipping the initial face region estimation step as commonly done in literature. We regard eye detection problem as a task of classifying each pixel of interest in the test image to belong to eye or not. To do this, a small patch around each pixel to be tested is considered. Two dictionaries, D_{eye} and $D_{background}$, are learned to label each interested pixel. We use the reconstruction error as a discriminant, with the idea that dictionary D_{eye} should be "good" at reconstructing eye and "weak" in reconstructing background, while the dictionary $D_{background}$ is the opposite. By comparing the reconstruction errors from the two dictionaries, the image can be separated into eye and background regions. We use eye-part patches instead of whole eye patches in training. By using eye-part patches as training samples, we do not need to align the training patches before training.

The organization of this paper is as follows. Section 2 introduces the numerical background of sparse representation. Experimental results are shown in Sect. 3. The paper ends in Sect. 4 with a conclusion of our work.

2 Sparse Representation for Signal Classification

Consider a signal $x_l \in R^n$. We say that x_l admits a sparse approximation over a dictionary D in $R^{n \times k}$, with k columns referred to as k atoms, when one can find a linear combination of a "few" atoms from D that is "close" to the original signal x_l. In this paper, x_l represents an image patch written as a column vector. Given an input matrix $X = [x_1, \ldots, x_m] \in R^{n \times m}$ of m signals, learning such a dictionary can be

formulated as an optimization problem over a dictionary $D = [d_1, \ldots, d_k] \in R^{n \times k}$ and the coefficient matrix $A = [\alpha_1, \ldots, \alpha_m] \in R^{k \times m}$. A number of practical algorithms, including the k-SVD algorithm [9] and the method of optimal direction (MOD) [10] with l_0-norm sparsity constraints, and the algorithm of Lee et al. [11]. with l_1-norm sparsity constraints, have been developed for learning such dictionary. All of these techniques are iterative approaches. After an initialization of D, e.g., from random signals, they iterate between a sparse coding step and a dictionary update step. The optimization problem with l_0-norm sparsity constraint can be written as:

$$\min_{\alpha_l, D} \sum_{l=1}^{m} \|x_l - D\alpha_l\|_2^2, \quad \text{s.t.} \left\|d_j\right\|_2^2 = 1 \text{ and } \|\alpha_l\|_0 \le L \tag{1}$$

During the sparse coding step, D is fixed and the coefficient matrix A is computed. In the l_0 case, sparse coding amounts to solving the following NP-hard optimization problem over α_l:

$$\min_{\alpha_l} \|x_l - D\alpha_l\|_2^2, \quad \text{s.t.} \|\alpha_l\|_0 \le L \tag{2}$$

A greedy algorithm called orthogonal matching pursuit (OMP) [12] is shown to be very efficient, although theoretically can only find suboptimal solution. In the l_1 case, sparse coding amounts to solving the following unconstrained problem over α_l:

$$\min_{\alpha_l} \|x_l - D\alpha_l\|_2^2 + \lambda \|\alpha_l\|_1 \tag{3}$$

where λ is a scalar regularization parameter that balances the tradeoff between reconstruction error and sparsity. It is a well-known fact that the l_1 constraint induces sparse solutions for the coefficient vector α_l. Furthermore, this is a convex problem that can be solved very efficiently using, e.g., the LARS-Lasso algorithm [13] and basis pursuit (BP) [14] to find its global optimum.

During the dictionary update step, D is updated with a fixed A [10, 11] or variable A [9]. When the coefficient matrix A is fixed, updating the dictionary D is a linear least-squares problem under quadratic constrains as follows:

$$\min_{D} \sum_{l=1}^{m} \|x_l - D\alpha_l\|_2^2, \quad \text{s.t.} \left\|d_j\right\|_2^2 = 1, \quad \text{for} j = 1, \ldots, k \tag{4}$$

An alternative way to perform sparse coding is to enforce positivity of both the coefficient matrix A and the dictionary D. The NN-k-SVD algorithm [15] and the NNSC algorithm [16] can be used to learn such non-negative constrained problem efficiently.

Assume that there are N classes of training signals C_i, $i = 1, \ldots, N$. The simplest strategy of using dictionaries for discrimination consists of first learning N dictionaries D_i, one for each class. Then approximating each signal using a constant

sparsity and N different dictionaries provides N different reconstruction errors, which can then be used as the features for classification. Thus, the way of estimating the class i_0 for an input signal x_l can be written as:

$$\hat{i}_0 = \arg\min_{i=1,\ldots,N} R(x_l, D_i) \tag{5}$$

here, $R(x_l, D_i)$ is the reconstruction error of the signal x_l using the dictionary D_i.

In this paper, we also use the reconstruction error $R(x_l, D_i)$ as a discriminant, with the idea that dictionary D_i associated with class C_i should be "good" at reconstructing this class, while "bad" for the other classes. We only classify the image patches into two classes: C_{eye} for the patches that are centered on a pixel located on the eye and $C_{background}$ for the ones that are not centered on the eye. Given C_{eye} and $C_{background}$, we learn two dictionaries D_{eye} and $D_{background}$ for representing the training image patches, and then associate each test patch to the dictionaries for which the "better" sparse decomposition is obtained. Subsequently, the image can be separated into eye and background regions by comparing the reconstruction errors from each of these two dictionaries:

$$\min\left(R\left(x_l, D_{eye}\right), R\left(x_l, D_{background}\right)\right) \tag{6}$$

We propose a supervised learning algorithm, which uses labeled training patches to learn D_{eye} and $D_{background}$. The strategies are detailed as follows:

Step 1: Let D_{all} be the trained dictionary with k_{all} columns, which is used to reconstruct all the labeled training sets $X_{all} = [X_{eye}, X_{background}]$. The columns number of X_{all} is $m_{\text{eye}} + m_{background}$. For each signal $x_l \in X_{all}$, we have the corresponding sparse representation $\alpha_l(x_l, D_{all})$, and we define two coefficient matrices A_{eye} and $A_{background}$ with m_{eye} columns and $m_{background}$ columns, respectively.

Step 2: Two signals belonging to different classes are expected to have decompositions that use different atoms. Inversely, two atoms in D_{all} would belong to different subspaces if they are used by signals belonging to different classes. Then, it is reasonable to believe that the atoms used by a vector x_l belonging to C_{eye} are different from those used by a vector x_l belonging to $C_{background}$. Thus, we can extract two sub-dictionaries D_{eye} and $D_{background}$ from D_{all} by comparing coefficient matrices A_{eye} and $A_{background}$. We compute two vectors S_{eye} and $S_{background}$ to find out which atoms in D_{all} are more likely belong to D_{eye} and which atoms are more likely belong to $D_{background:}$

$$\begin{aligned} S_{eye} &= \frac{1}{m_{eye}} \left|A_{eye}\right| \cdot [1]^{m_{eye} \times 1} \\ S_{background} &= \frac{1}{m_{background}} \left|A_{background}\right| \cdot [1]^{m_{background} \times 1} \end{aligned} \tag{7}$$

$$\mathrm{div}\left(S_{eye},\ S_{background}\right) = S_{eye}\ ./S_{background} \tag{8}$$

where operations $|\cdot|$ and ./ are element-wise absolute value symbol and element-wise division symbol. The bigger an element in div(S_{eye}, $S_{background}$) is, the more likely the corresponding atoms belongs to D_{eye}.

3 Experimental Results

In our experiments, the steps to collect eye-part and background sample patches are as follows. The Sobel edge detector is applied first to all the training images. Then, a small sliding window is used to scan the image into patches, and all the non-edge patches are discarded. In our experiments, all the training and test samples were scaled to a size of 25 × 25 pixels, which gives the length of the training vector to 1875 (= 25 × 25 × 3). Finally, a total of 20,550 eye-part patches and 40,450 background patches are generated. 14,384 eye-part patches and 28,315 background patches are used for training, producing an input training matrix X_{all} in the size of 1875 × 42699, and the rest are used for testing. Examples of the training samples are shown in Fig. 1.

First, we learn dictionary D_{all}, which is adapted to the input matrix $X_{all} \in R^{1875\times 42699}$. In the l_0 case, the number of atoms used in the sparse representation was set to $L = 8$. In the l_1 case, the parameter that balances the tradeoff between reconstruction error and sparsity was set to $\lambda = 100$. The number of atoms in dictionary D_{all} was set to $k_{all} = 960$, and the epochs of iteration was set to 40. Then, we apply the method mentioned in Sect. 2 to get D_{eye} and $D_{background}$. In our experiment, we consider that the atoms in D_{all}, with the corresponding elements in div(S_{eye}, $S_{background}$) bigger than 2 belong to D_{eye}, while the atoms with the corresponding elements in div(S_{eye}, $S_{background}$) smaller than 0.5 belong to $D_{background}$. The number of atoms in D_{eye} and $D_{background}$, for different dictionary training methods mentioned in Sect. 2, are shown in Table 1. The atoms learned by MOD are shown in Fig. 2.

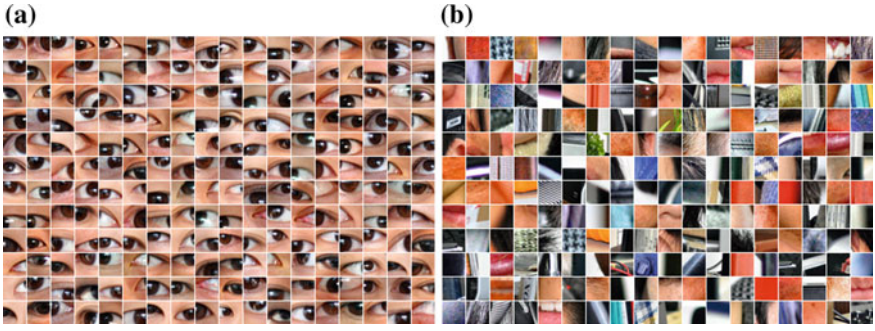

Fig. 1 Examples of the training sample patches: **a** examples of the eye-part samples for training and **b** examples of the background samples for training

Table 1 The number of atoms in D_{eye} and $D_{background}$ used in this paper

Method	k_{eye}	$k_{background}$
MOD	370	347
k-SVD	367	355
fast_sc [11]	340	439
NN-k-SVD	105	597
NNSC	275	500

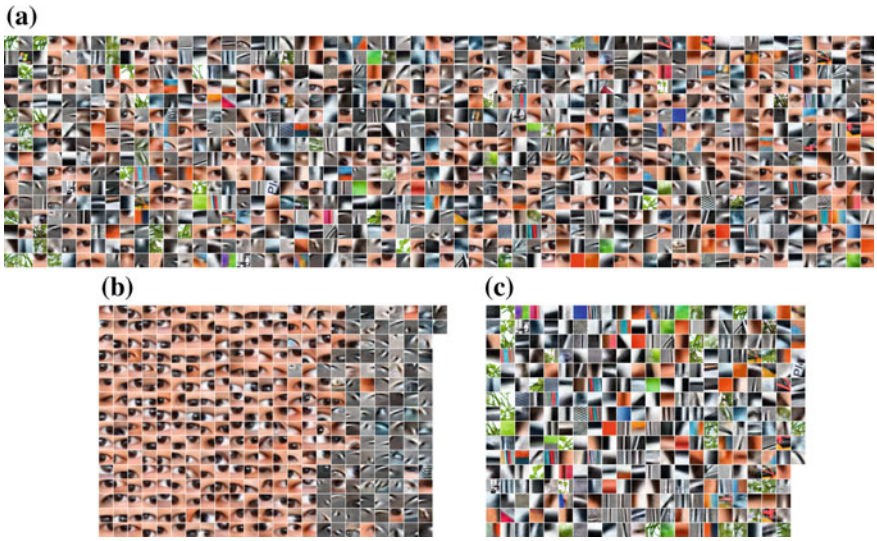

Fig. 2 Dictionaries learned by MOD: **a** dictionary with 960 atoms, **b** eye dictionary with 370 atoms, and **c** background dictionary with 347 atoms

Table 2 The recognition rate for the training samples

Method	True positive rate (%)	True negative rate (%)	Recognition rate (%)
MOD	97.713	92.460	94.229
k-SVD	95.599	94.310	94.745
fast_sc	98.471	88.730	92.012
NN-k-SVD	89.912	84.037	86.016
NNSC	92.471	88.095	89.569
LDA	92.811	87.826	89.506

The classification results for the training and testing sample patches are presented in Tables 2 and 3. As a comparison, the recognition rate calculated by linear discriminant analysis (LDA) is also presented.

Table 3 The recognition rate for the testing samples

Method	True positive rate (%)	True negative rate (%)	Recognition rate (%)
MOD	97.746	92.097	94.000
k-SVD	95.086	94.561	94.738
fast_sc	98.589	88.430	91.853
NN-k-SVD	89.247	83.997	85.766
NNSC	91.469	88.035	89.192
LDA	91.469	86.873	88.421

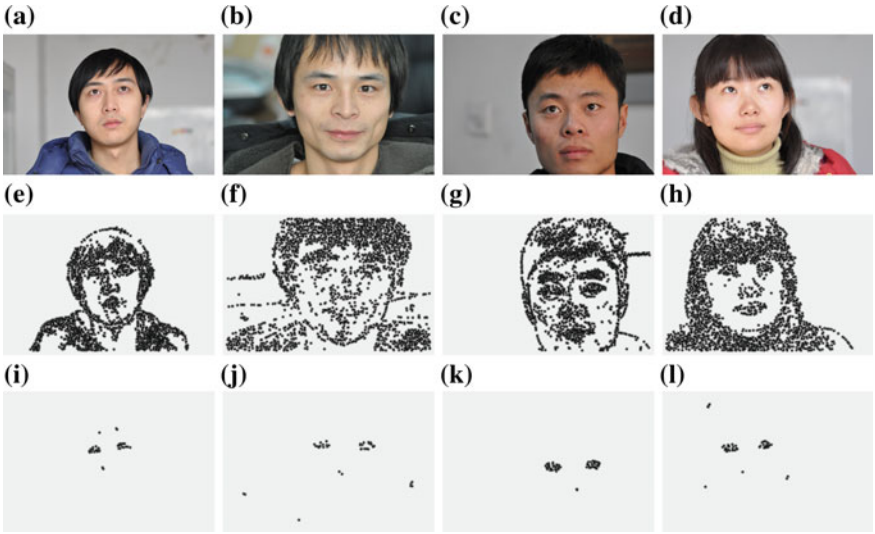

Fig. 3 The test images have a size of 613 × 407. None of these test images were used to generate training sample patches

Some results for testing images are shown in Fig. 3. Firstly, we apply Sobel detector to find all the edge points in a given image. Since the computational cost is too large if we test all the edge points, we only randomly choose 3000 detected edge points to test whether they locate on the eye or not. Then we calculate the difference of the reconstruction error from the chosen 3,000 points of interest. We discard all the interesting points with $R(x_l, D_{eye})$—$(x_l, D_{background})$ larger than −4, as a result, enough points located on eyes are saved and almost all the points not located on eyes are washed out. Here, the chosen dictionary training method is MOD. The results shown in Fig. 3 demonstrate that our method achieves high eye detection accuracy on face image captured under varying lighting conditions, general poses and viewpoints.

4 Conclusion

In this paper, we apply the method of sparse representation to solve the problem of human eye detection in color images under variable lighting conditions, general poses, and unconstrained background condition. The highest recognition rate is given by k-SVD, which demonstrates that sparse representation is accurate in human eye detection.

Acknowledgments This work is supported by National Natural Science Foundation of China (Grant No. 61401105).

References

1. Viola P, Jones MJ (2004) Robust real-time face detection[J]. Int J Comput Vis 57(2):137–154
2. Danafar S, Sheikh LT, Targhi AT (2006) A method for eye detection based on SVD transforms[J]. Int J Imaging Syst Technol 16(5):222–229
3. de Campos TE, Feris RS, Marcondes RC (2000) Eigenfaces versus eigeneyes: first steps toward performance assessment of representations for face recognition[M]. In: MICAI 2000: advances in artificial intelligence. Springer, Berlin, pp 193–201
4. Chen S, Liu C (2015) Eye detection using discriminatory Haar features and a new efficient SVM[J]. Image Vis Comput 33:68–77
5. El-Sayed MA, Khafagy MA (2014) An identification system using eye detection based on wavelets and neural networks[J]. arXiv:1401.5108
6. Zhu Z, Ji Q (2005) Robust real-time eye detection and tracking under variable lighting conditions and various face orientations[J]. Comput Vis Image Underst 98(1):124–154
7. Coetzer RC, Hancke GP (2014) Development of a robust active infrared-based eye tracker[J]. IET Comput Vis 8(6):523–534
8. Shimata R, Mitani Y, Ochiai T (2015) A study of pupil detection and tracking by image processing techniques for a human eye-computer interaction system[C]. Software Engineering, Artificial Intelligence, In: Networking and parallel/distributed computing (SNPD), 2015 16th IEEE/ACIS international conference on. IEEE, vol 2015. pp 1–4
9. Aharon M, Elad M, Bruckstein A (2006) K-SVD: an algorithm for designing overcomplete dictionaries for sparse representation[J]. IEEE Trans Signal Process 54(11):4311
10. Engan K, Aase SO, Husøy JH (1999) Frame based signal compression using method of optimal directions (MOD)[C]. In: Circuits and systems, 1999. ISCAS'99. Proceedings of the 1999 IEEE international symposium on. IEEE, 1999, vol 4. pp 1–4
11. Lee H, Battle A, Raina R et al (2006) Efficient sparse coding algorithms[C]. Adv Neural Inf Process Syst 2006: 801–808
12. Yaghoobi M, Wu D, Davies ME (2015) Fast non-negative orthogonal matching pursuit[J]. Sig Process Lett IEEE 22(9):1229–1233
13. Efron B, Hastie T, Johnstone I et al (2004) Least angle regression[J]. Ann Stat 32(2):407–499
14. Chen SS, Donoho DL, Saunders MA (1998) Atomic decomposition by basis pursuit[J]. SIAM J Sci Comput 20(1):33–61
15. Aharon M, Elad M, Bruckstein AM (2005) K-SVD and its non-negative variant for dictionary design[C]. Optics & photonics 2005. Int Soc Opt Photonics 2005:591411–591411-13
16. Hoyer PO (2000) Non-negative sparse coding[C]. Neural Networks for Signal Processing, 2002. Proceedings of the 2002 12th IEEE Workshop on. IEEE, vol 2002. pp 557–565

Infrared and Visible Image Fusion Based on Tetrolet Transform

Xin Zhou and Wei Wang

Abstract Tetrolet transform has a better directionality of the structure and can express texture features of image precisely in dealing with high-dimensional signal. This paper introduces tetrolet transform into infrared and visible images for fusion to obtain a greater amount of information. First, the tetrolet transform was performed on the images which are fused to obtain high-pass and low-pass subbands on different scales. Then, a method based on local region gradient information was applied to low-pass subbands to get the low-pass fusion coefficients. Finally, the inverse tetrolet transform was utilized to obtain fused image. Using a variety of images to perform fusion experiment, all the results have shown that the fused image has more abundant features and more amount of information by using tetrolet transform. Compared with the traditional fusion algorithms, the fusion algorithm presented in this paper provides better subjective visual effect, and the standard deviation and entropy value would be somewhat increased.

Keywords Infrared image · Visible image · Image fusion · Tetrolet transform · Multiscale directional analysis

1 Introduction

The information contained in the infrared image and the visible image is quite different and forms a complementary relationship, since the infrared image sensor's approach of acquiring the target information's band range and imaging mode is different from the visual one [1]. Through the fusion of the infrared image and the visible image, combing the complementary information and the redundant information of the two kinds of images, the fused image of the target has clear outline, rich information and the perception ability of the image sensor can be largely extended.

X. Zhou (✉) · W. Wang
College of Electronics and Communication Engineering, Tianjin Normal University, Tianjin, China
e-mail: zhouxintjnu@126.com

Q. Liang et al. (eds.), *Proceedings of the 2015 International Conference on Communications, Signal Processing, and Systems*, Lecture Notes in Electrical Engineering 386, DOI 10.1007/978-3-662-49831-6_72

Wavelet has become an important means in image fusion for its well-known time frequency localization analysis properties. However, the advantages of the wavelet transform primarily are embodied in the analysis and process towards the one-dimensional segmentation smooth and function of bounded variation. When it has been applied in two-dimensional or higher dimensional case, the separable wavelet formed by one-dimensional wavelet has limited direction, and then cannot optimally represent line singularity or face singularity high-dimensional function [2]. Therefore, the wavelet transform can only reflect the point singularity of the signal, and can not reflect the two-dimensional image's marginal, linear, characteristics.

Tetrolet transform is a geometric adaptive transform having tetromino support and the potential to adapt to the directional features of an image, it can be better applied in the image fusion [3].

2 Tetrolet Transform

A new adaptive Haar wavelet transform, called tetrolet transform provides efficient image representation. Tetrolet is wavelet based efficient and effective transform, whose supports tetrominoes which are shapes are made by connecting four equal-sized squares. The corresponding filter bank algorithm is simple but enormously effective. In every level of the filter bank algorithm the low-pass image is divided into 4 × 4 blocks. Then in each block a local tetrolet basis is determined, which is adapted to the image geometry in this block. In discrete wavelet transformation (DWT), horizontal and vertical directions only preferred, which fails to achieve optimal results with images that contain geometric structures in other directions. To improve the treatment of orientated geometric image structures, tetrolet transform is introduced [4–9].

In the Haar filter bank, the low-pass filter and the high-pass filters are just given by the averaging sum and the averaging differences of each four pixel values which are arranged in a 2 × 2 square. Then we can determine the low-pass part $a^l = \left(a^l[i,j]\right)_{i,j=0}^{\frac{N}{2}-1}$ with

$$a^l[i,j] = \sum_{(i',j') \in I_{i,j}} \in \left[0, L\left(i',j'\right)\right] a\left[i',j'\right] \tag{1}$$

as well as the three high-pass parts for l = 1, 2, 3, $w_l^1 = \left(w_l^1[i,j]\right)_{i,j=0}^{\frac{N}{2}-1}$ with

$$w_l^1[i,j] = \sum_{(i',j') \in I_{i,j}} \in \left[l, L(i',j')\right] a\left[i',j'\right] \tag{2}$$

where the coefficients $\in$[l, m], l, m = 0, …, 3 are entries from the Haar wavelet transform matrix

$$W = (a[l,m])_{l,m=0}^{3} = \frac{1}{2}\begin{pmatrix} 1 & 1 & 1 & 1 \\ 1 & 1 & -1 & -1 \\ 1 & -1 & 1 & -1 \\ 1 & -1 & -1 & 1 \end{pmatrix} \tag{3}$$

The decomposition algorithm of tetrolet transform is processed by four ways, which are as follows:

(1) Divide the image into 4 × 4 blocks.
(2) Find the sparsest tetrolet representation in each block.
(3) Rearrange the low- and high-pass coefficients of each block into a 2 × 2 block.
(4) Store the tetrolet coefficients (high-pass part).
(5) Apply Steps 1 to 4 to the low-pass image.

Input image is considered as $a^0 = (a|i,j|)_{i,j=0}^{N-1}$ with $N = 2^J, J \in N$ then J − 1 levels can be applied. In the *rth* level, r1, …, J − 1, the following computations are performed.

Step 1: Divide the low-pass image a^{r-1} into blocks $Q_{i,j}$ of size 4 × 4, $i,j = 0, \ldots, \frac{N}{4^r} - 1$.

Step 2: In each block of $Q_{i,j}$ there are 117 admissible tetromino coverings are considered, i.e., $c = 1, \ldots, 117$. For each tiling c Haar wavelet transform is applied to the four tetromino subsets $I_s^{(c)}, s = 0, 1, 2, 3$ In this way, four low-pass coefficients and 12 Tetrolet coefficients are obtained for each tiling of c. More precisely, in $Q_{i,j}$ we compute analogously to (1) and (2) the pixel averages for every admissible tetromino configuration $c = 1, \ldots, 117$ by $a^{r,(c)} = (a^{r,(c)}[s])_{s=0}^{3}$ with

$$a^{r,(c)}[s] = \sum_{(m,n) \in I_g^{(c)}} \in [0, L(m,n)] a^{r-1}[m,n] \tag{4}$$

as well as the three high-pass parts l = 1, 2, 3, $w_l^{r,(c)} = (w_l^{r,(c)}[s])_{s=0}^{3}$ with

$$w_l^{r,(c)}[s] = \sum_{(m,n) \in I_g^{(c)}} \in [l, L(m,n)] a^{r-1}[m,n] \tag{5}$$

where the coefficients $\in [l, L(m,n)]$ are given in (3) and where L is the bijective mapping, which relating the four index pairs (m, n) of $I_g^{(c)}$ with the values 0, 1, 2, and 3 in descending order. That means, by the one-dimensional indexing J (m, n) the smallest index is identified with the value 0, while the largest with 3.

Then the covering c^* is chose such that the l^{-1}-norm of the 12 Tetrolet coefficients becomes minimal

$$c^* = \arg\min_c \sum_{i=1}^{3} \left\| w_l^{r,(c)} \right\|_1 = \arg\min_c \sum_{l=1}^{3} \sum_{g=0}^{3} \left| w_l^{r,(c)}[s] \right| \tag{6}$$

Hence, for every block $Q_{i,j}$ we get an optimal Tetrolet decomposition $[a^{r,(c^*)}, W_1^{r,(c^*)}, W_2^{r,(c^*)}, W_3^{r,(c^*)}]$. By doing this, the local structure of the image block is adapted.

The best covering c^* is a covering whose tetrominoes do not intersect an important structure like an edge in the image a^{r-1}. Because the tetrolet coefficients become as minimal as possible a sparse image representation will be obtained. For each block $Q_{i,j}$ the covering c^* is stored such that has been chosen, since this information is necessary for reconstruction. If the optimal covering is not unique, then the tiling c^* has taken that already chosen most frequently in the previous blocks. Thus, the coding of the used coverings becomes cheaper.

Step 3: In order to be able to apply further levels of the tetrolet decomposition algorithm, the entries of the vectors $a^{r,(c^*)}$ are arranged and $W_l^{r,(c^*)}$ into 2×2 matrices using a reshape function R,

$$a^r_{|Q_{i,j}} = R(a^{r,(c^*)}) = \begin{pmatrix} a^{r,(c^*)}[0] & a^{r,(c^*)}[2] \\ a^{r,(c^*)}[1] & a^{r,(c^*)}[3] \end{pmatrix} \tag{7}$$

and in the same way $w^r_{l|Q_{i,j}} = R(w_l^{r,(c^*)})$ for $l = 1, 2, 3$. For an efficient representation in the next level, a suitable arrangement of the low-pass values is essential. That means, the order of labeling the tetrominoes of c^* in each block Qi, j by $s = 1, 2$ and 3 is very important. The labeling should be done in a way, such that the geometry of the tiling is suitably mapped to $\begin{pmatrix} 0 & 2 \\ 1 & 3 \end{pmatrix}$. Therefore the four shapes of the chosen partition c^* are labeled by comparing with the square case.

Step 4: After finding a sparse representation in every block Qi, j for $i, j = 0, \ldots, \frac{N}{4^r} - 1$, the low-pass matrix is stored.

$$a^r = (a^r_{|Q_{i,j}})_{i,j=0}^{\frac{N}{4^r}-1} \tag{8}$$

and the high-pass matrices

$$w_l^r = (w^r_{l|Q_{i,j}})_{i,j=0}^{\frac{N}{4^r}-1} \tag{9}$$

$L = 1, 2, 3$, replacing the low-pass image a^{r-1} by the matrix

$$\begin{pmatrix} a^r & w_2^r \\ w_1^r & w_3^r \end{pmatrix} \tag{10}$$

After a suitable number of decomposition steps, a shrinkage procedure to the Tetrolet coefficients in order to get a sparse image representation is applied.

$$S_\lambda(x) = \begin{cases} x, & |x| \geq \lambda \\ 0, & |x| \geq \lambda \end{cases} \tag{11}$$

For the reconstruction of the image, low-pass coefficients are needed from the coarsest level and the Tetrolet coefficients as usual. Additionally, the information about the respective covering in each level and block is necessary.

3 The Infrared and Visible Image Fusion Algorithm Based on Tetrolet

The paper introduced the tetrolet into fusion of the infrared and visible image. The characters of the tetrolet can be better used in extracting the geometric features of the source image and provide more information for the fused image. When the fusion is processing, the different scales and different directional subbands can adopt different fusion rules. The better fused effect can be achieved through sufficiently digging original multi-source image's visual information.

The high frequency subband after the tetrolet decomposition contains a lot of high frequency information of the image. The bigger coefficient's absolute value corresponds to the certain directional interval's significant characteristic, for example: marginal, linear, regional boundary, etc. The coefficients can better depict the image's structure's information, and have great influence upon human's vision. The low frequency subband contains most of low frequency information of the image, and is the primary perception part of the human's eyes to the image content. The paper judges and processes the fusion according to the characteristics of the low frequency subband and the high frequency subband with corresponding fusion rules, and the subband coefficient would thereby acquired.

According to the human visual system's characteristics, we can know that the human's eyes are not sensitive to the individual pixel's gray value. The distinctness of the image is decided by the all pixels in certain region. To improve the fused image's clearness, the pixel's regional feature should be considered in the design of fusion algorithm. Therefore, the coefficient with the bigger regional variance value should be adopted as the fused image's high frequency subband coefficient in tetrolet transform.

The specific fusion rules are show in the following:

(1) Tetrolet decomposition is applied in the visible image V and the infrared image I in the level L. the high frequency subband V_l^k and $I_l^k\left(k = 1, 2 \ldots, 2^{nl}, l = 1, 2, \ldots, L\right)$ and the low frequency subband V_L^0 and I_L^0. L is the value of the largest possible decomposition level. 2^{nl} is the directional value of each level's decomposition.

(2) The coefficient of the low frequency subband remains constant. The paper chooses two images' average value of the coefficient of the low frequency subband as the fused image's low frequency subband coefficient.
(3) As for the high frequency subband's coefficient, in the largest decomposition level L, the largest value of the two images which corresponds to decomposition scale values has been adopted as the fused image's coefficient.
(4) As for other $L-1$ level high frequency coefficient, the maximum principle of the local variance has been adopted, that is to say, in the transform domain, calculating the corresponding point $N \times N$ neighborhood's local variance C_X^k(X as V or I), and choosing the highest coefficient of the variance as the fused image's corresponding point's coefficient.

At last, tetrolet inverse transformation has been applied to the fused image's coefficient, and we get the fused image F.

4 Experiments

The paper has adopted several different approaches to fuse the two registrated infrared and visible images. The Fig. 1 presents a group of image fusion experimental results which is based on multi-image fusion approach. The Fig. 1a, b are infrared and visible image respectively. The Fig. 1c is the fused image based on the contrast pyramid decomposition. Figure 1d is the fused image based on the Laplacian pyramid decomposition. Figure 1f is the fused image based on the paper's approach (Tetrolet). Among these, the approaches CP, DWT and LP have

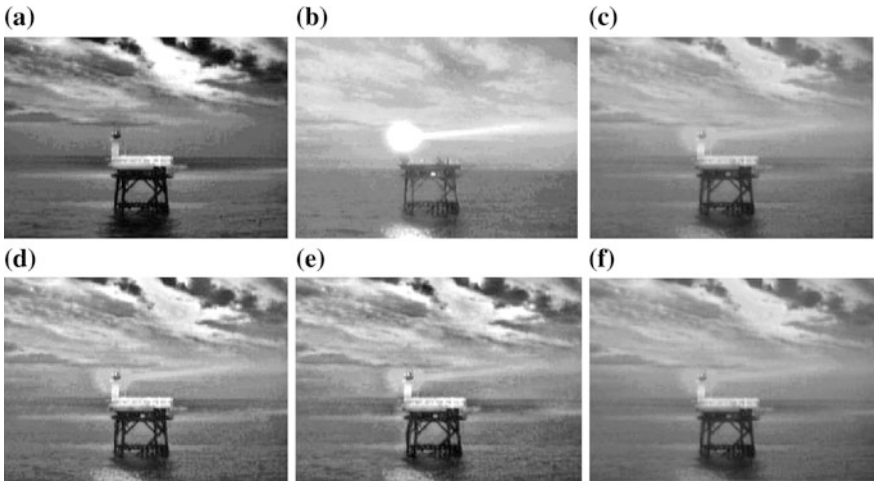

Fig. 1 Comparison of image fusion based on different rules. **a** Infrared image. **b** Visible image. **c** Fusion image using CP. **d** Fusion image using LP. **e** Fusion image using DWT. **f** Fusion image using Tetrolet

Table 1 Comparison of statistical parameters about fusion results according to different fusion rules

	Entropy	Cross entropy	Standard deviation	Average gradient
CP	10.319	0.874	24.291	28.416
LP	10.670	0.955	24.082	28.620
DWT	10.792	0.713	24.623	28.217
Tetrolet	10.623	0.601	24.949	28.904

adopted the same fusion rule as this paper. In calculating the local variance, the $N \times N = 3 \times 3$; LP, CT, DWT and tetrolet decomposition are all 3 levels.

From Fig. 1a–f are all much clearer than the infrared image (a), and contains the information of the visible image. But the Fig. 1c is a little obscure. There are some noisy spots in Fig. 1d. Compared with the figure (f), the figure (e) is much more obscure in the marginal part of the letter. Therefore, the fused figure (f) which is based on tetrolet transform has better visual effect.

To quantitatively evaluate the performances of the fusion approaches applied in the infrared and invisible image, we adopted many evaluation parameters to evaluate the approach mention in this paper and other approaches quantitatively. As the Table 1 shows, if the entropy and standard deviation acquired by a certain fusion approach is relatively larger, but the cross entropy is relatively smaller, and then we can say that the fusion approach is better. From the Table 1, as far as the infrared and the visible image are concerned, the tetrolet fusion approach which is put forward by the paper is better than LP, DWT and CP fusion approaches.

5 Conclusions

The paper put forward an infrared and visible fusion algorithm which is based on the tetrolet transform. Compared with the traditional wavelet transform, tetrolet has anisotropy and translation invariance. The tetrolet transform can preserve the infrared and visible image's feature information, enhance the fused image's space detail representation ability, and improve the fused image's information.

Acknowledgment The authors are grateful to the anonymous referees for constructive comments.

References

1. Zhou X, Liu R-A,Chen J (2009) Infrared and visible image fusion enhancement technology based on multi-scale directional analysis. Proc. Int. Congr. Image Signal Process., CISP
2. Naqvi SAR (2013) Image compression using Haar wavelet based tetrolet transform. In: 2013 International conference on open source systems and technologies (ICOSST), pp 4–50

3. Thayammal S, Selvathi D (2014) Multispectral band image compression using adaptive wavelet transform—Tetrolet transform. 2014. In: International conference on electronics and communication systems, ICECS
4. Shi C (2014) A novel hybrid method for remote sensing image approximation using the tetrolet transform. IEEE J Sel Top Appl Earth Obs Remote Sens 7(12):4949–4959
5. Krommweh J Tetrolet transform: a new adaptive Haar wavelet algorithm for sparse image representation. J Vis Commun Image Represent 21(4):364–74
6. Yan Xiang (2013) Image fusion based on Tetrolet transform. J Optoelectron Laser 24 (8):1629–1633
7. Zhang Chang-Jiang (2014) Multi-channel satellite cloud image fusion in the tetrolet transform domain. Int J Remote Sens 35(24):8138–8168
8. Shen Yu (2013) Infrared and visible images fusion based on tetrolet transform. Spectrosc Spectral Anal 33(6):1506–1511
9. Yang X (2014) Image enhancement based on tetrolet transform and PCNN. Comput Eng Appl 50(19):178–81

Image Quality Assessment via Adaptive Pooling

Zhong Zhang, Shuang Liu and Ao Li

Abstract The pooling operation is the key to image quality assessment (IQA), but the traditional pooling treats local quality map equally. In this paper, we propose a novel method named adaptive pooling for image quality assessment, which explicitly considers importance of different local regions. The adaptive pooling operation assigns different weights to local quality map according to the variance of local regions. The proposed method is verified on two challenging IQA databases (CSIQ and TID 2008 databases), and the results demonstrate that it achieves better results than the state-of-the-art methods.

1 Introduction

Image quality assessment (IQA) is an important issue in many fields, such as image acquisition, transmission, compression, restoration, and enhancement. Generally, there are three kinds of IQA models in terms of the availability of a reference image, full reference (FR) models, reduced reference (RR) models, and no reference (NF) models. This paper only discusses FR-IQA models. FR-IQA models can be classified into two types. The first one is built under a bottom-up framework [1], which simulates the various processing stages in the visual pathway of human visual system (HVS), including just noticeable differences [2], visual masking effect [3], etc. The second one is constructed in a top-down framework [4, 5] which designs to model

Z. Zhang · S. Liu (✉)
College of Electronic and Communication Engineering, Tianjin Normal University, Tianjin, China
e-mail: shuangliu.tjnu@gmail.com

Z. Zhang
e-mail: zhong.zhang8848@gmail.com

A. Li
School of Computer Science and Technology, Harbin University of Science and Technology, Harbin, China
e-mail: dargonboy@126.com

Q. Liang et al. (eds.), *Proceedings of the 2015 International Conference on Communications, Signal Processing, and Systems*, Lecture Notes in Electrical Engineering 386, DOI 10.1007/978-3-662-49831-6_73

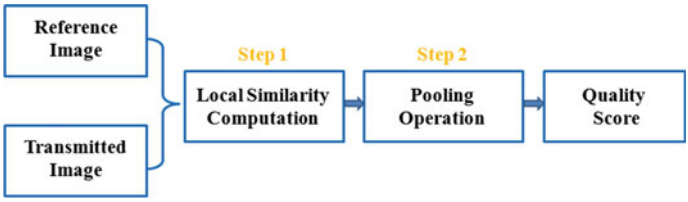

Fig. 1 The common flowchart of FR-IQA models

the overall function of HVS according to some global assumption. Recent studies [4, 5] have demonstrated the effectiveness of this kind of methods, and thus many approaches follow the top-down framework. The structural similarity (SSIM) [6], as a representative approach of top-down model, is based on the assumption that HVS is highly adapted to extract the structural information from the visual scene, and thus a measurement of SSIM should provide a good approximation of image quality.

From another point of view, many FR-IQA models consist of two stages [7] as shown in Fig. 1. The first step is local similarity computation. Considering the computational complexity, many approaches adopt image gradient as a measurement feature [8, 9] due to effectively capturing image local structure. Most gradient based FR-IQA models [4, 5] are inspired by SSIM [6]. They compute the similarity between the gradients of reference image and destroyed image. The second stage is the pooling operation which obtains a single overall quality score calculated from local similarity computation. The pooling operations, which aggregate similarity map or vectors into a single score or one vector, are widely used in many fields, such as image classification [10], human action recognition [11, 12]. The common used pooling operation is the average pooling, i.e., calculating the average of all local quality values as the final quality score. However, the average pooling treats each local region in an image equally, which neglects the local contrast information of the reference image.

In this paper, we propose a novel pooling operation namely adaptive pooling for image quality assessment. Natural images usually have diverse local structures which reflects the degree of importance of different local regions. Based on the consideration, the adaptive pooling assigns different weights according to the variance of local regions. Our method is verified by two challenging IQA databases, and the experimental results demonstrate that the proposed method achieves higher prediction accuracy than that of previous methods on image quality assessment.

2 Gradient Magnitude and Adaptive Pooling

2.1 Similarity

Many gradient based FR-IQA approaches utilize a similarity function to calculate gradient similarity [4, 8]. In addition to gradient magnitude, these approaches also adopt other similarity features, for example, luminance similarity and structural

similarity. Zhang et al. [4] combined phase congruency, which is a dimensionless measure of the significance of a local structure, with gradient magnitude. However, the computation of phase congruency is time consuming. In this paper, we adopt Roberts operator, and then calculate the similarity map.

2.2 Adaptive Pooling

The final quality score can be obtained from *SSM* via pooling operation. The most commonly used pooling operation is average pooling, i.e. averaging all the *SSM* values as the final quality score. However, this pooling operation equally treats each *SSM* value, i.e. each *SSM* value is assigned the same weight 1 regardless of what the local structure is. It fails to capture the local contrast information in the reference image. Figure 2 shows the reference image and its variance map of the 3×3 region. From this figure, we can see that the local regions with high contrast contain much structure information and therefore they should contribute more to evaluate the image quality. In order to exploit the local contrast information of reference image, we define the variance of a local region as a weight in the pooling stage

$$a(m,n)^2 = \frac{1}{(2R+1)^2} \sum_{p=m-R}^{m+R} \sum_{q=n-R}^{n+R} (ri(p,q) - v(m,n))^2 \tag{1}$$

where $v(m,n) = \frac{1}{(2R+1)^2} \sum_{p=m-R}^{m+R} \sum_{q=n-R}^{n+R} ri(p,q)$ is the mean value of reference image ri at location (m,n), and R is the radius of local region. Here, we set R to 1, i.e., we calculate the weight in a 3×3 local region. Furthermore, the pooling weight a should be normalized using the maximum value of a.

There are two advantages about the variance pooling. First, different local regions show different variance which considers microscopic structures of reference image. Specifically, when a local region is flat, its variance is low, while the variance is high at the boundaries of different regions. Second, the pooling weight a and *SSM*

Fig. 2 Reference image and its variance map of the 3×3 region

are complementary. Their joint distribution can better characterize the difference between reference image and transmitted image. The final quality score is computed by

$$score = \frac{1}{M \times N} \sum_{m=1}^{M} \sum_{n=1}^{N} a(m,n) SSM(m,n) \tag{2}$$

Note that the higher quality score, the higher image transmission quality.

3 Experimental Results

3.1 Experimental Setup

We verify the proposed algorithm on two publicly available databases: CSIQ, and TID2008 databases [13, 14]. The CSIQ database consists of 886 destroyed images and 30 reference images. The destroyed images contains six types of distortions at five different distortion levels. Concretely, the six types of distortions involve JPEG compression, JPEG 2000 compression, Gaussian blur (GB), additive white noise (AWN), additive pink Gaussian noise (APGN), and global contrast decrements (GCD). The TID 2008 database has 1700 destroyed images and 25 reference images with 17 kinds of distortions at 4 levels. Note that each images in IQA databases has been assessed by human beings under controlled conditions, and then assigned a quantitative quality score: mean opinion score (MOS) or difference MOS (DMOS).

For fair comparison, we employ three commonly used criteria to evaluate the proposed method. The first criterion is the Person linear correlation coefficient (PLCC) between MOS and the objective scores after nonlinear regression. The second criterion is the Spearman rank-order correlation coefficient (SROCC) which measures the prediction monotonicity of an IQA approach. The last one is the root mean square error (RMSE) between MOS and the objective scores.

3.2 Performance Comparison

Table 1 shows the comparative results on the CSIQ database according to PLCC, SROCC, and RMSE. We show the top three methods in boldface for each evaluation criterion. From this table, we can see that the proposed method achieves the best results based on all three criteria, because it explicitly considers the local structure contribution.

We also test the performance of the proposed algorithm on the TID2008 database. The results are shown in Table 2. The proposed algorithm achieves better results in all criteria. Once again, we prove the effectiveness of our algorithm through this database.

Table 1 Performance of the proposed method and other methods on the CSIQ database

	PLCC	SROCC	RMSE
SSIM [6]	0.861	0.876	0.133
GS [8]	0.896	0.911	0.116
MAD [13]	**0.950**	**0.947**	**0.082**
FSIM [4]	0.912	0.924	0.108
GMSD [9]	**0.954**	**0.957**	**0.079**
Ours	**0.958**	**0.961**	**0.071**

Table 2 Performance of the proposed method and other methods on the TID2008 database

	PLCC	SROCC	RMSE
G-SSIM [5]	0.760	0.731	0.873
SSIM [6]	0.773	0.775	0.851
GS [8]	0.842	0.850	0.723
MAD [13]	0.829	0.834	0.751
FSIM [4]	**0.874**	**0.880**	**0.653**
GMSD [9]	**0.879**	**0.891**	**0.640**
Ours	**0.8732**	**0.883**	**0.631**

4 Conclusion

This paper proposes a novel FR-IQA approach to overcome the limitation of traditional average pooling operation. We explicitly consider the local contrast information of reference images in the pooling stage. To this end, the variance of a local region is defined as a weight which is utilized to reflect the importance of local regions. The experimental results on CSIQ and TID 2008 databases show that the proposed algorithm achieves better results than previous approaches.

Acknowledgments This work is supported by National Natural Science Foundation of China under Grant No. 61401309, No. 61501327, and No.61501147; Natural Science Foundation of Tianjin under Grant No. 15JCQNJC01700; Natural Science Foundation of Hei Longjiang Province of China under Grant No. F2015040; Doctoral Fund of Tianjin Normal University under Grant No. 5RL134 and No. 52XB1405.

References

1. Wang Z, Bovik AC (2006) Modern image quality assessment. Synth. Lect. Image Video Multimed. Process. 2(1):1–156
2. Lubin J (1997) A human vision system model for objective picture quality measurements. In: International Broadcasting Convention, pp. 498–503

3. Ross J, Speed HD (1991) Contrast adaptation and contrast masking in human vision. Proc R Soc Lond Ser B Biol Sci 246(1315):61–70
4. Zhang L, Zhang L, Mou X, Zhang D (2011) FSIM: a feature similarity index for image quality assessment. IEEE Trans Image Process 20(8):2378–2386
5. Chen G, Yang C, Xie S (2006) Gradient-based structural similarity for image quality assessment. In: IEEE International Conference on Image Processing, pp. 2929–2932
6. Wang Z, Bovik AC, Sheikh HR, Simoncelli EP (2004) Image quality assessment: from error visibility to structural similarity. IEEE Trans Image Process 13(4):600–612
7. Zhang L, Zhang L, Mou X, Zhang D (2012) A comprehensive evaluation of full reference image quality assessment algorithms. In: IEEE International Conference on Image Processing, pp. 1477–1480
8. Liu A, Lin W, Narwaria M (2012) Image quality assessment based on gradient similarity. IEEE Trans Image Process 21(4):1500–1512
9. Xue W, Zhang L, Mou X, Bovik AC (2014) Gradient magnitude similarity deviation: a highly efficient perceptual image quality index. IEEE Trans Image Process 23(2):684–695
10. Murray N, Perronnin F (2014) Generalized max pooling. In: IEEE Conference on Computer Vision and Pattern Recognition, pp. 2473–2480
11. Zhang Z, Wang C, Xiao B, Zhou W, Liu S (2013) Attribute regularization based human action recognition. IEEE Trans Inf Forensics Secur 8(10):1600–1609
12. Zhang Z, Wang C, Xiao B, Zhou W, Liu S (2014) Cross-view action recognition using contextual maximum margin clustering. IEEE Trans Circuits Syst Video Technol 24(10):1663–1668
13. Larson EC, Chandler DM (2010) Most apparent distortion: full-reference image quality assessment and the role of strategy, J Electron Imaging, 19(1), 011006-1–011006-21
14. Ponomarenko N, Lukin V, Zelensky A, Egiazarian K, Carli M, Battisti F (2008) TID2008-a database for evaluation of full-reference visual quality assessment metrics. Adv Mod Radioelectron 10(4):30–45

Human Abnormal Behavior Detection Based on RGBD Video's Skeleton Information Entropy

Ziyang Bian, Tingfa Xu, Chang Su and Xuan Luo

Abstract Conventional human abnormal behavior detection is mostly done in videos taken by visible-light cameras, and it is usually designed for a certain task. In order to solve the human abnormal behavior detection problem in general situation, this paper proposes a detection algorithm based on skeleton information entropy, by using the information from RGBD videos. In this paper, we assume that abnormal behavior is disordered. To sample the accurate features of human, we use RGBD cameras to get the skeleton information. Then, we analyze the information entropy of the angles of the skeleton, and find that the values of the information entropy are significantly higher in abnormal videos than in normal videos. The methods are tested in our database taken by Kinect in our lab and we present superior results whose recall is 92 % and precision is 95.83 %, and accuracy is 94 %.

Keywords Human abnormal behavior detection · RGBD video · Information entropy

1 Introduction

Security problems receive growing attention in recent years, especially in China. Video cameras could help people watch and record important information. But the growing data of video need more and more people to monitor. An auto-abnormal human behaviors detection system is in need to help security guard work efficiently.

The media lab in MIT has developed a human tracking and behaviors recognition system named Pfinder [1]. And IBM has developed an intelligent monitoring

Z. Bian · T. Xu (✉) · C. Su · X. Luo
School of Optoelectronics, Beijing Institute of Technology, Beijing 100081, China
e-mail: tingfaxu@126.com

Z. Bian · T. Xu · C. Su · X. Luo
Key Laboratory of Photoelectronic Imaging Technology and System,
Ministry of Education of China, Beijing 100081, China

Q. Liang et al. (eds.), *Proceedings of the 2015 International Conference on Communications, Signal Processing, and Systems*, Lecture Notes in Electrical Engineering 386, DOI 10.1007/978-3-662-49831-6_74

system especially for airport security. And several Chinese companies like HKvision and Dahua have developed some product for specific security application.

Kinect is a new and widely available commodity sensor platform that incorporates a structured light based depth sensor. Using an on-board ASIC a 11-bit 640 × 480 depth map is generated at 30 Hz. And the quality of this depth map is generally remarkable given the cost of the device. Some start-up companies like DeepGlint are taking the advantage of the depth sensor to make security monitoring accurate and stable [2].

In data mining, anomaly detection is the identification of items, events or observations which do not conform to an expected pattern or other items in a data set [3]. Anomalies are also referred to as outliers, novelties, noise, deviations and exceptions [4].

Three broad categories of anomaly detection techniques exist. Unsupervised anomaly detection techniques detect anomalies in an unlabeled test data set under the assumption that the majority of the instances in the data set are normal by looking for instances that seem to fit least to the remainder of the data set. Supervised anomaly detection techniques require a data set that has been labeled as "normal" and "abnormal" and involves training a classifier. Semi-supervised anomaly detection techniques construct a model representing normal behavior from a given normal training data set, and then testing the likelihood of a test instance to be generated by the learnt model [5, 6].

In this paper, we assume that abnormal behavior is disordered [7]. We use RGBD cameras to get the skeleton information to sample the accurate features of human. Then, we analyze the information entropy of the angles of the skeleton, and train the classifier.

2 Human Detection and Skeleton Extraction in RGBD Video

2.1 The Skeleton Tracking Using NITE Middle Ware and Kinect

Skeletal Tracking allows Kinect to recognize people and follow their actions. Using the infrared (IR) camera and, Kinect can get the depth information. Depth acquisition is enabled by "light coding" technology. The process codes the scene with near-IR light, light that returns distorted depending upon where things are. The solution then uses a standard off-the-shelf CMOS image sensor to read the coded light back from the scene using various algorithms to triangulate and extract the 3D data. Finally, we can get RGBD data from Kinect.

Skeletal tracking is based on the RGBD data by machine learning (ML). First, depth image is used to identify whether each pixel belongs to the user, in order to segment the contour profile of human body and remove the back ground. Second,

different part of human body is classified from the contour profile. Finally, 20 joints are located from the human parts. The algorithm above is integrated in the middle ware named NITE. After we connect Kinect into computer and set up the NITE middle ware, we can recognize up to 15 users in details in the field of view of the sensor with frame rate of 30 fps. The application can locate the joints of the tracked users in space and track their movements over time.

As shown in Fig. 1, using Kinect and NITE middle ware, we can track human skeleton C based on RGB image A and depth image B. Specifically, in the depth image, the pixels' color close to blue means that they are close to the camera. On the contrary, the pixels' color close to red means that they are away from the camera.

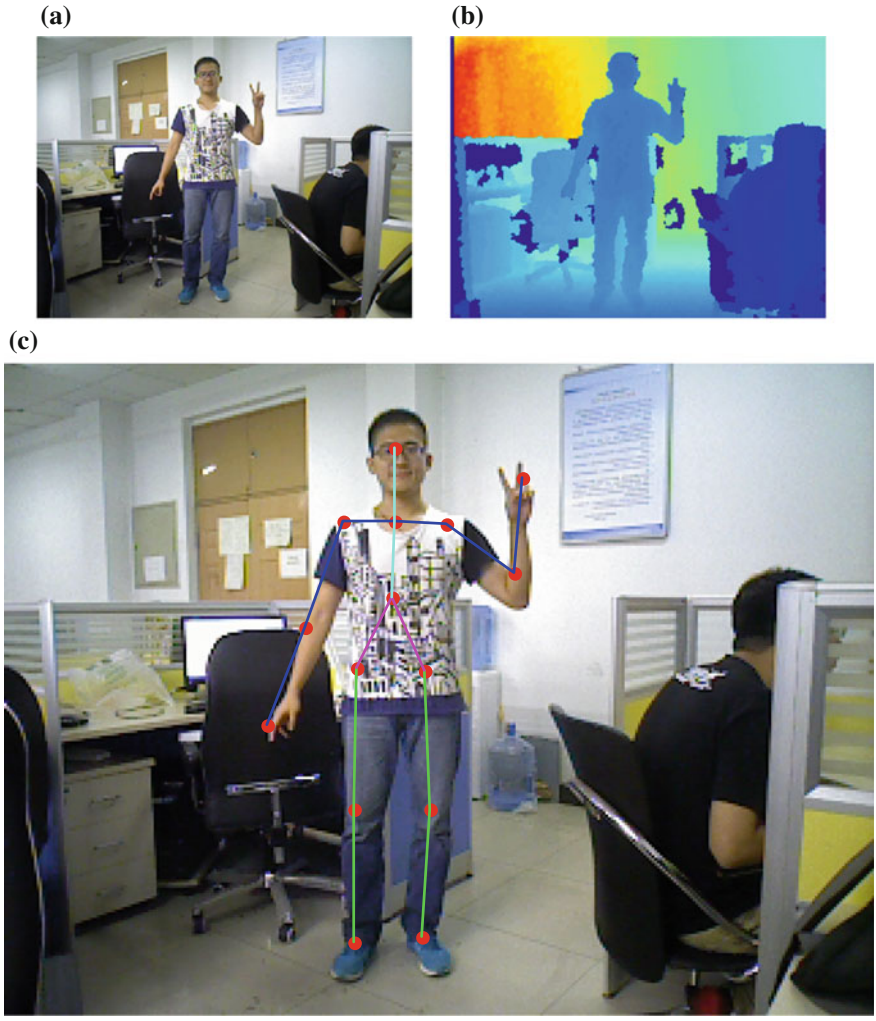

Fig. 1 The skeleton tracking using NITE middle ware and Kinect

2.2 The Feature Extraction of Joint Angles

To sample features in an efficient way, we can extract the joint angles as features, which is invariant in transition and rotation. In this way, the human pose in each frame can be represented by a vector A of angles as follows:

$$A = (a_1, a_2, a_3, \ldots, a_n) \tag{2.1}$$

where n denotes the number of joint angles, and a denotes the value of joint angles. On this basis, the behavior of a person in the video can be represented by a matrix B of angles as below:

$$B = (A_1, A_2, A_3, \ldots, A_m)^T \tag{2.2}$$

where m denotes the number of frames in the video.

The study finds that 15 joints have significant relation with human pose, which are denoted by letters from A to O as shown in Fig. 2.

And the corresponding relation of different letters and body joins is shown in Table 1.

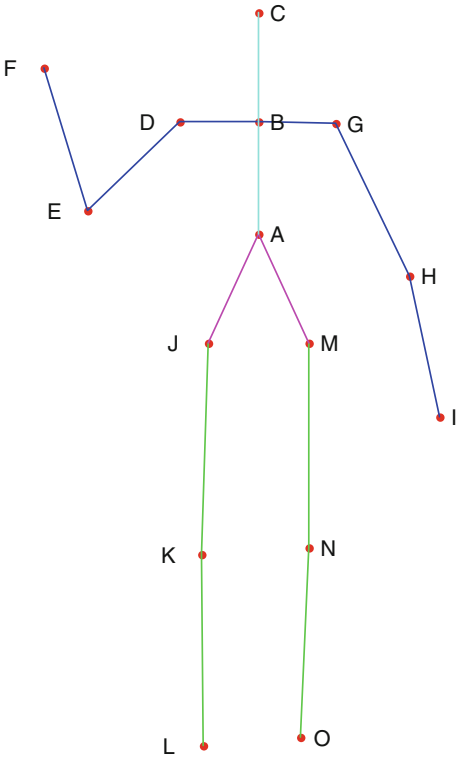

Fig. 2 Fifteen body joints

Table 1 Name of fifteen body joints

ID	Name	ID	Name	ID	Name
A	Torso	F	Right hand	K	Right knee
B	Neck	G	Left shoulder	L	Right feet
C	Head	H	Left elbow	M	Left hip
D	Right shoulder	I	Left hand	N	Left knee
E	Right elbow	J	Right hip	O	Left feet

Table 2 Name of 25 joint angles

ID	Description	ID	Description	ID	Description
1	(ED, EF)	10	(IH, axis + Y)	19	(MN, MA)
2	(HG, HI)	11	(LK, axis + Y)	20	(DB, DE)
3	(KJ, KL)	12	(ON, axis + Y)	21	(GB, GH)
4	(NM, NO)	13	(BC, axis + Y)	22	(AN, AK)
5	(ED, axis + Y)	14	(DG, axis + X)	23	(AO, AL)
6	(HG, axis + Y)	15	(JM, axis + X)	24	(JD, JK)
7	(KJ, axis + Y)	16	(DC, DE)	25	(MG, MN)
8	(NM, axis + Y)	17	(GC, GH)		
9	(FE, axis + Y)	18	(JK, JA)		

As shown in Table 2, 25 joint angles which have significant relation with human pose are extracted from the 15 joints.

In Table 2, angles from 1 to 4 and from 16 to 25 are angles between vectors. And angles from 5 to 13 are angles between vector and axis *Y*. Besides, angles 14 and 15 are angles between vector and axis *X*. The coordinate system is based on Kinect as its original point. And the axis *X* points to the left side of Kinect. And the axis *Y* points to the top of Kinect. And the axis *Z* points to the users in the view of Kinect. To simplify the model, all the angles are 2 dimensional in the image plane.

3 Abnormal Detection Based on Information Entropy

3.1 The Concept of Information Entropy

In information theory, entropy is the expected value of the information contained in each message received. It is a measure of unpredictability of information. In discrete system, the entropy *H* of a discrete random variable *X* with possible values $\{x_1, \ldots, x_n\}$ and probability mass function *P(X)* can explicitly be written as:

$$H(X) = \sum_{i=1}^{n} P(x_i)I(x_i) = -\sum_{i=1}^{n} P(x_i)log_b P(x_i) \tag{3.1}$$

Here I is the information content of X. $I(X)$ is itself a random variable. And b is the base of the logarithm used. Common values of b are 2, Euler's number e, and 10, and the unit of entropy is shannon for $b = 2$, nat for $b = e$, and hartley for $b = 10$. When $b = 2$, the units of entropy are also commonly referred to as bits.

Information entropy is one of several ways to measure diversity. Entropy is defined in the context of a probabilistic model. Independent fair coin flips have entropy of 1 bit per flip. A source that always generates a long string of B's has entropy of 0, since the next character will always be a 'B'. The example shows that the bigger the entropy is the more disordered the system.

3.2 *The Abnormal Detection Algorithm Based on Information Entropy*

Most abnormal behaviors like fight, robbery and chaos have a common feature that they are disordered. On the contrary, normal behaviors like walk and greeting are less disordered than abnormal behaviors. So to calculate the information entropy of skeleton can be a good method to distinguish abnormal behaviors.

18 clips of videos which have 300 frames per clip are taken in our lab using Kinect. Half of them are abnormal and the other half of them are normal. After we get the skeleton information using NITE, we discretely sample the joint angles in the interval of 5°. Then, each joint angle's information entropy in each video is calculated. When more than one person shows up in one clip, we will choose the highest entropy of each joint. Finally, we get the mean information entropy of all the joint angles in each video. The results are shown in Fig. 3. The symbols of plus denote the values of entropy of abnormal videos, and the symbols of circle denote the values of entropy of normal videos. The results show that the abnormal behaviors have higher value if entropy than the normal ones, and that using a

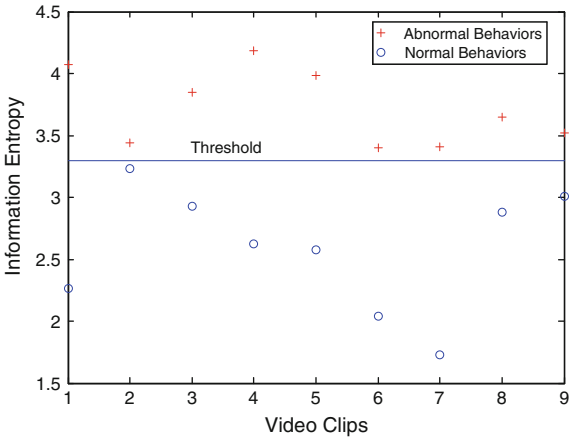

Fig. 3 The information entropy of different video clips of different type

threshold of entropy $H = 3.4$ can distinguish abnormal behavior well. Further studies have been done, and we find that the change of discrete interval and frames only impact the threshold but have no influence on the relative value of entropy. So when we keep the discrete interval as 5°, and the total frames as 300, the threshold of entropy $H = 3.4$ will still work.

4 Experimental Evaluation

4.1 Data Set

Because there is no common data set of abnormal behaviors in RGBD video, we have to make it ourselves. 100 clips of videos which have 300 frames (10 s) per clip are taken in our lab using Kinect. 50 of them are abnormal and the other 50 of them are normal. The number of person shown in the same video is from 1 to 4. And abnormal behaviors include fight, robbery and chaos. And normal behaviors include walk, hug and greeting.

Kinect is connected to MATLAB and all the sampling and calculating scripts run in MATLAB. Besides, Open Natural Interaction (OpenNI), an open source software project focused on certifying and improving interoperability of natural user interfaces and organic user interfaces for Natural Interaction (NI) devices, are set up to connect Kinect to computer. And the NITE middle ware is also set up to enable skeleton tracking. The software environment makes kinect able to track up to 15 users at the same time.

The typical frames of video data set are shown in Fig. 4. The pictures A and B on the top show abnormal behaviors like fight and robbery, and the pictures C and D on the bottom show normal behaviors like greeting and walking.

4.2 Results

The results are shown in Table 3. True Positive (TP) means that our classifier classifies the abnormal ones as abnormal ones. And False Positive (FP) means that our classifier classifies the normal ones as abnormal ones. And True Negative (TN) means that our classifier classifies the true normal ones as normal ones. And False Negative (FN) means that our classifier classifies the abnormal ones as normal ones.

For different threshold, we find that if we reduce the threshold, the recall rate will rise. In abnormal behavior detection, the recall is more important than precision or accuracy. So threshold $T = 3.0$ performs better than $T = 3.4$.

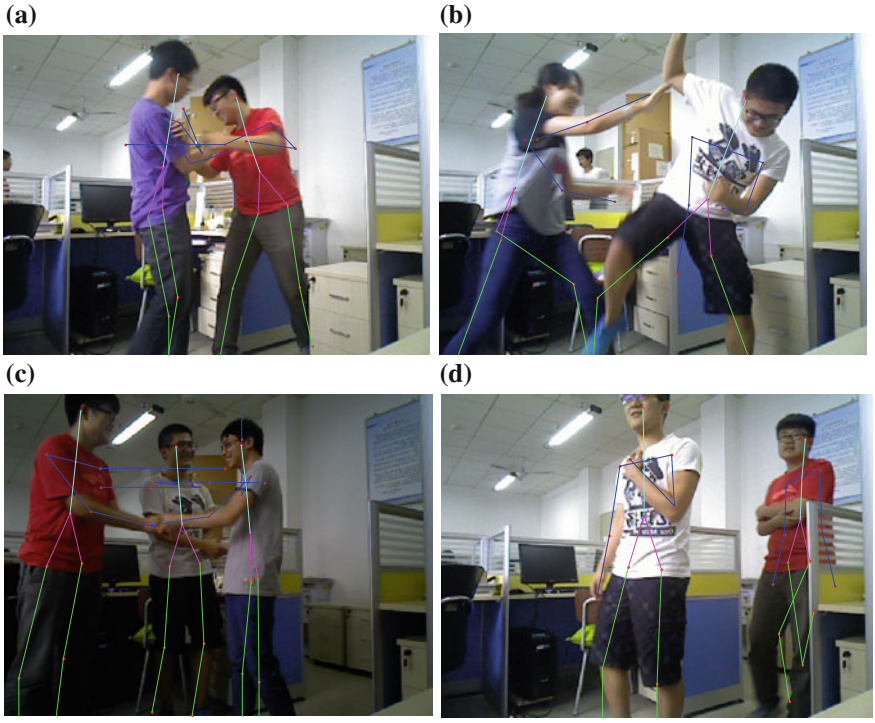

Fig. 4 The abnormal behavior and normal behavior RGBD video data set

Table 3 Results of test data set

Threshold	TP	FP	TN	FN	Precision (%)	Recall (%)	Accuracy (%)
$T = 3.4$	46	2	48	4	95.83	92	94
$T = 3.0$	50	7	43	0	87.72	100	93

5 Conclusion

The availability of commodity depth sensors such as Kinect and Xtion has the potential to revolutionize the field of security and monitoring. In this work we have taken a step towards bringing the ability to detect human abnormal behaviors which are disordered in general. The key concept in our abnormal behaviors detection algorithm is that the information entropy of skeleton angles in the video clips can distinguish abnormal behaviors with an excellent performance.

There are several ways in which the algorithm could be extended. First, the data set is still small. And a bigger data set can make the algorithm more reliable. Second, the algorithm needs the NITE middle ware and OpenNI environment, so that it can only run on personal computer. More work remains to be done to make it run in real-time embedded systems such as DSP or FPGA.

The final interesting direction is to perform abnormal human behaviors detection in common area and in real time.

Acknowledgments This work was supported by the National Natural Science Foundation of China [grant numbers 61172178, 61371132 and 61471043], the Specialized Research Fund for the Doctoral Program of Higher Education [grant number 20121101110022], and the International Science & Technology Cooperation Program of China [grant number 2014DFR10960].

References

1. Wren CR, Azarbayejani A, Darrell T, Pentland AP (1997) Pfinder: Real-time tracking of the human body. IEEE Trans Pattern Anal Mach Intell 19(7):780–785
2. Zhang Z, Liu Y, Li A, Wang M (2014). A novel method for user-defined human posture recognition using Kinect. In: 2014 7th International Congress on Image and Signal Processing (CISP), pp. 736–740. IEEE, Oct
3. Chandola V, Banerjee A, Kumar V (2009) Anomaly detection: A survey. ACM Comput Surv 41(3):1
4. Hodge VJ, Austin J (2004) A Survey of Outlier Detection Methodologies. Artif Intell Rev 22 (2):85
5. Popoola OP, Wang K (2012) Video-based abnormal human behavior recognition—a review. IEEE Trans Syst Man Cybern Part C Appl Rev 42(6):865–878
6. Kim H, Kim I, Chung, TM (2014). Abnormal behavior detection technique based on big data. In Frontier and Innovation in Future Computing and Communications, pp. 553–563. Springer, Netherlands
7. Mehran R, Oyama A, Shah M (2009). Abnormal crowd behavior detection using social force model. In: IEEE Conference on Computer Vision and Pattern Recognition, 2009. CVPR 2009, pp. 935–942. IEEE, June

Image Restoration Using the Alternation Direction Method Based on the Gradient Cepstrum Analysis PSF Estimation Strategy

Mingzhu Shi

Abstract Image restoration is a highly ill-posed problem and usually be regularized by alternating estimating point spread function (PSF) and recovering blur image, which lead to high complexity and low efficiency. In this paper, we propose an efficient PSF estimation algorithm based on gradient cepstrum analysis (GCA). Then, to verify the accuracy of the strategy, estimated PSFs are used to image deconvolution step, which exploits a novel total variation model coupling with a gradient fidelity term. We also adopt an alternating direction method (ADM) numerical algorithm with rapid convergence and high robustness to optimize the energy function. Experimental results show that our scheme can estimate PSF rapidly and produce comparable results without involving long time consuming.

Keywords Point spread function (PSF) · Gradient cepstrum analysis · Total variation (TV) · Image restoration

1 Introduction

Image restoration has long been a fundamental research problem in many science and engineering areas. Assuming that the imaging system is linear space-invariant, the image degraded process can be modeled as convolution of a latent image with a blur kernel. The progress is described as

$$g(x,y) = f(x,y) \otimes h(x,y) + n(x,y) \tag{1}$$

where (x,y) denotes the pixel coordinate in spatial domain. $g(x,y)$, $f(x,y)$ and $n(x,y)$ represent the observed blur image, the latent image, and the additive noise,

M. Shi (✉)
College of Electronic and Communication Engineering, Tianjin Normal University, Tianjin 300387, China
e-mail: smz_tjnu@163.com

Q. Liang et al. (eds.), *Proceedings of the 2015 International Conference on Communications, Signal Processing, and Systems*, Lecture Notes in Electrical Engineering 386, DOI 10.1007/978-3-662-49831-6_75

respectively. $\otimes$ denotes the convolution operator, and $h(x, y)$ is the blur kernel, which often be described as a point spread function (PSF).

Recent state-of-the-art PSF estimation algorithms tend to deploy effective priors about the statistics of natural images for single image deblurring. Fergus [1] use a zero-mean mixture-of-Gaussian model for natural image gradients distribution Krishan [2] models the heavy-tailed distribution by hyper-Laplacian priors and adopts an alternating minimization scheme, which is fast optimized by a lookup table (LUT) algorithm. Levin et al. [3] also propose an efficient marginal likelihood optimization method based on the maximum a posteriori (MAP). Yet it involves a challenging marginalization over latent images and computational complexity. Although above algorithms obtain good results, they are often time consuming. In this paper, we propose a novel efficient gradient cepstrum analysis (GCA) strategy into the single blurred image for PSF estimation.

The rest of this paper is organized as follows. In Sect. 2, we make a description of the proposed GCA strategy. Section 3 describes our novel TV-based image restoration model and the ADM numerical algorithm. Experimental results are shown in Sect. 4. Finally, a conclusion is made in Sect. 5.

2 PSF Estimation by Gradient Cepstrum Analysis Strategy

In this section, we focus on the PSF estimation process and the details are described in the following subsections.

2.1 PSF Estimated from the Blurred Image Gradient Cepstrum

The linear space-invariant degrade process is described as Eq. (1). In the case of ignoring the additive noise, it is formulated in frequency domain as

$$G(u, v) = F(u, v)H(u, v) \tag{2}$$

where (u, v) represents the index in frequency domain, $G(u, v)$, $F(u, v)$ and $H(u, v)$ denote the discrete Fourier transform of the blurred image, PSF, and latent image, respectively. In image restoration technology, cepstrum of the image $g(x, y)$ is defined as

$$C_g(p, q) = FFT^{-1}[|\log|(G(u, v)||] \tag{3}$$

where (p, q) and $C_g(p, q)$ indicate the index in cepstrum domain and the cepstrum of image $g(x, y)$, respectively. FFT^{-1} denotes the inverse Fourier transform. In practical applications, to avoid the ill-posed problem caused by $|G(u, v)| = 0$, $C_g(p, q)$ is often defined as

$$C_g(p, q) = FFT^{-1}\{\log[1 + |(G(u, v)|]\} \tag{4}$$

The cepstrum of degrade progress is described as

$$C_g(p, q) = C_f(p, q) + C_h(p, q) \tag{5}$$

where $C_f(p, q)$ and $C_h(p, q)$ represent the cepstrum of the latent image and the PSF. Obviously, the convolution in spatial domain is translated into the additive form, which is easy to separate the information of the PSF.

Considering that the laplace operator is isotropic and rotation invariant, we choose it as a gradient operator. It can reflect second-order differential properties of the image, thus extracting points, lines, and boundaries for the image. It is also known as a boundary extraction operator and defined $\nabla^2 = \partial^2/\partial x^2 + \partial^2/\partial y^2$. There is $\nabla^2 g(x, y) = \nabla^2 f(x, y) \otimes h(x, y)$. We get $C_{\nabla^2 g} = C_{\nabla^2 f} + C_h$. In this paper, $C_{\nabla^2 f}$ is proved to be approximate to a delta function in the following experiment, then

$$C_{\nabla^2 g} \approx C_h \tag{6}$$

It means that we can estimate the PSF by analyzing the cepstrum of the gradient of the blur image, just as the above-mentioned strategy, gradient cepstrum analysis (GCA).

2.2 Phase Retrieval

The PR [4, 5] technique is adopted here to derive the phase of the PSF. It recovers the phase just from the magnitude of a signal's Fourier transform, which is the iterative Fourier transform algorithm. The iterative process includes three constraints, i.e., positivity, compact support, and module constraints. To be exact, positivity and compact support constraints are spatial domain constraints and the module belongs to the frequency domain constraints. The flow chart for the algorithm is shown in Fig. 1.

In general case, iterative Fourier transforms for the image PR technique will take a long computing time, but in this paper, the PSF size is much smaller than that of the image and constrained by the module and the compact support. Therefore, the weakness of long time consuming is not exposed in our PSF estimation.

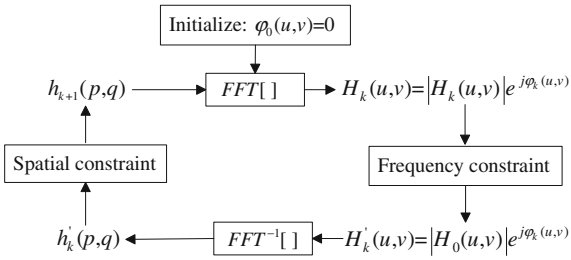

Fig. 1 Flow chart of the iterative Fourier transform algorithm

3 Proposed Model and Numerical Algorithm

In this section, we propose a total variation regularized model coupling with an image gradient fidelity term to evaluate the accuracy of our PSF estimation strategy and an alternating direction method (ADM) [6] with rapid and stable convergence is used to optimize the energy function.

3.1 The Proposed Model

Total variation image restoration has advantage of suppressing ringing effects and preserving sharp edges. However, it still has a potential shortcoming that does not meet the morphological principle of image processing, which is often referred to the staircase effect in the recovered image [7, 8]. In order to use the unique advantage of TV regularization and avoid its disadvantage,we propose a novel TV-based regularized model coupling with a gradient fidelity term to recover the latent image from the single blurred image.

The model is defined as

$$\min \Phi_{reg}(f) + \beta\Phi_{fid}(f,g) + \gamma\Phi_{fid}(\nabla f, \nabla g) \tag{7}$$

where $\Phi_{reg}(f)$ regularizes the solution by TV norm, and $\mathrm{TV}(f) = \sum_i \|D_i f\|$, i indexes pixels in the image. D is the first-order finite difference operator $D_x = [1, -1], D_y = [1, -1]^T$. $\Phi_{fid}(f,g)$ called the energy fidelity term is to measure the violation of the relation between f and the observation g. It is constrained by the noise and based on the assumption that noise random variables for all pixels are independent and identically distribute and each of them follows a Gaussian distribution. We define $\Phi_{fid}(f,g) = \|f \otimes h - g\|^2/2$. $\Phi_{fid}(\nabla f, \nabla g)$ is the gradient fidelity term that constraints the gradient of the recovered image to be similar with the gradient of the latent image. It plays an important part in maintaining image smoothing and suppressing the

staircase effect. And then, we get $\Phi_{fid}(\nabla f, \nabla g) = \|\nabla f - \nabla g\|^2/2$. β and γ are constraint coefficients chosen as constants. Then, we obtain the energy function

$$E(f) = \sum_i \left[\|D_i f\| + \frac{\beta}{2}\|f \otimes h - g\|^2 + \frac{\gamma}{2}\|\nabla f - \nabla g\|^2 \right] \tag{8}$$

3.2 Numerical Algorithm

In this paper, we use the ADM to optimize the energy function and realize fast image deconvolution with the purpose of not covering the fast advantage of our PSF estimation strategy.

We introduce an auxiliary variable $w = (w_1, w_2)^T$, where $w_1 = D_x f$, $w_2 = D_y f$ and the iterative parameter λ. Let $\nabla f \approx D_i f$ and the augmented Lagrangian function of the Eq. (8) is expressed as

$$\begin{aligned} L_A(f, w, \lambda) = \sum_i \left[\|w_i\| - \lambda_i^T (w_i - D_i f) + \frac{\alpha}{2}\|w_i - D_i f\|^2 + \frac{\gamma}{2}\left\|w_i - (\nabla g)_i\right\|^2 \right] \\ + \frac{\beta}{2}\|f \otimes h - g\|^2 \end{aligned} \tag{9}$$

We fix f^k, λ^k and optimize w. Equation (9) is transformed to minimizing

$$L_A(f^k, w, \lambda^k) = \|w_i\| + \frac{\alpha}{2}\left\|w_i - (D_i f^k + \frac{1}{\alpha}(\lambda^k)_i)\right\|^2 + \frac{\gamma}{2}\|w_i - \nabla g\|^2. \tag{10}$$

By solving its Euler-Lagrange equation, we obtain the solution that is given explicitly by the two-dimensional shrinkage [9]

$$w_i^{k+1} = \text{shrink}\left(D_i f^k + \frac{1}{\alpha}(\lambda^k)_i + \frac{\gamma}{\alpha}(\nabla g)_i, \frac{1+\gamma}{\alpha}\right) \tag{11}$$

Then, fix λ^k, w^{k+1} and optimize f. Equation (11) is transformed to minimizing

$$L_A(f, w^{k+1}, \lambda^k) = \sum_i (\lambda_i^T D_i f + \frac{\alpha}{2}\|w_i - D_i f\|^2) + \frac{\beta}{2}\|f \otimes h - g\|^2 \tag{12}$$

The minimization of Eq. (12) with respect to f is a least squares problem and its corresponding normal equation is

$$(D^T D + \frac{\beta}{\alpha} h^T h) f = D^T (w^{k+1} - \frac{1}{\alpha}\lambda^k) + \frac{\beta}{\alpha} h^T g \tag{13}$$

The ADM numerical algorithm can be described as follows.

(i) Initialization: $f = g, \lambda = \lambda_0, \alpha > 0, \beta > 0, \gamma > 0$;
(ii) Iteration:

- Compute w^{k+1} for given (f^k, λ^k) .
- Compute w^{k+1} via Eq. (13).
- Update λ^{k+1} via $\lambda^{k+1} = \lambda^k - \alpha(w^{k+1} - Df^{k+1})$.

(iii) Repeat (ii) and stop until $\left\|f^{k+1} - f^k\right\| / \max\left\{\left\|f^k\right\|, 1\right\} \leq tol$. Here *tol* is set to 10^{-3}.

4 Experimental Results

In order to evaluate the performance of our scheme, we carry out a series experiments and compare with some state-of-the-art algorithms. First, we carry out the experiment on the synthetic blurred image from [3] and their corresponding PSFs. The size of the tested kernel is 27 × 27 and results are shown in Fig. 2. Figure 2a and b are the cepstrum of the PSF itself and the cepstrum of the gradient of blur image. Figure 2c is the real PSF and Fig. 2d is the estimated PSF by our scheme. It can be seen that our estimated PSF is extremely similar to the true PSF.

It should be noted that original result might be a mirrored or shifted version of the true PSF, because all of them have the same cepstrum function. However, it is easy to validate and correct since wrong PSFs give very different deblurred result. Experimental results on other tested PSFs are shown in
We take the estimated PSFs to image deconvolution and adopt signal to noise (SNR) of restored images to evaluate the accuracy of our proposed PSF estimated method, as shown in the bottom-right of images in Fig. 3. Figure 3a is a clear image and degraded by convolving with the mentioned 13 × 13 PSF shown in the bottom-right in Fig. 3b. Figure 3c and d are results by Fergus and Levin's methods, respectively. Figure 3e provides the result by Hu's method that using gradient

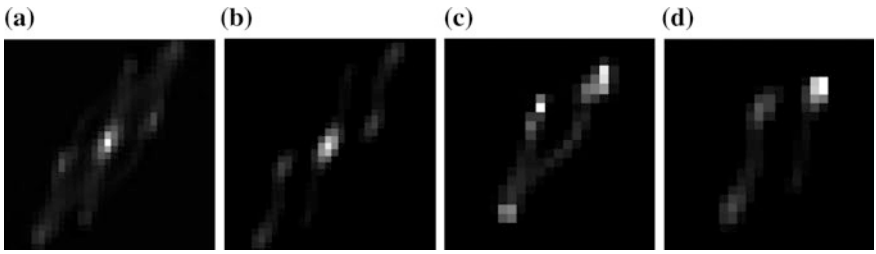

Fig. 2 The GAC of the blur image. **a** The cepstrum of the PSF itself. **b** The cepstrum of the gradient of blur image. **c** The true PSF. **d** Our estimated PSF

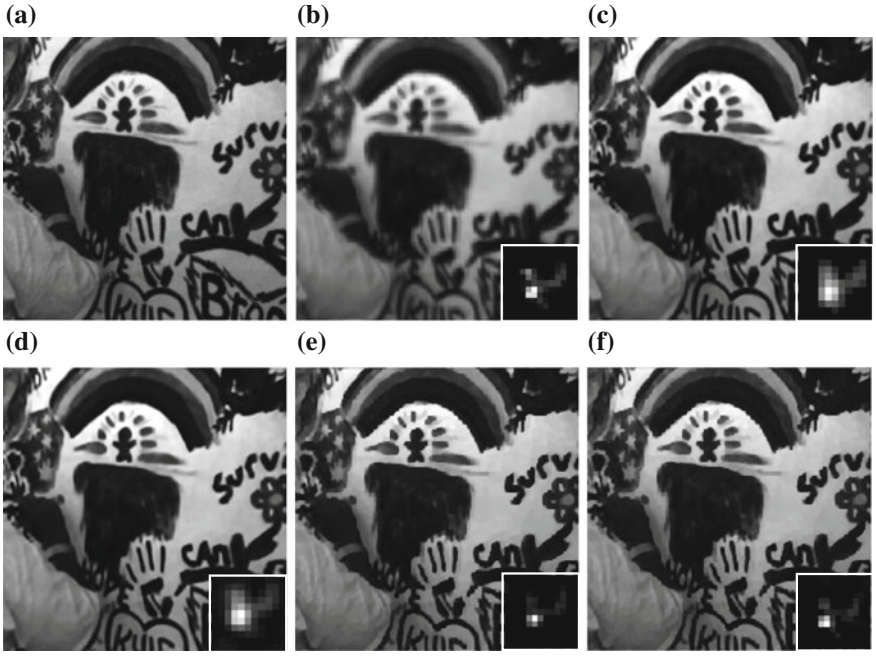

Fig. 3 Estimated PSFs and corresponding restored images by different algorithms. **a** The clear image. **b** Blurred image and the degrade PSF (SNR = 10.47). **c** Ref [1] (SNR = 15.76). **d** Ref. [3] (SNR = 18.90) **e** Ref. [4] (SNR = 16.04) **f** Our result (SNR = 17.58)

domain correlation based on a patch-based image degradation model. Figure 3f shows our result. Compared with other three state-of-art algorithms, it is evident that our scheme can also get the ideal restoration in visual although the SNR is slightly lower.

We also test other PSFs and SNRs between original images and recovered images using different estimated PSFs and computation time are listed in Table 1. As can be seen from the result data, our scheme can not only obtain a good recovery result, but also shortens the compute time remarkably.

Table 1 Processing time using different algorithms for PSFs in each size

PSF size	Time (s)			Time (s)		
	Ref. [1]	Ref. [3]	Ref. [4]	PSF estimation	Image restoration	Total
13 × 13	30.52	127.80	6.32	1.45	2.57	4.02
17 × 17	33.93	138.57	7.69	1.57	3.76	5.33
21 × 21	44.03	146.95	8.73	1.69	4.41	6.10
23 × 23	53.47	154.20	8.91	1.78	4.45	6.23
27 × 27	56.20	155.79	9.48	1.89	5.38	7.27

5 Conclusions

In this paper, an efficient PSF estimated strategy has been proposed based on image gradient cepstrum analysis. PSF power information is obtained from cepstrum properties of the blur image gradient and its phase information is retrieved by PR technique. To verify the accuracy of the strategy, the estimated PSF is used for recovering image with a novel total variation image restoration model that is coupling with a gradient fidelity term. An alternating direction method (ADM) numerical algorithm with rapid convergence and high robustness is adopted to optimize the energy function. Both synthetic and real blur experiments show that our scheme can rapidly produce comparable results with some state-of-the-art algorithms and greatly shorten the computing time.

Acknowledgments We thank the reviewer for helping us to improve this paper. This work is supported by National Science Foundation of China (Grant No.61501328) and Doctoral Found of Tianjin Normal University (Grant No.52XB1406).

References

1. Fergus R, Singh B, S.T. Hertzmann A, Roweis ST, Freeman W (2006) Removing camera shake from a single photograph. ACM Trans. Graph 25:787–794
2. Krishan D, Fergus R (2009) Fast image deconvolution using Hyper-Laplacian priors. Adv NIPS 22:1033–1041
3. Levin A, Wesis Y, Durand F, Freeman WT (2011) Efficient marginal likelihood optimization in blind deconvloution. In: IEEE conference on CVPR, Colorado Spring, CO, USA, pp 2657–2665
4. Hu W, Xue J, Zheng NR (2012) PSF estimation via gradient domain correlation. IEEE T. Image Process 21:386–392
5. Paganin D, Gureyev TE, Pavlov KM (2004) Phase retrieval using coherent imaging systems with linear transfer functions. Opt Commun 234:87–105
6. He BS, Xu MH, Yuan XM (2011) Solving large-scale least squares covariance matrix problems by alternating direction methods. SIAM J Matrix Anal Appl 32:136–152
7. Vogel C.R., Oman, ME (1998) Fast, robust total variation-based reconstruction of noisy, blurred images. IEEE Trans. Image Process 7:813–824
8. Goldstein T, Osher S (2009) The split Bregman method for L1-regularized problems. SIAM J Imaging SCI 2:323–343
9. Beck A, Tebolle M (2009) A fast iterative shrinkage-thresholding algorithm for linear inverse problems. SIAM J Imaging SCI 2:183–202

Image Denoising via Modified Multiple-Step Local Wiener Filter and Quaternion Wavelet Transform

Xiaobo Zhang

Abstract This paper proposes an image denoising algorithm via the modified multiple-step local Wiener filter in the quaternion wavelet transform domain. The multiple-step local Wiener filter has shown good performance on removing the Gaussian white noise. The quaternion wavelet transform (QWT) can provide a richer scale-space analysis when compared with wavelet transform or complex wavelet transform, and which is an efficient multiscale geometric analysis method. So the combination between them can remove noise more effectively and efficiently. Experimental results verify that the proposed method improves the denoising performance significantly and is very efficient in computation time.

Keywords Image denoising · Multiple-step local Wiener filter · Quaternion wavelet transform (QWT)

1 Introduction

Image quality is often degraded by noise since the imperfection of image acquisition and transmission channels. So the denoising became an essential step in image analysis. The aim of image denoising algorithms is to reconstruct the original image from its noisy observation as accurately as possible when reducing the noise level. Over the past several decades, many denoising techniques have been developed. Transform domain methods by using wavelets do well in removing the noise of images. Due to the sparsity of wavelet coefficients, noise is uniformly spread throughout the coefficients in the wavelet domain, while image information is mainly concentrated on the few largest ones. So, noise can be effectively removed by using different coefficient shrinkage methods, including BayesShrink [1], ProbShrink [2], BiShrink [3] and SUREShrink [4] and so on.

X. Zhang (✉)
Institute of Graphics and Image Processing, Xianyang Normal University, Xianyang 712000, China
e-mail: zhangxiaobo9876@163.com

Q. Liang et al. (eds.), *Proceedings of the 2015 International Conference on Communications, Signal Processing, and Systems*, Lecture Notes in Electrical Engineering 386, DOI 10.1007/978-3-662-49831-6_76

Although wavelet transform has been widely used in the design of image denoising, wavelets are only very efficient in dealing with point singularities. So, many new wavelets are proposed and used in image processing. They include contourlets, ridgelets, curvelets, shearlets, etc. However, these developed wavelets are a little expensive in computational time. The quaternion wavelet transform (QWT) proposed by Corrochano [5, 6] is an effective multiscale analysis tool in the process of image processing. It is designed by employing the advantages of discrete wavelet transform (DWT) and dual-tree complex wavelet transform (DT-CWT) [7]. So, the QWT attracted researcher's attention.

Recently, in [8], Shan et al. proposed a new image denoising algorithm via bivariate shrinkage based on QWT (QWT-Bishrink). Although this method is very simple, it did not produce the impressive denoised results. At this time, we noted that the diffusion scheme has been introduced into wavelet domain for image denoising unlike traditional wavelet shrinkage strategy. The iterative scheme based on diffusion has show good ability of removing noise.

So, in this paper, we also proposed an image denoising algorithm. It operates in the QWT domain. The multiple-step local Wiener filter [9] is modified to shrinkage the noisy coefficients. We also compare the proposed method with other related image denoising methods. In view of the combination between QWT and multiple-step local Wiener filter, our research is original.

The paper is organized as follows: Sect. 2 presents the proposed method. The QWT, modified multiple-step local Wiener filter and the algorithm structure are shown in turn. Section 3 provides the numerical simulation results. The good performance of the proposed method is demonstrated. Finally, Sect. 4 concludes the paper.

2 The Proposed Method

In this section, the denoising of an image corrupted by white additive independent white Gaussian noise with zero mean and variance σ^2 will be considered. Now, we describe the proposed algorithm in detail.

2.1 QWT

The QWT was invented in [5, 6] and is an extension of real wavelet transform and complex wavelet transform. It has one magnitude and three phase angles. Two phases represent local image shifts, and the third phase captures the image texture information.

Suppose $\phi(x, y)$ is a real separable scaling function, and $\psi^D(x, y)$, $\psi^V(x, y)$ and $\psi^H(x, y)$ are mother wavelets, respectively. The 2D QWT is written in terms of separable products as follows:

$$\begin{cases} \phi(x,y) = \phi_h(x)\phi_h(y) + I\phi_g(x)\phi_h(y) + J\phi_h(x)\phi_g(y) + K\phi_g(x)\phi_g(y) \\ \psi^D(x,y) = \psi_h(x)\psi_h(y) + I\psi_g(x)\psi_h(y) + J\psi_h(x)\psi_g(y) + K\psi_g(x)\psi_g(y) \\ \psi^V(x,y) = \phi_h(x)\psi_h(y) + I\phi_g(x)\psi_h(y) + J\phi_h(x)\psi_g(y) + K\phi_g(x)\psi_g(y) \\ \psi^H(x,y) = \psi_h(x)\phi_h(y) + I\psi_g(x)\phi_h(y) + J\psi_h(x)\phi_g(y) + K\psi_g(x)\phi_g(y) \end{cases} \tag{1}$$

In above, $\phi_g(x) = \mathrm{H}\phi_h(y)$ and $\psi_g(x) = \mathrm{H}\psi_h(y)$ (H represents Hilbert Transform). The I, J, and K obey the following rule: $I^2 = J^2 = K^2 = -1$, $IJ = -JI = K$, $IK = -KI = J$ and $JK = -KJ = I$.

The QWT can be implemented with separable filter banks and is carried out by using a dual-tree algorithm with linear computational complexity [9]. Compared to wavelet transform, QWT is shift invariance and has good directional selectivity. Compared to complex wavelet transform, QWT has abundant phases capturing the geometric structure of the nature images.

2.2 Modified Multiple-Step Local Wiener Filter

Since the QWT is linear transform, the problem can be formulated as:

$$v(i,j) = s(i,j) + n(i,j) \tag{2}$$

where $v(i, j)$ is the noisy quaternion wavelet coefficient, $s(i, j)$ is the true coefficient, and $n(i, j)$ is the noise which is Gaussian distribution with zero mean and variance $\hat{\sigma}^2$ which is estimated by using Monte–Carlo technique and independent of $s(i, j)$.

In [9], the multiple-step local Wiener filter scheme is formulated by multiple successive steps, and the output for one step is used as the input for next step.

Let D is QWT, D^{-1} inverse QWT, w_μ local Wiener filter used in every high frequency subband at the μth step, I_0 original noisy image, and I_λ the estimate of noise-free image.

$$I_\lambda = D^{-1}(w_\lambda \cdots w_\mu \cdots w_2 w_1 (DI_0)), (\mu = 1, 2, \ldots, \lambda) \tag{3}$$

In above, $DI_0 = v$.

Let s_μ and σ_μ^2 represent the signal to be restored and noise variance at the μth step Wiener filter, respectively. So, at the μth step, the form of the optimal Wiener filter is as follows:

$$w_\mu(i,j) = \frac{E\{s_\mu^2(i,j)\}}{E\{s_\mu^2(i,j)\} + \sigma_\mu^2} \tag{4}$$

The $E\{s_\mu^2(i,j)\}$ must be estimated since it is unknown. Because of the independence of the signal and the noise, and let $v_0 = v$, we can write

$$E\{s_\mu^2(i,j)\} = E\{v_{\mu-1}^2(i,j)\} - \sigma_\mu^2 \tag{5}$$

In Eq. (5), the expected value $E\{v_{\mu-1}^2(i,j)\}$ needs to be estimated. We assume that these estimates are computed by averaging the squared values of $v_{\mu-1}(i,j)$ in a window centered at (i,j), according to the formula:

$$q_\mu(i,j) = \frac{1}{M}\sum_{k=-R}^{R}\sum_{l=-R}^{R} v_{\mu-1}^2(i-k, j-l), M = (2R+1)^2 \tag{6}$$

After approximation of the expected value $E\{v_{\mu-1}^2(i,j)\}$ by a sample's mean, $E\{v_{\mu-1}^2(i,j)\} \approx q_\mu(i,j)$, the expected value $E\{s_\mu^2(i,j)\}$ can be re-expressed as

$$E\{s_\mu^2(i,j)\} \approx q_\mu(i,j) - \sigma_\mu^2 \tag{7}$$

Inserting Eq. (7) into Eq. (4), the Wiener filter is turned into

$$w_\mu(i,j) = \frac{\max(q_\mu(i,j) - \sigma_\mu^2, 0)}{\max(q_\mu(i,j) - \sigma_\mu^2, 0) + \sigma_\mu^2} \tag{8}$$

The estimated value v_μ of the restored coefficient s_μ at the μth step is then computed from the relation:

$$v_\mu = w_\mu v_{\mu-1} \tag{9}$$

The multiple-step local Wiener filter is presented by taking noise variance σ_μ^2 as $(1/\lambda)\hat{\sigma}^2$. It has been successfully implemented in DT-CWT domain. To effectively use the multiple-step local Wiener filter, we modify noise variance σ_μ^2 of every wiener filter as $(\eta/\lambda)\hat{\sigma}^2$. The η control the denoising amount of each step Wiener filter. The modified multiple-step local Wiener filter is turned into original multiple-step local Wiener filter in [9] when $\eta = 1$.

2.3 Algorithm Structure

We summarize the algorithm as follows:

(1) Perform QWT on the original noisy image.
(2) Modify the QWT coefficients by using modified multiple-step local Wiener filter.
(3) The noise-free image is finally estimated by computing the inverse QWT.

3 Experimental Results

In this section, the performance of the proposed algorithm will be demonstrated. Since the SURE-LET method armed with Stein's unbiased risk (SURE) and linear expansion of thresholds (LET) is very efficient. Furthermore, in term of [4], the SURE-LET method outperforms some state-of-the-art wavelet-based denoising methods, such as BayesShrink, ProbShrink, BiShrink, etc. For this, in this paper, we focus on the comparison between the proposed method and SURE-LET method.

For the proposed method, the QWT with five-level decomposition is used. The local window sizes are 5×5, 3×3, 1×1, 1×1, and 1×1 from the finest scale to the coarsest scale. The η and λ is taken to 1.05 and 2, respectively. As for the SURE-LET approach, the parameters have been set according to the values given in [4]. The corresponding Matlab code is provided on author's websites.

Table 1 presents the PSNR comparison of the SURE-LET approach and proposed method. Under all cases, the proposed method obtains higher PSNRs. Figure 1 presents the visual comparison of the SURE-LET approach and proposed method. The noisy Barbara image with $\sigma = 10$ was processed with two methods. We can see that the proposed method better preserve the image features, such as edges and details, and so on when removing noises well. Table 2 presents the comparison of the running time between two methods. Compared to the SURE-LET approach, the proposed method can save more time. In a word, the proposed method is more efficient and effective when dealing with noisy images.

In addition, QWT-Bishrink method based on QWT and bivariate shrinkage is also used to compare since this simple and effective method is carried out in QWT domain. But, we only present the reported PSNRs results since we have no source code. From Table 3, it is obvious that the proposed method is superior to QWT-Bishrink.

Table 1 Comparison of SURE-LET approach and proposed method in term of PSNR (dB)

σ	5	10	15	20	5	10	15	20
Method	Peppers				House			
SURE-LET	37.17	33.18	30.91	29.33	37.88	34.29	32.32	30.93
Proposed	**37.38**	**33.52**	**31.29**	**29.70**	**38.46**	**34.62**	**32.54**	**31.08**
Method	Al				Bridge			
SURE-LET	38.43	34.90	32.97	31.64	35.06	30.22	27.84	26.36
Proposed	**38.83**	**35.30**	**33.35**	**31.95**	**35.20**	**30.44**	**28.02**	**26.48**
Method	Barbara				Boat			
SURE-LET	36.71	32.18	29.66	27.98	36.70	32.90	30.85	29.47
Proposed	**37.41**	**33.35**	**31.03**	**29.41**	**36.94**	**33.26**	**31.28**	**29.88**
Method	Cowd				Goldhill			
SURE-LET	34.86	29.77	27.11	25.38	36.53	32.69	30.76	29.52
Proposed	**34.93**	**29.93**	**27.33**	**25.62**	**36.81**	**33.04**	**31.07**	**29.76**

Fig. 1 Comparison of the restoration results from SURE-LET and proposed method. Zoom into file three times for a better view. **a** original Barbara (512 × 512) image. **b** noisy image ($\sigma = 10$). **c**–**d** shows restored Barbara images using QWT-Bishrink and proposed, respectively

Table 2 Computational burdens (second) for SURE-LET and proposed method

Method	SURE-LET	Proposed
Unite of time	0.64 (256 × 256)	0.21 (256 × 256)
	1.42 (512 × 512)	1.25 (512 × 512)

Table 3 Comparison of QWT-Bishrink and proposed method in term of PSNR (dB)

σ	10	15	20	10	15	20	10	15	20
Method	Lena			Barbara			Boat		
QWT-Bishrink	29.82	29.89	29.93	29.02	28.11	27.48	28.03	26.23	24.14
Proposed	**35.03**	**33.12**	**31.72**	**33.35**	**31.03**	**29.41**	**33.26**	**31.28**	**29.88**

4 Conclusion

In this paper, an efficient image denoising algorithm is proposed. It is based on an integration of the multiple-step local Wiener filter and QWT. This method can be considered as extension and supplementary of diffusion-based Wiener filter. The effectiveness of multiple-step local Wiener filter is further embodied.

Acknowledgments This work is partially supported by National Natural Science Foundation of China (Grant No. 61401383) and Natural Science Foundation of Xianyang Normal University (Grant No. 14XSYK006) and Qinglan Talent Program of Xianyang Normal University (Grant No. XSYQL201503).

References

1. Chang SG, Yu B, Vetterli M Adaptive wavelet thresholding for image denoising and compression. IEEE Trans Image Process 9(9):1532–1546
2. Pi˘zurica A, Philips W (2006) Estimating the probability of the presence of a signal of interest in multiresolution single- and multi-band image denoising. IEEE Trans Image Process 15 (3):654–665
3. Sendur L, Selesnick IW (2002) Bivariate shrinkage functions for wavelet-based denoising exploiting interscale dependency. IEEE Trans Signal Process 50(11):2744–2756
4. Luisier F, Blu T, Unser M (2007) A new SURE approach to image denoising: inter-scale orthonormal wavelet thresholding. IEEE Trans Image Process 16(3):593–606
5. Corrochano EB (2006) The theory and use of quaternion wavelet transform. J Math Imaging Vis 24(1):19–35
6. Corrochano EB (2005) Multi-resolution image analysis using the quaternion wavelet transform. Numer Algorithms 39(1):35–55
7. Chan WL, Choi H, Baraniuk RG (2008) Coherent multiscale image processing using dual-tree dual-tree quaternion wavelets. IEEE Trans Image Process 17(7):1069–1082
8. Shan G, Liu P, Liu J, Tang X (2010) A new image denoising algorithm via bivariate shrinkage based on quaternion wavelet transform. J Comput Inf Sys 6(11):3751–3760
9. Zhang X, Feng X (2014) Multiple-step local Wiener filter with proper stopping in wavelet domain. J Vis Commun Image Represent 25(2):254–262

Adaptive Multiscale Block Compressed Sensing with Texture Information and Orientation Estimation

Donghong Gao, Haixia Wu and Wei Gao

Abstract The multiscale block compressed sensing algorithm gives an unreasonable resource distribution. This is because it deploys the same subrate within each decomposition level of a wavelet transform of an image. A novel adaptive sampling method applying the prior information is proposed to ameliorate the algorithm performance. Taking the importance differences of the wavelet coefficients of each decomposition level into account, texture information and directionality obtained by low frequency coefficients are combined. They are used to deploy the subrate adaptively into each image block of each subband of each level, realizing adaptive multiscale block compressed sensing. Experimental results reveal that, at each total subrate, the proposed algorithm significantly improves both the reconstruction quality and the visual effect with the maximum PSNR gain up to 1.38 dB.

Keywords Multiscale block compressed sensing · Wavelet transform · Image entropy · Orientation estimation · Adaptive sampling

1 Introduction

Compressed sensing (CS) theory shows that, if a signal which has a sparse representation in some orthonormal basis or tight frame, sampled at a rate significantly below the Nyquist rate, it can be reconstructed from several linear projections with a high probability [1]. This process achieves the purpose of simultaneous sampling and compressing. Currently, CS has already had a notable impact on several applications such as medical imaging, optics, pattern recognition, image compressing and super

D. Gao (✉) · H. Wu · W. Gao
School of Information and Electronics, Beijing Institute of Technology, Beijing, China
e-mail: taystupid@qq.com

H. Wu
e-mail: wuhaixia@bit.edu.cn

W. Gao
e-mail: Titigw@bit.edu.cn

Q. Liang et al. (eds.), *Proceedings of the 2015 International Conference on Communications, Signal Processing, and Systems*, Lecture Notes in Electrical Engineering 386, DOI 10.1007/978-3-662-49831-6_77

resolution [2–5]. One of the primary challenges for CS is the large computational cost in both sampling and reconstruction. The block CS with smoothed projected Landweber reconstruction (BCS-SPL) [6] significantly reduced the computational burden and the memory space, but at the cost of the reduced quality of image reconstruction. Flower et al. proposed another algorithm which named multiscale block compressed sensing with smoothed projected Landweber reconstruction (MS-BCS-SPL) [7]. This algorithm deploys block-based compressed sensing sampling within each subband of each decomposition level of a wavelet transform according to their different importance in different decomposition level and achieves good results.

In essence, not only the coefficient blocks between each level have different importance but the blocks within each level have because of the difference of their amount of information contained. It is worth mentioning that in MS-BCS-SPL, the low frequency coefficients of wavelet decomposition are completely ignored. However, the low frequency coefficients contain much useful prior image information. Under the framework of MS-BCS-SPL, we propose a texture-orientation-based adaptive sampling method using the prior information to ameliorate the reconstruction quality. The resulting technique, texture-orientation-based multiscale block compressed sensing (TO-BCS-SPL), illustrates in experimental results that at the same subrate, the proposed method gives a significant gain in reconstruction quality over MS-BCS-SPL.

2 Background

CS theory overcomes the limits of Nyquist rate meaning that if a vector $x \in R^n$ is sparse in some orthonormal basis or compressive in some tight frame, measured by a $M \times N$ matrix,

$$y = Ax \tag{1}$$

where y is an $M \times 1$ vector with M measurements, A is an $M \times N$ matrix, although $M \gg N$, x is still able to be reconstructed accurately.

In terms of the whole image, measurement matrix A is too large to be feasibly calculated and stored. An approach proposed in [6] solved this problem. This approach breaks the image into $B \times B$ nonoverlapping blocks and measures them with matrixes of corresponding size independently. Assume that x_j is a vector representing of block j of input image,

$$y_j = \boldsymbol{\Phi}_B x_j \tag{2}$$

where $\boldsymbol{\Phi}_B$ is an $M_B \times B^2$ measurement matrix. Then for the whole image, A is constrained to have a block-diagonal structure in the following formula. Therefore, only a measurement matrix $\boldsymbol{\Phi}_B$ needs to be stored, process burden is much mitigated.

$$A = \begin{bmatrix} \boldsymbol{\Phi}_B & 0 & \cdots & 0 \\ 0 & \boldsymbol{\Phi}_B & \cdots & 0 \\ \vdots & & \ddots & \vdots \\ 0 & \cdots & 0 & \boldsymbol{\Phi}_B \end{bmatrix} \tag{3}$$

3 Proposed TO-BCS-SPL Algorithm

In the wavelet domain, coefficients of each level consist of three subbands depicting the horizontal, vertical, diagonal details separately [8]. We deploy a 3-level DWT to be in accordance with MS-BCS-SPL. After that, calculate the inverse wavelet transform of the low frequency coefficients to obtain the estimated image and divide it into blocks.

3.1 Texture Information of Image Blocks

After dividing the estimated image, each block has variant texture information. In this paper, image entropy is applied to measure the amount of the texture information [9]. Let p_i represents the probability associated with gray level i which can be calculated by the gray histogram, the image entropy is defined as

$$H = -\sum_{i=0}^{255} p_i \log_2 p_i \tag{4}$$

Compute the image entropy of each image block and transform them to the preliminarily adaptive subrates. Steps of the process are as follows:

Step 1. Calculate the 3-level DWT of the original image I and get the estimated image I_0.
Step 2. Divide the estimated image I_0 into h(*in this paper*, $h = 64$) nonoverlapping blocks with size $B \times B$.
Step 3. Use Formula (4) to calculate the image entropy H_j of block $j(j = 1, 2, \ldots, h)$, and the total image entropy.
Step 4. Use Formula (5) to calculate the preliminarily adaptive subrate r_j.

$$r_j = (S - S_{min}) \cdot h \cdot H_j / \sum_{j=1}^{h} H_j + S_{min} \tag{5}$$

where S represents the target subrate, S_{min} is a minimum subrate threshold set to avoid too low values of the preliminarily adaptive subrates, shown in Formula (6).

$$S_{min} = \begin{cases} S/2, \ 0 < S \leq 0.1 \\ 0.05, \ 0.1 < S \leq 1 \end{cases} \tag{6}$$

3.2 Orientation Estimation of Image Blocks

Every image has a certain directionality. An image transformed to wavelet domain also has its directionalities reflected in the wavelet subbands of each decomposition level. The gradient vectors in an image block is on average orthogonal to the dominant orientation of the image pattern. So orientation estimation can be formulated as the task of finding the gradient information [10]. Steps are as follows.

Step 1. Determine the gradient matrix $\boldsymbol{G}$ and compute the SVD of $\boldsymbol{G}$.

$$\boldsymbol{G} = \boldsymbol{USV}^T = \boldsymbol{U} \begin{bmatrix} s_1 & 0 \\ 0 & s_2 \end{bmatrix} \begin{bmatrix} \boldsymbol{v}_1 \ \boldsymbol{v}_2 \end{bmatrix}^T = \boldsymbol{U} \begin{bmatrix} s_1 & 0 \\ 0 & s_2 \end{bmatrix} \begin{bmatrix} v_{11} & v_{12} \\ v_{21} & v_{22} \end{bmatrix} \tag{7}$$

where $\boldsymbol{v}_1$ represents the dominant orientation of the gradient field, $\boldsymbol{v}_1$ is orthogonal to $\boldsymbol{v}_2$ and $\boldsymbol{v}_2$ represents the dominant orientation in the image block.

Step 2. The difference between the singular value s_1 and s_2 is used to measure the accuracy or dominance of the estimate.

$$R = \frac{s_1 - s_2}{s_1 + s_2}^{[10]} \tag{8}$$

$R \in [0, 1]$, the larger the value of R, the more accurate the directivity of the image blocks is. $R \geq \tau$ (note that τ is the threshold value and usually is an experimental value) illustrates that the image block has an accurate dominant orientation.

Step 3. For image blocks with accurate dominant orientation, compute their dominant orientation angles.

$$\theta = 180/\pi \cdot arctan(v_{22}/v_{21}) \tag{9}$$

Step 4. Determine the dominant orientations according to the angles.

$$\theta = \begin{cases} (-30°, 30°] & : \textit{horizontal} \\ (-60°, -30°] \ \cup \ (30°, 60°) & : \textit{diagonal} \\ (-90°, -60°] \ \cup \ (60°, 90°) & : \textit{vertical} \end{cases} \tag{10}$$

3.3 TO-BCS-SPL

The low frequency coefficients of wavelet domain image $\widetilde{I}$ are set to full sampling. Each subband of each level is divided into h non-overlapping blocks to be consistent with the block number of the original image. Assume that the block sizes of each level are $B_l(l = 1, 2, 3)$, there exists a proportional relationship between B_l and the original image block size B and that is $B_1 : B_2 : B_3 : B = 1 : 2 : 4 : 8$. The whole steps of deploying the preliminarily adaptive subrate r_j to each image block of each subband of each level according to their dominant orientation are as follows. The flow chart of the process is shown in Fig. 1.

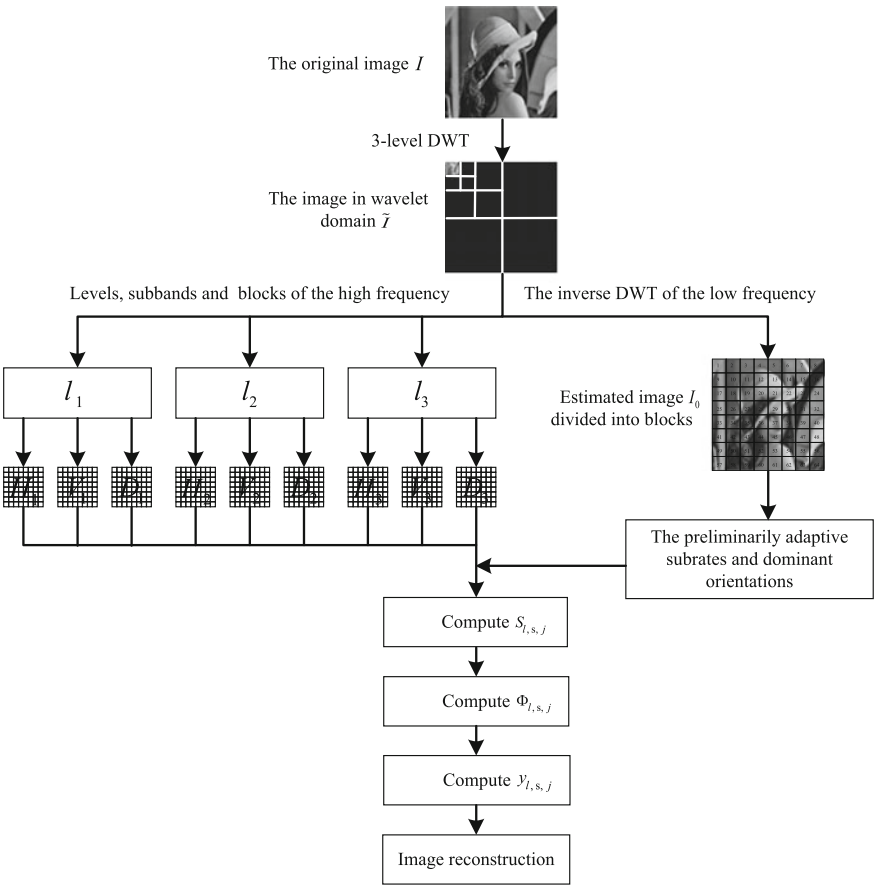

Fig. 1 The flow chart of the TO-BCS-SPL algorithm

Step 1. Calculate the subrate of the image block j of each subband of level l, represented by the symbol $S_{l,j}$. Set r_j as the target subrate of each level of the corresponding image block. Apply the following formulas to determine $S_{l,j}$.

$$r_j = \frac{1}{64} S_{0,j} + \frac{3}{64} S_{1,j} + \frac{3}{16} S_{2,j} + \frac{3}{4} S_{3,j} \tag{11}$$

$$S_{l,j} = W_l S' = 16^{L-l+1} S' \tag{12}$$

Step 2. Calculate the final subrate of the the image block j of subband $s(s \in H, V, D)$ of level l, represented by the symbol $S_{l,s,j}$. It is determined by $S_{l,j}$ and the dominant orientation. Assume that the dominant orientation of the image block j is horizontal, then we set the subrates as

$$S_{l,h,j} = 1/2 \cdot S_{l,j} \cdot 3, \quad S_{l,v,j} = 1/4 \cdot S_{l,j} \cdot 3, \quad S_{l,d,j} = 1/4 \cdot S_{l,j} \cdot 3 \tag{13}$$

Step 3. Calculate the measurement matrix of the image block j of subband s of level l, represented by the symbol $\boldsymbol{\Phi}_{l,s,j}$. Compute the number of adaptive measurements, $M_{l,s,j} = S_{l,s,j} \times B_l^2$. $\boldsymbol{\Phi}_{l,s,j}$ consist of $M_{l,s,j}$ row vectors randomly chosen from a $B_l \times B_l$ random orthogonal matrix $\boldsymbol{\Phi}_{B_l \times B_l}$, which is orthogonalized by the random matrix generated by the Gaussian distribution $N(0, 1)$.

Step 4. Measure the blocks with $\boldsymbol{\Phi}_{l,s,j}$ to obtain the measurement vector $y_{l,s,j}$.

$$y_{l,s,j} = \boldsymbol{\Phi}_l \widetilde{x}_{l,s,j} \tag{14}$$

where $\widetilde{x}_{l,s,j}$ represents the image block in wavelet domain.

Step 5. Reconstruct the image. The stage applies the SPL [7] method. First acquire the image in wavelet domain from $y_{l,s,j}$ and $\boldsymbol{\Phi}_{l,s,j}$. Compute the inverse wavelet transform and reduce the blocking artifacts by Wiener filtering. Then repeat the projection and filtering steps until the iteration termination condition is satisfied. Finally, the optimal solution is acquired.

4 Experimental Results

We now evaluate the performance of the TO-BCS-SPL algorithm described above on six grayscale images of size 512×512, they are Lena, Peppers, Barbara, Goldhill, Couple, and Airplane. TO-BCS-SPL uses 9/7 wavelet transform to compute a 3-level DWT of the test images with the block sizes of each level $B_l = 8, 16, 32 (l = 1, 2, 3)$. The block size of the original image is $B = 64$, the directivity threshold $\tau = 0.1$. Figures 2 and 3 shows the preliminarily adaptive subrate and orientation estimation of each block of Pepper. In Fig. 3, N indicates that the corresponding block has no

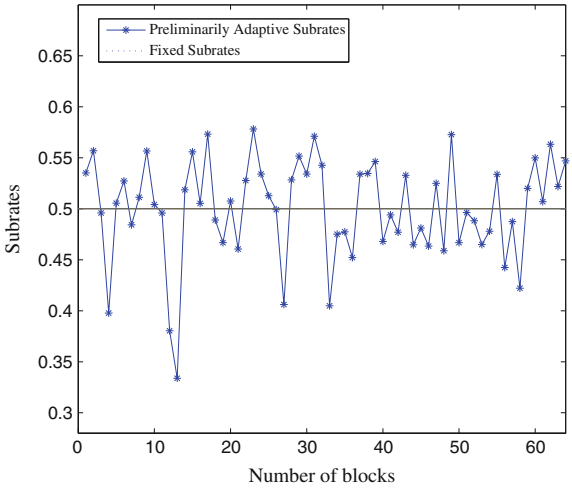

Fig. 2 Preliminarily adptive subrates of the blocks

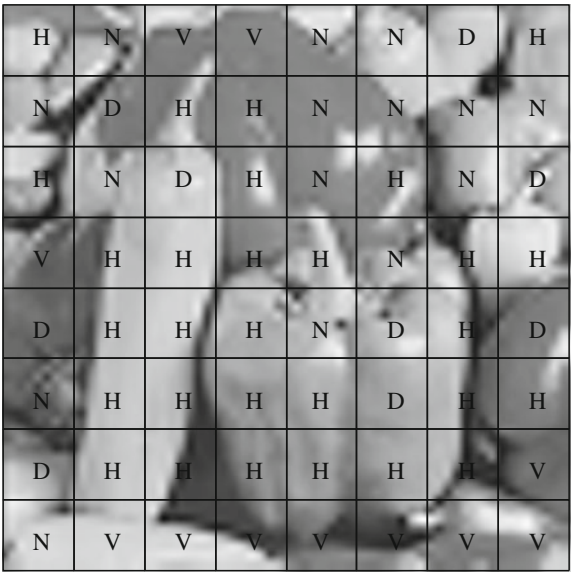

Fig. 3 The estimated orientations of the blocks

accurate dominant orientation, H, V and D indicate that the dominant orientations of the blocks are horizontal, vertical and diagonal separately.

We compared TO-BCS-SPL to algorithm MS-BCS-SPL, BCS-SPL and MS-GPSR [11]. Table 1 presents the reconstruction performance of the various algorithms of the images. All the results are the average value of three independent runs. To make it convenient for comparison, large PSNR values are highlighted by bold.

As is introduced, texture information and orientation both have their influences to the reconstruction quality, TO-BCS-SPL combines these two ideas and deploys them

Table 1 PSNR of each reconstructed image

Image	Algorithm	Subrate			
		$S = 0.3$	$S = 0.4$	$S = 0.5$	$S = 0.6$
Lena	TO-BCS-SPL	**36.75**	**37.99**	**39.19**	**40.68**
	MS-BCS-SPL	36.68	37.87	38.97	40.19
	BCS-SPL	33.52	35.21	36.74	38.29
	MS-GPSR	35.37	36.31	37.81	39.40
Peppers	TO-BCS-SPL	35.91	**36.88**	**37.81**	**38.92**
	MS-BCS-SPL	**35.92**	36.85	37.75	38.80
	BCS-SPL	33.75	35.14	36.39	37.67
	MS-GPSR	33.02	34.27	35.87	37.32
Barbara	TO-BCS-SPL	26.00	27.18	**28.77**	**30.65**
	MS-BCS-SPL	**26.06**	**27.26**	28.66	30.57
	BCS-SPL	25.28	26.88	28.54	30.27
	MS-GPSR	**26.09**	**27.53**	**29.64**	**32.34**
Goldhill	TO-BCS-SPL	**32.91**	**34.07**	**35.30**	**36.71**
	MS-BCS-SPL	32.78	33.72	34.68	35.81
	BCS-SPL	30.38	31.70	33.02	34.40
	MS-GPSR	32.11	32.94	34.25	35.78
Couple	TO-BCS-SPL	**31.61**	**32.99**	**34.37**	**35.98**
	MS-BCS-SPL	31.50	32.57	33.63	34.88
	BCS-SPL	28.63	30.12	31.57	33.12
	MS-GPSR	30.54	31.64	33.14	35.01
Airplane	TO-BCS-SPL	**36.41**	**38.29**	**40.55**	**42.66**
	MS-BCS-SPL	36.35	38.27	39.78	41.28
	BCS-SPL	32.32	34.47	36.44	38.40
	MS-GPSR	32.37	34.41	37.15	39.91

within the domain of a wavelet transform. As a consequence, at most subrates, TO-BCS-SPL achieves a significant gain with the maximum PSNR gain up to 1.38 dB. But it is not that perfect for Barbara which has too many details to deal with. It is because the adaptive sampling method is more effective to those images with distinguished smooth and complex regions. Anyway, compared to MS-BCS-SPL and BCS-SPL which use the same reconstruction method, TO-BCS-SPL achieves much better results except at extremely few subrates.

Figures 4 and 5 depicts the visual effects of the reconstruction images applying BCS-SPL, MS-BCS-SPL and TO-BCS-SPL at variant subrates. As is seen, the reconstructed image of our algorithm are clearer and smoother. Each figure also shows the PSNR and SSIM. As can be seen in all the figures, the reconstruction quality of the proposed algorithm has a significant advantage over the other algorithms.

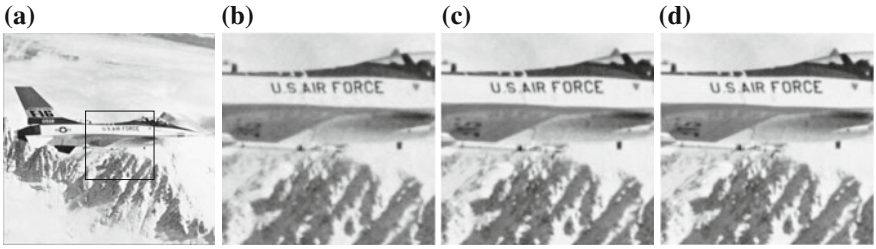

Fig. 4 S = 0.5, The reconstructed image of Airplane. **a** Original image of Airplane. **b** BCS-SPL, PSNR = 36.44 dB, SSIM = 0.95509. **c** MS-BCS-SPL, PSNR = 39.77 dB, SSIM = 0.97282. d TO-BCS-SPL, PSNR = 40.56 dB, SSIM = 0.97822

Fig. 5 S = 0.6, The reconstructed image of Barbara. **a** Original image of Barbara. **b** BCS-SPL, PSNR = 30.27 dB, SSIM = 0.90798. **c** MS-BCS-SPL, PSNR = 30.57 dB, SSIM = 0.89698. **d** TO-BCS-SPL, PSNR = 30.70 dB, SSIM = 0.9364

5 Conclusion

TO-BCS-SPL provides two other ideas in the framework of MS-BCS-SPL. Based on the idea that decomposition coefficients within each level has different importance to reconstruction quality, it combines the different importances of texture information and directivity. This results in a more effective adaptive sampling method. TO-BCS-SPL improved the PSNR as well as the visual effect of the reconstructed image while remains the approximate time complexity. The next work is to attempt to modify the reconstruction algorithm and complete the whole compressed sensing process and achieve further advances in the reconstruction quality.

References

1. Donoho DL (2006) Compressed sensing. IEEE Trans Inf Theory 52(4):1289–1306
2. Davenport MA, Duarte MF, Eldar YC et al (2011) Introduction to compressed sensing. Preprint 93:1–64
3. Tsaig Y, Donoho DL (2006) Extensions of compressed sensing. Signal Process 86(3):549–571

4. Jiao LC, Yang SY, Liu F et al (2011) Development and prospect of compressive sensing. Dianzi Xuebao (Acta Electronica Sinica) 39(7):1651–1662
5. Baraniuk RG (2007) Compressive sensing. IEEE Signal Process Mag 24(4)
6. Mun S, Fowler JE (2009) Block compressed sensing of images using directional transforms. In: 2009 16th IEEE International Conference on Image Processing (ICIP). IEEE, pp 3021–3024
7. Fowler JE, Mun S, Tramel EW (2011) Multiscale block compressed sensing with smoothed projected landweber reconstruction. In: 19th European signal processing conference. IEEE, vol 2011, pp 564–568
8. Mohideen SK, Perumal SA, Sathik MM (2008) Image de-noising using discrete wavelet transform. Int J Comput Sci Netw Secur 8(1):213–216
9. Sabuncu MR (2004) Entropy-based image registration. Princeton University, Princeton
10. Feng XG, Milanfar P (2002) Multiscale principal components analysis for image local orientation estimation. In: Conference record of the thirty-sixth Asilomar conference on signals, systems and computers, 2002. IEEE, vol 1, pp 478–482
11. Figueiredo MAT, Nowak RD, Wright SJ (2007) Gradient projection for sparse reconstruction: application to compressed sensing and other inverse problems. IEEE J Sel Top Signal Process 1(4):586–597

A Robust Tracking Combined with Texture Feature and Background-Weighted Color Histogram

Liang Chen, Qingquan Huang, Liang Pang and Fenglong Su

Abstract This paper proposed an adaptive tracking combined background weight with color-texture histogram on the basis of mean shift algorithm to achieve accurate tracking in complex scenes and similar background. Experimental results show that the proposed method is more efficient in dealing with complex background and occlusion than the traditional mean shift algorithm and corrected background-weighted mean shift algorithm with good computational efficiency.

Keywords Mean Shift · Color-texture histogram · Background-weighted

1 Introduction

Moving target tracking has been a hot issue in the field of computer vision and emerged various tracking algorithms [1, 2]. Mean shift (MS) algorithm [3] is applied to pattern recognition and image segmentation by Cheng [4] in 1995 for the first time and has been widely used in object tracking owing to its' easy implementation, fast iterations and less adjustment parameters. However, Mean shift algorithm using a single color histogram to indicate the target characteristics, and rectangular target template contains background information, the target feature cannot be accurately distinguish and describe in complex scenes.

In order to improve tracking accuracy in complex scenes, Comaneci [5] put forward BWH-MS (Background-Weighted Histogram MS) algorithm, integrate the local background information into the target color histogram to reduce the influence of background. Ning [6] proved BWH-MS does not realize the background information into the target model and raised a corrected background-weighted histogram (CBWH) MS algorithm, improved the robustness in complex scene.

L. Chen · Q. Huang (✉) · L. Pang · F. Su
PLA University of Science & Technology, Nanjing, China
e-mail: 554834712@qq.com; 1210524393@qq.com

Q. Liang et al. (eds.), *Proceedings of the 2015 International Conference on Communications, Signal Processing, and Systems*, Lecture Notes in Electrical Engineering 386, DOI 10.1007/978-3-662-49831-6_78

Texture information is a stable feature which can be used to improve the tracking robustness for it is not affected by light and background colors. Local Binary Pattern (LBP) descriptor [7] and its variants [8] (center symmetric local binary pattern (CS-LBP), local ternary pattern (LTP)) has applied to the target tracking due to the strong description ability and efficiency in computing texture feature extraction [9]. Literature [10] combined target texture with color histogram has improved tracking capabilities. These adaptive tracking algorithms based on color texture and Mean shift, although to some extent, improved the tracking performance in complex scenes, but did not consider background interference.

In this paper, an improved tracking which uses color histograms mixed with LBP texture to describe the target and compromises background-weighted based on CBWH-MS algorithm is proposed to solve the above problems effectively. Experiments show the improved method herein not only tracking more accurately in large background noise, but also more robust in complex scenes, and has better computational efficiency.

2 Mean Shift Tracking

Mean shift algorithm delineate a rectangle containing the interested object at the beginning frame by the mouse, the rectangular area called a target area, calculate the probability of each eigenvalue in the feature space of all the pixels in the target area for establishing the target model; establish target candidates model in possible candidate target region in subsequent frames; then measure Bhattacharyya coefficient between the target model and the target candidate models, seek to current position which obtain the maximum value of Bhattacharyya coefficient, thus achieving the target tracking.

2.1 Target Model

The target model based on weighted kernel function expressed as:

$$\hat{q}_u = C \sum_{i=1}^{n} k\left(\left\|\frac{y_0 - x_i}{h}\right\|^2\right) \delta[b(x_i) - u]_{u=1,2,\ldots,m} \tag{1}$$

wherein: $\hat{q}_u$ are value of histogram component u; m is component number; h is window width of kernel function $k(x)$; $\delta(x)$ is Kronecker Delta function; generally m value 32 or 16; $b(x)$ is color index of histograms corresponding to pixel x_i; constant C is Normalization factors with constraints: $\sum_{u=1}^{m} \hat{q}_u = 1$, so get: $C = 1/\sum_{i=1}^{n} k\left\|\frac{y_0 - x_i}{h}\right\|^2$

2.2 Candidate Target Model

The probability density function of candidate target model expressed as:

$$\hat{p}_u = C_h \sum_{i=1}^{n_k} k\left(\left\|\frac{y - x_i}{h}\right\|^2\right)\delta[b(x_i) - u]_{u=1,2,\ldots m} \tag{2}$$

wherein: $C_h = 1/\sum_{i=1}^{n_k} k\left\|\frac{y_0 - x_i}{h}\right\|^2$ is Normalization factors with constraints: $\sum_{u=1}^{n} \hat{p}_u = 1$.

2.3 Similarity Measure Target Model and Candidate Models

In order to determine the target location in the new frame, similarity between target histogram and candidate target histogram often using Bhattacharyya coefficient: $\hat{\rho}(y) = \sum_{u=1}^{m} \sqrt{\hat{p}_u(y)\hat{q}_u}$. Expansion by Taylor formula:

$$\rho(\hat{p}(y), \hat{q}) \approx \frac{1}{2}\sum_{u=1}^{m} \sqrt{\hat{p}_u(y_0)\hat{q}_u} + \frac{C_h}{2}\sum_{i=1}^{n_k} \omega_i k\left(\left\|\frac{y - x_i}{h}\right\|^2\right) \tag{3}$$

where weighting factor is:

$$\omega_i = \sum_{u=1}^{m} \sqrt{\frac{\hat{q}_u}{\hat{p}_u(y_0)}}\delta[b(x_i) - u] \tag{4}$$

Candidate model in different candidate area in the current frame is calculated, so the candidate region that has the smallest Bhattacharyya coefficient is the position of the target. MS algorithm is to determine the position of a candidate who making maximum Bhattacharyya coefficient in the new frame.

3 Background-Weighted Color-Texture Histogram Tracking

3.1 LBP Texture

LBP feature is an efficient local texture characteristic, because it has rotational invariance and local gray invariance, have been widely used in texture classification, feature identify, and other fields. LBP feature calculate the gray value of each

pixel and its adjacent pixel in picture, and use the binary pattern representing the comparison result to describe the texture. The Calculating formula is:

$$\mathrm{LBP}_{P,R}(x_c, y_c) = \sum_{p=0}^{P-1} s(g_p - g_c)2^p \tag{5}$$

wherein: g_c is gray value of center pixel (x_c, y_c); R is distance between the center pixel and adjacent pixels, P is the number of pixels in the field; g_p are gray values of P pixels in neighborhood whose center is (x_c, y_c) and radius is R. Function $s(x)$ defined as:

$$s(x) = \begin{cases} 1, & x \geq 0 \\ 0, & x < 0 \end{cases} \tag{6}$$

But the LBP get from formula (5) does not have rotational invariance, so it is not apply to the character modeling while the target posture is altering. For this problem, literature [11] gives a consistent pattern of LBP expansion:

$$\mathrm{LBP}_{P,R}^{riu2} = \begin{cases} \sum_{p=0}^{P-1} s(g_p - g_c), & U(\mathrm{LBP}_{P,R}) \leq 2 \\ P+1, & U(\mathrm{LBP}_{P,R}) > 2 \end{cases} \tag{7}$$

wherein:

$$U(\mathrm{LBP}_{P,R}) = |s(g_{P-1} - g_c) - s(g_0 - g_c)| + \sum_{p=1}^{P-1} \left| s(g_p - g_c) - s(g_{p-1} - g_c) \right| \tag{8}$$

3.2 Combined Color-Texture Histogram

According to the definition of a consistent pattern of LBP expansion, each pixel of the target object can be calculated as a corresponding $\mathrm{LBP}_{P,R}^{riu2}$, when $P = 8$, $R = 1$, it ranging from 0 to 9, then calculated texture histogram of the target object, so combined three color channels R, G, B with one-dimensional texture channel to define joint color-texture histogram.However, experimental results show that the combination in this way does not improve tracking performance compared to the use of color histogram, especially do not have a strong ability to distinguish when the target is similar to the background. In order to establish joint color-texture histogram which can identify the background and target zones preferably and reduce interference in the flat areas of image, literature [8] retain only five kinds of uniform pattern in nine patterns. In addition, so as to enhance noise immunity of LBP for flat areas, add an interference factor r, the greater the absolute value of r is,

the greater tolerance for gray value volatility. So in this paper using the following definitions:

$$\mathrm{LBP}_{P,R}^{riu2} = \begin{cases} \sum_{p=0}^{7} s(g_p - g_c - r), U(\mathrm{LBP}_{P,R}) \le 2 \\ \sum_{p=0}^{7} s(g_p - g_c - r) \in \{2,3,4,5,6\} \\ 0, \quad \text{others} \end{cases} \tag{9}$$

Such texture description only consider severe pixels change severely, eliminate most flat elements of the background and target area, can make up the deficiencies of color histogram. Combine three color channels R, G, B and $\mathrm{LBP}_{8,1}^{riu2}$, define the joint color-texture histogram as:

$$\hat{q}_u = C \sum_{i=1}^{n} k\left(\left\|x_i^*\right\|^2\right) \delta[\mathrm{bin}(x_i) - u]_{u=1,2,\ldots,m} \tag{10}$$

wherein, $\mathrm{bin}(x_i)$ represent area of color-texture histogram of pixel x_i, $\delta(x)$ is Kronecker Delta function; C is Normalization constant, with $\sum_{u=1}^{m} q_u = 1$, so get:

$$C = \frac{1}{\sum_{i=1}^{n} k\left(\left\|x_i^*\right\|^2\right)} \tag{11}$$

Select the dimension, the algorithm has $m = 8 \times 8 \times 8 \times 5$, the previous three dimension represent three color channel R, G, B, the fourth dimension represent selected five kinds of texture patterns in $\mathrm{LBP}_{8,1}^{riu2}$.

3.3 The Probability Distribution of Color-Texture Feature Based on Background Weights

Due to the target is usually represented by rectangular region which inevitably contains some background information, in order to reduce the interference of background information, the paper introduce background weights to the definition of color texture, redefine the target model, and candidate target model:

New target model:

$$\hat{q}_u^{'} = C^{'} v_u \sum_{i=1}^{n} k\left(\left\|x_i^*\right\|^2\right) \delta\left[b(x_i^*) - u\right] \tag{12}$$

New candidate target model:

$$\hat{p}_u^{'}(y) = C_h^{'} v_u \sum_{i=1}^{n_h} k\left(\left\|\frac{y - x_i}{h}\right\|^2\right)\delta[b(x_i) - u] \tag{13}$$

wherein: $\{v_u = \min(\hat{o}^*/\hat{o}_u, 1)\}_{u=1,\ldots,m}$ are background weights; $\{\hat{o}_u\}_{u=1,\ldots,m}$ $\left(\sum_{i=1}^{m} \hat{o}_u = 1\right)$ are background models, three times size of the target model; $\hat{o}^*$ is nonzero minimum of $\{\hat{o}_u\}_{u=1,\ldots,m}$. Calculating weight of candidate target area pixel x_i calculation according to background-weighted histogram:

$$\omega_i^{'} = \sum_{u=1}^{m} \sqrt{\frac{\hat{q}_u^{'}}{\hat{p}_u^{'}(y)}}\delta[b(x_i) - u] \tag{14}$$

In the first frame, the target is initialized to give its initial position and the background feature model $\{\hat{o}_u\}_{u=1,\ldots,m}\left(\sum_{i=1}^{m} \hat{o}_u = 1\right)$. Compute background characteristics of the current frame $\{\hat{o}_u^{'}\}_{u=1,\ldots,m}$ and $\{v_u^{'}\}_{u=1,\ldots,m}$; then, calculate Bhattacharyya coefficient between it and the previous background model $\{\hat{o}_u\}_{u=1,\ldots,m}$, just as:

$$\rho = \sum_{u=1}^{n} \sqrt{\hat{o}_u \hat{o}_u^{'}} \tag{15}$$

If $\rho < \varepsilon$, background show large changes, update background model:

$$\{\hat{o}_u\}_{u=1,\ldots,m} \leftarrow \{\hat{o}_u^{'}\}_{u=1,\ldots,m}, \{v_u\}_{u=1,\ldots,m} \leftarrow \{v_u^{'}\}_{u=1,\ldots,m}$$

Calculating target model using $\{v_u^{'}\}_{u=1,\ldots,m}$ and formula (12).

Else, do not update background model.

3.4 *Color-Texture and Background-Weighted Histogram MS Algorithm*

The procedure of the adaptive algorithm is:

Step1: Initialized, obtain the initial target position y_0. Calculating $\hat{q}$ of target model and $\{\hat{o}_u\}_{u=1,\ldots,m}$ of background model according to Eq. (10); Calculating $\{v_u\}_{u=1,\ldots,m}$ and $\hat{q}^{'}$ according to Eq. (12);

Step2: Assigning $k \leftarrow 0$;

Step3: Calculating $\hat{p}(y_0)$ of candidate target model in the current frame according to Eq. (13);

Step4: Calculating $\omega_i^{'}$ according to Eq. (14);

Step5: Calculating new location y_1 according to Eq. (3);

Step6: Assigning $d \leftarrow \|y_1 - y_0\|$, $y_0 \leftarrow y_1$, $k \leftarrow k+1$; $\varepsilon_1 \leftarrow 0.1$, maximum of iteration is N.

if $d < \varepsilon_1$ or $k > N$, computing the current background characteristics of $\{\hat{o}_u'\}_{u=1,\ldots,m}$ and $\{v_u'\}_{u=1,\ldots,m}$; if $\rho < \varepsilon_2$, update background model: $\{\hat{o}_u\}_{u=1,\ldots,m} \leftarrow \{\hat{o}_u'\}_{u=1,\ldots,m}$ $\{v_u\}_{u=1,\ldots,m} \leftarrow \{v_u'\}_{u=1,\ldots,m}$, update the target model: $\{\hat{q}_u'\}_{u=1,\ldots,m}$. Go to step2 for tracking of the next frame.
Else, $k \leftarrow k+1$ and go to step3.

4 Results and Discussions

To test the proposed algorithm, select a few standard test video sequence to conduct tracking experiment while comparing with traditional Mean shift tracking algorithm (MS) based only on the color histogram and tracking algorithm (CBWH-MS) based on the background-weighted color histogram. From top to bottom, MS, CBWH-MS, improved algorithm in this paper, respectively.

As Fig. 1, select video of pedestrians passing through the pole to test robustness under occlusion of the improved algorithm. After the pole, for the target is blocked, MS algorithm and CBWH-MS algorithm cannot distinguish target from occlusion environment, resulting in poor tracking performance. Improved algorithm track well, indicating that the improved algorithm have robustness in occlusion compared with the above two algorithms.

As Fig. 2, select video of fast shaking toy cat to test robustness in complex background and computational efficiency of the improved algorithm. In the process

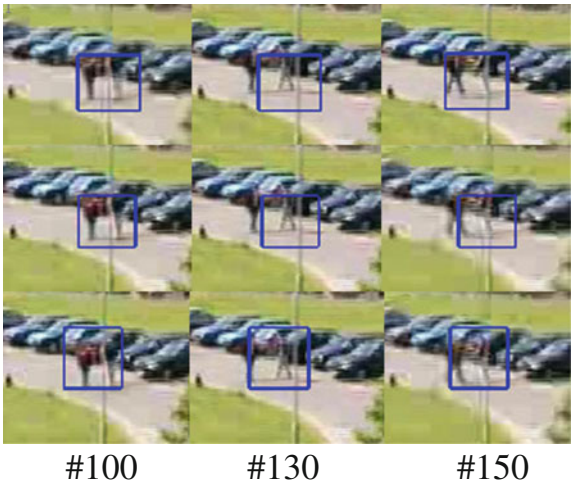

Fig. 1 Occlusion pedestrian tracking

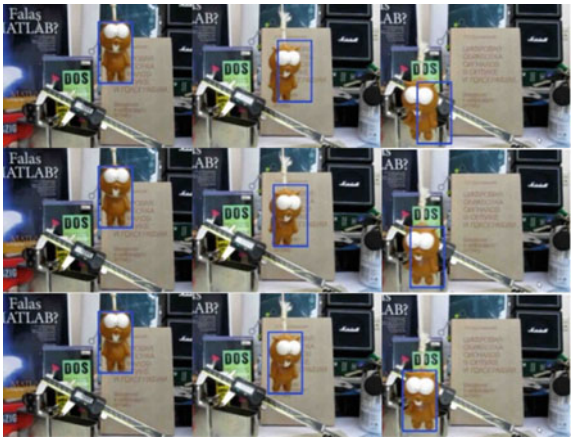

Fig. 2 Complex background tracking

Table 1 Algorithm performance comparison

Algorithm	Average per frame processed/s
MS	0.13
CBWH-MS	0.19
Improved Algorithm	0.21

of rapid movement of the toy cat, MS algorithm affected by complicated background, it is difficult to distinguish the target from the environment, CBWH-MS method added the background information, but slightly worse than improved algorithm with fusion of texture features in tracking, indicating that the improved algorithm improved the robustness in complex environments. At the same time, it is possible to track fast-moving target, show that the real-time performance of the improved algorithm is to meet the requirements.

Finally, computing performance of three algorithms were compared, as shown in Table 1, the computational efficiency of the proposed method is less efficient than the classic MS algorithm, but almost the same with CBWH-MS algorithm, to meet the real-time requirements.

5 Conclusions

This paper presents improved color-texture and background-weighted histogram MS algorithm, in the feature selection, chosen a blend of traditional RGB color histograms and texture features based on LBP. To reduce the influence of background on targeting updated background-weighted information selectively to accommodate larger changes of the background and complex environment.

Compared to traditional mean shift tracking algorithm (MS) based only on the color histogram and tracking algorithm (CBWH-MS) based on the background-weighted color histogram, the improved algorithm is possible to target more accurately and tracking more effectively in complex scenes, and has good computational efficiency.

References

1. Chen DY, Chen ZW (2013) Mean shift robust object tracking based on feature saliency. J Shanghai Jiao Tong Univ 47(11):1807–1812
2. Wang YX, Zhang YJ (2010) Meanshift object tracking through 4-D scale space. J Electron Inf Technol 32(7):1626–1632
3. Fukunaga K, Hostellerl D (1975) The estimation of the gradient of a density function with applications in pattern recognition. IEEE Trans Inf Theory 21(1):32–40
4. Cheng Y (1995) Mean shift mode seeking and clustering. IEEE Trans Pattern Anal Mach Intell 17(8):790–799
5. Ramesh DCV, Meer P (2000) Real-time tracking of non-rigid objects using mean shift. In: IEEE Conference on computer vision and pattern recognition, pp 142–149
6. Ning J, Zhang L, Zhang D, Wu C (2012) Robust mean shift tracking with corrected background-weighted histogram. IET Comput Vis 6:62–69
7. Heikkia M, Pietikainen M, Schmid C (2009) Description of interest regions with local binary patterns. Pattern Recogn 42(3):425–426
8. Tan X, Triggs B (2010) Enhanced local texture feature sets for face recognition under difficult lighting conditions. Image Process 19(6):1635–1650
9. Zhang HY, Hu Z (2014) Mean shift tracking method combining local ternary number with hue information. J Electron Inf Technol 36(3):624–630
10. Dai YM, Wei W, Lin YN (2012) An improved mean-shift tracking algorithm based on color and texture feature. J Zhejiang Univ (Eng Sci) 46(2):212–217
11. Heikkia M, Pietikainen M (2006) A texture-based method for modeling the background and detecting moving objects. IEEE Trans Pattern Anal Mach Intell 28(4):657–662

Part XI
Biological and Medical Signal Processing

Throat Polyp Detection Based on the KPCA and Neural Network Pattern Recognition

Wei Wang, Shan Qin, Shu Jiang, Dan Wang and Lei Xue

Abstract In this paper, we apply a new combination mode to detect throat polyp auxiliary. The Kernel principal component analysis is employed to extract characteristic value of the voice, and neural network pattern recognition to classify the voice data. This method can help diagnosis of throat polyps. As is known, In the modern clinical application, it is not widespread to use electronic laryngoscope. More cases need cutout, clamp or puncture to do pathological examinations, which is very hurt and it takes a long time to wait for the result that may delay the best treatment time. The results of pattern recognition show a beneficial correct rate of prediction under different number of samples and different random measurement matrices.

Keywords Kernel principal component analysis · Neural network pattern recognition · Probability and statistics

1 Introduction

It is common to have throat polyps and to be completely unaware of them, particularly if they are fairly small. The clinical symptoms are hoarseness and oropharyngeal discomfort. Traditionally, the methods of diagnosis are indirect laryngoscope, video-laryngoscope, and stroboscope light [1]. These polyps then break off and disappear inside the body or clear up by themselves. However, throat polyps can increase in size to the extent that they affect a person's ability to speak. Furthermore, most of these methods need special instrument, and mainly depend on the experience of the pathologists. Also, the patients will feel uncomfortable pain

W. Wang (✉) · S. Qin · D. Wang · L. Xue
College of Electronic and Communication Engineering,
Tianjin Normal University, Tianjin, China
e-mail: weiwangvip@163.com

S. Jiang
704 Institute, China Shipbuilding Industry Corporation, Shanghai, China

Q. Liang et al. (eds.), *Proceedings of the 2015 International Conference on Communications, Signal Processing, and Systems*, Lecture Notes in Electrical Engineering 386, DOI 10.1007/978-3-662-49831-6_79

usually. It would be desirable if throat polyps could be detected based on the patient vowel voices only [2].

Pattern recognition techniques, such as Bayesian classifier, known as the optimal classifier, could be used if the voice samples follow certain distribution, and this belongs to model-based statistical processing. In [3], the statistical characteristic root-mean square-delay spread and standard deviation were employed to describe the speech frequency domain characteristic and used as two antecedents. The Fuzzy logic system was used to make polyp patients' diagnosis. The results demonstrated that the proposed method could detect the throat polyps with low prob-48 ability of miss detection and 0 % false alarm rate. In [4], some methods of speech analysis for the diagnosis of the laryngeal function have been discussed. In humans' voices, the voice amplitude is highly bursty, and we believe that no statistical model can really demonstrate the uncertain nature of the voice.

Because of the complexity and diversity of voice, the data and information in many aspects, such as analysis, making decisions are nonlinear connection and complex. As an important branch of artificial intelligence, Neural network pattern recognition implements a mapping function from the input to the output, which is proved by mathematical theory that three layers neural network can approximate any nonlinear continuous function with arbitrary precision [5]. This makes it particularly suitable for solving complex problems, namely that has strong nonlinear mapping ability.

The remainder of this paper is organized as follows: Sect. 2 introduces KPCA and formulates the KPCA Sect. 3 briefly introduces pattern recognition. Experimental results are presented in Sect. 4 and conclusions are drawn in Sect. 5.

2 Kernel Principal Component Analysis

Principal component analysis is an appropriate model for data that are generated by a Gaussian distribution, or data that are best described by second-order correlations. In fact, PCA is based only on second-order correlations without taking higher-order statistics into account. It is well known, however, that the distribution of the actual data is highly non-Gaussian, and that the majority of the available information in data such as in-dependency or distances between different clusters cannot be described by second-order correlations [6]. So, when PCA is employed, the contribution of the index maybe scattered, and a comprehensive ability index can not be found.

2.1 Theory of the KPCA

When it comes to KPCA, the original variable space is mapped into a high dimensional feature space F by a nonlinear transformation Φ, and the do linear PCA in F, via the kernel trick, it only needs a dot product t between two input examples x and y in the original space,

$$k(x, y) = \Phi(x) \cdot \Phi(y) \tag{1}$$

It shows that, if k is a positive definite kernel, then there exists a map Φ into a dot product space F such that formula holds. Without knowing the concrete form of Φ, as long as selecting the proper kernel function, it can make the first principal component contribution rate reach more than 90 %, which is an advantage of KPCA. The space F then has the structure of a so-called Reproducing Kernel Hilbert Space (RKHS).

Express the implicit of the data for the feature space using a kernel [3], which make it possible for training a linear classifier in this feature space. With this kernel function, decision rules can be realized through [7] the kernel function:

$$f(x) = \sum_{i=1}^{l} \partial_i y_i k(x_i, x) + b \tag{2}$$

Samples of input space are $x_1, x_2, \ldots x_l$ transform into the samples of feature space is $\Phi(x_1), \Phi(x_2), \ldots, \Phi(x_l)$ [8]. Then, using principal components analysis in the feature space analysis, i.e., to solve eigenvalue problem:

$$\lambda_i u_i = C u_i, \quad i = 1, 2, \ldots, l \tag{3}$$

In which $C = \frac{1}{l} \sum_{i=1}^{l} \Phi(x_i)\Phi(x_i)^T$, is the sample covariance matrix of the feature space, and $\lambda_i \neq 0$, u_i is the feature vector. The formula (3) can be converted into the kernel eigenvalue problem:

$$\eta_i \partial_i = K \partial_i, \quad i = 1, 2, \ldots, l \tag{4}$$

In which $K = (k_{ij})_{i \times j}$ is kernel matrix, $k_{ij} = \Phi(x_i) \cdot \Phi(x_j)$, and $\eta_i \neq 0$, ∂_i is the feature vector. when reconstruct data, we use the fellow formula (5):

$$s_t(i) = u_i^T \Phi(x_t) = \sum_{j=1}^{l} \partial_i(j) K(x_j, x_t), \quad i = 1, 2, \ldots, l \tag{5}$$

If a function meets the Mercer conditions, it can be used as kernel function. The common kernel function includes linear function, polynomial function, the radial basis function, Sigmoid function and compound function [4].

2.2 Characteristics of the KPCA

The data that cannot be linear classified in a low dimensional space, will be very good in a high dimension space. The kernel function make it possible to transform

the original data from low dimensional space to high dimension space, then to analysis the principal component and to classify in high dimension space.

For the selection of kernel function, there is a lack of guidelines. Various experimental observations indeed show that some problems is well with some kernel function effect, but with some is very poor, in addition, generally speaking, the radial basis kernel function is a preferred one, which will not cause a too big deviation.

3 Pattern Recognition

Pattern recognition is a subject that researches identifying things by computer instead of human. It not only reduces the human physical and mental labor, but also improves the recognition ability, and accomplishes a lot of recognition which can not be completed by human before [9].

The intention of pattern is perfect specimens for imitating, so the pattern recognition is to identify a given thing with which specimen. In other words, the pattern recognition is a pattern classification. The feature variables of object of study consist of the spatial patterns, and according to the view of 'Like attracts like' to analysis the data structure, and to identify each pattern class [10]. Because of the computer, pattern recognition can deal with a lot of information with many influencing factors, decide to choose the characteristic variables of classification, and make the best decision.

It is a fundamental problem to recognize patterns in data. Applications in which the training data comprises examples of the input vectors along with their corresponding target vectors are known as supervised learning problems. In other pattern recognition problems, the training data consists of a set of input Vectors x without any corresponding target values. The goal in such unsupervised learning problems may discover groups of similar examples in the data, which is called clustering, or determine the distribution of data in the input space.

The most successful model of pattern recognition is the feedforward neural network. It is an alternative approach that fix the number of basis functions in advance but allow them to be adaptive, in other words, to use parametric forms for the basis functions in which the parameter values are adapted during training, it is also known as the multilayer perceptron.

When choose feedforward networks as pattern recognition networks, we can train to classify inputs according to target classes [11]. The target data for pattern recognition networks should consist of vectors of all zero values except for a 1 in element i, where i is the representative of the class.

3.1 Elementary Decision Theory

When it comes to class, we use Bayes decision rule to discrimination. We have an observation vector and we wish to assign an object to one of the C classes based on

the measurements x [12]. A decision rule based on probabilities is to assign x to class w_j if the probability of class w_j given the observation x, that is, $p(\omega_j|x)$, is greatest over all classes $\omega_1, \omega_2, \ldots, \omega_C$. That is, assign x to class w_j if

$$p(\omega_j|x) > p(\omega_k|x) \quad k = 1, 2, \ldots, C \quad k \neq j \tag{6}$$

And according to Bayes' theorem:

$$p(\omega_i|x) = \frac{p(x|\omega_i)p(\omega_i)}{p(x)} \tag{7}$$

3.2 The Process of Neural Network Pattern Recognition

Below is a picture of the flow chart of neural network pattern recognition. Trainscg is a network training function that updates weight and bias values according to the scaled conjugate gradient method [13] (Fig. 1).

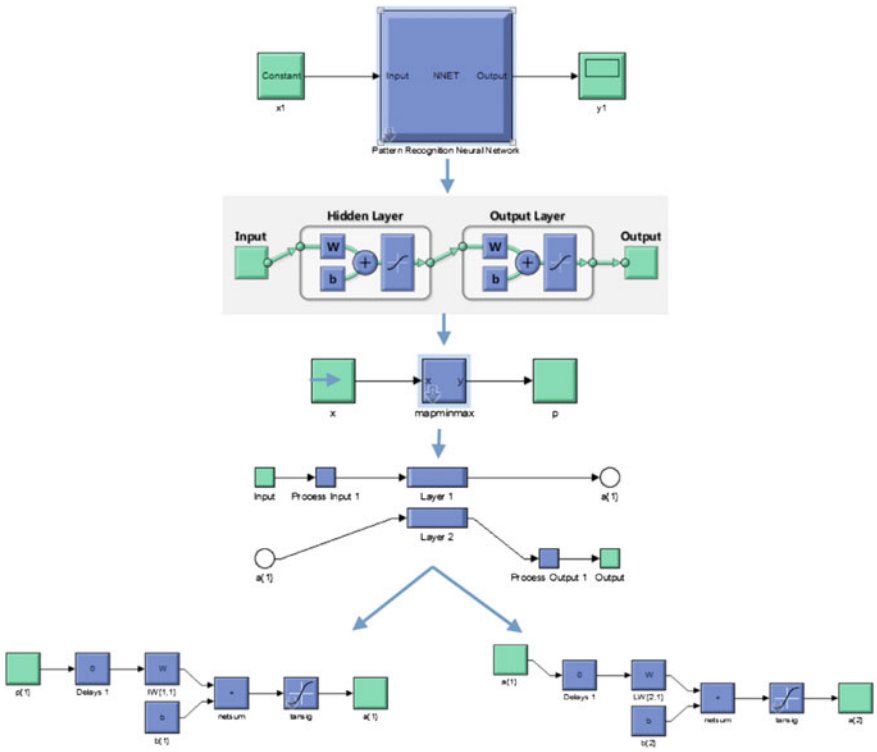

Fig. 1 The flow chart of neural network pattern recognition

4 Experiment

There are 33 samples of voice data, each sample has the two different vowels /a:/ and /i:/, each utterance has two sampling records. First, data normalization, and adjustment the ranks of matrix. Then use kernel principal component analysis to new data sample *X*, because of the use of nuclear techniques, The contribution rate of the first two principal components is up to 90 % or more, such as (Table 1):

We can calculate the contribution rate, in Normal 8 /a:/-2, the first two value is about 88.9 % of the total, and in sick 2 /a:/-2, the first two value is about 90.0 % of the total.

So, each group of data only need the first two principal components, and each sample has 4 parameters /a:/-1, /a:/-2,/i:/-1, and /i:/-2, each parameter has two values. We assume that the target output of sick is 1, the output of normal is 0, and then, the data will be processed by pattern recognition.

After the recognize, we obtain the final results as follows (Fig. 2):

According to the proportion to decide the numbers of each matrix, the proportion of training is 60 %, the proportion of validation is 10 %,and the proportion of test is 30 %.

Set the first picture on the upper left corner as an example, when training the samples, the green part is the correct number, that is to say, if the real value is 1, and the output also is 1. The red part is the error number, which means that the actual should have 1, but after judging is 0. The blue part is the total correct rate.

Here give a brief introduction of validation confusion matrix in Fig. 3. The validation confusion matrix is to verify the training network, at the beginning of training, the error rate will be reduced, then there will be a turning point, then the error rate will be increased. The validation matrix is to find the inflection point, and to stop training at the inflection point, then we achieve the best effect of training net.

Figure 4 is the two dimensional, visual result of pattern recognition. Figure 5 is the result of neural network classifier. By calculating in Fig. 5, It can be drawn that the correct rate of sick reaches 70 %, and the accuracy of normal is up to 60 %. So, the total accuracy is about 67 %. Compared with two result of test, obviously, the rate of correct of pattern recognition is higher.

Table 1 The principal component of two samples

	Normal 8 /a:/-2	Sick 2 /a:/-2
The first principal components	3.186143238	2.516873502
The second principal components	2.402175274	2.286803172
The third principal components	0.727210583	0.533577761

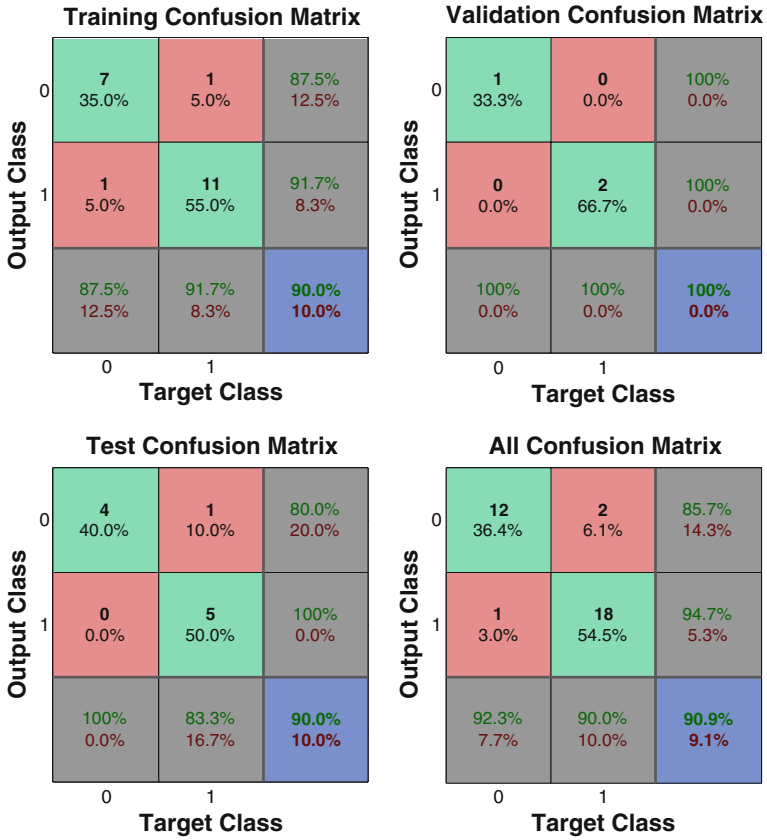

Fig. 2 The result of pattern recognition

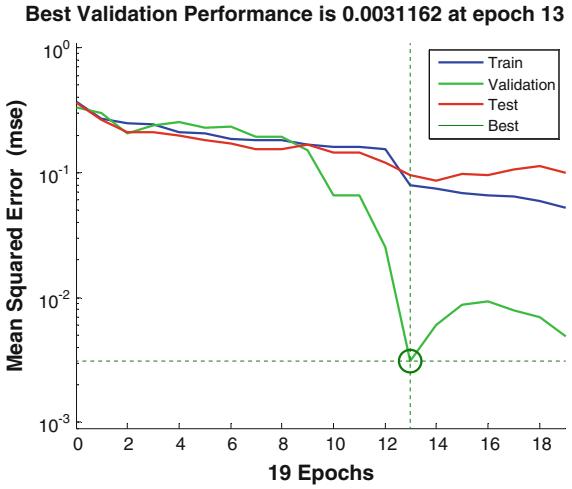

Fig. 3 Best validation performance

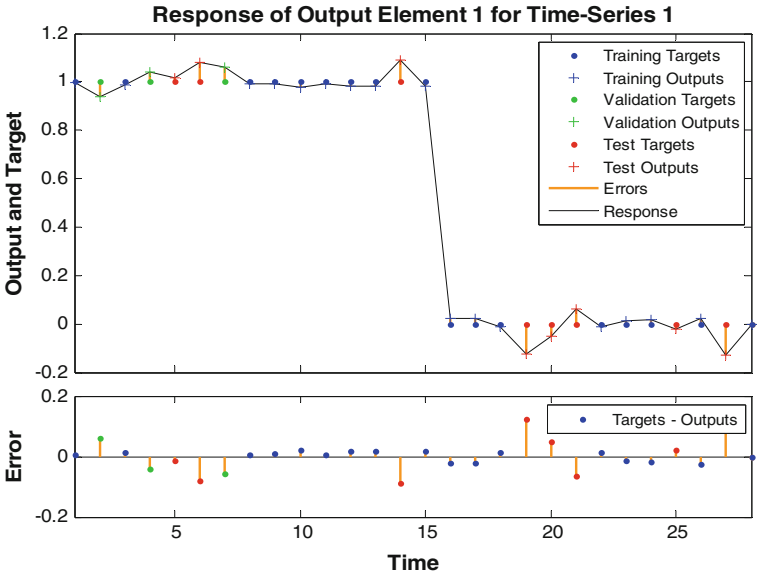

Fig. 4 Output of pattern recognition

Fig. 5 Output of neural network classifier

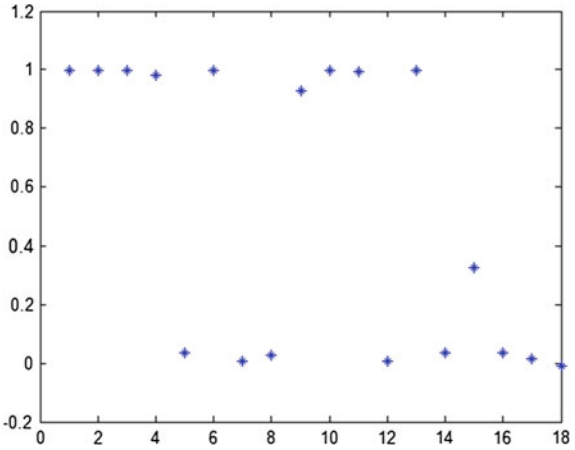

5 Conclusion

The experiment get the representative characteristics value by using the kernel principal component analysis, it provides a good precondition for pattern recognition classification, which promote the accuracy of classification.

The result illustrates that the correct rate of prediction is high under different number of samples and different random measurement matrices. However, more numbers of samples are needed to experiments, if we want to apply this approach in real life in the future.

Acknowledgments This work was supported by National Natural Science Foundation of China (61271411), National Natural Science Foundation of China (61372097), And it also was supported by The National Natural Science Foundation international (area) the cooperation and exchanges Project (61411130159) and National Youth Found of China (61501326).

References

1. Gyanli H et al. (2005) With the application of electronic laryngoscope laryngeal polyp forceps in operation of larynx. J Clin Otorhinolaryngol 06:276–277
2. Xincheng G (2010) The application of electronic laryngoscopy and laryngeal polyp forceps in operation of larynx. China Pract Med 25:115–116
3. Hongpin Y, Chunhong P (2006) A brief introduction to pattern recognition. Autom Panorama 01:22–26
4. Rongfang L, Tusheng L (2007) Finger crease pattern recognition using Legendre moments and principal component analysis. Chin Opt Lett 03:160–163
5. Christopher M (2007) Bishop. Pattern Recogn Mach Learn 10:91–295
6. Yingshu Y (2011) Matlab technology to realize the pattern recognition and intelligent Computing, vol 02. Publishing House of Electronics Industry, pp 217–238
7. Jia C, Shan X (2008) Fuzzy neural model for flatness pattern recognition. J Iron Steel Res (Int) 06:33–38
8. Wujingpei (2005) Analysis and application of principal component based kernel. Syst Eng 02:117–120
9. Youguo1 P et al (2007) The frame of cognitive pattern recognition. In: The twenty-sixth session of the China control conference, China hunan zhangjiajie
10. Science, W.S.S.o.I. et al (2010) The accelerated power method for kernel principal component analysis, China hubei wuhan
11. Choi JM, Sung MW, Park KS (2002) New method in acoustic analysis for the diagnosis of the Laryngeal functions. In: Proceedings of the Second Jt EMBS/BMES Conf10, pp 135–136
12. Zhong Z, Jiang T, Zhang WS, Yao H (2010) Analysis speech of polypus patients based on channel parameters and fuzzy logic systems. In: Proceedings of the 2010 seventh international conference on fuzzy systems and knowledge discovery, Yantai, pp 529–532
13. Xingtai W.S.X.P.C. et al (2011) Kernel principal component analysis fault diagnosis method based on sound signal processing and its application in hydraulic pump, China beijing

Dielectric Property Study of *Bacillus cereus* Spores at Microwave Frequency Region

Haiyun Wu, Yong Wei, Xiaoying Guo, Hua Liu, Ruokui Chang, Huiyong Shan and Yueming Zuo

Abstract Study on the dielectric phenomena of cells is critical to the further understanding of electromagnetic effect on cells. The dielectric properties of *Bacillus cereus* spores were measured for frequencies ranging from 500 to 8500 MHz using coaxial-line probe technology. The influence of *Bacillus cereus* spores concentration on the dielectric spectroscopy was explored at microwave frequency region. The results showed that the dielectric constant of the sample with *Bacillus cereus* spores and blank decreased with increasing frequency, especially at higher frequencies. The loss factor had a minimum of about 3420 MHz. What is more, when the frequency was lower than 3420 MHz, the dielectric constant of *Bacillus cereus* spores was lower than that of blank. While the loss factor and loss tangent were higher than that of blank. There was a more significant change for the loss factor than the dielectric constant between the *Bacillus cereus* spores and

H. Wu (✉) · Y. Wei (✉) · H. Liu · R. Chang · H. Shan
Engineering and Technology College, Tianjin Agriculture University, Tianjin, China
e-mail: haiyunwu2013@163.com

Y. Wei
e-mail: weiytj@tjau.edu.cn

H. Liu
e-mail: tjwqns@tjau.edu.cn

R. Chang
e-mail: changrk@163.com

H. Shan
e-mail: tjshy@sohu.com

X. Guo
Water Conservancy Engineering College, Tianjin Agriculture University, Tianjin, China
e-mail: guoxiaoying1974@126.com

Y. Zuo
Engineering College, Shanxi Agriculture University, Shanxi, China
e-mail: zuoyueming@163.com

Q. Liang et al. (eds.), *Proceedings of the 2015 International Conference on Communications, Signal Processing, and Systems*, Lecture Notes in Electrical Engineering 386, DOI 10.1007/978-3-662-49831-6_80

blank. Thus, the dielectric constant can be an indicator in *Bacillus cereus* spores qualitative analysis.

Keywords *Bacillus cereus* spores · Dielectric constant · Loss factor · Microwave frequency · Qualitative analysis

1 Introduction

Milk can provide rich nutrient while it also can be a potential source of chemical and biological hazards. The presence of spores in raw milk could produce toxins which may be lethal to the consumer, and they can compromise shelf life and quality of the final product. Hence, development of methods for the detection of spores in milk has attracted considerable interest.

Since traditional methods for detection of spores are time-intensive, costly, and are often specific to the genus and species of the spore itself, requiring differential media, various growth conditions, as well as, enrichment procedures [1]. Several rapid detection methods such as PCR technology [2, 3] and spectroscopy methodologies have been developed to detect spores. For example, Farquharson et al. Farquharson [4] designed a simple vacuum system to collect *Bacillus cereus* spores and detected it using Raman spectroscopy. Reynolds [5] used hyperspectral reflectance signatures with post-processing to differentiate live (viable) from dead (nonviable) endospores.

It is necessary to study the dielectric phenomena of cells for further understanding of the electromagnetic effect on cells. Open-ended coaxial-line probe method associated with network analyzers or impedance analyzers is a useful technique to determine dielectric properties, according to the reflection coefficient at the material–probe interface [6]. Dielectric measurement can be directly related to changes in cell behaviors [7]. Recently, dielectric measurement has been used to detect the movement of spores [8]. Also, researchers have verified that dielectric measurement can be directly related to viable biomass concentration [9–12] and spore growth [13]. But, most of the dielectric study about the dielectric phenomena on cells focused on the radio frequency range. There has been little study to explore the dielectric property at microwave range up to now.

In this work, coaxial-line probe method associated with network analyzers was used to determine dielectric properties, i.e., dielectric constant, dielectric loss factor, and loss tangent, of *Bacillus cereus* spores at microwave frequency region. The relationship between permittivity and spores concentration was explored.

2 Experimental Section

2.1 Reagents

Peptone, NaCl, Agar, Beef extract, and KCl were obtained from Solarbio Science & Technology CO., Ltd. (Beijing, China). The buffers and solutions used in this study were prepared as follows: PBS buffer (10 mM, pH 7.4) and *Bacillus cereus* culture media (10 g Peptone, 5 g NaCl, and 20–25 % Agar in 1000 mL Beef extract). All solutions were prepared with deionized water in a Heal Force water purification system (Smart Series, 18.2 MΩ cm, Hong Kong, China).

2.2 Instruments

The dielectric properties measurements were performed with an Agilent Technologies N5241A vector network analyzer and Agilent Technologies 85070E slim form coaxial probe (Agilent Technologies, Inc. USA). In order to eliminate cable instability and system drift errors, the slim form coaxial probe used in the experiment was calibrated with open (air), short circuit, and deionized water at 25 °C sequentially before experiment. The Agilent Electronic Calibration module microwave ports were connected in line between the probe and the network analyzer test port cable.

2.3 Preparation of Microbial Sample

Bacillus cereus was purchased from Beina Biotechnology Research Institute (Beijing, China). A 10 μL loop of *Bacillus cereus* isolate was grown in *Bacillus cereus* culture media at 28 °C for 40 h to make a stock culture. The stock cultures were serially diluted with PBS buffer (10 mM, pH 7.4). A conventional spread plating method was used for bacterial counts.

2.4 Measurement Procedure

A volume of 10 mL sample for test was applied to the beaker. Measurements were made by simply immersing the slim form coaxial probe into sample. Sample size required minimum 5 mm insertion and 5 mm around tip of probe.

For dielectric properties measurements, settings were made to provide 201 measurements on a logarithmic scale from 500 to 8500 MHz. All experiments were carried out at room temperature. Complex permittivity in a variety of formats,

including dielectric constant, dielectric loss factor, loss tangent, or Cole–Cole was recorded with three replications. Between replications, the probe was washed with deionized water and wiped dry. The average of the three replications was used in analysis.

To observe the permittivity change of samples with bacterial cells compared to blank, a calibration curve for normalized permittivity change (NPC) and concentrations of *Bacillus cereus* was drawn based on the difference of magnitude of permittivity with respect to blank. The value of NPC was given by the following Eq. (1):

$$NPC = \frac{\varepsilon_{\text{sample}} - \varepsilon_{\text{blank}}}{\varepsilon_{\text{blank}}} \tag{1}$$

where $\varepsilon_{\text{blank}}$ is the magnitude of permittivity for blank sample, and $\varepsilon_{\text{sample}}$ is the magnitude of permittivity for a sample containing *Bacillus cereus* spores. An average of three readings and their standard deviation was calculated and analyzed for each concentration of bacteria.

3 Results and Discussion

3.1 The Permittivities of Bacillus cereus Spores

The permittivities of *Bacillus cereus* spores pure culture at the concentration of 3.8×10^7 CFU/mL and the blank solution (PBS buffer (10 mM, pH 7.4) at the frequency range from 500 to 8500 MHz are shown in Fig. 1. As shown in Fig. 1a, the dielectric constant of the pure culture decreased with increasing frequency. Especially at the high frequency, the dielectric constant decreased sharply. Figure 1b shows the dielectric loss factor of the sample with *Bacillus cereus* spores and blank solution decreased lineally with increasing frequency, and reached a minimum at about 3420 MHz. When the frequency was higher than 3420 MHz, the dielectric loss factor increased with increasing frequency. The same trend can be observed as the loss tangent which is shown in Fig. 1c.

Theoretically, the measured loss of material can actually be expressed as a function of both dielectric loss due to dipole rotation (ε''_{rd}) and conductivity (S), which is shown in Eq. (2).

$$\varepsilon''_r = \varepsilon''_{rd} + \frac{\sigma}{\omega \varepsilon_o} \tag{2}$$

where σ is ionic conductivity of a material; ω is the frequence of excitation sources, and ε_o is the permittivity of free space. At low frequencies, the overall conductivity can be made up of many different conduction mechanisms, but ionic conductivity is the most prevalent in moist materials. ε''_r is dominated by the influence of

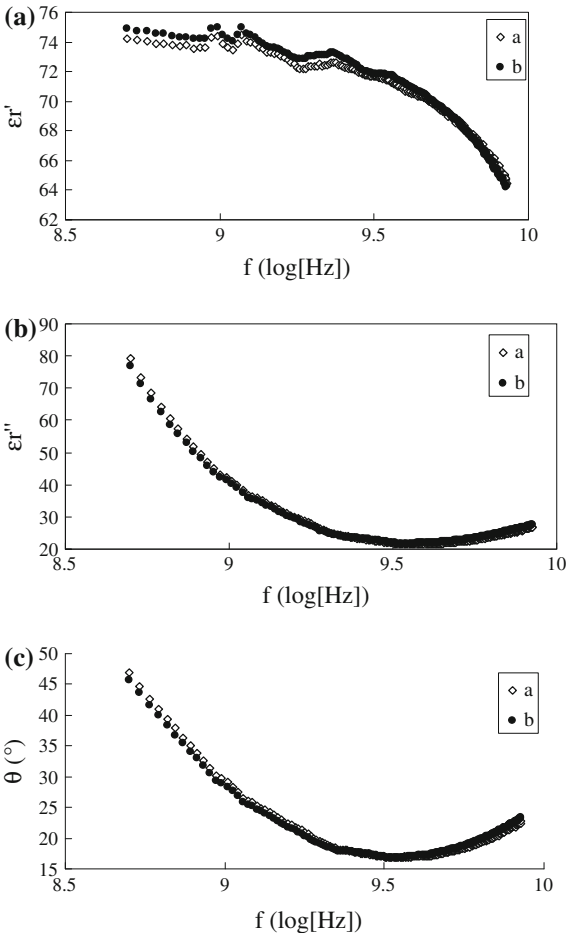

Fig. 1 The frequency dependent permittivities of *Bacillus cereus* pure culture at the concentration of 3.8×10^7 CFU/mL (*a*) and the blank (*b*). **a** Dielectric constant versus frequency. **b** Dielectric loss factor versus frequency. **c** Loss tangent versus frequency

electrolytic conduction caused by free ions which exist in the presence of a solvent. Ionic conductivity only introduces losses into a material. At low frequencies, the effect of ionic conductivity is inversely proportional to frequency and appears as a 1/f slope of the ε_r'' curve. Therefore, the measured dielectric loss factor decreased lineally with increasing frequency at the frequency lower than 3420 MHz.

3.2 The Influence of Bacillus cereus Spores Concentrations on Permittivities

In order to study the influence of *Bacillus cereus* spores concentrations on permittivities, a calibration curve for normalized permittivity change (NPC) between *Bacillus cereus* pure culture at the concentration of 3.8×10^7 CFU/mL and the

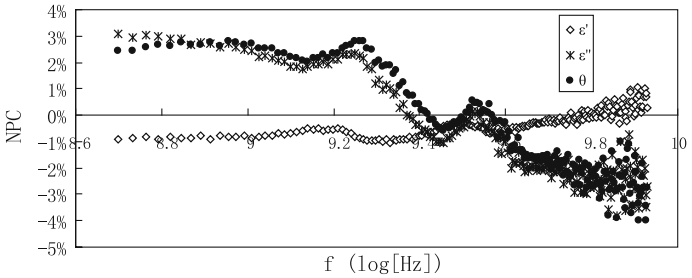

Fig. 2 The permittivity changes of *Bacillus cereus* pure culture at the concentration of 3.8×10^7 CFU/mL from 500 to 8500 MHz

blank was shown in Fig. 2. The dielectric constant of *Bacillus cereus* spores was observed to be lower than that of blank when the frequencies were less than about 3240 MHz, and were a little higher than that of blank over the frequency range more than 3240 MHz. Compared to dielectric constant, there was a significant change for dielectric loss factor and loss tangent, especially at the low frequencies. The dielectric loss factor and loss tangent of *Bacillus cereus* spores were observed to be higher than that of blank when the frequencies were less than about 3240 MHz. That was by the dielectric property of the cell suspensions. At low frequencies, the dielectric loss factor is dominated by the influence of electrolytic conduction. The cells increased the conductivity.

Figure 3 shows the loss factor changes of *Bacillus cereus* pure culture at serial concentrations from 3.8×10^7 to 3.8×10^9 CFU/mL. While the frequencies were less than about 3240 MHz (9.5 log scales), the dielectric loss factor of *Bacillus cereus* spores at concentrations of 3.8×10^8 and 3.8×10^9 CFU/mL was observed to be higher than that of blank too.

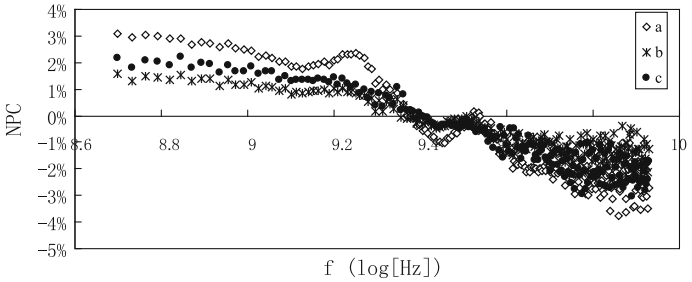

Fig. 3 The loss factor changes of *Bacillus cereus* pure culture at serial concentrations: (*a*) 3.8×10^7 CFU/mL; (*b*) 3.8×10^8 CFU/mL; (*c*) 3.8×10^9 CFU/mL

4 Conclusions

The dielectric properties of *Bacillus cereus* spores at microwave frequency region were explored from 500 to 8500 MHz. The dielectric constant of *Bacillus cereus* spores decreased with increasing frequency, especially at higher frequencies. The loss factor reached a minimum at about 3420 MHz (9.5 log scales). When the frequency was lower than 3420 MHz, dielectric constant of *Bacillus cereus* spores was lower than that of blank. While the loss factor and loss tangent were higher than that of blank. There was a significant change for loss factor than the dielectric constant between the *Bacillus cereus* spores and blank. Therefore, the loss factor could be an indicator in predicting whether the sample is contaminated by *Bacillus cereus* spores or not. Measurements are nondestructive and can be made in real time. It provides some useful information for developing a fast spore sensor.

Acknowledgments This research was funded by the Tianjin Natural Science Foundation of China through grant number 13JCYBJC25700, the Technology Development Fund in Tianjin Agricultural University of China through grant number 2013N02 and the Innovation and Entrepreneurship Training Plan for Undergraduate in Tianjin of China through grant number 201410061185, and 201510061140.

References

1. Harper NM, Getty KJ, Schmidt KA et al (2011) Comparing the mannitol-egg yolk-polymyxin agar plating method with the three tube most probably number method for enumeration of *Bacillus cereus* spores in raw and high-temperature, short-time pasteurized milk. J Food Prot 74(3):461–464
2. Guidi V, Respinis SD, Benagli C et al (2010) A real-time PCR method to quantify spores carrying the Bacillus thuringiensis var. israelensis cry4Aa and cry4Ba genes in soill. J Appl Microbiol 109(4):1209–1217
3. Scheldeman P, Herman L, Foster S et al (2006) Bacillus sporothermodurans and other highly heat-resistant spore formers in milk. J Appl Microbiol 101(3):542–555
4. Farquharson S, Grigely L, Khitrov V et al (2004) Detecting *Bacillus cereus* spores on a mail sorting system using Raman spectroscopy. J Raman Spectrosc 35:82–86
5. Anderson JE, Reynolds C, Reynolds C et al (2008) Differentiation of live-viable versus dead bacterial endospores by calibrated hyperspectral reflectance microscopy. J Microsc 232 (1):130–136
6. Guo W, Zhu X, Liu H et al (2010) Effects of milk concentration and freshness on microwave dielectric properties. J Food Eng 99(3):344–350
7. Fricke H (1925) A mathematical treatment of the electric conductivity and capacity of disperse systems II: The capacity of a suspension of conducting spheroids surrounded by a non-conducting membrane for a current of low frequency. Phys Rev 26:678–681
8. Zhong LS, Zhang Y, Zhang L et al (2006) The dielectric behaviors of cells under nonuniform AC fields. In: Proceedings of the IEEE international conference on Properties and Applications of Dielectric Materials (PADM'2006), Bali, Indonesia, pp 554–557
9. Ding C, Liu X, Shang P (2014) Progress of the technology and application of dielectric spectroscopy of cell suspensions. Beijing Biomed Eng 33(1):94–100

10. Heileman K, Daoud J, Tabrizian M (2013) Dielectric spectroscopy as a viable biosensing tool for cell and tissue characterization and analysis. Biosens Bioelectron 49C:348–359
11. Daoud J, Asami K, Rosenberg L et al (2012) Dieleclric spectroscopy for non-invasive monitoring of epithelial cell differentiation within three-dimensional scaffolds. Phys Med Biol 57(16):5097–5112
12. Carvell JP, Dowd JE (2006) On-line measurements and control of viable cell density in cell culture manufacturing processes using radio-frequency impedance. Cytotechnology 50 (1):35–48
13. Sarrafzadeh MH, Belloy L, Esteban G et al (2005) Dielectric monitoring of growth and sporulation of Bacillus thuringiensis. Biotechnol Lett 27(7):511–517

Improving Consensus Hierarchical Clustering Framework

Ashis Kumer Biswas, Baoju Zhang, Xiaoyong Wu and Jean X. Gao

Abstract Consensus clustering has been widely accepted in recent years as an effective alternative to the individual clustering. Individual clustering results may contain noise inherent to the original dataset that introduces instability and inconsistency during the interpretation. Consensus clustering strategies focus on combining different individual clustering results from a dataset and generates a single clustering result overcoming the inconsistencies that otherwise could not be avoided. Consensus partitional clustering has been thoroughly studied over the past decade, but only a few contributing research on the consensus hierarchical clustering domain has been done. In this paper, we present an improved and simplified consensus hierarchical clustering framework that is capable of producing a consensus aggregated hierarchical cluster given a set of individual hierarchical clustering results, denoted as dendrograms. Moreover, we propose an additional dendrogram descriptor matrix which is ultra-metric, and improves the consensus clustering performance to some extent than the others. We applied our framework on three generic datasets from the UCI machine learning repository to solve the consensus hierarchical clustering problem and the experimental results demonstrate the effectiveness of our framework.

A.K. Biswas (✉) · J.X. Gao (✉)
Department of Computer Science and Engineering, The University of Texas at Arlington, Arlington, TX 76019, USA
e-mail: ashis.biswas@mavs.uta.edu

J.X. Gao
e-mail: gao@uta.edu

B. Zhang · X. Wu
School of Communications and Electronic Information, Tianjin Normal University, Tianjin 300387, China
e-mail: wdxyzbj@163.com

Q. Liang et al. (eds.), *Proceedings of the 2015 International Conference on Communications, Signal Processing, and Systems*, Lecture Notes in Electrical Engineering 386, DOI 10.1007/978-3-662-49831-6_81

1 Introduction

Ensemble clustering became the *de facto* standard used by the researchers now-a-days to remedy instability in individual clustering results. It refers to the retrieval of a consensus clustering from a given set of individual clustering results obtained from various sources and methods with different parameter settings. There have been a fair amount of researches published to introduce effectiveness of the ensemble clustering strategies over the past decade [1, 3, 8].

Most of the ensemble clustering methods are introduced to build consensus out of partitional clustering results. Very few researches have been published for the consensus hierarchical clustering problem, for example [2, 5, 7, 9]. The results of the hierarchical clustering algorithms cannot be represented as a global objective function, thereby solution to the ensemble hierarchical clustering is even more challenging.

In this paper, we propose a consensus hierarchical clustering framework, where the input is a set of hierarchical clustering results, represented by dendrograms. The output is the consensus hierarchical clustering. The overall strategy of our framework can be described in the following three steps:

- Use a dendrogram descriptor measure to generate an ultra-metric dendrogram distance for each input dendrograms (Sect. 2.1.1).
- Aggregate the ultra-metric dendrogram distances (Sect. 2.2).
- Construct the final Hierarchical clustering from the aggregated distance matrix (Sect. 2.2).

Previous ensemble hierarchical clustering frameworks have considered finding the closest ultra-metric distance matrix from the aggregated distance matrix [9]. However, in this paper we argue that the step is not necessary, rather adapting it increases the computational complexity of the overall framework.

2 Materials and Methods

2.1 Dendrogram Descriptor

A hierarchical clustering result can be easily encoded as a binary tree, which explains the hierarchy of the individual data points (i.e. the leaf nodes), how they progressively merge together to form the clusters, as well as illustrate pairwise similarity between the leaf nodes in a cluster through appropriate scaling of the heights of the two hands emanating from the parent cluster representative node to the child nodes corresponding to the measured distance values. Such tree is called a dendrogram.

Given only a dendrogram of a certain hierarchical clustering result without any pairwise distance matrix of the leaf nodes, one can define an ultra-metric matrix encapsulating the pairwise distances among the leaf nodes. Here, an ultra-metric

distance function $d : \Omega \times \Omega \rightarrow \mathbb{R}$ between a set of leaf nodes from Ω is defined as

$$d(x, y) \geq 0, \quad \forall x, y \in \Omega \tag{1}$$
$$d(x, y) = 0, \quad \text{if} \quad x = y, \quad \forall x, y \in \Omega \tag{2}$$
$$d(x, y) = d(y, x), \quad \forall x, y \in \Omega \tag{3}$$
$$d(x, y) \leq \max\{d(x, z), d(y, z)\}, \quad \forall x, y, z \in \Omega \tag{4}$$

Equation 4 is known as the "strong triangle condition", also the "three-point condition". Such matrix is denoted as the dendrogram descriptor from which the given dendrogram can be reproduced and characterized [4].

In the following sub-section, we first define our proposed dendrogram descriptor—Nodal Hop Distance (NHD) and the next sub-section with few existing dendrogram descriptors. We will refer to Fig. 1 to explain the definitions.

2.1.1 Nodal Hop Distance

Nodal Hop Distance (NHD) is the number of hops required to reach from one leaf to the other in a dendrogram. For the dendrogram in Fig. 1, NHD$(b, d) = 4$, because there are 4 hops required to go from leaf node b to the leaf node d, which are: $b \rightarrow N_2$, $N_2 \rightarrow N_4$, $N_4 \rightarrow N_3$ and $N_3 \rightarrow d$.

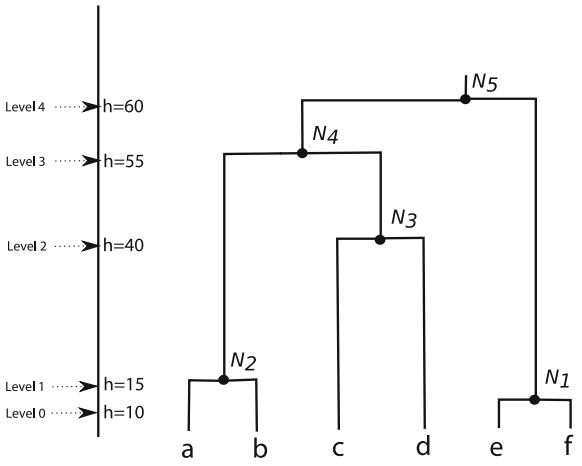

Fig. 1 A dendrogram representing hierarchical clustering of six data items, namely a, b, c, d, e, f. Nodes e and f are joined at height 10 at intermediate node N_1. Then, the nodes a and b merged at the intermediate node N_2 at height 15, c and d at height 40 merged at the intermediate node N_3. The two intermediate nodes N_2 and N_3 are merged at height 55 forming another intermediate node N_4. Eventually, N_4 is merged to the intermediate node N_1 at height 60 spawning the top-level node N_5. We can see that there are 5 levels of in this dendrogram and each of the merge operation increases the level of the dendrogram

2.1.2 Existing Dendrogram Descriptors

We have used the five existing dendrogram descriptors to compare results with our proposed descriptor. The five dendrograms were defined in earlier work by Podani et al. [6].

Cophenetic Difference (CD) is the lowest height of internal nodes in the dendrogram where the two given leaf nodes are merged. The Cluster Membership Divergence (CMD) between two leaf nodes denotes the number of leaf nodes of the smallest cluster in the dendrogram containing the two leaf nodes. The Maximum Edge Distance (MED) between two leaf nodes is recursively defined as the depth of the intermediate nodes containing the two, where depth of a leaf node is zero, and depth is incremented by one for every bottom-up recursive traversal. The Partition Membership Divergence (PMD) is the number of partitions of the dendrogram where the two given leaves do not belong to the same cluster. Finally, the Subdendrogram Membership Divergence (SMD) is the number of sub-dendrograms where the two given leaf nodes will not be in the same cluster.

Referring to Fig. 1, CD between the leaf nodes b and d is 55, and CD $(c,f) = 60$, CMD between b and c is 4, since the smallest cluster would contain the leaves a, b, c, d. Since MED is recursively defined, to calculate MED between b and d we solve it in a bottom-up fashion:

$$\begin{aligned}\text{MED}(b,d) &= \text{depth}(N_4) = \max(\text{depth}(N_2), \text{depth}(N_3)) + 1 \\ &= \max(\max(\text{depth}(a), \text{depth}(b)) + 1, \max(\text{depth}(c), \text{depth}(d)) + 1) \\ &= \max(\max(0,0) + 1, \max(0,0) + 1) + 1 = \max(1,1) + 1 = 2\end{aligned}$$

Again, PMD between the nodes c and d is 3, because there are three possible partitionings where c, d are not in the same cluster, which are: {a,b}{c}{d}{e,f}, {a}{b}{c}{d}{e}{f} and {a}{b}{c}{d}{e,f}. Finally, the SMD between the nodes a and d is 3. Because, in the subdendrograms rooted with N_1, N_2 and N_3, both a and d are not present at the same time.

Table 1 illustrates the six dendrogram descriptor matrices for the dendrogram presented in Fig. 1.

2.2 *Dendrogram Combination and Final Clustering*

Given a set of k ultra-metric dendrogram descriptors $\mathbb{D} = \{D^1, D^2, \cdots, D^k\}$ of the data objects in the dataset, the associated consensus distance matrix D^{con} can be computed using Eq. 5.

$$D^{\text{con}} = \frac{1}{k} \sum_{i=1}^{k} D^i \tag{5}$$

Table 1 Six Dendrogram descriptors for the example dendrogram presented in Fig. 1

$CD =$

	a	b	c	d	e	f
a	0	15	55	55	60	60
b	15	0	55	55	60	60
c	55	55	0	40	60	60
d	55	55	40	0	60	60
e	60	60	60	60	0	10
f	60	60	60	60	10	0

$CMD =$

	a	b	c	d	e	f
a	1	2	4	4	6	6
b	2	1	4	4	6	6
c	4	4	1	2	6	6
d	4	4	2	1	6	6
e	6	6	6	6	1	2
f	6	6	6	6	2	1

$MED =$

	a	b	c	d	e	f
a	0	1	2	2	3	3
b	1	0	2	2	3	3
c	2	2	0	1	3	3
d	2	2	1	0	3	3
e	3	3	3	3	0	1
f	3	3	3	3	1	0

$PMD =$

	a	b	c	d	e	f
a	0	2	4	4	5	5
b	2	0	4	4	5	5
c	4	4	0	3	5	5
d	4	4	3	0	5	5
e	5	5	5	5	0	1
f	5	5	5	5	1	0

$SMD =$

	a	b	c	d	e	f
a	2	2	3	3	4	4
b	2	2	3	3	4	4
c	3	3	2	2	4	4
d	3	3	2	2	4	4
e	4	4	4	4	3	3
f	4	4	4	4	3	3

$NHD =$

	a	b	c	d	e	f
a	0	2	4	4	5	5
b	2	0	4	4	5	5
c	4	4	0	2	5	5
d	4	4	2	0	5	5
e	5	5	5	5	0	2
f	5	5	5	5	2	0

That is, the (i,j)th entry of the D^{con} matrix indicates the average of the distance entries defined in all the k ultra-metric dendrograms. Then, the aggregated dendrogram was used to perform the final hierarchical clustering.

3 Results and Discussions

3.1 Evaluation Criteria

In order to evaluate clustering algorithms with respect to the applications of different dendrogram descriptors, we use one intrinsic and three extrinsic evaluation criteria. Cophenetic Correlation Coefficient (CPCC), being the intrinsic evaluation metric for a clustering result denotes how accurately the result reflects the input dataset. It is in-fact the normalized correlation coefficient among the distances between the leaf nodes and the corresponding lowest common ancestors. A CPCC score is bounded within the range [0,1] and the score close to 1 is desirable. CPCC is defined in Eq. 6.

$$CPCC = \frac{\sum_{i<j}(d_{ij} - \bar{d})(h_{ij} - \bar{h})}{\sqrt{[\sum_{i<j}(d_{ij} - \bar{d})^2][\sum_{ij}(h_{ij} - \bar{h})^2]}}, \tag{6}$$

where d_{ij} is the distance obtained from the given dendrogram between the ith and jth leaf-node, h_{ij} being the height of the lowest common ancestor of the leaf nodes, $\bar{d}$ and $\bar{h}$ are the mean values of d_{ij} and h_{ij} over all the pairs respectively.

Since all the dataset we used in this study have ground truth, clustering solutions can be assessed using the external criteria: F_1, Rand Index (RI) and the Adjusted Rand Index (ARI), as defined below:

$$F_1 = \frac{2a}{2a+b+c},$$

$$RI = \frac{a+d}{a+b+c+d}, \quad \text{and} \quad ARI = \frac{a - \binom{n}{2}(c+a)(b+a)}{\frac{1}{2}(2a+b+c) - \binom{n}{2}(c+a)(b+a)},$$

where a is the number of pair of objects which are both in the same clusters seen in the predicted and ground truth partitions, b denotes the number of pairs in the same cluster seen in ground truth, but not in the predicted partition, c denotes the number of pairs in the same cluster seen in the predicted partitioning result, but not in the ground truth, and d denotes the number of pairs in the same cluster seen neither in the ground truth nor in the predicted partitioning result.

The F_1, RI are bounded within the range [0,1], but ARI is bounded within the range $[-1, 1]$, and higher score indicates better performance. In order to accomplish the external validation on the hierarchical solutions, we generate partitional clusters from the obtained dendrograms, and then compute the performance metrics using the respective ground truth partitions.

3.2 Datasets

We used three datasets to evaluate our consensus hierarchical clustering framework. These are from UCI machine learning repository. Each of the datasets have labels which were used in the external validation of the clustering results. The datasets and their characteristic features are summarized in Table 2.

All the experiments were conducted on Ubuntu platform in a CPU with Intel core i5-2400 3.10 GHz processor, with 12 GB of RAM.

Table 2 The source and characteristics of the datasets used in the experiments

No.	Name	# of instances	# of features	# of classes
1	Libras movement	360	90	15
2	Wine	178	13	3
3	Parkinson's disease	197	23	2

3.3 Results

We generated 9 input dendrograms for each of the dataset using various hierarchical clustering methods on different distance metrics. The clustering methods include: single-link, average-link and complete-link. And the distance metrics include: Euclidean, Cosine and the city-block distance. For each of the dendrogram, we first computed the six ultra-metric dendrogram descriptors (as defined in Sect. 2.1).

Table 3 illustrates both internal and external evaluation performance of our consensus framework on the libras movement dataset. Overall the average-link and complete-link agglomerative clustering performance are superior than the single-link consensus clustering. The Sub-dendrogram Membership Divergence (SMD) and our proposed descriptor Nodal Hop distance (NHD) are the two ultra-metric descriptors performed better than the other descriptors.

Table 4 illustrates both internal and external evaluation performance of our consensus framework on the wine dataset. We can see that in terms of CPCC score, CD and CMD are the best descriptors when average-link and complete-link agglomerative clusterings have been employed. Although the SMD and NHD were not the best in this scenario, but in terms of the external evaluation criteria (F_1, RI and ARI), SMD and NHD are showing consistently good scores.

Table 5 illustrates both internal and external evaluation performance of our consensus framework on the Parkinson's disease dataset. Here, all the ultra-metric dendrogram descriptors show good performance except MED. Again, we see that the average-link and complete-link agglomerative clustering performance are superior than the single-link consensus clustering.

4 Conclusion and Future Research Direction

In this paper, we presented a simplified framework for consensus hierarchical clustering problem. In this framework, each input dendrogram is first represented by a ultra-metric dendrogram descriptor matrix. Then, we combined the descriptor matrices using simple averaging aggregator. We investigated six dendrogram descriptor matrices, including a proposed descriptor matrix namely Nodal Hop Distance (NHD). Experiments were performed on three generic machine learning datasets to evaluate our framework and underline the effectiveness of the proposal. There are several future research scopes that can begin from this study. First, scaling up the aggregation process to large-scale and distributed datasets. Second, the study shows that average link and complete link based consensus clustering is better. But, in terms of other agglomerative clustering methods, this avenue is yet to be investigated.

Table 3 Experimental results on the libras movement dataset

Descriptor	Average-link				Single-link				Complete-link			
	CPCC	F_1	RI	ARI	CPCC	F_1	RI	ARI	CPCC	F_1	RI	ARI
CD	0.907	0.139	0.305	0.024	0.747	0.128	0.288	0.011	0.907	0.126	0.227	0.008
CMD	0.926	0.339	0.866	0.276	0.875	0.217	0.740	0.126	0.926	0.284	0.864	0.217
MED	0.831	0.220	0.315	0.019	0.655	0.201	0.423	0.033	0.811	0.322	0.314	0.018
PMD	0.975	0.193	0.634	0.094	0.899	0.171	0.550	0.066	0.975	0.234	0.757	0.147
SMD	0.990	0.122	0.183	0.003	0.985	0.122	0.165	0.002	0.990	0.134	0.316	0.019
NHD	0.977	0.393	0.912	0.346	0.886	0.271	0.831	0.196	0.987	0.334	0.902	0.282

Table 4 Experimental results on the wine dataset

Descriptor	Average-link				Single-link				Complete-link			
	CPCC	F_1	RI	ARI	CPCC	F_1	RI	ARI	CPCC	F_1	RI	ARI
CD	0.926	0.656	0.700	0.413	0.713	0.499	0.373	0.011	0.926	0.501	0.360	0.007
CMD	0.931	0.602	0.724	0.391	0.845	0.500	0.343	−0.004	0.931	0.626	0.690	0.377
MED	0.874	0.712	0.403	0.113	0.519	0.710	0.618	0.013	0.788	0.575	0.544	0.012
PMD	0.943	0.618	0.637	0.324	0.675	0.483	0.374	−0.009	0.943	0.647	0.692	0.398
SMD	0.869	0.500	0.343	−0.004	0.742	0.500	0.343	−0.004	0.869	0.654	0.696	0.408
NHD	0.793	0.597	0.731	0.395	0.656	0.498	0.596	0.173	0.793	0.597	0.731	0.395

Table 5 Experimental results on the Parkinson's disease dataset

Descriptor	Average-link				Single-link				Complete-link			
	CPCC	F_1	RI	ARI	CPCC	F_1	RI	ARI	CPCC	F_1	RI	ARI
CD	0.908	0.774	0.638	0.042	0.699	0.774	0.638	0.042	0.908	0.768	0.627	0.014
CMD	0.956	0.734	0.597	−0.000	0.920	0.734	0.597	−0.000	0.956	0.726	0.593	0.005
MED	0.710	0.331	0.438	0.022	0.775	0.331	0.301	0.081	0.921	0.421	0.114	0.031
PMD	0.974	0.734	0.597	−0.000	0.835	0.738	0.602	0.006	0.974	0.734	0.597	−0.000
SMD	0.974	0.734	0.597	−0.000	0.936	0.734	0.597	−0.000	0.974	0.734	0.597	−0.000
NHD	0.947	0.772	0.603	0.011	0.902	0.766	0.622	−0.007	0.947	0.775	0.592	0.008

References

1. Fred AL, Jain AK (2005) Combining multiple clusterings using evidence accumulation. IEEE Trans Pattern Anal Mach Intell 27(6):835–850
2. Hossain M, Bridges SM, Wang Y, Hodges JE (2012) An effective ensemble method for hierarchical clustering. In: Proceedings of the fifth international C* conference on computer science and software engineering, pp. 18–26. ACM
3. Li T, Ding C (2008) Weighted consensus clustering, pp. 798–809. SIAM
4. Mirzaei A, Rahmati M (2008) Combining hierarchical clusterings using min-transitive closure. In: 19th international conference on pattern recognition, 2008. ICPR 2008, pp. 1–4. IEEE
5. Mirzaei A, Rahmati M (2010) A novel hierarchical-clustering-combination scheme based on fuzzy-similarity relations. IEEE Trans Fuzzy Syst 18(1):27–39
6. Podani J (2000) Simulation of random dendrograms and comparison tests: some comments. J Classif 17(1):123–142
7. Rashedi E, Mirzaei A, Rahmati M (2015) An information theoretic approach to hierarchical clustering combination. Neurocomputing 148:487–497
8. Strehl A, Ghosh J (2003) Cluster ensembles—a knowledge reuse framework for combining multiple partitions. J Mach Learn Res 3:583–617
9. Zheng L, Li T, Ding C (2014) A framework for hierarchical ensemble clustering. ACM Trans Knowl Discov Data (TKDD) 9(2):9

Part XII
Circuit Processing System and System Design

A Resistor Loaded Bow-Tie Antenna Fed by Gaussian Pulse

Jun Zheng, Jia-Wei Li and Ning-Ning Yan

Abstract A resistor loaded bow-tie antenna fed by Gaussian pulse which is generated by avalanche transistor Marx circuit is proposed in this paper. The Marx circuit generates very short pulse with high peak voltage and the width of the Gaussian pulse is 0.5 ns. The antenna has dimensions of 10 cm by 9 cm and is based on a dielectric substrate. The antenna with discrete exponential resistive loading minimizes the duration of the radiation pulse. The antenna has opposed structure whose two monopoles are separately placed on the top and bottom surfaces of the dielectric substrate that makes the antenna bear high voltage. The technical parameters of the antenna (such as fidelity, time-domain pattern, etc.) are optimized so that the antenna has good fidelity and wide time-domain pattern.

Keywords Gaussian pulse · Marx circuit · Resistor loaded bow-tie antenna · Fidelity · Time-domain pattern

1 Introduction

Nanosecond and subnanosecond pulse power generators are important in variety of applications, such as ground-penetrating radar (GPR) [1], see-through-wall (STW) radar technology [2], survivor detection, material processing, and medical treatment [3, 4]. The key point of all these technologies depends on the suitable

J. Zheng (✉)
Sichuan Electronic Military Equipment Technology Research Institute, Chengdu 611700, China
e-mail: lesterli3@163.com

J.-W. Li · N.-N. Yan
School of Physical Electronics, University of Electronic Science and Technology of China, Chengdu 611731, China
e-mail: 597071220@qq.com

N.-N. Yan
e-mail: 312924970@qq.com

Q. Liang et al. (eds.), *Proceedings of the 2015 International Conference on Communications, Signal Processing, and Systems*, Lecture Notes in Electrical Engineering 386, DOI 10.1007/978-3-662-49831-6_82

pulse generators. Several technologies exist for generation of nanosecond pulses such as spark gas [5], draft-step-recovery diode (DSRD) [6], semiconductor opening switch (SOS) [7] and fast-ionization device (FID) and all of them rely on fast high power switches. Avalanche transistor may be an ideal candidate as a high-speed switching device.

The GPR system is an effective tool for nondestructively sensing subsurface environment. Antenna is one of the most critical hardware components for the performance of the GPR system. The system demands an antenna with fewer multiple reflections of the input signal from different parts of the antenna [8]. There are only a few types of antennas that are widely used in GPR systems, such as resistively loaded cylindrical monopoles, TEM horns [9], resistor loaded bow-tie antennas [10, 11], and spiral antennas [12]. As ultra-wideband electromagnetic pulse is usually used in the system, the antenna should be wideband and couple electromagnetic from air to ground, which is lossy and dispersive medium [8]. In order to distinguish the scattered signal of the target from the clutter, it is very essential that the antenna should be able to transmit the input signal with subtle distortion. The late-time ringing of the signal should be reduced. Therefore, the resistively loaded bow-tie antenna with compact structure, flat input impedance for minimal antenna ringing, and stable radiation patterns for minimal impact on the shape of radiated waveforms is adopted in GPR system.

In this paper, a 15 classes Marx pulse generator is designed which could generate zero order Gaussian pulse with 1 kV peak voltage, 500 ps pulse width and 10 kHz repeat frequency. We present the design, simulation results, and experimental results of the antenna. The exponential resistive loading profile is an effective mode while most GPR antennas use resistive loading to terminate the reflections at the end of antenna [13] or they are linearly loaded [14]. The antenna is also manufactured more facilely than the continuous resistive loading antenna [15].

2 Typical Avalanche Transistor Waveform and Marx Circuit

2.1 Typical Avalanche Transistor Waveform

Figure 1a shows a typical circuit of avalanche transistor. The collector-to-emitter voltage E_C is very near to the breakdown voltage. As $R_L \gg R_C$, R_C mainly determines the current supplied to charge capacity C. As capacity charges, the collectors-to-emitter voltage approximately remains to E_C. The emitter junction becomes forward biased and junction into the base begins. It is the time that the transient shown in Fig. 1b (stimulated by Pspice) takes place.

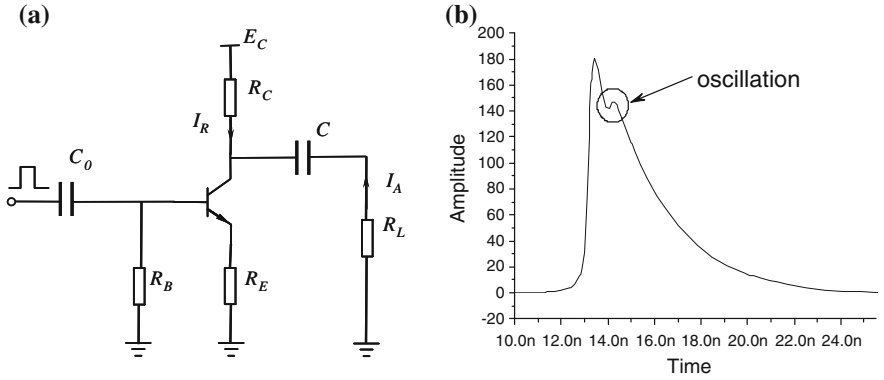

Fig. 1 **a** Avalanche transistor circuit **b** Typical waveform of the pulse

2.2 Marx Circuit Based on Avalanche Transistor

In order to achieve high peak voltage, Marx circuit was used [16]. By connecting avalanche transistor in series, the peak voltage of pulse could be multiplied effectively.

The capacity $C_{1\text{-}15}$ was charged by V_{CC} at the same time, until the first transistor was triggered. As the trigger input, avalanche transistor breaks down in sequence causes stored charges discharged though R_M and R_L. Regardless of leak current, the peak voltage of Marx circuit can be written as

$$V_{\text{peak}} = \frac{NV_{CC}R_L}{R_L + R_M} \tag{1}$$

where N is the class number of Marx circuit, V_{CC} is supply voltage.

Measured result is shown in Fig. 2 that the original falling edge of the pulse is not a perfect *RC* discharging curve. As we discussed before, each single avalanche transistor of 15 classes of the Marx circuit has an oscillation after capacity $C_{1\text{-}15}$ begins to discharge.

Since the oscillation is inevitable and the occurring time is mainly determined by transistor, we can make the oscillation move out of the falling edge. We gradually reduce capacitance of charging capacity. In this way, the waveform of the pulse is more symmetrical with less tailing. Experiment in Fig. 3 shows the gradual reduction in capacitance of charging capacity of the last six classes.

Figure 3a shows the comparison of the original measured pulse and the modified measured pulse. The output waveform in Fig. 3b is measured by Agilent digital oscilloscope with 6 GHz sampling bandwidth and 20 GS/s sampling rate via a 60 dB high-voltage attenuator. The pulse is with 200 ps rise time, 250 ps fall time, 500 ps (10–10 %) pulse width, and 1 kV amplitude (measured on 50 Ω load).This method can accelerate the discharging progress so that the oscillation of the pulse

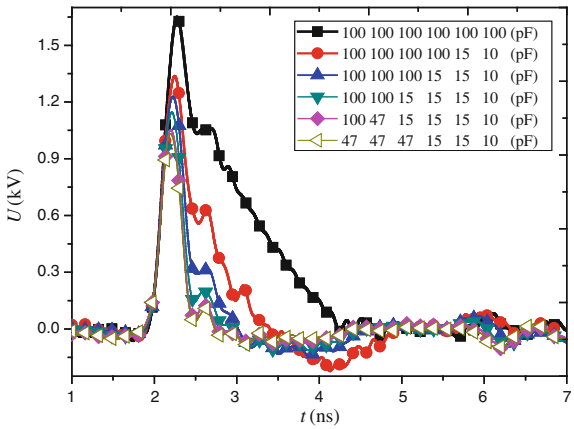

Fig. 2 The waveform of the pulse changes with lost six capacity gradually deduced

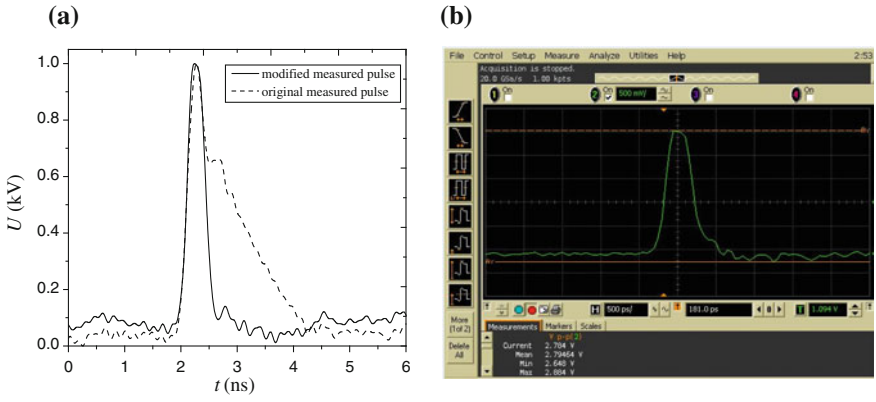

Fig. 3 **a** Comparison waveform of original and modified **b** Experimental final result

moves out of the falling edge. Taking on-resistance into consideration, R_M should be smaller than R_L and to reduce reflections from loading (normally 50 Ω).

3 Antenna Design and Antenna Results

3.1 The Design of Antenna

The geometry of the antenna illustrated in Fig. 4a indicates that it has a planar structure with the dimensions of only 10 cm by 9 cm which have been found optimal for the transmission of the abovementioned Gaussian pulse. The antenna is realized as a printed antenna on a dielectric substrate. The thickness and relative

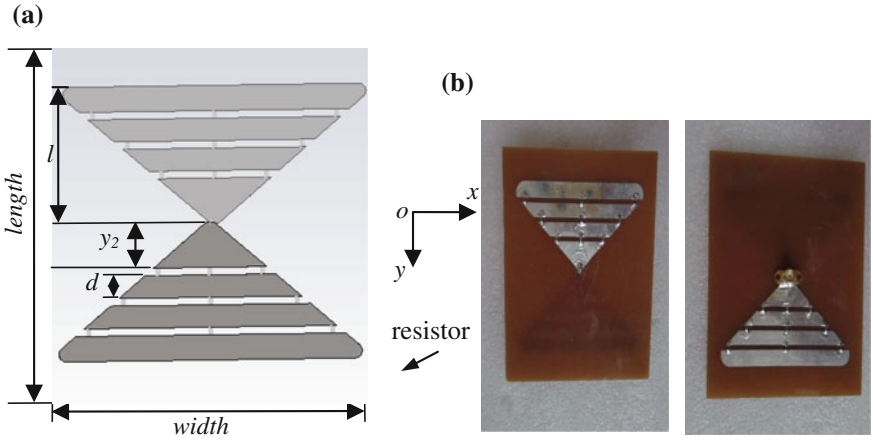

Fig. 4 **a** Geometry of the antenna: length = 10 cm, width = 9 cm, flare angle = 100°, y_0 = 1.2 cm, d_1 = 0.2 cm, d_2 = 0.6 cm; Resistors are the same in each gap; R_0 = 27 Ω, R_1 = 56 Ω, R_2 = 120 Ω **b** *Top* and *bottom* view of the manufactured single antenna

dielectric constant is 4 mm and 4.4, respectively. For suppression of late-time ringing, the monopoles of the antenna are loaded with chip resistors soldered across the gaps as indicated in Fig. 4a. The photograph of the manufactured antenna is shown in Fig. 4b and the proposed antenna is fed by a 50 Ω SMA connector. The resistive value increases exponentially from the position y_0 (the starting position of resistive loading along the dipole) to the end. The resistor profile is given as

$$R = R0\exp[k(y - y0)/l] \tag{1}$$

where, R_0 is the resistor value of the starting position, k is optional coefficient, y is the position along the resistive monopole, l is the total length of the resistive monopole.

Figure 5 shows the 0.5-ns Gaussian pulse and the frequency spectrum of the pulse. The antenna fed by the pulse is designed, simulated, and optimized (Fig. 6).

3.2 The Simulated and Experimental Results

The performance parameter of each antenna is obtained by the simulation software of CST 2011. In order to transmit short duration time pulses and distinguish the scattered signal of the target from the clutter, it is very essential that the antenna is able to transmit the input signal with little distortion. It demands an antenna with broadband input impedance characteristics and fewer multiple reflections of the input signal from different parts of the antenna. Figure 7 shows the simulated and measured S11(dB) of the antenna and we can see the S11 is about less than -10 dB

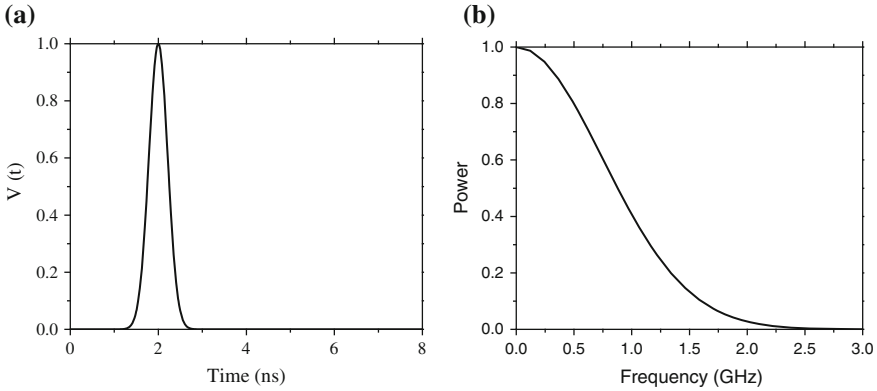

Fig. 5 **a** Diagram of 0.5-ns Gaussian pulse **b** Frequency spectrum of Gaussian pulse

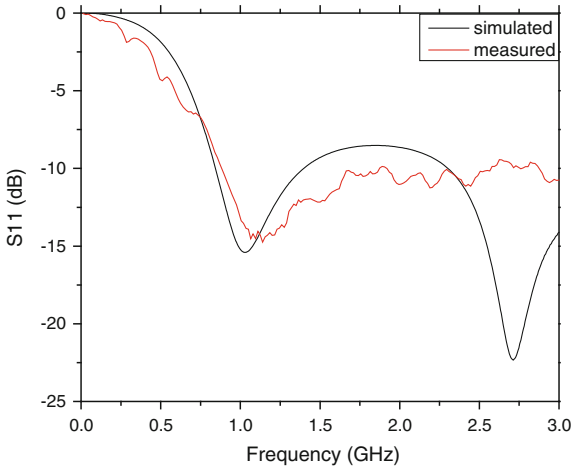

Fig. 6 Input reflection coefficients S11(dB) of simulated and measured results

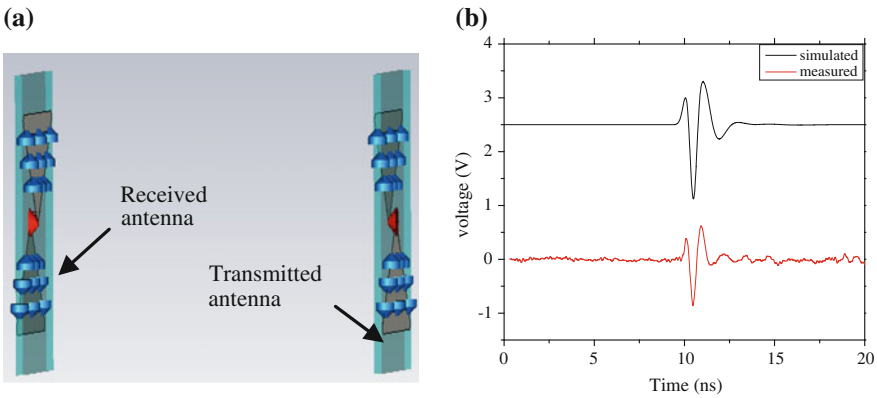

Fig. 7 The model of transmitted and received antennas and comparison of the transmitted waveforms simulated and measured of the antenna

when frequency is higher than 0.85 GHz. It indicates that the measured results are in good agreement with the simulated results with acceptable tolerance.

The distance r between transmitted and received antennas along the axial direction needs to meet the time-domain far-field Fraunhofer condition as following:

$$r \geq 2L^2/cT \approx 0.13\text{m} \tag{2}$$

where, L is the maximum size of the antenna, c is light velocity, and T is width of the excitation pulse. Taking $r = 1$ m to meet the far-field condition (r greater than 0.13 m) as shown in Fig. 7a. The simulated and measured time domain waveforms transmitted by the antenna are shown in Fig. 7b. The clutter signals shown in measured waveforms are partly carried out by the circuit radiation of the pulse generator, the reflections of the ground and the experiment environment. From the results, shown in Fig. 7b, it can be seen that the waveform has short duration time and the experiment and the simulation results have little difference.

Additionally, Fig. 3a presents the measured waveforms received by antenna in different directions in E plane. We can see there is a little change in the waveforms and it indicates that the antenna has high fidelity. The simulated and measured time-domain radiation patterns in E plane of the proposed antenna are shown in Fig. 3b. The simulated and measured half power beamwidth (HPBW) in E plane are about ±43, ±36°, respectively, which demonstrates the good directivity of the antenna. The trends between the simulated and measured time-domain radiation patterns are the same and they are accorded with each other (Fig. 8).

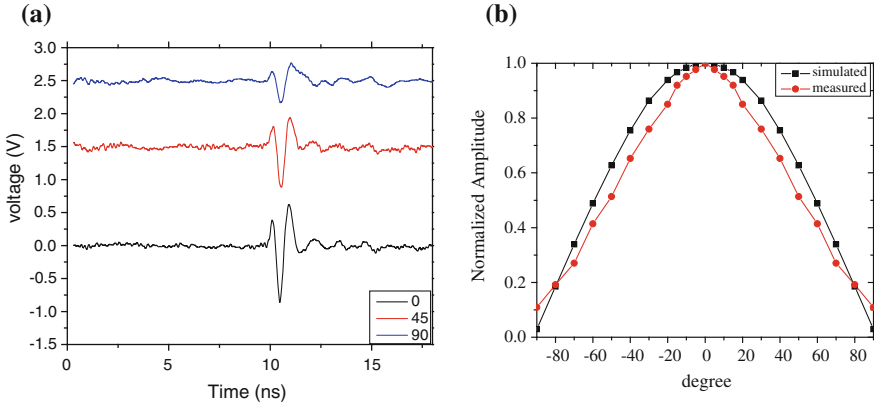

Fig. 8 **a** Time domain waveforms measured in different directions **b** the time-domain radiation pattern

4 Conclusion

The Marx pulse generator can produce very short pulse with high peak voltage and the final experiment pulse is much similar to the standard Gaussian pulse. Exponential loaded bow-tie antenna can be designed for large bandwidth, and transmitting the input signal with little distortion and high fidelity. The characteristic of the pulse generator and antenna in time domain behavior demonstrates that they can be used in GPR systems very well.

References

1. Persico R, Soldovieri F (2000) A microwave tomography approach for a differential configuration in GPR prospecting.[J]. IEEE Trans Antennas Propag 11:3541–3548
2. Liu Q, Wang Y, Fathy AE (2012) A compact integrated 100 GS/s sampling module for UWB see through wall radar with fast refresh rate for dynamic real time imaging. Radio Wirel Symp (RWS), pp. 59–62
3. Corbella C, Vives M, Oncins G, Canal C, Andujar JL, Bertran E. (2004) Characterization of DLC films obtained at room temperature bypulsed-DC PECVD. Diam Relat Mater, 13(4–8):1494–1499
4. Fridman A (2008) Plasma Chemistry. Cambridge University Press, Cambridge, U.K
5. OsmokroviC P, Arsie N, LazaxeviC' Z, KartaloviC' N. (1996) Triggered vacuum and gas spark gaps, IEEE Trans Power Deliv, 11(2)
6. Merensky LM, Kardo-Sysoev AF, Flerov AN, Pokryvailo A, Shmilovitz D (2009) A low-jitter 1.8-kV 100-ps Rise-time 50-kHz repetition-rate pulsed-power generator, Trans Plasma Sci 37(9)
7. Lyubutin SK, .Mesyats GA, Rukin SN, Slovikovskii BG (1997) Subnanosecond high-density current interruption in SoSdiodes. In: Pulsed Power Conference, vol 1, pp 664–666
8. Liu L, Su Y, Huang C, Mao J (2005) Study about the radition properties of an antenna for Ground-Penetrating Radar. In: IEEE international symposium on microwave, antenna, propagation and EMC technologies for wireless communications proceedings
9. Turk AS, Keskin AK (2011) Vivaldi shaped TEM horn fed ridged horn antenna design for UWB GPR systems. In: 2011 6th international workshop on advanced ground penetrating radar (IWAGPR), pp 22–24. Aachen
10. Lestari AA, Yulian D, Liarto, Suksmono A.B (2007) Improved bow-tie antenna for pulse radiation and its implementation in a GPR survey. In: 2007 4th International Workshop on Advanced Ground Penetrating Radar, pp 27–29. Aula Magna Partenope. June
11. Lestari AA, Yarovoy AG, Ligthart LP (2004) RC-Loaded bow-tie antenna for improved pulse radiation. IEEE Trans Antennas Propag 52(10)
12. Phelan M, Su H, LoVetri J (2002) Near field analysis of a wideband log-spiral antenna for 1–2 GHz GPR. In: Canadian Conference on Electrical and Computer Engineering, 2002, IEEE CCECE 2002
13. Nishioka Y, Maeshima O, Uno T, Adachi, S (1999) FDTD analysis of resistor-loaded bow-tie antennas covered with ferrite-coated conducting cavity for subsurface radar. In: IEEE Trans Antennas Propog, 47(6)
14. Waldschmidt C, Palmer K.D (2001) Loaded wedge bow-tie antenna using linear profile. Electron Lett, 37(4)
15. Lee K-H, Venkatarayalu NV, Chen C-C (2002) Numerical modeling development for characterizing complex GPR problems. SPIE, vol 4758, pp 652–656
16. Bailey V, Carboni V, Eichenberger C, Naff T, Smith I, Smith I (2010) A 6-MV pulser to drivr horizontally polarized EMP simulators. IEEE Trans Plasma Sci, 38(10)

A Cavity-Backed Time-Domain Oval Dipole Antenna Designed for Application in Anti-stealth Radar

Jun Zheng, Ya-Hua Ran, Zhi Liu and Yi Wang

Abstract A high peak power time-domain oval dipole antenna is designed for application in anti-stealth radar and high-power microwave system. A kind of Blumlein Reflection Line (BRL) is integrated with photoconductive semiconductor switches (PCSS) to generate monocycle pulse with 2 ns pulse width to feed the antenna. Opposed structure is adopted to make the antenna able to withstand high peak voltage. An idea of impedance load and adding back cavity for antenna is further proposed to get directed radiation signal with desirable front-to-back (F/B) ratio. Antenna is optimized and simulated with computer simulation tool (CST) Microwave Environment software. The experimental results show the performance parameters of the antenna radiation electromagnetic pulse is with about 3:1 front-to-back ratio in the amplitude scale which is practically measured as 2.2:1.

Keywords High peak power · Time-domain · Oval dipole antenna · Opposed structure · Impedance load · Back cavity

1 Introduction

Time domain antenna can efficiently solve the problem of frequency band that is being increasingly cramped as the traditional technology of frequency domain has grown-up. Time-domain antenna is also customized for anti-stealth radar. Time-domain antenna is required to feature high power, high fidelity, high radiation efficiency, wide bandwidth, and good directionality to apply in anti-stealth radar.

J. Zheng (✉)
Sichuan Electronic Military Equipment Technology Research Institute, Chengdu 610017, China
e-mail: lesterli3@163.com

Y.-H. Ran · Z. Liu · Y. Wang
School of Physical Electronics, University of Electronic Science and Technology of China, Chengdu 611731, China

Q. Liang et al. (eds.), *Proceedings of the 2015 International Conference on Communications, Signal Processing, and Systems*, Lecture Notes in Electrical Engineering 386, DOI 10.1007/978-3-662-49831-6_83

Based on the conventional design of time-domain antenna, F/B ratio among these properties is considered as the main merit of the proposed antenna.

Many methods have been proposed to control direction and improve F/B ratio of time-domain antenna such as structure optimization [1–3], Fresnel zone plate (FZP) lens focusing [4, 5], organizing array [5], compensation of distance traveled, and adopting dielectric director [6]. Structure optimization is popularly used to improve F/B ratio. FZP lens focusing is a novel idea which can more efficiently help in obtaining desirable F/B ratio. However, it is difficult to design and manufacture the lens because the low centre frequency of time-domain antenna causes the large dimension of the antenna and then the lens should be designed with relatively apposite size. Most of the time-domain array antennas obviously show disadvantage for its large dimension. Literature [6] shows the adoption of dielectric director to improve F/B ratio. High permittivity is the common feature of FZP lens and dielectric director, so both manufacture of FZP lens and dielectric director cost much. Taking these in consideration, conventional design is further proposed.

In this paper, photoconductive semiconductor switches are applied for signal source because of its fast response, low jitter, and high peak power. Opposed configuration is further adopted to make the dipole antenna able to withstand high peak voltage to realize high peak power. The BRL is designed to transform the Gaussian pulse generated by PCSS into monocycle pulse to improve the radiation efficiency [7]. CST is used to simulate the radiation pulse and calculate the parameters of the antenna. In order to keep current on antenna distributed as travelling wave, a method of loading resistance of 200 Ω on the corner of the antenna is proposed to decrease the amplitude of noise and guarantee high fidelity [8, 9]. In addition mirror effects are taken into consideration and then a rectangle back cavity with 200 mm height and the same length and width with the substrate is designed to improve radiation performance. Simulation results show that the parameter of the antenna is with about 3:1 front-to-back ratio in the amplitude scale. The experimental results are consistent with the simulation results so it's reliable to apply the proposed antenna in anti-stealth radar and high-power microwave system.

2 Antenna Design and the Proposed Directional Transceiver Models

2.1 Antenna Design

The configuration of the time-domain oval dipole antenna with a metal rectangular back cavity with opposed surface structure is illustrated in Fig. 1. In Fig. 1a, the optimized dimensions of the singular time-domain oval dipole antenna are presented as below: $a = 57.722$ mm, $b = 41.173$ mm, $c = 5.781$ mm, $d = 1$ mm, $r = 75.5$ mm. The size of FR4 epoxy substrate is $200.233 \times 200.233 \times 1$ mm^3 with dielectric constant $\varepsilon_r = 4.4$. In general, the time-domain oval dipole antenna in

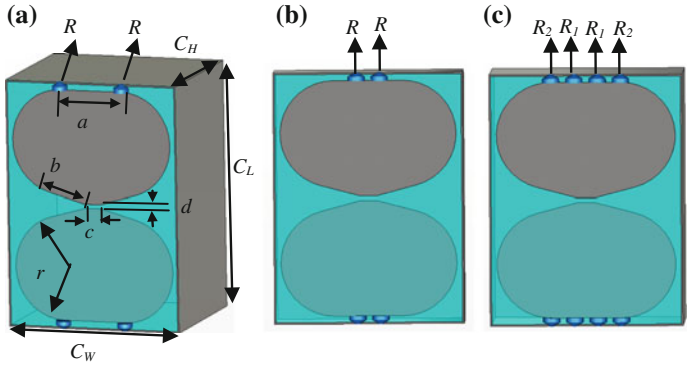

Fig. 1 The configuration of the time-domain oval dipole antenna with a metal rectangular back cavity. **a** The simulation model of the antenna. **b** The load resistors is close to *middle* position of the antenna. **c** The load eight resistors with two kinds of R1 and R2

free space radiates bidirectional patterns with the maximum gain in the normal directions of the antenna plane. Bidirectional patterns are not suitable for of the most wireless communication systems because the polarization senses of the two beams are opposite. To generate unidirectional patterns, the antenna is devised with a back cavity or reflector. As shown in Fig. 1a, a rectangular cavity of length C_L, width C_W, and height C_H is placed underneath the antenna and connected to the ground plane of the PCB. In practice, the cavity of length and width is slightly greater than the size of the oval dipole antenna so as to spare enough space for the margin for manufacturing and assembling. In order to decrease the reflection from the end of the oval dipole antenna and the backward radiation, four end-loaded resistors are symmetrically attached between the top of the oval dipole and the top of the metal rectangular reflector.

The dimensions of the design antenna are decided by the central frequency of the feeding electric pulse. Some parameters which have effects on the impedance matching, radiation waveform or its' power spectrum are discussed in following contents.

Figure 2 demonstrates the simulated results of the radiated waveforms and its power spectrum as the height C_H of the back cavity increases. It shows, when C_H is less than 200 mm, the waveform's peak is significantly reduced and the power spectrum's amplitude is also significantly reduced, when $C_H > 200$ mm, although the waveform peak is little different and the amplitude of trailing signal has been reduced, the number of rings increases and the power spectrum's amplitude is significantly reduced. After comprehensive analysis, 200 mm is the optimal height of the metallic back cavity to realize more power radiation and compact construction of the antenna.

Resistance parameters including the location of resistors, the number of load resistance, and the resistance value have influences on the antenna performance. Compared to Fig. 1a, the location of the load resistors, shown in Fig. 1b, is close to

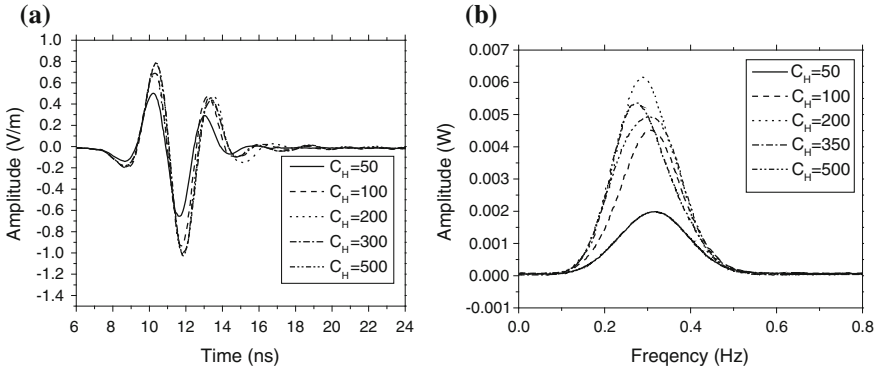

Fig. 2 Influence of parameter C_H. **a** The radiated waveform. **b** The power spectrum of the radiation waveform

middle position of the antenna, but the resistance is still 200 Ω. In Fig. 3, the input impedance bandwidth, as the resistance, located on the corner of the antenna is wider than the input impedance bandwidth as the resistance is set away from the corner of the antenna. The reason is shown by Fig. 3b, that a larger dish current density is distributed on the corner edge of antenna. So loading resistors on the corner edge of antenna is naturally a proper way to decrease the antenna reflection.

The next study is the influence on antenna performance as the number of loading resistors changes from 2 to 4 and 8. As shown in Fig. 1c, resistor R1 = 330 Ω and R2 = 470 Ω are symmetrical loaded at the side ends of the antenna. The resistor at each side of the antenna is equivalent to a parallel resistance, and the total resistance keeps 200 Ω. After abundant simulation, it is concluded that the number of load

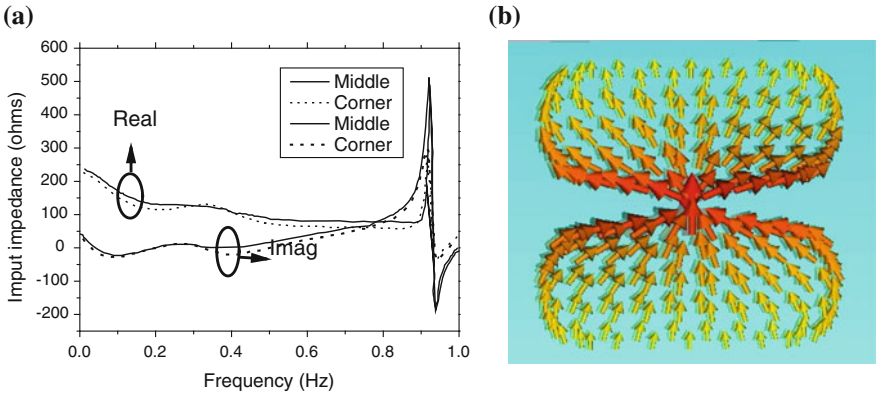

Fig. 3 **a** Input impedance of the antenna with the different loading resistance. **b** Current distribution

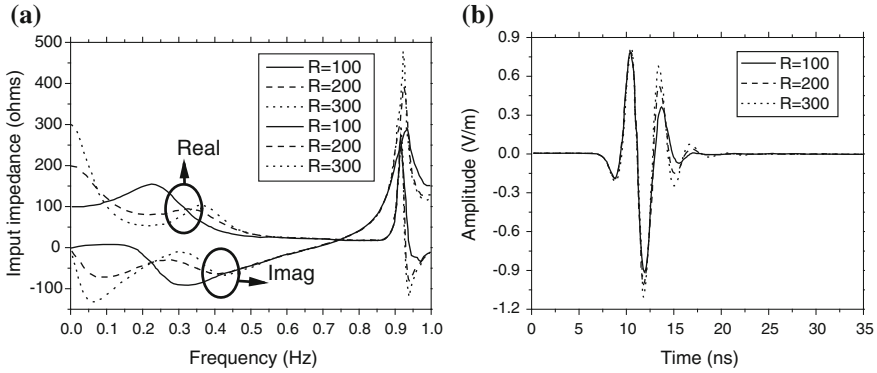

Fig. 4 The loaded different resistance. **a** The input impedance. **b** Waveforms of radiation

resistor has nothing to do with input impedance and radiation waveform of the antenna. Therefore, we choose to load four resistors.

Figure 4 demonstrates the simulation results of the impedance changing and the different radiation waveforms as the value of the loaded resistor R increases. Figure 4a shows the loaded resistance of the antenna can significantly affect the input impedance when frequency is low. The input impedance of the antenna increases as the loaded resistance increases. Figure 4b shows the radiation waveform and amplitude of trailing signal are larger as the total resistance increases. When R varies from 150 to 250 Ω, the amplitude of noise signal is small and waveforms fidelity is good. The final values for the parameters are given in Table 1.

2.2 *The Proposed Directional Transceiver Models*

The proposed three directional transceiver models are shown in Fig. 5a. The transmitting and receiving antennas are placed in the air-filled box face to face. The distance between transmitting antenna and receiving antenna is 2 m. The boundary conditions in the CST MWS are set as "open (add space)". The transient solver module is used in our simulation. The feeding pulse is a monocycle with 3 ns peak-peak duration. Figure 5a demonstrates the simulation results of the received waveforms from back and front. As show in Fig. 5b, front-to-back ratio in the amplitude scale of waveform which is received by the front antenna to that received

Table 1 The final values for the parameters

Parameters	A_1	B_1	C_1	D_1
Value (mm)	125.369	14.397	14.397	2.45
Parameters	r	C_L	C_W	C_H
Value (mm)	40	320	210.998	202.4

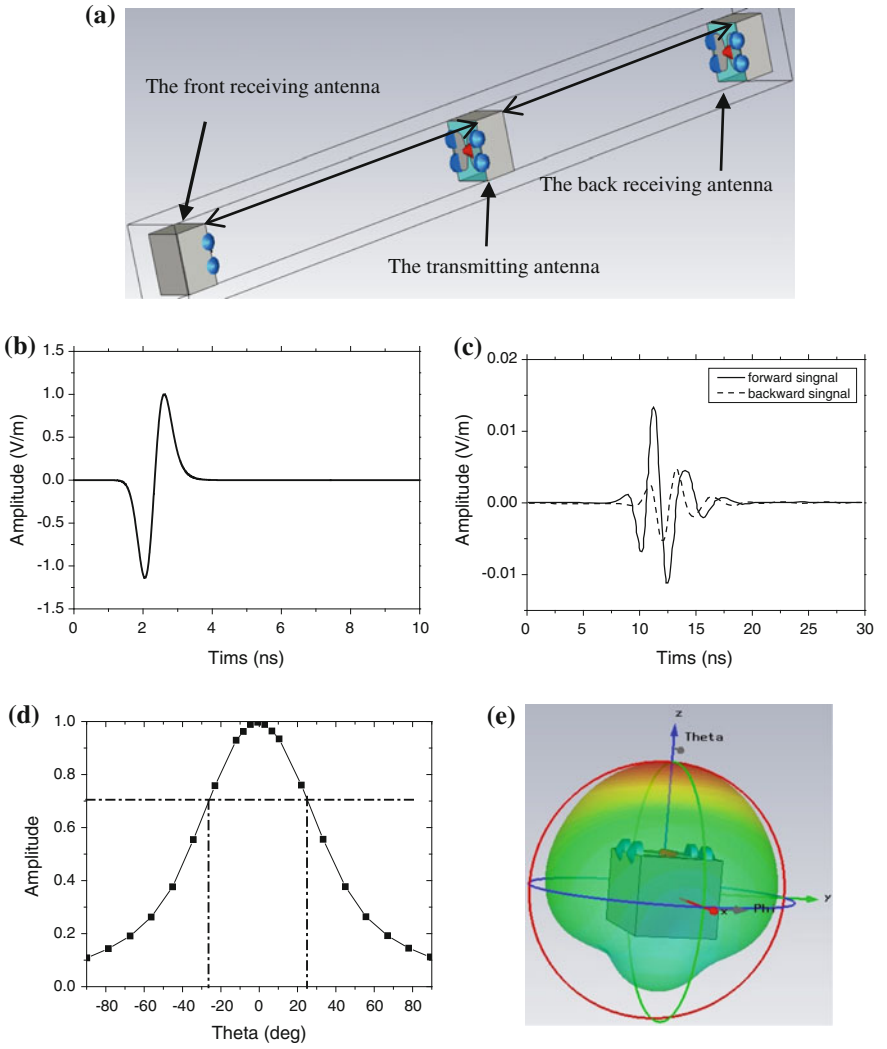

Fig. 5 Co-simulation. **a** The simulated model. **b** Waveforms of the monocycle pulse. **c** Waveforms accept by the receiving antennas in Co-simulation. **d** The normalized frequency patterns at 0.528 GHz. **e** Normalized energy pattern (NEP)

by the back one is 3 to 1. Figure 5c, d show the simulated normalized frequency patterns with 2.76 dB practical gain at 0.528 GHz and simulated normalized energy pattern (NEP) with about ±25°, respectively. It is indicated that the proposed antenna generates unidirectional patterns.

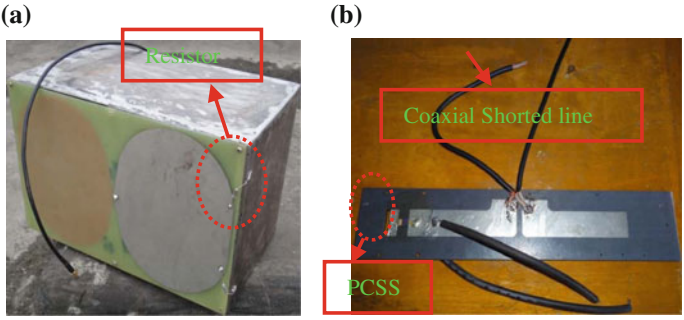

Fig. 6 **a** Prototype of the proposed antenna. **b** Prototype of the PCSS Blumlein line and BRL

3 Experiment of the Proposed Antenna

Figure 6 shows the fabricated prototype of the designed antenna with the same dimensions as indicated in Table 1. Figure 6b shows the prototype of the PCSS Blumlein line and BRL. The PCSS produces Gaussian pulse, so BRL is designed to transform the Gaussian pulse into a monocycle pulses with duration of 3 ns (central frequency of 0.528 GHz). In this letter, the PCSS fabricated on GaAs material which can output voltage 10 kV, pulse width 1.8 ns, trigger jitter root mean square value of 65 ps of high power transient electrical pulse. Figure 8a shows the experiment monocycle pulses generated through BRL, when the experiment PCSS and Blumlein line produce about 3 ns Gaussian pulse, and this Gaussian monocycle pulse is used to employ the antenna radiation.

Figure 7 shows simulation and experimental results of the proposed antenna. The measurement was performed with an Agilent E5071C network analyzer. The simulated −8 dB S11 bandwidth (0.265–0.458 GHz), and the measured bandwidth

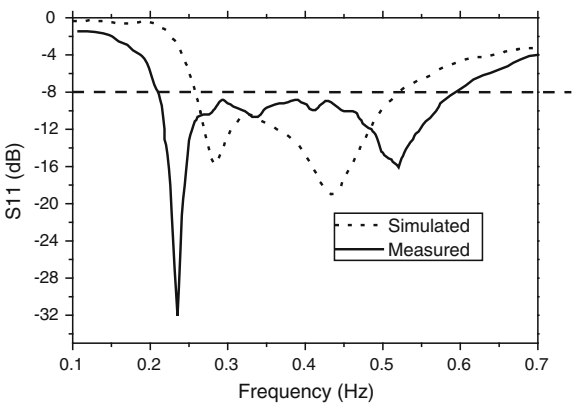

Fig. 7 Input reflection coefficients (dB) of simulation and measured results

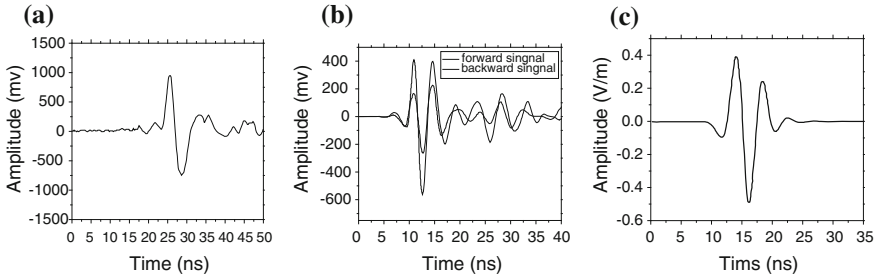

Fig. 8 **a** The measured waveform of the feeding pulse. **b** The measured waveform which is received by the front antenna and the measured waveform which is received by the back antenna. **c** The simulated waveform

with a return loss (RL) 8 dB is achieved from 0.21 to 0.59 GHz. The antenna can operate in the set bandwidth of the monocycle pulse spectrum.

In the experiment, we use the Agilent 54855A oscilloscope to collect the time-domain signals of the receiving antenna which is same with the transmitting antenna. The feeding pulse is a monocycle of 3 ns peak-peak duration. Figure 8a shows the measured feeding pulse with 3 ns peak-peak duration. The second and following periodic pulses shown in the measured waveform curve are reflected by the ground. Figure 8b shows the measured waveform which is received by the front antenna and the back antenna. The experimental results show that both the waveform is in good agreement with the simulation curves except for the ringing, which may come from multipath coupling and reflection from the surrounding. The measured amplitude front-to-back ratio is 2.22:1 while the simulated is 3:1. It indicates that the scheme to realize directional detection by the two proposed directional antennas is practicable.

4 Conclusion

In this paper, a cavity-backed time-domain oval dipole antenna has been proposed. The experimental results which are in good agreement with the simulation results show the performance parameters of the radiation electromagnetic pulse is with about ±25° time-domain amplitude pattern at half peak amplitude, and about 3:1 front-to-back ratio in the amplitude scale which is practically measured as 2.2:1. It is indicated that the proposed is good candidate for application in anti-stealth radar.

References

1. Qu S-W, Li J-L, Xue Q, Chan CH, Li S (2009) Wideband and unidirectional cavity-backed folded triangular bowtie antenna. IEEE Trans Antennas Propag AP-57(4):1259–1263
2. Thai TT, DeJean GR, Tentzeris MM (2008) Design and development of a novel compact soft-surface structure for the front-to-back ratio improvement and size reduction of a microstrip Yagi array antenna. IEEE Antennas Wirel Propag Lett 7:1525–1528
3. Ryu J, Chin H, Yeom J-H, Kim H-T, Kwon H-O, Han SH, Choi JS (2013) A high directive paraboloidal reflector antenna for high far voltage in an ultra wideband source system. IEEE Trans PLASMA SCI AP-41(8):2283–2290
4. Karimkashi S, Kishk AA (2011) Focusing properties of fresnel zone plate lens antennas in the near-field region. IEEE Trans Antennas Propag AP-59(5):1481–1487
5. Kadri I, Petosa A, Roy L (2005) Ka-band Fresnel lens antenna fed with an active linear microstrip patch array. IEEE Trans Antennas Propag AP-53(12):4175–4178
6. Bourqui J, Okoniewski M, Elise C (2010) Balanced antipodal Vivaldi antenna with dielectric director for near-field microwave imaging. IEEE Trans Antennas Propag AP-58(7):2318–2326
7. Lestari AA, Bharata E, Suksmono AB, Kurniawan A, Yarovoy AG, Ligthart LP (2010) A modified bow-tie antenna for improved pulse radiation. IEEE Trans Antennas Propag AP-58 (7):2184–2192
8. Lestari AA Yarovoy, AG, Ligthart LP (2004) RC-loaded bow-tie antenna for improved pulse radiation. IEEE Trans Antennas Propag AP-52(10):369–373
9. Liang H-Y, Yang H-C, Zhang J (2012) A cylindrical conformal directional monopole antenna for borehole radar application. IEEE Antennas Wirel Propag Lett 11:1525–1528

Improvement of Errors-and-Erasures Algorithm for JTIDS

Zengshan Tian, Liang Li, Mu Zhou and Wei He

Abstract The Joint Tactical Information Distribution System (JTIDS) is the communication terminal of Link-16. In this work, an improvement on the errors-and-erasures decoder (EED) is proposed for the JTIDS receiver to replace the original EED. Based on the analysis of every two adjacent pulses in JTIDS double pulses mode, we determine the current output symbol, and then reduce the symbol error rate, as well as improve the performance of JTIDS receiver in the complex electromagnetic environment. The simulation results show that as the additive white Gaussian noise and pulsed-noise interference exist, the JTIDS receiver with the proposed improved EED is featured with better anti-interference performance.

Keywords Joint tactical information distribution system · Errors-and-erasures decoder · Probability of symbol error · Pulsed-noise interference

1 Introduction

The Joint Tactical Information Distribution System (JTIDS) is system integrated with communications, navigation and identification, which has been widely used in the United States and North Atlantic Treaty Organization forces. The JTIDS is a time division multiple access (TDMA) system with the characteristics of the direct sequence spread spectrum, frequency hopping, and Reed–Solomon (RS) encoding.

The performance of symbol error rate (SER) of JTIDS using various modulation schemes under different types of interference and fading have been investigated in [1–7].The analytical expressions for the performance of SER of the coherently detected JTIDS-type were first given in [1]. The performance of JTIDS receiver using

Z. Tian · L. Li (✉) · M. Zhou · W. He
Chongqing Key Lab of Mobile Communications Technology, Chongqing University of Posts and Telecommunications, Chongqing 400065, People's Republic of China
e-mail: liliang_fpga@163.com; 707854950@qq.com

Z. Tian
e-mail: tianzs@cqupt.edu.cn

Q. Liang et al. (eds.), *Proceedings of the 2015 International Conference on Communications, Signal Processing, and Systems*, Lecture Notes in Electrical Engineering 386, DOI 10.1007/978-3-662-49831-6_84

the errors-and-erasures decoder (EED) for both the single- and double-pulse structures with Additive White Gaussian Noise (AWGN) and pulsed-noise interference (PNI) was investigated in [2]. The results in [2] showed that the EED outperforms the errors-only decoding as the PNI exists. The probability of symbol error with respect to the JTIDS/Link-16-type waveform transmitted over the slow and flat Nakagami fading channel was studied in [3].The results in [4] proved that the JTIDS receiver with the noise normalization combining (NNC) [5] and EED outperforms the conventional JTIDS receiver under the PNI in the aspect of SER. In [6, 7], the performance of the JTIDS-compatible waveform which uses the 32-ary orthogonal codes to replace the cyclic code shift keying (CCSK) was examined for errors-only RS decoding and EED, respectively.

The existing EED algorithms only focus on the situation that once a symbol is erased, it cannot be corrected. Based on this, the high symbol error rate is generally resulted after the CCSK decoding. To enhance the antijamming capability of JTIDS receiver, an improved EED approach is proposed to be used in the JTIDS receiver by replacing the conventional EED with the double-pulse structure. This approach relies on the characteristic that every two JTIDS pulses contain the same information to reduce the symbol error rate in the complex electromagnetic environment. In this paper, the performance of SER of the conventional EED and improved EED are compared under the AWGN and PNI by assuming that the modules of frequency dehopping, MSK demodulation, pulse synchronization, and descrambling in JTIDS receiver work well.

2 System Model Description

The block diagram of the JTIDS receiver using the improved EED is shown in Fig. 1. As seen from figure, after the demodulation, descrambling of the 32-chip sequence is obtained, and then the cross-correlation value of the 32-bit sequence with all the 32 possible local sequences is calculated. After that, the 5-bit channel symbol can be recovered based on the 32 cross-correlation values. The decision is made by choosing the 5-bit channel symbol with the maximum cross-correlation value [2]. After the 32-ary CCSK symbol demodulator, EED processing, and symbol de-interleaving, the information are recovered by the RS decoder.

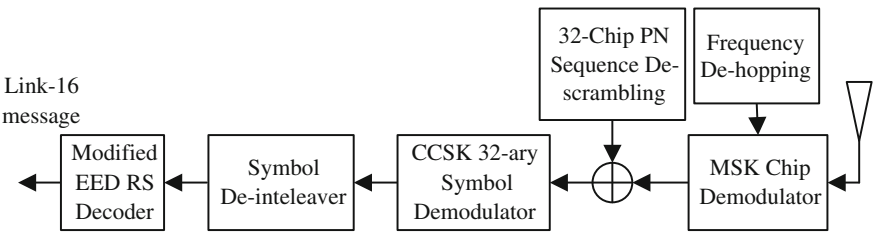

Fig. 1 JTIDS receiver using the improved EED

If the JTIDS receiver uses the conventional EED, a channel symbol will be erased as the largest CCSK cross-correlation value is smaller than the erasure threshold, which means a 5-bit channel symbol is erased and replaced by the symbol erasure when $R_i < T, 0 \leq i \leq 32$, where R_i is the cross-correlation value with respect to the ith local sequence and 32-bit sequence after the de-scrambling, and T is the erasure threshold. After EED processing, the CCSK symbol demodulator yields 33 possible outputs corresponding to the symbols 0, 1, 31, and symbol erasure.

In the improved EED, every two adjacent pulses contain the same Link-16 message as the JTIDS-type waveform is transmitted into the double pulses. Therefore, after the CCSK symbol demodulates, every two 5-bit channel symbols should be the same, and then we can merge these two same symbols into a group. Furthermore, a channel symbol is not immediately replaced by the symbol erasure as its CCSK cross-correlation value is smaller than the erasure threshold, but replaced by another channel symbol in the same group. The flowchart of the improved EED is shown in Fig. 2.

The steps of the improved EED are described as follows. First of all, we compare the largest CCSK cross-correlation value with the erasure threshold. If the largest CCSK cross-correlation values are not smaller than the erasure threshold, we output the 5-bit channel symbol directly. Otherwise, we examine whether this pulse is the first pulse or second pulse in the double pulses mode. If it is the first pulse, we delay

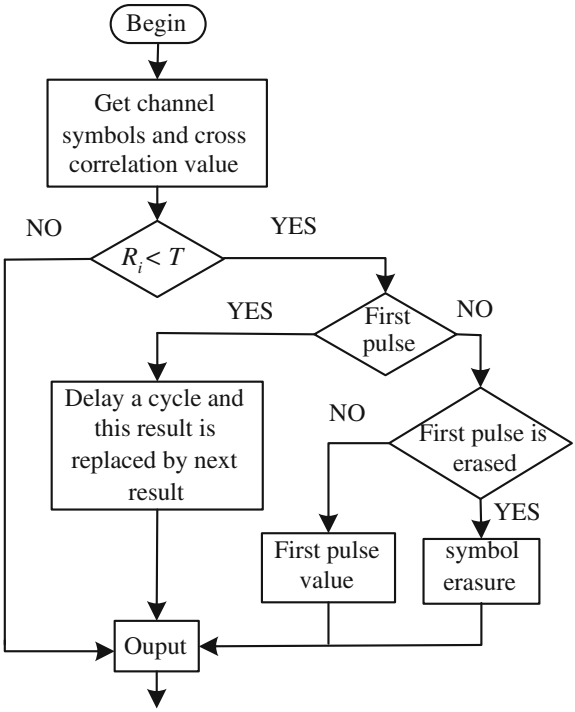

Fig. 2 Flowchart of the improved EED

the output by a cycle, and then replace the current result by the next one. If it is the second pulse, we examine whether the first pulse has been erased. If first pulse has been erased, we output the symbol erasure, otherwise we output the first pulse.

By using the improved EED, the joint decision of the two channel symbols in the same group is required to determine whether a channel symbol is erased. Based on this, the erased symbol could be corrected by another symbol in the same group. The symbol erasure is set as the output only when the correlation values of the two pulses in the same group are both smaller than the erasure threshold.

3 Performance Analysis

3.1 JTIDS Receiver Using Conventional EED

In this subsection, the performance of SER of JTIDS receiver using the conventional EED with AWGN and PNI is investigated. For the RS code, up to t symbol errors can be corrected in each block of n symbols. In the conventional EED, a block error does not occur under $d_{\min} \geq 2i + j + 1$, where i and j stand for the number of symbol errors and number of symbol erasure, respectively, in a symbol block, and $d_{\min}$ is the minimum hamming distance. A block error occurs under $i > t$ or $j > d_{\min} - 2i - 1$. Based on this, the probability of block error using the conventional EED [8] is calculated by

$$\begin{aligned} P_E = & \sum_{i=t+1}^{n} \binom{n}{i} {p_s}^i \sum_{j=0}^{n-i} \binom{n-i}{j} {p_e}^j {p_o}^{n-i-j} \\ & + \sum_{i=0}^{t} \binom{n}{i} {p_s}^i \sum_{j=d_{\min}-2i}^{n-i} \binom{n-i}{j} {p_e}^j {p_o}^{n-i-j} \end{aligned} \tag{1}$$

where p_s is the average probability of channel symbol error for the output of the CCSK symbol demodulator, p_e is the average probability of channel symbol erasure, and p_o is the average probability of channel symbol correct. The values of p_s, p_e, and p_o are given in [2]. Given the probability of block error, the probability of symbol error, P_S, is defined as

$$P_S = P\{\text{symbol error}|\text{block error}\}P_E \tag{2}$$

As there are i error symbols and j erased symbols, the conditional probability of symbol error [9] is approximated by

$$P\{\text{symbol error}|\text{block error}\} \approx \frac{i+j}{n} \tag{3}$$

By substituting (1) and (3) into (2), the probability of symbol error, P_S, is obtained as

$$P_S \approx \frac{1}{n}\Big[\sum_{i=t+1}^{n}\binom{n}{i}{p_s}^i\sum_{j=0}^{n-i}(i+j)\binom{n-i}{j}{p_e}^j{p_o}^{n-i-j} + \sum_{i=0}^{t}\binom{n}{i}{p_s}^i\sum_{j=d_{\min}-2i}^{n-i}(i+j)\binom{n-i}{k}{p_e}^j{p_o}^{n-i-j} \tag{4}$$

After that, substituting p_s, p_e, and p_o into (4), we can easily obtain the SER of the JTIDS receiver using the conventional EED under the AWGN and PNI.

3.2 JTIDS Receiver Using Improved EED

For the JTIDS receiver using the improved EED, the channel symbols to be erased are determined by not only their own correlation values at the CCSK decoder, but also the other pulses containing the same Link-16 information. Since the improved EED algorithm has no impact on the characteristics of the channel symbols, the values p_s, p_e, and p_o selected in [2] can be used to evaluate the performance of the JTIDS receiver using the improved EED under the AWGN and PNI. In this case, the probability of block error, P_{EM}, by using the improved EED is calculated by

$$P_{EM} = \sum_{i=t+1}^{n}\binom{n}{i}{p_s}^i\sum_{j=0}^{n-i}\binom{n-i}{j}{p_{ef}}^j{p_{ec}}^{n-i-j} + \sum_{i=0}^{t}\binom{n}{i}{p_s}^i\sum_{j=d_{\min}-2i}^{n-i}\binom{n-i}{j}{p_{ef}}^j{p_{ec}}^{n-i-j} \tag{5}$$

where p_{ef} is the probability of channel symbol error (or erasure) when the cross-correlation value is smaller than the erasure threshold. p_{ec} is the probability of channel symbol correct by using the improved EED.

Under the improved EED, as the cross-correlation value of a channel symbol is smaller than the erasure threshold, there are three possible outputs, the correct output channel symbol, error channel symbol, and erased channel symbol. The error channel symbol occurs as its cross-correlation value is smaller than the erasure threshold, while the other symbol in the same group is also an error channel symbol. The erased channel symbol occurs as the cross-correlation values of the two pulses in the same group are both smaller than the erasure threshold. Based on this, the value of p_{ef} is calculated by

$$\begin{aligned} p_{ef} &= p_e p_e + p_e p_s \\ &= \sum_{\theta}^{L} \binom{L}{\theta} \rho^{\theta} (1-\rho)^{L-\theta} p_{e|\theta} \sum_{\theta}^{L} \binom{L}{\theta} \rho^{\theta} (1-\rho)^{L-\theta} p_{e|\theta} \\ &\quad + \sum_{\theta}^{L} \binom{L}{\theta} \rho^{\theta} (1-\rho)^{L-\theta} p_{e|\theta} \sum_{\theta}^{L} \binom{L}{\theta} \rho^{\theta} (1-\rho)^{L-\theta} p_{s|\theta} \end{aligned} \tag{6}$$

where the values of p_s and p_e are given in [2], and $0 < \rho \leq 1$ is the ratio of time with the PNI. In (6), the first and second terms on the right-hand side stand for the probabilities of the erased and error channel symbols as the output, respectively.

Furthermore, the correct channel symbol can be selected as the output by using the improved EED under two cases. The first one is that the original channel symbol is correct, while the second one is that as the cross-correlation value of a channel symbol is smaller than the erasure threshold, whereas the other symbol in the same group is a correct channel symbol. Based on this, the value of p_{ec} is calculated by

$$\begin{aligned} p_{ec} &= p_o + p_e p_o \\ &= \sum_{\theta}^{L} \binom{L}{\theta} \rho^{\theta} (1-\rho)^{L-\theta} p_{o|\theta} \\ &\quad + \sum_{\theta}^{L} \binom{L}{\theta} \rho^{\theta} (1-\rho)^{L-\theta} p_{e|\theta} \sum_{\theta}^{L} \binom{L}{\theta} \rho^{\theta} (1-\rho)^{L-\theta} p_{o|\theta} \end{aligned} \tag{7}$$

In (7), the first and second terms on the right-hand side stand for the probabilities for the first and second cases, respectively. By substituting (5) and (3) into (2), the probability of symbol error, P_S, is calculated by

$$\begin{aligned} P_S \approx \frac{1}{n} [&\sum_{i=t+1}^{n} \binom{n}{i} {p_s}^i \sum_{j=0}^{n-i} (i+j) \binom{n-i}{j} {p_{ef}}^j {p_{ec}}^{n-i-j} \\ &+ \sum_{i=0}^{t} \binom{n}{i} {p_s}^i \sum_{j=d_{\min}-2i}^{n-i} (i+j) \binom{n-i}{j} {p_{ef}}^j {p_{ec}}^{n-i-j}] \end{aligned} \tag{8}$$

Then, by substituting p_s, p_e, and p_o into (6) and (7), the values of p_{ef} and p_{ec} can be easily calculated. Finally, based on p_{ef}, p_{ec}, and p_s in (8), the SER of the JTIDS receiver using the improved EED under the AWGN and PNI is obtained.

4 Simulation Results

In this section, we will compare the SERs achieved by the JTIDS receiver using the improved and conventional EED, respectively, under the AWGN and PNI. By selecting the erasure threshold $T = 14$ which is the optimal threshold has been demonstrated in [2], we obtain the simulation results in Figs. 3, 4, and 5. In these figures, N_I and N_o stand for the one side power density spectrum of the PNI and AWGN, respectively, and $E_{b'}$ is the average power of each bit in a pulse.

Figure 3 shows the results under the AWGN, while Figs. 4 and 5 show the results under the AWGN and PNI. As shown in Fig. 3, the improved EED outperforms the conventional EED in the aspect of the average power per bit per pulse, $E_{b'}$. For exam-

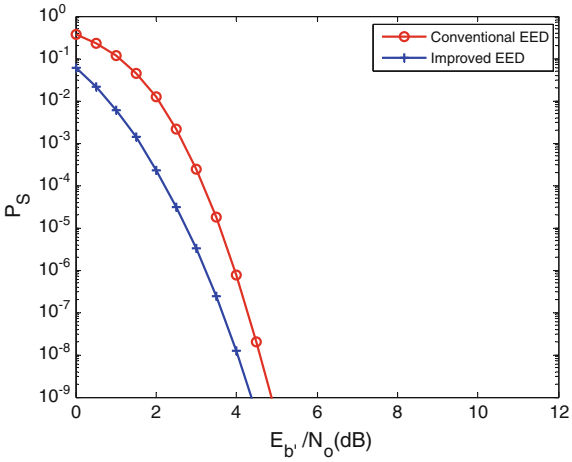

Fig. 3 SERs of JTIDS receiver under AWGN

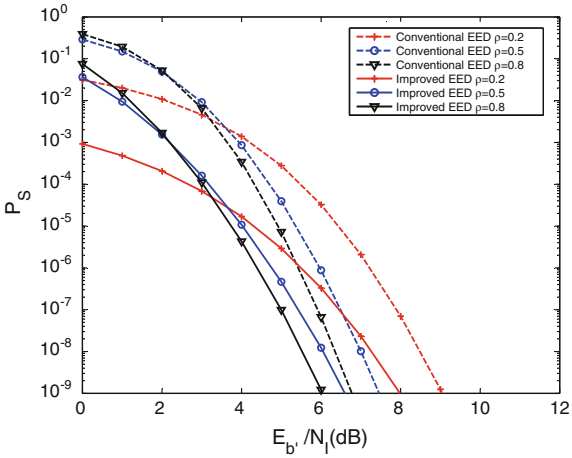

Fig. 4 SERs of JTIDS receiver under $E_{b'}/N_0 = 10\,\text{dB}$

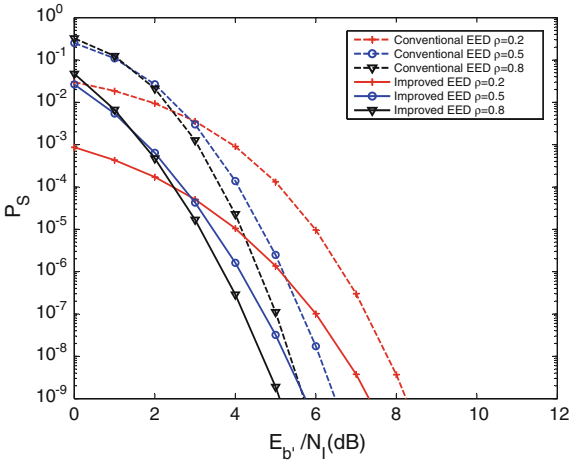

Fig. 5 SERs of JTIDS receiver under $E_{b'}/N_0 = 15$ dB

ple, to achieve $P_S = 10^{-5}$, the $E_{b'}/N_0$ required by the conventional EED is about 3.6 dB, whereas the $E_{b'}/N_0$ required by the improved EED is only about 2.7 dB.

Figure 4 shows the results under $E_{b'}/N_0 = 10$ dB. For simplicity, only three possible values of ρ ($\rho = 0.2$, 0.5, and 0.8) are considered in the simulations. $\rho = 0.8$ represents that the PNI exists for 80 %. As seen from Fig. 4, we observe that: (i) given the same value of ρ, the JTIDS receiver using the improved EED outperforms the one using the conventional EED in the aspect of $E_{b'}/N_I$. For example, under $\rho = 0.8$ and $P_S = 10^{-5}$, the $E_{b'}/N_I$ required by the improved EED is about 3.7 dB, whereas the $E_{b'}/N_I$ required by the conventional EED is about 4.9 dB; and (ii) given the same value of P_S, the improved EED outperforms the conventional EED by a greater margin as the value of ρ decreases. For example, given $\rho = 0.2$ and $P_S = 10^{-5}$, the improved EED outperforms the conventional EED by 2.2 dB and increase of 1 dB compared to when $\rho = 0.8$.

Similarly, under $E_{b'}/N_0 = 15$ dB, the results of SERs are shown in Fig. 5. From Fig. 5, we observe that: (i) first of all, based on the results in Figs. 4 and 5, the probability of symbol error decreases as $E_{b'}/N_0$ increases as expected; and (ii) given the same value of ρ, the JTIDS receiver using the improved EED outperforms the one using the conventional EED in the aspect of $E_{b'}/N_I$. For example, under $\rho = 0.2$ and $P_S = 10^{-5}$, the $E_{b'}/N_I$ required by the JTIDS receiver using the improved EED is 2 dB lower than the $E_{b'}/N_I$ required by the one using the conventional EED.

5 Conclusion

In this paper, an improvement of EED algorithm is proposed for JTIDS, and meanwhile the probability of symbol error under the AWGN and PNI has been significantly investigated. By using the improved EED, the channel symbol can be replaced

by another channel symbol that contains the same message in the same group as the CCSK cross-correlation value is smaller than the erasure threshold. To verify the performance of the proposed improved EED, we compare the probabilities of symbol error with the conventional EED. The simulation results demonstrate that the performance of SER of the JTIDS receiver using the improved EED is much better than the one using the conventional EED.

References

1. Wang H, Kuang J, Wang Z et al (2005) Transmission performance evaluation of JTIDS. In: Proceedings of the IEEE military communications conference, pp 2264–2268
2. Kao C, Robertson C, Kragh F (2009) Performance of a JTIDS-type waveform with errors-and-erasures decoding in pulsed-noise interference. In: Proceedings of the IEEE military communications conference, pp 1–7
3. Kao C, Kragh F, Robertson C (2008) Performance analysis of a JTIDS/Link-16-type waveform transmitted over Nakagami fading channels with pulsed-noise interference In: Proceedings of the IEEE military communications conference, pp 1–6
4. Kao, C Robertson C (2011) An improved link-16/JTIDS receiver in pulsed-noise interference. In: Proceedings of the IEEE military communications conference, pp 341–346
5. Kao C, Robertson C (2010) Performance of a JTIDS-type waveform with noise-normalization combining in pulsed-noise interference. In: Proceedings of the IEEE military communications conference, pp 1690–1694
6. Lekkakos D, Kragh F, Robertson C (2009) Performance analysis of a Link-16 compatible waveform using errors-and-erasures decoding when corrupted by pulse-noise interference. In: Proceedings of the IEEE military communications conference, pp 1–6
7. Lekkakos D, Robertson C, Lekkakos D et al (2009) Performance analysis of a LINK-16/JTIDS compatible waveform transmitted over a channel with pulse-noise interference. In: Proceedings of the IEEE pacific rim conference on communications, pp 29–34
8. Sargrad D, Modestino J (1990) Errors-and-erasures coding to combat impulse noise on digital subscriber loops. IEEE Trans Commun Process 1145–1155
9. Joiner L, Komo J (2003) Errors and erasures decoding of BCH and Reed-Solomon codes for reduced M-ary orthogonal signaling. IEEE Trans Commun Process 57–62

An X Band 40 W High Power Amplifier Based on Internally Matched

Zhengbo Yang, Fei Liang, Ping Yang and Jing Liu

Abstract An X band high power amplifier which is based on internally matched single chip 5 mm GaN on SiC high electron mobility transistors (HEMTs) is successful simulated and tested. LCL network and microstrip circuits are directly used to match the impedance of the 5 mm GaN on SiC HEMTs to 50 Ω with using two-way power combiner. The internally matched circuit structure is optimized and calculated using ADS software, designed with this method of working from 8.5 to 9.5 GHz, and tested in the labs. We use microwave signal source, DC power supply, attenuator, power meter, and the spectrum analyzers to test the high power amplifier, with the bias condition of $V_{ds} = 30$ V and $V_{gs} = -3.6$ V, in the range of 8.5−9.5 GHz, the test results are as follows: power gain (G) > 11 dB, the input VSWR < 1.8 and the output VSWR < 2.2, the output power (Pout) > 36.65 dBm and power added efficiency (η_{PAE}) > 30 %.

Keywords Internally-matched · High power amplifier · GaN HEMTs · Power divider

1 Introduction

With the continuous development of the microwave solid-state high power amplifiers, high power devices are not only widely used in radar technology and wireless communication technologies, but also enable us to improve the output power and the power additional efficiency of the microwave solid-state high power amplifier. Therefore, the power synthesis technology becomes one of the most simple and effective means to improve radar and wireless communication system output power. It not only has high research value, but also plays an important role in practical applications. Throughout the course of the microwave solid-state high power amplifiers in recent decades, microwave power synthesis technology is the

Z. Yang (✉) · F. Liang · P. Yang · J. Liu
The Second Research Institute of CAAC, Chengdu, China
e-mail: 196102849@qq.com

Q. Liang et al. (eds.), *Proceedings of the 2015 International Conference on Communications, Signal Processing, and Systems*, Lecture Notes in Electrical Engineering 386, DOI 10.1007/978-3-662-49831-6_85

direction of high-frequency, multichannel and broadband. Such as, based on hybrid designs and internally matched GaN HEMTs technology, 23 W at X band [1], and 500 W at 3.5 GHz [2] were achieved, respectively. And at X band, the reported internally matched GaN HEMTs amplifiers have demonstrated 45.2 W [3].

The project is mainly researching on X band (8.5−9.5 GHz) internally-matched in synthesis technologies of microwave solid-state high power amplifiers, such as the transistor matching technology, power divider/combiner technology and the DC bias technology. According to the input and output impedance of HEMT die and the characteristics of the output power, we design a high power amplifier based on the two-way matching synthesis technology using theoretical analysis and practical method of combining the microwave circuit simulation. Then the schematic simulation, layout, schematic co-simulation, processing and packaging, and debugging are also proceeding.

Based on these requirements that the high output power, the high power efficiency and the high gain of microwave solid-state high power amplifier, we first introduced the working principle of matching technology, detailed description the matching components and design process of the amplifier, and then tested it. By using the internally matched technology, the two-way internally matched GaN HEMTs die with 5 mm total gate width demonstrated a very high output power of 40 W at 8.5−9.5 GHz under the condition of continuous wave (CW), with a power added efficiency of 38.0 % and power gain of 9 dB with a drain voltage of 30 V and source voltage of −3.6 V. Finally, we test on the bias condition of $V_{ds} = 30$ V and $V_{gs} = -3.6$ V, in the range of 8.5 GHz−9.5 GHz, the test results are as follows: power gain (G) > 11 dB, the input VSWR < 1.8 and the output VSWR < 2.2, the output power (P_{out}) > 36.65 dBm, and power added efficiency (η_{PAE}) > 30 %.

2 Simulation

2.1 Principle of Matching Technology

With the increase in the gate width, the input impedance value of the FET dies by getting lower and lower, the device of the unloaded Q value will becomes higher and higher, the amplitude and phase unbalance problem of the feeding signal will be more serious. Therefore, it is difficult to use the external circuit for a certain width-band matching directly, but match the transistor in the packaging can solve this problem.

Internally-matched technology is a kind of technology which is to balance between the inside of a transistor die and each other transistor die on signal amplitude and phase, it can not only increase the input and output real part impedance of the transistor die, but also becomes part of power divider/combiner. Its design principle is, matching structure is respectively matched to the input and

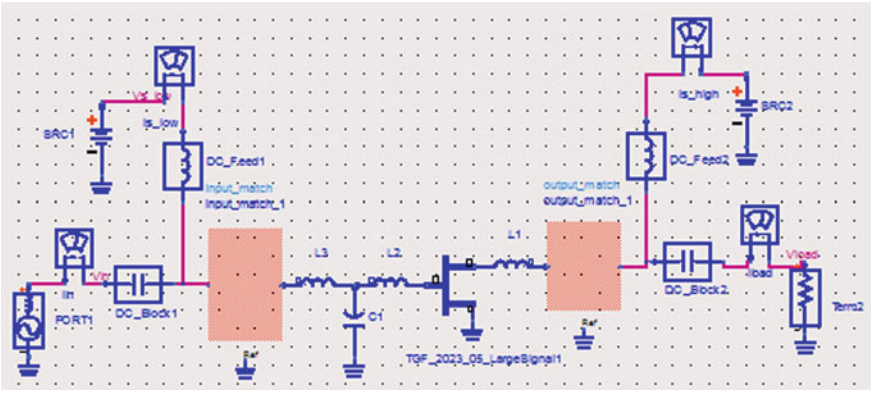

Fig. 1 Structure block diagram of the internally matched

output end of the transistor die. This means that we can change the port impedance values, offset the imaginary part impedance of transistor die, and improve its real impedance to the impedance values of a particular (the specific value of this project is 30 Ω).

In addition, the project requirement of devices power is very high, a single chip (called single cell) of the power output capacity always cannot meet the requirements. Therefore, we often use a plurality of chips (called multicellular) for power combiner to achieve the technical requirements. So, we design the two-way synthesis microwave solid-state high power amplifier circuit by using a plurality of chips in this project. Figure 1 is the one-way of structure block diagram of the internally-matched. It mainly consists of the bias structure, the "T"-type power divider/combiner network structure, the structure of the input and output matching, LCL filter network structure, and the matching circuit structure of HEMT die.

2.2 Matching Components

Based on the impedance and characteristics of transistor die, we choose the appropriate circuit structure to design the internally matched to meet the design requirements. One of the main structure is the matching components, which include banding wire, capacitance, resistor, and microstrip in the internally matched circuit.

Matching circuit often adopts the "T" type LC low pass filter network. Among them, the bonding wire inductance (L) and the MIM capacitance (C) are the most commonly used matching components. Bonding wire diameter (D) is commonly used for 20, 25, 30 μm, etc. Length l (cm) n roots of bonding wires inductance L (nH) is calculated by the following formula:

$$L = \frac{1}{\sqrt{n}}\left[1.97 + \frac{(n-1)l}{n(s+l)}\right]\left(\ln\frac{4l}{D} - 1 + \frac{2D}{l}\right)(nH) \tag{1}$$

The inductance value calculated by the formula (1) is too small to design because formula (1) is not accurate enough, the banding wire and microstrip leads impact on each other. So, we design the "T" type LC low pass filter network according to the actual circuit.

High dielectric constant ceramic, Al_2O_3, SiO_2, Si_3N_4, or GaAs are commonly used as capacitor. a is the length of the capacitor, b is width, and t is the capacitor dielectric thickness, the capacity C (pF) of capacitor is calculated by the following formula:

$$C = \frac{k\varepsilon_r\varepsilon_0 ab}{t}(pF) \tag{2}$$

In the general capacitance range, the correction constant k is generally within the range of 1.2−1.8, a and b are smaller, t greater, k value is usually greater.

2.3 Power Divide and Combiner

Power divider and combiner are developed on the basis of the tee joint. Hence, they are in the same circuit topology. When used as input circuit in high power GaN FET, the microwave input power can be assigned to each unit cell of FET, so it is called power divider. When used as output circuit in high power GaN FET, the respective units of the FET cell output power combiner as a large output power, so it is called power combiner. As a result, power divider and combiner is one of the most commonly matching components.

However, the impedance value of large gate width of the transistor die is very low, if the impedance transformation network upgrades directly to 50 Ω, a high Q value of the circuit, signal amplitude, and phase imbalance are very serious. So, it also caused a very narrow band in this matching and the outer circuit is also difficult to match. In power divider design, which synthesis the multicellular to the internally matched power output, we often use Wilkinson power divider forms which is different from the traditional Wilkinson power divider, as shown in Fig. 2; on the one hand, it is the role of impedance transformation to complete the transistor impedance through an impedance transformation network upgrade to 50 Ω, which is contributed to connect with the peripheral circuit, whereas, on the other hand, it is also subjected to the package size and the power divider is not large than the size of package.

In this kind of structure, the RF signal inputs from the left port while the power outputs from the right ports. If the right port is exactly in match state, there are electric current flows through the resistor R. If one of the right ports is in mismatch state, the current can through it and generate the extra power. When the power is

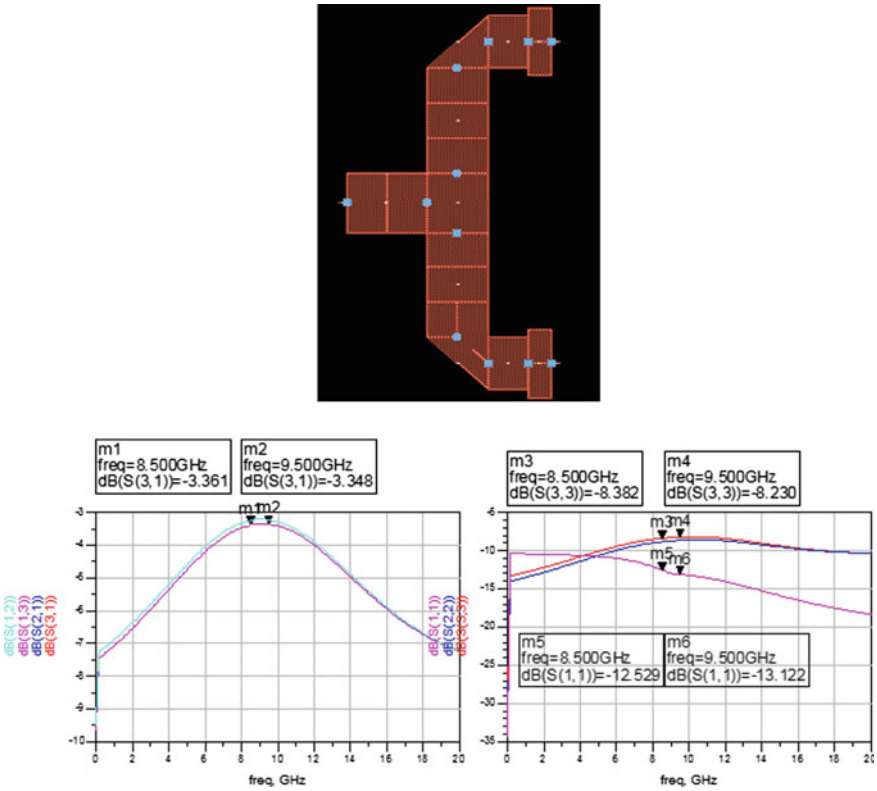

Fig. 2 Structure block diagram and result of power divider/power combiner

absorbed by the isolation resistor R, the "T" type power divider/combiner play the role of balancing or isolating. From the optimization results, we can get a good power divider/combiner.

2.4 Process of Simulation

For high-frequency mixed integrated circuits at X band, the main problems need to solve are reducing the parasitic reaction brought by the various connections, and reducing the microwave signal transmission path loss. Parasitic reaction of interconnect components not only makes the broadband characteristic degrade the device, but also brings additional losses and lower gain.

At 9 GHz, we designed the input and output matching circuits based on GaN HEMTs small signal S-parameters and load pull data. When the gain gets to the biggest matching in the input matching circuit of small signal and the transmission circuit gets the best efficiency, the output matching circuit for large signal optimal

load matching obtains maximum output power. In matching circuit, we use microstrip line and bonding wire to match, so that the device of input and output impedance value can match to 50 Ω. Bonding wire is not only used for transistor die and microstrip circuit connection, but also as part of the matching circuit. The input and output of the microstrip matching circuit are manufactured by the relative dielectric constant 9.5, the thickness of Al_2O_3 ceramic substrate is 0.5 mm, the

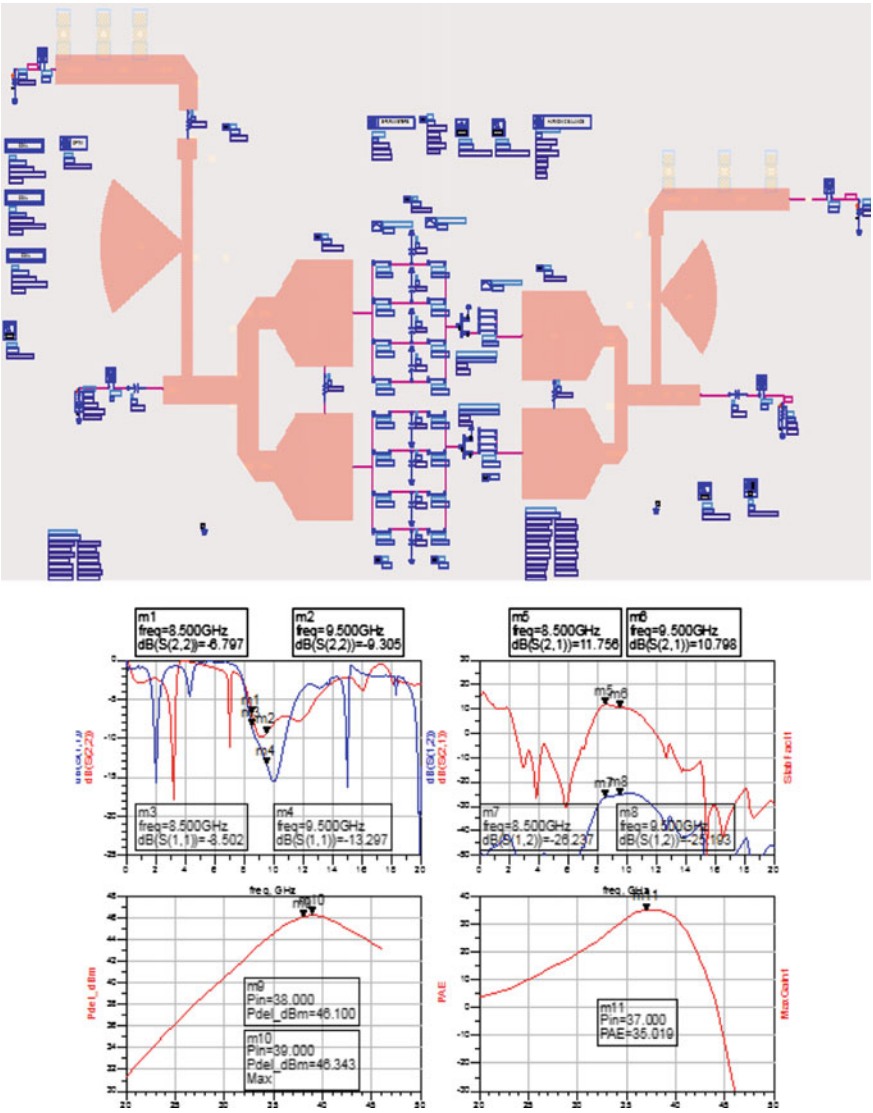

Fig. 3 Topology schematic diagram of the designed power amplifier

thickness of gold layer is 3 microns and the diameter of the bonding wire is 25 microns. Packaging shell is made of oxygen free copper, and its size is 15.2 mm * 13 mm. Transistor die and ceramic substrate will be packaged in the package shell through sintering and bonding.

By looking for GaN HEMTs small signal S-parameters and testing the load pull, the input and output impedance value calculated by the relevant formula is approximately 1 and 5 Ω, so two kinds of different impedance matching circuit can be designed by different circuit structure.

When using the λ/4 of the impedance conversion line, the drain of GaN HEMTs can be connected directly by a bonding wire impedance conversion line, in order to make the output characteristic impedance value reach to 30 Ω; while the source of GaN HEMTs must be use the "T" type of LC low pass filter network to make the source of impedance values raised to a certain value, and the bonding wire connected to the impedance transformation line, in order to make the output characteristic impedance value reach to 30 Ω; finally, by connecting "T" type power divider and power synthesizer the impedance of the specific value (30 Ω) changes to 50 Ω. Figure 3 shows the topology schematic diagram of the designed power amplifier.

3 Test

3.1 Test Procedure

When designing and simulating the high power amplifier is finished, we produced it. The high power amplifier mainly includes the external cavity structure, bias circuit structure, input and output of the "T" type power divider/combiner, input and output matching section, and so on. Internally matched structure and cavity structure of the high power amplifier are shown in Fig. 4.

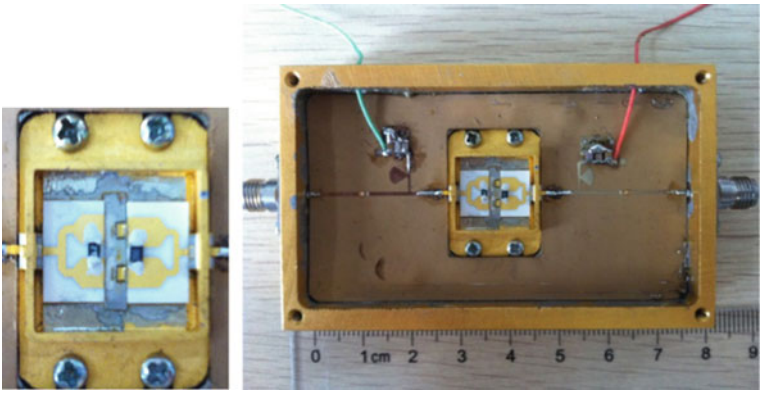

Fig. 4 Internally matched structure and cavity structure of the high power amplifier

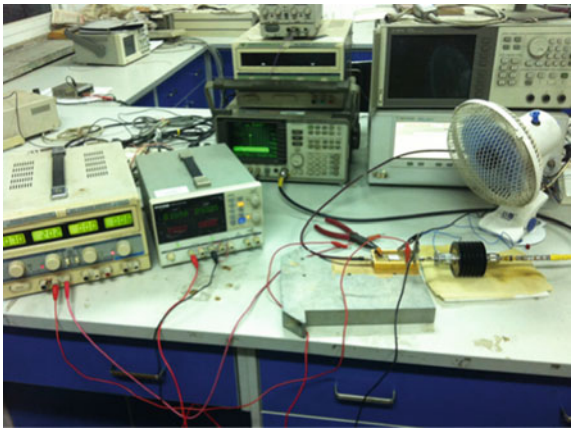

Fig. 5 The power gain and output power of the power amplifier test pattern

As is shown in Fig. 5, we use microwave signal sources, DC power supplies, attenuators, power meters, and the spectrum analyzers to test the high power amplifier, with the bias condition of $V_{ds} = 30$ V and $V_{gs} = -3.6$ V, in the range of 8.5−9.5 GHz, the test results are as follows: power gain (G) > 11 dB, the input VSWR < 1.8 and the output VSWR < 2.2, the output power (P_{out}) > 36.65 dBm, and power added efficiency (η_{PAE}) > 30 %.

3.2 Analysis of Test Result

From the above test results, we can analyze, with the bias condition of $V_{ds} = 30$ V and $V_{gs} = -3.6$ V, in the range of 8.5 GHz−9.5 GHz, the linear gain fluctuation range is bigger, but not less than 11 dB, and the measured output power is 36.65 dBm, all the test results do not reach the design requirements.

The bad test results are caused by the following reasons:

(a) The defect of design

As the matching module size is very small and the ceramic substrate heats faster, isolation resistor should be designed in the internally matched structure, rather than being welded after the assembly, this may cause the impact on the human factors in the process of welding; The difference between the large signal model based on ADS simulation design and the material object is mainly caused by the transistor processing technology.

(b) The error of the assembly process

The error of the assembly process greatly influenced the results of the design, such as the height and length of the bonding wire, the coupling effect between gold; also,

circuit connection and the wastage of the joint will cause great error and cannot reach the design requirements.

(c) Heat dissipation

Although we have considered the heat dissipation on the design of cavity and the selection of material, but high temperature will have great influence to the overall performance of the transistor die and disturbs the test results when we test.

4 Conclusions

Microwave power amplifier is a kind of device which can realize high output power and high power added efficiency. It is widely used in radar technology and wireless communication technology.

In order to achieve high output power and high power added efficiency, we adopted the matching technology of the transistor die to produce higher power output, it can make the inside of a transistor die and each other transistor die implementation on signal amplitude and phase equilibrium. By testing and analyzing, with the bias condition of $V_{ds} = 30$ V and $V_{gs} = -3.6$ V, in the range of 8.5 GHz−9.5 GHz, the linear gain is greater than 11 dB, the input VSWR is less than 1.8, the output VSWR is less than 2.2, and the maximum output power is 36.65 dBm. But on the whole, due to insufficiency of design experience and process technology and the limitation of test conditions, we failed to test the scheduled early indicators, but when compared with other design, our design structure is relatively simple and effective. Because in the case of high frequency and high power, we can inhibit the generation of self-excitation, heat dissipation problems, and deal well with stability, this is a very difficult thing to do well.

Acknowledgments This paper is supported by the Technology and Innovation Fund Program of CAAC (MHRD20140109). The authors would like to thank the anonymous reviewers and editors for their helpful comments and suggestions.

References

1. Schuh P, Leberer R, Sledzik H (2006) 20 W GaN HPAs for next generation X-band T/R-modules. In: IEEE MTT-S international microwave symposium digest, pp 726–729
2. Wu YF, Wood SM, Smith RP (2006) An internally-matched GaN HEMT amplifier with 550-watt peak power at 3.5 GHz. In: 2006 International electron devices meeting (IEEE Cat No. 06CH37807C), pp 1−3
3. Wang XL, Chen TS, Xiao HL, J. Tang, JX Ran (2009) An internally-matched GaN HEMTs device with 45.2 W at 8 GHz for X-band application. Solid-State Electron 332–335

A Virtualization Testbed Framework for Networked Information System

Lixin Zhu and Shuanghua Zhu

Abstract After a review on the existing testbed frameworks for networked information system, we proposed a new virtualization testbed framework which had the merits of scalability, configurability, security, programmability and efficiency. The testbed framework is defined with function components and running view in detail in this paper. The implementation methods for virtualization testbed framework are described and experimental results showed the advantage of virtualization testbed framework.

Keywords Networked information system · Virtualization testbed · Testbed framework

1 Foreword

The networked information system, which has features in network-centric topology and service oriented architecture, has become the mainstream of military information system development. To address the challenges proposed by networked information system development, many system architectures, concepts, services, protocols, and algorithms have been proposed in order to meet the technical requirements. The SOA-based and cloud computing-based system framework have been successful examples [1]. Nevertheless, before a new system architecture or protocol has been put into application, we must build testbed to do full-scale and rigorous experiments. By now, there are three types of testbed framework for networked information system [2].

The first one is simulation-based testbed framework. In simulations, models of real-world components (such as ICT infrastructure) are created, and these models are then made to interact [3]. Simulation has the advantage of being highly scalable

L. Zhu (✉) · S. Zhu
Science and Technology on Information Systems Engineering Laboratory, Nanjing 210007, China
e-mail: rambozhuzhu@aliyun.com

Q. Liang et al. (eds.), *Proceedings of the 2015 International Conference on Communications, Signal Processing, and Systems*, Lecture Notes in Electrical Engineering 386, DOI 10.1007/978-3-662-49831-6_86

since a large number of host and device models can be run on a single physical machine (assuming simple models). However, a disadvantage is that because these models are often high level abstractions of the real-world objects, the test results can lack fidelity and may not reflect reality. Developing models which capture the complex, dynamic, and stochastic nature of networked information system requires a significant effort.

The second one is overlay network-based testbed. The overlay network testbed operates on top of production networks. The overlay network can dynamically change the topology of the network for applications under test, while the underlying network remains static. It therefore provides flexibility in configuring testbeds for different experiments. Overlays are very common method for adding functionality to an existing service, for example the internet overlays the telephone network. Other networks such as peer-to-peer or cloud services now overlay the internet. FEDERICA project [4] funded by EU has interconnected the separated network widely distributed in Europe to build a specific testbed for next generation network. With this overlay testbed, the cybersecurity, protocol, and application for future Internet could be verified. Using overlays for test networks provide size, cost, and fidelity advantages compared to other approaches. This is because testing can be performed at the same scale as the production network it overlays, real hardware is used for high fidelity, and they avoid the additional cost of building a separate test network or laboratory. However, a disadvantage is the difficulty in performing formal testing including repeatability and experiment control (since the underlying network cannot always be controlled). Another disadvantage is the potential adverse impact of the experiment on the production network.

Recently, the emulation testbed for networked information system was proposed [5], that uses a standalone physical testbed to emulate any number of different experiment configurations. Emulation is the process of mapping a desired experimental networked information system topology and software configuration onto the physical infrastructure of the testbed. While the actual infrastructure may consist of a cluster of machines, the emulation component can configure the cluster to behave as per the desired experiment topology including routing, services and C3I applications. It supports experimentation with scientific rigor. Fidelity is high due to the use of real hardware and having total control of background traffic, workloads, and general events. This contrasts with simulations where it is not always easy to know which parts of the model can be abstracted without influencing the test results. Fidelity is also higher than with overlay networks where experiments are not always repeatable due to the shared infrastructure. Virtualization is commonly used as a tool for flexible emulation. However, the lack of a united platform was the main difficulty to build a emulation testbed for networked information system, which could allocate, deploy, control, and manage this kind of virtualization testbed and its resource.

2 Virtualization Testbed Functional Requirements

The networked information system has features in complex topology, large scale, and technology diversity, which lead to the new functional requirements for the virtualization testbed. In addition, the virtualization testbed should afford to hold cybersecurity test that probably induces physical damage to testbed infrastructure. Based on above analysis, we propose the functional requirements for virtualization testbed, including

- Scalability, the testbed infrastructure could scale its capability and the physical resources could extend on demands;
- Configurability, the testbed and its resource could be reconfigured according to the specific task and user's demand while keeping the physical infrastructure static;
- Security, the simultaneous experiments could not affect each other; the damage caused by disruptive test could be separated from the testbed infrastructure; the contaminated resource in the experiments could be refreshed and reused in next experiments;
- Programmability, the virtualization testbed resource could be reallocated and redeployed to build a new test object system; the physical production network could be logically reprogrammed to form a new topology;
- Efficiency, the reproduction of object system and its running environment could be executed time efficiently with the help of a suit of automated testbed tools.

To meet all above functional requirements, we propose a virtualization testbed framework, in which the management of testbed running and resource allocation are unified by the virtualization platform. The virtualization framework also brings the merit of enabling disruptive cyber attack tests.

3 Virtualization Testbed Functional Requirements

3.1 The Virtualization Framework Levels

The framework of the virtualization testbed was illustrated in Fig. 1. It could be divided into three levels including testbed infrastructure, virtualization testbed service, and reproductive testing environment.

The reproductive testing environment is the mapping of a real networked information system consistent with test design. The nature attributes and lifecycle of a test would be described with a set of formal syntax first and the recurrence of real scene would hold in this level. The virtualization testbed service level is the test service provider, which unified the management of LVC test resources and was responsible for reallocate, deploy, configure test resources to reproduce an object system. It has separated the testbed infrastructure from reproductive testing environment, which would lead to disruptive effect in a cybersecurity test probably.

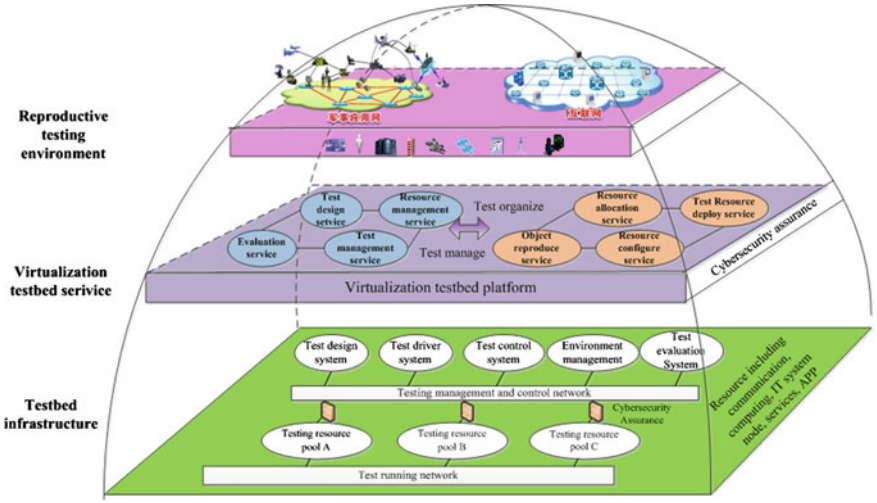

Fig. 1 The virtualization testbed framework

The data also is collected by the testbed virtualization platform efficiently. Testbed infrastructure is the real test capability supplier, which remains under cover the heterogeneous test resources and provides a unified access to them.

The running view of virtualization testbed is illustrated in Fig. 2.

Fig. 2 Testbed running view

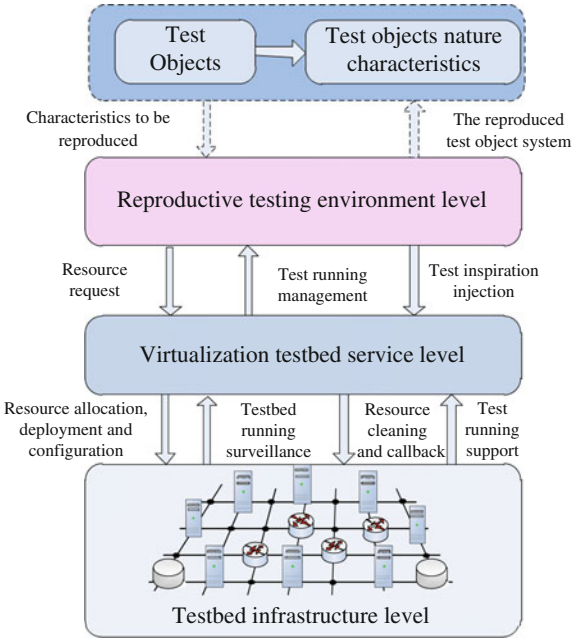

Step1. The user abstracts the intrinsic characteristics of test object and forms the configuration scripts. The nature characteristics are the most important features and models of the object system to be tested, including system structure, function components, running behavior, and configuration attributes;
Step2. The user puts out the requests of reproducing object system and allocating related resource to virtualization testbed service level, which would allocate resources and organize the test procedure. The virtualization testbed service level would reproduce the object system according to the configuration scripts that described the object attributes and deployment structure;
Step3. After the reproduction of object system had finished, the testing environment for specific task level would load emulation implies to drive the object system running. The resources in the testbed infrastructure level would have been logically occupied by this test and burden the actual computing;
Step4. The virtualization testbed service level records all the test data and events, and it makes preparation for evaluation;
Step5. The virtualization testbed service level organizes the cleaning and callbacking the test resource allocated in the test.

3.2 The Implementation of Virtualization Testbed Platform

The core function of virtualization testbed platform is the implementation of allocation, deployment, configuration and management all kinds of resources. The difficulties lie in three aspects, including the creation of basic test resources, the cybersecurity assurance of virtualization platform, the unified deployment and configuration of LVC resources.

The creation of basic test resources has great difficulty because of the diversity of networked information system components. Each characteristic to be reproduced is quiet different, which leads to the need of applying different way to emulate each

Table 1 The test resource emulation methods

Resource type		Emulation methods
Network resource	Router	Linux container-based router emulation
	Link	Link emulation based on traffic shaping
	Traffic	Traffic emulation based on logical network behaivor mapping
Computing resource	Computer device	Server virtualization method
	Operation system	Platform virtualization method
Service resource	System service	Interface encapsulation and message agent method
Application resource	Sensor	Radar and ESM system emulation
	Weapon	Aeroplane movement emulation
	C2 System	Real C2 system image

basic test resource. All kinds of methods applied in our test resource emulation are illustrated in Table 1.

Among these, the Linux container based router emulation would reproduce large scale network with a great number of emulated routers based on Qugga [6]. The server virtualization is implemented through VMware ESX software and OpenVZ. All above test resource emulation methods are not proposed by us originally and we cite them here to describe our implementation in detail.

The cybersecurity assurance of virtualization platform is an important merit of our framework. This is implemented by three kinds of logical seperations form testbed infrastructure and reproductive test environment, including testbed infrastructure, testbed services, and test data, as illustrated in Fig. 3.

(1) Testbed infrastructure security. In a destructive experiment, the malwares from the object system would probably penetrate residence and attack testbed infrastructure. In order to make sure of the cybersecurity, we have deployed firewall to avoid unlicensed access and misuse. After each test, we have cleaned and polymerized the resource to avoid the negative effect to next test.
(2) Testbed virtualization platform security. When carrying a test on virtualization testbed platform, we have assured the security by validating user's authority through certificate and key. We have also supervised the testing procedure to avoid exceptional behavior that would induce damage.
(3) Test data security. We proposed an agent based test data collection method to avoid the malware promulgated stealthily and to validate the correctness of them.

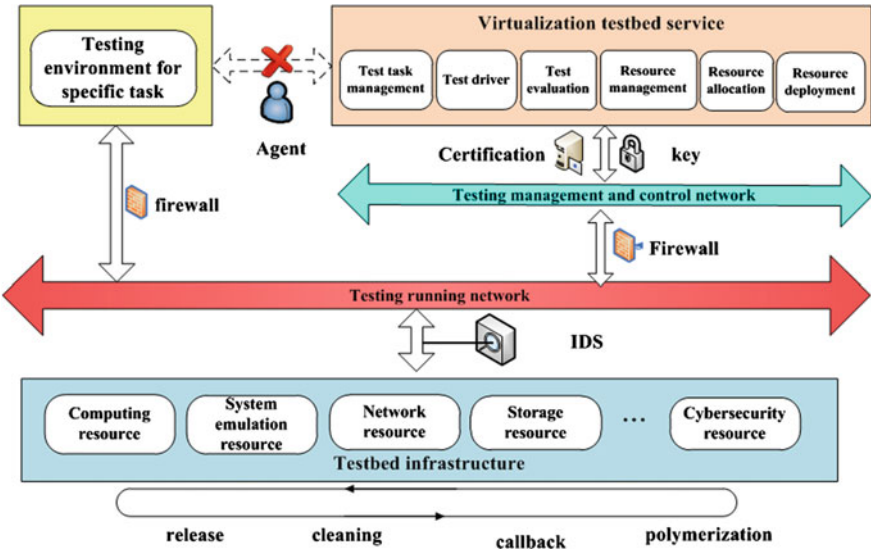

Fig. 3 The cybersecurity design of testbed

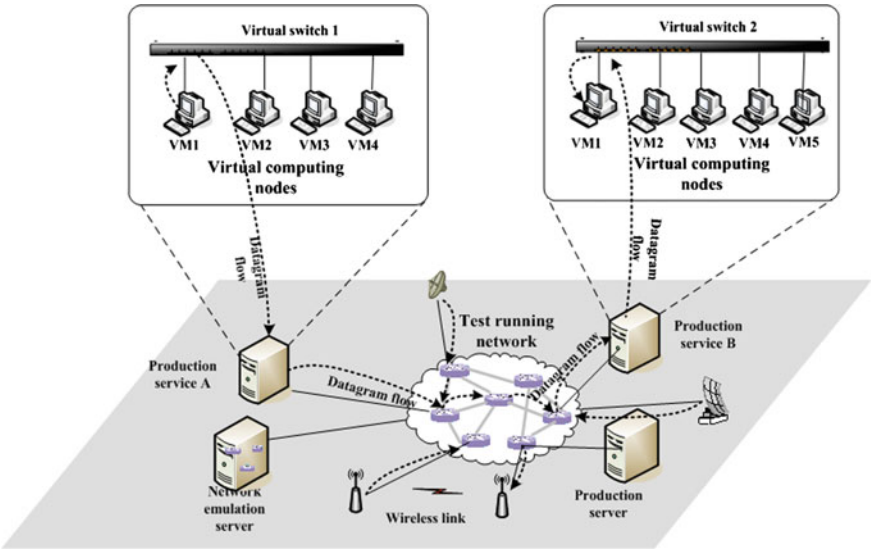

Fig. 4 Test resource virtualization management model

The unified deployment and configuration of LVC resources is another important merit of our testbed platform. It is implemented through port mapping and router redirection, as illustrated in Fig. 4.

(1) The port mapping was applied to interconnect virtual and real resources. The promiscuous mode was set on the virtual machine network interface first, and then all outstreams from the virtual machine was mapped onto the host network interface.
(2) The router redirection was applied in interoperating emulation and real resources. All emulation result flow would be redirected into real network and make the interoperation possible.
(3) The interoperation between virtual and emulation resources could be interacted directly because both kinds of resource are running on the same infrastructure level.

4 Experiments

With the virtualization testbed platform above, we have built a virtualization testbed prototype with ten servers (IBM M3 series) and one high performance router. On this testbed, we have reproduced a networked information system with 218 nodes (including sensors, routers, computers, and C3I nodes) and have validated the five merits of our testbed.

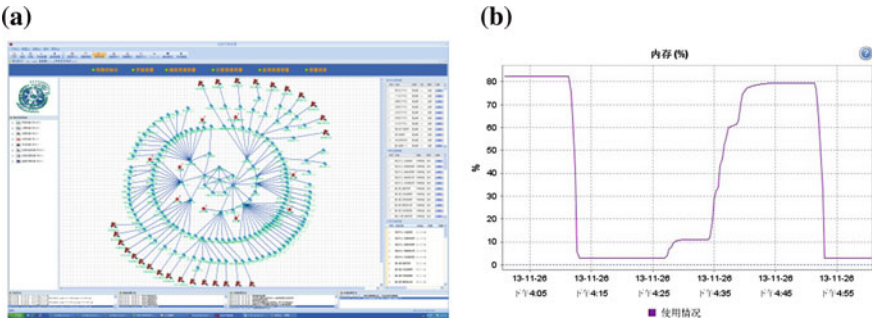

Fig. 5 Virtualization testbed running information **a** Object information system topology **b** Testbed resource changing profile

Table 2 Time on object system reproduction

Reproduction content	Results
Topology reproduction time	2 s
Network reproduction	2 min and 30 s
Computing device reproduction	12 min and 30 s
Applications deployment time	7 min
Test driver loading time	less than 10 s
Test resource callback time	6 min and 50 s
Total time	less than 29 min and 2 s

In Fig. 5a, we showed a networked information system topology that was visually configured by user. All available test resources are listed on the left side of this software and could be used to define a object system. Figure 5b showed testbed resource changing profile in a test. The left part of the profile indicted by dashed line is denoting the callback of memory resource and the right part showed the reallocation process of memory resource in the next test. This profile showed us the programmability of testbed.

The time cost in the reproduction of networked information system with 218 nodes is listed in Table 2, which is less than 30 min and quiet efficient.

5 Conclusion

This paper has analyzed the requirements of networked information system testing and proposed a new virtualization testbed framework, which has the merits of scalability, configurability, security, programmability, and efficiency. The implementation methods for virtualization testbed framework are described and experimental results show the advantage of virtualization testbed framework. Next, we will get further research in networked information system driving methods.

References

1. Yushi L, Heng W, Gangning Z et al (2013) Network-centric architecture for C4ISR system. Command Inf Syst Technol 4(6):1–7
2. Liang J, Lin Z, Ma Y (2013) Future internet experiment platform. Chin J Comput 36 (7):1364–1373
3. Xiaofeng H, Zhiqiang L (2011) The development of national critical infrastructure modeling and simulation. J Univ Shanghai Sci Technol 33(6):687–693
4. Szegedi P (2008) DJRA2.1: architectures for virtual infrastructure, new Internet paradigms and business models [EB/OL], In: FEDERicA project, European Union 7th Framework, Oct 2008. http://www.fp7-federica.eu/documents/FEDERICA-dJRA2.1.pdf
5. Wang J, Li Z, Lu G, et al (2008) Gragon-Lab: next generation Internet Technology Testbed. Sci China Ser E:Inf Sci 38(10):1783–1794
6. Carbone M, Rizzo L (2010) Dummynet revised. ACM SIGCOMM Comput Commun Rev 40 (2):12–20

Fixed-Frequency Sliding Mode Control of Buck Converter Based on Differential Geometry Theory

Li Kai, Li Jianbing, Zhou Dongfang and Kai Zheng

Abstract The paper establishes the state feedback accurate linearization model of buck converter by differential geometry theory. Based on the model, PWM fixed-frequency sliding mode controller is designed with the method of approach law. Experiment indicates that compared with PID control, new method has better dynamic and steady-state feature.

Keywords PID control · State feedback accurate linearization · Fixed-frequency sliding mode control

1 Introduction

With the development of controlling criterion and precision, new controlling method has amore important role in the research of modern converter. Compared with other methods, sliding mode control [1] is featured with its robustness and fast response, which can improve the dynamic and steady-state quality under wide range of disturbance in parameters, such as input voltage and load.

Ideal sliding mode control calls for infinite frequency. Sliding mode control based on hysteresis modulation reduces the frequency. The frequency is not stable and this goes against the design of the filter. Fixed-frequency sliding mode control [2] based on equivalent control not only reduces the frequency, but also guarantees the advantage of sliding mode control.

The paper takes buck converter as an example. The nonlinear system model of buck converter is transformed into linear system model with the method of state feedback accurate linearization [3, 4]. Then the fixed-frequency sliding mode

L. Kai (✉) · L. Jianbing · Z. Dongfang · K. Zheng
Communication Engineering College Information Engineering
University Science Avenue, Zhengzhou 450001, China
e-mail: 18695845556@163.com

Q. Liang et al. (eds.), *Proceedings of the 2015 International Conference on Communications, Signal Processing, and Systems*, Lecture Notes in Electrical Engineering 386, DOI 10.1007/978-3-662-49831-6_87

control is designed based on the linear system model of buck converter. The new method combines the advantages of fixed-frequency sliding mode control and state feedback accurate linearization, which has good dynamic and steady-state feature and is convenient to determine the parameters.

2 The State Feedback Accurate Linearization Model

2.1 The Affine Nonlinear Model of Buck Converter

First, the working principal of buck converter is illustrated in Fig. 1 as follows:

The state space equations are established by state space averaging method as follows:

$$\begin{cases} L\dfrac{\mathrm{di}_L}{\mathrm{dt}} = U_{\mathrm{in}}\mathrm{d(t)} - U_O \\ C\dfrac{\mathrm{du}_o}{\mathrm{dt}} = i_L - \frac{U_O}{R_o} \end{cases} \tag{1}$$

where d(t) is a function varying with time, also represents system control variable. Inductance current i_L (t) and capacitor voltage U_c (t) are chosen as two-dimensional state variables as follows:

$$X(t) = [x_1 \quad x_2]^T = [i_L(t) \quad U_c(t)]^T \tag{2}$$

The affine nonlinear model of buck converter can be established as follows in formula (3):

$$\begin{cases} X = f(X(t)) + g(X(t))u \\ y = h(X(t)) = x_2 \end{cases} \tag{3}$$

where $f(X(t)) = \begin{bmatrix} \frac{-x_2}{L} \\ \frac{x_1}{C} - \frac{x_2}{R_o C} \end{bmatrix}, g(X(t)) = \begin{bmatrix} \frac{U_{in}}{L} \\ 0 \end{bmatrix}$

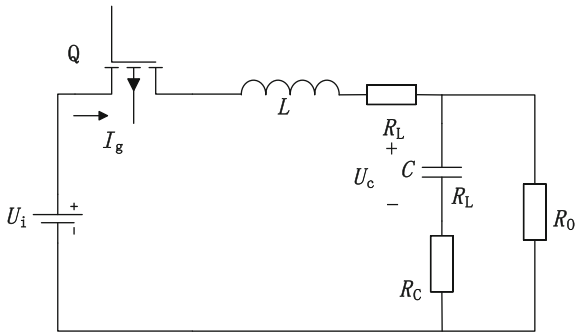

Fig. 1 Basic circuit of buck converter

2.2 Requirements of State Feedback Accurate Linearization

First we should confirm whether the model above meets the requirements of state feedback accurate linearization before coordinate transformation [5].

According to the law, the necessary and sufficient conditions are expressed as follows (the relation degree is set as **r**, and the system dimension is set as **n**):

1. The rank of the matrix $[\,g(X) \quad L_f g(X)\,]$ equals to system dimensions 2;
2. The vector field $D = \{g(X), L_f g(X)\}$ are involutions at $X = X^0$.

When both conditions are met, the nonlinear system can be turned into Brunovsky standard, which is a firmly anchored linear system.

The formula (4) can be calculated with Li function as follows:

$$L_f g(X) = \frac{\partial g(X)}{\partial X} f(X) - \frac{\partial f(X)}{\partial X} g(X) = \begin{bmatrix} 0 \\ \frac{U_{in}}{LC} \end{bmatrix} \tag{4}$$

The rank of matrix $[\,g(X) \quad L_f g(X)\,]$ (the rank is 2) equals to the system dimensions. At the same time vector field D meets condition 2. So the affine nonlinear model of buck converter can be turned into controlled linearity system (Brunovsky model).

2.3 Coordinate Transformation

New coordinates can be set as follows:

$$Z = [\,z_1 \quad z_2\,]^T = \varphi(X) = [\,h(X) \quad L_f h(X)\,]^T$$

$$\begin{cases} z_1 = \varphi_1(X) = x_2 \\ z_2 = \varphi_2(X) = \frac{x_1}{C} - \frac{x_2}{R_o C} \end{cases} \tag{5}$$

Through coordinate transformation [6], nonlinear system can be turned into Brunovsky model as follows:

$$\begin{cases} z_1 = \dot{z}_2 \\ z_2 = \alpha(X) + \beta(X) u \end{cases} \tag{6}$$

The controlled variable under new coordinate can be set as v:

$$v = \alpha(X) + \beta(X) u \tag{7}$$

Formula (8) can be attained from (5):

$$\begin{cases} x_1 = Cz_2 + \frac{x_2}{R_o} \\ x_2 = z_1 \end{cases} \tag{8}$$

Then

$$\dot{X} = \begin{bmatrix} C\dot{z}_2 + \frac{\dot{z}_1}{R_o} & z_1 \end{bmatrix}^T = \begin{bmatrix} -\frac{x_2}{L} & L_f h(x) \end{bmatrix}^T + \begin{bmatrix} CL_g L_f h(x) u & 0 \end{bmatrix}^T \tag{9}$$

Comparing between (7) and (9), (10) can be obtained as follows:

$$\begin{cases} \alpha(x) = \begin{bmatrix} -\frac{x_2}{L} & \frac{x_1}{C} - \frac{x_2}{R_o C} \end{bmatrix}^T \\ \beta(x) = \begin{bmatrix} \frac{U_{in}}{L} & 0 \end{bmatrix}^T \end{cases} \tag{10}$$

Combining (5) and (9), the relation of controlled variable under new and old coordinate system can be attained as follows in formula (11):

$$u = \frac{v + \frac{L_f h(x)}{R_o C} + \frac{h(x)}{LC}}{L_g L_f h(x)} = \frac{v - L_f^2 h(X)}{L_g L_f h(X)} \tag{11}$$

3 Fixed-Frequency Sliding Mode Control Based on State Feedback Accurate Linearization Model

Under the new coordinate system, controlled variable is set as $\boldsymbol{v}$, output variable is turned into $z_1 = x_2 = U_c(t)$. When system tends to be stable, the steady-state output voltage is $U_c(t) = z_{1ref}$. The error variable is set as $e = z_{1ref} - z_1$.

Linear switching function is selected as follows:

$$s = \alpha e + \dot{e} = \alpha\left(z_{1ref} - z_1\right) - z_2 \tag{12}$$

In other words,

$$s = \alpha\left(z_{1ref} - z_1\right) - v \tag{13}$$

Specific sliding mode controller is designed by approaching law.

$$\dot{s} = -\varepsilon \mathrm{sgn}(s) - ks \quad \varepsilon, k > 0 \tag{14}$$

Formula (15) can be obtained from (12) and (13) as follows:

$$v = -\alpha z_2 - \varepsilon \operatorname{sgn}(s) - ks \tag{15}$$

Through coordinate transformation, the relation between **v** and equivalent controlled variable **u** is expressed as follows in formula (16):

$$\begin{aligned} u &= \frac{LC}{U_{in}}\left[-\left(\frac{1}{R_o^2C^2}-\frac{1}{LC}\right)x_2+\frac{1}{R_oC}x_1+v\right] \\ &= \frac{LC}{U_{in}}\left[-\left(\frac{1}{R_o^2C^2}-\frac{1}{LC}\right)x_2+\frac{1}{R_oC}x_1-\alpha u_c(t)+\varepsilon\operatorname{sgn}(s)+ks\right] \end{aligned} \tag{16}$$

4 Simulation Experiment

4.1 Simulation Model

In this paper, Simulink tool is used for simulation experiment, specific parameters are shown as follows: $U_{in} = 12$ V, $U_c = U_{ref} = 5$ V, $L = 500$ μH, $R_o = 40\,\Omega$, $C = 1$ μH, $f = 100$ KHz.

From all the formulas above, u_{eq} can be obtained as follows in formula (17):

$$u_{eq} = K_i i_L(t) + K_u U_c(t) + \frac{LC}{U_{in}}\varepsilon\operatorname{sgn}(s) + \frac{LCK}{U_{in}}s \tag{17}$$

where $\begin{cases} K_{\mathrm{u}} = \frac{-L}{U_{\mathrm{in}}R_{\mathrm{o}}^2C} + \frac{1}{U_{in}} + \frac{L\alpha}{U_{in}R_o} \\ K_i = \frac{L}{RU_{in}C} - \frac{L\alpha}{U_{in}} \\ s = \alpha(5 - U_c(t)) - \frac{1}{C}i_L(t) + \frac{1}{R_oC}U_c(t) \end{cases}$

Specific parameters can be concluded as follows: $K_{\mathrm{u}} = -0.0741, K_i = 2.3633$. Controlled parameters can be attained by optimizing as follows:

$$\alpha = 5500000, \varepsilon = 2.56 \times 10^9, \mathrm{K} = 7.2 \times 10^8. \tag{18}$$

Figure 2 shows the simulation model established by Simulink tool. Simulation time is set to 0.02 s, load changes between 40 and 80 Ω for each 5 ms.

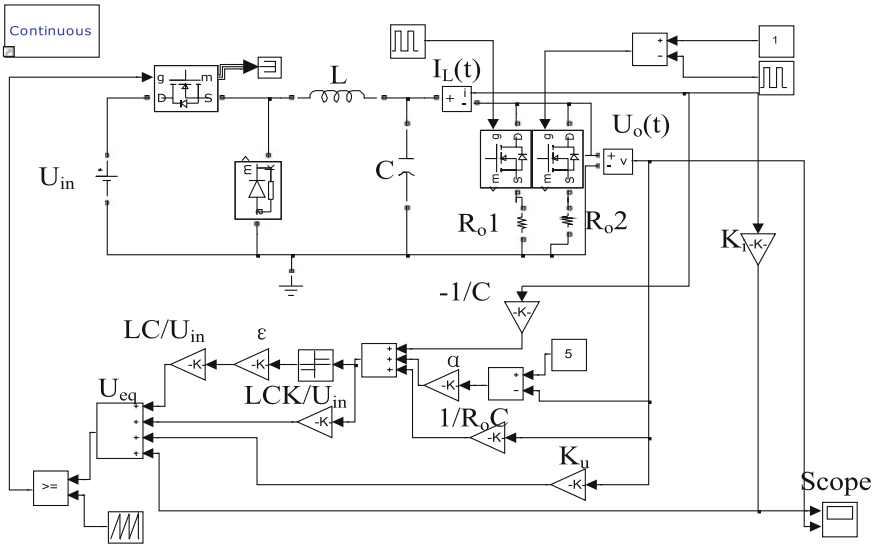

Fig. 2 The circuit simulation model

4.2 Simulation Results

Figure 3 shows the output voltage under the load mutation between 80 and 40 Ω based on fixed-frequency sliding mode control with the state feedback accurate linearization method.

It is indicated from Fig. 3 that almost no overshoot exists and system can transit to steady state quickly, in the meantime, the accommodation reflex time and oscillation time is short, the new control method has good dynamic response feature. When load does not change, its steady-state voltage seems to be stable, so it has good static characteristic, too.

Figure 4 shows the output voltage under the load mutation between 80 and 40 Ω based on traditional PID controller. Overshoot is about 0.3 V with PID controller, the accommodation reflex time is about 200 us. Compared with Fig. 3, it is

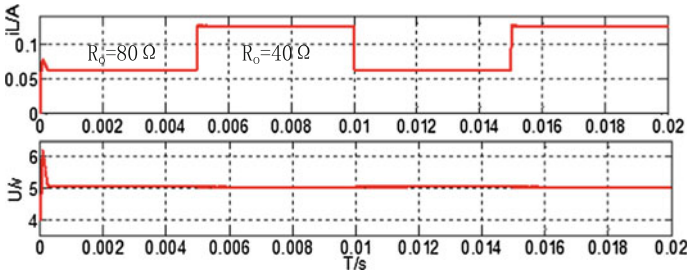

Fig. 3 Load mutation with new sliding mode controller

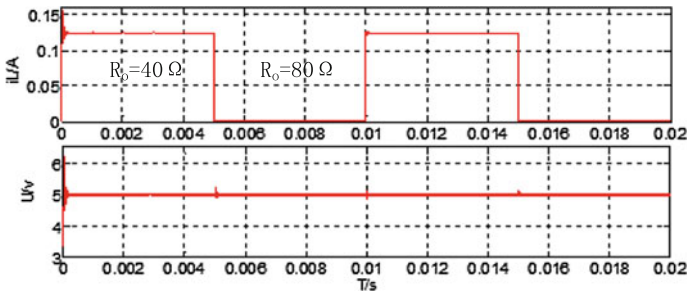

Fig. 4 Load mutation with PID controller

significant that new method has better dynamic performance, the accommodation reflex time is shorter and overshoot is smaller.

5 Conclusions

The paper combines nonlinear variable structure control theory and fixed-frequency sliding mode control, then designs a new fixed-frequency sliding mode controller for buck converter based on state feedback accurate linearization method. Simulation experiment indicates that new controller has better dynamic performance, the accommodation reflex time is shorter and overshoot is smaller. Moreover, new controller based on fixed-frequency sliding model control overcomes the disadvantages of sliding mode control based on hysteresis modulation. Compared with traditional controller, new controller has great effect and is convenient to be designed.

Otherwise, new method also has disadvantages that it is not very effective during light load.

References

1. Tan SC, Lai Y-M, Tse CK (2012) Sliding mode control of switching power converters techniques and impliementation. CRC Press
2. Martinez H, Ilic M (1988) A geometric approach to the feed-back control of switch mode DC-to–DC power supllies. IEEE Trans Circuits Syst. 35:1291–1298
3. Jiangyuan L, Yunxiang X et al (2012) Sliding mode control of CCM Buck converter based on state feedback accurate linearization. J South China Univ Technol 40:130–135
4. Hongbo Ma, Quanyuan Feng (2009) Fixed-frequency PWM sliding mode control of Buck converter based on accurate feedback linearization. Electr Power Autom. Equip 29:28–31
5. Deng Weihua (2005) The state feedback accurate linearization model and nonlinear control of the power electronic converter. Doctor thesis, South China University of Technology
6. Le Jiangyuan (2011) Research on nonlinear composite control of power electronic converter based on differential geometry. Doctor thesis, South China University of Technology

The Pre-application System of Real Estate Registration

Zhiqing Wang and Hao Luo

Abstract With the increase in network speed and the expansion of intelligent equipment, the establishment of real estate registration center is increasing year by year. The current model cannot meet the requirements of the registration center. Instead, there are some problems such as wastage of resources and time. To improve the efficiency of registered office and service levels, we want to establish "The Tianjin real estate trading center of registration and certification online pre-qualification platform". The purpose is to establish information, standardization, intelligent, all-weather network service platform. The system is adopting B/S operation mode and using Silverlight and related to the client. It can be applied for multiple subsystems such as examine and verify as a complete solution. System innovation is mainly for business. It will upload all the processing requirement by the Internet and it will do a preliminary application, then submit formal approval process.

Keywords Real estate registration · Preliminary application system · B/S structure operation mode

1 The Introduction

Tianjin real estate trading center of registration and certification (hereinafter referred to as center) is used for registration of the state land with the initiative registration of real estate [1], pre-sale registration of the commodity house, land mortgage registration and so on. It is an important window of national territory and

Z. Wang · H. Luo (✉)
Tianjin Real Estate Trading Center of Registration and Certification, Tianjin, China
e-mail: 40623249@qq.com

Q. Liang et al. (eds.), *Proceedings of the 2015 International Conference on Communications, Signal Processing, and Systems*, Lecture Notes in Electrical Engineering 386, DOI 10.1007/978-3-662-49831-6_88

housing administration industry and it is the national construction system of the national civilized unit. At present, there are some issues with such as the standard strictly, high social awareness, heavy working intensity and others [2], they already set up nine business windows in the registration center in bureau of administrative service hall. The businessmen and people are eager to establish a convenient and efficient information platform in the center to improve the efficiency of operations [3]. This platform can give the demands of the masses satisfaction and can promote the office efficiency and service level of the real estate registration. It is the only way for the long-term development.

According to the actual research situation and development trend in the future, we should make sure the project construction should be a high starting point. The overall project goals can be summarized as follows: (1) We will achieve the online application of registration center for all of the real estate registration project gradually [4]. We will realize the online application [5] (network or mobile phone APP) of the development enterprise and masses. We will achieve the database management of the real estate registration information [6] and archives, which will enhance the level of real estate registration information based on the realization of online office and paperless office. (2) We will realize the visual control in the whole process of the business registration based on the current real estate registration mode and explore a set of combined with ISO 9001:2008 management system, suitable for the real estate registration model of modern. (3) We will realize all kinds of registration and the summary of relevant information, query, statistics of intuitive visual and automatic generation and establish cooperative office platform. (4) We will realize the intelligent release of real estate registration information and cooperate with financial institutions and large real estate development enterprises. Thus, we can enhance the level of real estate registration management. (5) We will realize online publishing of the notification, announcement and related advocacy work and answer the various related consulting of the public by intelligent robot. We can realize the window service network of the real estate registration information and satisfaction survey of service network, etc. (6) We will realize the interconnection with utilization of archives system, realize the resource intensively and information standardization. System is divided into three parts: the real estate registration pre-application subsystem, real estate business subsystem and real estate registration service subsystem. The paper is organized as follows. In Sect. 1, we described the research status of real estate registration system, the research target and content. In Sect. 2, we introduced the development of national territory and housing administration application system in Tianjin. In Sect. 3, we introduced the research results of benefits. In Sect. 3, we addressed the application of research results. In Sect. 4, we are testing the system and obtained result. In Sect. 5, a summary is made for this paper.

2 The Development of National Territory and Housing Administration Application System in Tianjin

2.1 System Overall Design

There are three ways of application of software with current development [2, 7]: Independent development of completely independent; Pure secondary development based on commercial software platform; On independent programming language platform, use software to provide the basis of component integrated secondary development. This system is composed of four layers, respectively, and they are the Client Tier and WebTop Tier, Application Tier and the Database Tier.

According to the above analysis, the center of pre-registration system provided by our company will be established in the database based on the B/S application and it will pay attention to the compatibility and expansibility. The development environment is using Microsoft Visual Studio 2010, oracle10g database, using the c # development language and using Silverlight 3.0. In client running environment, the operating system are Microsoft Windows XP, Microsoft Windows 2003, Microsoft Windows 7 and so on. The customers will use browser IE 6.0 and above.

This system background is a new technology of Microsoft's Silverlight [8], and it is crossing platform and browser. Its generation has brought a lot of powerful tools for the Internet in the computer industry and it also improving the working efficiency. In this paper, we are relying on the composition and properties of Silverlight, discussing its actual application in related industries and development prospects.

Web development platform is a kind of trend. When many programmers were tired with the programming work, they are looking for highly efficient and different development methods. Thus, they will go into the development platform.

The system framework is as follows in (Fig. 1).

The system development environment and running environment is as follows:

(1) The development environment (Table 1)
(2) The operating environment (Table 2)

2.2 System Development of Key Technology

Microsoft Silverlight is a cross-browser, across the client platform technology. It can design, develop and launch a multimedia experience with rich interaction (RIA, Rich Interface Application) network interactive program. Silverlight provides a powerful platform. It not only can develop Web application with professional graphics, audio and video, but also enhance the user experience. Thus Silverlight attracted the attention of designers and developers.

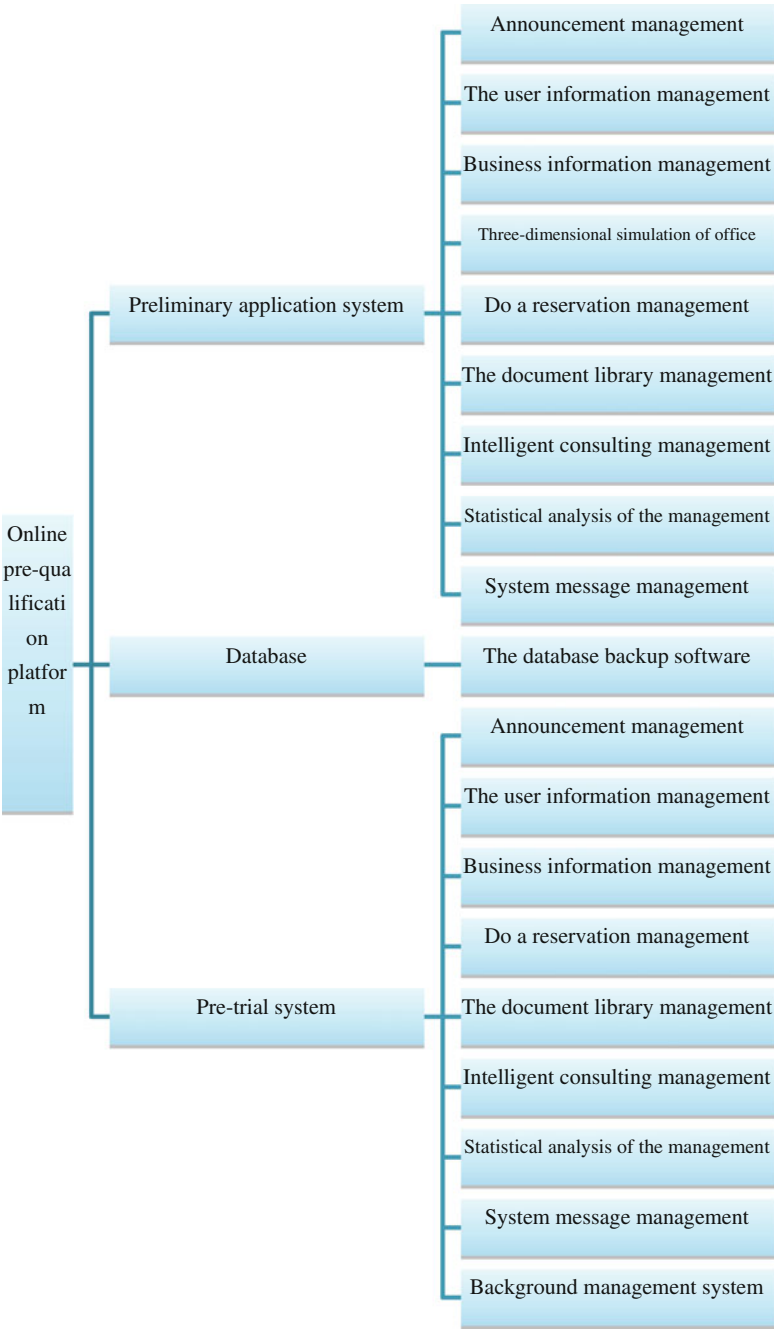

Fig. 1 The system framework

Table 1 The development environment of hardware environment

Hardware environment	
CPU	Intel® Pentium® 4 Processor 2.8 GHz
RAM	4 GB
Hard disk	120 GB Hard disk
Display	1600*900 Pixel true color LCD

Table 2 The hardware environment of running environment

Hardware environment	
CPU	Intel® Pentium® 4 Processor 2.4 GHz
RAM	1 GB
Hard disk	100 GB Hard disk

Silverlight can create a highly artistic application, it has the following characteristics: (1) A cross-browser, cross-platform technology. It can run in all popular browsers, including Microsoft Internet Explorer, Mozilla Firefox, Apple Safari and Opera. It also can run on Microsoft Windows and Apple Mac OS X. (2) No matter where to run, it can provide the same user experience. (3) The system is needed to download a small file to install to support, just a few seconds. (4) The user can be controlled directly in your browser and you can drag, flip, zoom pictures. (5) It reads the data and update the appearance but not interrupted by refresh the whole page to the user operation. Silverlight combines multiple technologies into a development platform, in which you can choose to conform to the requirements of the appropriate tools and programming languages.

2.3 System Implementation

The system is according to the requirement analysis [4]. In the early development of the system, we carried out preparation, project design work, organize relevant technical personnel for the requirements analysis and overall design of the system and we have determined the technical architecture, development platform and tools of the system. In the middle of the research and development, we are conducting the project implementation, achievement test to perfect and project promotion. According to the requirements of function and system architecture design, we formed a integrated application system which meet the requirements of end users. In the latter part of the system, we prepared reports and maintained the project. After a half-year of the system development, testing, modification, promote the use, the system function has been improved. And it has been applied to the daily work.

System implementation process as follows (Fig. 2).

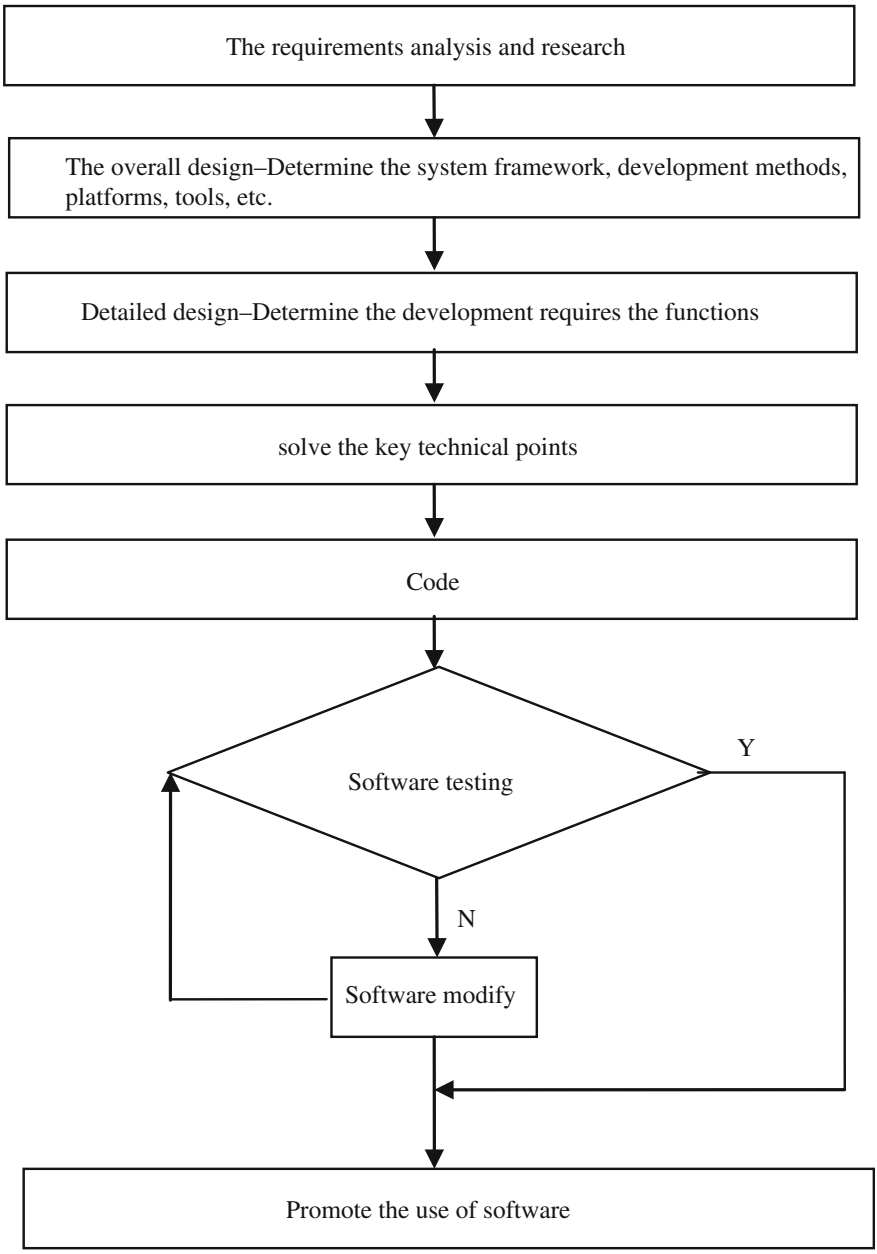

Fig. 2 The system development process

3 The Benefits and Application of Research Results

The development and application of national territory and housing administration application system in Tianjin has produced clear economic benefits [9]. Direct economic benefits include the following aspects: (1) The system has adapted to the working characteristics of the network, carried on the front of the government's service function, reduced the cost of the applying for personnel management, improved the work efficiency, reduced the service cost. (2) The system is integrated with the scanning system, reduced the amount of digital archives scanning, saved labor costs and equipment investment.

The system not only generates good economic benefits but also generates good social benefits, its main features are the following: (1) The system brings a change in the work way, improves the work efficiency, reduces the run time, and the number of the applicant to the hall for work, improves the user experience. (2) The system will provide good environment to the society and reduce social friction. (3) After the completion of this platform, it will greatly improve the soft environment, can effectively enhance the user quality and skill, reduce the overall cost, improve the image of the department. In order to speed up the construction of strong talent, build Tianjin development advantages to provide powerful guarantee.

4 The Test of the System

The test team from January 2014 began, based on the development of the report and user manual of "pre-application system of real estate registration" and based on the real estate registration procedures [10], we have conducted a comprehensive test to the system according to the following procedure. (1) The system customization. In the system of real estate surveying and mapping management, the system is the basis of real estate surveying and mapping management. In the test, the metering personnel authority and individual information will be truthfully recorded and classified according to the web access to personnel authorized. (2) The test of business process. The business flow is used in the pre-application management system is the core content, through entry the actual database on the basis of comprehensive consideration, give full consideration to the system. According to the set of permissions to log in the system and test. (3) The test of network environment. We can test according to the function of the frequently used in daily work, carry on the real data entry and reference to the daily work for testing. (4) The test of internal management environment. Through, entry the actual data and reference to the daily work for testing.

The conclusions of the system: the system interface esthetics, interface style friendly and easy operation; The system can meet the needs of the registration center of the daily work, fully functional, running accuracy; The system advanced design concept, high safety, easy to update maintenance and daily management.

5 Summary

We have completed the Tianjin national territory and housing administration application system research by our group. The system is based on the existing business registration of national territory and housing administration center of Tianjin and forming a set of system of efficient operation which the computer as support tools. The system uses modern methods to replace the traditional operation mode, achieves automation, standardization of the work window, improves the level, speed and efficiency of daily work, and enriches the work, provides the direction of the innovation and development for the national territory and housing administration work.

The research project have fully exercised the team members' independent innovation ability, research ability and accumulated valuable experience in scientific research project. We will make greater contribution according to the use of existing innovation platform, innovation environment. The development of this system is completed, just only one passage of the research. It is still demanded in further perfect and make it be more practical.

Acknowledgements This project is supported by "a figure project of Tianjin real estate". The implementation and operation maintenance is supported by the comprehensive information network of real estate in Tianjin. Tianjin Normal University and Tianjin EasyTech Corporation provides the technical support for the expanded function of the system.

References

1. Sun GD, Liang RH, Wu FL, Qu HM (2013) A web-based visual analysis system for real estate data. J Sci Chin 56(5):1–13. doi:10.1007/s11432-013-4830-9
2. Han Zonghie (2014) The practical implications of the unification of the real estate registration system in Korea. Int J Hous Markets Anal 7(2):254–265. doi:10.1108/IJHMA-04-2013-0023
3. Lu RQ, Jin Z (2008) From knowledge based software engineering to knowware based software engineering. J Sci Chin 51(6):638–660
4. Sun Y (2009) Real estate management information system development and design data. In: 2011 3rd IEEE International conference on information management and engineering
5. Hao Z (2011) Information-based construction of real estate enterprises. In: 2011 IEEE International conference on information theory and information security, Mar 2011
6. Chen L, Shen X, Wang L (2012) An application of extreme programming in development of management information system. In: 2012 International conference on intelligent control and information processing
7. Lee S-C (2001) Development of instructional strategy of computer application software for group instruction. J Comput Educ 37(1):1–9. doi:10.1016/S0360-1315(01)00020-3
8. Qiao D, Jun Y, Zhang P (2011) The research and implementation of IPTV system base on Silverlight. In: 2011 3rd IEEE international conference on information management and engineering, Mar 2011
9. Yazdanifard R, Micheal AO, Esimhenor IS (2011) Implementing real estate trading; it's vast improvement. In: 2011 International conference on information communication and management
10. Mei H, Liu XZ (2010) Software techniques for internet computing: current situation and future trend. J Chin Sci Bull 31:3510–3516

Research on Testing the Ultrasonic Wind Sensors in Circuit Wind Tunnel

Min Huang, Huiguo Lu, Baoqiang Wang and Yong Lu

Abstract Ultrasonic anemometer is suitable of a variety of industries which have wind demand because of the small start of wind speed, no moving parts, not destroying the wind farm and high accuracy. However, ultrasound test procedures related to wind measurements has not formalized in china. This article selected speed test point drawing on the wind cup test procedures and tests each point at different angles in the HDF-720 low-speed wind tunnel loop. The test results found that the ultrasonic wind sensor can be installed in a large wind tunnel for testing, but in the same wind speed, results of the measurement are slightly different at different angles due to the existence of wind instrument sensor shadow effect. Moreover, for different wind speeds, the differences are also different. Combined with the above test analysis, we must correct the measurement following the ultrasonic sensor installation angle when using ultrasonic anemometer to measure wind speed in real time.

Keywords Test · Ultrasonic anemometer · Circuit wind tunnel · Error analysis

1 Introduction

In the measurement of surface wind, the main test methods are mechanical, hot bulb, laser, ultrasonic, etc. [1], which are widely used to measure the surface wind. Mechanical sensors are subject to wear due to rotation, low measurement, large rotating inertia, and there are start-up wind speed. The mechanical moving parts of the ultrasonic sensor [2–6] are from the influence of the start wind speed and the inertia, having the advantage of fast response speed and high measurement accuracy. The main methods for measuring the velocity of ultrasonic sensors are vortex street method, correlation function method, Doppler method, time-difference method [1]. Vortex street method can only measure wind speed in one direction.

M. Huang (✉) · H. Lu · B. Wang · Y. Lu
Electronic Engineering College, CUIT, Chengdu 610225, China
e-mail: huangmin08@163.com

Q. Liang et al. (eds.), *Proceedings of the 2015 International Conference on Communications, Signal Processing, and Systems*, Lecture Notes in Electrical Engineering 386, DOI 10.1007/978-3-662-49831-6_89

Correlation function method has high accuracy, strong anti-interference ability, but it is only suitable for measuring air flow in a single direction. Doppler method calculates wind speed mainly by frequency offset, but this method is greatly influenced by environment and temperature. Due to the low development level of ultrasonic sensors in the domestic, a large number of ultrasonic sensors rely on imports, so ultrasonic wind measurement instrument testing technology is approximately blank. The methods of wind speed and direction detection based on ultrasonic time-difference are applied in the paper and test in the loop wind tunnel, and the result is discussed in this paper.

2 Principle of Ultrasonic Wind Which Is Based on the Time-Difference Method

The time-difference method [7, 8] uses one pair of 20 cm apart and high sensitivity ultrasonic probe which can be send and receive signal, a 90° angle layout, the overall height of 420 mm ultrasonic probe. The shape structure of two-dimensional ultrasound probe is as shown in Figs. 1 and 2.

Fig. 1 Ultrasonic probe structure shape

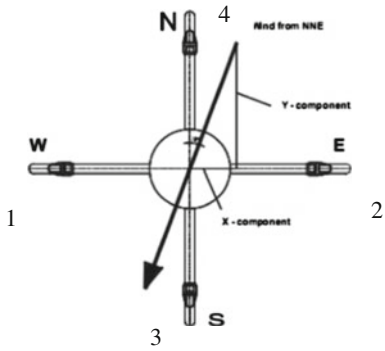

Fig. 2 Two-dimensional ultrasound probe principle

The distance of two ultrasonic sensors is d, When the ultrasonic wave spread between No. 1 and 2 probes, the propagation time of downwind and headwind is respectivelyt_{12}, t_{21}. The frequencies are f_{12},f_{21}, frequency difference is Δf_x; Similarly, when the ultrasonic wave spread between No. 3 and 4 probes, the propagation time of downwind and headwind are respectively t_{34}, t_{43}. The frequencies are f_{34}, f_{43}, frequency difference is Δf_y. The spread of ultrasonic wave is v_c under the condition of no wind speed, wind speed is v, winds from the east–west direction is v_x and from the north–south direction is v_y, so:

$$t_{12} = \frac{d}{v_{12}} = \frac{d}{v_c + v_x}; t_{21} = \frac{d}{v_{21}} = \frac{d}{v_c - v_x} \tag{1}$$

By (1), the wind speed v_x in east–west direction is deduced:

$$v_x = \frac{d}{2}\left(\frac{1}{t_{12}} - \frac{1}{t_{21}}\right) = \frac{d}{2}(f_{12} - f_{21}) = \frac{d}{2}\Delta f_x \tag{2}$$

Similarly, the wind in east–west direction is v_y:

$$v_y = \frac{d}{2}\left(\frac{1}{t_{34}} - \frac{1}{t_{43}}\right) = \frac{d}{2}(f_{34} - f_{43}) = \frac{d}{2}\Delta f_y \tag{3}$$

By (2), (3), we can get the actual wind speed and direction as follows:

$$v = \frac{d}{2}[(\Delta f_x)^2 + (\Delta f_y)^2]^{\frac{1}{2}}; \theta = \arccos \Delta f_x / [(\Delta f_x)^2 + (\Delta f_y)^2]^{\frac{1}{2}} \tag{4}$$

3 Ultrasonic Anemometer Test Based on Wind Tunnel

3.1 Wind Speed Detection Device

3.1.1 Wind Tunnel

This experiment adopts the HDF—720 wind tunnel [9] with the diameter of 720 mm, which is suitable for large size ultrasonic probe test. The device has wide range of wind speed, from 0.05 to 61.5 m/s, the uniformity of velocity's deviation is less than 0.5 % and the stability of velocity's deviation is less than 0.2 %. Wind speed verification device is made of wind tunnel body piercing, differential pressure gauge, Frequency converter, fan, computer software, wind and other parts.

3.1.2 The Pitot Tube

The main measurement standard device is the second-class pitot tube [10–12] at low-speed wind tunnel, L-type pitot tube is the most perfect kind of pitot. The Pitot tube has two inlet pressures, at the top of the probe is inlet total pressure, at the side of probe is static import. Total pressure and static pressure are tethered through soft rubber tube and DP-CALC, thus pitot tube differential pressure gauge measurement system is formed and we can read the differential pressure differential pressure gauge measuring velocity.

3.2 Standard Wind Measurements

Bernoulli equation [13] derived fluid velocity at work segment is as follows:

$$V = \sqrt{\frac{2}{\rho}(P - P_0)} = \sqrt{\frac{2}{\rho}\Delta P} \tag{5}$$

wherein, the calculation formula for air density [14] is $\rho = \frac{P_0 - 0.378He_w}{R_d(t+273.15)}$, among them, t is the temperature of the flow field, the unit is °C; H is the relative humidity of the flow field, the unit is %RH; P_0 is the ambient atmospheric pressure, the unit is Pa; e_w is the saturation vapor pressure when the flow field temperature is t °C, the unit is Pa; Rd is the gas constant of dry air, and generally Rd = 287 J/(K · kg).

4 The Testing Process and Data Analysis

In test experiments, Thies Clima ultrasonic wind measurement instrument made in Germany was used to test data, which can get real-time wind speed, wind direction and the actual temperature, the measured values are in the form of digital and analog output. This ultrasonic anemometer has the advantage of wide wind speed measurement range which can reach 0 ~ 65 m/s, high resolution, when wind speed is 0−5 m/s, the accuracy is ±0.1 m/s, when wind speed is greater than 5 m/s, the accuracy is ±2 %v m/s, high measurement precision (0.1 m/s), etc.

4.1 Obtaining Test Data

In the process of testing, reference the cup verification regulation [14, 15] to chose the wind test points for ultrasonic anemometer, which test data under the condition of 2, 5, 10, 15, 20, 30 m/s. Because the shape of the structure characteristics of

Table 1 The standard wind and the anemometer's test wind when the angle is 10° m/s

Test point	Standard wind			Anemometer test wind		
2	2.04	2.05	2.04	2.00	2.00	2.00
5	5.00	5.00	5.03	5.10	5.10	5.10
10	10.00	10.01	10.01	10.20	10.25	10.20
15	15.00	15.00	15.01	15.35	15.20	15.25
20	19.97	19.97	19.98	20.30	20.30	20.30
30	29.97	29.97	29.97	30.35	30.30	30.35

Table 2 Wind measurements test wind speed at different angles when the standard wind speed is 10 m/s V/m/s

Angle θ/°	10	20	30	40	50	60	70	80	90
The wind speed	10.01	10.1	10.08	10.1	10.07	10.05	10.12	10.07	9.98

ultrasonic anemometer, the above test points are tested at intervals of 10° from 0° to 90° (Table 1).

Because of numerous test data, choose a different wind speed as the data represent when the anemometer and wind direction of 10° as well as data of different angles when 10 m/s.

From Table 2, when the wind speed is close to the standard test wind speed, there exists errors between the instruments measured wind speed and the standard wind speed. In addition, there error is different in the same wind at different angles, the error source is the probe and has the shadow effect [9] caused by.

4.2 Data and Error Analysis

Absolute error expression [16] is

$$\delta_x = x - x_0 \tag{6}$$

In the formula, δ_x represents the absolute error (m/s); x represents the wind measurement instrument of wind speed; x_0 represents the standard wind speed. According to (6), it can be calculated that the absolute error between the wind anemometer's speed value and the standard value is shown in Table 3.

The distribution chart of absolute error between the measured wind speed and the standard speed under the same standard wind speed and different angles (Fig. 3).

The absolute error is minimum when the standard wind speed is 5 m/s, the absolute error of 10, 15, 20, 30 m/s increase gradually. The change of the absolute

Table 3 The absolute error between the wind anemometer's speed value and the standard value V m/s

Wind speed	Angle θ/°								
	10	20	30	40	50	60	70	80	90
2	−0.04	−0.05	−0.14	−0.15	−0.27	0.06	−0.06	−0.25	−0.38
5	0.09	0.02	−0.10	0.15	0.17	0.09	0.11	0.01	0.00
10	0.20	0.17	−0.06	0.12	0.31	0.24	0.22	0.13	0.02
15	0.27	0.26	0.23	0.21	0.31	0.32	0.30	0.26	−0.09
20	0.33	0.33	0.40	0.39	0.45	0.49	0.42	0.27	0.22
30	0.36	0.99	1.25	1.26	1.20	0.82	0.81	0.45	0.16

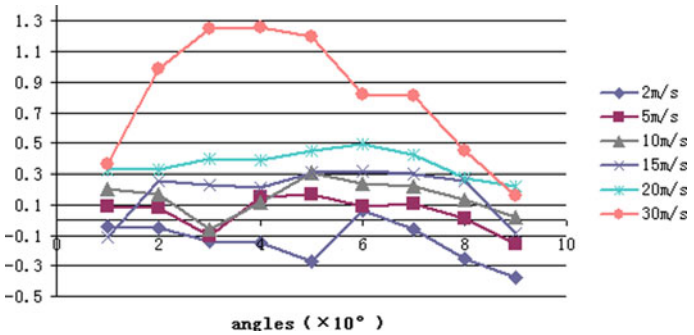

Fig. 3 The distribution chart of absolute error

error is the largest and fastest when 30 m/s, and reaches a maximum. The distribution map generally showed a trend of first increasing and then decreasing. According to the measurement performance requirement of wind cup sensor [14, 15], the maximum permissible error is ±(0.5 + 0.03v) m/s.

The expression for the relative error [13] is

$$E = \left|\frac{\delta_x}{x_0}\right| \times 100\,\% \tag{7}$$

In the formula, δ_x absolute error and x_0 represents the standard wind speed. The relative error between the instruments measured value and the standard wind speed, as shown in Table 4.

Shown in the table, in the standard wind speed of 20, 15, 10 and 5 m/s relative error value is smaller; Wind speed of 2, 30 m/s relative error is relatively large.

Table 4 The relative error between the instrument measured value and the standard wind speed

Standard wind speed (m/s)	Angle θ/°								
	10	20	30	40	50	60	70	80	90
2	1.96	2.44	6.86	7.09	13.04	2.94	3.06	12.20	18.27
5	1.80	0.40	2.00	2.97	0.00	1.80	2.20	0.20	3.10
10	0.20	1.69	0.59	0.90	3.10	2.20	2.20	1.30	2.00
15	1.80	1.73	1.53	1.40	2.06	2.13	2.00	1.73	0.60
20	1.65	1.65	2.00	1.95	2.24	2.45	2.10	1.35	1.10
30	1.20	3.3	4.18	4.20	4.00	2.73	2.70	1.50	0.53

5 The Absolute Error Curve and Its Correction Equation of Different Speed in All Direction

From Figs. 4 and 9, respectively, to draw the error curves and its correction equation at different angles in different wind speeds. According to the influence of the shadow effect [17] on different angles from 0 to 90°. So the error is corrected by quadratic polynomial, the correction equation is shown in the figure. From the figure, it can be found, the error rule is not too obvious when at 2, 5, 10 m/s, But error rule gradually approaches the shadow effect change rule when the wind is at 15, 20, 30 m/s, that also verified the size of the wind speed impact the shadow effect [17] (Figs. 5, 6, 7, 8).

The main factors that caused different errors at different angles is the shadow effect, second, also include the stability and uniformity of the wind field, the reflection interference of the ultrasonic in the tunnel wall, the wind energy loss in the process of transmission, etc.

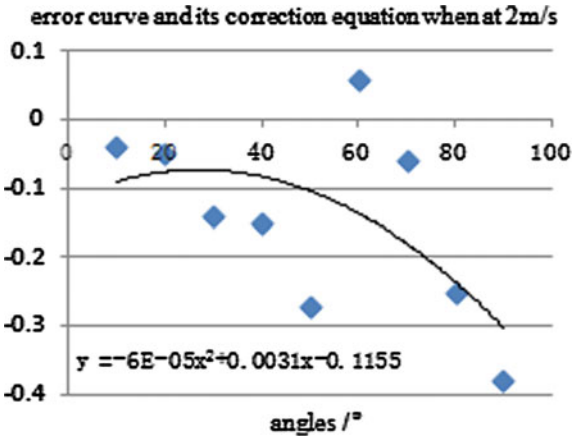

Fig. 4 The error correction curve at 2 m/s

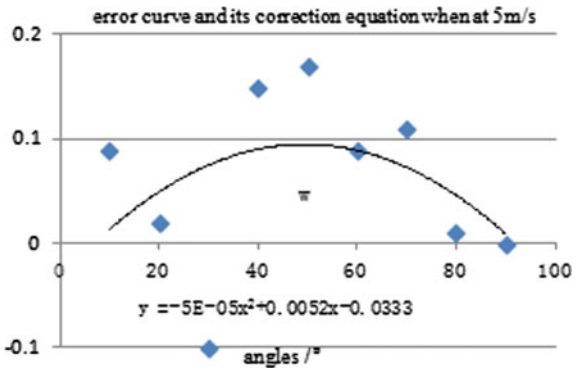

Fig. 5 The error correction curve at 5 m/s

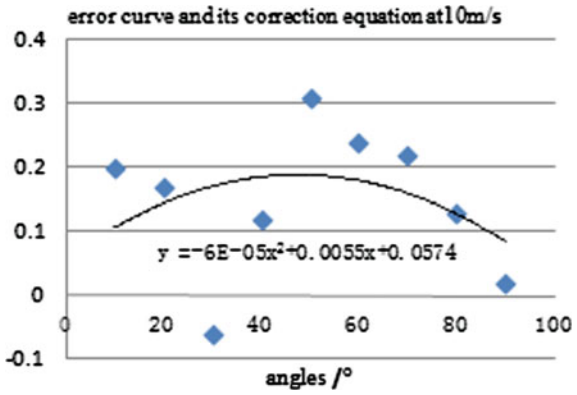

Fig. 6 The error correction curve at 10 m/s

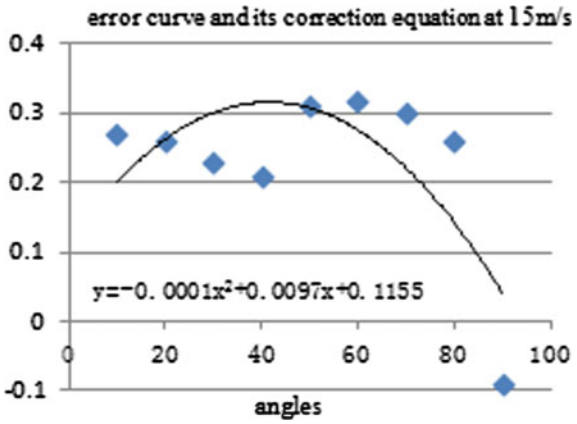

Fig. 7 The error correction curve at 15 m/s

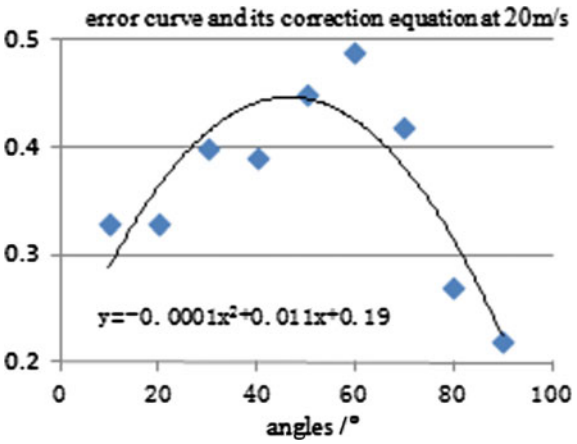

Fig. 8 The error correction curve at 20 m/s

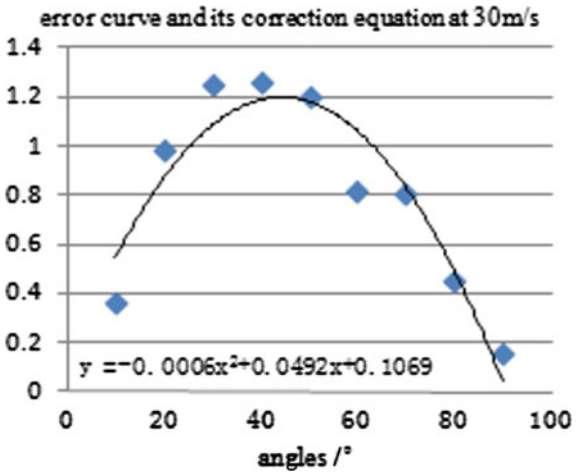

Fig. 9 The error correction curve at 30 m/s

6 Conclusion

This study choose German Thies Clima ultrasonic anemometer as instrument to be tested in the low-speed wind tunnel HDF-720. According to the verification regulation of wind speed sensor, set the test point and test in different angles. According to the analysis of the actual testing process and data statistics, conclusions are obtained as follows:

(1) Loop wind tunnel is used to analyze the ultrasonic anemometer verification test method is feasible;
(2) Ultrasonic anemometer should make use of the program testing, not only should be in accordance with the requirements for the wind sensor

measurement procedures, select a specific set of test wind speed, and must, according to the different aspects of ultrasonic sensor placement test data for the corresponding correction

(3) The main factors that caused different errors at different angles is the shadow effect, second, also include the stability and uniformity of the wind field, the reflection interference of the ultrasonic in the tunnel wall, The wind energy loss in the process of transmission, etc.

Based on the wind tunnel condition, the verification test study of the ultrasonic sensor is carried out in the paper. Due to the limited test conditions and test object, the above conclusion is hard to avoid has certain limitation, it is useful for further improve and deepen to the follow-up study.

References

1. Xie D (2013) Study of wind speed measurement method based on ultrasonic sensor [D]. Heilongjiang university
2. Quaranta AA, Aprilesi GC, Cicco GD et al (1985) A microproxcessor based three axes ultrasonic anemometer [J]. J Phys E Instrum 18(5):384–387
3. Banfield D, Dissly R (2005) A martian sonic anemometer[C]. In: 2005 IEEE aerospace conference, vol 2005. USA, pp 641–647
4. WS425 F/G ultrasonic wind sensor[Z] (2006) Vaisala Instruments Ltd
5. FT702 anemometer [Z] (1999) FT Technologies Ltd
6. User manual of windsonic-ultrasonic wind sensor [Z] (2005) Gill Instruments Ltd
7. Zhang Jieguang, Qi Wenxin, Qi Yu (2013) The principle and application of three dimensional ultrasonic anemometer[J]. Comput Digital Eng 41(1):124–130 in Chinese
8. Zhou Kang, Xin Xiaoshuai (2011) Design of wireless ultrasonic anemometer based on direct time difference method[J]. Appl MCU Embedded Syst 11(12):54–60
9. Sha Yizhuo, Chuang Shicong, Gao Qingting (2008) A design of low—speed meteorological wind tunnel for ultrasonic anemometer calibration. Chin J Sci instrum 29(8):296–300
10. Wang Min, Wei Genbao, Ma Jinguo (2013) Measurement error analysis and deviation simulation of second-class pitot tube. Meteorol Sci Technol 41(5):843–846
11. Cui Yanxia, Zhang Li (2000) Pitot tube test technology[J]. J Datong Vocat Tech Coll 14 (4):60–61
12. Wang Min, Zhou Shudao, Wang Yanjie (2010) Several factors affecting the accuracy of the pitot tube anemometer[J]. Lab Res Explor 29(3):35–37
13. Xu H (1987) Basic theory of air dynamics[M]. Beijing Institute of Aeronautics and Astronautics Press
14. CMA, JJG 004-2011 (2011)The verification regulation of the automation weather station wind direction and wind speed sensor[S]. Beijing:CMA, vol 6. Chinese, p 13
15. Zhang J, Wenhua LV (2011) Test guide for meteorological measurement[M], Beijing:Chinese quality inspection, vol 11
16. Qian Zheng, Jia Guoxin (2013) Error theory and data processing[M]. Science Press, Beijing, p 3
17. Zhang Aichen (2003) Modern weather observation[M]. Peking University Press, Beijing, p 10

The Experiment and Analysis of Image Acquisition System Based on the Hardware Platform

Baoju Zhang, Lei Xue, Shan Qin, Dan Wang and Yulong Gu

Abstract This paper introduced the hardware platform of image measurement reconstruction which is based on the theory of the compression sensing and its working process, the hardware platform consists of two parts, front-end acquisition circuit and rear reconstruction port. Acquisition port uses the Complementary Metal Oxide Semiconductor(CMOS) image sensor, it can achieve the real-time image acquisition, deposit the image in memory which is acquired in real time through a peripheral interface, to generate the corresponding gray level matrix. Then completing the transplantation of image reconstruction algorithm and the debugging of program through the hardware platform of the image measurement and the reconstruction system, achieving the reconstruction of Chinese characters and the complex image quiet clearly.

Keywords Compressive sensing · Image acquisition · Image reconstruction

1 Introduction of Image Acquisition System

The hardware platform of image acquisition system is shown in Fig. 1, it includes power supply unit, complementary metal oxide semiconductor (CMOS) image sensor [1], storage unit, central processing unit, image display screen, and communication unit, and its overall structure is shown in Fig. 1. The working voltage of power supply unit for other units to provide appropriate. The working process of image acquisition system is as follows:

(1) CMOS image sensor, which is in the front-end of the system [2], is responsible for the image acquisition in real time, the generated RGB image matrix visiting the access controller DMA through direct memory of the processor in

B. Zhang (✉) · L. Xue · S. Qin · D. Wang · Y. Gu
College of Electronic and Communication Engineering,
Tianjin Normal University, Tianjin, China
e-mail: wdxyzbj@163.com

Q. Liang et al. (eds.), *Proceedings of the 2015 International Conference on Communications, Signal Processing, and Systems*, Lecture Notes in Electrical Engineering 386, DOI 10.1007/978-3-662-49831-6_90

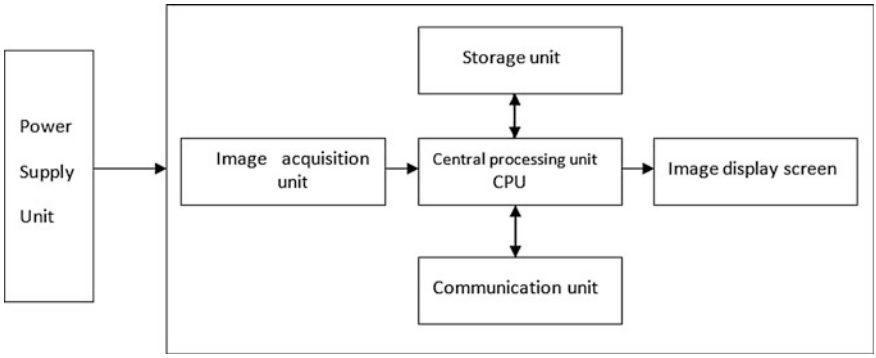

Fig. 1 Structure chart of image acquisition system

central processing unit [3], can be stored in the storage unit directly, have no need to occupy the resource of central processor unit CPU;

(2) The RGB image, which is stored in the storage unit, make it a gray one by processor to generate a corresponding two-dimensional matrix of the gray image, and then observing and reconstructing the two-dimensional matrix of the gray image by reconstructing image observation program;

(3) Finally, displaying the reconstructed gray-scale image through the image display screen;

(4) The whole working process is controlled by the upper machine through the communication module.

1.1 The Introduced of Processor OMAPL138

The embedded application processor with Da Vinci architecture of TI company started to use the combination of DSP [4] and ARM, which has the asymmetric nuclear structure [5], OMAPL138, as a classic processor, is a dual-core processor with low consumption. Dual-core architecture in OMAPL138, combined the advantages of high-speed digital signal processing performance in DSP and Reduced Instruction Set Computer (RISC) [6] in ARM, used TMS320C674xDSP kernel and ARM926EJ-S kernel which both have high performance. The internal resources structure of OMAPL138 is shown in Fig. 2.

2 Image Signal Measurement and Display Unit

Image signal acquisition unit, which used OV2640 image sensor, connected the processor OMAPL138 through the VPIF interface.

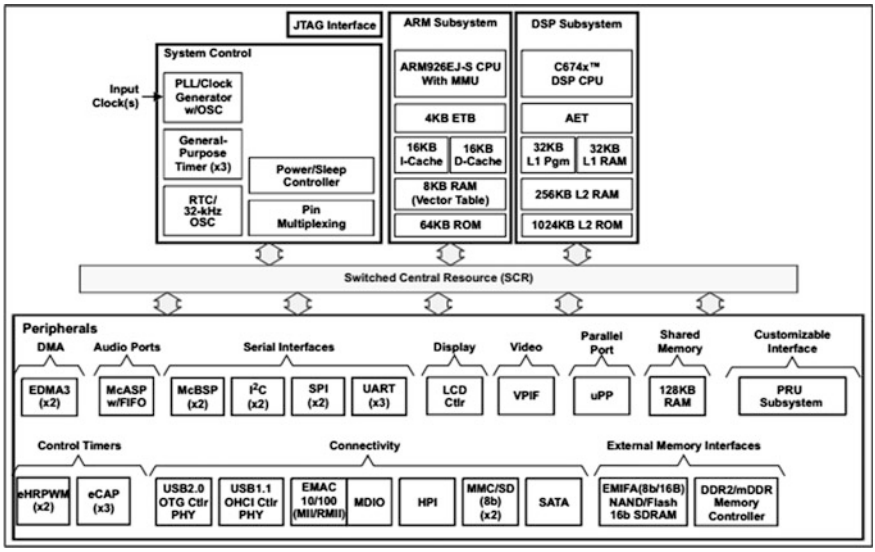

Fig. 2 The resource structure of OMAPL138

2.1 The Profile of Image Sensor OV2640

OV2640 is a CMOS image sensor [7], the first video sensor with 0.25 inches size and 2-million pixels, is a new image sensor with the architecture of 2.2 micron OmniPixel2. It can be assembled into mm-scale socket products, which is currently one of the miniature camera module. OV2640 uses high-tech and advanced OmniPixel2 architecture, with a richer color and zero-gap micro-lens structure, to increase the fill factor and quantum, and form a sensitive 2.2 micron pixel, improving the efficiency and effect of display [8]. Besides the benefits that OmniPixel2 architecture has brought, OmniVision integrates the advanced image signal processing module (OmniQSP), greatly improving the performance of the image. OV2640 has five units, including the analog signal processing unit, 10-bit A/D converter, digital signal processing unit, output format specification unit, and compression unit, it also has microcontroller, SCCB peripheral interface, and digital video output interface, Fig. 3 shows its internal structure function. It has the following features:

(1) Supporting 2-million pixels;
(2) Resolution can be as high as 1632 × 1232, as well supporting 320 × 240, 640 × 480, 800 × 600, 1024 × 768 [9];
(3) The refresh rate can be 30 frames/s, the rate is accessible in the highest yield 60 frames/s.

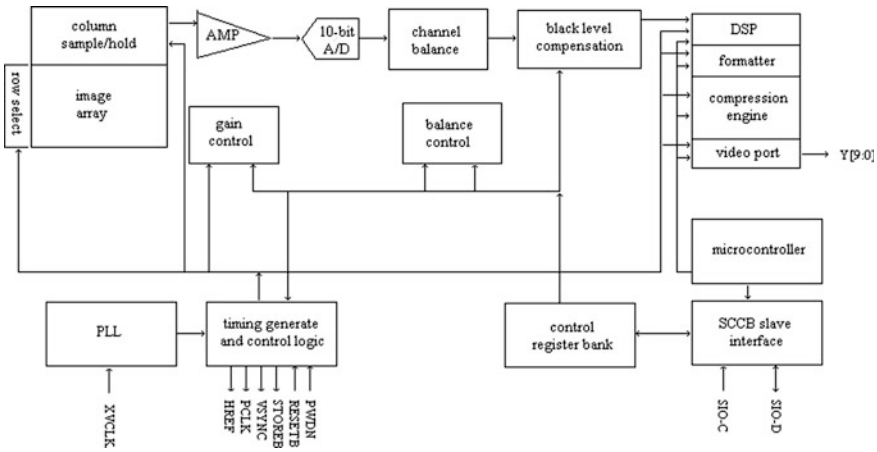

Fig. 3 The internal functional structure of image sensor OV2640

2.2 *Image/Video Peripheral Interface VPIF*

Image sensor OV2640 is connected to the processor OMAPL138 through VPIF interface, VPIF interface can capture and display the digital video. OMAPL138 VPIF interface includes two video input channels and two video output channels. Input channel 0 and input channel 1 share the same receiving structure, and output channel 2 and output channel 3 share the same transmission structure. Input and output channels of VPIF are as shown in Fig. 4. It has two input and output channels with embedded time code for 8-bit standard definition video signal, one input and output channel with embedded time code for 16-bit high definition video signals, and one input channel for 16-bit original video signal.

VPIF interface has four clock input pins and 2 clock output pins. Each channel has one clock input pin [10], can achieve the control of clock edges through the

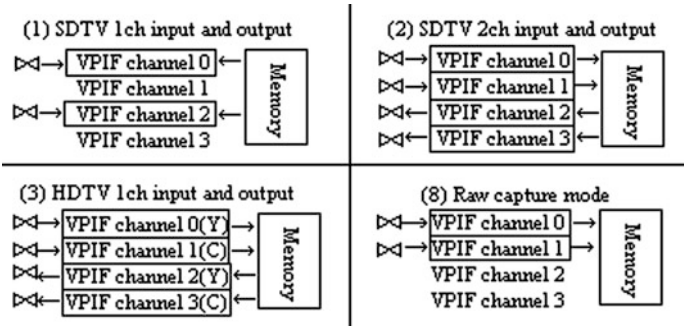

Fig. 4 The figure of input and output channels of VPIF

CLKEDGE which is in the register CnCTRL, 1, 2, 3 (n = 0), which is corresponding to each channel. VPIF interface can provide clocks for external devices through channels 2 and 3, and accomplish the setting of devices through the CLKEN digit in C2CTRL and C3CTRL registers which is corresponding to channels 2 and 3. The clock frequency produced by VPIF interface has the same frequency with input clock signal.

In this system, the image sensor OV2640 connect with OMAPL138 through VPIF interface, configuring VPIF interface as raw capture mode, in this mode, the output signal of image sensor can be transmitted to the processor directly. Processor can access controller DMA through direct memory to deposit data in the storage unit directly, do not take up the resource of CPU. In general, the format of the output signal which is produced by image sensor is RGB (sometimes can be RGrGbB). The format of the signal has the following characteristics:

(1) Storing the pixel data directly;
(2) Data bit width can be 8-bit pixels, 10-bit pixels or 12-bit pixels;
(3) Having selections of horizontal and vertical pixel signal polarity;
(4) Storing fields separately and crosswise.

2.3 LCD Display Unit

The image display unit adopts the AT070TN83 display screen made by INNOLUX Corporation. AT070TN83 is a 7-inch TFT-LCD screen, whose color-depth format is 16-bit RGB565, resolution with 800 × 400 pixel units, satisfies the need of displaying. AT070TN83 connects with the processor OMAPL138 through VPIF interface.

3 Experiments on the Hardware Platform

There are two sets of experiment in this paper. Experiment 1 used GPSR reconstruction algorithm combining with polynomial measurement matrix based on gram matrix. Experiment 2 used SAMP algorithm combining with Hada code measurement matrix based on pseudo-random sequence.

3.1 Experiment 1: GPSR Reconstruction Algorithm Combining with Polynomial Measurement Matrix Based on Gram Matrix

The GPSR algorithm adopted in the experiment combining with polynomial matrix measurement which based on gram matrix, the experiment was divided into three

groups. Each test adopted different measurement ratios, respectively, 20 %, 30 %, and 40 %. Two of these tests were simple Chinese character' images, "天" and "津"; the third group test is for the typical and quietly complex Lena image.

3.1.1 The Experimental Data

Figure 5 shows the corresponding reconstruction rendering of word "天" under different measurement ratios, Fig. 6 shows the corresponding reconstruction effect of word "津" under different measurement ratios, and Fig. 7 shows the corresponding reconstruction effect of the Lena image under the different measurements ratios. Table 1 shows the reconstruction time in each group under the different measurement ratios.

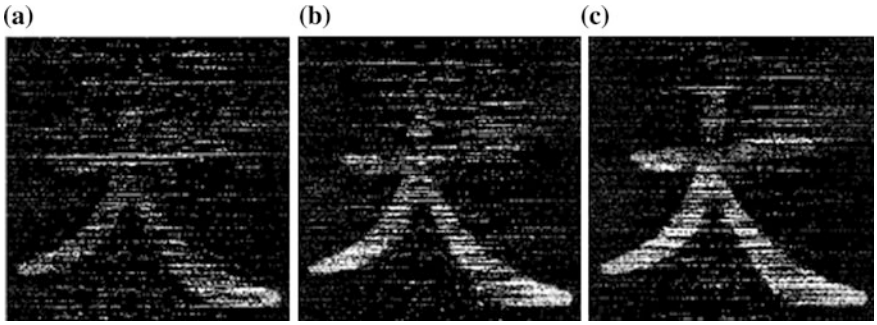

Fig. 5 The reconstruction effect chart of word "天". **a** Ratio is 20 %. **b** Ratio is 30 %. **c** Ratio is 40 %

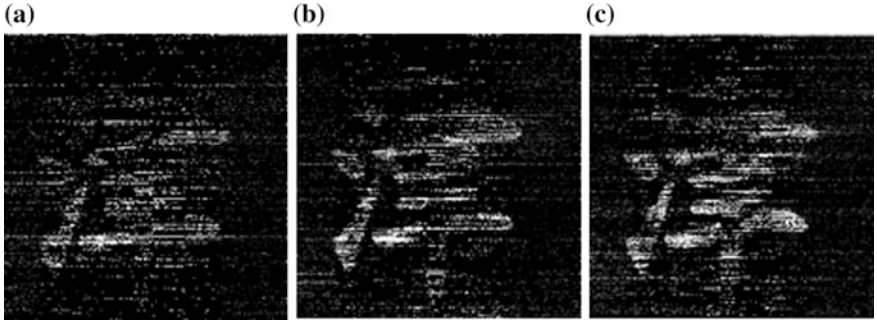

Fig. 6 The reconstruction effect chart of word "津". **a** Ratio is 20 %. **b** Ratio is 30 %. **c** Ratio is 40 %

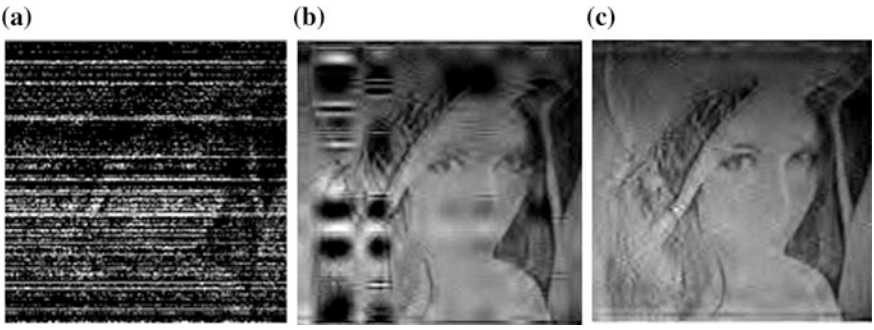

Fig. 7 The reconstruction effect chart of the Lena image. **a** Ratio is 20 %. **b** Ratio is 30 %. **c** Ratio is 40 %

Table 1 The reconstruction time under different measurement ratios of word "天", word "津", and the Lena image

Target image	Measurement ratio (%)	Reconstruction time (s)
The image of word "天"	20	13.75
	30	27.35
	40	43.56
The image of word "津"	20	13.87
	30	28.58
	40	44.54
The Lena image	20	56.56
	30	65.43
	40	75.54

3.1.2 The Experimental Analysis

It can be concluded from Figs. 5, 6, and 7 that under the same measurement ratio, the reconstruction effect of simple Chinese character images is superior to the quietly complex Lena image. By analyzing the data in Table 1, that for the same target image, along with the increase of the measurement ratio, the reconstructed image has a more clear effect, and the reconstruction time is in continual increase. Under the same measurement ratio, the Lena image needs the longest reconstruction time. Therefore, coming to a conclusion that GPSR reconstruction algorithm combining with polynomial measurement matrix based on gram matrix, along with the increase of the complexity of the image, the reconstruction time will increase.

3.2 *Experiment 2: SAMP Algorithm Combining with Hada Code Measurement Matrix Based on Pseudo-random Sequence*

3.2.1 The Experimental Data

SAMP reconstruction algorithm adopted in this experiment was combining with Hada code measurement matrix based on pseudo-random sequence, was divided into three groups. Figure 8 shows the reconstruction effect of word "天" under different measurement ratios, Fig. 9 shows the corresponding reconstruction effect of word "津" under different measurement ratios. Figure 10 shows the reconstruction effect of the Lena image under the different measurements ratios. Table 2 shows the reconstruction time in each group under the different measurement ratios.

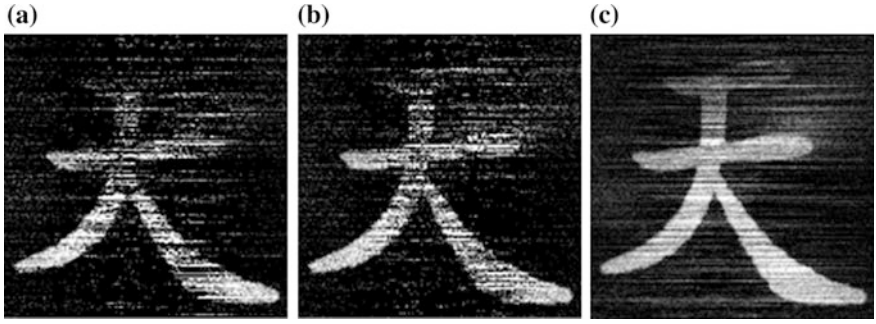

Fig. 8 The reconstruction effect chart of word "天". **a** Ratio is 20 %. **b** Ratio is 30 %. **c** Ratio is 40 %

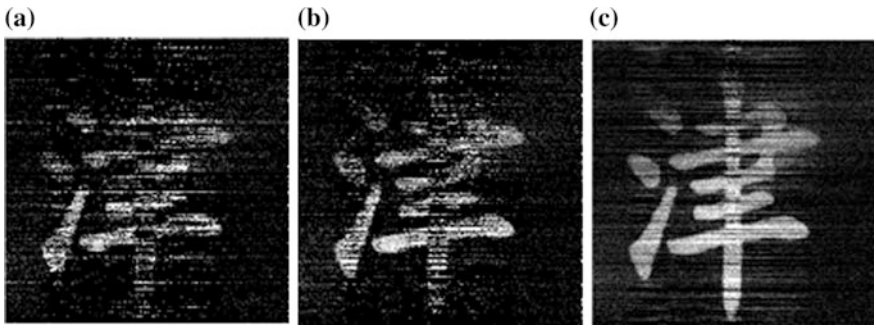

Fig. 9 The reconstruction effect chart of word "津". **a** Ratio is 20 %. **b** Ratio is 30 %. **c** Ratio is 40 %

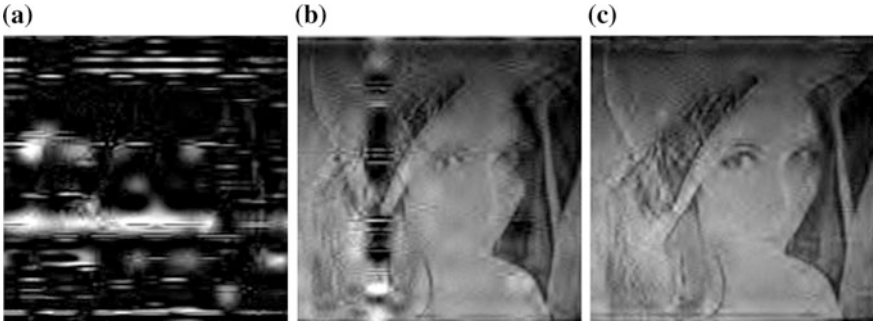

Fig. 10 The reconstruction effect chart of the Lena image. **a** Ratio is 20 %. **b** Ratio is 30 %. **c** Ratio is 40 %

Table 2 The reconstruction time under different measurement ratios of word "天", word "津", and the Lena image

Target Image	Measurement ratio (%)	Reconstruction time (s)
The image of word "天"	20	23.75
	30	22.35
	40	21.56
The image of word "津"	20	22.87
	30	21.58
	40	20.54
The Lena image	20	37.54
	30	36.43
	40	35.54

3.2.2 The Experimental Analysis

Observing from Figs. 8, 9, and 10, it can be concluded that, under the same measurement ratio, the reconstruction effect of simple Chinese character images is superior to the quietly complex Lena image. By analyzing the data in Table 2, for the same target image, along with the increase of the measurement ratio, the reconstructed image has a more clear effect, and the reconstruction time is in continual reduce. Under the same measurement ratio, the Lena image needs the longest reconstruction time. Therefore, it can come to a conclusion that SAMP reconstruction algorithm combining with polynomial measurement matrix based on gram matrix, along with the increase of the complexity of the image, the reconstruction time will increase.

3.3 The Compare and Analysis of the Results of Experiment 1 and Experiment 2

Analyzing the results of the two experiments, comparing Fig. 5 with Fig. 8, Fig. 6 with Fig. 9, and Fig. 7 with Fig. 10, the reconstruction effect of experiment 2 is superior to the experiment 1. Comparing Table 1 with Table 2, only when measurement ratio is 20 %, the reconstruction time of experiment is longer than experimental 1; and when measurement ratio is 30 % or 40 %, the reconstruction time of experiment is less than experimental 1. For the same target images, along with the increase of the measurement ratio, reconstruction time of experimental 1 become longer, reconstruction time of experimental 2 is reduced gradually.

As has been analyzed above, we can conclude that SAMP reconstruction algorithm combining with Hada code measurement matrix based on pseudo-random sequence is superior to GPSR reconstruction algorithm combining with polynomial measurement matrix based on gram matrix.

4 Conclusions

In this paper, two algorithms in image acquisition system based on compressed sensing on the hardware platform is introduced, and the results of the two groups of experimental data show that these two algorithms provide a viable option for the design of the image acquisition system based on the compressed sensing. SAMP reconstruction algorithm combining with Hada code measurement matrix based on pseudo-random sequence has a very important significance in designing the practical-value image acquisition system based on the compressed sensing.

Acknowledge This paper is supported by Natural Science Foundation of China (61271411), and cooperation project of 2014 annual national natural science fund committee with the Edinburgh royal society of British (613111215). It also supported by Tianjin Research Program of Application Foundation and Advanced Technology (15JCZDJC31500), National Natural Science Foundation of China (Grant No. 61501326), and Research on real time topology optimization and efficient broadcasting transmission algorithm in ZigBee networks for smart grid(NSFC:61401310).

References

1. Li Guike, Li Yulong, Feng Peng et al (2009) A novel single-Poly floating-gate UV sensor using standard CMOS process. Proc SPIE 7385:73852B
2. Stern A, Rivenson Y, Javidi B (2008) Single exposure optically compressed imaging and visualization using random aperture coding. J Phys 139:1–10
3. Deng Cai, He Xiaofei, Han Jiawei, TS Huang (2011) Graph regularized non-negative matrix factorization for data representation. IEEE Trans Pattern Anal Mach Intell 33(8):1548–1560

4. Merrett GV, Harris NR, A-l Hashimi BM (2007) Energy managed reporting for wireless sensor network. Sens Actuators 4:1–11
5. Wu L, Weaver C, Austin T (2001) A fast flexible architecture for secure communication. In: Proceedings of the 28th annual international symposium on computer architecture, Göteborg, Sweden
6. Fiskiran AM, Lee RB (2005) On-chip lookup tables for fast symmetric-key encryption. In: Proceedings of IEEE international conference on application-specific systems, architecture processors, Samos, Greece
7. Bigas M, Cabruja E, Forest J et al (2006) Review of CMOS image sensors. Microelectron J 37 (5):433–451
8. Lustig Michael, Donoho David, Pauly John M (2007) Sparse MRI: the application of compressed sensing for rapid MR imaging. Magn Reson Med 58(6):1182–1195
9. Ke Jun, Shankar Premchandra, Neifeld Mark A (2009) Distributed imaging using an array of compressive cameras. Optics Commun 282:185–197
10. Lei Xu, Liang Qilian, Cheng Xiuzhen, Chen Dechang (2013) Compressive sensing in distributed radar sensor networks using pulse compression waveforms. EURASIP J Wirel Commun Netw. doi:10.1186/1687-1499-2013-36

Kinematics Parameters Identification for IRB 1400 Using Improved Quantum Behaved Particle Swarm Optimization

Fengliang Wang, Yali Wang, Jie Li and Wei Fang

Abstract This paper presents an improved quantum behaved particle swarm optimization (IQPSO) algorithm to identify the robot kinematics parameter errors to improve the absolute accuracy of serial robots. The IQPSO algorithm is based on the quantum behaved particle swarm optimization (QPSO) algorithm. To improve the convergence speed, in the IQPSO algorithm, each dimension of the global best position is kept to be the best at each iterative process by comparing each dimension with the pre-value in the last iterative process. Comparing the IQPSO algorithm with least squared algorithm, the absolute accuracy of the robot can be improved 200 %. And compared with the standard particle swarm optimization (SPSO) algorithm and QPSO algorithm, the convergence speed is improved about 200 %. So the proposed algorithm can effectively identify the robot kinematics parameter errors.

Keywords Kinematics parameter errors · Quantum behaved particle swarm optimization · Robot positioning accuracy

1 Introduction

Knowledge of the stringent value of the robot end-effector pose is necessary in several industrial applications such as macroscopic structure measurement and assemblage. However, industrial robots cannot meet this challenge because of numerous errors. Five error sources are known to lead to robot inaccuracy, such as errors in kinematics parameters, environment, measurement, calculation, and use.

F. Wang (✉) · Y. Wang · J. Li
Zhonghuan Information College, Tianjin University of Technology, Tianjin, China
e-mail: wfl_yerkes@126.com

W. Fang
Beijing Aeronautical Science & Technology Research Institute of COMAC, Beijing, China

Q. Liang et al. (eds.), *Proceedings of the 2015 International Conference on Communications, Signal Processing, and Systems*, Lecture Notes in Electrical Engineering 386, DOI 10.1007/978-3-662-49831-6_91

The kinematics parameter errors are the dominant error source which account for 95 % of the errors [1]. So the robot positioning accuracy can be improved by identifying the error correction parameters.

Robot end-effector pose is usually obtained by kinematics models such as the D-H, the MD-H, or the S-model [2, 3]. Numerous robot calibration methods were proposed based on kinematics models with various parameter identification methods [4]. Wu et al. developed a linear Cartesian error model from the kinematics equations of an open-loop manipulator [5]. Most of the time, it is difficult to identify the kinematics parameters just by linear error models exactly. Optimizations are used to get more precise kinematics parameter errors. Gatti and Danieli proposed an effective and ready-to-apply computational approach using a nonlinear least-square optimization to estimate kinematics error parameters [6]. Gong investigated the methods to attain the errors in kinematics and non-kinematics parameters [7]. Meggiolaro et al. described a technique for determining kinematics and elastic deformation errors using polynomial approximations [8]. Lightcap et al. addressed a two-level optimization method to improve robot positioning accuracy by calibrating robot kinematics and flexibility parameters [9].

For most conventional optimization methods, least squared algorithm based on quadratic error functions whose iterative initial values have a great contribution to the results [10]. That means that the optimization results are not the global optimum but the approximate extreme points in the solution space. Now that the traditional methods cannot deal with nonlinear systems effectively, some new methods drawn from the field of biology are proposed to be the alternation. Genetic algorithms (GA), artificial neural networks, and particle swarm optimization algorithm are used to identify parameters to improve the robot accuracy [11, 12]. It has been proved that the particle swarm optimization algorithm had better optimization capability than other algorithms [13].

Though the PSO algorithm can solve some problems efficiently, it has disadvantage that it does not guarantee the global optimum. In the paper, an improved algorithm is proposed to overcome the shortcoming. The proposed approach is applied to the IRB 1400 robot kinematics parameter error identifying, and the parameter errors are identified efficiently.

2 The Algorithms

The kinematics model of the robot is usually expressed using Denavit–Hartenberg (DH) parameters [2]. IRB 1400 is an articulated serial robot with all of the rotary joints. There are six links and 24 kinematics parameters for the IRB 1400 robot. Because of the reasons of manufacturing, mounting or using, the kinematics parameters are disagree with their true value, making the robot positioning inaccuracy. To improve the robot accuracy, the correct kinematics parameters are need to obtained.

Due to the complexity of the robot kinematics system, it is difficult to determine kinematics parameter errors by gradient and differentiable information. Particle swarm optimization (PSO) which is a population-based stochastic optimization algorithm can achieve the work [14]. At first, the initial particles are generated in the searching space randomly. Then the particles as their personal best positions are used to evaluate the fitness function. Next, the swarms adjust their own velocities and positions dynamically based on the personal best positions and global best positions. Every swarm continuously updates itself through the above mentioned best positions. In this way, the particles tend to reach better and better solutions in the searching space.

In the PSO algorithm, the particles will follow a particular course after several iterations. And then the particles will be trapped into local optima. So the global convergence cannot be guaranteed [15]. To make sure the particles escape from a local minimum, QPSO optimization algorithm is proposed [16]. In the QPSO algorithm, the particle position is described not by the velocity but by the particle's appearing probability density function. There is no fixed orbit for the particles, and the particles can appear at any position in the feasible solution space with certain probability. So the QPSO has been proved to guarantee the global convergence [17].

The particle position updating equations are as follows:

$$C_j = (C_1, C_2, \ldots C_D) = \frac{1}{M}\sum_{i=1}^{M} P_i = (\frac{1}{M}\sum_{i=1}^{M} P_{i,1}, \frac{1}{M}\sum_{i=1}^{M} P_{i,2}, \ldots \frac{1}{M}\sum_{i=1}^{M} P_{i,D}) \quad (1)$$

$$p_{i,j} = \varphi \cdot P_{i,j} + (1-\varphi) \cdot G_{i,j} \quad \varphi \sim U(0 \sim 1) \quad (2)$$

$$x_{i,j} = p_{i,j} \pm \alpha \cdot \left| C_j - x_{i,j} \right| \cdot \ln[1/u], \quad u \sim U(0 \sim 1) \quad (3)$$

where D is the dimension of the problem space; M is the population size; $x_i = (x_{i1}, x_{i2}, \ldots x_{iD})$ are the particle current positions; $P_i = (P_{i,1}, P_{i,2}, \ldots P_{iD})$ are the personal best positions; $G_i = (G_{i,1}, G_{i,2}, \ldots G_{iD})$ are the global best positions; α is the Contraction–Expansion coefficient which is the only parameter in QPSO algorithm which is depicted as

$$\alpha = (1 - 0.5)*(MAXITER - t)/MAXITER + 0.5 \quad (4)$$

where t is the current iterative number, and the $MAXITER$ is the maximum iterative number.

To improve the searching ability of the QPSO algorithm, a local search operator around the global best position is obtained in a particular search area [18, 19]. Introduced an improved QPSO with the method that substituting every dimension of the best position for each particle with the corresponding element of the whole particle swarm, and reference [20] proposed a cooperative QPSO with five particles cooperate to find the personal best position for each particle. The approaches mentioned above can enhance the searching ability greatly, but they are time

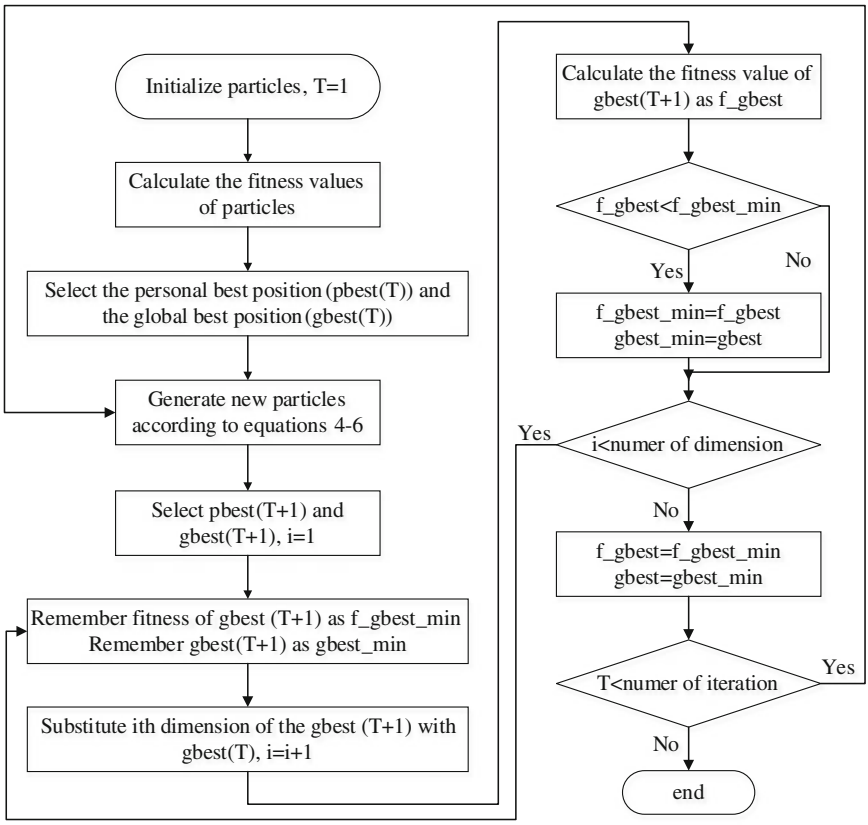

Fig. 1 Algorithm flow chart

consuming. In order to improve the convergence speed while reduce the time consuming, a new improved QPSO (IQPSO) algorithm is proposed. Figure 1 gives the IQPSO algorithm flow chart.

As shown in Fig. 1, at each iteration procedure, the previous global best position obtained in the last iteration procedure is remembered. After the new global best position attained, each dimension of the new global best position is substituted separately by the corresponding element of the former global best position, and the new positions are used to evaluate the objective function. If the replaced position's fitness value is better, substitute the global best position with the new position.

In the proposed algorithm, each dimension of the global best position is kept the best for every iteration procedure. The algorithm can improve the convergence speed greatly, while it is not time consuming.

3 Experiments

The experimental system consists of a six degree-of-freedom (DOF) serial robot IRB 1400 manufactured by ABB Inc., a laser tracker AT901-B manufactured by Leica Geosystems AG, and a personal computer (PC) manufactured by Lenovo. The laser tracker can obtain the Cartesian position in the laser tracker frame and has an accuracy of 0.015 mm. The system is shown in Fig. 2.

For the sake of measuring the robot end-effector positions conveniently using laser tracker, a precise extend pole is used, which is shown in Fig. 3. One end of the extend pole is fixed on the robot end-effector, and the other end can fix the laser tracker probe. The distance from the probe spherical center to the robot end-effector is known as l. The frame in the probe spherical center can be created having the same pose with the robot end-effector frame. When the robot axes are moved, the laser tracker probe positions are measured by the laser tracker at the same time. If the kinematics parameters are accurate, the distance of any two positions calculated by the robot kinematics model should be the same with the distance measured by the laser tracker. So the objective functions can be written as

$$F(\Delta\theta_1, \ \ldots, \Delta\theta_6, \Delta\alpha_1, \ \ldots, \Delta\alpha_6, \Delta a_1, \ \ldots, \Delta a_6, \Delta d_1, \ \ldots, \Delta d_6) = \sum_{i=1, j=i+1}^{n-1} \left(\left|\left(\left\|(X_r^i, Y_r^i, Z_r^i) - (X_r^j, Y_r^j, Z_r^j)\right\| - \left\|(X_l^i, Y_l^i, Z_l^i) - (X_l^j, Y_l^j, Z_l^j)\right\|\right)\right|\right) \tag{5}$$

where, (X_r^i, Y_r^i, Z_r^i) and (X_r^j, Y_r^j, Z_r^j) are the ith and jth position coordinates in the robot base frame, which are calculated using the robot kinematics model.

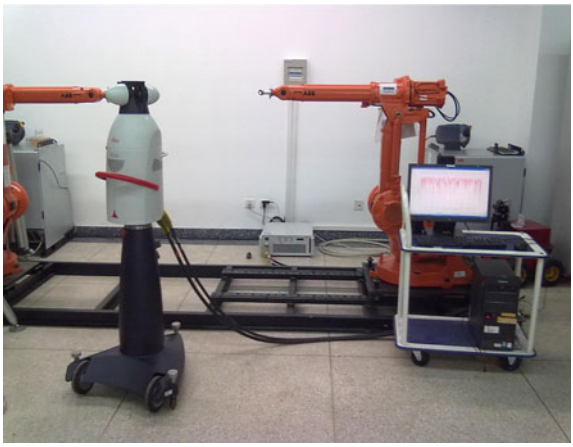

Fig. 2 Measurement system

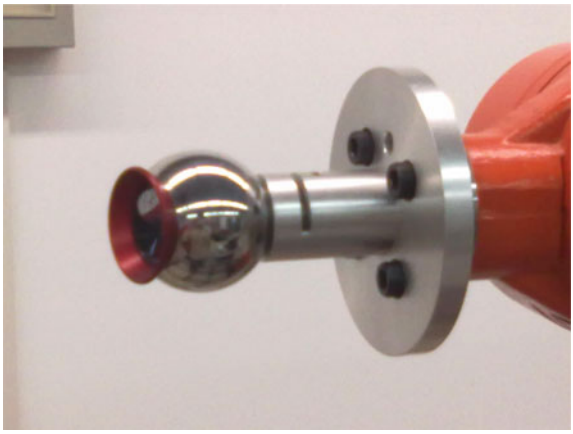

Fig. 3 The extend pole

(X_l^i, Y_l^i, Z_l^i) and (X_l^j, Y_l^j, Z_l^j) are the ith and jth position coordinates in the laser tracker frame measured by the laser tracker.

$\Delta\theta_1, \ldots, \Delta\theta_6, \Delta\alpha_1, \ldots, \Delta\alpha_6, \Delta a_1, \ldots, \Delta a_6, \Delta d_1, \ldots, \Delta d_6$ are the robot kinematics parameter errors, which are the global best position of the populations in the algorithm. n is the number of the calibration positions.

3.1 Application of the Proposed Algorithm

The joint angle of axis one is divided at intervals of 1 % of the whole range. The axis one is moved to those angles, while the rest axes stay zero. The positions of the probe measured by the laser tracker are recorded and the distance of any two positions are calculated.

The corresponding angle data supplied by the robot controller are recorded. Together with other kinematics parameters provided in Table 1, there are 100 group kinematics parameters. The same operation is carried out for the axis two to axis six. And 600 group kinematics parameters are obtained, which are considered as the

Table 1 IRB1400 robot kinematics parameters

No.	Joint angle range θ(°)	Link joint offset d / mm	Link length a / mm	Link twist angle α(°)
1	-170 ~ 170	475	150	-90
2	-70 ~ 70	0	600	0
3	-65 ~ 70	0	120	90
4	-150 ~ 170	720	0	-90
5	-115 ~ 115	0	0	90
6	-300 ~ 300	85	0	0

initial parameters. For each group, there are 24 kinematics parameters need to be identified. The positions of the probe measured by robot kinematics model can be obtained with the identified kinematics parameters. So the distance of any two positions can be calculated too. The identifying procedure is as follows:

Step 1. Setting the parameters of the algorithm. In the identifying process, the population size is set 100, the dimension is 24, the maximal iteration number is 600, the range of joint angle error is (−0.5, 0.5) rad, and the range of length parameter error is (−10, 10) mm.

Step 2. 100 group populations with 24 dimensions are generated in the range mentioned in Step 1, which are considered as the personal best positions of the 100 group populations. Each group population are added to the 600 group kinematics parameters, and then substituted to the robot kinematics model. The probe positions can be obtained and the distances between any two positions can be calculated. The min fitness value of all the 100 group populations is the global fitness value, and the corresponding population values are the global best position.

Step 3. New 100 group populations are generated using the QPSO algorithm. New personal best positions and new global best position can be obtained.

Step 4. According to the proposed method in the paper, each dimension of the global best position is substituted with the corresponding one of the global best position attained in the last iteration. Compare the fitness values of them, and the global best position of the iteration can be obtained.

Step 5. The number of iteration increases, if the number is less than the maximal number and the repeat number of the global best position is smaller than 200, steps 3–5 are repeated. Otherwise, this procedure is halted.

3.2 Results and Discussion

The robot is moved to 260 positions randomly and the relative kinematics parameter nominal values are obtained. Then the corrected parameter values are obtained by the nominal values plus the identified errors, and the corrected position values are attained by Eq. (5) with the corrected parameter values. The distance of two positions is denoted as

$$D_r^{ij} = \left\| (X_r^i, Y_r^i, Z_r^i) - (X_r^j, Y_r^j, Z_r^j) \right\| Z \tag{6}$$

The probe positions are measured by the laser tracker when the robot moves. The distance of two positions is denoted as

$$D_l^{ij} = \left\| (X_l^i, Y_l^i, Z_l^i) - (X_l^j, Y_l^j, Z_l^j) \right\| \tag{7}$$

The errors between the distances are used as verification set for the identify results. The kinematics parameter errors are identified using SPSO algorithm and QPSO algorithm with the same kinematics parameters and the same algorithm

setting. The distance errors are obtained by applying the corrected parameters, and the results are shown in Figs. 4, 5 and 6. For the sake of displaying simple, the results after 400 iterations are not displayed.

From Figs. 4, 5 and 6, we can see that the error is descending as the iterative number increase. After 218 iterations, the SPSO algorithm is trapped into local optima. The mean error of the SPSO algorithm is 1.648159 mm, the RMS error is 3.037922 mm, and the max error is 6.459807 mm.

After 400 iterations, the mean error of the QPSO algorithm is 0.214945 mm, the RMS error is 0.072696 mm, and the max error is 1.504699 mm. Of course, the error is descending as the iterative number increase. At the 764 iteration, the mean error of the QPSO algorithm is 0.079793 mm, the RMS error is 0.008972 mm, and the max error is 0.406252 mm. For the sake of displaying simple, the results after 400 iterations are not displayed.

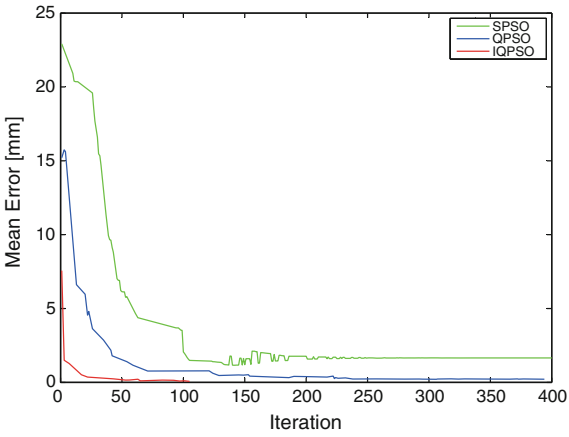

Fig. 4 Mean error

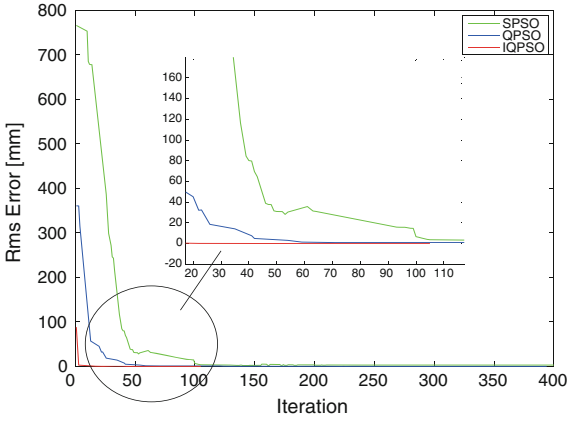

Fig. 5 Rms error

Fig. 6 Max error

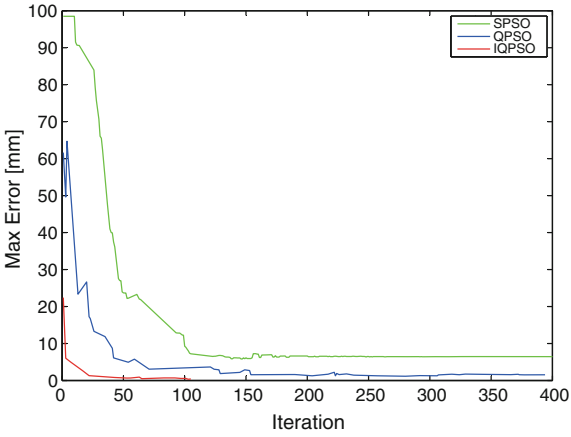

Table 2 The results of the accuracy comparison

	Kinematics model	NLS	SPSO	QPSO	IQPSO
Mean Error (mm)	2.8057	0.2342	1.6482	0.0798	0.0733
RMS Error (mm)	12.0907	0.0579	3.0379	0.0090	0.0087
Max Error (mm)	18.9690	1.2915	6.4598	0.4063	0.4470
Min Error (mm)	0.2145	0.1703	0.1147	0.0712	0.0684

After 105 iterations, the mean error of the IQPSO algorithm is 0.068603 mm, the RMS error is 0.007774 mm, and the max error is 0.414081 mm. From the comparison, we can see that the IQPSO algorithm has high convergence speed.

The results applying nonlinear least squared (NLS) algorithm are displayed to compare with the SPSO, QPSO and IQPSO algorithms, as shown in Table 2.

From Table 2 we can see that the errors without any optimization are very large, and the results of the IQPSO algorithm are the best.

4 Conclusions

A new Improved QPSO algorithm is proposed to identify the robot kinematics parameter errors. Compared with the SPSO algorithm and QPSO algorithm, the results show that the IQPSO algorithm has a high convergence speed. Compared with the traditional nonlinear least squared algorithm, the results show that the IQPSO algorithm has a good accuracy. The robot positioning accuracy is improved to be close to the robot repeatability level using the IQPSO algorithm. In addition, the proposed algorithm is general, and it has broad applications including numerous other kinds of serial robots and other parameter identifying applications.

References

1. Judd RP, Knasinski AB (1990) A technique to calibrate industrial robots with experimental verification. IEEE Trans Robot Autom 6:20–30
2. Denavit J, Hartenberg RS (1955) A kinematic notation for lower-pair mechanisms based on matrices. Trans ASME J 23:215–221
3. Stone HW (1986) Kinematic modeling, identification and control of robotic manipulator. Ph. D. thesis, Robotic Institute, Caregie Mellon University
4. Elatta AY, Li PG, Fan LZ et al (2004) An overview of robot calibration. Inf Technol J 3:74–78
5. Wu CH (1983) The kinematic error model for the design of robot manipulators. In: American control conference, pp 497–502
6. Gatti G, Danieli G (2008) A practical approach to compensate for geometric errors in measuring arms: application to a six-degree-of-freedom kinematic structure. Meas Sci Technol 19:015107
7. Gong CH (2000) Robotic measurement system: self-calibration, real-time error compensation and path planning. Ph.D. thesis, University of Michigan, USA
8. Meggiolaro MA, Dubowsky S, Mavroidis C (2005) Geometric and elastic error calibration of a high accuracy patient positioning system. Mech Mach Theor 40:415–427
9. Lightcap C, Hamner S, Schmitz T et al (2008) Improved positioning accuracy of the PA10-6CE robot with geometric and flexibility calibration. IEEE Trans Robot 24:452–456
10. Nubiola A, Bonev IA (2012) Absolute calibration of an ABB IRB 1600 robot using a laser tracker. Robot Comput Int Manuf
11. Tang YC, Xu Y (2005) Application of fuzzy Naive Bayes and a real-valued genetic algorithm in identification of fuzzy model. Inf Sci 169:205–226
12. Wang X, Liu H, Shi Y, Liang B, Zhang Y (2012) Research on identification method of kinematics for space robot. Proc Eng 29:3381–3386
13. Hassan R, Cohanim BK, Weck OD et al (2005) A comparison of particle swarm optimization and the genetic algorithm. In: Proceedings of the 46th AIAA/ASME/ASCE/AHS/ASC structures, structural dynamics and materials conference, Austin, TX
14. Kennedy J, Eberhart RC (1995) Particle swarm optimization. In: Proceedings of the IEEE international conference on neural networks, Perth, Western Australia, pp 1942–1948
15. Bergh FV (2001) An analysis of particle swarm optimizers. Ph.D. thesis, University of Pretoria, South Africa
16. Sun J, Feng B, Xu WB (2004) Particle swarm optimization with particles having quantum behavior. In: IEEE proceedings of congress on evolutionary computation, pp 325–331
17. Sun J, Xu W, Liu J (2005) Parameter selection of quantum-behaved particle swarm optimization. In: Advances in Natural Computation, pp 543–552
18. Wang J, Zhou Y (2007) Quantum-behaved particle swarm optimization with generalized local search operator for global optimization. In: Advanced intelligent computing theories and applications with aspects of artificial intelligence, pp 851–860
19. Huang Z, Wang Y, Yang C, Wu C (2009) A new improved quantum-behaved particle swarm optimization model. In: IEEE conference on industrial electronics and applications, pp 1560–1564
20. Li YY, Xiang RR, Li C et al (2012) An improved cooperative quantum-behaved particle swarm optimization. Soft Comput 16:1061–1069

Research and Design of the Communication Response Among Intelligent Cars

Haomeng Tong, An Zhao and Jie Li

Abstract The architecture of coordination is the basis of the coordination of multiple intelligent vehicles, as well as the framework for integrated control and decision-making. By analyzing the multiple intelligent vehicle coordination problems, the parallel coordination architecture based on the multiagent systems coordination model has been designed by considering the composition and operating characteristics of the local intelligent transportation system. This coordination architecture integrates the behavior coordination and the task coordination, and can meet the requirements of the multiple intelligent vehicle coordination in local transportation system. Refer to the above-mentioned coordination architecture, a multiple intelligent vehicle coordination system for the local intelligent transportation has been realized.

Keywords Intelligent vehicles · Wireless module · AVR microcontroller · Communication response

1 Introduction

Collaboration of multiple intelligent vehicles is a complex problem of distributed system, which involves intelligent vehicle technology, collaborative behavior among intelligent vehicle, task coordination, coordination architecture design, collaborative communication problems, etc. [1].

Collaboration of multiple intelligent vehicles has been researched from 1980s. As the practical degree intelligent vehicle is being increasingly improved, researching on the collaboration of multiple intelligent vehicles in the real trans-

H. Tong (✉)
Zhejiang University of Techonology, Hangzhou, China
e-mail: 1262375517@qq.com

A. Zhao · J. Li
Zhonghuan Information College, Tianjin University of Technology, Tianjin, China

Q. Liang et al. (eds.), *Proceedings of the 2015 International Conference on Communications, Signal Processing, and Systems*, Lecture Notes in Electrical Engineering 386, DOI 10.1007/978-3-662-49831-6_92

portation environment, especially environment of the plant facilities and urban road is becoming a research hotspot [2]. This paper mainly studies the design of the architecture of multiple intelligent vehicle cooperation, behavior coordination, and task coordination [3]. The purpose of research on the task coordination is to solve the problem that how multiple intelligent vehicle can finish the task under dynamic and random transportation conditions [4].

Coordination of intelligent vehicles requires communication among them. One intelligent vehicle sends its information to other vehicles in a self-organizing wireless network to spread its information in a certain region [5]. Communication enables vehicle to perceive the driving status and behavior potential of other vehicles in a large region, it can help the vehicle to acquire more information which is hard to acquire for conventional onboard sensors. Furthermore, it can take the place of some onboard sensors and achieve coordination of vehicles with more safety, effectiveness, and economization [6].

The operation of this system is that every two vehicles will send real state information between each other like speed, distance, etc., which in order to adjust the distance for ensuring there are no collision and friction. In term of the state of the small vehicles operating condition, if varies or faults, the vehicle will communicate with the main controlling system and send signals to let it intervene.

There is real communication that happened in the small vehicles, while there is interrupted communication between the small vehicles and the main controlling system. The real communication covers simple and inflexible information, while the interrupted covers flexible and changeable information according to different features of ways of communication, dealing with the different information, which assigns the resource of system communication reasonably, and improves the stability and reliability of the system as well at the same time.

Figure 1 shows the schematic of one testing field to simulate the vehicle functions. In this test, vehicle A should be at the position next to the start line and vehicle B should be next to the field boundary. Then they start simultaneously and at same direction, to test the overtaking function.

The hardware design includes design of the MEGA 16 basic module, driver module, and wireless module. The software involves route program, anti-off-field program, and wireless communication program. There is one control panel with three buttons in the vehicle. Button 1 enables the vehicle to run for one lap. Button 2 can activate the fore-vehicle program, which enables the fore-vehicle to be overtaken by the rear-vehicle at the first lap and overtake rear-vehicle at the second lap, and to continue this pattern. Button 3 can activate the rear-vehicle program, which enables the rear-vehicle to overtake the fore-vehicle at the first lap and also follow the same pattern with button 2. There are 3 infrared photoelectrical sensors and an infrared obstacle sensor to acquire essential data. The software controls the two vehicles to follow the test pattern automatically.

The two vehicles are both Atmega 16 microcontroller core, using PWM ports to control the velocity, serial communication to control the wireless module, and driver module to control the motors. Novel type of infrared photoelectrical sensors controlled by Atmega 16 were used to eliminate disturbs. A special algorism is

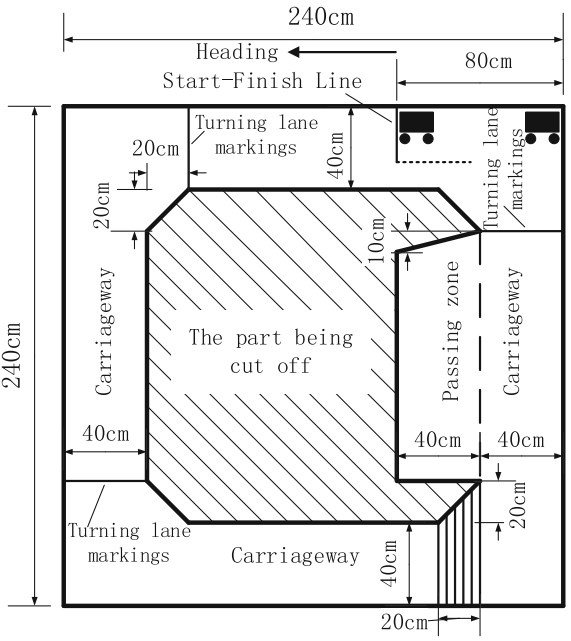

Fig. 1 Schematic of testing field

adopted to improve the stability of vehicles. When the sensors detect the boundary line, wheel of the inner side will stop until it is fixed to the right direction, and wheels of the outer side will stop for half of the stop time of the inner side wheels, to adjust the running direction and achieve route optimization [7].

2 Principle and Schematic of the System

The schematic of the system is shown in Fig. 2. Where the main control module and motion control module are responsible for scheduling of the entire system, and other modules achieve corresponding operations. Motion control module is to control the behaviors of the motors. Infrared photoelectrical sensors acquire the position information and send it to the motion control module through IO ports. After receiving this information and calculating the vehicle position, the control module will operate the motors by sending PWM signals to follow the trace [8].

The main control module is responsible for controlling the entire system, including processing of the obstacle information and turning line information, and wireless module communication [9], as well as the communication with the motion control module through the I/O ports, to achieve more running modes.

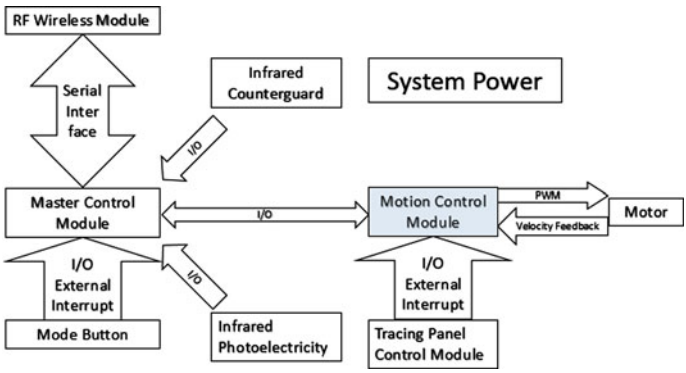

Fig. 2 Schematic of the system

3 System Design

AVR microcontroller is adopted in this design. Its main features are: Harvard architecture; reduced instruction set computer (RISC); fast access registers, single-cycle instruction; the same as PIC HI/LOW when works as output, and can be set as tri-state high-impedance input or pull-up resistor input when works as input, and has the ability to sink current of 10–20 mA; multifrequency RC oscillators are integrated, automatically reset, watchdog, startup delay, and other functions, the external circuit is easier, the system is more stable and reliable; most of AVR chips have abundant resources: with EEPROM, PWM, RTC, SPI, UART, TWI, ISP, AD, Analog Comparator, WDT, etc.

In this design, the L298 N DC/stepper motor driver is adopted for motion control module, which has the following characteristics: motor reversing and speed adjustment; good starting performance with high starting torque; operating voltage up to 36 V, 4A; ability to drive two DC motors; suitable for robot design and intelligent vehicle design.

This design uses L298 to drive two DC geared motor. Pin A, B can be used for PWM control. If the robot project requires only straight ahead, IN1, IN2 and IN3, IN4 two pairs of pins should be connected to high and low, respectively, only using two ports of the microcontroller sending PWM signals to control A, B, to achieve running straight, turning, acceleration/deceleration, etc.

Tracked vehicle chassis is adopted instead of the traditional tricycles or four-wheel vehicles chassis. With the constraints of the test field, the tracked vehicle chassis performs more stably. This design chooses high-power RP5 tracked vehicle chassis which has high torque 280 motor, helical + metal teeth gear set. This chassis has strong power, high stability, ability of in situ steering, turning flexibility, and low noise at the same time. It is a very good embedded control platform.

It requires vehicle to detect many marker lines in the running process, e.g., turning lines and field boundary lines, which needs infrared photoelectrical sensor

to achieve the detection. Sharp GP2A200 infrared photoelectrical sensor is used as its high precision and sensitivity. Infrared obstacle sensor is applied to acquire the position of the fore-vehicle in the overtaking procedure. When it detects the information, it will send a high signal to I/O port of the microcontroller.

Wireless communication is needed when the overtaking occurs. RF1100SE wireless communication module is selected in this design. This module adopts the CC1100 wireless communication chip from Chipcon, with the maximum data rate 500 kbps, changeable baud rate, maximum transmission distance of 300 meters, wireless wake-up function, sensitivity to −110 dBm, high reliability, and can be applied in many fields of short distance communication. This module is connected to the RXD/TXD port of the MEGA 16.

The applied voltage needed for MEGA16 is 5 V, for L298 drive is 12 V. This system uses the delay program to shift. Therefore, 7805 should be used to regulate the voltage for microcontroller, and 7812 is also needed to regulate the voltage for the L298 driver chip. To exceed 16 V as the power source of the entire system, there is a need 5 16850 lithium-ion battery which has high operating voltage, high energy density, light weight, small size, long life time, low self-discharge, no memory effect, no pollution, environmental protection, and high security.

4 System Hardware

This design adopted the MCU controller of ATmega 16. It is a low-power 8-bit CMOS microcontroller based on an enhanced AVR RISC architecture, which is based on the AVR core with Harvard architecture, with independent data and program bus. Program in the memory operates at the first level. While its advanced instruction set and single clock cycle execution time make the data rate up to 1 MIPS/MHz, thereby allowing the system optimization between power consumption and processing speed.

As shown in Fig. 3, it is the MEGA16 minimum system schematic for an ATmega16 microcontroller core, which is surrounded by some common interface circuit, including an external crystal oscillator circuit, reset circuit, 5 V power supply circuit, JTAG download interface, and serial communication interface circuits. It can be linked to a number of sensors through I/O ports.

L298 chip is used to achieve driving the motor, as shown in Fig. 4, the motor is connected to the L298 chip through photocoupler using four 4140 diode. Eight LEDs are used to detect the driving signal which is the input to the motor. Four pins OUT1, OUT2, OUT3, and OUT4 are connected to the four connectors of two motors. L298 inputs and PWM ports are connected to the microcontroller (PD4.PD5), to constitute the driver circuit.

Infrared photoelectric sensors are used in this system. The I/O port will be high when it scans the black line, otherwise will be low, which are connected to the PC0, PC1, PC2 three I/O ports, and then using LED to determine whether the sensor signal is detected, as shown in Fig. 5.

The flow chart and the practice product of this system are shown in Figs. 6 and 7.

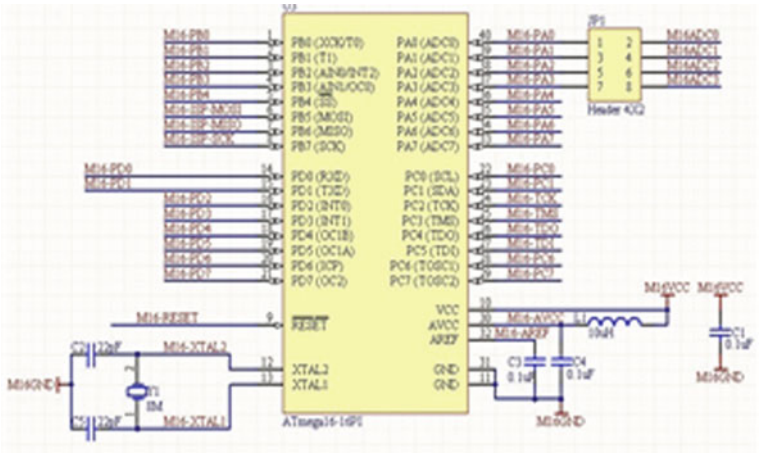

Fig. 3 Minimum system

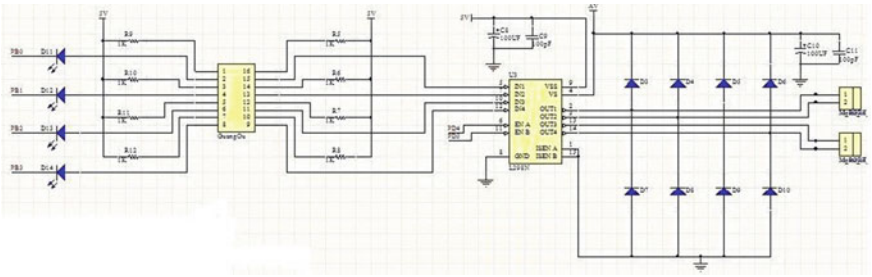

Fig. 4 L298 driver circuit

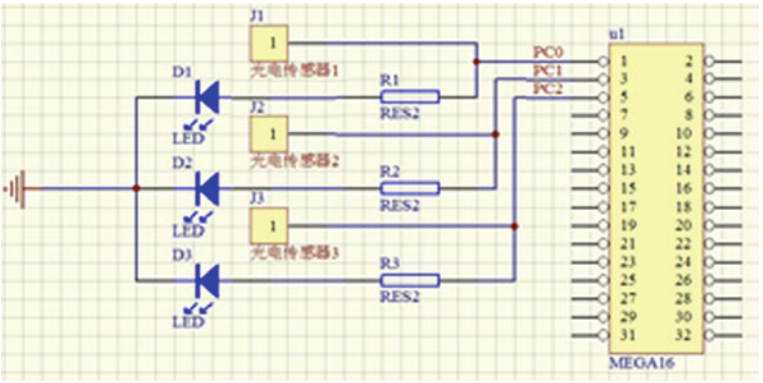

Fig. 5 Sensor module circuit

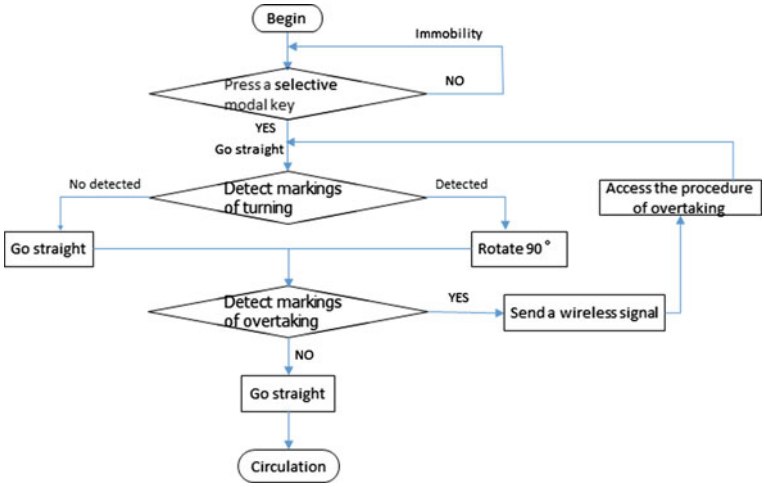

Fig. 6 System flow chart

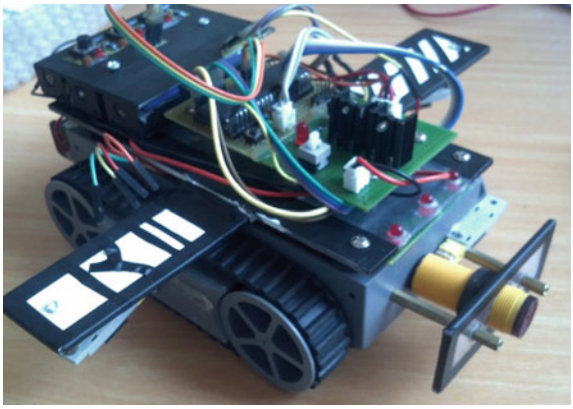

Fig. 7 Practice system product

5 Conclusions

Transport task allocation is an important factor that affects the system efficiency, service levels, and the transport costs. A closely related issue is to determine the transport routes, namely the vehicle routing problem. Mathematical programming or heuristic methods are commonly used to solve the centralized task allocation problem. Mathematical programming method takes transportation amount and costs as the objective function, vehicle loading, number of tasks, and time consumption as the constrains, such as integer programming, 0–1 programming, branch and

bound, etc. Heuristic methods commonly used simulated annealing, genetic algorithms, etc. Compared with mathematical programming methods, heuristic method, although not always able to determine the optimal solution, can solve the problem with high speed and in real time, therefore it is suitable for solving dynamic task allocation problems. Problems of task allocation and vehicle routing in the dynamic environment become a research hotspot in recent years.

In the area intelligent transportation systems, the collaborative task of intelligent vehicles which is generated dynamically needs to be done, and the running routes of vehicles also need to be corrected dynamically with transportation tasks. Thus, the problem of tasks collaboration needs to be considered in the dynamic situation.

Design of the collaboration architecture should primarily consider how to integrate collaboration and decision method, which is crucial for the realization of cooperation among members within a system. Currently, in the multiple intelligent robot systems, collaboration among intelligent robots generally adopts the distributed collaboration technology which is based on the multiple intelligent model. Multiagent system is an important research direction in the field of distributed artificial intelligence. Intelligent vehicle in the area intelligent transport systems can also be treated as an intelligent robot, but as a transport system, the involved collaboration in this system has its own features, it is more complex than conventional robot and more types of collaborative problems should be considered.

Area intelligent transportation system also can be treated as a large system, and as the intelligent vehicle has the abilities of independent control, decision-making, and autonomous behavior, thus, it has the characteristics of collaborative distribution. Combined with the characteristics of the area intelligent transport systems, the large system control theory and multiagent collaborative theory can be taken as reference for design of the collaborative architecture.

This research establishes the platform of multi-vehicles' operating and communication researching in smart vehicles. The passage is aimed at researching the operation from the same direction in double vehicles, and the model of communication and methods in a condition of complex path programming and complex tasks model in three vehicles or more on the platform as well.

References

1. Liu Y, Xuan H (2005) Summarizing research on models and algorithms for vehicle routing problem. J Ind Eng/Eng Manag 19(1)
2. Ershi Q, Qing T, Ninghua S (2003) Review of methods of the planning for the logistic chain network. J Tianjin Univ (Soc Sci) 5(3):225–228
3. Shi S, Gao F, Du F, Zhang Y (2007) Modeling and simulation of stop-and- go vehicle cruise system. Chin J Highw Transp 20(3)
4. Youchun X, Rongben W, Bin L, Bing L (2001) A summary of worldwide intelligent vehicle. Autom Eng 23(5):289–295

5. Li J, Guo Y (2001) Theory and method of logistics delivery vehicle scheduling. China Logistics Publishing House
6. Ren H, Dong Q, Li X, Shi W (2007) Simple intelligent electric vehicle. Xidian University, Research Center of Measurement & Control Technology and Instrument, Xian
7. Tan M, Xu J, Xu L, Li D (2005) Control strategy of vechicle's lane-changing and its sensitivity analysis. J Sys Eng 21(2):206–210
8. Jun Z, Changying J (2003) Lateral control of intelligent vehicle. Robot 25(1):26–30
9. Wu C, Yan X (2001) Research on lateral control in automated highway system. Comput Commun 19(99)

Research on Impact of AVC Control Action Sequence via Optimization Parameter System in Hebei Low Voltage Grid

Xiao Yang, Nan Wang, Wenping Hu, Liang Meng and Peng Luo

Abstract Proposing the optimal AVC coordinating parameters and comparing effects of different control action sequence in a scientific manner is one of the functional characteristics of smart AVC. In this paper, Optimization Parameter(OP) system is developed in Hebei low voltage grid for this purpose. The data are taken from EMS. The state estimation is carried out periodically after obtaining real-time data. Taking state estimation results as the basic power flow and simulating AVC operations, the voltage variations and line loss analysis can be calculated for comparison. The system can compare optimization parameters for the real grid or for the virtual grid. It s depends on whether to consider the actual capacity of reactive power compensation equipments. The structure, hardware configuration and data exchange of the system are illustrated. And several analysis tools of the OP system are introduced. The paper gives the formula of voltage fluctuation and example in which evaluating effects of voltage fluctuation benefited from different control action sequences. With the system, users can get the optimal AVC coordinating parameters and the optimal control action sequence expediently.

Keywords Smart grid · Automatic voltage control · Control action sequence · Voltage fluctuation · Real-time data · Optimization parameter

1 Introduction

With the smart grid developing and voltage level upgrades, the researchers pay more attention to the reactive power balance and voltage control. These control actions lead to voltage fluctuation, which must be beared by the insulation of transformation, transmission and consumer equipment, greatly affecting the safe

X. Yang (✉) · W. Hu · L. Meng · P. Luo
Hebei Electric Power Research Institute, Shijiazhuang 050021, China
e-mail: 15831160430@163.com

N. Wang
Shijiazhuang University of Economics, Shijiazhuang 050021, China

Q. Liang et al. (eds.), *Proceedings of the 2015 International Conference on Communications, Signal Processing, and Systems*, Lecture Notes in Electrical Engineering 386, DOI 10.1007/978-3-662-49831-6_93

operation and probably shortening the life of them [1–3]. Automatic Voltage Control (AVC) system has been applied as a means for controlling voltage and adjusting reactive power because it has many special excellences [4–8]. However, in low voltage grid or rural grid, AVC system needs to control equipment of different voltage levels at the same time, without considering optimal control action sequences. Meanwhile there are few ways to compare effects of different control action sequences on the voltage regulation. And it is a problem to evaluate effects of voltage fluctuation when different voltage level operations in one AVC control action strategy.

The main function of AVC system for smart grid can be described usually as follows: (a) It can check whether the available AVC coordinating parameters are optimization. (b) It can evaluate reducing line loss benefited from the operations. (c) It can provide the decision-supporting function for planning new power capacitors or on-load regulating transformer of substation, which can adjust the layout of reactive power compensation equipments [9–12]. The Optimization Parameter (OP) system has all these functions, and has another important function in addition. (d) It can evaluate voltage fluctuation benefited from the optimal operation sequences.

The main motive of this paper is to provide the purpose, system structure, hardware configuration and data exchange of the OP system. Blueprint of developing OP system to smart AVC system is shown. Furthermore, a number of important concepts about the coordinating priority, such as the voltage-capacitor sensitivity and the voltage-tap sensitivity, are also given. Finally, the formula of voltage fluctuation is introduced. And the example of control action sequences for Hebei low grid is given.

2 The Optimization Parameter System

With the real-time data from EMS, the OP system is the on-line monitoring and analyzing system for Hebei low voltage grid. The state estimation is carried out periodically after obtaining real-time data. Taking state estimation results as the basic power flow, the theoretical voltage variations and line loss analysis can be carried out within the virtual equipments such as capacitors and transformers. It can calculate the voltage-capacitor sensitivity, which is voltage variation of one key bus dividing the reactive variation when regulating a unit of capacitor. Also the OP system can calculate the voltage variation of one key bus while regulating the transformer tap, which is voltage-tap sensitivity. These sensitivities decide the coordinating priority of capacitors or transformers. All the voltage variations can be viewed with Hebei grid geographical diagram.

The OP system in Hebei grid contains five subsystems. The flowchart of it is illustrated in Fig. 1.

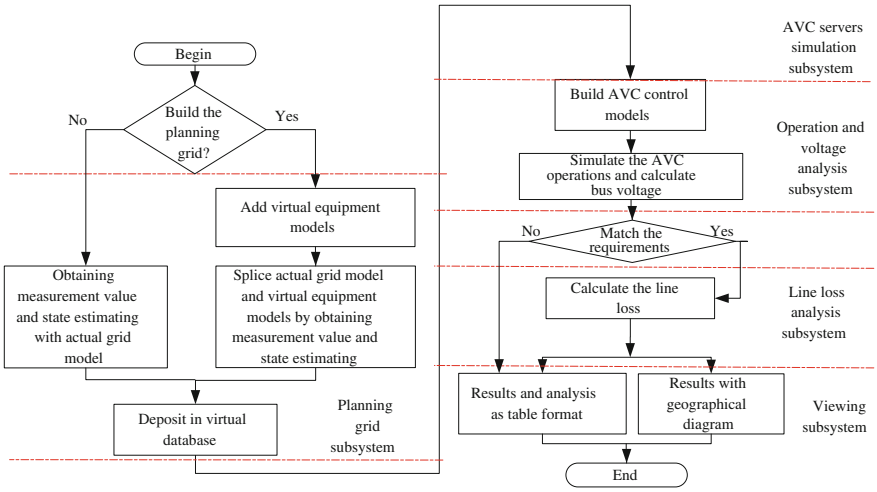

Fig. 1 Flowchart of OP system

2.1 Planning Grid Subsystem

The planning grid subsystem can establish and save different planning grid models. The planning grid models include actual grid model and virtual equipment models (transformer, line, bus, generator, capacitor, etc.). Based on two data sources (real-time data and historical data), the virtual equipment models can be added via user interface. The subsystem can splice actual grid model and virtual equipment models by obtaining measurement value of actual grid model and carrying state estimation with the planning grid model. If establishing the virtual equipment models is not needed, the subsystem only obtains measurement value and carries state estimating with actual grid model. The models deposit in virtual database.

2.2 AVC Servers Simulation Subsystem

It is used to build AVC control models and save different AVC coordinating parameters such as capacitors coordinating velocity and minimum capacitors amount by one operation. They can affect the reactive power controlling and voltage coordinating. Every AVC control model can deposit a number of parameter schemes.

2.3 Operation and Voltage Analysis Subsystem

It is used to simulate the AVC operations. First users should define whether the operations are taking place in one day or in any time segment. And via the subsystem users can use real-time EMS data or historical EMS data for simulation. The operations include switching of capacitors or adjusting on-load regulating transformer taps. Then the accurate results of power flow and voltage variations are calculated. These data are stored in virtual database for the line loss analysis subsystem. If the AVC servers parameters cannot match the coordinating requirements, the next step will go to viewing subsystem and propose the incompetent parameters in the form of table. Otherwise, go to line loss analysis subsystem. The analysis of voltage fluctuation and the optimal control action sequence will use subsystems B and C.

2.4 Line Loss Analysis Subsystem

It can calculate line loss of the actual grid or the planning grid. First users should establish line loss models and parameters. It can define or modify range of line loss statistics areas via user interface. The line loss models and parameters of added virtual equipments are stored in database and initialized automatically if updated. According to the aforesaid power flow stored in virtual database, the integral calculation for line loss can be carried out. The results can be shown with Hebei grid geographical diagram. This subsystem is usually used for planning new transformer substation with the Planning grid subsystem.

2.5 Viewing Subsystem

It is used to provide analysis tables and comparison curves for users. It also shows bus voltage or line loss with the geographical diagram of low voltage grid.

3 Hardware Configuration and Data Exchange

The hardware configuration of OP system is shown in Fig. 2. The EMS server, EMS workstation, and EMS database are built in power dispatch or control center of county in Hebei province. A data receiving server in Hebei Electric Power Research Institute is configured to receive models, graphics, and data of Hebei low voltage grid. Two network cards are used in data receiving server. One network

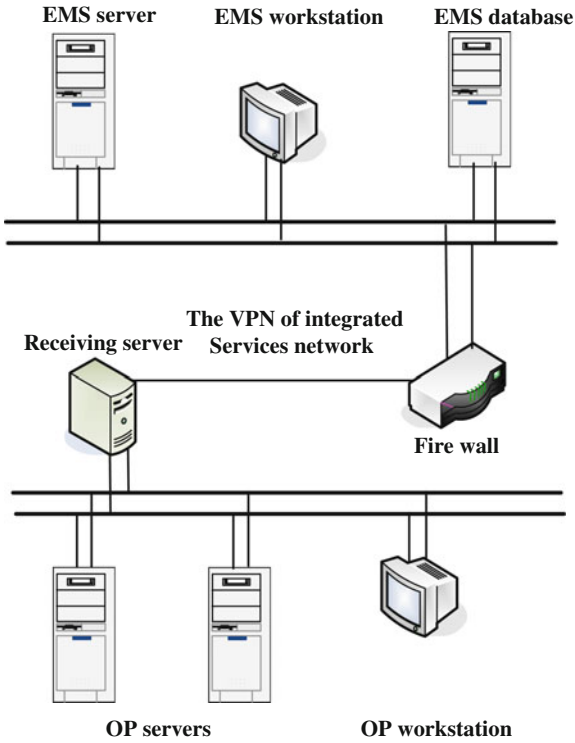

Fig. 2 Hardware configuration

card connects with the EMS server to get power system data. The other one connects with OP system.

Two OP servers are configured for storing five subsystems and the virtual database, they are used for calculation and analysis functions. And the system has data backup and recovery function. The files of it can be automatically forwarded to other storage facilities for data mirroring, disaster recovery, or backup applications. A workstation is used for monitoring and operating. With the workstation, users can login OP servers, modify parameters and view the results.

Figure 3 shows data exchange between five subsystems and EMS server. After state estimation, the EMS server sends correction value to OP system. As it is shown, the virtual database is very important in the system. It not only receives EMS real-time data or historical data, and stores voltage analysis and line loss results.

Broken line means the data is sent from OP system to AVC system. With control orders via AVC system, the purpose is sending the optimization coordinating parameters and optimal control action sequence to AVC severs in substations. Moreover, it could modify AVC coordinating parameters on-line when large load variation happened or structure of low voltage grid changed. This is one of the functional characteristics of smart AVC [10–14], and it is still in research.

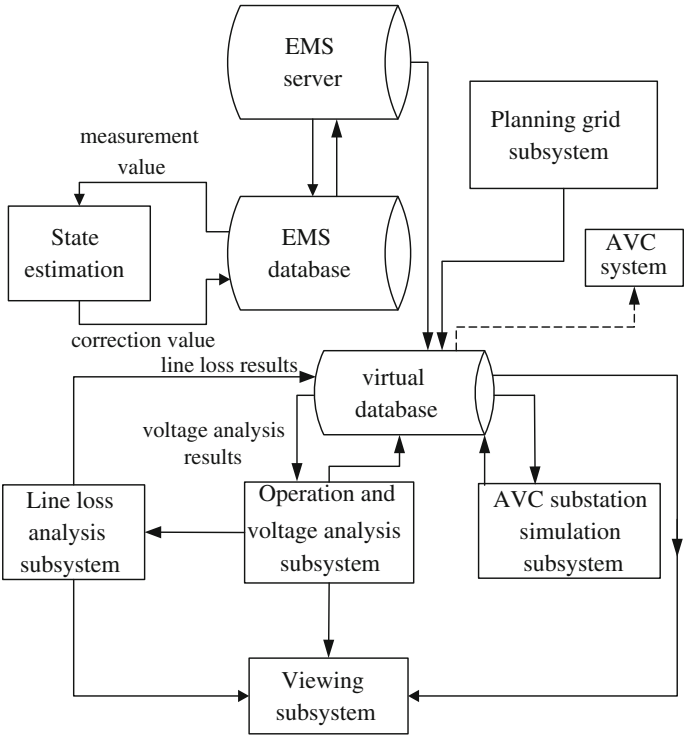

Fig. 3 Data exchange of OP system

4 The Introduction of Analysis Tools and Applications

4.1 Sensitivity and Priority Calculator

It can calculate the voltage-capacitor sensitivity. The reactive variation of switching one unit of capacitor in one substation is first defined. Then the system calculates reactive output and voltage variation of different key points. Using the same reactive output variation, the tool simulates every substation with different load situations. The load situations include spring load, summer load, and winter load, for their distinct load characteristics in Hebei low voltage grid. When all voltage-capacitor sensitivities are given, users can define capacitor coordinating priority for some key point in different load situations. Capacitors with bigger voltage-capacitor sensitivity have higher coordinating priority. The process of providing voltage-tap sensitivity and on-load regulating transformer coordinating priority is similar.

4.2 Comparison Curve

The main function of the tool is to show comparison curves for different types of data. A series of comparison curves have built in system such as active power, reactive power, voltage, line loss, and so on. Users can display these comparison curves easily. Through the comparison, it is illustrated which planning new capacitors of substation or new on-load regulating transformers have better effects on controlling voltage or reducing line loss. The system also provides a user-defined interface for comparison curve. Users can define various comparison curve schemes according to their requirements.

4.3 Table Report

The main function of table report is to provide customization reports for users. The stored data in system can be proposed in the tables such as sensitivities data, priorities data, capacitors data, on-load regulating transformers data, integral time section of line loss, line loss, and so on. Via the report, better layout planning for reactive equipment are revealed. The arithmetic of data in tables can be investigated by users. The format of tables can be defined flexibly. The customization report can be generated and published automatically.

5 Application on Impact of AVC Control Action Sequence

Different control action sequences lead to obviously different effect on voltage fluctuation, which can be defined as follows:

$$V_f^* = \sum_{n=1}^{l} \sqrt{\sum_{i \in \pi} (V_i^{n^{*2}} - V_i^{n-1^{*2}})} \tag{1}$$

where $V_i^{n^*}$ is normalized value of bus i voltage after control action sequence n. $V_i^{0^*}$ is normalized value of the original voltage of bus i before control actions. And π is ensemble of key points in the voltage control area. l is the final control action. Because $l \in \mathrm{N}$, certainly exist permutation l_α, which makes $\alpha = \min(V_f^*)$. For existing different voltage levels in the voltage control area, the normalized value is used. Users can get l_α via subsystems B and C as describe above.

Table 1 shows schemes of control action strategy at one time in Hebei low voltage grid. Bus A, B, C, and D constitute voltage control area 7. Table 2 shows

Table 1 Control strategy of voltage control area 7

Bus name	Voltage level (kV)	Coordinating priority	Strategy (kV)
A	35	1	34.17 → 34.05
B	35	1	34.98 → 34.91
C	10	2	10.98 → 10.71
D	10	3	10.88 → 10.83

Table 2 Control action sequence and results

Sequence	V_f^*	Sequence	V_f^*	Sequence	V_f^*
ABCD	0.037	BDCA	0.034	CDBA	0.036
ABDC	0.035	BDAC	0.036	CDAB	0.037
ACDB	0.038	BADC	0.037	DABC	0.035
ACBD	0.038	BACD	0.035	DACB	0.037
ADBC	0.037	CBAD	0.035	DBAC	0.036
ADCB	0.036	CBDA	0.033	DBCA	0.035
BCDA	0.033	CADB	0.037	DCBA	0.034
BCAD	0.034	CABD	0.037	DCAB	0.035

different control action sequence and results of V_f^*. And it reveals both C → B → D → A and B → C → D → A lead to the least voltage fluctuation. Because capacitors of bus B have higher coordinating priority, best control action sequence is B → C → D → A, and α is 0.033.

6 Conclusions

In this paper Optimization Parameter system is developed. The structure, hardware configuration, and data exchange of it are introduced. With the OP system, the traditional reactive compensate equipments can be united and developed to smart AVC system for rural grid. And via the OP system, the voltage fluctuation with different control actions sequence can be researched. The system can propose coordinating priority of capacitors or on-load regulating transformers. It can evaluate reducing line loss benefited from the AVC coordinating parameters or the AVC operations. And it can provide the optimal AVC coordinating parameters and the optimal control action sequence, which lead to better voltage controlling and better power quality for users.

References

1. Dmitriev MV, Evdokunin GA, Gamilko A (2005) EMTP simulation of the secondary arc extinction at overhead transmission lines under single phase automatic reclosing. In: IEEE Conference on Power Technology. Russia, pp 1–6. IEEE
2. Malewski R, Douville J, Lavallee L (1988) Measurement of switching transients in 735 kV substations and assessment of their severity for transformer insulating. IEEE Trans Power Deliv 3(4):1380–1386
3. Qiu JY, Ren JJ, Hu DC (2007) Lightning overvoltage analysis of 110 kV transformer neutral point (in Chinese). High Volt Eng 33(1):99–101
4. Guo QL, Wang B, Ning WY et al (2008) Applications of automatic voltage control system in North China power grid (in Chinese). Autom Electr Power Syst 32(5):95–98
5. Guo QL, Sun HB, Zhang BM et al (2005) Study on coordinated secondary voltage contro1 (in Chinese). Autom Electr Power Syst 29(23):19–24
6. Ruiz PA, Sauer PW (2007) Voltage and reactive power estimate for contingency analysis using sensitivities. IEEE Trans Power Syst 22(2):639–647
7. Chowdhury FD, Crow BH, Acar ML et al (2005) Improving voltage stability by reactive power reserve management. IEEE Trans Power Syst 20(1):338–345
8. Wu D, Li DC, Dong R et al (2005) Actualization and effect of An-hui automatic voltage control system (in Chinese). Power Syst Equip 6(5):63–67
9. Yang X, Fan H, Tang BF, Wang XW (2011) Development of auxiliary optimization parameter system for smart AVC in Hebei grid. In: 2011 international conference on advanced power system automation and protection, pp 242–245. IEEE, China
10. Yu YX (2009) Technical composition of smart grid and its implementation sequence (in Chinese). South Power Syst Technol 3(2):1–5
11. Zhang ZZ, Li XY, Cheng SJ (2010) Structures, functions and implementation of united information system for smart grid (in Chinese). Proc CSEE 30(34):1–7
12. Hu XH (2009) Smart Grid- A Development Trend of Future Power Grid (in Chinese). Power Syst Technol 33(14):1–5
13. Cui SY, Sun SF, Li LX et al (2009) Survey on Smart Grid Technology (in Chinese). Power Syst Technol 33(8):1–8
14. Yu YX, Liang WP (2009) Smart grid (in Chinese). Power Syst Clean Energy 25(1):7–11

A Study on Micro-Grid Power Quality Management and Simulation Based on RTW Toolkit

Zhiqiang Gao, Zhongji Sun, Liang Meng, Xiao Yang, Lingming Meng and Peng Luo

Abstract For improving micro-grid power quality, this paper elaborates a method of using energy storage system to stabilize power and active power filter (APF) to govern harmonic. The control principle of energy storage system and APF is introduced, and the simulation model of the micro-grid is established, which can generate C code automatically through MATLAB real-time code generation tool RTW (Real-Time Workshop). The code is applied to the running real micro-grid system. By comparing APF simulation results and actual running results, the effectiveness and practicability of the simulation based on RTW were verified. At the same time, it shows that the application of APF has a positive role in micro-grid power quality improvement.

Keywords Micro-grid · Power quality · Battery · Active power filter (APF) · Real-time workshop (RTW)

1 Introduction

Micro-grid is increasingly attended in society as an effective means to achieve the diversification of new energy utilization. For a mature micro-grid, the good power quality is one of its essential characteristics [1]. However, due to the volatility of distributed power factor and a large number of power electronics devices, micro-grid power quality issues cannot be ignored [2]. For power fluctuations and harmonic pollution, the energy storage system and APF are, respectively, used to stabilize

Z. Gao · Z. Sun · L. Meng (✉) · X. Yang · P. Luo
State Grid Hebei Electric Power Research Institute, 238 Tiyu South Street, Shijiazhuang 050022, China
e-mail: 15133128069@139.com

L. Meng
Electrical and Electronic Engineering Institute, North China Electric Power University, 619 Yonghua North Street, Beijing 071003, China
e-mail: 15233128878@139.com

Q. Liang et al. (eds.), *Proceedings of the 2015 International Conference on Communications, Signal Processing, and Systems*, Lecture Notes in Electrical Engineering 386, DOI 10.1007/978-3-662-49831-6_94

power fluctuations and to compensate harmonic. Simulation in MATLAB can verify compensation effect and provide help for the improvement of control strategy.

In order to carry out the further research, establishing accurate simulation system is an urgent demand of the study technology. In order to build a more accurate model, we use the RTW digital simulation tool as the actual system control system uses a digital control system. The RTW tool generates real-time C code based on the micro-grid simulation model which can be applied to the actual system control. This method not only avoids the tedious process of hand-written programs, but also ensures the accuracy and efficiency of the program code, and achieves the organic combination of simulation and real control system [3–5].

2 Structure of the Micro-Grid

The micro-grid studied in this paper, shown in Fig. 1, consists of photovoltaic cells, an energy storage system, an active power filter (APF), inverters, loads, and other means. Among them, the energy storage system is a hybrid energy storage system which is composed of a battery and super capacitor. As an energy storage device with high energy density, the battery can achieve a large-capacity storage, but is not suitable for frequent charging and discharging. On the other hand, the super capacitor, as power-type energy storage device, has a high power density, long cycle life, charging time is short, high reliability, and low energy density characteristics. According to these characteristics, the energy storage system combined by the two devices has complementary advantages, which can stabilize power in micro-grid comprising intermittent power supply. The APF can compensate harmonics and reactive power in micro-grid. Both of the energy storage system and the APF is used to ensure higher power quality in micro-grid. The breaker K is used to make the micro-grid run in grid operation or island operation.

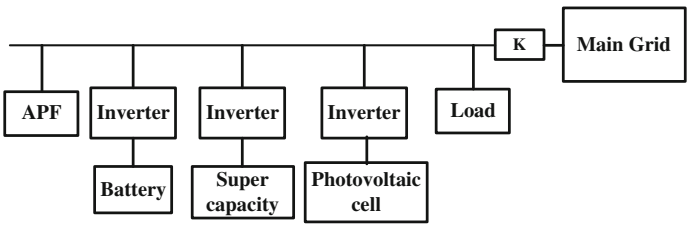

Fig. 1 The micro-grid system

3 Control Principle of the Energy Storage System

Micro-grid has flexible modes of operation, it can work in grid operation and in island operation. In different modes of operation, the control principle of the energy storage system is different.

3.1 Control Theory of Grid Operation

The voltage and frequency is guaranteed by the grid when it operates in the grid-connected mode. Both of the batteries and the super capacitors are controlled with PI double loop control strategy which is composed by outer loop power control and inner current control, as shown in Fig. 2.

As shown in Fig. 2, the AC bus voltage (u) and current (i) of the outlet of the inverter are collected. Via the Park transformation (as formula 1), they are divided into the direct-axis component and the quadrature-axis component respectively. Then active component (P) is obtained by multiplying the voltage direct-axis component and the current direct-axis component. In the same way, we can get reactive component (Q) by the calculation of the quadrature-axis component of voltage and current. By calculating the difference between the measured value and the set value, $i_{\_ref}$ which is the setpoint of inner current control is got after the adjustment of PI link and Park inverse transformation. In the inner current control, i calculated by $i_{\_ref}$ minus i is put into PWM generator to control the inverter bridge after filtering, clipping, and other links.

$$P = \frac{2}{3}\begin{bmatrix} \cos\theta & \cos(\theta - 120°) & \cos(\theta + 120°) \\ -\sin\theta & -\sin(\theta - 120°) & -\sin(\theta + 120°) \\ \frac{1}{2} & \frac{1}{2} & \frac{1}{2} \end{bmatrix} \tag{1}$$

3.2 Control Theory of Island Operation

The voltage and frequency of the micro-grid need to be supplied by the energy storage device, so the control method is different from the grid operation mode. In

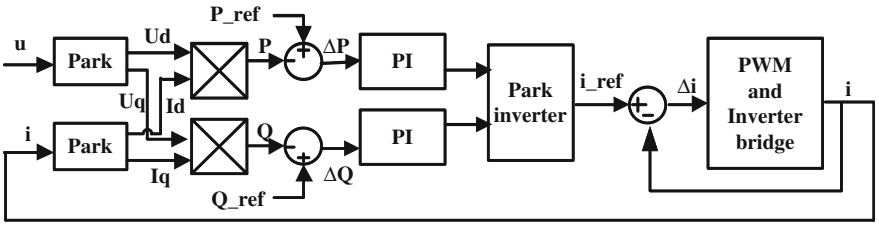

Fig. 2 Principle of power−current control

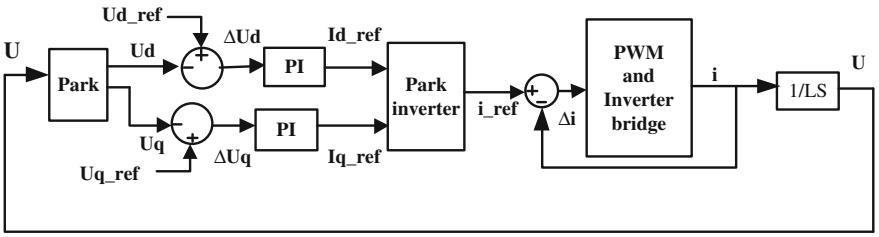

Fig. 3 Principle of voltage−current control

this paper, the voltage and frequency support are provided by the battery which is controlled by outer loop voltage control and inner current control. Then the super capacitors are still controlled by outer loop power control and inner current control.

The U-I double loop control strategy of the battery is shown in Fig. 3. The AC output voltage of the inverter is decomposed into U_d and U_q after the Park transform. Compare U_d and U_{d_ref} which is the set value and input the difference into the PI link, then the output is i_{d_ref}. In the same way, i_{q_ref} can be calculated. Through the calculation of the Park inverse transformation, i_{d_ref} and i_{q_ref} are transformed into $i_{\_ref}$ which is the setpoint of inner current control. Then achieve the control of the battery after the current loop control.

4 Control Principle of the APF

The control strategy of APF is designed to compensate the harmonic according to different harmonic orders. For example, to compensate the fifth harmonic, the APF is controlled to output the reverse fifth current waves until the fifth harmonic is disappear. For any other orders of harmonic, add the input to the control loop can do it. The control diagram is shown in Fig. 4.

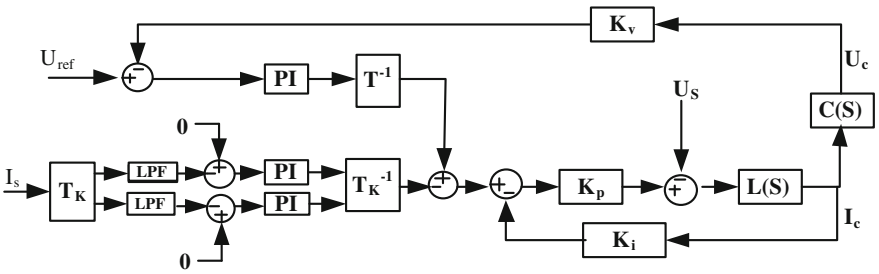

Fig. 4 Principle of APF control

I_s is the high-order harmonic current, it can be decomposed into direct-axis component I_{s_d} and quadrature-axis component I_{s_q} through conversion matrix T_K and low pass filter (LPF). Let set value (0) minus I_{s_d} and I_{s_q}, respectively, and input the answers to the PI link, then the harmonic current signal is got after inverse conversion matrix T_K^{-1}. After proportion and integral control link, this signal controls APF to output compensation current. The function of the voltage control loop is to stabilize the fundamental voltage.

$$T_K = \frac{2}{3} \cdot \begin{bmatrix} \cos(k\omega \cdot t) & \cos\left(k\omega \cdot t - \frac{2}{3}k\pi\right) & \cos\left(k\omega \cdot t + \frac{2}{3}k\pi\right) \\ -\sin(k\omega \cdot t) & -\sin\left(k\omega \cdot t - \frac{2}{3}k\pi\right) & -\sin\left(k\omega \cdot t + \frac{2}{3}k\pi\right) \\ \frac{1}{2} & \frac{1}{2} & \frac{1}{2} \end{bmatrix} \tag{2}$$

$$T_K^{-1} = \begin{bmatrix} \cos(k\omega \cdot t) & -\sin(k\omega \cdot t) & 1 \\ \cos\left(k\omega \cdot t - \frac{2}{3}k\pi\right) & -\sin\left(k\omega \cdot t - \frac{2}{3}k\pi\right) & 1 \\ \cos\left(k\omega \cdot t + \frac{2}{3}k\pi\right) & -\sin\left(k\omega \cdot t + \frac{2}{3}k\pi\right) & 1 \end{bmatrix} \tag{3}$$

5 Establishment and Analysis of Simulation

According to the control theory, a micro-grid working in island mode of operation, as an example, was established in MATLAB/Simulink environment which is shown in Fig. 4. In this model, the Pv module consists of photovoltaic cells and inverter, the battery module is a combination module which contains battery and inverter, the EDLC module is a combination of super capacitors and inverter, the APF module is active power filter and the load module is loads of the micro-grid. Design simulation parameters are as follows: micro-grid bus voltage of 100 V, battery and super capacitor DC voltage are both 700 V, super capacitor rated power 50 W, PV power 20 W, and parameters of loads depend on the specific set of simulations.

In addition, the simulation model can be compiled by using RTW into executable C language code which can be accessed directly downloaded to the target

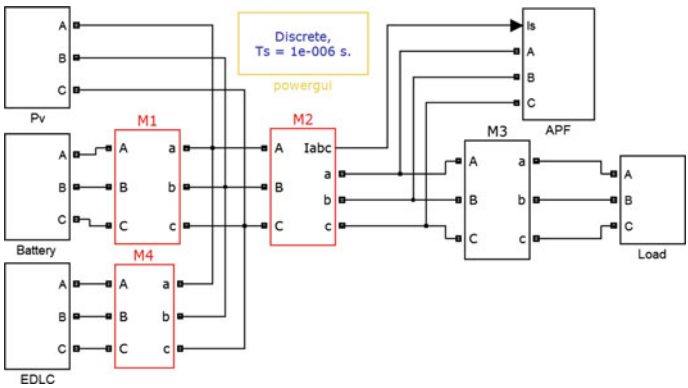

Fig. 5 Simulation model of micro-grid system

machine and run in the actual system. It is of great meaning which will integrate the control system simulation and practical system to achieve real-time semi-physical simulation [4–7] (Fig. 5).

5.1 Simulation of Load Mutation

The value of phase resistance of the load which is connected in triangle connection mode is 40 Ω. Run this simulation and test voltage dynamic characteristics of the main inverter in AC side. In order to observe the dynamic process, this article will invert direct-axis voltage through the DA per unit of output (at 100 V line voltage direct-axis voltage DA output by 1 V). The load capacity is mutated In 0.304 s, Figs. 6 and 7 show the simulation result.

In summary, when the load increasing suddenly, the main inverter output voltage has dropped, but the energy storage system control strategy can achieve power

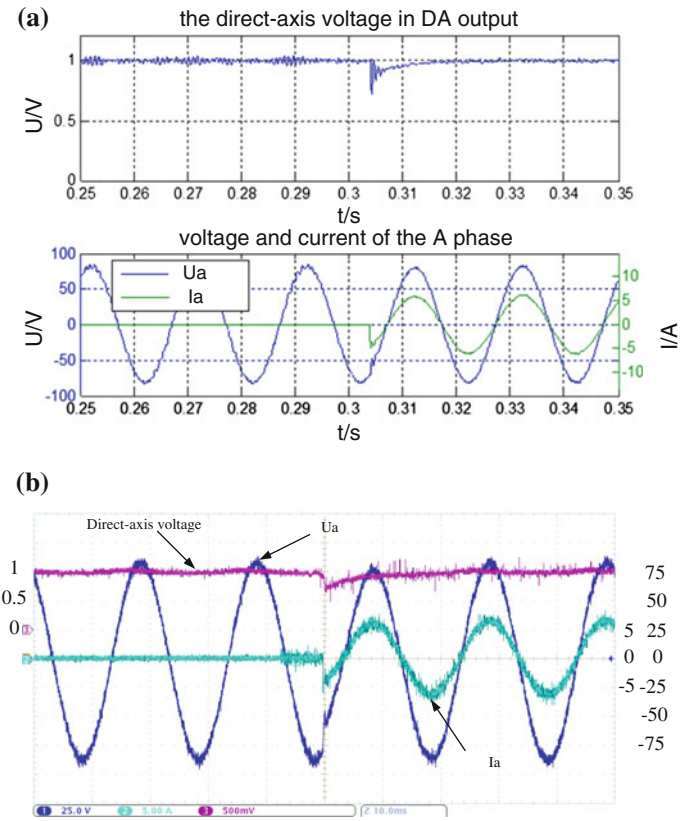

Fig. 6 Simulation datas of increasing load **a** Simulation curves of increasing load (b) Collected curves of increasing load in system

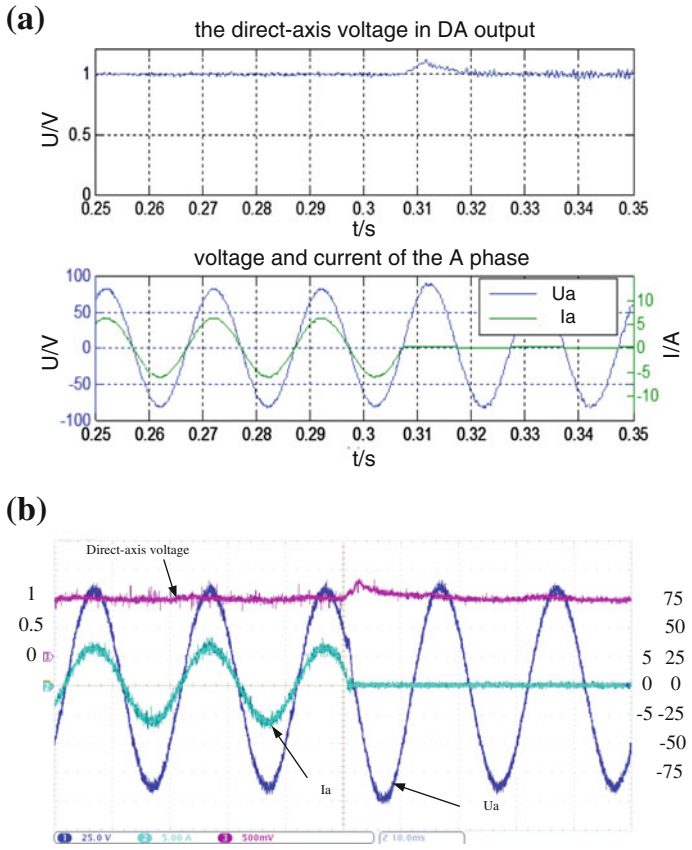

Fig. 7 Simulation datas of reduce load **a** Simulation curves of reduce load **b** Collected curves of reduce load in system

tracking adjustment, the voltage returns to normal in about 0.01 s; when load reduction, the direct-axis voltage sudden rise can be dropped to normalcy in 0.01 s in a very short time. In addition, the simulation is highly consistent with the experimental results, proving the accuracy and practicality of RTW toolkit directly.

5.2 Simulation of Harmonic Compensation

The loads consist of the rectifier and DC load, a DC load RL series impedance, where R is 40 Ω and L is 0.66 mH. To compensate the five-order harmonic and the seven-order harmonic current, for example, simulate the APF harmonic current compensation effect in micro-grid. According to the control principle of the APF, the simulation model shown in Fig. 8, where "5 modules" and "7 modules" are the five-order harmonic and the seven-order harmonic current calculation module.

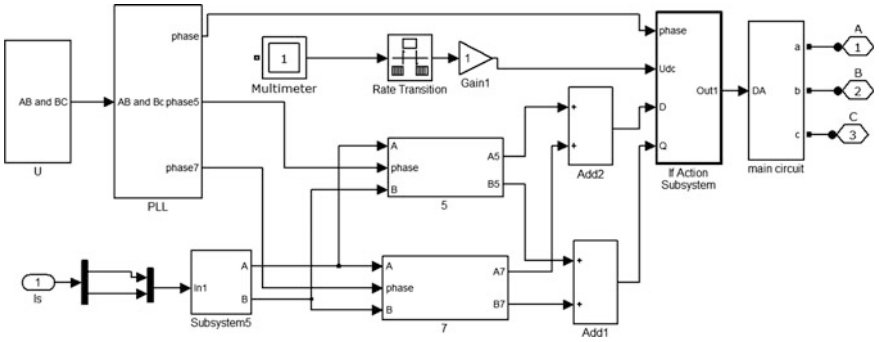

Fig. 8 Simulation model of APF

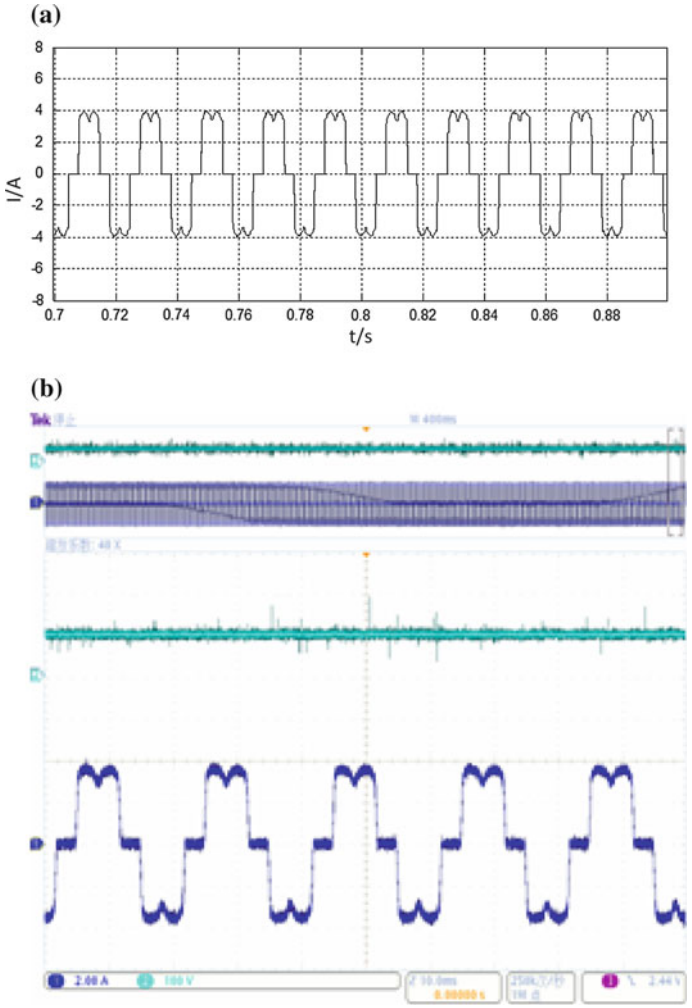

Fig. 9 Simulation without APF compensation **a** Simulation curves without APF compensation **b** Collected curves without APF in system

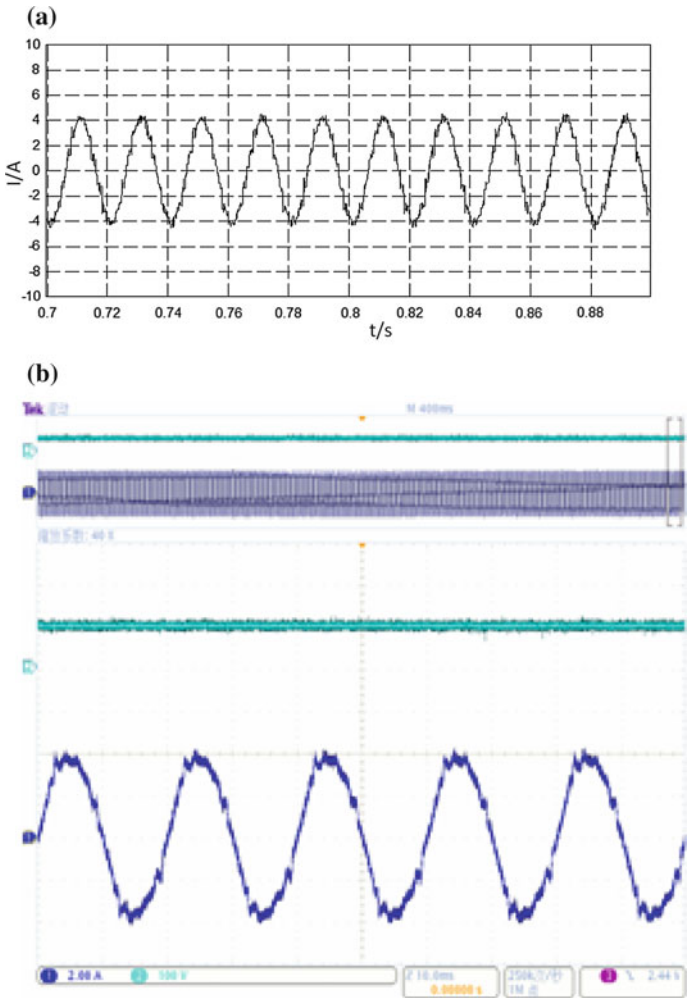

Fig. 10 Simulation with APF compensation **a** Simulation curves with APF compensation **b** Collected curves with APF in system

Table 1 FFT analysis of actual test in micro-grid

	Five-order harmonic (%)	Seven-order harmonic (%)
Without APF	21.56	18.02
With APF	0.23	0.03

Figures 9 and 10 show the simulation current waveform. Visibly, the non-sinusoidal grid current becomes a sine wave after the APF compensation. FFT analysis data of the current waveform is shown in Table 1, the five-order harmonic and the seven-order harmonic wave components are close to zero. In a word, the

simulation shows the accuracy of the APF control strategy. Comparing the simulation waveforms and waveforms measured in practical micro-grid, the results are almost identical, proving once again the accuracy and usefulness of RTW toolbox.

6 Conclusion

As an essential part of the promotion micro-grid, the energy storage system plays a crucial role in promoting power quality. The multiple energy storage device used in this paper which consists of batteries and super capacitors can enhance the micro-grid dynamic performance, keep the system power being balance in the load mutation and maintain the normal operation of bus voltage stability. The analysis and simulation verify that the control strategy is effective and practical. Then harmonic pollution is a major threat to the micro-grid power quality, the active power filter (APF) described in this paper can compensate harmonic current effectively and stably which improves the micro-grid power quality. At last, the Real-Time Workshop (RTW) simulation can be achieved in practice micro-grid, which is easy to use, and avoids the manual code written and improves efficiency. It provides feasible and effective research methods for the future micro-grid simulation study.

References

1. Lasseter RH, Piagi P (2004) Micro-grid: a conceptual solution [C]. In: Power Electronics Specialists Conference. IEEE, vol 6, pp 4285−4290
2. Wang C, Peng L (2010) Distributed generation, micro-grid and smart distribution grid development and challenges. Electric Power Syst 34(2):10–14
3. Chen Y (2002) Realization from Matlab/Simulink model to code. Tsinghua University Press, Beijing
4. Shaoqiang Y, Zhang P (2009) Design platform of computer control system based on RTW.J Electric Electron Educ 31 (Suppl.):65–68
5. Zhang Y, Zhao Z, Ting L (2009) Control system for three-level dual-PWM converter based on RTW. Electric Power Autom Equip 29(10):128–131
6. Song J (2012) Analysis using symmetrical components and software labview lack of three-phase asynchronous motors running. Sci Technol Innov Herald (21)
7. Sun Z (2009) Technical overview soft start motor. Jilin Institute of Chemical Technology (3):70–75

Design and Analysis of Coil with Ferrite Core for Wireless Power Transfer Systems

Xiu Zhang and Xin Zhang

Abstract The key of wireless power transfer technology rests on finding the most suitable means to improve the power transfer efficiency when the transfer distance is extended. In this paper, a new shape of transmitter coil, which is developed as part of a deep brain stimulator for stroke patients, is proposed. Because the receiver coil to be implanted in the patients' skull is very small, a ferrite core is inserted into the coils to improve the performance of the wireless power transfer system. In this paper, the finite element method (FEM) is used to analyze the system. The relative positional relationship between the transmitter coil and receiver coil is optimized. The length of ferrite core inserted into the transmitter coil is also analyzed. The optimal shape of the transmitter coil is also derived and reported.

1 Introduction

Since the new century, the technology of wireless power transfer has received increasing attentions from all over the world because of its intrinsic safety and convenience characteristics. Compared with the far-field wireless power transfer system, the near-field wireless system has high power transfer efficiency but short power transfer distance and hence such systems are mainly exploited in electric toothbrushes. When the power transfer distance is up to centimeters, the power transfer efficiency of near-field systems is only about 1 % [1–3].

To extend the power transfer distance, the magnetic resonant coupling method (also called mid-distance field mode) has become the most popular method. In 2007, the MIT research team published their findings in *Science*, and since then, this method has become the hottest methodology to realize wireless power transfer

X. Zhang · X. Zhang (✉)
College of Electronic and Communication Engineering, Tianjin Normal University, Tianjin, China
e-mail: ecemark@mail.tjnu.edu.cn

X. Zhang
e-mail: zhang210@126.com

Q. Liang et al. (eds.), *Proceedings of the 2015 International Conference on Communications, Signal Processing, and Systems*, Lecture Notes in Electrical Engineering 386, DOI 10.1007/978-3-662-49831-6_95

system. In this method, the receiver coil and the transmitter coil must have the same resonant frequency which is also the same as that of the power source. The transmission distance of wireless power transfer system with this method can be significantly extended with no undue reduction on power transfer efficiency [4].

With the advent of power electronics, various implanted medical devices, such as deep brain stimulator, nerve stimulator, and cardiac pacemaker, are widely used in the medical field [5, 6]. These devices can effectively prolong the patients' lives. In order to alleviate the patients' financial burden and their suffering, the technology of wireless power transfer has become popular in biomedical engineering.

As an electromagnetic problem, the wireless power transfer system can be analyzed using Maxwell's electromagnetic field equations. Indeed, numerical methods for solving the Maxwell's equations have been applied successfully to study a wealth of problems in science and engineering [7, 8]. In this paper, the numerical method of electromagnetic field computation, such as finite element method (FEM) is applied to appreciate and analyze, quantitatively, the performance of wireless power transfer systems [9, 10].

In this paper, the ferrite material is employed as the core to be applied into the wireless power transfer system to extend the power transfer distance. According to the application of the system, a new shape of the transmitter coil is proposed to improve the performance of the system.

2 Structure of Wireless Power Transfer Systems

Unlike other studies analyzing common structures, the wireless power transfer system with ferrite core is analyzed in this paper. As shown in Fig. 1, the transmitter coil and receiver coil in the common structure have the same axis. In the new structure, the axes of the transmitter coil and the receiver coil are parallel to each other and a ferrite rod is inserted into the coils to reduce the magnetic reluctance. Thus, the receiver coil can pick up more magnetic flux linkage which induces voltage in the receiver coil. Indeed, the current in the coil with ferrite core can generate about 50 times stronger magnetic field intensity than the coil without core [11]. The longer core length is, the larger is magnetic flux density in the secondary core.

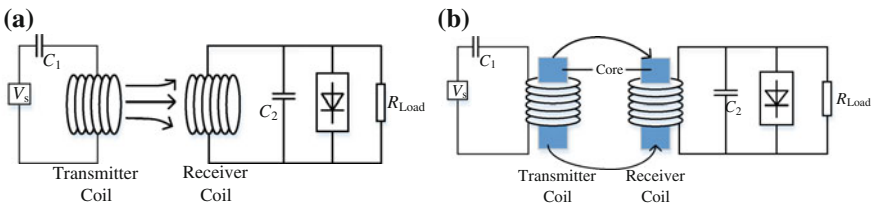

Fig. 1 **a** Wireless power transfer system without a core. **b** Wireless power transfer system with a core

In this paper, the wireless power transfer system is applied to the deep brain stimulator which is implanted inside the skull of patients. Transmitter coil with a novel shape as shown in Fig. 2 is proposed. In this system, the transmitter coil with a ferrite core has an arc along with the shape of the human head.

For deep brain stimulator, the receiver coil should be as small as possible. In order to obtain the maximum power transfer efficiency, the ferrite core inserted into the transmitter coil needs to be optimized. As shown in Fig. 2, the angle θ represents the length of the ferrite core, while the angle α represents the relative position of the transmitter coil and the receiver coil. In addition, the angle φ represents the chord of the transmitter coil. The specifications of the system are listed in Table 1.

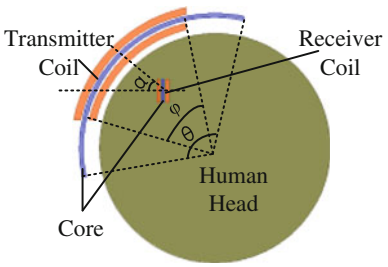

Fig. 2 Novel shape of the wireless power transfer system with core applied to a deep brain stimulator

Table 1 Specifications of the wireless power transfer system

Parameters		Values
Angles	α	−40 ~ 40°
	θ	70 ~ 180°
	φ	70°
Diameter of wire		1 mm
Diameter of coil		4 mm
Length of receiver coil		5 mm
Number of stranded of the wire		70
Turn number of transmitter coil		10
Turn number of receiver coil		5
Resonant frequency		3 MHz
Complementary capacitance in transmitter coil		2.33 nF
Complementary capacitance in receiver coil		4.23 nF
Saturation magnetic flux density of NiZn Ferrite core		0.3 ~ 0.5 T

In this paper, the resonant frequency of the coils is 3 MHz. The nickel–zinc (NiZn) ferrite core is chosen as the core material which is inserted into the coils. NiZn ferrite has higher resistivity which is more suitable for applications with operating frequencies above 1 MHz.

3 Methods and Analysis

3.1 Finite Element Method

In order to reduce the AC resistances of the coils, the transmitter coil and the receiver coil are fabricated using litz wires. According to the Maxwell Equations, the two-dimensional (2-D) magnetic field equation in the regions of air, iron cores, and stranded windings can be expressed as

$$\nabla \cdot (\nu \nabla A) - \sigma \frac{\partial A}{\partial t} = -J_s \tag{1}$$

where A is the magnetic vector potential; ν and σ are the reluctivity and the conductivity of the material, respectively; J_s is the given current density.

The basic equations of the transient magnetic field-circuit coupled problem can be summarized as the following set of equations [7, 8]

Field equation:

$$\nabla \cdot (\nu \nabla A) - \sigma \frac{\partial A}{\partial t} + \frac{d_p N}{Sap} i_{ad} + \frac{d_p N}{Sap} i_w = -J_s \tag{2}$$

Additional equation:

$$-\frac{d_p N}{Sa} \iint_{\Omega} \frac{\partial A}{\partial t} d\Omega + \frac{R_{dc}}{l} i_{ad} = 0 \tag{3}$$

Electric circuit branch equation:

$$-\frac{d_p N}{Sa} \iint_{\Omega} \frac{\partial A}{\partial t} d\Omega - \frac{R_{dc}}{l} i_w = -\frac{1}{l} u_w \tag{4}$$

where d_p is the polarity (+1 or –1) to represent the forward paths or return paths of the windings, respectively; p is the symmetry multiplier which is defined as the ratio of the original full cross-sectional area to the solution area; N is the total conductor number of this winding; S is the total cross-sectional area of the region occupied by the winding in the solution domain; a is the number of parallel branches in the winding; R_{dc} is the d.c. resistance of the winding; i_w and u_w are the branch current and voltage of the winding, respectively. The additional current i_{ad} is introduced in

regions of solid conductors to ensure the last coefficient matrix of the field-circuit coupled equations is symmetrical.

The induced voltage V_2 in the receiver coil is

$$V_2 = \omega \bar{B}_2(x) A_2 N_2 \tag{5}$$

where ω is the angular frequency; A_2 is the cross-section area of the receiver coil; N_2 is the number of turns of the receiver coil; $\bar{B}_2(x)$ is the average magnetic flux density in the receiver coil determined by

$$\bar{B}_2(x) = \frac{1}{l_r} \int_{-l_r/2}^{l_r/2} B_2(x) dx \tag{6}$$

where l_r is the length of the receiver coil. The power transfer efficiency of the system can be calculated by

$$\eta = \frac{P_2}{P_1} = \frac{V_2^2 / R_2}{I_1^2 R_1} = \frac{\left(\omega \overline{B}_2(x) A_2 N_2\right)}{I_1^2 R_1 R_2} \tag{7}$$

where P_1, P_2 are the input power in the transmitter coil and the output power induced in the receiver coil, respectively; R_1 and R_2 represent the resistance of the transmitter coil and the receiver coil, respectively; I_1 is the input current in the transmitter coil.

Magnetic flux lines between the transmitter coil and the receiver coil are shown in Fig. 3. It can be seen that the receiver coil can pick up the major bulk of the magnetic fluxes generated by the transmitter coil.

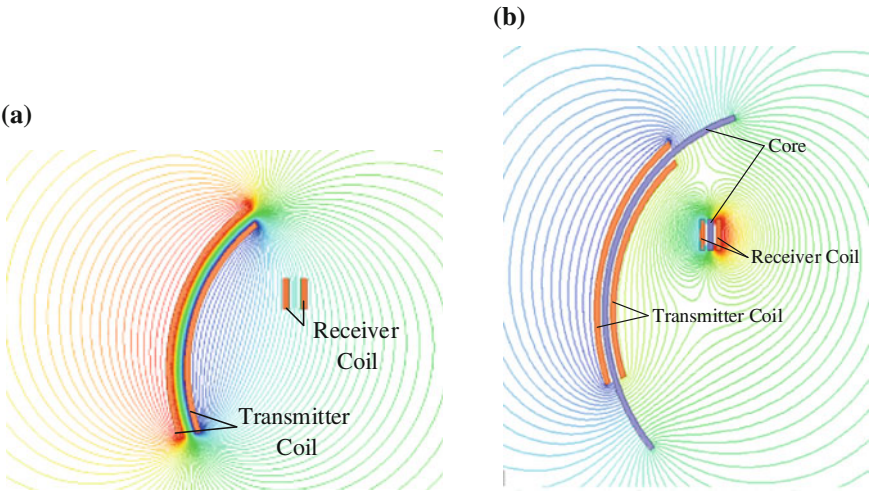

Fig. 3 Simulation result of the magnetic flux lines of the proposed coil configuration. **a** without core; **b** with core

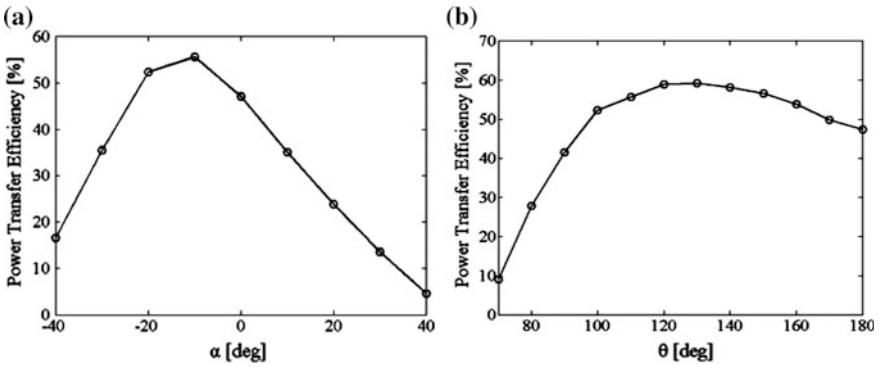

Fig. 4 **a** Power transfer efficiency varies with the angle α. **b** Power transfer efficiency varies with the angle θ

3.2 Analysis

The angle α represents the positional relationship between the transmitter coil and receiver coil. When the line connecting the centers of the transmitter coil and the receiver coil is parallel to x-axis, the value of angle α is equal to zero. The curve of power transfer efficiency varying with different α values is shown in Fig. 4a. It can be seen that the power transfer efficiency is maximum when the angle α is equal to −10°.

The angle θ represents the length of the core inserted into the transmitter coil. The initial value of the angle θ is equal to 70° when the lengths of the core and the transmitter coil are the same. The curve of power transfer efficiency varying with the different angle θ is shown in Fig. 4b. It can be seen that the power transfer efficiency is maximum when the angle θ is equal to 120°.

4 Results

Practically, the core loss in the ferrite material will increase the temperature of the coil, meanwhile, the higher temperature will decrease the saturation flux density of the ferrite material. The NiZn ferrite material used in this paper has a saturation flux density of about 400 mT at room temperature. Considering the temperature caused by the core loss, the flux density in the core should not exceed 250 mT. For the deep brain stimulator, however, the security of the system to the patients is the most important problem that should be considered. According to the standard established by the Minister of Public Works and Government Services of Canada, the maximum magnetic field strength should not exceed 2.05 μT [12].

In order to the guarantee the security of the system, the distribution of the magnetic field strength in the human head is given in Fig. 5a. The curve of the magnetic field strength from left to right is shown in Fig. 5b. It can be seen that

the maximum magnetic field strength in the human head if under 2 μT which meets the above-mentioned standard. In this case, the input current in the transmitter coil is about 5 mA. It indicates that the induced voltage in the receiver coil is above 3 V when the input current in the transmitter coil is about 5 mA.

The magnetic flux density profile in the ferrite core when the input current is about 5 mA in the transmitter coil is about 100 μT which is much less than 250 mT.

According to the above analysis, the wireless power transfer system will operate with the best performance when the angle α is equal to $-10°$ and the angle θ is equal to 120°. The maximum power transfer efficiency of the system is about 60 % when the frequency of the excitation is 3 MHz as shown in Fig. 6. When the operating frequency deviates from the resonant frequency, the power transfer efficiency of the system will have a sharp decline.

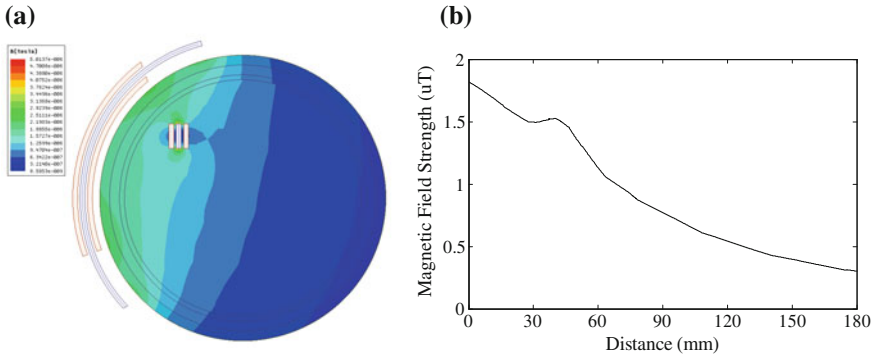

Fig. 5 **a** Distribution of the magnetic field strength in the human head. **b** Curve of the magnetic field strength from left to right of the human head

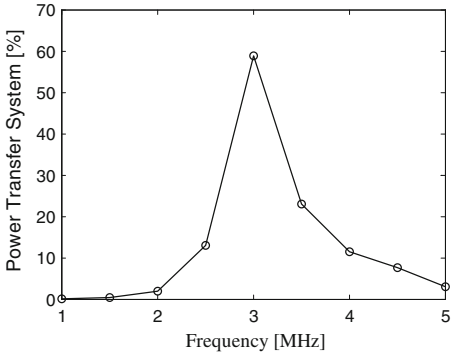

Fig. 6 Power transfer efficiency with different frequencies

5 Conclusion

In this paper, a transmitter coil with a novel shape is proposed for wireless power transfer system in implanted medical devices. A ferrite core which is suitable for high-frequency application is inserted into both the transmitter coil and the receiver coil. The simulation results indicate that the receiver coil with the core can pick up more magnetic fluxes when compared with receive coils without the core. In addition, the relative positional relationship of the transmitter coil and the receiver coil and the length of the ferrite core inserted into the transmitter coil are both quantitatively analyzed. The power transfer efficiency of the system can reach as high as 60 %. Such findings are instrumental for building a solid theoretical basis for future work in wireless power transfer systems.

Acknowledgments This research was supported by the Tianjin Thousand Youth Talents Plan Project of Tianjin Normal University (ZX110023). This research was also supported in part by the Applied Basic Research Program of Tianjin (15JCYBJC52300).

References

1. Hui SY (2013) Planar wireless charging technology for portable electronic products and Qi. Proc IEEE 101(6):1290–1301
2. Hui SYR, Zhong W, Lee CK (2014) A critical review of recent progress in mid-range wireless power transfer. IEEE Trans. Power Electron. 29(9):4500–4511
3. McSpadden JO, Mankins JC (2002) Space solar power programs and microwave wireless power transmission technology. IEEE Microwave Mag 3(4):46–57
4. Sample A, Yeager D, Powlede P, Mamishev A, Smith J (2008) Design of an RFID-based battery-free programmable sensing platform. IEEE Trans Instrum Meas 57(11):2608–2615
5. Kurs A, Karalis A, Moffatt R, Joannopoulos JD, Fisher P, Soljacic M (2007) Wireless power transfer via strongly coupled magnetic resonances. Science 317(5834):83–86
6. Liu X, Zhang F, Hackworth S, Sclabassi RJ, Sun M (2009) Wireless power transfer system design for implanted and worn devices. In: Proceedings of IEEE 35th Annual Northeast Conference Bioengineering, Boston, MA, USA
7. Fu WN, Zhou P, Lin D, Stanton S, Cendes ZJ (2004) Modeling of solid conductors in two-dimensional transient finite-element analysis and its application to electric machines. IEEE Trans Magn 40(2):426–434
8. Fu WN, Ho SL (2010) Extension of the concept of windings in magnetic field electric circuit coupled finite element method. IEEE Trans Magn 46(6):2119–2123
9. Zhang X, Ho SL, Fu WN (2011) Quantitative analysis of a wireless power transfer cell with planar spiral structures. IEEE Trans Magn 47(10):3200–3203
10. Zhang X, Zhao Y, Ho SL, Fu WN (2012) Analysis of wireless power transfer system based on 3-D finite element method including displacement current. IEEE Trans Magn 48(11): 3692–3695
11. Park C, Lee S, Cho G, Rim CT (2015) Innovative 5-m-off-distance inductive power transfer systems with optimally shaped dipole coils. IEEE Trans Power Electron 30(2):817–827
12. Code S (1999) Limits of human exposure to radiofrequency electromagnetic fields in the frequency range from 3 kHz to 300 GHz. Minister of Public Works and Government Services, Canada

Fiber Bragg Grating Arrays in All-Solid Photonic Bandgap Fiber

Tingting Han and Jingping Yang

Abstract The fiber Bragg grating arrays are inscribed into the Ge-doped cladding rods in an all-solid photonic bandgap fiber. Different resonance wavelengths and widths are observed by launching light into different rods from two reverse directions. The diverse resonance dips from different rods may have different responses to the environment changes, hence the fiber Bragg grating arrays will have good capacity to be employed as the multi-parameter sensor.

Keywords Photonic crystal fiber · Fiber Bragg gratings · Multi-parameter sensor

1 Introduction

The photonic bandgap fiber (PBGF) as a specific photonic crystal fiber (PCF) [1, 2] guides light in the low index core through photonic bandgap effect. In recent years, many researchers pay more attention to the all-solid PBGFs [3], which are composed of a two-dimensional periodic array of high-index rods embedded in a low-index background and a low-index core formed by omitting one or more rods. The all-solid PBGFs have more advantages of easy fabrication, convenience to splice to the conventional single mode fiber (SMF) and no surface mode excited, compared with the hollow-core PBGFs. Moreover, the fiber core and the fiber cladding rods can be doped for fiber Bragg grating (FBG) inscription by UV illumination. Jin et al. [4, 5] realized a fiber Bragg grating photoinscribed into the Ge-doped cladding rods in an all-solid PBGF and observed the resonances between the guided core mode and the guided LP_{01} supermode. Bigot et al. [6] realized the fiber Bragg grating with reflectivity up to 25 dB, photo-written in the Ge-doped core of a 2D all-solid PBGF. Cook et al. [7] demonstrated the successful inscription

T. Han (✉) · J. Yang
College of Electronic and Communication Engineering,
Tianjin Normal University, Tianjin 300387, China
e-mail: hanting608@163.com

Q. Liang et al. (eds.), *Proceedings of the 2015 International Conference on Communications, Signal Processing, and Systems*, Lecture Notes in Electrical Engineering 386, DOI 10.1007/978-3-662-49831-6_96

of Bragg gratings in the germanium rings of Yb^{3+}-doped photonic bandgap fiber, and reflection bands were observed from the guided modes of the concentric annular rings, rather than from the core mode.

In this letter, the fiber Bragg grating arrays are realized by inscribing into the Ge-doped cladding rods in an all-solid PBG hydrogen loaded fiber using the KrF excimer laser. The resonance dips are observed only if the light is launched into the Ge-doped cladding rods. When the light is launched into the all-solid PBGF and then passed through the FBG, there will be two kinds of mode couplings. The one kind is the coupling occurring between the adjacent rods of the all-solid PBGF when light is traveling through the all-solid PBGF, and the other kind is the coupling to the reversed guided supermode in the cladding rods of the PBGF when light is traveling through the FBG. Then we launch the light into the Ge-doped rods from two reverse directions, in other words, the light travels through different lengths in the PBGF before passing through the FBG, different resonance wavelengths and the resonance width are observed.

2 Experimental Setup

The microscope image of the all-solid PBGF used in our experiment, which was fabricated by Yangtze Optical Fiber and Cable Company Ltd of China, is shown in the inset of Fig. 1b. Five layers high-index rods (germanium doped) with single rod surrounded by an index depressed layer (fluorine doped) are embedded in the pure silica background. The core is formed by omitting a high-index rod and a low-index ring. The diameter of the fiber is 125 μm, and the distance between the adjacent rods Λ is 10 μm. The outer diameters of the high-index rod and the low-index ring are 0.3786 Λ and 0.7572 Λ, respectively. Compared with the pure silica background, the average refractive index difference of the high-index rods and the low-index rings are 0.034 and −0.08, respectively.

A 1.5 m all-solid PBGF, with 3 cm section which is stripped the coating at the distance of 9 cm from the beginning end, is loaded in a hydrogen atmosphere at 100 atm, 100 °C for 48 h to enhance its photosensitivity. Then the stripped section is exposed by focused pulses from a 248 nm KrF excimer laser with average energy of single pulse of 40 mJ at a repetition rate of 2 Hz for 2 min. The grating period is 593 nm. The FBG is fabricated, as shown in the right part of Fig. 1b. A broadband source covering from 1520 nm to 1580 nm passing through the SMF is coupled into the core and the Ge-doped rods of the all-solid PBGF. An ANDO Q8383 optical spectrum analyzer is connected to the other end of the all-solid PBGF for measuring transmission spectrum of the FBGs, as shown in Fig. 1a. Figure 1b is a blow up of the section circled by the dotted ellipse in Fig. 1a.

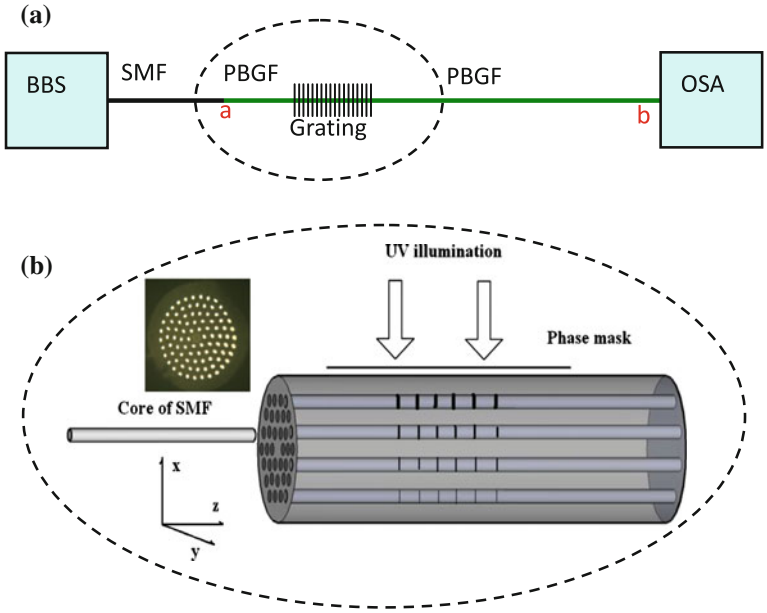

Fig. 1 **a** The schematic diagram of the experimental setup. **b** The schematic diagram of the blow up of the section circled by the *dotted ellipse* in Fig. 1a. The *right part* is the fiber Bragg grating inscribed into the high-index Ge-doped rods by UV illumination using phase mask. The *left part* is the core of the SMF transporting the light from BBS into the individual rod of the cladding of the all-solid PBGF

3 Experimental Realization and Analysis

Figure 2a shows the transmission spectra when the light is launched into the core and the six rods of the first ring (see the inset) of the all-solid PBGF after FBG fabrication. It is obviously seen that no Bragg resonance dip appears when the light is launched into the core of the PBGF. While Bragg resonance dips occur if the light is separately launched into the six rods of the first ring of the all-solid PBGF. The resonance wavelength of each rod is different. This is because each rod experienced different pulse energies due to the different vertical distances from the phase mask to the rod, and the index modulation for the rods is different resulting in different effective indices of the coupled modes neff for the rods. Hence, according to the fiber Bragg grating phase matching condition $\lambda_{res} = 2n_{eff}\,\Lambda$, where λ_{res} is the Bragg resonant wavelength and Λ is the period of the FBG, the resonant wavelengths are different. Since the above-mentioned experiment is based on that the light is first passing through the shorter length of the all-solid PBGF (as shown in Fig. 1a), for the convenience of description, we call the situation forward-launching.

Then, we launch the light into the core and the same rods from the right end of the all-solid PBGF, i.e., the b point as shown in Fig. 1a, and the OSA is connected with the left end. We call the situation back-launching. The transmission spectra are shown in

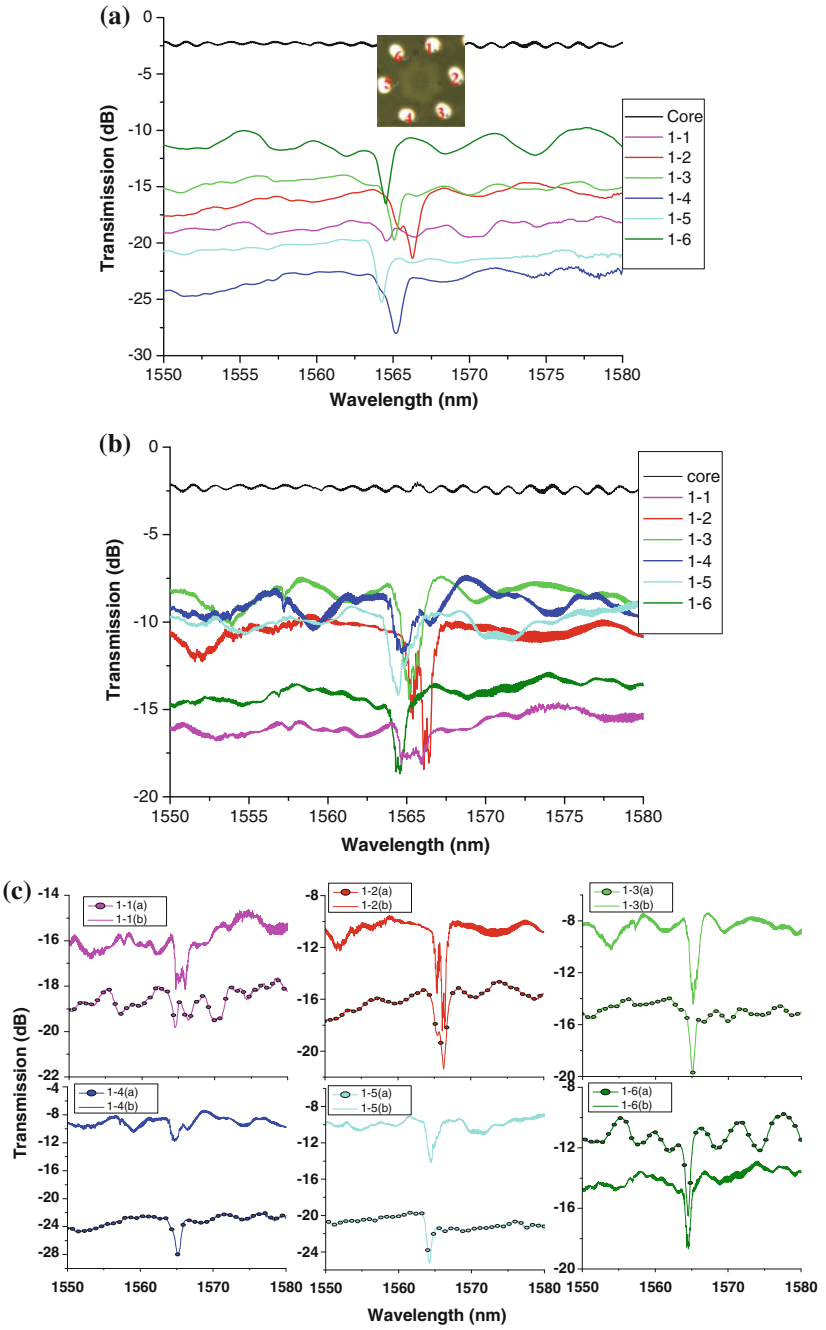

Fig. 2 The transmission spectra of the FBGs from the core and the six rods in the first ring of the all-solid PBGF after FBG fabrication for the two situations: **a** light forward-launching and **b** light back-launching. **c** Comparison of the transmission spectrum of the FBG from the same rod for the two situations: forward-launching (*dotted lines*) and back-launching (*solid lines*)

Fig. 2b. Similarly, there is no resonance dip if light is coupled into the core of the PBGF, and Bragg resonance dips with different resonance wavelengths and resonance widths also occur if the light is launched into the six rods of the first ring of the PBGF.

For comparison, we depict the transmission spectra of the FBG from the same rod for the two situations: forward-launching and back-launching, as shown in Fig. 2c. We can observe the transmission spectra of the FBGs from the same rod for the two situations have similar resonant wavelength. However, for the back-launching, the curves are not enough smooth. This is because, for the back-launching, light is first coupled into the rods of the longer length PBGF section, and the couplings between the adjacent rods occur. Then the coupled light in some rods is traveling through the FBG, and the transmission spectrum is not only simple Bragg resonance dips of the single rod, and they consist of the resonance dips of the adjacent rods. On contrary, for the forward-launching, the light is coupled into the shorter length PBGF section, which is short enough to couple the light between the adjacent rods and the light is restricted in the single rod. When the light travels through the FBG, the transmission spectrum is formed by the Bragg resonance dips of the single rod. Hence its resonance width is larger than the former situation (see the first figure in Fig. 2c). We also observe the transmission spectrum of the FBG from the rods of the second and the third ring, as shown in Fig. 3. The resonant dips from every rod are also

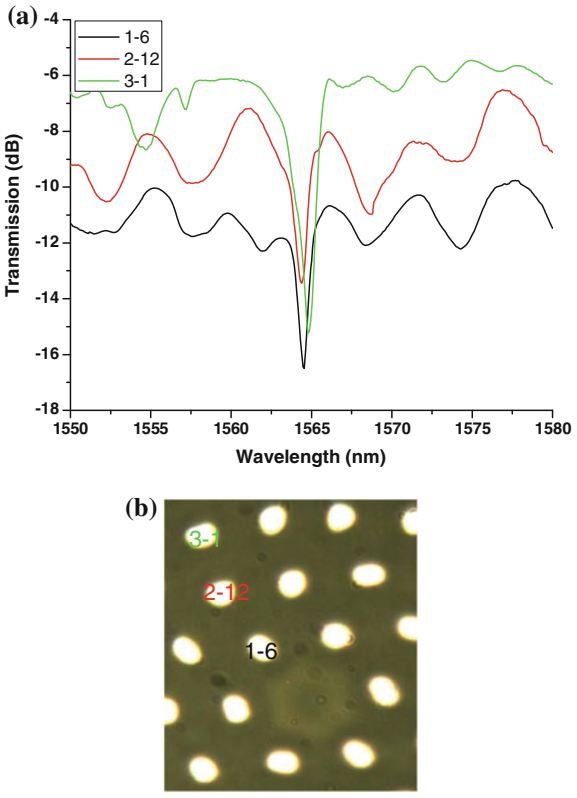

Fig. 3 **a** The transmission spectra of the FBG from three rods from the first, second and third rings, respectively. **b** The relative position of the three rods

obviously observed with different resonant wavelengths. In our experiments, the resonance wavelength width is larger than the Bragg resonance width in ordinary single mode fiber (SMF); this is because the mode couplings in the rods of the PBGF occur between the rods-guided supermodes, not the simple guided fundamental mode in the core of the SMF.

4 Conclusion

In conclusion, we realize the fiber Bragg grating arrays by inscribing into the Ge-doped cladding rods of an all-solid PBG hydrogen loaded fiber using KrF excimer laser. We launch the light into the Ge-doped rods from two reverse directions, and different resonance wavelengths and resonance widths are observed. The diverse resonance dips from different rods may have different responses to the environment changes, hence the fiber Bragg grating arrays will have good capacity to be employed as the multi-parameter sensor. If we control the length of the all-solid PBGF before the FBG, we may realize diverse resonance dips, and the fiber Bragg grating arrays can be used to be study the properties of the supermode coupling in the rods. Still, there should be further research on the specific mode couplings in the rods of all-solid PBGF and in the FBG.

Acknowledgments This work was supported by the National Natural Science Foundation of China under Grant No. 11404240, and by the Doctoral Scientific Foundation of Tianjin Normal University under No. 52XB1307. The authors would like to thank Yangtze Optical Fiber and Cable Co. LTD (Wuhan, China) for providing PCFs.

References

1. Russell P (2003) Photonic crystal fibers. Science 299(5605):358–362
2. Knight JC (2003) Photonic crystal fibres. Nature 424(6950):847–851
3. Luan F (2004) All-solid photonic bandgap fiber. Opt Lett 29:2369–2371
4. Jin L (2007) Bragg grating resonances in all-solid bandgap fibers. Opt Lett 32:2717–2719
5. Jin L (2007) Spectral characteristics and bend response of Bragg gratings inscribed in all-solid bandgap fibers. Opt Express 15:15555–15565
6. Bigot L (2009) Efficient fiber Bragg gratings in 2D all-solid photonic bandgap fiber. Opt Express 17:10105–10112
7. Cook K (2010) Bragg gratings in Yb^{3+}-doped solid photonic bandgap fibre, OSA

The Design of Temperature and Humidity Measure Based on USB Interface

Yuchan Xie

Abstract To expand the using occasions, a kind of temperature and humidity measurement based on USB interface has been completed in which SHT10 is used as the temperature and humidity data collecting sensor, and the relative humidity is compensated by temperature at the same time. The USB interface chip CH340T is used to transfer the received data to PC for processing. In this paper, the system is described in detail from two aspects, hardware and software. Experiment shows the system has good measurement results.

Keywords Temperature measure · Humidity measure · USB interface

1 Introduction

Along with the social development, temperature and humidity measurements have been applied in more and more industrial and agricultural scenes [1, 2]. For example, in the warehouses for food or medicine or tobacco, etc., the temperature and humidity need real-time monitoring. There are strict requirements in semiconductor production environment, too warm or too wet will lead to its performance depressing. So temperature and humidity need to be strictly inspected and controlled.

By traditional method, the temperature and humidity are measured separately, the compatibility is poor among sensors, measurement process is disturbed easily, and the measurement circuit is too complex. It already cannot satisfy the needs of the development of modern science and technology [3].

At present most of the communications between the temperature and humidity detection system and PC are through RS-232 serial port [4]. To catch up with the trend of interface development, USB interface is used in the system, which makes

Y. Xie (✉)
College of Computer and Communication Engineering,
Northeastern University at Qinhuangdao, Qinhuangdao, China
e-mail: xieyuchan@neuq.edu.cn

Q. Liang et al. (eds.), *Proceedings of the 2015 International Conference on Communications, Signal Processing, and Systems*, Lecture Notes in Electrical Engineering 386, DOI 10.1007/978-3-662-49831-6_97

it either as a disk to read and write or as a peripheral to communicate with a PC, so as to achieve the ideal of intelligent temperature and humidity testing requirements. In general the structure of the system is simple with higher intelligent degree and higher measurement precision.

2 The Design Scheme

A STC89C52 chip is used as the core of the system to control the whole system as shown in Fig. 1. SHT10 is used as the temperature and humidity sensor. DS1320 generates the time information. The liquid crystal display module LCD1602 displays temperature and humidity value. A set of temperature and humidity data is stored in AT24C02 every 5 s, which is transmitted to PC by CH340T in USB interface. PC can receive data with serial port assistant.

3 Hardware Design

The STC89C52 peripheral circuit is shown in Fig. 2.

3.1 Temperature and Humidity Sensor

SHT10 communicates with STC89C52 through two lines. P1.3 in STC89C52 is connected with SHT10 to transmit DATA. P1.4 is connected with SCK to generate the clock signal. VDD in SHT10 is connected with power and GND with grounding. The connection between SH10 and STC89C52 is shown in Fig. 3.

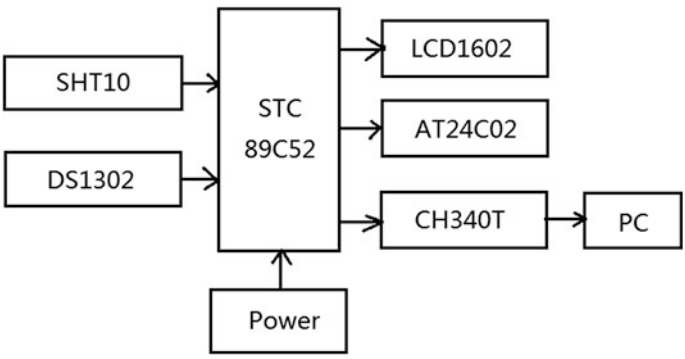

Fig. 1 The system structure

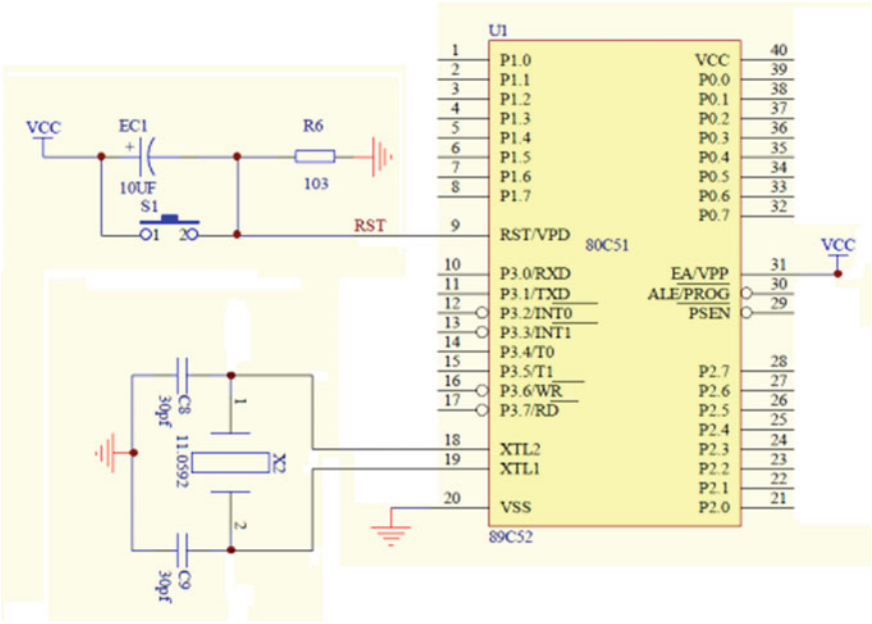

Fig. 2 The STC89C52 peripheral circuit

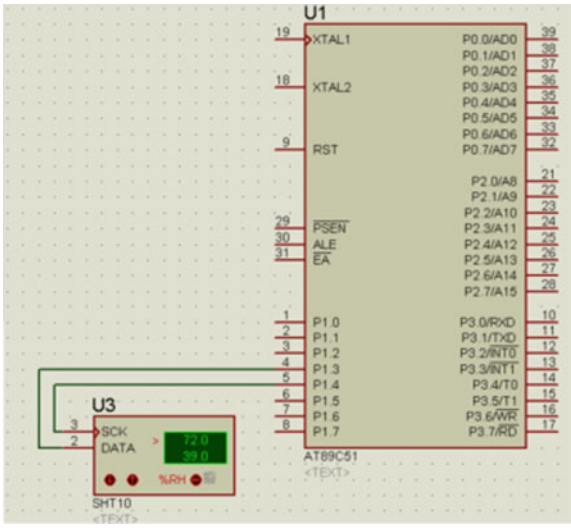

Fig. 3 Connection between SHT10 and STC89C52

Memory chip AT24C02 connected with the main control chip is shown in Fig. 4. Address line in AT2402 is used to determine the chip hardware address, they are grounded in the system. SDA is connected with P2.1, the main control chip

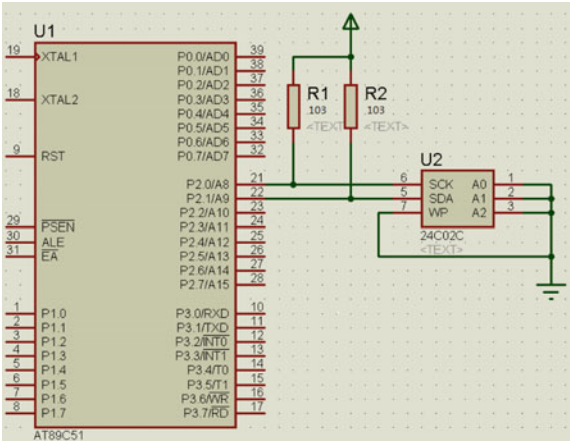

Fig. 4 AT24C02 connects with control pins

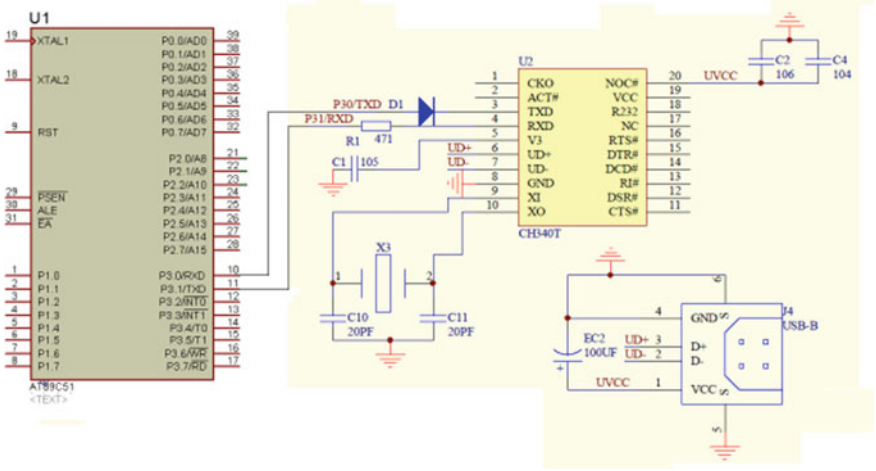

Fig. 5 CH340T is connected with the main control pin

simulate data transmission by IIC bus communication. SCL is connected with P2.0, the clock signal is generated by the main control chip. WP is grounding, which allowing normal read and write operations.

Ch340T is connected with STC89C52 for serial communication by two lines, in which P3.0 is connected with TXD and P3.1 with RXD is shown in Fig. 5.

4 Software Design

4.1 Temperature and Humidity Measuring

The main program related with the temperature and humidity sensor SHT10 includes: writing section, read bytes, temperature and humidity measurement, temperature and humidity value scale transform, temperature compensation and so on, which is shown in Fig. 6.

- Signal sampling: The control pins start transmission timing is shown in Fig. 6. When the clock signal SCK changes from low level to high electricity, data line becomes low. After the next high level of SCK, data line is changed to be high level. A measure initialization is completed by now. A measurement course begins after measuring instruction was set out. The measuring instruction and measuring precision are different according to the measure time. The measurement is end when DATA is low again. Signals have been read out when the "data ready" come, which is shown in Fig. 7.

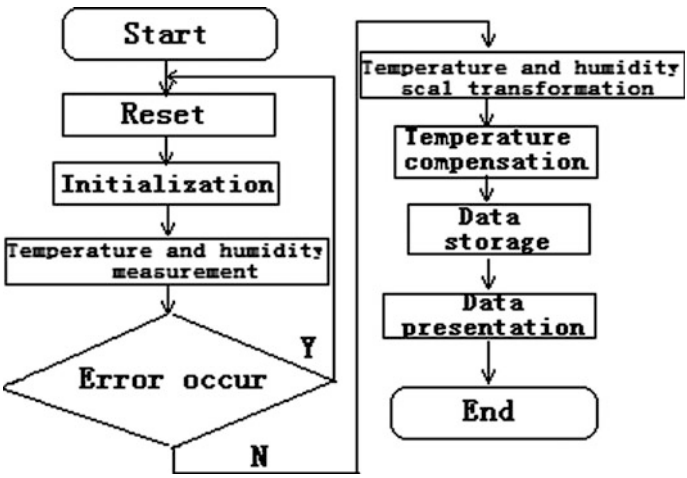

Fig. 6 Temperature and humidity measure flow chart

Fig. 7 Initiate transmit

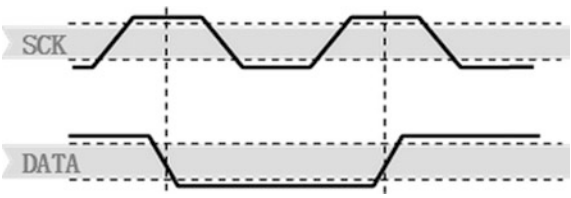

- Temperature measurement by SHT10 has good linear. Temperature T can be obtained directly by equation:

$$T = d_1 + d_2 \cdot SOT \tag{1}$$

In which, *SOT* is the output temperature data from SHT10. *d1* and *d2* are constants, which can be obtained by looking up a handbook.

- Relative humidity *RH* can be obtain by the following equation:

$$RH = C1 + C2 \cdot SORH + C3 \cdot SORH^2 \tag{2}$$

In which, *SORH* is the output humidity data through SHT10, *C1*, *C2,* and *C3* are constants, which can be achieved by looking up a handbook too.

- The compensation for relative humidity temperature
If there is large difference between the measured temperature with 25 °C, the humidity value needs to be correct by its temperature. The compensation formula is shown as following:

$$HTRUE = (T\,^\circ C - 25) \cdot (t1 + t2 \cdot SORH) + RH \tag{3}$$

T °C is the temperature data that comes from SHT10, whose unit is degree centigrade. *SORH* is the output humidity data. *RH* is the relative humidity, which has been transformed. *t1* and *t2* are constants, which can be achieved by looking up the handbook.

4.2 Data Storage and Reading

- Writing process: There are 7 address codes in AT24C02. The 4 high address codes are fixed, which are 1010. The other 3 low ones, which are A2, A1, A0 are achieved according to their level. When the main control chip is in writing, its (R/W) pin is set to 0. The 7 address codes are sending in the SDA line. The SDA line is released after writing.
- Reading process: When reading, the "0" in pin (R/W) and 7 address codes are sending in SDA line. After confirming the codes in SDA line is its address information, AT24C02 generates response signals on line. Then, the first address is sent to AT24C02, and then wait for the response signal. After its pin (R/W) is set "1", the control chip sending device address to AT24C02. After receiving the device response, the data on line is reading.
- Data transfer: The measure system communicates with PC through CH340T. After installing the drive program in PC, a serial port assistant can receive data. An asynchronous communication is taken between the measure system and PC. In order to guarantee the coordination in both transceiver side, the transmitting device and receiving device with the same data format and transmission speed.

It takes character as asynchronous communication unit. The time interval between characters is arbitrary, but the bits in each character are transmitted at a fixed time. That is, the distances between bits in the same character are the integer times of the minimum interval.

5 Simulation Experiment

In the temperature and humidity measuring system, data acquisition was by SHT10, data was processed in STC89C52. Temperature, humidity, and time were shown in LCD1602. Data was stored in AT24C02 and was transmitted to PC through CH340T.

The simulation exercise was based on proteus software tool. Its result was shown in Fig. 8. In the LCD, time information was shown in the above line. Temperature and humidity parameters were displayed in the following line. Every 5 s a set of temperature and humidity data would be stored in AT24C02, and received by the serial port assistants. Experiment shows each module in the temperature and humidity measuring instrument work normally, realize basic functions. Actual test result is shown in Fig. 9.

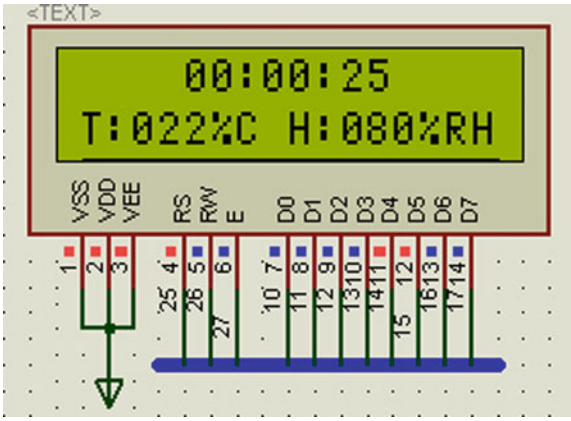

Fig. 8 Simulation result

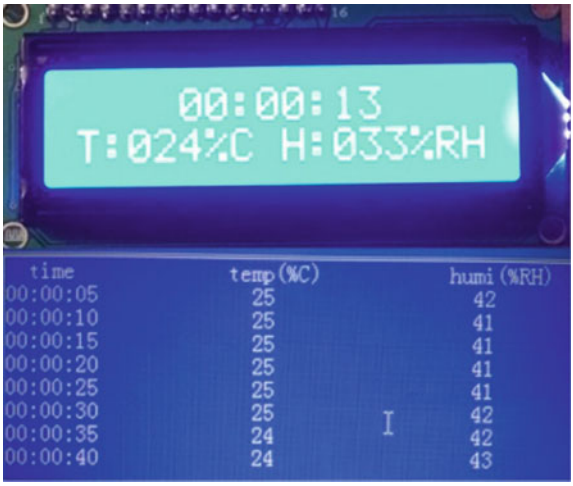

Fig. 9 Real test result

6 Conclusions

The temperature and humidity detecting system is composed of the new type of digital integrated temperature and humidity sensor SHT10, large capacity memory chip AT24C02, and the convenient and reliable USB interface, which are used to communicate with PC. According to these, the temperature and humidity can be acquired and saved at any time without manual intervention. It can work at lots of occasions. The testing system has a simple structure and reliable data and easy to use.

References

1. Xiaoping Y (2011) The design of temperature and relative humidity measurement system based on AT89S52 and DHT21. J Wuxi Inst Technol 10:62–63
2. Lei Y (2013) Temperature and humidity monitoring system based on USB interface in the greenhouse. Agric Mech Res 7:110–114
3. Buli X, Keqin D, Lihong L (2009) USB communication intelligent measure system of temperature and humidity. Modern Sci Instrum 3:40–43
4. Jing Z, Lei Z, Yang N (2012) Design of test program for RS232-USB converter. Electron Test 5:50–54

The Demodulation System of Fiber Bragg Grating Based on Edge Filter

Wenjie Shen, Jing Jiang, Yun Tian and Hao Sun

Abstract Fiber Bragg grating is used for monitoring various parameters. In this paper, a set of demodulation system is built based on the principle of edge filter. The system can realize static and dynamic demodulations for the Fiber Bragg grating. Besides, in order to reduce the influence caused by temperature and strain to the filtering device, the appropriate compensation and packaging are designed. As a result, the temperature drift coefficient of the filtering device reduces from 112 to 45 pm/°C, and the stability of the system is improved obviously. The experimental result shows that the wavelength resolution of the system is 0.01 nm and the bandwidth can achieve to 3.5 nm. The error is less than 1 % when the system is used for dynamic signal demodulation.

Keywords Fiber sensing technology · Fiber Bragg grating · Demodulation · Edge filter · Temperature drift coefficient

1 Introduction

Fiber Bragg grating (FBG) is one of sensing components. It has many ad vantages, such as small size, good reliability, high sensitivity, anti-interference ability, and so on. Because of so many advantages, the FBG has a good and wide application in the sensing area. When the FBG is used to measure, the change of the central wavelength is linear with the strain or the temperature. So how to extract the information about the central wavelength is one of the core technologies in fiber sensing area at present. In order to get better demodulation method of FBG, researchers proposed many methods, include matching demodulation method for FBG [1], tune optical fiber F-P filter demodulation method [2, 3], balance and unbalance Michelson interference demodulation method [4], ring cavity fiber laser lasing demodulation method, chirped grating detection method, and so on.

W. Shen (✉) · J. Jiang · Y. Tian · H. Sun
Tianjin Institute of Metrological Supervision and Testing, Tianjin, China
e-mail: wenjie8612@163.com

Q. Liang et al. (eds.), *Proceedings of the 2015 International Conference on Communications, Signal Processing, and Systems*, Lecture Notes in Electrical Engineering 386, DOI 10.1007/978-3-662-49831-6_98

According to the basic principle of edge filter demodulation methods [5, 6], the system we mentioned is built. It can demodulate the central wavelength of FBG using the long period grating (LPG) as the edge filter device. Because the system is based on the detection of light intensity and only includes a set of simple photoelectric detection circuit, it can reduce the influence to the demodulation frequency caused by the mechanical device. And the system can achieve static and dynamic demodulations of FBG. Besides, in order to improve the stability of FBG, the appropriate temperature compensation and packaging technology are adopted.

2 Basic Principles of the System

The demodulation system is built based on the principle of edge filter and the details are as follows. A beam of light emitted from the light source enters FBG by through the 3 dB coupler. Then the light reflected from FBG is divided into two channels evenly. One beam of light enters the photoelectric detection device through a linear filter of LPG. And the other one enters the photoelectric detection device with the same parameters as the reference beam. So we can get the signal of measurement from a ratio. The ratio is got from the two voltage signals from the photoelectric detection device. We determine the relationship between the ratio and the central wavelength of the FBG in further.

The coupled principle of LPG is that, the coupling between the forward transmission mode and the core of the optical fiber can lead to attenuation of the specific wavelength [7], and it shows a broad bandwidth loss peak in the transmission spectrum. The diagram of the demodulation system is showed in Fig. 1.

In our system, there are two sides of linear band in the transmission spectrum of LPG. In the linear band, there is a linear relationship between the transmission and the central wavelength of FBG. So we use the band as a linear filter. The intensity of the light detected changes according to the central wavelength of the reflected

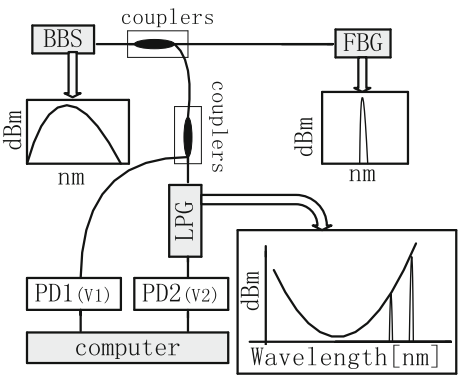

Fig. 1 The diagram of the demodulation system

light in FBG. We get the signals of measurement from the photoelectric detection device.

Assuming that the filter transfer function of LPG is expressed by the normalized spectral transmittance curve H (λ), the spectral density of the reflected optical light is expressed by R (λ). So the optical power of the reflected light in the FBG which is filtered by LPG can be expressed as follows.

$$I(\lambda) = \int_{-\infty}^{+\infty} R(\lambda - \lambda')H(\lambda')d\lambda'$$

According to the transmission spectrum of LPG, H (λ) is a linear function in the band we chose and the spectral bandwidth of R (λ) is less than wavelength rang of LPG, the optical power function I(λ) can be transformed into the following form.

$$I(\lambda) = H(\lambda) \int_{-\infty}^{+\infty} R(\lambda - \lambda')d\lambda'$$

The light power of the reference beam does not change with the changes of the central wavelength of FBG, and it can be expressed as follows.

$$I_1(\lambda) = \int_{-\infty}^{+\infty} R(\lambda - \lambda')d\lambda'$$

When the central wavelength changes, the ratio of I (λ)/I_1 (λ) also changes in linear form. So we can get the information about the central wavelength of FBG, and realize the detection and demodulation to the signal of the central wavelength.

According to the mathematical relationship and the characteristics of LPG, the optical power of the reflection spectrum which obtained by LPG can be simplified to the following form.

$$I(\lambda) = k^* \Delta\lambda$$

$\Delta\lambda$ is expressed as the changes of the central wavelength of the FBG, and k is a constant only related to the characteristic of FPG.

Actually, the central wavelength of FBG can also be detected only by the signal filtered by LPG, but so many unstable factors be found in the experimental process, such as the micro-bending effect of the light path in the transmission process, the changes of light intensity when reflected back in FBG, the distribution of the light source, the ups and downs of the light power, and so on. All of these will affect the measurement results. Therefore, when the system is built, we take the methods that the information of the central wavelength is obtained by the ratio of the two kinds of signals, one was filtered and the other one was without filtering. Experiment shows that, with the method, the unfavourable factors can be eliminated effectively.

3 The Packing of LPG and Temperature Compensation

The most important part of the demodulation system is LPG, but the LPG is very sensitive to the external environment. The fluctuation of environmental temperature will cause the drift of the central wavelength of LPG, and bring a bad impact on the experimental results. In order to improve the stability and accuracy of the system, we must take methods to package the LPG. Before, researchers have done a lot of research and experiments on the temperature compensation of LPG, such as packaging LPG by metal casing to compensate temperature drift [8], coating resin in the surface of LPG to reduce the temperature drift [9], and so on.

According to the characteristics of the LPG chosen, that is the temperature coefficient is positive and the strain coefficient is negative, we determine to package the LPG using three kinds of materials with different coefficient of thermal expansion. By analysis and comparison, the materials used to temperature compensation and the method of packaging are selected. In experiments, LPG is pasted on three kinds of material. They are the organic glass, the thin aluminum sheet, and the copper plate. Then we make heating test and cooling test. Observing the changes of the central wavelength with the temperature and comparing the experimental data between uncompensated and compensated.

Figure 2 shows the temperature characteristic curve of LPG under different packaging, which can be known that the brass plate make a good effect in temperature compensation. The temperature compensation effect packaged by aluminum is weaker than packaged by copper. And due to the thermal expansion coefficient of organic glass, the LPG is over stretched, so the waveform and 3 dB bandwidth are unable to recover.

By comparing the experimental results of three kinds of packaging materials, we choose the copper plate as the temperature compensated material. The experimental

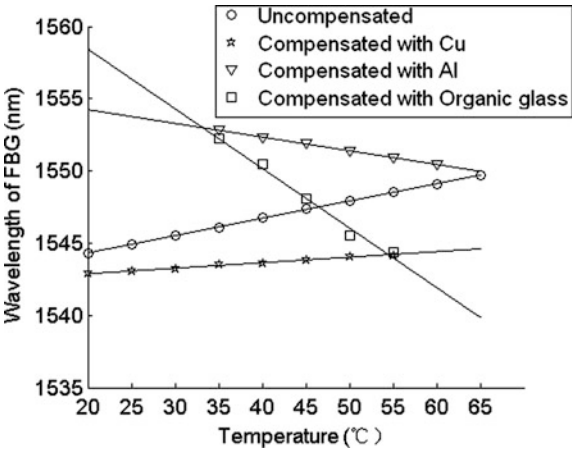

Fig. 2 The temperature characteristic curve of LPG under different packaging

data shows that the temperature drift coefficient of LPG uncompensated is 112 pm/°C, and it is 45 pm/°C when compensated with copper plate.

The packaging with the copper plate can not only effectively reduce the temperature drift, but also avoid the appearance of bending in the grid of LPG. So the method improves the stability of the demodulation system.

4 The Demodulation System and Experiment Analysis

The light source used in the system is ASE broadband light source with a better flatness, which can ensure the stability of the light source power and advantage to the demodulation of the FBG.

The transmission spectrum of LPG used in the system is showed in Fig. 3. As we have said in the front of the page, there are two linear bands in the sides of the central wavelength of LPG, and we choose one side of the band from 1548 to1554 nm as a filter in our system.

The system uses InGaAs PIN fiber couple output photodiode as a photoelectric detector to convert the light intensity signal to electrical signal, and design the circuit board to convert the current signal to voltage signal using some kinds of chip, such as OP657, OP37 and INA 143. The circuit board can detect the weak signal. The, the signal is sent to the computer by AD collector. And at last, the data processing and display are realized using computer program.

The device supplying the signal of the sensing grating is a structure of equal intensity beam. FBG paste along the central axis of the beam, and the displacement

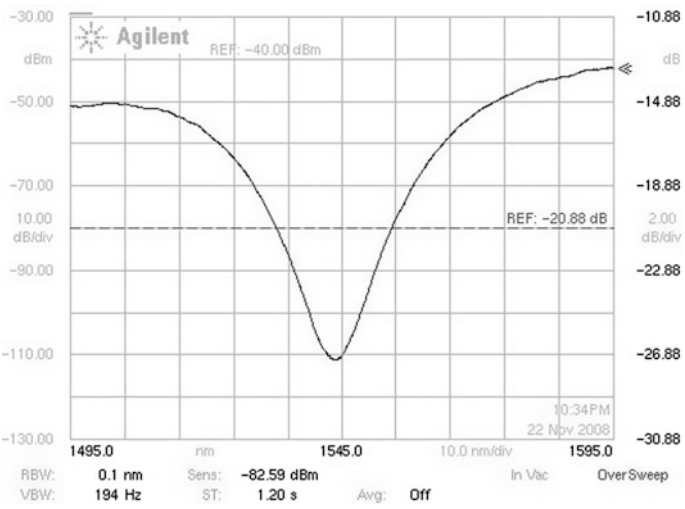

Fig. 3 The transmission spectrum of LPG

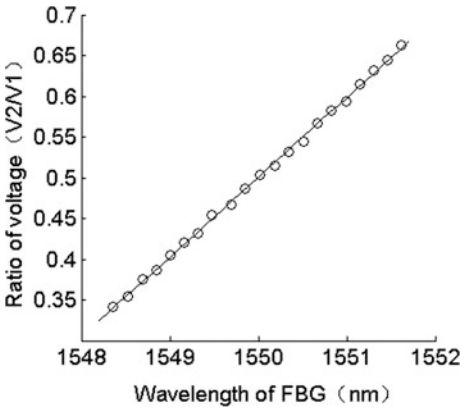

Fig. 4 The sensing curve of the demodulation system

happens by the feed of screw micrometer head. Then we observe the central wavelength of FBG using a spectrometer. The photoelectric detection converts the optical power signal into the voltage signal with the sensitivity of 100 mv/nw. The voltage signal is sent to the computer and processed by the computer.

Figure 4 shows the relationship between the ratio of the two voltage signal detected by and the changes of the central wavelength of the FBG reflected wave.

From the figure, we can see that there is a good linear relationship between the ratios of the two voltage signals to the central wavelength of FBG, the fitting degree of the curve is 0.9962. Experimental data shows that the demodulation range of the system is 3.5 nm, the wavelength sensitivity is 0.092 nm^{-1}, and the wavelength resolution is 0.01 nm.

The system is based on the detection of light intensity, and only using simple photoelectric detection circuit. The designs effectively reduce the frequency limit which is caused by the mechanical device. The system can realize static and dynamic demodulation for FBG.

The vibration test experiment is made in equal strength beam vibration test bench. The micro-motor is fixed in the free end of the beam, and send driving signal as sine shape in order to drive the equal strength beam vibration. The speed of the motor can be changed by adjusting the motor speed regulator. The FBG is pasted on the central position of the equal strength beam, and the detected signal can be observed using the computer program. The information about the central wavelength of FBG detected at 50 and 100 Hz is shown in Fig. 5. The figure above is the curve when the frequency is 50 Hz, and the figure below is the curve when the frequency is 100 Hz.

The detected signal shows that the central wavelength changes with the signal waveform and frequency sent by the micro-motor. The detection signal is stable and the waveform has good quality. Experimental data shows that when the system is used to dynamic measurement, the frequency error is less than 1 % t.

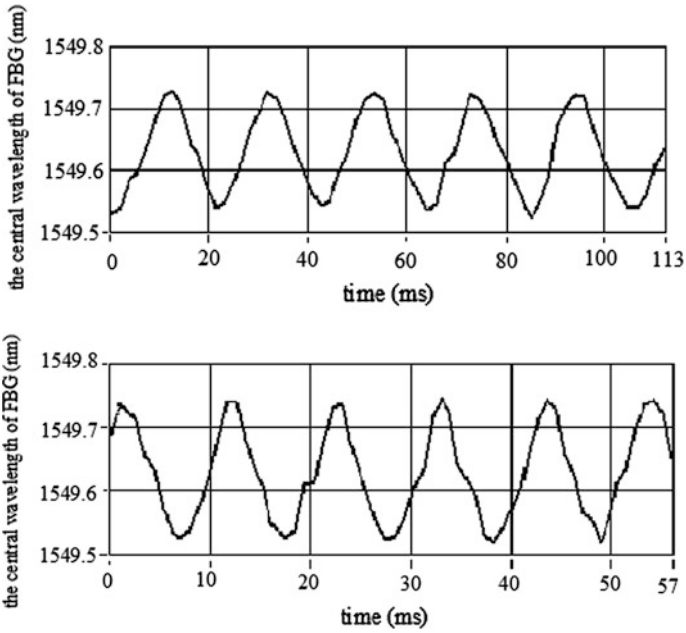

Fig. 5 The waveform of detection at different frequency

5 Conclusions

In this paper, the FBG demodulation system based on the linear filter of LPG is introduced. The linear demodulation range of the system can reach to 3.5 nm, the wavelength sensitivity is 0.092 nm^{-1} and the wavelength resolution is 0.01 nm. Due to the use of all optical fiber technology, the system can realize static and dynamic demodulations of FBG. When used in dynamic demodulation, the signal is stable and the frequency error is less than 1 %.

In order to solve the problems that the LPG is sensitivity to the changes of temperature and strain, appropriate temperature compensation and packaging technology is adopted. By taking measures, the temperature drift coefficient of LPG is decreased from 112 to 45 pm/°C. It not only compensates the drift cased by temperature changes, but also avoids the appearance of bending phenomenon in grid and the stability of the system is improved. In a word, the demodulation system has good performance.

References

1. Zhang D, Guo D, Luo P et al (2007) Researches on fiber grating vibration sensor based on matching filter demodulation[J]. Chin J Sens Actuators 20(2):311–313
2. Kersey AD, Berkoff TA, Morey WW (1993) Multiplexed fiber Bragg grating strain sensor system with a fiber Fabry-Perot wavelength filter [J]. Opt Lett 18(16):1370–1372
3. Zhao B, Zhang Z, Zhong Q et al (2009) F-P Demodulation method of fiber Bragg grating and scale changeable sampling technique[J]. Laser Infrared 39(1):59–62
4. Kersey AD, Berkoff TA (1992) Dualwavelength fiber interferometer with wavelength selection via fiber Bragg grating elements [J]. Electron Lett 28(13):1215–1216
5. Zhou G, Zhao Q, Kai G, Dong X (2003) A novel ede filter demodulation techique by using high birefringence fiber sagnac loop mirror[C]. In: Proceedings of the 8th optoelectronics and communication conference(OECC2003), vol II. pp 855–856
6. Liu B, Tong Z, Chen S (2004) A novel method of edge filter linear demodula-tion using long-period grating in fiber sensor system[J]. Acta Optica Sinica 24(2):199–202
7. Lee BH, KimYJ, ChungY et al (2001) Analytic solution for cascaded long-period fiber gratings. IEICE Trans E84-C:621–628
8. Qin L, Wei EX, Wang QY et al (2000) Compact temperature-compensaring package for Long-period fiber gratings[J]. Opt Mater 14(8):239–242
9. He WW, Shiwenkang J et al (2002) Broadband wavelength tuning an temperature compensation of long period fiber grating[J]. J Shang Hai Jiao Tong Univ 36(7):1029–1031

Part XIII
Signal Processing and Machine Learning Algorithm

Convergence and Steady-State Properties of the Affine Projection Mixed-Norm Algorithms

Ling Liqian, Lin Bin, Wang Fei and Luo Lingling

Abstract The affine projection algorithm (APA) attracts a wide attention for its advantages such as simple frame, fast convergence rate, and so on. This paper is based on the AP algorithm to introduce nonlinear update equation for the weight error vector. So the affine projection mixed-norm (APMN) algorithm is proposed. In this paper, we use a new approach to analyse the APMN algorithm. In this thesis, the stability and convergence rate of APMN algorithm are analyzed in theory and, simulation and verification of theoretical analysis is also performed.

Keywords Adaptive filter · Steady-state analysis · Mean-square error · Convergence rate

1 Introduction

Adaptive filters have become a vital part of many modern communication and control systems, which can be used in system identification, adaptive equalization, echo cancelation, beam-forming, and so on [1, 2]. Adaptive signal-processing algorithms are conventionally based on a single error norm, such as the established last mean square (LMS) and the lesser known least mean fourth (LMF) algorithms. [3] The LMF algorithm is particularly appropriate for applications in which the measurement noise has a probability density function with short tails. However, its convergence properties are very sensitive to the proximity of the adaptive weights to the optimum Wiener solution. The least mean mixed norm (LMMN) adaptive algorithm overcomes this sensitivity and reduces misadjustment performance [4, 5]. The normalized least mean square (NLMS) algorithm is a popular method used in adaptive filtering. It is a simple, stable adaptation technique with low complexity. However, NLMS convergence is sensitive to the spectral flatness of the reference

L. Liqian (✉) · L. Bin · W. Fei · L. Lingling
College of Information Science and Technology, Dalian Maritime University, Dalian 116026, China
e-mail: lingliqian1117@163.com

Q. Liang et al. (eds.), *Proceedings of the 2015 International Conference on Communications, Signal Processing, and Systems*, Lecture Notes in Electrical Engineering 386, DOI 10.1007/978-3-662-49831-6_99

input and may be very slow when the input signal is colored. By employing several input vectors, APA provides faster convergence than NLMS, especially when the reference input of the adaptive filter is highly colored [6–9]. APMN algorithm is used find the error signal mixed power based on AP algorithm.

Adaptive-signal-processing algorithms are conventionally based on a single error norm, for example the established Affine Projection Algorithm (APA) [6], the Least Mean Mixed Norm (LMMN) adaptive algorithm [3] and the APMN adaptive algorithm is proposed in this paper.

2 APMN Adaptive Algorithm

The input signal x_{n} of the adaptive filter and the unknown system which was assumed to be time invariant and have a finite impulse response (FIR) structure. The objective is to minimize the difference between the desired signal d_n and the output of the adaptive filter according to some optimization criterion (Fig. 1).

APMN algorithm is used to regulate the error function based on AP algorithm. So the weight update formula is

$$w_{n+1} = w_n + \mu \frac{X_n}{X_n^T X_n} f(e_n) \tag{1}$$

$$\mathrm{e_n} = \mathrm{d_n} - \hat{\mathrm{d}}_\mathrm{n} = \mathrm{X_n^T}(\mathrm{w_{n+1}} - \mathrm{w_n}) \tag{2}$$

$$f(e_n) = \left(\delta + \delta |e_n|^2\right) e_n \tag{3}$$

where

μ is step-size;
$X_{\mathrm{n}} = (x_n, x_{n+1}, \ldots, x_{n-M})$ is input matrix;
$x_{\mathrm{n}} = (x_n, x_{n-1}, \ldots, x_{n-N+1})$ is input vector;
w_0 is unknown column vector that we wish to estimate;
$w_{\mathrm{n+1}}$ is weight vector, which is the estimation for $\mathrm{w_0}$, at time constant n;

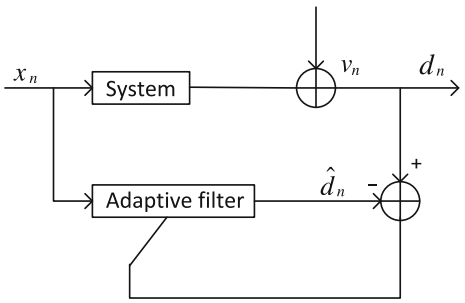

Fig. 1 Adaptive-system identification in additive measurement noise

We should find the weight w_{n}^1 so minimized that $\|w_{\mathrm{n}}^1 - w_{\mathrm{n}}\|$ is subject to $d_n - x_n^T w_n^1 = 0$. This solution is given by

$$w_n^1 = w_n + \mu_0 x_n \tag{4}$$

where $\mu_0 = \frac{f(e_n)}{x_n^T x_n}$ and $e_n = d_n - x_n^T w_n$.

Then, the weight w_{n}^2 forces the a posterior estimation error an (n − 1) to zero, while maintaining the zero a posterior estimation error at n, and keeping the norm of the increment in weights to a minimum. That is, to find the weight w_{n}^2 minimize $\|w_{\mathrm{n}}^2 - w_{\mathrm{n}}\|$ that is subject to $d_n - x_n^T w_n^2 = 0$ and $d_{n-1} - x_{n-1}^T w_n^2 = 0$. If the increment in weights $\left(w_{\mathrm{n}}^1 - w_{\mathrm{n}}^2\right)$ is orthogonal to x_{n}. Hence, it decomposes $x_{\mathrm{n}-1}$ into a component along x_{n} and a component x_{n}^1 that is orthogonal to x_{n}. It increases the weights along x_{n}^1 so that the second constraint is satisfied. This solution is given by

$$w_n^2 = w_n^1 + \mu_1 x_n^1 = w_n + \mu_0 x_n + \mu_1 x_n^1 \tag{5}$$

where $\mu_1 = \frac{f\left(e_n^1\right)}{x_n^{1T} x_n^1}$ and $e_n^1 = d_{n-1} - x_{n-1}^T w_n^1$.

And so on $w_n^{k+1} = w_n^1 + \mu_0 x_n + \mu_1 x_n^1 + \ldots + \mu_k x_n^k$

where $\mu_k = \frac{f\left(e_n^k\right)}{x_n^{kT} x_n^k}$, $e_n^k = d_{n-k} - x_{n-k}^T w_n^k$ and $f\left(e_n^k\right) = \left(\delta + \vec{\delta}\left|e_n^k\right|^2\right) e_n^k$.

Thus the weight update that forces the most recent (M + 1) posterior estimation errors to zero is given by

$$w_{n+1} = w_n + \mu_0 x_n + \mu_1 x_n^1 + \cdots + \mu_m x_n^M \tag{6}$$

where M + 1 is the number of input vectors used for adaptation, x_n is the input vector at the nth instant, x_n^k, for $k = 1,2, \ldots, M$, is the component of x_{n-k} that is orthogonal to $x_n, x_{n-1}, x_{n-2}, \ldots x_{n-(k-1)}$, and μ_k, for $k = 0,1,\ldots, M$ is chosen as in the next formula.

$$\mu_k = \begin{cases} \frac{e_n}{x_n^T x_n} & k = 0, \|x_n\|^2 \neq 0 \\ \frac{e_n^k}{x_n^T x_n} & k = 1, 2, \ldots, M, \|x_n\|^2 \neq 0 \\ 0 & others \end{cases}$$

where $e_n = d_n - x_n^T w_n$,

$$e_n^k = d_{n-k} - x_{n-k}^T w_n^k,\ k = 1, 2, \ldots, M$$
$$w_n^k = w_n + \mu_0 x_n + \ldots + \mu_{k-1} x_n^{k-1}$$

So the weight vector updating formula of affine projection mixed-norm adaptive algorithms is

$$w_n^k = w_n + \mu_0 x_n + \mu_1 x_n^1, \ \ldots + \mu_m x_n^{M-1}$$

The error in variable weight vector is $\tilde{w}_n = w^0 - w_n$, after pushing to get $\tilde{w}_{n+1}$

$$\tilde{w}_{n+1} = \tilde{w}_n - \sum_{j \in Jn} \frac{\tilde{\mu} f\left(e_n^j\right)}{x_{n-jD}^T x_{n-jD}} x_{n-jD} \tag{7}$$

3 Steady-State Performancee

In the stability analysis of AP adaptive algorithm is the use of calculation $cov\left(\|\tilde{w}_{n+1}\|^2\right)$. Steady state performance is obtained by analysis. In this paper, let Σ denote any $M \times M$ Hermitian positive-definite matrix, and define the weighted priori and posteriori error signals:

$$\begin{gathered} e_a^{\Sigma}(n-jD) = x_{n-jD}^T \Sigma \tilde{w}_n, e_p^{\Sigma}(n-jD) = \mathbf{x}_{n-jD}^T \Sigma \tilde{w}_{n+1} \\ \tilde{w}_{n+1} = \tilde{w}_n - \sum_{j \in Jn} \frac{\tilde{\mu} f\left(e_n^j\right)}{x_{n-jD}^T x_{n-jD}} x_{n-jD} \end{gathered} \tag{8}$$

Multiplying both sides of the above equation by $x_{n-jD}^T \Sigma$ and substituting (8) into them, we have

$$e_p^{\Sigma}(n-jD) = e_a^{\Sigma}(n-jD) - \frac{\tilde{\mu} f\left(e_n^j\right)}{x_{n-jD}^T x_{n-jD}} \tag{9}$$

The following equation concerning the energy conservation relation during an equalizer update is used to solve the steady-state performance analysis for adaptive algorithms

$$\|x_{n-jD}\|_{\Sigma}^2 \|\tilde{w}_{n+1}^2\|_{\Sigma}^2 + \|e_a^{\Sigma}(n-jD)\|^2 = \|x_{n-jD}\|_{\Sigma}^2 \|\tilde{w}_n\|_{\Sigma}^2 + \|e_p^{\Sigma}(n-jD)\|^2$$

Introducing (9) into the above equation and taking expectations, we get

$$\begin{gathered} E\|\tilde{w}_{n+1}\|_{\Sigma}^2 = E\|\tilde{w}_n\|_{\Sigma}^2 + E\left[\frac{\tilde{\mu}^2 \|x_{n-jD}\|_{\Sigma}^2}{\left(x_{n-jD}^T x_{n-jD}\right)^2} \left|f\left(e_n^j\right)\right|^2\right] - 2\tilde{\mu} E\left[\frac{e_a^{\Sigma}(n-lD) f\left(e_n^j\right)}{x_{n-jD}^T x_{n-jD}}\right] \\ E\|\tilde{w}_{n+1}\|_{\Sigma}^2 = E\|\tilde{w}_n\|_{\Sigma}^2 + \tilde{\mu}^2 E\left[S_{\Sigma}\left|f\left(e_n^j\right)\right|^2\right] - 2\tilde{\mu} h Re\left(E\left[e_a^{\Sigma}(n-lD) f\left(e_n^j\right)\right]\right) \end{gathered} \tag{10}$$

where $S_{\Sigma} = \frac{\|x_{n-jD}\|_{\Sigma}^2}{\left(x_{n-jD}^T x_{n-jD}\right)^2}, h = E\left[\frac{1}{x_{n-jD}^T x_{n-jD}}\right]$

We adopt the following three assumptions

A.1: The noise sequence v_n with zero-mean and variance $\sigma_v^2 \neq 0$ is statistically independent and identically distributed of the regressor sequence is x_n.

A.2: The priori estimation error $e_a(n-jD)$ with zero-mean is independent of x_n. And for complex-valued cases, it satisfies the circularity condition, namely, $Ee_a(n-jD)=0$ and $Ee_a(n-jD)e_a^{\Sigma}(n-jD)=0$.

A.3: The priori estimation error $Ee_a(n-jD)$ and its weighted estimation error $e_a^{\Sigma}(n-jD)$ are jointly circular Gaussian.

The error function $f\left(e_n^j\right)$ is for the Fourier series expansion, deducing

$$E\|\tilde{w}_{n+1}\|_{\Sigma}^2 = E\|\tilde{w}_n\|_{\Sigma}^2 + \tilde{\mu}^2 E\left(C_{n-jD} + B_{n-jD}|e_a(n-jD)|^2\right)S_{\Sigma} - \tilde{\mu}E\left(hA_{n-jD}\|\tilde{w}_n\|_{\Sigma R_x}^2\right)$$

$$E\|\tilde{w}_{n+1}\|_{\Sigma}^2 = E\|\tilde{w}_n\|_{\Sigma}^2 + \tilde{\mu}^2 E\left(C_{n-jD} + B_{n-jD}\|\tilde{w}_n\|_{R_x}^2\right)S_{\Sigma} - \tilde{\mu}E\left(hA_{n-jD}\|\tilde{w}_n\|_{\Sigma R_x}^2\right)$$

where $A_{n-jD} = 2E\left|f_{e_n^j}^{(1)}(v_n)\right|$, $B_{n-jD} = E\left|f_{e_n^j}^{(1)}(v_n)\right|^2 + f_{e_n^j}^{(2)}(v_n)f\left(e_n^j\right)$, $C_{n-jD} = \left|f\left(e_n^j\right)\right|^2$

Substituting $\Sigma = I$, we get

$$E\|\tilde{w}_{n+1}\|^2 = E\|\tilde{w}_n\|^2 + \tilde{\mu}^2 E\left(C_{n-jD} + B_{n-jD}\|\tilde{w}_n\|_{R_x}^2\right)S_I - \tilde{\mu}E\left(hA_{n-jD}\|\tilde{w}_n\|_{R_x}^2\right) \tag{11}$$

At steady-state, under the assumption $E\|\tilde{w}_{n+1}\|^2 = E\|\tilde{w}_n\|^2$, $n \to \infty$, which is often used in the steady-state performance analysis, (11) can be rewritten as

$$\left(A_{n-jD} - \tilde{\mu}B_{n-jD}\eta_{\mu}\right)\xi = \tilde{\mu}C_{n-jD}\eta_{\mu} \tag{12}$$

where, $\xi = \|\tilde{w}_n\|_{R_x}^2$, $\eta_{\mu} = \frac{S_I}{h}$

Since $\tilde{\mu}C_{n-jD}\eta_{\mu} \geq 0$ and $\xi \geq 0$. If the following condition about the step-size is satisfied,

$$0 < \tilde{\mu} < \frac{A_{n-jD}}{B_{n-jD}\eta_{\mu}}$$

The steady-state EMSE performance can be expressed by

$$\xi = \frac{\tilde{\mu}C_{n-jD}\eta_{\mu}}{A_{n-jD} - \tilde{\mu}B_{n-jD}\eta_{\mu}} \tag{13}$$

and the steady-state mean square error is given by $MSE = \sigma_v^2 + \xi$.

4 Simulation Results

In this section, the theoretical result is demonstrated by carrying out simulations in the system FIR filter with 11 taps. The input signal is correlated and the signal-to-noise ratio (SNR) is 20 dB. Each simulation results are obtained by ensemble averaging over 200 independent trials.

Figure 2 compares the $\delta = 0.01$, $\delta = 0.1$, and $\delta = 0.8$ of convergence rate of the APMN algorithm for $\sigma = 10^{-2}$ and $\mu = 0.1$. The figure also shows that with the increase of δ, the convergence rate is also increasing. Figure 3 compares the $\mu = 0.01$, $\mu = 0.1$, and $\mu = 0.5$ of convergence rate of the APMN algorithm for $\sigma = 10^{-2}$ and $\delta = 0.5$. The figure also shows that with the increase of μ, the convergence rate is also increasing.

Figure 4 compares the simulation and theoretical results of steady state MSE of the APMN algorithm for $\sigma = 10^{-2}$ and $\delta = 0.5$. It is seen in the figure that the theoretical and experimental MSE are in good match. Figure 5 compares the simulation and theoretical results of steady state MSE of the APMN algorithm for $\sigma = 10^{-2}$ and $\mu = 0.1$. It is seen in the figure that the theoretical and experimental MSE are in good match.

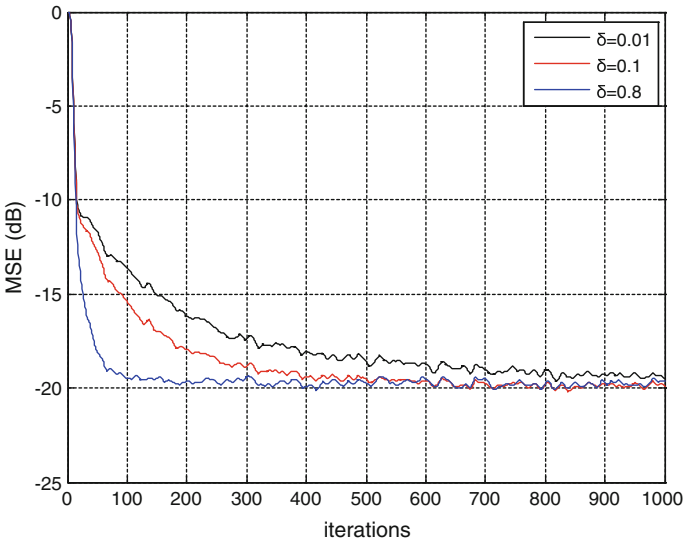

Fig. 2 Comparison of learning curves for the proposed algorithm with δ

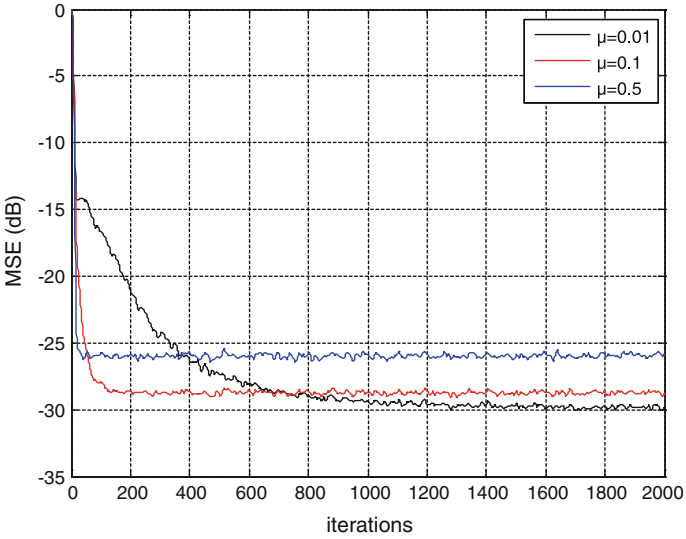

Fig. 3 Comparison of learning curves for the proposed algorithm with μ

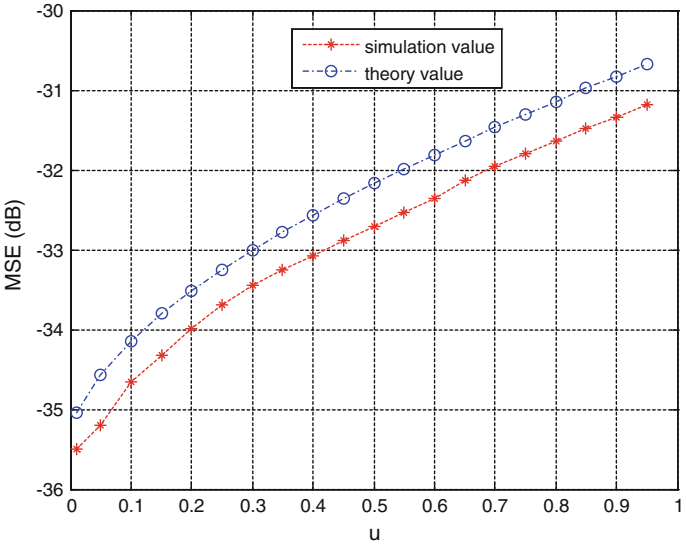

Fig. 4 Theory and simulation MSE versus μ

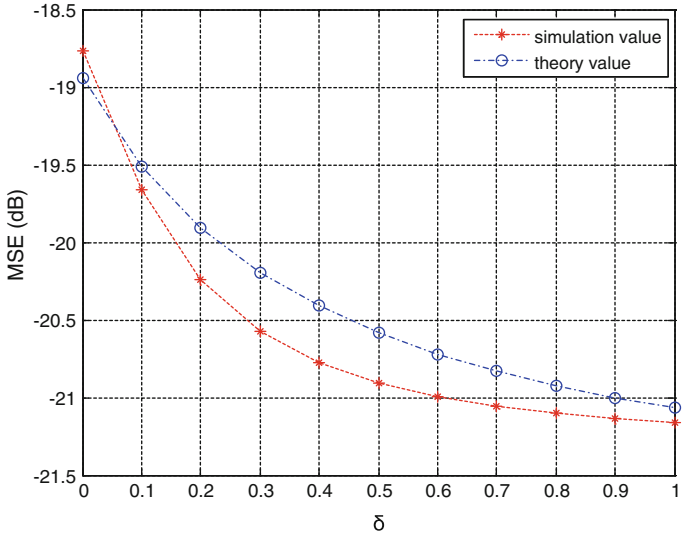

Fig. 5 Theory and simulation MSE versus δ

5 Summary

This paper is based on the AP algorithm to introduce nonlinear update equation for the weight error vector and the APMN algorithm is proposed. The above simulation results show the steady-state performance and convergence of the APMN algorithm. The results of simulation and theoretical results of steady state MSE of the APMN algorithm for σ and μ meet the requirements. The APMN algorithm retains the advantages of AP algorithm and has better steady state.

References

1. Zhou D, DeBrunner VE (2006) Affine projection algorithm based direct adaptations for adaptive nonlinear predistorters. In: Fortieth Asilomar conference on signals, systems and computers, 2006. ACSSC'06, 29 Oct 2006–1 Nov 2006, pp. 144–147
2. Shubair RM, Jimaa SA (2007) Improved adaptive beamforming using the least mean mixed-norm algorithm. In: 9th international symposium on signal processing and its applications, 12–15 Feb 2007. ISSPA 2007, pp 1–4
3. Zerguine A, Cowan CFN, Bettayeb M (1997) Adaptive echo cancellation using least mean mixed-norm algorithm. IEEE Trans Sig Process 45(5):1340–1343
4. Chambers JA, Tanrikulu O, Constantinides AG (1994) Least mean mixed-norm adaptive filtering. Electron Lett 30(19):1574–1575
5. Tanrikulu O, Chambers JA (1996) Convergence and steady-state properties of the least-mean mixed-norm (LMMN) adaptive algorithm. In: Vision, image and signal processing, IEEE proceedings, vol 143, no 3, pp 137–142

6. Joy J, Mathurakani M (2013) A switching variable step size affine projection adaptive algorithm for acoustic echo cancellation. In: 2013 Annual international conference on emerging research areas and 2013 international conference on microelectronics, communications and renewable energy (AICERA/ICMiCR), 4–6 June 2013, pp 1–5
7. Bouchard M, Albu F (2003) The multichannel Gauss-Seidel fast affine projection algorithm for active noise control. In: Seventh international symposium on signal processing and its applications, proceedings, 1–4 July 2003, vol 2, pp 579–582
8. Ban SJ, Lee CW, Kim SW (2009) Adaptive regularization parameter for pseudo affine projection algorithm. IEEE Sig Process Lett , May 2009, vol 16, no 5, pp 382–385
9. Gonzalez A, Ferrer M, Albu F, de Diego M (2012) Affine projection algorithms: evolution to smart and fast algorithms and applications. In: Signal processing conference (EUSIPCO), 2012 proceedings of the 20th european, 27–31 Aug 2012, pp 1965–1969

A Parameter-Free Gradient Bayesian Two-Action Learning Automaton Scheme

Hao Ge, Yan Yan, Jianhua Li, Ying Guo and Shenghong Li

Abstract Reinforcement learning is one of the subjects of Artificial Intelligence and learning automata have been considered as one of the most powerful tools in this research area. A learning automaton (LA) is a learning machine that can learn an optimal action through interacting with stochastic environments. However, its performance highly depends on the selection of a configurable learning speed. Granmo proposed a Bayesian Learning Automaton (BLA), which is reported to not rely on such external parameters, to solve Two-Armed Bernoulli Bandit problem in 2010. In this paper, we demonstrate the BLA algorithm from a learning automata perspective. Furthermore, we devote efforts to improving the convergence speed of BLA by incorporating a gradient descent-like method and then proposed a novel Gradient Bayesian Learning Automaton (GBLA). It has been demonstrated by extensive simulations that GBLA is faster than BLA and traditional algorithms such as DP_{RI}, and outperforms the state-of-art SE_{RI} algorithm as well.

Keywords Learning automata · Parameter-free · Bayesian estimation · Two-action environment

H. Ge (✉) · Y. Yan · J. Li · Y. Guo · S. Li
Shanghai Jiao Tong University, Shanghai 200240, China
e-mail: sjtu_gehao@sjtu.edu.cn

Y. Yan
e-mail: yevita94@hotmail.com

J. Li
e-mail: lijh888@sjtu.edu.cn

Y. Guo
e-mail: guoying2014vip@sjtu.edu.cn

S. Li
e-mail: shli@sjtu.edu.cn

Q. Liang et al. (eds.), *Proceedings of the 2015 International Conference on Communications, Signal Processing, and Systems*, Lecture Notes in Electrical Engineering 386, DOI 10.1007/978-3-662-49831-6_100

1 Introduction

Learning Automaton (LA) have been long used as a powerful tool for maximizing the reward attained in stochastic environments [2, 5, 8, 9]. If we define the action with the maximum reward probability as the optimal action, the automaton will converge to the optimal action almost surely as long as a sufficiently large resolution parameter (or sufficiently small learning speed) is set, which is also known as the *ϵ-optimal* property. Generally, a larger resolution parameter will lead to a more accurate convergence but more interactions with the environment. For that reason, parameter tunning is necessary to balance accuracy and convergence speed in practical applications. Typically, the resolution parameter varies from tens to hundreds in different environments (see a comparison of various pursuit learning schemes [4], including DP_{RI} which will be discussed later). Worse still, the state-of-art algorithm (SE_{RI} [5]) has two such tunable parameters, making the scheme more flexible but harder to be applied.

In this paper, we proposed a parameter-free scheme, which means the procedure of manually choosing a learning speed can be omitted. Meanwhile, the accuracy is ensured by a Bayesian inference method.

Our work presents a set of novel contributions that we summarize in the following:

1. We present the first *parameter-free* scheme in the field of LA, for learning in two-action stochastic environments. The meaning of the terminology *parameter-free* is twofold: (1) The resolution parameter does not need to be manually configured. (2) Unlike other estimator based schemes, initializations of estimators are also unnecessary in our scheme.
2. Most conventional LA algorithms employ a stochastic exploration strategy in literatures, on the contrary, we design a deterministic gradient descent like method instead of probability matching as the exploration strategy to further accelerate the convergence rate of the automaton.
3. Numeric simulations confirm that our scheme can converge correctly, and our scheme also possesses a relatively fast convergence speed compared to SE_{RI}, which is reported to be the fastest scheme over the past decades. Moreover, our scheme always has a higher accuracy with no more interactions than SE_{RI}, which indicates that the proposed scheme can learn the environments better.

The rest of this paper is organized as follows. In Sect. 2, we introduce the Bayesian learning automaton for solving Two-Armed Bernoulli Bandit (TABB) problem, and present the BLA algorithm from a LA perspective. We point out its limitation and propose a solution in Sect. 3. The results of extensive simulations are presented in Sect. 4. Section 5 concludes the paper.

2 Bayesian Learning Automaton

In [3], a Bayesian learning automation (BLA) is proposed for solving TABB problem. The TABB problem is a classical optimization problem that explores the trade-off between exploitation and exploration in reinforcement learning. One distinct difference between learning automata and Bandit playing algorithms is the metrics used for performance evaluation. Typically, the probability of selecting the optimal action is used for evaluating LA algorithms while *regret* is usually used in bandit playing algorithms.

We summarize the BLA proposed in [3] briefly as follows: The BLA maintains two Beta distribution to estimate the reward probabilities of each arm. At each time instance, two values are randomly drawn from the two Beta distributions. The arm with the higher random value is selected, and the feedback is used to update the parameter of the Beta distribution associated with the selected arm. One advantage of BLA is that it doesn't involve any explicit computation of Bayesian expression.

In order to construct an absorbing learning automaton counterpart, however, the probability of each arm being selected must be explicitly computed to judge the convergence of the algorithm. Now, we describe the corresponding BLA algorithm from a LA perspective as below.

Algorithm 1 Bayesian Learning Automaton

1: initial $\alpha_1 = 1, \beta_1 = 1, \alpha_2 = 1, \beta_2 = 1$;
2: **repeat**
3: Compute the probability $P_1 = P(e_1 > e_2)$ where e_1 and e_2 are random variables that follow distribution $Beta(\alpha_1, \beta_1)$ and $Beta(\alpha_2, \beta_2)$, respectively, and $P_2 = 1 - P_1$
4: Choose an action a_i according to probability distribution P_1, P_2
5: Receive a feedback from the environment and update the parameter of Beta distributions: $\alpha_i = \alpha_i + 1$ if a reward is received and $\beta_i = \beta_i + 1$ if a penalty is received.
6: **until** $\max(P_1, P_2) > 0.99$

The probability P_1 of choosing action a_1 can be calculated by

$$P_1 = \int_0^1 \int_0^u \frac{v^{\alpha_2 - 1}(1-v)^{\beta_2 - 1}}{B(\alpha_2, \beta_2)} \frac{u^{\alpha_1 - 1}(1-u)^{\beta_1 - 1}}{B(\alpha_1, \beta_1)} dvdu \tag{1}$$

$$= \frac{1}{B(\alpha_1, \beta_1)B(\alpha_2, \beta_2)} \sum_{i=0}^{\beta_2 - 1} \frac{(1-\beta_2)_i}{i!(\alpha_2 + i)} B(\alpha_1 + \alpha_2 + i, \beta_1) \tag{2}$$

where $B(\alpha, \beta)$ is beta function with parameter α and β, respectively, and the denotation $(x)_i$ is a *Pochhammer Symbol*. e_1 and e_2 are Bayesian estimates of the reward probabilities for the two actions. It is noted that the direct computation of P_1 is avoided in [3] by random sampling.

As revealed in [3], the performance of Algorithm 1 does not rely on an external parameter which must be manually configured in other algorithms. Besides, as it employs a Bayesian estimate rather than a maximum likelihood estimate of reward probability, the initialization of estimators can be omitted then.

However, Algorithm 1 suffers from one weakness that it needs more iterations to get converged. Numeric support can be found in Sect. 4. To overcome this problem, we proposed a gradient descent like method to accelerate the convergence. Algorithm 1 and the proposed algorithm are experimentally verified and the results are demonstrated in Sect. 4.

3 Gradient Bayesian Learning Automaton

As mentioned above, BLA algorithm takes more iterations to get converged, which is undesired in most scenarios. On one hand, more iterations means more interactions with the environment. In some applications, interacting with environments could be expensive, such as drug trials, destructive tests or financial investments. On the other hand, as claimed in [3], the computation time of Eq. (2) is unbounded, rising with the number of actions being selected.

Considering the above two drawbacks of BLA, in this paper, we are dedicated to accelerating the convergence by incorporating a gradient descent like method. First, we shall present the Gradient Bayesian Learning Automaton (GBLA) algorithm.

Algorithm 2 Gradient Bayesian Learning Automaton

1: initial $\alpha_1 = 1, \beta_1 = 1, \alpha_2 = 1, \beta_2 = 1$;
2: **repeat**
3: Compute the probability $P_1 = P(e_1 > e_2)$ where e_1 and e_2 are random variables that follow distribution $Beta(\alpha_1, \beta_1)$ and $Beta(\alpha_2, \beta_2)$, respectively, and $P_2 = 1 - P_1$
4: Choose the action according to Eq. (14).
5: Receive a feedback from the environment and update the parameter of Beta distributions: $\alpha_i = \alpha_i + 1$ if a reward is received and $\beta_i = \beta_i + 1$ if a penalty is received.
6: **until** $\max(P_1, P_2) > 0.99$

Obviously, the major difference between Algorithms 1 and 2 lies in line 4. The exploration strategy used in Algorithm 1 is the so-called *probability matching*. Probability matching occurs when an action is chosen with a frequency equivalent to the probability of that action being the best choice. This sub-optimal behavior has been reported repeatedly by psychologists and experimental economists [6]. While Algorithm 2 adopts a gradient descent like method, which will be elaborated hereinafter.

As P_1 and P_2 can be perceived as functions with arguments $\alpha_1, \beta_1, \alpha_2, \beta_2$. The partial derivatives with respect to $\alpha_1, \beta_1, \alpha_2, \beta_2$, respectively, are listed below:

$$\frac{\partial P_1}{\partial \alpha_1} = P_1(\alpha_1 + 1, \beta_1, \alpha_2, \beta_2) - P_1(\alpha_1, \beta_1, \alpha_2, \beta_2) \tag{3}$$

$$\frac{\partial P_1}{\partial \beta_1} = P_1(\alpha_1, \beta_1 + 1, \alpha_2, \beta_2) - P_1(\alpha_1, \beta_1, \alpha_2, \beta_2) \tag{4}$$

$$\frac{\partial P_1}{\partial \alpha_2} = P_1(\alpha_1, \beta_1, \alpha_2 + 1, \beta_2) - P_1(\alpha_1, \beta_1, \alpha_2, \beta_2) \tag{5}$$

$$\frac{\partial P_1}{\partial \beta_2} = P_1(\alpha_1, \beta_1, \alpha_2, \beta_2 + 1) - P_1(\alpha_1, \beta_1, \alpha_2, \beta_2) \tag{6}$$

An intuitive way is to calculate the expected gradient $\mathbb{E}[\nabla P_1]$ condition on each action has been selected

$$\mathbb{E}[\nabla P_1 | a_1 \text{ is selected}] = \frac{\alpha_1}{\alpha_1 + \beta_1} \frac{\partial P_1}{\partial \alpha_1} + \frac{\beta_1}{\alpha_1 + \beta_1} \frac{\partial P_1}{\partial \beta_1} \tag{7}$$

$$\mathbb{E}[\nabla P_1 | a_2 \text{ is selected}] = \frac{\alpha_2}{\alpha_2 + \beta_2} \frac{\partial P_1}{\partial \alpha_2} + \frac{\beta_2}{\alpha_2 + \beta_2} \frac{\partial P_1}{\partial \beta_2} \tag{8}$$

However, as reported in [1], the *recurrence relationships* of $P_1(\alpha_1, \beta_1, \alpha_2, \beta_2)$ can be shown as

$$P_1(\alpha_1 + 1, \beta_1, \alpha_2, \beta_2) - P_1(\alpha_1, \beta_1, \alpha_2, \beta_2) = h(\alpha_1, \beta_1, \alpha_2, \beta_2)/\alpha_1 \tag{9}$$

$$P_1(\alpha_1, \beta_1 + 1, \alpha_2, \beta_2) - P_1(\alpha_1, \beta_1, \alpha_2, \beta_2) = -h(\alpha_1, \beta_1, \alpha_2, \beta_2)/\beta_1 \tag{10}$$

$$P_1(\alpha_1, \beta_1, \alpha_2 + 1, \beta_2) - P_1(\alpha_1, \beta_1, \alpha_2, \beta_2) = -h(\alpha_1, \beta_1, \alpha_2, \beta_2)/\alpha_2 \tag{11}$$

$$P_1(\alpha_1, \beta_1, \alpha_2, \beta_2 + 1) - P_1(\alpha_1, \beta_1, \alpha_2, \beta_2) = h(\alpha_1, \beta_1, \alpha_2, \beta_2)/\beta_2 \tag{12}$$

where $h(\alpha_1, \beta_1, \alpha_2, \beta_2) = \frac{Beta(\alpha_1+\alpha_2, \beta_1+\beta_2)}{Beta(\alpha_1, \beta_1) \times Beta(\alpha_2, \beta_2)}$.

Therefore, Eqs. (7) and (8) are always being zeroes. As a consequence, applying gradient descent directly on P_1 won't work properly.

An alternative way is to choose action which will probably lead to a bigger increase/decrease of the P_1. In case of $P_1 > P_2$, action a_1 is promising to be optimal action. Hence, we will make trails that is possible to maximize P_1 shortly. Simply, we choose action a_1 provided that $\max(\frac{\partial P_1}{\partial \alpha_1}, \frac{\partial P_1}{\partial \beta_1}) > \max(\frac{\partial P_1}{\partial \alpha_2}, \frac{\partial P_1}{\partial \beta_2})$ and choose a_2 the other way around.

$$a_i = \begin{cases} \text{argmax}_i(\frac{\partial P_1}{\partial \alpha_i}, \frac{\partial P_1}{\partial \beta_i}) & \text{when } P_1 > P_2 \\ \text{argmin}_i(\frac{\partial P_1}{\partial \alpha_i}, \frac{\partial P_1}{\partial \beta_i}) & \text{when } P_1 < P_2 \\ \text{randomly chosen} & \text{when } P_1 = P_2 \end{cases} \tag{13}$$

It is easy to know that $h(\alpha_1, \beta_1, \alpha_2, \beta_2)$ is (trivially) larger than zero, so $\frac{\partial P_1}{\partial \alpha_1}$ and $\frac{\partial P_1}{\partial \beta_2}$ are (trivially) positive while $\frac{\partial P_1}{\partial \beta_1}$ and $\frac{\partial P_1}{\partial \alpha_2}$ are (trivially) negative.

So, Eq. (13) can be simplified as:

$$a_i = \begin{cases} \text{argmin}_i(\alpha_i + \beta_i) & \text{when } P_1 \neq P_2 \\ \text{randomly chosen} & \text{when } P_1 = P_2 \end{cases} \tag{14}$$

Intuitively, the action which has been tried less in previous iterations will be chosen in the next iteration according to our exploration strategy. Particularly, if $P_1 = P_2$ or $\alpha_1 + \beta_1 = \alpha_2 + \beta_2$ holds, we just randomly choose one action from the two candidates.

The above procedure is referred as *gradient descent like method* within this paper.

The learning process proceeds until the probability of hypothesis $e_1 > e_2$ or $e_2 > e_1$ is greater than a threshold (typically 0.99).

4 Simulation Results

In this section, the proposed GBLA is compared to the deterministic estimator based DP_{RI} [7], stochastic estimator based SE_{RI} scheme [5] and BLA [3].

We start the experiments with four two-action environments and the actions' reward probabilities for each environment are as follows:

$E_1 : \{0.90, 0.60\}$.
$E_2 : \{0.80, 0.50\}$.
$E_3 : \{0.80, 0.60\}$.
$E_4 : \{0.20, 0.50\}$.

E_1 is the most simple environment, with low variance and a large difference between the two actions. E_2 keeps the same difference between the two actions but with a larger variance. E_3 reduces the difference thus forming a harder environment. E_4 is similar with E_2 but more penalties will be received. E_2 to E_4 are also used to compare continuous and discretized pursuit learning schemes in [4].

In all the tests performed, an algorithm is considered to have converged if the probability of choosing an action is greater than or equal to a threshold $T(0 < T < 1)$. If the automaton converges to the action that has the highest reward probability, it is considered to have converged correctly.

Before a large number of simulations being carried out, parameter tunning is necessary to find the "best" external parameter for DP_{RI} and SE_{RI} in each environment. The resolution parameter is considered to be "best" provided that the automaton converges correctly in a sequence of 750 experiments. And the value of "best parameter" is averaged over 20 independent tunings to minimize the variance.

And after we get the "best" parameter, 250,000 independent simulations are performed to get averaged iterations and accuracy. For DP_{RI} and SE_{RI}, all actions are sampled 10 times to initialize the estimator vector, and these extra 20 iterations are also included in the iteration counts.

The iterations and accuracy (*number of correctly converged/number of experiments*) of each algorithm is summarized in Table 1.

Table 1 Performance comparison of DP_{RI}, SE_{RI}, BLA and GBLA

Env.	DP_{RI}			SE_{RI}			BLA		GBLA	
	Param.	Itera.	Acc. (%)	Param.[a]	Itera.	Acc. (%)	Itera.	Acc. (%)	Itera.	Acc. (%)
E_1	n = 22	46	99.76	(15, 3)	43	99.84	80	99.93	42	99.99
E_2	n = 29	61	99.78	(18, 3)	51	99.78	118	99.92	49	99.94
E_3	n = 74	127	99.67	(38, 5)	99	99.73	231	99.55	99	99.79
E_4	n = 18	64	99.83	(12, 3)	54	99.86	185	99.99	49	99.93

[a]The parameter of SE_{RI} is represented by a 2-tuple which means (n, γ)
Env. Environment, *Param.* Parameter, *Itera.* Iteration, *Acc.* Accuracy

From the table, we can obtain that GBLA improved[1] the convergence rate by 8.71 %, 19.67 %, 22.05 %, and 23.44 % in the four environments, respectively, compared with DP_{RI}.

To show the superiority of gradient descent-like method to probability matching strategy, GBLA is also compared with BLA. GBLA dramatically improved the convergence rate by 47.5 %, 58.47 %, 57.14 %, and 73.51 % in the four environments, respectively. It confirms the effectiveness and efficiency of the proposed gradient descent-like method.

Finally, GBLA is compared with the state-of-art learning algorithm—SE_{RI}. The improvement of convergence rate is not so remarkable as it in the former two comparisons. From the table, we can infer that GBLA is as fast as SE_{RI}, further more, it has a higher accuracy in the benchmark environments. So, we may safely draw the conclusion that GBLA is better than SE_{RI} in two-action environments.

5 Conclusions

In this paper, we incorporate the Bayesian learning automata with a gradient descent-like method. As a result, the Gradient Bayesian Learning Automaton is proposed. Different from traditional LA algorithms, it does not rely on external manually configured parameters and neither the initialization of estimators. Our simulation results have shown that the proposed algorithm converges as fast as SE_{ri} algorithm in the four two-action environments with a higher accuracy.

Nevertheless, our algorithm is still far from perfect, and it has its own limitations. Our work aims to evoke researches on these limitations, such as reducing the computation complexity without compromising convergence speed and accuracy and how the scheme can be extended to be applicable in multi-action environments.

[1]The improvement of GBLA is obtained by calculating $\frac{Iterations_{\{ComparedAlgorithm\}} - Iterations_{\{GBLA\}}}{Iterations_{\{ComparedAlgorithm\}}}$.

Acknowledgments This research work is funded by the National Science Foundation of China (61271316), Shanghai Key Laboratory of Integrated Administration Technologies for Information Security, and Chinese National Engineering Laboratory for Information Content Analysis Technology.

References

1. Cook JD (2008) Numerical computation of stochastic inequality probabilities. Technical report, UT MD Anderson Cancer Center Department of Biostatistics
2. Ge H, Jiang W, Li S, Li J, Wang Y, Jing Y (2015) A novel estimator based learning automata algorithm. Appl Intell 42(2):262–275
3. Granmo OC (2010) Solving two-armed Bernoulli Bandit problems using a Bayesian learning automaton. Int J Intell Comput Cybern 3(2):207–234
4. Oommen BJ, Agache M (2001) Continuous and discretized pursuit learning schemes: various algorithms and their comparison. IEEE Trans Syst Man Cybern Part B: Cybern 31(3):277–287
5. Papadimitriou GI, Sklira M, Pomportsis AS (2004) A new class of ϵ-optimal learning automata. IEEE Trans Syst Man Cybern Part B: Cybern 34(1):246–254
6. Rivas J (2013) Probability matching and reinforcement learning. J Math Econ 49(1):17–21
7. Thathachar MAL, Sastry PS (1985) A new approach to the design of reinforcement schemes for learning automata. IEEE Trans Syst Man Cybern 1:168–175
8. Zhang J, Wang C, Zhou M (2014) Last-position elimination-based learning automata. IEEE Trans Cybern 44(12):2484–2492. doi:10.1109/TCYB.2014.2309478
9. Zhang X, Granmo OC, Oommen BJ (2013) On incorporating the paradigms of discretization and Bayesian estimation to create a new family of pursuit learning automata. Appl Intell 39(4):782–792

An Adaptive Method of Signal Separation Based on Spatial Filter

Biao Cheng, Hong-yi Yu, Zhi-xiang Shen and Yun-peng Hu

Abstract This paper addresses the problem of parameter estimation and adaptive separation by antenna arrays. The technique of Sparse Bayesian Learning (SBL), with remarkable performance in low SNR and limited snapshots, is introduced to estimate Direction-of-Arrival (DOA), as no information about the statistical property or deterministic property is known in advance. The spatial filter is designed based on the DOA estimates to separate signals from different directions. It is shown that the spatial filter can separate the signals with the noise power decreased. To enhance the performance of separation, an iteration processing is utilized until satisfying the convergence criterion. Experimental results are used to evaluate the performance of the spatial filter.

Keywords Array signal processing · Sparse bayesian learning · Spatial filter · Diversity processing · Direction-of-Arrival

1 Introduction

As an important technique of signal processing, spatial filtering is widely applied in communication system, biomagnetic source imaging [1], surface electromyography [2], electroencephalogram analysis [3] and fiber transmission [4]. It is well-known that it can obtain signal from certain direction and suppress unwanted signals from other directions, with SINR increased and system performance improved. As the electromagnetic environment becomes more congested, the effective spatial filtering of communication signals seems to be necessary and essential. Consequently in this paper we present a new method to spatially filter communication signals.

The existing spatial filtering techniques generally consist of two main structures: classical spatial filter [5–7] and adaptive spatial filter [8, 9]. The former is computed as an optimization problem and derives closed-form solution according to the prior

B. Cheng (✉) · H. Yu · Z. Shen · Y. Hu
Information Engineering University, Zhengzhou, Henan 450001, China
e-mail: chengb_cn@163.com

Q. Liang et al. (eds.), *Proceedings of the 2015 International Conference on Communications, Signal Processing, and Systems*, Lecture Notes in Electrical Engineering 386, DOI 10.1007/978-3-662-49831-6_101

information. A null phase-shift spatial filter (NPSF) in [5] is designed by subspaces of target signal and interference which aims to cover a narrow band rather than a single direction, and can avoid the amplitude and phase distortion caused by the filters. A spatial filter is designed in an efficient manner by formulating the design procedure as a rank-deficient linear least-squares problem in [6]. The combination of the subspace-based bearing-estimation and spatial filter algorithms is capable of resolving sources that are below the resolution limit. Spatial filter can also separate the ultra-wideband signals. A spatial filter [7] is proposed for one-dimensional time-of-arrival localization and its performance is comparable to basic time-reversal systems.

The adaptive spatial filter is computed without prior parameters; however, it needs to utilize the characteristics of signals. An adaptive blind spatial filter [8] is proposed by utilizing a constant modulus criterion and Kalman filter without prior information about the signals. An algorithm with less computational complexity [9] is proposed to filter signals with cyclostationary characteristic and this subspace projection-based method achieves better performance than the original algorithms.

In this paper, we propose a method to design adaptive blind spatial filter without prior information or signal characteristic. The proposed method generally combines direction estimation and spatial filter design. The direction can be estimated by Sparse Bayesian Learning (SBL) and then spatial filter based on direction estimates is proposed to separate the signals. Generally the algorithm can blindly separate the signals and adaptively adjust filter parameter to changing directions.

This paper is organized as follows. Section 2 presents a review of the array output model. Section 3 introduces the estimation of sparse matrix and exploitation of spatial filters, and the overall scheme of proposed method is also illustrated in Sect. 3. Section 4 contains numerical simulations to examine the performance of the proposed method, and conclusions are given in Sect. 5.

2 Model Formulation

Suppose that K independent far-field stochastic and stationary signals impinge onto an M-element array from directions of $\boldsymbol{\theta} = [\theta_1, \ldots, \theta_K]$ simultaneously, the array output $\mathbf{y}(t) = [y_1(t), \ldots, y_M(t)]^T$ at time t is

$$\mathbf{y}(t) = \mathbf{A}(\boldsymbol{\theta})\mathbf{s}(t) + \boldsymbol{\upsilon}(t) \tag{1}$$

where the array responding matrix to all the incident signals is denoted by $\mathbf{A}(\boldsymbol{\theta}) = [\mathbf{a}(\theta_1), \ldots, \mathbf{a}(\theta_K)]$, with each column being the array responding vector of the kth incident signal $\mathbf{a}(\theta_k) = [e^{j\varphi_{k,1}}, \ldots, e^{j\varphi_{k,M}}]^T$. $\varphi_{k,m}$ is the phase shift of the kth signal propagating from the reference antenna to the mth antenna. $\mathbf{s}(t) = [s_1(t), \ldots, s_K(t)]^T$ is the complex waveform vector of the signal. $\boldsymbol{\upsilon}(t) \sim N(0, \sigma^2\mathbf{I}_M)$ is the zero-mean white Gaussian noise with power σ^2. In the scenario of N snapshots, the array output

formulation presented in (1) can be extended and rewritten as $\mathbf{Y}=\mathbf{A}(\boldsymbol{\theta})\mathbf{S}+\mathbf{V}$, where $\mathbf{Y}=[\mathbf{y}(t_1),\ldots,\mathbf{y}(t_N)]$, $\mathbf{S}=[\mathbf{s}(t_1),\ldots,\mathbf{s}(t_N)]$, $\mathbf{V}=[\boldsymbol{\upsilon}(t_1),\ldots,\boldsymbol{\upsilon}(t_N)]$.

In fact, the signals only impinge on the array from limited directions. In order to utilize the sparsity characteristics, we partition the potential space of the incident signals with $\boldsymbol{\Psi}=[\theta_1,\ldots,\theta_P]$ and the direction set is $\boldsymbol{\Phi}=[\mathbf{a}(\theta_1),\ldots,\mathbf{a}(\theta_P)]$. Generally, the cardinality of the direction set is much larger than the antenna number and the dictionary is overcomplete. When substituting $\boldsymbol{\Phi}$ for $\mathbf{A}(\boldsymbol{\theta})$, (1) can be rewritten as

$$\mathbf{Y}=\boldsymbol{\Phi}\mathbf{X}+\mathbf{V} \tag{2}$$

where $\mathbf{X}=[\boldsymbol{\rho}(t_1),\ldots,\boldsymbol{\rho}(t_N)]\in C^{P\times N}$ is sparse matrix with K non-zero rows. Then signal direction can be derived by scanning the location of non-zero rows in sparse matrix. When $P\gg K$ the waveform matrix $\mathbf{X}$ presents sparsity characteristics which can be solved by sparsity recovery.

3 Spatial Filtering for Signal Separation

3.1 Sparse Matrix Estimation

The likelihood function of $\boldsymbol{\rho}(t_n)\in C^{P\times 1}$ is

$$P\left(\mathbf{y}(t_n)|\boldsymbol{\rho}(t_n),\sigma^2\right)=\left(2\pi\sigma^2\right)^{-M/2}\exp\left[-\frac{1}{2\sigma^2}\left(\mathbf{y}(t_n)-\boldsymbol{\Phi}\boldsymbol{\rho}(t_n)\right)^H\left(\mathbf{y}(t_n)-\boldsymbol{\Phi}\boldsymbol{\rho}(t_n)\right)\right] \tag{3}$$

To complete the structure of hierarchical prior, we define the individual hyperparameter $\alpha_p(p=1,\ldots,P)$ to independently moderate the strength of each row in sparse matrix $\mathbf{X}$. Suppose that the column $\boldsymbol{\rho}(t_n)$ is Gaussian distributed, i.e., $\boldsymbol{\rho}(t_n)\sim CN(0,\boldsymbol{\Gamma})$ and $\boldsymbol{\Gamma}=\mathrm{diag}\left(\alpha_1,\ldots,\alpha_P\right)$. Then the probability of $\mathbf{X}$ with respect to $\boldsymbol{\Gamma}$ and σ^2 can be derived by Bayesian criterion as follows

$$P\left(\mathbf{X}|\mathbf{Y},\boldsymbol{\Gamma},\sigma^2\right)=(2\pi)^{-NP/2}|\boldsymbol{\Sigma}|^{-N/2}\exp\left[-\frac{1}{2}\sum_{n=1}^{N}\left(\boldsymbol{\rho}(t_n)-\boldsymbol{\mu}_n\right)^H\boldsymbol{\Sigma}^{-1}\left(\boldsymbol{\rho}(t_n)-\boldsymbol{\mu}_n\right)\right] \tag{4}$$

where $\boldsymbol{\Sigma}_t=\sigma^2\mathbf{I}+\boldsymbol{\Phi}\boldsymbol{\Gamma}\boldsymbol{\Phi}^H$, the posterior covariance and mean are, respectively

$$\boldsymbol{\Sigma}=\left(\sigma^{-2}\boldsymbol{\Phi}^H\boldsymbol{\Phi}+\boldsymbol{\Gamma}^{-1}\right)^{-1}=\boldsymbol{\Gamma}-\boldsymbol{\Gamma}\boldsymbol{\Phi}^H\boldsymbol{\Sigma}_t^{-1}\boldsymbol{\Phi}\boldsymbol{\Gamma} \tag{5}$$

$$\boldsymbol{\Lambda}=[\boldsymbol{\mu}_1,\ldots,\boldsymbol{\mu}_N]=\boldsymbol{\Gamma}\boldsymbol{\Phi}^H\boldsymbol{\Sigma}_t^{-1}[\mathbf{y}_1,\ldots,\mathbf{y}_N] \tag{6}$$

We regard posterior mean $\mathbf{\Lambda}$ as the sparse matrix estimate which is directly influenced by $\mathbf{\Gamma}$. SBL estimates $\mathbf{\Gamma}$ by maximizing the marginal likelihood known as type-II maximum likelihood method. The EM algorithm is an iterative method to implement the maximum likelihood estimation. The E-step step is derived by calculating the conditional mean according to $E_{\mathbf{X}} \ln P(\mathbf{Y}, \mathbf{X}|\mathbf{\Gamma}, \sigma^2)$. The M-step is expressed via the update rule [10]

$$\alpha_p^{(\text{new})} = \frac{1}{N}\left\|\mathbf{\Lambda}_p\right\|_2^2 + \mathbf{\Sigma}_{pp}, \quad \forall\, p = 1, \ldots, P \tag{7}$$

$$\left(\sigma^2\right)^{(\text{new})} = \frac{\frac{1}{N}\left\|\mathbf{Y} - \mathbf{\Phi}\mathbf{\Lambda}\right\|_F^2}{M - P + \sum_{p=1}^{P} \frac{\Sigma_{pp}}{\alpha_p^{(\text{new})}}} \tag{8}$$

where $\mathbf{\Lambda}_p$ is the pth row of $\mathbf{\Lambda}$ at last iteration and $\mathbf{\Sigma}_{pp}$ is the pth diagonal value of $\mathbf{\Sigma}$. Essentially the learning processing is composed of two steps. Firstly we calculate posterior covariance and mean based on (5) and (6), then update parameters based on (7) and (8). The iteration will stop when reaching the final convergence criterion.

3.2 Spatial Filters Design

The K spatial filters aim to separate the signals in space domain based on the DOA estimates. Define the kth spatial filter by $\mathbf{T}_k (k = 1, \ldots, K)$. The most intuitive expression of output filtered by $\mathbf{T}_k$ can be written by

$$\mathbf{T}_k\mathbf{X} = \mathbf{T}_k\mathbf{A}(\boldsymbol{\theta}) \begin{bmatrix} \mathbf{s}_1(t) \\ \vdots \\ \mathbf{s}_K(t) \end{bmatrix} + \mathbf{T}_k\mathbf{V} = \begin{bmatrix} \mathbf{s}_k(t) \\ \vdots \\ \mathbf{s}_k(t) \end{bmatrix} + \mathbf{T}_k\mathbf{V} \tag{9}$$

From the above equation, we aim to obtain sufficient samples of signal $\mathbf{s}_k(t)$ for further processing. In this subsection, we utilize the subarray composed of K successive antennas to filter each sample of the kth signal. Denote the partial responding matrix consisting of the mth to $(m + K - 1)$th rows of the original matrix $\mathbf{A}(\boldsymbol{\theta})$ by $\mathbf{A}_m(\boldsymbol{\theta})$ $(m = 1, \ldots, M - K + 1)$, and inverse matrix by $\mathbf{B}_m(\boldsymbol{\theta}) = [\mathbf{A}_m(\boldsymbol{\theta})]^{-1}$, with its kth row denoted by $\mathbf{b}_m^{(k)} \in C^{1\times K}$, then

$$\mathbf{B}_m(\boldsymbol{\theta})\mathbf{A}_m(\boldsymbol{\theta})\mathbf{S} = \begin{bmatrix} \mathbf{b}_m^{(1)} \\ \vdots \\ \mathbf{b}_m^{(K)} \end{bmatrix} \mathbf{A}_m(\boldsymbol{\theta})\mathbf{S} = \mathbf{S} \tag{10}$$

where $\mathbf{b}_m^{(k)}\mathbf{A}_m(\boldsymbol{\theta})\mathbf{S} = \mathbf{s}_k$, indicating that kth row of $\mathbf{B}_m(\boldsymbol{\theta})$ can filter kth signal from the sources impinging onto array. Then the kth spatial filter $\mathbf{T}_k \in C^{(M-K+1)\times M}$ can

be designed by $(\mathbf{T}_k)_{m\bullet} = \left[\mathbf{0}_{1\times(m-1)}, \mathbf{b}_m^{(k)}, \mathbf{0}_{1\times(M-K+1-m)}\right]$. The kth spatial filter output $\mathbf{u}_k \in C^{(M-K+1)\times N}$ is

$$\mathbf{u}_k = \mathbf{T}_k\mathbf{A}(\boldsymbol{\theta})\begin{bmatrix}\mathbf{s}_1(t)\\ \vdots \\ \mathbf{s}_K(t)\end{bmatrix} + \mathbf{T}_k\mathbf{V} = \begin{bmatrix}\mathbf{b}_1^{(k)}\mathbf{A}_1(\boldsymbol{\theta})\\ \vdots \\ \mathbf{b}_{M-K+1}^{(k)}\mathbf{A}_{M-K+1}(\boldsymbol{\theta})\end{bmatrix}\begin{bmatrix}\mathbf{s}_1(t)\\ \vdots \\ \mathbf{s}_K(t)\end{bmatrix} + \mathbf{T}_k\mathbf{V} = \begin{bmatrix}\mathbf{s}_k(t)\\ \vdots \\ \mathbf{s}_k(t)\end{bmatrix} + \mathbf{T}_k\mathbf{V} \tag{11}$$

It can be inferred from the above equation that the output $\mathbf{u}_k$ through kth spatial filter $\mathbf{T}_k$ contains the kth signal and effectively eliminates the other signals. Furthermore, each row in $\mathbf{u}_k$ represents the identical kth signal $\mathbf{s}_k(t)$, indicating that every subarray consisting of K successive antennas can spatially filter the signal. It ends up with $M - K + 1$ identical signals and then we formulate the kth signal estimation as

$$\tilde{\mathbf{s}}_k(t) = \frac{1}{M-K+1}\sum_{j=1}^{M-K+1}(\mathbf{u}_k)_{j\cdot} \tag{12}$$

where $(\mathbf{u}_k)_{j\cdot}$ is the jth row of the output $\mathbf{u}_k$. Similar to diversity processing, it can be concluded that (12) can decrease noise power and improve filtering performance.

3.3 Overall Scheme of the New Method

During the above procedure, the design of the spatial filter relies on accurate matrix estimate and directly influences the algorithm performance. Therefore, a refined DOA estimation should be introduced to obtain the accurate value iteratively until it satisfies the convergence criterion.

Remark 1 Denote the signal passed through the kth spatial filter in qth iteration by $\tilde{\mathbf{s}}_k^{(q)}(t)$. The iteration satisfies the convergence criterion when the difference of signal filtered in the qth iteration and $(q + 1)$th iteration is smaller than a fixed threshold ε_1. We set the convergence criterion as

$$\sum_{k=1}^{K}\left\|\tilde{\mathbf{s}}_k^{(q+1)}(t) - \tilde{\mathbf{s}}_k^{(q)}(t)\right\|^2 < \varepsilon_1 \tag{13}$$

Remark 2 To obtain coarse DOA estimates, the potential space of the incident signals is divided into P samples in the initialization step. However, the coarse sampling cannot promise to include the actual DOA into the direction set which results in inaccurate DOA estimates. In the simulation, the mismatch of direction set leads to cluster peak emerging beside the real value. Therefore, we propose a probabilistic method to redesign the direction set. Denote the DOA estimate of the

kth signal in qth iteration by $\theta_k^{(q)}$ and the direction set in $(q+1)$th iteration is updated by $\boldsymbol{\Psi}^{(q+1)} = \left[\boldsymbol{\beta}_1^{(q+1)}, \ldots, \boldsymbol{\beta}_K^{(q+1)}\right]$. $\boldsymbol{\beta}_k^{(q+1)} \sim \mathrm{N}\left(\theta_k^{(q)}, \sigma_\varphi^2\right)$ is a sub-dictionary with σ_φ^2 being the perturbation variance.

4 Simulation Results

Consider a uniform linear array with 16 half-wavelength spaced antennas and two signals modulated with binary-phase-shift-keying (BPSK) arrive from 30° and 60°, respectively. The carrier frequency is set to 5 MHz and the sampling frequency is set to 15 MHz. The baud rates are 1 MHz and 0.6 MHz, respectively. In the initialization step, the sparsity-inducing space is sampled form 0° to 180° with 2° interval to obtain the direction set $\boldsymbol{\Psi}$. The threshold ε_1 and the perturbation variance σ_φ^2 are set to 0.01 and 0.05 respectively.

In the initialization, we sample the potential space uniformly to obtain the coarse estimates and refine the dictionary set for the next iteration. The performance of DOA estimates versus iteration index is demonstrated to prove the effectivity of proposed method. 300 independent simulations are carried out. The average root-mean-square-error (RMSE) in qth iteration is defined as

$$\mathrm{RMSE}^{(q)} = \sqrt{\sum_{w=1}^{W}\sum_{k=1}^{K}\left(\theta_k^{(w,q)} - \theta_k\right)^2 / KW} \tag{14}$$

where $\tilde{\theta}_k^{(w,q)}$ is the DOA estimate in qth iteration and θ_k is the actual value. The signal-to-noise ratio (SNR) is set to 0 dB for both of the signals. In Fig. 1, the simulation result indicates that the estimation performance improves with respect to

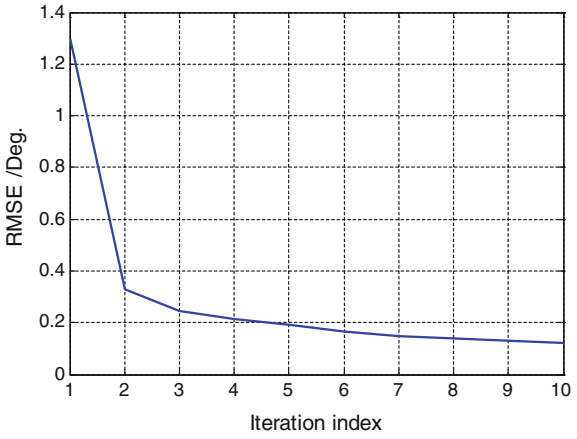

Fig. 1 DOA estimation RMSE versus iteration index

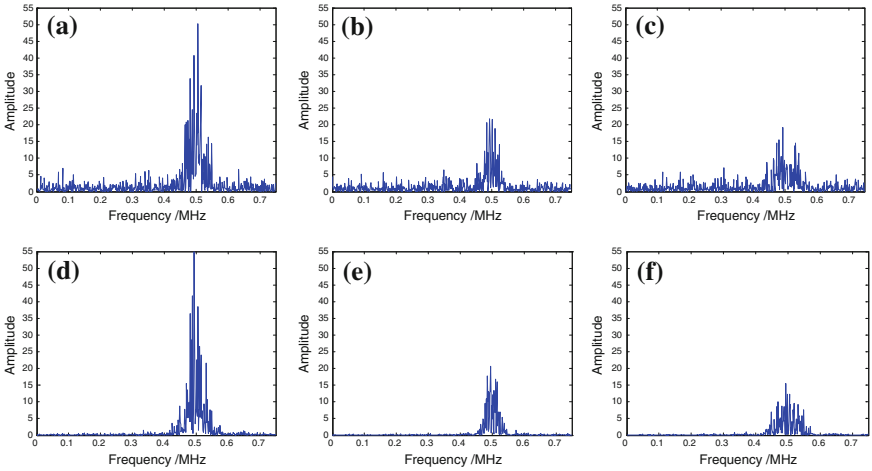

Fig. 2 Power spectrum of signals: **a** original signals; **b** original signal 1; **c** original signal 2; **d** filtered signals; **e** filtered signal 1; **f** filtered signal 2

increased iteration index. The RMSE of DOA becomes stable when iteration index reaches to 7.

Figure 2 demonstrates the spectrum of original signals and filtered signals when satisfying the stop criterion. Figure 2b, c show two original signals that arrive at the array and Fig. 2a is the sum of two original signals. From Fig. 2e, f, it is obviously that the spatial filters based on final direction estimates can effectively separate two signals and as a result of (12) the noise power is decreased distinctly.

The performance of signal separation by different algorithms is to be demonstrated. The signal-to-interference-plus-noise ratio (SINR) of all the incident signals is used for precision evaluation. In this subsection SNR is changing from −30 to 30 dB for both of the signals. 75 snapshots are collected and 300 independent simulations are carried out in each scenario. We define signal from $\theta_e = 30°$ as expected signal $\mathbf{s}_e$ and signal from $\theta_i = 60°$ as interference $\mathbf{s}_i$. Then we evaluate the performance of spatial filter $\mathbf{T}_e$ designed for expected signal. The SINR of the proposed spatial filter is defined as

$$\mathrm{SINR} = \frac{\left\| \sum_{j=1}^{M-K+1} \left[\mathbf{T}_e\, \mathbf{a}(\theta_e)\, \mathbf{s}_e\right]_{j\cdot} \right\|^2}{\left\| \sum_{j=1}^{M-K+1} \left[\mathbf{T}_e\, \mathbf{a}(\theta_i)\, \mathbf{s}_i\right]_{j\cdot} \right\|^2 + \left\| \sum_{j=1}^{M-K+1} \left(\mathbf{T}_e \mathbf{V}\right)_{j\cdot} \right\|^2} \tag{15}$$

Figure 3 demonstrates the performance of the proposed method based on the spatial filter (SF), Stimulate Covariance Matrix Inversing (SMI) algorithm, and Eigenspace-Based (ESB) algorithm. The SNR of expected signal and the interference is identical in each scenario. The performance of SMI deteriorates because the power of expected signal is high. The performance of ESB under high SNR surpasses SMI. However, the performance of ESB under low SNR is not satisfactory.

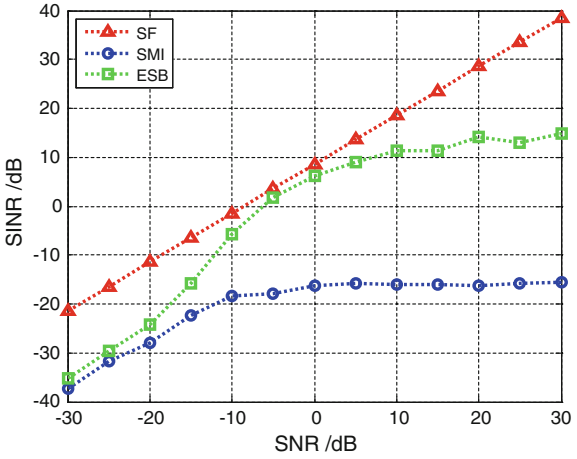

Fig. 3 Performance evaluation of different algorithms

By contrast, the spatial filter can increase SINR and outperforms the subspace-based algorithms remarkably.

5 Conclusions

In this paper, we proposed a novel method to separate signals devised by the combination of SBL algorithm and spatial filters. The SBL algorithm is utilized to estimate the directions without any prior information or characteristic of signals. We design spatial filters based on direction of each signal to achieve efficient separation. The filtering outputs obtain sufficient samples which can be used to calculate the mean values of each signal with the noise power reduced extremely. The simulation results indicate that the proposed algorithm can spatially filter the signals and outperform existing subspace-based algorithms.

References

1. Kumihashi I, Sekihara K (2010) Array-gain constraint minimum-norm spatial filter with recursively updated gram matrix for biomagnetic source imaging. IEEE Trans Bio Med Eng 57(6):1358–1365
2. Hahne JM, Graimann B, Muller K (2012) Spatial filtering for robust myoelectric control. IEEE Trans Bio Med Eng 59(5):1436–1443
3. Ghaderi F (2013) joint spatial and spectral filter estimation for single trial detection of event related potentials. IEEE International workshop on machine learning for signal processing. IEEE Press, Southampton, pp 1–6

4. Sudhakar MV, Mallikarjuna Reddy Y, Prabhakara Rao B (2013) Analysis of spatial filtering to enhance transmission capability of single mode optical fibers. In: International conference on information communication and embedded systems. IEEE Press, Irbid, pp 619–622
5. Hong H, Mao X-P, Hu C, Guo R, Deng W-B, Jiang P (2013) Narrow-band null phase-shift spatial filter based on oblique projection. In: Radar conference. IEEE Press, Ottawa, pp 1–5
6. MacInnes CS (2004) Source localization using subspace estimation and spatial filtering. IEEE J Oceanic Eng 29(2):488–497
7. Jones NA, Hum SV (2013) An ultra-wideband spatial filter for time-of-arrival localization in tunnels. IEEE Trans Antennas Propag 61(10):5237–5248
8. Bhotto MZA, Bajic IV (2015) Constant modulus blind adaptive beamforming based on unscented Kalman filtering. IEEE Signal Process Lett 22(4):474–478
9. Lee J, Huang C (2009) Blind adaptive beamforming for cyclostationary signals: a subspace projection approach. IEEE Signal Process Lett 8(4):1406–1409
10. Wipf DP, Rao BD (2007) An empirical bayesian strategy for solving the simultaneous sparse approximation problem. IEEE Trans Signal Process 55(7):3704–3716

Function Optimization via a Continuous Action-Set Reinforcement Learning Automata Model

Ying Guo, Hao Ge, Fanming Wang, Yuyang Huang and Shenghong Li

Abstract Learning automata as a tool for machine learning, could search the optimal state adaptively in random environment. Function optimization is a fundamental issue and many practical models are ultimately the mathematical optimization problems. In this paper, we apply the basic continuous action-set reinforcement learning automata (CARLA) model to function optimization. An application model called equiCARLA is constructed by means of equidistant discretization and linear interpolation, and it presents a superiority over the existing algorithms not only in speed but also in precision. The experimental results demonstrate the effectiveness and efficiency of our model for function optimization.

Keywords Function optimization · CARLA · Equidistant discretization · Linear interpolation

1 Introduction

Methods for function optimization have achieved a revival with the steepest descent method, Newtons method, conjugate gradient method and quasi-Newton method proposed in succession [1]. For all these methods there is a common requirement,

Y. Guo (✉) · H. Ge · S. Li
Department of Electronic Engineering, Shanghai Jiao Tong University, Shanghai, China
e-mail: guoying2014vip@sjtu.edu.cn

H. Ge
e-mail: sjtu_gehao@sjtu.edu.cn

S. Li
e-mail: shli@sjtu.edu.cn

F. Wang
Riffle Institute, Singapore, Singapore
e-mail: fanmingwang@gmail.com.sg

Y. Huang
Shanghai Starriver Bilingual School, Shanghai, China
e-mail: markhuanghyy@outlook.com

Q. Liang et al. (eds.), *Proceedings of the 2015 International Conference on Communications, Signal Processing, and Systems*, Lecture Notes in Electrical Engineering 386, DOI 10.1007/978-3-662-49831-6_102

that is, the gradient ∇f is supposed to be explicitly available. Usually in most real situations, the lack of sufficient information concerning the structure of function f makes optimization a challenging task. So does the complexity of mathematical computation. In this case, a number of limitations are exposed when adopting these classical methods.

Motivated by the shortcomings of the aforementioned algorithms, recent scholars increasingly focus on modeling the optimization problem whose function expression is unknown. Among the multiple solutions, learning automata-based algorithms are one of the most promising means and attract extensive research efforts [2]. Learning automata, an adaptive decision device that interacts with an unknown random environment, has a range of applications in past publications [3–5]. In this paper, we are dedicated to applying the concept of *learning automata* to solve the *function optimization* problems.

2 Related Work

Generally, LA can be divided into two types, i.e., finite action-set learning automaton (FALA) and continuous action-set learning automaton (CALA) [6]. When FALA is used for function optimization, one needs to discretize the parameter space[1] so that actions of LA can be possible values of the corresponding parameter. The accuracy of the solution is increased by choosing the finer discretization and hence increasing the number of actions of LA. However, increasing the number of actions leads to slow convergence of the learning algorithm [7]. A more satisfying solution would be to employ CALA. And several CALA algorithms for function optimization have been developed during past years.

The earliest CALA algorithm is given by Santharam et al. [8]. In his model, the action probability distribution $P(n)$ is a normal distribution with mean μ_n and standard deviation σ_n. Given a pair of initial parameters (μ_0, σ_0), $N(\mu_n, \sigma_n)$ eventually converges to $N(\alpha^*, \sigma_l)$ after a period of time. α^* is the optimum of function f and σ_l is a sufficiently small number. However, the experiments with regard to function optimization reveal that the performance of CALA closely depends on its initial parameters.

Beigy et al. presented a new CALA algorithm in 2006 [9]. The updating rules of μ_n and σ_n are modified on the basis of Santharam's algorithm. However, in [10] the authors asserted that Beigy's algorithm is unable to converge as expected when programming to optimize a function, and they subsequently proposed a refined vision called ASCALA to fill the flaw. But in this algorithm the function to be optimized may get stuck in its local optimal area.

[1] The parameter space is the scope where we search for an optimum.

Another CALA algorithm is shown in [11], and we denote it as CARLA. The author put forward this novel model, applying it to vehicle suspension control. Since we believe LA is a fabulous tool to solve the optimization problems, we apply it to function optimization in the following section.

3 Our Model

3.1 Basic CARLA Model

This section presents the exhaustive procedures of the basic CARLA model.

- Initialization. The initial probability $p_\alpha(0)$ is uniformly distributed.

$$p_\alpha(0) = \frac{1}{\alpha_l - \alpha_s}, \ \forall \alpha \in (\alpha_s, \alpha_l] \tag{1}$$

- Action Selection. A normalized and uniformly distributed random number p^* is produced, then action selection at any instant $\alpha(n)$ is achieved via the cumulative probability function.

$$p^* = \int_{\alpha_s}^{\alpha(n)} p_\alpha(n) d\alpha \tag{2}$$

- Environment Feedback. The feedback by Env $\beta(n)$ depends on the current and previous function evaluations. From Eq. (3) we can see that if $g(.)$ obtains its minimum, Env will trigger a feedback $\beta = 1$ and reward the selected action to maximum extend. It could efficiently solve a minimizing problem.

$$\beta(n) = max \left\{ 0, \frac{G_{med} - g(n)}{G_{med} - G_{min}} \right\} \tag{3}$$

- Probability Updating.[2] The probability function $P_\alpha(n)$ is changed based on the rule in Eq. (4). Here λ and σ are parameters, which could be defined in terms of the range of actions, namely $\lambda = \frac{g_h}{\alpha_l - \alpha_s}$ and $\sigma = g_w(\alpha_l - \alpha_s)$. γ is a normalization factor to ensure the property of a standard probability density function.

$$p_\alpha(n+1) = \gamma \left\{ p_\alpha(n) + \beta(n)\lambda exp \left\{ -\frac{[\alpha - \alpha(n)]^2}{2\sigma^2} \right\} \right\}, \ \forall \alpha \in (\alpha_s, \alpha_l] \tag{4}$$

[2]Consider a minimizing problem here. G is a dynamic set containing function evaluations to be minimized. G_{med} and G_{min} are median and minimum values in the set G. $g(n)$ is the evaluation of function g(.) at the time n. Due to the negative correlation between $g(n)$ and $\beta(n)$, *min* $g(.)$ is equivalent to *max* $E(\beta|\alpha)$. That is what the learning objective of LA is.

Now we make an intuitive explanation for the learning algorithm above. Since the increasing component of $P_\alpha(n)$ is a Gaussian neighbourhood function centered on the selected action $\alpha = \alpha(n)$, the selected action will get the largest increase in its choosing probability. And the greater it is rewarded by Env, the greater it will increase. On the other hand, an increased probability for the selected action means more chances of being selected again in the next cycle. This repeated mechanism eventually results in a convergence to the optimal action.

3.2 Application Model

In this section, we apply the basic CARLA model to function optimization and construct an application model. Due to the inability for a computer to deal with infinite datas on practical implementation, in this paper we utilize the technique of *discretization*. Moreover, *interpolation* is adopted so as to keep the property of continuous action-set. Therefore, the application model is a combination of discretization and interpolation. There are mainly two ways of discretization: equidistance and equifrequency [12]. The former could maintain the original distribution of data, so we choose equidistant discretization in our application model. Interpolation consists of linear interpolation, quadratic interpolation, etc. [13], and the simplest one, i.e., linear interpolation is used in this paper.

Specifically, any continuous variable such as action-set A or probability function $P(t)$ is discreted into some points, whose distances to its neighbour are equal. We call them the sampling points while others are denoted as non-sampling points. When optimizing a function, the first step is to get the sampling points by discretizing. Then we handle the sampling points in the same way as the basic CARLA model. And for non-sampling points we obtain their values by means of linear interpolation. A plain instruction about the application model is shown in Fig. 1.

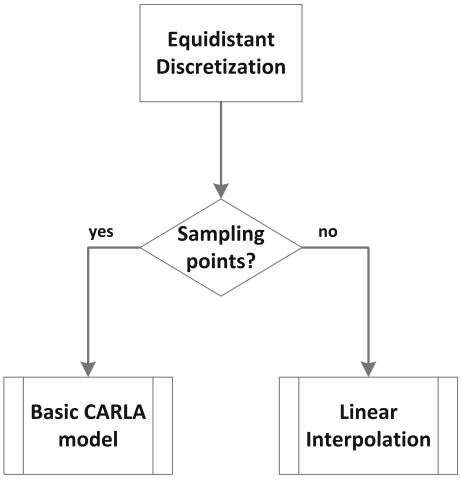

Fig. 1 The application model. We denote it as equiCARLA where equi is short for equidistant discretization

4 Experiments and Analysis

4.1 Experimental Environment

To test and verify our model, we consider the penalized Shubert function, which is one of the benchmark problems to test global optimization algorithms. The function has 19 minima, but only three are global optimal points. The global minimum evaluation is −12.8709.

$$F(x) = \sum_{i=1}^{5} icos((i+1)x+1) + u(x, 10, 100, 2) \tag{5}$$

where

$$u(x, b, k, m) = \begin{cases} k(x-b)^m, & x > b \\ 0, & |x| \le b \\ k(-x-b)^m, & x < -b \end{cases} \tag{6}$$

Our model is aimed at modeling the optimization problems in the circumstances that the only information is the function evaluation at the chosen point. In engineering, the function evaluation is usually a noise-corrupted value. Therefore, we set up three groups of experiments: noiseless, uniform noise $U(-0.5, 0.5)$ added to $F(.)$, Gaussian noise $N(0, 0.1)$ added to $F(.)$. The corresponding observed evaluations at a certain moment are $g(n) = F(.)$, $g(n) = F(.) + U(-0.5, 0.5)$, and $g(n) = F(.) + N(0, 0.1)$, respectively.

4.2 Parameter Setting

- g_h—The parameter in the probability updating equation determining: 0.3
- g_w—The parameter in the probability updating equation determining σ: 0.02
- $(\alpha_s, \alpha_l]$—The initial interval for action selection: (0,10]
- *Iters*—The overall number of iterations: 1000
- *Nums*—The number of repeated time of an experiment: 1000
- N—The number of sampling points for the equiCARLA model: 100

4.3 Evaluation Criterion

4.3.1 The Average Results (*ave*)

We carried out 1000 repeated experiments, so 1000 results is averaged to get *ave*. An ideal situation is that $ave = -12.8709$.

$$ave = \frac{\sum_{i=1}^{Nums} Res(i)}{Nums} \tag{7}$$

4.3.2 The Number of Global Convergence ($\sharp$ *gol*)

If any final result lies in the scope of $[-12.8709, -12.8709 + \varepsilon]$, where ε is a predefined noise margin, we claim that this result converges to its global minimum. So $\sharp$ *gol* is computed after finishing 1000 experiments according to the equation below. We choose 0.2 as the noise margin in our model to evaluate its capability.

$$\sharp gol = \sum_{i=1}^{Nums} D(i),\ D(i) = \begin{cases} 1,\ Res(i) \in [-12.8709, -12.8709 + \varepsilon] \\ 0,\ Res(i) \notin [-12.8709, -12.8709 + \varepsilon] \end{cases} \tag{8}$$

4.3.3 Root-mean-square Error (*RMSE*)

RMSE is a common index to measure the deviation of the result and the objective value.

$$RMSE = \sqrt{\frac{\sum_{i=1}^{Nums} [Res(i) - (-12.8709)]^2}{Nums}} \tag{9}$$

4.4 Experimental Results

Table 1 presents the results of *ave* and $\sharp$ *gol* over 1000 experiments for CALA and ASCALA. As a contrast, Table 2 shows the same index of the application model in Sect. 3.2, i.e., the equiCARLA model. The performance of CALA is susceptible to its initial parameters (μ_0, σ_0). Once the parameters are chosen unsuitably, it will be a terrible failure. For example, in case 1 with no noise, the *ave* is equal to -2.95168 and the $\sharp$ *gol* is only 19, far away from our target. ASCALA is superior to CALA to a certain extent, but a local minimum convergence rather than a global one is still inevitable. However, when employing equiCARLA model, both the noiseless and the noised scenarios display obvious advantages over the original algorithms. All the *ave*

Table 1 The *ave* and the ♯ *gol* over 1000 experiments (each consisting of 8000 iterations) for CALA, ASCALA

Case	No noise				Uniform noise $U(-0.5, 0.5)$				Gaussian noise $N(0, 0.1)$			
	CALA		ASCALA		CALA		ASCALA		CALA		ASCALA	
	ave	♯ *glo*	*ave*	♯ *glo*	*ave*	♯ *glo*	*ave*	♯ *glo*	*ave*	♯ *glo*	*ave*	♯ *glo*
1	−2.95168	19	−11.5481	793	−2.68737	3	−10.1912	594	−2.75491	5	−9.97313	573
2	−4.38881	136	−9.97655	523	−12.7478	834	−12.5041	952	−12.8534	999	−12.4701	943
3	−8.57354	81	−10.4651	519	−11.764	644	−11.6355	809	−11.7197	761	−11.6545	815
4	−11.3576	761	−8.48706	387	−7.42936	374	−9.61443	570	−7.27992	418	−9.60872	580
5	−11.9364	878	−11.6604	826	−8.11979	18	−10.4232	502	−8.16983	23	−10.4555	497
6	−10.462	537	−8.90681	422	−9.4282	213	−9.81494	510	−9.54619	256	−9.94501	520

Different cases represent different initial parameters μ_0 and σ_0. For the noiseless scenario, (μ_0, σ_0) in case 1–6 is equal to (3, 5), (3, 6), $(-10, 5)$, $(-10, 7)$, (10, 5) and (10, 7), respectively. And for the noised scenario, from the top-down they are (4, 6), (8, 3), (8, 5), (12, 6), $(-10, 5)$, $(-10, 6)$

Table 2 The *ave* and the ♯ *gol* over 1000 experiments (each consisting of 1000 iterations) for equiCARLA

Scenario	equiCARLA	
	ave	♯ *glo*
No noise	−12.3691	919
Uniform noise $U(-0.5, 0.5)$	−12.416	911
Gaussian noise $N(0, 0.1)$	−12.3491	907

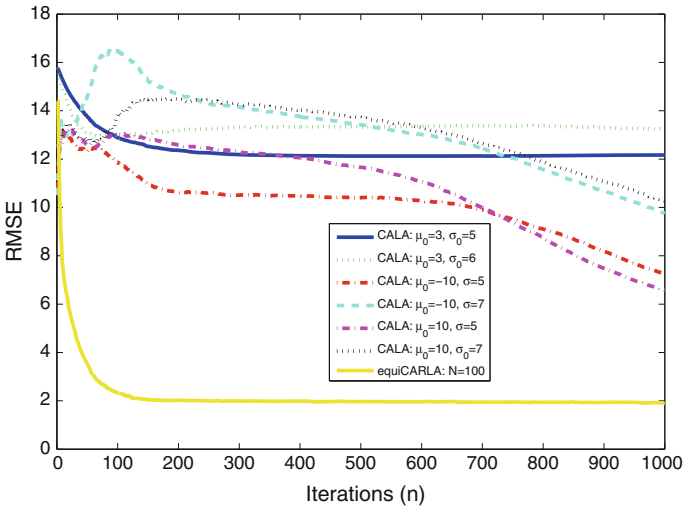

Fig. 2 The *RMSE curve* varied with iterations for CALA and equiCARLA in the noiseless scenario

is less then −12.34 and the ♯ *gol* surpasses 900. What's more, the equiCARLA model could achieve such an effect in just 1000 iterations while it requires 8000 iterations for CALA and ASCALA.

Figure 2 is a more perspective contrast. Taking the noiseless scenario for a case, the equiCARLA model converges in about 100 iterations, and the final *RMSE* is approximately 2. But for CALA, the *RMSE* is changing all the time. In addition, no matter what the initial parameters of CALA are, the *RMSE* curves are always above the equiCARLA's. From what has been discussed above, we may conclude that equiCARLA precedes CALA not only in precision but in speed.

5 Conclusion

In this paper, we apply the basic CARLA model to function optimization and construct an application model. The core in this model is the combination of equidistant discretization and linear interpolation. Once equidistant discretization has been fin-

ished, the sampling points are dealt with the basic CARLA model, but for the non-sampling points the linear interpolation technique is taken into consideration. Compared with the existing algorithms, the learning process of the new model becomes accelerated and constantly precise, presenting a superiority both in speed and in precision. The experimental results demonstrate the effectiveness and efficiency of our model for function optimization. In further study, other discretization and interpolation techniques may be some novel research directions.

Acknowledgments This research work is funded by the National Science Foundation of China (61271316), 973 Program of China (2013CB329605), Shanghai Key Laboratory of Integrated Administration Technologies for Information Security.

References

1. Yuan Y, Sun W (1997) Optimization theory and methods. Science Press, Beijing
2. Najim K, Poznyak AS (2014) Learning automata: theory and applications, Elsevier
3. Misra S, Krishna PV, Kalaiselvan K, Saritha V, Obaidat MS (2014) Learning automata-based Qos framework for cloud Iaas. IEEE Trans Netw Serv Manag 11(1):15–24
4. Misra S, Krishna PV, Saritha V, Obaidat MS (2013) Learning automata as a utility for power management in smart grids. IEEE Commun Mag 51(1):98–104
5. Rezvanian A, Rahmati M, Meybodi MR (2014) Sampling from complex networks using distributed learning automata. Phys A Stat Mech Appl 396:224–234
6. Thathachar M, Sastry PS (2002) Varieties of learning automata: an overview. IEEE Trans Syst Man Cybern Part B Cybern 32(6):711–722
7. Beigy H, Meybodi M (2005) Stochastic optimization using continuous action-set learning automata. Sci Iran 12(1):14–25
8. Santharam G, Sastry P, Thathachar M (1994) Continuous action set learning automata for stochastic optimization. J Frankl Inst 331(5):607–628
9. Beigy H, Meybodi M (2006) A new continuous action-set learning automaton for function optimization. J Frankl Inst 343(1):27–47
10. Guo Y, Ge H, Yan Y, Huang YY, Li SH (2015) A new continuous action-set learning automaton for function optimization. In publishing
11. Howell MN, Frost GP, Gordon TJ, Wu QH (1997) Continuous action reinforcement learning applied to vehicle suspension control. Mechatronics 7(3):263–276
12. Rabaseda S, Rakotomalala R, Sebban M (1996) A comparison of some contextual discretization methods. Inf Sci 92(1):137–157
13. https://en.wikipedia.org/wiki/Interpolation. Accessed August 2015

Quality Test and Track System Based on Neural Network

Lu Yao, Zhou Hailiang, Guo Jingtao, Shi Xin and Wang Xigang

Abstract This paper researched a hot rolling product's quality test expert system which was on the basics of radial basis function (RBF) neural network combined with quality-trace. Due to the insufficiency in the explanation facility of the conventional neural network expert system while it also could not afford the process of reasoning, this paper raises a new method which combined four RBF neural networks while it used Multiquadratic Functions as its kernel function. Besides, according to the characteristic of the products in Steel & Iron Industry, this paper takes combined neural network in the part of physical properties test. In order to solve the insufficiency in explanation facility of the conventional neural network expert system this system makes quality-trace after it judged the four results from the four neural networks.

Keywords RBF neural network · Multiquadratic · Quality-trace

1 Introduction

In the torrent of economic development in the society, the development of Steel & Iron Industry experiences reformations on the technology again and again. At the same time, the conventional concept of the quality in Steel & Iron Industry has changed a lot. Quality assurance system (QAS) is now gradually becoming the target of enterprises' work and the focus from the social attention. At present, the characteristic in the metallurgy industry has changed its direction. Now it requires strict quality specifications of the products. There are strict quality-traces and quality test in the whole productive process. And the enterprise must afford its clienteles with corresponding quality certificates. So, quality control takes the more important position in the Steel & Iron Industry. And the most pivotal technology to realize quality control is quality test. In this part we need to analyze the reason of

L. Yao (✉) · Z. Hailiang · G. Jingtao · S. Xin · W. Xigang
Tianjin Institute of Metrological Supervision and Testing, Tianjin, China
e-mail: 13820204398@163.com

Q. Liang et al. (eds.), *Proceedings of the 2015 International Conference on Communications, Signal Processing, and Systems*, Lecture Notes in Electrical Engineering 386, DOI 10.1007/978-3-662-49831-6_103

the waste products accurately and trace back to the link which leads to the defects. Our final target is to control the quality to the best level. In order to make quality test accurate and intelligent, enterprises use expert system when they test the quality of products. However, in the conventional expert system there are bottleneck problem and low automaticity which restrict the function of it. So, the expert system which combines with neural networks brings quality test to a new stage which develops better.

2 RBF Neural Network in the Basis of Multiquadratic

RBF neural network is a kind of effective feedforward network which has three layers and one of them is hidden layer. Its neurons basis function has a local performance which only produces effective nonzero response on the very small local scale. So it attains high speed in the process of study while it can avoid the default of falling into local optimum in the BP neural network [1–3]. RBF neural network can reflect nonlinear separable problems which exist in low-dimensional subspace to a high-dimensional subspace and makes it linearly separable. In the RBF neural network the neurons in the hidden layer makes the high-dimensional hidden unit space. At the same time, the transfer function in the hidden layer is a nonlinear function. This makes the nonlinear transformation from input space to the hidden unit space. In reference [4] the writer invented a superconducting power supply which makes uses of this characteristic of radial basis function neural networks. In the condition of enough neurons in the hidden layer the input data can be linear separable in the output mode of high-dimensional space. The network topology structure of RBF neural network is shown in the following picture.

This system uses a new RBF neural network which uses Multiquadratic as its kernel function and gradient descent as its training method to test the products. It uses gradient descent to optimize RBF neural network. The details of the training steps refer to reference [5]. The conventional methods all get used to make Gaussian function as its kernel function. But, Multiquadratic has its unique advantages such as highly symmetry, simple form, better smoothness, derivable at any degree and its rate of approach becomes faster near the training center. It can approach an input–output reflection with a higher precision. So, we use Multiquadratic as the activation function of hidden layer. Its main work is to calculate the output of hidden layer unit.

$$h_j = (\|X - c_j\|^2 + b_j^2)^{\frac{1}{2}}, j = 1, 2, \ldots, n \tag{1}$$

In the above formula, h_j is the output of the jth hidden layer unit. $c_j = [c_{j1}, c_{j2}, \ldots, c_{jm}]$ is the center of the jth basis function unit. It is also the centric vector. $b = [b_1, b_2, \ldots, b_n]^T$ is the expand constant or width of the basis function. The smaller the value is, the smaller the width of the basis functions is and the basis

function is more selectable. b_j is a standardization constant whose value is bigger than zero. $W = [w_1, w_2, \ldots, w_n]^T$ is the weight vector of the network.

There are two adjustable parameters in the whole network when we use Multiquadratic as the basis function. They are the center of the function, and the width and the weight of output unit. To RBF neural network the conventional method to ensure the parameters usually is K-means cluster. In reference [6] the writer used RBF neural network to check the defect of slab. He used K-means cluster to confirm the center and width. However, although the K-means cluster can confirm the expand constant according to the distance during every center there are two shortcomings about it: The first is when it confirm the center of data it only uses the input data of the samples but not together with the output data of the samples or the error. The second one is this method cannot conform the numbers of cluster. Gradient descent takes the direction of negative gradient as the direction of descending. It is a kind of minimization arithmetic. And it overcomes the shortcomings in the K-means cluster. It realizes unrestraint optimization with the fastest rate of convergence [7–10].

In Fig. 1 the structure of RBF neural network the input vector $X = [x_1, x_2, \cdots, x_{\mathrm{m}}]$ with its number of the input unit is m. $H = [h_1, h_2, \cdots, h_{\mathrm{n}}]^T$ is the radial basis function vector. In it h_j is the kernel function and we use Multiquadratic as its kernel function, as it is shown in formula (1). The output of RBF neural network is a linear combination of the output of hidden layer unit. It is:

$$\hat{y}(k) = w_1 h_1 + w_2 h_2 + \cdots + w_{\mathrm{n}} h_{\mathrm{n}} \tag{2}$$

From formulas (1) and (2) we could see the parameters we need to confirm in RBF neural network are weight vector W, centric vector c_j, the width B and the number of hidden layer units m.

To the number of hidden layer units there is no specific theory at the moment. We confirm it by experiences at the most cases. To the width B, centric vector c_j and weight vector W we use gradient descent which is on the basis of Delta learning rule to confirm them.

Suppose $y(k)$ is the practical output at the kth moment and the performance index function of the RBF neural network is:

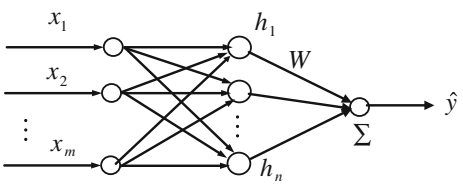

Fig. 1 The structure of conventional RBF neural network

$$\mathrm{E} = \frac{1}{2}\sum_{\mathrm{k}=1}^{m}[y_k - \hat{y}_k]^2 \tag{3}$$

We use gradient descent to adjust W, B, and c_j:

$$w_j(k) = w_j(k-1) + \eta\frac{\partial \mathrm{E}}{\partial w_j(k-1)} + \alpha[w_j(k-1) - w_j(k-2)] \tag{4}$$

Therefore,

$$\begin{aligned}\frac{\partial \mathrm{E}}{\partial w_j(k-1)} &= \sum_{k=1}^{m} e(k-1)\left(\left\|x_j - c_j(k-1)\right\|^2 + b_j^2\right)^{\frac{1}{2}} \\ b_j(k) &= b_j(k-1) + \eta\frac{\partial \mathrm{E}}{\partial b_j(k-1)} + \alpha[b_j(k-1) - b_j(k-2)]\end{aligned} \tag{5}$$

Therefore,

$$\begin{aligned}\frac{\partial \mathrm{E}}{\partial b_j(k-1)} &= \sum_{k=1}^{m} e(k-1)w_j(k-1)\left(\left\|x_j - c_j(k-1)\right\|^2 + b_j^2\right)^{-\frac{1}{2}}\left\|x_j - c_j(k-1)\right\| \\ c_{ji}(k) &= c_{ji}(k-1) + \eta\frac{\partial \mathrm{E}}{\partial c_{ji}(k-1)} + \alpha[c_{ji}(k-1) - c_{ji}(k-2)]\end{aligned} \tag{6}$$

Therefore,

$$\frac{\partial \mathrm{E}}{\partial c_{ji}(k-1)} = \sum_{k=1}^{m} e(k-1)w_j(k-1)\left(\left\|x_j - c_j(k-1)\right\|^2 + b_j^2\right)^{-\frac{1}{2}}b_j(k-1)$$

Therefore, α is the momentum factor, η is the learning rate, and the value of α and η is between 0 and 1.

3 The Hot Rolling Products Quality Test Expert System Using Radial Basis Function (RBF) Neural Network

The RBF neural network can change the nonlinear information in one space into the linear information in another space with the effect of mapping. And in the hot rolling products quality test system the parameters of hot rolling products quality are highly nonlinearly so we need to use the neural network to generate the results which can be understand and accept by the users.

At present the newest method of quality test is to take use of expert system. In conventional expert system the part of knowledge acquisition is accomplished by labour. Workers summarize the knowledge and experiences and then analyze and

trim them. However, by the use of expert system which combines with neural network we do not need labour anymore in disposing those knowledge. What we need to do is only to input the previous examples and parameters into the new system and then train the neural network. After we finish training the neural network the prepared network will dispose these parameters and output the results which are accurately similar with the answers of experts. So it can replace the labour in dealing with some nonlinear problems with a more effective and accurate method [5, 11–13].

The main job of this system is to investigate the relationship between the defects of products and parameters in operations and inspect the quality of the products. And store the parameters of every inspection into the data base of expert system. Then dispose those data in the RBF neural network and sent the results to the transfer layer. After all the steps there will be a final results brought out on the transfer layer (UI).

The hot rolling products quality test expert system mainly detects the chemical properties, physical properties, dimensional accuracy and the quality of surface of the products. It produces the results after the processing of RBF neural network and determines whether the product is an acceptable product or a waste product. The process of quality test is very complex. This system need to input and check dozens of parameters. There are 38 parameters in the part of chemical properties(C) including C, Mn, S, Pi, Si, Ni, Alt, Als, Cu, Ca/Als, etc.; And nine parameters in the part of physical prosperities(P) including yield strength, strength of extension, percentage elongation after fracture, blow-test (under the condition of 20, 0, –20, –40 °C), bending test and etc.; And 9 parameters in the part of dimensional accuracy(D) including the width of edge, the thickness of edge, the arc radius of inside, etc.; And 41 parameters in the part of the surface of the products including silted, edge crack, lapped, indentation, pitting surface, etc.

At present, most methods which the enterprise uses to detect the quality of products is to detect the chemical properties,physical properties,dimensional accuracy, and the quality of surface of the products separately. This leads to low confluent level in every performance index of the products. However, the chemical properties, physical properties, dimensional accuracy, and the quality of surface of the products are related to each other. For example, the reasons which results in the low tensile strength are maybe because there appears inclusion, shrinkage cavity or air bubble in steel. It cannot be welded together very well so as to fissure in the steel. Superficial fissure may cause edge crack or corner crack. Or maybe because of the serious segregation in the chemical composition in steel. When the purity of carbon and other alloying element is too high there maybe difficulty in rolling while it also results in low elongation. It is also easy to result in fissures which make tensile strength low. Besides, the high heating temperature or the long heating time may also results in low tensile strength. So, we can see there is connotative relevance in every parameters of section steel. And chemical properties are almost relevant to physical prosperities directionally. It is the content level of chemical element can influence the parameters of physical properties directly. So we take use of the relativity of chemical–physical prosperities of products to forecast the

physical properties of the products after the process of the neural network to the chemical parameters. This method simplifies the link of instrument detection to physical prosperities and saves amount of manpower and material while it saves the testing cost. When testing the physical properties of section steel we take combined neural network. There are four neural network layers in the whole structure. In the first neural network input part of the first layer input the chemical properties parameters and after the processing in the hidden layer the first neural network output part output the predicted physical properties parameters which form the input part of the second neural network part. After the processing of the hidden layer of the second neural network part the final testing results of physical properties will be outputted in the output part of the second neural network part. The following three neural network layers test the chemical properties parameters, dimensional accuracy parameters and the surface of the products. The structure of the combined neural network is showed in the following figure. In Fig. 2, at the input part of the first neural network layer, x_{c1} to x_{c38} are chemical properties parameters. At the end of the first neural network part which is also the input part of the second neural network part $y_{c1}(x_{p1})$ to $y_{c9}(x_{p9})$ are physical properties parameters. In the following there neural network layers the x_{c1} to x_{c38} are chemical properties parameters, x_{D1} to x_{D9} are dimensional accuracy parameters, x_{s1} to x_{s41} are about the parameters of the surface of the products. For the test of the surface of the products the mainly method are human check. There are not different degrees of the defect of the surface, so if there exist any defect the input value is 1 or else 0. To the test of chemical properties, dimensional accuracy and the surface of the products we adopt the common neural network.

After the conversion of all the hidden layers there are four results generated: y_c, y_p, y_d, y_s. The four results are all digital outputs. Later they would be adjusted in

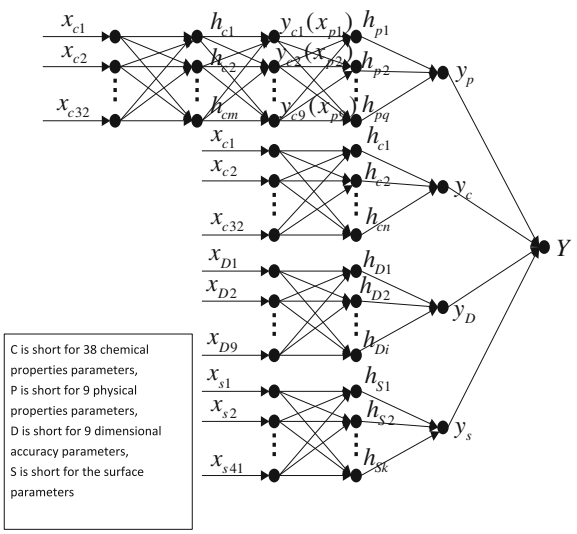

Fig. 2 Structure of the mul-RBF neural network

the results testing layer. The final output of the whole neural network part is Y, which is composed by two parts: qualified and disqualified. If the product is disqualified there is a further checking about it. Then the system would give out the reasons of disqualification. Then it transfers the digital outputs to the practical outputs and the final results shown on the UI are two possible results: qualified and disqualified (with its reasons).

In this system the data base software is Oracle11g. There two kinds of data in the data base which are input data and feedback data. The input data serve for the knowledge acquisition part of the expert system while the feedback datas are the result data outputted from the inference engine after the processing of the RBF neural network. The feedback data also includes the weight and other coefficients of the neural network. They are all stored in the data base to form a knowledge base.

The whole system included a secondary database server, a three-stage database server, an industrial personal computer (IPC) which is used to exhibit the data in the proscenium. This system adopted the browser/server (B/S) model. And it is developed by ASP.NET. The programming language is C#. The operating system on the server is Windows Server 2008. The Web server is IIS7 while the operating system we used Windows Server 2008. The database management system we used Oracle11g.

The data from product quality test has the following characteristics: the data size is large (generally speaking the data is from the latterly 5–10 years), the types of the parameter are not sole (in this system there are four types), the result is complex (if the result is not qualified there are many different cases to the rejected product), it does not need to update the data. According to the characteristics of the data from product quality test the whole structure of the expert system is shown in Fig. 3. The knowledge base is supported by the Oracle database. It organized and managed the knowledge base under the database management mechanism. The RBF neural network is used in knowledge acquisition and inference machine part. The data is

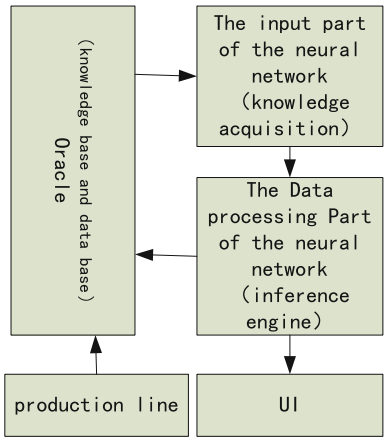

Fig. 3 Structure of the expert system

transferred and disposed according to the direction of arrow. At last the UI and the database share the output result.

The reasoning process of the expert system is a process of parallel computing. There are five steps about it: I. Input the parameters from the input layer of RBF neural network. II. The data are transferred to the input end of the hidden layer by a specific transmission mode. III. After the training of Multiquadratic in the hidden layer the data which are processed are output in the output end of the hidden layer. IV. Linearize the data and output the results y_c, y_p, y_d, y_s. V. Transfer the result to the UI and the data base at the same time after the process of judging layer.

4 Analysis of Test Results

At present, the qualified rate of the section steel product is up to 96.27 %. This experiment extracts 200 samples of the section steel product to test the expert system. Thereinto, we extract four sets of data from the unqualified products and 1 set of data from the qualified product as the followings. In order to inspect the generalization ability of the neural network the five sets of data are not included in the training samples. Table 1, 2, 3, 4 takes the chemical prosperities parameters, physical properties parameters, dimensional accuracy parameters and the surface of the products parameters of i-beam as the representative of the four sets of input data. Table 5 is about the results and analysis after the comprehensive judgment about the chemical constituents, physical properties parameters, dimensional accuracy and the surface of the products. Suppose the weight of chemical properties is W_{ci}, the weight of physical prosperities is W_{pi}, the weight of dimensional accuracy parameters is W_{di}, the weight of the surface quality parameters is W_{si}. So, the final outputs of the four neural network are $y_c = \sum_{i=1}^{38} W_{ci}h_{ci}$, $y_p = \sum_{i=1}^{9} W_{pi}h_{pi}$, $y_d = \sum_{i=1}^{9} W_{di}h_{di}$, $y_s = \sum_{i=1}^{41} W_{si}h_{si}$. The $W_{ci}, W_{pi}, W_{di}, W_{si}$ and $h_{ci}, h_{pi}, h_{di}, h_{si}$ are confirmed by the formulas of gradient-decent at the beginning of the paper. The brand of the products is Q295 with A level.

Table 1 Chemical properties data

Chemical composition (%)	C	Mn	Si	P	S	……
Low range	0.16	0.8				……
High range	0.18	1.5	≤0.55	≤0.05	≤0.045	……
Unqualified sample 1	0.41	1.84	0.37	0.043	0.038	……
Unqualified sample 2	0.16	1.26	0.42	0.047	0.042	……
Unqualified sample 3	0.24	1.13	0.51	0.049	0.031	……
Unqualified sample 4	0.16	0.94	0.49	0.045	0.021	……
Qualified sample 5	0.18	1.32	0.51	0.05	0.029	……

Table 2 Physical properties data

Physical properties	Yield point	Strength of extension	Percentage elongation after fracture	……
Normalized value	≥ 295	390–570	≥ 23	……
Unqualified sample 1	300	232	28	……
Unqualified sample 2	301	391	16	……
Unqualified sample 3	302	492	23	……
Unqualified sample 4	272	391	42	……
Unqualified sample 5	297	412	29	……

Table 3 Dimensional accuracy data

Dimensional accuracy (mm)	Leg width	Girdle thickness	Height	Outer slope	……
Normalized value	400 (±4.0)	400 (±0.9)	400 (±4.0)	T ≤ 1.5 % b	……
Unqualified sample 1	397	400	399	5.82	……
Unqualified sample 2	398	400.3	403	5.96	……
Unqualified sample 3	402	399.8	401	5.99	……
Unqualified sample 4	400	399.5	396	5.83	……
Unqualified sample 5	403	400.2	398	8.82	……

Table 4 Surface of the products data

Surface of the products	Slit	Edge crack	Indentation	Pitted surface	……
Unqualified sample 1	0	0.84	0	0.92	……
Unqualified sample 2	0	0	0	0.67	……
Unqualified sample 3	0	0	0	0	……
Unqualified sample 4	0	0	0	0	……
Unqualified sample 5	0	0	0	0	……

This system detects the products from four aspects and gives out the reasons of disqualification. This is good for the following quality-trace and analyzing the results detailedly. Compare with the traditional way, it saves 60 % of the time.

Table 5 Comprehensive judgment

Comprehensive judgment	Chemical prosperities	Physical properties	Dimensional accuracy	The surface	Result analysis
Unqualified sample 1	0.806	11.02	30.41	0.26	Unqualified:chemical properties, physical properties, the surface
Unqualified sample 2	0.737	12.46	30.79	0.13	Unqualified:chemical properties, the surface
Unqualified sample 3	0.798	12.46	30.295	0	Unqualified:chemical properties, physical properties
Unqualified sample 4	0.71	12.77	33.382	0	Unqualified: dimensional accuracy
Qualified sample 5	0.749	13.55	30.418	0	Qualified

5 Quality-Trace on Basis of RBF Neural Network Expert System

At present neural network expert system can solve the "bottleneck" problem in the conventional expert system very well. However, the black box problems in the explanation mechanic of the neural network expert system have not been solved up to now [14–17]. Although the system can provide a result which is close to the idea from experts infinitely, it cannot provide the further explanation to the result. It also cannot provide the whole reasoning process. In order to overcome the shortcoming of neural network expert system this system raised a new idea on the module settings. This system set a quality analysis module and a quality trace module which is based on the essential data real time data acquisition module and the neural network expert system quality test module. After the quality test all the data and the result from the expert system would be recorded in the database. Due to the large test data and result this system set a quality analysis module which was suit for the characteristic of the steel industry. It combined the data and the specific actual situation to analyze deeply. And summarize the internal relations of the parameters and the law of the production achievement. Then made a conclusion under these information and made quality trace with right direction. This paper raises a method that combines neural network expert system and quality-trace. According to the result from the neural network expert system it makes quality-trace to the unqualified products. The part of quality-trace reappears the reasoning process in the conventional expert system while it also makes up the drawback of the explanation mechanic in the neural network expert system on the one hand. On the other hand it can trace to the process which induces the problem and can help the workers to know the responsible part.

The production of hot rolled steel is belonged to the type of process industry. The productive process from the primal raw material to the final product is continuous. So the information to the productive process is also continuous. And the technological parameters to every process are so many. At the same time the production environment is complex so there are many factors can influence the quality of the final products. And it is also important that the products are formed from a kind of raw material which is changed in chemical properties and physical properties in many processes and is finally turned into many kinds of products. So the quality problem in the productive process would influence many down-stream products. So when it traces the quality of the hot rolled steel product it needs to trace to the raw material widdershins according to the production technology process of the products [18, 19].

There must be reliable trace- basis when realize the process of quality trace. If an enterprise wants to realize quality trace it must establish an impeccable and effective quality management mechanism to record the identification of product well. An identification of product is the only sign during the whole manufacturing process. It includes the product ID, batch number, sequence number, date, etc. At the same time it must establish a search mechanism about these information accurately and fastly. According to the characteristic of the steel industry the identifier records the raw material batch number, batch number, procedure parameter, etc. When there happens any quality problem the workers can review the information during the whole life cycle according to the identifier.

By means of the records of all the information during the whole life cycle the system accumulates product data and quality test data continually through the expert knowledge database. So as to realize tracking back management of the product quality automatically and effectively.

In order to solve the problem of the neural network that cannot afford reasoning process we made some trace-rules especially to the expert system:

1. Input the identification of product you can inquire the corresponding slab number, steel type number, semi-finished numbers, material group numbers, executive standard number, heating furnace number and the mill number, roll number, continuous casting number during the productive process and other information in the pivotal link.
2. Input the identification of product you can inquire the test results in the quality test neural network expert system and all the parameters in the quality test about chemical properties, physical properties, dimensional accuracy and the surface of the products. The unqualified item would be colored red. At the same time you can inquire the detailed overweight data.
3. Input the productive time and the information as mill number, furnace number, etc. you can inquire product batch at the same time which passed the corresponding equipment.
4. Input the process name and time you can inquire the corresponding classes and teams information so as to search the department information, role information, user information, job number and name.

In the process of quality-trace the informations are divided into two types. They are lateral tracing and lengthways tracing.

(1) Lateral tracing
When there appears any problem in the products the quality-trace system can trace to the heating process, steel rolling process or sizing operation according to the informations of the code on the product. And the quality-trace information link can be crosswise expanded on the basis of the associated content from all the information. It traces strictly according to the reversed order of production technology process. Then it locks the specific link which causes the quality problems. After separately confirmation to the four neural networks it finds out the problematical parameters and review to the parameters of the other products which is also belonged to the same brammennummer. The specific steps are shown in Fig. 4.

(2) Lengthways tracing
When there occurs any quality problem and after it has locked the problematical link by the lateral tracing we need to develop the lengthways tracing about the problematical link. That is the case-by-case. First, we need to make sure about the batch of the problematical products according to the reason which resulted in the defect. Then trace the storage informations and the informations of the production department of the same batch. The aim is to lock the scope of the problematical products. Then analyze the reason which leads to the defect in detail so as to improve the method of quality control and improve the quality of products.

The process of tracing is a kind of reversed order to the process flow of the production. It is from the finished product number to the semifinished product number, intermediate blank number, raw materials number, furnace time number, and slab number.

The quality trace to the steel products can be divided into 4 parts according to the productive technology: chemical properties tracing, physical properties tracing, dimensional accuracy tracing, the surface of the products tracing. The objective of quality trace is not only to find out the negligence of the craft and to improve the process, but also to trace back the products of the same batch. Then checkout these products again to ensure the products of the same batch are safe.

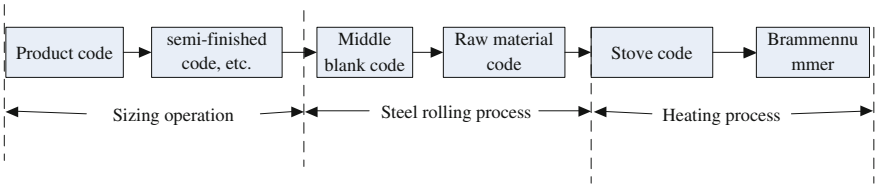

Fig. 4 Structure of lateral tracing

In the chemical properties tracing part, the fault is not resulted from the hot rolling productive process. There are two sources to the slabs: home-grown and outsourcing. To the outsourcing slabs, the workers can trace the manufacturers according to the order number and some other informations. To the home-grown slabs, the workers can trace the craft process to the steel-making part. And trace the process in accordance with the "tree- rule." We see every process of every product as a panel point. The production sequence is from up to down while the trace sequence is from down to up, as is shown in Fig. 5. At the same time trace back the product from the same batch.

When trace to the slab number do the lateral tracing and find out all the slabs which are the same batch. Then sample randomly from the same batch and recheck the quality. If the result is eligible, only downgrading the former subquality product. If the result is disqualification, dispose the slabs from the same batch unitively.

In the physical properties tracing part, we trace the heating link, rolling link, cooling link and dephosphorization link according to the craft process. If there is any defect on the physical properties, trace the product from the same batch and recheck the quality. Lock the bottleneck link according to the inquiring to every parameter. And trace the other products which experienced the same equipment and the same process. Sample and recheck the products to ensure their quality.

In the dimensional accuracy tracing part, trace the cut to length cold saw cutting part. In the surface of the products tracing part, we need to consider the chemical

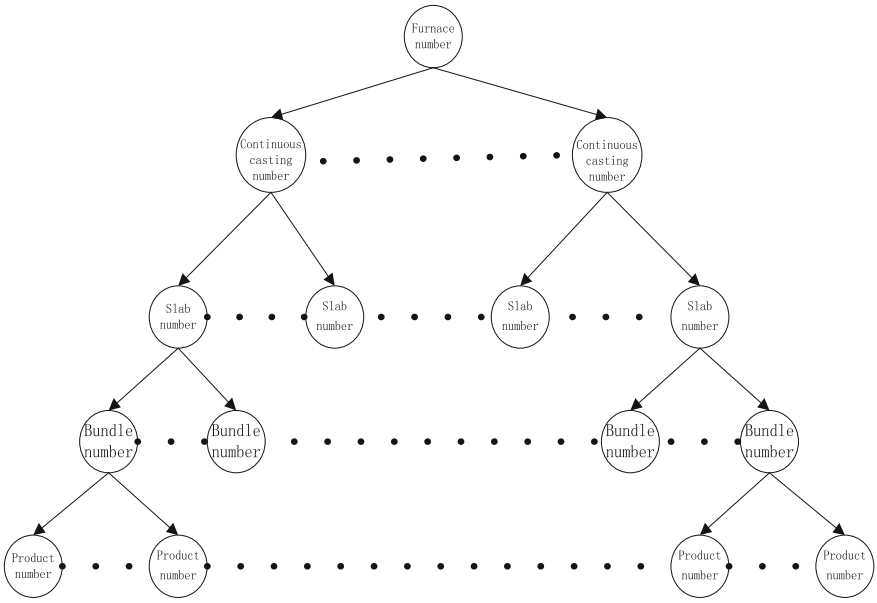

Fig. 5 "tree-rule" tracing

properties. The defect of the surface of the products is mainly because of the chemical properties problem. If there is any defect on the surface of the products, trace directly to the slab. Inquire if the slab is home-grown or outsourcing to lock the problem part.

6 Conclusion

This paper expounded a hot rolling products quality test expert system which combined the RBF neural network and quality-trace. It tested the quality of the products in four aspects which were chemical properties, physical properties, dimensional accuracy and the surface of the products. It made the final results by the comprehensive judgment and gave a kind of rough analysis about the result. Then it made all-around quality-trace. On one hand the trace result can explain the result from the expert system on the other hand it can find out the responsible process during the course of manufacture. This system can explain the detailed reasons about the result so it mends the shortcoming of explain facility in the conventional neural network expert system. And it also offers the theory basis for the later improved work about the whole system. In addition, because of the powerful ability in data processing of RBF neural network it can also be incorporated into the detection control and fault diagnosis of chemical energy storage device such as rechargeable batteries, super capacitor. etc. However, how to make this theory helpful in the daily detective work is which we need to research further.

Acknowledgments [1] AQSIQ Nonprofit Industry SPecialized Research Funding Projects (201310003). [2] AQSIQ Science and Technology Plan Projects (2014QK186)

References

1. Galushkin AI (2010) Neural networks theory. Springer, Germany
2. Wen-yu LV, Wei-ming LI, Wei-hong LI (2012) Research on the Optimization selection of thin coal seam mining method based on ANNES. China Min Mag 32(4):132–138
3. Park H-S, Pedrycz W, Chung Y-D, Oh S-K (2012) Modeling of the charging characteristic of linear-type superconducting power supply using granular-based radial basis function neural networks. Expert Syst Appl 39(1):1021–1039
4. Shi Z (2009) Neural network. Higher Education Press, China
5. Du Z (2010) Application study of RBF in crack testing of steel. Harbin University of Science and Technology, China
6. Liang ZHOU, Kai-junIntrusion WU (2010) Detection system based on combination of expert system and BP neural network. Microcomput. Inf 18(5):456–461
7. Hanafizadeh P, Ravasan AZ, Khaki HR (2010) An expert system for perfume selection using artificial neural network. Expert Syst Appl 37(12): 8879–8887
8. Niu X, Zhao X (2012) The study of fault diagnosis the high-voltage circuit breaker based on neural network and expert system. Procedia Eng 29(11): 3286–3291

9. Rosa ES, Salgado RM, Ohishi T, Mastelari N (2010) Performance comparison of artificial neural networks and expert systems applied to flow pattern identification in vertical ascendant gas–liquid flows. Int J Multiph Flow 36(9):738–754
10. Du L-J, Zhang S-F, Yan E-L (2010) A Study on diagnostic expert system of electronic engine based on fuzzy neural network. J Agric Univ Hebei 5(8):156–162
11. Xu-jin LIU, Jian-ping LI, Chang-long DU, Zheng-wei HU (2011) Coal-mining Machine Fault Diagnosis Expert System Simulation Based on Fuzzy Neural Network. Coal Mine Mach 4 (8):98–105
12. Li J, Han S-J, Chang Y-Q, Nie S-Y (2011) Application of artificial intelligence in sea cucumber cultivate expert system. J Comput Appl S1(3):188–192
13. Zhang X-H, Zhen T, Bao H (2010) Research and application of measurement and control expert system for grain storage based on neural network. J Henan Univ Technol (Nat Sci Edition) 3(6):228–234
14. Molina JM, Isasi P, Berlanga A, Sanchis A (2000) Hydroelectric power plant management relying on neural networks and expert system integration. Eng Appl Artif Intell 13(3):357–369
15. Ao Z (2010) Artificial intelligence and expert system. China Machine Press, China
16. Hai Z-H, Tian M-Q (2010) Research of expert system of fault diagnosis for asynchronous motor based on neural network. Industry and Mine Automation 4(7):557–562
17. Chen X (2010) Research on order tracking and product quality tracing system for discrete manufacturing. Zhejiang University, China
18. Li W (2011) The study of the tracing management system design about the white spirit products. Beijing University of Posts and Telecommunications, China
19. Ohshima M, Tanigaki M (2000) Quality control of polymer production processes. J Process Control 10(2): 135–148

A New Vector Measurement Method for Power System Based on All-Phase Fourier Transform

Peng Luo, Xiaoguang Hao, Yuhao Zhao and Lei He

Abstract A novel vector measurement method for power system based on all-phase Fourier transform (apFFT) is proposed. Due to apFFT's excellent performance in suppressing spectral leakage and the property of 'phase invariant', this method can realize the accurate estimation of PMU phase angle, and then the time-shift phase difference correcting spectrum method is used to estimate the frequency and amplitude parameters. Simulation shows that, for the noise-free case, the proposed method is close to unbiased estimation, and the estimation accuracy is also higher than conventional method.

Keywords Power system · Phasor measurement unit · Vector measurement · All-phase fourier transform

1 Introduction

With the development and wide application of smart grid, the security and stability of power system is especially important [1, 2]. Phasor measurement unit (PMU) is based on the global positioning system (GPS) and high precision timing signal, which has been widely used in wide area measurement system (WAMS) to realize synchronous acquisition of different nodes in wide-area power system [3]. Many PMUs have been applied in areas including power grid dynamic estimation, fault location, wide-area protection and on-line parameter estimation [4, 5], and the measuring accuracy of PMU algorithm will directly affect the performance of whole system.

Synchronous phasor measurement algorithms for PMU are mainly designed to estimate the frequency, phase angle, and amplitude of power system, and the mainstream PMU algorithms include zero crossing method, discrete Fourier transform (DFT) method, Kalman filtering method and wavelet transform method

P. Luo (✉) · X. Hao · Y. Zhao · L. He
Hebei Electric Power Commissioning Institute, Shijiazhuang 050021, China
e-mail: luopeng1984@sohu.com

Q. Liang et al. (eds.), *Proceedings of the 2015 International Conference on Communications, Signal Processing, and Systems*, Lecture Notes in Electrical Engineering 386, DOI 10.1007/978-3-662-49831-6_104

[6, 7]. Due to DFT's excellent harmonic suppression performance in static conditions, this method is mostly used at present. However, the inherent defects of DFT method such as spectral leakage and frequency aliasing will cause a large error in parameter estimation. To solve this problem, many works were developed in this field. In paper [8], length of the data window is variable to improve frequency estimation precision, but the calculation cost is significantly increased. In paper [9], the sampling frequency is adjusted adaptively by system frequency to satisfy the restrictive conditions of integer-period sampling. However, bay level IEDs cannot usually control the sampling frequency of process level in practical substations, which will cause the difficulties of application.

In this paper, a novel vector measurement method for power system based on apFFT [10, 11] is proposed. The rest of this paper is organized as follows: Sect. 2 will briefly introduce the related contents in all-phase spectrum analysis, the phase estimation performance of deterministic signal will be proposed in Sect. 3. In Sect. 4, a time-shift phase difference correcting spectrum method is proposed to estimate the frequency and amplitude parameters. Finally, simulation results are presented in Sect. 5 and the conclusion is shown in Sect. 6.

2 All-Phase Spectrum Analysis

The signal processing flow of all-phase spectrum analysis is shown in Fig. 1. Input samples are pretreated by a convolution window of length $2N - 1$, and a new N-points data samples $y(n)$, $(n = 0, 1, \ldots, N - 1)$ are obtained by superposition of two data groups with N points interval, then the spectrum analysis result is calculated by traditional Fourier transform of $y(n)$.

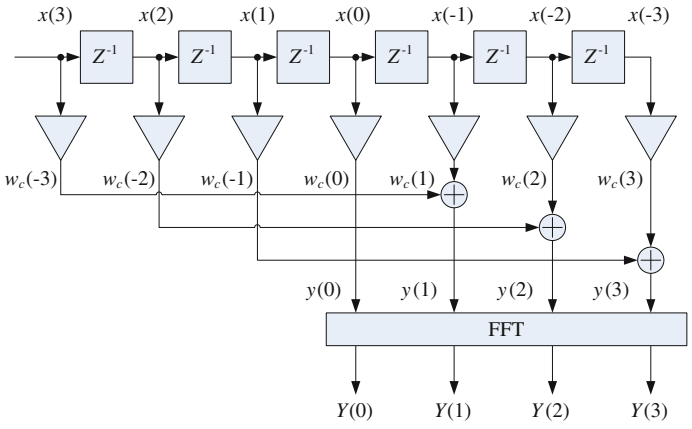

Fig. 1 All-phase FFT spectrum analysis ($N = 4$)

In Fig. 1, convolution window $\boldsymbol{w}_c = [w_c(-N+1), \ldots, w_c(-1), w_c(0), w_c(1), \ldots, w_c(N-1)]^{\mathrm{T}}$ is constructed by front-window $\boldsymbol{f}$ convolved with reversal back-window $\boldsymbol{b}$, calculated as (1):

$$w_c(n) = \begin{cases} f(n) * b(-n), & n \in [-N+1, N-1] \\ 0, & |n| \geq N \end{cases} \tag{1}$$

The Fourier transform of $\boldsymbol{w}_c$ is as follows:

$$W_c(e^{j\omega}) = F(e^{j\omega})B(e^{-j\omega}) = F(e^{j\omega})B^*(e^{j\omega}) \tag{2}$$

Above analysis shows that the FFTs of all N kinds of data groups including $x(0)$ are comprehensively considered in all-phase spectrum analysis, which brings many good performance such as suppression of amplitude spectral leakage and flat phase distribution nearby the spectral peak. In addition, although the FFTs of N different data groups are considered, the apFFT can be calculated by only one FFT, which improves the computing efficiency.

3 Phase Estimation Performance of Deterministic Signal

Consider a compound cosine signal containing three components with different frequency and phase:

$$x(n) = \sum_{m=1}^{3} \cos(2\pi\omega_m n/N + \varphi_m),\ n \in [-N+1, N-1] \tag{3}$$

where $\omega_1 = 20.0$, $\varphi_1 = 10°$, $\omega_2 = 60.2$, $\varphi_2 = 50°$, $\omega_3 = 100.4$, $\varphi_3 = 90°$, $N = 256$. The windowed FFT and double-window apFFT of $x(n)$ are shown in Figs. 2 and 3, and rising-cosine window is adopted as window function here.

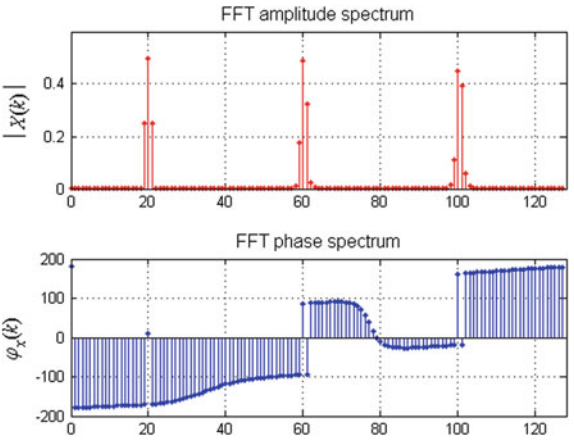

Fig. 2 FFT spectrum of $x(n)$

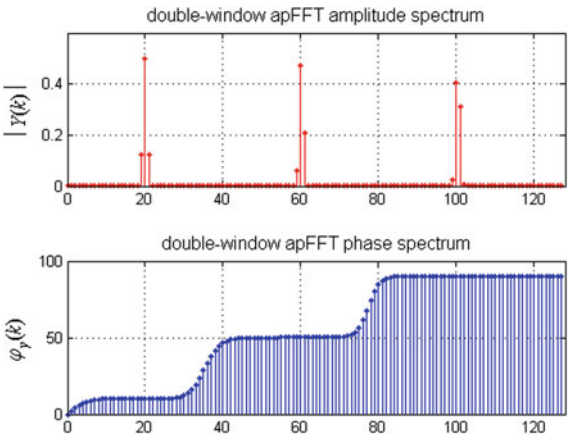

Fig. 3 Double-window apFFT spectrum of $x(n)$

Table 1 Comparison of phase estimation results ($N = 256$)

	Real value	Windowed FFT	Double-window apFFT
$k = 20$	10°	9.9997939384°	10.0000000006°
$k = 60$	50°	85.8592933936°	50.0000000006°
$k = 100$	90°	161.7187408919°	89.9999999999°

$$w_h(n) = 0.5\left[1 - \cos\left(\frac{2\pi n}{N-1}\right)\right],\ n \in [0, N-1] \tag{4}$$

From above results, the apFFT has better property of leakage reduction than conventional FFT, the energy leakage caused by non-integer-period sampling and cross talks among different frequency components are restricted in two spectral lines. For the phase spectrum, the apFFT phase spectrum presents a regular flat distribution nearby the target frequency, which is the property of 'phase invariant'. The phase measurement results of these two analysis method are given in Table 1.

4 Frequency and Amplitude Estimation Algorithm

In this paper, the data intercepting method of observed sequence is improved, and new time-shift phase difference correcting spectrum algorithm is proposed to estimate the frequency and amplitude parameters of PMU vectors. The concrete steps are listed as the following:

- The observed PMU signal is sampled (may not be integer-period sampled) and be divided into two data series $x_1(n)$ and $x_2(n)$ with fixed length $2N + 1$, and the time delay between two series is n_0;

$$x_1(n) = Ae^{j\left(\omega^* n + \theta\right)},\ n \in [-N+1,\ N-1] \tag{5}$$

$$x_2(n) = Ae^{j\left[\omega^*(n-n_0)+\theta\right]},\ n \in [-N+1,\ N-1] \tag{6}$$

- Perform N-point double-window apFFT about $x_1(n)$ and $x_2(n)$, and the phase difference between two series as shown in Eq. (7) is obtained based on the phase spectrum at the main spectral line k^*, where $2n_0k^*\pi/N$ is the compensation value of digital angular frequency $2\ k^*\pi/N$ of main spectrum k^* with delay n_0;

$$\Delta\varphi = \varphi_1(k^*) - \varphi_2(k^*) + 2n_0k^*\pi/N = \omega^* n_0 \tag{7}$$

- Based on Eq. (7), the frequency estimation with phase compensation and frequency deviation at main spectral line k^* are derived as (8) and (9);

$$\hat{\omega}^* = [\varphi_1(k^*) - \varphi_2(k^*)]/n_0 + 2k^*\pi/N \tag{8}$$

$$d\omega = \hat{\omega}^* - 2k^*\pi/N + [\varphi_1(k^*) - \varphi_2(k^*)]/n_0 \tag{9}$$

- Estimate the signal amplitude using frequency deviation $d\omega$, for the double-window apFFT case, the estimation formula is given as

$$\hat{A} = \frac{\left|Y(k^*)\right|}{F_g^2(d\omega)} \tag{10}$$

- In this paper, the Hanning window (rising-cosine window) is used for window function, then the amplitude estimation is adjusted to Eq. (11);

$$\hat{A} = \left[\frac{2\pi d\omega(1-d\omega^2)\sqrt{Y(k^*)}}{2\sin\ (\pi d\omega)}\right]^2 \tag{11}$$

- Altogether, the algorithm flow chart of proposed PUM vector measurement based on apFFT is given as Fig. 4.

5 Simulations

The fundamental frequency and phase angle of test signal are set at 50.5 Hz and 40°, two harmonic components are also contained in the test signal, with the expression (12).

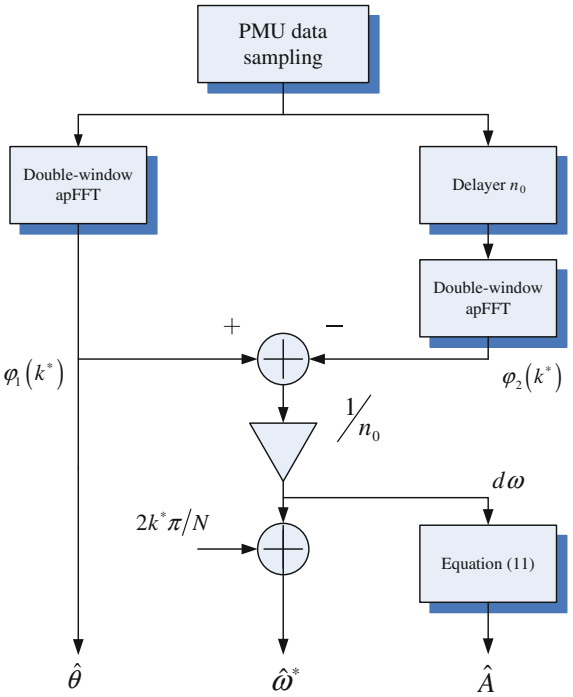

Fig. 4 Flowchart of PUM vector measurement

$$x(t) = 5\cos(50.5 \times 2\pi t/f_s + 40\pi/180) + 0.25\cos(200 \times 2\pi t/f_s) + 1.75\cos(300 \times 2\pi t/f_s) \quad (12)$$

The double-window apFFT of $x(t)$ is shown in Fig. 5.

Two different estimation methods proposed in this paper, and paper [9] are used to estimate the frequency, phase angle and amplitude parameters of the test signal, and the estimation results is given in Table 2.

From above simulation results we find that, compare with the conventional DFT method, the apFFT method proposed in this paper has a better performance in estimation precision and noise suppression.

6 Conclusions

With development and wide application of smart grid, the estimation performance of PMU vectors will directly affect the reliability of power system applications such as relay protection, measuring and controlling. According to this problem, a new vector measurement method for power system is proposed which is based on all-phase spectrum analysis. In this method, the observed signals need not be

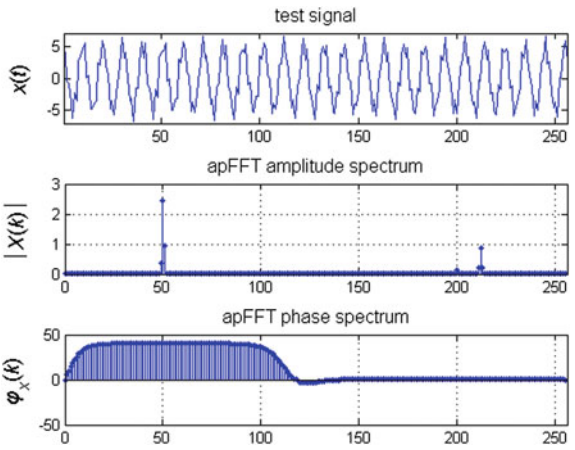

Fig. 5 Test signal and its apFFT spectrum

Table 2 Parameter estimation results of test signal

	Real value	Method in [9]	Method in this paper
f	50.5	50.5018709238	50.5000000000
θ	40°	40.1024310871°	39.9999999996°
A	5	4.9404296603°	4.9978567797

sampled by strictly integrated periods, and the spectral leakage and barrier effect are suppressed significantly. Simulation shows that the apFFT method proposed in this paper has a better performance in estimation precision and noise suppression than conventional method. It can be expected that this method would be used in areas of vector measurement and harmonic analysis in power automation, which has a good research value.

References

1. Phadke AG, Thorp JS (2008) Synchronized phasor measurements and their applications. Springer, Berlin, Germany
2. Novosel D, Madani V, Bhargava B et al (2008) Dawn of the grid synchronization. IEEE Power Energy Mag 6(1):49–60
3. Wang Z, Zhang J, Qian C (2012) Topology error identification based on synchronized measurements for power network. Electric Power Autom Equip 32(1):1–8
4. Meng F, Dong X, Gao Z et al (2012) Online PSS evaluation based on WAMS/PMU technology. Electric Power Autom Equip 32(10):146–149
5. Zhang Y, Markham P, Xia T et al (2010) Wide area frequency monitoring network (FNET) architecture and applications. IEEE Trans Smart Grid 1(2):159–167
6. Jafarian P, Sanaye-Pasand M (2011) Weighted least error squares based variable window phasor estimator for distance relaying application. IEEE Proc Gener Transm Distrib 5 (3):298–306

7. Ghahremani E, Kamwa I (2011) Dynamic state estimation in power system by applying the extended Kalman filter with unknown inputs to phasor measurement. IEEE Trans Power Syst 26(4):2556–2566
8. Hart D, Novosel D, Hu Y et al (1997) A new frequency tracking and phasor estimation algorithm for generator protection. IEEE Trans Power Delivery 12(3):1064–1073
9. Chen M, Zheng X, Wang X et al (2005) A novel algorithm for reducing spectrum leakage based on equal angle-interval sampling principle. Trans China Electrotech Soc 20(8):94–98
10. Wang Z, Hou Z, Su F (2003) All phase FFT spectrum analysis. J China Inst Commun 24 (11A):16–19
11. Huang X, Wang Z, Luo P et al. Discrimination and correction for dense all-phase FFT spectrums. Acta Electron Sin 39(1):172–177

Comparative Presentation of Machine Learning Algorithms in Flood Prediction Using Spatio-Temporal Data

Piraporn Jangyodsuk, Dong-Jun Seo, Ramez Elmasri and Jean Gao

Abstract The development of accurate flood prediction model could reduce number of fatalities by assisting local government in decision making. In this paper, three well-known machine learning algorithms, including Support Vector Machine, Decision Tree, and Lasso, are compared in terms of flood prediction accuracy. The selected algorithms are applied to learn flood prediction models for six U.S. Geological Survey gauges in North Texas. Three data sets from different sources had been used to learn flood prediction models. The data sets include Water level time series from gauges, spatio-temporal precipitation from National Weather Service's Weather Surveillance Radar-1988 Doppler, and hydrological data from Hydrology Laboratory-Distributed Hydrologic Model. Although Support Vector Machine usually performs well in many applications, the results suggest that Lasso is the most appropriate for flood prediction while Support Vector Machine performs the worst.

1 Introduction

Flash flood is a natural threat typically caused by heavy rainfall from a severe thunderstorm, hurricane, or tropical storm. The dangerous aspect of flash flood is its sudden occurrence and fast moving water. In May 2015, heavy rainfall caused many flash floods and river floods across Texas and Oklahoma which resulted in fatalities

P. Jangyodsuk (✉) · R. Elmasri · J. Gao
Computer Science and Engineering Department, University of Texas at Arlington, Arlington, TX, USA
e-mail: piraporn.jangyodsuk@mavs.uta.edu

R. Elmasri
e-mail: elmasri@uta.edu

J. Gao
e-mail: gao@uta.edu

D.-J. Seo
Department of Civil Engineering, University of Texas at Arlington, Arlington, TX, USA
e-mail: djseo@uta.edu

Q. Liang et al. (eds.), *Proceedings of the 2015 International Conference on Communications, Signal Processing, and Systems*, Lecture Notes in Electrical Engineering 386, DOI 10.1007/978-3-662-49831-6_105

and damages. Although flash flood alerts were issued by National Weather Service, they are issued by county. Local government could use this warning along with local finer scaled information to give more accurate flood warning by city or neighborhood. Because of data availability and river floods in the area of interest are usually associated with heavy rainfall like flash floods, river floods at U.S. Geological Survey (USGS) gauges are used in this paper. The purpose of this paper is presenting and comparing three machine learning algorithms for flood prediction. The compared algorithms are Support Vector Machine, or SVM [1], decision tree [2], and Lasso [3], which are well-known machine learning algorithms for classification and predictions.

Many regression-based flood prediction methods, such as SVM [4–6] and Artificial Neural Network [7], use past values of water level or water level from nearby locations as the input features, so the number of features considered is low. Our work integrates data sets from different sources for flood prediction. These data sets are water level time series, and spatio-temporal precipitation and hydrological data, which means data used in this work has more features and possibly is more noisy.

2 Compared Algorithms

2.1 Support Vector Machine

Support Vector Machine or SVM [1] is one of the most popular discriminative model classifier. The intuition of SVM is simple yet powerful, maximizing the distance between two classes of data by drawing a line. While this seems like too simple and might not cover more complex data, using Kernel will make this line become any arbitrary shape in the space. As such, fitting the data well even if the number of features dimensions is high.

The intuition of Kernel trick in SVM is projecting the data into higher dimensional space. While at first, this looks counter intuitive, it enables the data to be separable with linear line in higher dimensional space. Furthermore, the embedding function is not necessarily required. As what truly needed is only the Kernel function $K(x_i, x_j)$ between pairs of data points.

2.2 Decision Tree

Decision tree [2] is one of the most popular classification models in machine learning and data mining due to the fact that it supports high-dimensional data and is very scalable. At each node, the tree split data points into two subsets where the decision is based on a selected objective function. Usually, the most popular one is maximizing information gain.

The idea of decision tree is extended to forest and fern. In decision forest, the final classification is based on the vote of multiple trees (hence forest). This eliminates the well-known problem of overfitting. For fern, it speeds up the classification of decision tree by having every decision function at every node on the same level to be the same.

2.3 Lasso

Lasso, or Least Absolute Shrinkage and Selection Operator, is a linear regression method that penalizes the summation of all absolute coefficients. This penalty makes the result sparse. In other words, some coefficients are exactly zeros. As such, Lasso can also be used to solve feature selection problem. Furthermore, Lasso is good for solving linear regression problem which the data are large and highly correlated because result from Lasso is sparse and the final model uses less features than the model from standard regression. Lasso can be written as the Eq. 1 where $\mathbf{x} \in \mathbb{R}^{d \times m}$ and λ defines the strength of the penalty.

$$\min_{\mathbf{w} \in \mathbb{R}^d} \frac{1}{m} \sum_{i=1}^{m} \frac{1}{2} \|y_i - \mathbf{w}\mathbf{x}_i\|_2^2 + \lambda \|\mathbf{w}\|_1 \tag{1}$$

There are many methods for solving Lasso, for example, coordinate descent [8], block coordinate descent [9], stochastic gradient descent (SGD) [10], and truncated gradient algorithm [11]. It has been theoretically analyzed that SGD is the best approach for large data. Since flood prediction involves in high dimensional spatio-temporal data, SGD-based Lasso is an appropriate method to solve the problem.

3 Experiments

The experiments are designed to evaluate the accuracy of three well-known algorithm on flood prediction. The data used in these experiments are from three sources, water level from U.S. Geological Survey (USGS) gauges, Multi-sensor Precipitation Estimates (MPE) from National Weather Service's Weather Surveillance Radar-1988 Doppler (WSR-88D), and streamflow and runoff data from MPE and Hydrology Laboratorys Distributed Hydrologic Model (HLRDHM) [12]. Six experiments were conducted for six USGS gauges, BCHT2, FWHT2, FWOT2, ERMT2, BOYT2, and SPMT2. In each experiment, we use USGS observed stream, MPE, streamflow, and runoff at time t as predictors to predict whether flood occurs in the next 1–6 h. The comparison metrics are precision, recall, and F_1 score. Precision is the ratio of correctly predicted flood events to all flood predictions. Recall is the ratio of correctly predicted flood events to all flood events. Lastly, F_1 score is the summarized measurement that takes both precision and recall into account.

3.1 Data Sets

3.1.1 USGS Water Level Data Sets

For flood identification, we use water level from U.S. Geological Survey (USGS) gauges, stage information from National Weather Service (NWS), and flood records from the city of Fort Worth. Water level time series, sampled at every 15 min from October 1, 2007 to present, at USGS gauges are publicly available in USGS website. Because other data sets are available at every 1 hour, we re-sampled and used 1-h water level time series. Six gauges in North Texas area, as shown in Table 1, have been used in the experiments.

Most of USGS gauges have flood stage and action stage provided by NWS. In collaboration with the city of Fort Worth (CoFW), we have records of 2001–2010 flood events at the first four USGS gauges from Table 1. We defined flood stage* from the minimum value between NWS's action stage and the minimum gauge height during flooding period. Water level higher than flood stage* means it is flooding.

3.1.2 Precipitation Data Set

The precipitation data we used is Multi-sensor Precipitation Estimates, or MPE, which are generated every 1 hour at 4×4 km resolution from NWS's WSR-88D Radar. MPE data we used covers West Gulf River Forecast Center area, or WGRFC. One HRAP cell represents 4×4 km area. We have MPE data at every hour from January 1996 to December 2012. In total, there are 425×390 MPE values for every hour.

Table 1 Six USGS gauges used in the experiments

Site name	Address	Flood stage*	Number of flood events		
			Training	Cross-val.	Testing
BCHT2	W Fk Trinity Rv at Beach St, Ft Worth, TX	18.10	146	521	128
FWHT2	Clear Fk Trinity Rv at Ft Worth, TX	10.05	294	231	158
FWOT2	W Fk Trinity Rv at Ft Worth, TX	3.60	28	12	23
ERMT2	Village Ck at Everman, TX	12.01	30	13	21
BOYT2	W Fk Trinity Rv nr Boyd, TX	15.32	206	748	147
SPMT2	Palo Duro Ck nr Spearman, TX	9	73	13	77

3.1.3 Hydrological Data Set

In collaboration with with Hydrology and Water Resources Laboratory, University of Texas at Arlington, we have streamflow and runoff data, which are generated from MPE and NWS Hydrology Laboratorys Distributed Hydrologic Model (HLRDHM) at 500×500 m resolution. The coverage is the city of Fort Worth area. We have streamflow and runoff data at every hour from January 1996 to December 2012. For each hour, there are 236×164 values.

3.2 Experiment Setup

The period that all data sets are available is October 2007 to December 2012. We separated data into three sets, October 2007 to December 2009 for training, 2010 for cross-validation, and 2011 to 2012 for testing. In total, there are 19,775 samples in training set, 8,760 samples for cross-validation, and 17,520 samples for testing. The numbers of flood occurrences in each set are shown in Table 1.

For each gauge, six experiments were conducted to compare the predictive power at different lead times, from one to six hours. Because using all 243,158 features in precipitation data and hydrological data is too high dimensional, we used data from 25×25 cells or 41×41 around each gauge as input.

1. For site BCHT2, FWHT2, FWOT2 and ERMT2, 25×25 MPE, streamflow, and runoff values around the gauge are used so there are 1,250 hydrological features and 625 precipitation features in total.
2. For site BOYT2 and SPMT2, 41×41 MPE values around the gauge are used so there are 1,681 precipitation features in total. Hydrological data are not used for these two sites because data are not available.

3.3 Experimental Results

Because flood may cause fatalities, recall is an important factor to consider in flood prediction. Good flood prediction method should have high recall so that it alerts the authorities to take action in time for most of the actual floods. Precision is also significant because actions and preparations require expense and manpower, low precision leads to unnecessary spending. As such, we compared all four methods on F_1 score which consider both precision and recall (Table 2).

All quantitative results for six gauges can be found in Tables 3 and 4. The mean precision, recall, and F_1 score of all three methods are compared in Fig. 1. Lasso has the best F_1 score and precision in 1 to 6 lead times predictions. Lasso and decision tree give the best comparable recall in 1 to 3 lead times predictions. It can be concluded that Lasso is the most appropriate method for all 1–6-h lead time flood predictions.

Table 2 Experimental results: comparison of precision from three algorithms on six USGS gauges

Lead time	Method	Site name					
		BCHT2	FWHT2	FWOT2	ERMT2	BOYT2	SPMT2
1-h	SVM	0.3860	0.4915	0.1707	0.3636	0.7667	0.4903
	Decision tree	0.5469	0.7005	0.6129	0.8235	0.9444	**0.9559**
	Lasso	**0.8440**	**0.9324**	**0.9474**	**0.9500**	**0.9538**	0.9200
2-h	SVM	0.2696	0.3357	0.1765	0.0469	0.5815	0.5034
	Decision tree	0.5519	0.4661	0.4000	0.6190	0.8897	0.8209
	Lasso	**0.8218**	**0.8121**	**1**	**0.7895**	**0.9318**	**0.8378**
3-h	SVM	0.1970	0.2548	0.0556	0.0488	0.5579	0.4762
	Decision tree	0.2182	0.3686	0.1875	**0.6250**	0.8777	**0.7541**
	Lasso	**0.7700**	**0.7770**	**0.9231**	0	**0.9213**	0.7432
4-h	SVM	0.1244	0.1810	0	0	0.4803	0.4452
	Decision tree	0.2007	0.1898	0.1538	0.1500	0.8000	0.6721
	Lasso	**0.6036**	**0.6486**	**0.9167**	**0.6923**	**0.8923**	**0.6769**
5-h	SVM	0.1039	0.0558	0	0	0.3620	0.4110
	Decision tree	0.1611	0.2084	0.0444	0.1000	0.6412	**0.6216**
	Lasso	**0.5536**	**0.6181**	**0.8333**	**0.6667**	**0.8480**	0.5846
6-h	SVM	0.0613	0.0357	0	0	0.3324	0.3767
	Decision tree	0.0664	0.1877	0.0090	0.2000	0.6853	**0.5405**
	Lasso	**0.4211**	**0.5490**	**0.7273**	**0.5714**	**0.8548**	0.5231

Table 3 Experimental results: comparison of recall from three algorithms on six USGS gauges

Lead time	Method	Site name					
		BCHT2	FWHT2	FWOT2	ERMT2	BOYT2	SPMT2
1-h	SVM	0.6484	0.7342	0.3043	0.1905	**0.9388**	**0.9870**
	Decision tree	**0.8203**	0.8291	**0.8261**	0.6667	0.9252	0.8442
	Lasso	0.7188	**0.8734**	0.7826	**0.9048**	0.8435	0.8961
2-h	SVM	0.4297	0.5949	0.3913	0.1429	**0.8980**	**0.9610**
	Decision tree	**0.6641**	0.7405	0.5217	0.6190	0.8776	0.7143
	Lasso	0.6484	**0.7658**	**0.6522**	**0.7143**	0.8367	0.8052
3-h	SVM	0.3125	0.5000	0.0870	0.1905	**0.8844**	**0.9091**
	Decision tree	**0.6172**	0.5506	**0.5217**	**0.2381**	0.8299	0.5974
	Lasso	0.6016	**0.6835**	**0.5217**	0	0.7959	0.7143
4-h	SVM	0.1875	0.3608	0	0	**0.8299**	**0.8442**
	Decision tree	0.4375	0.3544	**0.6087**	0.1429	0.7891	0.5325
	Lasso	**0.5234**	**0.6076**	0.4783	**0.4286**	0.7891	0.5714
5-h	SVM	0.1875	0.0886	0	0	**0.8027**	**0.7792**
	Decision tree	0.2266	0.5316	0.0870	0.0952	0.7415	0.2987
	Lasso	**0.4844**	**0.5633**	**0.4348**	**0.1905**	0.7211	0.4935
6-h	SVM	0.1016	0.0506	0	0	**0.8027**	**0.7143**
	Decision tree	0.1563	0.4810	0.0435	0.1429	0.6667	0.2597
	Lasso	**0.4375**	**0.5316**	**0.3478**	**0.3810**	0.7211	0.4416

Table 4 Experimental results: comparison of F_1 Score from three algorithms on six USGS gauges

Lead time	Method	Site name					
		BCHT2	**FWHT2**	**FWOT2**	**ERMT2**	**BOYT2**	**SPMT2**
1-h	SVM	0.4840	0.5888	0.2188	0.2500	0.8440	0.6552
	Decision tree	0.6563	0.7594	0.7037	0.7368	**0.9347**	0.8966
	Lasso	**0.7764**	**0.9020**	**0.8571**	**0.9268**	0.8953	**0.9079**
2-h	SVM	0.3313	0.4292	0.2432	0.0706	0.7059	0.6607
	Decision tree	0.6028	0.5721	0.4528	0.6190	**0.8836**	0.7639
	Lasso	**0.7249**	**0.7883**	**0.7895**	**0.7500**	0.8817	**0.8212**
3-h	SVM	0.2417	0.3376	0.0678	0.0777	0.6842	0.6250
	Decision tree	0.3224	0.4416	0.2759	**0.3448**	0.8531	0.6667
	Lasso	**0.6754**	**0.7273**	**0.6667**	0	**0.8540**	**0.7285**
4-h	SVM	0.1495	0.2410	0	0	0.6085	0.5830
	Decision tree	0.2752	0.2472	0.2456	0.1463	0.7945	0.5942
	Lasso	**0.5607**	**0.6275**	**0.6286**	**0.5294**	**0.8375**	**0.6197**
5-h	SVM	0.1337	0.0685	0	0	0.4989	**0.5381**
	Decision Tree	0.1883	0.2995	0.0588	0.0976	0.6877	0.4035
	Lasso	**0.5167**	**0.5894**	**0.5714**	**0.2963**	**0.7794**	0.5352
6-h	SVM	0.0765	0.0419	0	0	0.4701	**0.4933**
	Decision Tree	0.0932	0.2700	0.0149	0.1667	0.6759	0.3509
	Lasso	**0.4291**	**0.5402**	**0.4706**	**0.4571**	**0.7823**	0.4789

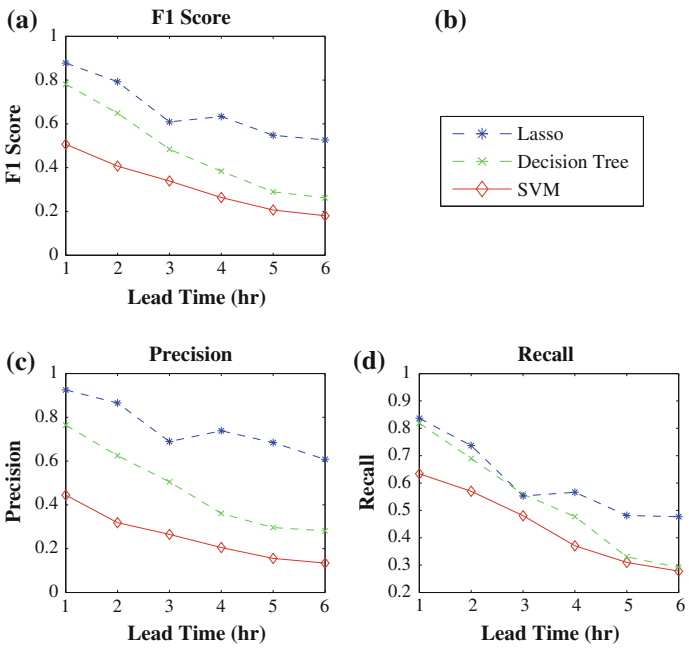

Fig. 1 Plots summarize performance of four algorithms on six lead times flood predictions. These scores are the average score from six gauges

The results suggest that Lasso performs well both with and without hydrological features and the performances of SVM and decision tree improves when using only precipitation features. This result can be explained by the fact that runoff and streamflow are calculated from MPE and HLRDHM model so they have information from MPE. SVM and decision tree are better when unprocessed MPE features are used than when the features are processed by a model.

4 Conclusion

Lasso has the best precision, recall, and F_1 score in all lead times predictions. Decision tree has the comparable recall in 1–3-h lead time prediction. Even though decision tree is scalable which is good for high-dimensional data like spatio-temporal data, it does not perform as well as Lasso. Although SVM usually performs well in many applications, it is not suitable for flood prediction using spatio-temporal data. On the other hand, the other linear regression-based method, Lasso, performs well on flood prediction. The reason could be because of the sparsity of the coefficients in results from Lasso which means Lasso chooses only some variables and spatial locations which highly correlated to future flood while SVM uses all variables and all locations. In other words, SVM is more prone to noisy data than Lasso. For spatio-temporal data like precipitation data and hydrological data, which are noisy and highly correlated, Lasso is the most appropriate methods in three compared machine learning algorithms.

Acknowledgments This work is supported by the National Science Foundation under Grant No. IIP-1237767 (Brenda Philips, Unversity of Massachusetts Amherst, Principal Investigator), CyberSEES-1442735 (Dong-Jun Seo, University of Texas at Arlington, Principal Investigator), and by the City of Fort Worth.

References

1. Cortes C, Vapnik V (1995) Mach Learn 20(3):273
2. Quinlan J (1987) Int J Man-Mach Stud 27(3):221
3. Tibshirani R (2011) J Roy Stat Soc Ser B (Stat Methodol) 73(3):273
4. Lin GF, Chou YC, Wu MC (2013) J Hydrol 486:334
5. Theera-Umpon N, Auephanwirivakul S, Suteepohnwiroj S, Pahasha J, Wantanajittikul K (2008) In: IEEE international joint conference on neural networks, IJCNN 2008. (IEEE World Congress on Computational Intelligence), pp 3039–3043
6. Han LCD, Zhu N (2007) J Hydroinformatics 9(4):267
7. Ruslan FA, Samad AM, Zain ZM, Adnan R (2014) In: 2014 IEEE 10th international colloquium on signal processing its applications (CSPA), pp 204–207
8. Friedman J, Hastie T, Tibshirani R (2010) J Stat Softw 33(1):1
9. Treister E, Turek JS (2014) In: Advances in neural information processing systems 27, pp 927–935
10. Shalev-Shwartz S, Tewari A (2011) J Mach Learn Res 12:1865

11. Langford J, Li L, Zhang T (2009) In: Advances in neural information processing systems 21, pp 905–912
12. Rafieeinasab A, Norouzi A, Kim S, Habibi H, Nazari B, Seo DJ, Lee H, Cosgrove B, Cui Z (2015) J Hydrol

Neuro-Space Mapping Method for Nonlinear Device Modeling

Shuxia Yan, Jing Jin, Lisen Zhang, Zhihong Feng, Peng Xu and Qijun Zhang

Abstract A proposed Neuro-Space Mapping (Neuro-SM) method for nonlinear device modeling is presented, which can modify the output signals of the given model to improve the direct current (DC) characteristic and adjust the input signals of the given model to improve the small signals characteristic by the mapping of neural networks. The novel Neuro-SM formulations and structure for DC and small-signal simulation are proposed to obtain the mapping network automatically. The simulation results demonstrate that the accuracy of the Neuro-SM model using the proposed method is higher than the existing model and the training process is methodical.

Keywords Neuro-SM · Neural networks · Training method · Modeling

1 Introduction

Neuro-space mapping (Neuro-SM), combining artificial neural networks (ANNs) [1, 2] with space mapping (SM) [3], uses a novel formulation of space mapping with a neural network to automatically modify the voltage or current signals of the existing device model until the simulation results can match the device data accurately. The technology not only has the capability of learning the physical behavior of devices from component data, but also can employ mathematical link between fast yet approximate models and accurate yet expensive models to achieve

S. Yan (✉)
School of Electronics and Information Engineering,
Tianjin Polytechnic University, Tianjin 300387, China
e-mail: tjuysx@163.com

S. Yan · L. Zhang · Z. Feng · P. Xu
National Key Laboratory of ASIC,
Hebei Semiconductor Research Institute, Shijiazhuang 050051, China

J. Jin · Q. Zhang
School of Electronic Information Engineering, Tianjin University, Tianjin 300072, China

Q. Liang et al. (eds.), *Proceedings of the 2015 International Conference on Communications, Signal Processing, and Systems*, Lecture Notes in Electrical Engineering 386, DOI 10.1007/978-3-662-49831-6_106

circuit design fast and accurately [4]. It is an advance over several previous ANN-based methods for device modeling. Neuro-SM method has been used in metal–semiconductor–field-effect transistor (MESFET) modeling [5], heterojunction bipolar transistor (HBT) modeling [6], high-electron mobility transistor (HEMT) modeling [4], etc.

An analytical Neuro-SM model was proposed for the first time in [4], where analytical equations are derived so that mapping neural networks in the model can be trained more efficiently. The models built by the method mentioned in [4] are formulated by only mapping the voltage relationship in the existing model. Because the voltage signals are input signals, the mapping neural network was called input mapping. However, when the existing model is too coarse, or when the modeling requirement is too stringent, such simple input mapping may be insufficient to achieve the desired accuracy. The work in [7] considers employing the output mapping in addition to the input mapping to adjust the current signals; this is made possible by utilizing new mapping mechanisms for the voltage and current at gate and drain to modify the voltage and current signals in the existing model. But the accuracy of the model was affected by all the internal synaptic weights of the mapping neural networks, which increases the training difficulty.

This paper presents an advance of Neuro-SM over previously published Neuro-SM. The proposed technique uses the output mapping to match the direct current (DC) characteristic of fine model, and the input mapping to match the small signals characteristic of fine model. The proposed model can be trained by the fine DC data and the fine S-parameter data separately, which can greatly simplify the training process. In addition, analytical relationship between typical types of transistor data and the corresponding mapping neural networks will be derived. Examples of InP PHEMT modeling demonstrate that the proposed Neuro-SM can obtain more accurate model with less neurons.

2 Proposed Neuro-SM Method for Nonlinear Device Modeling

Coarse model and fine model: Suppose that the existing models give only rough approximation of the device data, but cannot accurately match the actual device data. Let the existing nonlinear device model be called the coarse model. The fine model is only a fictitious model implied by actual device data from measurement or detailed device simulator. The differences between the coarse model and the device data cannot be ignored even after the parameters in the coarse model are optimized as much as possible. Let the terminal voltage and current signals of the coarse model be defined as $\boldsymbol{v_c} = [v_{gc}, v_{dc}]^T$ and $\boldsymbol{i_c} = [i_{gc}, i_{dc}]^T$, respectively. Let the terminal voltage and current of the fine model be defined as $\boldsymbol{v}_f = [v_{gf}, v_{df}]^T$ and $\boldsymbol{i}_f = [i_{gf}, i_{df}]^T$, respectively.

The efficiency of Neuro-SM model depends on both the suitability of the mapping structure and the quality of the coarse model [7]. There are two main structures of Neuro-SM for nonlinear device modeling. One is formulated to exceed the present capabilities of device models built by existing equivalent circuits by mapping the gate and drain voltage relationship in the coarse model through two voltage-controlled voltage sources, such as the traditional Neuro-SM method. The other one is formulated to overcome the accuracy limit of the previous Neuro-SM methods by adding the input and output mapping networks in the coarse model, such as the modified Neuro-SM method. However, the two types of Neuro-SM models were trained with all fine data including DC data, S-parameter data, and HB data which lead to different characteristics of the Neuro-SM model affecting each other and make the structure of the mapping network complicated. Here, we propose an enhanced Neuro-SM method to get an accurate model with simple training by separating the input mapping network and output mapping network.

2.1 Analytical DC Mapping

The proposed method uses output mapping to change the DC feature of the Neuro-SM model. Figure 1 shows the proposed Neuro-SM DC model for two-port transistor. The interpretation of the operations of the proposed Neuro-SM DC model is as follows: First of all, voltage signals at the external terminals of the gate and drain $v_{gf.dc}$ and $v_{df.dc}$ are fed into the gate and drain of the coarse model. Then, the current signals at the gate and drain of the coarse model are evaluated by the coarse model computation (defined as $i_{gc.dc}$ and $i_{dc.dc}$). At the end, the current signals at the gate and drain of the coarse model $i_{gc.dc}$ and $i_{dc.dc}$ as well as the voltage signals of the fine model $v_{gf.dc}$ and $v_{df.dc}$ are mapped onto the external current signals of the fine model $i_{gf.dc}$ and $i_{df.dc}$ by mapping neural networks.

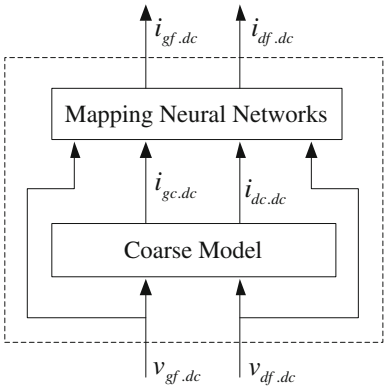

Fig. 1 Two-port representation of the proposed Neuro-SM DC model where mapping neural networks are used to provide gate and drain current mapping between the coarse model and the fine model

In the proposed model, the new and separated output mappings are added to modify the current relationship between the coarse model and the fine model. Only DC signals were fed into the current mapping networks, so the mapping will not affect the small-signal characteristics of the Neuro-SM model. Voltage signals $v_{gf.dc}$ and $v_{df.dc}$ are added as additional inputs to the current mapping neural networks by utilizing the prior-knowledge input concept. Current mapping is applied on the gate and drain voltages of the fine model and gate and drain currents of the coarse model through two controlled current sources. The mapping characteristic for DC output current $i_{gf.dc}$ and $i_{df.dc}$ at gate and drain of the fine model can be generally described in functional form, proposed as

$$i_{gf.dc} = f_{\mathrm{ANN1}}(v_{gf.dc}, v_{df.ac}, i_{gc.dc}, i_{dc.dc}, \boldsymbol{w}_1) \tag{1}$$

$$i_{df.dc} = f_{\mathrm{ANN2}}(v_{gf.dc}, v_{df.ac}, i_{gc.dc}, i_{dc.dc}, \boldsymbol{w}_2) \tag{2}$$

Where $i_{gf.dc}$ and $i_{df.dc}$ are the final values of the gate and drain currents at the external gate and drain terminals of the proposed Neuro-SM model, respectively. f_{ANN1} and f_{ANN2} denote current mapping neural networks for current signals at gate and drain, respectively. Vectors $\boldsymbol{w}_1$ and $\boldsymbol{w}_2$ contain all internal synaptic weights of the neural networks f_{ANN1} and f_{ANN21}, respectively. Normally, the mapping formula f_{ANN} was obtained by the multilayer perceptron (MLP).

2.2 Analytical Small-Signal Mapping

Input mapping networks were used to adjust the small-signal characteristics of the proposed Neuro-SM model. In the proposed method, *Y* matrix and *S* matrix were used to present the small-signal characteristics of the models. In this step, the coarse model and the output mapping neural networks make up the new coarse model. In the input mapping, the AC voltage signals of the device will not be applied directly to the coarse model. Instead, they are mapped into corresponding voltages in the coarse model. Voltage mapping can be realized by adding two voltage-controlled voltage sources to achieve mappings of $v_{gf.\mathrm{ac}}$ and $v_{df.\mathrm{ac}}$ onto $v_{gc.\mathrm{ac}}$ and $v_{dc.\mathrm{ac}}$, respectively.

$$v_{gc.\mathrm{ac}} = h_{\mathrm{ANN1}}(v_{gf.ac}, v_{df.ac}, \boldsymbol{w}_3) \tag{3}$$

$$v_{dc.\mathrm{ac}} = h_{\mathrm{ANN2}}(v_{gf.ac}, v_{df.ac}, \boldsymbol{w}_4) \tag{4}$$

where $v_{gc.\mathrm{ac}}$ and $v_{dc.\mathrm{ac}}$ are intermediate voltage values at gate and drain of the coarse model, respectively. h_{ANN1} and h_{ANN2} denote the neural networks that can represent the voltage mapping equations for the gate and drain voltage signals, respectively. $\boldsymbol{w}_3$ and $\boldsymbol{w}_4$ are vectors containing all internal synaptic weights of neural networks

h_{ANN1} and h_{ANN2}, respectively. Normally, the mapping formula h_{ANN} was obtained by the MLP.

In transistor modeling, with the proposed Neuro-SM method, Y matrices are used to represent the small signals. The analytical mapping combining the coarse matrices Y_c and the fine matrices Y_f is presented as

$$Y_f = Y_c \cdot \left[\begin{array}{cc} \frac{\partial v_{gc.ac}}{\partial v_{gf.ac}} & \frac{\partial v_{gc.ac}}{\partial v_{df.ac}} \\ \frac{\partial v_{dc.ac}}{\partial v_{gf.ac}} & \frac{\partial v_{dc.ac}}{\partial v_{df.ac}} \end{array} \right] \Big|_{v_{gf} = v_{gf.dc},\, v_{df} = v_{df.dc}} \tag{5}$$

where Y_c of the new coarse model is evaluated at the bias $v_{gf.dc}$ and $v_{df.dc}$. The relationship of Y parameter between fine model and coarse model is the derivative of neural network mapping [8].

Neuro-SM model will not be good unless all the four mapping neural networks are trained with the device data. The device data implies the device behavior of a fine model. Therefore, the four neural networks represent the mappings between the coarse model and the fine model. In order to get an accurate model with the proposed method, the output mapping neural networks, that is f_{ANN1} and f_{ANN2}, should be trained with the fine DC data first. Then, make the coarse model and the trained output mapping neural networks as the new coarse model, and train the input mapping networks h_{ANN1} and h_{ANN2} with the fine S-parameter data. After training, the proposed Neuro-SM model can be more accurate than the coarse model, and it can replace the fine device to be used in an original circuit for design and simulation.

3 Demonstration Examples

This example illustrates the proposed Neuro-SM method and its training process. The fine data is based on the on-wafer measurement results of InP HEMT. The Angelov model is used as the existing coarse model. We optimized the coarse model in Advanced Design System (ADS) first and built the Neuro-SM model in NeuroModelerplus. Even though the variables in the Angelov model are optimized as much as possible, the optimized coarse model cannot fit the fine data accurately. Then, output mapping neural networks and input mapping neural networks are added to the optimized coarse model constituting an accurate Neuro-SM model.

In this example, 3-layer MLP was used as the output and input mapping neural networks. Training was done using DC and S-parameter data separately. In order to make the DC characteristic of the proposed Neuro-SM model to match the device data, the output mapping networks were adjusted. Four hidden neurons are used and 22 variables are optimized. The training was stopped until the DC error between the proposed model and the fine model met the requirement. In order to make the small-signal characteristic of the proposed model to match the device data, the input mapping networks were adjusted. Ten hidden neurons are used and 52 variables are

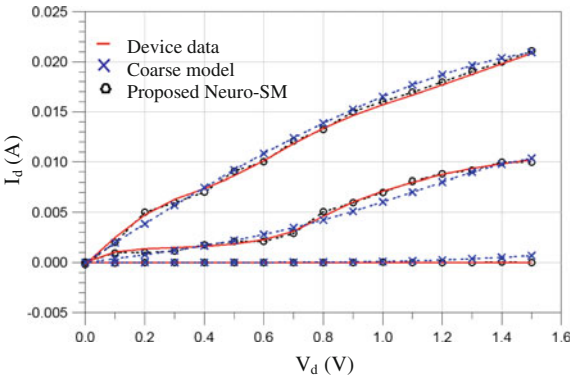

Fig. 2 I-V comparison of the InP HEMT models (the coarse model and the proposed Neuro-SM model)

optimized. The training was stopped until the S-parameter error between the proposed model and the fine model met the requirement. After training, the proposed Neuro-SM model and the coarse model were compared as shown in Figs. 2, 3, and 4.

Figure 2 shows the accurate model with the proposed Neuro-SM method to improve the coarse model which has been optimized with DC data in ADS. The DC feature of the coarse model can match with the fine model roughly, but the model built with the proposed Neuro-SM method can be mapped to the device data with better accuracy because the neural network training can automatically adjust the mappings according to the differences between the device data and the coarse model. Figures 3 and 4 show the comparison of the magnitude and phase of the transmission coefficients among the proposed Neuro-SM model, coarse model, and fine model, respectively. Both the magnitude and phase of the transmission coefficients of the proposed Neuro-SM model are more accurate than the coarse model. The result demonstrates that the proposed Neuro-SM approach improves the current capabilities of the existing model and matches the fine device data with higher accuracy.

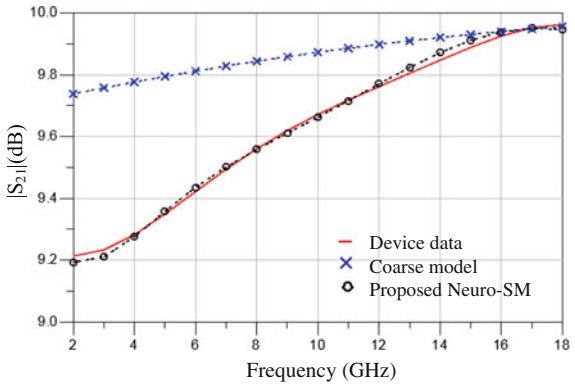

Fig. 3 Plot of the magnitude of the transmission coefficients for the InP HEMT models (the coarse model and the proposed Neuro-SM model)

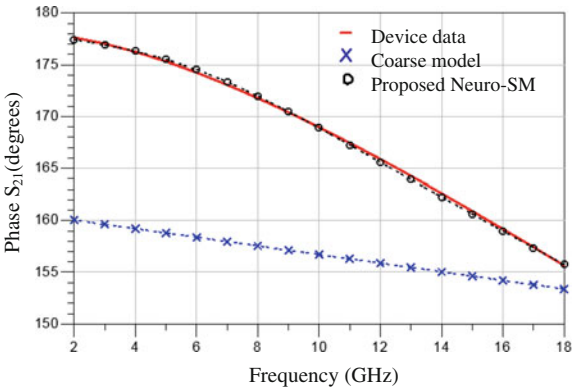

Fig. 4 Plot of the phase of transmission coefficients for the InP HEMT models (the coarse model and the proposed Neuro-SM model)

Table 1 Test error comparison of coarse model and Neuro-SM models for DC and S-parameter simulation

Model type	DC error (%)	$\|S_{21}\|$ error (%)	Phase S_{21} error (%)
Coarse model	2.36	2.98	6.99
Traditional Neuro-SM model	1.9	1.05	1.31
Modified Neuro-SM model	0.37	0.23	0.25
Proposed Neuro-SM model	0.28	0.14	0.12

In order to further demonstrate the advantage of the proposed Neuro-SM method, we also use the traditional Neuro-SM method and the modified Neuro-SM method to do modeling for this example. The comparison results of the simulations are shown in Table 1. The errors between the fine data and the modified and the proposed Neuro-SM model are much smaller than that between the coarse model and the traditional Neuro-SM model. Accurate models can be built by the modified Neuro-SM method with 30 hidden neurons and the proposed Neuro-SM method with 14 hidden neurons. The proposed Neuro-SM model has higher accuracy with simpler structure.

4 Conclusions

A proposed Neuro-SM method for nonlinear device modeling has been presented to reduce the difficulty of the new model. The model can minimize the difference between the existing model and the fine data by adjusting the neural network mapping. In this paper, novel Neuro-SM formulations have been presented in order to train the Neuro-SM model separately and effectively. The technique can improve the small signals characteristic of Neuro-SM model without changing the DC characteristic. After training, the proposed Neuro-SM model can replace the fine

data to work in design and simulation directly. The proposed method can make the training process more methodically.

References

1. Zhang QJ, Gupata KC (2000) Neural network for RF and microwave design. Artech House, Norwood, MA
2. Kabir H, Wang Y, Yu M, Zhang QJ (2010) High-dimensional neural-network technique and applications to microwave filter modeling. IEEE Trans Microw Theory Tech 58(1):145–156
3. Bandler J, Zhang QJ, Dakroury S, Mohamed A, Bakr M, Madsen K, Sondergaard J (2004) Space mapping: the state of the art. IEEE Trans Microw Theory Tech 52(1):337–361
4. Zhang L, Xu JJ, Yagoub MCE, Ding RT, Zhang QJ (2005) Efficient analytical formulation and sensitivity analysis of neuro-space mapping for nonlinear microwave device modeling. IEEE Trans Microw Theory Tech 53(9):752–2767
5. Zhang L, Xu JJ, Yagoub MCE, Ding RT, Zhang QJ (2003) Neuro-space mapping technique for nonlinear device modeling and large-signal simulation. In: IEEE MTT-S international microwave symposium. Philadelphia, USA, pp 173–176
6. Yan S, Cheng Q, Wu H, Zhang Q (2015) Neuro-space mapping for modeling heterojunction bipolar transistor. Trans Tianjin Univ 21(1):90–94
7. Zhu L, Ma YT, Zhang QJ et al (2012) An enhanced Neuro-space mapping method for nonlinear microwave device modeling. In: 2012 IEEE International Symposium on Circuits and Systems. Seoul, Korea, pp 2087–2090
8. Xu JJ, Yagoub MCE, Ding RT et al (2003) Exact adjoint sensitivity for neural based microwave modeling and design. IEEE Trans Microw Theory Tech 51(1):226–237

General Framework for Parameter Learning and Optimization in Stochastic Environments

Wen Jiang, Yan Yan, Hao Ge and Shenghong Li

Abstract The existing strategies on Stochastic Point Location (SPL) are adopted to search a point or parameter on a real line under stochastic environment, which have been demonstrated to be effective. However, one problem which still has not been addressed yet is how to learn a point in multidimensional space under stochastic environment. This problem will become more difficult when the environment itself is a deceptive one in which the probability (p) of the correct response emitted from the environment is $p < 0.5$. In this paper, a general framework is proposed to deal with all the above-mentioned problems. A key aspect of our method worth mentioning is that it can transform learning a point in space into one of searching d optimal points on d different super lines, where d is the dimension size. Finally, the excellent performance of our proposed algorithm has been proved by our rigorous mathematical proof and validated by a great number of experiments.

Keywords SPL problem · Parameter learning · Stochastic optimization · Learning automata

1 Introduction

The problem that an entity (a robot, algorithm, learning mechanism) guided with the information provided by environment attempts to locate a particular point or parameter is named as point location problem. Generally speaking, the point location

W. Jiang (✉) · Y. Yan · H. Ge · S. Li
Department of Electronic Engineering, Shanghai Jiao Tong University,
800 Dongchuan Road, Min Hang, Shanghai 200240, People's Republic of China
e-mail: wenjiang@sjtu.edu.cn

Y. Yan
e-mail: yevita94@hotmail.com

H. Ge
e-mail: sjtu_gehao@sjtu.edu.cn

S. Li
e-mail: shli@sjtu.edu.cn

Q. Liang et al. (eds.), *Proceedings of the 2015 International Conference on Communications, Signal Processing, and Systems*, Lecture Notes in Electrical Engineering 386, DOI 10.1007/978-3-662-49831-6_107

problem could be classified into two categories: deterministic point location (DPL) problem and stochastic point location (SPL) problem. In practical applications, if the entity (a robot, algorithm, learning mechanism) is guided by the environment with deterministic information or deterministic responses, then it will fall in the category of DPL problem [1], while if the environment might tell the entity (robot, algorithm or learning mechanism) to go to the wrong direction with the probability of $1 - p$ ($0 < p < 1$), then the point location problem will be called as SPL problem [1] which is the main focus of this paper.

All these algorithms in the existing literatures [2–6] are only concerned about how to locate an unknown parameter η^* on a real line (one dimensional space). For example, in literature [2], a discretized random search algorithm was proposed and proven to be e-optimal, which means that this scheme can converge to a point arbitrarily close to the true point with an arbitrarily high probability. However, one main drawback of this method is that the steps made by this random search learning algorithm are very conservative, which has been overcome by the Continuous Point Location with Adaptive Tertiary Search (CPL-ATS) strategy [3] and Continuous Point Location with Adaptive d-ARY search (CPL-AdS) strategy [4]. One key improvement of the CPL-AdS strategy [4] over the CPL-ATS strategy [3] is that the former could operate in the deceptive environment in which the probability (p) of the correct response emitted from the environment is $p < 0.5$. The scheme introduced in [5] is mainly concerned with how to solve stochastic point location problem in no-stationary meta-level environments, where a student receives information from a teacher. And it is interesting to note that the student performs better than the teacher. Recently, we proposed a generalized CPL-AdS methodology [6] which can overcome the bottleneck of [3, 4] by a decision formula and introduces a new paradigm to solve the stochastic dynamic point location problem. In addition, simulation results demonstrated that the method that we proposed in [6] is able to learn a key parameter, named as Contagion Parameter, which is the probability of a healthy person getting infected when he/she meets with an infected one in stochastic disease spreading model. And this paper further shows that even if this Contagion Parameter has changed because of virus variation, the algorithm [6] is still capable of tracking the changes.

The existing solutions to SPL problem have been found in applications [7–13]. Literature [7] shows that the solutions to the SPL problem have been applied to Goore Game. In [8], the authors built a new epidemic model and utilized the theory of the SPL problem to estimate the key fixed parameter, i.e., the contagion parameter, which is the probability of being infected when interacting with an infected person. Furthermore, though literatures [9–13] aim at solving resource allocation problems, it is worth of mentioning that these are actually SPL problem. Literature [11] tries to learn the parameters of the multinomial distribution via interacting with stochastic environment. In each time instant, the environment suggests increasing or decreasing the estimated parameter. Of course, these suggestions are not reliable, which means that the learning algorithm might be misled by environment. Furthermore, literatures [11–13] consider the stochastic nonlinear resource allocation problems which aim at finding the optimal resource allocation strategy based on the noisy or

incomplete information. Again, the environment is stochastic in nature; hence the stochastic nonlinear resource allocation problems are actually SPL problem.

However, as mentioned above, these solutions to the SPL problem are only focused on how to locate a particular point on a real-line or to learn one parameter, which greatly limits their applications.

The rest of this paper is organized as follows. In Sect. 2, we shall give the details of the proposed general framework employing the random search strategy [2], and then present the stochastic optimization algorithm originated from our proposed framework, which can deal with unimodal SPL problem. In Sect. 3, some experiments are conducted to verify the performance of the stochastic optimization algorithm. The last Section will conclude this paper.

2 Search Problems in Higher Dimensional Space

In the following, we shall focus on discussing how to solve the multi-dimensional SPL problem. As far as we know, this is the first paper that handles the multi-dimensional SPL problem. The main idea of our proposed algorithm is to convert the optimization problem into the one that searches the solutions on super lines and then reconstruct the optimization results with these solutions. We shall first introduce the scheme described in [2, 6], which will be embedded into our proposed framework, and then concentrate on discussing how to optimize unimodal function problems.

2.1 Review of Solutions to the SPL Problem

Before introducing the concepts of multi-dimensional SPL problem, we shall first review those existing solution schemes to the SPL problem, which will be adopted in our proposed framework.

First, let us turn to the discretized random search learning algorithm [2]. Assuming $\eta(n)$ to be denoted as the guess of the learning algorithm at the *nth* step, there are the following updating rules:

$$\begin{cases} \eta(n+1) = \eta(n) + 1/N; \textit{if } E \textit{ suggests increasing } \eta, 0 < \eta(n) < 1 \\ \eta(n+1) = \eta(n) - 1/N; \textit{if } E \textit{ suggests decreasing } \eta, 0 < \eta(n) < 1 \\ \eta(n+1) = \eta(n); \textit{Otherwise} \end{cases} \tag{1}$$

where E denotes Environment.

It has been proved that this scheme is $\varepsilon - optimal$. That is to say, this algorithm will eventually converge to a point arbitrarily close to the true point with an arbitrarily high probability, which is presented in the following Lemma.

Lemma 1 *Let the search interval [0, 1] be subdivided into* $(\mathrm{N}+1)$ *sub-intervals,* $[0, 1/\mathrm{N}]$, $[1/\mathrm{N}, 2/\mathrm{N}], \ldots, [(\mathrm{N}-1)/\mathrm{N}, 1]$, *and be the true search point. Assuming that there exists a* $\delta > 0$ *such that for each* $\varepsilon > 0$, *we have [2]:*

$$\lim_{N \to \infty} Pr[|\eta(\infty) - \eta^*| < \delta] > 1 - \varepsilon \tag{2}$$

where $\eta(\infty) = \lim_{n \to \infty} \eta(n)$

Please refer to literature [2] for the detailed proof.

As Eq. (2) indicates, once given the parameter N, the algorithm has to move along these discretized points, which implies that the step size has been predefined by the parameter N. This leads us to believe that the algorithm is very conservative.

The above discussions address one of the existing solutions [2–6] to one-dimensional SPL problem and their applications. However, in many real-world problems, we have to learn several parameters simultaneously. In the following subsection, a unified framework for resolving multidimensional SPL problem based on these solutions will be introduced in details.

2.2 The Proposed Framework for Multidimensional SPL Problem

From certain analyses, it can be found that our proposed scheme will be able to locate the unknown multidimensional point while sharing the similar properties to the employed one dimensional SPL problem strategy. In detail, the proposed framework can be summarized as follows.

Algorithm 1 Procedure of GDR framework

Input: the search region T, the number of parameters d and the contaminated function value.
Output: the global optimal point $\eta^* = \arg\max(F(x))$.
Begin:

1. Randomly select d unparallel super lines
2. **for** j = 1 : d **Par do**
   a. Use the above mentioned one dimensional SPL algorithms to get $\overline{PO_j}$ (the point which has the shortest distance to η^*);
   b. Based on each line and the $\overline{PO_j}$, the hyper plane can be easily arrived at.

   end for
3. Get $\hat{\eta}^* = (\hat{\eta}_1^*, \hat{\eta}_2^*, \ldots, \hat{\eta}_d^*)$;

end

In the following, we shall introduce this framework to address the above-mentioned optimization problem when the available information are only the function values corrupted by noises.

2.3 Experimental Simulations

Think about this circumstance where random noise occurring with the probability of $1 - \mathrm{p}$. For instance, when an aircraft crashes, its black-casket drops on the ground, and the black-casket emits weak Hertzian waves with certain frequency. And our goal is how to locate this black-casket. However, for certain reasons, i.e., due to bad weather, the waves that the black-casket emitted might be unstable and thus untraceable. In addition, the received signal is also probably mixed with random noise. As a matter of fact, this problem of searching the black-casket could be regarded as SPL problem in three dimensional spaces. Here, the original signal mentioned can be simulated by the following function

$$f(x_1, x_2, \ldots, x_d) = \sum_{i=1}^{d} (x_i - \eta_i^*)^2 \tag{3}$$

It is very straight forward to see that the minimization of this cost function will easily arrive at $x_i = \eta_i^*$, $i = \{1, 2, \ldots, d\}$. In addition, assuming that the noise follows uniform distribution, and that the only information available to us is the function values corrupted by random noise.

In order to specify the signal intensity, we introduce the signal-to-noise ratio, *SNR*, which is defined as follows:

$$SNR = 10\log_{10}\frac{|\text{Signal Power}|}{|\text{Noise Power}|} \tag{4}$$

Assuming that the searching region is $T = \{(x, \mathrm{y})|x \geq 0, y \geq 0, x \leq 1, y \leq 1\}$, and that the location of the black-box (unknown point) is $\eta^* = (0.422, 0.289)$. We calculated the values of $\hat{E}[\{\eta(n)\}]$ for different p's and noises where $p = 1 - p - Noise$. The variances for two cases are calculated and demonstrated in Figs. 1 and 2, respectively. For every case, it can be found that the results are remarkable. Figure 1 illustrates that when $p = 0.1$, the algorithm couldn't work very well. As Fig. 2 depicts, for all the cases, all the variances of $\hat{E}[\{\eta(n)\}]$ are less than 3.0×10^{-4} when $p \geq 0.6$. That is to say, the difference between $\hat{E}[\{\eta(n)\}]$ and η^* is too small to be ignored. Taking another example with $p = 0.7$ and $SNR = -6.39$ dB, it can be found that the asymptotic value, $\hat{E}[\{\eta(n)\}]$, is almost able to locate the unknown parameter in such stochastic environment.

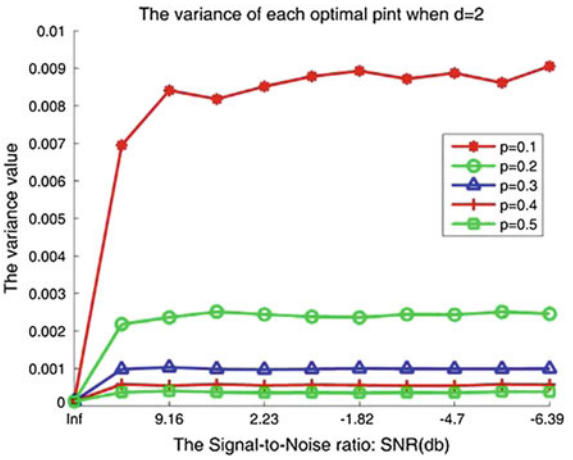

Fig. 1 The variances *cures* of the asymptotic values of $\hat{E}[\{\eta(n)\}]$ with p varying from 0.1 to 0.5, the step parameter $N = 500$, $d = 2$, and the SNR varying from ∞ to -6.39 dB. The results shown are the averaged values for 500 independent experiments

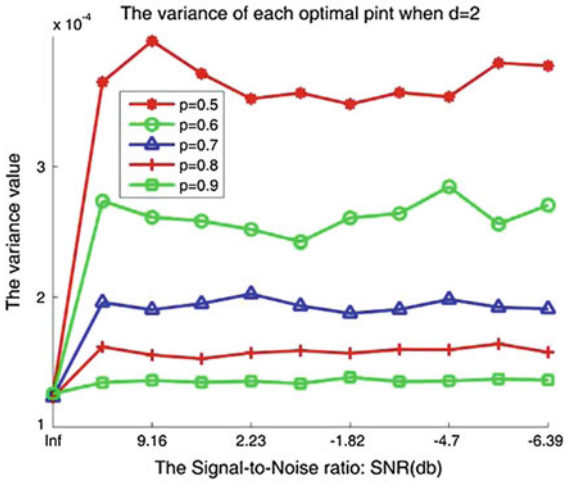

Fig. 2 The variances *cures* of the asymptotic values of $\hat{E}[\{\eta(n)\}]$ with p varying from 0.5 to 0.9, the step parameter $N = 500$, $d = 2$, and the SNR varying from ∞ to -6.39 dB. The results shown are the averaged values for 500 independent experiments

3 Conclusion

In this paper, we propose a framework that can address multi-dimensional SPL problem, and analyze its applications to unimodal optimization problem with unknown cost function. First of all, to the best of our knowledge, this is the first paper that reports the solutions to the multidimensional Stochastic Point Location problems. It is proved that under certain assumptions, the proposed framework will be able to converge to the unknown point. Second, this is also the first paper that deals with the optimization problem with the function values contaminated by stochastic noises from the viewpoint of SPL. We set d different unparallel straight lines to drill through the convex searching space, where for each line the efficient search space was defined and used as the constraints so as to guarantee that the optimal

point η^*could be located. Then each line will be able to get an optimal result. By using Eq. (15), we can finally reach the unknown point η^*.

Next, it should be pointed out that even if the probability of the occurrence of unbiased noise is above 0.5, the proposed framework will still be able to work with a good performance. A set of experiments have been conducted to validate the performance of our proposed framework. It is acknowledged that as the SNR decreases, the original signal is more difficult to detect. Nevertheless, it was found that although in these experiments, the unknown point η^* is still able to be located. In the first set of experiments, it was observed that even when p is as small as 0.2, where the noise intensity has reached two times of the original signal; the unknown parameter can still be found. These results are really very impressive and exciting.

References

1. Baeza-Yates RA, Culberson JC, Rawlins GJE (1998) Searching with uncertainty. In: Proceedings of scandinavian workshop algorithms and theory (SWAT). Halmstad, Sweden, pp 176–189
2. Oommen BJ, Raghunath G (1998) Automata learning and intelligent tertiary searching for stochastic point location. IEEE Trans Syst Man Cybern B Cybern 28(6):947–954
3. Oommen BJ (1997) Stochastic searching on the line and its applications to parameter learning in nonlinear optimization. IEEE Trans Syst Man Cybern B Cybern 27(4):733–739
4. Oommen BJ, Raghunath G, Kuipers B (2006) Parameter learning from stochastic teachers and stochastic compulsive liars. IEEE Trans Syst Man Cybern B Cybern 36(4):820–836
5. Oommen BJ, Kim S-W, Samuel M, Granmo, OC (2008) A solution to the stochastic point location problem in metaleval nonstaionary evironments. IEEE Trans Syst Man Cybern B Cybern 38(2):820–836
6. Huang DS, Jiang W A General CPL-AdS methodology for searching dynamic parameter in dual environments. IEEE Trans Syst Man Cybern B Cybern. (In Press)
7. Oommen BJ, Granmo OC, Pedersen A (2007) Using stochastic AI techniques to achieve unbounded resolution in finite player goore games and its applications. In: Proceedings of IEEE-CIG07. Hawaii, pp 161–167
8. Oommen BJ, Cali-toiu D (2008) Modeling simulating a disease outbreak by learning a contagion parameter-based model. In: Proceedings of spring simulation multi-conference, Ottawa, Canada, 14–17 Apr 2008
9. Oommen BJ, Rueda L (2006) Stochastic learning-based weak estimation of multinomial random variables and its applications to pattern recognition in non-stationary environments. Pattern Recogn 39:328–341
10. Yazidi A, Granmo OC, Oommen BJ (2012) A novel stochastic discretized weak estimator operating in non-stationary environments. In: Proceedings of ICNC 2012, the 2012 international conference on computing, networking and communications. Hawaii, USA
11. Granmo OC, Oommen BJ, Myrer SA, Olsen MG (2007) Learning automata-based solutions to the nonlinear fractional knapsack problem with applications to optimal resource allocation. IEEE Trans Syst Man Cybern B Cybern 37(1):166–175
12. Granmo OC, Oommen BJ (2008) A hierarchy of twofold resource allocation automata supporting optimal web polling. In: Proceedings of 21st international conference industrial and engineering applications of artificial intelligence and expert systems (IEA/AIE 08). pp 347–358
13. Granmo OC, Oommen BJ (2010) Solving stochastic nonlinear resource allocation problems using a hierarchy of twofold resource allocation automata. IEEE Trans Comput 59(4):545–560